14th SGA Biennial Meeting

Quebec City, Canada

August 20-23, 2017

MINERAL RESOURCES TO DISCOVER

Proceedings

Volume 4



14th SGA Biennial Meeting

August 20-23 2017

Québec City, Canada

Mineral Resources to Discover

Proceedings

Volume 4

Legal Deposit – Bibliothèque et Archives nationales du Québec
ISBN: 978-2-9816898-0-1
© Society for Geology Applied to Mineral Deposits, 2017

The 14th SGA Biennial Meeting is jointly organized by the Université Laval, Natural Ressources Canada (Geological Survey of Canada), the Ministère de l'Énergie et des Ressources naturelles du Québec, and the Institut national de la Recherche scientifique, Centre Eau Terre Environnement.

The theme for this 14th edition is "**Mineral Resources to Discover**".

Suggested citation for the entire volume:
Proceedings of the 14th SGA Biennial Meeting, 20-23 August 2017, Québec City, Canada, 1628 pages.

Suggested citation for an individual paper:
Hannington M, Petersen S, Monecke T, Mercier-Langevin P (2017) Divining gold in VMS systems: news from the seafloor. Proceeding of the 14th SGA Biennial Meeting, 20-23 August 2017, Québec City, Canada: pages 43-46

This publication cannot be reproduced in whole or in part without the permission of The Society for Geology Applied to Mineral Deposits (SGA).

A digital version of theses volumes is available from the SGA website at www.e-sga.org

Set of 4 volumes
Layout: Patrick Mercier-Langevin GSC
Claude Dion, André Tremblay MERN

Cover photograph: Kerr-Addisson mine "Glory Hole", green carbonate ore resulting from the fuchsite alteration of ultramafic rocks along the Larder Lake-Cadillac Fault Zone. Larder Lake, Ontario, Canada. (Photo: P. Mercier-Langevin, GSC).

SPONSORS

Diamond

AREVA

OSISKO GOLD ROYALTIES

Gold

ABITIBI GEOPHYSICS

AngloAmerican

GOLDCORP

InnovExplo
LA NOUVELLE RÉALITÉ MINIÈRE

INTEGRA GOLD CORP

ZEISS

COREM

Mira Geoscience
...modelling the earth

BARRICK

RESSOURCES 21

QUÉBEC MINES

ios services GÉOSCIENTIFIQUES inc.

Silver

NEW BOLIDEN

KNOWLEDGESCAPE
ADAPTIVE OPTIMIZATION AND EXPERT CONTROL

SGS

SOQUEM

newgold

Copper

Fonds de recherche Nature et technologies Québec

srk consulting

stornoway

ORGANIZERS

INRS
UNIVERSITÉ DE RECHERCHE
A RESEARCH UNIVERSITY

Canada

IVEX DIVERSIFICATION DE L'EXPLORATION MINÉRALE AU QUÉBEC

UNIVERSITÉ LAVAL

Québec

QUÉBEC VOTRE VILLE
DESTINATION AFFAIRES

TABLE OF CONTENT
Volume 4

SY04 – Critical and precious metal deposits: theory, experiment and nature – a symposium to recognize the work of A.E. Williams-Jones 1255

Couple Dissolution Precipitation (CDP) processes applied to rare-metal ore systems 1257
Kontak, D.J.

The roles of magma and fluid in concentrating HFSE/REE at Strange Lake, Québec 1261
Vasyukova, O.V. and Williams-Jones, A.E.

The late Archean Au epoch: By - product of Earth degassing triggered by electrical instabilities on the core-mantle boundary? 1265
Walshe, J.L. and Bath, A.B.

The nature and origin of REE mineralization in the Ashram Deposit, Eldor carbonatite complex, Quebec 1269
Beland, C.M.J. and Williams-Jones, A.E.

A mesothermal greisen-hosted Sn-Zn-Cu-Ag-In deposit at East Kemptville, Nova Scotia, Canada 1273
Bickerton, L., Kontak, D.J., Samson, I.M. and Murphy, J.B.

Semi-metal and base metal mobility in the metasedimentary contact aureole surrounding the Dublin Gulch reduced intrusion-related gold system (RIRGS), Yukon, Canada 1277
Cave, B.J., Barnes, S.-J., Sack, P.J., Pitcairn, I.K., Johnson, S.C. and Kuikka, H.

The role of pegmatites and acidic fluids for hydrothermal Zr and REE transport in the Strange Lake peralkaline granitic pluton 1281
Gysi, A.P.

Geochemical signature of rare-metal magmatic fluids exsolved from the Beauvoir granite (Massif Central, France) revealed by LA-ICPMS analysis of primary fluid inclusions 1285
Harlaux, M., Mercadier, J., Marignac, C., Cuney, M., Bonzi, W. and Kremer, V.

The Weijia scheelite magnesian skarn in the Nanling Range, South China: a special case related to high fluorine activity 1289
Huang, X., Lu, J., Sizaret, S., Barbanson, L., Chauvet, A., Wang, R., Ma, D., Li, X., Zhao, X., Chen, G. and Zhang, Q.

Numerical simulations of the transport of metals in vapour-like fluids applied to porphyry ore formation 1293
Hurtig, N.C. and Williams-Jones, A.E.

Linking channel-flow processes to pegmatite potentially mineralized in REE in the central Grenville Province 1297
Jannin, S., Gervais, F., Moukhsil, A., Crowley, J.L., Augland, L.E., Turlin, F., André-Mayer, A.-S. and Vanderhaeghe, O.

An early magmatic fluid pulse at Cononish orogenic gold deposit? Tellurium enrichment and implications for orogenic gold formation 1301
Jenkin, G.R.T., Spence-Jones, C., Boyce, A.J., Hill, N.J. and Sangster, C.J.S.

Two stages of skarn formation in the Hämmerlein tin-skarn deposit, western Erzgebirge, Germany 1305
Lefebvre, M.G., Romer, R.L., Glodny, J. and Roscher, M.

Texture and composition of pyrite and arsenopyrite in the Stibnite Au-Sb-W district, central Idaho, USA 1309
Marsh, E.E., Hofstra, A.H., Adams, D.T., Lowers, H.A. and Bennett, M.M

The physical and chemical evolution of fluids in rare-element (Be, Li, Nb-Ta) pegmatites associated with the Lacorne pluton, Québec, Canada 1313
Mulja, T. and Williams-Jones, A.E.

Hydrothermal record of Fe-Ti oxides breakdown: insights into understanding Sb mineralisation 1317
Pochon, A., Boulvais, P., Gapais, D., Beaudoin, G., Gloaguen, E. and Branquet, Y.

Discovery of REE minerals hosted in karst bauxite ores from the Sierra de Bahoruco, Pedernales, Dominican Republic 1321
Proenza. J.A., Aiglsperger, T., Villanova-de-Benavent, C., Torró, L., Rodríguez -García, D., Ramírez, A. and Rodríguez, J.

Why are IOCG deposits iron-oxide-rich? Insights from the Prominent Hill hematite breccia deposit, Gawler Craton 1325
Schlegel, T.U., Heinrich, C.A., Wagner, T. and Boyce, A.

Geochemistry and mineralogy of the Dotson Zone HREE deposit in the Bokan Mountain peralkaline igneous complex, southeastern Alaska, USA 1329
Taylor, C.D., Lowers, H.A., Adams, D.T. and Robinson, R.J.

The Parautochthonous Belt as a source of Grenvillian LREE-rich pegmatitic granite dykes 1333
Turlin, F., André-Mayer, A.-S, Crépon, A., Caumon, M.-C., Vanderhaeghe, O., Gervais, F., Jannin, S., Zeh, A., Deloule, É., Moukhsil, A. and Solgadi, F.

Genesis of the Bianjiadayuan Ag-Pb-Zn deposit, NE China: Mineralogical, textural, sulfur and lead isotope studies 1337
Zhai, D., Liu, J. and Cook, N.J.

Reduction of arsenite and sulfate by elemental copper, nickel and cobalt: implications to the formation of arsenide minerals in low temperature hydrothermal deposits 1341
Allin, N.C. and Gammons, C.H.

Granite-related ore deposits in the NW Amazonian Craton, Colombia 1345
Bonilla Pérez, A., Franco Victoria, J.A., Cramer, T. and Amaya Perea, Z.

Hydrothermal monazite and xenotime related to granites associated with the North Zone Mount Pleasant Sn-Zn-Cu-In (& W) deposits, NB, Canada: preliminary studies 1349
Charnley, B., Lentz, D.R. and McFarlane, C.R.M.

Spatial relations between gold, associated metals and lithologies at the Miwah acid-sulfate (high sulfidation) epithermal deposit, Aceh, North Sumatra, Indonesia 1353
Heriawan, M.N. and Mulja, T.

The Otanmäki rare metal (Nb, Zr, REE) mineralization, central Finland 1357
Kärenlampi, K., Paulick, H., Hanski, E., Pohjolainen, E., Kontinen, A., Huhma, H. and Jylänki, J.

Paragenetic constraints on hydrothermal origin of xenotime mineralization in the Maw Zone REE deposit, Athabasca Basin, Canada 1361
Rabiei, M., Chi, G. and Normand, C.

EU Critical Raw Materials in the Czech Republic – Cínovec (Zinnwald) ore district 1365
Rembousek, P., Vymazalová, A., Poňavič, M. and Pašava, J.

Sm-Nd isotopic signatures of the St-Honoré, Crevier, and Shortt Lake REE deposits in Québec (Canada) 1367
Sappin, A.-A, Beaudoin, G., Stevenson, R. and Constantin, M.

HFSE evolution of the Eldor Carbonatite 1371
Schmidt, P.T., Samson, I.M., Williams-Jones, A.E. and Smith, D.L.

Halite at the Saint-Honoré carbonatite: an insight into a magmatohydrothermal process 1375
Tremblay, J., Bédard, L.P. and Matton, G.

Indium mineralization in the East Kemptville Sn-Cu-Zn-Ag-In deposit, Nova Scotia 1379
Willson, J., Samson, I.M. and Kontak, D.J.

Fluid Inclusion, H-O, S, Pb and noble gas isotope studies of the Aerhada Pb-Zn-Ag Deposit, Inner Mongolia, NE China 1383
Zhang, H., Zhai, D. and Liu, J.

Petrographic and mineral chemical characteristics of the Jianfengling granite stock in the Nanling Range, South China: Insights to the evolutionary process of the highly evolved Li-F granitic magma 1387
Zhao, X., Lu, J. and Wang, R.

S10 – GSC@175: How can government promote exploration success? 1391

Geoscience Australia's contribution to Australian mineral exploration 1393
Huston, D.L. and Blewett, R.S.

Promoting mineral exploration in Sweden from the perspective of the government 1397
Ingvald, E. and Lax, K.

The role of the U.S. Geological Survey Mineral Resources Program in aiding mineral exploration 1399
Kelley, K.D., Anderson, E., McCafferty, A., Hitzman, M.W., Meinert, L., Goldfarb, R.J. and Leach, D.L.

Supporting innovation for sustainable mineral development in Canada: 175 years of public geoscience 1403
Kirkwood, D., Villeneuve, M. and Mercier-Langevin, P.

Long-term investment in geoscience has made Finland a top-ranking exploration target 1407
Nurmi, P.A., Eilu, P., Nykänen, V. and Vuollo, J.

The Geological Survey of Argentina (SEGEMAR) and its support to the Argentinian mineral industry 1411
Rios Gómez, J. and Zappettini, E.

Promoting and assisting mineral exploration: Québec's approach 1415
Roy, P., Dubé-Loubert, H., Goutier, J., Guemache, M., Labbé, J.-Y., Roy, C. and Giguère, R.

Precompetitive geoscience for mineral exploration –
the Western Australian Government's Exploration Incentive Scheme 1419
Tyler, I.M. and Ellis, M.J.

Living on the edge of the Cambrian Australian proto-continent:
potential for subduction-related mineral systems in the Stavely Arc, western Victoria, Australia 1423
Duncan, R., Cayley, R., Taylor, D., Skladzien, P., Cairns, C., McLean, M., Haydon, S., Middleton, M., Weatherman, M., Schofield, A., Lewis, C., McAlpine, S., Huston, D., Bastrakov, E., Goodwin, J., Thomas, M., Neumann, N. and Barton, T.

Finnish historical and current Ni-Cu-PGE deposits highlight country-wide exploration potential 1427
Konnunaho, J., Makkonen, H.V., Halkoaho, T., Rasilainen, K. and Eilu, P.

S11 – Resources development and perception/acceptability: The role of geosciences 1431

Social geology applied to mineral deposits (keynote) 1433
Jébrak, M.

Comparing social risk for mining projects located in different jurisdictions 1437
Bergeron, K.M., Jébrak, M. and Krolik, C.

Social acceptability of mining project in Québec: Evidence from stated preference method 1441
Corneille, A. and He, J.

Perception regarding mineral resources development and
social acceptability in the province of Québec, Canada 1445
Malo, F., Bédard, K., Malo, M., Rivard, C. and Lavoie, R.

Nickel mining potential for evaluating land-use pressure in the Sodankylä region, Finnish Lapland 1449
Markovaara-Koivisto, M., Kiniven, M. and Eilu, P.

Long-term pollution and impacts on local communities from defunct gold tailings deposits:
a case study of Davidsonville, South Africa 1453
Nwaila, P.C., Nwaila, G.T. and Broadhurst, J.L.

Trace metal transfer in the environment: a key issue for the acceptability of mining projects 1457
Rossi, M., Camizuli, E. and Gasquet, D.

S12 – Gem research: Beautiful windows into Earth's interior 1461

Origin of scapolite-hosted sapphire near Kimmirut, Baffin Island, Nunavut, Canada 1463
Belley, P.M., Dzikowski, T.J., Fagan, A., Cempírek, J., Groat, L.A., Mortensen, J.K., Fayek, M., Giuliani, G. and Fallick, A.E.

Sapphire corundum anomalies with different gold anomalies in heavy mineral fractions of
stream sediments on CLY gold + bismuth telluride prospect, British Columbia, Canada 1467
Howard, W.R.

Genesis of emerald at Lened, NWT 1471
Lake, D.J., Groat, L.A., Falck, H., Cempírek, J., Kontak, D., Marshall, D. and Mulja, T.

The impurities, defects, inclusions and gemological characteristics of diamonds
from the M.V. Lomonosov deposit 1475
Posukhova, T.V., Kriulina, G.Y., Garanin, V.K. and Shaimardanova, A.

GS01 – General session 1479

Geochemical survey for rare earth elements in the Hongcheon area, Korea 1481
Ahn, J.S., Youm, S.-J. and Cho, Y.-C.

The Northern Manitoba Mining Academy: providing resource-related trades training and support for research 1485
Alexandre, P.

Tetrahedrite-freibergite from Ag-Pb-Zn Prognoz deposit (Russia, Sakha-Yakutia): Implication for ore genesis 1487
Anikina, E. and Bortnikov, N.S.

The spatial variation of mineralogy in the vanadiferous magnetite deposit of the Lac Doré Complex (Chibougamau, Québec) and its implications on the chemical purity of magnetite concentrates 1491
Arguin, J.-P., Pagé, P., Girard, R. and Barnes, S.-J.

Estimate of alteration zones and type of deposit by multispectral satellite image interpretation and correlation with geology and geochemistry in the SW Loja-Ecuador Province 1495
Caiza Cañar, E.K.

Heavy minerals related to nepheline syenites in the Guaviare Department, southeastern Colombia 1499
Campos Rodríguez, H.R.C., Franco Victoria, J.A., García Romero, D.F., Cramer, T., Bonilla Pérez, A. and Amaya Perea, Z.

Measurements of gold in ores by laser-induced breakdown spectroscopy (LIBS) 1503
Castello, M., Constantin, M., Laflamme, M., Rifai, K. and Kamwa, B.N.

Replacement processes of the early-stage sulphides in the Kupferschiefer series of SW Poland 1507
Chmielewski, A. and Oszczepalski, S.

Mineral exploration guidelines for the Ba-Sr ore deposits of the Neuquén Basin, West Argentina 1511
De Barrio, R.E.

The potential of phosphate and associated critical raw materials in Europe 1515
Decrée, S., Ihlen, P.M., Schiellerup, H., Hallberg, A., Demetriades, A., Raha, M. and Soesoo, A.

Mineralizing events in the Vosges massif: insights from the Mn-W Haut-Poirot deposit (NE France) 1519
Dekoninck, A., Rochez, G., Yans, J. and Fluck, P.

Geochronology and mineralogical evolution of the Koudiat-El-Hamra silver ore veins deposits (Central Jebilet, Morocco) 1523
El Arbaoui, A., Wafik, A., Essaifi, A. and Jarni, A.

Geology and genesis of El-Dob tungsten ore deposit (North Eastern Desert, Egypt): Insights from fieldwork, petrography and remote sensing 1527
El Desouky, H., Dawoud, M. and Salah, M.

The Filon 7/5 (Bou Azzer district, Morocco): an example of Co-Ni ores formation under disequilibrium conditions 1531
Fanlo, I., Arranz, E., Subías, I. and Gervilla, F.

Volcanic stratigraphy and mineralisation of the Archean Colomb-Chaboullié greenstone belt, James Bay, Québec, Canada 1535
Galloway, S., Ross, P.-S., Bandyayera, D. and Daoudene, Y.

First record of garnierite in serpentinites from the Eastern Desert of Egypt: a witness to Ni-laterization in the Arabian Nubian Shield 1539
Hamdy, M.M., Abdel Wahed, M.A., El Dien, H.G. and Morishita, T.

What's inside the Temagami geophysical anomaly, Sudbury district, Ontario? 1543
Kawohl, A., Frimmel, H.E., Bite, A. and Whymark, W.

The association between granitoids and skarn mineralisation in the Taebaeksan mineralized province, South Korea 1547
Kim, G.-B., Choi, S-G., Choi, E.J., Kim, C.S. and Kang, J.G.

Impacts of the ore mining and processing on the environment in the Berg Aukas area, Namibia 1551
Kříbek, B., Majer, V., Pašava, J., Knésl, I., Kamona, F., Mapani, B. and Sracek, O.

Greisenisation and permeability changes in granitic intrusions related to Sn-W deposits: Case of Panasqueira 1555
Launay, G., Sizaret, S., Guillou-Frottier, L., Gloaguen, É., Melleton, J., Pichavant, M., Champallier, R., Pinto, F. and Ferraz, P.

Petrogenesis and tectonic implications of the Triassic granitoid plutons in west Qinling Mountains, China: insights from LA-ICP-MS zircon U-Pb ages, and Lu-Hf isotope of the Zhongchuan pluton 1559
Liu, J., Yang, S., Zhai, D., Wang, J., Wang, Y., Liu, Z., Zhang, F and Yuan, F.

Trace elements in sphalerite from the Stan Terg Pb-Zn deposit, Kosovo 1563
Mederski, S., Kołodziejczyk, J. and Pršek, J.

Rare earth elements in the Marinkas Quellen carbonatite, southwestern Namibia 1567
Ogungbuyi, I., Janney, P. and Harris, C.

New data on the origin of the Fe-Cu-As skarn deposit at Obrí důl, West Sudetes, Bohemian Massif 1571
Pašava, J., Veselovský, F., Dobeš, P., Erban, V., Pour, O., Žák, K., Ackerman, L., Haluzová, E., Creaser, R. and Tásler, R.

New insights into hydrothermal Zn-Cu mineralization in the West Troms Basement Complex, northern Norway 1575
Paulsen, H.-K, Palinkas, S.S. and Bergh, S.G.

Mn deposits in karstic and pseudo-karstic landforms at the Iberian Range (Teruel, NE Spain) 1579
Subias, I., Fanlo, I., López Pomar, A.E. and Ares G.

Mineral survey and characterization of talc indices of Bodi, north of Boumnyebel, Cameroon 1583
Tangko, E. and Nkoumbou, C.

Graphite veins mineralization in the Beni Bousera Massif (Internal Rif, Morocco) 1587
Wafik, A., Hajjar, Z., Gervilla, F. and Bendaouad, R.

Mineralization in the serpentinites from the Kizhnica area, Kosovo 1591
Werner, K.

The 234U/238U isotopic ratio as a vector to kimberlite pipes: the example the Arkhangelsk diamondiferous province, Russia 1595
Yakovlev, E. and Druzhinin, S.

Genesis of the mottramite-bearing Jbel Haouanit Cu-Pb-Zn-V supergene ore deposit (Eastern High Atlas, Morocco) 1599
Yans, J., Verhaert, M., Dekoninck, A., Bernard, A., Gautheron, C. and Saddiqi, O.

Zircon U-Pb dating and Sr-Nd-Pb-Hf isotopes of the ore-associated granite porphyry at the Longgen Pb-Zn deposit, Tibet 1603
Zhang, Y.-C., Zheng, Y.-Y and Gao, S.-B.

SY04 – Critical and precious metal deposits: theory, experiment and nature – a symposium to recognize the work of A.E. Williams-Jones

Convenors:

Iain Samson

Robert Linnen

Stefano Salvi

Sponsored by:



Keynote presentation

Couple Dissolution Precipitation (CDP) processes applied to rare-metal ore systems

Daniel J. Kontak
Laurentian University, Ontario, Canada

Abstract. Rare-metal (RM) mineralization (e.g., REE, Ta, Nb, Y, Sn) in felsic host rocks frequently coincides with zones of metasomatism, which suggests secondary processes are an integral and important part of the mineralizing process. Several case studies from granite and pegmatite settings are presented as further evidence of this process. In addition, it is suggested that the process of coupled dissolution-precipitation (CDP) creates the porosity and permeability necessary for this process to advance. The latter also involves the reacting-out of RM- or high field strength elements-bearing phases, which release elements for upgrading in these systems, which is an important economic factor.

1 Introduction

Alteration is an important aspect of many ore systems and an integral part of ore deposit models; the presence of well-defined alteration zones in VMS and porphyry deposits are classic examples. Formation of alteration reflects the sequential equilibration of host rocks and fluids, but more specifically with pre-existing minerals. Studies of zoned alteration profiles in a variety of ore settings include orogenic gold (Gammons and Williams-Jones 1988), tin greisens (Halter et al. 1996), and rare-metal (RM) pegmatites (Gysi and Williams-Jones 2013); these studies document well such reactions of rock and fluids. In zoned alteration profiles, discrete reactions occur that define mineral assemblage interfaces (e.g., muscovite = topaz + quartz in greisens). The mass transfer of components in such reactions can be an important part of ore systems, as mass loss generates porosity and permeability. The latter is important, as it enhances continued ingress of new, unreacted fluid and removal of components. This process is an important part of ore systems for several reasons: 1) alteration of primary phases can liberate ore elements - examples being liberation of HFSE in amphibole in RM granites and invisible gold in pyrite within oxide caps of epithermal settings; and 2) filling porosity by later ore phases, such as tin- and base metal phases in granite-hosted greisen systems. In some cases it is the ingress of an external fluid unrelated to the primary ore system that is important, as was well documented by Salvi and Williams-Jones (2005) in the case of the Strange Lake RM deposit.

Despite the well documented nature and general acceptance of alteration in many hydrothermal ore settings (e.g., VMS, porphyry-epithermal, orogenic gold), the same cannot be said for RM deposits. In fact, Strange Lake is a case in point where it is the overprint of metasomatism on proto-ore that is important in the economics of this deposit. Recent work at the Nechalacho RM deposit, NWT, Canada (e.g., Sheard et al. 2013; Feng and Samson 2015), has also shown the importance of metasomatism in modifying and upgrading RM ore zones.

The intent of this paper is to present and discuss two independent but related aspects of RM systems: 1) provide further support for the significance of metasomatism in these systems; and 2) highlight the importance of coupled dissolution-precipitation (CDP) as an essential component of metasomatism. This latter aspect is of particular importance in LCT-type RM pegmatites, where there has been a general lack of recognition of its presence and significance (see Kontak, 2006), which has implications for how the RM enrichment is present and formed.

2 Importance of CDP in ore systems

Metasomatism has been recognized as an important process in ore systems for decades – it is an essential aspect that accounts for the implied large-scale mass transfer involved in alteration zones (e.g., vuggy silica zones in epithermal settings). The scale of how this process occurs and progresses in an actively forming ore system has, however, rarely been investigated at the scale necessary to understand the process, this being microns or smaller (e.g., Putnis 2002). In addition, but on a related matter, has been the general inference of the immobility of HFSEs. The latter two aspects bear significantly on interpreting the formation of RM deposits and, in the author's opinion, have limited the recognition and hence significance of hydrothermal processes in theses ore systems. The overview of Williams-Jones et al. (2012) provides insight into this issue and significance of fluids in mobilising the REEs and its relevance to ore systems.

In recent years there has been increasing recognition that minerals react to form new, stable phases at the mineral:fuid interface via CDP processes – that is minerals dissolve and new ones precipitate rather than solid state transformation via diffusion. Importantly this process also generates pore space. Thus, CDP involves the sequential dissolution of a primary phase, creation of space and its subsequent occlusion by new material; generally the latter involves only partial infilling, hence the porosity and permeability are generated (see Putnis et al. 2005). Textural evidence of CDP is the pitted texture in the product phase, as is common when plagioclase is saussuritized (Fig. 1). Thus, CDP provides the means for further ingress of fluid and solutes, removal of mass and development of alteration zones. For example, development of both zoned (cm- to 10s cm scale) and massive (m to 10s m scale) greisens at the East Kemptville Sn-Zn-Cu-Ag deposit reflects CDP, and formation of reaction zones at these different scales (Halter et al. 1996, 1998).

Detailed studies of accessory phases that are important proto-ore hosts for RM, such as zircon (Hf, Zr, HREEs) and monazite (LREEs), have shown that these minerals

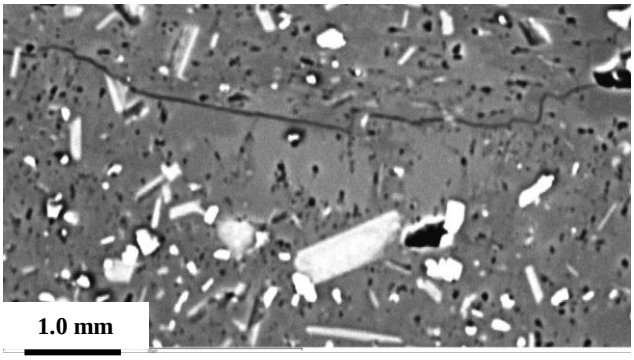


Figure1. A SEM BSE image of altered plagioclase showing remnant core (centre; An_{30}) surrounded by a zone of albite-epidote-muscovite due to CDP process. Note the pitted texture of the albite, which typifies the product of the CDP process.

are not as robust to mineral:fluid interaction as once considered (e.g., Geisler et al. 2007). This provides the basis for considering hydrothermal processes as an important component of ore formation in RM systems. In fact, where these phases are present as products in hydrothermal settings the means to date the systems is provided. As further evidence of this, the author notes the common occurrence of altered zircon in almost all of his studies of granitic rocks, with new zircon characterized by its enrichment in Ca, Sr, Al and Fe (cf. Geisler et al. 2007).

3 Examples of CDP in ore settings

In the section below, examples of CDP accompanied by RM mineralization are presented beginning with granitic settings, then a simple pegmatite, followed by LCT-type pegmatites.

3.1 Proterozoic Khetri granites, India

The Proterozoic ca. 1650 Ma Khetri granites of northern India represent A-type magmatism. They are amphibole-biotite - bearing granites with rare miaroles and pegmatites and have been implicated genetically in the formation of the regional IOCG Khetri Cu belt. Detailed microscopic and SEM-EDS studies (Kontak and Kaur 2013) indicate that although magmatic textures are preserved, all primary phases record CDP processes; e.g. feldspars are pitted and record low T metasomatism (Ab_{100}, Or_{100}). Low abundances of RM are present as U-Th-LREE-F phases with fluorite, calcite, apatite and titanite in secondary cavities. Furthermore, L-V-Halite inclusions cut quartz and fill pores where CDP of feldspar occurs.

3.2 Bokan Mountain, Alaska

The U-Th-Y-Nb-REE mineralization at Bokan Mountain is hosted by a ~177 Ma, circular (3 km diameter), peralkaline granite complex with an arfvedsonite core zone and an aegerine-augite border phase that is partially surrounded by a pegmatite border zone (Dostal et al. 2014). The granite records a transition from an early subvolvus to later hypersolvus granite phase and early magmatic enrichment of HFSE (e.g., Zr, Y, REEs) in the border pegmatites and late dike rocks. Thereafter, ingress of orthomagmatic fluids resulted in extensive element modification of the feldspars and mafic minerals via CDP processes and enrichment of the RM phases, while preserving primary textures. The latter is exemplified, for example, by the replacement of magmatic pyroxene by quartz-arfvedsonite-hematite with associated RM mineralization (Fig. 2). Such fluid enhanced element mobility was common and resulted in elevated Nb-Ta-Zr-Y-Th-U-REE concentrations with formation of related phases including allanite monazite, thorite, zircon, bastnaesite, parasite and ferro-columbite.

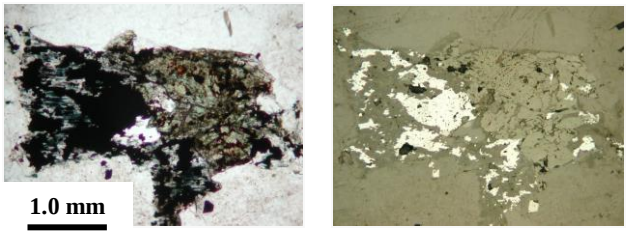


Figure 2. A sample of altered granite from the Bokan Mountain RM deposit. Transmitted (Left) and reflected (Right) light images of the same area showing primary aegerine augite replaced by an assemblage of quartz-hematite-riebeckite which may also include RM phases in some cases.

3.3 The Mongolian ongonites

The Cretaceous (~120 Ma) Mongolian ongonites have long been referred to as pristine RM-enriched felsic dike rocks – quartz-two feldspar, topaz-bearing glassy rocks. Work on samples from the type locality (Dostal et al. 2015) shows these rocks record both textural and mineral-chemical evidence of re-equilibration with orthomagmatic fluids, while retaining an overall magmatic texture (Fig. 3).

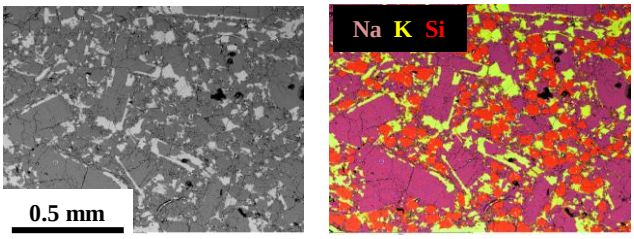


Figure 3. A sample of Mongolian ongonite in SEM-BSE image (Left) and equivalent false coloured X-ray map (Right). Images show the preservation of the original magmatic texture despite intense metasomatism. X-ray map shows albite (An_{100}; mauve), K-feldspar (Or_{100}; yellow), and quartz (red).

The feldspar phases (Ab_{100} and Or_{100}) are richly pitted, and associated with quartz containing low-density L-V±Halite inclusions. Abundant secondary RM phases (Zr-Hf-U-Nb-Ta-Sn-W-REE) phases, some containing F and CO_2, are also present. LA ICP-MS analysis shows RM enrichment

in secondary, relatively F-poor (4 wt. % F; 700 ppm Sn, 150 ppm Nb, 30 ppm Ta) muscovite that replaces primary F-rich (8 wt. % F) muscovite.

3.4 Sudbury pegmatites

An extensive swarm (ca. 10 kms) of simple, two feldspar-quartz pegmatites with abundant graphic texture outcrop south of Sudbury, Ontario. They intrude Proterozoic ortho- and paragenesis of the Killarney magmatic zone. Although the dikes only host low levels of RM mineralization (U-Th-Sn-Ta-Nb), it is the abundant metasomatism in them that is of interest. The latter reflects the contrasting nature of the mafic wall-rocks versus the felsic pegmatites, in particular sulfidic amphibolites. Current research focuses on documenting fluid:rock interaction in this setting and the CDP processes. The latter is reflected by; 1) variable reddening of feldspars due to micron-size Cr-Ti bearing hematite in pitted feldspar; 2) the presence of micron-size uraninite in hematite zones; 3) extreme development of new, porous feldspar due to CDP; and 4) formation of secondary Fe-rich (<3.5 wt. % FeO) muscovite, Mn-rich garnet, Ca-sulfate, and calcic (An_{30}) plagioclase (Fig. 4).

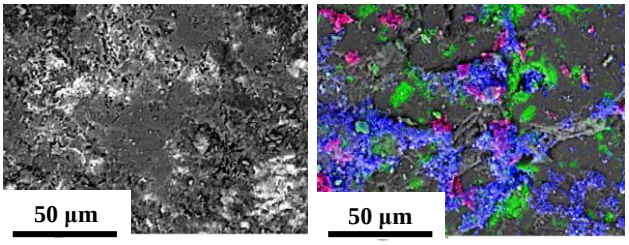


Figure 4. Sample of a simple Sudbury pegmatite. Left: A SEM-BSE image showing pitted K-feldspar with pores lined by Fe-rich muscovite and hematite. Right: A false coloured X-ray map showing albite (grey), Fe-rich muscovite (green), calcic plagioclase (An_{20}; blue), and Ca-sulfate phase (red).

3.5 LCT pegmatites: Tanco, Manitoba, LNPG, N.W.T., and Brazil Lake, Nova Scotia

The LCT-type pegmatites represent one of the most important sources of RM, in addition to being among the most fractioned igneous rocks known. Thus this rock suite has been the focus of many studies in their natural setting and related samples and experimental equivalents (e.g., Kontak 2006; London 2008; Maneta and Baker 2014). Whereas the primary mineralogy (i.e., quartz-K-feldspar-albite-spodumene) is simple, their internal textures (e.g., skeletal, graphic, line-rock, crenulated, colloform) are not and it this feature that distinguishes the suite from other rock types (London 2008). Here we are concerned, however, with the nature and origin of the RM mineralization in this suite which, as with their contained textures, remains an area of debate, as recently summarized by Linnen et al. (2012). On the one hand there is clear evidence for some magmatic mineralization, such as the coarse intergrowth of tantalite and glassy K-feldspar at Tanco, whereas at the same deposit there is an abundance of tantalite intergrown with inferred secondary muscovite and albite (Fig. 5). In addition, at many other LCT settings there is pervasive development of secondary albite that contains abundant RM phases. The latter observation suggests RM phases were introduced during the secondary metasomatic stage of pegmatite evolution. It is the latter type of occurrence that the following discussion focuses on.

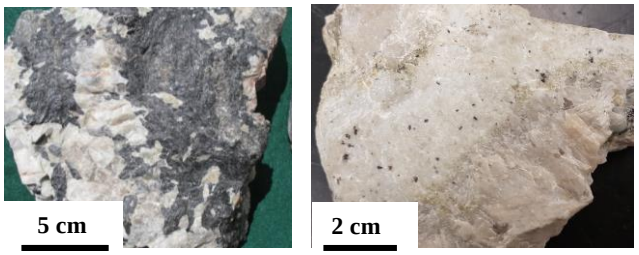


Figure 5. Samples from Tanco LCT-type pegmatite showing RM mineralization. Left: Coarse-grained tantalite intergrown with glassy, primary K-feldspar; image 20 cm wide. Right: Fine-grained saccharoidal albite with disseminated tantalite cutting coarse primary K-feldspar; image 10 cm wide.

The 395 Ma Brazil Lake LCT pegmatites, Nova Scotia, intrude basic metavolcanic rocks interbedded with quartzite and slates (see Kontak (2006) for details). Early magmatic quartz-spodumene-K-feldspar is pervasively overprinted by zones of saccharoidal and cleavelanditic albite and reflect CDP processes (Fig. 6). The latter is accompanied by abundant secondary muscovite and minor spessartine garnet. Whole-rock geochemistry (n=350) indicates a strong correlation of the RM mineralization with the albitic alteration zones. Interestingly, analyses of secondary fluid inclusions in the quartz via LA ICP-MS

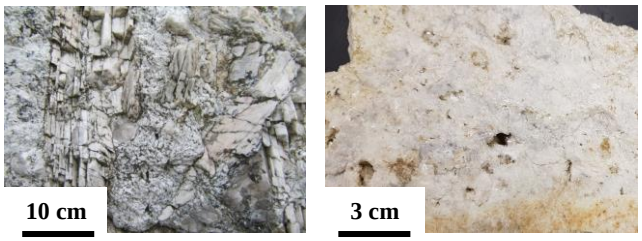


Figure 6. Samples from the Brazil Lake LCTtype pegmatite. Left: Intergrowth of cleavelandite, after blocky K-feldspar, and elongate spodumene. Right: Secondary albite after blocky K-feldspar with abundant pores that are lined with platy albite and muscovite.

indicate a lack of RM elemental (i.e., Ta, Nb , Sn, W all <5 ppm) enrichment, which suggests the RM and albitic alteration relate to metasomatism by a sodic-rich melt rather than a fluid phase (Kontak et al. 2016).

The 82 Ma Little Nahanni pegmatite group (LNPG), NWT, Canada, outcrops over 15 km and comprises several hundred dikes of 10s to 100s metres strike length and cm- to multi-metre width. The primary assemblage is

dominated by quartz-spodumene-K-feldspar with subordinate albite and lepidolite. Whereas some RM mineralization (mm size Ta-Nb oxides, cassiterite, wolframite) is of magmatic origin, most of it coincides with development of secondary plagioclase which ranges from albitic (An_{0-5}) to slightly calcic (An_{10-15}) (Fig. 7). The latter plagioclase records exchange with the calcic metasedimentary wall rocks, which is also reflected by the presence of Ca, S, Co, Zn, and As in analysis of fluid inclusion evaporate mounds (Burns 2017).

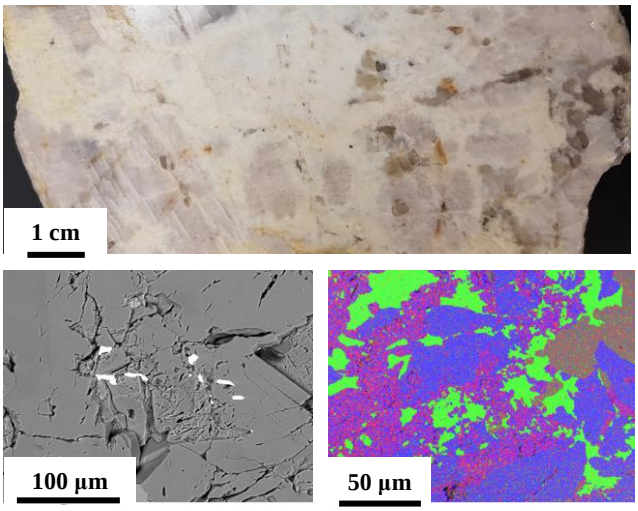


Figure 7. Samples from the LNPG LCT-type pegmatites. Top: Fine-grained albite (white) replacing primary, glassy K-feldspar (grey phase). Bottom left: SEM-BSE image showing primary albite (An_5, upper left, dark grey) replaced by pitted calcic plagioclase (An_{15}) with its pores lined by cassiterite. Lower right: A false coloured X-ray map showing primary K-feldspar (blue) and albite (green) replaced by secondary calcic plagioclase (mauve; An_{10-15}).

4 Conclusions

The above discussion presents ample evidence that further strengthens the case for the role of metasomatism in RM mineralization. In addition, it is suggested that CDP is the process which accounts for replacement of the primary magmatic phases, including, in some cases, RM proto-ore, and facilities continued reactions and development of alteration zones. These ideas were presented in an eloquent model based on the Strange Lake work by Salvi and Williams-Jones (2005) a decade ago. Since then this model has been supported by subsequent studies (e.g., Thor Lake, Misery Intrusion, Strange Lake) by A.E. Williams-Jones and colleagues. The additional studies summarized here thus concur with the aforementioned conclusions.

Acknowledgements

The ideas presented reflect interaction with many colleagues, but in particular A.E. Williams-Jones, R.F. Martin and I. Parsons. I also thank many others who I have had the pleasure to interact with and learn from and whose contributions are presented here. Any errors or omissions are however due solely to the author.

References

Burns, MGG (2017) A fluid Inclusion study of the Little Nahanni LCT-Type Pegmatite Group, NWT Canada: Implications for the nature and origin of fluids in LCT-type pegmatites. Unpubl MSc thesis, Laurentian Univ, Sudbury, ON, Canada.

Dostal, J, Kontak, DJ, Karl, S (2014) The Early Jurassic Bokan Mountain peralkaline granitic complex, (southeastern Alaska): Geochemistry, petrogenesis and rare-metal mineralization. Lithos 202-203: 395-412.

Dostal, J, Kontak, DJ, Gerel, O, Shellnutt, G, Fayek, M (2015) Cretaceous ongonites (topaz-bearing albite-rich micro-leucogranites) from Ongon Khairkhan, Central Mongolia: Products of extreme magmatic fractionation and pervasive metasomatic fluid: Lithos 236-237: 173-179.

Feng, Y, Samson, IM (2015) Replacement processes involving high field strength elements in the T Zone, Thor Lake rare-metal deposit. Can Mineral 53: 31-60.

Halter, W, Williams-Jones, AE, Kontak, DJ (1996) The role of greisenization in cassiterite precipitation at the East Kemptville tin deposit, Nova Scotia. Econ Geol 91: 368-385.

Geisler, T, Schaltegger, U, Tomaschek, F. (2007) Re-equilibration of zircon in aqueous fluids and melts. Elements 3(1), 43-50.

Gysi, AP, Williams-Jones, AE (2013) Hydrothermal mobilization of pegmatite-hosted REE and Zr at Strange Lake, Canada: A reaction path model. Geochim Cosmochim Acta 122: 324-352.

Kontak, DJ (2006) Nature and origin of an LCT-suite pegmatite with late-stage sodium enrichment, Brazil Lake, Yarmouth County, Nova Scotia. I. Geological setting and petrology. Can Mineral 44: 563-598.

Kontak, DJ and Kaur, G (2013) What about the fluids? Re-examining the peptrology of Proterozoic A-type granites, north Khetri Cu belt, Rajasthan, India. Geol Assoc Can-Mineral Assoc Can Meeting, Abstr with Program, St. John's, Nfld, Canada.

Kontak, DJ, Burns, MGG, Alimohammadi, M., Ulrich, T (2016) Fluid inclusion study of the Brazil Lake LCT-type pegmatite, Nova Scotia, Canada provides insight into the origin of rare-metal enrichment and occurrence of wallrock-derived CO_2. Abstr with Program, PACROFI-XIIII, Columbus, Missouri, USA.

Linnen, R.L, Van Lichtervelde, M, and Černý, P (2012) Granitic pegmatites as sources of strategic metals. Elements, 8, 275-280.

London, D (2008) Pegmatites, Can Mineral, Spec Publ 10, Mineral Assoc Can, 347 p.

Maneta, V and Baker, D. (2014) Exploring the efect of lithium on pegmatitic textures: An experimental study. Amer Mineral 99: 1383-1403.

Mountain, B, Williams-Jones, AE (1988) Mass transfer and the path of metasomatic reactions in mesothermal gold deposit: An example from Flambeau Lake, Ontario. Econ Geol 91: 302-321.

Putnis, A (2002) Mineral replacement reaction: from macroscopic observations to microscopic mechanisms. Mineral Mag 66: 689-708.

Putnis, CV, Geisler, T, Schmid-Beurmann, P, Stephan, T, Giampaolo, C (2005) An experimental study of the replacement of leucite by analcime. Amer Mineral 92: 19-26.

Salvi, S and Williams-Jones, AE (2005) Alkaline granite-syenite deposits: Geol Assoc Canada Short Course Notes, 17, 315–341.

Sheard, Williams-Jones, AE, Heiligmann, M, Peterson, C, Trueman, DL (2012) Controls on the Concentration of Zirconium, Niobium, and the Rare Earth Elements in the Thor Lake rare metal deposit, Northwest Territories, Canada. Econ Geol 107: 81-104.

Williams-Jones, AE, Midgisov, AA, Samson, IM (2012) Hydrothermal mobilisation of the rare earth elements: A tale of "ceria" and "yttria": Elements 8: 355–360.

Keynote presentation

The roles of magma and fluid in concentrating HFSE/REE at Strange Lake, Québec

Olga V. Vasyukova and Anthony E. Williams-Jones
McGill University, Montréal, Canada

Abstract. The granites and pegmatites of the Strange Lake pluton show extreme enrichment in high field strength elements (HFSE), including rare earth elements (REE). Three main processes contributed to the enrichment. Silicate-fluoride liquid immiscibility occurred during magma emplacement. Globules of the fluoride melt scavenged the REE and Ca from the silicate melt and acted as nucleation surfaces for rare minerals that consumed components from both the silicate and the fluoride melt (e.g., chevkinite-(Ce)). Fractional crystallisation of major minerals (mostly alkali feldspar) drove evolution of the melt towards an alkaline composition, which lead to its enrichment in Zr, Nb and Ti. This highly evolved residual melt and the associated fluoride melt intruded fractures and formed pegmatites. Finally, saturation of the silicate (pegmatite) magma with an aqueous fluid lead to subsolidus alteration and hydrothermal remobilisation of elements and evolution of the fluid through a combination of cooling, decreasing pH, and increasing oxygen fugacity. These changes in physicochemical conditions, particularly in pH and temperature, ensured efficient mobilisation of the HFSE and their concentration in the pegmatites and adjacent granites. Each of the three processes (immiscibility, fractional crystallisation and hydrothermal remobilisation) cumulatively help explain the HFSE enrichment of the Strange Lake pluton.

1 Introduction

Alkaline and peralkaline igneous rocks commonly show significant enrichment in HFSE. Examples of such enrichment include the Khibiny and Lovozero complexes (Russia), the Thor Lake and Strange Lake complexes (Canada), the Ilímaussaq complex (Greenland), the Tamazeght massif (Morocco), Pilanesberg (South Africa), the Khaldzan-Buregtey Massif (Mongolia) and the Amis complex (Namibia). All of the above-mentioned intrusions have high concentrations of Zr, REE, Nb and Ti (and in some case cases U, Ta and P). The Strange Lake pluton (Québec-Labrador, Canada), the subject of this paper, is an example of a peralkaline granitic pluton that is enriched in HFSE to potentially economic levels. It contains a resource of 278 Mt. grading 0.93 wt.% total REE oxides (of which 39% are HREE), 1.92 wt.% ZrO_2 and 0.18 wt.% Nb_2O_5. This includes a high grade spine comprising 20 Mt. grading 1.44 wt.% total REE oxides (of which 50% are HREE), 2.59 wt.% ZrO_2 and 0.34 wt.% Nb_2O_5 (www.questrareminerals.com).

The question of whether the HFSE mineralisation of the Strange Lake pluton is magmatic, hydrothermal or both, has long been debated. There is compelling evidence that the mineralisation is dominantly secondary and that hydrothermal fluids therefore played an important role in forming the deposit (Gysi and Williams-Jones 2013; Gysi et al. 2016; Salvi and Williams-Jones 1996; Salvi and Williams-Jones 2006). The confinement of the potentially economic mineralisation to pegmatites and immediately adjacent granite, and the high concentrations of HFSE in unaltered granites, however, indicate that magmatic processes were also important in HFSE concentration.

Fractional crystallisation is well-known to be a powerful mechanism for enriching magmas in incompatible elements. In the case of the Strange Lake pluton, however, although it has been shown that fractional crystallisation, dominantly of alkali feldspar, satisfactorily explains the behaviour of the major elements, it does not explain the hyper-enrichment in the HFSE or the enrichment in Ca in the pegmatites (Boily and Williams-Jones 1994). To explain such enrichment of the HFSE, Boily and Williams-Jones (1994) proposed that the excess alkalis and high concentration of F in the magma promoted the formation of stable HFSE complexes involving these components, permitting them to remain in solution until the end stages of crystallisation of an extremely depolymerised residual, pegmatite-forming melt. The enrichment in Ca was attributed to late low temperature fluids of external origin (Salvi and Williams-Jones 1990).

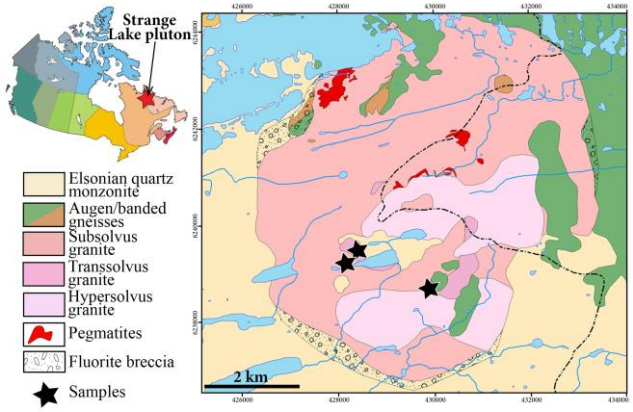


Figure 1. A geological map of the Strange Lake pluton showing the distribution of the principal rock types and the locations of the samples on which this study was based.

Evidence of an additional magmatic mechanism of HFSE enrichment, known previously only from experiments (Veksler et al. 2005), namely silicate-fluoride melt immiscibility, emerged later, based on a melt inclusion study (Vasyukova and Williams-Jones 2014). In this study, crystallised melt inclusions in quartz from granite were re-homogenised at 700-950°C, and after

quenching, some inclusions were shown to contain silicate glass, and others fluoride glass or fluoride glass surrounded by silicate glass. The silicate melt was shown to concentrate Zr, Nb and Ti, whereas the fluoride melt was found to be highly enriched in Ca and the REE (percentage levels). A model was proposed in which droplets of a fluoride melt exsolved during (or shortly after) magma emplacement, scavenged the REE and Ca from the silicate melt, and eventually accumulated in the cores of the pegmatites, thereby explaining the localisation of the deposits in these rocks.

Macroscopic evidence of silicate-fluoride liquid immiscibility was found recently in the early granite in the form of an inclusion ~5 cm in diameter, containing ~25 wt.% REE, ~6 wt.% Ca and F and only ~40 wt.% SiO_2 (Vasyukova and Williams-Jones 2016). This inclusion is believed to represent a globule of the fluoride melt. Textural relationships among primary and secondary minerals in this inclusion revealed their paragenesis. The relationships also showed that the immiscible fluoride globules not only scavenged the REE and Ca, but also acted as a locus of crystal nucleation, in which the crystallising phases were supplied by elements from two melts, thereby forming unusual minerals, e.g., chevkinite-(Ce) and fluorbritholite-(Ce).

The evolution of the hydrothermal fluid was reconstructed in (Vasyukova et al. 2016), based on fluid inclusion data. These data showed that fluid evolution was governed by cooling-induced oxidation at isobaric (~1.1kbar) conditions. A high salinity (~25 wt.% NaCl) CH_4-bearing fluid exsolved from the silicate melt at ~450-500°C. This fluid had a high capacity to transport the light REE. Methane was gradually oxidised, firstly to CH_4 with admixture of higher hydrocarbons (at ~360°C) and then to CO_2 (~300°C). The aqueous component of the fluid evolved towards lower salinity, driven by fluid-rock interaction. At ~220°C, the aqueous fluid had an apparent salinity of ~4.5 wt.% NaCl eq. and coexisted with CO_2 gas. This fluid was particularly aggressive causing decomposition of Na-zircono- and titano-silicates and re-mobilisation of Zr and Ti.

During the ensuing cooling, the fluid lost its gas component due to crystallisation of REE-fluocarbonates and interstitial calcite. Water was largely consumed by the formation of K and Fe-phyllosilicates (Gysi and Williams-Jones 2013). Consequently, at 150°C the fluid salinity increased to ~19 wt.% NaCl eq. This fluid was responsible for remobilisation of the HREE.

As a result of the studies referred to above, data are available on the composition of the melt from which the Strange Lake granites crystallised, and the hydrothermal fluids responsible for the alteration of the granites and pegmatites. A key body of data that is missing, however, is that relating to the melt from which the pegmatites crystallised. Here we report results of a study of melt inclusions in quartz from the border zone of the Strange Lake pegmatites. The inclusions represent the latest and most evolved melt and, together with previous inclusion data, allow reconstruction of the full crystallisation and alteration history of the pluton.

2 Geological setting

The Strange Lake pluton is Mid-Proterozoic, comprising three granite units (Fig. 1), an early and least evolved hypersolvus granite containing a single alkali feldspar, perthite, a more evolved, transsolvus granite (perthite, K-feldspar and albite) and a most evolved subsolvus granite containing two alkali feldspars (Salvi and Williams-Jones 1990). There are two main pegmatite fields, one in the north-eastern part of the pluton and the other in the centre (Fig. 1). Both fields comprise sub-horizontal lenses and sheets (tens of cm up to 20 m in thickness) in altered subsolvus granite. The HFSE mineralisation is confined to the pegmatites and the most altered adjacent subsolvus granites.

3 Methods

Melt inclusions were heated in cold-seal autoclaves at 650-700°C and 1.5-3 kbar. Homogenised inclusions were exposed by polishing (using kerosene instead of water to preserve water soluble phases) and analysed using an electron microprobe (EPMA at McGill University: JEOL JXA-8900L at 15 kV, with a 6.5 nA beam current and a beam diameter of 15 µm).

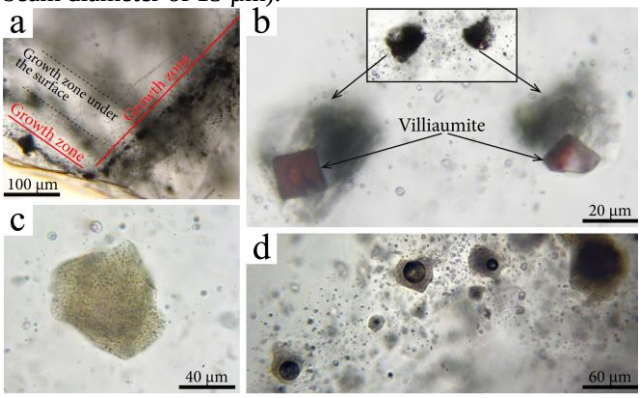


Figure 2. Photomicrographs (transmitted light) showing melt inclusions before (a and b) and after (c and d) heating. (a) – melt inclusion arrays along growth zones. (b) – two inclusions at low (the inset) and high magnification, containing villiaumite crystals. (c and d) – inclusions from the same growth zone after re-homogenisation displaying different melt/fluid ratios.

4 Results

Melt inclusions in the Strange Lake pegmatites are found along growth zones (Fig. 2a and b) or in rare cases as isolated inclusions. The inclusions are dark, 20-100 µm in diameter, fully crystallised and spatially associated with fluid inclusions (Fig. 2). They contain (before heating) K-feldspar, albite, arfvedsonite ($NaNa_2(Fe^{2+}{}_4Fe^{3+})Si_8O_{22}(OH)_2$), astrophyllite ($(K,Na)_3(Fe^{2+},Mn)_7Ti_2Si_8O_{24}(O,OH)_7$), Na- and K-zirconosilicates (elpidite $Na_2ZrSi_6O_{15}\cdot 3H_2O$ or vlasovite $Na_2ZrSi_4O_{11}$), villiaumite (NaF, Fig. 2c)

and in some cases interstitial bastnäsite-(Ce), REE-fluoride and an unidentified Nb-Pb mineral (possibly plumbo-pyrochlore).

After heating, the inclusions were quenched, forming a light brown silicate glass, which is either homogeneous or contains numerous minute globules (Fig. 2c and d). Many, but by no means all of the inclusions, contain a fluid bubble (Fig. 2e) and even within the same growth zone the melt/fluid ratio varies significantly (Fig. 2d).

The average compositions of the melt inclusions from the pegmatites are shown in Table 1. For comparison, the compositions of the granite-hosted melt inclusions studied by (Vasyukova and Williams-Jones 2014) and the bulk pegmatite composition are also shown in Table 1. The melt trapped in pegmatite-hosted quartz is depleted, compared to the melt trapped in granite-hosted quartz, in SiO_2 and Al_2O_3 (62.3 and 5.7 wt.% in pegmatite vs 73.1 and 8 wt.% in granite, respectively) and highly enriched in Na_2O, F, Cl and ZrO_2 (1.4, 2.9, 5 and 2.1 times, respectively). Other elements show more modest enrichment (see TiO_2, FeO, K_2O in Table 1). Niobium concentrations are the same in the granitic and pegmatitic melts. The water content, a maximum, was roughly estimated from the difference between the total composition and 100%, and is ~3 times higher in the pegmatitic melt. The calculated aluminium saturation index (ASI), on average, is 0.4 in the pegmatite melt, which is nearly half that of the granitic melt.

Table 1. Average compositions (wt.%) of melt inclusions in granites (Vasyukova and Williams-Jones, 2014) and pegmatites (this study) and the average bulk rock pegmatite composition (drill holes ALT11002 and ALT11003, data provided by Quest Rare Minerals LTD).

	Granite		Pegmatite		Pegmatite bulk rock	
Nr[1]	39	σ	26	σ	36	σ
SiO_2	73.1	2.3	62.3	3.0	70.2	6.3
TiO_2	0.5	0.4	0.6	0.1	0.6	0.5
Al_2O_3	8.0	2.2	5.7	0.7	6.2	1.6
FeO	4.1	2.0	5.3	0.5	4.3	1.8
CaO	0.08	0.06	0.11	0.02	2.9	1.6
Na_2O	4.5	1.1	6.1	1.9	2.4	1.7
K_2O	4.1	1.3	4.3	1.0	3.7	1.2
ZrO_2	1.5	1.3	3.2	1.0	2.6	1.3
Nb_2O_5	0.4	0.3	0.4	0.2	0.5	0.4
F	0.8	0.4	2.3	0.8	1.2	0.7
Cl	0.1	0.1	0.5	0.3	-	-
Ce_2O_3	bdl	-	0.3	0.1	0.3	0.1
H_2O[2]	3.2	2.2	9.4	1.7	-	-
Total	100		100		100	
ASI	0.7	0.2	0.4	0.2	0.8	0.2

[1] Nr – number of analyses; [2] roughly estimated by the 'difference' method (100% minus the EPMA analyses totals).

Compared to the pegmatite-hosted melt inclusions, the bulk pegmatite (fully crystallised) is significantly enriched in SiO_2 and CaO and depleted in Na_2O, F, ZrO_2 and FeO (Table 1). The proportions of TiO_2, Al_2O_3 K_2O, Nb_2O_5 and Ce_2O_3 in the melt inclusions, however, are very similar to those of the bulk pegmatite. The aluminium saturation index of the bulk pegmatite is twice as high as that of the pegmatitic melt inclusions.

5 Discussion

A key observation is that the glass/fluid ratio of the melt inclusions is highly variable (Fig. 2c and d). This indicate that exsolution of the fluid occurred early, i.e., before crystallisation of the pegmatite border zones. We propose that the depletion of the pegmatitic melt (relative to the granitic melt) in Si and Al was most likely caused by partitioning of these elements into the fluid due to the high alkalinity of the latter. Our calculations (Hch, Shvarov and Bastrakov (1999)) show that at 450°C and pH=10 an aqueous fluid can dissolve up to 10 wt.% of Si and 7 wt.% of Al, if it equilibrated with quartz and corundum (a simple proxy for the Al-bearing phases), respectively.

Owing to the increase in alkali content (Table 1), the ability of the pegmatite melt to dissolve incompatible elements and volatiles increased significantly (see the much higher concentrations of F, Cl, Zr, and Ce in the pegmatite-hosted melt inclusions compared to those in the granite-hosted melt inclusions, Table 1), which is consistent with the earlier model of (Boily and Williams-Jones 1994) and experimental studies on the solubility of HFSE minerals in peralkaline melts (Linnen and Keppler 1997; Linthout 1984; Watson 1979).

Interestingly, the CaO concentration of the bulk pegmatite is considerably higher than that of the corresponding melt inclusions. It is possible that the Ca was introduced by an external fluid, as proposed by Salvi and Williams-Jones (1990). In subsequent studies the same proposal has been made for other peralkaline and alkaline plutons, including quartz syenite intrusions in the Gallinas Mountains (Williams-Jones et al. 2000) and the Tamazeght complex in Morocco (Salvi et al. 2000).

Another possible explanation for the high bulk Ca content of the pegmatite is that the immiscible fluoride melt served as the source for Ca (and REE). As was discussed earlier, the pegmatitic melt was extremely alkaline and F-rich, allowing it to dissolve a high concentration of HFSE. This very low viscosity melt coexisted with a high salinity fluid, which therefore would also have been alkaline. We propose that the melt and fluid formed an extremely reactive emulsion that readily dissolved the coexisting fluoride melt. As the corresponding glass has a low Ca content, we further propose that Ca partitioned preferentially into the fluid.

Since the fluid exsolved from the melt before crystallisation of pegmatite, the fluid/melt ratio in pegmatite was probably very high (physical accumulation of fluid bubbles as a result of fluid buoyancy). At a high fluid/melt ratio, even the partitioning of Ca into the fluid will not affect its composition significantly so that its detection by microthermometry can be difficult. This is consistent with previous conclusions that the fluid coexisting with the melt has a composition in the system NaCl-H_2O (Salvi and Williams-Jones 1996; Salvi and

Williams-Jones 2006; Vasyukova et al. 2016).

6 Conclusions

The compositions of melt inclusions in the Strange Lake pegmatites provide important insights into the evolution of the silicate melt and the hydrothermal fluid. Together with earlier compositional data on melt inclusions in the granites, the composition of a palm-size REE-rich fluoride melt inclusion, and fluid inclusion data, they allow us to reconstruct the evolution of the system from magma emplacement until complete solidification and alteration.

The peralkaline Strange Lake magma was emplaced at shallow depth (~1.1 kbar) and underwent silicate-fluoride immiscibility, either during or shortly after emplacement. The immiscible fluoride globules served as sources for REE and Ca, and the silicate melt evolved to become alkali-rich (with an ASI of ~0.4) allowing it to dissolve high proportions of HFSE.

The alkaline pegmatite melt exsolved an aqueous fluid during or shortly after intrusion, and border pegmatite zones (containing microcline, arfvedsonite, quartz and Ti- and Zr-silicates) crystallised from the resulting melt-fluid emulsion. During this crystallisation, the fluid migrated to the core, where quartz later precipitated.

The subsolidus fluid evolution was governed by cooling-induced oxidation, which caused formation of CO_2 from CH_4 and, as a result, a significant decrease in fluid pH. This low pH fluid was especially corrosive for sodium Ti- and Zr-silicates, which were completely destroyed. The fluid was also responsible for formation of K- and Fe-phyllosilicates (Gysi and Williams-Jones 2013). The decrease in the fluid pH from strongly alkaline to acidic played a crucial role in the re-distribution of the REE.

The Strange Lake deposit formed as a result of three processes, namely silicate-fluoride immiscibility, fractional crystallisation and hydrothermal re-mobilisation, each of which was essential for REE concentration. Without the separation of a fluoride melt, the REE would have been dispersed in early granitic units making them unavailable for further concentration in the melt. Fractional crystallisation within the silicate melt lead to the formation of a low viscosity residual melt which later exsolved an aqueous fluid that combined with the melt to form an emulsion capable of dissolving high concentrations of REE from the coexisting fluoride globules. Finally, the exsolved fluid re-mobilised the HFSE by dissolving primary REE-minerals and precipitating secondary minerals more amenable to beneficiation.

Acknowledgements

The research was funded by Discovery and Collaborative Research and Development grants (Quest Rare Minerals Ltd.) from NSERC (Canada), and a team grant from FQRNT (Québec). We thank Anastasia Kostyuk who performed a number of re-homogenisation experiments for this study.

References

Boily M, Williams-Jones AE (1994) The role of magmatic and hydrothermal processes in the chemical evolution of the Strange Lake plutonic complex, Quebec-Labrador. Contrib Mineral Petr 118:33-47.

Gysi AP, Williams-Jones AE (2013) Hydrothermal mobilization of pegmatite-hosted REE and Zr at Strange Lake, Canada: A reaction path model. Geochimica et Cosmochimica Acta 122:324-352.

Gysi AP, Williams-Jones AE, Collins P (2016) Lithogeochemical Vectors for Hydrothermal Processes in the Strange Lake Peralkaline Granitic REE-Zr-Nb Deposit. Econ Geol 111:1241-1276.

Linnen RL, Keppler H (1997) Columbite solubility in granitic melts: consequences for the enrichment and fractionation of Nb and Ta in the Earth's crust. Contrib Mineral Petr 128:213-227.

Linthout K (1984) Alkali-zirconosilicates in peralkaline rocks. Contrib Mineral Petr 86:155-158.

Salvi S, Williams-Jones AE (1990) The role of hydrothermal processes in the granite-hosted Zr, Y, Ree deposit at Strange Lake, Quebec Labrador - evidence from fluid inclusions. Geochimica Et Cosmochimica Acta 54:2403-2418.

Salvi S, Williams-Jones AE (1996) The role of hydrothermal processes in concentrating high-field strength elements in the Strange Lake peralkaline complex, northeastern Canada. Geochimica Et Cosmochimica Acta 60:1917-1932.

Salvi S, Fontan F, Monchoux P, Williams-Jones AE, Moine B (2000) Hydrothermal mobilization of high field strength elements in alkaline igneous systems: Evidence from the Tamazeght complex (Morocco). Economic Geology and the Bulletin of the Society of Economic Geologists 95:559-575.

Salvi S, Williams-Jones AE (2006) Alteration, HFSE mineralisation and hydrocarbon formation in peralkaline igneous systems: Insights from the Strange Lake Pluton, Canada. Lithos 91:19-34.

Shvarov YV, Bastrakov EN (1999) HCh: a software package for geochemical equilibrium modelling. User's Guide. Australian Geological Survey Organisation, Record 1999/25.

Vasyukova O, Williams-Jones AE (2016) The evolution of immiscible silicate and fluoride melts: Implications for REE ore-genesis. Geochimica et Cosmochimica Acta 172:205-224.

Vasyukova OV, Williams-Jones AE (2014) Fluoride–silicate melt immiscibility and its role in REE ore formation: Evidence from the Strange Lake rare metal deposit, Quebec-Labrador, Canada. Geochimica et Cosmochimica Acta 139:110-130.

Vasyukova OV, Williams-Jones AE, Blamey NJF (2016) Fluid evolution in the Strange Lake granitic pluton, Canada: Implications for HFSE mobilisation. Chemical Geology 444:83-100.

Veksler IV, Dorfman AM, Kamenetsky M, Dulski P, Dingwell DB (2005) Partitioning of lanthanides and Y between immiscible silicate and fluoride melts, fluorite and cryolite and the origin of the lanthanide tetrad effect in igneous rocks. Geochimica Et Cosmochimica Acta 69:2847-2860.

Watson EB (1979) Zircon saturation in felsic liquids - experimental results and applications to trace-element geochemistry. Contrib Mineral Petr 70:407-419.

Williams-Jones AE, Samson IM, Olivo GR (2000) The genesis of hydrothermal fluorite-REE deposits in the Gallinas Mountains, New Mexico. Economic Geology and the Bulletin of the Society of Economic Geologists 95:327-341.

Keynote presentation

The late Archean Au epoch: By - product of Earth degassing triggered by electrical instabilities on the core-mantle boundary?

John L. Walshe and Adam B. Bath
CSIRO Mineral Resources, WA, Australia

Abstract. The epoch of Late Archean Au deposits, at ~ 2.7 to 2.63 Ga, can be interpreted as one manifestation of planetary degassing of highly reduced and oxidized volatiles. It is hypothesized that the ultimate driver of this Au epoch was an electron flux from the core-mantle boundary that released H from the mantle ($e + OH^- = O^{2-} + H$), drove redox reactions and sustained the volatile flux of the late Archean. The interaction between fluxes of mantle volatiles and crustal hydrothermal systems constrained the formation of Au deposits/camps.

1 The scale of mineral systems?

Metal accumulations within the Earth are rare occurrences and the accumulations of high grade, large tonnage metal deposits much more so. Most models of formation of these deposits are based on some combination of processes that operate within the middle to upper crust and the hydro- and bio-sphere: metamorphism, basin dewatering, de-volatilization of magmas, sea floor metamorphism, meteoric fluid circulation, fluvial winnowing and detrital accumulations. But these are relatively common Earth processes. Arguably such common processes ought to give rise to more common occurrences of the giant deposits. So is the "special-ness" of the major metal accumulations a function of rare combinations of common processes or have we yet to understand some key elements of the mineral systems that produced the giant deposits? Typical length scales of major mineral provinces are of the order of 100s to 1000s of kilometres across the earth's surface. Given that aspect ratios (length to depth) of systems can be expected to be of the order of 1:1 then the depth of mineral systems may well be 100s to 1000s of kilometres rather than 10s of kilometres as commonly assumed. The distance from the surface of the Earth to the core is approximately 3000 km making it conceivable that some components in mineral systems originate in the lower mantle, if not the core of the Earth.

Au ± Cu deposits are distributed heterogeneously through Earth history with two Precambrian peaks at about 2800 to 2500 and 2200 to 1600 Ma. There is a notable gap in the record from 1600 to 600 Ma with major gold provinces and deposits (including Cu-Au deposits) occurring in the last 600 million years of Earth history. The formation of Au deposits may be broadly related to tectonic processes and production of juvenile continental crust (Groves et al. 2005) but these "Earth-scale" epochs of metallogenic province formation lasting up to 0.5 billion years with time gaps up to approximately a billion years (Figure 1) suggest an additional control beyond tectonic processes.

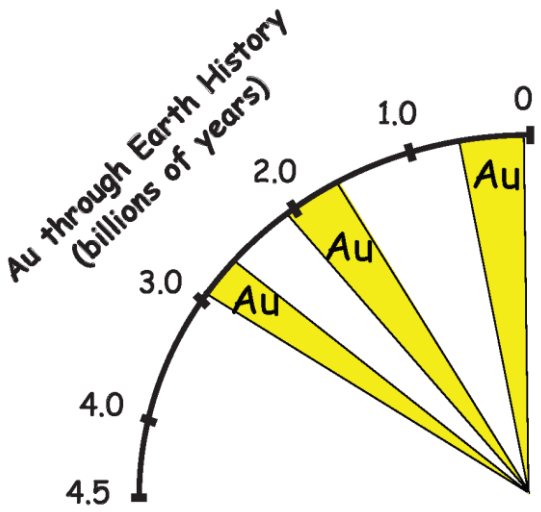


Figure 1. Au epochs through Earth history. Date from Groves et al. 2005

2 Volato - thermal systems with roots deep in the mantle

It is possible to think of the mineral systems that created the Earth's major mineral deposits and provinces as volato-thermally driven chemical engines with roots deep in the mantle. It may be argued that the major gradients in chemical potential in systems were linked to this degassing history and reflect the interplay of deep-Earth anhydrous fluids with the Earth's hydrous outer layers. Metal transport and deposition capacities will be closely linked to propagation of redox and related physico-chemical gradients through the system. Such arguments imply quite specific links between the formation of the Earth's resources across time and space, secular changes in architecture and geochemistry of the planet over some 4.5 billion years of evolution and Earth phenomena such as mass extinction events, global anoxia and atmospheric evolution. Conceivably a better understanding of large-

scale linkages may lead to better techniques for differentiating productive terrains and epochs of Earth history as well as the links between metallogenesis and other Earth processes.

3 Mineral and isotopic zoning of volato-thermal Au systems, Late Archean, eastern Yilgarn Craton

The Late Archaean gold deposits are known from five continents, are hosted within supra-crustal volcano-sedimentary sequences and are spatially associated with trans-crustal structures, 100s of kilometres in length, as exemplified by the deposits of the eastern Yilgarn Craton, Western Australia. All the productive gold camps of the eastern Yilgarn gold province show evidence of deposit to district scale mineral zoning and systematic patterns in $^{13}C_{carbonate}$ and $\delta^{34}S_{sulfide}$ that can be related to chemical gradients sustained by fluxes of reduced (H_2, CH_4) and oxidized gases (SO_2), triggered by tectonic events and related magmatism (Bath et al., 2013; Neumayr et al., 2008). In the Kundana Camp (> 8 million ounce resource) the major deposits are focused on a ~ 15km long, NW striking zone of biotite ± andesine ± amphibole alteration subparallel with the Zuleika Shear. Flanking alteration is dominated by K-feldspar ± muscovite with albite. Minor magnetite ± barite are best developed with the K-feldspar - muscovite assemblage suggesting the transition from biotite to K-feldspar – muscovite defines a camp-scale redox boundary defined by: $KFe_3AlSi_3O_{10}(OH)_2+0.5O_2 = KAlSi_3O_8+Fe_3O_4+H_2O$, with a reduced inner core to the system and oxidized margins. In the St Ives Camp (> 10 million ounce resource) a reduced core to a system was defined between the Athena and Hamlet deposits by systematic mapping of stable isotopes ($\delta^{13}C_{carbonate}$, $\delta^{34}S_{pyrite}$, $\delta^{34}S_{pyrrhotite}$). Elevated $\delta^{13}C$ values (> 0 ‰), relative to reservoir values of -5±2 ‰, define the core of the system and indicate domains of partial reduction of CO_2 via: $H_2CO_3 + 4H_2 = CH_4 + 3H_2O$. Domains of depleted values of $\delta^{13}C$ values (< -6 ‰) define zones of methane oxidation on the margins of the system by oxidized sulfur species, e.g. $3CH_4 + 4SO_2 + H_2O = 4H_2S + 3H_2CO_3$

4 Physico - chemical constraints on Au transport by anhydrous volatiles

Physico-chemical constraints lead to the conclusion that Au was transported by anhydrous, volatile-rich fluids of variable redox state. H_2O concentration is estimated at less than 1wt % and potentially only a few ppb, from stability of the tschermakite component in amphibole, with anorthite and calcite in the system Ca-Mg-Al-Si-O-H (calculations at 450 °C and 2kbar). Gold precipitation is associated with an increase in water activity to ~ 30 to 50 wt %, calculated from the stability of ilmenite-rutile-pyrrhotite-quartz-calcite in the system Ca-Fe-Ti-Si-S-C-O-H. Water activity was likely constrained by mixing of hydrous fluids (metamorphic, crustal fluids) with anhydrous fluids (mantle volatiles). Au deposition occurred at alkaline conditions with fluid pH values of 7 to 8 at (2 to 3 units pH above neutrality @ 300-450 °C and 2kbar) based on aegirine, riebeckite micro-alteration selvages associated with Au veins (data from Wattle Dam Au deposit). pH likely decreased with increasing water activity. Charge balance across the anhydrous domains of the system was possibly maintained by electrical discharges.

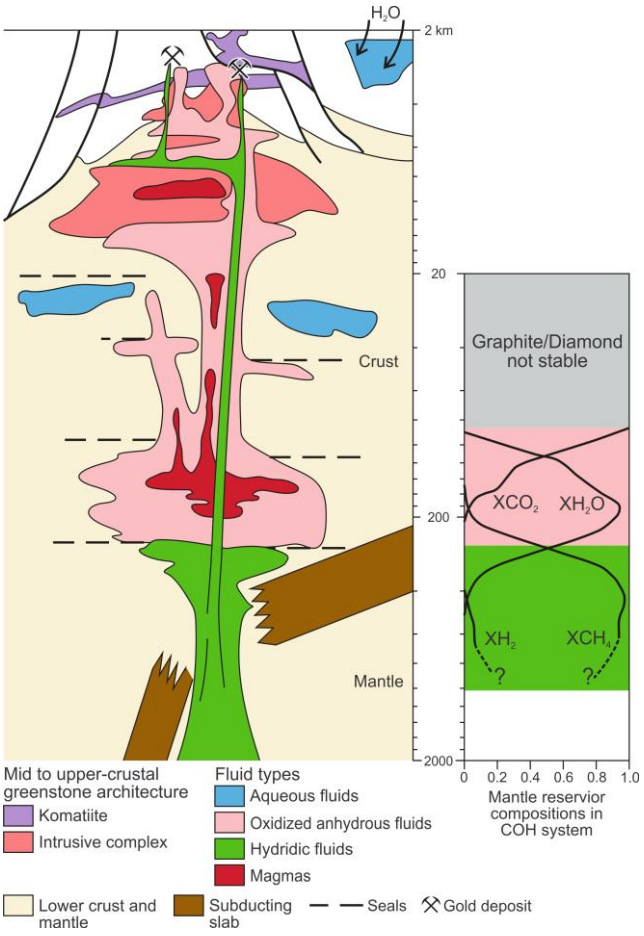


Figure 2. Crust–mantle depth perspective of volatile reservoirs of reduced and oxidized species in the COH system and "volato-thermal engines" of Au systems. a: Section based on the mid to upper crustal architecture of the eastern Yilgarn gold province, Western Australia. b. Shows the depth vs X_i (mole fraction) for species in COH fluid for a given geotherm.

5 The Late Archean Au epoch: by-product of Earth degassing

Late Archean Au deposits of the eastern Yilgarn can be interpreted as one manifestation of planetary degassing of highly reduced and oxidized volatiles at ~ 2.7 to 2.5 Ga and provide insight into the fluid history of a significant section of the Earth's crust for this epoch. Oxidised

volatiles were of magmatic/mantle affinity ($\delta^{34}S$ $SO_{2(g)}$ ~ 1 ‰; $\delta^{13}C$ $CO_{2(g)}$ ~ -5 ‰). Possible sources of reduced volatiles include serpentinisation reactions in the deep-crust or mantle wedge. Thermodynamic studies, and inclusion mineralogy of diamondiferous kimberlites and lamproites suggest hydric fluids could dominate in the Earth at depths greater than 300 - 400 km (Figure 2). It is hypothesized that the ultimate driver of the volatile fluxes may have been an electron flux from the core-mantle boundary that released H from the mantle ($e + OH^-min = O^{2-}min + H$) leading to reduction of oxidized C and S species in the upper mantle/lower crust (Figure 3).

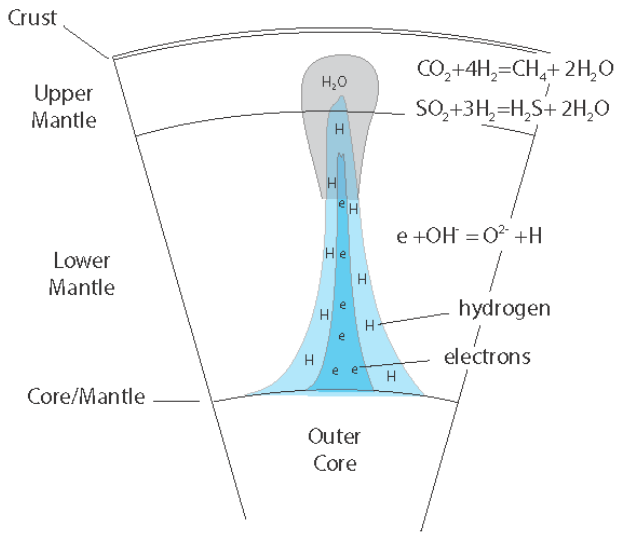


Figure 3. Reactions driven by electron flux from core-mantle boundary.

6 Earth degassing and MIF of S isotopes in the Late Archean

Large amplitude mass-independent fractionation (MIF) of ^{33}S and ^{36}S in sulphides and sulphates (up to ~ +9.5 ‰ $\Delta^{33}S$; is known only from the Late Archean at ~ 2.7 to 2.45 Ga (Farquhar et al., 2007) and is uniquely accounted for by ultra-violet photolysis of gaseous sulphur bearing species such as SO_2 under O_2-free conditions, yielding elemental sulphur and sulphuric acid. The high fluxes of SO_2 in an O_2-depleted, CH_4-rich atmosphere required to sustain this level of MIF (Halvey et al. 2010) suggests a common heritage with the reduced - oxidized volatile fluxes sustaining formation of gold deposits and provinces globally in the mid to upper crust. Gold metallogeny and enhanced MIF can be considered bi-products of late Archean degassing of volatiles of contrasting redox state.

Acknowledgements

Many colleagues contributed to the conversation, notably Willy Jones, Larry Cathles and Dave Cooke. Work on Late Archean Au deposits of the eastern Yilgarn supported by the Minerals Research Institute of Western Australia (M410, M452 and M494) together with Northern Star Resources, Evolution Mining, Ramelius Resources, Saracen Resources, Gold Road Resources, Goldfields, Echo Resources, Blackham Resources and Excelsior Gold.

References

Bath, A.B., Walshe, J.L., Cloutier, J., Verrall, M., Cleverley, J.S., Pownceby, M.I., Macrae, C.M., Wilson, N.C., Tunjic, J. and Nortje, G. (2013) Biotite and apatite as tools for tracking pathways of oxidized fluids in the Archean East Repulse gold deposit. Econ. Geol. 108(4): 667-690

Farquhar, J., Peters, M., Johnston, D.T., Strauss, H., Masterson, A., Wiechert, U. and Kaufman, A.J. (2007) Isotopic evidence for Mesoarchaean anoxia and changing atmospheric sulphur chemistry. Nature 449(7163): 706-709

Groves, D.I., Condie, K.C., Goldfarb, R.J., Hronsky, J.M.A. and Vielreicher, R.M. (2005) Secular changes in global tectonic processes and their influence on the temporal distribution of gold-bearing mineral deposits. Econ. Geol. 100: 203-224

Halevy, I., Johnston, D.T. and Schrag, D.P. (2010) Explaining the Structure of the Archean Mass-Independent Sulfur Isotope Record. Science, 329(5988): 204-207

Neumayr, P., Walshe, J.L., Hagemann, S.G., Petersen, K., Roache, R., Frikken, P., Horn, L. and Halley, S. (2008) Oxidized and reduced mineral assemblages in greenstone belt rocks of the St. Ives gold camp, Western Australia: vectors to high- grade ore bodies in Archaean gold deposits? Mineral Deposita 43: 363–371

The nature and origin of REE mineralization in the Ashram Deposit, Eldor carbonatite complex, Quebec

Caitlin M.J. Beland and Anthony E. Williams-Jones
McGill University, Montréal, Canada

Abstract. A growing number of studies suggest that hydrothermal remobilization is crucial for the formation of carbonatite-hosted rare earth element (REE) deposits. The Ashram REE deposit, hosted by the Eldor Carbonatite Complex (Quebec), is an example of a REE deposit formed mainly due to hydrothermal remobilization. The REE minerals at Ashram deposit are secondary and were precipitated from hydrothermal fluids. They are mainly monazite-(Ce), bastnäsite-(Ce), xenotime-(Y) and minor aeschynite-(Y), and occur as disseminations in breccia matrices, in veins, and as vug fillings. Monazite-(Ce) was the earliest mineral to form, followed by xenotime-(Y) and bastnäsite-(Ce). Compositions of the main REE minerals vary with location in the deposit, particularly in respect to their Nd_2O_3 and ThO_2 contents. Early monazite-(Ce) formed by replacing apatite through substitution of Ca^{2+} by REE^{3+}, whereas a later generation formed from apatite by dissolution-reprecipitation, inheriting the parent REE chemistry. Bastnäsite-(Ce) developed as a replacement of monazite-(Ce) through ligand exchange (F^-, CO_3^{2-} for PO_4^{3-}), while preserving the original REE chemistry. Together, magmatic zone-refinement and hydrothermal remobilization contributed to the formation of a carbonatite-hosted REE deposit.

1 Introduction

Carbonatites are an important source of REE. Historically, the ores have been considered to be magmatic. Recent studies, however, suggest that hydrothermal fluids play an important role in the formation of carbonatite-hosted REE deposits (e.g. Moore et al. 2015; Xie et al. 2015; Trofanenko et al. 2016). It is now well documented from experimental studies and natural samples that the REE can be transported in aqueous solutions (e.g., Buhn & Rankin 1999; Migdisov et al. 2009). The bulk of REE transport in hydrothermal fluids is thought to be achieved through complexation with chloride and sulfate, whereas carbonate and phosphate are considered depositional ligands (Migdisov et al. 2016 and references therein).

The Eldor Carbonatite Complex and its Ashram deposit provide an ideal natural laboratory in which to identify the dominant controls (magmatic and hydrothermal) on ore formation. The current study presents textural observations of the REE mineralization and major and trace element compositions of the principal ore minerals and associated phases. These are used to determine the mineral paragenesis. From these data, the composition and evolution of the mineralizing fluids is inferred.

2 Geology of the Eldor Carbonatite Complex

The Eldor carbonatite complex is located approximately 130 km south of Kuujjuaq, in northern Quebec and is hosted by rocks of the Labrador Trough. It is an elliptical body comprising a series of intrusive carbonatites ranging in composition from calcio- through magnesio- to ferro-carbonatite. The complex is subdivided into a rim (calcio- and magnesio-carbonatite) and core, with the core being the Ashram REE deposit.

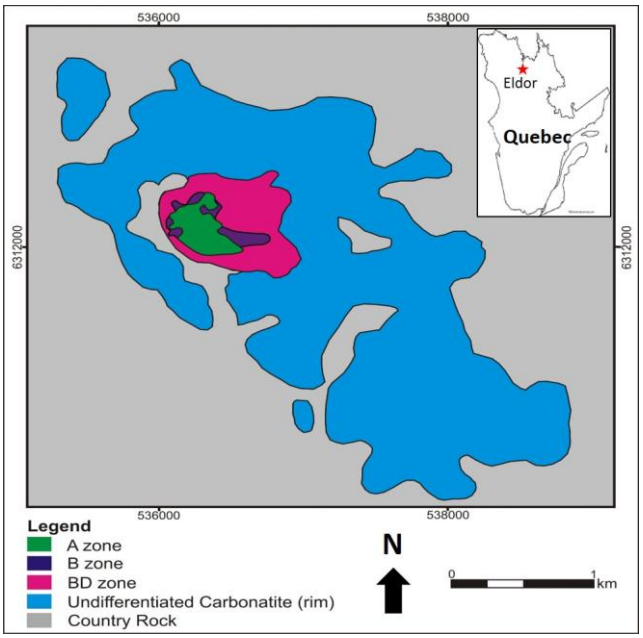


Figure 1. A simplified geological map of the Eldor Carbonatite Complex at 100 m depth.

Ashram contains three main zones of mineralization: BD, B, and A (Fig. 1). In addition, there is the MHREO zone, which is a subdivision of the A zone. The outermost BD zone is an apatite-rich magnesiocarbonatite with rare earth fluorocarbonate (REEflc) mineralization (bastnäsite-(Ce) ($REECO_3F$), parisite-(Ce) ($Ca(Ce,La)_2(CO_3)_3F_2$), synchisite-(Ce) ($CaCe(CO_3)_2F$)). The B zone is also a magnesiocarbonatite, but with a dominant assemblage of fluorite + monazite ($REEPO_4$). This assemblage continues into the A zone magnesiocarbonatite. The innermost MHREO zone is a ferrocarbonatite. This zone contains monazite-(Ce) and subordinate xenotime-(Y) (YPO_4) and aeschynite-(Y) ($(Y,Ca,Fe)(Ti,Nb)_2(O,OH)_6$).

3 Methods

A preliminary petrographic study was carried out using a combination of optical and scanning electron microscopy (SEM). Cathodoluminescence (CL) was essential to identify different generations of apatite.

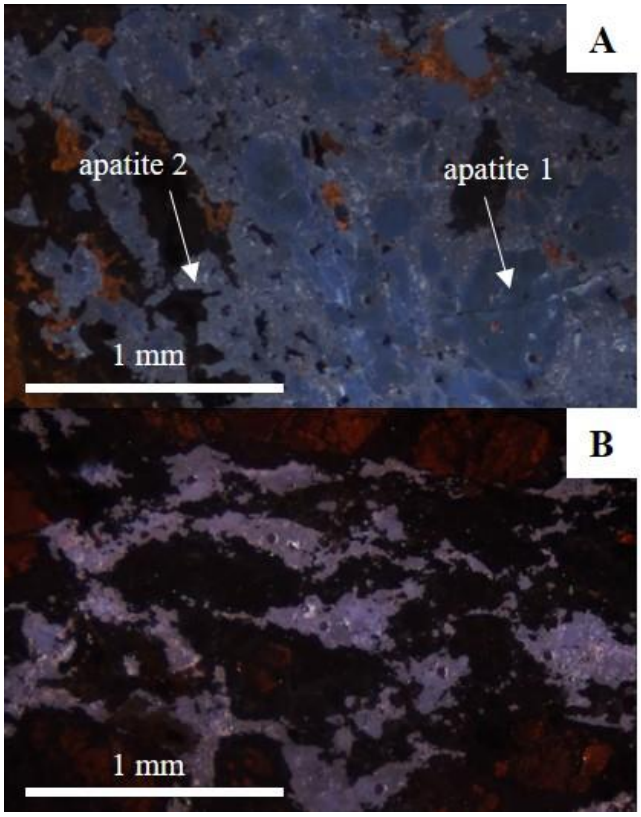


Figure 2. Cathodoluminescence images of selected samples of apatite. A) Cluster of apatite 1 (characteristic of the rim) locally mantled by sucrosic pale blue-violet-luminescing apatite. B) Veins of apatite 2 (locally violet-luminescing) brecciating BD zone dolomite carbonatite.

Mineral chemical data (WDS) were collected on apatite (n=336), monazite (n=352), and bastnasite (n=155), using an electron microprobe (EPMA at McGill University: JEOL JXA-8900L at 20 kV, with a 30 nA beam current and a beam diameter of 10 µm).

Trace element data for apatite (n=204) were collected using a laser ablation inductively-coupled plasma mass spectrometer (LA-ICP-MS). Analyses were performed at McGill University using a NewWave 213 nm ND-YAG laser, operated at a fluence of 12 J/cm^2. Ablation of 30 µm spots were performed with a 30s laser warm-up, 45s ablation and 30s washout. Aerosols were transported into a FINNIGAN iCapQ ICP-MS. The dwell time was 20 ms for the REE. Blocks of ≤ 15 analyses were collected, bracketed by two analyses of SRM NIST 610 external standard, to apply a linear instrument drift correction. Quantification of element concentrations was performed using the software, Iolite. The internal standard used was the Ca content obtained by EMPA.

4 Results

4.1 Petrographic observations

Primary assemblages and textures dominate in the Eldor calciocarbonatites. All other units exhibit variable but significant hydrothermal overprinting, as evidenced by secondary textures (e.g., veins and vug infill). Fluorite and apatite are major hydrothermal minerals in the Ashram deposit. Apatite is an important component of all the rim lithologies and the BD zone. In the rim units, apatite is a coarse-grained, primary phase with ovoid crystal shapes (apatite 1), and blue-violet in CL. It is locally mantled by fine-grained, pale violet to pale pink apatite (Fig. 2A). Apatite in the BD zone is fine-grained and sucrosic, commonly with irregular grain boundaries, and is pale violet to pale pink in CL (apatite 2) (Fig. 2B). Fluorite occurs in the late rim units, the BD zone, and is most abundant in the B and A zones. There are multiple generations of fluorite, some of which are observed to have replaced apatite.

The REE minerals, monazite-(Ce), bastnäsite-(Ce), xenotime-(Y) and minor aeschynite-(Y), occur in veins, as vug fillings, and as disseminations in breccia matrices in all Ashram zones (Fig. 3). The different REE minerals are rarely observed in contact with each other, but where they are in contact, the REEflc invariably mantles monazite-(Ce). Where apatite and monazite-(Ce) are observed in contact, monazite-(Ce) mantles apatite or occurs in fractures in the latter (Fig 3C).

4.2 Mineral chemistry

The compositions of monazite-(Ce) and bastnäsite-(Ce) vary with location in the deposit, particularly in respect to their Nd_2O_3 and ThO_2 contents. Monazite-(Ce) from the A and B zones comprises two distinct groups, showing high- and low-Nd content (Fig. 4A). Monazite-(Ce) from the MHREO zone has a high Nd content and falls into the trend formed by the low-Nd group from the A and B zones. Extremely rare BD zone monazite-(Ce) lies in the high-Nd group. Compositions of bastnäsite-(Ce) from the A, B and MHREO zones define a trend identical to that shown by monazite-(Ce) (Fig. 4B). The BD zone bastnäsite-(Ce) and high-Nd monazite-(Ce) have similar Nd and Th contents. Both groups of monazite-(Ce) can occur within a given sample or even vein. High-Nd bastnäsite-(Ce), however, has been observed in very late coarse-grained veins that cross-cut the major mineralization.

Monazite-(Ce) groups are also distinct in their chondrite-normalized REE (REE_{CN}) distribution patterns (Fig. 5). Low-Nd monazite-(Ce) of the A and B zones is LREE-enriched (steeper slope) relative to MHREO zone and high-Nd monazite-(Ce). The size of the negative Eu anomaly decreases from low- to high-Nd monazite-(Ce) and towards the center of the deposit. Apatite 1 is LREE-enriched and HREE-depleted, very similar to the high-Nd monazite-(Ce) group. Notably, the violet-luminescent apatite of the BD zone has an identical profile to apatite 1. The profile of apatite 2 (BD zone) is convex-upward through the LREE, flat through the MREE and HREE-enriched relative to apatite 1.

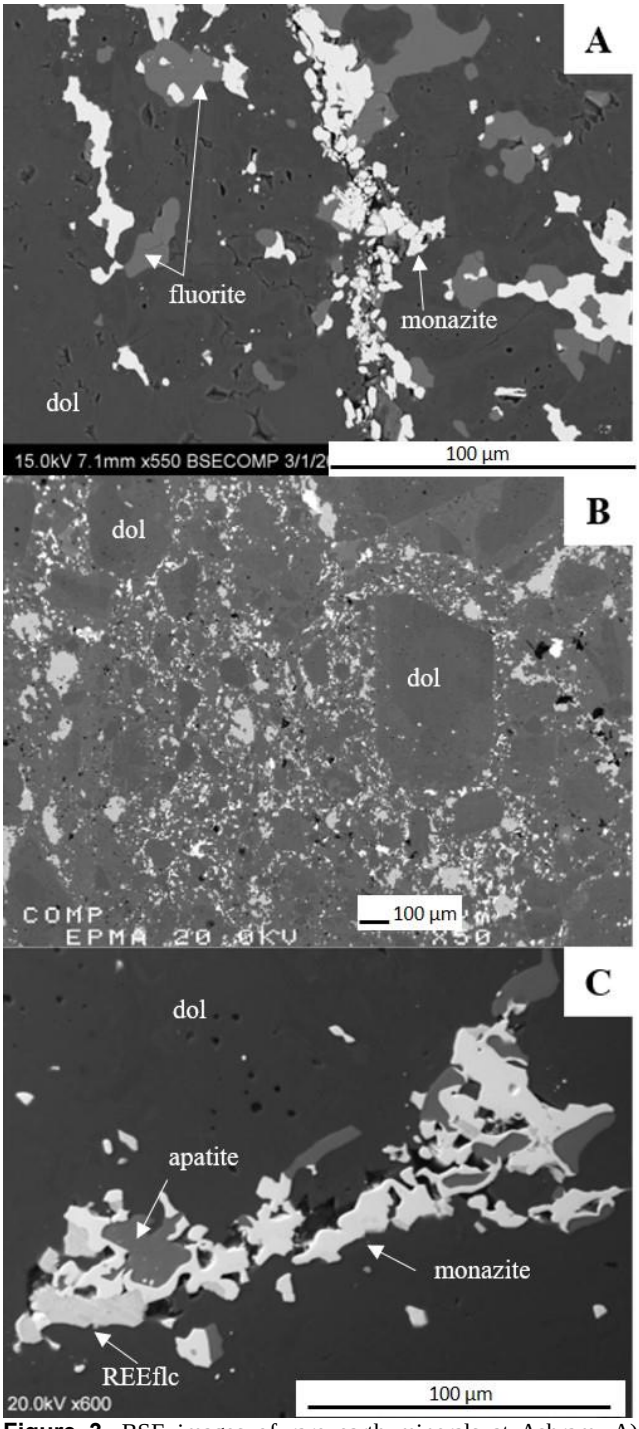


Figure 3. BSE images of rare earth minerals at Ashram. A) Monazite-(Ce) (white) ± fluorite (light grey) veins illustrating A and B zone textures. B) REEflc (white) and apatite (light grey) disseminated in dolomite breccia in the BD zone. C) Apatite is mantled by monazite-(Ce), which in turn is mantled by the REEflc.

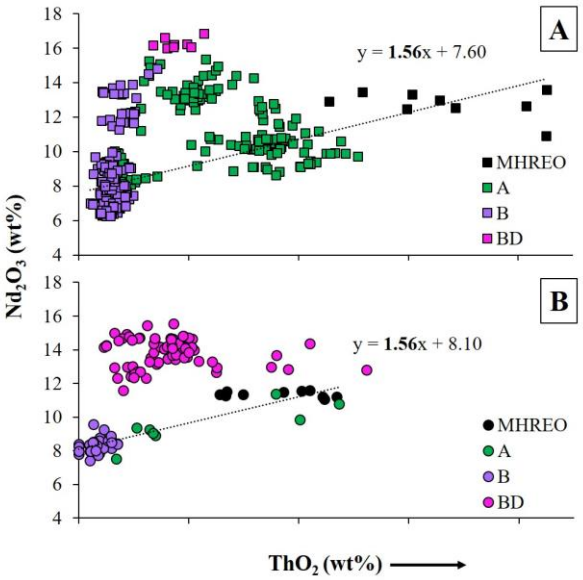


Figure 4. Compositions of Ashram A) monazite-(Ce) and B) bastnäsite-(Ce). Note that MHREO zone monazite-(Ce) and low-Nd monazite-(Ce) of the B and A zones define a positive linear trend in Nd_2O_3 – ThO_2 space. Bastnäsite-(Ce) from the B, A and MHREO zones show an identical trend. Some monazite-(Ce) from the B and A zones is more Nd-rich, and overlaps in composition with BD zone bastnäsite-(Ce) and monazite-(Ce).

5 Discussion

The occurrence of REE minerals in veins and vug-fillings indicates precipitation from a hydrothermal fluid, though this does not rule out the possibility of magmatic pre-concentration. Monazite-(Ce) was the earliest ore mineral to form, followed by bastnäsite-(Ce).

Apatite 2 (BD zone) is interpreted to have formed by dissolution-reprecipitation of apatite 1. The former mantles the latter, with a sharp boundary between the two phases, satisfying the textural criteria for dissolution-reprecipitation proposed by Putnis (2009).

Textural relationships between monazite-(Ce) and apatite suggest that monazite-(Ce) replaced apatite. Monazite-(Ce) compositions suggest that there were two mineralizing events (distinguished by Nd content). The similarity in slopes of REE_{CN} profiles of apatite 1, MHREO zone and high-Nd monazite-(Ce) can be explained by fluid-mediated dissolution of apatite (removal of Ca^{2+}) and reprecipitation of monazite-(Ce), preserving the original apatite REE chemistry. In contrast, replacement of apatite to form the low-Nd monazite-(Ce) group occurred by substituting REE^{3+} for Ca^{2+}. Addition of REE^{3+} from solution is required to explain the LREE-enrichment of low-Nd monazite-(Ce) relative to both apatite varieties. Alternatively, the low-Nd group may have formed from a parent apatite not yet identified.

Textural relationships between monazite-(Ce) and bastnäsite-(Ce), combined with the mineral chemistry (the similar Nd and Th contents of monazite-(Ce) and bastnäsite-(Ce)), indicate that bastnäsite-(Ce) developed as a replacement of monazite-(Ce). This replacement occurred through ligand exchange (F^-, CO_3^{2-} for PO_4^{3-}), while preserving the original REE chemistry. In the B, A, and MHREO zones, where monazite-(Ce) is the dominant REE mineral, bastnäsite-(Ce) partially replaced low-Nd monazite-(Ce), whereas the BD zone (with essentially no

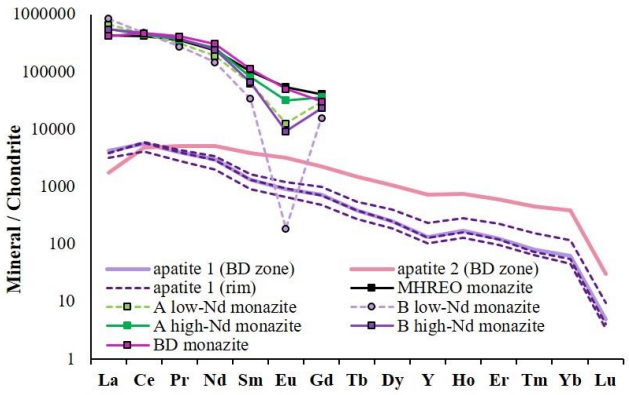


Figure 5. Chondrite-normalized (McDonough & Sun 1995) REE distribution plots of monazite-(Ce) compared to apatite. Apatite line colours reflect CL colour.

monazite-(Ce)) represents total replacement of high-Nd monazite-(Ce) by bastnäsite-(Ce). This paragenetic sequence (apatite→monazite→bastnäsite) has been documented in other REE-depositing hydrothermal systems, including that of Bayan Obo (Smith et al. 1999).

Textural relationships suggest that the high-Nd monazite-(Ce) (and bastnasite-(Ce)) is later than the low-Nd group, consistent with the smaller Eu anomalies in monazite-(Ce) in the former group (Fig 5). Together, these observations suggest a cooling-induced oxidation trend.

5.1 Inferred fluid compositions

The fluid responsible for the dissolution of apatite 1 and its reprecipitation as apatite 2 was likely Na-poor, as sodic fluids have been shown to suppress the removal of Na^+ (and REE^{3+}, to maintain charge balance) from apatite (Harlov 2015). Nonetheless, as the LREE were mobilized, the fluid was likely Cl^-- (or sulfate-)-enriched. The replacement of apatite by low-Nd monazite-(Ce) was likewise probably mediated by a Cl^- - and REE^{3+}-bearing fluid for reasons described above. The La and Ce in low-Nd monazite-(Ce) may have been supplied by the apatite 1 to apatite 2 dissolution-reprecipitation reaction. In contrast, preservation of the parent REE chemistry, suggests that the fluids responsible for the replacement of apatite 1 by high-Nd monazite-(Ce), and monazite-(Ce) by bastnäsite-(Ce) were poor in transport ligands. The latter replacement reaction must have been mediated by a F-bearing fluid, as F is an essential constituent of bastnäsite-(Ce) ($REECO_3F$). This is supported by the abundance of fluorite. Formation of bastnäsite-(Ce) was likely triggered by the availability of CO_3^{2-} (Migdisov et al. 2016) either in the fluid and/or interaction with the host carbonate rocks.

This sequence of reactions described above is consistent with progressive evolution of a carbo-hydrothermal fluid in response to cooling and fluid-rock interaction. The study emphasises the essential role that such fluids play in carbonatite-hosted REE ore genesis.

6 Conclusion

The REE mineralization at Ashram is hydrothermal in origin and was produced through a series of fluid-mediated replacement reactions. Dissolution-reprecipitation of apatite was an important process. The REE were mobile during the formation of apatite 2 and (possibly) the low-Nd monazite-(Ce). Together, the mineral paragenesis and chemistry suggest an overall cooling-induced oxidation. Ashram had a long-lived history in which the combination of magmatic zone-refinement and hydrothermal mobilization contributed to the formation of a potentially economic carbonatite-hosted REE deposit.

Acknowledgements

We would like to thank Commerce Resources Corp. and Dahrouge Geological Consulting Ltd. for providing access to the site and drill core, and DIVEX and Mitacs for providing funding for the research.

References

Buhn B & Rankin AH (1999) Composition of natural, volatile-rich Na-Ca-REE-Sr carbonatitic fluids trapped in fluid inclusions. Geochim Cosmochim Acta 63:3781-3797.

Harlov DE (2015) Apatite: A fingerprint for metasomatic processes. Elements 11:171-176.

McDonough WF, Sun SS (1995) The composition of the Earth. Chem Geol 120:223-253.

Migdisov AA, Williams-Jones AE, Wagner T (2009) An experimental study of the solubility and speciation of the Rare Earth Elements (III) in fluoride- and chloride-bearing aqueous solutions at temperatures up to 300°C. Geochim Cosmochim Acta 73:7087-7109.

Migdisov AA, William-Jones AE, Brugger J, Caporuscio FA (2016) Hydrothermal transport, deposition and fractionation of the REE: Experimental data and thermodynamic calculations. Chem Geol 439:13-42.

Moore M, Chakhmouradian AR, Mariano AN, Sidhu R (2015) Evolution of rare-earth mineralization in the Bear Lodge carbonatite, Wyoming: Mineralogical and isotopic evidence. Ore Geol Rev 64:499-521.

Putnis A (2009) Mineral replacement reactions. Rev Mineral Geochem 70:87-124. doi: 10.2138/rmg.2009.70.3.

Smith MP, Henderson P, Zhang P (1999) Reaction relationships in the Bayan Obo Fe-REE-Nb deposit Inner Mongolia, China: implications for the relative stability of rare-earth element phosphates and fluorocarbonates. Contrib Mineral Petrol 134:294-310.

Trofanenko J, Williams-Jones AE, Simandl GJ, Migdisov AA (2016) The nature and origin of the REE mineralization in the Wicheeda carbonatite, British Columbia, Canada. Econ Geol 111:199-223.

Xie Y, Li Y, Hou Z, Cooke DR, Danyushevsky L, Dominy SC, Yin S (2015) A model for carbonatite hosted REE mineralisation – the Mianning-Dechang REE belt, Western Sichuan Province, China. Ore Geol Rev 70:595-612.

A mesothermal greisen-hosted Sn-Zn-Cu-Ag-In deposit at East Kemptville, Nova Scotia, Canada

Luke Bickerton, Daniel J. Kontak
Laurentian University, Ontario, Canada

Iain M. Samson
University of Windsor, Ontario, Canada

J. Brendan Murphy
St. Francis Xavier University, Nova Scotia, Canada

Abstract. The 375 Ma South Mountain Batholith (8000 km^2) is a large syn- to post-tectonic composite intrusion of metaluminous to peraluminous plutons; several of which are highly evolved and mineralized (Sn-W-Mo-U). Only one, the Davis Lake, hosts significant mineralization in the East Kemptville Sn-Cu-Zn-Ag-In greisen-style deposit. Two main ore zones, the Baby and Main, have ore-grade greisens but dissimilar lithological characteristics. The Main Zone mineralization is concentrated along a NE-trending, sub-vertical fault zone, whereas the Baby Zone mineralization occurs beneath magmatic-hydrothermal breccias localized along the same fault zone. Mineralization resulted from the exsolution of metal-bearing orthomagmatic fluids from a near-crystallized melt at high pressure and temperature (ca. 3.5-4 kbars and ~650°C) that interacted with the host granite and little, if any, input of other fluids; hence it is similar to other greisen-style deposits. Unique to this deposit, however, is the interpreted depth of ore precipitation (ca. 3.5 kbars), which is ca. 2 kbars higher than typical greisen-style deposit formation. This high P during formation and its status as the only significant tin occurrence in a large batholith with multiple highly evolved plutonic centres, makes the deposit an outlier on the global scale.

1 Introduction

The nature of tin deposits has been described extensively in the literature for over 150 years (e.g., Taylor, 1979; Heinrich, 1990; Lehmann, 1990). The variable character of tin deposits has generated a range of classifications, each with an epigenetic magmatic inference. Various features can be applied to describe different tin deposit styles: 1) mineralization is associated with highly fractionated felsic intrusions and subvolcanic rocks that are enriched in lithophile elements (e.g., Černy et al., 2005), 2) deposits are concentrated provincially into metallogenic districts (e.g., South East Asia, western Europe [Erzgebirge to Cornwall], Central Andes), and 3) the depth of mineralization is typically 2-4 km for intrusion-proximal deposits and 0.35-2 km for subvolcanic deposits (Taylor, 1979).

In comparison to other tin provinces, eastern Canada has fewer major tin deposits, East Kemptville (EK) being the only past-producer. This Sn-Cu-Zn-Ag-In deposit in southwestern Nova Scotia has features that differ from the characteristics prevalent in primary tin deposits. Primarily, these differences are its apparent depth of formation (i.e., ca. 3.5 kbars) and its apparent isolation with respect to significant mineralization across an entire batholith of 8000 km^2. Additional data and insights into the nature and genesis of mineralization in the EK deposit and its regional setting are being investigated to determine the controls and therefore distribution of mineralization in the district. Here we focus on geology of the ore zones and the hydrothermal evolution and origin of mineralizing fluids.

2 Geological setting

2.1 Regional geology

A variety of base- and rare-metal mineralized centres, including Cu, Sn, W-Mo, Sb and Ta, are associated with widespread granitic magmatism in the Canadian Appalachians (e.g., van Staal, 2007). These deposits range in age from ca. 410 to 360 Ma and extend from Atlantic Canada into eastern Quebec, varying from shallow porphyry and epithermal systems (e.g., Lake George Sb, NB; Gaspé Cu-Mo, QC) to mesothermal granite-hosted greisens and veins (EK). Other deposits that host Sn in this region are commonly found in shallow porphyry to epithermal systems (e.g., Ackley greisen deposit, NFLD, Mt. Pleasant greisen, vein and breccia deposit, NB).

Southern Nova Scotia is predominantly underlain by metasedimentary and granitoid rocks. The former is the extensive Meguma Supergroup, an Ediacaran to Early Ordovician package of metasandstones and metasiltstones/slate (White, 2010). The sedimentary package was deformed during the ca. 410-380 Ma Acadian orogeny (i.e., Neoacadian of van Staal, 2007), which recorded dextral oblique translation of the Meguma terrane along the eastern Laurentian margin (Fig. 1). During the waning stages of this event (ca. 375 Ma), the Meguma was intruded by metaluminous to peraluminous granitoids of the voluminous (~8000 km^2) South Mountain Batholith (SMB; Fig. 1). Field studies indicate basement structures controlled the emplacement of the SMB and were important conduits for later mineralizing fluids (e.g., Horne et al., 1992; Kontak, 1994; MacDonald, 2001).

Detailed mapping of the SMB (MacDonald, 2001) revealed the batholith to be a composite, multi-phase

intrusive complex with an outer primitive zone of somewhat foliated granodiorite that was intruded by more evolved leucogranitoid plutons. The most westerly of these evolved plutons is the 800 km^2 Davis Lake Pluton (DLP), which contains the EK deposit. Rare- and base-metal mineralization is present in the SMB and other similar-aged felsic intrusions in the Appalachians. There have not been, however, any other significant discoveries of Sn-mineralized centres in the batholith which makes the SMB a metallogenic anomaly, unusual for Sn-enriched regions (see Lehmann, 1990 and references therein).

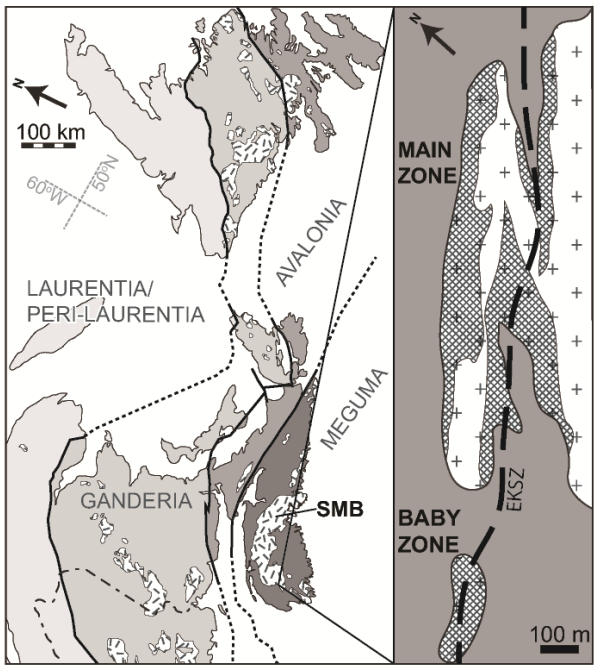


Figure 1. Eastern Canadian Appalachian terrane map (left) showing Devonian-Carboniferous intrusions (after Hibbard et al., 2006). Inset shows a bedrock geology at East Kemptville (right) with the leucogranites, metasedimentary wallrocks (grey), extent of the greisens (hatched) and the two ore zones (Main and Baby).

2.2 Deposit geology

Several studies have constrained the formation of the EK deposit (e.g., Richardson, 1988; Kontak, 1990; Halter et al., 1996) and evolution of the DLP (Dostal and Chatterjee, 1995). The ca. 375 Ma DLP is zoned, from an early biotite granodiorite to a highly fractionated (i.e., Rb, Li, U, F, Ta and Sn rich) biotite muscovite leucomonzogranite, which gives way to the EK topaz-muscovite leucogranite (EKL). The EKL has a distinct geochemical signature (depleted ΣREE, low $(La/Sm)_N$ and Nb/Ta; Kontak, 1990), stockscheider-type pegmatites, and miaroles, locally lined with cassiterite (Kontak et al., 2001; Fig. 2). These features suggest EK was a product of crystal-fluid fractionation of the DLP which generated an evolved melt and related metal-rich fluid responsible for mineralization (e.g., Halter et al., 1996).

Two ore zones, the Main (MZ) and Baby (BZ) (Fig. 2), make up the deposit and combined to give initial estimated reserves of 56 Mt @ 0.17% Sn (Richardson et al., 1982); however, the relationship between the two ore zones remains poorly documented. Both zones contain the same element suite (Sn, Zn, Cu, Ag and In) and both are localized to a NE-trending structural corridor, the East Kemptville shear zone (EKSZ, Fig. 1; 2), but the character of the host rocks and ore grades are dissimilar. The MZ is primarily hosted by the EKL and its highest grades are present along the EKSZ, whereas the higher-grade, lower tonnage BZ is locally hosted by a magmatic-hydrothermal breccia and is possibly related to a different intrusive pulse, as indicated by lithogeochemical data (Fig. 3).

Cassiterite, the principal Sn ore mineral, occurs in both zoned and massive greisens. Zoned greisens have symmetrical alteration haloes about a central quartz-cassiterite vein; they represent progressive alteration of the EKL from a muscovite-leucogranite to sericite-albite-quartz and quartz-topaz greisens, with subhedral cassiterite in the latter. The massive greisens typically have inconsistent mineral assemblages, ranging from dominantly quartz-topaz, quartz-mica, phengite-zinnwaldite, to quartz-chlorite; each may contain disseminated to patchy cassiterite of variable grain-size and habit. The In-enriched Cu-Zn sulfide stage post-dates greisenization and occurs either as micro-veins filling dissolution features in massive greisens, or as larger veins.

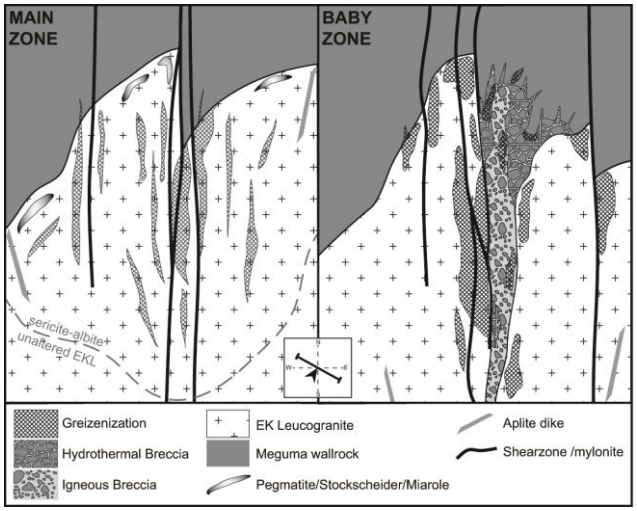


Figure 2. Schematic geologic cross-sections of the two ore zones at the EK deposit. Note the presence of discontinuous greisens and ductile deformation in the Main Zone, whereas the Baby Zone displays breccias and massive greisen development.

3 Sampling and methodology

Samples were collected during logging of drill core from the deposit and were used in tandem with archived samples from previous work (i.e., Kontak, 1990). Down-hole geochemical data was provided by Avalon Advanced Materials Inc.

Quartz- and topaz-hosted fluid inclusions (FI) of indeterminate origin (Bodnar 2003) from greisens and veins were used for thermometry. The data were collected

using a Linkham THMSG600 heating-freezing stage at Laurentian University. A scanning electron microscope (SEM) with energy dispersive X-ray spectroscopy (EDS) at Laurentian University was used for mineral identification and chemistry, greisen textures, and evaporate mound chemistry.

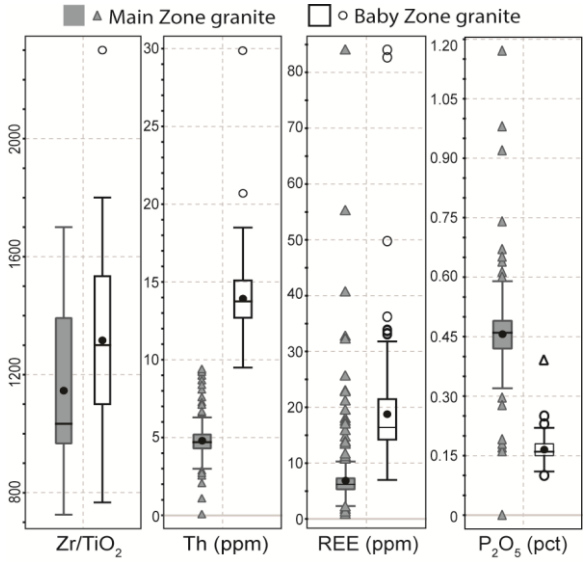


Figure 3. Select Tukey box-plots of relatively unaltered granite samples from two ore zones at EK (unpublished geochemical data, Avalon Advanced Materials Inc.).

4 Results

The ore zones at EK have dissimilar size, ore tenor, geology and geochemistry. The large MZ has abundant discontinuous zoned greisens that are dominantly fracture controlled and parallel to a through-going fault zone. The host rock to the MZ quartz-topaz greisens is a fine- to medium-grained, sericitized leucogranite with alteration grading to albitization at depth; it is relatively unaltered by approx. 200 m below surface. The host to the BZ is similar to the latter rock at depth, however the near-surface granite-wallrock transition is unique to the deposit area. This transition is a pervasively altered igneous breccia with a quartz-phyric matrix that is locally intermingled with a clast-supported hydrothermal breccia with a quartz-mica cement. The granite beneath the breccia zone hosts massive greisens with variable thickness, ore concentration, and greisen orientation.

The geochemistry of ore-hosting granite in each zone is also slightly contrasting. The granites are indistinguishable in hand sample and major element chemistry due to extensive alteration, but subtle differences in their trace element chemistry indicate a spatial variation in the granite composition between the MZ and BZ (Fig. 3). The BZ granites, relative to those of the MZ, are depleted in P_2O_5 and markedly more enriched in Th and REE.

Examination of FI in the EKL and ore-bearing samples reveals abundant decrepitated fluid inclusions. Where unmodified, fluid inclusion assemblages (FIAs) are seen with FIs that are equant and 5-15 µm in size. Three main FIAs are present: (1) two phase $L_{H2O}+V_{H2O}$, (2) three phase $L_{H2O}+V_{H2O}$+halite, and (3) hypersaline $L_{H2O}+V_{H2O}$+H ± other solid phases. Low temperature observations indicate the rare presence of a $CO_2 \pm CH_4$-bearing inclusion type, but only in vein samples. As further study is required to define this inclusion type, it is not discussed. Types 2 and 3 are mainly in the EKL and associated pegmatites; these have salinities ≤ 38 wt. % equiv. NaCl. Greisen and vein FIAs have salinities of 10-23 wt. % equiv. NaCl, with a depressed eutectic. This suggests the presence of divalent cations such as Fe, which has been confirmed with decrepitate mound analysis (Fig. 4). Homogenization temperatures (T_h) for inclusions vary across the paragenesis: for the EKL T_h = 258-393ºC, for the EK greisens Th = 220-313ºC, and for sulfide-bearing veins Th = 280-317ºC.

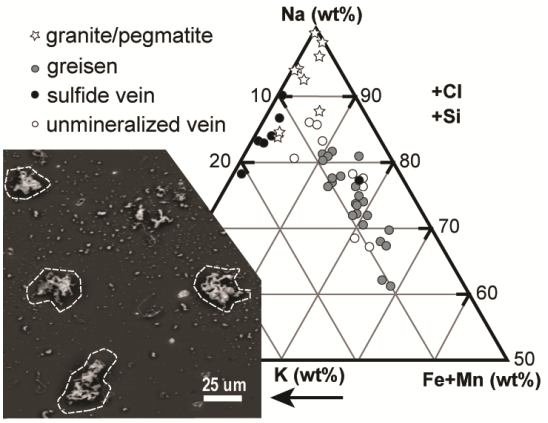


Figure 4. SEM-BSE image of evaporate mounds from decrepitated fluid inclusions on quartz surface (left). Dashed outlines are areas rastered for EDS analyses. Salinities were used as an internal standard to calculate the weight % of elements measured in FIAs from each stage of the paragenesis (right).

5 Discussion

The EK ore zones accommodate mineralization in different ways. Preliminary interpretation of the trace-element geochemistry of the host granites in both ore zones suggest these are separate, although mineralogically and texturally similar, intrusive events. The MZ contains ductile deformation, protracted with respect to mineralization, and ore grade is closely related to these shear zones; the BZ, on the other hand, displays brittle deformation (breccias) and its ore grade does not clearly favor local shear zones. Greisen style (massive versus zoned) is not exclusive to either ore zone, however the zoned greisens in the MZ are predominantly restricted to discontinuous fractures and massive greisens identified in this zone may be an example of coalesced zoned greisens. Conversely, the BZ contains pervasive greisens beneath the wallrock contact that show variable mineralogy and morphology. More work is required to determine if these differences reflect multiple mineralizing events, or changing P-T-X conditions of fluids across the deposit.

Isochores for FIAs in the EKL (+pegmatites), greisens and sulfide-bearing veins are compared to H_2O-saturated and F-rich granite solidi in Figure 5. Based on the intersection of the isochores with the solidi, the estimated depth of emplacement for the SMB (ca. 3.5 kbars; Kontak and Kyser, 2011) is shown as a likely upper constraint on the pressures for EK. A dominant mineralizing fluid of moderate salinity (25-28 wt. % NaCl-$FeCl_2$) has a P-T path consistent with a fluid that equilibrated after exsolving from a near-crystallized melt at high pressure and temperature (ca. 3.5-4 kbars and ~650°C). Subsequent formation of cassiterite-bearing pegmatites at ~500°C was followed by greisen-formation at 600-400°C. These conditions are unusual for Sn deposits, which generally form at shallow depths (< 1 kbar; Taylor, 1979).

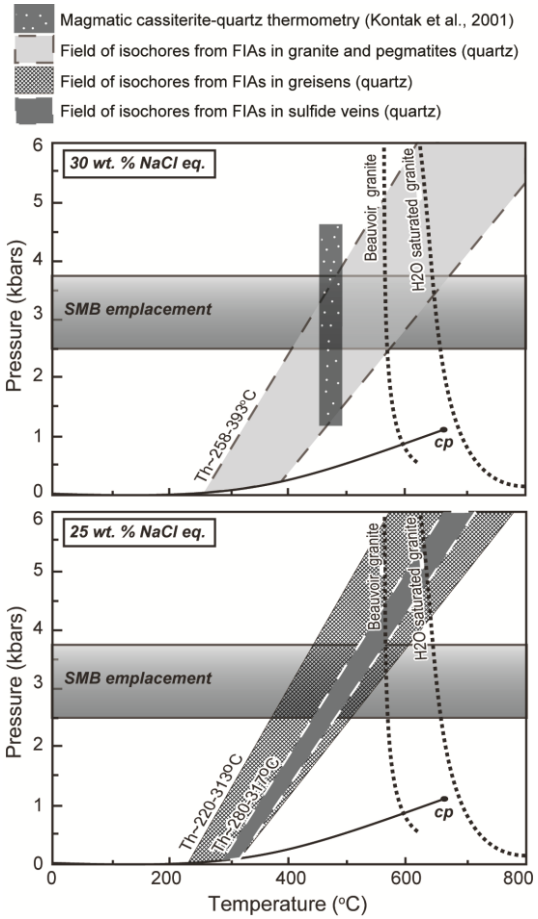


Figure 5. P-T plots with isochores (from T_h on LV-curve) for FIAs in the EKL (above) and mineralized greisens and veins (below); calculated using ISOC (Bakker, 2003). Calculated cassiterite-quartz thermometry from EK pegmatites is shown (Kontak et al., 2001) in addition to the estimated emplacement P for the SMB, the solidi of volatile-rich granites (H_2O-saturated, Tuttle and Bowen, 1958; F-rich, Cuney et al., 1992).

Acknowledgements

This study is supported by a NSERC-CRD grant co-funded by Avalon Advanced Materials, Inc.

References

Bakker RJ (2003) Package FLUIDS 1. Computer programs for analysis of fluid inclusion data and for modelling bulk fluid properties. Chemical Geology 194: 3-23.

Bodnar RJ (2003) Introduction to fluid inclusions. In Samson, I, Anderson, A., and Marshall, D (eds.) Fluid Inclusions: Analysis and Interpretation. MAC, Short Course 32: 1-8.

Černý, P, Blevin, PL, Cuney, M, London, D (2005) Granite related ore deposits. Econ Geology 100th Anniversary Volume, 337–370.

Cuney, M, Marignac, C, Weisbrod, A (1992) The Beauvoir topaz-lepidolite albite granite; the disseminated magmatic Sn-Li-Ta-Nb-Be mineralization. Econ Geol 87(7): 1766-1794.

Dostal, J, and Chatterjee, AK (1995) Origin of topaz-bearing and related peraluminous granites of late Devonian Davis Lake pluton, Nova Scotia, Canada. Chemical Geology 123: 67–88.

Halter, WE, Williams-Jones, AE and Kontak, DJ (1996) The role of greisenization in cassiterite precipitation at the East Kemptville tin deposit, Nova Scotia. Econ Geol 91: 368-385.

Heinrich, CA (1990) The chemistry of hydrothermal tin(-tungsten) ore deposition. Econ Geol 85: 457-481.

Hibbard, JP, van Staal, CR, Rankin, DW, and Williams, H, (2006) Lithotectonic map of the Appalachian orogen (South), Canada–United States of America: Geological Survey of Canada Map 02096A, 2 sheets: 1:1,500,000.

Horne, RJ, MacDonald, MA, Corey, MC, and Ham, LJ (1992) Structure and emplacement of the South Mountain Batholith, soutlwestern Nova Scotia. Atlantic Geology 28: 29-50.

Kontak, DJ (1990) The East Kemptville topaz-muscovite leucogranite, Nova Scotia. I. Geological setting and whole rock geochemistry. Canadian Mineral 28: 787–825.

Kontak, DJ (1994) Geological and geochemical studies of alteration processes in a fluorine-rich environment: the East Kemptville Sn-(Zn-Cu-Ag) deposit, Yarmouth County, Nova Scotia, Canada. In Lentz, DR (ed.) Alteration and Alteration Processes associated with Ore-forming Systems: GAC SC Notes 11: 261-314.

Kontak, DJ, Dostal, J, Ansdell, K, Halter, W, Martin, RF, and Williams-Jones, AE (2001) The nature and origin of pegmatite in a fluorine-rich leucogranite, East Kemptville, Nova Scotia. Transact of the Royal Society of Edinburgh: E Sci 92: 173-2000.

Kontak, DJ and Kyser, TK (2011) Fingerprinting multiple fluid reservoirs in a 380 Ma Intrusion-Related Gold (IRG) setting, Nova Scotia, Canada: Implications for the nature and origin of IRG deposits. Mineralium Deposita 46: 337-363.

Lehmann, B (1990) Metallogeny of Tin. Springer, Berlin.

MacDonald, MA (2001) Geology of the South Mountain Batholith, southwestern Nova Scotia. NSDNR Open File Rep ME2001-2.

Richardson, JM (1988) Field and alteration relationships of alteration and greisen-hosted mineralization at the East Kemptville tin deposit, Davis Lake monzogranite, southwest NS, Canada. In Granite related mineral deposits. Taylor, RP, and Strong, DF (eds) Cdn Inst of Mning and Metallur, Spcial 39: 265 -279.

Richardson, JMG, Spooner, ETC, and McAuslan, DA (1982) The East Kemptville tin deposit, Nova Scotia: an example of a large tonnage, low grade, greisen-hosted deposit in the endocontact zone of a granite batholith: GSC Current Research: 27-32.

Taylor, RG (1979) Geology of Tin Deposits. Elsevier, Amsterdam.

Tuttle OF, Bowen NL (1958) Origin of granite in light of experimental studies in the system $NaAlSi_3O_8$–KAl–Si_3O_8–H_2O. Geol Soc Am Mem 74: 153.

van Staal, CR (2007) Pre-Carboniferous tectonic evolution and metallogeny of the Canadian Appalachians. In Mineral Deposits of Canada, Goodfellow, WD (ed), GAC, SP 5: 793-818.

White, CE (2010) Stratigraphy of the Lower Paleozoic Goldenville and Halifax groups in southwestern Nova Scotia. Atl Geol 46: 136-154.

Semi-metal and base metal mobility in the metasedimentary contact aureole surrounding the Dublin Gulch reduced intrusion-related gold system (RIRGS), Yukon, Canada

Ben J. Cave, Sarah-Jane Barnes
Université du Québec à Chicoutimi, Québec, Canada

Patrick J. Sack
Yukon Geological Survey, Canada

Iain K. Pitcairn
Stockholm University, Sweden

Sean C. Johnson
CODES ARC Centre of Excellence in Ore Deposits, University of Tasmania, Australia

Helena Kuikka
Victoria Gold Corp.

Abstract. Precious, semi-, and base metals have been shown to be mobilised from metasedimentary rocks during prograde metamorphism. These form an important source of metals for orogenic gold systems. Similar metal enrichments are observed in reduced intrusion-related gold systems (RIRGS) hosted in the Selwyn basin area. However, no assessment has previously been attempted to determine whether prograde metamorphism of the surrounding metasediments could represent an important metals source for RIRGS. In this study, we focus on the availability and mobilisation of semi- and base metals through mineral reactions occurring in the contact aureole around the Dublin Gulch RIRGS. Pyrite and chlorite are observed in the regionally metamorphosed rocks dominating the semi- and base metals budget. During contact metamorphism, these recrystallise to pyrrhotite and chalcopyrite, and biotite, respectively. These mineral phases contain significantly lower concentrations of metals, compared to their precursor minerals (except Cu and Zn in chalcopyrite). Whole rock geochemistry shows that relative to the contact metamorphosed rocks, the regionally metamorphosed rocks are enriched in As, Sb, Te, Bi, Pb, Zn, and H_2O. This suggests, mobilisation of these elements has occurred, possibly as a metal-rich fluid that could provide an alternative or additional metal source for RIRGS.

1 Introduction

Marine clastic metasedimentary rocks have been the focus of several recent studies (e.g., Pitcairn et al, 2006, 2010 2014; Large et al, 2011, 2012; Hammerli et al, 2016; Thomas et al, 2011; Cave et al, 2015, 2016) on local- and regional- scale trace element mobility associated with regional or contact prograde metamorphic events.

Mineralogical changes with prograde metamorphism are crucial in explaining the mobilisation of trace elements. In the studies of the Otago and Alpine schists, diagenetic or detrital metal-rich mineral phases recrystallise with prograde metamorphism [pyrite to pyrrhotite: Au, As, Ag, Hg, Sb and Mo (Pitcairn et al, 2006, 2010, 2014; Large 2012); rutile to titanite: W (Cave et al, 2015, 2016)]. During this recrystallisation a significant proportion of these metals have been shown to be released into concurrently developing metamorphic fluids that can subsequently be structurally focused to form orogenic gold systems (e.g., Pitcairn et al, 2006, 2010 2014; Large et al, 2011, 2012; Hammerli et al, 2016; Thomas et al, 2011; Cave et al, 2016).

The same prograde mineral recrystallisation reactions are observed in the Selwyn basin area, in contact aureoles associated with reduced intrusion-related gold systems (RIRGS) (e.g., Maloof et al, 2001). This class of deposit forms an important source for global gold, and area also enriched in significant quantities of other metals, including W, As, Te, Sb, Bi, Pb, and Zn (Maloof et al, 2001). Metal source models for RIRGS predominantly suggest metals are derived from the same source regions as the magmas (e.g., Hart et al, 2004). However, the potential that contact metamorphism could provide a significant amount of these metals to RIRGS has not been assessed. In addition, the assimilation of country rock metasediments has been shown to introduce semi- and base metals into magmas (e.g., Samalens et al, 2017), and may provide an additional or alternative source for these metals to RIRGS. This study, aims to establish the framework for future work to address this. Critical to this is understanding metal availabilities in the metasediments. The Yusezyu Formation of the Selwyn basin area, north western Canada (Fig. 1) provides an excellent natural laboratory in which to test this hypothesis. With the Yusezyu Formation hosting numerous RIRGS, being accessible for study, and importantly simplifying this study to one formation.

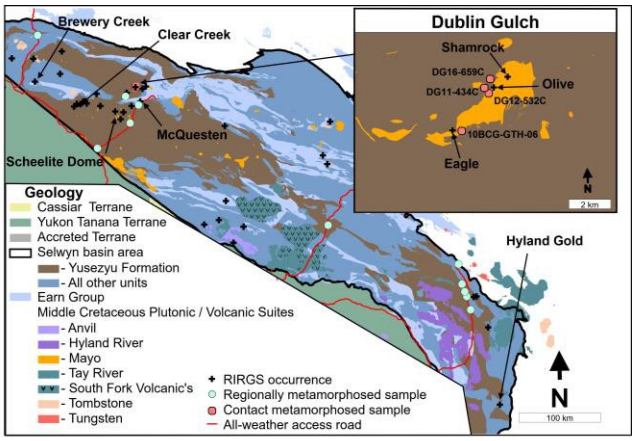


Figure 1. Geological map of the Selwyn basin area (outlined in heavy black) and selected adjacent terranes.

2 Geological setting

The Selwyn basin area (Fig 1) is an extensive Neoproterozoic to Siluro-Devonian continental margin basin that developed on the western margin of Ancestral North America (Gordey and Andersen, 1993). Comprised of a thick (up to 6.65 km) sequence of variably metamorphosed Neoproterozoic to Siluro-Devonian turbiditic metasandstones, shales, and limestones (Gordey and Anderson, 1993; Murphy, 1997). Stratigraphy in the Selwyn basin area is divisible into two groups and seven formations. These are, the Neoproterozoic to Lower Cambrian Hyland Group (Yusezyu, Algae Lake, and Narchilla formations), the Lower Cambrian Gull Lake Formation, the Cambro-Ordovician Rabbitkettle Formation, and the Ordovician-Silurian Road River Group (Duo Lake and Steel Formations) (Gordey and Andersen, 1993). Unconformably overlying the Selwyn basin stratigraphy, and included here in the Selwyn basin area stratigraphy, is the Devono-Mississippian Earn Group (Gordey and Andersen, 1993).

Rocks of the Selwyn basin area are part of the Selwyn fold belt, a domain deformed and metamorphosed (sub-greenschist to middle greenschist facies) during the Jurassic-Cretaceous period, as a response to the accretion of the Yukon- Tanana to the continental margin (Mair et al, 2006). Numerous post-tectonic, mainly mid-Cretaceous (96–90 Ma; Hart et al, 2004) granitic plutons (e.g., the Tay River, and Tombstone suites) intrude the Selwyn basin area. Compositionally these plutons vary, however, an overall trend of subalkalic and weakly to strongly alkalic intrusions is recognised in the western to southern and northern and eastern Selwyn basin area, respectively (Rasmussen et al, 2010). These correspond to the Hyland-Anvil and Tay River suites in the western to southern Selwyn basin area, and the Tungsten, Mayo, and Tombstone suites in the northern and eastern Selwyn basin area (Rasmussen et al, 2010). Around these mid-Cretaceous plutons, contact aureoles are developed that overprint regional structures and metamorphic isograds.

Associated with these intrusions are numerous RIRGS that are observed throughout the Selwyn basin area. These RIRGS form the eastern portion of the globally significant Tintina Gold Belt (TGB). Past production and *in situ* resources from placer and hard rock deposits in the TGB exceeds 1700 tonnes of Au. Dublin Gulch is the most significant RIRGS in the Selwyn basin area, containing constrained in-pit resources of 100 tonnes Au (at 0.63 g/t) (Victoria Gold Corp, 2016). Mineralisation at Dublin Gulch, is typical of many RIRGS in the Selwyn basin area. The deposit is hosted within sheeted veins in the Dublin Gulch granodiorite and contact metamorphosed metasediments (Yusezyu Formation), and is characterised by enrichments in precious (Au, Ag), semi- (As, Te, Sb, Bi), and base metals (Mo, W, Pb, and Zn), with Au having a strong correlation with Bi ($r^2 = 0.9$) (Maloof et al, 2001).

3 Methodology

3.1 Sample selection and analytical techniques

Regionally metamorphosed Yusezyu Formation samples were obtained along the Dempster Highway, Silver Trail Highway, access road to Dublin Gulch, Canol Road, Nahanni Range Road, and from unmineralised sections of drillholes at the 3Aces orogenic gold occurrence (Fig. 1). Contact metamorphosed samples were taken from drillholes in the contact aureole surround the Dublin Gulch granodiorite (Fig. 1).

Mineralogical and textural associations in the samples (n 29) were examined under reflected and transmitted light, and under scanning electron microscope (SEM).

Laser ablation traverses were performed using a 100 μm beam moving at 100 μm/s relative to the sample at a repetition rate of 10 Hz and fluence of 2.5 J/cm^2. Traverses were conducted perpendicular to the major bedding/foliation. Laser ablation traverses were used to evaluate the distribution of elements of interest among mineral phases, to aid the identification of important metal-rich mineral phases.

Trace element compositions of pyrite (Py; n 180), pyrrhotite (Po; n 67), chalcopyrite (Ccp; n 18), chlorite (Cld; n 15), and biotite (Bt; n 7) were determined by LA-ICP-MS spot analyses from samples (n 29) distributed throughout the Selwyn basin area (Fig. 1). These *in situ* analyses were performed using a Resonetics Resolution laser ablation system equipped with a Coherent COMPex Pro 110 ArF Excimer laser, housed at CODES/Earth Sciences, University of Tasmania. The ArF excimer laser operates at a 193-nm wavelength with a 20-ns pulse width and was coupled to an Agilent 7700 quadrupole inductively coupled plasma mass spectrometer (ICP-MS). Quantitative LA-ICP-MS trace element analyses were performed following methods described by Gregory et al, (2015) for sulphide minerals, and methods described in Cave et al, (2016) for other minerals.

Whole rock and select trace element analyses were performed on regionally (n 31) and contact metamorophsed (n 9) samples by Actlabs and LabWest on XRF discs and pellets, and multiacid digestions finished

with either ICP-OES or ICP-MS depending on the element. LOI was performed gravimetrically.

4 Results

4.1 Metal-rich mineral phases

Regionally metamorphosed samples: Laser ablation traverses completed on representative psammitic and pelitic samples, show irregular distributions of most trace elements, however some trends are recognised. Relatively high levels (counts per second; cps) of As, Sb, Te, Bi, Cu, Pb, and Zn predominately appear to correspond to relatively high levels in Fe and S. Reflected light microscopy shows these relatively high levels of As, Sb, Te, Bi, Cu, Pb, and Zn, as corresponding to the laser beam having passed through grains of pyrite. Zinc additionally appears as relative high levels at periods with corresponding relatively high levels of Mg, Al, Fe, and Si, with these corresponding to the laser beam having passed through chlorite lathes. Laser spot analyses show pyrite contains appreciable amounts of all these metals (Table 1), whereas chlorite contains significant amounts of Zn (Table 1).

	Unit	As ppm	Sb ppm	Bi ppm	Te ppm	Cu ppm	Pb ppm	Zn ppm
Py (n 180)	Min	<2.8	<0.19	<0.020	<0.082	<0.27	0.518	<0.35
	Max	11235	296	144	19.1	3521	3781	8537
	Median	612	22	3.5	1.5	237	216	21
Po (n 67)	Min	<1.4	<0.081	<0.020	<0.14	<0.84	<0.067	<0.48
	Max	37	7.3	18.8	5.8	5.3	53	4.4
	Median	<2.6	<0.20	0.67	<0.55	<2.2	0.57	<0.92
Ccp (n 11)	Min	<10.6	<0.37	<0.095	<0.92	340982	<0.40	475
	Max	<24	5.1	9.7	3.6	418599	16.9	822
	Median	<14.3	0.74	1.4	<1.3	360034	1.7	667
Cld (n 15)	Min	<5.8	<0.22	<0.074	<0.33	<2.3	<0.78	345
	Max	12.1	<0.79	0.322202	<6.0	22	7.3	952
	Median	<9.7	<0.66	<0.19	<2.3	<5.4	1.2	713
Bt (n 7)	Min	<8.5	<0.52	<0.02	<0.72	<3.7	<0.68	226
	Max	<13.3	<1.07	<0.29	<3.5	10.4	4.1	387
	Median	<9.3	<0.78	<0.16	<1.9	<4.9	0.88	335

Table 1. Minimum, Maximum, and median values for select mineral phases determined by LA-ICP-MS.

Contact metamorphosed samples: Laser ablation traverses completed on representative psammitic to pelitic biotite-bearing contact metamorphosed samples from Dublin Gulch, show extremely heterogeneous distributions of As, Sb, Te, Bi, Cu, Pb, and Zn. Distribution of these elements systematically vary with metamorphic textures, with these elements generally below detection in the quartz-albite segregations, whereas being detectable in the biotite ± mica segregations. In the quartz-albite and biotite ± mica metamorphic segregations large pyrrhotite grains with associated chalcopyrite are observed. When the laser beam passed over these grains relatively high levels (cps) of As, Sb, Te, Bi, Cu, Pb, and Zn are observed. However, *in situ* analyses shows these elements are significantly lower in pyrrhotite and chalcopyrite, relative to pyrite (from which it formed), except Cu and Zn in chalcopyrite (Table 1). Zinc is also present in relatively high levels (cps) at periods that corresponding with relatively high levels (cps) of Mg, K, Al, Fe, and Si, with SEM showing these as corresponding to the laser beam having passed through biotite lathes. Spot analyses performed on biotite show it contains significant amounts of zinc, however significantly less than chlorite (from which it formed) (Table 1).

4.2 Semi-metal, base metal, and volatile concentrations in whole rock

The Yusezyu Formation metasediments show heterogeneity in whole rock concentrations among individual samples, however, overall trends are recognised. Median values reveal regionally metamorphosed samples contain appreciable concentrations of As (28.4 ± 24.5 ppm), Bi (0.32 ± 0.26 ppm), Sb (3.4 ± 3.8 ppm), Te (0.09 ± 0.08 ppm), Pb (33.0 ± 24.3 ppm), and Zn (100.0 ± 29.2 ppm) that are all significantly higher than concentrations observed in the contact metamorphosed samples (As, 10.5 ± 7.7 ppm; Bi, 0.17 ± 0.12 ppm; Sb, 1.1 ± 2.2 ppm; Te, 0.03 ± 0.01 ppm; Pb, 11.2 ± 6.4 ppm; Zn, 65.1 ± 24.0 ppm). In contrast, Cu concentrations are observed being relative enriched, but more heterogenous in the contact metamorphosed samples (53.4 ± 31.6 ppm) relative to the regionally metamorphosed samples (42.2 ± 12.6 ppm). Sulphur median values are similar between the regionally metamorphosed samples (1.2 ± 1.2 wt %) and contact metamorphosed samples (1.1 ± 1.0 wt %).

Loss on ignition (LOI) values represent the loss of volatile phases (e.g., organics, H_2O, CO_2, and S) during high-temperature heating of the samples. These values are often used to show the potential of rocks to produce fluid (H_2O) during prograde metamorphism. Loss on ignition (LOI) values are significantly lower in the contact metamorphosed samples (2.1 ± 1.1 wt %) than in the regionally metamorphosed samples (5.9 ± 1.7 wt %). We suggest this indicates a significant proportion was lost as H_2O.

5 Discussion and conclusion

Mineral reactions are crucial in explaining the mobility of trace elements in metasediments during prograde metamorphism. In the regionally metamorphosed Yusezyu Formation samples, pyrite and chlorite are the most important host phases for semi- (As, Sb, Te, and Bi) and base metals (Cu, Pb, and Zn). Through prograde metamorphism these are converted to pyrrhotite and chalcopyrite, and biotite, respectively. These minerals contain significantly lower concentrations of semi- and base metals relative to the minerals from which they formed from (except for Cu and Zn in chalcopyrite), suggesting these mineral reactions make these metals available for mobilisation.

Whole rock concentrations show that relative to the contact metamorphosed samples, the regionally metamorphosed samples contain significantly higher concentrations of As, Sb, Te, Bi, Pb, and Zn (Fig. 2), and slightly higher concentrations of S (Fig. 2). Whereas Cu appears to be enriched (Fig. 2). Leaching of elements by

concurrently produced metamorphic fluids, can efficiently mobilise elements from metasedimentary rocks during prograde metamorphism (e.g., Pitcairn et al., 2006, 2010; Hammerli et al. 2016). We suggest the significantly lower LOI values in the contact metamorphic samples (Fig. 2) reflects significant metamorphic fluid production that likely leached elements made available through mineral recrystallisation reactions.

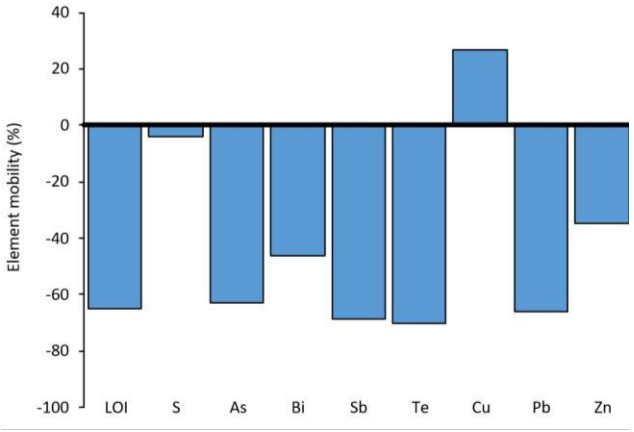


Figure 2. Element mobility diagram, showing percentage loss or gain of selected trace elements and the volatiles.

Mobilisation of this suite of elements could provide an alternative or additional metal source for RIRGS. Furthermore, the early assimilation of regionally metamorphosed sediments or later assimilation of contact metamorphosed sediments, could provide metals to the RIRGS. However, the assimilation of regionally metamorphosed metasedimentary rocks could provide significantly greater amounts of metals that are observed enriched in these deposits. Further work is required to: (1) Understand whether the metal-rich metamorphic fluid produced in the contact aureole interacted with the causative magma and was an important metal source for the RIRGS; (2) Investigate whether the assimilated metal-rich metasediments were an important metal source for the RIRGS.

Acknowledgements

This study is part of a larger project funded by the Geological Survey of Canada through the TGI-5 grant program and the Canada Research Chair in Magmatic Ore Deposits. We also wish to acknowledge the Yukon Geological Survey and Victoria Gold Corp. for access and support for this project. Daniel Gregory, Leonid Danyushevsky, Sarah Gilbert, Ivan Belousov, and Elena Lounejeva are thanked for their assistance with the Laser Ablation Induced Coupled Plasma-Mass Spectrometer analyses.

References

Cave BJ, Stepanov AS, Craw D, Large RR, Haplin JA, Thompson J (2015) Release of trace elements through the sub-greenschist facies breakdown of detrital rutile to metamorphic titanite in the Otago Schist, New Zealand. Can Min 53:379–400

Cave BJ, Pitcairn IK, Craw D, Large RR, Thompson J, Johnson SC (2016) A metamorphic mineral source for tungsten in the turbidite-hosted orogenic gold deposits of the Otago Schist, New Zealand. Mineral Deposita (2016) doi:10.1007/s00126-016-0677-5

Gregory DD, Large RR, Halpin JA, Baturina EL, Lyons TW, Wu S, Danyushevsky L, Sack PJ, Chappaz A, Maslennikov VV, Bull SW (2015) Trace element content of sedimentary pyrite in black shales. Econ Geol 110:1389-410

Gordey SP, Anderson RG (1993) Evolution of the northern Cordilleran miogeocline, Nahanni map area (105I), Yukon and Northwest Territories. Geol Surv Can Mem 428: 1–214

Hammerli J, Spandler C, Oliver N (2016) Element redistribution and mobility during upper crustal metamorphism of metasedimentary rocks: an example from the eastern Mount Lofty Ranges, South Australia. Contrib Mineral Petr 171:36

Hart, CJR, Goldfarb RJ, Lewis LL, Mair JL (2004) The Northern Cordilleran Mid-Cretaceous Plutonic Province: Ilmenite/Magnetite-series Granitoids and Intrusion-related Mineralisation. Resour Geol 54:253–280

Pitcairn IK, Teagle DAH, Craw D, Olivo GR, Kerrich R, Brewer TS (2006) Sources of metals and fluids in orogenic gold deposits: insights from the Otago and Alpine Schists, New Zealand. Econ Geol 101:1525–1546

Pitcairn IK, Olivo GR, Teagle DAH, Craw D (2010) Sulfide evolution during prograde metamorphism of the Otago and Alpine Schists, New Zealand. Can Min 48:1267–1295

Pitcairn IK, Craw D, Teagle DA (2014a) The gold conveyor belt: largescale gold mobility in an active orogen. Ore Geol Rev 62:129–142

Large RR, Bull SW, Maslennikov VV (2011) A carbonaceous sedimentary source-rock model for carlin-type and orogenic gold deposits. Econ Geol 106:331–358

Large R, Thomas H, Craw D, Henne A, Henderson S (2012) Diagenetic pyrite as a source for metals in orogenic gold deposits, Otago Schist, New Zealand. NZ J Geol Geophys 55:137–149

Mair JL, Hart CJ, Stephens JR (2006) Deformation history of the northwestern Selwyn Basin, Yukon, Canada: Implications for orogen evolution and mid-Cretaceous magmatism. Geol Soc Am Bull 118:304-23

Maloof TL, Baker T, Thompson JF (2001) The Dublin Gulch intrusion-hosted gold deposit, Tombstone plutonic suite, Yukon Territory, Canada. Mineral Deposita 36:583 doi:10.1007/s001260100190

Murphy DC (1997) Geology of the McQuesten River region, northern McQuesten and Mayo map areas, Yukon Territory. Yukon Geol Surv. Bull 6:1–95

Rasmussen KL, Arehart GB, (2010) Preliminary O-S isotopic compositions of Cretaceous granitoids in the Cassiar Platform and Selwyn Basin, Yukon and Northwest Territories. Yukon Geol Surv 2010: 279-292

Samalens N, Barnes SJ, Sawyer EW (2017) The role of black shales as a source of sulfur and semimetals in magmatic nickel-copper deposits: Example from the Partridge River Intrusion, Duluth Complex, Minnesota, USA. Ore Geol Rev 81:173-87

Thomas HV, Large RR, Bull SW, Maslennikov V, Berry RF, Fraser R, Froud S, Moye R, (2011) Pyrite and pyrrhotite textures and composition in sediments, laminated quartz veins, and reefs at Bendigo gold mine, Australia: insights for ore genesis. Econ Geol

Victoria Gold Corp (2016) Victoria Gold: Fully Permitted Eagle Gold Project Feasibility Study Demonstrates Post Tax NPV of $508M and IRR of 29.5%. TSX release http://www.vitgoldcorp.com/i/pdf/nr/NR-2016-09-12.pdf accessed 22 Feb 2017

The role of pegmatites and acidic fluids for hydrothermal Zr and REE transport in the Strange Lake peralkaline granitic pluton

Alexander P. Gysi
Colorado School of Mines, U.S.A.

Abstract. Strange Lake is mid-Proterozoic peralkaline granitic pluton located in Quebec/Labrador, Canada. It is a world class REE-Zr-Nb mineral deposit host to two potential ore zones (the B zone and Main zone). Several studies have demonstrated that hydrothermal processes have played a significant role for metal mobilization and mineralization in this system (Salvi and Williams-Jones 2006, and references therein). The mineralization in the B zone occurs in pegmatite-rich domains, where it was shown that >90 % of the mineralized REE and Zr occurs in hydrothermal minerals with a significant secondary enrichment process (Gysi et al. 2016). The hydrothermal alteration can be spatially related to the pegmatites, which were interpreted to be the source of saline acidic HF-HCl-bearing fluids (Gysi and Williams-Jones 2013). I present here the different alteration types related to these pegmatitic fluids by combining field observations at the outcrop and thin section scales with mineral and bulk rock compositions to illustrate the effects of hydrothermal fluid-rock reactions on chemical mass fluxes and associated ore mineralization. Numerical modeling of fluid-rock equilibria is used to explore the controlling factors for REE and Zr mobilization in these hydrothermal fluids, and discuss the key factors affecting metal mobility at Strange Lake.

1 Field relations and alteration mechanisms

The B zone consists of numerous flat lying pegmatite sheets forming a mineralized pegmatite spine hosted in the peralkaline granite. The pegmatites are zoned (Fig. 1) into a core enriched in quartz, fluorite and light (L)REE-bearing minerals (i.e., REE fluorocarbonates), and a border at the contact to the granite, enriched in granitic minerals (quartz, arfvedsonite, K-feldspar) and zirconosilicates (i.e., pseudomorphs after elpidite host to Zr and HREE). The pegmatite spine also displays rock alteration textures and an associated hydrothermal REE/Zr mineralogy interpreted to be related to acidic pegmatitic fluids that led to an "auto-metasomatism" of the pegmatite and alteration of the granite (Gysi et al. 2016). The interpretation that the pegmatite was the source of these acidic fluids is supported by the presence of an alteration halo surrounding the pegmatite spine. This halo is characterized by aegirinized/hematized amphibole (replacement of arfvedsonite) restricted to the border of the pegmatite sheets and surrounding granite. This "acidic alteration" stage was also shown to be responsible for the border/core zoning observed in the pegmatites. During this fluid-rock interaction, the quartz/fluorite-rich core of the pegmatites was buffered by the acidic fluids and favorable for the mobilization of REE and Zr, whereas the border was rock buffered, and consequently less acidic with respect to its fluid chemistry (Gysi and Williams-Jones, 2013).

The acidic alteration is characterized by the following alteration types and textures: (1) pseudomorphic replacement of Na zirconosilicates by Ca zirconosilicates (Ca-metasomatism), (2) aegirinization/hematization, (3) the formation of late-stage quartz and fluorite veins (Ca-F metasomatism), (4) phyllic alteration, and (5) brecciation. These alteration features can be grouped according to whether they occurred at high temperature (e.g. pseudomorphic replacement reactions; 1 and 2) or low temperature (e.g. quartz/fluorite vein formation; 3 to 5). The distribution and characteristics of these two alteration events also record a change from a closed (restricted to the pegmatite) to an open (veining and alteration reaching

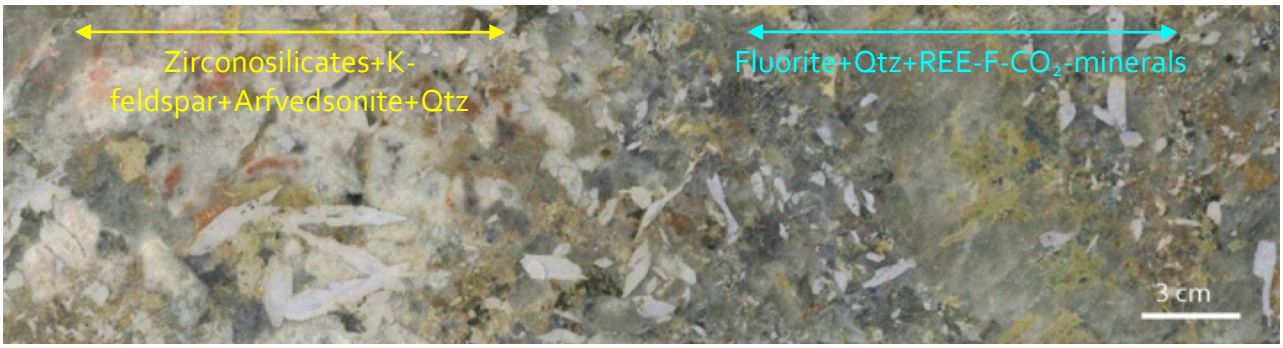


Figure 1. Drill core of a B zone pegmatite showing the zoning into core (right) and border (left). The white boat-shaped minerals are pseudomorphs after elpidite (Na-zirconosilicate). Modified after Gysi and Williams-Jones (2013).

into the granite) fluid-rock reaction system, where the high temperature alteration event can be related to Ca-metasomatism, and the low temperature alteration to Ca-F metasomatism (Gysi et al. 2016).

The dominant hydrothermal REE-bearing minerals include ferriallanite-(Ce) and gadolinite-group minerals, which occur as mineral replacement, in fractures and hydrothermal veins. The Zr-bearing minerals include three generations of zircons that record different hydrothermal evolution stages (Gysi et al. 2016). The earliest zircon I, corresponds to pseudomorphic replacement of elpidite characteristic for the Ca-metasomatic stage, followed by zircon II that occurs as hydrothermal crystal clusters intergrown with quartz and/or fluorite in the pegmatite (Gysi and Williams-Jones, 2013). The latest generation, zircon III, occurs in the granite and forms spherules intergrown with hydrothermal quartz and fluorite, which are characteristic for the Ca-F metasomatic alteration stage. These late zircons have a flat chondrite-normalized REE profile and are LREE enriched compared to the more typical HREE enriched zircon compositions.

2 Numerical modeling

Numerical simulations (Fig. 2) were carried out using the program GEM-Selektor (http://gems.web.psi.ch) and the MINES thermodynamic database (http://tdb.mines.edu) to test different possible fluid-rock interaction scenarios responsible for the transport of REE and Zr associated to these pegmatitic aqueous fluids. Multi-pass simulations conducted at 150 to 500 ºC and 1 kbar, indicate that the pH of an acidic fluid reacted with the pegmatite decreases progressively from rock to fluid buffered pH values upon increased fluid-rock reaction. The mobility of the LREE and HREE/Zr was dependent on the stability of bastnäsite-(Ce)/fluocerite-(Ce) and zircon, respectively. The LREE were more mobile at high temperature, due to the decreased stability of bastnäsite-(Ce)/fluocerite-(Ce) with decreasing pH. The mobility of Zr and HREE were increased at lower temperature due to the retrograde solubility of zircon, and again, a low pH fluid was required to mobilize these metals.

The simulated aqueous complexes of these metals (not shown in the figure) indicate that the REE are preferably transported as chloride complexes at low pH and high temperatures, resulting in a fractionation of LREE vs. HREE. Zirconium, on the other hand, was preferably transported at low temperatures as Zr hydroxyfluoride complexes ($ZrF_2(OH)_2^0$ and $ZrF(OH)_3^0$; Migdisov et al. 2011) due to its retrograde solubility and the requirement of low pH fluids with high F concentrations. Besides showing that the acidic alteration is a possible mechanism for REE/Zr transport, the simulations also indicate that the zoning into border and core pegmatite can be achieved by interaction of these acidic saline HF-HCl-bearing fluids with the pegmatites upon cooling. The quartz/fluorite dominated mineralogy in the core pegmatite corresponds to zones of increased fluid-rock reactions, where low pH fluids are stable and create an ideal pathway for the hydrothermal transport of REE and Zr.

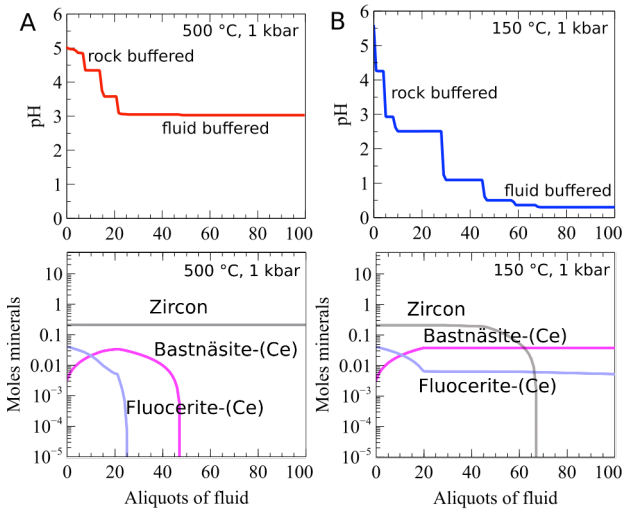


Figure 2. Simulated pH and stable REE/Zr minerals (moles) present in the altered pegmatite as a function of the number of 0.2 kg aliquots of fluid reacted with an initial mass of 1 kg of fresh Strange Lake pegmatite at 150-500 °C and 1 kbar. The calculations were carried out using a saline acidic HF-Cl-bearing fluid (1 molal total acid), assuming that the mobility of LREE was dependent on the stability of bastnäsite-(Ce)/fluocerite-(Ce) and the mobility of HREE/Zr was dependent on the stability of zircon. rock buffered pH: quartz +feldspar +hematite +phyllosilicates +fluorite; fluid buffered pH: quartz ±fluorite ±hematite. **a** multi-pass model at 500 °C

3 Hydrothermal evolution stage

Figure 3 depicts a conceptual model for the hydrothermal transport and mineralization of REE and Zr based on an interpretation of field observations and the numerical model. In a first stage (Fig. 3a), the fluids that were exsolved during the crystallization of the pegmatites, reacted at high temperature with the zirconosilicates from the border of the pegmatites, which led to a pseudomorphic replacement of elpidite (Ca-metasomatism; zircon I). These pseudomorphic reactions led to a Na-Ca exchange and depletion of the pegmatitic fluids in Ca with a corresponding enrichment in Na. In a second stage (Fig. 3b) and upon further crystallization, the high temperature fluids released from the core of the pegmatites reacted in focused zones of increased fluid-rock reactions, which led to a local remobilization of Zr (zircon II), LREE and beginning of aegirinization of the granite adjacent to the pegmatite spine. In a third stage (Fig. 3c), the system cooled down sufficiently for the fluids to become strongly acidic (fluid 1). An opening of the pegmatite system released these fluids to the surrounding granite. These fluids were likely enriched in HF-HCl and had a very low pH (pH<2; see Gysi and Williams-Jones, 2013) to be able to transport significant

concentrations of Zr and REE. Mixing with an externally derived meteoric Ca-rich fluid (fluid 2), led to the mineralization of zircon spherules (III), fluorite, ferriallanite-(Ce) and gadolinite-group minerals in fractures and veins in the granite and to the formation of a large fluorite breccia observed in the northwest of the B zone. The main factors contributing to the hydrothermal mobilization of REE and Zr, were the formation of a low pH fluid-rich pegmatite subsystem in the Strange Lake granitic pluton and the change from a closed to open system fluid-rock system behavior. Future simulation work will necessitate to include more detailed observations from fluid inclusions studies (Vasyukova and Williams-Jones, 2016a) to be able to further fine tune the numerical model, and better understand the chemistry of these fluids, including redox, salinity, temperature and ligand activities for metal transport.

4 Where does the Ca come from?

Several factors remain controversial in these peralkaline systems, one of them being the possible source of Ca since peralkaline melts are apparently depleted in this element. A more detailed discussion describing possible causes for Ca enrichment processes in Strange Lake is given by Gysi et al. (2016). In many peralkaline and alkaline igneous systems, there is evidence that interaction of fluids from the parent pluton with the surrounding rock units (e.g. carbonates) or mixing with externally derived meteoric fluids is capable of adding Ca to the system (Salvi et al. 2000; Martin and De Vito, 2014). For Strange Lake, it was initially proposed, based on studies of fluid inclusions, that high-salinity, NaCl-rich (~20–25 wt % NaCl) orthomagmatic fluids exsolved from the pegmatites and were mixed with low-temperature (<200°C), lower-salinity, Ca-rich fluids to produce the observed Ca metasomatism and Ca-bearing REE/HFSE phases (Salvi and Williams-Jones 2006, and references therein). Recently, however, Vasyukova and Williams-Jones (2016b) provided melt inclusion evidences for the presence of immiscible Ca-F–bearing melts, and proposed that these melts may have accumulated and later dissolved by hydrothermal fluids. From textural relationships it appears that two separate sources of Ca may have been present at Strange Lake: i) one that was responsible for the Ca metasomatism at high temperature, which permitted a closed-system Ca-Na exchange during the formation of pseudomorphs in the border pegmatites, and ii) another source that was responsible for the low-temperature Ca-F metasomatic event represented by late zircon, gittinsite, and fluorite in the granite when the pegmatite system was open. The presence of a large fluorite breccia surrounding the pluton in the northwest, south, and northeast, further suggests that most of the F and Ca did not originate from the same source, and that both elements were not transported together on a large scale.

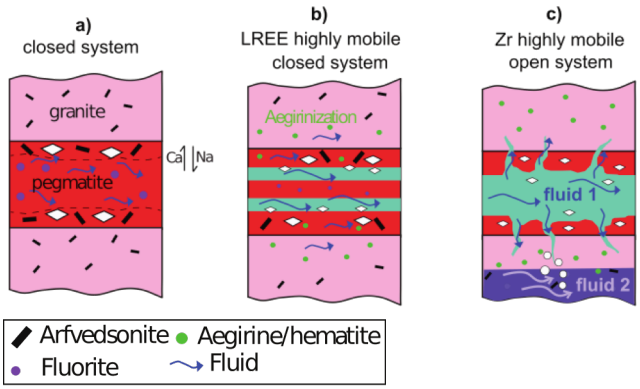


Figure 3. Evolution model of the Strange Lake pegmatite spine (see text for details). Modified after Gysi et al. (2016).

5 Conclusions and outlook

Strange Lake is a valuable natural laboratory for studying the role of hydrothermal fluids during the genesis of peralkaline granitic systems. In particular, a better know-how of the different alteration stages, their effects on mineralogy and rock geochemistry, and their relations to ore metal distribution is paramount for future REE exploration strategies. Determining geochemical vectors for mineral exploration requires an in depth knowledge on how to relate geochemistry with changes in rock chemistry. A combination of field, mineralogical and numerical simulation studies permit to build a genetic evolution model for this deposit type, which aims at facilitating the interpretation of field relations in other similar REE mineral deposits.

Acknowledgments

I would like to thank wholeheartedly A.E. Williams-Jones (Willy) for his support and enthusiasm during my Postdoctoral Fellowship at McGill University. This work was possible through collaboration with Willy, and Quest Rare Minerals Ltd. This project was also funded by a fellowship from the Swiss National Science Foundation to A. Gysi (SNSF grant PBSKP2_134329).

References

Gysi AP, Williams-Jones AE (2013) Hydrothermal mobilization of pegmatite-hosted REE and Zr at Strange Lake, Canada: A reaction path model. Geochim Cosmochim Acta 122: 324-352.

Gysi AP, Williams-Jones AE, Collins P (2016) Lithogeochemical vectors for hydrothermal processes in the Strange Lake peralkaline granitic REE-Zr-Nb deposit. Econ Geol 111: 1241-1276.

Martin R, De Vito C (2014) The late-stage miniflood of Ca in granitic pegmatites: An open-system acid-reflux model involving plagioclase in the exocontact. Can Mineral 52: 165–181.

Migdisov AA, Williams-Jones AE, Van Hinsberg V, Salvi S (2011) An experimental study of the solubility of baddeleyite (ZrO_2) in fluoride-bearing solutions at elevated temperature. Geochim Cosmochim Acta 75: 7426–7434.

Salvi S, Williams-Jones AE (2006) Alteration, HFSE mineralisation and hydrocarbon formation in peralkaline igneous systems: Insights from the Strange Lake Pluton, Canada. Lithos 91: 19–34.

Salvi S, Fontan F, Monchoux P, Williams-Jones AE, Moine B (2000) Hydrothermal mobilization of high field strength elements in alkaline igneous systems: Evidence from the Tamazeght complex (Morocco). Econ Geol. 95: 559–576.

Vasyukova O, Williams-Jones AE (2016a) Fluid evolution in the Strange Lake granitic pluton, Canada: Implications for HFSE mobilisation. Chem Geol 444: 83-100.

Vasyukova O, Williams-Jones AE (2016b) The evolution of immiscible silicate and fluoride melts: Implications for REE ore-genesis. Geochim Cosmochim Acta 172: 205–224.

Geochemical signature of rare-metal magmatic fluids exsolved from the Beauvoir granite (Massif Central, France) revealed by LA-ICPMS analysis of primary fluid inclusions

Matthieu Harlaux, Julien Mercadier, Christian Marignac, Michel Cuney, Wilédio Bonzi and Valentin Kremer
Université de Lorraine

Abstract. The Beauvoir granite (Limousin, French Massif Central) represents an exceptional case in the European Variscan belt of a peraluminous rare-metal granite crosscutting an early W stockwork. The latter was strongly overprinted by the rare-metal magmatic-hydrothermal fluids derived from the Beauvoir granite, resulting in a massive topazification. This work presents a complete study of primary fluid inclusions hosted in quartz and topaz from the Beauvoir granite and the metasomatized stockwork in order to characterize the geochemical composition of the early magmatic fluids exsolved during the crystallization of this highly evolved rare-metal granite. Microthermometric data show that the earliest fluid (L1) is high temperature (500 to >600°C), saline (17-28 wt.% NaCl eq) and Li-rich (Te<-70°C). LA-ICPMS analyses of fluid inclusions show that its chemical composition is dominated by Li, Na, K, Cs, Sn, and Rb as major elements, with significant concentrations (10^2-10^3 ppm) of Nb, W and Ta. These results demonstrate that primary fluid inclusions preserved the pristine signature of the magmatic fluids in the Beauvoir granite, but also in the metasomatized W stockwork despite the distance from the granitic cupola (>100 m) and interaction with external fluids.

1 Introduction

Rare-metal deposits are mainly associated with peraluminous to peralkaline granites and pegmatites, which represent major economic resources for strategic elements such as Li, Be, Nb, Ta, Sn, W and REE (Linnen and Cuney 2005; Linnen et al. 2012). The European Variscan belt represents an important metallogenic province for rare-metal granites and pegmatites, which are located mainly in the Bohemian Massif, the Iberian Massif, Cornwall, and the French Massif Central (FMC). These deposits formed during Carboniferous to Permian times between 330 and 280 Ma in relation with the late-Variscan orogenic evolution (Chen et al. 1993; Marignac and Cuney 1999; Cuney et al. 2002; Melleton et al. 2012, 2015). In France, the Beauvoir granite represents one of the best examples of a peraluminous high phosphorus rare-metal granite (Černý et al. 2005) and was intensively studied during the 1980s-1990s, with a 900 m of continuous core drilling GPF1 from the "Géologie Profonde de la France" program (Cuney and Autran 1987).

In this study, we present a complete study of primary fluid inclusions hosted in quartz and topaz crystals from the Beauvoir granite and the metasomatized stockwork with three main objectives: (i) to characterize the geochemical composition of the early rare-metal-rich magmatic fluids exsolved during the crystallization of the Beauvoir granite; (ii) to study the partitioning of elements between the co-existing volatile and brine phases during the magmatic-hydrothermal transition; and (iii) to determine the geochemical evolution of the magmatic fluids during their ascent and their interaction with the enclosing micaschists with distance from the granitic cupola.

2 Geological setting

The Beauvoir granite is located in the Echassières granitic complex in the NE part of the FMC in the Limousin area, which consists of a stack of metamorphic nappes emplaced during the Variscan orogeny during the Upper Paleozoic (Faure et al. 2009). The Echassières complex includes an early W-bearing quartz-vein system, the so-called La Bosse stockwork, and is composed of at least three successive granitic units that intruded into the micaschists of the Para-Autochtonous Unit (Cuney et al. 1992; Raimbault et al. 1995). From oldest to youngest, these granitic units are: (i) the La Bosse granite, which is concealed at depth and is presumed to be related to the formation of the W deposit; (ii) the Colettes granite, which is a porphyritic biotite-muscovite-cordierite granite that overprints the La Bosse stockwork; and (iii) the Beauvoir granite, which crosscuts the Colettes granite and consists of a topaz-lepidolite-albite granite with disseminated Sn, Li, Ta, Nb and Be mineralization, corresponding to accessory minerals of cassiterite, columbite-tantalite, lepidolite and Li-Be-phosphates.

The latter is characterized by a vertical internal zoning marked by the succession of three granitic units (B3, B2, B1) emplaced successively, which present a magmatic foliation underlined by lepidolite and show a progressive magmatic differentiation upwards (Cuney et al. 1992; Raimbault et al. 1995). The emplacement of the Beauvoir granite has been dated at 308 ± 2 Ma (^{40}Ar-^{39}Ar on lepidolite; Cheilletz et al. 1992). However, a recent U-Pb dating of columbite-tantalite yielded an age of 317 ± 6 Ma (Melleton et al. 2015), which is significantly older than the

previous age. Considering that no late, high-temperature hydrothermal alteration event is recorded at Echassières (Merceron et al. 1992), the age obtained on lepidolite is likely close to the magmatic emplacement age of the Beauvoir granite and does not represent a late, disturbed age. Thus, a possible emplacement age of 310 Ma for the Beauvoir granite seems consistent within uncertainty with the two existing U-Pb and ^{40}Ar-^{39}Ar ages.

The La Bosse W stockwork consists in a network of up to 0.6 m-thick quartz-ferberite veins, which are hosted in the enclosing micaschists and have been dated at 334 ± 2 Ma (U-Pb on wolframite; Harlaux et al. 2017). The stockwork outcrops about 100 m above the Beauvoir granite contact and several 100 metres laterally from the cupola. It was strongly overprinted by the magmatic fluids derived from the Beauvoir granite, resulting in massive topazification of the vein system, partial dissolution of quartz, and crystallization of late Li-micas and Nb-Ta-oxides (Aïssa et al. 1987a).

3 Fluid inclusion study

Samples from the Beauvoir granite (B1 facies) and the metasomatized La Bosse stockwork were studied. Double-polished thick sections (150-200 µm) were prepared for the study of fluid inclusions in quartz and topaz. All analyses were performed at the GeoRessources laboratory (Université de Lorraine, Vandoeuvre-lès-Nancy, France).

3.1 Petrography and microthermometry of fluid inclusions

In the Beauvoir granite and La Bosse stockwork, quartz and topaz crystals contain numerous fluid inclusions, found as dense clouds of disseminated individual or clustered inclusions. This represents a severe limitation for the identification of different generations of fluid inclusions based on criteria of relative position or arrangement. Nevertheless, three main types of fluid inclusions can be distinguished in quartz and topaz based on petrography and microthermometry results (Fig. 1):

(i) L1-type fluid inclusions: these consist of multi-phase fluid inclusions with a dominant aqueous phase containing a vapour bubble (~40%) and small isotropic cubic solids, interpreted as halite. The fluid inclusions have irregular shapes, and range in size from 10 to 23 µm, typically. They are characterized by very low eutectic temperatures (Te<-70°C) and low ice-melting temperatures (-40°C<Tm_{ice}<-2°C). Halite melting occurred between 275 and 300°C, before total homogenization by vapour disappearance. In the Beauvoir granite, homogenization occur to the liquid phase at temperatures from 491 to 600°C, with an average value of 542°C. They are lower in the La Bosse stockwork, where they range from 377 to 468°C, with an average value of 422°C. Estimated salinities range from 16.7 to 28.1 wt.% NaCl eq in the Beauvoir granite and from 27 to 28.7 wt.% NaCl eq in the La Bosse stockwork.

(ii) L2-type fluid inclusions: these comprise multi-phase fluid inclusions composed of a dominant aqueous phase with a small vapour phase (~30%) and contain multiple cubic crystals of salts, including halite. These fluid inclusions are characterized by irregular to regular shapes and have sizes between 10 and 35 µm. They have very low eutectic temperatures (-80°C<Te<-52°C) and low ice-melting temperatures (-42°C<Tm_{ice}<-1.6°C). Halite melting occurred consistently before total homogenization at temperatures between 215 and 407°C, with average values of 359°C in the Beauvoir granite and 286°C in the La Bosse stockwork. Bulk homogenization occur to the liquid phase at temperatures ranging from 377 to 542°C in the Beauvoir granite (average: 455°C), whereas they range from 305 to 439°C in the La Bosse stockwork (average: 375°C). Estimated salinities are between 32.6 and 48.2 wt.% NaCl eq in the Beauvoir granite and between 36.7 and 40.4 wt.% NaCl eq in the La Bosse stockwork.

(iii) V2-type fluid inclusions: these consist of two-phase fluid inclusions and contain a dominant vapour phase (>80%) with a minor liquid phase. They comprise irregularly shaped fluid inclusions and range from 12 to 24 µm in size. They have very low eutectic temperatures (Te<-65°C) and low ice-melting temperatures (-19°C<Tm_{ice}<-1.4°C). They homogenize to the vapour phase at temperatures between 375 and 595°C in the Beauvoir granite (average: 465°C) and between 342 and 490°C in the La Bosse stockwork (average: 403°C). Estimated salinities range from 4.7 to 21.9 wt.% NaCl eq in the Beauvoir granite and from 1.4 to 9.2 wt.% NaCl eq in the La Bosse stockwork.

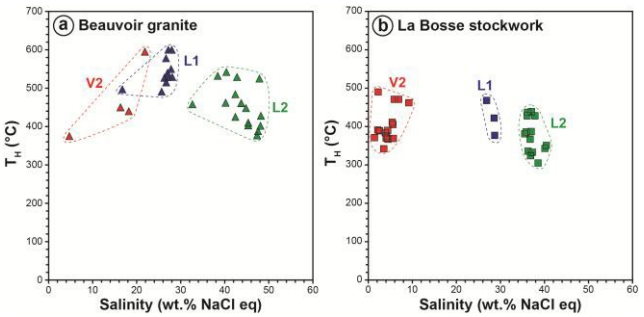


Figure 1. Salinity vs T_H diagram for the different generations of fluid inclusions identified in the Beauvoir granite (a) and the La Bosse stockwork (b).

3.2 LA-ICPMS analyses of fluid inclusions

LA-ICPMS analyses were performed on selected fluid inclusions previously studied by microthermometry using an Agilent 7500c Q-ICPMS. An example of LA-ICPMS spectrum of an L1-type fluid inclusion from the Beauvoir granite is shown in Fig. 2. The fluid inclusion signal is ca. 56 s in length and shows high signal/background ratios (10^1-10^4) for most of the measured elements (Na, Sn, Cs, Mg, Fe, Li, W, Nb, Ta). The salinities of fluid inclusions were used to estimate the Na content for the quantification of the LA-ICPMS signals. Results of concentrations

determined by LA-ICPMS are shown on Fig. 3. In the Beauvoir granite, L1-type fluid inclusions are characterized by high concentrations in Na (10^5 ppm), Sn (1,100-38,000 ppm), Cs (22,000-76,000 ppm), K (3,200-42,000 ppm), Mn (9,000-30,000 ppm), Fe (12,000-17,000 ppm), Rb (4,000-14,000 ppm), Li (4,500-18,000 ppm) and minor concentrations in W (900-3,000 ppm), Nb (40-1,500 ppm) and Ta (18-180 ppm). The L2- and V2-type fluid inclusions have, respectively, higher and lower concentrations for most of the elements compared to the L1-type fluid inclusions, but within the same order of magnitude. In contrast, L1-, L2- and V2-type fluid inclusions from the La Bosse stockwork have generally lower concentrations compared to those from the Beauvoir granite, except for K, Mn, Fe and Sr, which have higher concentrations.

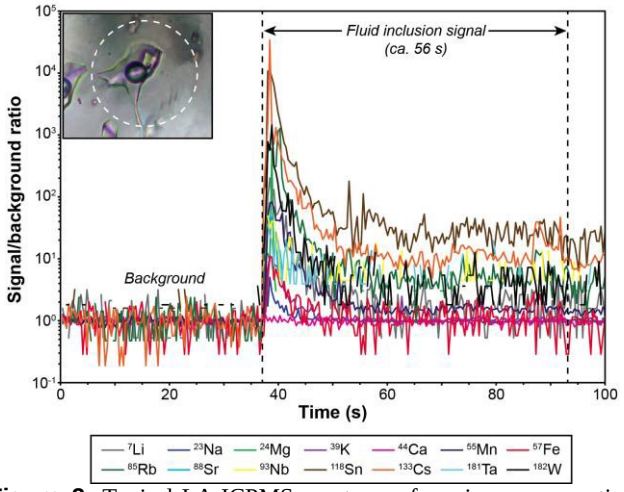


Figure 2. Typical LA-ICPMS spectrum of a primary magmatic L1-type fluid inclusion hosted in a globular quartz crystal from the Beauvoir granite. The ablated fluid inclusion (picture in inset) was 17 µm in size using a laser spot diameter of 32 µm (dashed white circle).

4 Discussion

The different types of fluid inclusions identified represent different generations of fluids trapped in primary quartz and topaz during the magmatic-hydrothermal transition of the Beauvoir granite. These data appear to be in good agreement with previously reported microthermometry results (Aïssa et al. 1987b; Cuney et al. 1992). L1-type fluid inclusions represent the earliest record of the primary fluid exsolved during the crystallization of the Beauvoir granite. Microthermometric data indicate that this fluid was high temperature (500 to >600°C), saline (17-28 wt.% NaCl eq) and Li-rich (Te<-70°C). LA-ICPMS analyses reveal that the chemical composition of the L1 fluid is dominated by Li, Na, K, Cs, Sn, and Rb as major elements, and Nb, Ta, and W as minor elements. The Nb content is higher on average than the Ta content in the fluid (Nb/Ta~5), which may indicate the higher hydrothermal mobility of Nb compared to Ta. Indeed, Nb is known to have precipitated during the topazification of the W stockwork (Aïssa et al. 1987b). Ca was systematically below the limits of detection (LOD~3,000 ppm) in the L1-type fluid inclusions, which indicates that its concentration was low in the primary fluid, in agreement with the low Ca content of the Beauvoir granite (Cuney et al. 1992; Raimbault et al. 1995). Moreover, the massive topazification overprinting the La Bosse stockwork at surface suggests that the L1 fluid contained high concentrations in F (not analyzed by LA-ICPMS), which is also known to efficiently increase the solubility of Nb and Ta in hydrothermal fluids (Zaraisky et al. 2010; Timofeev et al. 2015).

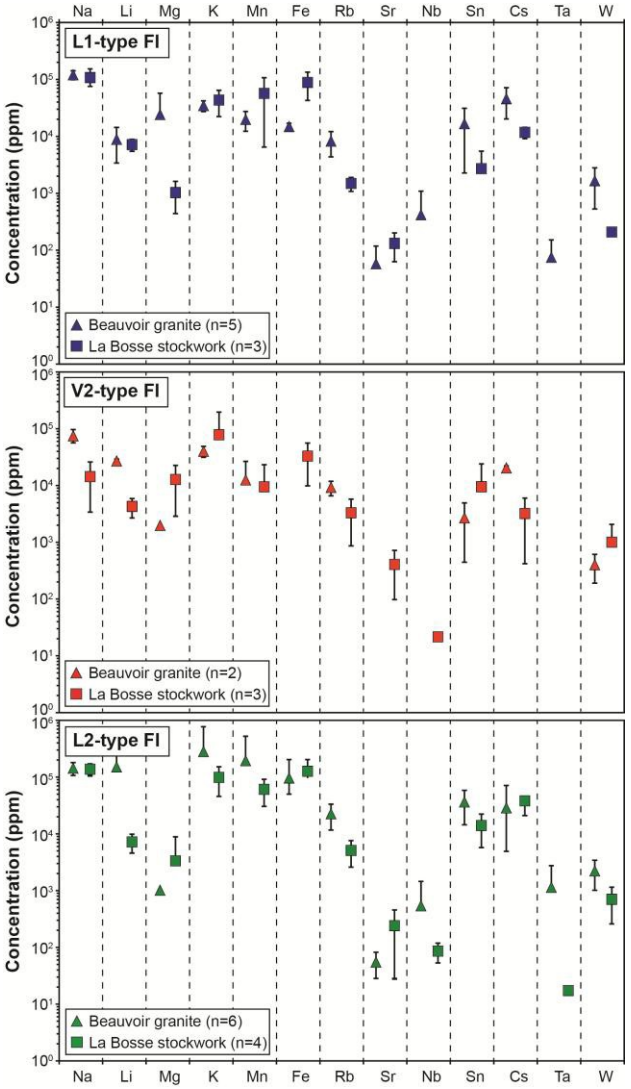


Figure 3. Minor and trace elements contents in L1-, V2- and L2-type fluid inclusions (FI) from the Beauvoir granite and the La Bosse stockwork determined by LA-ICPMS. The values represented correspond to the average and standard deviations of the concentrations determined.

Boiling of the primary L1 fluid yielded to the phase separation of a low- to moderate-salinity vapour (V2; 4.7-22 wt.% NaCl eq) and a high-salinity brine (L2; 32-48 wt.% NaCl eq) at ca. 450°C (Cuney et al. 1992). LA-ICPMS analyses of the co-existing V2- and L2-type fluid

inclusions revealed that the L2-fluid has the highest concentrations of metals and shows a preferential enrichment in most of the elements compared to the V2 fluid. This indicates that the majority of the elements partition preferentially into the aqueous phase in the Beauvoir granite. This behaviour is similar to the results of Audétat et al. (2000a,b) on the Mole granite (Australia), where most of the elements, including W, Sn, Na, K, Li and Cs, are partitioned preferentially into the brine phase.

The evolution of the exsolved magmatic fluids percolating through the enclosing micaschists with distance from the Beauvoir granite is characterized by a decrease in temperature (60-120°C) and salinity (3-10 wt.% NaCl eq), which can be interpreted in terms of cooling and thermal equilibration around the intrusion. The salinity decrease may indicate that the magmatic-hydrothermal fluids were more or less diluted by a very low-salinity fluid, which may correspond to meteoric water, considering the relatively shallow depth of emplacement (ca. 3 km) of the Beauvoir granite (Aïssa et al. 1987b). These results also show that the geochemical signature of the rare-metal magmatic fluid is preserved in fluid inclusions from the metasomatized La Bosse stockwork, despite the distance from the granitic cupola (>100 m) and interaction with external fluids. Consequently, the geochemical signature of fluid inclusions may represent a highly reliable pathfinder for the discovery of hidden rare-metal granitic cupolas at Echassières and more widely in the Limousin area, as well as elsewhere in the world.

Acknowledgements

This work was supported by the French National Research Agency through the national program “Investissements d'avenir” of the Labex Ressources 21 with the reference ANR-10-LABX-21-RESSOURCES21 and has also taken part of the project ERAMIN “New Ores”. The authors would like to thank Imerys, and especially Hubert Sauvage for their support and access to the Beauvoir quarry. We thank also Dr Chantal Peiffert and Dr Marie-Christine Boiron for technical support in providing analytical data with LA-ICPMS analyses.

References

Aïssa M, Marignac C, Weisbrod A (1987a) Le stockwerk à ferbérite d’Echassières : évolution spatiale et temporelle ; cristallochimie des ferbérites. Géol Fr 2-3:311-333.

Aïssa M, Weisbrod A, Marignac C (1987b) Caractéristiques chimiques et thermodynamiques des circulations hydrothermales du site d’Echassières. Géol Fr 2-3:335-350.

Audétat A, Günther D, Heinrich CA (2000a) Magmatic-hydrothermal evolution in a fractionating granite: A microchemical study of the Sn-W-F-mineralized Mole Granite (Australia). Geochim Cosmochim Ac 64:3373-3393.

Audétat A, Günther D, Heinrich CA (2000b) Causes for large-scale metal zonation around mineralized plutons: fluid inclusion LA-ICP-MS evidence from the Mole Granite, Australia. Econ Geol 95:1563-1581.

Černý P, Blevin PL, Cuney M, London D (2005) Granite-related ore deposits. Econ Geol 100th Anniversary Volume:337-370.

Cheilletz A, Archibald D, Cuney M, Charoy B (1992) Ages $^{40}Ar/^{39}Ar$ du leucogranite à topaze-lépidolite de Beauvoir et des pegmatites sodolithiques de Chédeville (Nord Massif Central, France). Significations pétrologique et géodynamique. CR Acad Sci Paris 315:329-336.

Chen Y, Clark AH, Farrar E, Wasteneys HAHP, Hodgson MJ, Bromley AV (1993) Diachronous and independent histories of plutonism and mineralization in the Cornubian Batholith, southwest England. J Geol Soc 150:1183–1191.

Cuney M, Autran A (1987) Objectifs généraux du projet GPF Echassières n°1 et résultats essentiels acquis par le forage de 900 m sur le granite albitique à topaze-lépidolite de Beauvoir. Géol Fr 2-3:7-24.

Cuney M, Marignac C, Weisbrod A (1992) The Beauvoir topaz-lepidolite albite granite (Massif Central, France): the disseminated magmatic Sn-Li-Ta-Nb-Be mineralization. Econ Geol 87:1766-1794.

Cuney M, Alexandrov P, Le Carlier de Veslud C, Cheilletz A, Raimbault L, Ruffet G, Scaillet S (2002) The timing of W-Sn-rare metals mineral deposit formation in the Western Variscan chain in their orogenic setting: the case of the Limousin area (Massif Central, France). Geol Soc London Spec Publ 204:213-228.

Faure M, Lardeaux JM, Ledru P (2009) A review of the pre-Permian geology of the Variscan French Massif Central. CR Geosci 341:202–213.

Harlaux M, Romer RL, Mercadier J, Morlot C, Marignac C, Cuney M (2017) 40 Ma years of hydrothermal W mineralization during the Variscan orogenic evolution of the French Massif Central revealed by U-Pb dating of wolframite. Miner Deposita DOI 10.1007/s00126-017-0721-0.

Linnen RL, Cuney M (2005) Granite-related rare-element deposits and experimental constraints on Ta-Nb-W-Sn-Zr-Hf mineralization. In Rare-Element Geochemistry and Mineral Deposits (eds. RL Linnen and IM Samson). Geological Association of Canada, Short Course Notes, 17:45-68.

Linnen RL, Van Lichtervelde M, Černý P (2012) Granitic pegmatites as sources of strategic metals. Elements 8:275-280.

Marignac C, Cuney M (1999) Ore deposits of the French Massif Central: insight into the metallogenesis of the Variscan collision belt. Miner Deposita 34:472-504.

Melleton J, Gloaguen E, Frei D, Novák M, Breiter K (2012) How are the emplacement of rare-element pegmatites, regional metamorphism and magmatism interrelated in the Moldanubian domain of the Variscan Bohemian Massif, Czech Republic? Can Mineral 50:1751-1773.

Melleton J, Gloaguen E, Frei D (2015) Rare-elements (Li-Be-Ta-Sn-Nb) magmatism in the European Variscan Belt, a review. Proceedings of the 13th Biennial SGA Meeting, 24–27 August 2015, Nancy, France 2:807-810.

Merceron T, Vieillard P, Fouillac AM, Meunier A (1992) Hydrothermal alterations in the Echassières granitic cupola. Contrib Mineral Petr 112:279-292.

Raimbault L, Cuney M, Azencott C, Duthou JL, Joron JL (1995) Geochemical evidence for a multistage magmatic genesis of Ta-Sn-Li mineralization in the granite at Beauvoir, French Massif Central. Econ Geol 90:548-576.

Timofeev A, Migdisov AA, Williams-Jones AE (2015) An experimental study of the solubility and speciation of niobium in fluoride-bearing aqueous solutions at elevated temperature. Geochim Cosmochim Ac 158:103-111.

Zaraisky GP, Korzhinskaya V, Kotova N (2010) Experimental studies of Ta_2O_5 and columbite–tantalite solubility in fluoride solutions from 300 to 550°C and 50 to 100 MPa. Miner Petrol 99:287-300.

The Weijia scheelite magnesian skarn in the Nanling Range, South China: a special case related to high fluorine activity

Xudong Huang
Nanjing University, China
Institut des Sciences de la Terre d'Orléans, Université d'Orléans, France

Jianjun Lu
Nanjing University, China

Stanislas Sizaret
Institut des Sciences de la Terre d'Orléans, Université d'Orléans, France

Luc Barbanson
Institut des Sciences de la Terre d'Orléans, Université d'Orléans, France

Alain Chauvet
Université Montpellier 2, France

Rucheng Wang, Dongsheng Ma, Xiaoyu Li, Xu Zhao, Guanghong Chen, Qiang Zhang
Nanjing University, China

Abstract. Different from most other W-skarns in the world, the Late Jurassic Weijia scheelite skarn in the Nanling Range of South China is magnesian, and is characterized by the occurrence of serpentine and phlogopite, and the lack of forsterite and spinel. Because of the high abundance of fluorite, an investigation of the relationship between fluorine and the unusual magnesian skarn and tungsten mineralization was undertaken. A high fluorine activity for the granite-related mineralization is indicated by the abundances of fluorine-rich minerals and the estimated HF concentrations. A fall of fluorine activity with decreasing temperature is reflected by the compositions of different micas. The decrease of fluorine activity should be directly induced by the progressive formation of fluorite and other fluorine-rich minerals. The obvious positive correlation between the grade of WO_3 and the content of fluorite indicates a strong coupling relationship of tungsten and fluorine. The scheelite mineralization is most probably triggered by the decrease of fluorine activity. The low temperature condition of ore-forming fluids which exsolve from the fluorine-rich melts and experience a further evolution in sedimentary strata is not favourable for the development of high-temperature prograde forsterite and spinel in the magnesian skarn.

1 Introduction

Essentially, all economic W-skarns are calcic throughout the world (Kwak 1987). Magnesian skarns are of importance for Sn, Fe, and sometimes Au mineralization, and mostly exhibit a diagnostic mineralogy that includes forsterite, spinel, and serpentine (Kwak 1987; Meinert et al. 2005). However, the Weijia scheelite skarn in the Nanling Range of South China is a special case, which comprises dominant magnesian skarn and secondary calcic skarn. The magnesian skarn minerals are mainly serpentine and phlogopite, without forsterite and spinel. Another remarkable feature of the Weijia W deposit is the occurrence of abundant fluorite. The relationship between fluorine and the unusual magnesian skarn, and also tungsten mineralization requires further investigation.

The Weijia W deposit, a recently discovered super-large scheelite skarn deposit related to the Late Jurassic granite, is located in the western part of the Nanling Range W-Sn metallogenic province, and in southern Hunan Province. It has a total WO_3 resource of ca. 300,000 tons estimated by a cut-off grade of 0.12 wt.%, in which 240,000 tons are from the magnesian skarn and the rest 60,000 tons from the calcic skarn.

2 Ore deposit geology

The stratigraphy of the Weijia area is dominated by Devonian carbonate rocks, which were deformed before Jurassic. The Middle Devonian Qiziqiao Formation, which is composed of a 350 m thick upper member of limestone, a 390 m thick middle member of dolostone, and a 340 m thick lower member of limestone, was intruded by a Late Jurassic granite, and acts as the ore-bearing horizon.

The Weijia granite is porphyritic (Fig. 1a), and contains quartz (ca. 35 vol.%), K-feldspar (ca. 37 vol.%), albite (ca. 25 vol.%), and minor biotite (ca. 2 vol.%) and muscovite (ca. 1 vol.%). Accessory minerals include fluorite, zircon, thorite, xenotime, monazite, niobite, samarskite, fergusonite, scheelite, parisite, ilmenite, etc. It belongs to the ilmenite series granites, and is a highly fractionated peraluminous S-type granite (Huang et al. 2017). Zircon U-Pb dating yielded an age of ca. 158 Ma (Zhao et al. 2016;

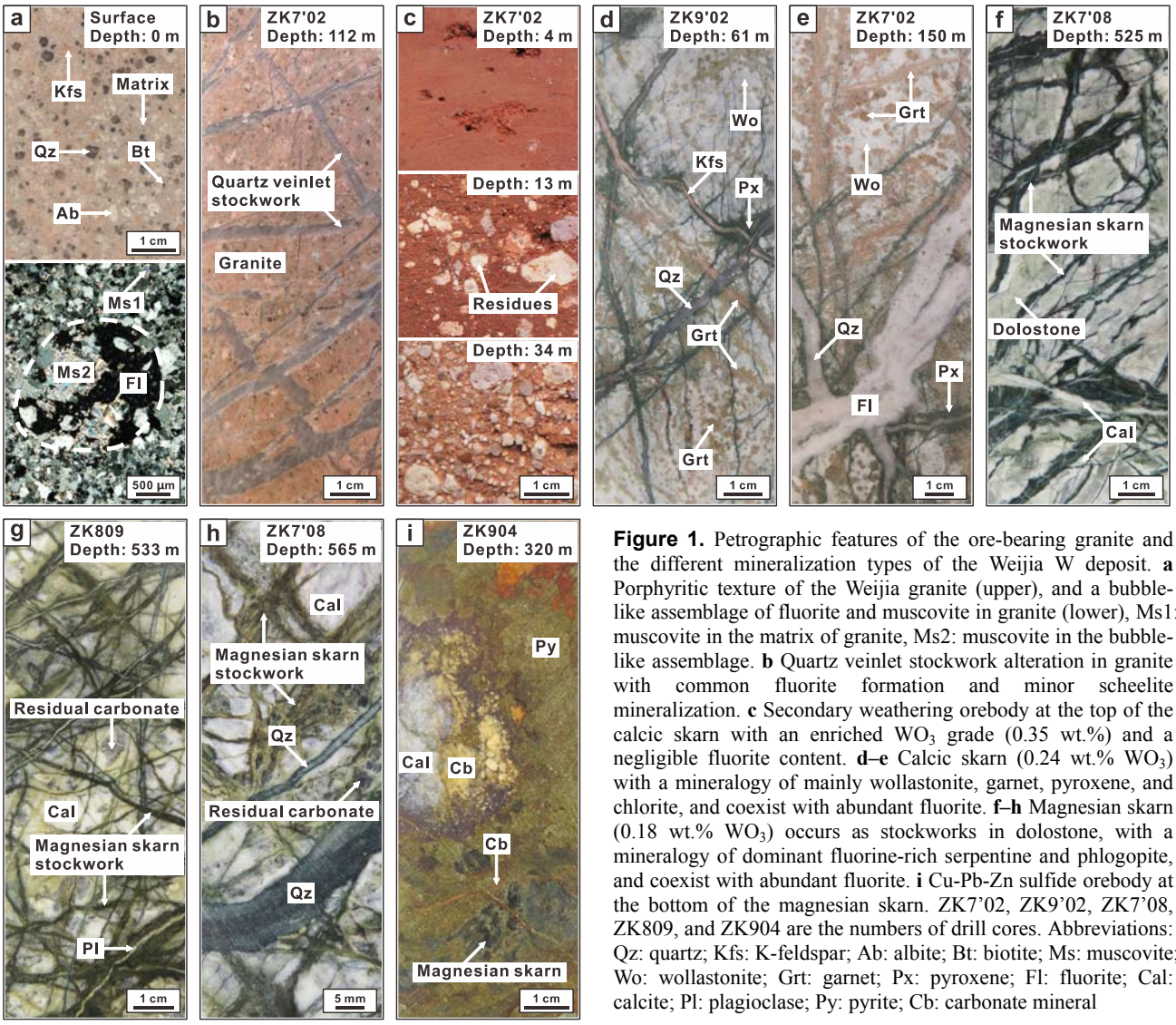


Figure 1. Petrographic features of the ore-bearing granite and the different mineralization types of the Weijia W deposit. **a** Porphyritic texture of the Weijia granite (upper), and a bubble-like assemblage of fluorite and muscovite in granite (lower), Ms1: muscovite in the matrix of granite, Ms2: muscovite in the bubble-like assemblage. **b** Quartz veinlet stockwork alteration in granite with common fluorite formation and minor scheelite mineralization. **c** Secondary weathering orebody at the top of the calcic skarn with an enriched WO_3 grade (0.35 wt.%) and a negligible fluorite content. **d–e** Calcic skarn (0.24 wt.% WO_3) with a mineralogy of mainly wollastonite, garnet, pyroxene, and chlorite, and coexist with abundant fluorite. **f–h** Magnesian skarn (0.18 wt.% WO_3) occurs as stockworks in dolostone, with a mineralogy of dominant fluorine-rich serpentine and phlogopite, and coexist with abundant fluorite. **i** Cu-Pb-Zn sulfide orebody at the bottom of the magnesian skarn. ZK7'02, ZK9'02, ZK7'08, ZK809, and ZK904 are the numbers of drill cores. Abbreviations: Qz: quartz; Kfs: K-feldspar; Ab: albite; Bt: biotite; Ms: muscovite; Wo: wollastonite; Grt: garnet; Px: pyroxene; Fl: fluorite; Cal: calcite; Pl: plagioclase; Py: pyrite; Cb: carbonate mineral

Huang et al. 2017). A unusual bubble-like assemblage of fluorite and muscovite occurs in the Weijia granite (Fig. 1a). The petrographic evidences, such as the porphyritic texture (Fig. 1a), the hexagonal bipyramidal quartz phenocryst with resorption texture, and the micrographic texture of K-feldspar, indicate a shallow emplacement depth, which is different from the most granites related to W-skarns in the world (Meinert et al. 2005).

The alteration within the Weijia granite includes the feldspar-quartz veins and the quartz veinlet stockworks (Fig. 1b). Fluorite is commonly observed in the quartz veinlet stockworks, and coexists with minor scheelite. The calcic skarn orebodies (Fig. 1d, e), with thicknesses of 14 ~ 46 m and an average grade of about 0.24 wt.%, generally occur along the contact zone between the Weijia granite and the limestone of the upper member of the Qiziqiao Formation. Zhao et al. (2016) reported a Re-Os age of 159.0 ± 5.6 Ma for molybdenite from the calcic skarn, which is consistent with the zircon U-Pb age of the Weijia granite. The magnesian skarn orebodies (Fig. 1f–h), with thicknesses of 85 ~ 182 m and an average grade of about 0.18 wt.%, occur as stratiform within the dolostone of the middle member of the Qiziqiao Formation, and have a consistent strike-dip with the host strata. These magnesian skarn orebodies strike north-northwest, and extend down southwest, with a dip angle of 10 ~ 35°. There is a 0.85 m thick stratiform Cu-Pb-Zn sulfide orebody (Fig. 1i) at the bottom of the magnesian skarn. Both the magnesian and the calcic skarn scheelite ores contain abundant fluorite (generally 3 ~ 18 wt.%), and the grade of WO_3 has an obvious positive correlation with the content of fluorite (Fig. 2).

Surficial weathering and leaching of the calcic skarn resulted in a sharp decrease of fluorite content (drop to 0.4 ~ 0.8 wt.%) and an enrichment of WO_3 (increase to an average grade of about 0.35 wt.%) (Fig. 2), and the formation of a 3 ~ 40 m thick secondary weathering orebody (Fig. 1c).

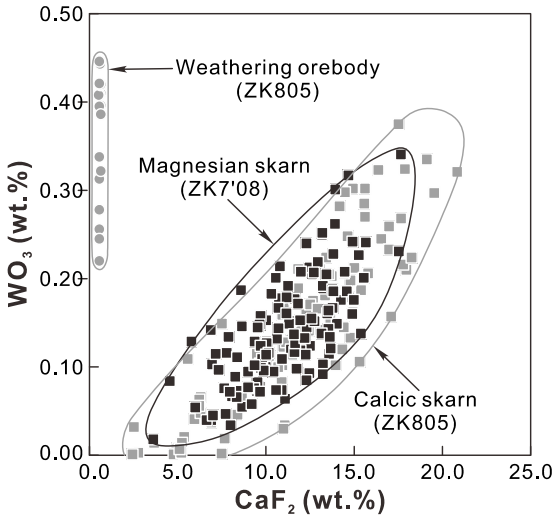


Figure 2. The relationship between WO_3 and CaF_2 contents of scheelite ores from the Weijia W deposit (The data are from No. 418 Geological Team of Bureau of Geology and Mineral Exploration and Development of Hunan Province, internal report)

3 Magnesian skarn

The magnesian skarn of the Weijia W deposit occurs as stockworks in dolostone (Fig. 1f–h). It was formed through replacement of wall rocks by hydrothermal fluid infilling in fractures. This process caused decarbonation and magnesium release of the surrounding dolostone, and led to the later crystallization of purified calcite (Fig. 1f–h). Serpentine and phlogopite, as the predominant skarn minerals, coexist with disseminated scheelite and abundant fluorite. The other skarn minerals include minor pyroxene, garnet, chlorite, chondrodite, fluoborite, and sellaite. Forsterite and spinel are absent (Fig. 3). This kind of magnesian skarn is remarkably different from the most other magnesian skarns in mineralogy, such as the contemporary Hehuaping magnesian Sn skarn (Yao et al. 2014), which occurs in the same dolomitic horizon of the Qiziqiao Formation in southern Hunan Province, and has a prograde stage well developed with forsterite and spinel.

4 Fluorine-rich minerals

In addition to fluorite, other fluorine-rich minerals (Table 1) are also widely spread in the Weijia W deposit, especially in the magnesian skarn.

5 Estimation of fluorine activity

The magmatic biotite 1 (T > 800 °C, Table 1) of the Weijia granite is plotted in the field of porphyry Mo deposits in the [IV (F/Cl)]-[IV (F)] diagram, reflecting a high fluorine activity of granitic melts. The biotite 2 (T = 600 ~ 800 °C, Table 1) has a significantly lower fluorine activity than the biotite 1 (Table 1, Fig. 4), and may indicate a later hydrothermal effect on the primary biotite. The two different types of muscovites in the Weijia granite have lower temperatures than the biotites, and a similar [IV (F)] to the biotite 2 (Table 1).

Quantitative estimation of fluorine activity by biotite 1, biotite 2, and hydrothermal phlogopite of the magnesian skarn, using the biotite and phlogopite fluorimeters (Aksyuk 2000), yields HF concentrations of $10^{-1.3}$ to $10^{-1.0}$ mole/dm^3, $10^{-2.3}$ to $10^{-1.5}$ mole/dm^3, and $10^{-3.0}$ to $10^{-2.6}$ mole/dm^3, respectively. The decreasing trend of HF concentration from biotite 1 to biotite 2 is consistent with that reflected by the F and F/Cl intercept values (Fig. 4).

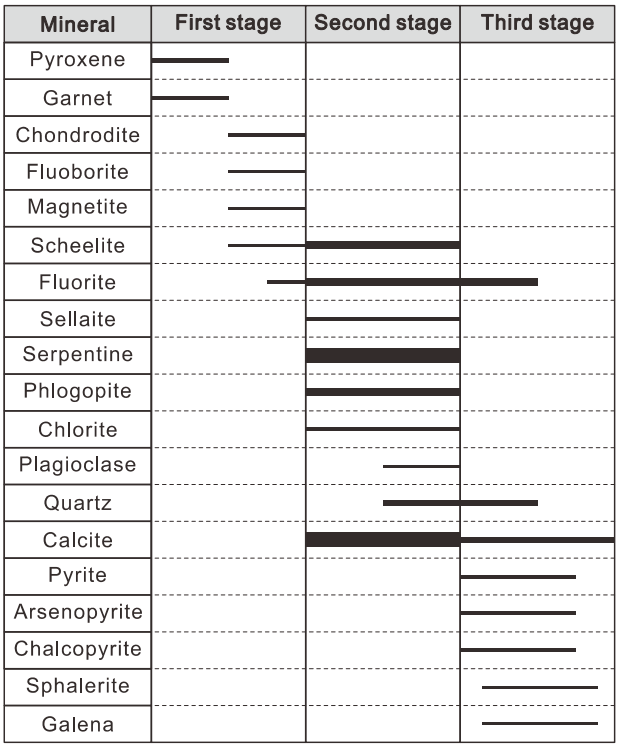


Figure 3. Paragenetic sequence of the Weijia magnesian skarn

Table 1. Fluorine-rich minerals of the Weijia W deposit

Host rock	Mineral	T (°C)[1]	F (wt.%)[2]	IV (F)[3]
Granite	Biotite 1	> 800	2.42 ~ 4.84	0.80 ~ 1.07
	Biotite 2	600 ~ 800	0.32 ~ 1.95	1.17 ~ 1.96
	Muscovite 1	450 ~ 600	0.15 ~ 1.47	1.19 ~ 2.54
	Muscovite 2	300 ~ 400	0.29 ~ 1.14	1.34 ~ 2.03
Calcic skarn	Garnet		0.00 ~ 1.45	
	Vesuvianite		2.59 ~ 4.03	
Magnesian skarn	Serpentine		1.21 ~ 3.01	
	Phlogopite		2.65 ~ 6.88	1.61 ~ 2.04
	Garnet		2.44 ~ 4.36	

[1]Temperature is estimated by the method of muscovite solid solutions (Monier and Robert 1986). [2]F content is determined by electron microprobe analysis. [3]Fluorine intercept value [IV (F)] is defined by Munoz (1984). Biotite is divided into biotite 1 and biotite 2 according to the fluorine content and temperature. Muscovite 1: muscovite in the matrix of granite; muscovite 2: muscovite in the bubble-like assemblages of fluorite and muscovite

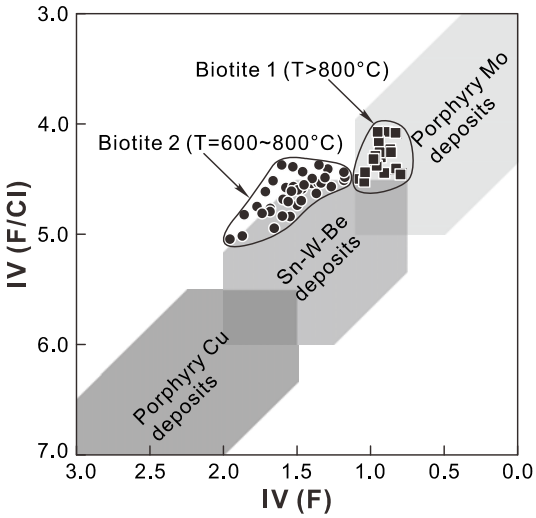


Figure 4. Diagram of F/Cl intercept value [IV (F/Cl)] vs. F intercept value [IV (F)] for the biotite of the Weijia granite (after Munoz 1984). [IV (F)] and [IV (F/Cl)] are quantitative parameters for F enrichment degree defined by Munoz (1984), both higher values indicate lower F enrichment degree

6 Discussion and conclusions

Fluorine can effectively reduce the viscosity and the minimum liquidus temperature of granitic melts (Manning 1981), and lead to a high degree of evolution and a resulting enrichment of tungsten in melts, even though the tungsten solubility in granitic melts is nearly independent of the fluorine content (Audétat et al. 2000; Linnen and Cuney 2005; Che et al. 2013). The Weijia granite was crystallized from the fluorine-rich melts that have HF concentration of $10^{-1.3}$ to $10^{-1.0}$ mole/dm^3, which is similar to the rare metal granites ($10^{-1.5}$ ~ $10^{-1.0}$ mole/dm^3) and significantly higher than the granitoids related to W-skarns in the western Cordillera ($10^{-2.8}$ ~ $10^{-1.8}$ mole/dm^3) (Audétat et al. 2000), and also those of the porphyry Cu deposits (Fig. 4, Audétat et al. 2000). The distinctive properties of high evolution and shallow emplacement for the Weijia granite, are most probably related to the high fluorine activity of granitic melts, and can be interpreted by a low-viscosity and long-distance emplacement.

The regularity of increasing IV (F) (Table 1) and decreasing HF concentration along with decreasing temperature, which is reflected by the compositions of different micas, reveal a fall of fluorine activity. The decrease of fluorine activity should be directly induced by the progressive formation of fluorite and other fluorine-rich minerals. The positive correlation between the grade of WO_3 and the content of fluorite (Fig. 2) indicates a strong coupling relationship of tungsten and fluorine, even though the effect of fluorine on tungsten transport in magmatic-hydrothermal systems is still indistinct. The formation of fluorite and other fluorine-rich minerals, which lowered the fluorine activity, is in all probablity the trigger for scheelite mineralization.

The low liquidus temperature of granitic melts, which is induced by the high fluorine activity, lead to a relatively low temperature of exsolved fluids. Along with the migration in sedimentary strata, the ore-forming fluids with further evolution result in a lower temperature condition, which is not favourable for the development of high-temperature prograde minerals, such as forsterite and spinel.

Acknowledgements

This study was supported by the National Natural Science Foundation of China (Grant No. 41273053), National Key Basic Research Program of China (Grant No. 2012CB416702), and Sino-French Cai Yuanpei Program of China Scholarship Council.

References

Aksyuk AM (2000) Estimation of fluorine concentrations in fluids of mineralized skarn systems. Econ Geol 95: 1339–1347

Audétat A, Günther D, Heinrich CA (2000) Magmatic-hydrothermal evolution in a fractionating granite: A microchemical study of the Sn-W-F-mineralized Mole Granite (Australia). Geochim Cosmochim Acta 64: 3373–3393

Che XD, Linnen RL, Wang RC, Aseri A, Thibault Y (2013) Tungsten solubility in evolved granitic melt: An evaluation of magmatic wolframite. Geochim Cosmochim Acta 106:84–98

Huang XD, Lu JJ, Sizaret S, Wang RC, Ma DS, Zhang RQ, Zhao X, Wu JW (2017) Petrogenetic differences between the Middle-Late Jurassic Cu-Pb-Zn-bearing and W-bearing granites in the Nanling Range of South China: A case study of the Tongshanling and Weijia deposits in southern Hunan Province. Sci China Earth Sci 60:in press

Kwak TAP (1987) W-Sn skarn deposits and related metamorphic skarns and granitoids. Elsevier, Amsterdam

Linnen RL, Cuney M (2005) Granite-related rare-element deposits and experimental constraints on Ta-Nb-W-Sn-Zr-Hf mineralization. In: Linnen RL, Samson IM (eds) Rare-Element Geochemistry and Mineral Deposits. Geological Association of Canada Short Course Notes 17, pp 45–68

Manning DAC (1981) The effect of fluorine on liquidus phase relationships in the system Qz-Ab-Or with excess water at 1kb. Contrib Mineral Petrol 76:206–215

Meinert LD, Dipple GM, Nicolescu S (2005) World skarn deposits. Economic Geology 100th Anniversary Volume:299–336

Monier G, Robert J-L (1986) Muscovite solid solutions in the system K_2O-MgO-FeO-Al_2O_3-SiO_2-H_2O: an experimental study at 2 kbar P_{H2O} and comparison with natural Li-free white micas. Mineral Mag 50:257–266

Munoz JL (1984) F-OH and Cl-OH exchange in micas with applications to hydrothermal ore deposits. In: Bailey SWB (ed) Micas. Mineralogical Society of America, Washington DC, pp 469–493

Yao Y, Chen J, Lu JJ, Wang RC, Zhang RQ (2014) Geology and genesis of the Hehuaping magnesian skarn-type cassiterite-sulfide deposit, Hunan Province, Southern China. Ore Geol Rev 58:163–184

Zhao PL, Yuan SD, Mao JW, Santosh M, Li C, Hou KJ (2016) Geochronological and petrogeochemical constraints on the skarn deposits in Tongshanling ore district, southern Hunan Province: Implications for Jurassic Cu and W metallogenic events in South China. Ore Geol Rev 78:120–137

Numerical simulations of the transport of metals in vapour-like fluids applied to porphyry ore formation

Nicole C. Hurtig
Colorado State University, U.S.A.

Anthony E. Williams-Jones
McGill University, Montréal, Canada

Abstract. The solubility of Au, Cu, Ag and Mo is simulated as a function of temperature, pressure, redox condition, and the sulphur and chlorine contents of the volatile phase. The information is used to show the role of these variables in controlling metal budgets and zoning in porphyry ore deposits. In an intermediate-density fluid, Au and Cu reach a maximum solubility at ~460 °C and ~540 °C, respectively, whereas Mo and Ag concentrations decrease with decreasing temperature and pressure. The solubility maximum of gold occurs at 340 °C for low-density fluids, indicating a potential for remobilization of gold to shallower, and more distal environments at a late stage. The solubility maximum of Cu, on the other hand, is dependent on the sulphur content of the fluid, and ranges between 540 and 600 °C. It increases at higher temperature and lower sulphur concentration. The fluid composition exerts a major control on the metal ratios of magmatic fluids and therefore the overall metal budget of the ore deposit. The P-T evolution path way of the magmatic volatile phase during cooling and decompression plays an important role in the spatial distribution of metals and the formation of ore deposits.

1 Introduction

Porphyry Cu-Au-(Mo) deposits constitute the largest source of Cu and Mo ore world-wide and contain significant recourses of Au, W and Ag (Sillitoe 2010; Singer et al. 2005). Low- and intermediate-density fluids are commonly the dominant volatile phases in magmatic-hydrothermal systems, and are the most likely agents of metal transport to sites of ore deposition (Heinrich et al. 1999; Williams-Jones et al. 2002; Williams-Jones and Heinrich 2005; Weis 2015). These fluids are highly compressible, and the metal solubility is controlled by fluid density. There are no free electrons in a vapour phase and thus the metallic species are molecular. These fluid characteristics indicate that metal precipitation is related to decompression and sharp pressure gradients.

The early experiments were performed mainly at very low water vapour pressures and the relationship between metal solubility and water fugacity was assumed to be linear (Migdisov et al. 1999; Archibald et al. 2001, 2002, Rempel et al. 2006, 2008). Because of this, the hydration number was assumed to be constant at constant temperature. However, the absolute hydration number generally decreased with increasing temperature, thereby preventing the formulation of a thermodynamic model with which to predict the metal solubility for a range of temperature and pressure. Later experiments aimed at extending the range of water vapour pressures investigated the critical region of saturated water vapour pressure, where fluid density has the greatest effect on metal solubility. These experiments showed that there is an exponential increase in metal solubility with increasing water vapour pressure as illustrated in Figure 1 (Migdisov and Williams-Jones 2013; Hurtig and Williams-Jones 2014a, b; Migdisov et al. 2014). This exponential increase in metal solubility is interpreted to reflect the changing sizes of the hydration clusters (Fig. 1) i.e., the number of water molecules y in metallic gaseous species such as, for example, $AuCl(H_2O)_y$. Recognizing that hydration numbers increase with increasing water vapour pressure and decrease with increasing temperature was a key observation that permitted the implementation of a hydration model (Pitzer and Pabalan 1986) for metallic gaseous species. This model bridges the entire density range between vapour-like and liquid-like fluids and makes it possible to conduct pressure sensitive numerical simulations.

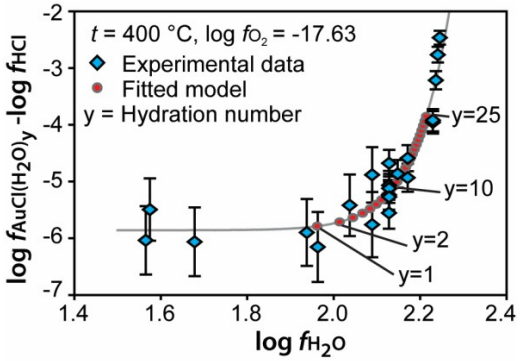


Figure 1. Experimental results showing gold fugacity normalized to HCl fugacity as a function of water vapour pressure at 400 °C. The experimental data were fitted to a power function for extracting integer hydration numbers, y. Modified after (Hurtig and Williams-Jones 2014a).

Experimentally-derived formulations of metal solubility in low- and intermediate-density fluids (Rempel et al. 2006; Zezin et al. 2007, 2011; Migdisov and Williams-Jones 2013; Hurtig and Williams-Jones 2014b; Migdisov et al. 2014) allow for the thermodynamic modelling of metal solubility and mineral precipitation during cooling and decompression of a magmatic high-temperature volatile phase. Previous numerical models investigated the mobilization of Au-Ag-Mo in porphyry and epithermal environments (Hurtig and Williams-Jones 2015). Here we present results from simulations focusing

on Cu-Au-Mo porphyry ore deposits. The geochemical modelling is applied to better understand the factors controlling ore formation, and focuses on the effect of pressure fluctuations.

2 Numerical simulations

2.1 Thermodynamic data and modelling procedure

Geochemical simulations were performed using the GEM-Selektor geochemical modelling package (Kulik et al. 2013). Thermodynamic data for individual gaseous metal species were implemented into the GEMS data base using experimentally derived temperature dependent logarithmic equilibrium constants. The following metallic gaseous species were considered for the numerical simulations: $AuCl(H_2O)_y$, $AgCl(H_2O)_y$, $CuCl(HCl)(H_2O)_{2.5}$, $CuCl(H_2O)_y$, $MoO_3(H_2O)_y$ and $AuS(H_2S)_{x-1}(H_2O)_y$, where y is the number of water molecules in the hydration cluster and x-1 is the number of hydrogen sulphide molecules that participate in mixed solvation clusters.

The major gases, H_2O_g, $H_{2,g}$, $CO_{2,g}$, $CH_{4,g}$, CO_g, $Cl_{2,g}$, $O_{2,g}$, HCl_g, H_2S_g, and $SO_{2,g}$ were treated as non-ideal and their fugacity coefficients were determined using the Peng-Robinson-Stryjek-Vera equation of state (Stryjek et al. 1986; Poling et al. 1988; Proust and Vera 1989). The minor gas species, $S_{2,g}$, $S_{8,g}$ and $SO_{3,g}$ were treated as ideal gases. In gas-mineral equilibrium simulations, all gases were treated as ideal initially, and the fugacity of major gases was calculated manually in a subsequent step using the fugacity coefficients for the appropriate pressure-temperature conditions. The conventional Van der Waals mixing rule with one binary interaction parameter was used to describe the properties of the non-ideal mixtures.

The assumption that minor gas species, such as $S_{2,g}$, $S_{8,g}$ and $SO_{3,g}$, are ideal did not introduce significant errors, because these gases are non-polar and only occur in low concentrations in the gas mixtures considered. The nature of the gaseous metal species, on the other hand, indicates that their behaviour in aqueous vapour is non-ideal. By using a set of hydration reactions, which are linked to the water fugacity, we were able to partly account for the non-ideal behaviour of these species.

2.2 Compositional controls on metal mobility

The simulations investigating the compositional control of the high-temperature magmatic volatile phase on metal solubility and metal ratios were performed for a fluid at 600 °C and 810 bar with a density of 300 kg/m^3. The magmatic volatile phase was buffered by mineral assemblages and saturated with ore forming constituents. We evaluated the effects of changing redox conditions, and the Cl and the S content of the fluid on metal solubility and metal ratios.

The effect of the redox condition on metal solubility is shown in Figure 2. The redox condition is expressed as R_H = log f_{H2}/log f_{H2O}, and is reflected in the buffering mineral assemblage in Figure 2a. The fluid has a composition of 0.3 wt.% Cl, 2 wt.% S and 10 wt.% CO_2. Under reduced conditions buffered by magnetite-calcite-ilmenite, Au and Ag are transported in the vapour, whereas Cu and Mo are in very low concentrations. Under highly oxidized conditions buffered by hematite-anhydrite-rutile, Mo is predominant, Ag and Cu undergo increased solubility and the Au solubility is slightly decreased. Gold solubility reaches a maximum buffered by magnetite-anhydrite-rutile, as it shows limited solubility under reduced conditions and the solvated AuS species are destabilized under highly oxidizing conditions. The buffering of magnetite-anhydrite-rutile by a high-temperature volatile phase is very common in porphyry ore-forming systems. To further investigate the compositional control of a fluid buffered by magnetite-anhydrite-rutile, subsequent models were involved changing the Cl (Fig. 2) and S (Fig. 3) concentrations.

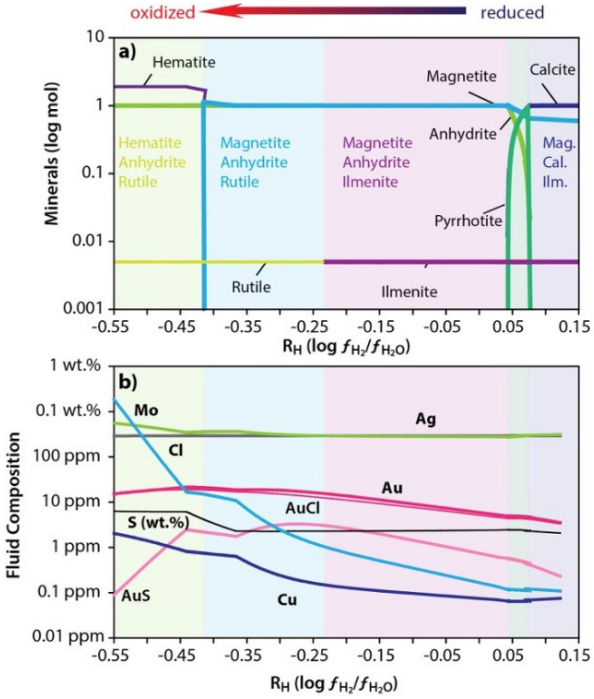


Figure 2. Numerical simulation of **a** the buffering mineralogy and **b** the fluid composition as a function of redox conditions (R_H = log f_{H2}/log f_{H2O}) at 600 °C and 810 bar.

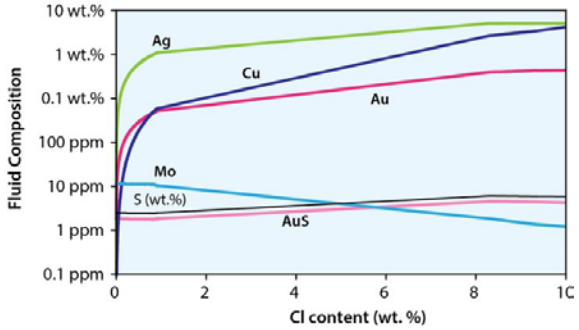


Figure 3. Numerical simulations of the fluid composition as a function of chlorine concentration at 600 °C and 810 bar. The

redox condition is buffered by the mineral assemblage, magnetite-anhydrite-rutile.

In Figure 3 it is evident that Cu becomes predominate over Mo at 0.2 wt.% Cl, over Au at 0.8 wt.% Cl and over Ag at >10 wt.% Cl. The redox condition of the fluid is buffered by magnetite-anhydrite-rutile and the fluid has a composition of 0-10 wt.% Cl, 2.5 wt.% S and 10 wt.% CO_2. At 600 ºC, the Cu solubility is controlled by the species $CuCl(HCl)(H_2O)_{2.5}$, whereas the solubility of Au and Ag is controlled by hydrated AuCl and AgCl complexes. Molybdenum solubility on the other hand shows a negative correlation with increasing Cl content; molybdenum-oxychloride species were not considered in the model, although they might be present in solutions with elevated Cl concentration (Rempel et al. 2008; Ulrich and Mavrogenes 2008).

The control of the sulphur content on metal solubility is illustrated in Figure 4. The redox condition is buffered predominantly by magnetite-anhydrite-rutile and at >5.2 wt.% S by magnetite-anhydrite-rutile-pyrite. The fluid has a composition of 0-6 wt.% S, 0.3 wt.% Cl and 10 wt.% CO_2. Molybdenum concentration is highest at low S concentration, and Ag and Cu concentrations decrease with increasing S content. Gold concentration, on the other hand, increases with increasing S content, because of the increasing importance of solvated AuS species.

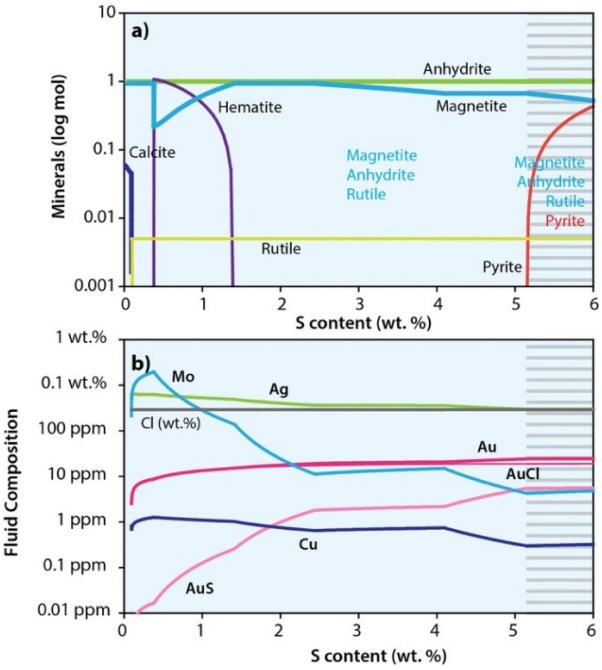


Figure 4. Numerical simulations of **a** the buffering mineralogy and **b** the fluid composition as a function of sulphur concentration at 600 °C and 810 bar.

2.3 P-T dependence of metal solubility

The effect of water vapour pressure on Cu and Au solubility was modelled at 600 ºC (Fig. 5). Copper solubility is controlled by the species $CuCl(HCl)(H_2O)_{2.5}$ and gold solubility is governed by the species $AuCl(H_2O)_y$ with hydration numbers (y) of 1 to 10. At low water fugacity, Au solubility is higher than Cu solubility, however at moderate water fugacity Cu solubility overtakes Au solubility, which becomes more important at elevated water fugacity.

During cooling and decompression of an intermediate-density fluid, Au concentration reaches a maximum at 460 °C and Cu at 540 °C, whereas Mo and Ag concentrations decrease with decreasing T and P. The solubility maximum of gold occurs at 340 °C at lower fluid density, indicating a potential for re-mobilization of gold to shallower, and more distal environments at a later stage. The Cu solubility maximum increases to higher temperature if the sulphur concentration of the fluid is increased.

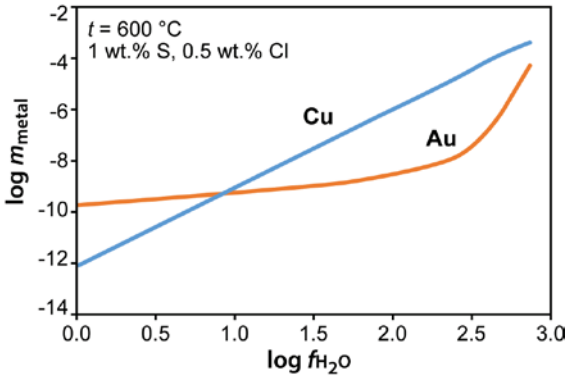


Figure 5. Numerical simulations showing the concentration of Cu and Au (mol/kg) as a function of water fugacity at 600 ºC in a fluid with 1 wt.% S and 0.5 wt.% Cl.

3 Conclusions and outlook

The composition (S, Cl, H_2) and density of the fluid exert important controls on metal solubility and the metal ratios of ore-forming vapour-like fluids and therefore the overall metal budget of the corresponding ore deposit. Sulphur-rich, low-density fluids generally favour the transport of Au and Ag in vapour-like magmatic fluids, whereas Mo and Cu will be more enriched in intermediate-density fluids with lower S contents. The path of fluid evolution during cooling and decompression controls the metal zoning of a porphyry ore deposit. Whereas systems with elevated S contents will exhibit compact overlapping metal zonation, S-poor systems will be characterised by more disseminated metal zoning styles.

These numerical simulations can be applied to a variety of porphyry ore-forming systems as a means of better understanding the factors controlling metal enrichment and improving exploration models.

Acknowledgements

We would like to thank Artas Migdisov who contributed to this work by performing experiments and deriving thermodynamic properties for gaseous hydrated Cu- and

Ag-chloride species. We also want to acknowledge his contribution to the idea and development of the hydration model.

References

Archibald S, Migidisov A, Williams-Jones, AE (2002) An experimental study of the stability of copper chloride complexes in water vapor at elevated temperatures and pressures. Geochim Cosmochim Acta 66:1611–1619.

Archibald SM, Migdisov A.A., Williams-Jones A.E. (2001) The stability of Au-chloride complexes in water vapor at elevated temperatures and pressures. Geochim Cosmochim Acta 65:4413–4423.

Heinrich CA, Günther D, Audétat A, Ulrich, T, Frischknecht, R (1999) Metal fractionation between magmatic brine and vapor, determined by microanalysis of fluid inclusions. Geology 27:755.

Hurtig NC, Williams-Jones AE (2015) Porphyry-epithermal Au-Ag-Mo ore formation by vapor-like fluids: New insights from geochemical modeling. Geology 43:587–590.

Hurtig NC, Williams-Jones AE (2014a) An experimental study of the transport of gold through hydration of AuCl in aqueous vapour and vapour-like fluids. Geochim Cosmochim Acta 127:305–325.

Hurtig NC, Williams-Jones AE (2014b) An experimental study of the solubility of MoO_3 in aqueous vapour and low to intermediate density supercritical fluids. Geochim Cosmochim Acta 136:169–193.

Kulik DA, Wagner T., Dmytrieva SV, et al (2013) GEM-Selektor geochemical modeling package: Revised algorithm and GEMS3K numerical kernel for coupled simulation codes. Comput Geosci 17:1–24.

Migdisov AA, Bychkov AY, Williams-Jones AE, van Hinsberg VJ (2014) A predictive model for the transport of copper by HCl-bearing water vapour in ore-forming magmatic-hydrothermal systems: Implications for copper porphyry ore formation. Geochim Cosmochim Acta 129:33–53.

Migdisov AA, Williams-Jones AE, Suleimenov OM (1999) Solubility of chlorargyrite (AgCl) in water vapor at elevated temperatures and pressures. Geochim Cosmochim Acta 63:3817–3827.

Migdisov AA, Williams-Jones AE (2013) A predictive model for metal transport of silver chloride by aqueous vapor in ore-forming magmatic-hydrothermal systems. Geochim Cosmochim Acta 104:123–135.

Pitzer KS, Pabalan RT (1986) Thermodynamics of NaCl in steam. Geochim Cosmochim Acta 50:1445-1454.

Poling BE, Prausnitz JM, O'Connell JP (1988) The properties of gases & liquids, 5th Edn. McGraw-Hill Companies Inc.

Proust P, Vera JH (1989) PRSV: The Stryjek-Vera modification of the Peng-Robinson equation of state. Parameters for other pure compounds of industrial interest. Can J Chem Eng 67:170–173.

Rempel KU, Migdisov AA, Williams-Jones AE (2006) The solubility and speciation of molybdenum in water vapour at elevated temperatures and pressures: Implications for ore genesis. Geochim Cosmochim Acta 70:687–696.

Rempel KU, Williams-Jones AE, Migdisov AA (2008) The solubility of molybdenum dioxide and trioxide in HCl-bearing water vapour at 350 °C and pressures up to 160 bars. Geochim Cosmochim Acta 72:3074–3083.

Sillitoe RH (2010) Porphyry copper systems. Econ Geol 105:3–41.

Singer D a., Berger VI, Moring BC (2005) Porphyry Copper Deposits of the World Database, Map, and Grade and Tonnage Models. Menlo Park

Stryjek R, Vera JH, Engineering C, Ha C (1986) PRSV - An Improved Peng-Robinson Equation of State with New Mixing Rules for Strongly Nonideal Mixtures.

Ulrich T, Mavrogenes J (2008) An experimental study of the solubility of molybdenum in H2O and KCl-H2O solutions from 500 °C to 800 °C, and 150 to 300 MPa. Geochim Cosmochim Acta 72:2316–2330.

Weis P (2015) The dynamic interplay between saline fluid flow and rock permeability in magmatic-hydrothermal systems. Geofluids 15:350–371.

Williams-Jones AE, Heinrich CA (2005) Vapor transport of metals and the formation of magmatic-hydrothermal ore deposits. Econ Geol 100:1287–1312.

Williams-Jones AE, Migdisov AA, Archibald SM, Xiao Z (2002) Vapor-transport of ore metals. Water-rock Interact Ore Depos Environ geochemistry A Tribut to David A Crerar Geochemical Soc Spec Publ 7:279–305.

Zezin DY, Migdisov AA, Williams-Jones AE (2007) The solubility of gold in hydrogen sulfide gas: An experimental study. Geochim Cosmochim Acta 71:3070–3081.

Zezin DY, Migdisov AA, Williams-Jones AE (2011) The solubility of gold in H2O-H2S vapour at elevated temperature and pressure. Geochim Cosmochim Acta 75:5140–5153.

Linking channel-flow processes to pegmatite potentially mineralized in REE in the central Grenville Province

Sophie Jannin, Félix Gervais
?cole Polytechnique, Montréal, Canada

Abdelali Moukhsil
Ministère de l'Énergie et des Ressources naturelles du Québec, Québec, Canada

James L. Crowley
Boise State University, Idaho, U.S.A.

Lars E. Augland
GEOTOP, Université du Québec à Montréal, Canada

François Turlin, Anne-Sylvie André-Mayer
Université de Lorraine, CNRS, CREGU, France

Olivier Vanderhaeghe
Université de Toulouse, France

Abstract. We present an integrated structural-metamorphic-geochronological study of the central Grenville Province aimed at testing the recently proposed channel flow model and investigated its potential control on the generation, emplacement and geometry of leucogranite/ pegmatite, which can be enriched in rare-earth elements (REE). Three deformation stages (Dp1-Dp3) are documented within the Parautochthonous Belt (PB), Dp1 indicate top-to-the-NW reverse-shearing at 1002 ± 2 Ma. Dp2 structures were developed by oblique-reverse, top-tothe-NNE shearing occurring along an exhumation path bracketed between 986 and 961 Ma. In the overlying Allochthonous Belt (AB), two deformation stages (Da1-Da2) are documented. Da1 was developed by reverse, top-tothe-NNW shearing associated with 1080-1030 Ma granulite-facies metamorphism, whereas Da2 developed by oblique-normal shearing within the newly-identified Thachic shear-zone (TSZ). Synkinematic pegmatite dykes are abundant in the TSZ and yielded an age of 986.2 ±0.5 Ma. These data are best compatible with a channel flow model in which the upper part of the PB and the lower part of the AB flowed together. Granitic material segregated out of the partially molten channel material to be emplaced as synkinematic dykes increasing in volume towards the top of the channel and as crosscutting dykes in its hanging wall: the upper part of the AB.

1 Introduction

Tectonic models involving channel flow processes have bee, proposed for several orogens, such as the Himalayas (e.g. Cottle et al., 2015), the Canadian Cordillera (Gervais and Brown, 2011) and the Grenville Province (Rivers, 2008). As these models generally require partial melting of channel material, these systems are linked to extensive granitic magmatism. Because these orogenic leucogranites and pegmatites can be enriched in rare-earth elements (REE) as documented in the Himalayas (Searle et al., 2016) and the Grenville Province (Turlin et al., this volume), it is crucial to gain a better understanding of these processes.

The Grenville Province is a large hot orogen with a complex convergent Mesoproterozoic history that culminated in a continental collision from 1090 to 980 Ma (Rivers, 2008). Channel flow models have been proposed for this orogen based on thermomechanical numerical modelling (Jamieson et al., 2010), or orogen-wide data compilation (Rivers, 2008), but remains to be rigorously tested by modern and integrated structural, metamorphic and geochronological studies of a specific field area. We present such integrated studies from the central Grenville Province (Fig.1), that allow us to conduct a field-based test similar to that applied to the southeastern Canadian Cordillera by Gervais and Brown (2011). The proposed tectonic model offers an interesting explanation for the generation of the REE-rich pegmatites found in the structurally overlying tectonic domain (Turlin et al., submitted and this volume).

2 Geological context

Two belts form the Grenville Province: the Parautochthonous Belt (PB), composed of rocks from the North American craton basement and its meta-sedimentary cover, and the Allochthonous Belt (AB) composed of rocks formed outboard of the cratonic margin that were thrusted on the PB. The Allochthon Boundary Thrust (ABT) separates these two belts along the entire length of the Grenville Province in Canada.

In the central Grenville Province, the AB underwent reverse, top-to-the-NW deformation associated with protracted granulite metamorphism in the sillimanite field between 1080 and 1030 Ma (Fig. 1; Dunning and Indares, 2010; Lasalle et al., 2014). U/Pb ages on titanite indicate cooling of the AB below 600-700°C between 1006 and

987 Ma (Dunning and Indares, 2010). In contrast, rocks from the PB, followed a tight Pressure-Temperature clockwise path at granulite conditions in the kyanite field at 995-985 Ma during the Rigolet stage of the Grenvillian Orogeny (Jordan et al., 2006), but the age and type of deformation associated with the metamorphic event remains elusive. U/Pb dates on titanites constraint the cooling below 700600°C at 961-956 Ma (Jordan et al., 2006). These data suggest that cooling of the AB was synchronous with the paroxysm of metamorphism in the structurally underlying PB (Dunning and Indares, 2010).

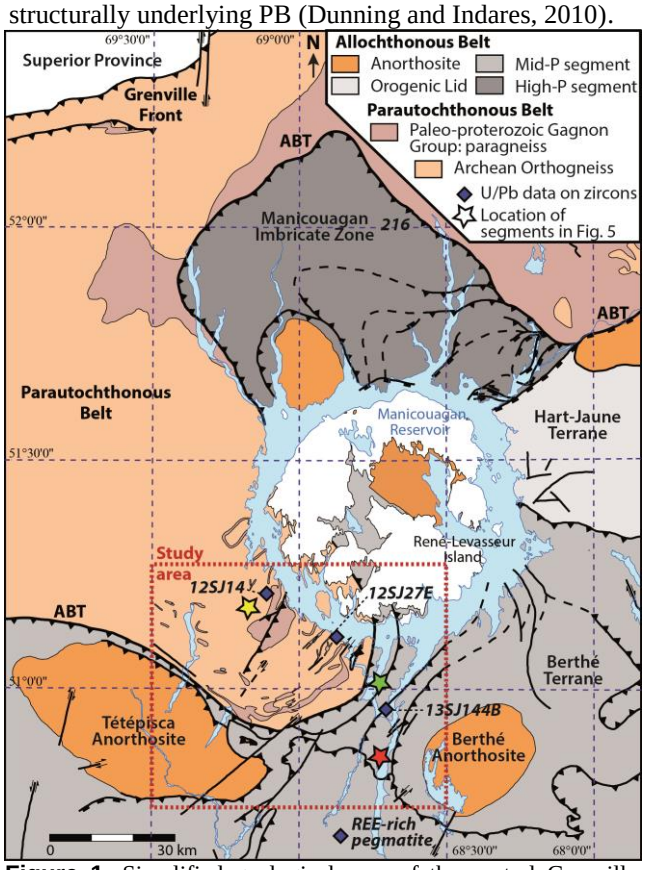


Figure 1. Simplified geological map of the central Grenville Province (Quebec) with the localisation of the dated syn-deformation samples and the REE-rich pegmatites of Turlin et al. (this volume).

3 Results

3.1 Deformations and U-Pb dating in the Parautochthonous Belt

Three deformation stages were mapped in the PB (labelled Dp1-Dp3). A NW-SE Dp1 foliation with a SSE plunging lineation indicates reverse, top-to-the-NW shearing, whereas a NE-SW Dp2 foliation with a SSW plunging lineation indicates oblique-reverse, top-to-the-NNE shearing (Fig. 2). Dp1 is folded by Dp2 and becomes completely transposed towards the ABT. Local Dp3 structures indicate oblique-normal, down-to-the-SW shearing with a WSW plunging lineation (Fig. 2).

The age of Dp1 and Dp2 were constrained by combining results of two techniques of U-Pb geochronology on zircon: laser ablation (LA-ICP-MS) for its high spatial resolution and chemical abrasion isotope dilution (CA-IDTIMS) for its high precision. The age of Dp1 can be inferred by linking deformation, metamorphism and geochronology. Dp1-foliation is defined by kyanite and kyanite-bearing leucosome. The presence of kyanite in this leucosome suggests partial melting by muscovite dehydration-melting in the kyanite field predating or synchronous with Dp1. An early-Dp2 leucosome (12SJ14) was collected at an outcrop where Dp1 is defined by migmatitic banding (Fig. 3A). The oldest zircon group in this leucosome (Fig. 3B) yielded a weighted mean $^{206}Pb/^{207}Pb$ date of 1008 ± 18 Ma (LA-ICP-MS) and three analyses from tips yielded a weighted mean $^{206}Pb/^{238}U$ date of 1002 ± 2 Ma (CA-ID-TIMS, Fig. 3D). Because, prismatic zircon overgrowths in granulite-paragneiss is generally infer to occur only in the presence of melt and that zircon of this group is depleted in HREE (Rubatto et al., 2001, 2002), we interpret Dp1 to have formed at 1002 ± 2 Ma at high pressure near the thermal peak. The older age-bracket of Dp2 is provided by the overgrowth-2 zircon in this same sample interpreted as dating the crystallization of this axial-planar Dp2 leucosome (Fig. 3A-B). It yielded a weighted mean $^{206}Pb/^{207}Pb$ date of 995 ± 21 Ma (LA-ICP-MS) and one analysis of a tip yielded a $^{206}Pb/^{238}U$ date of 986 ± 4 Ma (CA-ID-TIMS, Fig. 3D). The younger age-bracket for Dp2 is provided by a crosscutting gabbro co-magmatic with a pegmatite (12SJ27E) that yielded a weighted mean $^{206}Pb/^{207}Pb$ date of 961 ± 22 Ma (LA-ICP-MS).

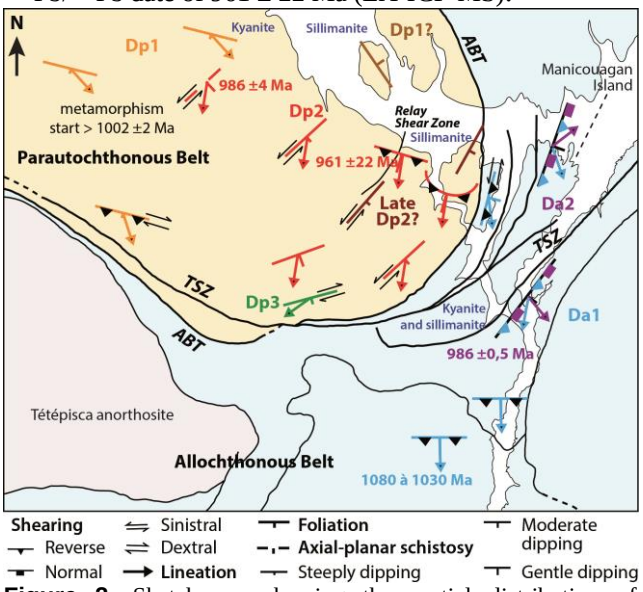


Figure 2. Sketch-map showing the spatial distribution of deformation stages and their ages in the study area (not to scale).

The Dp2 lineation defined by retrograde hornblende in this gabbro coupled to the presence of the reactants of the biotite dehydration-melting reaction (biotite + sillimanite) in the tails of a syn-Dp2 δ garnet porphyroblast imply that Dp2 occurred along a retrograde metamorphic path. Dp2 is thus bracketed between 986 ± 4 and 961 ± 22 Ma, which imply a minimum of 14 myr of reverse shearing along a

retrograde P-T path, throughout which time, leucogranite were generated and emplaced in a ductile crust.

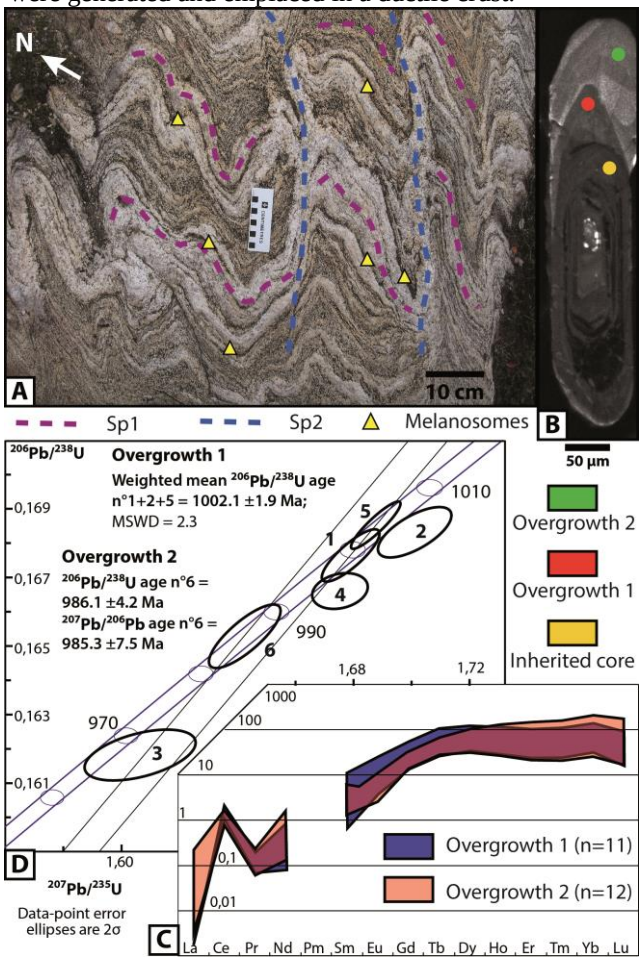


Figure 3. 12SJ14 outcrop. A) Pre- to syn- Dp2 axial-planar leucosomes. B) Zircon from leucosome 12SJ14 with two overgrowths surrounding an inherited core. C) Similar REE profiles of the two zircon overgrowths (results from LA-ICP-MS). D) Concordia diagrams of U-Pb analyses of overgrowth 1 and 2 (results from CA-ID-TIMS).

3.2 Deformations and U-Pb dating in the Allochthonous Belt

Two deformation stages were mapped in the AB (Da1 and Da2). In the northern part of the Manicouagan Island (Fig. 2), a NNE-SSW Da1 foliation with a SSE plunging lineation indicates sinistral-reverse, top-to-the-NNW shearing that is reworked by a NNE-SSW Da2 foliation with a SE plunging lineation indicating down-to-the-SE shearing. On the southern part of this island, a folded EW Da1 foliation, with a S plunging lineation, indicates reverse, top-to-the-N shearing that is reworked by a NE plunging lineation indicating a sinistral-normal down-tothe-NE shearing. We interpret this localized Da2 deformation as a normal shear zone that we named the Thachic shear-zone (TSZ).

Kinematic indicators allow us to link the Da1 and Da2 to metamorphism. Similar to Dp2, the presence of the reactants of the biotite dehydration-melting reaction (biotite + kyanite) in the tails of a syn-Da1 δ garnet porphyroblast imply that Dp2 occurred along a retrograde metamorphic path in the kyanite field.

Because monazite that yielded ages between 1080-1030 Ma were interpreted to have crystallized along a cooling path in in anatectic metapelites of the AB (Lasalle et al., 2014), Da1 most likely occurred during that timeframe as well. A syn- to post- Da2 spiral-shape garnet showing rational faces in leucosome (Fig. 4B), indicates that part of the normal shearing along the TSZ proceeded at high temperature.

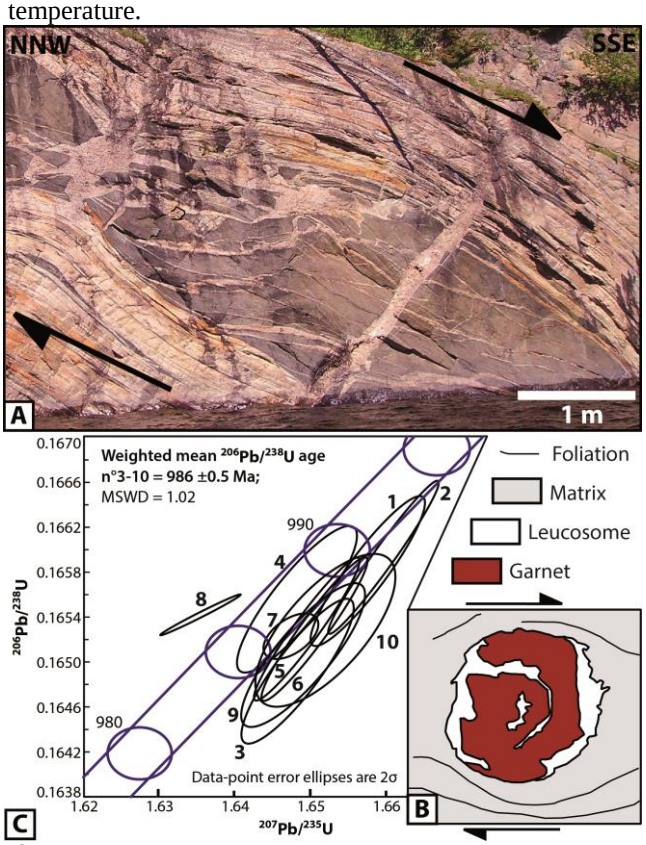


Figure 4. A) Syn-Da2 pegmatitic dykes. Their drag along the lower and upper boundaries of the mafic boudins indicate a normal sense of shear. B) A faceted spiral shape garnet in leucosome indicates crystallisation of the garnet and the leucosome syn- to post- Da2 normal sense-shear. C) Concordia diagrams of U-Pb analyses of a syn-Da2 pegmatite (results from CA-ID-TIMS).

A key characteristic of the TSZ is the abundance of synkinematic pegmatite. These pink pegmatites embody biotite and magnetite and can be distinguished from an older generation of white pegmatite by their colour, the presence of biotite and a lower proportion of quartz. The white pegmatites are more abundant at structurally lower levels where they show evidence of solid-state deformation. The synkinematic nature of the pink pegmatite within the TSZ is notably demonstrated by the entrainment at the margin of mafic boudin (Fig. 4A) in undeformed pegmatite that show evidence of solid-state, C/S-type deformation elsewhere on the same outcrop.

The timing of Da2 is provided by of the age of a synkinematic pink pegmatite. It yielded a weighted mean

$^{206}Pb/^{238}U$ date of 986.2 ±0.5 Ma (CA-ID-TIMS on zircons; Fig. 4C). Normal shearing along the TSZ was, therefore, synchronous, within errors, with the 986-961 Ma Dp2 reverse-deformation in the PB (Fig. 2-4).

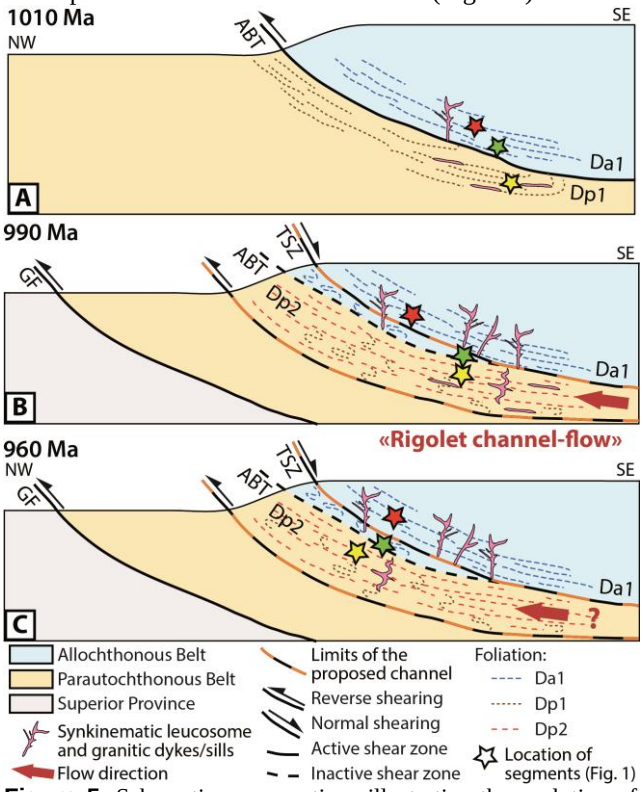


Figure 5. Schematic cross-sections illustrating the evolution of the study area with a Rigolet channel-flow providing crosscutting REE-rich pegmatites in upper structural domains.

4 Interpretation & conclusions: Channel flow control on leucogranites/pegmatite generation & emplacement

This integrated structural, metamorphic, geochronological study allows us to test tectonic models for the exhumation of the PB. The presence of two synchronous shear zones, reverse at the base and normal at the top of a panel laden with melt that was recording an exhumation path are key characteristics of channel-flow (Fig. 5; Gervais and Brown, 2011). The fact that the normal-sense TSZ is located within the AB implies that the lower portion of the AB was incorporated in the PB channel, which contrast with upper parts of the AB that was at upper crustal levels at that time.

Our study further documents the strong control that channel-flow processes exert on leucogranite/pegmatite generation, emplacement and geometry. During their underthrusting, fertile metasedimentary rocks of the PB were partially melted, which allowed their viscosity to drop to allow their flow down pressure gradients. Segregation of the melt led to protracted leucogranite/pegmatite emplacement as synkinematic dykes and sills within the channel with an increasing volume towards the normal-sense shear-zone at its roof (Fig. 5).

Although not documented in this study, it is likely that the passive hanging wall would be intruded by swarms of cross-cutting leucogranite/pegmatite dykes generated within the channel. Evidence for this is provided by the REE-rich pegmatite dykes emplaced at a structurally upper level of the AB between 1000 and 1005 Ma, which is the same timing as Dp1-leucosome (Fig. 3; Turlin et al., this volume and submitted). As similar granitic magmatism distribution was documented in other orogens for which channel flow models were proposed (SE Canadian Cordillera and the Himalayas), such systems appears like good REE-exploration targets.

Acknowledgements

The authors would like to thank the Ministère de l'Énergie et des Ressources naturelles du Québec for providing technical and financial support for the field work and analyses.

References

Cottle JM, Larson KP, and Kellett DA (2015) How does the mid-crust accommodate deformation in large, hot collisional orogens? A review of recent research in the Himalayan orogen. Journal of Structural Geology, 78: 119–133.

Dunning G, and Indares A (2010) New insights on the 1.7–1.0 Ga crustal evolution of the central Grenville Province from the Manicouagan – Baie Comeau transect. Precambrian Res., 180: 204–226.

Gervais F, and Brown RL (2011) Testing modes of exhumation in collisional orogens: Synconvergent channel flow in the southeastern Canadian Cordillera. Lithosphere, 3: 55–75.

Jamieson RA, Beaumont C, Warren CJ, et al. (2010) The Grenville Orogen explained? Applications and limitations of integrating numerical models with geological and geophysical data. Can. J.Earth Sci., 47: 517–539.

Jordan SL, Indares A, and Dunning G (2006) Partial melting of metapelites in the Gagnon terrane below the high-pressure belt in the Manicouagan area (Grenville Province): pressure–temperature (P–T) and U–Pb age constraints and implications. Can. J. Earth Sci., 43: 1309–1329.

Lasalle, S., Dunning, G. and Indares, A. (2014). In situ LA–ICP–MS dating of monazite from aluminous gneisses: insights on the tectono-metamorphic history of a granulite-facies domain in the central Grenville Province. Can. J. Earth Sci. 51:558-572.

Rivers T (2008) Assembly and preservation of lower, mid, and upper orogenic crust in the Grenville Province—Implications for the evolution of large hot long-duration orogens. Precambrian Res., 167: 237–259.

Rubatto D (2002) Zircon trace element geochemistry: partitioning with garnet and the link between U-Pb ages and metamorphism. Chem. Geo., 184: 123–138.

Rubatto D, Williams IS, and Buick IS (2001) Zircon and monazite response to prograde metamorphism in the Reynolds Range, central Australia. Contrib. Mineral. and Petrol., 140: 458–468.

Searle MP, Robb LJ, and Gardiner NJ (2016) Tectonic Processes and Metallogeny along the Tethyan Mountain Ranges of the Middle East and South Asia (Oman, Himalaya, Karakoram, Tibet, Myanmar, Thailand, Malaysia). Soc. Econ. Geol., Spec. Publ., 19: 301–327.

Turlin F, André-Mayer A-S, Crépon A, et al. (this volume). The Parautochthonous Belt as a Source of Grenvillian LREE-Rich Pegmatitic Granite Dykes.

Turlin F, André-Mayer A-S, Moukhsil A, et al. Unusual LREE-rich, post-tectonic, monazite- or allanite-bearing pegmatitic granite in the central Grenville Province, Québec. Submitted to Ore Geol. Rev. 2017.

An early magmatic fluid pulse at Cononish orogenic gold deposit? Tellurium enrichment and implications for orogenic gold formation

Gawen R.T. Jenkin
University of Leicester, U.K.

Carl Spence–Jones
University of Leeds, U.K.

Adrian J. Boyce
Scottish Universities Environmental Research Centre, U.K.

Nyree J. Hill, Christopher J.S. Sangster
Scotgold Resources

Abstract. Tellurium enrichment occurs in many orogenic gold deposits. Fractionation of Te from Se and S could offer insight into source/pathway processes of auriferous fluids. In the Te–rich metasedimentary–hosted Cononish vein gold deposit, Scotland, Ag in Au–Ag alloy increases from ~20 to 80 wt.% through the paragenesis, correlating with decreasing hessite abundance. This suggests the Au–Ag alloy composition was controlled by the fluid Te activity, which decreased through time. This is coupled to an increase in pyrite $\delta^{34}S$ from -1.9‰ to +11.4‰ through the paragenesis. Thus, the deposit formed from a primary fluid with a low–$\delta^{34}S$ and high Te+Au+Ag that evolved towards a high $\delta^{34}S$–low Te fluid. The high $\delta^{34}S$ of the later fluid suggests it can only be a metamorphic fluid sourced from nearby SEDEX horizons. The early fluid that deposited most of the gold could be metamorphic fluid from other units in the stratigraphy, or magmatic in origin. Two observations taken together suggest it is most likely that this fluid was magmatic; the age of the mineralisation is identical to the last stage of crystallization of nearby granite batholiths, and the fluid has a S–isotope signature consistent with a magmatic source. Tellurium in *some* orogenic gold deposits may relate to magmatic input.

1 Introduction

Orogenic gold deposits are a broad class of deposits exhibiting a common set of features (Goldfarb et al. 2005) and are typically deposited from low–salinity CO_2–bearing fluids (Goldfarb and Groves 2015). Despite commonality of broad features, variations in isotopic composition, mineral assemblage, and metal enrichments exist (Chapman and Mortensen 2016; Goldfarb and Groves 2015; Groves et al. 1998), and the interpreted source of the ore fluids, and the dissolved constituents they transport, remains controversial (Goldfarb et al. 2005; Goldfarb and Groves 2015; Wyman et al. 2016). Whilst a metamorphic fluid source remains the most likely model for the majority of orogenic deposits, input of magmatic fluids may be important in some deposits (Goldfarb et al. 2005). The cause of Te–enrichment in orogenic gold deposits mirrors this dichotomy, with some workers advocating that this indicates a magmatic source (Burrows and Spooner 1989) whereas others suggest it need not (Goldfarb et al. 2000).

The planned development of the Cononish gold mine, Scotland (estimated reserves of 555,000 tonnes of ore grading at 11.1 g/t Au and 47.7 g/t Ag; Scotgold Resources Limited 2015), alongside the development of Curraghinalt and Cavanacaw mines in Ireland, has catalysed a re–evaluation of gold metallogenesis in the Caledonides. The Cononish deposit, located 3 km south west of Tyndrum, contains significant Te (Te/Au by weight ~≥1, suggesting >7 t Te; Science and Technology Committee 2011) and provides an excellent system in which to study the fluids and processes that formed the mineralisation. Fluid inclusion and stable isotope data are available, along with textural and mineralogical descriptions of the mineralised veins (Pattrick et al. 1988; Earls et al. 1992; Curtis et al. 1993). However, the detailed paragenesis of the veins has never been described and linked to mineral chemistry and stable isotope data. Furthermore, the genesis of the deposit remains contentious, with either magmatic or metamorphic fluids (±meteoric) interpreted to have formed the deposit (Pattrick et al. 1988; Curtis et al. 1993; Craw and Chamberlain 1996). Here, a combined study of the paragenesis, Au–Ag alloy composition, and sulfur isotopes provides evidence for an early Te–bearing magmatic fluid.

2 Geological setting

The Tyndrum area comprises Neoproterozoic Dalradian Supergroup metasediments that were subjected to amphibolite–grade metamorphism and deformation (D_1–D_4) during the Grampian Orogeny, ~470 Ma (Stephenson et al. 2013). The sequence is dissected by major NE–trending sinistral faults with a normal component that developed late in the orogeny, including the Tyndrum fault. The Cononish deposit comprises a composite vein structure hosted within the sub–vertical Eas Anie Structure (041/89SE) that is associated with a splay off the Tyndrum Fault (see geological map in Hill et al. 2013).

The Eas Anie Structure crosscuts Grampian and lower– Appin Group units that were deformed into large north– east verging nappe structures during the Grampian orogeny (Tanner and Thomas 2010; Tanner 2012). The Cononish deposit is situated on the "upper" southerly

dipping limb of an anticline. The stratigraphy on the lower limb of the fold is overturned and inferred to exist at depth below the deposit (Earls et al. 1992; Stephenson et al. 2013; Tanner 2014). The Cononish Au–Ag (±Cu, Pb) mineralisation was dated by Rice et al. (2012) at 408 ± 2 Ma and 407 ± 1 Ma using Ar/Ar of K–feldspar.

3 Vein stages

The vein is predominantly formed from massive milky white quartz, produced by multiple, sub–millimetre wide vein generations with minor pyrite, chalcopyrite, and galena. The multigenerational quartz has recrystallized, however, the form of the finer veinlets is preserved and can be distinguished through translucency and inclusion density variations in plane–polarised light. Through examining crosscutting relationships, textures and mineral associations, a detailed paragenesis has been determined (Spence–Jones 2013)(Fig. 1):

Stage 1 – early quartz veining

The majority (up to an estimated 70–80% by volume) of the multigenerational quartz breccia making up the vein formed early in its development and is classified as Stage 1. This comprises a milky white quartz dominated matrix–supported breccia. The clasts (up to ~80 cm) are composed of silicified host rocks that are significantly rotated in relation to the orientation of fabrics in the host lithologies. The quartz was originally formed by a multitude of fine 50–1000 µm stringer veins but has now recrystallized.

Stage 2 – early Au–Ag mineralisation

Coarse, up to 2 cm, euhedral cubic pyrite crystals occur within the early quartz veins in sulfide–rich pods that range in size from 1 cm to up to 30 cm. These pods are hosted within the quartz vein and also form 1–10 cm halos around altered clasts. This early euhedral pyrite is interpreted to have formed later than the Stage 1 quartz veinlets since the pyrite has not been crosscut by any of the quartz veinlets nor do they contain any quartz inclusions.

The coarse pyrite crystals host the earliest Au–Ag (±Cu, Pb) mineralisation within fractures and as trails of inclusions. The fractures contain the assemblage hessite + Au–Ag alloy + galena ± altaite ± chalcopyrite that is diagnostic of the Au–Ag mineralisation.

Stages 3–4 – evolution of the Au–Ag mineralisation

The vein material formed during Stages 1 and 2 is cross cut and comminuted by later narrow, 0.5–10 cm–wide shears that typically form anastomosing arrays up to half a metre wide. These shears host abundant chalcopyrite and galena with subordinate pyrite, sphalerite, calcite and Au–Ag alloy. The sulfides comprise >50% by volume of the late vein mineralogy. Stage 3 and 4 veins have been separated to represent end–members of a continuous trend based on the relative proportions of chalcopyrite and galena, progressing from 90% galena to 90% chalcopyrite (the latter often observed with calcite). The galena–rich veins are inferred to be earlier (Stage 3) as they are crosscut by later calcite–chalcopyrite veins. Whether a particular vein in an individual sample is Stage 3 or 4 is difficult to decide due to variations in mineralogy along the veins. The distinction is made for the deposit as a whole taking into account the compositions of the associated Au–Ag alloy, and the dominance of galena over chalcopyrite in the early Au–Ag mineralisation stages.

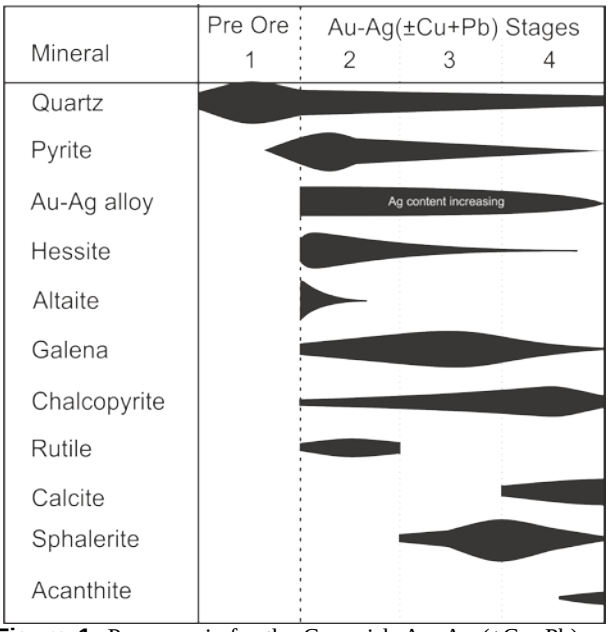


Figure 1. Paragenesis for the Cononish Au–Ag (±Cu, Pb) vein after Spence–Jones (2013).

4 Au–Ag alloy composition and association

The gold and silver concentrations in 215 individual Au–Ag alloy grains (formerly "electrum") were measured by SEM–EDX (Spence–Jones 2013). Compositions are highly variable, ranging from ~10% to ~90 wt.% Ag (Fig. 2). This is in contrast to many hydrothermal gold deposits, with the exception of epithermal deposits, which show much narrower compositional ranges with Au–Ag alloy ranging between 75–90% Au, or 60–90% as reported from placers (Chapman and Mortensen 2006, 2016; Chapman et al. 2010; Morrison et al. 1991).

Narrower ranges in composition (10–20% variation) occur within individual samples, indicating that the gold formed under similar conditions within a thin section sized sample of the vein. This supports the textural observations that later fluid phases have overprinted the earlier phases chemically and texturally, unless minerals are shielded from the late fluid as inclusions within early minerals.

There is a distinct association of the Au–rich alloy (gold) grains with hessite, whereas Ag–rich alloy (silver) is strongly associated with chalcopyrite (Fig. 2). Galena is associated with the whole range of Au–Ag alloy compositions.

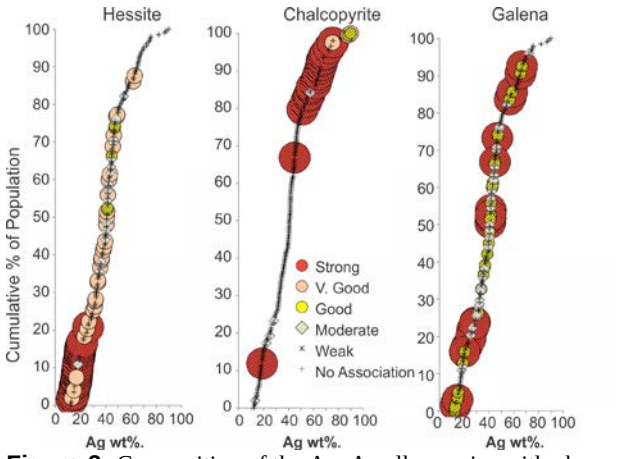


Figure 2. Composition of the Au–Ag alloy grains with observed mineral associations for hessite, chalcopyrite and galena using a qualitative scale. The size of the circle indicates the qualitative strength of the association: Strong association indicates the phases are clearly related, for example intergrown mineral textures. Moderate association indicates minerals that are observed together in a fracture or a veinlet. Weak association represents a tenuous link, such as Au–Ag alloy occurring in veins sets that contain the associated mineral distally. No association indicates the minerals were not observed with Au–Ag alloy in a vein.

5 Sulfur isotope data

Figure 3A shows 16 new pyrite S–isotope analyses along with the combined published S–isotope dataset for Cononish. These show a range of $\delta^{34}S$ values from -1.9 to +11.4‰. Samples for this study were taken from coarse pyrite crystals that are temporally constrained in the paragenetic sequence described above. This reveals a trend of increasing $\delta^{34}S$ through the paragenetic sequence (Fig. 3B). Two samples that could relate to either Stage 3 or 4, as they show mineralogical and textural features of both stages, were plotted as Stage 3.5. To avoid bias in the results, the position of the samples in the paragenesis was determined and recorded prior to analysis.

6 Discussion

6.1 Evolution of Au–Ag alloy composition

At Cononish, the Au–Ag alloy coexists with hessite, in which case the activity of Ag will be buffered by this phase (Gammons and Williams–Jones 1995) and the composition of Au–Ag alloy will thus be dependent on the activity of Te_2 in the system (Afifi et al. 1988). Put simply, if aTe_2 is high then large proportions of hessite will precipitate removing Ag available to the Au–Ag alloy and keeping the activity of Ag low. This will produce Au–rich alloy, as the buffered ratio of the Au/Ag activity will be high. In Stage2, hessite is abundant along with Au–rich alloy; 90–75% Au. In Stages 3 and 4, the abundance of hessite decreases (Fig. 1), with no hessite seen in Stage 4, and here associated Au–Ag alloy grains have higher silver contents; 10%–75% Au. In late Stage 4 veinlets, acanthite occurs instead of hessite. It is interpreted that high aTe_2 in the early fluid controlled the composition of the early Au–Ag alloy and a progressive decrease in aTe_2 over time led to the deposition of progressively more Ag–rich alloy until aTe_2 decreased sufficiently in late Stage 4 that acanthite was deposited. To reduce aTe_2 with time *via* temperature change, a temperature rise would have been required (Afifi et al. 1988), which would seem unlikely given the limited range of fluid inclusion temperatures (Curtis et al. 1993). More likely it relates to a change in fluid source.

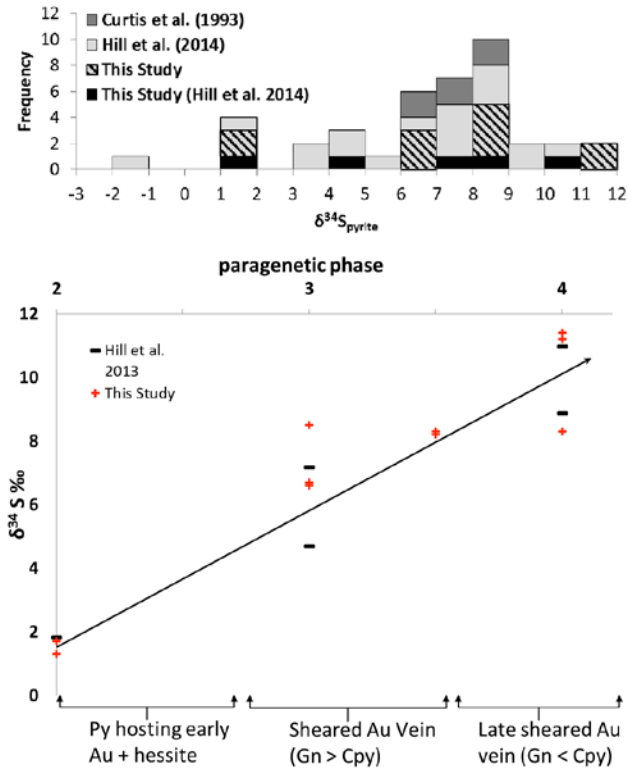


Figure 3. A. Histogram of compiled pyrite $\delta^{34}S$ for the Cononish deposit. **B.** Pyrite $\delta^{34}S$ vs. paragenetic stage.

6.2 Sulfur sources

The evolution in $\delta^{34}S_{pyrite}$ represents a significant shift in the sulfur isotope composition of the fluid, which is interpreted as a change of the sulfur source. Hill et al. (2013) examined the $\delta^{34}S$ of the local stratigraphy and discussed potential sulfur reservoirs. They demonstrated that it is possible to produce the full range of S–isotope values at Cononish, either from mixing of sulfur from different units in the local stratigraphy, or by mixing of magmatic sulfur with metasedimentary derived sulfur with $\delta^{34}S \geq +12‰$ from particular SEDEX–bearing stratigraphic units. Hill et al. (2013) advocated the latter scenario given the timing of the mineralisation long after metamorphism, but synchronous with the final stages of nearby granite magmatism and its mineralisation (Neilson et al. 2009). The paragenetically constrained pyrite $\delta^{34}S$ data support this interpretation, with the increase through the paragenesis interpreted as an early magmatic fluid progressively mixing over time with metasedimentary

sulfur. To produce the same trend in $\delta^{34}S$ values over time from a purely metasedimentary–sourced hydrothermal system would have required mixing of fluids from different reservoirs that changed during deposit formation.

7 Implications

The Cononish Au deposit formed as the result of an early fluid pulse from a low–$\delta^{34}S$ (~1‰), high Te+Au+Ag source that evolved towards a high–$\delta^{34}S$ (≥11‰), low Te fluid with time. The low $\delta^{34}S$ source is interpreted here as a magmatic pulse of fluid and the evolution away from the strongly Te–saturated initial fluid is interpreted as a waning of magmatic fluid input and regaining of geochemical equilibrium with the Dalradian metasediments. Thus in *some* orogenic Au deposits it would seem that high Te relates to an input of magmatic fluid.

Acknowledgements

NH was funded by the Natural Environment Research Council (NERC) Open CASE studentship NE/H017755/1 with Scotgold Resources Ltd. Scotgold are acknowledged for financial and logistical field support and access to company information. S–isotope analyses were carried out at SUERC under NERC Isotope Facilities grant IP–1317–0512. AJB is funded by NERC support of the Isotope Community Support Facility. GRTJ is supported by NERC Minerals Security of Supply (SoS) grant NE/M010848/1 Tellurium and Selenium Cycling and Supply (TeaSe).

References

Afifi AM, Kelly WC, Essene EJ (1988) Phase relations among tellurides, sulfides, and oxides; I, thermochemical data and calculated equilibria. Econ Geol 83:377–394.

Burrows DR, Spooner ETC (1989) Relationships between Archean gold quartz vein–shear zone mineralization and igneous intrusions in the Val d'Or and Timmins areas, Abitibi subprovince, Canada. Econ Geol Monograph 6:424–444.

Chapman RJ, Mortensen JK (2016) Characterization of gold mineralization in the northern Cariboo Gold District, British Columbia, Canada, through integration of compositional studies of lode and detrital gold with historical placer production: A template for evaluation of orogenic gold. Econ Geol 111:1321–1345.

Chapman RJ, Mortensen JK, Crawford EC, Lebarge W (2010) Microchemical studies of placer and lode gold in the Klondike district, Yukon, Canada: 1. Evidence for a small, gold–rich, orogenic hydrothermal system in the Bonanza and Eldorado Creek area. Econ Geol 105:1369–1392.

Craw D, Chamberlain CP (1996) Meteoric incursion and oxygen fronts in the Dalradian metamorphic belt, southwest Scotland: A new hypothesis for regional gold mobility. Miner Deposita31:365–373.

Curtis SF, Pattrick RAD, Jenkin GRT, Fallick AE, Boyce AJ, Treagus JE (1993) Fluid inclusion and stable isotope study of fault–related mineralization in Tyndrum area, Scotland. Trans Inst Min Metall Section B–Appl Earth Sci 102:B39–B47.

Earls G, Patterson RTG, Clifford JA, Meldrum AH (1992) The geology of the Cononish gold silver deposit, Grampian Highlands of Scotland. In Bowden AA (ed) The Irish minerals industry 1980–1990, Irish Association for Econ Geol pp 89–103.

Gammons CH, Williams–Jones AE (1995) Hydrothermal geochemistry of electrum – thermodynamic constraints. Econ Geol 90:420–432.

Goldfarb RJ Groves DI (2015) Orogenic gold: Common or evolving fluid and metal sources through time. Lithos 233:2–26.

Goldfarb RJ, Hart C, Miller M, Miller L, Farmer GL, Groves DI (2000) The Tintina Gold Belt – A global perspective. In Tucker TL, Smith MT (eds) The Tintina gold belt – Concepts, exploration, and discoveries. British Columbia and Yukon Chamber of Mines Spec Vol 2:5–34.

Goldfarb RJ, Baker T, Dubé B, Groves DI, Hart CJR, Gosselin P (2005) Distribution, character, and genesis of gold deposits in metamorphic terranes. Econ Geol 100th Anniv Vol pp 407–450.

Groves DI, Goldfarb RJ, Gebre–Mariam M, Hagemann SG, Robert F (1998) Orogenic gold deposits: A proposed classification in the context of their crustal distribution and relationship to other gold deposit types. Ore Geol Rev 13:7–27.

Hill NJ, Jenkin GRT, Boyce AJ, Sangster CJS, Catterall DJ, Holwell DA, Naden J, Rice CM (2013) How the Neoproterozoic S–isotope record illuminates the genesis of vein gold systems: An example from the Dalradian Supergroup in Scotland. Geol Soc, London, Spec Pub 393:213–247.

Morrison GW, Rose WJ, Jaireth S (1991) Geological and geochemical controls on the silver content (fineness) of gold in gold–silver deposits. Ore Geol Rev 6:333–364.

Neilson JC, Kokelaar BP, Crowley QG (2009) Timing, relations and cause of plutonic and volcanic activity of the Siluro–Devonian post–collision magmatic episode in the Grampian terrane, Scotland. J Geol Soc 166:545–561.

Pattrick RAD, Boyce A, MacIntyre RM (1988) Gold–silver vein mineralization at Tyndrum, Scotland. Mineral Petrol 38:61–76.

Rice CM, Mark DF, Selby D, Hill NJ (2012) Dating vein–hosted Au deposits in the Caledonides of N. Britain. Trans Inst Min Metall (Section B. Appl Earth Sci) 121:199–200.

Science and Technology Committee, House of Commons (2011) Strategically important metals. HC 726, The Stationery Office Limited, London.

Scotgold Resources Limited (2015) Cononish gold project study update and JORC 2012 ore reserve estimate http://www.asx.com.au/asxpdf/20150526/pdf/42yt26kn3xqj6x.pdf.

Spence–Jones C (2013) Metallurgical investigation of ore at Cononish Gold Mine, Scotland. MGeol thesis, University of Leicester.

Stephenson D, Mendum JR, Fettes DJ, Leslie AG (2013) The Dalradian rocks of Scotland: An introduction. Proc Geol Ass 124:3–82.

Tanner PWG (2012) The giant quartz–breccia veins of the Tyndrum–Dalmally area, Grampian highlands, Scotland: Their geometry, origin and relationship to the Cononish gold–silver deposit. Earth and Environ Sci Trans Roy Soc Edinburgh 103:51–76.

Tanner PWG (2014) Structural controls and origin of gold–silver mineralization in the Grampian terrane of Scotland and Ireland. Geol Mag 151:1072–1094.

Tanner PWG, Thomas PR (2010) Major nappe–like D2 folds in the Dalradian rocks of the Beinn Udlaidh area, Central Highlands, Scotland. Earth and Environ Sci Trans Roy Soc Edinburgh 100:371–389.

Wyman DA, Cassidy KF, Hollings P (2016) Orogenic gold and the mineral systems approach: Resolving fact, fiction and fantasy. Ore Geol Rev 78:322–335.

Two stages of skarn formation in the Hämmerlein tin-skarn deposit, western Erzgebirge, Germany

Marie G. Lefebvre, Rolf L. Romer, Johannes Glodny
German Research Centre for Geosciences GFZ, Potsdam, Germany

Marco Roscher
Saxore Bergbau GmbH, Freiberg, Germany

Abstract. The Hämmerlein Sn-skarn deposit of the western Erzgebirge is hosted in early Palaeozoic schists and gneisses and is closely associated with one of the most voluminous granite intrusions of the Erzgebirge, the Eibenstock granite. The main valuable ore mineral in Hämmerlein is cassiterite which is disseminated in the four types of skarn occurring in the deposit, i.e., garnet, amphibole, pyroxene, and magnetite skarn. There are two scenarios for deposit formation: (1) formation of the skarn during the regional metamorphism at 340 Ma followed by mineralization during granite emplacement at 320 Ma and (2) skarn formation and mineralization directly related to the granite intrusion. Theriak-Domino thermodynamic P-T-XCO_2 modelling shows that both scenarios are possible for the formation of the skarn series, but as the Rb-Sr muscovite-based age of skarn samples is 340 Ma, the first scenario is the relevant one. The skarn mineral assemblages formed during regional metamorphism, whereas cassiterite mineralization is related to younger granite emplacement and is associated with chloritization of biotite and precipitation of fluorite. These reactions changed the fluid composition and induced cassiterite mineralization.

1 Introduction

The Hämmerlein Sn-skarn deposit is located in the western Erzgebirge and is hosted in gneisses and schists with intercalated marbles. The host rocks dominantly consist of early Paleozoic rocks that have been subducted during the Variscan orogeny and reached peak metamorphic conditions at c. 340 Ma (Rötzler at al., 1998; Kroner & Romer, 2013). The metamorphic nappes have been intruded later by a wide range of geochemically contrasting granites, some of which with important tin mineralization (Förster et al., 1999). The S-type Eibenstock granite, which covers an area of 25 by 22 km, is the most voluminous granite of the Erzgebirge. It has given rise to a series of greisen-type and skarn-type Sn-W mineralizations, including the Hämmerlein Sn-skarn deposit (Schuppan & Hiller, 2012).

In the Hämmerlein deposit, cassiterite is the most valuable ore mineral. On a small scale it is irregularly distributed within the skarns subunits and in the mica schist wall-rocks. On a large scale however, its occurrence is structurally controlled. In the skarns, cassiterite generally is fine-grained and dominantly occurs in amphibole skarn. In contrast, local cassiterite occurrences in the mica schists are typically coarse-grained. In addition to Sn, the Hämmerlein skarn also contains two

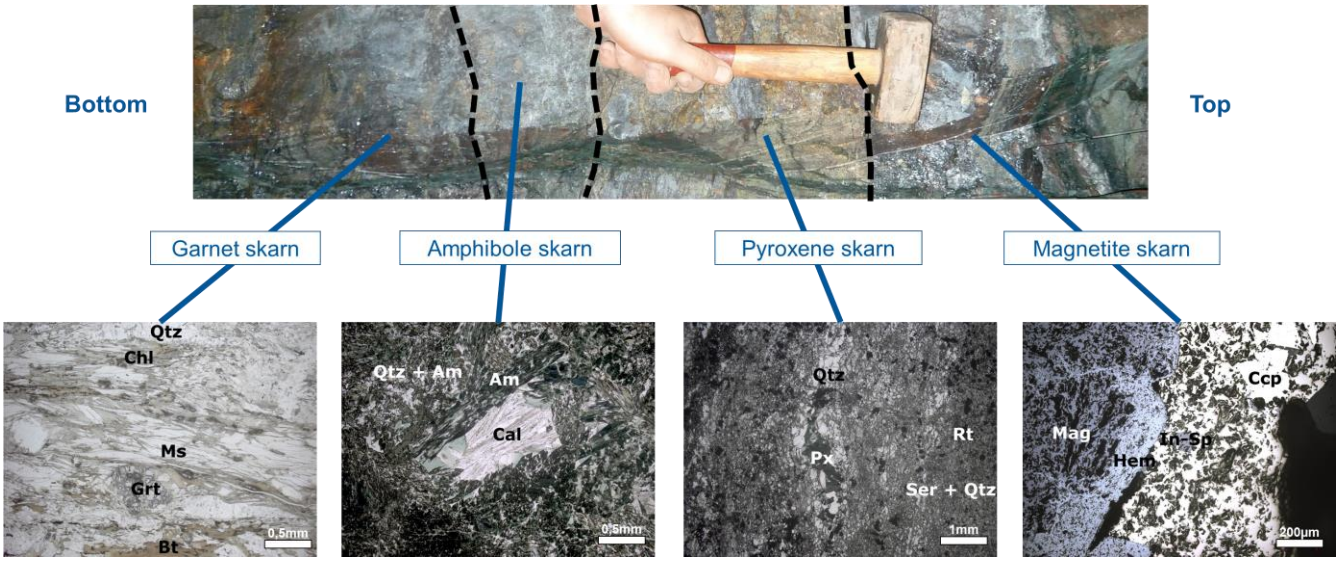


Figure 1. Hämmerlein skarn profile (Am: amphibole, Bt: biotite, Cal: calcite, Ccp: chalcopyrite, Chl: chlorite, Grt: garnet, Hem: hematite, In-Sp: In-sphalerite, Mag: magnetite, Ms: muscovite, Px: pyroxene, Qtz: quartz, Rt: rutile, Ser: sericite)

types of In mineralization. Indium is markedly enriched in a discontinuous sphalerite layer beneath the magnetite skarn, and In-sphalerite exsolutions occur in chalcopyrite lenses in the magnetite skarn.

There are two Variscan events during which fluids were available to induce skarn formation: (1) regional metamorphism at c. 340 Ma and (2) fluid escape from the Eibenstock granite, which intruded at around 320-325 Ma (Kempe et al., 2004; Romer et al., 2007). As the introduction of Sn is apparently related to the emplacement of the Eibenstock granite, as also indicated by the numerous tin greisen mineralizations related to this granite, there are two scenarios for the skarn formation: (1) the skarns crystallized at 340 Ma when metamorphic fluids produced by dehydration of the shales induced the formation of the zoned skarns. Tin was introduced later by magmatic fluids that reacted with remaining carbonates from the protolith and/or altered the existing mineral assemblage of the skarn. In this case, there were two separate skarn-forming events. (2) No fluids were available to induce skarn formation during regional metamorphism at 340 Ma and the skarn was formed by a magmatic fluid that also introduced the metals into the skarn. In this case, the skarn mineralization would reflect one single event.

We present P-T models based on the chemistry of skarn samples. Rb-Sr mineral data have been used to determine the chronology of skarn formation, and to distinguish between the two mineralizations scenarios.

2 Samples

There are four skarn types at Hämmerlein that at the sample location form a profile (Fig. 1) from bottom to the top of the skarn unit: garnet skarn, amphibole skarn, pyroxene skarn and magnetite skarn. The brownish-red garnet skarn is composed of phenocrysts of almandine or grossular in a feldspar-quartz-muscovite matrix. Biotite is largely altered to chlorite. The amphibole skarn is greyish-green and shows a feldspar-quartz matrix with clusters of altered grunerite surrounding calcite. Some foitite (tourmaline) crystals occur disseminated in the matrix. The light brown pyroxene skarn is similar to the amphibole skarn except for the presence of augite lenses (surrounded by quartz) instead of grunerite and the absence of tourmaline. Late veins of calcite crosscut the matrix and the augite lenses. Rare sulfides and oxides, including pyrite, arsenopyrite, and magnetite, occur as disseminated crystals in the various calc-silicate skarns. In the magnetite skarn, magnetite is strongly altered to hematite. In addition, there are irregular patches of pyrite and chalcopyrite with exsolutions of In-sphalerite in the chalcopyrite. Minor arsenopyrite and Bi-Cu minerals occur disseminated in the magnetite matrix.

The distribution of Sn within the different skarn units is heterogeneous. Sn enrichment occurs between grunerite and magnetite-hematite assemblages and within the amphibole skarn. Typically, cassiterite grains are small (~10 µm) and occur disseminated in a quartz-chlorite matrix. Only at the contact between amphibole and magnetite skarns, cassiterite crystals may locally be coarse grained (up to 10 mm).

3 Whole rock composition of the various skarn units

Despite their contrasted mineralogy, the major element chemistry of the various skarn systems, obtained by XRF analysis, is quite homogeneous averaging around 35.9% SiO_2, 0.6% TiO, 15.3% Al_2O_3, 18.7% Fe_2O_3, 1.3% MnO, 4.3% MgO, 17.6% CaO, 1.2% Na_2O and 1.6% K_2O. All silicate skarns produced from decarbonation of the protolith have high Mg and Ca contents. Furthermore, the skarns have high Fe and K contents and are enriched, to different extents, in Cu, As, In and Sn. The REE pattern of the skarns is flat and shows a positive Eu anomaly (Fig. 2). Differences among skarns are related to element concentrations, i.e., to variable dilution by phases with low REE contents. The REE patterns of skarns markedly differ from the one of mica schists and gneisses that also have a flat REE pattern but without Eu anomaly. Mineralized and barren rocks show similar REE pattern, indicating the REE were essentially immobile during skarn formation and, thus, were inherited from the protolith.

Trace element concentrations are highly variable among different skarn types, largely reflecting the ability of the various skarn minerals to incorporate different groups of trace elements.

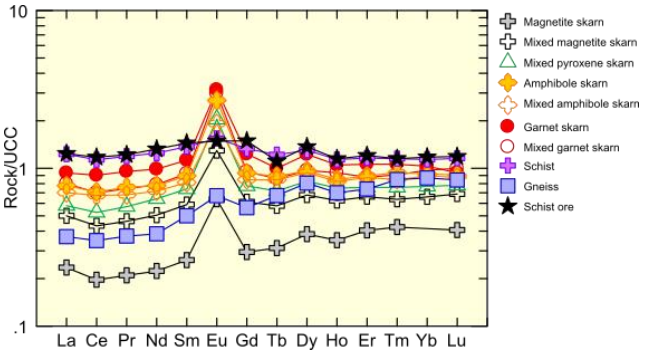


Figure 2. REE patterns of skarns, gneiss and schists from Hämmerlein deposit normalized to Upper Continental Crust (UCC) REE composition from Taylor & McLennan (1985).

4 P-T-XCO_2 models

The similarity of the whole rock composition of different skarn types implies that the mineralogical variability is controlled by P, T, and the fluid composition, most importantly XCO_2, which is modified by consumption of carbonates and possibly by phase separation. Using the average chemical composition of the skarns (except for the magnetite skarn that had been calculated with the actual composition), we modelled the mineral assemblage of the skarns for 5 kbar (regional metamorphism) and 2 kbar (contact metamorphism) in terms of temperature and

XCO_2 (Fig. 3) using the Theriak-Domino thermodynamic modelling software package of de Capitani & Petrakakis (2010).

At 2 kbar, the stability fields of the various skarn mineral assemblages differ in temperature and XCO_2 range. The garnet skarn is stable at high temperature and high XCO_2 (Fig. 3). The other skarn types show stability fields at systematically lower XCO_2 from amphibole and pyroxene to magnetite skarn (Fig. 3). Amphibole and pyroxene skarns are stable at the same temperature as the garnet skarn, but they can also be stable at lower temperature. The magnetite skarn forms at even lower temperature. Note, the temperature of formation is modelled the same for the amphibole and pyroxene skarns because the only difference between their assemblages is the occurrence of amphibole versus pyroxene + calcite veins, which can be explained by contrasting XCO_2. If the skarn formed at 2 kbar, the temperature range would imply that the various types of skarn did not form from the same fluid at the same time and that there must have been heat input with the fluid. Later formed skarns (pyroxene and magnetite skarns) would have formed at lower XCO_2 when much of the wall rock carbonates had been consumed.

At 5 kbar, the stability fields of the various skarn types are larger and shifted to higher temperatures. For the temperature range of 400-450°C all skarns types are stable, although at different XCO_2 (Fig. 3). This implies that at higher pressure, the various skarn assemblages may be produced by variation in XCO_2 alone and the skarn mineral assemblage also may have formed during regional metamorphism, when an ambient temperature of c. 450°C at 5 kbar was reached. The fluid source to form the skarns was dehydration of silicate wall-rocks, whereas the variations in XCO_2 reflect decarbonation during skarn formation and metamorphism.

5 Rb-Sr ages and mineral data

Rb-Sr multi-mineral data have been determined for a calc-silicate associated to pyroxene skarn (CSV1) and an amphibole (HAS3) skarn. Six mineral analyses define an age of 341.2 ± 3.8 (MSWD = 325) for skarn CSV1. Five mineral analyses define an age of 338.0 ± 5.0 Ma (MSWD = 77) for skarn HAS3. This implies that the skarn has formed during regional metamorphism rather than during granite emplacement. Reduced isochron diagrams (Fig. 4) show significant isotopic heterogeneity in the samples, which is also reflected in the high MSWD values. The isotopic heterogeneity is most obvious for albite and fluorite of sample CSV1 and for blue fluorite of sample HAS3 that have highly radiogenic initial $^{87}Sr/^{86}Sr$ values (Fig. 4). Textural evidence shows that fluorite along with chlorite formed later than white mica. The Sr isotopes support this observation as they imply that fluorite and, to some degree, also albite obtained their Sr from a different reservoir than white mica. To develop a Sr isotopic composition as radiogenic as observed in fluorite, the Sr

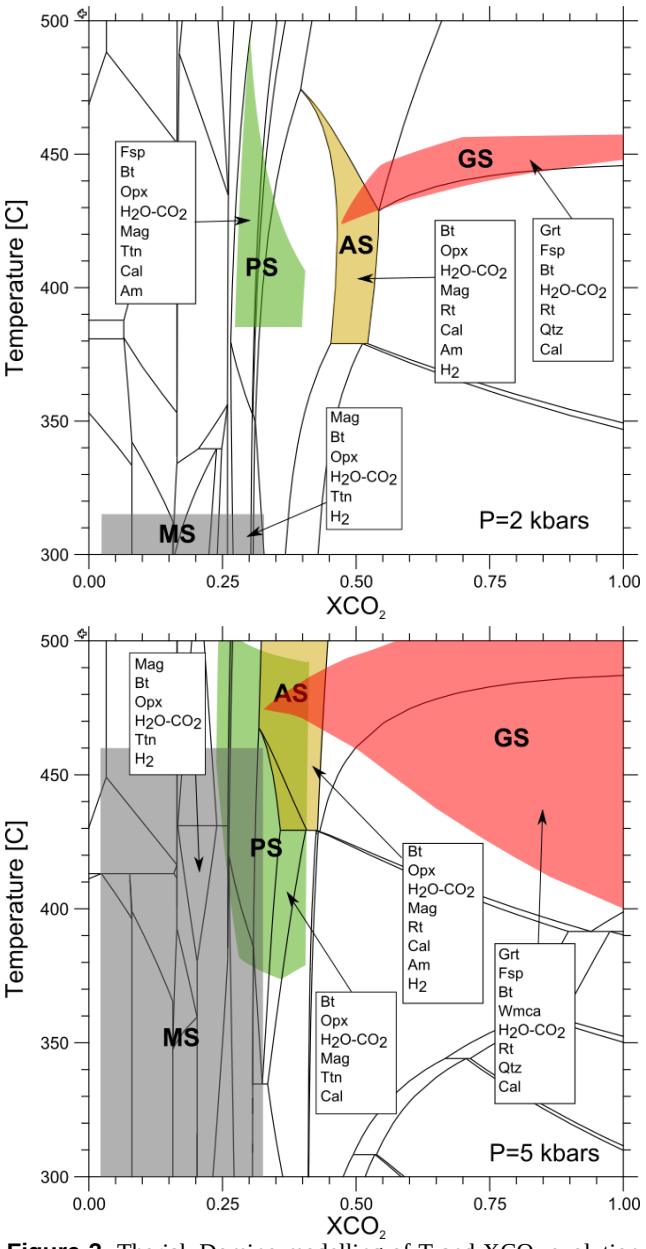


Figure 3. Theriak-Domino modelling of T and XCO_2 evolution of Hämmerlein skarns at 2 kbar (up) and 5 kbar (down) (Am: amphibole, Bt: biotite, Cal: calcite, Fsp: feldspar, Grt: garnet, Mag: magnetite, Opx: orthopyroxene, Qtz: quartz, Rt: rutile, Ttn: titanite, Wmca: white mica)

source needs a very high $^{87}Rb/^{86}Sr$ ratio for quite some time. It should be noted that the white mica did not record the younger crystallization event giving rise to fluorite, albite, and chlorite. Instead, white mica dates the regional metamorphism at 340 Ma.

6 Discussion

The muscovite-based Rb-Sr ages of the skarn samples demonstrate that the skarn formed at around 340 Ma. This age is identical to the age of regional metamorphism of the host-rocks of the skarns. Thus, the skarn formation is likely to have been induced by fluids derived from the

metamorphism of the silicate wall rocks. Textural evidence shows that one generation of fluorite is related to a later event, during which albite and chlorite crystallized. Chlorite formed at the expense of biotite, which is present only as rare relics. Chlorite also forms pseudomorphs after amphibole. Cassiterite in the skarns always occurs together with chlorite. Therefore, cassiterite crystallization may be related to chloritization of biotite and alteration of amphibole. The fluid that induced chloritization may have transported Sn along with F. The destruction of biotite released the radiogenic Sr incorporated in fluorite and albite. The dissolution of biotite and/or the precipitation of fluorite may have changed the ability of the fluid to complex and transport Sn, thus, eventually leading to the precipitation of cassiterite. The martitization of magnetite can also be in part responsible for the precipitation of cassiterite.

The source of the fluid inducing the precipitation of fluorite and cassiterite and the chloritization of biotite in the skarn is not related to the regional metamorphism at 340 Ma, but is likely related to the intrusion of the Eibenstock granite because of the following reasons: (i) cassiterite, chlorite, and fluorite are texturally related and (ii) the Sr isotopic data show that one generation of fluorite was formed later than 340 Ma as it is out of equilibrium with the skarn assemblages.

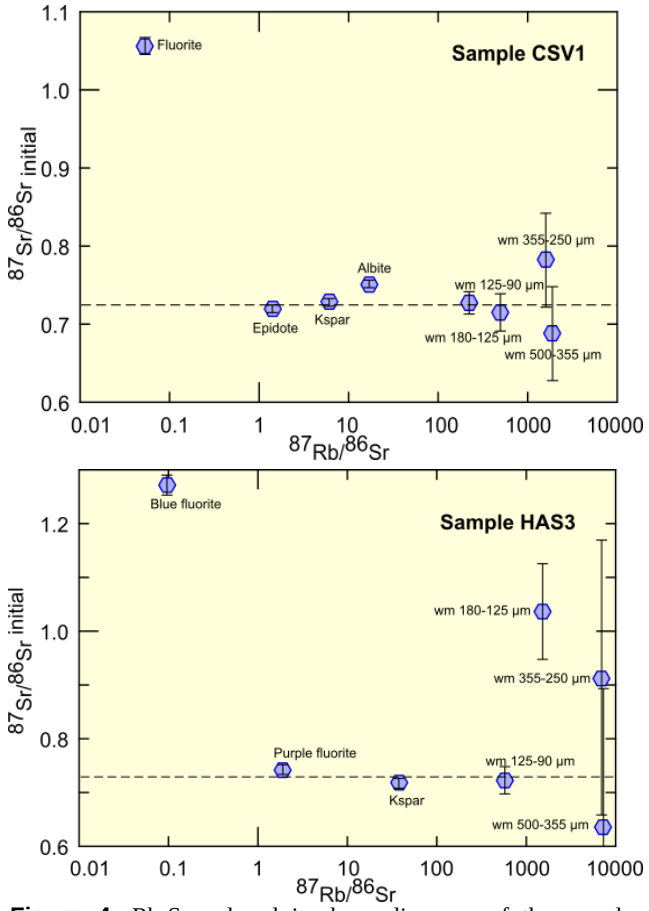


Figure 4. Rb-Sr reduced isochron diagrams of the samples CSV1 (up) and HAS3 (down).

Thus, Sn mineralization in the Hämmerlein skarn is the result of two separate events, i.e. (i) the formation of a zoned skarn during regional metamorphism at 340 Ma and, (ii) the local retrogression of the original skarn assemblage by granite-derived fluids that introduced Sn, In, and F and that led to chloritization and deposition of cassiterite and fluorite. The dated muscovite formed during regional metamorphism and did not record the partial retrogression by this late fluid. Our study demonstrates that dating of skarn minerals in poly-stage skarns not necessarily provides the age of skarn mineralization.

Acknowledgements

This project was supported by German government BMBF grant (033R134A) awarded to RLR.

References

de Capitani C and Petrakakis K (2010) The computation of equilibrium assemblage diagrams with Theriak/Domino software. American Mineralogist 95:1006-1016

Förster H-J, Tischendorf G, Trumbull RB and Gottesmann B (1999) Late-Collisional Granites in the Variscan Erzgebirge, Germany. Journal of Petrology 40(11):1613-1645

Kempe U, Bombach K, Matukov D, Schlothauer T, Hutschenreuter J, Wolf D and Sergeev S (2004) Pb/Pb and U/Pb zircon dating of subvolcanic rhyolite as a time marker for Hercynian granite magmatism and Sn mineralisation in the Eibenstock granite, Erzgebirge, Germany: Considering effects of zircon alteration. Mineralium Deposita 39:646-669

Kroner U and Romer RL (2013) Two plates – Many subduction zones: The Vaariscan orogeny reconsidered. Gondwana Research 24:298-329

Romer RL, Thomas R, Stein HJ and Rhede D (2007) Dating multiply overprinted Sn-mineralized granites – examples from the Erzgebirge, Germany. Mineralium Deposita 42:337-359

Rötzler K, Schumacher R, Maresh WV and Wilmer AP (1998) Characterization and geodynamic implications of contrasting metamorphic evolution in juxtaposed high-pressure units of the Western Erzgebirge (Saxony, Germany). European Journal of Mineralogy 10:261-280

Schuppan W and Hiller A (2012) Die Komplexlagerstätten Tellerhäuser und Hämmerlein. Landesamt für Umwelt, Landwirtschaft und Geologie. Bergbaumonografie. Freiberg 157p

Taylor SR and McLennan SM (1985) The continental crust: Its composition and evolution. Blackwell Scientific Publications Oxford 312p

Texture and composition of pyrite and arsenopyrite in the Stibnite Au-Sb-W district, central Idaho, USA

Erin E. Marsh, Albert H. Hofstra, David T. Adams, Heather A. Lowers, and Mitchell M. Bennett
U.S. Geological Survey

Abstract. High-contrast backscattered electron (BSE) images and electron microprobe (EMP) analyses of pyrite from Au-Sb-W deposits in the Stibnite mining district reveal alternating growth zones that are enriched in Au, Ag, Sb, As, and Cu. Textures indicate periods of replacement, dissolution, and open-space growth. The Au and As contents show that ore fluids were generally undersaturated with Au. Such pyrite is indicative of low temperatures of formation and reducing conditions.

1 Introduction and geologic setting

The Stibnite mining district is located in east-central Idaho on the eastern margin of the Atlanta Lobe of the Cretaceous Idaho Batholith, which is near the western margin of the Eocene Thunder Mountain Caldera (Fig. 1). Mineralization occurred within second order faults and damage zones of the regional Meadow Creek fault (Lewis et al. 2012). This district is an important domestic source of the critical element Sb, with an estimated resource of 49,000 metric tons (SRK Consulting, 2012). The district is also well endowed in Au, Ag, and W.

The Yellow Pine, Hangar Flats, and West End Au-Sb-W deposits, along with numerous prospects have been defined on the Stibnite Gold Project property (Fig. 1). In the Yellow Pine and Hangar Flats deposits, ore is hosted in Cretaceous granodiorite, alaskite/aplite dikes, and granite porphyry. In the West End deposit, ore is hosted in the Stibnite roof pendant composed of metamorphosed Lower Paleozoic and Neo-Proterozoic sedimentary rocks. Ore occurs as veins and disseminations in both intrusive and metamorphic hosts.

Cretaceous and Eocene ages have been reported for mineralization in this district. In the West End deposit, veinlets and alteration halos contain adularia that yielded Ar^{40}/Ar^{39} ages of ~51 Ma (Gillerman et al. 2014). Molybdenite in paragenetically early veins gave a Re-Os age of ~86 Ma (Konyshev and Muntean 2016). Scheelite associated with stibnite in the Hangar Flats deposit gave LA-ICP-MS U-Pb ages of ~45 to 35 Ma (Wintzer et al. 2016). Sericite from Yellow Pine was dated by Ar^{40}/Ar^{39} at ~78 Ma (Lewis 1984).

Lewis (1984) documented arsenic zonation and etch gaps in pyrite (see Fig. 2A) associated with sericite that replaces igneous biotite in Cretaceous intrusions. Konyshev and Muntean (2016) reported native gold in zoned arsenian-pyrite rims on pyrite from the West End deposit.

Textural and microanalytical studies of pyrite and arsenopyrite were conducted to aid interpretation of geochronologic results on sericite and K-feldspar and microthermometric results on fluid inclusion assemblages in quartz and stibnite, as well as to compare texture and geochemistry with other hydrothermal ore deposits types.

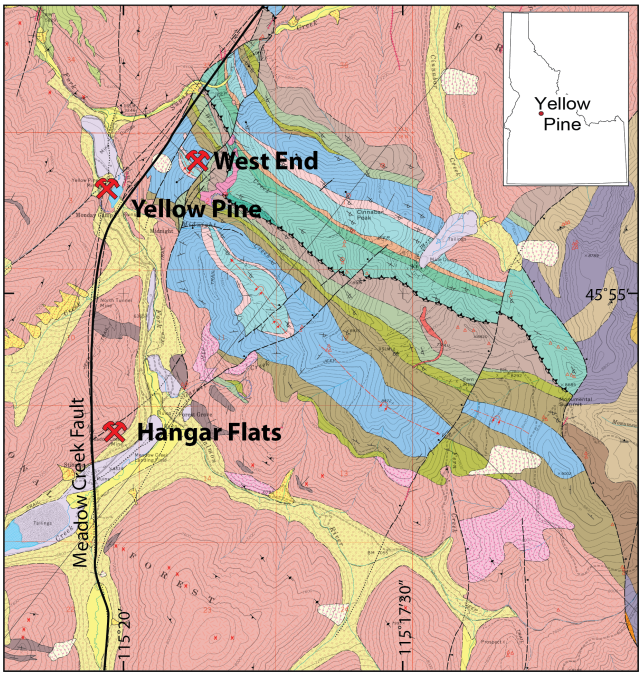


Figure 1. Regional geologic map showing the Stibnite mining district in east-central Idaho. Please refer to Stewart et al. (2015) for map units.

2 Textures and microanalyses of pyrite and arsenopyrite

High-contrast BSE images and EMP analyses revealed four pyrite types based on texture and chemistry in both intrusion-hosted and roof pendant-hosted mineralization: type 1) dark barren cores of euhedral pyrite with bright oscillatory rims and etch gaps that are overgrown by stibnite or arsenopyrite; type 2) oscillatory zoned arsenian-pyrite with trace-element-poor rims; type 3) irregular replacement pyrite with oscillatory growth zones, etch gaps, and arsenopyrite overgrowths; and type 4) fracture filling fine-grained euhedral pyrite with moderate trace element contents (Fig. 2). Arsenopyrite is generally zoned with respect to Sb and occurs in fine- to medium-grained euhedral crystals. Stibnite, as mentioned above, is found rimming zoned pyrites and in massive veins that cross cut pyrite/arsenian-pyrite and arsenopyrite veins and disseminations. These textural types corroborate the paragenetic sequence previously defined by Lewis (1984;

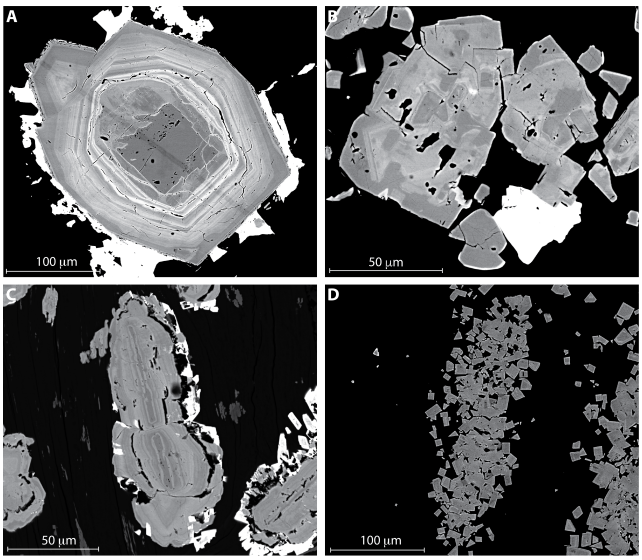


Figure 2. SEM-BSE images of zoned pyrite (light gray) and arsenopyrite (white) in quartz and feldspar (black) and sericite (dark gray). A) type 1 pyrite; B) type 2 pyrite; C) type 3 pyrite; and D) type 4 pyrite–see text for descriptions.

see his figure 7) except for his exclusion of early barren pyrite.

Microanalyses of pyrite and arsenopyrite plot in a data array (Fig. 3) that is similar to one defined by microanalyses of pyrite in a variety of ore deposit types (Deditius et al. 2014; Fig. 3). At Yellow Pine, Hangar Flats, and West End, it is apparent that arsenic substitutes as As^{1-} for sulphur in pyrite (Fig. 3).

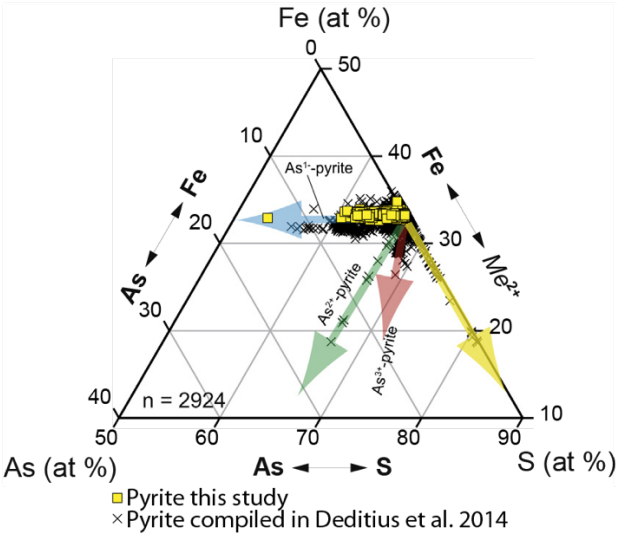


Figure 3. Yellow Pine pyrite EPMA data plotted with compiled data from Deditius et al. (2014) on As-Fe-S ternary diagram. Deditius et al. (2014) outlined three trends for substitution of As into pyrite (As^{1-} for S, blue arrow; As^{2+} for Fe green arrow; and As^{3+} for Fe, red arrow) and one of divalent metals for Fe (yellow arrow). Yellow Pine pyrites plot on the As^{1-} pyrite trend.

Gold ranges from the detection limit of 200 ppm to a maximum of 2100 ppm and is positively correlated with arsenic in the pyrite. Copper is zoned, with values ranging from ~400-1700 ppm. Silver shows a similar trend to gold and arsenic. Tungsten was not detected.

Gold occurs with arsenic in zoned pyrite. In Figure 4, the data plot on and below the gold saturation curve of Reich et al. (2005), which suggests that ore fluids generally were undersaturated with gold. The values that lie on the gold saturation curve, and the observation by Kunyshev and Muntean (2016) of native gold indicate that either there are two gold events, perhaps a later event was saturated producing native gold and the earlier event was undersaturated, or perhaps the visible gold has been subsequently remobilized from the earlier event. A consideration must be made about analytical techniques used. Spot sizes for SIMS data (the Midas data plotted in Fig. 4; as well as some of the data Deditius et al. (2014), drew on their conclusions regarding the undersaturation of gold) are larger than those for the electron probe, which could cause a dilution effect if an analysis incorporates multiple growth zones of varying Au content. This could result in the misrepresentation of the system being undersaturated in gold. The positive correlation between Au and As may reflect the temperature and activity of reduced sulfur in hydrothermal solutions (Deditius et al. 2014). They compared trace element chemistry from a variety of deposit types, discovering a correlation with the upper wedge of the As vs Au plot indicating ore formation at moderate to lower temperature.

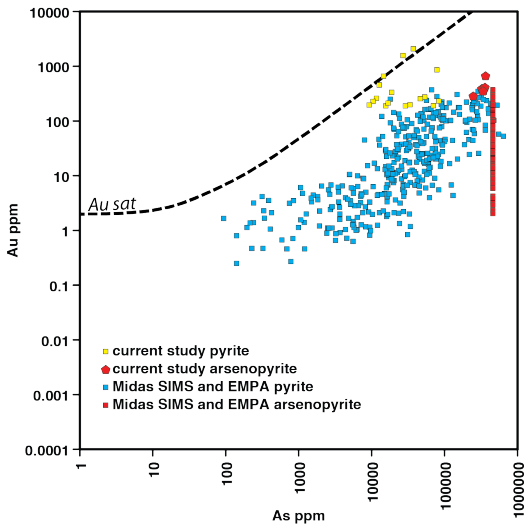


Figure 4. Arsenic vs. gold plot of current EPMA data along with previous SIMS and EPMA data from Midas Gold. *Au sat* is the gold saturation curve from Reich et. al (2005).

Knowing that gold resides in zoned pyrite, optical and scanning electron microscopy confirm that zoned pyrite is associated with crosscutting sericitic alteration (Fig 5). Sericite separates from this event have been submitted for argon geochronology. Cathodoluminescence and optical microscopy confirm that early H_2O-NaCl-CO_2-bearing quartz phenocryst-hosted secondary inclusions (Bennett et al., 2016) in altered monzonite are related to the auriferous

zoned pyrite.

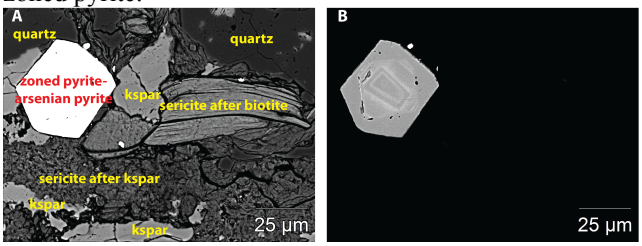


Figure 5. Zoned pyrite associated with sericitic alteration. A) BSE image of sericite replacing potassium feldspar and biotite along a structure hosting zoned pyrite/arsenian-pyrite. B) Highly contrasted BSE image illustrating zonation in pyrite form A.

Conclusions

Growth textures and trace-element chemistry of pyrite and arsenopyrite from the Yellow Pine, Hangar Flats, and West End deposits show that hydrothermal activity along the Meadow Creek fault was episodic and compositionally variable. Multiple fluid events produced zoned sulfides within the altered wall rock and multiple episodes of vein fill. Gold occurs in solid-solution in zoned arsenian-pyrite and arsenopyrite, unlike the thin trace element-rich rims on diagenetic pyrite in most Nevadan Carlin-type gold deposits, and similar to pyrite from Chinese Carlin-type and orogenic gold deposits. This careful paragenesis of precious metal events corroborates previous geochemical studies used to define the deposit formation history.

Acknowledgements

This work could not have been done without access to Midas Gold's Stibnite Gold Project property and exploration drill cores. Field, laboratory, and sample preparation help from Leslie Logan is greatly appreciated. We thank Ryan Taylor, Cliff Taylor, Chris Dail, and Niki Wintzer for their thoughtful reviews.

References

Bennett M, Marsh E, Hofstra A (2016) Cathodoluminescence and Fluid Inclusion Investigations in Quartz: Preliminary Results from the Yellow Pine Au-Sb deposit, Idaho: Pan-American Current Research on Fluid Inclusions (PACROFI-XIII) University of Missouri—Columbia, May 24-26, 2016, Abstract Volume

Deditius AP, Reich M, Kesler SE, Utsunomiya S, Chyssoulis SL, Walshe J, Ewing RC, (2014) The coupled geochemistry of Au and As in pyrite from hydrothermal ore deposits. Geochim Cosmochim Acta, 140: 644-670

Gillerman VS, Schmitz MD, Benowitz J, Layer PW, (2014) Geochronology of intrusive rocks and hydrothermal alteration at the structurally controlled Stibnite Au-Sb-W deposit, Idaho: Geol Soc of Amer Abstracts with Programs , 46/6:165

Konyshev SA, Muntean JL (2016) Diversity of sedimentary rock-hosted gold deposits in the Stibnite mining district, Idaho, Geol Soc of Amer Abstracts with Programs, 48/7 doi: 10.1130/abs/2016AM-281194

Lewis RD (1984) Geochemical investigations of the Yellow Pine, Idaho and Republic, Washington mining districts, Dissertation, Purdue University, 204

Lewis RS, Link PK, Stanford LR, Long SP (2012) Geologic map of Idaho: Idaho Geological Survey, Moscow, Idaho, Geologic Map 9.

Reich, M, Kesler SE, Utsunomiya S, Palenik, CS, Chryssoulis, SL, Ewing RC (2005) Solubility of gold in arsenian pyrite. Geochim Cosmochim Acta, 69:2781-2796

Stewart DE, Stewart ED, Lewis RS, Weppner KN (2015) Geologic map of the Stibnite quadrangle, Valley County, Idaho: Draft Plate 1, Idaho Geological Survey, University of Idaho, Moscow, Idaho. (http://www.idahogeology.org/PDF/Maps_(M)/Geologic_Maps_(GM)/PDF/Stibnite_GM-51_P1_P2_M.pdf_

SRK Consulting (Canada) Inc. (2012) NI 43-101 Technical Report on Mineral Resources Golden Meadows Project Valley County, Idaho

Wintzer NE, Gillerman VS, Schmitz MD (2016) Eocene U-Pb scheelite LA-ICP-MS dates of the stibnite-scheelite mineralization in the Yellow Pine Au-Sb-W mining area, Central Idaho, USA, Geol Soc of Amer Abstracts with Programs. 48:7 doi: 10.1130/abs/2016AM-283926

The physical and chemical evolution of fluids in rare-element (Be, Li, Nb-Ta) pegmatites associated with the Lacorne pluton, Québec, Canada

Thomas Mulja
Consulting geologist, North Vancouver

Anthony E. Williams-Jones
McGill University, Montréal, Canada

Abstract. Co-magmatic rare-element (Be, Li, Nb, Ta) granitic pegmatites associated with the Lacorne monzogranite pluton of the Preissac-Lacorne batholith (Québec), which range from a least evolved beryl-type in the pluton to a most evolved spodumene-type in mafic country rocks, possess internal lithologic fabrics and primary fluid inclusions that provide evidence that the magma was saturated with aqueous fluids pene-contemporaneously with emplacement. On the basis of microthermometric fluid inclusion measurements and oxygen isotope thermometry, the trapping temperatures of the initial fluids decreased from approximately 550°C in beryl and beryl + spodumene pegmatites to about 400-450°C in spodumene pegmatite; the pressure was 3.5 kb. The last fluids were trapped at between 250 and 360°C. Fluid composition evolved from being NaCl-dominated (4-16 wt% NaCl eq.) with appreciable Fe and dissolved CO_2 to aqueous carbonic-dominated (6-10 wt% NaCl eq.), with significant Mn, Li and Cs. This reflects corresponding trends in the chemical evolution of the host rock. At a late stage of crystallization, the beryl pegmatites underwent local fluid overpressure leading to brecciation and the incursion of external $CaCl_2$-rich fluids into the beryl pegmatites. Aqueous fluids exsolved from the spodumene-forming melt escaped into the country rocks and induced lithium metasomatism.

1 Introduction

Aqueous fluids or water-rich solutions are believed by some to play a critical role in the formation of granitic pegmatites (see review by Thomas et al. 2012) and by others, e.g. London (2014), to play no significant role at all. Opinion is also divided on the timing of their exsolution from the pegmatite-forming melts. Nebalek et al. (2010), for example, interpreted them to be early and voluminous, whereas Michalik et al. (2017) interpreted them to be late and exsolved in relatively minor quantities. These differences of opinion notwithstanding, there is a need to document the nature of the fluid, particularly that related to the genesis of rare-element (Be, Li, Nb, Ta, P) granitic pegmatites. Such information can be, and has been, successfully extracted through microthermometric analysis of fluid inclusions trapped in pegmatite minerals (e.g., Sirbescu and Nebalek 2003). In this contribution, we present data on fluid inclusions in early to late primary minerals from a series of co-magmatic beryl-, beryl + spodumene- and spodumene-type pegmatites associated with the Lacorne pluton of the Archean Preissac-Lacorne batholith in western Québec, Canada (Fig. 1). Our aim is to determine the timing of fluid saturation, and the pressure, temperature and composition of the pegmatite-related fluids throughout the differentiation trajectory of the melts.

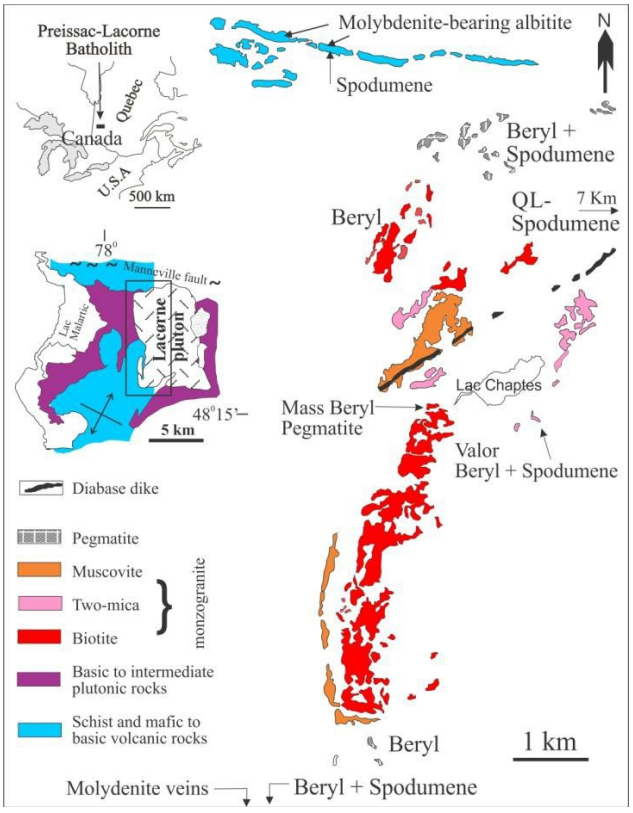


Figure 1. Location map of the Lacorne pluton in Québec, and the regional zoning of beryl, beryl + spodumene and spodumene pegmatites. The spodumene pegmatites studied here came from the former Quebec Lithium mine (QL; measured and indicated resource of 46.6 Mt @ 1.19% Li_2O, Blanchet et al. 2012), about 7 km east of the figure border (After Mulja et al. 1995).

2 The Lacorne rare-element pegmatites

2.1 Beryl pegmatite

Beryl pegmatites range in size from small lenses to 8 m

wide dikes and have either a sharp or a gradational contact with the host pluton. This study is based on 0.5 to 1 m wide pegmatites. They are zoned symmetrically from a sodic aplite margin, through a medial assemblage of beryl, quartz, K-feldspar, muscovite, and albite, to a quartz + K-feldspar core. Layers of fine-grained garnet and small pockets of quartz + muscovite are common in the aplite. The K-feldspar crystals are commonly perthitic and form graphic intergrowths with quartz (Fig. 2). Ferrocolumbite, monazite-(Ce), gahnite, molybdenite and magnetite are minor minerals. Brecciation is observed in a number of the pegmatites, in which angular fragments are either sealed by granitic infill or albite masses.

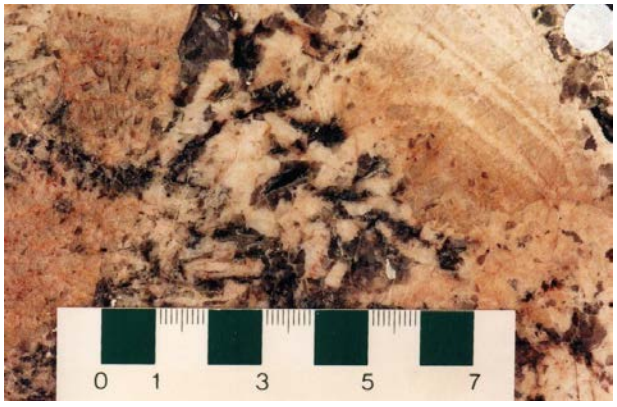


Figure 2. Brecciated beryl pegmatite from the Mass Beryl prospect, showing perthitic K-feldspar fragments cemented by coarse-grained feldspar + quartz + muscovite crystals. The early-formed K-feldspar exhibits a graphic intergrowth with quartz, whereas the later-formed K-feldspar displays growth zones of pink and white laminae. This breccia is evidence for a hydraulic fracturing event, most likely induced by a magmatic-hydrothermal fluid overpressure inside the pegmatite-generating magma chamber.

2.2 Beryl + spodumene pegmatite

Beryl + spodumene pegmatites are located between beryl and spodumene pegmatites (Fig. 1) and the one at the Valor prospect is best suited for this study. This pegmatite is hosted in the Lacorne two-mica monzogranite and appears lensoidal (it has a maximum width of 4 m). It has a discontinuous, corrugated and layered aplite border zone that is locally truncated by euhedral beryl crystals up to 4 cm across and spodumene abutting against the monzogranite. A narrow zone of muscovite books and small beryl crystals marks the transition from the aplite to an intermediate zone that comprises mainly 3 to 4 cm wide rosettes of cleavelandite (albite), quartz, K-feldspar and spodumene, and minor pollucite, manganocolumbite and pyrophanite ($MnTiO_3$). Spodumene in this zone varies in size from small laths to a 20 cm × 2 m prism that extends into the pegmatite core. The spodumene, quartz, albite and lepidolite constitute the core minerals.

2.3 Spodumene pegmatites

Occurrences of spodumene pegmatite are restricted to drill core, and include both massive and zoned varieties. They vary from small lenses to dikes generally 1-2 meters wide (a 45 m wide pegmatite was reported by Blanchet et al. 2012) and display either a sharp or gradational contact with the host rocks. Thin rims of holmquistite [$Li_2(Mg,Fe^{+2})(Al,Fe^{+3})_2(Si_8O_{22})(OH)_2$] after biotite are commonly developed in the host rocks where the contacts are sharp. The pegmatites contain 10-30% spodumene, and 30-50% each of quartz and feldspars (albite and K-feldspar). Some albite crystals have overgrowths ranging from oligoclase to andesine in composition. In the massive variety, spodumene forms 1 cm x 3 cm prismatic crystals that are randomly distributed from wall to wall and oriented at 45-90 degrees to the contacts. Many of this lithium pyroxene is also intergrown with quartz, and we interpret these two interlocking phases to be a replacement of petalite. The discrete quartz and feldspars occur as subhedral to euhedral crystals averaging 5 mm across. The zoned spodumene pegmatites are symmetrical, consisting of a discontinuous < 5-cm wide border aplite, an intermediate assemblage of spodumene + quartz + minor plagioclase, and a quartz-dominated core with minor spodumene + feldspars. These silicate minerals display textural and fabric characteristics akin to those of their counterparts in the massive pegmatites. Manganocolumbite, pollucite, beryl and apatite are minor minerals.

3 Materials and analytical methods

Beryl and quartz from the inner zone of beryl pegmatites, border zone beryl from beryl + spodumene pegmatite and border spodumene and inner quartz from spodumene pegmatite were sampled for fluid inclusion microthermometric analysis with a Fluid Inc. USGS-adapted gas-flow heating and freezing stage (Werre et al. 1979). The chemical compositions of precipitates from decrepitated inclusions and of solids in opened inclusions were determined with an energy-dispersive X-ray spectrometer attached to a JEOL 840 scanning electron microscope, and in a few cases, Raman spectroscopic analyses. Three samples of beryl and quartz were analyzed for the anion contents of the fluid inclusions using the crush-leach method (cf. Roedder 1984) and a Dionex ion chromatograph at the University of Windsor in Ontario. Oxygen isotope compositions of quartz and garnet in beryl and beryl + spodumene pegmatites were determined at the University of Saskatchewan in order to provide estimates of the temperature of equilibration of these minerals in their respective pegmatites.

4 Results and discussion

4.1 Conditions and timing of fluid saturation and entrapment

On the basis of data for the hornblende-plagioclase geobarometer, garnet-quartz oxygen isotope geothermometry, phase equilibria for petalite, spodumene

and quartz, beryl saturation, and fluid inclusion microthermometry, we estimate that the pegmatites studied were emplaced at a pressure of approximately 3.5 kb, and that the aqueous fluids in beryl in beryl and beryl + spodumene pegmatites were trapped at 500 and 560°C, in spodumene from spodumene pegmatite at 400 - 450°C, and in quartz from all pegmatites at a temperature as low as 250 - 350°C. The Lacorne pegmatite-forming melts have been inferred from the structural state of columbite-tantalite from all pegmatite types to have crystallized rapidly with the distal spodumene pegmatite having the fastest rate of crystallization (Mulja et al. 1996). Such rapid crystallization is generally considered to result in aplite due to the high nucleation density and fast growth rate (London 2014). As crystallization of the melt progresses inward to precipitate larger crystals of a smaller number of minerals, this textural transition is interpreted to induce massive fluid exsolution, which reduces the nucleation density but also enhances crystal growth (Sirbescu et al. 2009; Nebalek et al. 2010). In addition, the precipitation of early beryl and the development of graphic K-feldspar + quartz intergrowths are related to the release of volatiles from the crystallizing melts (Eversen et al. 1999; Lentz and Fowler 1992). Significantly, recent experiments have demonstrated that this intergrowth can form early in Li + H_2O-saturated pegmatite melts (Maneta 2015). All of the above features are consistent with the heterogeneous internal textures of the Lacorne pegmatites, including a 2 m long spodumene prism and the inward growth of spodumene. The regional zonation of the Lacorne pegmatites with the beryl pegmatites located within the intrusion and the spodumene pegmatites furthest from it was made possible by a progressive decrease in melt viscosity due to H_2O saturation, and later the high concentration of Li. Therefore the Lacorne pegmatite-forming melt is interpreted to have become water-saturated after the crystallization of the border zone aplite in the beryl variant and upon the emplacement of the beryl + spodumene and spodumene pegmatites. This condition continued until the terminal stages of their magmatic history

4.2 Nature and evolution of the pegmatite-related fluids

Results from microthermometric measurements and analyses of residues from decrepitated fluid inclusions indicate that the primary aqueous fluids (liquid + vapor ± solids) have low salinity (10 ± 6 wt% NaCl eq.), high initial melting temperature (> –20ºC), and have compositions dominantly in the NaCl-H_2O system, irrespective of their host mineral and pegmatite type. The subordinate components vary from Ca and Fe in beryl and beryl + spodumene pegmatites to Mn, Li and Cs in spodumene pegmatites. This compositional variation is reflected by the presence in fluid inclusions, of calcite in beryl pegmatite and manganoan calcite in beryl + spodumene and spodumene pegmatites. It is also corroborated by the presence of zabuyelite (Li_2CO_3) and pollucite in some fluid inclusions (zabuyelite was confirmed by Raman spectroscopic analyses and both minerals by EDS analyses of opened inclusions) hosted in spodume pegmatites. As mentioned earlier, holmquistite replaced biotite adjacent to spodumene pegmatite. In addition to the low salinity fluid referred to above, beryl and quartz from beryl and beryl + spodumene pegmatites host a higher salinity fluid (19 ± 5 wt% NaCl eq.) with a much lower initial ice melting temperature (–30 to –70ºC) reflecting the presence of significant $CaCl_2$. This fluid is considered to be of secondary origin and to have circulated in the partially crystallized pegmatites during hydraulic fracturing (Figs. 2, 3). The latest fluid was CO_2-dominated with a trapping temperature of 260 ± 40ºC) and was observed only in late quartz. It likely represents a residual orthomagmatic fluid containing small proportions of CO_2 that underwent unmixing during the terminal stage of pegmatite crystallization.

5 Conclusions

We propose a five-stage evolution for the Lacorne pegmatite-forming magmas (Fig. 3): (1) Emplacement of magma at ~550°C, and 3.5 kb, at or near saturation with a low-salinity, CO_2-bearing, NaCl-dominated fluid; (2) Crystallization of beryl in beryl pegmatite and beryl and spodumene in spodumene pegmatite, and entrapment of NaCl brines containing appreciable concentrations of Ca and Fe. Later and distal to the pluton, spodumene pegmatite began crystallizing and entrapped Mn + Li + Cs-bearing NaCl brines at 400-450°C; (3) Local hydraulic fracturing led to a temporary drop in fluid pressure; (4) Entrapment of high salinity and Ca-rich fluid inclusions by beryl and quartz in the beryl pegmatite, and incursion of external Ca-bearing brines into the spodumene pegmatite (most beryl and beryl + spodumene pegmatites were largely shielded from these external fluids by their intrusion into the host monzogranite pluton); and (5) Unmixing of the orthomagmatic fluid into aqueous and CO_2 phases and their heterogeneous entrapment in late quartz at between 250 and 350°C. In summary, the results of this study suggest, at least in the case of the Lacorne pegmatites, that aqueous fluid saturation can take place at an early stage of crystallization, and that magma evolution is matched by the changes of the solute chemistry of the exsolving aqueous fluid. Carbon dioxide is an important component of this fluid, and the common occurrence of aqueous-carbonic fluid inclusions in quartz is a natural consequence of the cooling of the system.

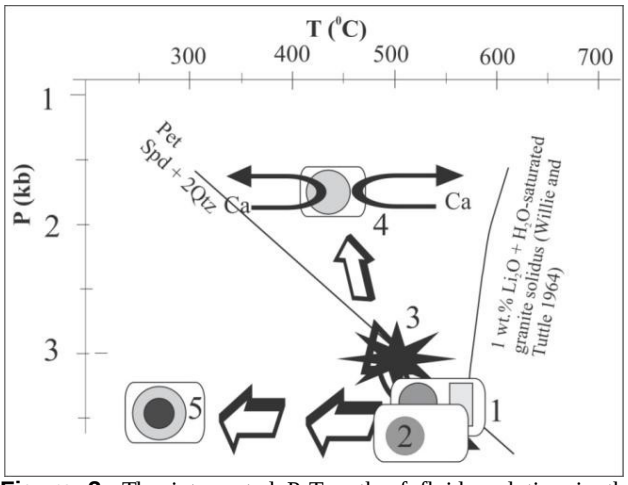


Figure 3. The interpreted P-T path of fluid evolution in the Lacorne rare-element pegmatite system. See text for explanation. The 3.5 kb pressure for the metamorphic aureole is after Powell (1994). The solidus of the Lacorne spodumene pegmatite with an average grade of 1.19% Li_2O is inferred from that of the lithium-bearing granite of Wyllie and Tuttle (1964).

Acknowledgements

This research was supported by a NSERC Discovery grant to AEW-J. Anne Préfontaine supplied some of the fluid inclusion microthermometric data for the spodumene pegmatite. We thank the referee and editor for their reviews.

References

Blanchet D, Hardie C, Lavery M, Lemieux M, Nussipakyonova D, Shannon JM, Woodhouse P (2012) Feasibility study update NI 43-101 technical report Quebec lithim project La Corne Township, Quebec, Canadian Lithium Corp.

Eversen JME, London D, Wendlandt, RFW, (1999) Solubility and stability of beryl in granitic melts. Am Mineral 84: 733–745 London D (2014) A petrologic assessment of internal zonation in granitic pegmatites. Lithos,184–187:74–104

Lentz DR, Fowler A (1992) A dynamic model for graphic quartz feldspar intergrowths in granitic pegmatites in the southwestern Grenville Province, Can Min 30: 571-585

London D (2014) A petrologic assessment of internal zonation in granitic pegmatites. Lithos 187: 74-104

Maneta V (2015) The effect of Li on the petrogenesis of granitic pegmatites. Ph.D thesis, McGill University, Montreal, Canada

Michalik RM, Wagner T, Fusswinkel T, Heinonen JSH, Heikkilä P (2017) Chemical evolution and origin of the Luumäki gem beryl pegmatite: constraints from mineral trace element chemistry and fractionation modeling, Lithos 274-275: 147-168

Mulja T, Williams-Jones AE, Martin RF, Wood SA (1996) Compositional variation and structural state of Nb-Ta oxide minerals in rare-element granitic pegmatites from the Preissac-Lacorne batholith, Quebec. Am Mineral 81: 146-157

Mulja T, Williams-Jones AE, Wood SA, Boily M (1995) The rare-element-enriched monzogranite-pegmatite-quartz vein system in the Preissac-Lacorne batholith, Quebec. II. Geochemistry and Petrogenesis, Can Min 33: 817-833

Nabelek PI, Whittington AG, Sirbescu M-LC (2010) The role of H_2O in rapid emplacement and crystallization of granite pegmatites: resolving the paradox of large crystals in highly undercooled melts, Contributions to Mineralogy and Petrology, 160/3: 313–325

Powell WG (1994) A petrological and geochronological study of the metamorphic history of the Rouyn-Noranda area, Quebec. Unpublished Ph.D thesis, Queen's University, Kinston, Ontario.

Roedder E (1984) Fluid inclusions. Mineralogical Society of America, Rev Mineral 12: 212-218

Sirbescu M-LC, Nabelek PL (2003) Crystallization conditions and evolution of magmatic fluids in the Harney Peak Granite and associated pegmatites, Black Hills, South Dakota—evidence from fluid inclusions, Geochim Cosmochim Acta 67-13: 2443-2465

Sirbescu M-LC, Wilke M, Veksler LV (2009) Understanding Pegmatite Texture: Kinetics of Crystallization in the Haplogranite-Li-B-H_2O System, American Geophysical Union, Fall Meeting 2009, abstract #V43B-2233

Thomas R, Davidson P, Beurlen H (2012) The competing models for the origin and internal evolution of granitic pegmatites in the light of melt and fluid inclusion research. Miner Petrol 106:55–73

Werre RWJr, Bodnar RJ, Bethke PM, Barton PB (1979) A novel gas-flow fluid inclusion heating/freezing stage (Abstr.). Geol. Soc. Ame. Abstrc. Progs. 11: 539

Wyllie P, Tuttle OF (1964) Experimental investigation of silicate systems containing two volatile components. III. The effects of SO_3, P_2O_5, HCl and Li_2O, in addition to H_2O, on the melting temperatures of albite and granite. Amer. Jour. Sci. 262: 930-939

Hydrothermal record of Fe-Ti oxides breakdown: insights into understanding Sb mineralisation

Anthony Pochon, Philippe Boulvais, Denis Gapais *Université de Rennes 1, France*

Georges Beaudoin
Université Laval, Canada

Eric Gloaguen
Bureau de Recherche Géologique et Minière (BRGM), France

Yannick Branquet
Institut des Sciences de la Terre d'Orléans (ISTO), France

Abstract. Fe-Ti oxide breakdown is frequently observed within hydrothermally altered dolerites in the Semnon Sb-Au district in the Variscan Armorican belt, France. Hydrothermal alteration has totally replaced primary ilmenite-hematite series minerals to rutile. Trace element analyses reveal some variations between parent minerals and their alteration product, characterized by a relative enrichment of Sb and W in rutile. For a better understanding of mineral replacement reactions, the redistribution of trace elements during the transition of ilmenite-hematite series into rutile was estimated by mass balance calculations. Comparison between the mean compositions of hydrothermal rutile and hydrothermal sulphide, from the same event, was also performed. Key findings from this work show that (1) almost all elements (especially Fe, Mn and Zn) are released from ilmenite-hematite series minerals during hydrothermal breakdown, (2) Sb and W are dominantly incorporated into the rutile structure from external fluid sources, (3) the Sb content of rutile evolves through time with sulphide precipitation as a result of Sb-partitioning and (4) the input of sulphur into the hydrothermal system controls the behaviour of Sb. Fe-Ti oxide breakdown is a key to understand Sb mineralisation.

1 Introduction

Rutile is a common accessory mineral in a wide variety of rocks and hydrothermal systems (Meinhold 2010). Like most accessory minerals, rutile has a remarkable ability to incorporate significant amounts of trace elements into its lattice, especially HFSE, Sb and W (Zack et al. 2002). Rutile is stable during supergene alteration and, consequently, its trace element geochemistry has a wide range of applications in geosciences. For example, it has been used to trace metal sources in an orogenic gold province (Cave et al. 2015). The breakdown of Fe-Ti oxides is common under metamorphic and hydrothermal conditions (Luvizotto et al. 2009, Rabbia et al. 2009), which makes it an important process to investigate in order to understand the redistribution of trace elements in hydrothermal systems. Furthermore, a good understanding of the breakdown of Fe-Ti oxides during alteration may help better constrain mineralising processes (Rabbia et al. 2009). Our work focuses on the breakdown of Fe-Ti oxides into hydrothermal rutile from mafic dykes in the Semnon Sb-Au deposit. SEM, EPMA and LA-ICP-MS analyses were performed in order to study the petrographic features of Fe-Ti oxides and the geochemical behaviour of trace elements, Sb in particular, during breakdown.

2 Geological background

A major part of French Sb-mineralisation belongs to the Variscan Armorican belt in the western part of France. This belt comprises several domains with different tectonic and metamorphic histories separated by two major crustal-scale shear zones (Gumiaux et al. 2004). Four main antimony districts are recognized in the Armorican Massif: the La Lucette district, the Vendée district, the Le Semnon district and the Quimper-Cap Sizun district. These stibnite-bearing lode deposits are usually considered to be related to a late-Variscan hydrothermal event (Bouchot et al. 2005). In spite of previous studies, the mineralisation history remains unconstrained. It involves felsic magmatic events from the Cambrian to late Variscan, control by Variscan shear zones (Chauris and Marcoux 1994) and a spatial relationship with high-density and magnetic zones, likely reflecting mafic bodies at depth (Pochon et al. 2016a).

Our study focuses on the Semnon Sb-Au district, where relations between Sb-mineralisation and mafic rocks can be well documented. The district contains numerous dolerite dykes that are up to 25 m thick. They strike NW – SE and are steeply dipping to the north. They intrude lower Ordovician slates and are affected by the regional E – W trending sub-vertical cleavage. The dyke swarm is dated at 363.4 ± 5.8 Ma by U-Pb LA-ICP-MS on apatite (Pochon et al. 2016b).

In map view, dykes are spatially associated with mineralisation. In the field, Sb-bearing quartz-carbonate flat veins cut across the cleavage and the contact between dolerite and slates. Some mineralised veins are also affected by folding and the regional sub-vertical cleavage. The mineralisation mainly consists of berthierite, stibnite, pyrite, sphalerite, and native gold. Arsenopyrite is scarce inside the veins, but abundant in the hydrothermally

altered dolerite and slate vein wallrocks.

The hydrothermal alteration is potassic (illitization), with associated carbonatisation and silicification of country rocks. Within dolerite dykes, this hydrothermal alteration is responsible for replacement of magmatic Fe-Ti oxides by rutile and leucoxene. Noteably, this destabilization is restricted to altered dolerites.

3 Sampling and methods

Three samples of unaltered dolerites and two samples of altered dolerite were collected from the Semnon Sb-Au deposit. The dolerite samples belong to the same dyke swarm, with the same age, in order to compare the effects on Fe-Ti oxides breakdown by hydrothermal fluids.

Reflected light microscopy and SEM were used to identify the different phases and to describe textures of unaltered and altered oxides in order to characterize and decipher parent from product minerals. Mineral compositions were measured using a Cameca SX-100 electron microprobe at IFREMER (France) and Université Laval (Québec). Trace elements were obtained by LA-ICP-MS at Université du Québec à Chicoutimi (Québec).

4 Results

4.1 Mineral textures of Fe-Ti oxides

Within unaltered dolerites, Fe-Ti oxides mainly consist of ilmenite and ilmenite-hematite solid solution (Ilm-Hem_{ss}) with a grain size range of 50-500 µm. These oxides coexist with various textures. Lamellar exsolutions (<2 µm) of ilmenite, hematite and possibly magnetite in Ilm-Hem_{ss} are common. Lamellae are often composite as they contain the three types of exsolution. Other types of texture consist of ilmenite and hematite "fish bone" exsolution within Ilm-Hem_{ss} (nm-scale) and a mosaic texture (µm-scale) with a few pores (Fig. 1a).

Within altered dolerites, rutile (here used in the general sense of "TiO_2-polymorph") is the only Ti-oxide, and it is a product of the breakdown of primary ilmenite and Ilm-Hem_{ss} crystals (Fig. 1b). The grain size is variable and ranges between 10 and 80 µm. Rutile crystallizes with an irregular habit, or in places along the Ilm-Hem c-axis, within the preserved shape of the parent crystal (Fig. 1b). In the altered dyke, the replacement of the parent Ilm-Hem crystal by rutile is complete. The rutile is partially replaced around the rim by leucoxene, preserving the original habit. It is frequently cracked and also partially altered to leucoxene. Micron-scale pores inside the preserved shape of parent crystals are mainly filled by illite and carbonate (Fig. 1b). Sb-sulphides are frequently observed as inclusions or in micro-cracks in rutile.

4.2 Trace element composition

The trace-element composition of ilmenite crystals is rather homogeneous between individual grains. Compatible elements (Mn, V, Cr, Co, Ni) and HFSE show small concentration variations, whereas Mo, Sb, W and Pb, considered as incompatible elements, exhibit relatively large compositional variations, up to 2 orders of magnitude.

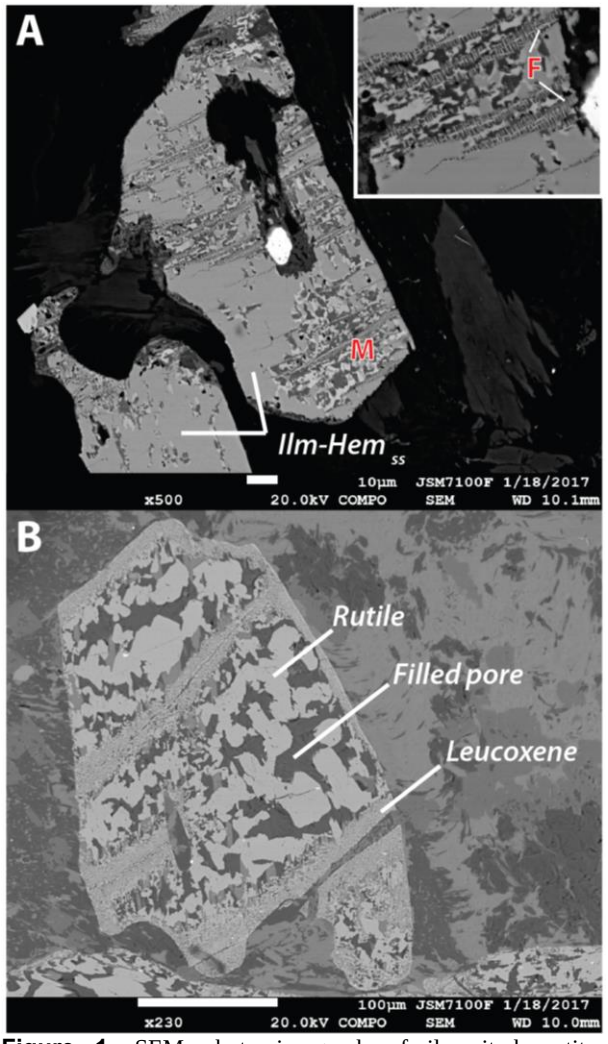


Figure 1. SEM photomicrograph of ilmenite-hematite crystals with "fishbone" exsolution (F) and mosaic textures (M) in an unaltered dolerite (a). Insert width is 30 µm. SEM photomicrograph of hydrothermal rutile from altered dolerite from the Semnon Au-Sb deposit (b).

Composition of the Ilm-Hem_{ss} is homogeneous between individual crystals, with most compatible elements and HFSE showing no significant variation. The only exception is the moderately compatible Cr, which is highly variable (2-11000 ppm). Others elements (As, Mo, Sb, W and Pb) display larger variations. Note that Sb is more enriched in Ilm-Hem $_{ss}$ than ilmenite (Fig. 2a). With respect to the parent mineral crystals analysed, the mean trace-element composition shows a relatively high concentration of Zn (80-7300 ppm), which is considered compatible in Fe-Ti oxides (Klemme et al. 2006).

Rutile displays a similar homogeneity of trace-element compositions with some elements more or less enriched

compared to parent minerals. Rutile is depleted in Mn, Co and Ni and enriched in Sb and W (Fig. 2a). One of the main feature of rutile is the large variation in Sb, up to 2 orders of magnitude which allows the definition of two types of rutile: Sb-rich (> 90 ppm) and Sb-poor rutile (<10 ppm). Also Zn concentrations (< 15 ppm) are much lower than in ilmenite and Ilm-Hem$_{ss}$.

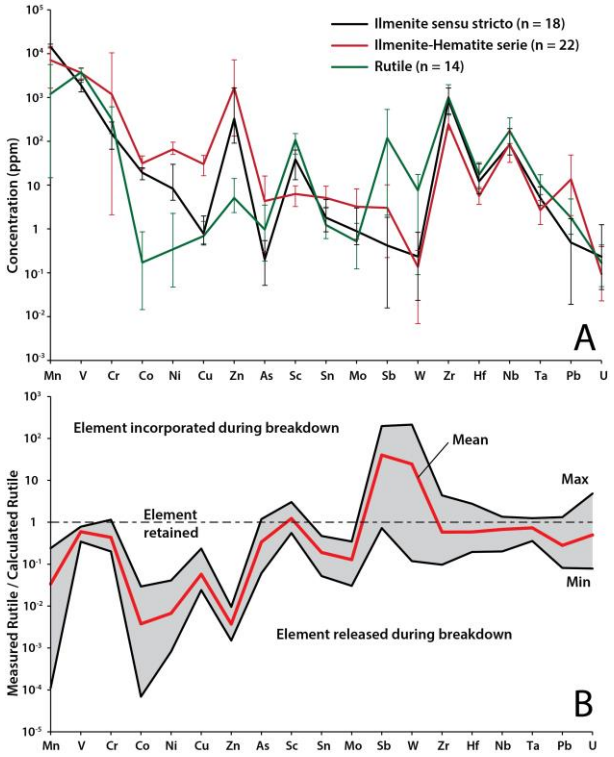


Figure 2. (a) Trace element composition of Fe-Ti oxides determined by LA-ICP-MS: ilmenite, ilmenite-hematite solid solution and rutile. Vertical bars represent min-max values. (b) Composition of hydrothermal rutile normalized to mean composition of hydrothermal rutile calculated using Gresens (1967).

5 Interpretation and discussion

As shown above, Fe-Ti oxide breakdown is common in hydrothermally altered dykes. The most common parent minerals are composite Fe-Ti oxides with complex exsolution textures. The mineralogical reaction is interpreted to have resulted from hydrothermal breakdown, rather than deuteric alteration, because rutile is only present in hydrothermally altered dolerite. The mineral replacement reaction can be described as follow:

$$\text{Ilmenite} + \text{Ilm-Hem}_{ss} + \textit{Fluids} \rightarrow \text{Rutile}$$

The variation of most trace elements in the parent mineral can be explained using trace element behaviour between ilmenite and silicate melts (e.g. Klemme et al. 2006). However, the distribution of trace elements during breakdown between rutile and fluids is less well constrained. The mass balance of this reaction has been calculated following the approach of Gresens (1967) with three assumptions: (1) Ti is immobile during breakdown, (2) trace elements from the replaced parent mineral are conservatively incorporated in rutile and (3) LA-ICP-MS measurements of trace element contents of Fe-Ti oxides are representative of trace element compositions of Fe-Ti oxides. Mass balance for the reaction is written as 100 g ilmenite + 24 g Ilm-Hem $_{ss}$ + 0.02 g SiO_2 = 54.4 g rutile (TiO_2) + 72 g Fe_2O_3 total + 2.21 g MnO + 0.05 g Al_2O_3 + 0.04 g MgO with a calculated concentration factor of 2.3 for trace elements incorporated from a parent mineral into rutile. Most elements, iron in particular, are partitioned in the fluid during this reation.

Using the concentration factor, we calculated the expected mean trace-element composition of hydrothermal rutile from the average measured trace element composition of the precursor mineral (Gresens 1967, Cave et al. 2015). Mean hydrothermal rutile trace-element compositions were normalized against calculated hydrothermal rutile trace element values (Fig. 2b). Values > 1 indicate an element concentration is higher than predicted and therefore this element was incorporated from an external source (fluids). Values < 1 and ≈ 1 correspond to release or retention of the element during breakdown, respectively.

In the Figure 2b, comparison between calculated and measured values of hydrothermal rutile show that HFSE (Nb, Ta, Zr, Hf), V, Cr and Sc were retained by rutile during crystallisation. This is expected because these elements are often considered to be the least mobile. Sb and W are strongly incorporated into the structure of rutile during hydrothermal alteration. This indirectly suggests that percolating hydrothermal fluids were relatively enriched in Sb and W. Inversely, others elements (Mn, Co, Ni, Cu, Zn) are incompatible in rutile and remained in solution and/or partitioned into sulphides. Zn, which is rather incompatible in rutile compared to ilmenite (Klemme et al. 2006; Meinhold 2010), appears to have been leached by fluids (Fig. 2b). This may constitute a potential and local metal source for the sphalerite found in the veins. Thus, the hydrothermal fingerprint seems to be have been, in part, well-recorded in rutile chemistry.

Hydrothermal rutile is considered to be early in the paragenetic evolution of the Semnon Sb-Au deposit. It is probably older or synchronous with arsenopyrite and pyrite found in hydrothermally altered dolerite dykes. Because these three minerals are closely associated, the chalcophile element compositions of hydrothermal rutile have been compared with that of pyrite in order to understand partitioning between them (Fig. 3). Comparison with arsenopyrite could not be made because of a lack of LA-ICP-MS data, but EPMA analyses show a high concentration of Sb in arsenopyrite (0.2-1.3 % Sb). LA-ICP-MS data for pyrite is used below to illustrate the impact of sulphide crystallisation on Sb partitioning.

First, the range in concentrations of Sb is similar between rutile and pyrite (1-600 ppm, Fig. 3). This indicates that these minerals record the same hydrothermal event and that Sb is present early in the hydrothermal system, before the stibnite and berthierite late

crystallisation. Sb-rich and Sb-poor rutile (Fig. 3) indicate a decrease of Sb content incorporated into rutile through time. This can be interpreted as a consequence of Sb partitioning between rutile and sulphides, with formation of Sb-rich rutile before sulphide precipitation, and Sb-poor rutile after sulphide precipitation. Indeed, Sb may behave like HFSE with respect to the rutile structure, but it is also a chalcophile element (Meinhold 2010). The Sb-content variation may reflect the input of sulphur in the hydrothermal system, as documented by the Mo content in hydrothermal rutile from Cu-Mo porphyry (Rabbia et al. 2009). This potential duality of Sb behaviour between rutile and sulphides can provide important information about the incremental history of mineralisation.

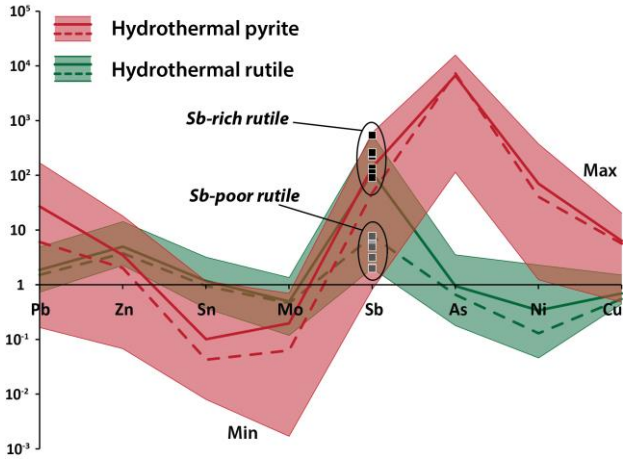


Figure 3. Diagram of chalcophile element composition of hydrothermal rutile and hydrothermal pyrite from the Semnon Sb-Au deposit. Bold and dashed line correspond to mean and median values, respectively.

6 Concluding remarks

The ongoing work on the breakdown of Fe-Ti oxides has shown that hydrothermal alteration is responsible of formation of rutile. Consequently, it results in a redistribution of trace elements during the alteration of ilmenite to rutile that is mainly characterized by: (1) a near total release of iron, Mn and Zn and (2) a strong incorporation of Sb via an external input, interpreted as hydrothermal fluid circulation. Mean chalcophile element compositions of coeval hydrothermal rutile and pyrite indicate that Sb partitioning between these two phases controls the Sb content of rutile. These results demonstrate a consistent record of hydrothermal alteration by Sb behaviour in rutile. Because Sb is frequently associated with orogenic and subduction-related gold and base-metal deposits, it is suggested that experimental data are required in order to better constrain the partitioning of Sb between ilmenite, rutile, sulphides, and hydrothermal fluids, particularly at temperatures lower than 400°C. This would provide quantitative information about the HFSE and chalcophile-like behaviour of Sb in Fe-Ti oxides and sulphides.

Acknowledgements

This work was funded by the French Geological Survey (BRGM), the region of Brittany, the OSUR and the doctoral school SDLM, with contributions from the Natural Sciences and Engineering Research Council of Canada. The author thanks Jessica Langlade (UBO), Marc Choquette (Laval), Dany Savard and Philippe Pagé (UQAC) for their assistance with EPMA and LA-ICP-MS analyses.

References

Bouchot V, Ledru P, Lerouge C, Lescuyer JL, Milesi JP (2005) 5: Late Variscan mineralizing systems related to orogenic processes: the French Massif Central. Ore Geol Rev 27:169–197.

Cave BJ, Stepanov AS, Craw D, Large RR, Halpin JA, Thompson J (2015) Release of trace elements through the sub-greenschist facies breakdown of detrital rutile to metamorphic titanite in the Otago Schist, New Zealand. Can Mineral 53:379-400.

Chauris L, Marcoux E (1994) Metallogeny of the Armorican Massif. In: Chantraine J, Rolet J, Santallier DS, Piqué A, Keppie JD (eds.) Pre-Mesozoic Geology in France and Related Areas, IGCP-Project 233. Springer Berlin Heidelberg, pp 243–264.

Gresens RL (1967) Composition-volume relationships of metasomatism. Chem Geol 2:47-65.

Gumiaux C, Brun JP, Gapais D (2004) Strain removal within the Hercynian Shear Belt of Central Brittany (western France): methodology and tectonic implications. Journal of the Geological Society of London 224:287–305.

Klemme S, Günther D, Hametner K, Prowatke S, Zack T (2006) The partitioning of traces elements between ilmenite, ulvospinel, armacolite and silicate melts with implications for the early differentiation of the moon. Chem Geol 234:251-263.

Luvizotto GL, Zack T, Triebold S, von Eynatten H (2009) Rutile occurrence and trace element behavior in medium-grade metasedimentary rocks: example from the Erzgebirge, Germany. Miner Petrol 97:233-249.

Meinhold G (2010) Rutile and its applications in earth sciences. Earth-Sci Rev 102:1-28.

Pochon A, Gapais D, Gloaguen E, Gumiaux C, Branquet Y, Cagnard F, Martelet G (2016a) Antimony deposits in the Variscan Armorican belt, a link with mafic intrusives? Terra Nova 28:138-145.

Pochon A, Poujol M, Gloaguen E, Branquet Y, Cagnard F, Gumiaux C, Gapais D (2016b) U-Pb LA-ICP-MS dating of apatite in mafic rocks: Evidence for a major magmatic event at the Devonian-Carboniferous boundary in the Armorican Massif (France). Am Mineral 101:2430-2442.

Rabbia OM, Hernández LB, French DH, King RW, Ayers JC (The El Teniente porphyry Cu-Mo deposit from hydrothermal rutile perspective. Miner Deposita 44:849-866.

Zack T, Kronz A, Foley SF, Rivers T (2002) Trace element abundances in rutiles from eclogites and associated garnet mica schists. Chem Geol 184:97-122.

Discovery of REE minerals hosted in karst bauxite ores from the Sierra de Bahoruco, Pedernales, Dominican Republic

Joaquín A. Proenza, Thomas Aiglsperger, Cristina Villanova-de-Benavent, Lisard Torró, Daniel Rodríguez-García *Universitat de Barcelona, Spain*

Australia Ramírez, Jesús Rodríguez
Servicio Geológico Nacional, Dominican Republic

Abstract. Karst bauxite ore samples (n=37) from active and inactive mining sites from Sierra de Bahoruco, SW Dominican Republic, have been investigated for their potential to host REE. Geochemical whole rock analyses reveal elevated contents up to ~0.5 wt.% total REE with LREE/HREE ratios from ~1 to ~25 (average ~8). Hydroseparation techniques in combination with magnetic separation were applied to three bauxite ores and led to the discovery of numerous REE-bearing mineral phases, which can be classified into (1) primary REE-phosphates; (2) secondary REE-phosphates; (3) REE carbonates and (4) REE oxides. With the exception of primary monazite, REE-bearing minerals show features (e.g., coatings; infills) suggesting significant REE mobilization and re-deposition within the bauxite host. This observation is supported by rather heterogeneous chondrite-normalized patterns, which are characterized by negative Ce and Eu anomalies in most cases. Considering the relatively high REE contents in all studied karst bauxite ores, as well as the secondary nature of most REE-bearing minerals here presented, karst bauxite ores from the Dominican Republic potentially represent an unconventional REE ore deposit of economic significance, where REE could be obtained as by-products during Al production.

1 Introduction

Bauxite ores are the main source for Al in the world, and two main types are defined: i) lateritic bauxites, formed due to intense weathering of the source rock (e.g. granites, basalts, shales) and ii) karst bauxites, characterized by a strong association with a carbonate host rocks. However, the formation of karst bauxites is a topic of ongoing scientific debate and two theories compete. One is that bauxite formation is a direct result of carbonate dissolution, whereas the other requires an external contribution of Al-bearing minerals during or after carbonate deposition (Bárdossy 1982; Mameli et al. 2017). Recently, bauxite ores have attracted economic geologists because of their capacity to accumulate rare earth elements (REE) (Liu et al. 2016 and references therein). Of special interest in this context are the heavy rare earth elements (HREE, Eu-Lu) because of their greater economic value compared with light rare earth elements (LREE, La-Sm).

At present, ~90% of the worldwide REE demand is supplied by China (Hatch 2012). As a consequence, REE were defined as critical metals for western countries as they are needed for numerous technological applications in sophisticated industries ("high-tech metals") (e.g., Duta et al. 2016). This work forms part of a joint investigation between the geological survey of the Dominican Republic and the University of Barcelona and aims to report first results of a detailed geochemical and mineralogical survey of karst bauxite ores from the Sierra de Bahoruco, SW Dominican Republic. Special emphasis is given to assess their potential to accumulate REE as well as to identify and characterize the main REE carriers.

2 Geological overview

The study area lies in the so-called Sierra de Bahoruco which is located in the south-western part of the Dominican Republic, next to the border with Haiti (Fig. 1).



Figure 1. Map showing the island Hispaniola in the Caribbean; the study area, located in the province of Pedernales, is highlighted.

Its crystalline basement is formed by the basaltic Dumisseau Formation (Campanian to lower Eocene) which is overlain by a thick sequence of carbonates (Eocene to Quaternary), representing the major components of the Sierra de Bahoruco (Escuder-Viruete et al. 2016). The carbonate sequence records the progressive shift in the environment of deposition from Eocene deep, outer slope, Pliocene shallow, inner platform and reef boundstones, and to Pleistocene emersion (Pérez-Valera 2010; Pérez-Valera and Abad 2010).

The collision of the Greater Antilles belt with the Bahamas Platform caused the progressive uplift of the Sierra de Bahoruco from latest Middle Miocene to the

present (Pérez-Valera 2010). Intense weathering under tropical conditions resulted in the development of locally well-developed karst systems and bauxite formation. Repeated Pleistocene-Holocene sea-level highstands associated with fast sea-level oscillations favored the development of important alteration profiles and karstification (de León 1989; Pérez-Valera 2010; Pérez-Valera and Abad 2010).

Karst bauxite deposits in Sierra de Bahoruco, SW Dominican Republic, stand out as an important endowment for this ore type. Mining activities in the district began in 1959 by the Alcoa exploration company, which produced a total of ~23 million DMTU (dry metric ton unit) in 26 deposits until 1982 (Ramirez 2015). Since 2006, the only remaining active mining operation in the study area is Las Mercedes, which represents the largest deposit (2.31 km^2) in the study area. Current reserves for karst bauxite deposits in Sierra de Bahoruco are estimated in 28 Mt of bauxite ore (Nelson et al. 2011).

3 Sample selection and methods

A total of 100 samples (1 kg each) of bauxite ore (incl. associated carbonates) from active and inactive mining sites were collected throughout the study area. 52 samples were selected, homogenized and sent for geochemical analysis to Actlabs Laboratories (Ontario, Canada). Major, minor and trace elements of samples were determined using fusion inductively coupled plasma emission (FUS-ICP) and inductively coupled plasma emission mass spectrometry (ICP-MS).

Three samples with elevated REE signatures were chosen for a detailed heavy mineral investigation. Each sample (100 g) was first crushed and hand-sieved to obtain three size fractions: <30, 30-50 and 50-75 µm. Next, the two coarser size fractions were processed by means of hydroseparation (HS) techniques and magnetic separation (FRANTZ) at the HS laboratory Barcelona (www.hslab-barcelona.com) (Aiglsperger et al. 2015). Subsequently, polished monolayers were prepared from heavy mineral concentrates and were studied with optical microscopy (OM), scanning electron microscope (SEM) using a Quanta 200 FEI XTE 325/D8395 as well as a field emission scanning electron microscope (FE-SEM) at the Centres Científics i Tecnòlogics, University of Barcelona (CCiT-UB), Spain. At the same institution, quantitative electron microprobe analyses (EMPA) were obtained with a JEOL JXA-8230 electron microprobe, operating in wavelength-dispersive spectroscopy (WDS) mode with an accelerating voltage of 20 kV, a beam current of 15 nA, and a beam diameter of 5 µm. Analytical standards and lines used for analyses were: wollastonite (Si Kα), apatite (Ca Kα, P Kα), barite (Ba Lα), celestine (Sr Lα), UO_2 (U Mβ), ThO_2 (Th Mα), GaAs (Ga Lα), YAG (Y Lα), LaB_6 (La Lα), CeO_2 (Ce Lα), REE-1 (Pr Lβ, Er Lα), REE-2 (Ho Lβ, Tm Lα, Eu Lα), REE-3 (Yb Lα, Sm Lβ, Gd Lα) and REE-4 (Lu Lα, Tb Lα, Nd Lβ).

4 REE geochemistry

All investigated bauxite ores have yielded relatively high total REE (La-Lu) contents in the range ~400 to ~5000 ppm (average ~1200 ppm), and LREE/HREE ratios between ~1 and ~25 (average ~8). The associated carbonates have low REE contents (~10 ppm in average) and LREE/HREE ratios around 5. In general, REE show a positive correlation with Al, Fe, Mn and P.

Chondrite-normalized patterns are variable. However, in most cases they are showing negative Ce and Eu anomalies and slight to intense positive trends from Ce to Pr (and to Nd in some cases), whereas slopes for HREE are rather flat for all samples (Fig. 2). Interestingly, one carefully selected, pure white (without bauxite contamination) carbonate sample next to the bauxite ore is characterized by similar chondrite-normalized patterns (Fig. 2).

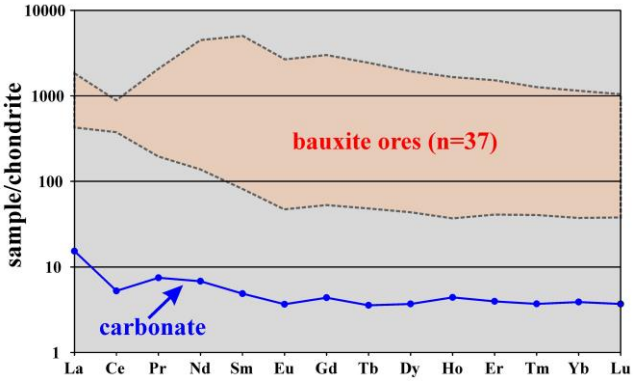


Figure 2. Chondrite-normalized patterns for the investigated bauxite ores and one characteristic carbonate sample from the study area. Normalization values were taken from Anders and Grevesse (1989).

5 REE mineralogy

In all the studied bauxite samples and in all the size fractions, REE-bearing mineral phases were discovered. Based on their chemical composition and textural appearance they can be classified into four main groups:

i) primary REE-phosphates
ii) secondary REE-phosphates
iii) REE-carbonates
iv) REE-oxides

Primary REE-phosphates are Ce- and La-rich monazite, characterized by euhedral to subhedral crystal shapes (Fig. 3A). Monazite crystals occur either as free single grains or intergrown (included) in zircon and host Si-rich (according to EDS analyses) melt inclusions of unknown mineralogy. The average compositions in the monazite include, normalized to 4 oxygens, Ce 0.44 a.p.f.u., La 0.25 a.p.f.u., Nd 0.14 a.p.f.u., Sm 0.04 a.p.f.u and Gd 0.04 a.p.f.u.

Neodymium represents the most abundant REE in secondary REE-phosphates, which generally occur either as anhedral single grains or as coatings on other grains.

However, secondary REE-phosphates also show replacement and infill textures associated with their Al-oxide(s) host (Fig. 3B). According to our EPMA analyses rhabdophane, churchite and florencite are present in the Sierra de Bahoruco karst deposits.

REE-carbonates are characterized by diverse morphologies, ranging from zoned, euhedral crystals and zoned nodules to grains without zoning and rather irregular shapes (Fig. 3C). However, high contents of Nd and/or Gd are general features of all REE-carbonates. ¡

REE-oxides occur as coatings and/or infills associated with their Al-oxide(s) host. Ce-rich REE-oxides most likely represent cerianite (CeO_2). However, HREE-bearing oxides of unknown mineralogy were also detected (Fig. 4).

6 Discussion

Unconventional REE ore deposits formed by intense weathering of source rocks in tropical climates have a significant economic potential. Simandl (2014), for example, reports on grades of economic interest as low as 500 ppm REO when conditions are favourable (i.e. easy open pit mining; beneficial LREE/HREE ratios; simple mineral processing). Karst bauxite ores from the Sierra de Bahoruco in the Dominican Republic are characterized by relatively high contents of up to 0.5 wt% REE, and hence are an excellent candidate for such unconventional REE ore deposits. This is particularly true as mines are already economic due to the presence of high quality Al ore (Si content ~4 wt%). The REE geochemistry presented here of the studied karst bauxite ores suggests that REE could be mined as by-products.

However, understanding the ore mineralogy is crucial for any exploration project, and very limited information on the REE mineralogy related to bauxites is currently available.

REE minerals identified in bauxite deposits worldwide include cerianite, parisite, röntgenite, synchysite, rhabdophane, and churchite (Mongelli 1997; Mameli et al. 2007; Wang et al. 2010; Li et al. 2013; Liu et al. 2016).

First results of heavy mineral investigations of three karst bauxite ores have shown the presence of primary and secondary REE minerals in the Sierra de Bahoruco bauxite deposits (Fig.3). REE minerals identified include rhabdophane, cerianite and churchite, among others.

In general, rhadophane is considered to precipitate in the lower horizon of the bauxite profile under high pH conditions (Berger et al. 2014; Liu et al. 2016 and references therein). In contrast, examination of Eh-pH predominance diagrams reveals that cerianite is formed at pH from 5 to 6, and Eh values of 0.38–0.61; whereas churchite is formed in acidic environments (pH=0.5–3.0) Liu et al. 2016).

Secondary REE phosphates and carbonates often show clear evidence for REE mobilization and re-deposition (e.g. infills; coatings). They reveal a strong spatial

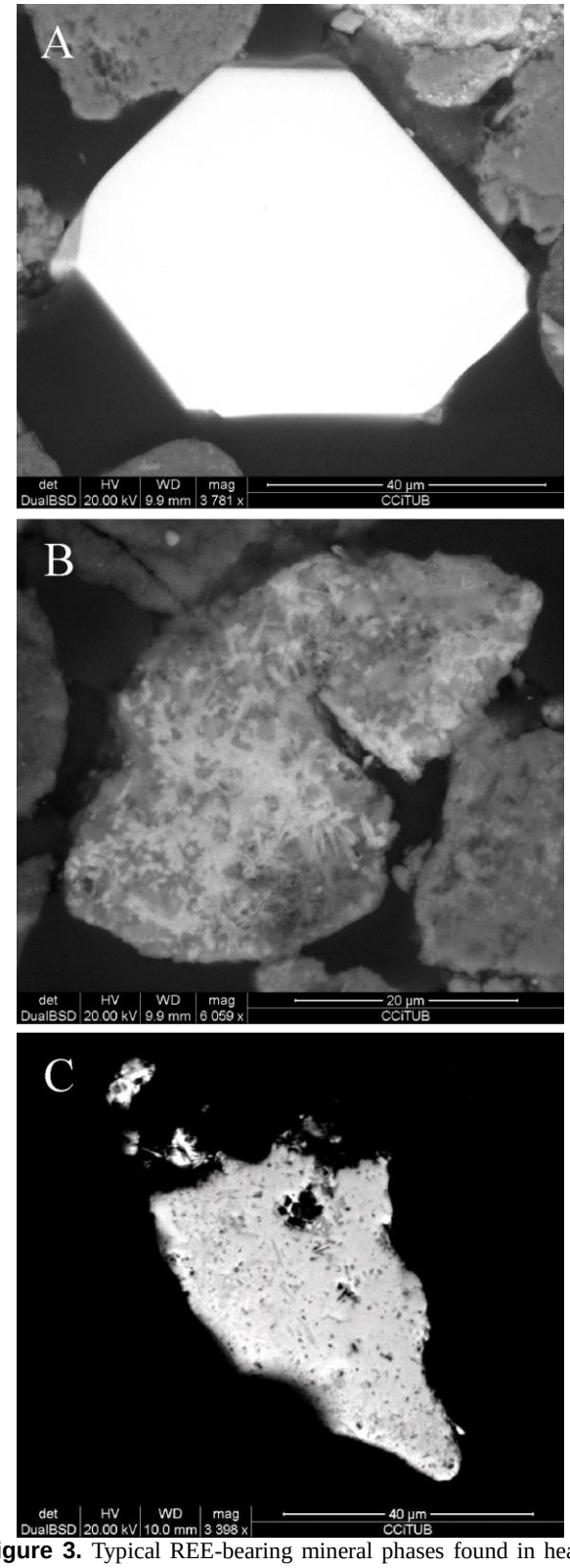


Figure 3. Typical REE-bearing mineral phases found in heavy mineral concentrates of the studied karst bauxite ores. A) Euhedral crystal of primary monazite; B) Secondary, Nd-rich phosphate crystals (white) within Al-oxide(s) matrix (grey); C) Gd-bearing REE carbonate.

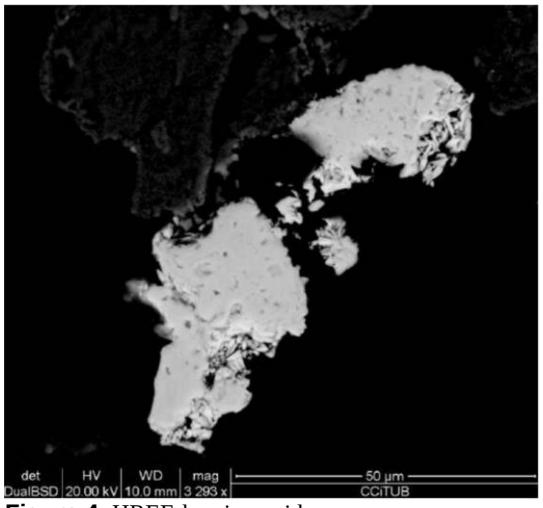


Figure 4. HREE-bearing oxide.

relationship with their Al-oxide(s) host and are systematically enriched in more valuable, heavier REE (e.g. Nd, Sm, Gd). REE absorbed on the surface of clay-minerals are believed to occur as well.

7 Concluding remarks

Karst bauxite ores hosted in the Sierra de Bahoruco contain REE contents of economic significance when seen as cost-inexpensive by-products during the production of Al. Hydroseparation in combination with magnetic separation is a powerful tool to achieve REE-bearing mineral concentrates. Results of this investigation contribute to a better understanding of REE cycling in the supergene environment.

Acknowledgements

This research has been funded by the project 2014-1B4-133 of the Ministerio de Educación, Ciencia y Tecnología (MESCyT) of the Dominican Government. The help and hospitality extended by the staff of DOVEMCO as well as by driver Mr. Wilson and assistants Mr. Jhonny and Mr. Lily during fieldwork are gratefully acknowledged. Special thanks go to Dr. X. Llovet for excellent technical support in EMP sessions.

References

Anders E, Grevesse N (1989) Abundances of the elements: Meteoritic and solar. Geochim Cosmochim Acta 53:197-214

Aiglsperger T, Proenza JA, Zaccarini F, Lewis JF, Garuti G, Labrador M, Longo F. (2015) Platinum group minerals (PGM) in the Falcondo Ni laterite deposit, Loma Caribe peridotite (Dominican Republic). Mineral. Deposita 50:105–123

Bárdossy G (1982) Karst bauxites. Bauxite deposits on carbonate rocks. Developments in Economic Geology 14. Elsevier, Budapest

Berger A, Janots E, Gnos E, Frei R, Bernier F (2014) Rare earth element mineralogy and geochemistry in a laterite profile from Madagascar. Appl Geochem 41:218–228

de León O (1989) Geología de la Sierra de Bahoruco (República Dominicana). Museo Nacional de Historia Natural, Santo Domingo

Dutta T, Kim KH, Uchimiya M, Kwon EE, Jeon BH, Deep A, Yun ST (2016) Global demand for rare earth resources and strategies for green demand. Environ Res 150:182-190

Escuder-Viruete J, Joubert M, Abad M, Pérez-Valera F, Gabites J (2016) The basaltic volcanism of the Dumisseau Formation in the Sierra de Bahoruco, SW Dominican Republic: A record of the mantle plume-related magmatism of the Caribbean Large Igneous Province. Lithos 254-255:67-83

Hatch GP (2012) Dynamics in the Global Market for Rare Earths. Elements 8:341-346

Li Z, Din J, Xu, J, Liao Ch, Yin F, Lü T, Cheng, L, Ch, Li J (2013) Discovery of the REE minerals in the Wulong–Nanchuan bauxite deposits Chongqing, China: Insights on conditions of formation and processes. J Geochem Explor 133:88–102

Liu X, Wang Q, Zhang Q, Zhang Y, Li Y (2016) Genesis of REE minerals in the karstic bauxite in western Guangxi, China, and its constraints on the deposit formation conditions. Ore Geol Rev 75:100-115

Mameli P, Mongelli G, Oggiano G, Dinelli E (2007). Geological, geochemical and mineralogical features of some bauxite deposits from Nurra (Western Sardinia, Italy): insights on conditions of formation and parental affinity. Int J Earth Sci 96:887-902

Mongelli G (1997) Ce-anomalies in the textural components of Upper Cretaceous karst bauxites from the Apulian carbonate platform (southern Italy). Chem Geol 140:69–79

Nelson CE, Proenza JA, Lewis JF, Lopez-Kramer J (2011) The metallogenic evolution of the Greater Antilles. Geol Acta 9:229-264

Pérez-Valera F (2010) Geologic Map Sheet 1:50.000 num. 5970-III and corresponding memoir. Proyecto 1B de Cartografía Geotemática de la República Dominicana. Programa SYSMIN. Dirección General de Minería, Santo Domingo

Pérez-Valera F, Abad M (2010) Informe Estratigráfico y Sedimentológico. Proyecto 1B de la Cartografía Geotemática de la República Dominicana. Programa SYSMIN. Dirección General de Minería, Santo Domingo

Ramirez RE (2015) El oro de Pedernales. Geonoticias 12-38:12-14

Simandl GJ (2014) Geology and market-dependent significance of rare earth element resources. Mineral. Deposita 49:889–904

Wang QF, Deng J, Liu XF, Zhang QZ, Sun S, Jiang CZ, Zhou F (2010) Discovery of the REE minerals and its geological significance in the Quyang bauxite deposit, West Guangxi, China. J Asian Earth Sci 39:701–712

Why are IOCG deposits iron-oxide-rich? Insights from the Prominent Hill hematite breccia deposit, Gawler Craton

Tobias U. Schlegel and Christoph A. Heinrich *ETH Zurich, Switzerland*

Thomas Wagner
RWTH Aachen, Germany

Adrian Boyce
Scottish Universities Environmental Research Centre, U.K.

Abstract. Prominent Hill is an iron oxide – copper – gold (IOCG) deposit hosting high-grade chalcocite – bornite ores in hematitic breccias derived from sedimentary and volcanic rocks of the Gawler Craton in South Australia. The deposit shows evidence of replacement of partly carbonate, chlorite, muscovite and pyrite bearing host rocks by phengitic sericite, hematite and Cu-rich copper sulfides. A hydrothermal sulfide stage I with sub-economic pyrite – chalcopyrite mineralization is overprinted by high-grade mineralization of sulfide stage II, along an alteration front, transgressive to lithological contacts, indicating that acid neutralization was an essential component of ore deposition. Spatially-resolved sulfur isotopes of sulfides and ore-related barite reveal a large variation in $\delta^{34}S$, which can be explained by one dominant source of magmatic sulfur that was oxidized to variable degrees. Fluid inclusions preserved in quartz, fluorite and barite associated with high-grade chalcocite mineralization were studied by micro-thermometry and a new quantification scheme for LA-ICPMS microanalysis. Four end-member fluids include a highly acidic, low-salinity Cu- and U-enriched fluid carrying magmatic solute components that were previously oxidized by exposure to atmospheric oxygen. This main copper-introducing fluid mixed and interacted with a modified magmatic brine and local basement brines. Surface-oxidized sulfur and copper of ultimately magmatic origin are proposed to have been the oxidants of a process involving Fe^{2+} from the brines as reductant, resulting in redox-balanced reactions producing the low-sulfidation copper sulfide – hematite – fluorite ore assemblage. Our process model combines aspects of magmatic-hydrothermal ore formation (magmatic heat ± brine) with features of sediment-hosted copper deposition (oxidized Cu^{2+} + sulfate + replacement of pre-ore pyrite) and characteristics of epithermal ore formation in a possibly evaporitic setting (likely convection of ultimately surface-derived basement brines).

1 Introduction

Iron oxide hosted copper – gold (IOCG) ± U ± REE deposits are characterized by the presence of magnetite or hematite as a major if not dominant component, of commonly large, breccia-hosted orebodies. Genetic models have focused on tectonic setting and crustal magmatism associated with this broad class of ore deposits, on stable and radiogenic isotopes, and on fluid inclusions to characterize their specific hydrothermal setting and the possible sources of ore-forming components (Barton and Johnson, 1996; Williams et al. 2005; Bastrakov et al. 2007; Barton 2014). No consensus exists, however, on the defining characteristic of these deposits, notably why IOCG are so rich in iron oxides. Answering this question requires a quantitative understanding of hydrothermal redox reactions by the fluids involved in ore formation, which needs to be based on a clear paragenetic understanding of geological evolution in the ore-forming system.

Prominent Hill, in the Gawler Craton of South Australia, is a word-class deposit, showing many similarities with the giant Olympic Dam deposit, and has been the focus of intense study over the last decades (Belperio et al. 2007; Freeman and Tomkinson 2010, Schlegel and Heinrich 2015). This paper summarizes a collaborative PhD project supported by OZ Minerals, Scottish Universities Environmental Research Centre, the Swiss National Science Foundation and ETH Zurich. We attempted to combine a solid geological understanding of orebody geometry and hydrothermal alteration with a texturally-resolved sulfur isotope study and a fluid inclusion analytical investigation using recent advances in LA-ICPMS (Schlegel et al. 2012). We were attracted to Prominent Hill by the fact that fluorite is present in abundance, as an integral part of the high-grade copper ore. The presence of fluorite (besides barite and typically minor or very fine-grained quartz) was paramount to the success of a quantitative fluid inclusion study.

2 Geology and alteration zoning

The geology and lithochemistry of the Prominent Hill iron oxide – copper – gold (IOCG) deposit has been published by Schlegel and Heinrich (2015), upon which this section is based, and which provides extensive references to previous work. Prominent Hill is the second-largest mine in the Gawler Craton of South Australia and contained about 278 Mt of ore at 0.98 % Cu, 0.75 g/t Au and 2.5 g/t Ag (Freeman and Tomkinson, 2010). Whereas the super-giant deposit of Olympic Dam is dominated by granite breccias, Prominent Hill is hosted mainly by breccias of sedimentary rocks

comprising coarse clastic to argillic lithologies with some volcanoclastic components and variable carbonate content. These sedimentary rocks and underlying mafic to intermediate-composition lavas are unmetamorphosed and inferred to be members of the lower Gawler Range Volcanics (Belperio et al., 2007). The volcano-sedimentary package hosting the high-grade copper-mineralized hematite breccias was downfaulted and overturned into near-vertical position along the E-W oriented Hanging Wall fault, north of which similar but greenschist-facies regionally metamorphosed rocks were mineralized by sub-economic magnetite skarns and intruded by granitic and more distal gabbroic bodies. Economic copper mineralization at Prominent Hill involved texturally-destructive replacement of formerly carbonate-bearing and siliciclastic breccia components, which were altered to assemblages including hematite, siderite, ankerite, quartz, chlorite, phengitic sericite, (fluor)-apatite, fluorite, barite, REE-U minerals including monazite, uraninite, and coffinite, together with Cu-sulfides including chalcopyrite, bornite, and chalcocite in the highest-grade ore.

Brecciation and replacement also caused some mechanical mixing of primary lithologies, obscuring but not entirely eliminating the original sedimentary contacts. Mass-balance estimation identified Al, Ti, Si and Zr as least mobile components during hematite – chlorite – sericite to weak hematite – quartz alteration. A lithochemical model, based on one horizontal and five vertical sections, formed the basis for alteration mapping, using molar (Fe+Si)/(Fe+Si+Al), K/Na and K/Al ratios. Spatial patterns of chemical variation indicate that the alteration-forming hematite, chlorite, phengitic sericite, ± quartz mineral assemblages are superimposed on a steeply-dipping, E-W oriented pattern of former lithological contacts. Hematite enrichment correlates only partially with the distribution of high Cu grades. Intense hematite – quartz alteration resulted in an aluminosilicate-poor, sub-vertical body replaced completely by fine-grained hematite and quartz. It forms a Cu-poor but Au-mineralized core east of the Cu-rich zones of the deposit. Zones of increasing K/Al and K/Na ratios extend upward and westward, with alteration boundaries and Cu-grade contours transgressively overprinting lithological contacts.

Copper ore deposition and hematite alteration developed after tilting of the host sequence into its present overturned orientation, as indicated by geopetal structures in the breccia matrix (Schlegel and Heinrich, 2015). Thus, the economic mineralization occurred late in the deformation history of the region and after extrusion of the lower Gawler Range Volcanics. The Prominent Hill orebodies formed after upthrusting of deeper-seated rocks that probably already contained the sub-economic chalcopyrite mineralization in magnetite skarns that are preserved north of the fault. Hematite in part formed together with hydrothermal introduction of high-grade Cu ore, but some iron oxide introduction preceded ore formation. Alteration geochemistry and petrography indicate that the best Cu mineralization occurred together with hematite – chlorite – sericite ± siderite alteration of originally carbonate-, muscovite, illite- and feldspar-bearing sedimentary lithologies. Deposit-scale zoning and smaller-scale mineral textures show that high-grade copper ore deposition was driven by acid neutralization of an initially low-pH metal-transporting fluid.

3 Sulfur isotopes

The Prominent Hill ore is characterized by a high Cu/S ratio with bornite and chalcocite in the most richly mineralized hematite breccias. With a study of sulfur isotope compositions we addressed the question of whether sulfur and copper originated from the same source rocks, and tried to identify the redox processes that created the associated iron oxide enrichment (Schlegel et al. 2017). Highly variable sulfur isotope compositions of sulfides and sulfates are typical in IOCG deposits but have been variably used to suggest sulfur contributions from sedimentary, seawater, evaporitic and magmatic sources

Prominent Hill records a wide range of $\delta^{34}S$, ranging from –34 ‰ to +30 ‰ for Cu-(Fe) sulfides, and a narrower range of 4 ‰ to 16 ‰ for barite. Iron sulfides (pyrite, pyrrhotite) also show a comparatively narrow range of more negative $\delta^{34}S$ values, mostly between -15 and +4‰. These data, together with the textural observations, are interpreted with a two-stage sulfide mineralization model, in which all hydrothermal sulfur is ultimately derived from a magmatic source that had a composition of 4.4 ± 2 ‰. The diversity in sulfur isotope composition can be produced by different fluid evolution paths along reducing or oxidizing trajectories. A dominantly reduced sulfur evolution pathway is responsible for sulfide stage I mineralization, by intrusion-derived magmatic-hydrothermal fluids producing early pyrite and minor chalcopyrite in the host rocks of Prominent Hill, and magnetite ± copper sulfides in regional magnetite skarns. By contrast, during stage II sulfide mineralization, initially surface-venting magmatic fluids and subaerial volcanic gases were completely oxidized by reaction with atmospheric oxygen. This produced sulfate and sulfuric acid with a sulfur isotope composition approximating the original magmatic source. This highly oxidized fluid, derived from the surface environment, was probably dominated by meteoric water, but contained dominantly magmatic solute components — notably sulfate, acidity, and copper. Reduction of these igneous solute components produced hydrothermal Cu sulfides with a wide range in sulfur isotope compositions. Partial reaction with stage I sulfides already existing in the host rocks resulted in mixing of sulfur derived from sulfate reduction and from sulfides deposited during stage I. Modeling of the sulfur isotope fractionation processes in response to reducing and oxidizing pathways demonstrates that the full spectrum of sulfur isotope data at Prominent Hill can be explained with a single, ultimately magmatic sulfur source. We argue that an essentially magmatic sulfur source is also adequate to explain the spectrum of published sulfur isotope data of other IOCG prospects and deposits in the Gawler province, including Olympic Dam.

4 Fluid inclusion investigations

Based on the geological logging of alteration distribution, we selected a large number of drill-core samples for polished thin sections, to study the relation between mineral textures and contained fluid inclusions (Schlegel et. al., in preparation). Fluid inclusions are abundant and their presence in fluorite and barite allowed a clear textural association of inclusion types with chalcocite ± bornite precipitation in high-grade breccia ore. Inclusions in replacement and infill textures within the breccia matrix predominate, whereas veins are rare but provide additional fluid data that can be tentatively related to stage I pre-ore mineralization and the waning of economic sulfide stage-II mineralization.

From numerous doubly-polished sections, a subset was studied by a combination of microthermometry with LA-ICPMS microanalysis. Wherever possible, micro-thermometry included measurement of two low-temperature phase transitions (last melting of ice and of hydrohalite or dissolution of halite) following internal recrystallization of the inclusions by temperature cycling. This procedure allows quantification of Ca/Na ratios of all except for the lowest-salinity fluids. Its precision is superior to that of LA-ICPMS, which however confirmed that Ca is the dominant additional cation in the fluid inclusions besides Na and minor K. All fluid inclusion data were obtained from several inclusions in texturally defined fluid inclusion assemblages (FIA), to assess analytical significance and precision. Heating experiments were subject to limitations of inclusion stretching, hence greater attention was paid to phase proportions (bubble size) showing that the deposit experienced significant variations in temperature between ~ 120 and 350 °C. Vapor inclusions are rare but a few essentially 'empty' FIA indicate that the deposit formed at shallow depth and that the homogenization temperatures do not require major pressure correction. High temperatures at shallow depth require that ore formation temporally overlapped with magmatism, as a source of heat and possibly chemical components.

LA-ICPMS was carried out with a highly-sensitive Sector-Field mass spectrometer. Calculation of absolute element concentrations from the concentration ratios obtained by LA-ICPMS was achieved by using, as far as possible, the true Na concentration of fluid inclusions derived from the two microthermometric measurements (Schlegel et al. 2012). Unfortunately, total sulfur concentrations of the fluid inclusions are not well defined due to high analytical backgrounds.

Compositional results indicate a wide range of systematic variation in salinity and Ca/Na ratio, which together with textural occurrence was used to group the FIA into four compositional groups. These in turn define four end-member fluids that were involved in the formation of the Prominent Hill deposit.

Fluid A has low to intermediate salinity, dominated by NaCl and is intimately associated with high-grade stage-II ore deposition. This fluid is interpreted to be the main copper-bearing fluid, on account of its variably high Cu and U content. Textural relations suggest that this fluid was acidic (driving alteration to the extreme of Al depletion in hematite – quartz altered zones), and that it also contributed F to the precipitation of fluorite by mixing with more calcic fluids. This fluid is interpreted to be of meteoric origin, in former contact with an oxidized atmosphere, but containing fully oxidized magmatic solutes including S as sulfuric acid (and presumably also Cu and F) derived from volcanic degassing with contributions of Cu from near-surface leaching of concurrently erupting lavas of the Gawler Range Volcanics.

Fluid B is a high-salinity brine with low to moderate Ca/Na ratios but high concentrations of K, Fe Cs and Pb, which are interpreted as magmatic brine components. They occur in veins that may represent the waning of sub-economic magnetite – chalcopyrite skarns in the hanging wall of Prominent Hill, but they also occur in veins containing siderite and chalcopyrite that cross the high-grade mineralized breccias. Both sites of occurrence of this fluid include consistently high-temperature assemblages (>250 °C) confirming the input of magmatic heat and inferred magmatic brine before and after, and plausibly also during the main, stage II ore formation.

Fluids C and D have intermediate salinity, and range in composition from moderately (C) to very high (D) ratios of Ca/Na. Hypothetical mixing lines of major and minor compositions preclude that these calcic-sodic brines are derived by mixing of low-salinity surface-derived ore Fluid A with the inferred magmatic brine B. Mass-balance considerations also preclude that Fluids C and D acquired their high Ca/Na ratios by alteration reactions within the orebody and the associated alteration front. Rather, these fluids have acquired their distinct composition by larger-scale equilibration with sedimentary or basement rocks at very low fluid/rock ratios. These brines have Br/Cl ratios that are 2-10x higher than present-day seawater, which is usually taken as an indication that their salinity originates from residual Br enrichment in a halite-precipitating evaporitic environment at the surface.

5 The chemistry of IOCG ore deposition

Even though geological and fluid-geochemical data from Prominent Hill are restricted and still tentative due to numerous technical challenges, we can combine them to a plausible model for hydrothermal ore formation that may extend to other hematite-rich IOCG deposits. Elevated temperatures indicate that Prominent Hill is a magmatic-hydrothermal deposit in the broader sense. Temperatures broadly span the epithermal range: lower than those of porphyry copper deposition, and ranging down to those of sediment-hosted copper deposits. A viable process model for ore formation must provide a chemical explanation why hematite-breccia hosted IOCG deposits differ from porphyry-type ore deposits in lacking extensive quartz vein development, but contain tens of percent of hematite. The genetic model should also explain the mineralogical traits

shared with sediment-hosted copper deposits, notably the very low sulfidation state of assemblages forming the highest-grade copper ores (including textural evidence of bornite and chalcocite precipitation by replacement of a restricted supply of preexisting pyrite; stage I at Prominent Hill).

Fluids at temperatures below 300 °C contain very low concentrations of free O_2 even if saturated with air, and very low concentrations of H_2 even at moderately reduced conditions near the SO_4/H_2S boundary in the Earths interior. We therefore expect that major mass transfer between fluids and minerals, notably tens of percent of hematite addition in the copper-mineralized breccias, is effected by O_2-conservative reactions involving more abundant redox couples in the hydrothermal fluids. Sulfate as a major and highly soluble oxidant, and Fe^{2+} as a reductant required for iron transport and iron oxide precipitation, are likely to play a major, if not dominant role (Gow et al. 1994). Magmatic brine (Group B fluids) would contains all necessary ingredients including high concentrations of Fe^{2+} as well as sulfur, which would come in as SO_2 and disproportionate to H_2S and sulfate on cooling. It also contains abundant Cu, but if injection of magmatic brine was the single essential contributor to IOCG mineralization we would expect geological characteristics resembling those of the barren quartz – magnetite core of porphyry deposits or those of several sub-economic magnetite – pyrite dominated prospects in the eastern Gawler Craton.

The virtual absence of quartz veining, the predominance of delicate replacement textures and the addition of abundant hematite in intimate association with the Cu-rich copper sulfides and fluorite are more distinctively explained by a process of fluid mixing and fluid-rock reaction, probably including net volume generation by replacement and local dissolution of carbonates, which possibly contributed to breccia collapse, as another distinctive feature of most IOCG deposits. This opens the possibility of redox-coupled hematite + chalcocite deposition, in which Cu^{2+} and sulfate are reduced to copper-(iron-) sulfides, while Fe^{2+} is oxidized to hematite:

$$2Cu^{2+} + HSO_4^- + 10Fe^{2+} + 11H_2O = 5Fe_2O_3 + Cu_2S + 23H^+$$

The reaction, also when written for bornite, liberates H^+ and will therefore be promoted by carbonate dissolution or acid-consuming Al-silicate alteration, as indicated by the observed orebody-scale zonation. A second contributing set of reactions involves reaction with preexisting pyrite, such as:

$$14Cu^{2+} + 5FeS_2 + 12H_2O = 3HSO_4^- + 7Cu_2S + 5Fe^{2+} + 21H^+$$

In either reaction, the availability of sulfur probably limited reaction progress towards high-grade copper deposition, which would explain the characteristic low sulfidation state of the highest-grade ore assemblage. Ferrous iron for net hematite addition was provided by either a small contribution of magmatic brine (B) or by reduced rock-equilibrated basement brines (C or D), mixing with the more copious ore fluid A.

In conclusion, our data are consistent with a magmatic-hydrothermal origin for IOCG deposits, differing from the formation of porphyry – epithermal ore systems by surface-venting of magmatic fluids in a continental volcanic setting. This leads to atmospheric oxidation of magmatic copper and sulfur, preparing a sulfur-bearing but sulfide-depleted ore fluid. Iron oxide deposition is linked to copper deposition by redox reactions between this oxidized ore fluid and subsurface brines rich in ferrous iron, producing limited sulfide for the low-sulfidation copper sulfide assemblages of hematite-rich IOCG deposits.

Acknowledgements

We acknowledge financial support by the Swiss National Science Foundation and are most grateful for field support and intense discussion with Pat Williams and geologists of OZ Minerals.

References

Barton MD and Johnson DA (1996) Evaporitic-source model for igneous-related Fe oxide-(REE-Cu-Au-U) mineralization: Geology, 24, 259-262.

Barton MD (2014) Iron Oxide(–Cu–Au–REE–P–Ag–U–Co) Systems, in Holland HD, Turekian KK, eds, Treatise on Geochemistry (Second Edition): Oxford, Elsevier, 13, 515-541.

Bastrakov EN, Skirrow RG, Davidson GJ (2007) Fluid evolution and origins of iron oxide-Cu-Au prospects in the Olympic Dam district, Gawler craton, South Australia: Economic Geology 102, 1415-1440.

Belperio A, Flint R, and Freeman H (2007) Prominent Hill: A hematite-dominated, iron oxide copper-gold system: Economic Geology 102, 1499-1510.

Freeman H and Tomkinson M (2010) Geological setting of iron oxide related mineralisation in the southern Mount Woods domain, South Australia, in Porter TM, ed, Hydrothermal iron oxide copper-gold & related deposits: A global perspective - Advantages in understanding of IOCG deposits: Adelaide, PGC Publishing 3, 171-190.

Gow PA, Wall VJ, Oliver NHS, and Valenta RK (1994) Proterozoic iron oxide (Cu-U-Au-REE) deposits – Further evidence of hydrothermal origins: Geology 22, 633-636.

Schlegel TU, Wälle M, Steele-MacInnis M, and Heinrich CA (2012) Accurate and precise quantification of major and trace element compositions of calcic-sodic fluid inclusions by combined microthermometry and LA-ICP-MS analysis: Chemical Geology 334, 144-153.

Schlegel TU and Heinrich CA (2015) Alteration and lithology control Cu mineralization at Prominent Hill iron oxide-copper-gold deposit, Gawler craton, South Australia: Economic Geology 110, 1953-1994.

Schlegel TU, Wagner T, Boyce AJ, and Heinrich CA (2017) A magmatic source of hydrothermal sulfur for the Prominent Hill deposit and associated prospects in the Olympic iron oxide copper-gold (IOCG) province of South Australia: Ore Geology Reviews 2016, in press.

Schlegel TU, Wagner T, Wälle M, and Heinrich CA (in preparation) Hematite-breccia hosted iron oxide – copper – gold deposits require magmatic fluid components exposed to atmospheric oxidation: Prominent Hill, Gawler Craton, South Australia.

Williams PJ, Barton MD, Johnson DA, Fontbote L, de Haller A, Mark G, Oliver NHS, and Marschik R (2005) Iron oxide copper-gold deposits: geology, space-time distribution, and possible modes of origin, in Hedenquist JW, Thompson JFH, Goldfarb RJ, and Richards JP, eds, Economic Geology 100th Anniversary Volume: Littleton, Colorado, 371-405.

Geochemistry and mineralogy of the Dotson Zone HREE deposit in the Bokan Mountain peralkaline igneous complex, southeastern Alaska, USA

Cliff D. Taylor, Heather A. Lowers, David T. Adams
U.S. Geological Survey
R. James Robinson
Aurora Geosciences Inc.

Abstract. The Bokan Mountain igneous complex (BMIC) is a typical example of a peralkaline intrusive system that has evolved to the point of developing late stage HFSE- and REE-rich silicic pegmatites and dikes. The Dotson Zone comprises a series of felsic dikes that extend from the southeast margin of the composite pluton and may represent an important resource of critical HREEs. Petrographically, the primary igneous mineral assemblage is altered by late-igneous and hydrothermal fluids resulting in redistribution and enrichment of REEs. An area of flexure in the southeastern end of the Dotson Zone was the primary locus of enrichment as shown by the pervasive alteration and consistently high REE+Y values. We favor a model in which the dikes were emplaced concurrently with the marginal intrusions, and then altered during emplacement of the inner, main intrusion in a relatively rapid series of overlapping intrusive and late magmatic fluid-high temperature hydrothermal events as the complex cooled. A much later sodic intrusive event focused on the BMIC may have resulted in additional silica-Na-Zr-rich alteration in proximity to the pluton.

1 Introduction

The Early Jurassic Bokan Mountain igneous complex (BMIC) intruded lower Paleozoic island arc volcanosedimentary rocks of the Alexander terrane in southeastern Alaska on southern Prince of Wales Island, ~40 km west of Ketchikan. The BMIC is roughly circular, 3 km in diameter, composed of peralkaline granitic rocks, exhibits late-stage heavy rare earth (HREE)-enriched pegmatite enclaves and felsic dikes, and is associated with numerous U-Th-HREE-fluorite hydrothermal and skarn mineral occurrences at its margin. The BMIC hosts the Ross-Adams mine, Alaska's only past-producer of uranium and one of the highest grade granite-hosted uranium mines in the world. Recent exploration at Bokan Mountain has focused on the Dotson Zone (DZ), a ~2-km-long, 50-m-wide zone of felsic dikes extending from the southeast margin of the pluton. Ucore Rare Metals Inc. reported an indicated resource of 4.79 million tonnes and an inferred resource of 1.05 million tonnes at 0.6% total rare earth oxides (TREO), of which about 39% consists of the valuable HREOs (Ucore, May, 2015). Thus, the DZ deposit represents a potential future domestic source of critical HREEs (Taylor et al. 2016).

Recent SHRIMP and LA-ICP-MS U-Pb ages on zircon and monazite and $^{40}Ar/^{39}Ar$ ages on sodic amphibole from the major lithologies of the BMIC reveal a complex history of progressive intrusion and development of highly incompatible-element-enriched pegmatites and dikes from ca. 182-176 Ma. These igneous events were followed by hydrothermal enrichment of HREE and hydrothermal zircon growth during at least two subsequent episodes. An initial hydrothermal event is recorded in arfvedsonite from the main intrusion of the BMIC (ca. 173 Ma) as well as in hydrothermal zircons from the DZ (ca. 172-170). A second, much younger event is recorded in zircons (ca. 123-121 Ma) and monazite (ca. 115 Ma) from the DZ. The youngest event within the BMIC is recorded by zircon in widespread fine-grained, felty aegirine dikes at ca. 116 Ma. This work suggests that progressive emplacement of the BMIC and hydrothermal HREE-enrichment of felsic dikes took place over 10-12 m.y. Sodic metasomatism of the oldest marginal and interior phases of the complex provided a source of high field strength elements (HFSE) and REE components to magmatic fluids from the main body of the BMIC, resulting in the emplacement of the felsic dikes. A separate pulse of alkaline magmatism, or an as-yet unidentified metamorphic/metasomatic event, resulted in emplacement of quartz-aegirine dikes and further hydrothermal enrichment of the DZ approximately 55-50 m.y. later (Taylor et al. 2016). In this contribution we present the results of a geochemical and mineralogical study of the DZ.

2 Geology

In detail, the DZ extends from the Connector Fault, which truncates its northwestern end, to Kendrick Bay; a strike length of 2140 m. It has an average width of 50 m, and a vertical extent of 450 m (open at depth). On average, the DZ strikes 288° and dips 75°-85°. The DZ consists of a sub-parallel network of at least 25 dikes. Dikes are rarely >2 m thick and more commonly form arrays of numerous dikes 1-10 cm thick over intervals of several meters. The Dotson Main dike is the most persistent and has a strike length of 1900 m and is up to 3 m thick in places. Dikes are remarkably planar over 10s of meters; dike splays and junctions occur occasionally. A major north-trending fault named the Camp Creek Fault Zone (CCFZ) cuts the DZ at a distance of ~1200 m from the west end. The CCFZ displaces dikes on the west side ~20m to the north. Dikes

on the west side are more tightly clustered. Strike of dikes on the east side are rotated several degrees to clockwise. Evidence suggests the CCFZ is a steeply dipping normal fault of minimal displacement, west side down. There is a flexure in the DZ from about 1400 to about 1650 m where the veins changes from steeply north-dipping (west) to steeply south-dipping (east). Here, the width of the DZ flares to ~100 m and dikes are more numerous and closely spaced (Robinson et al. 2011).

There are two basic types of dikes, all which exhibit very sharp, straight, and unaltered contacts with the surrounding wallrock: 1) simple dikes, consisting of a homogeneous mixture of fine to very coarse crystalline equigranular minerals, and 2) zoned dikes, having similar mineralogy but exhibiting distinct mineralogical zonation from margin to interior usually consisting of dark, aphanitic to very fine crystalline dark minerals adjacent to the dike walls grading or changing abruptly to leucocratic coarse crystalline minerals in the core of the dikes. Chlorite-calcite veins consisting of contorted black to very dark green-gray chlorite with fine to medium crystalline, often contorted calcite are found peripheral to the mineralized dikes, either sub-parallel to or at the distal ends of an individual mineralized dike (Robinson et al. 2011).

3 Methods

Forty two whole rock samples were collected from Ucore test pits and trenches at 80-300 m intervals along the entire 2 km length of the DZ. Thirty eight of the 42 samples represent REE-mineralized felsic dikes of the DZ deposit. All samples were analyzed by wavelength dispersive X-ray fluorescence (WDXRF) for major oxides and inductively coupled plasma mass spectrometry plus atomic emission spectroscopy (ICP-AES-MS) with an alkaline sinter for 55 elements. All greater-than-detection-limit analyses of HFSE and REE were reanalyzed either by dilution and ICP-AES-MS or by ICP-16 to obtain absolute values. Thin sections were cut for most samples and examined for petrography. Scanning electron microscopy with energy dispersive spectroscopy (SEM-EDS) of twenty one thin sections was completed for reconnaisance mineral identification and location for subsequent analyses by electron probe microanalysis (EPMA). EPMA acquisition parameters were optimized for the determination of REE, and detection limits of ca. 400-1300 ppm were achieved for most of the HFSE and REE.

4 Results

Petrographically and in back-scattered electron (BSE) imagery, the samples show evidence of partial to complete alteration. Less altered samples typically exhibit coarse- to fine-grained equigranular intergrowths of subhedral quartz, primary albite, and anorthoclase ± aegirine, muscovite, annite-phlogophite, and magnetite. The REE minerals are subhedral to anhedral and occur in intergranular space. Progressively more altered samples show subhedral to anhedral quartz and anorthoclase with embayed and irregular crystal boundaries, growth of secondary lath-shaped albite and partial to near-complete replacement of primary albite, anorthoclase and especially aegirine with a complex mixture of spongy zircon, chlorite, epidote, HFSE and REE minerals, fluorite, barite, calcite, and base metal sulfides. In zoned dikes and dikes with a higher content of primary mafic minerals, elongate phenocrysts of Na-amphibole, aegirine, and possibly earlier-formed elpidite (Mariano 2009) are preferentially and completely replaced by hydrothermal quartz, zircon, and fine-grained, intimately intergrown mixtures of HFSE and REE minerals (Fig. 1).

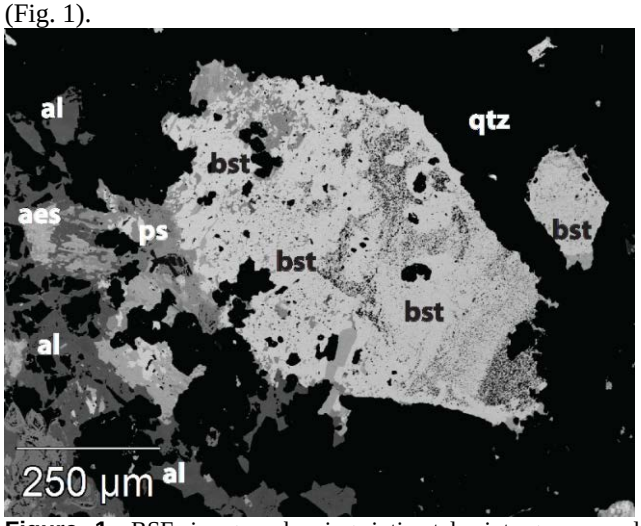


Figure 1. BSE images showing intimately intergrown and spongy textures of bastnasite, parisite, aeschynite, and allanite completely replacing an amphibole phenocryst. Matrix is quartz. aes=aeschynite; bst=bastnasite, al=allanite, ps=parisite, qtz =quartz.

Although over 40 HFSE and REE minerals have been reported from the BMIC by previous workers (Staatz 1978, Thompson 1988, Warner and Barker 1989, Philpotts et al. 1998, Mariano 2009, Wilson 2010, Dostal et al. 2011, Robinson et al. 2011, Stoeser and Lowers, 2013) we have only confirmed a suite of 30 minerals in the DZ based on preliminary SEM-EDS spectra followed by EPMA analyses. Minerals we have identified are the LREE phases bastnasite-(Ce), allanite-(Ce), parisite-(Ce), synchysite-(Ce), aeschynite-(Y), monazite–(Ce), bastnasite-(La), bastnasite-(Nd), parisite-(Nd), synchysite-(Nd), synchysite-(Y), fluorbritholite-(Ce), lanthanite-(Ce), an unknown Fe-Ti-Y-Ce-U-Th silicate, an unknown Fe-Ti-Y-Ce oxide, and an unknown Fe-Ca-Ce-Y carbonate, and the HREE phases zircon, fergusonite-(Y), fluorthalenite-(Y), xenotime-(Y), thalenite-(Y), tengerite-(Y), hingganite-(Y), caysichite-(Y), polycrase-(Y), an unknown Zr-Y-Nd-silicate, an unknown Al-Y-Dy-Fe-silicate, and an unknown Al-Y phosphate (roughly in decreasing order of abundance, respectively). Hydrothermal zircon is the most ubiquitous and abundant phase present and includes Ti- and Nb-rich variants. The Th minerals calciothorite, ferrithorite and

thorite were identified in minor amounts. Polycrase-(Y) is the only discrete U-bearing mineral identified in our work although thorite, calciothorite or ferrithorite, aeschynite-(Y), tengerite-(Y), fergusonite-(Y), and zircon (in order of decreasing U-content) all contain uranium in the range of 1-5 wt. percent.

Whole rock major element geochemistry of the dikes is unusual and reflects their highly silicic and alkaline compositions. SiO_2 ranges from 59 to 85 with an average of 75 wt. %. Average values for Al_2O_3, Na_2O, K_2O are 7.4, 3.2, and 1.4 wt. % respectively and CaO and MgO are 0.92 and 0.33. Average values for Fe_2O_3, MnO, P_2O_5, and TiO_2 are 4.8, 0.21, 0.12, and 0.32 wt. %. Loss on ignition (LOI) varies from 0.4 to 2.0 with an average of 1.1 wt. %. Major element zonation from west to east along the ~2 km length of the DZ is apparent with the greatest change in character occurring at the CCFZ. In general, major element abundances are more erratic in the western portion and less variable with more consistent trends to the east of the CCFZ. SiO_2 increases towards the CCFZ and is then consistently ~75 wt. % to the east. Al_2O_3, Na_2O, and K_2O decrease along the entire length of the DZ with a steeper decrease to the west of the CCFZ and nearly flat to slightly decreasing profiles to the east. CaO, P_2O_5, MnO, and LOI all have flat and erratic profiles to the west of the CCFZ and then increase to the east. Fe_2O_3 and TiO_2 decrease eastward to the CCFZ and are then flat to the east. MgO exhibits a consistent, flat profile along the entire length.

HFSE and REE geochemistry is extremely enriched and shows similar zonation patterns along the length of the DZ. Extremely high Zr and Total (T) REE+Y abundances are most striking with average values of 1.1 and 2.3, and maximum values of 3.3 and 6.7 wt. %, respectively. Zr is highly erratic to the west of the CCFZ but generally has a flat or slightly decreasing pattern along the entire length of the DZ. TREE+Y, TLREE, and THREE all increase along the length of the DZ with more steeply increasing TREE+Y and TLREE to the east of the CCFZ. This is reflected in the %HREE value, which decreases to the east (Fig. 2). The increase in the preponderance of the LREE with distance along the DZ is also shown by the shape and slopes of chondrite-normalized REE patterns. The $(La/Lu)_N$ values range from 0.1 to ~4 west of the CCFZ and steadily increase from ~2 to a high of 40 to the east. $(La/Sm)_N$ values are relatively constant, averaging 1.9 throughout the DZ whereas $(Gd/Lu)_N$ values range from 0.1 to 2.5 west of the CCFZ and steadily increase from 1.3 to 8.4 to the east. A negative Eu anomaly is present in all samples and is remarkably constant throughout the DZ ranging from a $(Eu/Eu^*)_N$ of 0.27 to 0.32 with an average of 0.29. Small to moderately positive Ce anomalies are larger and more erratic west of the CCFZ and decrease in size to the east. Nb and Ta values are flat and relatively constant to the west of the CCFZ and increase steeply and become more erratic to the east. Hf and Th values are flat and erratic throughout the DZ, and U rises to the east resulting in a highly erratic U/Th profile that rises east of the CCFZ. Th abundance is greater than U in all but one sample, with an average U/Th of 0.4.

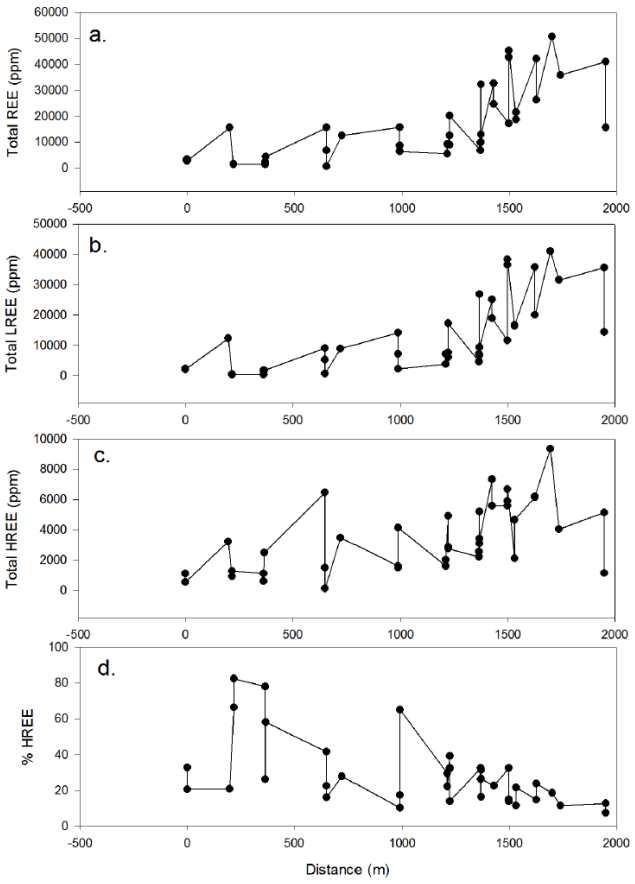


Figure 2. Profiles of REE abundances along the Dotson Zone (a) Total REE+Y; (b) Total LREE; (c) Total HREE; (d) % HREE.

5 Discussion

The new petrography and geochemistry of the dike samples along the >2 km length of the DZ presented in this study provide the clearest picture to date of the mineralogical and geochemical variations present within the deposit. Petrographically, the rock-forming mineralogy of the dikes is quite simple, being predominantly composed of quartz, albite, and anorthoclase with a variable suite of accessory minerals as described above. Without having performed quantitative evaluation of the mineralogy in each thin section we do not have direct evidence to suggest that the proportions of the minerals change significantly along the length of the DZ. The degree of alteration, however, increases notably with distance and reaches a maximum in the flexure zone to the east of the CCSZ where the DZ also flares in width. Geochemistry to the west of the CCSZ is characterized by erratic abundances of most elements. High Al_2O_3 and Na_2O probably reflect greater proportions of albite, high Fe_2O_3 and TiO_2 are likely from high primary magnetite and ilmentite contents, and elevated and highly erratic Zr is due to introduction of hydrothermal zircon. The erratic and moderate-sized Ce anomalies present to the west of the CCSZ also suggest a greater degree of hydrothermal alteration than to the east. However, this alteration was

probably a silica-Na-Zr-rich event as opposed to a carbonate-rich event as suggested by the low CaO content and low and erratic LOI. Our data clearly show that the main locus of REE-Y-Nb-Ta mineralization occurred in the flexure zone east of the CCFZ. The increase of the relative abundances of LREE to HREE in the flexure as well as the increasing CaO, LOI, suggest the predominance of REE-carbonate, -phosphate, and -niobate minerals over REE-silicates in this part of the DZ. Although HREE-enriched niobate, carbonate and phosphate minerals such as fergusonite, tengerite, and xenotime are also present in greater abundance than to the west, they are not as abundant as bastnasite, parisite, synchysite, and monazite.

5 Conclusions

Reasons for the observed differences in mineralogy and geochemistry along the DZ may be explained by a model in which the dikes were emplaced concurrently with the marginal intrusions of the BMIC and then subjected to a first phase of alteration related to emplacement of the inner, main phase of the BMIC in a relatively rapid series of overlapping intrusive and late magmatic fluid-high temperature hydrothermal events as the BMIC cooled. A much later sodic intrusive event focused on the BMIC may have resulted in additional silica-Na-Zr-rich alteration in proximity to the pluton.

Acknowledgments

We are grateful to the management and staff of Ucore Rare Metals Inc. for field support and permission to visit and sample their Dotson Zone Project. Reviews by Erin Marsh and Ryan Taylor greatly improved the manuscript. This study was financially supported by the U.S. Geological Survey Mineral Resources Program. Any use of trade, firm, or product names is for descriptive purposes only and does not imply endorsement by the U.S. Government.

References

Dostal J, Kontak DJ, Hanley J, Owen V (2011) Geological investigation of rare earth element and uranium deposits of the Bokan Mountain Complex, Prince of Wales Island, Southeastern Alaska. U.S. Geological Survey Mineral Resources External Research Report G09AP00039, p122

Gehrels GE (1992) Geologic map of the southern Prince of Wales Island, southeastern Alaska. U.S. Geological Survey Miscellaneous Investigations Series Map I-2169, scale 1-63,360, 1 plate and explanatory.pamphlet, p23

Mariano AN (2009) Report on Mineralogy of Mary Rose Outcrop Samples – Bokan Mountain, for Ucore Rare Metals Inc., p10

Philpotts JA, Taylor CD, Tatsumoto M, Belkin HE (1998) Petrogenesis of late-stage granites and Y-REE-Zr-Nb-enriched vein dikes of the Bokan Mountain stock, Prince of Wales Island, southeastern Alaska. U.S. Geological Survey Open File Report, OFR 98–0459, p71

Robinson RJ, Power MA, Barker JC (2011) Technical report on the exploration program and mineral resource estimate for the Bokan Mountain property, Prince of Wales Island, Alaska, for Ucore Rare Metals Inc., p190

Staatz MH (1978) I&L uranium and thorium vein system, Bokan Mountain, southern Alaska. Econ Geol 73;512-523

Stoeser D.B, Lowers HA (2013) Mineralogy and mineral paragenesis of the Dotson Ridge HREE deposit, Bokan Mountain, Prince of Wales Island, Alaska. 2013 Geological Society of America Annual Meeting, Denver, Colorado. Abstracts with Programs 45:276

Taylor CD, Aleinikoff JN, Holm-Denoma CS, Neymark LA, Bala SA, Pascarelli SE, Pillers RM, Karl SM, Van Gosen BS, Morgan LE, Cosca MA (2016) New geochronologic constraints on the formation and hydrothermal enrichment of the Bokan Mountain peralkaline igneous complex and associated HREE deposits, southeastern Alaska, USA. 2016 Geological Society of America Annual Meeting, Denver, Colorado. Abstracts with Programs. 48:7

Thompson TB (1988) Geology and uranium-thorium mineral deposits of the Bokan Mountain granite complex, southeastern Alaska. Ore Geol Rev 3: 193-210

Ucore (May (2015) Press Release. Ucore Increases Resource at Bokan Dotson-Ridge, accessed at: http://ucore.com/ucore-increases-resource-at-bokan-dotson-ridge.

Warner JD, Barker JC (1989) Columbium and rare earth element-bearing deposits at Bokan Mountain, southeast Alaska. Open-File Report 33-89, U.S. Bureau of Mines, p196

Wilson GC (2010) Mineralogy of rock samples from the Bokan Mountain property, Alaska. TGSL Report 2010-09P for Great Western Minerals Group Ltd, Saskatoon, p33

The Parautochthonous Belt as a source of Grenvillian LREE-rich pegmatitic granite dykes

François Turlin, Anne-Sylvie André-Mayer, Alexandre Crépon, Marie-Camille Caumon *Université de Lorraine, CNRS, CREGU, France*

Olivier Vanderhaeghe
Université de Toulouse, France

Félix Gervais, Sophie Jannin
Ecole Polytechnique de Montréal, Canada

Armin Zeh
Karlsruhe Institute of Technology, Germany

Étienne Deloule
Centre National de la Recherche Scientifique, France

Abdelali Moukhsil
Ministère de l'Énergie et des Ressources naturelles du Québec, Canada

Fabien Solgadi
Ministère de l'Énergie et des Ressources naturelles du Québec, Canada

Abstract. The central Grenville Province (Quebec) hosts numerous monazite- or allanite-rich pegmatitic granite dykes that display evidence for a post-tectonic timing of emplacement and a rooting in deep units. Investigations of zircon grains, through U-Pb-Hf-O isotopes and trace element analyses from three of these dykes provide evidence that all dykes were emplaced during the early-Rigolet phase (at 1000-1005 Ma), and that the magmas were mainly formed by the deep-seated partial melting of crustal units at depth belonging to the Parautochthonous Belt. This is suggested by $\varepsilon Hf_{(t)}$ signatures which are more negative than those of exposed Allochthonous units and spread along a distinct crustal evolution curve.

Zircon grains in monazite-bearing dykes show $\delta^{18}O$ mainly between +6.0 to +9.0‰ (VSMOW), pointing to partial melting of paragneisses of the Gagnon Terrane (Parautochthonous Belt), in agreement with $\varepsilon Hf_{(t)}$ signatures of ca. -6.0±1.3. In contrast to the monazite-bearing dykes zircon grains in allanite-bearing ones show significantly lower $\delta^{18}O$ (mostly +2 to +5‰ VSMOW), and less radiogenic hafnium ($\varepsilon Hf_{(t)}$ = -7 to -9). It is therefore suggested that these dykes formed by remobilization of a metasomatized crustal protolith belonging to the Superior Province.

1 Introduction

The Grenville Province spreads along the south-eastern margin of the Canadian Shield and results from a long history of tectonic accretion during the Mesoproterozoic and a subsequent continent-continent collision, the Grenvillian Orogeny *sensu stricto*, in the late-Mesoproterozoic to early-Neoproterozoic (e.g. Rivers et al. 2012). As such, it is a perfect target to decipher crustal growth and differentiation processes (Dunning and Indares 2010).

This province hosts various magmatic rare-earth elements (REE) occurrences, associated with numerous granitic pegmatites among others, mostly described in the western and eastern parts of the Grenville Province (e.g. Ayres and Černý 1982; Lentz 1996) and recently in the central Grenville (Turlin et al. accepted). Even though a derivation from the late-orogenic partial melting of a deep source was inferred (Turlin et al. accepted), whether the source is the Allochthonous or the underlying Parautochthonous belts is not constrained.

2 Geological context

2.1 Regional geology

The Grenville Province is divided into two main tectonometamorphic domains, namely the Allochthonous Belt (terranes accreted to Laurentia during the Mesoproterozoic), and the Parautochthonous Belt (rocks of the Superior Province and its metasedimentary cover reworked during the Grenvillian Orogeny) (e.g. Rivers 2008), which recorded diachronously the Grenvillian deformation. The Allochthonous Belt (Fig. 1) was metamorphosed during the Ottawan crustal thickening phase (ca. 1090-1020 Ma) with a H*T*-H*P* peak of metamorphism reaching granulite- to eclogite-facies at ca. 1080-1040 Ma (Rivers 2008; Lasalle et al. 2013). The Parautochthonous Belt (Fig. 1) was metamorphosed during the relatively short-lived Rigolet crustal thickening phase (ca. 1005-965 Ma) that reached granulite-facies peak of metamorphism (Jannin et al. this volume, in press; Jordan et al. 2006). The absence of metamorphic ages or ductile deformation in the Allochthonous Belt during that time suggest a passive setting at upper crustal level.

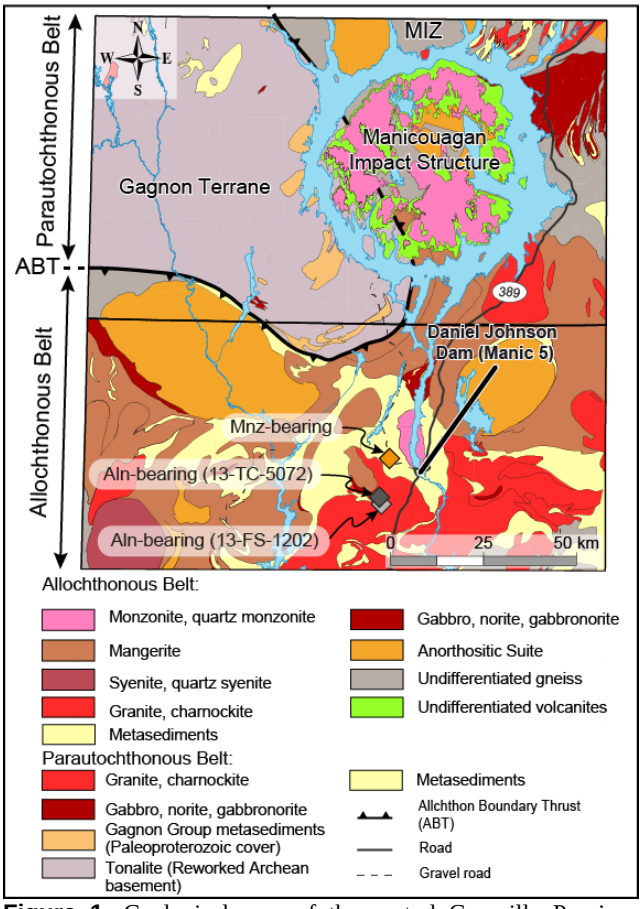


Figure 1. Geological map of the central Grenville Province (Quebec) with the localisation of the investigated LREE-rich pegmatitic granite dykes (modified after Turlin et al. accepted). Abbreviations: ABT = Allochthon Boundary Thrust; MIZ = Manicouagan Imbricate Zone; Aln = allanite; Mnz = monazite.

These features were incorporated into a model of channel flow during the Ottawan phase with the formation of an orogenic plateau between ca. 1080-1050 Ma (Rivers 2008). In this model, the Allochthon Boundary Thrust (ABT) is the basal thrust of the channel.

2.2 LREE-rich pegmatitic granite dykes from the central Grenville

Seven LREE-rich pegmatitic granite dykes have been identified in the Allochthonous Belt of the central Grenville Province. They intrude either paragneisses (Plus-Value Complex, the oldest unit of the region, ca. 1765-1497 Ma, Lasalle et al. 2013), or distinct metaplutonic complexes, the Bardoux (dyke 13-TC-5072) and the Castoréum (dyke 13-FS-1202) Plutonic Suites, which both emplaced in an arc-setting at ca. 1490 Ma and ca. 1390 Ma respectively (Augland et al. 2015). LREE are hosted either in monazite ('Mnz-bearing') or allanite ('Aln-bearing') for dykes hosted in paragneisses or in metaplutonic complexes respectively (Turlin et al. accepted).

All dykes are interpreted to have formed by partial melting of deep-seated crustal units during the early-Rigolet orogenic phase, as is suggested by (i) sharp intrusive contacts, (ii) lack of macroscopic and microscopic evidence for solid state deformation, (iii) lack of evidence for in-situ collect of melt, (iv) peraluminous signature of all investigated samples, and (v) U-Pb monazite ages of ca. 1000-1005 Ma (Turlin et al. accepted).

However, whether the Aln- and Mnz-bearing dykes are derived from the same or from different sources within the Allochthonous and/or Parautochthonous belts remains unclear. To provide new constraints on this problem, we present new data derived from zircon grains in one Mnz-bearing and two Aln-bearing pegmatitic granite dykes; comprising results of U-Pb-Hf isotope and trace elements analyses (LA-ICP-SF-MS, Goethe-University, Frankfurt), and oxygen isotope analyses (SIMS, CRPG, Nancy). These data will provide new information about (i) the timing of dyke intrusion, (ii) their source(s), (iii) their genetic links with the Allochthonous and/or the Parautochthonous Belt, and (iv) implications on the tectonic framework of this part of the Grenville Province at the time of emplacement.

3 Results

3.1 Zircon characteristics and U-Pb dating

Zircon grains from the three samples show rough oscillatory, banded or a sharp hourglass zoning (Aln-bearing dykes only) (Figs. 2d-f). Inherited cores have nowhere been observed, and porous domains have been avoided during analyses, wherever possible. Zircon domains in all samples reveal moderate Th/U ratios between 0.1 and 0.7 and mostly contain low Ca+Fe contents (<250 ppm), indicating that the zircon domains are pristine and crystallized directly from the melt. Only a few domains yield high Ca+Fe contents (up to 7800 ppm), pointing to a post-zircon growth hydrothermal alteration (Fig. 2g). U-Pb isotope analyses of zircon gave Concordia ages of 1004.2±2.1 Ma, 1001.9±3.9 Ma and 1004.2±2.3 Ma (Figs. 2a-c) for the Mnz-bearing, the Aln-bearing 13-TC-5072 and 13-FS-1202, respectively, recording the time of crystallization of the pegmatite dykes during the Rigolet phase.

3.2 Trace elements and Hf-O isotopes

Trace element data of zircon in Mnz- and Aln-bearing pegmatitic granite dykes clearly point to a crustal source for the parent magmas, as is reflected by U and Yb contents and ratios (Fig. 2h). However, significant differences in U/Yb in Mnz- and Aln-bearing dykes might reflect melting of distinct sources, in agreement with distinct Hf-O signatures.

Zircon grains in the Mnz-bearing dyke show negative $\varepsilon Hf_{(t)}$ values of -7.27 to -4.27, and that from Aln-bearing dykes -9.23 to -6.23 (dyke I: 13-TC-5072), and -11.99 to -8.19 (dyke II: 13-FS-1202). These values do not overlap with that reported from surrounding Allochthonous units (compiled from Augland et al. 2015) (Fig. 2i).

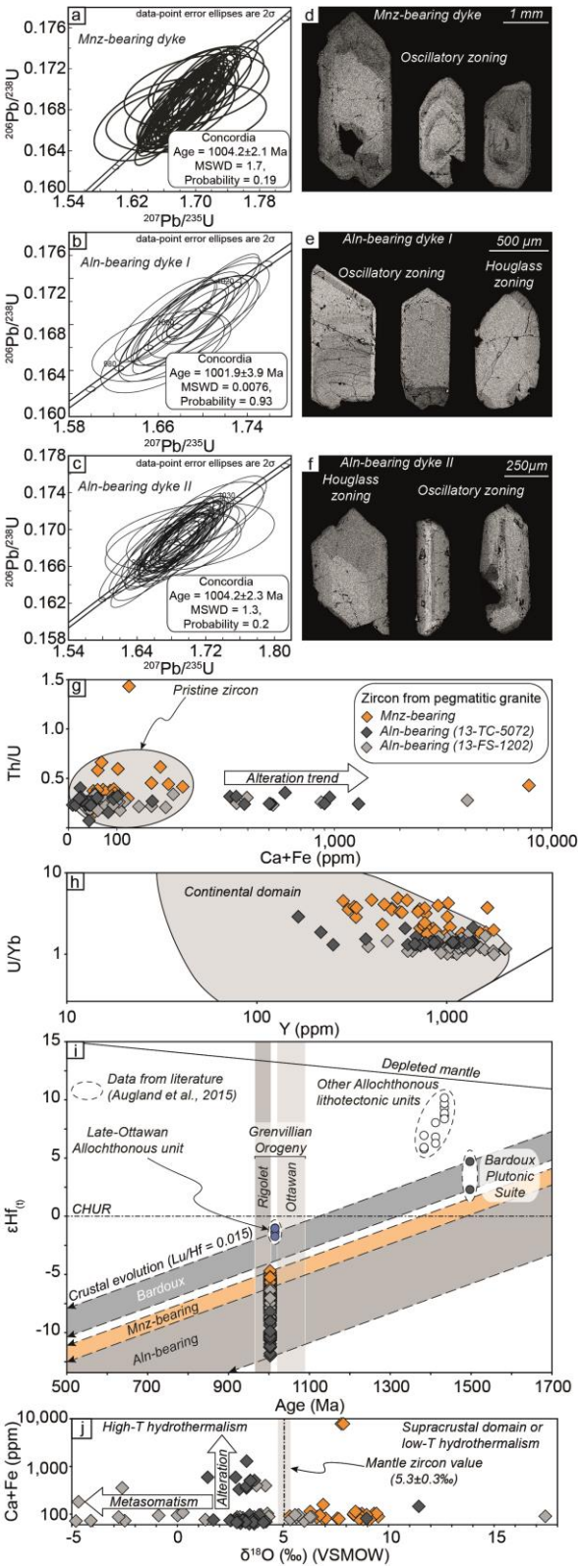


Figure 2. Data obtained on zircon grains from the Mnz- and Aln-bearing pegmatitic granite dykes. a-f: Concordia diagrams of zircon U-Pb analyses and BSE images of representative grains; g-h: Zircon compositions plotted in a Th/U and Ca+Fe (ppm) and U/Yb vs Y (ppm) diagrams; i: $\varepsilon Hf_{(t)}$ vs age (Ma) of the zircon grains compared to the surrounding units compiled from Augland et al. (2015); j: Ca+Fe (ppm) vs $\delta^{18}O$ with reported mantellic value after Valley et al. (2005).

Oxygen isotopes analyses of zircon in Mnz-bearing dyke display $\delta^{18}O$ values ranging from -2.83 to 10.48‰ (VSMOW), but most of them yield values between 6 to 9‰, i.e., higher than mantle composition (i.e., 5.3±0.3‰, Valley et al. 2005). Such values are typical for crustal sediments and S-type granite. In contrast, zircon from Aln-bearing dykes show $\delta^{18}O$ values mostly lower than mantle composition (mostly between 1 and 4 ‰), with a total ranges from -4.84 to 17.43‰ (dyke II: 13-FS-1202), and from 1.44 to 11.43‰ (dyke I: 13-TC-5072) (Fig. 2j). The most extreme $\delta^{18}O$ values in all samples are not correlated to partially altered zircon domains, and therefore do not result from post-zircon growth hydrothermal alteration. Nevertheless, most domains show pristine compositions as is indicated by plotting our data in Ca+Fe vs $\delta^{18}O$ diagram (Fig. 2j). The below mantle $\delta^{18}O$ values for the zircon grains in the two Aln-bearing dykes cannot be explained by melting of Proterozoic (meta)sedimentary rocks and related S-type granite, but rather require an alteration of the source through high-temperature hydrothermalism. Such an interpretation is in agreement with results of (Bindeman and Valley 2002; Valley et al. 2005).

4 Discussion

U-Pb ages of zircon reveal that LREE-rich Mnz- and Aln-bearing pegmatitic granite dykes from the central Grenville Province emplaced nearly contemporaneous at the onset of the Rigolet orogenic phase at 1000-1005 Ma (e.g. Rivers et al. 2012). This timing is consistent with field relationships indicating a post-Ottawan intrusion event, e.g. discordant contact, lack of solid state deformation, no interconnection with leucosomes. These zircon ages are similar to those obtained by Turlin et al. (accepted) on magmatic monazite grains from the Mnz-bearing dyke (ca. 1000 Ma). This, and the lack of any xenocryst zircon cores provide evidence that all investigated zircon grains/domains crystallized within the dykes and are not inherited.

The crustal character of the parental melt of the pegmatitic granite dykes is evidenced by the trace elements analyses that plot in the continental domain (Grimes et al. 2007). However the Mnz- and the Aln-bearing dykes display significantly different $\varepsilon Hf_{(t)}$ and $\delta^{18}O$ signatures, indicating that Mnz- and Aln-bearing dykes were derived from different sources at 1000 Ma (Figs. 2i-j). The strongly negative $\varepsilon Hf_{(t)}$ values of zircon in the Mnz- and Aln-bearing granite dykes exclude their formation by melting of surrounding rocks of the Allochthonous Belt, having all much higher $\varepsilon Hf_{(t)}$ at 1000 Ma. Thus, it appears more likely that all dykes result from partial melting of the underlying Parautochthonous Belt, in agreement with metamorphic studies and field observations made by Jannin et al. (this volume, in press) and Jordan et al. (2006), even though no Hf isotopic data are available from the Parautochthonous Belt to support this suggestion. The results presented in this study are compatible with models involving a downward migration of the syn-Ottawan channel flow developed in the Allochthonous Belt (Rivers 2008) at the initiation of the Rigolet, or of the development of a second

channel in the Gagnon terrane, i.e. structurally below the ABT at ca. 1005 Ma as proposed by Jannin et al. (this volume, in press).

The $\delta^{18}O$ signatures indicate that the Mnz- and Aln-bearing dykes result from the melting of different sources. The oxygen isotope values of the Mnz-bearing dyke (clearly above 5.3‰, Fig. 2j) point to a metasedimentary protolith, most probably paragneisses of the Gagnon Terrane (Fig. 1).

Hf-O isotopes systematics of zircon from the two Aln-bearing dykes are very similar (such as mineral assemblages and whole-rock geochemistry, Turlin et al. accepted) (Figs. 2i-j) suggesting that the dykes were derived from a common source. Their peraluminous character (Turlin et al. accepted), and zircon U-Pb-Hf-trace elements signatures clearly point to derivation from a crustal protolith (Figs. 2h-i). The low $\delta^{18}O$ values of zircon (below 5.3 ‰, Fig. 2j) additionally indicate that the parental melts were derived from an altered protolith which was intensely affected by high-temperature hydrothermalism (Valley et al. 2005). This protolith could have been either crustal rocks or paragneisses of the Parautochthonous Belt, but no data support one of these hypotheses.

5 Conclusion

Mnz-bearing and Aln-bearing LREE-rich pegmatitic granite dykes intruding the Allochthonous Belt in the central Grenville yield U-Pb ages on zircon ranging from 1001 to 1004 Ma. The presence of monazite or allanite is correlated with zircon trace elements, $\varepsilon Hf_{(t)}$ and $\delta^{18}O$ signatures. These signatures preclude an origin of these dykes by partial melting of rocks from the Allochthonous Belt and point to a dominant contribution of the underlying Parautochthonous Belt that was being partially molten at that time. Zircon signature from the Mnz-bearing dyke are consistent with a generation by partial melting of the paragneisses from the Gagnon Terrane, whereas that of the Aln-bearing dykes could suggest a generation by partial melting of a metasomatized crustal protolith.

Acknowledgements

The authors would like to thank the Ministère de l'Énergie et des Ressources naturelles (Québec) for providing technical and financial support for the field work and analyses. This work was founded by the Labex Ressources 21 (supported by the French National Research Agency through the national program "Investissements d'avenir", reference ANR-10-LABX-21–LABEX RESSOURCES 21) and the Region Grand-Est. It benefited from the framework of the DIVEX "Rare earth element" research program.

References

Augland LE, Moukhsil A, Solgadi F, Indares A, McFarlane C (2015) Pinwarian to Grenvillian magmatic evolution in the central Grenville Province: new constraints from ID-TIMS U-Pb ages and coupled Lu-Hf S-MC-ICP-MS data. Can J Earth Sci 52:701–721.

Ayres LD, Černý P (1982) Metallogeny of granitoid rocks in the Canadian Shield. Can Mineral 20:439–536.

Bindeman IN, Valley JW (2002) Oxygen isotope study of the Long Valley magma system, California: isotope thermometry and convection in large silicic magma bodies. Contrib Mineral Petrol 144:185–205.

Dunning G, Indares A (2010) New insights on the 1.7–1.0 Ga crustal evolution of the central Grenville Province from the Manicouagan – Baie Comeau transect. Precambrian Research 180:204–226.

Grimes CB, John BE, Kelemen PB, Mazdab FK, Wooden JL, Cheadle MJ, Hanghøj K, Schwartz, JJ (2007) Trace element chemistry of zircons from oceanic crust: A method for distinguishing detrital zircon provenance. Geology 35:643–646.

Jannin S, Gervais F, Moukhsil A, Crowley JL, Augland LE (this volume). Linking channel-flow processes to REE-rich pegmatites in the Central Grenville Province. *In*: Proceedings of the 14th Biennial Meeting of the SGA 2017, submitted.

Jannin S, Gervais F, Moukhsil A, Crowley JL, Augland LE (in press) Datation U/Pb des déformations inverses et normales dans la Province de Grenville central (Manicouagan, Québec): évidence d'un chenal orogénique dans le Parautochtone, in: Géologie et Ressources Minérales de La Partie Centrale de La Province de Grenville; Abdelali Moukhsil Coordonnateur, Ministère de l'Énergie et Des Ressources Naturelles, Québec.

Jordan SL, Indares A, Dunning G (2006) Partial melting of metapelites in the Gagnon terrane below the high-pressure belt in the Manicouagan area (Grenville Province): pressure–temperature (P–T) and U–Pb age constraints and implications. Can J Earth Sci 43:1309–1329.

Lasalle S, Fisher CM, Indares A, Dunning G (2013) Contrasting types of Grenvillian granulite facies aluminous gneisses: Insights on protoliths and metamorphic events from zircon morphologies and ages. Precambrian Research 228:117–130.

Lentz D (1996) U, Mo, and REE mineralization in late-tectonic granitic pegmatites, southwestern Grenville Province, Canada. Ore Geology Reviews 11:197–227.

Rivers T (2008) Assembly and preservation of lower, mid, and upper orogenic crust in the Grenville Province—Implications for the evolution of large hot long-duration orogens. Precambrian Research 167:237–259.

Rivers T, Culshaw N, Hynes A, Indares A, Jamieson R, Martignole J (2012) The Grenville Orogen - A Post-LITHOPROBE Perspective. In: Tectonic Styles in Canada: The LITHOPROBE Perspective. J.A. Percival, F.A. Cook, and R.M. Clowes, pp 97–236

Turlin F, André-Mayer A-S, Moukhsil A, Vanderhaeghe O, Gervais F, Solgadi F, Groulier PA, Poujol M (accepted) Unusual LREE-rich, peraluminous, monazite- or allanite-bearing pegmatitic granite in the central Grenville Province, Québec. Ore Geol. Rev.

Valley JW, Lackey JS, Cavosie AJ, Clechenko CC, Spicuzza MJ, Basei MAS, Bindeman IN, Ferreira VP, Sial AN, King EM, Peck WH, Sinha AK, Wei CS (2005) 4.4 billion years of crustal maturation: oxygen isotope ratios of magmatic zircon. Contrib Mineral Petrol 150:561–580.

Genesis of the Bianjiadayuan Ag-Pb-Zn deposit, NE China: Mineralogical, textural, sulfur and lead isotope studies

Degao Zhai, Jiajun Liu
China University of Geosciences, Beijing, China

Nigel J. Cook
University of Adelaide, Australia

Abstract. The Bianjiadayuan Pb-Zn-Ag deposit (4.81 Mt @157.4 g/t Ag and 3.94% Pb+Zn) is located in the Great Hinggan Range Pb-Zn-Ag-Cu-Mo-Sn-Fe polymetallic metallogenic belt, NE China. Vein-type Pb-Zn-Ag ore bodies are characterized by silver-rich ores with Ag grades up to 3,000 g/t. Freibergite is identified as the dominant and most important Ag-mineral in the deposit. Detailed ore mineralogical and textural investigations of freibergite reveal evidence of chemical heterogeneity down to the microscale. Late-stage silver-rich sulfosalts are largely derived from a series of retrograde and solid-state reactions that redistribute Ag via decomposition and exsolution during cooling. We document post-crystallization decomposition of freibergite, rarely described in the literature before now, illustrating that an acknowledgment of post-mineralization processes is essential for a coherent understanding of ore genesis. Sulfur and lead isotope compositions of sulfides indicate the origin of sulfur from magma, whereas lead and other metals were possibly derived from both host rock and magma. Fluid cooling, coupled with decreases in pH, fO_2 and fS_2, are the factors inferred to have led to a decrease of silver solubility in the ore fluid, and successively promote extensive Ag deposition.

1 Regional geology and mineralization

The Bianjidayuan Ag-Pb-Zn deposit occurs in the Great Hinggan Range (GHR) Metallogenic Belt, which lies in the easternmost part of the Central Asian Orogenic Belt. The region is characterized by widespread Mesozoic volcanic and intrusive rocks. The regional Cretaceous granitoids show an eastwards-younging trend, which indicates their emplacement in an extensional setting (Wu et al. 2003). It is proposed that early Paleo-Pacific subduction in the Jurassic caused subsequent lithospheric delamination or rollback and extension of the back-arc area, successively enabling the emplacement of large volumes of Cretaceous granitoids (Zhang et al. 2010). Compared with other areas in the CAOB, NE China was significantly affected by the Paleo-Pacific subduction.

The Great Hinggan Range hosts porphyry, skarn, epithermal and hydrothermal vein-type ore deposits, which have been related to Mesozoic magmatism (Chen et al. 2007; Zhai et al. 2013, 2014). Regionally, mineralization and Mesozoic granites demonstrate a close spatial distribution. Numerous ore deposits, including porphyry Cu-Mo, skarn Fe-Sn and polymetallic veins, occur in the southern segment of the GHR Metallogenic Belt (Zhai et al. 2014). With the discovery of numerous vein-type Ag-Pb-Zn ore deposits in this district, the southern segment of the GHR has, in recent years, arguably become an important vein-type Ag-Pb-Zn metallogenic belt in northern China.

2 Ore deposit geology

The strata exposed in the ore district belong mainly to the Permian Zhesi Formation, comprising metasedimentary rocks including slates and siltstones that dip to the NNW at 50–55°, and Quaternary paleoplacers (Fig. 1). Many of the Ag-Pb-Zn veins are hosted by Permian slate. The dominant igneous rocks exposed in the ore district are gabbro, quartz porphyry, and numerous NE- and NW-trending diorite and granite dykes (Fig. 1).

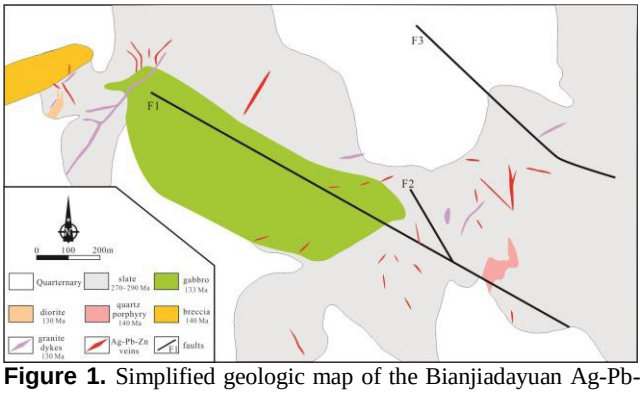


Figure 1. Simplified geologic map of the Bianjiadayuan Ag-Pb-Zn deposit

Gabbro is the main igneous rock, accounting for >20% of the surface outcrop across the mine area. Quartz porphyry is present below surface mainly in the western part of the ore district, with a small occurrence in the southeast (Fig. 1). Contact relationships between gabbro and quartz porphyry are not clear. Relationships between Ag-Pb-Zn mineralization and quartz porphyry are also poorly constrained at the present time due to the absence of sufficient spatial contacts. However, recent exploration identified Cu-Mo mineralization within the quartz porphyry, and Cu-Sn mineralization in breccia above the porphyry in the western part of the main Ag-Pb-Zn district (Fig. 1). Numerous NE-SW and rare N-S-trending, dioritic to granitic sills and dykes intrude Permian slate and the main gabbro body (Fig. 1).

The Bianjiadayuan Ag-Pb-Zn vein system is primarily

hosted in Permian slate. More than 20 major veins, numerous stockworks, as well as minor disseminations have been identified during mine-scale exploration. The Ag-Pb-Zn ores are mainly hosted by NW and NE trending open-space filling veins with a length between 50 and ~200 m, and extend vertically at least as much as 300 m. Numerous stockworks, veinlets and disseminations occur on the margins of the major veins in altered slate or gabbro. Distinct episodes of alteration are recognized: an early episode of silicification, two intermediate episodes (propylitic and phyllic), and a late argillic episode. There is no apparent spatial zonation of alteration types as, in most places, alteration assemblages are superimposed upon one another.

3 Sulfur and lead sources

The $\delta^{34}S$ compositions of sulfides from Ag-Pb-Zn veins at Bianjiadayuan display a narrow range (-0.7 to +2.7‰), with only minor variation with respect to either vertical location of the veins, or from grain to grain within a specific sample (Fig. 2). This indicates a single, homogeneous sulfur source, most likely from magma. The S isotope data obtained for sulfides in the Bianjiadayuan deposit are very similar to published sulfur isotopic data for sulfides in nearby hydrothermal ore deposits (Zhai et al. 2014).

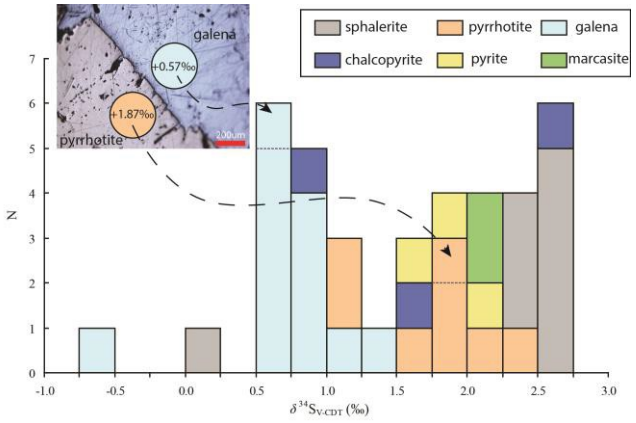


Figure 2. Histogram of sulfur isotope compositions of sulfides with a typical textual equilibrium sulfide pair

Based on $^{206}Pb/^{204}Pb$ vs. $^{208}Pb/^{204}Pb$ binary plots, the Pb isotope ratios for the Bianjiadayuan ores are obviously distinct from sulfides from other magmatic-hydrothermal deposits (Fig. 3), suggesting a distinct metal source for the Bianjidayuan deposit compared to other ore deposits in the district. Lead isotope ratios for the Bianjiadayuan ores differ not only from those of the Mesozoic and Hercynian granites but also Cretaceous andesites. Instead, they show similarities to values for Cretaceous gabbros and basalts, and to a lesser extent, Permian strata such as the slate hosting the veins (Fig. 3). This information indicates that the metal contribution within the deposit may be largely derived, inherited, or leached from basic rocks, and subordinate sedimentary strata.

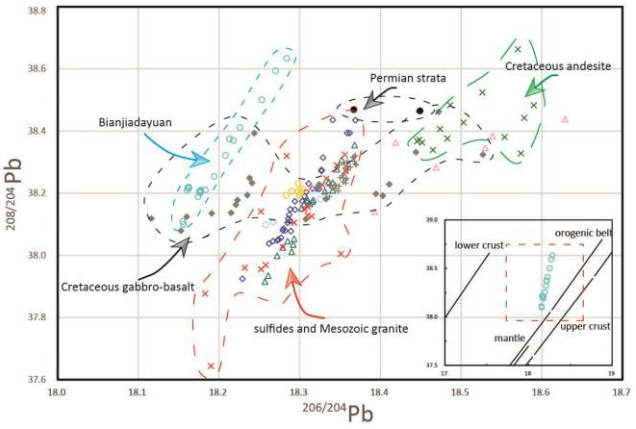


Figure 3. Lead isotope plots of the Bianjiadayuan sulfides compared to local magmatic-hydrothermal deposits and different rock units

4 Ore mineralogical and textural implications

The obtained compositions of fahlore, the most important and widespread Ag-host in the Bianjiadayuan ores, reveal that compositions equate to both argentian tetrahedrite and freibergite, as defined by Riley (1974) on the basis of Ag content (~20 wt% Ag limit between the two phases). Freibergite is the more abundant in the Bianjiadayuan ores but both high- and low-Ag components can be identified in different grains, and, notably, also within single mineral grains. The existence of compositionally heterogeneous domains in natural freibergite has been rarely reported. Barroso et al. (2003) considered that tetrahedrite grains compositionally zoned with respect to Ag related to a late influx of Ag-rich fluids coeval with the late stages of freibergite growth. Sack et al. (2003), on the other hand, reported that freibergite with clear Ag heterogeneity was originally a single grain that exsolved into regions of Ag-rich and Ag-poor compositions.

In appearance, the Bianjiadayuan freibergites (Fig. 4) display similarities with those reported by Sack et al. (2003) and are distinct from those characterized by Barroso et al. (2003). We therefore speculate that the observed freibergites are attributable to a series of retrograde reactions that resulted in diverse decomposition and exsolution of primarily phases during cooling. Additionally, freibergite in the assemblage galena + boulangerite + pyrrhotite shows apparent Cu ↔ Ag and Zn — Fe variations, both among different minerals, and individual mineral grains, respectively, also suggesting the possibility of solid-state reactions during cooling.

In summary, the observed host phases for Ag are mostly late stage and may represent products of retrograde, solid-state reactions involving sulfosalt phases that redistributed Ag via decomposition and exsolution, resulting in ore textures that display compositional heterogeneity down to the sub-micron scale. Despite the critical importance of mineralogy for not only a

sustainable genetic model for the deposit, as well as selection of processing technology for extraction of silver, mineralogical aspects of silver distribution are often poorly characterized.

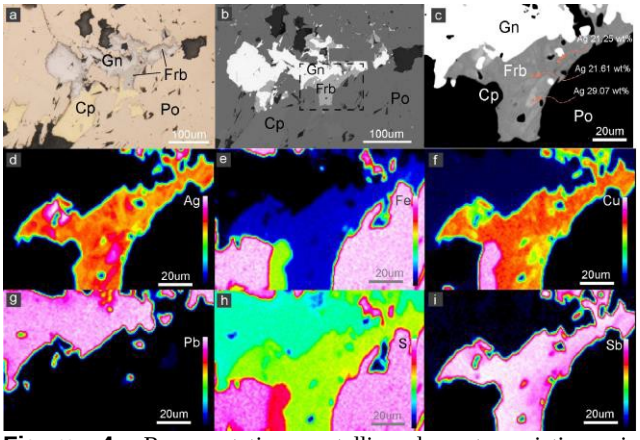


Figure 4. Representative metallic element variations in heterogeneous freibergite from the Bianjiadayuan deposit

Freibergite decomposition, as described here, has rarely been reported previously, and carries significant implications for any genetic model for the deposit. Although the key factors critical for initial ore deposition have been evaluated, post-formational redistribution processes are also clearly important, and have impacted on the ore. Evidence of analogous processes may exist, albeit undocumented, in other silver deposits. Our findings therefore indicate that acknowledgment of potential post-mineralization processes is essential for coherent genetic and exploration models in a wide variety of settings.

5 Mechanisms of Ag-rich ore formation

Silver, like gold, occurs dominantly as Ag^{+} in hydrothermal fluids (Williams-Jones and Migdisov 2014), and speciation for silver transport in hydrothermal fluids is dominated by bisulfide and chloride species (Stefansson and Seward 2003). Reliable thermodynamic data are available for both bisulfide and chloride species, based on a number of experimental inverstigations (e.g., Seward 1976; Gammons and Williams-Jones 1995; Stefansson and Seward 2003). These experimental studies demonstrate that, at lower temperatures (<200 °C), silver bisulfide species (AgHS°) predominate at near-neutral conditions; whereas silver chloride species ($AgCl_2^-$) are dominant under mildly acidic to acidic conditions. In contrast, at relatively high temperatures (>400 °C), silver is transported dominantly as a chloride complex in most hydrothermal fluids; whereas silver bisulfide species are only stable at mildly basic to basic conditions.

To determine the transport and deposition of silver in hydrothermal fluids responsible for formation of the Bianjiadayuan ores, we have thermodynamically modeled silver speciation at the likely conditions of silver ore deposition. Physicochemical conditions during precipitation of ore and alteration minerals were estimated from stability relationships among sulfides and silicates using the SUPCRT92 database (Johnson et al. 1992).

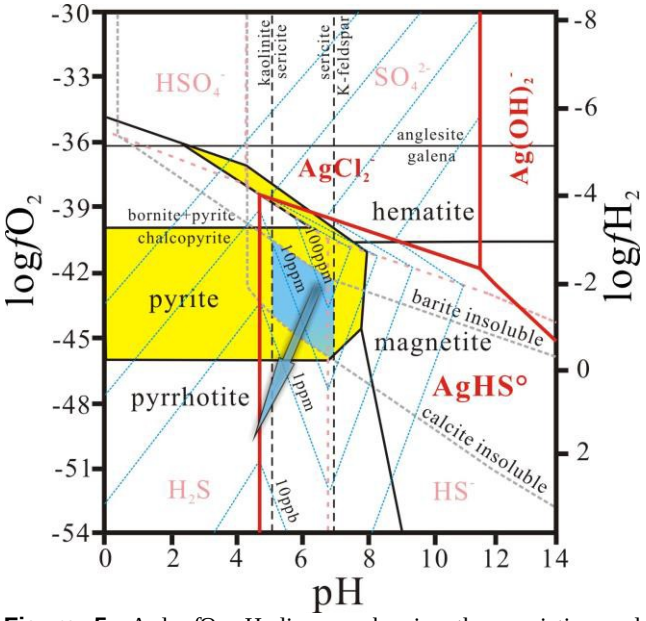


Figure 5. A logfO_2-pH diagram showing the speciation and solubility of silver in an aqueous fluid containing 1 *m* NaCl and 0.001 *m* ΣS at 200 ºC and 500 bars

The constrained pH range for stage III mineral deposition varies from 5.1 to 7.0, and the logfO_2 values range from -46.1 to -40.7 (Fig. 5). The above conditions support an interpretation in which the silver bisulfide species (AgHS°) was the sole species responsible for transport. As the ore fluid evolved to lower temperature, the hydrothermal system transformed to both decreasing pH and log fO_2 conditions (Fig. 5), which significantly reduced AgHS° solubility in the fluid, favoring silver precipitation. Such physicochemical evolution is consistent with the variation in mineral assemblage from stages III to IV, i.e., sericite followed by kaolinite, chalcopyrite prior to pyrrhotite, and deposition of late-stage calcite. We thus conclude that decrease in temperature, pH and logfO_2 were important triggers for silver ore deposition.

6 Genetic type and exploration implications

The classification of Ag-Pb-Zn vein type mineralization is controversial and a topic of considerable debate. A recent review (Kissin and Mango 2014) considers that these deposits can be divided into the following subtypes: Ag-Pb-Zn veins, five-element (Ag–Ni–Co–As–Bi) veins, epithermal deposits (low/high sulfidation), tin mineralization and skarn-associated silver-bearing veins. In the case of the Bianjiadayuan deposit, mineralization occurs as epigenetic veins generally formed by open-space filling. The mineralized veins are mainly hosted by slate, but subordinately also by gabbro, with an alteration assemblage of quartz, sericite, epidote and chlorite. Ore

minerals comprise galena, sphalerite, pyrite, chalcopyrite, pyrrhotite, and a suite of sulfosalt minerals, with in particular freibergite as the major silver carrier. The above summarized features are very like both 'epithermal ore deposits' and 'Ag-Pb-Zn veins', as classified by Kissin and Mango (2014).

Geochemical studies demonstrate that epithermal deposits mostly precipitate from hydrothermal fluids derived from granitic melts with variable modifications due to interaction with wall-rock (Deyell et al. 2005). This consideration is consistent with the sulfur and lead isotope results in this study. In the mine district considered here, it is logical to relate the Ag-Pb-Zn veins to the adjacent porphyry Cu-Mo system, an interpretation consistent with the sulfur source considered above. Abundant previous studies have showed a close genetic relationship between porphyry Cu-Mo and hydrothermal vein Ag-Pb-Zn systems in other ore districts (Sillitoe 2010; Catchpole et al. 2015). Should this hypothesis be correct in Bianjiadayuan, future ore exploration in the district should target similar Ag-Pb-Zn ore bodies in the western part of the distinct, since most of the current Ag mineralization is mined in the eastern part.

Conclusions

(1) Sulfur and lead isotopes indicate the origin of S from a felsic magma; ore metals originate from magma and host rock;

(2) Decreases in temperature, pH and log fO_2 of the ore- forming fluid were likely the key triggers for silver ore deposition;

(3) Mineralogical and textural evidence indicate that freibergite is the most important silver host, and largely derives from decomposition and exsolution processes associated with retrograde and solid-state reactions during cooling;

(4) Compositional heterogeneity is recognized in freibergite down to the sub-micron scale, a phenomenon rarely reported in the literature, demonstrating that an understanding of post-ore processes is critical for establishing coherent genetic and exploration models in diverse geological settings;

(5) The Bianjiadayuan Ag-Pb-Zn deposit is interpreted as an intermediate- to low-sulfidation epithermal deposit, which is a useful concept for exploration in the district.

Acknowledgements

We are very grateful to Anthony E. Williams-Jones for his long time support and helpful suggestions on numerous aspects. We thank Ed Ripley and Ben Underwood (both from IU) for the sulfur isotope analyses, Chusi Li (IU) and Zhenyu Chen (CAGS) for the EPMA analyses, and Dongjie Tang (CUGB) for the FESEM analyses. This research was supported financially by the National Natural Science Foundation of China (Grant 41672068), the Fundamental Research Funds for the Central Universities (Grant 2652015045), the Open Research Funds for GPMR (Grant GPMR201513) and the Chinese "111" project (Grant B07011).

References

Barroso M, Figueiras J, Alves LC, Mateus A (2003) Chemical nature of Ag-bearing tetrahedrites from the Enfermarias prospect (Moura, Portugal) revealed by EPMA and Micro-PIXE analysis. Abstract, http://webpages.fc.ul.pt, 50-52

Catchpole H, Kouzmanov K, Bendezú A, Ovtcharova M, Spikings R, Stein H, Fontboté L (2015) Timing of porphyry (Cu-Mo) and base metal (Zn-Pb-Ag-Cu) mineralisation in a magmatic-hydrothermal system—Morococha district, Peru. Miner Deposita 50(8): 895-922

Chen YJ, Chen HY, Zaw K, Pirajno F, Zhang ZJ (2007) Geodynamic settings and tectonic model of skarn gold deposits in China: an overview. Ore Geol Rev 31: 139–169

Deyell CL, Leonardson R, Rye RO, Thompson JFH, Bissig T, Cooke DR (2005) Alunite in the Pascua-Lama high-sulfidation deposit: Constraints on alteration and ore deposition using stable isotope geochemistry. Econ Geol 100: 131–148

Gammons CH, Williams-Jones AE (1995) Hydrothermal geochemistry of electrum; thermodynamic constraints. Econ Geol 90(2): 420-432

Johnson JW, Oelkers EH, Helgeson HC (1992) SUPCRT92: A software package for calculating the standard molal thermodynamic properties of minerals, gases, aqueous species and reactions from 1 to 5000 bars and 0° to 1000°C. Comput Geosci 18: 899-947

Kissin SA, Mango H (2014) Silver Vein Deposits. Treatise on Geochemistry, Second Edition. Elsevier, Oxford, 425-432

Riley JF (1974) The tetrahedrite-freibergite series, with reference to the Mount Isa Pb-Zn-Ag orebody. Miner Deposita 9(2): 117-124

Sack RO, Lynch JVG, Foit F (2003) Fahlore as a petrogenetic indicator: Keno Hill Ag-Pb-Zn District, Yukon, Canada. Miner Mag 67(5): 1023-1038

Seward TM (1976) The stability of chloride complexes of silver in hydrothermal solutions up to 350 °C. Geochim Cosmochim Acta 40(11): 1329-1341

Sillitoe RH (2010) Porphyry copper systems. Econ Geol 105: 3-41

Stefansson A, Seward TM (2003) Experimental determination of the stability and stoichiometry of sulphide complexes of silver(I) in hydrothermal solutions to 400 °C at 500 bar. Geochim Cosmochim Acta 67: 1395−1413

Williams-Jones AE, Migdisov AA (2014) Experimental constraints on the transport and deposition of metals in ore-forming hydrothermal systems. Society of Economic Geologists 18: 77-96

Wu FY, Jahn BM, Wilde SA, Lo CH, Yui TF, Lin Q, Ge WC, Sun DY (2003) Highly fractionated I-type granites in NE China (I): geochronology and petrogenesis. Lithos 66, 241–273

Zhai D, Liu J, Zhang H, Yao M, Wang J, Yang Y (2014) S-Pb isotopic geochemistry, U-Pb and Re-Os geochronology of the Huanggangliang Fe-Sn deposit, Inner Mongolia, NE China. Ore Geol Rev 59: 109-122

Zhai DG, Liu JJ, Wang JP, Yao MJ, Wu SH, Fu C, Liu ZJ, Wang SG, Li YX (2013) Fluid evolution of the Jiawula Ag-Pb-Zn deposit, Inner Mongolia: Mineralogical, fluid inclusion, and stable isotopic evidence. Int Geol Rev 55: 204-224

Zhang JH, Gao S, Ge WC, Wu FY, Yang JH, Wilde SA, Li M (2010) Geochronology of the Mesozoic volcanic rocks in the Great Xing'an Range, northeastern China: implications for subduction-induced delamination. Chem Geol 276: 144–165

Reduction of arsenite and sulfate by elemental copper, nickel and cobalt: implications to the formation of arsenide minerals in low temperature hydrothermal deposits

Nicholas C. Allin and Christopher H. Gammons
Deptartment of Geological Engineering, Montana Tech, U.S.A.

Abstract. Experiments are being conducted to determine the relative rates of reduction of aqueous sulfate and aqueous arsenite ($As(OH)_{3,aq}$), using foils of copper, nickel, or cobalt as the reductant, at temperatures of 100 to 300ºC. At the highest temperature, sulfate was partly reduced to sulphide with precipitation of Cu_2S (chalcocite) on copper foil and NiS_2 (vaesite) + $NiSO_4 \cdot xH_2O$ on nickel foil. In the 300ºC arsenite reduction experiments, Cu_3As (domeykite), Ni_5As_2, and CoAs (langisite) formed. Whereas reduction of sulfate has not been observed below 250ºC, reduction of arsenite by copper to form domeykite is rapid to at least 150ºC. The implication is that a low temperature fluid carrying both aqueous sulfate and arsenite will quickly precipitate metal-arsenide minerals at a reducing interface, whereas sulfate reduction is much slower, especially at temperatures below 250ºC. This helps to explain the abundance of metal-arsenide minerals and relative lack of metal-sulfide minerals in certain ore deposit types, including unconformity-type U-Ni and "5-element suite" vein deposits.

1 Introduction: Scope of work

The goal of this study is to investigate the rates of reduction of sulfate and arsenite ($As(OH)_{3,aq}$) in the temperature range 100 to 300ºC. Thermochemical sulfate reduction (TSR) has been extensively studied in the field and in the laboratory, due to its importance in the petroleum industry. The consensus is that TSR is potentially important at geologic time scales at temperatures as low as 150ºC, which overlaps with the temperatures of deep natural gas reservoirs (Krouse et al. 1988; Goldhaber and Orr 1995). However, in laboratory experiments, TSR does not appear to take place at temperatures below 250ºC at time scales of days to weeks (Shanks et al. 1981; Goldstein and Aizenshtat 1994).

In contrast to TSR, thermochemical arsenate or arsenite reduction (TAR) has not been addressed in the scientific literature, other than a preliminary study by Blair (1997). Although the +5 arsenate ion (AsO_4^{3-}) is stable in oxidized environments at ambient temperature, the dominant aqueous form of arsenic in hydrothermal fluids is +3 arsenite (Heinrich and Eadington 1986). Unlike the reduction of sulfate to sulphide, which involves a transfer of 8 electrons, reduction of arsenite to arsenide (As^{3-}) is a 6-electron step. Also, whereas the sulfate molecule has a very stable, rigid structure with S=O double bonds, dissolved arsenite ($As(OH)_3$) is comprised of relatively weak As-OH bonds. Therefore, theoretically, one would predict that TAR should proceed at a more rapid rate than TSR under equivalent conditions.

In the current study, the native elements Cu, Ni, and Co are being used in a set of parallel hydrothermal experiments to test the relative rates of TAR and TSR. The redox couples Cu/Cu^{+}, Ni/Ni^{2+} and Co/Co^{2+} are arranged in order of increasing strength in terms of their reductive capacity. Another reason we chose Cu, Ni, and Co is that these elements occur as both sulphide and arsenide minerals in nature. Although preliminary, the early results reported below have interesting applications to the formation of hydrothermal arsenide minerals in nature.

2 Experimental methods

The experiments were performed using sealed silica (quartz glass) tubes, following the methods of Gammons et al. (1997). The tubes were fashioned with a constriction placed two thirds up from the sealed base. Pieces of pure Cu, Ni, or Co foil were perched above the constriction, with 3 to 4 mL of solution below. The initial solution composition was either 0.1N H_2SO_4 (for the sulfate experiments) or 1000 ppm $As(OH)_3$ + 2% HCl (for the arsenite experiments). The tubes were sealed under partial vacuum and placed within a stainless steel pressure vessel containing about 30 mL of water to equalize pressure across the tube walls at high temperature. The vessels were placed upside-down in a forced-air convection oven to allow interaction between solution and foil at the temperature of the experiment. After 7 to 9 days, the vessels were removed from the oven, inverted to separate the solids from the solutions, and placed in cold water. Within 5 minutes, the vessels were opened and the tubes photographed to document changes in mineralogy or color of the solutions.

Experiments have been completed for Cu + sulfate and Cu + arsenite at 300˚, 250˚, 200˚ and 150˚C. Also, experiments using Ni + sulfate, Ni + arsenite, Co + sulfate, and Co + arsenite were completed at 300˚C. Most of the run products from the two cobalt experiments were lost, due to breaking of the tubes during the experiment (see below).

After rinsing and drying at 40˚C, the solid run products from the experiments were examined by microRaman spectroscopy and scanning electron microscopy (SEM-EDS). All quenched solutions have been saved, and will eventually be analysed for concentrations of ligands (sulfate, arsenite) and metals (Cu, Ni, Co).

3 Results

3.1 Sulfate reduction by copper foil

At temperatures ≥250°C, copper foils reacted with 0.1M H_2SO_4 to form chalcocite:

$$8Cu(s) + HSO_4^- + 7H^+ \leftrightarrow Cu_2S(s) + 6Cu^+ + 4H_2O \quad (1)$$

The morphology of the large (up to 0.5 mm long), needle-like crystals (Fig. 1) suggests that the chalcocite grew during the experiment, and not after quenching. No chalcocite was observed on the surface of copper foils reacted with H_2SO_4 at 200˚C or 150˚C.

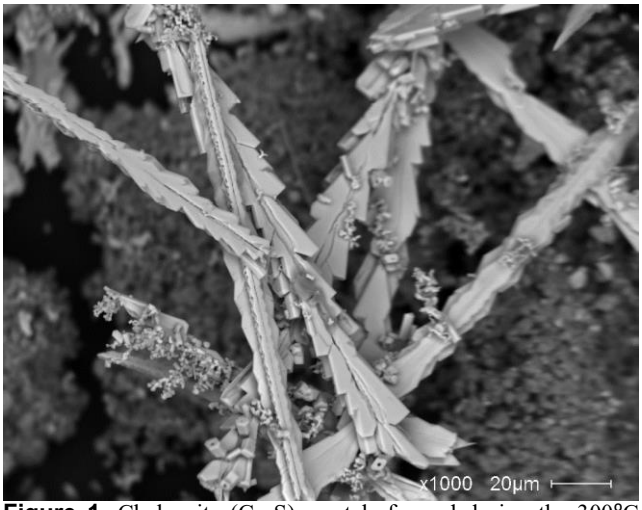


Figure 1. Chalcocite (Cu_2S) crystals formed during the 300°C sulfate reduction experiment. Background is corroded copper foil. Tiny grains are elemental copper formed during quench.

On quench, the cuprous ions (Cu^+) released via reaction (1) disproportionated to cupric ion (Cu^{2+}) and elemental copper:

$$2Cu^+ \rightarrow Cu^{2+} + Cu(s) \quad (2)$$

You can see some of the fine-grained elemental copper in Figure 1. Reaction (2) is analogous to the gold(I) disproportionation reaction studied by Gammons et al. (1997):

$$3AuCl_2^- \rightarrow AuCl_4^- + 2Au(s) + 2Cl^- \quad (3)$$

3.2 Arsenite reduction by copper foil

In all experiments in which copper was reacted with $As(OH)_3$, the surface of the copper foil was completely coated with Cu-arsenide phases. The foil reacted at 300˚C was a mix of domeykite (Cu_3As) and lesser amounts of paxite ($CuAs_2$) (Fig. 2). This experiment also had a large amount of nantokite (CuCl) in the bottom of the tube after quench. The foil reacted at 150˚C was converted to a mix of domeykite and nantokite (Fig. 3). The formation of domeykite can be written:

$$6Cu(s) + As(OH)_3 + 3H^+ \rightarrow Cu_3As + 3Cu^+ + 3H_2O \quad (4)$$

The increase in dissolved Cu from the corrosion of the foil led to precipitation of nantokite:

$$Cu^+ + Cl^- \rightarrow CuCl(s) \quad (5)$$

This phase was initially white, but turned blue upon exposure to light.

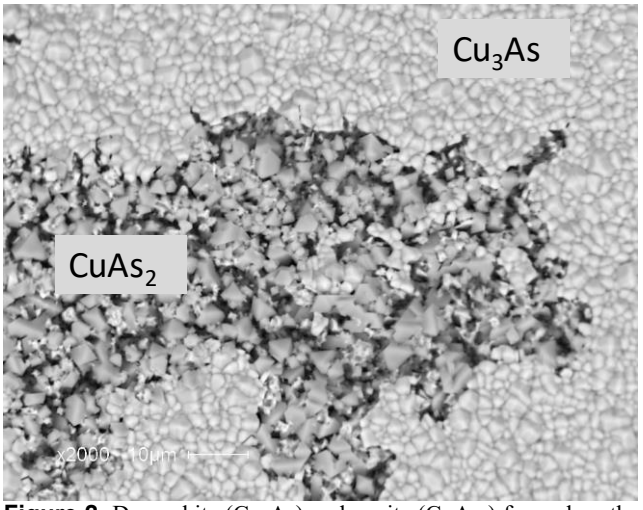


Figure 2. Domeykite (Cu_3As) and paxite ($CuAs_2$) formed on the surface of the copper foil during the 300°C arsenite reduction experiment.

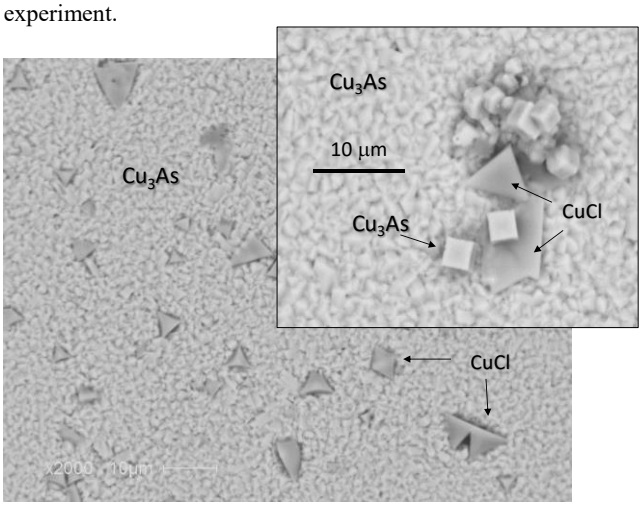


Figure 3. Domeykite (Cu_3As) and nantokite (CuCl) completely coating the surface of the copper foil after the 150˚C experiment.

3.3 Sulfate reduction by nickel foil

An experiment in which Ni foil was reacted with dilute H_2SO_4 at 300˚C produced a small amount of vaesite (NiS_2) and a large amount of a bright green Ni-sulfate, possibly retgersite ($NiSO_4 \cdot 6H_2O$). The reaction to form vaesite can be written:

$$7Ni(s) + 2HSO_4^- + 12H^+ \rightarrow 2NiS_2(s) + 5Ni^{2+} + 8H_2O \quad (6)$$

The vaesite has a cubic morphology, often twinned (Fig. 4). As shown by reaction (6), each mole of sulfate reduced by Ni foil produced one mole of vaesite and 2.5 moles of aqueous Ni^{2+}. The extra Ni^{2+} led to precipitation of a large amount of $NiSO_4 \cdot 6H_2O$ during the experiment.

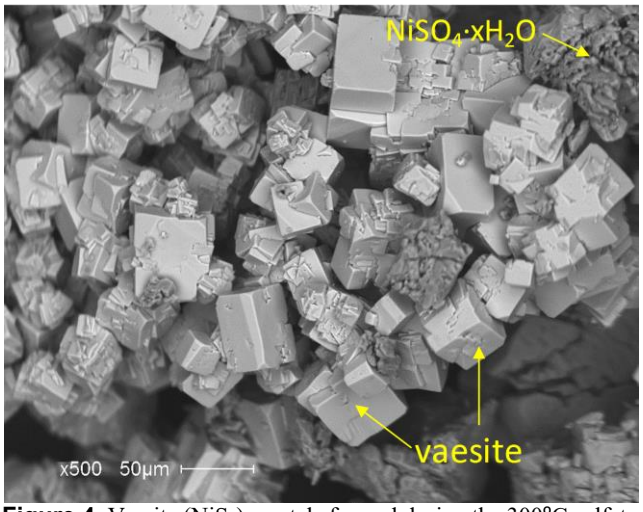


Figure 4. Vaesite (NiS_2) crystals formed during the 300°C sulfate reduction experiment on nickel foil. There is also some hydrous Ni-sulfate (amorphous with darker gray scale).

3.4 Arsenite reduction by nickel foil

When Ni was reacted with dilute $As(OH)_3$ at 300˚C, an unnamed Ni-As phase formed on the surface of the nickel foil (Fig. 5). The new phase has a stoichiometry that is close to Ni_5As_2, an arsenide that appears on the As-Ni phase diagram of Singleton and Nash (1987) but is not recognized as a mineral. Tredoux et al. (2016) reported $Ni_5(As,Sb)_2$ in their investigation of the Bon Accord deposit, S Africa. It is possible that the phase made in our experiment is similar to that found by Tredoux et al. (2016), but without the Sb content. The reaction of interest can be written as follows:

$$8Ni + 2As(OH)_3 + 6H^+ \rightarrow Ni_5As_2 + 3Ni^{2+} + 6H_2O \quad (7)$$

No other Ni-phases were observed to form in this experiment, and the starting Ni foil, where exposed, showed no evidence of oxidation to NiO.

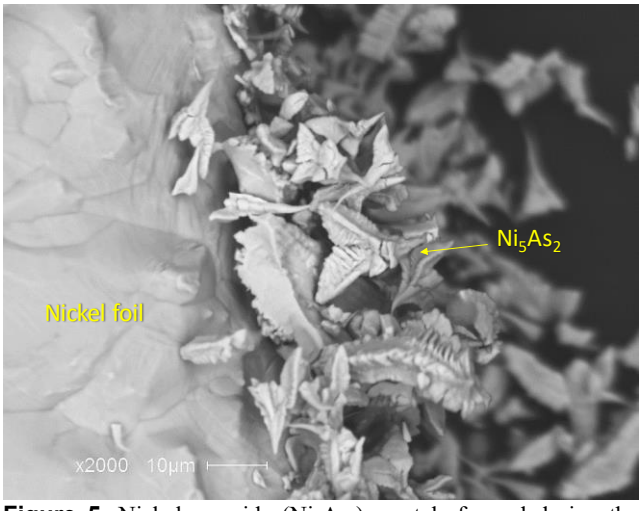


Figure 5. Nickel arsenide (Ni_5As_2) crystals formed during the 300°C arsenite reduction experiment on nickel foil (left). Some of the smaller Ni_5As_2 crystals may have formed during quench.

3.5 Experiments with cobalt foil

Experiments in which cobalt foils were reacted with dilute H_2SO_4 or $As(OH)_3$ at 300˚C generated a gas that caused the H_2SO_4 tube to crack during the run, and the $As(OH)_3$ tube to explode unexpectedly after quench when it was scored with a glass cutter. The gas was probably $H_2(g)$, formed by oxidation of elemental cobalt:

$$Co(s) + 2H^+ \rightarrow Co^{2+} + H_2(g) \quad (8)$$

A small amount of reacted foil was recovered from the broken $As(OH)_3$ tube and was shown to be completely transformed to a mixture of Co-chloride + CoAs (langisite). The formation of langisite can be written:

$$5Co(s) + 2As(OH)_3 + 6H^+ \rightarrow 2CoAs + 3Co^{2+} + 6H_2O \quad (9)$$

There was no indication that any elemental cobalt survived the experiment. The quenched solution had a deep pink color prior to exploding, consistent with a high concentration of Co^{2+}.

3.6 Future experiments

We will repeat similar Co and Ni metal foil experiments to see if sulfate and/or arsenite reduction persists to lower temperature. We hypothesize that sulfate reduction will not take place below about 250˚C, as was the case for our copper foil experiment (section 3.1), and as was found in previous laboratory studies of thermochemical sulfate reduction (Goldstein and Aizenshtat 1994). In contrast, we expect that arsenite reduction will occur at a rapid rate at lower temperature, possibly as low as 100˚C.

4 Implications to the formation of metal arsenide minerals in nature

Our experiments show that thermochemical reduction of sulfate and arsenite occurs rapidly at 300˚C using native metal substrates (Cu, Ni, Co foils). At lower temperature (150˚C), arsenite is easily reduced in the presence of copper to form domeykite (Cu_3As), but no comparable reduction of sulfate to Cu-sulfide minerals occurs. We conclude that a relatively low temperature, oxidized brine carrying copper along with both sulfate and arsenite will be much more likely to precipitate Cu-arsenide minerals (domeykite, paxite) as opposed to Cu-sulfide minerals at a reducing front. This is consistent with the occurrence of domeykite in the native copper deposits of the Keeweenawan Peninsula, Michigan (Koenig 1900; Moore 1962), and red-bed copper deposits of the Siwalik sandstones of Hamirpur district, India (Singh et al. 2002) and the Corocoro district, Bolivia (Avila-Salinas 1990), among others.

Other ore deposit types in which metal-arsenide minerals are abundant and sulfide minerals are scarce include unconformity U-Ni deposits, and the “five element suite” polymetallic vein deposits (Kissin 1992). In the Athabaska Basin of northern Saskatchewan, home of the world’s

richest uranium deposits, nickel-arsenide minerals are locally of sufficient concentration to make Ni an important by-product of uranium mining (Dahlkamp 1978). Like red-bed copper deposits, most models of formation of unconformity-type U deposits involve transport of metals by an oxidized fluid and precipitation near a reduction interface.

In the five element (Co-Ni-As-Ag-Bi) suite deposits, paragenetically early native silver and bismuth are surrounded by complex rosettes of Co-Ni-Fe arsenides, with sulfide minerals lacking or appearing very late in the sequence. Examples of five-element suite deposits include the polymetallic veins of the Cobalt-Gowganda, Echo Bay, and Thunder Bay Districts, Canada (Petruk 1971; Robinson and Ohmoto 1973; Franklin et al., 1986), the Schneeberg and Odenwald Districts, Germany (Staude et al. 2012; Burisch et al. 2017), the Jachymov area of the Czech Republic (Dolníček et al. 2009), the Anarak district of central Iran (Bagheri et al. 2007), and the Imiter and Bou Azzer districts of Morocco (Ahmed et al. 2009). Markl et al. (2016) and Burisch (2017) have proposed that 5-element suite deposits form when metalliferous brines mix with hydrocarbon-rich fluids, the organic carbon playing the role of a reductant that forces precipitation of elemental silver and Co-Ni-arsenides. The geologic settings of the deposits mentioned above may be too diverse to propose a single mechanism. However, the paragenetic sequence of native metals → metal arsenides → metal sulfides is consistent with precipitation at a reducing front where the kinetics of arsenite reduction are much faster than sulfate reduction.

Acknowledgements

This study builds on work done at McGill University in the 1990s by the second author and undergraduate student Trevor Blair. We thank Gary Wyss (Montana Tech) for help with the SEM-EDS work. This study is indirectly funded by a grant from the National Science Foundation (NSF#1624420).

References

Ahmed AH, Arai S, Ikenne M (2009) Mineralogy and paragenesis of the Co-Ni arsenide ores of Bou Azzer, Anti-Atlas, Morocco. Econ Geol 104:249-266.

Avila-Salinas W (1990) Origin of the copper ores at Corocoro, Bolivia. In Stratabound Ore Deposits in the Andes (pp. 659-670). Springer Berlin Heidelberg.

Bagheri H, Moore F, Alderton DHM (2007) Cu–Ni–Co–As (U) mineralization in the Anarak area of central Iran. J Asian Earth Sci 29:651-665.

Blair T (1997) Thermochemical arsenite reduction (TAR): a new hypothesis for the origin of "Cobalt-type" Ni-Co-arsenide vein deposits. B.S. Thesis, McGill University, 38pp.

Burisch M, Gerdes A, Walter BF, Neumann U, Fettel M, Markl G (2017) Methane and the origin of five-element veins: Mineralogy, age, fluid inclusion chemistry and ore forming processes in the Odenwald, SW Germany. Ore Geol Rev 81:42-61.

Dahlkamp FJ (1978) Geologic appraisal of the Key Lake U-Ni deposits, northern Saskatchewan. Econ Geol 73:1430-1449.

Dolníček Z, Fojt B, Prochaska W, Kučera J, Sulovský P (2009) Origin of the Zálesí U–Ni–Co–As–Ag/Bi deposit, Bohemian Massif, Czech Republic: fluid inclusion and stable isotope constraints. Min Deposita 44:81.

Franklin J, Kissin S, Smyk M, Scott S (1986) Silver deposits associated with the Proterozoic rocks of the Thunder Bay District, Ontario. Can J Earth Sci 23:1576-1591.

Gammons CH, Yu Y, Williams-Jones AE (1997) The disproportionation of gold (I) chloride complexes at 25 to 200˚C. Geochim Cosmochim Acta 61:1971-1983.

Goldhaber MB, Orr W.L (1995) Kinetic controls on thermochemical sulfate reduction as a source of sedimentary H_2S. ACS Symp Series 612:412-425.

Goldstein TP, Aizenshtat Z (1994) Thermochemical sulfate reduction: a review. J Thermal Anal 42:241-290.

Heinrich CA, Eadington PJ (1986) Thermodynamic predictions of the hydrothermal chemistry of arsenic, and their significance for the paragenetic sequence of some cassiterite-arsenopyrite-base metal sulfide deposits. Econ Geol 81:511-529.

Kissin SA (1992) Five-element (Ni-Co-As-Ag-Bi) veins. Geosci Canada 19(3).

Koenig GA (1900) Mohawkite, stibiodomeykite, domeykite, algodonite and some artificial copper arsenides. Am J Sci 60:439-448.

Krouse HR, Viau CA, Eliuk LS, Ueda A, Halas S (1988) Chemical and isotopic evidence of thermochemical sulphate reduction by light hydrocarbon gases in deep carbonate reservoirs. Nature 333:415-419.

Markl G, Burisch M, Neumann U (2016) Natural fracking and the genesis of five-element veins. Mineral Dep 51:703-712.

Moore PB (1962) Copper arsenides at Mohawk, Michigan. Rocks & Minerals 37(1-2):24-26.

Petruk W (1971) Mineralogical characteristics of the deposits and textures of the ore minerals. Can Mineral 11:108-139.

Robinson BW, Ohmoto H (1973) Mineralogy, fluid inclusions, and stable isotopes of the Echo Bay U–Ni–Ag–Cu deposits, Northwest Territories, Canada. Econ Geol 68:635–656.

Shanks WC, Bischoff JL, Rosenbauer RJ (1981) Seawater sulfate reduction and sulfur isotope fractionation in basaltic systems: interaction of seawater with fayalite and magnetite at 200-350˚C. Geochim Cosmochim Acta 45:1977-1995.

Singleton M, Nash P (1987) The As-Ni (Arsenic-Nickel) system. J Phase Equil 8:419-422.

Singh Y, Singh KDP, Chhabra J, Srinivasan S, Sharma YC, Gupta RK (2002) First report of domeykite and koutekite (copper arsenides) in Siwalik sandstones of Romehra, Hamirpur district, Himachal Pradesh. Geol Soc India 60:695-699.

Staude S, Werner W, Mordhorst T, Wemmer K, Jacob DE, Markl G (2012) Multi-stage Ag–Bi–Co–Ni–U and Cu–Bi vein mineralization at Wittichen, Schwarzwald, SW Germany: geological setting, ore mineralogy, and fluid evolution. Min Deposita 47:251-276.

Tredoux M, Zaccarini F, Garuti G, Miller DE (2016) Phases in the Ni-Sb-As system which occur in the Bon Accord oxide body, Barberton greenstone belt, South Africa. Mineral Mag 8:187-198.

Granite-related ore deposits in the NW Amazonian Craton, Colombia

Amed Bonilla Pérez, José Alejandro Franco Victoria, Thomas Cramer and Zeze Amaya Perea
Universidad Nacional de Colombia, Bogotá, Colombia

Abstract. In the Colombian portion of the northwestern Amazonian Craton, the crystalline basement is intruded by several anorogenic granites of Mesoproterozoic age, partly covered by Tertiary sedimentary rocks and Quaternary deposits. Petrographically and geochemically most of them are holocrystalline, leucocratic, and coarse-grained monzonites to granodiorites, often with wiborgite-type rapakivi texture. LA-ICP-MS U/Pb zircon dating yields concordant zircon enclosure ages of 1343 ± 8 Ma, 1392 ± 5 Ma and 1402 ± 2 Ma for a long lasting magma crystallization process.

Metallic minerals in host rocks (monzogranite and alkali feldspar granite), pegmatites and associated alluvial deposits sampled in eastern Colombia were characterized by means of reflected light petrography, SEM and XRF. The studied samples reveal a heterogeneous mineralogy as for example ilmenites with pyrochlore inclusions, Nb-rutile and struverite with columbite and cassiterite inclusions, as well as cassiterite, wolframite or monazite. Minerals from both alluvial and pegmatitic deposits point to alkaline granite and pegmatite complex origin. The U/Pb zircon ages suggest episodic intrusions of A-type granites between 1300-1400 Ma, associated with Nb, Ta, U, Sn and REE mineralizations, possibly related with coeval deposits in the southwestern Amazonian Craton and a large tin province from Bolivia to Brazil.

1 Localization and regional geology

The Amazonian Craton in the NE of South America formed mainly between the Paleo and Mesoproterozoic. Actually, the Amazonas River divides it into two large areas, the "Brazil or Guapore Shield" to the south and the "Guyana Shield" to the north. The latter comprises parts of Venezuela, Colombia, Guyana, Surinam and Brazil (fig. 1). In Colombia, several outcrops show that anorogenic granites of Mesoproterozoic age (1300-1400 Ma) intruded the crystalline basement known as Mitu-Complex (García et al. 2012; López et al. 2007; López and Cramer 2012). The Mitu-Complex is part of the 1.8-1.55 Ga old Rio Negro-Juruena (Tassinari and Macambira 2004) or 1.82-1.52 Ga Rio Negro (Santos et al. 2006) geochronological province consists mainly of orthogneisses, migmatites and granitoides.

Isolated Inselberg domes of porphyritic rapakivi granite rocks, mainly wiborgites, are locally intruded by pegmatitic dikes, were initially correlated with the Parguaza Magmatic Event with reported U–Pb zircon ages of 1530-1540 Ma in Venezuela (Gaudette et al. 1978) because of their anorogenic affinity.

However, Laser Ablation Inductively Coupled Plasma Mass Spectrometry U/Pb zircon dating yields concordant zircon enclosure ages of 1343 ± 8 Ma, 1392 ± 5 Ma and 1402 ± 2 Ma for the magma crystallization, in other words, an 100-200 Ma younger magmatism (Bonilla et al. 2013; Bonilla et al. 2016).

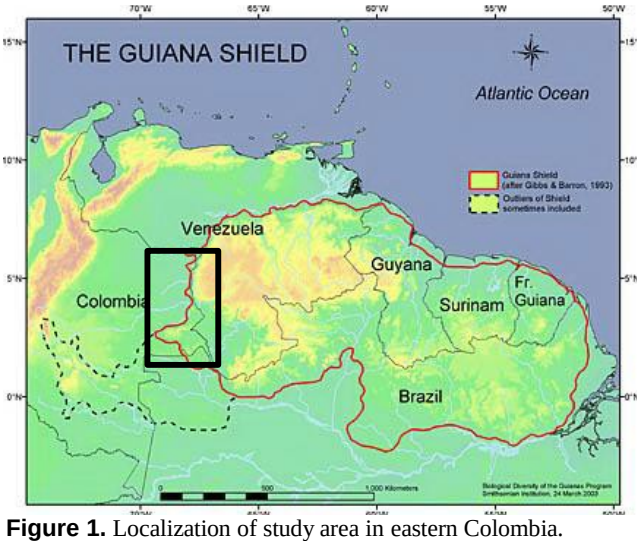


Figure 1. Localization of study area in eastern Colombia.

2 Ore deposits

The reported rapakivi granites in Colombia cover a large area and their attractive rapakivi texture gives them an economic potential as ornamental stones. Also lateritic and bauxite deposits, product of tropical weathering of the granites, may be of interest for aluminum and iron. However, the major potential of these granites comes from elements like tantalum, niobium, tin, titanium, etc.

Currently, the eastern Colombian rain-forest area is lacking a good vial or fluvial communication with the major urban centers which makes the transport of materials very difficult, and favors only low-volume high-value mining activity with materials like gold, Ta, Nb, REE, etc., not seldom associated with anorogenic granites (Breiter and Müller 2009; Rämö 2005; Vigneresse 2004; Rahal Lenharo 2003; Cerny 1992; Stein and Hannah 1990; Lehmann 1990; Pollard 1989a; Pollard 1989b; Taylor et al. 1988; Bonin 1986; Mehnert 1968).

2.1 Tantalum and niobium

One of the anorogenic granite outcrops in the area of the indigenous communities Matraca and Danta, at the middle Inirida River Basin. Surprisingly, the heterogeneous ilmenite grains contain niobium-rich pyrochlore inclusions with 5-10% Nb (fig. 2).

Near the Cachicamo River, in the Vichada-Department, coarse-grained colluvial deposits contain fragments of rapakivi granite, pegmatitic dikes and quartz veins as well as crystals of Nb-rutile and struverite uo to 5 cm long. These deposits are more likely associated with the big Parguaza Granite intrusion (Franco 2014; Bonilla et al. 2013; Gonzalez and Pinto 1990; McCandless 1965).

Energy Dispersive Spectroscopy (EDS) analyses of struverite and Nb-rutile indicate that they contain up to 10 % of both Ta and Nb, whereas back-scattered imaging and punctual EDS analyses reveal columbite inclusions or exsolutions in a rutile-matrix with up to 47% Nb and 14% Ta (fig. 3).

Preliminary results of a study of an alluvial deposit with similar mineralogy, discovered by our group near San José in the Guainia-Department last year, indicate Mn-columbites with up to 74% Nb, 6% Ta and 11% Mn measured as ROI in a Bruker Tracer V-III handheld X Ray Fluorescence hXRF (fig. 4).

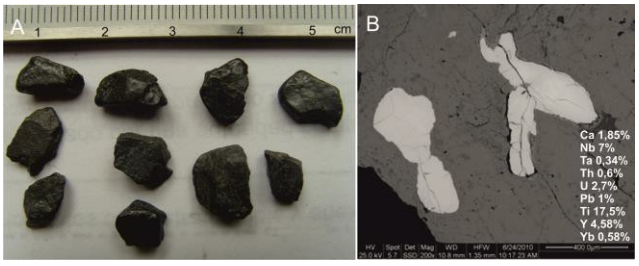
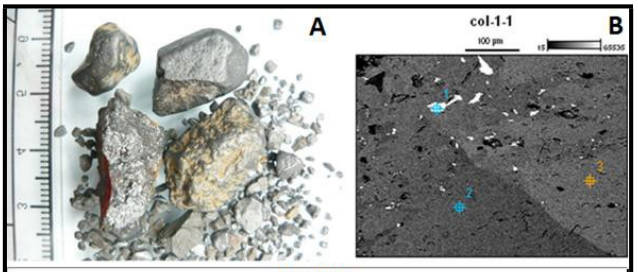


Figure 2. A) Ilmenite crystals from Matraca community B) Backscattering image of ilmenite with Nb, REE, U-rich inclusions (grat. Torsten Graupner and Frank Melcher BGR Hannover) (in Cramer et al. 2011).



Weight %						
POINT	Ti	Mn	Fe	Nb	Sn	Ta
col-1-pt1	7.91	4.79	23.17	47.77	1.63	14.74
col-1-pt2	68.88		7.04	9.92	4.01	10.14
col-1-pt3	67.45		7.17	9.93	5.05	10.40

Figure 3. (A) Nb-Rutile and struverite crystals from the alluvial Cachicamo deposit, (B) Backscattering image and EDS analysis showing bright columbite inclusions (pt1) in a Nb-rutile matrix with some Sn- and Ta- enrichment (pt2 and pt3).

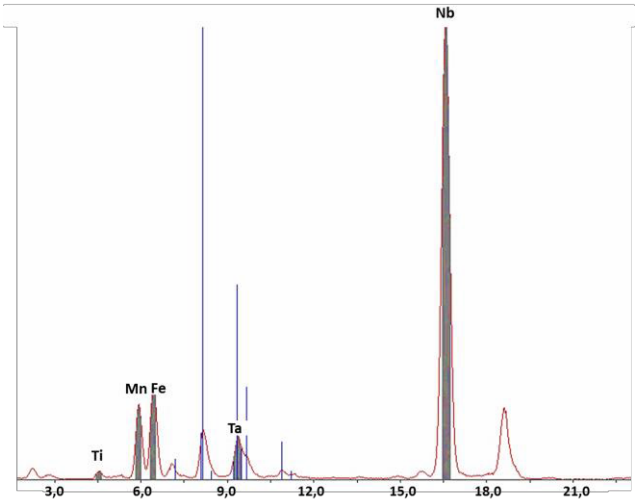


Figure 4. hXRF analyses of Mn-columbites from San José Guainía with Nb>Ta content (40kV, 3.40 µA, 30seg).

2.2 Uranium, Thorium and REE

As shown in Figure 3, inclusions in ilmenites from the Matraca and Danta granites were identified for their Ca, Yb, Y, U, Th contents as pyrochlore-group minerals (Cramer, Graupner, et al. 2010; Cramer, et al. 2010; Bonilla et al. 2010).

The pegmatitic dikes in San José - Guainía need to be studied additionally because of their anomalous high radioactivity, associated with magnetite and monazite crystals. Large crystals of monazite in the alluvial deposits contain high ROI-values of up to 25% Ce, 44% Th, 2% U and 2% Y (fig. 5).

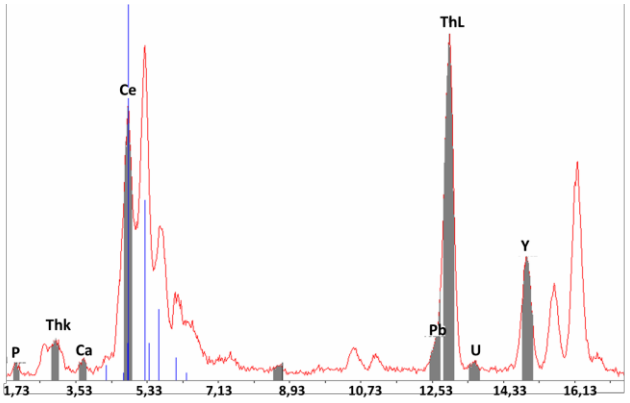


Figure 5. hXRF analyses of monazites from San Jose Guainía with high Ce, Th and Y content (40kV, 3.40 µA, 30seg).

2.3 Other commodities

Tonnes of wolframite have been illegally extracted from the Zancudo mining site in the central Guainía Department and carried to Bogotá for marketing. Bismuth and small amounts of gold genetically related to hübnerites (fig. 6) probably of greissen origin are hosted in metasedimentary rocks of the Maimachi Formation (Renzoni 1989) with WO_3 contents from 70 to 84wt%, MnO 12-22 wt% and FeO

of 5 – 13 wt%.

Tin occurs as an important component in form of cassiterite inclusions in Nb-rutiles, struverites and columbites, but is also found as large cassiterite crystals in alluvial deposits as for example in La Ceiba and Casuarito, in the Vichada Department, possibly associated with a larger tin province from Bolivia to Brazil (Romer and Kroner 2014; Bettencourt et al. 1999; Lehmann 1990).

Quartz and pegmatitic dikes in granites near Barranquillita in the Guainia-Departement contain columbites, but also large beryl crystals and beautiful garnets, possibly suitable for future handicraft incomes of the indigenous communities.

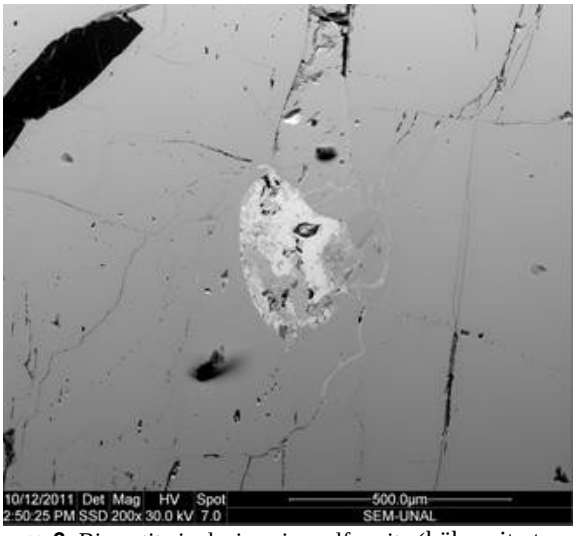


Figure 6. Bismutite inclusions in wolframite (hübnerite type) (SEM BS).

Conclusions

The rapakivi granites in the northwestern Amazonas craton are remains of one of the largest magmatic provinces in the world, which have also developed an economic potential for critical elements like tin, tantalum, niobium, tungsten and rare earth elements.

The extent of these widely distributed granites is still unknown; however, the Parguaza Granite is estimated to be larger than 30,000 km^2. Therefore, the prospective area for related ore deposits is very large. The association and morphological (size and shape) characteristics of minerals from alluvial deposits and from pegmatitic dikes infer alkaline granite and complex pegmatite sources. Neither the Sn nor the W occurrences show clear evidence of greissenization, but further studies are necessary as well as about interactions with mafic intrusions, or with older metamorphic and younger sedimentary processes. Also is it difficult to assess whether the near-by pyrochlore-enriched carbonatite complexes of Cerro Impacto in Venezuela and Seis Lagos in Brazil have their equivalents in Colombia, but especially in the Guainía Department this should not be excluded.

The continuous exploration of the Amazonian tropical rain forest often leads to the discovery of new deposits. In Brazil, Venezuela and Bolivia some of them are mined by private or government companies. In Colombia, however, civil war, drug trafficking, illegal mining, disrespect to the indigenous communities and damages to the sensitive ecosystems, increased the concerns about mining in general. Only political decisions that take serious account of social and environmental issues in the context of the actual peace process will allow Colombia to use its mineral resources in a rational way.

Acknowledgements

We express our gratitude to the native communities of Cachicamo, La Ceiba, Casuarito, Matraca, Danta, Barranquillita and San José for allowing our studies in their areas. Thanks to Ingeominas (today SGC), Colciencias and the Vaupes-Department as leader of the SGR-financed project “Strategic Minerals in the Llanos-Region”. The first author also wishes to thank Colciencias for the PhD’s scholarship and field trip financial support.

References

Bettencourt, J.S., R.M. Tosdal, W.B. Leite Jr., and B.L. Payolla. 1999. “Mesoproterozoic Rapakivi Granites of the Rondonia Tin Province, Southwestern Border of the Amazonian Craton, Brazil-I. Reconnaissance U-Pb Geochronology and Regional Implications.” Precambrian Research 95 (1–2): 41–67. doi:10.1016/S0301-9268(98)00126-0.

Bonilla, Amed, José Carlos Frantz, Juliana Charão-Marques, Thomas Cramer, José A. Franco-Victoria, y Zeze Amaya-Perea. 2016. “Magmatismo rapakivi en la cuenca media del río Inírida, departamento de Guainía, Colombia. Boletín de Geología, 38 (1): 17-32.

Bonilla, Amed, José Carlos Frantz, Juliana Charão-Marques, Thomas Cramer, José A. Franco-Victoria, Elise Mulocher, y Zeze Amaya-Perea. 2013. “Petrografía, Geoquímica y Geocronología del Granito de Parguaza en Colombia.” Boletín de Geología, 35 (2): 83–104.

Bonilla, Amed, Zeze Amaya Perea, José Alejandro Franco Victoria, y Thomas. Cramer. 2010. Caracterización de Depósitos Aluviales En La Comunidad de Matraca, Departamento del Guainía, Colombia. VI Congreso Uruguayo de Geología.

Bonin, Bernard. 1986. “Ring Complex Granites & Anorogenic Magmatism.” Paris: Bureau de Recherches Geologiques et Minieres.

Breiter, Karel, and Axel Müller. 2009. “Evolution of Rare-Metal Granitic Magmas Documented by Quartz Chemistry.” European Journal of Mineralogy 21 (2): 335–46. doi:10.1127/0935-1221/2009/0021-1907.

Cerny, Petr. 1992. “Rare-Element Granitic Pegmatites. Part II: Regional to Global Environments and Petrogenesis.” Geoscience Canada 18 (2): 68–81.

Cramer, Thomas, Zeze Amaya Perea, José Alejandro Franco Victoria, Amed Bonilla Perez y Ángela Patricia Poveda. 2011. Caracterización de Depósitos Aluviales Con Manifestaciones de Tantalio Y Niobio (Coltán) En Las Comunidades Indígenas de Matraca Y Caranacoa En El Departamento Del Guainía) - Contrato Interadministrativo No 021 de 2010 Ingeominas- Universidad Nacional de Colombia.

Cramer, Thomas, Amed Bonilla Perez, José Alejandro Franco Victoria, Zeze Amaya Perea, and Ignacio Iregui. 2010. “Mineralizations of Tantalum and Niobium in Vichada and Guainía, Eastern Part of Colombia.” Acta Mineralogica-Petrographica, Abstract Series 6 (Abstracts of the 20th World Congress of the International Mineralogical Association IMA2010, Budapest, 21st-27th August 2010).

Cramer, Thomas, Thorsten Graupner, Amed Bonilla Perez, José Alejandro Franco Victoria, and Zeze Amaya Perea. 2010. Erste Einblicke in Ta- Und Nb- Mineralisierungen Im Kolumbianischen Amazonasgebiet. Frankfurt: Vortrag DMG Sektionstreffen Petrologie/Petrophysik, Goethe-Universität Frankfurt, 26.6.2010.

Franco, José Alejandro. 2014. Contribución a la geología histórica del Oriente Colombiano: Proveniencia de minerales metálicos con Nb, Ta, Mn, Fe, Ti, Sn y W, de un depósito laterizado, en cercanías a la Comunidad Indígena de Cachicamo, al NE del Departamento del Vichada. Tesis Maestria. Universidad Nacional de Colombia, Bogotá.

García, Gabriel Rodríguez, Janeth Sepúlveda Ospina, Carolina Ramírez Cardona, Francy Helena Ortiz Párraga, Keepler Ramos Carvajal, José Gilberto Bermúdez Cordero, y María Isabel Sierra Rojas. 2012. “Unidades, Petrografía y Composición Química del Complejo Migmatítico de Mitú en los alrededores de Mitú.” Boletín de Geología, 33 (1).

Gaudette, Henry E, Vicente S Mendoza, Patrick M Hurley, and Harold W Fairbairn. 1978. “Geology and Age of the Parguaza Rapakivi Granite.” Geol. Soc. Am. Bull. 89 (9): 1335–40.

Gonzalez, Carlos F, y Hernando Pinto. 1990. “Petrografia Del Granito de Parguaza Y Otras Rocas Precambricas En El Orient de Colombia.” Geologia Colombiana 17: 107–21.

Lehmann, Bernd. 1990. Metallogeny of Tin. Vol. 32. Lecture Notes in Earth Sciences 32. Berlin, London: Springer.

López, J A, S Khurama, L E Bernal, and M A Cuéllar. 2007. El Complejo Mitú: Una Nueva Perspectiva. XI Congreso Colombiano de Geología. Bucaramanga.

López, J A, y Thomas Cramer. 2012. “Ambiente geológico del complejo Mitú y perspectivas de ocurrencias minerales de niobio y tantalio en el territorio colombiano.” Geología Colombiana 37 (2): 75–95.

McCandless, G.C. 1965. “Reconocimiento Geológico de La Parte Occidental Del Estado Bolívar.” Boletin Geológico 7 (13): 19–28.

Mehnert, K R. 1968. Migmatites and the Origin of Granitic Rocks. Amsterdam, New York [etc.]: Elsevier Pub. Co.

Pollard, P J. 1989a. “Exploration for Granite-Hosted Tantalum Deposits; an Approach via District Analysis.” In Lanthanides, Tantalum and Niobium: Mineralogy, Geochemistry, Characteristics of Primary Ore Deposits, Prospecting, Processing and Applications - Proceedings of a Workshop in Berlin, Nov. 1986, edited by Peter Möller, Petr Cerny, and Francis Saupé, 266–73. Berlin, Heidelberg, New York, London, Paris, Tokyo: Springer.

Pollard, P J. 1989b. “Geochemistry of Granites Associated with Tantalum and Niobium Mineralization.” In Lanthanides, Tantalum and Niobium: Mineralogy, Geochemistry, Characteristics of Primary Ore Deposits, Prospecting, Processing and Applications - Proceedings of a Workshop in Berlin, Nov. 1986, edited by Peter Möller, Petr Cerny, and Francis Saupé, 145–68. Berlin, Heidelberg, New York, London, Paris, Tokyo: Springer.

Rahal Lenharo, Sara Lais; 2003. Petrology and Textural Evolution of Granites Associated with Tin and Rare-Metals Mineralization at the Pitinga Mine, Amazonas, Brazil. Edited by Peter J.; Pollard and Helmut; Born. Lithos. 66thed. International: Elsevier : Amsterdam, International.

Rämö, O. Tapani. 2005. “Granitic Systems—a Special Issue in Honor of Ilmari Haapala.” Lithos, Granitic Systems Ilmari Haapala Volume Symposium “Granitic Systems –State of the Art and Future Avenues,” 80 (1–4): xi–xix. doi:10.1016/j.lithos.2004.09.015.

Renzoni, Giancarlo. 1989. “Comparación entre las secuencias metasedimentarias de la Serranía de Naquén y de la Serra da Jacobina.” Boletin Geológico Ingeominas 30 (2): 25–42.

Romer, Rolf L., and Uwe Kroner. 2014. “Sediment and Weathering Control on the Distribution of Paleozoic Magmatic Tin–tungsten Mineralization.” Mineralium Deposita 50 (3): 327–38. doi:10.1007/s00126-014-0540-5.

Santos, J O S, L A Hartmann, M.S.G.de Faria, S R L Riker, M.M.de Souza, M E Almeida, y N J McNaughton. 2006. A Compartimentação Do Cráton Amazonas Em Províncias: Avanços Ocorridos No Período 2000-2006. Edited by SBG-Núcleo Norte. Simp.Geol. Amaz., 9. Belém.

Stein, Holly J, and Judith L Hannah. 1990. Ore-Bearing Granite Systems : Petrogenesis and Mineralizing Processes. Boulder, Colo.: Geological Society of America.

Tassinari, C G, and J B Macambira. 2004. “Geological Provinces of the Amazonían Craton.” In Geología Do Continente Sul-Americano: Evolução Da Obra de Fernando Flávio Marques de Almeida, 471–86.

Taylor, R P, and D F Strong,. 1988. Recent Advances in the Geology of Granite-Related Mineral Deposits : Proceedings of the CIM Conference on Granite-Related Mineral Deposits, September, 1985. Montréal, Québec: Geology Division of CIM.

Vigneresse, J. L. 2004. “A New Paradigm for Granite Generation.” Transactions of the Royal Society of Edinburgh-Earth Sciences 95: 11–22..

Hydrothermal monazite and xenotime related to granites associated with the North Zone Mount Pleasant Sn-Zn-Cu-In (& W) deposits, NB, Canada: preliminary studies

Brittany Charnley, David R. Lentz, Chris R.M. McFarlane
University of New Brunswick, Canada

Abstract. All REE and Y are significantly enriched to the ores in the North Zone Sn-Zn-Cu-In and Fire Tower Zones W-Mo-Bi deposits at Mount Pleasant NB. Geochemical attributes and U-Pb geochronology is consistent with a cogenetic relationship between REE+Y and ore formation.

1 Introduction

Monazite and xenotime have long been known as hydrothermal phases within the various mineralized zones at Mount Pleasant deposits. We have used pXRF to help select areas to examine in further detail for this preliminary study to help constrain the mechanisms for mineralization, but also constrain them geochronologically (Charnley and Lentz 2016; Zhang et al. in press)

2 Geological setting

The Mount Pleasant granophile element deposits are located in along the southwestern margin of the Late Devonian Mount Pleasant Caldera in southwestern New Brunswick (Fig. 1). These deposits are associated with three Late Devonian hypabyssal granitic intrusions: Granite I (GI), Granite II (GII), and Granite III (GIII), which are near the contact between the Mount Pleasant caldera complex and the deformed Silurian rocks of the Piskahegan Group. These granophile element deposits are quite different and divided into two zones; the Fire Tower Zone (FTZ) and the North Zone (NZ). Tungsten-molybdenum-bismuth (W-Mo-Bi) mineralization is predominant in the FTZ, although a subzone of W-Mo also occurs in the NZ. The tin and indium mineralization with base metals (Cu-Zn-Sn-In) occurs predominantly in the NZ, but has also been locally intersected during drilling in the FTZ (Samson 1990; Sinclair et al. 2006) some of which is exposed at surface. Porphyry W-Mo-Bi mineralization is associated with Granite I (the oldest phase) and is hosted in zones of extensive brecciation, along with stockwork zones, quartz veinlets as well as disseminations in breccia matrix (Samson 1990; Sinclair 1994). The majority of the Sn deposits and other base metals (including In) seem to be associated with GII and occur as exogranitic vein, lode, and replacement deposits, although endogranitic mineralization also occurs. Granite III, the youngest phase, only has minor Sn mineralization associated with it (Sinclair et al. 1988), although Inverno and Hutchinson (2004) stated that there is potential for significant Sn in association with GIII, likely in the highly developed endogranitic tin zone within this granite.

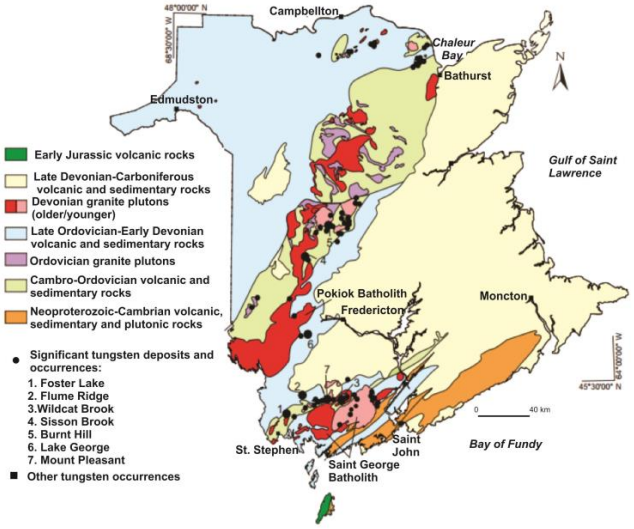


Figure 1. Regional tectonostratigraphic map of New Brunswick showing the distribution of tungsten occurrences throughout the province. The Mount Pleasant deposit is located at No. 7. (from Stewart et al. 2011).

Radiometric dates were determined for GIII using $^{40}Ar/^{39}Ar$ dates of biotite in sedimentary breccia underlain by a granite showing an age of ca. 361 Ma (Sinclair and Kooiman 1990). Other dates were obtained for the Bailey Formation (exocaldera rhyolite in the northern part of the Mount Pleasant caldera) using U-Pb zircon with an age of 363.4±1.8 Ma (Tucker et al. 1998) and for the Piskahegan Group (late fill sequence), an age of 368 Ma was discerned using Rb-Sr data (Anderson 1992). Thorne et al. (2013) have presented Re-Os model ages from samples of molybdenite related to the GI intrusive phase and the W-Mo-Bi mineralization from the Fire Tower Zone with overlapping ages of 369.7±1.6 Ma and 370.1±1.7 Ma, respectively. These dates confirm that caldera formation and volcanism and emplacement of sub-volcanic intrusions happened over a relatively short amount of time (see Yang et al. 2003).

3 Analytical methods

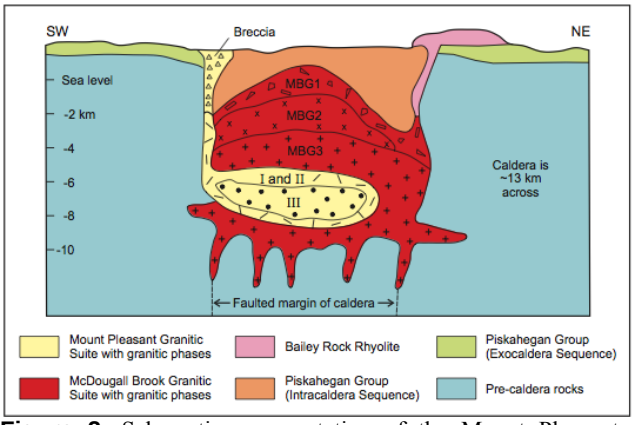


Figure 2. Schematic representation of the Mount Pleasant caldera sequence showing the various intrusions and the subvolcanic GI (as oldest) to GIII (youngest) granites (modified from McCutcheon et al.1997).

A hydrothermal monazite crystal (~200 μm across), hosted within a quartz vein cross-cutting GII was discovered in sample BC14-02-06 (polished thick section). The monazite is believed to have crystallized during quartz saturation in a vein from hydrothermal fluids during the cooling stages of GII. The JEOL JSM-6400 Scanning Electron Microscope (SEM) instrument at the University of New Brunswick was used to obtain a backscattered electron (BSE) image of the polished thick section sample using Digital Micrograph (Gatan Inc.) at an accelerating voltage of 15 kV, and a beam current of 15 nA. Photographs were taken with 30 times (low) magnification in order to obtain an image of a larger area of the sample and the gamma was adjusted to help see zoning in the monazite.

Laser Ablation Inductively Coupled Plasma-Mass Spectrometry (LA ICP-MS) was used to ablate and date the hydrothermal monazite that was found in the quartz vein. The instrument was a Resonetics S-155-LR 193nm Excimer laser ablation system coupled to an Agilent 7700x quadrupole ICP-MS. For this method the sample was analyzed for ^{204}Pb, ^{207}Pb, ^{235}U, ^{206}Pb, and ^{238}U (see McFarlane and Luo 2012). The certified standard used was Mnz-8153 (monazite), which had a date of ~507.5 Ma. The ablation diameter was 17 μm and the machine was running at 3 Hz/sec. Figure 3 shows the offcut scan from the sample that the monazite was found. Figure 4 shows a back-scattered electron image of the monazite and the hosting quartz vein, and Figure 5 shows a high magnification SEM-BSE image of the monazite. The monazite had a weak yellow pleochroism and had high relief, which is characteristic of hydrothermal monazite (Schandl and Gorton 2004).

4 Results

Using laser ablation inductively coupled plasma spectrometry (LA ICP-MS) analysis, the ^{204}Pb, ^{206}Pb, ^{207}Pb, ^{238}U and ^{235}U contents of the monazite were measured from 20 ablations to determine the age (Fig. 5).

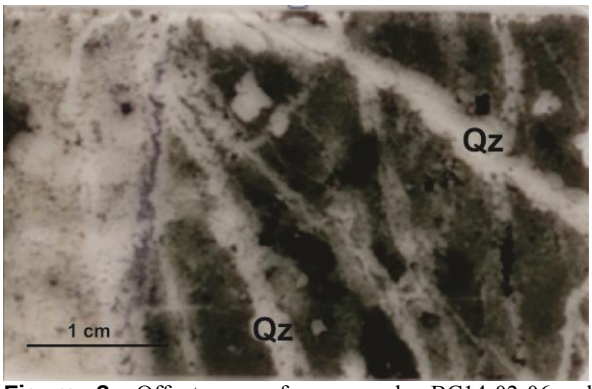


Figure 3. Offcut scan from sample BC14-02-06 where hydrothermal monazite was located in a quartz vein cutting GR II.

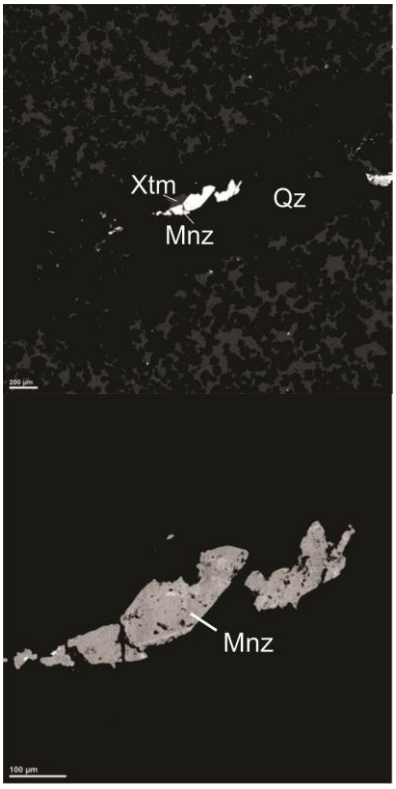


Figure 4. SEM-BSE image of monazite found in sample BC14-02-06 in a quartz vein cutting GR II (top and bottom).

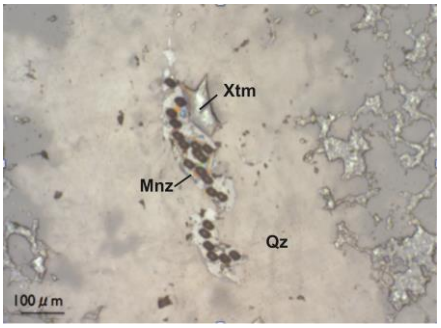


Figure 5. Reflected light photograph of the monazite found in sample BC14-02-06 showing ablation pits (GRII).

In order to improve the accuracy of the date, corrections were done for the common lead found in the sample (^{204}Pb) and for comparison purposes; the data was plotted on two different Concordia diagrams: the conventional Concordia plot and the inverse Concordia plot. An intercept was found on the conventional Concordia plot at 371.9±2.5 Ma (Fig.6). Another analysis was done on an inverse Concordia diagram and yielded an intercept at 371.0 ± 2.5 Ma that was anchored at 0.85 on the ^{207}Pb/^{206}Pb axis. Another intercept found at 371.0 ± 2.0 Ma, which intercepted at 3977± 750 on the ^{207}Pb/^{206}Pb axis (Fig. 7).

The ore elements that were found associated to this sample using the pXRF were; Mo, Bi, Zn, Sn, W,and Cu, with the following concentrations respectively; 1763 ppm, 776 ppm, 356 ppm, 28 ppm, 25 ppm, and 25 ppm . (Charnley and Lentz 2015; Zhang et al. in press). With respect to the rare earth elements (REE), this sample contained anomalous counts for several light REE, although no calibration standards were used for Ce and La.

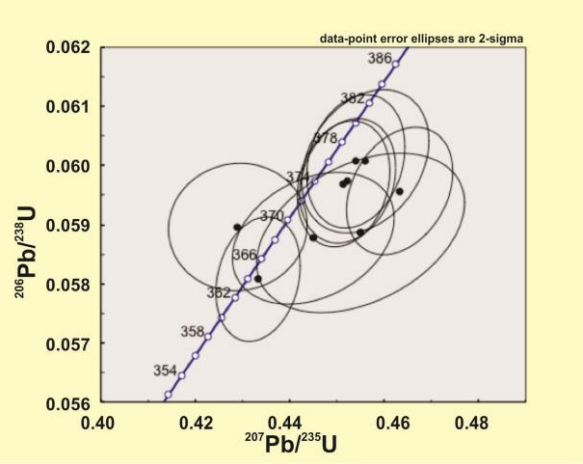


Figure 6. Concordia graph with ^{207}Pb/^{235}U vs. ^{206}Pb/^{238}U showing common intercept

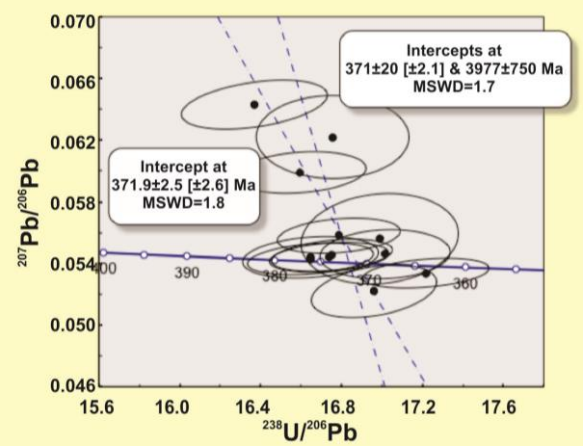


Figure 7. Graph of inverted Concordia Intercept at 371 ± 3 Ma MSWD=1.8 and anchored at 0.85 ^{207}Pb/^{206}Pb. Intercepts at 371 ± 2 Ma and 3977 ± 750 MSWD = 1.7.

5 Discussion

Monazite has a high thermal closure temperature, ~700°C and therefore is a good geochronometer to date hydrothermal ore deposits (Schandl and Gorton 2004), and is commonly associated with ore-related alteration minerals (Vielreicher et al. 2003). Other monazite studies in the Fire Tower Zone W-Mo-Bi deposit on Mount Pleasant has concluded that it has high uniform Gd_2O_3 content that gives it a high magnetic susceptibility (Petruk and Owen 1975); this makes it more valuable being MREE enriched and maybe geometallurgically important. The granites on Mount Pleasant are believed to be low temperature-fractionated granites; this allows monazite to be able to crystallize. Because monazite has a nine coordinated site, it is more favorable to accommodate the large light rare earth elements, including La to Eu, this means that these elements are decreasing in the system. Other elements including the HREE along with Y, as well as U and Th, are in increasing in these magmas, because they continue to be incompatible during crystal fractionation in the system (Ni et al. 1995).

The mobility of these REE seems to be related to the anion ligands present in solution. Williams-Jones et al. (2012) states that LREEs are more mobile in hydrothermal process than HREEs, and that chloride (Cl^-) and fluoride (F^-) seem to favour complexing with LREE's. Other ligands that aid in the mobility of REE's include $CO_3^{-2}{}_3$and HPO_4^{3-} (Yougliang and Yusheng 1991). Base metals like the ones seen at Mount Pleasant are primarily mobilized with Cl^- complexes at high temperature and low pH and therefore high abundances of these metals are seen with a decrease of temperature and increasing pH (Williams-Jones et al. 2012). An experiment of REEs with monazite by Williams-Jones et al. (2012) concluded that a system with hydrothermal fluid and primary magmatic REE mineralization could aid in the mobilization of LREEs and the transport of those elements from the area of mineralization.

6 Conclusions

Previous ^{40}Ar/^{39}Ar dating, on a biotite grain in sedimentary breccia found underlain by GIII, has shown a data of ca. 361 Ma (Sinclair and Kooiman 1990) and is related to cooling the biotite below its closure T of ~ 250°C and could be similar in age to the earlier granites. Thorne et al.'s (2013) Re-Os dates from GI in the Fire Tower Zone yielded ages of 369.7±1.6 and 370.1±1.7 Ma from samples of molybdenite related to the W-Mo-Bi mineralization. This study has concluded that the U-Pb date obtained in this study for monazite hosted within a quartz vein that cuts the North Zone GII are within error of those Re-Os dates found for the GI – related W-Mo-Bi mineralization. Therefore the GI and GII intrusions are spatially and temporally related, but further geochronology is needed on the igneous and hydrothermal system. The Ar-Ar biotite cooling age obtained for GIII (ca. 361 Ma) is much younger than both dates obtained for GI and GII intrusions,

and needs to be dated to ascertain its high T emplacement age, as geochemically these all seem related to a single magmatic system. It is important to note that GI is associated with W-Mo-Bi mineralization, based on Inverno and Hutchinson's (2004). This dated sample has anomalous Mo and Bi associated with it, which could mean there is an uncertainty with calling this granite GII versus Gi; this means more work is needed in the area to verify the detailed geochemical characteristics between these three Mount Pleasant granites (G1, G2, and GIII) so as to enhance mapping of the various granite-ore associations in better detail. Also, absolute ages need to be determined on all of the granites in the Mount Pleasant area, as well as their ores. Also, further work is needed on the REEs associated with the various types of mineralization, as noted above, some mineralization has higher REE that form hydrothermal monazite. In fact, the CANMET MP-2a standard (W-Mo-Bi ore) has very anomalous light to heavy REE contents that merits further investigation.

Acknowledgements

We thank Adex Mining Inc. and Roger Young of Adex for allowing us to take samples on Mount Pleasant, as well as the New Brunswick Museum for their generous grant, which was used on the LA ICP-MS to date the granite. We also thank the New Brunswick Department of Energy and Resource Development. DL and CM are supported by NSERC Discovery grants.

References

Anderson, HE (1992) A chemical and isotopic study of the age, petrogenesis and magmatic evolution of the Mount Pleasant caldera complex, New Brunswick. Unpublished Ph.D. thesis, Carleton University, Ottawa, Ontario, 188p.

Charnley, BE, Lentz, DR (2016) Petrogeochemical assessment of the various felsic volcanic and subvolcanic igneous rocks associated with Sn-Cu-Zn and W-Mo-Bi mineralization in the North Zone, Mount Pleasant, New Brunswick: A pXRF study. New Brunswick Department of Energy and Mines, Geoscience Report 2015-5, 31p.

Inverno, CMC., Hutchinson, RW (2004) The endogranitic tin zone, Mount Pleasant, New Brunswick, Canada and its metallogenesis. Applied Earth Science113261-288.

Inverno, CMC, Hutchinson, RW (2006) Petrochemical discrimination of evolved granitic intrusions associated with Mount Pleasant deposits, New Brunswick, Canada. Institution of Mining and Metallurgy Transactions (Section B-Applied Earth Science) 115: 23–39.

Kooiman, GJA, McLeod MJ, Sinclair, WD (1986) Porphyry tungsten-molybdenum ore bodies, polymetallic veins and replacement bodies and tin-bearing greisen zones in the Fire Tower Zone, Mount Pleasant, New Brunswick. Economic Geology 18: 1356-1373.

McCutcheon, SR, Anderson, HE, Robinson, PT (1997) Stratigraphy and eruptive history of the Late Devonian Mount Pleasant calderacomplex, Canadian Appalachians. Geological Magazine 134:17-36.

McFarlane, CRM, Luo, Y (2012) U-Pb geochronology using 193 nm excimer LA-ICP-MS optimized for *in situ* accessory mineral dating in thin sections. Geoscience Canada 39: 158-172.

Ni, Yunxiang, Hughes, JM, Mariano, AN (1995) Crystal chemistry of the monazite and xenotime structures. American Mineralologist 80: 21-26.

Petruk, W, Owens, D (1975) Monazite from the Mount Pleasant deposit, New Brunswick. Canadian Mineralogist 13: 289-299.

Samson, IM (1990) Fluid Evolution and Mineralization in a Subvolcanic Granite Stock: The Mount Pleasant W-Mo-Sn Deposits, New Brunswick, Canada. Economic Geology 85: 145-163.

Schandl, ES, Gorton, MP (2004) A textural and geochemical guide to the identification of hydrothermal monazite: criteria for selection of samples for dating epigenetic hydrothermal ore deposits. Economic Geology 99: 1027-1035.

Sinclair, WD, Kooiman, GJA (1990). The Mount Pleasant tungsten-molybdenum and tin deposits. In Mineral Deposits of New Brunswick and Nova Scotia (Field Trip 2), D.R. Boyle (editor). 8th IAGOD Symposium, Field Trip Guidebook. Geological Survey of Canada, Open File 2157, p. 78-87.

Sinclair, WD, Kooiman, GJA, Martin, DA (1988). Geological setting of granites and related tin deposits in the North Zone, Mount Pleasant, New Brunswick; Current Research, Part B, Geological Survey of Canada, Paper 88-lB: 201 -208.

Sinclair, WD (1994) Tungsten-molybdenum and tin deposits at Mount Pleasant, New Brunswick, Canada: products of ore–fluid evolution in a highly fractionated granite system. In Metallogeny of Collisional Orogens Focussed on the Erzgebirge and Comparable Metallogenic Settings, R Seltmann, H Kampf, P Moller (editors), p. 410–417.

Sinclair, WD, Kooiman, GJA, Martin, DA, Kjarsgaard, IM 2006. Geology, geochemistry and mineralogy of indium resources at Mount Pleasant, New Brunswick, Canada. Ore Geology Reviews 28: 123–145.

Stewart, HJ, McLeod, MJ, Thorne, KG (2011) Tungsten. New Brunswick Department of Natural Resources; Lands, Minerals and Petroleum Division, Mineral Commodity Profile No. 7, 7 p.

Thorne, KG, Fyffe, LR, Creaser, RA (2013) Re-Os geochronological constraints on the W-Mo mineralizing event in the Mount Pleasant Caldera Complex: implications for the timing of subvolcanic magmatism and caldera development. Atlantic Geology 49: 131-150.

Tucker, RD, Bradley, DC, ver Straeten, CA, Harris, AC, Ebert, JR, McCutcheon, SR 1998. New U-Pb zircon ages and the duration and division of Devonian time. Earth and Planetary Science Letters 158: 175–186.

Vielreicher, NM, Groves , DI, Fletcher, IR, McNaughton NJ, Rasmussen, B 2003. Hydrothermal monazite and xenotime geochronology: A new direction for precise dating of orogenic gold mineralization. SEG Newsletter, No. 53: 1, 10-16.

Williams-Jones, AE, Migdisov, AA, Samson, IM 2012. Hydrothermal Mobilisation of the Rare Earth Elements – a Tale of "Ceria" and "Yttria". Elements 8: 355-360.

Yang, X, Lentz, DR, McCutcheon, SR 2003. Petrochemical evolution of subvolcanic granitoid intrusions within the Late Devonian Mount Pleasant Caldera, southwestern New Brunswick, Canada: comparison of Au versus Sn-W-Mo-polymetallic mineralization systems. Atlantic Geology 39: 97-117.

Yongliang, X, Yusheng, Z (1991) The mobility of rare-earth elements during hydrothermal activity: A review. Chinese Journal of Geochemistry 10: 295-306.

Zhang, W, Lentz, DR, Charnley, B (2017). Petrogeochemical assessment of rock units and identification of alteration/mineralization vectors using portable X-ray fluorescence measurements: applications to the Fire Tower Zone (W-Mo-Bi) and the North Zone (Sn-Zn-In), Mount Pleasant deposit, New Brunswick, Canada. Journal of Geochemical Exploration, in press.

Spatial relations between gold, associated metals and lithologies at the Miwah acid-sulfate (high sulfidation) epithermal deposit, Aceh, North Sumatra, Indonesia

Mohamad Nur Heriawan
Institute of Technology Bandung (ITB), Indonesia

Thomas Mulja
Consulting Geologist, Canada

Abstract. The tabular Miwah acid-sulphate epithermal gold deposit occurs within a prominent peak dominated by a vuggy silica +/- sulphide +/- alunite core that grades into peripheral argillic and propylitic zones. These altered rocks replaced phreatomagmatic diatreme breccia, other breccias, and andesite. Gold is spatially correlated with Ag, Cu, As and Sb in the mineralized vuggy silica and massive sulphide-silica zones, and negatively with Pb and Zn. A multivariate statistical analysis shows that for surface samples, the mean of Au in the silica and undifferentiated breccia domains, is 1.97 ppm and 1.06 ppm, respectively, and the spatial range of Au span 200 - 350 m laterally. In drill core the mean of Au is 0.94 ppm in silica rocks, 1.06 ppm in hydrothermal breccias and 2.07 ppm in undifferentiated breccias, and the spatial range of Au vary from 150 - 300 m laterally and 10 - 20 m vertically. On the basis of these metal associations, lithologic units and geology, the Miwah gold deposit is structurally controlled by fracture zones through which the mineralizing vapors or brines ascended from a hydrothermal system at some depth in a maar-diatreme volcano. These brines flowed laterally along vug-enhanced permeable host rocks to develop the tabular deposit.

1 Introduction and geology

With an inferred resource of 3.14 M oz gold and 9 M oz silver at a cut-off grade of 0.2 ppm Au (East Asia Minerals Ltd. 2011), the Miwah acid-sulphate Au + Ag deposit is one of the largest on Sumatra Island (Fig. 1). Following its discovery and initial drilling by Highland Gold in 1992 (William and Fleming 1995), East Asia Minerals Ltd. in the 2000s systematically assayed outcrops and drilled 77 core holes to delineate the deposit. We present herein the spatial characteristics of gold and associated elements (Ag, Cu, As, Sb) with respect to host rocks, and integrate this information with other geological data to generate a mineralization model for the Miwah deposit.

Miwah rises as a 1980-m high prominent peak in the north-western backbone of the Barisan Mountains in Aceh, North Sumatra (Fig. 1). Mulja et al. (2003) summarized the geology and metallogeny of this region, which hosts many magmatic-hydrothermal precious and base-metal deposits. The local geology of Miwah comprises a sequence of basic to felsic porphyritic volcanic rocks of the 2.7 Ma Leuping Formation (Corbett and Leach 1997), and associated intrusive breccias, a volcanic dome, and andesite dikes (Fig. 2). Topographically the Miwah deposit is divisible into a lower western Miwah Bluff and a hilly eastern Block M, which consist mainly of phreatomagmatic diatreme breccia, and andesite and other breccias, respectively (Corbett and Leach 1997; Meldrum 2009). Subsequent logging of the drill core noted some breccias with textures indicative of both phreatomagmatic and hydrothermal origins. The deposit is cut by northerly trending faults, which are interpreted from satellite images to be related to the regional lineaments.

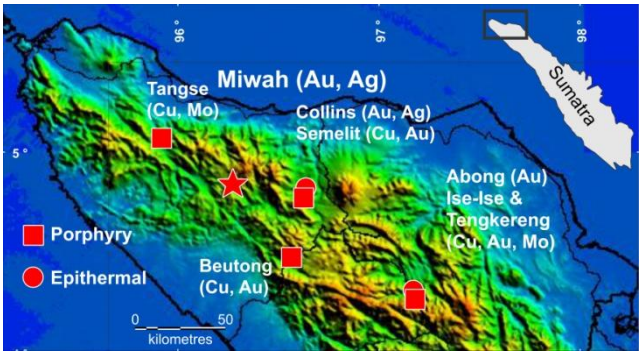


Figure 1. Location map of the Miwah deposit in Aceh, Northern Sumatra (after Mulja et al. 2003). The NW-trending fractures bisecting the Barisan orogenic belt and traversing adjacent to the mineral deposits belong to the Sumatra Transform Fault System.

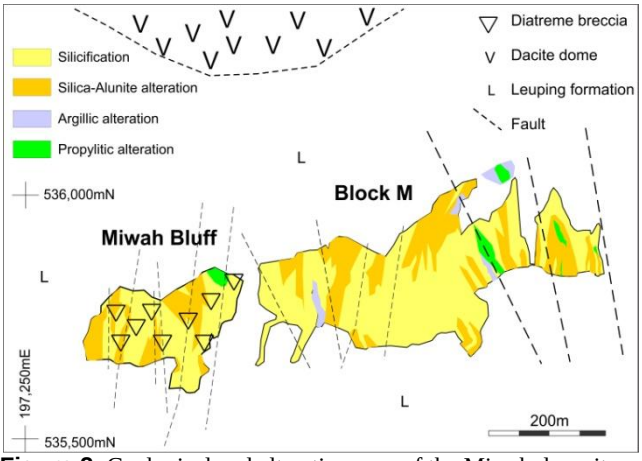


Figure 2. Geological and alteration map of the Miwah deposit (after Corbett and Leach, 1997; Taylor, 2011).

2 Alteration and mineralization

Forming a nearly horizontal body ~900m long, 300m wide, and up to 250m thick, Miwah is hosted by pervasively silicified volcanic rocks and breccias, and this alteration is dominated by vuggy (residual) silica (Fig. 3) and

subordinate massive sulphide-silica. Enclosed within this silicified rock are linear zones of silica-alunite or alunite-silica (alunite > silica; advanced argillic), many of which are associated with fractures/faults. Argillic (illite + kaolinite + smectite) and propylitic (chlorite + carbonate) alteration occur adjacent to silica-alunite zones, around the perimeters and in deeper parts of the deposit. Supergene oxidation ranges from 20 m to ~150 m.

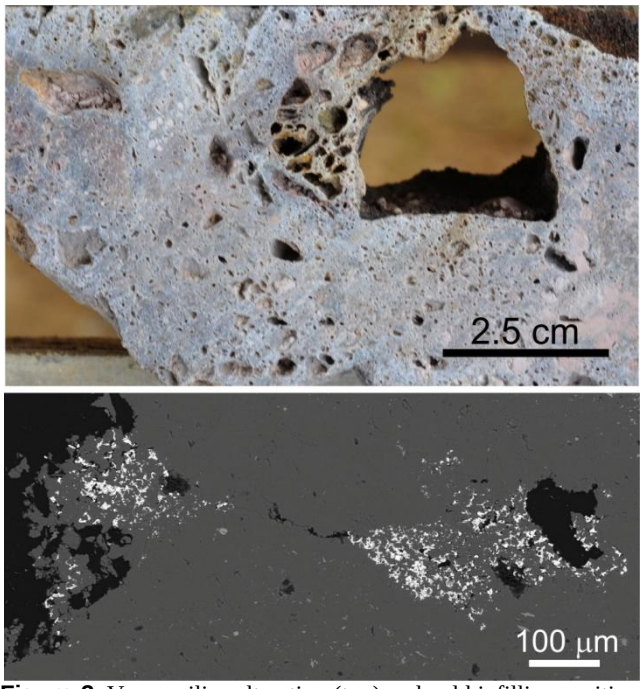


Figure 3. Vuggy silica alteration (top) and gold infilling cavities (back-scattered image, bottom).

Main stage gold mineralization developed mostly in the upper part of the vuggy silica alteration zone, where its highest grade on outcrops and cliff-walls is 23m@125 ppm Au (Fig. 5). Gold zones of various grades in the entire deposit crudely trend northerly, and many coincide with faults and breccias. In drill core, the vertical profile of gold grades displays a single spike (e.g. 20m@5.38 ppm Au) or multiple spikes with broad bases (as wide as 323m@1.34 ppm Au). Gold is correlated positively with Ag, Cu, As, Sb and Te, and negatively with Pb and Zn, which are anomalously high in silica-alunite and less commonly in argillic zones. Across the deposit the median and range of bulk rock Ag/Au is 2.6 and 0.5 to 9.5, respectively. Generally the Ag/Au, Cu/Au and As/Au values are higher in silica-alunite rocks than in the main stage auriferous zones. This decoupling of Au from Ag, Cu and As could be controlled by enargite, of which its paragenesis spans from pre- to post-gold deposition (James Clark, pers. comm). Native gold occurs as discrete and clustered grains, lining vugs and along fractures in the vuggy silica (Fig. 3). Sulphides consist mainly of pyrite, along with significant enargite in direct association with the gold mineralization, especially in the massive sulphide-silica alteration. Some refractory gold likely also occurs in sulphides as inferred by the 63-84% recovery in cyanide leach tests (Hawthorn 1997). Late-stage gold and Cu-sulphide veinlets cut the silicified rocks.

3 Statistical and geostatistical analysis

A multivariate geostatistical method was used to quantify the spatial correlation (ρ) of Au and associated metals in outcrop and drill core samples, and of Au with different rock and alteration types. These calculations were achieved with variogram and cross-variogram fitting models (for details see Heriawan et al. 2015). The dataset was differentiated into 4 domains: (1) surface (outcrop) alteration (2) surface rock types, (3) subsurface (drill core) alteration, and (4) subsurface rock types. Generally, a strong statistical correlation (r) between two elements is defined when $r > 0.70$, and this study deals only with the strongly correlated elements.

4 Results and discussion

4.1 Spatial correlations

The surficial silica and argillic zones have the highest average gold grade of 1.97 ppm and 1.87 ppm, respectively (Table 1). In most cases the latter alteration contains less than 0.05 ppm Au, and hence the highly auriferous argillized outcrop might have been overprinted by gold-bearing brines or supergene fluids. The lateral distance of influence (range) of gold zones is 350 m in the silica rocks and 300m in the argillic zone (Table 2). Among all outcrop types, the undifferentiated breccia has the highest Au mean of 1.06 ppm and its lateral range is 200 m. In drill core the silica zone contains the highest mean gold grade of 0.94 ppm and its range is 300 m and 10 m respectively in lateral and vertical directions. The average gold grade for each of the breccia subtypes is as follows (ppm Au, lateral:vertical range): undifferentiated (2.07 ppm, 350:20 m), hydrothermal (1.13 ppm, 150:15 m), and phreatomagmatic (1.06 ppm, 250:15 m). These results show that the anomalous gold mineralization is laterally segmented and that each segment is connected to a single or multiple vertical to steep feeder zones.

Table 1. Summary of gold statistics (ppm).

Geological Domain	Mean	Median	St.Dev.
A. Surface Alteration			
1. Argillic	1.87	0.38	14.56
2. Alunite Silica	0.08	0.02	0.18
3. Silica (vuggy ± sulphidized)	1.97	0.42	14.97
B. Surface Rock Types			
1. Undifferentiated Breccia	1.06	0.49	1.77
2. Phreatomagmatic Breccia	0.38	0.14	0.95
3. Hydrothermal Breccia	0.51	0.30	0.63
C. Subsurface Alteration			
1. Argillic	0.04	0.01	0.24
2. Alunite-Silica	0.07	0.03	0.14
3. Silica (vuggy ± sulphidized)	0.94	0.39	2.24
D. Subsurface Rock Types			
1. Undifferentiated Breccia	2.07	1.31	1.93

2. Fault Breccia	0.16	0.46	2.28
3. Hydrothermal Breccia	1.13	0.68	1.56
4. Phreatomagmatic Breccia	1.06	0.46	2.28

Table 2. Area of influence (range) of domains

Geological Domain	Range (m)
A. Surface Alteration	
1. Argillic	300 (Lateral)
2. Alunite-Silica	200 (Lateral)
3. Silica (vuggy ± sulphidized)	350 (Lateral)
B. Surface Rock Types	
1. Undifferentiated Breccia	200 (Lateral)
2. Phreatomagmatic Breccia	450 (Lateral)
3. Hydrothermal Breccia	300 (Lateral)
C. Subsurface Alteration	
1. Argillic	400 (Lateral)/15 (Vertical)
2. Alunite-Silica	300 (Lateral)/15 (Vertical)
3. Silica (vuggy ± sulphidized)	300 (Lateral)/10 (Vertical)
D. Subsurface Rock Types	
1. Undifferentiated Breccia	350 (Lateral)/20 (Vertical)
2. Fault Breccia	250 (Lateral)/15 (Vertical)
3. Hydrothermal Breccia	150 (Lateral)/15 (Vertical)
4. Phreatomagmatic Breccia	250 (Lateral)/15 (Vertical)

The spatial correlation (ρ) between Au and associated metals (co-variable) for each geological domain varies from 0.73 to 1 (Table 3). In general, gold displays a strong spatial correlation with Ag, Cu, As and Sb in all lithologic domains, and in the silica and silica-alunite alteration zones.

Table 3. Spatial correlation between metals in various domains.

Geological Domain	Co-variables	ρ
A. Surface Rock Types		
1. Phreatomagmatic Breccia	Au vs. As	0.90
	Au vs. Cu	0.74
B. Subsurface Alteration		
2. Alunite Silica	Au vs. As	0.90
	Au vs. Sb	0.98
3. Silica (vuggy ± sulphidized)	Au vs. Ag	0.94
	Au vs. Sb	1.00
C. Subsurface Rock Types		
1. Phreatomagmatic Breccia	Au vs. Ag	0.94
2. Fault Breccia	Au vs. Ag	0.99
	Au vs. As	0.86
	Au vs. Cu	0.80
	Au vs. Sb	1.00
3. Hydrothermal Breccia	Au vs. Ag	0.97
	Au vs. As	0.99
	Au vs. Cu	0.98

4.2 Hypothetical Miwah plumbing networks

The phreatomagmatic breccias of the Miwah Bluff and Block M indicate that the Miwah Hill is a remnant of a single- or multiple-vent maar-diatreme volcano. Such volcanogenic precious and base-metal deposits develop through hydrothermal processes related to sub-volcanic intrusions (e.g., Sillitoe 1985; Corbett and Leach 1997): the latter authors hypothesized a concealed porphyritic stock between Miwah and the dacite dome in the north to drive the mineralizing fluids (Fig. 2). Based on the above concept, recent advances in gold geochemistry, and the data in the preceding sections, we envisage SO_2-, H_2S- and HCl-rich vapours carrying Au, Ag, Cu and As as sulphide or chloride complexes (see Williams-Jones and Heinrich 2005; Zezin et al. 2011; Hurtig and Williams-Jones 2014) exsolved from magmatic-hydrothermal brines at some depth in a maar-diatreme volcano. These vapours ascended via fractures and breccias (feeder zones; Fig. 4) to reach a certain level where they condensed, or contracted, to become highly acidic fluids, which leached and altered the Leuping volcanic rocks and breccias into vuggy silica and advanced argillic zones. Either contemporaneously, or immediately after these alteration processes, gold precipitated mainly in the vugs, and together with Cu-As and other sulphide minerals, in the massive sulphide-silica rocks, and less commonly in the advanced argillic zones. Alternatively, the early volatiles may not have been the cause of mineralization, but rather became highly acidic fluids upon mixing with groundwater (at or above the paleo-water table), which then induced silicification and advanced argillic alteration (cf. Hedenquist et al. 2000). Subsequent metal-bearing fluids would have then risen along the feeder zones, and upon cooling and mixing with groundwater, precipitated gold and sulphide minerals in the silica and silica-alunite rocks. In either model, the early acidic fluids evolved by fluid-rock interaction towards higher pH and lower temperature residual liquids that further migrated laterally from the silica center to produce argillic and propylitic alteration along the margins. Repeated incursions of the vapours/brines developed additional individual gold zones along major fractures, as well as multiple gold horizons along previously-formed mineralized structures. Many earlier-formed feeder zones must have been completely sealed during the up-welling of successive brines. These one-time conduits are reflected in solitary gold horizons. Should the proposed maar-diatreme volcano setting for Miwah be proven correct, then similar gold deposits could exist nearby as these types of volcanoes tend to occur in clusters (Ross et al. 2017).

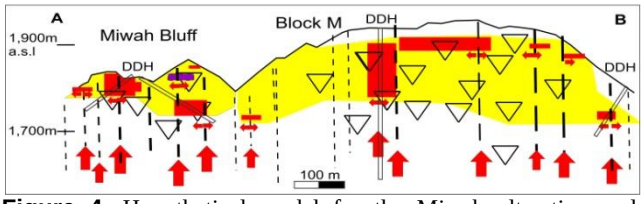


Figure 4. Hypothetical model for the Miwah alteration and mineralization illustrate the ascending vapours and fluids along fractures and breccias (feeder zones). Notes: purple: > 5 ppm Au; red: 1 - 4.9 ppm Au; yellow: drill-delineated deposit area.

5 Conclusions

The Miwah gold deposit displays typical geological, vuggy silica and silica-alunite alteration, and metal association

(Au, Ag, Cu, As, Sb) characteristics similar to its volcanogenic acid-sulphate epithermal counterparts developed elsewhere (e.g., Corbett, 2013). The spatial continuity of gold mineralization at Miwah, with auriferous zones ranging from 150 to 350 m long, is controlled by the local hydrologic regime and lithologies to produce the tabular deposit, and by fractures and breccias as conduits for the ascending brines, which subsequently became high-grade gold feeder zones. With the exception of minor faulting, supergene oxidation and erosion, the deposit appears to have remained intact since its formation. The multivariate statistical method employed in this study, particularly the domain (lithology, alteration, mineralization) and range (distance of influence) analyses, is effective to predict the probable lateral and vertical extents of gold mineralization.

Acknowledgements

This research was funded by East Asia Minerals Ltd. under a collaborative agreement between the company and the first author. We thank James Clark of McGill University for his constructive review on early drafts of this extended abstract. Comments by the editor and reviewer are appreciated.

References

Corbett G (2013) Pacific Rim Au-Ag, World Gold Conference, Brisbane, Australian Institute of Mining and Metallurgy, 14 p

Corbett G, Leach T (1997) High sulfidation gold-copper systems. In: Southwest Pacific rim gold-copper systems: Structure, alteration and mineralization. Short course manual, pp. 95-118

East Asia Minerals Ltd. Press release May 9, 2011

Hawthorn G (1997) Mineral process testing, Miwah gold-copper deposit, Indonesia. Colony Pacific Explorations Ltd. 34 p.

Hedenquist JW, Arribas JrA, Gonzalez-Uren E (2000) Exploration for epithermal gold deposits, Rev Econ Geol 13:245-277.

Heriawan MN, Sirait J, Margianto D, Wibawa RR (2015) Resources estimation of gold vein deposit using multivariate geostatistical method, Proceedings of International Symposium on Earth Science and Technology 2015, Fukuoka, Japan

Hurtig NC, Williams-Jones AE (2014) An experimental study of the transport of gold through hydration of AuCl in aqueous vapour and vapour-like fluids. Geochimica et Cosmochimica Acta 127: 305-325

Meldrum SJ (2009) Miwah High Sulphidation Epithermal Gold Complex, Aceh Province, Indonesia, unpublished report, 10 December 2009

Mulja T, Collins M, Wong HH, Rizal R, Brown T, Zainuddin M. (2003) An integrated mineral exploration programme in the Takengon tenement, Aceh magmatic arc, north Sumatra. Geochemistry: Exploration, Environment, Analysis 16: 321-335

Ross PS, Núñez GC, Hayman P (2017) Felsic maar-diatreme volcanoes: a review. Bull Volcanol 79:1-20

Sillitoe RH (1985) Ore-related breccias in volcanoplutonic arcs. Econ Geol 80:1467-1514

Taylor I (2011) A technical report on exploration and resource estimation of the Miwah project, Sumatra, Indonesia. Mining Associates Pty Ltd., Australia

Williams-Jones AE, Heinrich CA (2005) Vapor transport of metals and the formation of magmatic-hydrothermal ore deposits. Econ Geol 100:1287-1312

Williamson A, Fleming GJ (1995) Miwah prospect high sulphidation Au-Cu mineralisation, northern Sumatra, Indonesia. PACRIM '95: 637-642

Zezin DY, Migdisov AA, Williams-Jones AE (2011) The solubility of gold in H_2O-H_2S vapour at elevated temperature and pressure. Geochimica et Cosmochimica Acta 71: 3070-3081

The Otanmäki rare metal (Nb, Zr, REE) mineralization, central Finland

Kimmo Kärenlampi, Holger Paulick, Eero Hanski
University of Oulu, Finland

Esa Pohjolainen, Asko Kontinen, Hannu Huhma
Geological Survey of Finland

Jouko Jylänki
Otanmäki Mine Oy, Finland

Abstract. The Otanmäki rare metal mineralization is confined to silicified alteration zones within a 2.05 Ga A-type monzogranite gneiss. The mineralized zones range from 0.1-12 m in thickness and host allanite, fergusonite(-Y), yttropyrochlore(-Y), ferrocolumbite and zircon. The ore minerals are associated with brittle microfractures developed in the altered zones in the host granite. They are generally associated with fluorite and calcite, suggesting that HFSE (e.g., Zr, Nb, U, Th) and REE (e.g., La, Ce, Dy, Y) were transported in hydrothermal solutions complexed with the hard ligands F^- and CO_3^{2-}. In-situ laser ablation U-Pb isotope dating of the mineralization has given dates scattering between 1.95 and 1.85 Ga, implying that their formation possibly significantly postdates the formation of the host granite. Alternatively, the age variation may indicate resetting of zircon in mineralized rocks by tectono-thermal overprinting during the Svecofennian orogeny (1.9 to 1.8 Ga), suggesting the possibility that the mineralization is primarily magmatic-hydrothermal in origin and related to the 2.05 Ga A-type magmatism.

1 Introduction

Glacial boulders with elevated contents of U and Th were found in the Otanmäki area during ground follow up of aeroradiometric anomalies in 1981 (Äikäs 1990). These were tracked up to their bedrock sources in 1982, which led to the discovery of the Otanmäki rare metal (Nb, Zr, REE) occurrences. Drilling campaigns carried out by the mining company Rautaruukki in 1983-1985 outlined two deposits: Katajakangas and Kontioaho, located within 1 km of each other. According to preliminary mineral resource estimates, the Katajakangas deposit contains 0.46 Mt (million tonnes) at 2.7 wt% TREO (incl. Y_2O_3 and excl. Sc_2O_3), 0.76 wt% Nb_2O_5, and 1.13 wt% ZrO_2 (Hugg 1985a), while the Kontioaho deposit resources are estimated to be 4 Mt at 0.68 wt% TREO, 0.12 wt% Nb_2O_5 and 2.8 wt% ZrO_2 (Hugg 1985b).

In this paper, we provide preliminary descriptions of the geological setting and mineralogical, geochemical and textural characteristics of the rare metal mineralization based on field, petrographic and drill core studies conducted in 2016. U-Pb radiometric dating of the mineralization and its immediate wall-rock suite were performed using the in-situ laser ablation method (SC-ICP-MS).

2 Geological background

The Otanmäki complex, that hosts the mineralization, is located in the Archean Karelian Province, just 20 km east from the NE boundary of the Paleoproterotzoic Svecofennian terrane. The complex consists of a suite of 2050 Ma A-type granitoids (Otanmäki Granitoid Suite; OGS), such as peralkaline-metaluminous alkali feldspar granite and syenite, and peraluminous monzogranite. The granitoids were strongly deformed during the Svecofennian orogeny (1900–1800 Ma), resulting in gneissose structures and blastomylonite textures. The Otanmäki complex is fault-bound between the Archean Manamansalo and Iisalmi TTG-gneiss complexes (Hölttä et al. 2012; Kontinen et al. 2013). Also, in the south, it has a fault-defined contact with a 2065 Ma gabbro-anorthosite intrusion hosting numerous lenses of massive-disseminated Fe-Ti-V-oxide ore (Talvitie and Paarma 1980).

3 Rare metal mineralization

3.1 Geological setting

The mineralization consist of schistosity-concordant, subhorizontal, silica-rich, alkali- and alumina-depleted veins (silicified zones) in a fine-grained, pervasively foliated monzogranite, with K-feldspar, plagioclase (An_{30}), quartz, and biotite (annite) as the main mineral constituents. Accessory minerals include titanite, zircon, allanite, muscovite, and spotty to finely disseminated magnetite. The host granite shows little variation in appearance, having generally a pinkish-grey color and occasionally containing zones rich in K-feldspar porphyroblasts. Microstructures of the granite indicate that it underwent a strong early dynamic recrystallization, overprinted later by static recrystallization. However, in places, protomylonite zones do occur, implying localized movements during late stages of metamorphism.

The host granite forms a triangle-shaped, 16 km^2 block, flanked in the north by evolved, peralkaline aegirine-granites (Fig. 1), which, on average, contain 1500 ppm TREE+Y, 1400 ppm Zr, and 270 ppm Nb. The host monzogranite carries slivers of metaturbidite composed of alternating mica-schist and quartz-rich metapsammite interlayers. In the contacts between the metasediments and

granite occur thin calc-silicate reaction zones with quartz, biotite, epidote, amphibole, and garnet representing possibly primary but metamorphosed intrusive contacts. The mica schists contain garnet and staurolite porphyroblasts ± fibrolitic sillimanite, indicating amphibolite facies conditions of metamorphism. In addition, the granite and the metasedimentary slivers both contain sharply bound, 3- to 15-m-thick amphibolite layers. These are dikes with fine-grained margins, coarser central parts, and locally also apophyses.

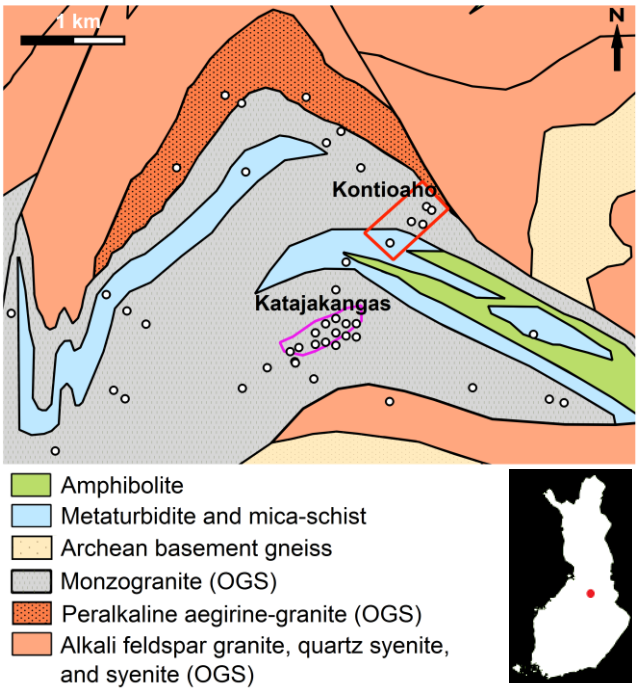


Figure 1. Simplified geological map of a triangle-shaped monzogranite block located within the Otanmäki complex, showing locations of drill holes (white circles) and the rare metal deposits. Minimap of Finland shows the location of Otanmäki.

The host granite has a peraluminous, ferroan rhyodacite composition with 67–72 wt% SiO_2, elevated HFSE and REE (350 ppm Zr, 40 ppm Nb, 340 ppm TREE+Y), LREE-enriched OIB-type chondrite-normalized REE patterns and moderate negative Eu anomalies. Samples are classified as within-plate and rift-related (A_1-type) A-type granitoids in the trace element discrimination plots of Pearce et al. (1984), Whalen et al. (1987) and Eby (1992). LA-SC-ICP-MS analyses on best-preserved zircon domains yielded an age of 2055 ± 8 Ma, interpreted to be the magmatic crystallization age of the granite. The obtained zircon age, field relationships, and textural information (e.g., fine grain size) suggest that the emplacement of the granite took place at a shallow crustal level. The granitic body seems to represent a hypabyssal variant of the A-type magmatism of the OGS, which was previously dated at 2050 Ma using a sample of peralkaline granite (Kontinen et al. 2013).

3.2 Katajakangas

The Katajakangas deposit is confined to strongly silicified and mineralized zones 0.1–1.4 m in thickness, which represent strongly altered granite. Sharp contacts are typically observed between the typically pinkish-grey host granite and greenish-grey mineralized zones.

The main minerals in the mineralized zones are quartz and allanite, accompanied by variable amounts of biotite, pyrite, calcite, fluorite, zircon, muscovite, fergusonite-(Y), ferrocolumbite, pyrrhotite, magnetite, yttropyrochlore-(Y), K-feldspar, ilmenorutile, manganoan ilmenite, titanite, and chalcopyrite (Fig. 2). Ferrocolumbite, fergusonite-(Y), and yttropyrochlore-(Y) are the major carriers of Nb and Ta, whereas HREE were incorporated into fergusonite-(Y), LREE in allanite, Y in fergusonite-(Y) and yttropyrochlore-(Y), and Zr in zircon. Fergusonite-(Y) and yttropyrochlore-(Y) are the dominant hosts to U, whereas Th occurs in allanite and fergusonite-(Y). The mineralized zones contain up to 470 ppm U and 1100 ppm Th.

Plagioclase is absent in the mineralized zones and is scarce in the immediate wall rocks. Some K-feldspar is variably present, but quartz is the dominant gangue mineral in the highly altered zones. Some of these mineralized zones might also represent quartz veins which were later affected by mineralizing fluids. Quartz is typically corroded and replaced by calcite and ore minerals, showing that it predates the ore formation. This is also indicated by the fact that quartz grains do not contain ore minerals as inclusions. Also, quartz grains in the mineralized zones are characterized by abundant brittle fractures, that are filled by the major ore and associated minerals (e.g., calcite, biotite). Brittle fractures are not present in ore minerals or calcite precipitated from ore-forming solutions, indicating that these minerals precipitated subsequent to late brittle fracturing.

The main LREE-bearing mineral, allanite, occurs predominantly as metamict crystals, being typically 20–200 µm but occasionally up to 500 µm in size. Volume increase and swelling of allanite due to metamictization has resulted in radial cracks in surrounding quartz grains. Fergusonite-(Y), typically 5–50 µm in size, is the dominant host to HREE. Ferrocolumbite is typically 5–100 µm in size and compositionally homogeneous.

Yttropyrochlore-(Y), typically 5–100 µm in size, is compositionally heterogeneous, with the abundances of Y, Ca, Ti, Ta and U being particularly variable. Crystals show discontinuous compositional zoning with abrupt changes in compositions between cores and rims. Variation in the temperature, pressure, and composition of parent fluids is also reflected by the differences in the compositions of cores and rims of yttropyrochlore and fergusonite crystals.

Zircon is abundant and occurs typically as spherical to ovoidal grains 5–50 µm in size. U-Pb dating of zircon grains (~90 analysis spots) in polished thin sections by laser ablation SC-ICP-MS yielded highly variable results. Obvious hydrothermal grains give dates scattering between 1.95 and 1.85 Ga, suggesting that the mineralization was related to repeated fluid flux events.

However, as a similar age variation is common in altered zircon domains of non-mineralized OGS rocks, this variation in ages may rather be related to alteration by Svecofennian tectono-thermal processes and related hydrothermal activity.

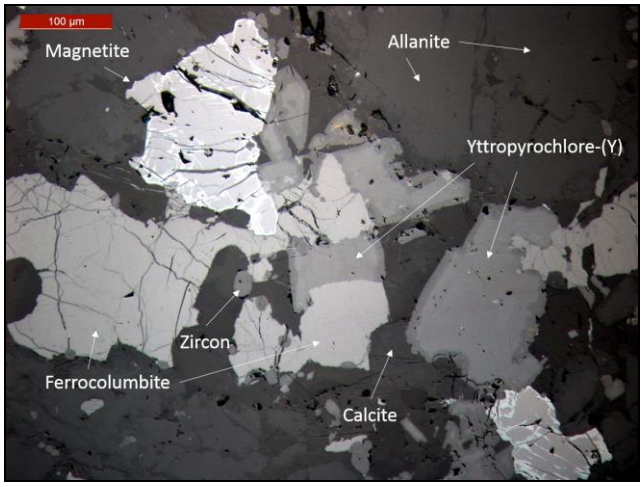


Figure 2. Some of the main ore minerals in the Katajakangas Nb-REE ore under reflected light. Sample KAT-012-1, drill core Katajakangas 12, depth: 31.80 m.

3.3 Kontioaho

The Kontioaho deposit represents a more diffusive type of rare metal mineralization distributed over a wider zone when compared to the highly concentrated set of veins at Katajakangas. The mineralization at Kontioaho is manifested as brownish to reddish zones that contain fine-grained, greenish-grey bands composed of rare metal-bearing minerals (Fig. 3). The footwall contact to the host granite is relatively sharp, whereas the hanging wall contact is gradational. The maximum thickness of the mineralized zone is 30 m, in which the highest-grade mineralization is 7 to 12 m in thickness.

The mineralized zones are mostly composed of fine-grained quartz-K-feldspar mosaic, which was derived by alteration of the host granite, adding quartz and removing plagioclase and biotite. Finely disseminated magnetite crystals occur throughout the mineralization, partly as a relict phase and partly as newly grown grains. K-feldspar crystals occur as tabular-blocky, variably rounded and corroded-looking crystals, but occasionally as rounded inclusions in quartz. Quartz crystals are anhedral, with irregular boundaries, and highly variable size. The mineralized zones are intensively cut by 1- to 5-cm-thick quartz veins/quartz-rich bands (or silicified seams) and rarely by pure quartz veins 30–80 cm in thickness.

Allanite and zircon are the major ore minerals and carriers of LREE, Th and Zr. Titanite is also present and it carries minor Nb, LREE and Y. Fergusonite-Y and/or yttropyrochlore-(Y) occur in minor amounts and contain highly variable amounts of HREE, Y, Nb and U. In addition, some minor LREE-fluorocarbonate occurs together with allanite.

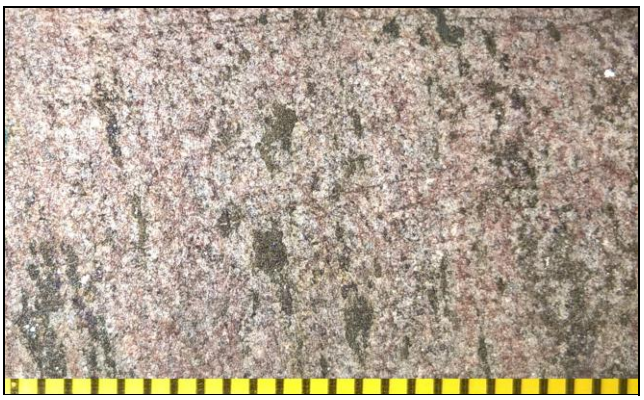


Figure 3. Drill core sample of Kontioaho ore. Sample 116-KA-R3-198.46m, drill core Kontioaho-3, depth: 198.46m. Scale bar in millimeters.

The ore minerals are associated with microfractures and fluorite-filled seams or veins, which cut and seem to have brecciated the quartz-K-feldspar mosaic (Fig. 4) and the quartz-rich veins/bands. Quartz and K-feldspar crystal fragments enclosed by fluorite are rounded and seem corroded, and occasionally have been replaced by minerals precipitated from ore forming solutions. The main ore minerals are never found as inclusions in quartz or K-feldspar. The mineralized microfractures also contain biotite and calcite, and occasionally abundant calcium-rich garnet (andradite), epidote, and amphibole, all clearly restricted to the microfractured zones. Brittle fracturing is not present in ore minerals and associated minerals in the microfractures.

The mineralizing fluid appears to have channeled along networks of predominantly schistosity-condordant microfractures, which can be fully or partially filled by ore minerals and/or fluorite. The density of microfractures in the mineralized zones seems to have had some control on the degree of mineralization. Sparsely spaced, ultrathin microfractures are only associated with the growth of bands or disseminations of ore minerals, while networks of interconnected fractures are associated with abundant allanite, zircon, and fluorite. In addition, quartz-rich mineralogical domains tend to be more fractured and more mineralized.

Allanite occurs as euhedral, metamict crystals 20–100 µm in size, forming bands and disseminations. Occasionally, allanite occurs with quartz in cm-sized lenses, which resemble the Katajakangas mineralization. Zircon crystals range from small roundish crystals 10–60 µm in size, to clusters of euhedral, up to 200-µm-sized grains. They are generally strongly metamict, though occasionally have non-metamict rims grown on strongly metamict cores, pointing to different growth periods or changes in fluid composition. Titanite can make up 5–10 vol% of the mineralized rock as subhedral grains that are 50–500 µm in size and are usually aggregated together with other ore minerals, especially zircon. Results of microprobe analyses show that titanite contains on average 2.04 wt% Nb_2O_5, 1.20 wt% LREO (La, Ce, Pr, Nd) and 1.04 wt% Y_2O_3.

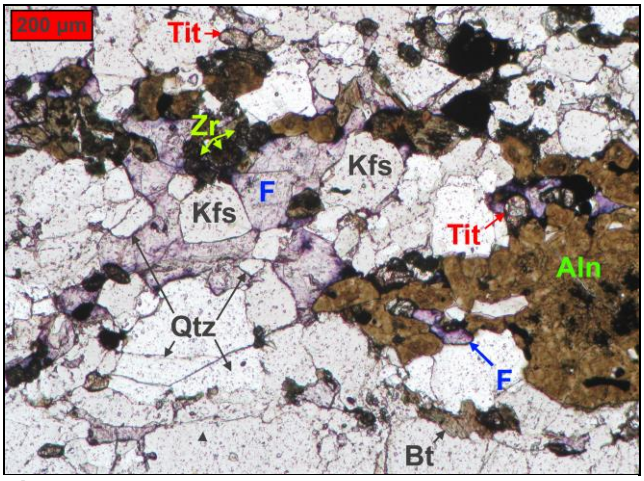


Figure 4. Main ore minerals in the Kontioaho ore under plane polarized light. Sample KA-R3-188.23 m, drill core Kontioaho-3, depth: 188.23 m. Mineral abbreviations: Aln=allanite, Bt=biotite F=fluorite, Kfs=K-feldspar, Qtz=quartz, Tit=titanite and Zr=zircon.

4 Discussion

The Otanmäki rare metal mineralization is composed of two types of deposits: 1) highly concentrated occurrences of Nb-Zr-REE in microfractures in strongly silicified zones that are rich in allanite, zircon, and Nb-Y-U oxides, and 2) wider, more diffuse occurrences of Nb-Zr-REE mineralization in microfractures filled with fluorite, allanite, and zircon, developed in partially silicified quartz-K-feldspar-rich zones.

The characteristics of the Otanmäki rare metal deposits suggest the mineralization originated from F-CO_2-H_2O-REE-HFSE-enriched hydrothermal solutions channeled into brittle microfractures in previously silicified, altered zones in a 2.05 Ga biotite monzogranite host. This scenario would imply that the mineralizing fluid was introduced to the altered zones under low-T metamorphic conditions (<300 °C), in the regime of brittle fracturing of quartz. Thus, the observed microfractures must be late in relation to orogenic events, perhaps 1.8 Ga in age or even younger. The Otanmäki complex underwent its main metamorphism and deformation phases between 1.8 and 1.9 Ga in relatively high peak-metamorphic temperature (>500 °C). Therefore, all lower temperature microstructures, that predate the peak-T metamorphic conditions have been strongly overprinted.

It is uncertain whether the formation of the mineralization and silicification represent simultaneous or separate events. Simultaneous formation could be related to the highly fractionated, fluorine- and rare metal-enriched peralkaline aegirine-granites of the OGS. The aegirine-granites seem to have intrusive, but metamorphosed, contacts against the host monzogranite, and they contain zones of narrow veins/dykes of pegmatoidal quartz, K-feldspar, amphibole, and occasional coarse quartz, fluorite and calcite veins. Microscopic studies also indicate that the aegirine-granites are characterized by abundant, small (5-50 µm in diameter), spherical zircon crystals and intergranular fluorite associated with thin veins of REE-bearing phases, suggesting high mobility and enrichment of volatiles, REE, and HFSE. If the mineralized zones represent primary, ca. 2050 Ma hydrothermal metasomatism caused by late-stage magmatic hydrothermal fluids injected into to the monzogranite, they must have been strongly overprinted by Svecofennian metamorphism. This makes it challenging to explain the brittle microfractures that were infiltrated by injections of F-rich fluid. However, it may also be considered that the primary mineralization may have been affected by metamorphic fluid flow during Svecofennian metamorphism, resulting in remobilization of fluorine, CO_2, REE, and HFSE by dissolution and precipitation mechanisms at low temperatures, perhaps in relatively young brittle microfractured zones developed during the waning stages of the metamorphism. Also, there is a possibility that the overprinted and remobilized primary mineralization is masked by young microfractures, which may also have been formed due to radiation damage caused by U-Th-bearing ore minerals, and that the microfractures ultimately had no association with the mineralizing processes.

5 Acknowledgements

This study is part of PhD project of Kimmo Kärenlampi supported by the K.H. Renlund Foundation, the Tauno Tönning Foundation, and the Geological Survey of Finland's SEXUM project funded by the Academy of Finland. The Otanmäki Mine Oy (www.otanmaki.fi) has provided material and logistical assistance during the study.

6 References

Eby GN (1992) Chemical subdivision of the A-type granitoids: Petrogenetic and tectonic implications: Geology 20: 641–644

Hugg R (1985a) Katajakangas. Geological mineral resource estimate. Rautaruukki Oy Exploration, Report OU 12/85 (in Finnish)

Hugg R (1985b) Kontioaho. Geological mineral resource estimate. Rautaruukki Oy Exploration, Report OU 11/85 (in Finnish)

Hölttä P, Heilimo E, Huhma H, Juopperi H, Kontinen A, Konnunaho H, Lauri L, Mikkola P, Paavola J, Sorjonen-Ward P (2012) Archaean complexes of the Karelia Province in Finland. Geological Survey of Finland, Special Paper 54: 9−20

Kontinen A, Huhma H, Lahaye Y, O'Brien H (2013) New U-Pb zircon age, Sm-Nd Isotope and geochemical data on Proterozoic granitic rocks in the area west of the Oulunjärvi Lake, Central Finland. In: Hölttä P (ed) Geological Survey of Finland, Report of Investigation 198: 70–74

Pearce JA, Harris NBW, Tindle AG (1984) Trace element discrimination diagrams for the tectonic interpretation of granitic rocks: Journal of Petrology, v. 25: 956–983

Whalen JB, Currie KL, Chappell BW (1987) A-type granites: geochemical characteristics, discrimination and petrogenesis. Contributions to Mineralogy and Petrology 95: 407–419

Äikäs O (1990) Thorium and niobium-lanthanide ore prospects in Otanmäki, Vuolijoki municipality. GTK, Report M19/3431/-90/1/6 (in Finnish)

Paragenetic constraints on hydrothermal origin of xenotime mineralization in the Maw Zone REE deposit, Athabasca Basin, Canada

Morteza Rabiei, Guoxiang Chi
University of Regina, Saskatchewan, Canada

Charles Normand
Saskatchewan Geological Survey, Canada

Abstract. The Maw Zone REE mineralization represents one of the largest HREE and yttrium (Y) deposits in the Athabasca Basin. The mineralization is hosted by a vertical brecciated zone in sandstone of the Manitou Falls Formation. This deposit was subjected to different generations of silicification, tourmalinization and hematitization. The tourmaline alteration is divided into three generations labelled as A, B and C. Generation A is coeval with syntaxial quartz in the sandstone. Generation B followed generation A, where it filled open spaces between detrital grains and formed aggregates and cement in breccia. Generation C is locally developed within drusy quartz near the centre of veins. Xenotime is associated with tourmaline B and postdates major compaction in the host sandstone. These observations, together with fluid inclusion microthermometric data, indicate that the xenotime in the Maw Zone area was not formed during early diagenesis, but is rather of hydrothermal origin. This is further supported by the paragenetic similarities between the Maw Zone and unconformity-related uranium deposits in the region, which formed from hydrothermal fluids.

1 Introduction

Xenotime occurrences in the Athabasca Basin comprise two major categories: diagenetic (e.g. Rainbird et al. 2003; Davis et al. 2008) and hydrothermal (e.g. Quirt et al. 1991; Fayek and Kyser 1997; Rabiei et al. 2015). Diagenetic xenotime in the basin mostly occurs as replacement rims and topotactic overgrowths around detrital zircon and is dispersed in the sandstone and in the alteration haloes around unconformity-related uranium (URU) deposits (Fayek and Kyser 1997; Rainbird et al. 2003; Davis et al. 2008). In contrast to the widespread occurrence of overgrowth xenotime, crystalline xenotime aggregates have only been found in a few places, including the Maw Zone deposit (Quirt et al. 1991; Normand 2014; Rabiei et al. 2015).

The Maw Zone deposit, which represents one of the largest heavy rare earth element (HREE) and Y concentrations inside the Athabasca Basin, contains a pre-NI 43-101-compliant resource estimated at 462 664 tonnes of ores averaging 0.21% Y_2O_3, mainly occurring as xenotime (Normand 2014). This deposit is located at the southeastern corner of the basin, between the Key Lake and McArthur River uranium deposits. Several previous studies have been carried out on the Maw Zone deposit, with the aim of understanding the genetic relationship between this deposit and the URUs in the region (Quirt et al. 1991; Hanly 2001; Rabiei et al. 2015). However, a detailed paragenetic study of the Maw Zone deposit, especially with respect to the timing of xenotime deposition relative to silicification and tourmalinization, is necessary. Such a study is also essential for determining the diagenetic versus hydrothermal nature of the xenotime mineralization.

2 Geological setting

The Maw Zone area is characterized by variably brecciated and silicified sandstones of the Manitou Falls Formation. The Manitou Falls Formation in the area is divided into, from bottom to top, the Bird member (MFb), the Collins member (MFc) and the Dunlop member (MFd), and is underlain by the Read Formation which overlies the basement (Kerr 2010). The Maw Zone REE deposit is hosted by a pipe-like brecciated zone, and xenotime mineralization is mainly developed in the Dunlop member, extending from approximately 130 m above the unconformity to the surface. The Dunlop member is characterized by quartz arenite with more than 1% clay intraclasts (Ramaekers et al. 2007).

The Maw Zone deposit is located within a regional alteration corridor of illite, kaolinite and tourmaline, as defined by Earle and Sopuck (1989), which encompasses several world-class URU deposits in the southeastern part of the Athabasca Basin. Extensive silicification and hematitization, and locally developed light green tourmalinization are easily identifiable in the field and in hand samples. The intensity of the alteration (particularly tourmalinization) is proportional to the intensity of brecciation and fracturing (Barker 2007). The breccias are mostly fragment-supported and are generally characterized by variably sized, subangular fragments.

3 Petrography and paragenesis

In the Maw Zone area, the predominant detrital minerals are quartz with minor muscovite, hematite, and zircon. The quartz grains are generally rounded and measure typically less than 1 mm in diameter.

Early diagenetic stages are represented by quartz

overgrowths, which generally contain iron oxides. This generation of syntaxial quartz is not intergrown with tourmaline and predates tourmalinization. The second generation of syntaxial quartz is coeval with the beginning of hydrothermal tourmalinization and is much more common than the first (Fig. 1a). Two major modes of drusy quartz can be distinguished in the Maw Zone area: drusy quartz that grew in crystallographic continuity with the second generation of syntaxial quartz and drusy quartz that nucleated directly on the walls of fractures without evidence of topotaxy (Fig. 1c). Drusy quartz in both types protrudes into open spaces and forms veins and breccia cement (Fig. 1c).

Tourmaline in the Maw Zone deposit, which is compositionally classified as magnesiofoitite (O'Connell et al. 2015; Rabiei et al. 2015), is grouped into three different generations, A, B and C, based on their paragenetic position, crystal habit and mineral associations (Fig. 1). These three generations of tourmaline formed during an uninterrupted process and we cannot define temporal boundaries between them. The earliest generation, A, comprises tourmaline that co-precipitated with the second generation of syntaxial quartz (Figs. 1a and c). The formation of tourmaline A was followed by that of tourmaline B, which is much more abundant and occurs as rims on detrital quartz grains (Figs. 1b and c), as cement for breccia, and as aggregates filling open spaces (Figs. 1b and c). The occurrence of tourmaline C is much more restricted than the earlier generations and forms intergrowths with drusy quartz (Figs. 1a and c).

Another mineral phase that developed pervasively in the area is hematite. In addition to rounded detrital hematite grains, several generations of diagenetic and hydrothermal hematite can be recognized in this area. The earliest generation consists of flakes of hematite (H1) riming detrital quartz and is spatially associated with the early phase of syntaxial quartz. The second generation of hematite, H2, is the most pervasive one and is coeval with the formation of tourmaline B. Similar to tourmaline B, H2 occupies open spaces between brecciated sandstone fragments and detrital quartz grains. The latest generation of hematite (H3) partially fills open spaces and crosscuts previously formed alterations and fractures.

Xenotime is the main ore mineral and rarely occurs in concentrations visible with the naked eye. However, where local concentrations of xenotime occur, the aggregates consist of micron-scale xenotime crystals that replace detrital quartz grains and fill the open spaces between them (Fig. 1). These xenotime crystals are coeval with tourmaline B (Fig. 1b). In xenotime-rich patches, the detrital quartz grains exhibit float textures which might be interpreted to suggest that the xenotime mineralization took place during early diagenesis (before significant compaction). However, counting the number of detrital quartz grains in areas inside and outside of the mineralized patches along single bedding intervals reveals that the number of detrital grains per view area is similar in both mineralized and unmineralized areas. This indicates that mineralization occurred by replacement of the detrital quartz grains after major compaction in this part of the basin.

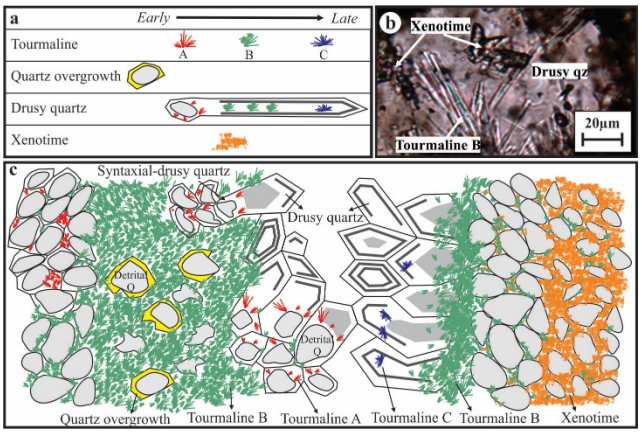


Figure 1. a Schematic paragenetic sequence of xenotime, diagenetic quartz overgrowths, drusy quartz and tourmaline. **b** Co-precipitation of stage B tourmaline and xenotime within an early phase of the drusy quartz. **c** Occurrences and crosscutting relationships of tourmaline, drusy quartz and xenotime.

4 Constraints on the hydrothermal origin of the xenotime

The xenotime in the Maw Zone deposit is interpreted to be of hydrothermal origin, based on three considerations: 1) petrographic studies suggesting replacement of sandstone by xenotime after significant compaction, as described above; 2) the similarities between the alteration associated with xenotime and those found in the URUs, and 3) geochronological and fluid inclusion data documented in other studies, as discussed below.

A detailed comparison between the paragenetic sequence in the Maw Zone deposit and the McArthur River uranium deposit (Derome et al. 2005) indicates remarkable similarity in their paragenetic histories, suggesting that they shared a similar paragenetic evolution. The predominant species of the tourmaline-supergroup mineral in both the Maw Zone REE deposit and in the McArthur River uranium deposit is magnesiofoitite in both cases. Tourmaline A in the Maw Zone deposit corresponds to tourmaline 1 of Derome et al. (2005) in the McArthur River deposit, which coexists with a phase of quartz that is interpreted to have formed by percolation of diagenetic fluids (Derome et al. 2005). Tourmaline B in the Maw Zone deposit is similar to the tourmaline 1 of Kotzer and Kyser (1995) and the tourmaline 2 of Derome et al. (2005) in the McArthur River deposit. In the McArthur River deposit, this phase of tourmaline is paragenetically associated with illite, Al-Mg-chlorite, hematite and varying amounts of uranium minerals (Kotzer and Kyser 1995; Derome et al. 2005). Considering that the URU deposits were formed through hydrothermal processes, it may be inferred that xenotime mineralization in the Maw Zone

deposit also originated from a hydrothermal fluid that may have shared part of the history of the URU mineralizing systems.

Recent geochemical studies (Rabiei et al. 2015 and in review) also support the hydrothermal origin of the xenotime mineralization in the Maw Zone deposit. SHRIMP U-Pb dating of xenotime yielded a $^{207}Pb/^{206}Pb$ age of 1547±14 Ma (Rabiei et al. in review), which is much younger than the host rocks (>1660 Ma; Rayner et al. 2003), confirming that the xenotime mineralization did not take place during early diagenesis. This age also corresponds to the ages of uranium mineralization in the southeastern part of the Athabasca Basin (Alexandre et al. 2009), further strengthening the inference that the xenotime mineralization in the Maw Zone area has a genetic link with the URU mineralization systems. This conclusion is also supported by the homogenization temperatures of fluid inclusions and the fluid temperatures estimated from the quartz-tourmaline oxygen isotope geothermometry, which range from 63° to 337°C.

Acknowledgements

This study was supported by the Saskatchewan Ministry of the Economy and a Natural Sciences and Engineering Research Council (NSERC) Discovery grant to Normand and in part by an NSERC Discovery grant to Chi. Zenghua Li and Kewen Wang are thanked for their assistance in the fieldwork, and Ken Ashton is thanked for help in core examination and discussion. Mostafa Fayek, William J. Davis and Nigel Blamey, who were involved in the isotopic and fluid inclusion studies, are thanked for their contributions. We are grateful to Denison Mines for accommodation during our fieldwork.

References

Alexandre P, Kyser K, Thomas D, Polito P, Marlat J (2009) Geochronology of unconformity-related uranium deposits in the Athabasca Basin, Saskatchewan, Canada and their integration in the evolution of the basin. Mineral Deposita 44:41–59

Barker M (2007) Structural analysis of the Maw zone: a sub-economic REE deposit. B.Sc. thesis, St. Francis Xavier University, Antigonish, 82 p

Davis WJ, Rainbird RH, Gall Q, Jefferson CJ (2003) In situ U-Pb dating of diagenetic apatite and xenotime: Paleofluid flow history within the Thelon, Athabasca and Hornby Bay basins. Geochim Cosmochim Acta Supplement 72:A203

Derome D, Cathelineau M, Cuney M, Farbe C, Lhomme T (2005) Mixing of sodic and calcic brines and uranium deposition at McArthur River, Saskatchewan, Canada: a Raman and laser-induced breakdown spectroscopic study of fluid inclusions. Econ Geol 100:1529–1545

Earle S, Sopuck V (1989) Regional lithogeochemistry of the eastern part of the Athabasca Basin Uranium province. No. IAEA-TECDOC 500:263–296

Fayek M, Kyser TK (1997) Characterization of multiple fluid-flow events and rare earth-element mobility associated with formation of unconformity-type uranium deposits in the Athabasca Basin, Saskatchewan. Can Mineral 35:627–658

Hanly AJ (2001) The mineralogy, petrology and rare earth element geochemistry of the Maw Zone, Athabasca Basin, Canada. M.Sc. thesis, Rolla, Missouri, University of Missouri 168 p

Kerr W (2010) The discovery of the Phoenix deposit: a new high-grade, Athabasca Basin unconformity-type uranium deposit, Saskatchewan, Canada; in The Challenge of Finding New Mineral Resources: Global Metallogeny, Innovative Exploration, and New Discoveries, Volume 2: Zinc-Lead, Nickel-Copper-PGE, and Uranium, Goldfarb RJ, Marsh EE, Monecke, T (eds). Soc Econ Geol, Spe Pub 15:703−728

Kotzer TG, Kyser TK (1995) Petrogenesis of the Proterozoic Athabasca Basin, northern Saskatchewan, Canada, and its relation to diagenesis, hydrothermal uranium mineralization and paleohydrogeology. Chem Geol 120:45–89

Normand C (2014) Rare Earths in Saskatchewan: Mineralization Types, Settings, and Distributions; Saskatchewan Ministry of the Economy. Sask Geol Surv Rep 264:105 p

O'Connell I, Hattori K, Chen S, Adlakha E, Sorba C (2015) Characterization of tourmaline from the Maw zone, Gryphon zone and sandstones above the Phoenix uranium deposits, Athabasca Basin, Saskatchewan, Canada. Geol Surv Can Sci Pres 37

Pan Y, Yeo G, Rogers B, Austman C, Hu B (2013) Application of radiation induced defects in quartz to exploration for uranium deposits: a case study of the Maw Zone, Athabasca Basin, Saskatchewan. Expl Mining Geol 21:115–128

Quirt D, Kotzer T, Kyser TK (1991) Tourmaline, phosphate minerals, zircon and pitchblende in the Athabasca Group: Maw Zone and McArthur River areas. Summary of Investigations: Saskatchewan Geological Survey, Sask Energy Mines Rep 91-4:181–191

Rabiei M, Chi G, Normand C (2015) Field and Petrographic Investigations of the Maw Zone REE Deposit, Athabasca Basin, Saskatchewan. Sum Inves 2:16 p

Rainbird RH, Rayner N, and Stern RA (2003) SHRIMP U-Pb geochronology of apatite cements and zircon bearing tuff clasts in sandstones from the Athabasca Group, Athabasca Basin, northern Saskatchewan and Alberta. Sask Indus Res, Open House, Proceedings p. 6

Ramaekers P, Jefferson CW, Yeo GM, Collier B, Long DGF, Catuneanu O, Bernier S, Kupsch B, Post R, Drever G, McHardy S, Jiricka D, Cutts C, Wheatley K (2007) Revised geological map and stratigraphy of the Athabasca Group, Saskatchewan and Alberta. Geol Surv Can Bull 588:155−191

Rayner NM, Rainbird RH, Stern RA (2003) SHRIMP U-Pb detrital zircon geochronology of Athabasca Group sandstones, northern Saskatchewan and Alberta. Natural Resources Canada, Geol Surv Can 2003-F2:20 p

Richard A, Cathelineau M, Boiron MC, Mercadier J, Banks DA, Cuney M (2016) Metal-rich fluid inclusions provide new insights into unconformity-related U deposits (Athabasca Basin and Basement, Canada). Mineral Deposita 51:249−270

EU critical raw materials in the Czech Republic – Cínovec (Zinnwald) ore district

Petr Rambousek, Anna Vymazalová, Michal Poňavič, and Jan Pašava
Czech Geological Survey

Abstract. Critical raw materials in the Czech Republic have been studied under the frame of the project Competence Centre for Effective and Ecological Mining of Mineral Resources. The detail study was focused on the Czech part of the Cínovec (Zinnwald) ore district. Type ore samples from the boreholes were evaluated using a QEMSCAN technique. All studied samples have shown a good liberation of Li-micas. The highest liberation was attained in greisens (89%). Liberation of fluorite showed the highest values in greisens and liberation of topaz in the Zinnwald granite. Residual cassiterite, columbite, scheelite and REE- bearing minerals are very difficult to be liberated due to small size of grains (< 75 μm) and are predominantly bound to Li-micas. Contents of lithium (2360-7840 ppm) from Cínovec (Zinnwald) ores are predominantly contained in zinnwaldite.

1 Introduction

This study has been performed under the project
„Competence Centre for Effective and Ecological Mining of Mineral Resources“ (CEEMIR), funded by the Technology Agency of the Czech Republic (TA ČR) under the leadership of the Technical University of Ostrava. The aim of the project is to study critical raw materials (CRM) of the European Union (EU), assess the suitable resources of CRM in the Czech Republic and propose a possible efficient and environment-friendly way of their mining and processing. The main task of the Czech Geological Survey is a collection of the current knowledge, evaluation of the knowledge and mineralogical and geochemical characterization of selected mineral deposits and prospective resources.

The list of CRM includes 21 non-energy and non-agricultural raw materials: antimony (Sb), beryllium (Be), borates, chromium (Cr), cobalt (Co), coking coal, fluorspar, gallium (Ga), germanium (Ge), indium (In), magnesite, magnesium (Mg), natural graphite, niobium (Nb), platinum group metals (PGM), phosphate rock, rare Earth elements (REE), silicon metal and tungsten (W). Further lithium (Li) and kaolin were also assigned as important priority commodities on a national scale, listed among EU non-critical raw materials (NCRM). Raw materials used for the production of metallic silicon and coke coal were excluded from studied CRM although there are their deposits and resources in the Czech Republic.

The area of the Czech Republic (CZ) was divided into four districts and accordingly in four tasks of the project. Each area/district considers the regional geological units and documents the approximate number of deposits and potential resources. Small and mostly low-grade deposits of fluorspar, graphite and W are registered on the territory of the CZ. In addition to these three CRM, further potentially prospective resources of Sb, Ge, In and Nb have been defined. The area of the eastern Erzgebirge (NW part of CZ) was classified as promising in terms of occurrences of W and Nb ores. Besides this, among NCRM, the deposits and resources of Sn, Li, Rb, Ta and Cs were defined.

The most promising part related to the Task 1 is the Czech part of the Cínovec (Zinnwald) ore district. The Cínovec (Zinnwald) granite cupola, located in the Erzgebirge Mountains, at the Czech-German border, about 10 km N-NW from Teplice (Czech Republic) was actively mined for Sn and W until 1990. The Cínovec cupola consists of an extremely differentiated granite intrusion characterized by high concentrations of Li, Sn and W in its apical part, and the intrusion also contains high concentrations of F, Nb, Ta, Th, REE, Y, Sc. The Sn-W-Li potential of German part of the Zinnwald deposit has also attracted researchers (e.g. Nessler et al. 2015).

2 Samples and methods

At present time, the mines on the Czech side of Cínovec (Zinnwald) are not accessible and the only materials available to study are archive samples and cores. The core for drill hole CS-1 is unique because that covers the full lithological sequence of granitic rocks including vein and greisen Sn-W-Li (Nb, Ta, Rb, Cs) mineralization (Fig. 1) and was therefore selected for this study. The hole CS-1 was drilled to a depth of 1596 m by the Czech Geological Survey in 1961-63. The core samples have been the object of various mineralogical and petrological studies, e.g. Štemprok (1965), Štemprok and Šulcek (1969), Rub et al. (1998), Johan and Johan (1993, 1994, 2005), Breiter et al. (1999), Johan et al. (2012), among others; and more recently by Breiter (2015, 2016).

We have studied type ore samples and 0.5-0.1 mm samples from the sludge lagoon. The crushed and milled material from the drill core was studied by means of multi- element chemical assay by ICPMS. Mineralogical studies were performed using the Quantitative evaluation of minerals by scanning electron microscopy (QEMSCAN) at SGS Canada Inc.



Figure 1. Photograph illustrating the archive drill core CS-1 (the scale bar is 1 m).

3 Results and discussion

The study of the type ores has resulted in a number of distribution maps, diagrams and identifications measurements. The following are the observations from the QEMSCAN analyses:

1) All studied samples have shown a good liberation of Li-micas. The highest liberation was attained in greisens – 89%, in the samples from sludge where it reaches about 84% to 79%.
2) Liberation of fluorite showed the highest values in greisens 75 %.
3) Liberation of topaz showed the highest values in the Cínovec/Zinnwald granite up to 97 %, however it has been influenced by low modal content of topaz; in greisens the liberation reached about 83%.
4) Residual cassiterite, columbite, scheelite and mineral carries of REE are very difficult to be liberated due to small size of grains (< 75 µm) and are predominantly bound to Li-micas.

A schematic genetic model of the evolution of the host granitic intrusion and related mineralization that is applicable to other granitic domes in the area was constructed from subsequent petrological, litho-geochemical and mineralogical classification of 254 studied samples.

The study of ores has shown the variability in the distribution of ore elements: Li (avg. 1300 ppm) and Rb (avg. 1650 ppm) in greisens; Rb reaches the highest average values (1300-1700 ppm) in the Zinnwald microgranite and granite. Slightly elevated average contents of W (93 ppm) and Sn (29 ppm) are related to greisens. Enriched average values of Nb (96 ppm) and Ta (39 ppm) are associated with upper altered granites. The content of Ta is relatively low in the Zinnwald granites whereas Nb content varies between 66 to 84 ppm on average.

4 Conclusions

Contents of lithium in Cínovec (Zinnwald) ores (ranging from 2360 to 7840 ppm), are predominantly bound to zinnwaldite. The recent study of the Cínovec-south, being under exploration, has shown that an important carrier of Nb-Ta is pyrochlore and that scheelite contains up to 16 % MoO_3 (Breiter 2016).

Acknowledgements

Financial support through the project „Competence Centre for Effective and Ecological Mining of Mineral Resources“ (CEEMIR) from the Technology Agency of the Czech Republic (TA ČR) is gratefully acknowledged. Scientific collaboration with Dr. K.Breiter from the Geological Institute of the CAS, v.v.i. is greatly acknowledged.

References

Breiter K (2015) Geochemical a petrography characterization of samples from archive boreholes in Cínovec region. MS-Arch. CGS.

Breiter K (2016) Results from correlation comparation of geochemical, minerogical a mineralogical data between ore deposit Cínovec-jih (South) and the typical profile of CS-1 borehole. MS-Arch. CGS

Breiter K, Förster H-J, Seltmann R (1999) Variscan silicic magmatism and related tin–tungsten mineralization in the Erzgebirge-Slavkovský les metallogenic province. Mineral Deposita 34: 505–521

Johan V, Johan Z (1994) Accessory minerals of the Cínovec (Zinnwald) granite cupola, Czech Republic, part 1. Nb-, Ta- and Ti-bearing oxides. Mineral Petrol 51: 323–343

Johan Z, Johan V (1993) Accessory minerals of the Cínovec granitic cupola; behaviour of REE in F- and CO2-rich fluids. In: Fenoll Hach-Ali P, Torres-Ruiz J, Gervilla F (eds) Current research in geology applied to ore deposits. University of Granada, Granada, pp 625–628

Johan Z, Johan V (2005) Accessory minerals of the Cínovec (Zinnwald) granite cupola, Czech Republic: Indicators of petrogenetic evolution. Miner Petrol 83:113-150

Johan Z, Strnad L, Johan V (2012) Evolution of the Cinovec (Zinnwald) granite cupola, Czech Republic: composition of feldspars and micas, a clue to the origin of W, Sn mineralization. Can Mineral 50:1131-1148

Nessler J, Seifert T, Gutzmer J (2015) New Sn-W Potential at the Zinnwald/Cinovec Deposit, Eastern Erzgebirge, Germany. In: Andre-Mayer AS, Cathelineau M, Muchez P (eds) Mineral Resources in a Sustainable World, CNRS, Univ Lorraine, Nancy, 1-5: 819-822

Rub AK, Štemprok M, Rub MG (1998) Tantalium mineralization in the apical part of the Cínovec (Zinnwaldú granite stock. Mineral Petrol 63: 199-222

SGS Canada Inc. (2016): An investigation by high definition mineralogy into the mineralogical characteristic of five composite samples from a lithium ore MS-Arch. CGS

Štemprok M (1965) Petrology and the vertical extent of mineralization in the Cínovec (Zinnwald) granite cupola. Sbor Geol Věd Prague, LG 5: 7-106

Štemprok M, Šulcek Z (1969) Geochemical profile trhough ano re- bearing lithium granite. Econ Geol 64: 392-404

Sm-Nd isotopic signatures of the St-Honoré, Crevier, and Shortt Lake REE deposits in Québec (Canada)

Anne-Aurélie Sappin, Georges Beaudoin
Université Laval, Québec, Canada

Ross Stevenson
Université du Québec à Montréal, Québec, Canada

Marc Constantin
Université Laval, Québec, Canada

Abstract. The St-Honoré carbonatite complex (565 Ma) and Crevier alkaline intrusion (957.5 Ma), both located in the Grenville Province, and the Shortt Lake carbonatite complex (2652 Ma), emplaced within the Superior Province, host significant REE deposits. In each igneous complex, the intrusive rocks and minerals have similar trace element geochemical signatures and Nd isotopic compositions, suggesting that in each intrusion the different lithofacies have a genetic link. In addition, the εNdt values of the St-Honoré carbonatite, syenite, and carbonate (+3.2 to +3.8), Crevier carbonatite and syenite (+1.8 to +2.6), and Shortt Lake syenite and diorite (+1.1 to +1.5) indicate mixing between enriched crustal sources and depleted mantle sources. Together, the geochemical and isotopic data suggest that the St-Honoré, Crevier, and Shortt Lake alkaline complexes crystallized from magmas derived from a depleted mantle source that have undergone crustal contamination by local country rocks during their ascent toward the surface.

1 Introduction

Quebec hosts numerous rare earth elements (REE) occurrences and deposits, many of which have substantial REE resources (e.g., Ashram, Montviel, Strange Lake, Kipawa, and Kwyjibo deposits). Previous studies on the REE deposits in Quebec primarily focused on geological, mineralogical, and geochemical characteristics of the mineralization and its host rocks. Systematic studies on isotopic compositions of these deposits are rare and only a few studied their Sm-Nd isotopic signatures (e.g., Bell and Blenkinsop 1987; Chen and Simonetti 2014; Kamenetsky et al. 2015; Kerr 2015; Nadeau et al. 2016).

This study presents new Sm-Nd isotopic data for three of the main REE deposits in Quebec to complete data already available. The selected deposits are the St-Honoré, Crevier, and Shortt Lake deposits, all associated with carbonatite complexes. The main goal of this study is to determine the nature of the mantle/crustal sources involved in the genesis of the alkaline complexes that host the mineralization and evaluate the crustal contribution in order to better constrain the processes that led to the formation of these REE deposits.

2 Local geology

2.1 St-Honoré carbonatite complex

The St-Honoré carbonatite complex was emplaced at 565 Ma (Doig and Barton 1968) within the Grenville Province. It is hosted by diorite, syenite, and biotite-pyroxene gneiss (Fig. 1), which were fenitized during the injection of the alkaline complex, and covered by Paleozoic limestone and shale (Tremblay et al. 2015). The emplacement of this intrusive complex appears to be related to an extensional event which would have led to the formation of the Saguenay graben and St-Laurent rift (Kumarapeli and Saull 1966).

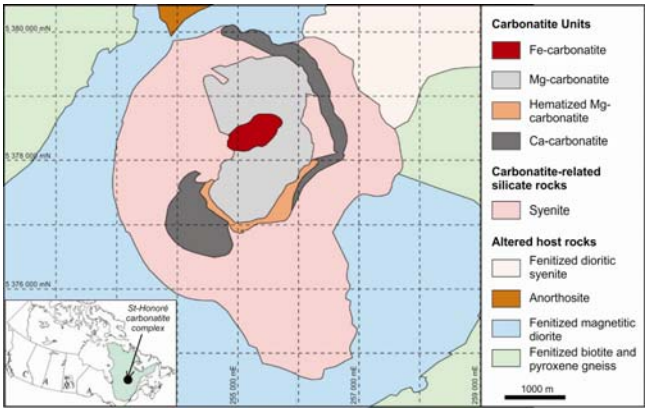


Figure 1. Simplified geological map of the St-Honoré carbonatite complex (modified from Tremblay et al. 2015).

The St-Honoré carbonatite complex forms a vertical intrusion with a roughly elliptical shape. It is composed of a rim of alkaline silicate rocks (mostly syenite) and a carbonatite core, which comprises from the outside to the inside, Ca-carbonatite, Mg-carbonatite, and Fe-carbonatite (Fig. 1; Néron 2015). Among the different types of carbonatite, Ca-carbonatite is the oldest and the most primitive one and Fe-carbonatite represents the youngest and the most evolved rock (Néron 2015). Ca-carbonatite and Mg-carbonatite contain the Niobec Nb ore deposit (estimated reserves of 416 Mt at 0.41% Nb_2O_5: Vallières et al. 2013), whereas the Fe-carbonatite hosts the REE mineralization. In this intrusive complex, Nb is commonly extracted from pyrochlore and columbite (Tremblay et al.

2015), whereas the main REE-bearing minerals are fluorocarbonates, such as bastnaesite, parisite, and synchysite (Gauthier 1979; Fournier 1993).

2.2 Crevier alkaline intrusion

The Crevier alkaline intrusion, dated at 957.5 Ma (Groulier et al. 2014), is located near the Waswanipi-Saguenay structural corridor, which is related to the Saguenay graben, within the Grenville Province. It is hosted by granitoid and charnockitic gneiss. This intrusion and its Nb-Ta mineralization were described in detail in Groulier (2013) and Groulier et al. (2014) and their main characteristics are summarized in the following paragraph.

At the surface, the Crevier alkaline intrusion is oval in its northern part and sub-circular in its southern part (Fig. 2). The intrusion is composed of nepheline syenite crosscut by banded syenite, fine-grained nepheline syenite dykes, carbonatite dykes, and alkaline syenite (Fig. 2). Nepheline syenite, banded syenite, and carbonatite are crosscut by pegmatitic nepheline syenite dykes. The latter are also crosscut by sodalite-rich veins. The Crevier Nb-Ta mineralization is associated with the pegmatitic nepheline syenite dykes, although the highest Nb and Ta contents were observed in the area rich in late sodalite-bearing veins. The Crevier deposit has indicated mineral resources of 12.9 Mt grading 0.19% Nb_2O_5 and 234 ppm Ta_2O_5 and inferred mineral resources of 15.4 Mt at 0.17% Nb_2O_5 and 252 ppm Ta_2O_5 using a 0.10% Nb_2O_5 cut-off grade (Duplessis and Girard 2010). Carbonatite associated with the Crevier intrusion also displays enrichment in REE (up to 1400 ppm). Niobium and Ta are mostly hosted by pyrochlore, whereas REE appear to be predominantly contained in monazite and REE carbonates.

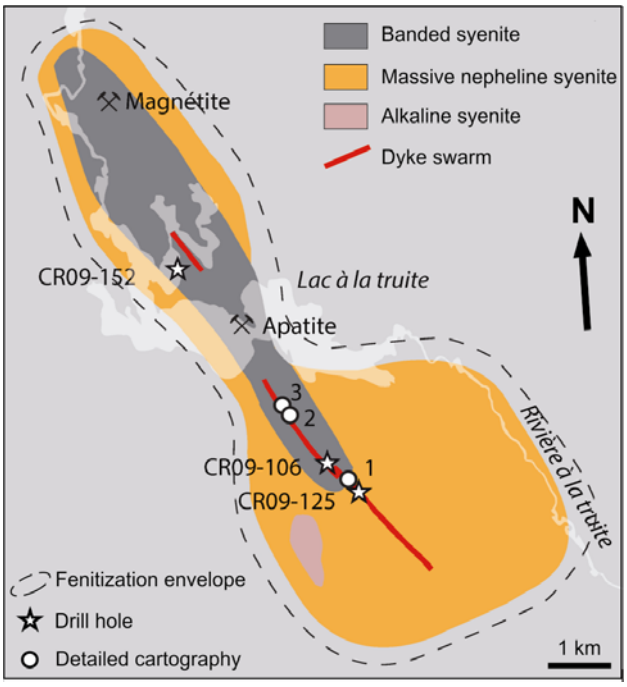


Figure 2. Simplified geological map of the Crevier alkaline intrusion (modified from Groulier et al. 2014)

2.3 Shortt Lake carbonatite complex

The Shortt Lake carbonatite complex is located in the eastern part of the Abitibi greenstone belt, within the Superior Province. It was formed at 2652 Ma (Thorpe et al. 1984; Morasse 1988) and is hosted by the volcanic rocks of the Obatogamau Formation and volcanogenic and sedimentary rocks of the Ruisseau Dalime formation (Fig. 3; Brisson 1998). The emplacement of this alkaline complex is syn- to post-deformation and is related to the Lamarck shear zone (Fig. 3; Brisson 1998; Nadeau et al. 2014).

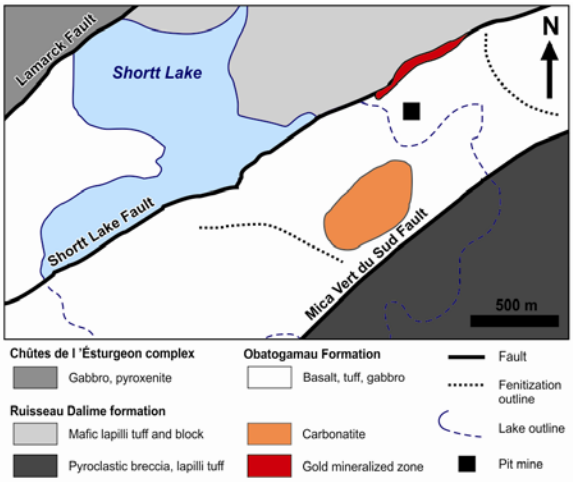


Figure 3. Simplified geological map of the Lake Shortt area (modified from Prud'homme 1990)

The Shortt Lake carbonatite complex is composed of a wide range of intrusive rocks, comprising alkaline gabbro, syenite, Ca-carbonatite and Si-carbonatite dykes, hornblendite dykes, undifferentiated mafic to intermediate sills, and lamprophyre dykes (e.g., Morasse 1988; Prud'homme 1990; Nadeau et al. 2014). All these lithofacies, as well as the REE occurrence, appear to be genetically related (Nadeau et al. 2014). The Shortt Lake REE mineralization is mainly hosted by carbonatite dykes and contains up to 2.2% rare-earth oxides (Quirion 1991). Common REE-bearing minerals include monazite, bastnaesite, pyrochlore, ancylite, and synchysite (Quirion 1991; Nadeau et al. 2014).

3 Methodology

Trace elements, including incompatible lithophile elements and REE, were analyzed at Actlabs (Ontario, Canada) by inductively-coupled plasma mass spectrometry (ICP-MS) or inductively-coupled plasma atomic emission spectroscopy (ICP-AES) following a lithium borate fusion and nitric acid dissolution.

Sm and Nd concentrations and Nd isotopic compositions were measured by isotope dilution – thermal ionization mass spectrometry (ID-TIMS) in static collection mode at the GEOTOP (UQAM, Montréal, Canada). Nd isotopic ratios were normalized to

$^{146}Nd/^{144}Nd$ = 0.7219. Reported values were adjusted to the JNdi-1 standard ($^{143}Nd/^{144}Nd$ = 0.512115 ± 0.000007; Tanaka et al. 2000) which yielded a mean value of $^{143}Nd/^{144}Nd$ = 0.512100 and 2σ errors of 0.000009 (6 analyses). Precision on Nd isotopic ratios is given at the 95% confidence level and errors are <0.009%. εNd values were calculated using the present-day values of the chondritic uniform reservoir (CHUR) of $^{143}Nd/^{144}Nd$ = 0.512638 and $^{147}Sm/^{144}Nd$ = 0.1966.

4 Trace element data

Chondrite-normalized REE patterns are presented in Figure 4. Overall, carbonatite and syenite of the St-Honoré carbonatite complex display REE patterns strongly enriched in LREE relative to HREE, with no Eu anomaly. However, Fe-carbonatite of this igneous complex has REE signatures slightly different compare to other St-Honoré carbonatites. The Fe-carbonatite is characterized by strongly fractionated REE profiles and, locally, has very high LREE contents or shows a slightly negative Eu anomaly. Carbonatite, lamprophyre, syenite, diorite, and ore samples of the Shortt Lake carbonatite complex display parallel REE patterns with a pronounced enrichment in LREE relative to HREE. These rocks do not exhibit Eu anomaly. Among these various lithologies, carbonatite has the highest contents in REE. Carbonatite and syenite of the Crevier alkaline intrusion have similar REE patterns, enriched in LREE compared to HREE, with no Eu anomaly. As in the Shortt Lake intrusive complex, Crevier carbonatite have higher REE contents than syenite.

5 Sm-Nd isotope data

The various lithologies of the St-Honoré igneous complex and the carbonate minerals from carbonatite have similar Nd isotopic ratios. Their εNd (565 Ma) values range from +3.2 to +3.8. Carbonatite and syenite of the Crevier intrusion have a narrow range of εNd (957.5 Ma) values, between +1.8 and +2.6. Syenite and diorite of the Shortt Lake carbonatite complex have slightly lower εNd values, with εNd (2652 Ma) ranging from +1.1 to +1.5.

6 Discussion

The Nd isotopic ratios of rocks and minerals of the St-Honoré carbonatite complex are consistent with the εNdt values recently obtained by Kamenetsky et al. (2015) for dolomite (from +3.2 to +4.0), phlogopite (+3.8), and apatite (+3.6) from Mg-carbonatite samples and the εNdt value obtained by Bell and Blenkinsop (1987) for a carbonatite (+3.6) of this igneous complex. Coupled with the lithogeochemical results, these isotopic compositions suggest that the different intrusive rocks of the St-Honoré complex are cogenetic. In addition, the similarity between the chondrite-normalized REE patterns (Fig. 4) and the low variations of the Nd isotopic ratios of the carbonatite and syenite of the Crevier intrusion and the syenite and diorite of the Shortt Lake carbonatite complex may also indicate that in each of these intrusive complexes, the various lithofacies are genetically associated.

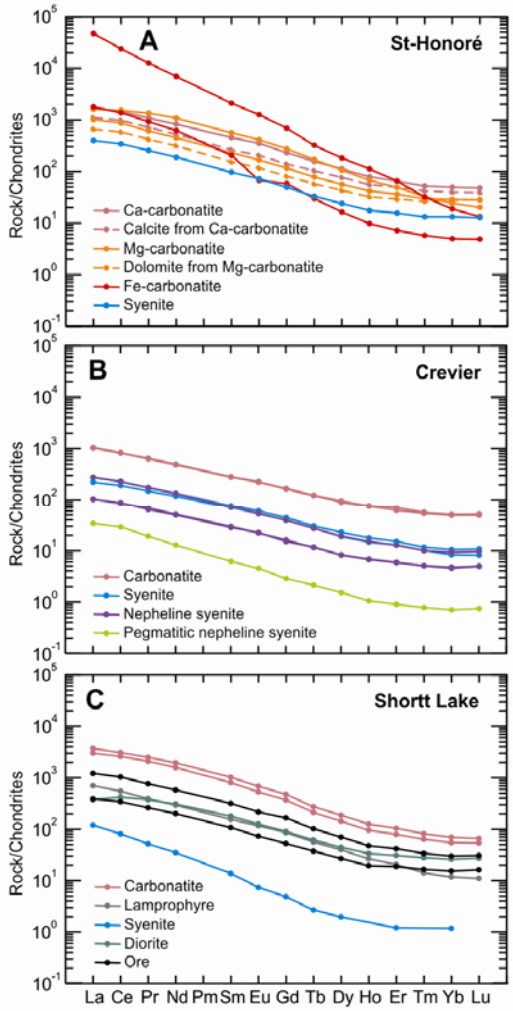


Figure 4. Chrondrite-normalized REE patterns. **a** St-Honoré carbonatite complex. **b** Crevier alkaline intrusion (data from http://sigeom.mines.gouv.qc.ca). **c** Shortt Lake carbonatite complex. Chondrite values from Sun and McDonough (1989).

The εNdt values obtained for rocks and minerals of the St-Honoré, Crevier, and Shortt Lake intrusive complexes are lower than the expected values for the depleted mantle at, respectively 565 Ma, 957.5 Ma, and 2652 Ma (Fig. 5). These isotopic compositions may be a result of mixing between a depleted mantle component and an enriched component, suggesting the implication of a crustal source in the formation of these igneous complexes.

7 Conclusions

Preliminary geochemical and Nd isotopic results on intrusive rocks and minerals of the St-Honoré, Crevier, and Shortt Lake alkaline complexes suggest that, in each complex, the emplacement of the different lithofacies is related to a same magmatic episode, involving magmas generated by the partial melting of a depleted mantle

source and their local contamination by an enriched crustal component.

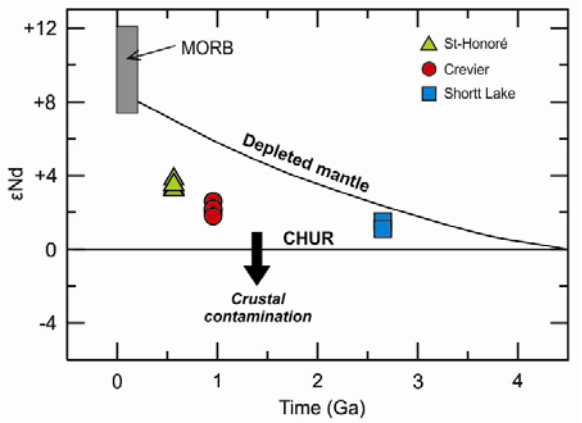


Figure 5. εNd versus time for the CHUR and depleted mantle models (modified from DePaolo 1981). Field of mid-ocean ridge basalts (MORB) from DePaolo and Wasserburg (1976).

Acknowledgements

We thank Patrice Roy and Fabien Solgadi from the Ministère de l'Énergie et des Ressources naturelles du Québec (MERN) for their assistance and André Poirier and Julien Gogot from the GEOTOP for their help in laboratory works and Nd measurements with the TIMS. Thanks are also extended to Olivier Nadeau (University of Ottawa), Jonathan Tremblay (UQAC), and Paul Bédard (UQAC) for providing samples and to Émilie Bédard, Anne-Marie Beauchamp, and Marjorie Lapointe-Aubert (UL) for sample preparation. This study is funded by the MERN.

References

Bell K, Blenkinsop J (1987) Archean depleted mantle: Evidence from Nd and Sr initial isotopic ratios of carbonatites. Geochim Cosmochim Acta 51: 291-298

Brisson H (1998) Caractéristiques, chronologie et typologie des minéralisations aurifères de la région du lac Shortt (Québec), Sous-province archéenne de l'Abitibi. PhD thesis, Université du Québec à Chicoutimi

Chen W, Simonetti A (2014) Evidence for the multi-stage petrogenetic history of the Oka carbonatite complex (Québec, Canada) as recorded by perovskite and apatite. Minerals 4: 437-476

DePaolo DJ (1981) Neodymium isotopes in the Colorado Front Range and crust-mantle evolution in the Proterozoic. Nature 291: 193-196

DePaolo DJ, Wasserburg GJ (1976) Inferences about magma sources and mantle structure from variations of 143Nd/144Nd. Geophys Res Lett 3: 743-746

Doig R, Barton JM (1968) Ages of carbonatites and other alkaline rocks in Québec. Can J Earth Sci 5: 1401-1407

Duplessis C, Girard R (2010) Technical report, niobium and tantalum resource estimation update of the Crevier deposit, north of Lac St-Jean, Quebec, Canada. NI 43-101 technical report

Fournier A (1993) Magmatic and hydrothermal controls of LREE mineralization of the St-Honoré carbonatite, Québec. MSc thesis, McGill University

Gauthier A (1979) Étude minéralogique, pétrographique et géochimique de la zone à terres rares de la carbonatite de St-Honoré. MSc thesis, Université du Québec à Chicoutimi

Groulier PA (2013) Étude des minéralisations en Nb-Ta du complexe igné alcalin de Crevier (Québec). MSc thesis, Université de Lorraine

Groulier PA, Ohnenstetter D, André-Mayer AS, Zeh A, Solgadi F, Moukhsil A, El Basbas A (2014) Étude des minéralisations en Nb-Ta de l'intrusion alcaline de Crevier. Ministère de l'Énergie et des Ressources naturelles, Québec, MB 2014-33: 68p

Kamenetsky VS, Mitchell RH, Maas R, Giuliani A, Gaboury D, Zhitova L (2015) Chlorine in mantle-derived carbonatite melts revealed by halite in the St.-Honoré intrusion (Québec, Canada). Geology 43: 687-690

Kerr A (2015) Sm-Nd isotopic geochemistry of rare-earth-element (REE) mineralization and associated peralkaline granites of the Strange Lake intrusion, Labrador. Newfoundland and Labrador Department of Natural Resources, Geological Survey, Current Research, Report 15-1: 63-83

Kumarapeli PS, Saull VA (1966) The St. Lawrence valley system: a North American equivalent of the East African rift valley system. Can J Earth Sci 3: 639-658

Morasse S (1988) Geological setting and evolution of the Lac Shortt gold deposit, Waswanipi, Quebec, Canada. MSc thesis, Queen's University

Nadeau O, Stevenson R, Jébrak M (2014) The Archean magmatic-hydrothermal system of Lac Shortt (Au-REE), Abitibi, Canada: Insights from carbonate fingerprinting. Chem Geol 387: 144-156

Nadeau O, Stevenson R, Jébrak M (2016) Evolution of Montviel alkaline-carbonatite complex by coupled fractional crystallization, fluid mixing and metasomatism — Part II: Trace element and Sm–Nd isotope geochemistry of metasomatic rocks: implications for REE-Nb mineralization. Ore Geol Rev 72: 1163-1173

Néron A (2015) Caractérisation de la minéralisation de la zone à terres rares de la carbonatite de Saint-Honoré, Québec, Canada. MSc thesis, Université du Québec à Chicoutimi

Prud'homme N (1990) Caractérisation pétrographique et géochimique de la carbonatite et de la syénite de la mine Lac Shortt. MSc thesis, Université du Québec à Chicoutimi

Quirion D (1991) Géologie de la mine d'or Lac Shortt. In: Guha J, Chown EH, Daigneault R (eds) Litho-tectonic framework and associated mineralization of the eastern extremity of the Abitibi greenstone belt, Quebec (field trip 3). Geological Survey of Canada, Open File 2158, pp. 116-131

Sun SS, McDonough WF (1989) Chemical and isotopic systematics of oceanic basalts: implications for mantle composition and processes. In: Saunders AD, Norry MJ (eds) Magmatism in the ocean basins. Geological Society of London, Special Publication 42, pp. 313-345

Tanaka T, Togashi S, Kamioka H, Amakawa H, Kagami H, Hamamoto T, Yuhara M, Orihashi Y, Yoneda S, Shimizu H, Kunimaru T, Takahashi K, Yanagi T, Nakano T, Fujimaki H, Shinjo R, Asahara Y, Tanimizu M, Dragusanu C (2000) JNdi-1: a neodymium isotopic reference in consistency with LaJolla neodymium. Chem Geol 168: 279-281

Thorpe RI, Guha J, Franklin JM, Loveridge WD (1984) Use of a Superior Province lead isotope framework in interpreting mineralization stages in the Chibougamau District. In: Guha J, Chown EH (eds) Chibougamau - Stratigraphy and mineralization. Canadian Institute of Mining and Metallurgy, Special Volume 34, pp. 496-516

Tremblay J, Bédard LP, Matton G (2015) A petrographic study of Nb-bearing minerals at the Saint-Honoré niobium deposit. In: Simandl GJ, Neetz M (eds) Symposium on strategic and critical materials proceedings, November 13-14, 2015, Victoria. British Columbia Geological Survey, Paper 2015-3, pp. 75-81

Vallières D, Pelletier P, Gaultier P, Ferlatte G, Tremblay JF, Sirois R (2013) NI 43-101 technical report, update on Niobec Expansion, December 2013

HFSE evolution in the Eldor Carbonatite

P. T. Schmidt, I.M. Samson
University of Windsor, Ontario, Canada

A. E. Williams-Jones
McGill University, Montréal, Canada

D. L. Smith
Dahrouge Geological Consulting Limited

Abstract. The Eldor Carbonatite Complex comprises three magmatic calcite carbonatite stages (1-3) which have been partially metasomatized to dolomite carbonatite. Pyrochlore-group minerals are the dominant high-field-strength element (HFSE)-bearing mineral group, fersmite is common in stage 1 and 3. The Ta/Nb and U/Th ratios of the pyrochlore-group minerals, as well as the whole rock chemistry of the carbonatites, change systematically with each stage. Stage 1 has Nb/Ta ratios <40 and U/Th >1, stage 2 has Nb/Ta ratios <100 and U/Th <1, and Stage 3 has Nb/Ta ratios >100 and U/Th <1. The metasomatism mobilized Ca^{2+} from the A-site and added Fe^{2+}, transforming fersmite into columbite-(Fe). HFSE were not, however mobilized on a large scale. Assay data can be used to classify drill core into 3 stages, based on Nb/Ta and U/Th ratios, and evaluation of HFSE changes over the geological evolution of the complex, reflecting an increase in Nb concentrations and a decrease in Ta and U concentrations. Th increases from the first to the second stage and decreases in the third stage.

1 Introduction

The Paleoproterozoic Eldor carbonatite (formerly known as the Lac Lemoyne carbonatite), located in northern Quebec, comprises several magmatic and carbohydrothermal stages including the Ashram Deposit, which is currently being assessed for its rare earth element (REE) and fluorspar potential. The carbonatites form an elliptical-shaped complex, with magmatic stages on the rim and the Ashram Deposit in the centre (Fig. 1). Drill results on the magmatic stages confirm that favourable grades of Ta and Nb are present and suggest that there is also potential for good tonnages.

Crosscutting relationships of calcite carbonatite in outcrop and drill core show three main stages (1-3), and are distinct in their pyrochlore-group mineral colour and morphology, and degree of deformation. The first calcite carbonatite shows a high degree of deformation and the pyrochlore-group minerals are anhedral with reddish-brown to black colours. The second calcite carbonatite is, by volume, the most dominant. A common characteristic feature is tabular aggregates of calcite carbonatite in a phoscorite matrix. Subhedral to euhedral pyrochlore-group minerals are brown to light brown. The third stage appears as undeformed layered calcite carbonatite with euhedral, light-brown pyrochlore group minerals. The most common accessory minerals in all calcite carbonatites are magnetite, apatite, olivine (serpentinized), amphiboles and phlogopite.

A large-scale metasomatizing event, dominant on the outer parts of the complex, altered the calcite carbonatite to dolomite carbonatite. The target of this contribution is to answer two main questions: 1) Is the change in Ta and Nb (and other HFSE) consistent with the geological evolution of the complex?, and 2) Were Nb and Ta mobilized during metasomatism? The focus in this paper is on the pyrochlore-group minerals as they are the dominant Nb- and Ta-bearing minerals, and are ubiquitous in all stages.

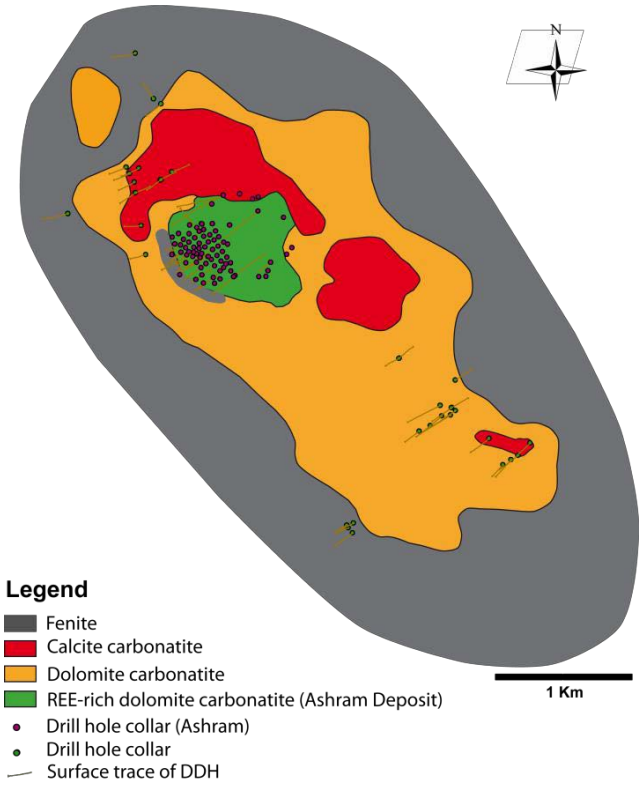


Figure 1. Simplified map of the Eldor Carbonatite Complex.

2 Methodology and results

2.1 Mineral chemistry

Mineral analyses were carried out using an FEI Quanta 200 FEG SEM with Energy Dispersive Spectroscopy (SEM-EDS) at the University of Windsor. Accelerating voltage was 25 kV with a 3.9 µm beam width and 30-100 second count times. The accuracy of EDS analysis of Ta and Nb was assessed by Wu et al. (2016), using the JEOL JXA-8530F field-emission electron microprobe with wavelength-dispersive analysis (WDS) at Western University.

Stage 1 calcite carbonatite hosts zoned pyrochlore-group minerals and fersmite. The core is a Ta- and U- rich oxycalciopyrochlore variety and is overgrown by fersmite (Fig. 1). The pyrochlore-group minerals in the dolomite carbonatite also have Ta and U-rich oxycalciopyrochlore cores, but the fersmite is altered to columbite-(Fe) (Fig. 1).

The pyrochlore group minerals of stage 2 calcite carbonatite are euhedral, but consist of a complex intergrowth between intermediate Th-bearing oxycalciopyrochlore, a Th-poor oxycalciopyrochlore, and a Th-rich oxycalciopyrochlore along fractures (Fig. 1). Metasomatism pseudomorphed the pyrochlore-group minerals of the calcite carbonatite to form columbite-(Fe) or nioboaeschynite-(Ce) (Fig. 1). Anhedral grains of Th- and Ta- rich oxycalciopyrochlore occur in close proximity (Fig. 1).

Pyrochlore-group minerals of stage 3 are subhedral to euhedral and consist of fersmite, often with a porous alteration rim of fluornatropyrochlore (Fig. 1). The pyrochlore-group mineral in the dolomite carbonatite is homogeneous fluornatropyrochlore, with pervasive porosity. Patches of columbite-(Fe) occur along the rim or fractures of these grains (Fig. 2).

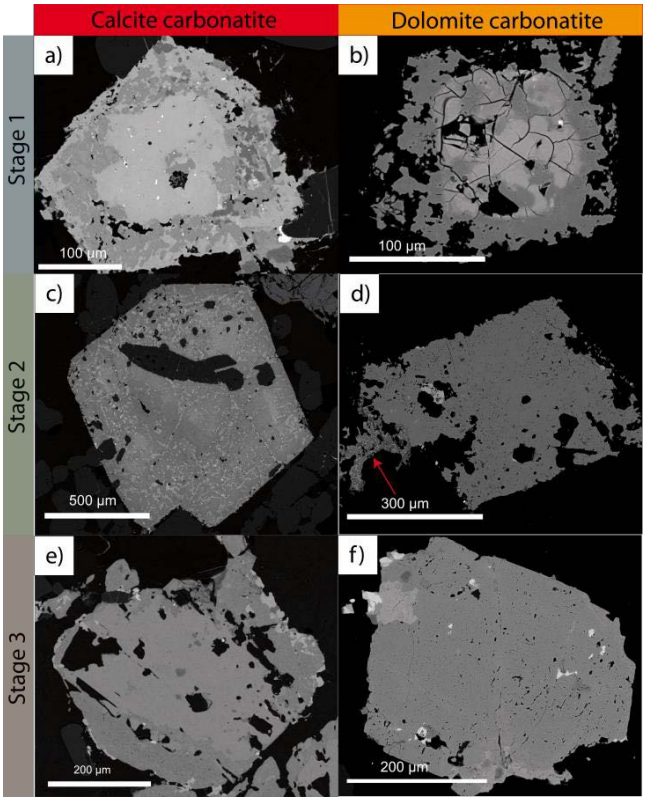


Figure 2. BSE images of pyrochlores and associated HFSE-minerals in different stages and rock types. a): core of U-Ta rich oxycalciopyrochlore mantled by fersmite (Sample ID: 47493). b): U-Ta rich oxycalciopyrochlore with columbite-(Fe) altered rim (67990). c): bright spots are intermediate Th-bearing oxycalciopyrochlore, dark spots Th-poor oxycalciopyrochlore. Very bright Th-rich oxycalciopyrochlore varieties occur in fractures (68185). d): columbite-(Fe) pseudomorph after pyrochlore, including in a gel like texture comprising a mixture of Th-and Ta-rich oxycalciopyrochlore (marked with red arrow) (68186). e): Fersmite in the core with an alteration rim of fluornatropyrochlore (68172). f): Fluornatropyrochlore with brighter patches of columbite-(Fe) (68164).

2.2 Whole rock chemistry

Whole rock analyses were carried out by Activation Laboratories Ltd. A lithium metaborate/tetraborate fusion flux was produced and analyzed by Inductively Coupled Plasma Mass Spectrometry (ICP-MS). A glass disc was produced to analyze Nb_2O_5 and Ta_2O_5 by X-ray fluorescence (XRF). Representative analyses are presented in Table 1.

A total of 5803 carbonatite whole-rock drill core sample were assayed. It shows an increase in total concentration for Nb and a decrease in Ta and U over the geological evolution of the complex (Fig. 3). Th increases from the first to the second stage and decreases in the third stage.

Table 1. Whole rock chemistry of representative samples

Sample ID	47493	67990	68185	68186	68172
Type/Stage:	Cal/1	Dol/1	Cal/2	Dol/2	Cal/3
Major Elements (wt. %):					
SiO_2	1.57	3.65	0.85	0.78	1.28
Al_2O_3	0.25	0.79	0.13	0.18	0.35
Fe_2O_3(T)	7.1	7.15	4.03	8.35	1.31
MnO	0.25	0.405	0.21	0.43	0.18
MgO	2.43	13.92	3.27	11.37	1.99
CaO	47.28	30.23	49.53	35.3	52.04
Na_2O	0.04	0.13	0.04	0.1	0.05
K_2O	0.13	0.52	0.07	0.04	0.28
TiO_2	0.079	0.18	0.04	0.1	0.02
P_2O_5	2.75	3.47	6.43	9.2	2.97
LOI	35.35	37.08	34	32.6	38.2
Total	97.21	97.52	98.66	98.46	98.64
Trace Elements (ratios):					
Nb/Ta	14	11	62	69	198
U/Th	1.36	5.43	0.14	0.10	0.07

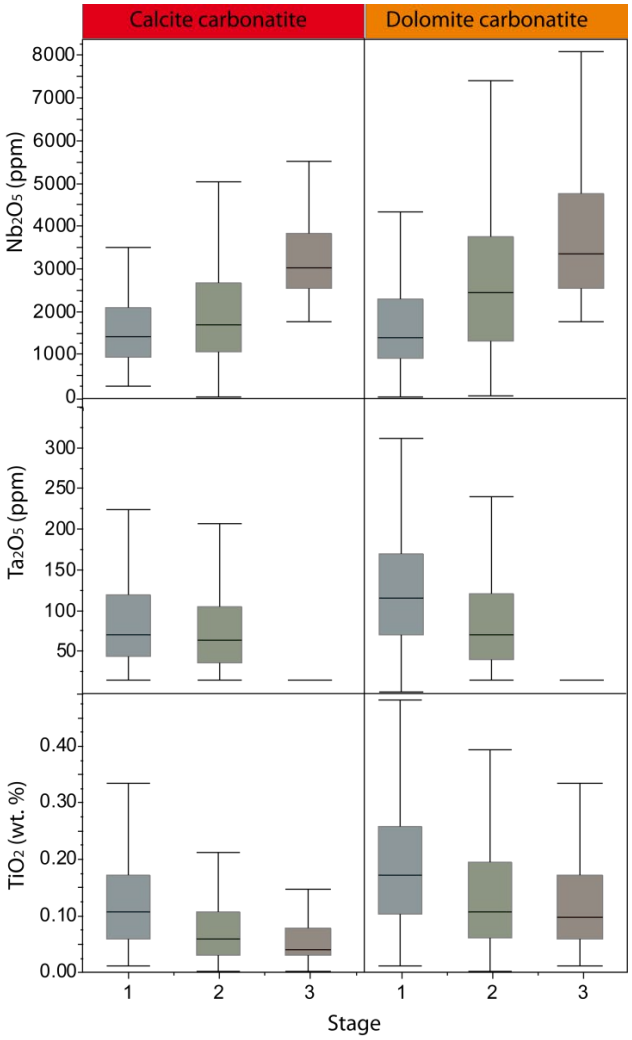


Figure 3. Boxplots of Nb_2O_5, Ta_2O_5, and TiO_2 over the three stages for calcite carbonatite and dolomite carbonatite. Whiskers show 3rd quartile + 1.5*(interquartile range) and 1st quartile - 1.5*(interquartile range). Outliers are not displayed.

3 Discussion

The first question raised was whether the change in Ta and Nb (HFSE) is consistent with the geological evolution of the complex. Whole rock assays and pyrochlore-group minerals in the three stages of calcite carbonatite show a systematic change from high U/Th and low Nb/Ta ratios in the early stage, intermediate U/Th and intermediate Nb/Ta ratios in the second stage and finally low U/Th and high Nb/Ta ratios in the last magmatic stage (Fig. 4), which demonstrate that there is a consistent change in magma chemistry that is consistent with the sequence of intrusion.

The observed trend of the pyrochlore-group mineral chemistry is similar to that reported from the Kola Alkaline Province (Lee et al. 2006), but euhedral fluornatropyrochlore at Eldor was found in dolomite carbonatite rather than calcite carbonatite. Another similarity is the tabular texture of the second stage of calcite carbonatite, which was also described from the Kola Alkaline Province (Vartiainen 1980). However, further research on melt petrogenesis in the Eldor Complex is necessary to determine if the evolution of the pyrochlore-group minerals was the result of partial melting processes in the mantle, or differentiation as a result of carbonated silicate melt immiscibility or crystal fractionation.

Metasomatism of calcite carbonatite to dolomite carbonatite altered fersmite to columbite-(Fe) through substitution of Ca^{2+} by Fe^{2+}, but the HFSE were not mobilized on a large scale, as reflected in the petrography, mineral chemistry and the whole-rock assays (Fig. 4). This is in agreement with Chakhmouradian (2015), who showed that HFSE were immobile in the dolomitized part of the Aley carbonatite.

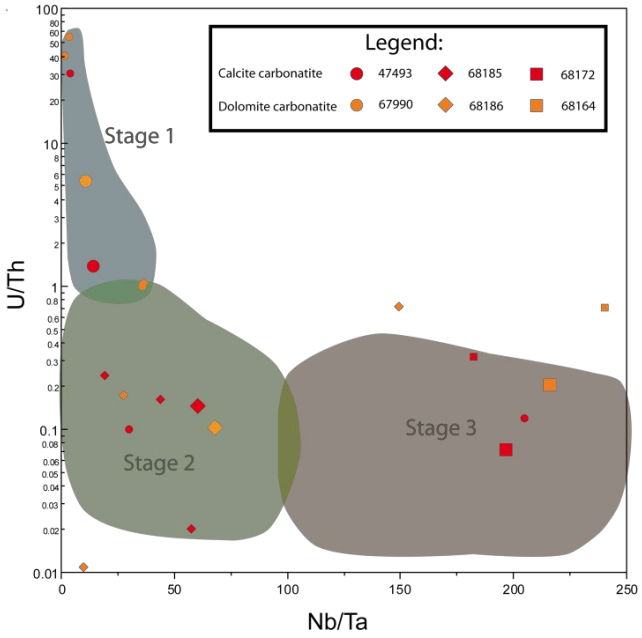


Figure 4. U/Th ratio (wt. %) vs. Nb/Ta ratio (wt. %) of whole rock analyses (big symbols for specific samples) and mineral chemistry of HFSE-minerals (small symbols of specific samples). Note: Y-axies is logarithmic. Coloured fields represent whole rock data of stage 1 (blue), stage 2 (green), and stage 3 (brown). Circles: Stage 1 (Sample ID: 47493 and 67990; data in Table 1). Diamond: Stage (68185, 68186). Squares: Stage 3(68172, 68164). Note that U and Th for mineral chemistry in stage 3 are below detection limit.

Therefore further exploration at the Eldor carbonatite for Ta should focus on the early carbonatite stages. Whereas the late stage is highly prospective for Nb. There are no systematic changes in Nb and Ta content between the magmatic calcite carbonatite and the metasomatic dolomite carbonatite.

Acknowledgments

Funding for this project was provided by NSERC, Commerce Resources Corp., and Dahrouge Geological Consulting Ltd. The authors would like to especially thank Chris Grove, Jenna Hardy, and Dave Hodge (Commerce Resources Corp.), as well as Jody Dahrouge and Darren Smith (Dahrouge Geological Consulting Ltd.) for their ongoing support and providing access to their geological information and drillcore. We are very grateful to Alex Knox and Caitlin Beland for their insights in to the Eldor Carbonatite geology and would like to thank Melissa Price and Sharon Lackie (University of Windsor) for their assistance in operating various analytical instruments

References

Chakhmouradian AR, Reguir EP, Kressall RD, Crozier J, Pisiak LK, Sidhu R, Yang P (2015) Carbonatite-hosted niobium deposit at Aley, northern British Columbia (Canada): Mineralogy, geochemistry and petrogenesis. Ore Geology Reviews. 64: 642-666.

Lee MJ, Lee JI, Garcia D, Moutte J, Williams CT, Wall F, Kim Y (2006) Pyrochlore chemistry from the Sokli phoscorite-carbonatite complex, Finland: implications for the genesis of phoscorite and carbonatite association. Geochemical Journal. 40(1): 1-13.

Vartiainen H (1980) The petrography, mineralogy and petrochemistry of the Sokli carbonatite massif, northern Finland

Wu M, Samson MI, Zhang, D (in press) Textural and Chemical Constraints on the Formation of Disseminated Granite-hosted W-Ta- Nb Mineralization at the Dajishan Deposit, Nanling Range, Southeastern China. Economic Geology

Halite at the Saint-Honoré carbonatite: an insight into a magmatohydrothermal process

Jonathan Tremblay, L. Paul Bédard
Université du Québec à Chicoutimi, Québec, Canada

Guillaume Matton
Mine Niobec inc., Québec, Canada

Abstract. Halite is a ubiquitous mineral in the Saint-Honoré carbonatite (Saguenay, Québec, Canada). It has remained present within the deposit as the deeper carbonatite has not been weathered. Halite is either disseminated or occurs as veinlets throughout the dolomitic unit associated with Nb mineralization. It is also found in pores of weakly to moderately altered pyrochlore crystals. The two main Nb-bearing minerals, fluorcalciopyrochlore and columbite-(Fe), are related through hydrothermal alteration (columbitization). Sodium is from pyrochlore (magmatic) whereas Cl is from hydrothermal fluid as there is no significant Cl in any mineral, except columbite-(Fe), which is hydrothermal. These interpretations suggest that halite has a hybrid magmatohydrothermal origin. The role of Cl to the transport of REEs and the contribution of columbitization in the fenitization of the host rocks are investigated.

1 Introduction

Oldoinyo Lengai has been intensely studied as it is the only known active carbonatite volcano having sodium carbonate lavas (Mangler et al. 2014). Studies of this volcano have raised numerous questions about the presence of sodium in carbonatites and the implication for its genesis, one question in particular being the origin of halite in carbonatites. Halite is observed in the groundmass of Oldoinyo Lengai lavas (Zaitsev and Keller 2006) but its origin and, more precisely, the reason for the presence of chlorine remains unclear.

The Saint-Honoré carbonatite offers an ideal location to study the presence of halite in carbonatites. Halite is a ubiquitous mineral in the carbonatite. Moreover, the carbonatite has not been affected by metamorphism, nor it is deformed, and it is accessible to roughly 800 metres in depth, thereby preserving it from weathering.

This communication focuses on the presence of halite in the Saint-Honoré carbonatite, its petrographic distribution as well as its origin.

2 Geology

2.1 Regional geology

The Saint-Honoré carbonatite is part of an alkaline complex of 10 km², located near the city of Saguenay, Québec, Canada. The complex is surrounded by Mesoproterozoic Grenvillian fenitized gneiss and diorite with an upper amphibolite and lower granulite metamorphic facies (Dimroth et al. 1981; Higgins and van Breemen 1996). The alkaline magmatism is referred to as the Iapetan rift and is related to the St-Lawrence River rift activity (Kumarapeli and Saul 1966).

Alkaline silicate rocks associated with the carbonatite are characterized by nepheline-bearing syenites and foidolites. Baddeleyeite from a lamprophyre dyke related to the alkaline complex yielded a U-Pb age of 582.1±1.8 Ma (Michael Higgins, personal communication, 2015).

2.2 Carbonatite

The Saint-Honoré carbonatite is composed of concentric subvertical layers of carbonates with variable compositions (Fortin-Bélanger 1977; Thivierge et al. 1983). The outer part of the carbonatite is a sövite (calcio-carbonatite) that is barren of any mineralization and has been only poorly documented. The core of the carbonatite displays ankeritic breccias and is enriched in LREEs (Fournier 1993; Grenier et al. 2013; Néron 2015). A dolomitic unit (magnesio-carbonatite) lies between the calcio- and ferro-carbonatite and hosts the Nb mineralization.

The dolomitic rocks have been the best studied portion of the carbonatite as they have been drilled for exploration and exploitation. The dolomitic rocks are characterized by medium-grained hypidiomorphic dolomite grains with no apparent cleavage. Accessory minerals are columbite-(Fe), fluorcalciopyrochlore, phlogopite, magnetite, pyrite, and various types of apatite. There are also minor traces of ilmenite, hematite, sphalerite, chlorite, quartz, zircon, baddeleyite, barite, and REE minerals throughout the unit. Accessory and trace minerals are generally disseminated, but may occur as lenses. There is a pervasive alteration affecting dolomite and accessory minerals, leaving a grey aspect to carbonates and alter phlogopite into chlorite.

3 Halite

Halite concentrations in the Saint-Honoré carbonatite are surprisingly high. Halite is observed as veins, varying from a few millimetres to a decimetre in width (Fig. 1). It is mainly observed in the dolomitic rocks where the Nb mineralization is economically viable. In the dolomitic unit of the carbonatite, except for halite and pyrochlore, no other mineral has a significant Na content. Thin sections were prepared using a water-free lubricant to preserve chlorides. Halite was not observed as inclusions in apatite or phlogopite. It was observed in pores of weakly to

moderately altered pyrochlore (Fig. 2), but never in fresh pyrochlore.



Figure 1. Halite (Hl) crystallized as veinlets and observed in core samples. In some cases it is conserved during drilling, but most halite is usually dissolved during drilling and logging. The core diametre is 3.65 cm.

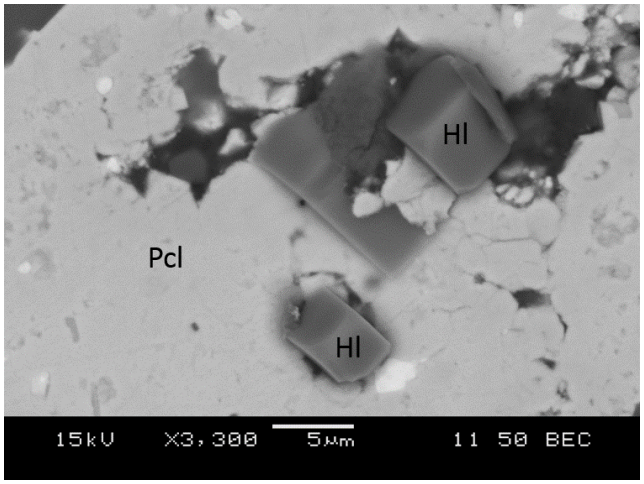


Figure 2. Halite (Hl) grains crystallized in pores of a moderately altered pyrochlore (Pcl). Grains of halite are roughly less than 10 µm. This backscattered electron (BSE) image was obtained by SEM analysis.

4 Pyrochlore, a source of sodium

To better understand the presence of halite in the carbonatite, we studied the mineral assemblages of the carbonatite (Tremblay et al., in preparation). Pyrochlore and columbite-(Fe) of the dolomitic unit are interpreted to be related by columbitization, an alteration process first described by James and McKie (1958) in the Tanganyika carbonatite. The alteration process releases Na, a major cation in pyrochlore (Lumpkin and Ewing 1995). Considering that the proportion of columbite-(Fe) slowly increases with depth, the quantity of leached Na is also expected to increase. Microprobe analyses of pyrochlore and columbite-(Fe) grains show that Cl is higher in columbite-(Fe) compared to fresh (unaltered) pyrochlore. Apatite and phlogopite associated with mineralization have Cl concentrations below detection limits.

5 Columbitization by hydrothermalism

The origin of pyrochlore alteration can be determined using a ternary diagram of the relative proportions of monovalent (Na), divalent cations (Ca, Sr, Fe^{2+} and Mn), and vacancies in pyrochlore (Lumpkin and Ewing 1995; Nasraoui and Bilal 2000; Zurevinski and Mitchell 2004). Based on microprobe results from this study and historical values (Tremblay et al., in preparation), the alteration trend is clearly hydrothermal (Fig. 3).

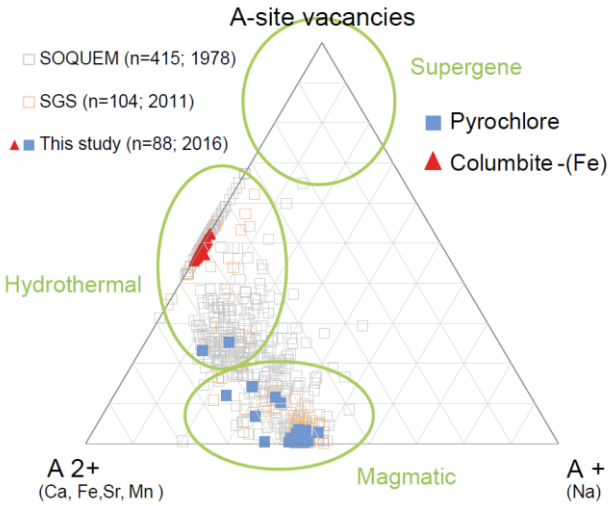


Figure 3. Ternary diagram of monovalent and divalent cations and vacancy of pyrochlore (based on Lumpkin and Ewing 1995) from the Saint-Honoré carbonatite. Although the diagram is not designed to plot columbite-(Fe), its position fits well with the hydrothermal field.

6 Discussion

The presence of halite, and therefore Na and Cl, raises questions regarding its contribution to the transport of economic elements and the origin of Na and Cl in carbonatites. Na is without doubt magmatic in the Saint-Honoré carbonatite, as it is a major constituent of fluorcalciopyrochlore (up to 8% Na_2O), one of the first minerals along with apatite to crystallize in a carbonatitic magma (Hogarth et al. 2000; Knudsen 1989). The strong relationship of pyrochlore to apatite and textural evidence argue for its magmatic origin.

The origin of Cl is, however, enigmatic. Based on the spatial distribution of halite in and around magmatic minerals from the Saint-Honoré carbonatite, Kamenetsky et al. (2015) proposed halite, and therefore Cl, to be mantle-derived. However, the study of the Nb-bearing minerals of the carbonatite suggests a slightly different interpretation of the petrogenesis of halite.

Petrographic observations and geochemical analysis of pyrochlore and columbite-(Fe) have shown that Na was leached during alteration, whereas Cl was related to

hydrothermal fluids. Thus, the Na is considered as magmatic in origin and Cl as being hydrothermal (Tremblay et al., in preparation). Our results show that the halite is not entirely magmatic, as argued by Kamenetsky et al. (2015), but rather magmatohydrothermal. The absence of Cl in other magmatic minerals (e.g., apatite and phlogopite) reinforces this idea of a non-igneous origin.

A mass balance exercise was applied to determine if the alteration of pyrochlore was an important source of Na. Pyrochlore accounted for only approximately 15% of total halite. However, the proportion of halite is uncertain due to its high solubility, and pyrochlore is mostly distributed as lenses and, therefore, its realistic proportion becomes difficult to estimate. Moreover, the deposit is open at depth and the proportion of pyrochlore might be higher at greater depths, suggesting that the input of Na from pyrochlore could have been even more substantial. Nevertheless, the alteration of pyrochlore contributed significantly to the formation of halite. It might be possible that this Na also contributed to the fenitization of the host rocks. This alteration is characteristic of alkaline rocks and more specifically to carbonatites. Silicate rocks are not in equilibrium with a carbonatitic magma and are probably less resilient to a salt-bearing hydrothermal fluid.

7 Conclusion

Halite, an enigmatic mineral in carbonatites, has one clear source: pyrochlore. Although alteration of pyrochlore is not the sole source, it contributes significantly to the total amount of halite. Furthermore, the presence of halite, and thus Cl, could have significantly increased the solubility of light rare earth elements (Migdisov and Williams-Jones 2014) and even Nb during magmatism and hydrothermalism. Halite would then be only a remnant of the transportation and/or concentration processes of Nb and REE mineralization in carbonatites.

Acknowledgements

This work is supported by a NSERC grant to LPB. J Tremblay thanks Niobec Mine Inc. for their ongoing support and the access to samples. The UQAC Foundation and DIVEX are also thanked for scholarship funds to J Tremblay. The extended abstract was corrected by Murray Hay (Maxafeau Editing Services).

References

Dimroth E, Woussen G, Roy, DW (1981) Geologic history of the Saguenay Region, Quebec (Central Granulite Terrain of the Grenville Province): a working hypothesis. Can J Earth Sci 18: 1506–1522

Fortin Bélanger M (1977) Le complexe annulaire à carbonatites de St-Honoré (P.Q. Canada) et sa minéralisation à niobium : étude pétrographique et géochimique. MSc thesis, Université du Québec à Chicoutimi, Chicoutimi, Canada, 210p

Fournier A (1993) Magmatic and hydrothermal controls of LREE mineralization of the St-Honoré Carbonatite, Québec. Unpublished M.Sc. thesis, McGill University, Montréal, Canada, 95p

Grenier L, Tremblay JF, Sirois R (2013) NI 43-101 Technical report, updated mineral resource estimate for rare earth elements, 2012. IAMGOLD Corporation, 166p

Higgins MD, van Breemen O (1996) Three generations of anorthosite-mangerite-charnockite-granite (AMCG) magmatism, contact metamorphism and tectonism in the Saguenay-Lac-Saint-Jean region of the Grenville Province, Canada. Precambrian Res 79:327–346

Hogarth DD, Williams CT, Jones P (2000) Fresh rock zoning in pyrochlore group minerals from carbonatites. Miner Mag 64:683–697

James TC, McKie D (1958) The alteration of pyrochlore to columbite in carbonatites in Tanganyika. J Min Soc 31:889–902

Kamenetsky VS, Mitchell RH, Maas R, Giuliani A, Gaboury D, Zhitova L (2015) Chlorine in mantle-derived carbonatite melts revealed by halite in the St.-Honoré intrusion (Québec, Canada). Geol 43:687–690

Knudsen C (1989) Pyrochlore group minerals from the Qaqarssuk carbonatite complex. In: Möller P, Cerný P, Saupé F (eds.) Lanthanides, Tantalum and Niobium, Springer-Verlag, Berlin-Heidelberg, 80–99

Kumarapeli PS, Saul VA (1966) The St. Lawrence valley system: A North American equivalent of the East African rift valley system. Can J Earth Sci 3:639–658

Lumpkin GR, Ewing RC (1995) Geochemical alteration of pyrochlore group minerals: Pyrochlore subgroup. Am Miner 80:732–743

Mangler MF, Marks MAW, Zaitzev AN, Eby GN, Markl G (2014) Halogens (F, Cl, and Br) at Oldoinyo Lengai volcano (Tanzania): Effects of magmatic differentiation, silicate-natrocarbonatite melt separation and surface alteration of natrocarbonatite. Chem Geol 365:43–53.

Migdisov A, Williams-Jones, AE (2014) Hydrothermal transport and deposition of the rare earth elements by fluorine-bearing aqueous liquids. Miner Deposita 49:987–997

Nasraoui M, Bilal E (2000) Pyrochlores from the Lueshe carbonatite complex (Democratic Republic of Congo): a geochemical record of different alteration stages. J Asian Earth Sci 18 :237–251

Néron A (2015) Caractérisation de la minéralisation de la zone à terres rares de la carbonatite de Saint-Honoré, Québec, Canada. MSc thesis, Université du Québec à Chicoutimi, Québec, Canada, 70p

Thivierge S, Roy DW, Chown EH, Gauthier A (1983) Évolution du complexe alcalin de St.-Honoré (Québec) après sa mise en place. Miner Deposita 18 :267–283

Zaitsev AN, Keller J (2006) Mineralogical and chemical transformation of Oldoinyo Lengai natrocarbonatites, Tanzania. Lithos 91:191–207

Zurevinski SE, Mitchell RH (2004) Extreme compositional variation of pyrochlore-group minerals at the Oka carbonatite complex, Quebec: Evidence of magma mixing? Can Miner 42:1159–1168

Indium mineralization in the East Kemptville Sn-Cu-Zn-Ag-In deposit, Nova Scotia

Jason Willson, Iain M. Samson
University of Windsor, Ontario, Canada

Daniel J. Kontak
Laurentian University, Ontario, Canada

Abstract. The past-producing East Kemptville Sn-Zn-Cu-Ag-In greisen deposit is located in the ca. 375 Ma Davis Lake Complex of the South Mountain Batholith of southwest Nova Scotia, Canada. The mine operated from 1985-1992 and was the only large primary past producing tin deposit in North America. Initial operations did not recognize the potential to recover In, and was more recently discovered during a re-investigation of the property. In mineralization occurs as trace element substitution in sphalerite, chalcopyrite, and, to a lesser extent, stannite and cassiterite. Preliminary results from this study indicate that minerals in greisen style mineralization contain higher In concentrations, than late, base-metal sulfide veins. This suggests that the source of the fluids that formed the greisens and sulfide veins was different, or that the physio-chemical character of fluids from a single source changed over time. The distribution of In varies among the different In-bearing minerals in different ore zones, further suggesting that different fluids or conditions existed.

1 Introduction

Granitoid-related magmatic-hydrothermal ore deposits are an important source of a range of commodities including Sn, W, Cu, and Mo. In addition, they are an important source of critical metals, where supply is globally limited and vulnerable. In is one of these critical metals, and is becoming widely used in several high technology applications such as photovoltaics, liquid crystal displays, and semiconductors. Currently, In is mostly recovered from base metal sulfide deposits, although high-grade In mineralization is known to be associated with granitoid-related deposits, such as the Mount Pleasant Sn-W-Mo-Bi-In deposit, in New Brunswick, Canada, with an estimated 680 t of In, at an average grade of 133 g/t (Green, 2009).

A less-studied example of granitoid-related In mineralization that occurs in a similar geological framework as Mount Pleasant is the East Kemptville Sn-Zn-Cu-Ag-In deposit, located in Yarmouth County of southwestern Nova Scotia. The deposit is the only large primary past-producing Sn deposit in North America, operating from 1985 to 1992, with pre-mining reserves of 56 Mt of 0.165% Sn (Kontak, 1994). The potential to recover In was not recognized during the initial mining operation, but was more recently realized during a re-examination by Avalon Rare Metals Inc. in 2007. Minimal work has been carried out the mineralogical distribution of In mineralization and its timing relationship relative to the Sn- and base-metal mineralization. In this contribution we examine how In is distributed between different ore zones and ore types that occur in the East Kemptville deposit, to determine if there are favourable mineralization styles, paragenetic stages or zones for In mineralization. These are related to the broader questions for the character and sources of fluids responsible for the different assemblages.

2 Geological setting

The East Kemptville deposit is located in the Meguma terrane of the northern Appalachian orogen and is hosted within the Davis Lake Complex, an 800 km^2 internally zoned granitic pluton at the western margin of the late Devonian (ca. 375 Ma) South Mountain Batholith. The Davis Lake Complex consists of a highly evolved suite of biotite monzogranites to leucomonzogranites, with the East Kemptville deposit hosted by a muscovite leucogranite (Kontak, 1994).

The deposit consists of structurally controlled greisen-style mineralization with two separate zones of mineralization: the Main and Baby zones. The greisen mineralization is further subdivided into 'zoned' and 'massive' mineralization types (Richardson, 1988; Halter et al., 1998). Massive greisens consists of large, elongate bodies (>20 m length) that exhibit quartz-topaz alteration and abundant, disseminated mineralization (Richardson, 1988). Zoned greisens are smaller, confined to individual veins, and typically exhibit a zoned alteration halo of quartz-topaz alteration near the vein with peripheral quartz-muscovite alteration. In both greisens, granite was altered by hydrothermal fluids to initially form a quartz-albite-muscovite greisen, and with further alteration forming quartz-muscovite and then quartz-topaz greisen. The quartz-topaz greisen alteration is accompanied by significant cassiterite and sulfide mineralization (Halter et al., 1998). Sulfide mineralization also occurs in the late, base-metal sulfide veins that cross-cut both zoned and massive greisens, and are found throughout the deposit (Kontak, 1994).

3 Analytical methods

Electron Microprobe analysis (EMPA) was carried out to determine In concentrations of selected minerals using a JEOL JXA-8530F field-emission electron microprobe located at the Earth and Planetary Materials Analysis (EMPA) laboratory at the University of Western Ontario,

Canada. The operating conditions used comprise a 25 kV accelerating voltage, 60 nA beam current, and a 1 µm beam diameter.

4 Results

4.1 Ore mineralogy and petrology

Two main ore mineral assemblages occur throughout the East Kemptville deposit. Assemblage 1 is characterized by cassiterite, wolframite ± arsenopyrite. This assemblage occurs only in massive- and zoned greisens, with arsenopyrite being more abundant in zoned greisens and in the Main Zone. Cassiterite typically occurs as fine- to medium-grained, subhedral to euhedral crystals that commonly exhibit growth zonation and can be found as aggregates or discrete grains (Fig. 1a). Wolframite is much less abundant than cassiterite, ranges from fine- to coarse-grained, occurs as tabular crystals, and forms discrete grains and shares mutual grain boundaries with cassiterite (Fig. 1b). Arsenopyrite is medium- to fine-grained, and occurs as euhedral- to subhedral crystals (Fig. 1c). In massive-greisen samples, arsenopyrite typically forms discrete grains, whereas in zoned greisens they more often occur as aggregates (Fig. 1d).

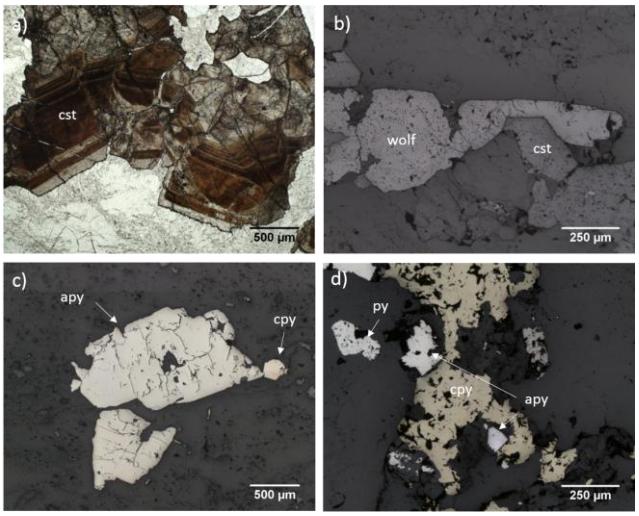


Figure 1. Photomicrographs of ore mineral associations of assemblage 1; a transmitted light, b-d reflected light. a) medium-grained cassiterite (cst) exhibiting growth zonation. b) tabular wolframite (wolf) sharing mutual grain boundaries with cassiterite. c) medium-grained suhedral arsenopyrite (apy) with adjacent chalcopyrite (cpy) in greisen vein. d) discrete euhedral arsenopyrite in massive greisen.

Assemblage 2 predominantly consists of pyrrhotite, pyrite, chalcopyrite, sphalerite, and stannite. This assemblage occurs in all of the types of mineralization. Pyrrhotite, chalcopyrite, and sphalerite commonly occur together and, in greisen mineralization, typically forms a mosaic texture, sharing smooth mutual grain boundaries (Fig. 2a). Discrete, euhedral crystals of pyrrhotite, chalcopyrite, and sphalerite also occur in the greisens. Sphalerite uncommonly contains chalcopyrite and/or pyrrhotite inclusions (Fig. 2b). Stannite often occurs as small grains (< 50 µm), and typically rims sphalerite, chalcopyrite, and cassiterite; discrete grains are rare (Fig. 2c). Pyrite and marcasite form incipient partial replacement to complete replacement of pyrrhotite. Assemblage 2 occurs in fractures, voids, and surrounding assemblage 1 minerals (Fig. 2d). In late, base-metal sulfide veins, assemblage 2 predominantly consists of sphalerite, with lesser amounts of chalcopyrite, pyrrhotite, and stannite. Sphalerite and chalcopyrite typically occur as coarse grains, whereas pyrrhotite typically forms medium- to fine grains and occurs as inclusions in sphalerite. Assemblage 2 does not vary mineralogical between the Main and Baby zones.

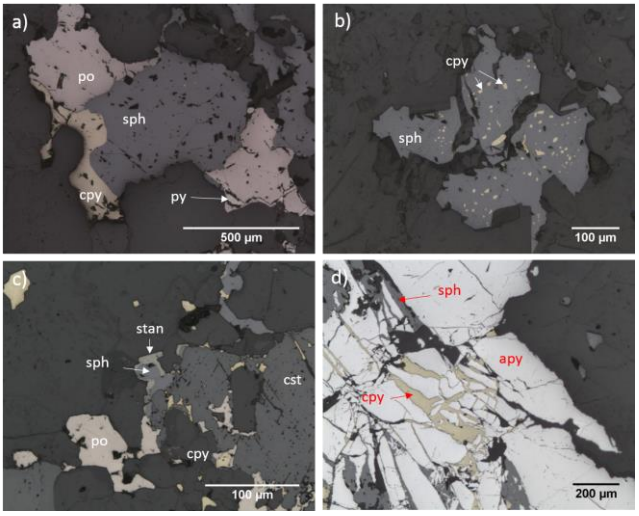


Figure 2. Photomicrographs of ore mineral associations of assemblage 2; a-d reflected light. a) pyrrhotite (po), sphalerite (sph), and chalcopyrite exhibiting smooth boundaries. Pyrite replacement of pyrrhotite. b) Sphalerite with chalcopyrite and pyrrhotite inclusions; in the former this may be chalcopyrite disease. c) stannite (stan) partially rimming sphalerite. d) Chalcopyrite and sphalerite infilling fractures in arsenopyrite.

4.2 Distribution of indium in oxide and sulfide minerals

Table 1 summarizes preliminary EMPA results on the concentration of In in the various oxide and sulfide minerals. Sphalerite, chalcopyrite, and stannite have the highest concentrations of In. Sphalerite is the most important host of In due to its overall high modal abundance in the deposit, and because it consistently contains high In concentrations of 1500 to 3000 ppm. Sphalerite contains moderate iron concentrations ranging from 7.1 to 10.3 wt. %, and minor amounts of Cd (0.55 to 0.70 wt. %). In concentrations in sphalerite generally correlate with Cu concentrations in sphalerite (Fig. 4.). The sphalerite with the highest In concentrations from this study (12,200 ppm) exhibits chalcopyrite 'disease' (Fig. 2b). Chalcopyrite can also contain significant amounts of In, although it is typically less abundant than sphalerite,

with In concentrations ranging from 140 to 1,300 ppm with an average concentration of 780 ppm. High-In chalcopyrite appears to form proximal to high-In sphalerite. EMPA data suggest that In is homogeneously distributed in individual crystals of both sphalerite and chalcopyrite. Stannite contains highly variable In concentrations, ranging from below detection to 19,600 ppm. High In concentrations in stannite typically correspond to high Zn concentrations. Cassiterite appears to be a less important host of In, and does not contain significant In concentrations (<250 ppm). Overall, assemblage 1 contains low In concentrations, due to the low abundance of In in cassiterite, whereas assemblage 2 contains the bulk of the In in the deposit.

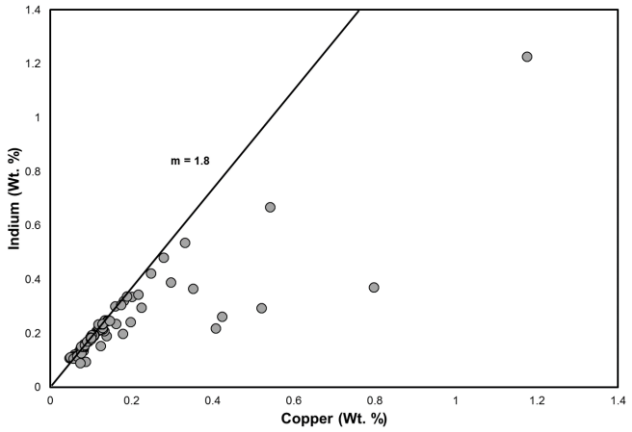


Figure 3. Cu vs In concentrations in sphalerite from EMPA. The control line with a slope of 1.8 reflects the idealized (Cu^{1+}+ In^{3+}) → 2(Fe^{2+},Zn^{2+}) coupled substitution in sphalerite. Samples that plot off the trend line contain higher Cu than expected from the coupled substitution.

	Minerals			
Indium (ppm)	Cassiterite (n= 16)	Sphalerite (n=78)	Chalcopyrite (n=53)	Stannite (n=20)
Minimum	< 100	90	140	0
Maximum	230	12270	1280	19600
Average	125	2265	780	1453
Median	115	1930	830	20

Table 1. In concentration by microprobe analysis for selected minerals.

The available data indicate differences in the In concentration of minerals between greisen and late-sulfide vein mineralization. However, these observations are based on a limited number of analyses and should be considered preliminary. Sphalerite from greisens in the Baby Zone overall contain higher concentrations of In than those in the Main Zone (Fig. 4a). For chalcopyrite there is greater overlap in the concentration ranges than for sphalerite, although the chalcopyrite average is also higher for the Baby Zone (Fig. 4b). The opposite appears to be the case for stannite, although the data is few in number (Fig. 4c).

The relationships are reversed for the late-sulfide veins with overall higher concentrations in the Main Zone sphalerite and chalcopyrite than in the Baby Zone (Fig. 4 a, b). For cassiterite in the greisens, In concentration shows the opposite trends to the sulfides in that the concentrations are overall higher in the Main Zone (Fig. 5).

In both the Main and Baby zones, chalcopyrite, sphalerite and stannite in the greisen-type mineralization contain higher In concentrations compared to the late-stage sulfide veins. Stannite in late sulfide veins contains low In concentrations (<200 ppm), whereas in greisens, stannite has variable In concentrations (Fig. 4c). Low-In stannite in greisens (100s ppm) typically rims and infills fractures in cassiterite, whereas high-In stannite (1000s to 10,000s ppm) typically rims high-In-bearing chalcopyrite and sphalerite.

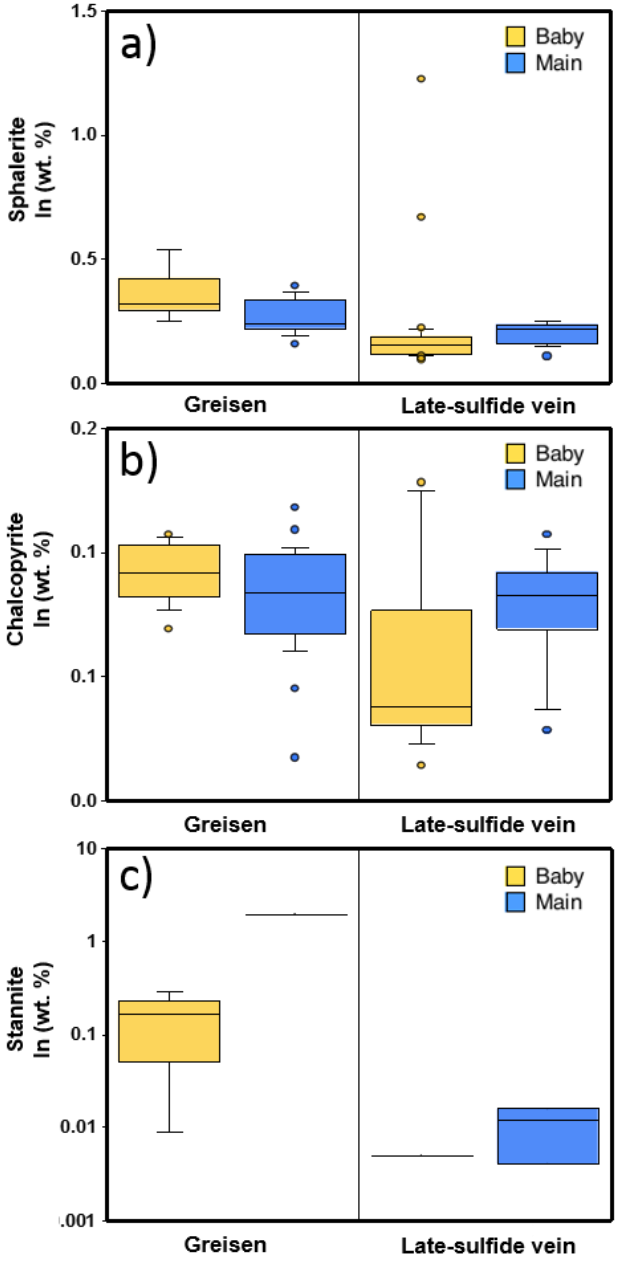


Figure 4. Box-whisker plots for In concentration in selected minerals from greisens and sulfide veins in the Main and Baby

Zone a) sphalerite, b) chalcopyrite, c) stannite. Note that the whiskers represent the 10th and 90th percentile, the lower end and upper end represent the 25th and 75th percentile, the line inside the box represents the median, and circles represent data below the 10th and above the 90th percentile.

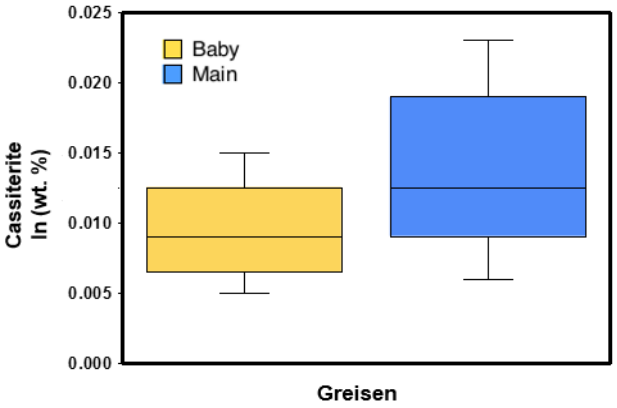


Figure 5. Box-whisker plots for In concentration in cassiterite from greisens from the Main and Baby Zone.

5 Discussion

The observed distribution of In carrier minerals at East Kemptville is similar to that observed from other In-bearing greisen deposits (e.g. Mt. Pleasant, Sinclair et al., 2003; Cornwall District, Anderson et al., 2016) where the principal In-bearing minerals are sphalerite, chalcopyrite, and stannite, with the highest In concentrations being observed in sphalerite and stannite and, to a lesser, extent chalcopyrite. In all deposits, sphalerite crystals with the highest In concentrations are those containing chalcopyrite inclusions (i.e., chalcopyrite disease). Unlike Mt. Pleasant and Cornwall, however, no minerals with In as a primary constituent (e.g., roquesite) have yet been recognized at East Kemptville. Cassiterite consists of low (10s to 100s ppm) In concentrations, which has been documented for other tin deposits (e.g., Pavlova et al.,2015). This suggests that cassiterite has a poor ability to sequester In.

In-bearing sulfide mineralization occurs in two mineralization styles: early greisens and late-stage base-metal sulfide veins, with the base-metal sulfide veins crosscutting greisen mineralization. This poses the question of whether the sulfides in the greisens represent a distinct, earlier event or are an overprint on the greisens where the sulphides precipitated from the same fluids as the fluids that formed the late-stage veins. In concentrations in the sulfide minerals from two mineralization styles appear to be different. Greisens contain minerals with higher In concentrations compared to the late-sulfide veins. This suggests that the sulfide mineralization in greisens represent a different fluid source or that the physio-chemical character of a fluid from a single source changed over time. The distribution of In between In-bearing minerals is different between the two ore zones. This further suggests that different fluids or physio-chemical conditions existed in the deposit.

Acknowledgements

The authors would like to gratefully acknowledge Dr. Bill Mercer for his support on the project. This work has been supported by Avalon Advanced Materials and NSERC through the Collaborative Research and Development grant.

References

Anderson JCO, Strickland RJ, Rollinson GK, Shail RK (2016) Indium mineralization in SW England: Host parageneses and mineralogical relations. Ore Geol Rev 78: 213-238

Green, MA (2009) Estimates of Te and In prices from direct mining of known ores. Prog Photovolt: Res Appl 17:347-359

George L, Cook NJ, Ciobanu CL (2016) Partitioning of trace elements in co-crystallization sphalerite-galena-chalcopyrite hydrothermal ores. Ore Geol Rev 77:97-116

Halter WE, Williams-Jones AE, Kontak D (1998) Origin and evolution of the greisenizing fluids at the East Kemptville tin deposit, Nova Scotia, Canada. Econ Geol 93:1026-1051.

Kontak D (1994) Geological and geochemical studies of alteration processes in a fluorine rich environment: The East Kemptville Sn-(Zn-Cu-Ag) deposit, Yarmouth County, Nova Scotia, Canada. In: Lentz D (ed), Alteration and alteration processes associated with ore-forming systems: Geological Association of Canada, Short course notes 11:261-314

Pavlova G, Palessky S, Borisenko A, Vladimirov A, Seifert TH, Luu Anh Phan (2015) Indium in cassiterite and ores of tin deposits. Ore Geol Rev 66:99-113

Richardson J (1988) Genesis and geochemistry of the East Kemptville greisen-hosted tin deposit, Davis Lake complex, southwestern Nova Scotia, Canada. Dissertation, Carleton university.

Sinclair WD, Kooiman GJA, Martin DA, Kjargaard IM (2006) Geology, geochemistry, and mineralogy of indium resources at Mount Pleasant, New Brunswick, Canada. Ore Geol Rev 28:123-145.

Fluid inclusion, H-O, S, Pb and noble gas isotope studies of the Aerhada Pb-Zn-Ag deposit, Inner Mongolia, NE China

Hongyu Zhang, Degao Zhai, Jiajun Liu
China University of Geosciences, Beijing

Abstract. The Aerhada Pb-Zn-Ag deposit is located in the western segment of the Great Hinggan Range Ag-Pb-Zn-Cu-Mo-Au-Fe metallogenic belt in NE China. Mineralization mainly occurs as ore-bearing quartz veins hosted by sandstone and siliceous slate. The ore-forming processes can be divided into three stages, including an early arsenopyrite-pyrite-quartz, a middle polymetallic sulfides-silver minerals-quartz and a late sphalerite-pyrite-calcite-fluorite stages. Microthermometric investigations on fluid inclusions reveal that homogenization temperatures for early to late stages range from 253º to 430°C, 195º to 394°C and 133º to 207°C. Fluid salinities show a range from 2.9 to 14.0 wt. % NaCl equiv. The fluid $\delta^{18}O_{H2O}$ and δD_{H2O} data mostly reflect a mixed magmatic and meteoric hydrothermal system. The calculated $\delta^{34}S_{H2S}$ values of hydrothermal fluids in equilibrium with sulfides suggest a sulfur source from mixtures of local magmatic and sedimentary rocks. The Pb isotope compositions of sulfides are similar to those of the local magmatic and sedimentary rocks, suggesting Pb and possibly other metals from both sources. The noble gas isotope compositions of fluid inclusions hosted in ore minerals demonstrate that the ore-forming fluids were dominantly derived from the deep mantle. Fluid mixing is inferred as the dominant mechanism for ore deposition.

1 Introduction

The Great Hinggan Range (GHR), which lies in the easternmost part of the Central Asian Orogenic Belt, is an important Ag-Pb-Zn-Mo-Cu-Au-Fe metallogenic belt in NE China. The Aerhada Pb-Zn-Ag deposit (1.0 Mt Pb+Zn@5.18% and 1000 t Ag@57.66g/t) is located in the East Ujimqin in the west segment of the GHR in NE China. This study draws on detailed field investigations together with new data from fluid inclusions and multiple isotope (H-O, S, Pb, He-Ar) compositions from the Aerhada deposit. Combined with previous published data from the deposit, we mainly address the following aspects: (1) the source, nature and evolution of the ore-forming fluids, (2) the source of metals, and (3) the mechanism of Pb-Zn-Ag mineralization and ore deposit type.

2 Regional geology

The western part of the GHR is part of a Paleozoic orogenic belt on the south side of the large-scale South Mongolian arcuate tectonic belt between the North China plate and the Siberian plate. This region is an important part of the Central Asian Orogenic Belt and an important metallogenic belt. The upper Paleozoic strata are widely exposed in the region. The regional Paleozoic Central Asian–Mongolian orogeny, and the Mesozoic volcanism and magmatism are favourable for the local mineralization (Zhang et al. 2015).

3 Ore deposit geology

The strata exposed in the ore district are mainly volcano-sedimentary rocks of the Upper Devonian Angeryin Wula Formation and the Upper Jurassic Baiyin Gaolao Formation as well as Tertiary and Quaternary sediments (Fig. 1). The Devonian Angeryin Wula strata, which are the main host rocks, are widely distributed in the mining area with a relatively complex lithology, including andesitic tuff, sandstone, siltstone, argillaceous slate and siliceous slate.

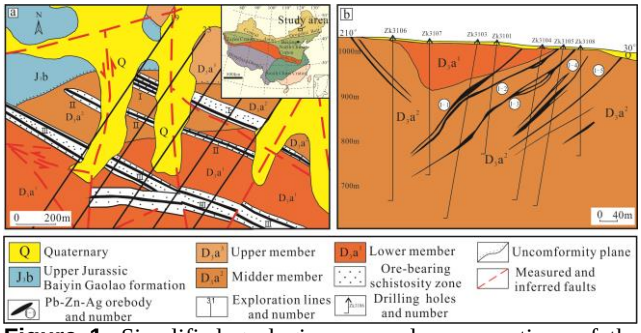


Figure 1. Simplified geologic map and cross sections of the Aerhada Pb–Zn–Ag deposit.

Three distinct ore belts (I, II and III) have been identified in the Aerhada deposit (Fig. 1a). All Pb-Zn-Ag mineralization occurs as veins in different belts. Ore belt I hosts the main ore, which is located in the northern part of the district. It has a length of 3200 m and width of 350 m to >600 m with a general strike of 305° (Fig. 1a). The ore-bearing veins decline southwest, with a dip between 25° and 55° (Fig. 1b).

The main ore minerals include galena, sphalerite, and pyrite, with minor proportions of arsenopyrite, chalcopyrite, chalcocite and argentite. The gangue minerals include quartz, chlorite, epidote, kaolinite, sericite, calcite, and fluorite. In general, mineral assemblages of quartz-epidote, quartz-chlorite-epidote-sericite, and calcite-fluorite-kaolinite-clay minerals formed from early to late

stages, respectively. Hydrothermal alteration is limited, and the most intense alteration occurred around the mineralized Pb-Zn-Ag veins, including silicification and carbonatization. Other alteration types consist of kaolinization, sericitization, chloritization and epidotization. The alteration zonation is not clearly developed as in most places the different alteration types were superimposed upon one another.

On the basis of the field cross-cutting relationship of veins, ore mineral assemblages and their textural relationships, ore and alteration minerals in the deposit can be divided into three paragenetic stages, i.e., arsenopyrite-pyrite-quartz stage (stage I), galena-sphalerite-pyrite-silver-bearing sulfosalts-quartz stage (stage II) and sphalerite-pyrite-calcite-fluorite period.

4 Fluid inclusions

Microthermometric investigations on fluid inclusions hosted in quartz and fluorite in textural equilibrium with sulfide minerals from early to late mineralization stages showed a gradual decrease for fluid temperature (Fig. 2). Similarly, as hydrothermal fluid evolved, fluid salinity demonstrated a decreased trend, i.e., average salinity values from 9.6 to 6.6 wt. % NaCl equiv. Therefore, the Aerhada hydrothermal system was characterized by both temperature and salinity decrease during fluid evolution (Fig. 3). A decrease in average salinity with drop in temperature is suggestive of fluid mixing (Fig. 3).

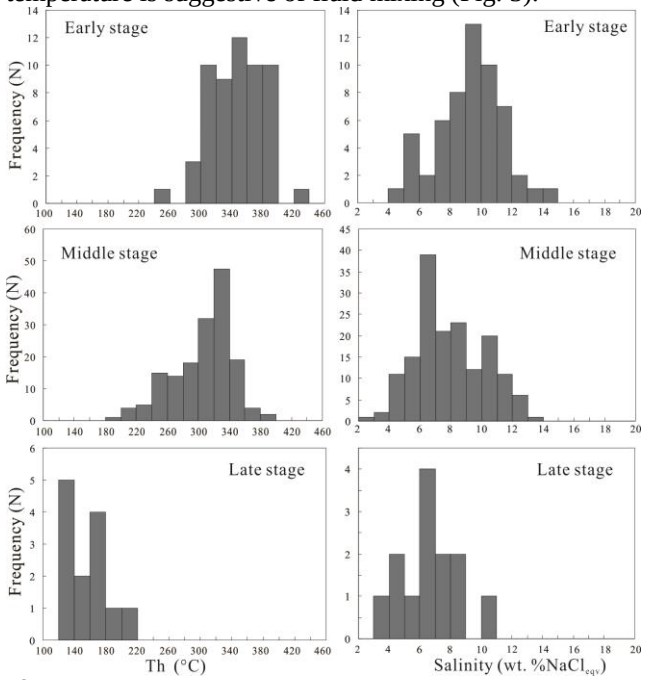


Figure 2. Histogram of homogenization temperature and salinity of the ore fluid for the Arehada Pb-Zn-Ag deposit.

Evidences from laser Raman analyses on fluid inclusions from early stage samples indicated that the vapor phase was dominated by H_2O and CO_2 with minor proportions of CH_4; whereas the vapor phases in fluid inclusions from middle and late stage samples were mainly composed by H_2O, CH_4 and CO_2 with minor amounts of N_2. Consequently, from early to late stages, the CO_2 contents of the ore-forming fluids gradually decrease, whereas CH_4 contents gradually increase, suggesting that the ore-forming fluid evolved from an oxidation state to a relative reduction state.

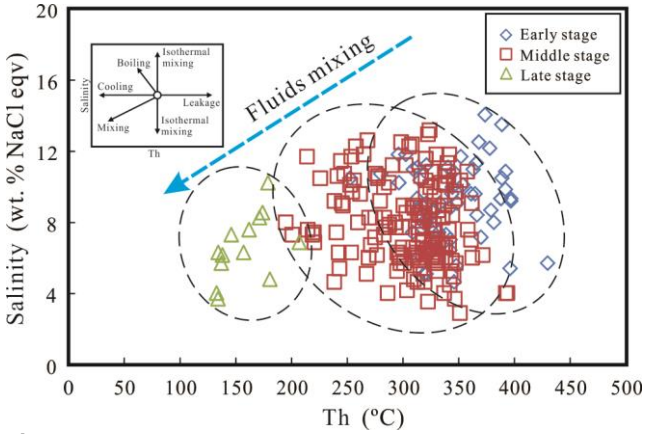


Figure 3. Homogenization temperature (Th) versus salinity plots of ore fluids for the Aerhada deposit. Inset illustration for different fluid evolution paths is based on Shepherd et al. (1985).

Based on the characteristics and evolution of hydrothermal system, we conclude that the ore-forming fluid responsible for the formation of the Aerhada deposit was characterized by a fluid mixing, accompanied with a large involvement of relative cool, reducing and dilute fluid in the hydrothermal system during mineralization, which are important to trigger sulfide precipitation.

5 Source of ore-forming fluids, sulfur and metals

Six different quartz and calcite samples from various mineralized stages were analyzed for oxygen (quartz and calcite) and hydrogen (fluid inclusions) isotopes using a MAT-253 stable isotope ratio mass spectrometer. The $\delta^{18}O_{H2O}$ values for early and middle stage veins are similar to those of magmatic water, and those for late stage are even lower; whereas the δD_{H2O} values for early and middle stage fluids plot below the field for typical magmatic water and those for late stage are similar to magmatic water (Fig. 4). The drop of the $\delta^{18}O_{H2O}$ values can mostly be explained as the addition of meteoric water, resulting in a migration of D-O isotope data points to the meteoric water line. The relatively low δD_{H2O} ratios in the early and middle stage and rise of δD_{H2O} values in late stage fluids are likely attributed to a bulk fluid inclusion analysis containing probably both primary and secondary inclusions (Goldfarb and Groves 2015).

The $\delta^{34}S$ values of sulfides and combined with previous data (Zhang et al., 2007) from the Aerhada Pb-Zn-Ag deposit demonstrate a range from +1.2 to +8.6‰ (mean = +5.8‰, n=30), which are similar to but more positive than the $\delta^{34}S$ values of sulfides from the majority of magmatic

hydrothermal deposits (−3 to +1‰; Hoefs 2009). The average $\delta^{34}S$ values of pyrite, sphalerite and galena from the deposit are 6.52‰, 6.50‰, 4.16‰, respectively, which are in general agreement with the equilibrium sequence of $\delta^{34}S_{Py}>\delta^{34}S_{Sp}>\delta^{34}S_{Gn}$, suggesting that the ore-forming system is in equilibrium (Ohmoto 1986). In addition, the calculated $\delta^{34}S_{H2S}$ values of ore-forming fluids in equilibrium with sulfides vary from 5.2 to 7.1‰ and average in 6.1‰, which lie between that of magmatic and sedimentary rocks (Ohmoto and Rye 1979), indicating sulfur in the Aerhada deposit was mainly derived from local magmatic and sedimentary sources.

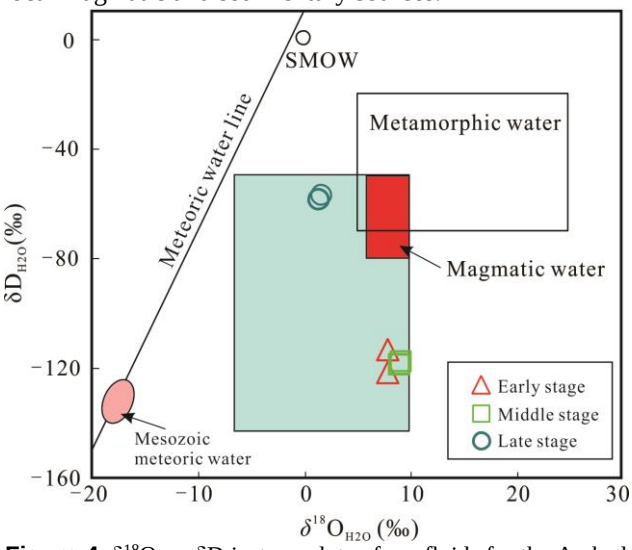


Figure 4. $\delta^{18}O_{H2O}$-δD isotope plots of ore fluids for the Aerhada Pb-Zn-Ag deposit. The green rectangle area represents the D-O isotope compositions for numerous hydrothermal Pb-Zn-Ag deposits in southern part of the GHR.

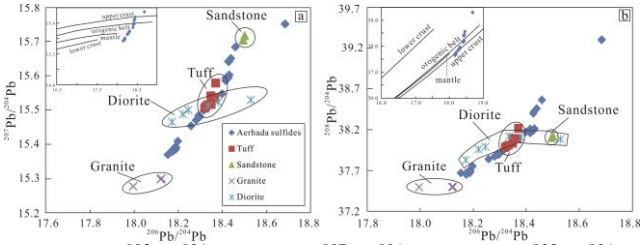


Figure 5. $^{206}Pb/^{204}Pb$ versus $^{207}Pb/^{204}Pb$ (a) and $^{206}Pb/^{204}Pb$ versus $^{208}Pb/^{204}Pb$ (b) plots of sulfides and various rocks from the Aerhada deposit.

In order to evaluate the metal source, we have collected previously published Pb isotope data, including Pb isotope ratios for local tuff, sandstone, Trassic diorites, and Jurassic to Cretaceous granites (Zhang et al. 2007). Based on $^{206}Pb/^{204}Pb$, $^{207}Pb/^{204}Pb$ and $^{208}Pb/^{204}Pb$ ratios in binary plots (Zartman and Doe 1981) (Fig. 5), the Pb isotopic compositions of the Aerhada sulfides plot mainly in the area between the upper crust and the orogenic belt with several data in the mantle. These plots could not distinguish the likely source for the metal. To further evaluate the metal source, we have compared the newly obtained Pb isotope data with previously reported data from various samples. Notably, the Pb isotope ratios of the sulfides were plotted between the local Mesozoic magmatic (i.e., granite) and the sedimentary rocks (i.e., sandstone) (Fig. 5). This suggests that Pb and possibly other metals are derived from both sources.

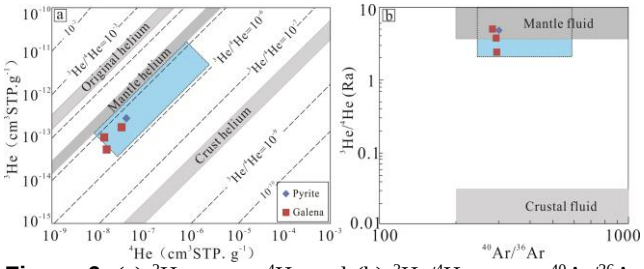


Figure 6. (a) ^{3}He versus ^{4}He and (b) $^{3}He/^{4}He$ versus $^{40}Ar/^{36}Ar$ plots of fluid inclusions hosted in sulfides from the Aerhada deposit.

The $^{3}He/^{4}He$ ratios (2.5-5.4 Ra) of ore-forming fluids responsible for formation of Pb-Zn-Ag ores in the main mineralization stage from the deposit are much higher than that of the crust (0.01-0.05 Ra; Stuart et al. 1995) but very close to that of the mantle (6-7 Ra; Burnard et al. 1999). This suggests that the ore-forming fluids are mainly composed by mantle helium. In the ^{3}He versus ^{4}He (Fig. 6a) and $^{3}He/^{4}He$ versus $^{40}Ar/^{36}Ar$ (Fig. 6b) plots, all the obtained data fall near or in the mantle He origin, indicating a significant contribution of mantle helium into the Aerhada ore system. The noble gas isotope data from the studied deposit are consistent with numerous Pb-Zn-Ag ore deposits from the central and south segment of the Great Hinggan Range (Wang et al. 2008), reflecting that those hydrothermal deposits might share some similar processes for their genesis. With consideration of their tectonic settings, a large number of hydrothermal deposits formed in NE China are related to the subduction of Paleo-Pacific plate and some with the Paleo-Asian plate subduction (i.e., the Duobaoshan Cu deposit, Zeng et al. 2014). In such a tectonic setting, the possible addition of radiogenic helium from the subducted crustal materials into the hydrothermal system would lead helium isotopic ratios for the mantle lower than typical MORB (8 Ra; Ozima and Podosek 2002). In addition, we have calculated the percentage of the mantle helium for ore system on the basis of the equation proposed by Kendrick et al. (2001). The results show that mantle-derived helium are in the range of 32 to 69% with an average of 53% for the Aerhada deposit, indicating that mantle fluid accounts for a considerable proportion.

6 Implications for Pb-Zn-Ag mineralization

Both hydrothermal fluid temperature and salinity gradually decreases from the early to late mineralization stages for the Aerhada deposit are consistent with a fluid-mixing scenario (Zhai et al. 2013). This further reflects that the homogenization temperature and salinity of the mineralizing fluids responsible for arsenopyrite and pyrite associated with quartz precipitation in the early stage

decreased through later stages of mineralization (Pb-Zn-Ag minerals with fluorite and calcite precipitation). Ore-forming fluids ascended along the NE- and NW-trending extensional fractures/faults and reacted with wall rock, changing the physicochemical conditions and isotopic compositions of the fluids. The addition of the meteoric water into the hydrothermal system might have extracted variable amounts of metals and sulfur from the host sedimentary rocks. Fluid mixing accompanied with variations of physicochemical properties and metal contents would destroy the chemical equilibrium of solutions and initiate relevant chemical reactions, ultimately resulting in ore mineral precipitation from solution during formation of the ore deposit. This is consistent with the concept that fluid mixing, cooling, and fluid-rock interactions play important roles in deposition of sulfides from hydrothermal fluids (Heinrich 2007).

The obtained D-O, S, Pb isotopic compositions from the deposit suggest that the ore fluids are most likely derived from deep magma with addition of meteoric waters, and the metals are mostly originated from both local magmatic and sedimentary sources. Moreover, our obtained noble gas isotopes indicate that the ore fluids show a deep mantle origin, which is consistent with the regional tectonic evolution involved large-scale oceanic plate subduction and subsequent lithospheric delamination and extension. Under such tectonic settings, the regional NE- and NW-trending extensional fractures and faults are favourable channels for ore fluid transportation (Tao 2006).

As discussed above, our geologic, fluid inclusion and isotope studies suggest that the Aerhada deposit shares numerous geological and geochemical characteristics with the majority magmatic-hydrothermal ore deposits in south segment of the Great Hinggan Range (Zhai et al. 2014). Therefore, based on ore deposit geology, fluid inclusion and isotope data, this deposit could be classified as a typical medium-low temperature hydrothermal vein type Pb-Zn-Ag deposit.

Conclusions

(1) Fluid inclusion studies indicate that the ore-forming fluid responsible for the formation of the deposit was characterized by a fluid mixing, accompany with a large involvement of relative cool, reducing and dilute fluid into the hydrothermal system during Pb-Zn-Ag mineralization.
(2) The obtained multiple (D-O, S, Pb, He-Ar) isotopic compositions suggest that the ore fluids are most likely derived from deep magma with addition of meteoric waters, and the metals are mostly originated from both local magmatic and sedimentary sources.
(3) The Aerhada deposit could be classified as a typical medium-low temperature hydrothermal vein type Pb-Zn-Ag deposit.

Acknowledgements

This research was financially supported by the NSFC (41672068), the Inner Mongolia Academician project (No. 2014-01-YS01), and the Chinese "111" project (No. B07011).

References

Burnard PG, Hu R, Turner G, Bi XW (1999) Mantle, crustal and atmospheric noble gases in Ailaoshan Gold deposits, Yunnan Province, China. Geochim Cosmochim Acta 63: 1595-1604

Goldfarb RJ, Groves DI (2015) Orogenic gold: common or evolving fluid and metal sources through time. Lithos 233: 2-26

Heinrich CA (2007) Fluid-fluid interactions in magmatic-hydrothermal ore formation. Rev Mineral Geochem 65: 363-387

Hoefs J (2009) Stable isotope geochemistry, 6th ed.: Berlin Heidelberg, Springer-Verlag, pp. 1-285

Kendrick MA, Burgess R，Pattrick RAD, Turner G (2001) Fluid inclusion noble gas and halogen evidence on the origin of Cu-Porphyry mineralising fluids. Geochim Cosmochim Acta 65: 2651-2668

Ohmoto H (1986) Stable isotope geochemistry of ore deposits. Rev Mineral Geochem 16: 491-559

Ohmoto H, Rye RO (1979) Isotopes of sulfur and carbon. In: Barnes, H.L. (Ed.). Geochemistry of Hydrothermal Ore Deposit. Wiley, New York, pp. 509–567

Ozima M, Podosek FA (2002) Noble Gas Geochemistry. Cambridge University Press, Cambridge, pp. 1-286

Shepherd TJ, Rankin AH, Alderton D (1985) A practical guide to fluid inclusion studies. Blackie and Son, Ltd., London, pp. 1-239

Stuart FM, Burnard PG, Taylor RP, Turner G (1995) Resolving mantle and crustal contributions to ancient hydrothermal fluids: He-Ar isotopes in fluid inclusions from Dae Hwa W-Mo mineralisation, South Korea. Geochim Cosmochim Acta 59: 4663-4673

Tao Z (2006) Geological characteristics of Aerhada lead & zinc deposit in Dongwuqi county, Inner Mongolia, China. Contrib Geol Miner Resour Res 21: 74-76 (in Chinese with English abstract)

Wang BD, Niu SY, Sun AQ, Hu HB, Liu YM, Guo LJ, Wang S (2008) Helium-argon isotopic tracing for the Pb-Zn-Ag polymetallic ore deposits in the central-south segment of the Da Hinggan Ling Range. Chin J Geochem 27: 235-241

Zartman RE, Doe BR (1981) Plumbotectonics: the model. Tectonophys 75: 135-162

Zeng QD, Liu JM, Chu SX, Wang YB, Sun Y, Duan XX, Qu WJ (2014) Re–Os and U–Pb geochronology of the Duobaoshan porphyry Cu–Mo–(Au) deposit, northeast China, and its geological significance. J Asian Earth Sci 79: 895-909

Zhai DG, Liu JJ, Wang JP, Yang YQ, Zhang HY, Wang XL, Zhang QB, Wang GW, Liu ZJ (2014) Zircon U-Pb and molybdenite Re-Os geochronology, and whole-rock geochemistry of the Hashitu molybdenum deposit and host granitoids, Inner Mongolia, NE China. J Asian Earth Sci 79: 144-160

Zhai DG, Liu JJ, Wang JP, Yao MJ, Wu SH, Fu C, Liu ZJ, Wang SG, Li YX (2013) Fluid evolution of the Jiawula Ag-Pb-Zn deposit, Inner Mongolia: Mineralogical, fluid inclusion, and stable isotopic evidence. Int Geol Rev 55: 204-224

Zhang WY, Nie FJ, Liu SW, Zuo LY, Yao XF, Jia DL, Liu JT (2015) Characteristics and genesis of mineral deposits in East Ujimqin Banner, western segment of the Great Xing'an Mountains, NE China. J Asian Earth Sci 97: 459-471

Zhang WY, Nie FJ, Liu Y, Jiang SH, Xu Z, Hu P, Lai XR, Pi XD (2007) Studies on sulfur and lead isotope of the Arehada Pb–Zn–Ag deposit, Dong Ujmqin Qi (County), Inner Mongolia. J Jilin Univ (Earth Sci Ed) 37(5): 868–883 (in Chinese with English abstract)

Petrographic and mineral chemical characteristics of the Jianfengling granite stock in the Nanling Range, South China: insights into the evolution of a highly evolved Li-F granitic magma

Xu Zhao
Nanjing University, China

Jianjun Lu
Nanjing University, China

Rucheng Wang
Nanjing University, China

Abstract. The Jianfengling granite stock in the Western Nanling Range of South China, represents a highly evolved, strongly peraluminous, Li-F rich and P-poor granite system of Late Jurassic age (~ 156 Ma). There is a distinct vertical zonation developed in the Jianfengling granite stock. Based on paragenesis, textural characteristics, and rock-forming mineral compositions, four petrographic units can be distinguished from the bottom to the top: protolithionite K-feldspar granite, zinnwaldite-albite granite, topaz greisen and greisenized granite, and stockscheider. The principal W-Sn-Ti-Nb-Ta minerals include columbite group minerals, microlite, wolframite, wolframoixiolite, cassiterite, ilmenorutile, and strüvertite; these minerals exhibit continuous compositional trends related by progressive fractionation from protolithionite K-feldspar granite to topaz greisen. However, in the uppermost stockscheider, the composition of mica and W-Sn-Nb-Ta minerals show less-differentiated characteristics. In addition, the Zr/Hf ratio and REE pattern of zircon also imply that the formation of stockscheider is not from the most fractionated granitic melt stage but at the early stage caused by liquid immiscibility between aluminosilicate and hydrosaline liquids. Meanwhile, the variation of accessory mineral assemblages and W, Sn, Nb, and Ta contents of zircon may provide information about the behavior of rare-metals during volatile-rich magma evolution and subsequently the magmatic-hydrothermal transition.

1 Introduction

Rare element mineralization, including W, Sn, Nb, Ta, Li, Rb, Cs, Be, etc., is closely associated with peraluminous granites (e.g. Beauvoir granite, France: (Cuney et al. 1992; Raimbault et al. 1995), Yichun granite, China: (Yin et al. 1995); Orlovka granite, Russia(Badanina et al. 2004)) and granitic pegmatites (Tanco pegmatite, Canada (Cerny and Siivola 1980); Nanping No. 31 pegmatite dyke, China (Rao et al. 2009)). Vertical zonation, accompanied by geochemical and mineralogical variation, is a common characteristic in highly evolved Li-F rich peraluminous granites (Kovalenko and Kovalenko 1984; Pollard 1989; Huang et al. 2002). It is generally agreed that fractional crystallization is the major controlling factor during magmatic differentiation. Enrichment of ore elements such as Nb, Ta, Sn, W etc., and volatile components (H_2O, F, P, B) during intense fractional crystallization, results in disseminated economic concentrations of Nb, Ta, Sn, and Li in the roof zone of plutons (Pollard 1989; Cerny et al. 2005). However, the liquid immiscibility phenomenon found in experimental studies of melt/fluid inclusions in natural and synthetic granitic samples (Veksler et al. 2002; Badanina et al. 2004; Veksler 2004; Thomas et al. 2006) draws wide attention in deciphering the magmatic processes and the magmatic-hydrothermal transition stage.

Hence, study on the vertical zonation of highly evolved peraluminous granites by systematic mineralogy not only can reveal the details of processes from the early to late stages of magmatic evolution, but also provide information about the role of liquid immiscibility. The purpose of this work is to describe the highly evolved granitic melts, using accessory mineral assemblages and mineral chemical variations and then access whether liquid immiscibility can occur in the early stages of the evolution of volatile-rich natural granitic magmas.

2 Geological setting

2.1 Mesozoic events in South China

Zhou (2006) Mesozoic magmatism in South China can be divided into two periods: the Triassic (251-205 Ma) and the Middle-Late Jurassic (180-142 Ma). Hundreds of W-Sn-Nb-Ta ore deposits are found in the Nanling Range, related to Mesozoic large-scale granitic magmatism, especially between 165 and 155 Ma (Sun et al. 2012). The dominant tectonic regime changed from Tethyan to paleo-Pacific domains in Mid-Late Jurassic due to the oblique subduction of the paleo-Pacific plate beneath the Eurasian continent (Mao et al. 2013). The rare-metal bearing granites in the Nanling Range were formed in an intracontinental extensional environment.

2.2 The Jianfengling W-Nb-Ta ore district

The Jianfengling W-Nb-Ta ore district is located in the

western Nanling Range, approximately 20 km west of the Qitianling batholith, and occurs to the west of the deep-seated NNE-SSW trending Chenzhou-Linwu fault.

The Jianfengling granite has an exposed area of approximately 4.4 km^2, and intruded Devonian and Carboniferous limestones and dolomites. This stock was emplaced in the late Jurassic period (156~160 Ma, Xuan et al. 2014 and unpublished coltan U-Pb data from Dr. Xudong Che). Geochemically, the Jianfengling granite is characterized by high silica (~67-74 wt.% SiO_2), high alkali (7.0-9.4 wt.% Na_2O+K_2O) and high alumina (13.4-18.2 wt.% Al_2O_3). It is poor in FeO (0.4-1.9 wt.%), MgO (<0.4 wt.%), CaO (0.4-0.9 wt.%), and TiO_2 (<0.04 wt. %), and is alkaline and strongly peraluminous in composition with alkalinity ratios (A.R.) of 3.5-7.8 and alumina saturation indices (ASI) of 1.18-1.57. The Jianfengling granite has elevated F (0.9-4.5 wt. %) but low P (~0.01wt.%) contents and thus can be classified into the low-P subtype topaz granite (Raimbault et al., 1991; Taylor, 1992).

Polymetallic mineralization, including Nb, Ta, W, Sn, Pb, Zn, Be, and F, has spatial and genetic relationships with the Jianfengling granite (e.g. Jianfengling Nb-Ta deposit; Xianghuapu scheelite-fluorite deposit; Dongshan scheelite-fluorite deposit; and Paojinshan galena-sphalerite-sulphide deposit; Fig 1a). The Jianfengling Nb-Ta ore deposit hosts 7478t of (Ta_2O_5+ Nb_2O_5), with an average grade of 0.026% (Ta_2O_5 + Nb_2O_5).

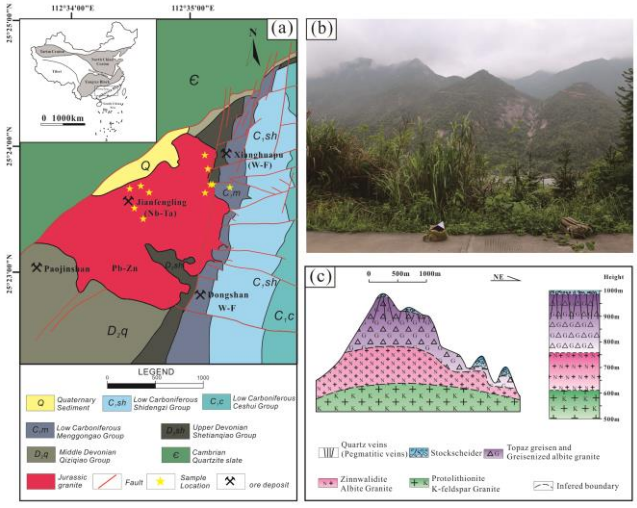


Figure 1. (a) Sketch geological map of the Jianfengling granite stock (Wang 1993). (b) Photograph showing the outcropping of the Jiafengling granite stock. (c) Simplified cross-section of the Jianfengling granite stock in NE direction

3 Petrographic study

Based on observation by optical microscopy and scanning electron microscope (SEM) and analytical data for feldspar and mica by electron probe microanalysis (EPMA), four petrographic units can be distinguished from the bottom to the top: protolithionite K-feldspar granite, zinnwaldite albite granite, topaz greisen and greisenized granite, and stockscheider (Fig 1c). These units are subhorizontal and the boundaries between the two granite units are gradual transitions without sharp intrusive contacts, suggesting in-situ magmatic differentiation of a single intrusion rather than successive magma batches. Detailed petrographic description of these four units are as follows:

1) Protolithionite K-feldspar granite
   The protolithionite K-feldspar granite is white to grey, medium to coarse grained, and has an inequigranular texture. It consists of quartz (35~40 vol.%), perthite (30~35 vol.%), albite (15~20 vol.%), and protolithionite (5~10 vol.%). Quartz and K-feldspar are generally subhedral and anhedral, respectively, while albite laths vary from subhedral to euhedral and occur as poikilitic inclusions inside quartz and K-feldspar phenocrysts. This unit is characteristized by mica with distinct pleochroism, from light brown to light green, and perthitic K-feldspar. The accessory minerals include zircon, monazite, xenotime, ilmenorutile etc.
2) Zinnwaldite albite granite
   The zinnwaldite albite granite is white to grey and medium to fine grained, and contains quartz (25~30 vol. %), albite (30~40 vol. %), K-feldspar (20~25 vol. %), and zinnwaldite (5~10 vol. %), as well as minor amount of topaz and fluorite. Its accessory minerals include zircon, monazite, xenotime, bastnäsite, amblygonite, and etc. Zinnwaldite shows a weak pleochroism from light green to colorless.
3) Topaz greisen and greisenized granite
   In this unit, there is no boundary between topaz greisen and greisenized granite in vertical direction. It seems that greisenized granite is embedded irregularly in the topaz greisen. The topaz greisen mainly consists of quartz, zinnwaldite, and topaz. In the greisenized granite, euhedral to subhedral albite laths and mica flakes are concentrically arranged along the growth zone inside quartz and K-feldspar phenocrysts. This texture is referred as “snowball texture”, which is a typical phenomenon in rare-metal granite, especially the albite-rich zone (Zhu et al. 2001). In the topaz greisen, the proportion of rock-forming minerals (quartz, zinnwaldite, topaz) have a wide range value of loss on ignition (LOI) due to the heterogeneity in topaz greisen. Sulfide (galena, sphalerite) mineralization is pervasive through the topaz greisen and greisenized granite. This unit is closely associated with the Nb and Ta mineralization, and columbite-group minerals, high-Ta cassiterite, and microlite occur as the main ore minerals.
4) Stockscheider
   The stockscheider unit occurs in the uppermost part of the Jianfengling granite stock, with a thickness of 10~20 m, and comprises protolithionite, quartz, and topaz. The protolithionite crystals are up to several centimeters in size. Topaz is present as aggregates of long prismatic crystals. Wolframite occurs as an accessory mineral associated with protolithionite.

According to the empirical equation and the classification diagram of Li-bearing trioctahedral mica (Tischendorf et al. 1997), combined with Li content of

bulk rock samples (564 ppm, protolithionite K-feldspar granite; 998 ppm, zinnwaldite albite granite; 2357 ppm, greisenized granite), Li-bearing mica can be classified into three types: protolithionite, zinnwaldite, lepidoite. There is a continuous chemical evolution trend from early-stage protolithionite through zinnwaldite to late-stage lepidoite, suggesting a volatile (Li, F) enrichment process through progressive fractional crystallization. However, towards the uppermost stockscheider, the Fe_2O_3 content increases up to 21 wt. %, while the F and calculated Li_2O contents reduce to 5.23 wt. % and 1.43 wt. %, respectively, which is consistent with an increasing K/Rb ratio of Li-bearing mica, reflecting a less-differentiated characteristic.

4 W-Sn-Ti-Nb-Ta minerals and zircon

4.1 W-Sn-Ti-Nb-Ta mineral assemblages

W-Sn-Ti-Nb-Ta mineral assemblages were studied by SEM, and analyzed by EPMA at the State Key Laboratory for Mineral Deposits, Nanjing University. Based on the observation of W-Sn-Ti-Nb-Ta minerals in different units, The W-Sn-Ti-Nb-Ta mineral assemblages changed during magmatic differentiation.

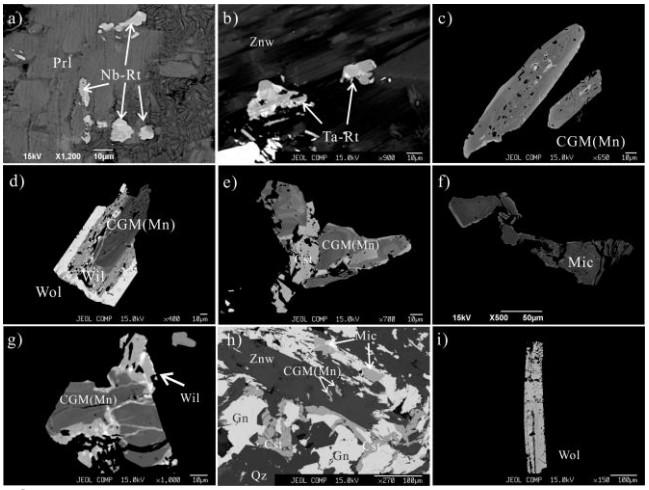


Figure 2. Backscattered electron images of the W-Sn-Ti Nb-Ta minerals from the four petrographic units.

In the protolithionite K-feldspar granite, the main assemblages are ilmenorutile (Fig. 3a), wolframoixiolite (Fe), and ferrocolumbite, with minor Nb-bearing wolframite (up to 10 wt.% Nb_2O_5+Ta_2O_5) and cassiterite. In the zinnwaldite albite granite, the W-Sn-Ti-Nb-Ta minerals change to columbite, Nb-bearing wolframite and minor wolframoixiolite and cassiterite (Figs. 2c, d). Ferrocolumbite gives way to mangancolumbite upwards in this unit and wolframoixiolite is rare in the upper part of this unit. In the topaz greisen and greisenized granite, the W-Sn-Ti-Nb-Ta mineral assemblages mainly contain manganocolumbite, microlite, and minor manganotantalite (Figs. 2b, e, f, g, h). Typical hydrothermal wolframite and cassiterite, have very low concentrations of Nb and Ta (<1 wt.% Nb_2O_5+Ta_2O_5 in wolframite, lower than detection limit in cassiterite), and which are intergrown with sulphides (galena and sphalerite), suggest that crystallization of W-Sn minerals can occur both at the magmatic and hydrothermal stages.

As for the stockscheider, the W-Sn-Ti- Nb-Ta accessory minerals mainly consist of wolframoixiolite, wolframite and small amount of columbite, which shows a distinctly lower Mn/(Mn+Fe) and Ta/(Ta+Nb) (Fig 3). This is consistent with the chemical evolution of mica and represents a less-fractionated characteristic.

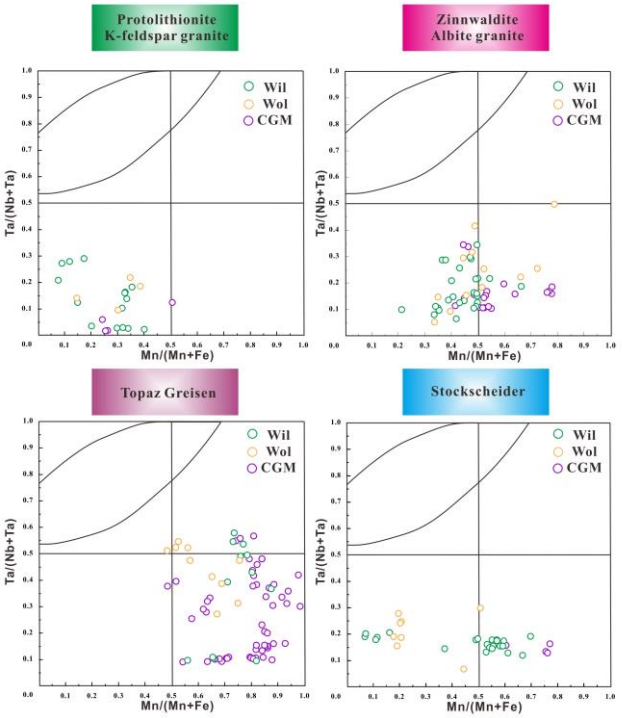


Figure 3. Compositional plots of the Nb-Ta-W minerals of different petrographic units (columbite-group minerals, wolframite, wolframoixiolite) expressed in terms of the Mn/(Mn+Fe) versus Ta/ (Nb+Ta) quadrilateral diagram

4.2 Major and trace element characteristics of zircon

In situ trace element analyses of zircon were obtained by laser-ablation-inductively coupled plasma mass spectrometry (LA-ICP-MS, using an Agilent 7700x ICP-MS coupled GeoLasPro 193nm laser ablation system) at the State Key Laboratory of Ore Deposit Geochemistry, Institute of Geochemistry, Chinese Academy of Sciences, Guiyang, China)

Zircon, as a ubiquitous accessory mineral in granitic rocks, is the most extensively used mineral for U-Pb dating and in situ microanalysis of major and trace elements, as well as isotope ratios, because it has a high resistance to postmagmatic hydrothermal overprinting and weathering (Hoskin and Schaltegger 2003). In the Jianfengling granite stock, zircon occurs as subhedral to euhedral inclusions in mica, topaz, or interstitially to quartz and feldspar. The amount and grain size of zircon decreases upwards.

Compared to the early magmatic stage (protolithionite K-feldspar granite) and the late magmatic-hydrothermal stage (topaz greisen and greisenized granite), zircon from the stockscheider shows affinity of zircon of the late magmatic stage and the higher Zr/Hf ratios than the pegmatitc melts derived from the most fractionated granitic melts.

Given the high W, Sn, Nb, and Ta contents in zircon (W up to 6036 ppm in the stockscheider unit; Sn up to 2782 ppm in the protolithionite K-feldspar granite unit; Nb up to 2851 ppm, and Ta up to 1940 ppm in the topaz greisen and greisenized granite unit) and the diversity of rare-metal elements enrichment at the different stages, the mobility of rare-metal elements presents the differences. Nb and Ta prefer to retain in the volatile-rich melt during the fractional crystallization, while W and Sn incorporated in the fluid phase under the sub-solidus condition, which results in the depletion of W and Sn in the zircon of the late magmatic stage or magmatic-hydrothermal stage.

5 Discussion

The main evolutionary trends in the chemistry of mica and W-Sn-Nb-Ta minerals in the Jianfengling granite are similar to those of peraluminous rare-metal granites and rare-element granitic pegmatites worldwide (Cerny et al. 1985; Beurlen et al. 2008). Our study provides further information about the variation of accessory mineral assemblages of Li-F rich, P-poor rare-metal granites during the magmatic differentiation, the magmatic-hydrothermal transition, and the hydrothermal alteration.

On the other hand, the mineralogical study of the stockscheider in the Jianfengling granite system indicates that liquid immiscibility between aluminosilicate melt and F-rich hydrosaline melt may occur in the early stages of granitic magma evolution; the coexisting liquids then undergo parallel chemical evolution (Veksler et al. 2004).

Acknowledgements

This study was supported by Major State Basic Research Development Program of China (2012CB416702) and the National Science Foundation of China (Grant No. 41572045).

References

Badanina EV, Veksler IV, Thomas R, Syritso LF, Trumbull RB (2004) Magmatic evolution of Li–F, rare-metal granites: a case study of melt inclusions in the Khangilay complex, Eastern Transbaikalia (Russia). Chemical Geology 210:113-133.

Beurlen H, Da Silva MR, Thomas R, Soares DR, Olivier P (2008) Nb–Ta–(Ti–Sn) oxide mineral chemistry as tracer of rare-element granitic pegmatite fractionation in the Borborema Province, Northeastern Brazil. Mineralium Deposita 43:207-228.

Cerny P, Siivola J (1980) The Tanco pegmatite at Bernic Lake, Manitoba. XII. Hafnian zircon. Can Mineral 18:313-321.

Cerny P, Meintzer RE, Anderson AJ (1985) Extreme fractionation in rare-element granitic pegmatites; selected examples of data and mechanisms. The Canadian Mineralogist 23:381-421.

Cerny P, Blevin PL, Cuney M, London D (2005) Granite-related ore deposits. Economic Geology 107:383-384.

Cuney M, Marignac C, Weisbrod A (1992) The Beauvoir topaz-lepidolite albite granite (Massif Central, France); the disseminated magmatic Sn-Li-Ta-Nb-Be mineralization. Economic Geology 87:1766-1794.

Hoskin PW, Schaltegger U (2003) The composition of zircon and igneous and metamorphic petrogenesis. Reviews in mineralogy and geochemistry 53:27-62.

Huang XL, Wang RC, Chen XM, Hu H, Liu CS (2002) Vertical variations in the mineralogy of the Yichun topaz–lepidolite granite, Jiangxi Province, southern China. The Canadian Mineralogist 40:1047-1068.

Kovalenko V, Kovalenko N (1984) Problems of the origin, ore-bearing and evolution of rare-metal granitoids. Physics of the earth and planetary interiors 35:51-62.

Mao JW, Cheng YB, Chen MH, Franco P (2013) Major types and time–space distribution of Mesozoic ore deposits in South China and their geodynamic settings. Mineralium Deposita 48:267-294.

Pollard P (1989) Geochemistry of granites associated with tantalum and niobium mineralization Lanthanides, tantalum and niobium. Springer, pp 145-168.

Raimbault L, Charoy B, Cuney M, Pollard P (1991) Comparative geochemistry of Ta-bearing granites. Source, transport and deposition of metals Balkema, Rotterdam:793-796.

Raimbault L, Cuney M, Azencott C, Duthou J-L, Joron JL (1995) Geochemical evidence for a multistage magmatic genesis of Ta-Sn-Li mineralization in the granite at Beauvoir, French Massif Central. Economic Geology 90:548-576.

Rao C, Wang RC, Hu H, Zhang WL (2009) Complex internal textures in oxide minerals from the Nanping No. 31 dyke of granitic pegmatite, Fujian province, southeastern China. The Canadian Mineralogist 47:1195-1212.

Sun WD, Yang XY, Fan WM, Wu FY (2012) Mesozoic large scale magmatism and mineralization in South China: Preface. Lithos 150:1-5.

Taylor R (1992) Petrological and geochemical characteristics of the Pleasant Ridge zinnwaldite-topaz granite, southern New Brunswick, and comparisons with other topaz-bearing felsic rocks. The Canadian Mineralogist 30:895-921.

Thomas R, Webster J, Rhede D, Seifert W, Rickers K, Förster H-J, Heinrich W, Davidson P (2006) The transition from peraluminous to peralkaline granitic melts: evidence from melt inclusions and accessory minerals. Lithos 91:137-149.

Tischendorf G, Gottesmann B, Foerster H-J, Trumbull RB (1997) On Li-bearing micas; estimating Li from electron microprobe analyses and an improved diagram for graphical representation. Mineralogical Magazine 61:809-834.

Veksler IV, Thomas R, Schmidt C (2002) Experimental evidence of three coexisting immiscible fluids in synthetic granitic pegmatite. American Mineralogist 87:775-779.

Veksler IV (2004) Liquid immiscibility and its role at the magmatic–hydrothermal transition: a summary of experimental studies. Chemical Geology 210:7-31.

Wang CS (1993) The Jianfengling granite complex and the associated polymetallic mineralisation, Hunan Province, PR China. University of Southampton.

Xuan Y, Yuan S, Yuan Y, Mi J (2014) Zircon U–Pb age, geochemistry and petrogenesis of Jianfengling pluton in southern Hunan Province. Mineral Deposits 33:1379-1390. (In Chinese with English abstract)

Yin R, Wang RC, Zhang A-C, Hu H, Zhu JC, Rao C, Zhang H (2013) Extreme fractionation from zircon to hafnon in the Koktokay No. 1 granitic pegmatite, Altai, northwestern China. American Mineralogist 98:1714-1724.

Zhu J-C, Li R-K, Li F-C, Xiong X-L, Zhou F-Y, Huang X-L (2001) Topaz–albite granites and rare-metal mineralization in the Limu district, Guangxi Province, southeast China. Mineralium Deposita 36:393-405.

S10 – GSC@175: How can government promote exploration success?

Convenors:
David Huston
Karen D. Kelley
Patrick Mercier-Langevin

Sponsored by:

Canada

Geoscience Australia's contribution to Australian mineral exploration

David L. Huston
Geoscience Australia

Richard S. Blewett
Geoscience Australia

Abstract. Since 1946 Geoscience Australia has been providing pre-competitive (non-rivalous) data and information to the minerals and petroleum exploration industries which have played an important part in resource discovery, including the Olympic Dam and Lihir deposits, and the Browse Basin hydrocarbon field. The modest investment in precompetitive data has resulted in economic benefits to Australia that are orders of magnitude greater than cost.

Australia is currently seen by industry as a mature exploration destination as most of the exposed regions have been extensively explored. However, Australia has large areas of basement covered by younger sedimentary rocks and regolith, which is both an opportunity and a challenge. To address this challenge, Geoscience Australia has begun a data collection program aimed at determining what data are required to explore undercover and providing that data in northern Australia. Data acquisition will include a range of non-traditional geophysical and geochemical methods and the data will be used to assess mineral potential on regional and national scales. In the future, Geoscience Australia will extend this data coverage into southern Australia and develop methods of assessing the viability of resource development in remote Australia.

1 Introduction

In June 1946, the Bureau of Mineral Resources, Geology and Geophysics (BMR) was founded with the aim of 'mapping the nation' using geology and geophysics, thereby assisting the mineral and petroleum exploration industry. In 1992, the BMR changed its name to the Australian Geological Survey Organisation (AGSO), and in 2001 AGSO was merged with the Australian Surveying and Land Information Group (AUSLIG) to become Geoscience Australia. As a consequence, Geoscience Australia's role is much broader than the BMR, incorporating aspects of community safety, providing independent information on groundwater resource management, managing aspects of Australia's marine jurisdiction, providing national- and local-scale topographic information, and maintaining geoscientific knowledge and capability to provide independent advice to government. However, one of Geoscience Australia's primary roles remains to encourage investment and facilitate the discovery and development of mineral and petroleum resources.

Since establishment in 1946, Geoscience Australia and its predecessors have not only provided traditional and routine geological information (e.g. geological maps), but it has also pioneered the acquisition of a variety of datasets at the national and regional scales that have played important roles in the discovery of mineral and petroleum resources in Australia and its former Trust Territory, Papua-New Guinea. The need for innovation is becoming more critical and Australia is currently considered a mature exploration destination, with most of exposed basement terranes considered well explored. About two-thirds of Australia's landmass, however, is blanketed by younger sediments and regolith that obscure the prospective geology of the basement. With the important exceptions of the Olympic Dam and nearby deposits in South Australia, virtually all of Australia's discovered resources are in exposed terranes. Hence, covered basement is Australia's exploration opportunity, but also the greatest challenge to exploration success.

2 Historical successes

Since 1946, data acquired by Geoscience Australia and its predecessors has played in important role in discovery of mineral and petroleum resources. The cost of these data is generally a small portion of the value of the resources discovered (see below), making precompetitive geoscience data acquisition a highly effective investment for the Commonwealth (and State) government. Below we give several examples — the Olympic Dam Cu-U-Au deposit, the Lihir Au deposit, and the Browse hydrocarbon field — to illustrate how data supplied by Geoscience Australia and its predecessors has contributed to discovery, and quantify some of the economic impacts of this investment.

2.1 Olympic Dam copper-uranium-gold

Discovery of the Olympic Dam deposit in South Australia by Western Mining Corporation (WMC) in 1975 was the consequence of high risk, deep exploration using a conceptual model (Haynes 2006). Two of the key datasets used by WMC to focus exploration were gravity and magnetic data acquired by BMR over the Stuart Shelf. These data, combined with the conceptual exploration model, new data acquisition and geophysical modelling by WMC led to the siting of drill hole RD1, which intersected 38 m grading 1.0% Cu. The potential of the deposit was confirmed with hole RD10, which intersected 170 m assaying 2.1% Cu and 0.06% U_3O_8 (McKay and Miezitis

2001). At 30 June 2012, resources and reserves at Olympic Dam totalled 9.576 Gt grading 0.82% Cu, 0.31 g/t Au, 0.26 kg/t U_3O_8 and 1.39 g/t Ag (Ehrig et al. 2013), for a total value of over $US700 billion (calculated using March 2017 metal prices).

2.2 Lihir gold

Between 1969 and 1974, the BMR and the Papua-New Guinea Geological Survey undertook a mapping program in the Tabar-Feni island chain including Lihir Island. The final results of this mapping program were released in 1982 and included the recognition of an active geothermal system and strong zones of alteration on Lihir. Shortly following release of these results, the Kennecott-Niugini joint venture discovered anomalous gold in rock chip samples from the island. Since initial gold production in 1997, the Lihir deposit has produced over 10 Moz of gold and has a current mining reserve of 28 Moz and a resource of 57 Moz (newcrest.com.au; data current at December 2015). At the March 2017 price of gold, total production and resources equate to approximately $US120 billion.

2.3 Browse Basin hydrocarbon

Although natural gas was discovered in the Browse Basin off the northwest coast of Australia in the 1970s, the lack of a market for gas at the time stymied hydrocarbon exploration, and the hydrocarbon potential of this basin was poorly understood (http://www.ga.gov.au/value-to-the-nation#s1). In 1996, Geoscience Australia acquired geophysical and other data in this basin to better understand its potential, releasing the data in 1997 (Blevin et al. 1997, Boreham et al. 1997). As a consequence of these new results INPEX Corporation began exploring in the Browse Basin in 1998 and defined the Ichthys gas discovery in 2000-2001, which has resources of 12.8 trillion cubic feet of gas and 527 million barrels of liquids (http://www.inpex.com.au/our-projects/ichthys-lng-project/ichthys-at-a-glance/). The Browse Basin study cost the Commonwealth government $AU3 million and has yielded the Ichthys project which has a value of $AU33 billion .

2.4 Discussion

The above three examples indicate that small quantities of high quality and useful data in new or remote areas can trigger the discovery of large resources in the short to medium term, and that exploration and discovery lead directly to major investments. In terms of government's role in facilitating economic development, the direct benefits of these small investments can be huge.

A more difficult impact to assess is the role of government data as a long-term or indirect contributor to discovery. Industry use the free pre-competitive data as they download it through the various portals such as AUSGIN, the collective Australian Government Information Network portal (http://www.geoscience.gov.au/). The geophysical archive and data delivery system (GADDS) for example has delivered 5 Tb of data since its inception in 2003. Over the last 12 years geophysical datasets worth over $AU180 million have been collected. To maximise the value of this investment, data collection standards have been set and continuously improved. The result is Australian explorers can access the same geophysical data providers who are proficient at providing world-best practice in terms of quality and price.

Another example of impact is the discovery of the Gruyere orogenic gold deposit in the Yamarna greenstone belt to the northeast of Kalgoorlie. This belt had a few minor mineral occurrences, but no significant deposits until the discovery of Gruyere (6.2 Moz: www.goldroad.com.au) in 2013. In 2001, Geoscience Australia, in collaboration with the Geological Survey of Western Australia and the Predictive Mineral Discovery Co-operative Research Centre (*pmd**CRC) acquired a reflection seismic profile across the Eastern Goldfields Superterrane into the Yarmana belt. Interpretation of the seismic data suggested that the Yamarna belt exhibited a similar crustal architecture to the well-endowed Kalgoorlie Terrane that contains the Kalgoorlie Golden Mile and other major orogenic gold deposits, and, therefore, would be highly prospective (Goleby et al., 2002). Based upon this analogy, exploration commenced in the Yamarna belt, initially without much success, until the Gruyere discovery in 2012 (some 10 years later). This example illustrates the medium- to long-term influence of concepts developed using government-supplied data in exploration.

Traditionally the role of Australian Commonwealth and State/Territory geological surveys has been to provide 'pre-competitive' data in remote regions, but as most of Australia is now covered by relatively high-quality geological maps and 'traditional' geophysical data (magnetics, radiometrics and gravity), the challenge for the surveys is to provide new types of data and new methods of interpreting the data. This new role is particularly important to provide industry a scientific and economic impetus to explore through cover in remote parts of Australia or to view the potential of well explored provinces with new concepts of mineral potential. The current role, as described below is to provide this impetus and turn around the perception that Australia is a mature exploration destination.

3 The present

In November 2016 Geoscience Australia began a new four-year program of data acquisition and interpretation termed "Exploring for the Future" (EFTF) with the aim of encouraging resource development in northern (tropical) Australia. This new program builds upon concepts of data acquisition and interpretation developed over the last decade or so within Geoscience Australia, partly as part of the UNCOVER initiative, a collaborative program to enhance exploration under cover between geological surveys, industry and universities in Australia. The

program will acquire a range of new geophysical and geochemical data, from which interpretations of the geology and mineral potential of northern Australia will be developed and tested by drilling.

In addition to the "tried and true" methods of ground gravity and aeromagnetics, the EFTF program will acquire new airborne electromagnetic, magnetotelluric and passive seismic data systematically through northern Australia. Until relatively recently, these techniques have been acquired in an ad hoc manner, and the provision of consistent and regularly spaced data will enable a more robust understanding of the structure of Australia's cover, crust and mantle.

In addition to geophysical data acquisition, the program will also acquire new regional-scale catchment and groundwater geochemical and national-scale isotopic data. Between 2007 and 2009, Geoscience Australia collected geochemical data from catchment sediments in the National Geochemical Survey of Australia (NGSA: de Caritat et al. 2011). The results of NGSA demonstrated the usefulness of these data in fields that vary from agriculture to mineral exploration, and the techniques developed during NGSA will be used in a more detailed data acquisition program in the Greater McArthur Basin, the North Australian Geochemical Survey (NAGS). This program will be accompanied by a regional project of borehole groundwater geochemistry.

Spatial variations in Nd and Pb isotopic data have recently been demonstrated to reflect tectonic and metallogenic characteristics of Australian crust (cf. Champion and Huston 2016). The EFTF program will complete national coverage of ore Pb isotope data and initiate new coverages of Hf-Lu and Ar-Ar data. These data will provide new insights into the tectonic and metallogenic framework of Australia.

The newly acquired data, along with existing data and our understanding of mineral systems that have affected northern Australia, will be used during the second half of the project to undertake a regional drilling program in the McArthur Basin. This drilling will not directly target mineralisation, but rather test geological models and test for evidence of the operation of mineral systems. The program will also be a critical test of cover thickness estimates produced from geophysical data (e.g. AEM, aeromagnetics).

Discussions with industry through the UNCOVER initiative have identified the most important impediment to exploration in Australia is understanding the impact of cover — its thickness and composition — and determining ways of exploring through it. Much of the data acquisition program under EFTF (AEM, aeromagnetics and passive seismic) is intended to address this problem, and some of the most important products of EFTF will be maps showing the distribution, thickness and composition of cover, tested using the regional drilling program. In addition, some of the geochemical programs (NAGS and the groundwater survey) are designed to test for the response of mineralised rock through cover. As part of these programs, surveys will be undertaken over known, undeveloped resources under various depths of cover.

The isotopic (Nd, Pb and Hf) and some geophysical (MT and passive seismic) data will be used to understand the composition, tectonics and metallogenesis of the Australian continent. The new data, along with existing data will be used to update the current crustal boundary map of Australia (Korsch and Doublier 2014). Recent research (Korsch and Doublier 2016) has highlighted the importance of crustal boundaries or 'big cracks' in controlling mineral systems at the regional scale.

Using all data available, Geoscience Australia is embarking on a long-term project to produce a national-scale 3D model of Australia's geology. This model will include a solid geology interpretation of basement along with 3D volumes showing the extent, thickness and composition of cover sequences of various ages. This project will be open-ended as the availability of new data will continually refine the model.

Over the last two decades, metallogenic research at Geoscience Australia has followed the "mineral systems" approach (cf. Wyborn et al. 1994), which is based on the "petroleum system" concept (Magoon and Dow 1994) now used extensively in the oil and gas industry. This approach has been developed through national collaborative research programs including the Australian Geodynamic and Predictive Mineral Discovery Cooperative Research Centres and the UNCOVER initiative. At Geoscience Australia we have concentrated on documenting the larger-scale (district to continental) and temporal characteristics of mineral systems, leaving the more detailed deposit-scale studies to Universities. The ultimate aim of Geoscience Australia's mineral system work is to provide mineral potential maps at the regional- (e.g. Schofield et al. 2011) and national- (e.g. Dulfer et al. 2016) scales for a range of commodity types (Cu, Zn-Pb, Ni, Au and U) using the data acquired from regional and national data acquisition and geological interpretations of these data.

The economic viability of developing a remote resource depends not only on the quality (grade, tonnage and metal recovery) of the deposit, but also on its depth below the surface and proximity to existing infrastructure. Hence, Geoscience Australia is currently developing GIS-based economic viability assessments of northern Australia for a range of commodities using depth to basement estimates and infrastructure data provided by other parts of Geoscience Australia and relevant State and Territory authorities. The purpose of this analysis is to identify the most economically favourable areas of undercover Australia for resource development.

4 The future

Geoscience Australia's current EFTF program is designed to begin systematic collection of a new range of data sets across northern Australia. It is important to realise that many of the data sets collected as part of EFTF are the same datasets collected by University groups at a much smaller scale or less systematically as part of 'academic'

studies. One of Geoscience Australia's continuing roles will be to assess the potential of novel academic studies as pre-competitive data sets for exploration.

Upon completion of EFTF in 2020, the role of Geoscience Australia is likely to remain the same in many aspects, but could change in others. In particular, many of the data coverages developed as part of EFTF will be extended southwards, with the goal of national coverages. These data will be used for national- and regional-scale mineral potential analysis for a range of mineral systems. In addition to these business-as-usual programs, Geoscience Australia will encourage the use of our data by the mining and exploration finance sector. To support this, we will provide economic assessments to determine regions that have a higher likelihood to develop a resource in collaboration with external organisation.

5 Industry intelligence

Discussion, both formal and informal, with industry highlight the fact that different parts of the exploration industry use data and interpretations provided by Geoscience Australia and the State/Territory surveys differently. Some (mainly the major and mid-size companies) prefer only the data, whereas others (commonly the juniors) value our interpretations in addition to the data. This diversity provides challenges in product delivery, but also allows engagement with industry to address important scientific questions at the regional and national scales.

Geoscience Australia and the State/Territory surveys have been advocating adopting the mineral systems (Wyborn et al. 1994) approach to understanding how mineral deposits form. After initial reluctance on the part of some in industry and academia, the mineral systems paradigm is gaining traction, particularly for mineral potential analysis.

6 Conclusions

Historically, data and knowledge provided by Geoscience Australia and its predecessors have played an important role in the discovery of new mineral and petroleum resources, particularly in remote and frontier areas of Australia and Papua-New Guinea. As high-quality geological and geophysical data exist for virtually all of Australia, the opportunity for contributing to discovery by providing data in frontier areas is decreasing. Rather, Geoscience Australia can contribute to discovery by providing new and novel data sets and ideas, particularly in areas of Australia where bedrock is covered. Currently Geoscience Australia is developing these datasets in northern Australia as part of the EFTF, with an ultimate aim of producing national maps covering a range of non-traditional geophysics, geology and geochemistry. In addition, the feasibility of developing remote resources is also being assessed.

Acknowledgements

Murray Richardson is thanked for reviewing this contribution, which is published with permission of the Chief Executive Officer of Geoscience Australia.

References

Blevin JE, Struckmeyer HIM, Boreham CJ, Cathro DL, Sayers J, Totterdell JM (1997) Browse Basin high resolution study, interpretation report, North West Shelf, Australia AGSO Record 1997/38

Boreham CJ, Roksandic Z, Hope JM, Summons RE, Murray AP, Blevin JE, Struckmeyer HIM (1997) Browse Basin organic geochemistry study, North West Shelf, Australia. Volume 1, interpretation report. AGSO Record 1997/57

Champion DC, Huston DL (2016) Radiogenic isotopes, ore deposits and metallogenic terranes: Novel approaches based on regional isotopic maps and the mineral systems concept. Ore Geol Rev 76:229–256

de Caritat P, Cooper M, Jaireth S, Bastrakov E (2011) National Geochemical Survey of Australia: Preliminary Implications for Energy and Mineral Exploration. Geoscience Australia Record 2011/29

Dulfer H, Skirrow RG, Champion DC, Highet LM, Czarnota K, Coghlan RA, Milligan PR (2016) Potential for intrusion-hosted Ni-Cu-PGE sulfide deposits in Australia: A continental-scale analysis of mineral system prospectivity. Geoscience Australia Record 2016/01

Ehrig K, McPhie J, Kamenetsky VS (2012) Geology and mineralogical zonation of the Olympic Dam iron oxide Cu-U-Au-Ag deposit, South Australia. Soc Econ Geol Spec Pub 16:237–268

Goleby BR, Korsch RJ, Fomin T, Bell B, Nicoll MG, Drummond BJ, Owen AJ (2002) Preliminary 3-D geological model of the Kalgoorlie region, Yilgarn Craton, Western Australia, based on deep seismic-reflection and potential-field data: Austr J Earth Sci 49:917–933

Haynes D (2006) The Olympic Dam ore deposit discovery – A personal view. SEG Newsletter 66:1–15

Korsch RJ, Doublier MP (2014) Major crustal boundaries of Australia. 1st Edition. Scale 1:2,500,000. Geoscience Australia, Canberra

Korsch RJ, Doublier MP (2016) Major crustal boundaries of Australia, and their significance in mineral systems targeting. Ore Geol Rev 76:211–228

Magoon LB, Dow WG (eds) (1994) The petroleum system: From source to trap. AAPG Memoir 60

McKay AD, Miezitis Y (2001) Australia's uranium resources, geology and development of deposits. AGSO – Geoscience Australia

Schofield A, Huston D, Kemp C (2011) Iron oxide-copper-gold potentia of the soutehrn Aileron Region. Geoscince Australia, Canberra

Wyborn LAI, Heinrich CA, Jaques AL (1994) Australian Proterozoic mineral systems: essential ingredients and mappable criteria. In The AusIMM Annual Conference 1994:109–115

Promoting mineral exploration in Sweden from the perspective of the government

Erika Ingvald
Geological Survey of Sweden

Kaj Lax
Geological Survey of Sweden

Abstract. Sweden has a long history of mining, the mineral industry being one of the backbones in developing the Swedish society during several centuries. Governmental organisations carried out exploration until the early 1990ies, when state financed exploration was essentially dropped. This was a result of several different factors, ranging from economical to political, and also a lack of success in opening new mines, although several mineral deposits have been found. Instead, the task for SGU became to focus on providing information and advice to privately owned companies, and to market Sweden as a country well suited for mineral exploration. This has been the task for SGU since 1992, through a decision by the Swedish parliament.

Today SGU is expected to increase efforts in areas outside "traditional" survey domains. Examples include government support regarding policy issues, legislation, and marketing. One of the greatest challenges is to keep up production of modern and relevant geological data at the same time as expanding in other areas. SGU recently completed a large project producing geological information in Northern Sweden, the so called Barents project. At the same time, SGU has scanned (hyperspectral imaging) more than 200 000 m of drill core from the area.

1 1600 years of mining

Copper and iron ore mining in Sweden has been going on for more than 1600 years, with well-known deposits as Garpenberg, Falun and Sala. It has been proposed that domestic mining in Bergslagen formed the starting point of the Swedish state from the Medieval times.

Mining has thus been been an important part of establishing Sweden as a nation, and today it is one of the important base industries in the country. As one of the few nations within EU that produces metals Sweden plays and will play a significant role in securing raw materials for the European Union.

2 The role of the survey

The Geological Survey of Sweden was founded in 1858, with the commission to secure raw materials to a society strongly exposed to the industrial revolution. For many years its role was to run extensive mapping and exploration. In 1982 SGU was divided into a government agency and a state owned exploration company, SGAB.
As most geological surveys, SGU still performs mapping programmes and investigations of interest to the mineral industry, bedrock geology, geophysics (airborne and ground measurements), till geochemistry included. During the past two years SGU has focussed on improving data storage and accessibility of data, but mapping commences again this year, this time in the mineral district of Bergslagen (2017). Such recently produced data is also available at the Mineral Information office.

The access not only to the information itself, but also to knowledge on possibilities and limitations of data, is of course rather important for improving success for the exploration campaigns of visiting companies.

2.1 New conditions for the mineral industry

The state exploration company founded in 1982 was not considered sufficiently successful and was shut down ten years later. Simultaneously, Sweden adapted to the legislation of EC, later to become EU, and also adjusted its mining act. The legislative changes opened up for mineral exploration in Sweden for international companies.

To support investment from private companies, the Swedish parliament decided to form an information office at one of the SGAB locations, in Malå in northern Sweden. In this location SGU stores thousands of exploration reports, maps, databases and drill cores (more than 3 million meters; the oldest cores are from the 1800s) from the state driven exploration. All this material is available for visitors. Additionally, a large share of the reports has been digitized and is accessible online.

Also, over the last couple of years SGU has scanned 230 000 meters of selected drill cores, representing most of the known ore types in Sweden, with infrared hyperspectral imaging (fig.1). RGB-photos and false composite colour images for entire drill cores are available online. The raw data can be ordered from our customer service and can be used to develop drill core mineral maps. Already the data from this project has shown to be extremely valuable in various projects, since the IR-data reveals much more information than what is visible to the naked eye.

Part of the marketing efforts includes participation in

international meetings such as SGA, PDAC, FEM and Mining Indaba.

Pointing out direct contribution of survey data to successful exploration projects is not always easy. This is essentially due to the fact that survey data is often used at early stages in order to discriminate between areas with high and low mineral potential.

However, studies done after the Barents project showed that release of data and reports significantly contributes to increased exploration. Also, at the other end of the spectrum, SGU data and information has led to reopening of a mine as late as 2008 (Dannemora, iron ore, in prod 2008-2015).

2.2 The Barents project

In 2012 SGU received additional funding from the Ministry of Enterprise in order to increase knowledge of the geology in northern Sweden, and to produce data for mineral exploration. The project ran for four years, and included airborne full tensor gravity and transient electromagnetic (VTEM), a 74 km long seismic reflection and AMT profile from the Kiruna area, bedrock mapping in key areas (representing specific parts of supracrustal rocks), regional bedrock mapping, till geochemical mapping. The results were published as SGU reports.

Acknowledgements

Acknowledgments to Helge Reginiussen (SGU) for assistance with graphics and interpretation of drill cores.

References

Bindler R, Karlsson J, Rydberg J, Karlsson B, Berg Nilsson L, Biester H, Segerström U (2017) Copper-ore mining in Sweden since the pre-Roman Iron Age: lake-sediment evidence of human activities at the Garpenberg ore field since 375 BCE. Jour Arch Science 12:99-108

http://www.sgu.se/en/mineral-resources/geological-information-for-mineral-exploration/drill-core-collection/drill-core-scanning-at-sgu

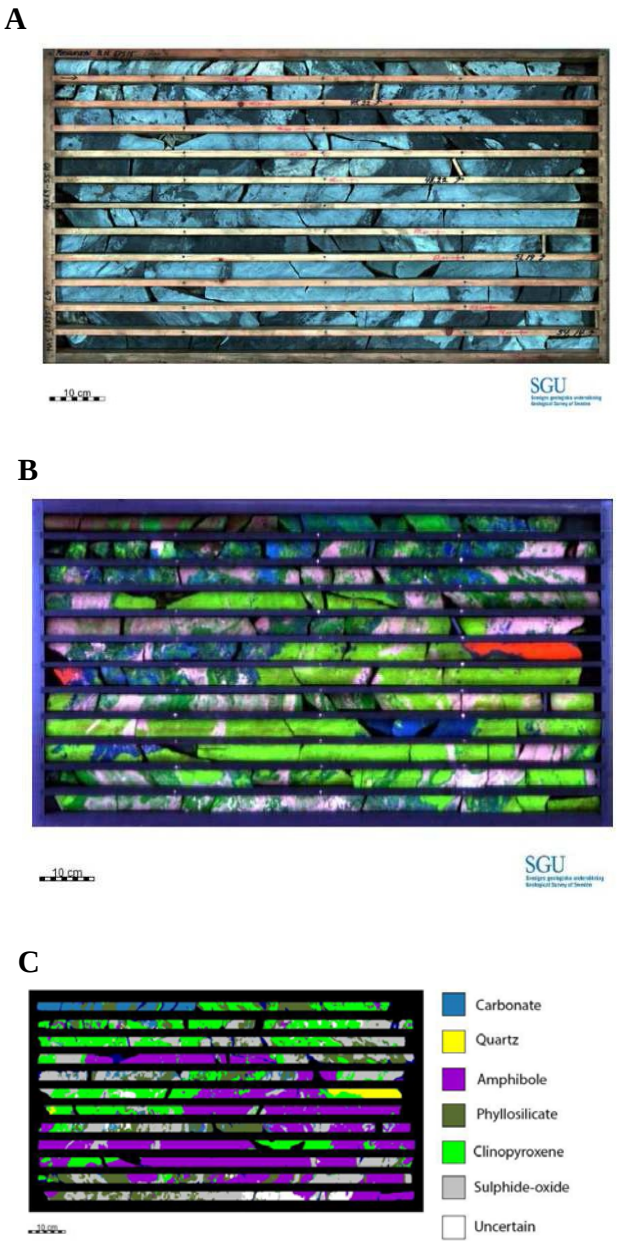


Figure 1. Comparison between results from drill core scanning. **a** RGB image, **b** False color composite (LWIR), **c** Mineral map. Original corelog "Tremolite-diopside skarn with irregular magnetite-serpentine-sulphide (po-py(cpy)) zones comprising 20-25% of the section."

The role of the U.S. Geological Survey Mineral Resources Program in aiding mineral exploration

Karen D. Kelley, Eric Anderson, Anne McCafferty
U.S. Geological Survey (Denver, Colorado)

Murray W. Hitzman, Lawrence Meinert
U.S. Geological Survey (Reston, Virginia)

Richard J. Goldfarb, David L. Leach
Colorado School of Mines

Abstract. Many discoveries of large deposits in the United States, including the Carlin, Mountain Pass, Henderson, Red Dog, and Eagle deposits, were based in part on U.S. Geological Survey (USGS) geologic, geochemical, or geophysical data. The Mineral Resources Program contributes to exploration success by (1) providing geologic, geochemical, and geophysical data; (2) developing mineral deposit models that target permissive areas; and (3) developing techniques that are used by industry in exploration. Basic geoscience data, particularly USGS geological maps, form the foundation for mineral exploration. Development and refinement of deposit models impact how exploration is focused. Two models that significantly changed based on USGS research include orogenic gold and sediment-hosted Pb-Zn. The new data from these models have changed exploration strategies. Indirect contributions by the USGS include development of techniques, such as the initiation of fluid inclusion research in the 1950s, and the development of geochemical and geophysical techniques that play a major role in exploration programs. The USGS also has contributed directly to exploration through collaborative studies with industry in well-known districts in the United States.

1 Introduction

The USGS Mineral Resources Program plays a role in US mineral exploration in three primary ways: (1) providing geologic, geochemical, and geophysical data; (2) constructing mineral deposit models; and (3) developing and documenting new techniques and technologies for exploration. All data produced by the USGS are freely available to the public.

2 Geological, geochemical, and geophysical data

One of the primary goals of the USGS, historically and currently, is to assess the nation's mineral resource potential. Basic geologic mapping, regional geochemical and geophysical data collection, and mineral deposit research are the foundation for these assessments. Geologic mapping of mineral districts was an important task of the USGS in the late 19th and early to mid-20th centuries and remains critically important as a framework dataset necessary for effective mineral exploration. During the 1970s to middle 1990s, the USGS undertook a major assessment program that covered much of the nation. This resulted in multiple mineral resource assessment reports, as well as public access to the underlying geologic, geochemical, geophysical, and mineral deposit databases (U.S. Geological Survey 2017).

A number of major mineral discoveries in the United States have utilized USGS data (Table 1). The Mountain Pass REE deposit was initially identified in March 1949 by local prospectors who discovered radioactive veins (Hewett 1954). One of the veins with high concentrations of REE oxides contained an unidentified mineral. This sample was sent to DF Hewett of the USGS, who was concurrently mapping the area. He identified the mineral as bastnaesite. In February 1950, MolyCorp bought the claims and mine development quickly followed. Continued mapping of the area by USGS geologists outlined additional REE prospects.

Table 1. USGS work that led to or contributed to major deposit discoveries by industry in the United States.

Deposit	Company/year of discovery	USGS reference
Mountain Pass, CA	MolyCorp/1950	Hewett (1954)
Carlin, NV	Newmont/1961-1962	Roberts (1960)
Henderson, CO	Climax Molybdenum Corp/1964	Theobald and Thompson (1959)
Red Dog, AK	Cominco/1978	Tailleur (1970)
Eagle, MI	Kennecott/1995	Klasner et al. (1977)

Discovery of the Carlin gold deposit in Nevada in 1961-1962 was the result of intensive prospecting by Newmont geologists concurrent with and following suggestions by Ralph J. Roberts and others in the USGS that gold deposits might be found along certain belts in north-central Nevada (Roberts 1960). These USGS geologists recognized favourable stratigraphy along the Robert Mountains thrust and identified geochemical anomalies indicative of gold enrichment.

As part of mineral resource investigations in the Berthoud pass quadrangle in Colorado, Theobald and Thompson (1959) completed an exploration geochemical survey in and around the known Urad porphyry Mo deposit. High W and Mo contents in heavy-mineral-concentrate samples from tributaries to Clear Creek

outlined a new region of potential for mineralization; this area became the world class Henderson mine.

Initial discovery of the Red Dog Pb-Zn deposit is also credited to USGS. During regional mapping in 1968, USGS geologist Irv Tailleur visited an iron-oxide stained creek at the current Red Dog mine site. High concentrations of Pb and Zn were reported (Tailleur 1970). Follow up work by the US Bureau of Mines and industry geologists led to discovery in 1978.

Another example of USGS research that influenced mineral discovery was a study of the Yellow Dog peridotite in Michigan (Klasner et al. 1977). The study, conducted in collaboration with Michigan Technical University concluded that there was significant potential for copper-nickel deposits in the area. Many years later, Kennecott Exploration discovered highly mineralized float boulders of peridotite in the area, leading to eventual drilling and delineation of the Eagle Cu-Ni deposit.

3 Mineral deposit models

Mineral deposit models elucidate the essential characteristics as well as variations within a group of deposits. Models may be used to predict regions with potential for a given mineral deposit type. The USGS developed models for a number of deposit types (Cox and Singer 1986) and USGS research over the past three decades continues to refine such models. USGS models of two deposit types have greatly impacted exploration: orogenic gold and sediment-hosted Pb-Zn deposits.

3.1 Orogenic gold deposits

Numerous models have been proposed for the genesis of orogenic gold deposits (Goldfarb et al. 2005) ranging from a syngenetic sea-floor exhalative origin, to deep convection of meteoric fluids. Some early models assumed that gold deposits in metamorphic rocks were intimately associated with magmatic processes. Classifications of orogenic gold deposits were based on the supposed temperature and depth of formation, mineralogical character of the ores, and host rock lithologies. Exploration criteria based on such genetic models were ill-defined.

In the early 1980s and over the next several decades, increased research largely by the USGS, greatly refined the model for this deposit type. Important criteria are now thought to include: (1) low salinity H_2O-CO_2-CH_4-N_2-H_2S fluids typical of devolatilization processes; (2) isotopically heavy $\delta^{18}O$ and δD values for hydrothermal minerals; (3) a wide range in $\delta^{34}S$ values reflecting variable host terranes undergoing metamorphism; (4) a lack of ores in high-grade metamorphic rocks; and (5) a decrease in ore-related metals at increasing metamorphic grades. Today most workers agree that orogenic gold ores are epigenetic and a product of metamorphic devolatilization; results from resource assessment studies in Alaska showed the timing of deposit formation is related to major changes in plate motions and far-field stresses. An understanding of structure, as well as host rock rheology, composition, and distribution, are keys for development of an exploration strategy within permissive terranes (Goldfarb et al. 2005).

3.2 Sediment-hosted Pb-Zn deposits

MVT and CD (Clastic-Dominated) Pb-Zn deposits (commonly, but often incorrectly, termed SEDEX or sedimentary exhalative ores) are the two most important types of sediment-hosted Pb-Zn ores (Leach et al. 2005; 2010). Early models for MVT deposits called upon ore formation by dilute meteoric groundwater, magmatic, and (or) connate fluids, and invoked processes that ranged from synsedimentary-exhalative to supergene activity. The incoherence of the model limited its usefulness for exploration. In the past 20-35 years, fluid inclusion, geochronologic, and other geologic studies demonstrated that MVT ores form by basinal fluids derived from evaporated seawater. USGS geologists recognized that orogeny led to continental-scale flow systems critical in generation of MVT deposits (Leach and Rowan 1986). It was shown that deposits formed in specific time intervals in Earth history related to tectonic events, the major ones being Devonian to Permian during assimilation of Pangea, Cretaceous to Tertiary during compression along the western margin of North America, and Tertiary to Neogene during closure of the Tethyan ocean from Europe and North Africa into Asia (Leach et al. 2010).

Early models for CD Pb-Zn deposits called upon formation by exhalation of metalliferous fluids onto the ocean floor with sulphide precipitation in brine pools (Model 31a: Cox and Singer 1986). Recent studies indicate that many CD Pb-Zn deposits form by replacement of shallowly buried carbonate rocks within a thick clastic rock sequence, although some are still thought to have formed by brine exhalation (Leach et al. 2005). Importantly, fluids that form CD Pb-Zn deposits are similar to MVT fluids in that they formed from sedimentary brines with similar temperatures and ore depositional paths (Leach et al. 2010). The refined models allow more focused exploration in terms of parameters such as deposit age, tectonic environment, and paleolatitude (within ~30 degrees of equator necessary to form brines).

4 Technique development and application

One of the most revolutionary developments by the USGS was the pioneering work by Edward Roedder in the 1950s (Roedder 1962) that led to the recognition that fluid inclusions represent ore fluids and that fluid inclusions can be used to determine compositions and temperatures of such fluids. Fluid inclusion research has become foundational for ore genesis studies and development of mineral deposit models, thus significantly impacting mineral exploration.

In the 1960s, the USGS developed or refined laboratory and field-based geochemical analytical techniques for exploration purposes (Ward et al. 1963). The total and

partial extraction of metals with subsequent analyses by atomic absorption spectrophotometry, emission spectrography, and colorimetric methods are among those developed internally by USGS scientists (Ward et al. 1963; Chao et al. 1971). Enzyme leach, a highly discriminating selective extraction for enhancing subtle geochemical anomalies in surficial geological materials, was developed by the USGS in 1976 (Clark et al. 1990). These methods were used primarily for government-funded assessment work, but some were subsequently incorporated by commercial laboratories and became standard commercial methods for exploration.

The USGS was also an integral partner in developing geophysical techniques applied to mineral deposit studies. They began developing software for reduction and interpretation of potential-field geophysical data shortly after they pioneered the airborne magnetometer in the late 1940s. Over subsequent decades, the USGS wrote much of the software code and developed algorithms for interpretation and analyses of potential field data that has become the industry standard (Phillips 2016).

5 Collaborations with industry

Over the past two decades, the Mineral Resources Program has participated in numerous collaborative studies with industry partners. Such partnerships allow comprehensive research that result in a better understanding of the origin of deposits and improved techniques for predicting areas with potential for mineral resources. Three examples are highlighted to illustrate these efforts.

5.1 Red Dog CD Pb-Zn deposit, Alaska

A collaborative project between the USGS and then Cominco American Inc. was initiated to identify the factors responsible for formation of the deposit, and possible exploration tools. Results are summarized in separate papers in Kelley and Jennings (2004). The Red Dog area is structurally complex, having formed in a basin in the Mississippian and then disrupted by thrust faulting during mid-Jurassic to Cretaceous orogeny. Outcomes of the studies included: (1) paleogeographic reconstruction of the Carboniferous basin using structural and detailed sedimentologic data, required for determining other prospective sites within the basin; (2) identification of carbonate platforms adjacent to the basin, which served to limit siliciclastic material and preserve organic carbon that became a reductant during mineralization as well as to provide carbonate turbidites to deeper parts of the basin; (3) the discovery that these carbonate turbidites in shale were important sites of sulphide ore deposition in the district, and thus their presence is an important added exploration criteria; (4) the finding that ore fluids were sourced from brines generated in the shallow carbonate platforms; (5) determinations of the age of mineralization and relative timing of barite and sulphide deposition; and (6) understanding the importance of high concentrations of Tl as a vectoring tool.

5.2 Pebble porphyry Cu-Au-Mo deposit, Alaska

The Pebble deposit in Alaska (Fig. 1) is one of the largest porphyry deposits in the world in terms of contained Cu and Au. The deposit is almost entirely concealed by glacial deposits and post-mineral younger volcanic and sedimentary rocks, particularly in the eastern part that is buried by more than 300 m of material. A collaborative research project between the USGS and Northern Dynasty Minerals Ltd. was designed to better understand how the deposit formed and to develop and identify tools for exploration of similar concealed deposits (Kelley et al. 2013). Both geochemical (Eppinger et al. 2013) and geophysical (Anderson et al. 2017) methods were tested.

One of the most effective geochemical tools for identifying deep mineralization at Pebble is shown by soil samples analysed using partial leach techniques (Fig. 1).

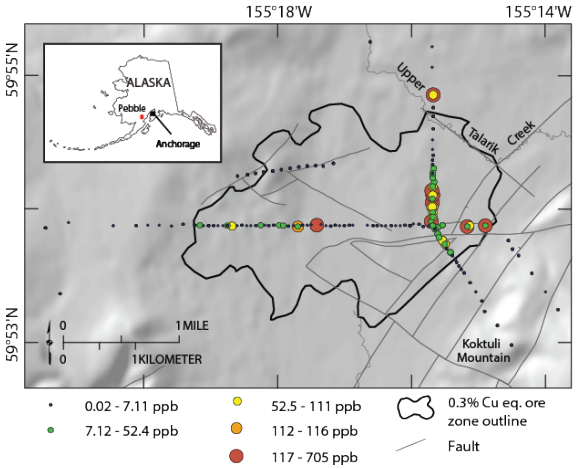


Figure 1. Molybdenum concentrations (ppb) in soil samples at the Pebble deposit analysed by enzyme leach. Modified from Eppinger et al. (2013)

Partial extractions release elements from different target phases within soil, and may better reflect concealed deposits at depth (Eppinger et al. 2013). The numerous anomalies along the north-south traverse in the eastern (deep) part of the deposit (Fig. 1) contrast with only a few select samples with anomalous Au, Cu, or Mo analysed by traditional aqua regia methods. Some of the geochemical techniques applied at the Pebble deposit were subsequently used successfully to re-establish drill targets at a porphyry deposit southwest of Pebble (John Harrop, TNR Gold Corp, written communication, 2011).

Aeromagnetic data acquired over the Pebble deposit indicate that the Pebble deposit is within a cluster of magnetic anomaly highs. Combined with surface geologic data and regional metallogenic constraints, aeromagnetic data, filtered to enhance the anomalous magnetic field and map magnetic domains, were used to produce a mineral potential map of southwest Alaska (Anderson et al. 2017)

5.3 IOA (Iron Oxide Apatite) and IOCG (Iron Oxide Copper Gold) deposits, southeast Missouri

Recent work by USGS geologists on IOA/IOCG deposits in southeast Missouri has led to refined genetic models and exploration strategies for these deposit types (results summarized in Slack et al. 2016). Among the significant findings important for exploration are (1) deposits are hosted not only in A-type felsic volcanic rocks, but also in S- and I-type granites; (2) sulphur isotope signatures of sulphide minerals correlate with elevated Cu concentrations and suggest a possible exploration tool; and (3) a better understanding of deposit signatures.

The USGS in conjunction with the Doe Run Company acquired high-resolution airborne magnetic and gravity gradiometry data in southeast Missouri (McCafferty et al. 2016). The geophysical data delineated the footprints of four known iron oxide deposits, but also highlighted five other prospective areas (Fig. 2). Utilizing the geophysical and geochemical tools developed in the southeast Missouri project could have significant application for mineral exploration for these deposit types in buried terranes of similar age in the Midcontinent region.

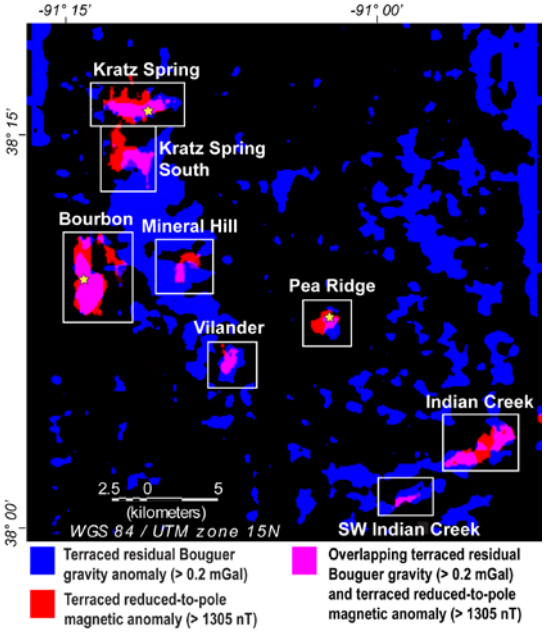


Figure 2. Prospectivity map for IOA\IOCG deposits in SE Missouri. Yellow stars are known deposits. Several areas with no known deposits are identified by gravity and magnetic anomalies

Acknowledgements

We thank Steve Smith and Garth Graham for their reviews and thoughtful comments.

References

Anderson ED, Monecke, T, Hitzman, MW, Zhou W, Bedrosian PA (2017) Mineral potential mapping in an accreted island-arc setting using aeromagnetic data: An example from Southwest Alaska. Econ Geol 112:375-396

Chao TT, Ball JW, Nakagawa HM (1971) Determination of silver in soils, sediments, and rocks by organic chelate extraction and atomic absorption spectrophotometry. Anal Chim Acta 54:77-82

Clark, JR, Meier, AL, Riddle, G. (1990) Enzyme leaching of surficial geochemical samples for detecting hydromorphic trace-element anomalies associated with precious-metal mineralized bedrock buried beneath glacial overburden in northern Minnesota. In Gold'90, Society of Mining Engineers, Chapter 19:189-207

Cox DP, Singer DA (1986) Mineral deposit models. US Geol Surv Bull 1693:379 p

Eppinger RG, Fey DL, Giles SA, Grunsky EC, Kelley KD, Minsley LM, Smith SM (2013) Summary of exploration geochemical and mineralogical studies at the giant Pebble Cu-Au-Mo deposit, Alaska: Implications for exploration under cover. Econ Geol 108:495-527

Goldfarb RJ, Baker T, Dube B, Groves DI, Hart C, Gosselin P (2005) Distribution, character, and genesis of gold deposits in metamorphic terranes. Econ Geol 100th Ann Vol:407-450

Hewett DF (1954) History of discovery at Mountain Pass, California. In Olson JC, Shawe DR, Pray LC, and Sharp WN. US Geol Surv Prof Paper 261:91 p

Kelley KD, Jennings S (2004) A special issue devoted to barite and Zn-Pb-Ag deposits in the Red Dog district, western Brooks Range, northern Alaska. Econ Geol 99:1267-1280

Kelley KD, Lang JR, Eppinger RG (2013) The giant Pebble Cu-Au-Mo deposit and surrounding region, southwest Alaska. Econ Geol 108:397-404

Klasner JS, Snider DW, Cannon WF, Slack JF (1977) The Yellow Dog peridotite and a possible buried igneous complex of Lower Keweenawan age in the northern peninsula of Michigan. US Geol Surv Open-File Rept 77-93:50 p.

Leach DL, Rowan EL (1986) Genetic link between Ouchita foldbelt tectonics and the Mississippi Valley-Type lead-zinc deposits of the Ozarks: Geol 14:931-935

Leach DL, Sangster DF, Kelley KD, Large RR, Garven G, Allen CR, Gutzmer J and Walters S (2005) Sediment-hosted lead-zinc deposits: A global perspective. Econ Geol 100th Ann Vol: 561-608.

Leach DL, Bradley DC, Huston D, Pisarevsky SA, Taylor RD and Gardoll SJ (2010) Sediment-hosted lead-zinc deposits in Earth history. Econ Geol 105: 593-625.

McCafferty, AE, Phillips JD, Driscoll RL (2016) Magnetic and gravity gradiometry framework for Mesoproterozoic iron oxide-apatite and iron oxide-copper-gold deposits, Southeast Missouri. Econ Geol 111:1859-1882

Phillips JD (2016) Potential-field software *in* Smith KS, Phillips JD, McCafferty AE, and Clark RN eds, 2016, Developing integrated methods to address complex resource and environmental issues. US Geol Surv Circ 1413:35-37

Roberts RJ (1960) Alinement of mining districts in north-central Nevada. US Geol Surv Prof Paper 400-B:17-19

Roedder E (1962) Studies of fluid inclusions I: Low temperature application of a dual-purpose freezing and heating stage. Econ Geol 57:1045-1061

Slack JF, Corriveau L, Hitzman MW (2016) A special issue devoted to Proterozoic Iron Oxide-Apatite (+/- REE) and Iron Oxide Copper-Gold and affiliated deposits of southeast Missouri, USA, and the Great Bear magmatic zone, Northwest Territories, Canada. Econ Geol 111:1803-1814

Tailleur IL (1970) Lead-, zinc-, and barite-bearing samples from the western Brooks Range, Alaska: US Geol Surv Open File Rept 70-319:16 p

Theobald PK, Thompson CE (1959) Geochemical prospecting with heavy mineral concentrates used to locate tungsten deposit. US Geol Surv Circular 411:13 p

U.S. Geological Survey (2017) Mineral Resources On-Line Spatial Data. U.S. Geol Surv Web site, accessed March 7, 2017, at https://mrdata.usgs.gov

Ward FN, Lakin HW, Canney FC (1963) Analytical methods used in geochemical exploration by the U.S. Geological Survey. US Geol Surv Bull 1152:106 p

Supporting innovation for sustainable mineral development in Canada: 175 years of public geoscience

Donna Kirkwood
Office of the Chief Scientist, Natural Resources Canada

Mike Villeneuve
Geological Survey of Canada (Ottawa, Ontario)

Patrick Mercier-Langevin
Geological Survey of Canada (Québec, Québec)

Abstract. The Geological Survey of Canada (GSC), Canada's oldest scientific organization and among the world's first national geological surveys, was founded in 1842 by Sir William Logan to establish a geological base on which to develop a mineral industry. It has been the driving force behind the mapping of Canada's nearly 10 million square km of land and freshwater lakes, and more than six million square km of continental margin. Through current research programs, Geo-mapping for Energy and Minerals, and the Targeted Geoscience Initiative, efforts continue to define prospective areas for resource extraction and develop tools and methods to assist in discovery. Program investigations have successfully supported industry exploration efforts and stimulated exploration investments, contributing to economic development across the country. The GSC has been intent on change, allowing programming to remain adaptable over time – focusing on industry needs, and collaborating with Indigenous peoples and communities, academia and other levels of government. On the latter, the Intergovernmental Geoscience Accords (first signed in 1996) and 30 years of federal-provincial-territorial government collaboration have been instrumental in creating a robust national base of public geoscience knowledge. This has supported Canada's competitive advantage and exploration successes. It is thus of utmost importance to continue evolving approaches to meet the challenges faced by industry in today's complex global economy.

1 Introduction

One of the leading mining nations in the world, Canada produces more than 60 minerals and metals and ranks first in the production of potash, and among the top five countries for the production of aluminium, cobalt, diamonds, nickel, platinum group metals, tungsten and uranium. As a result, Canada's minerals and metals industry employs more than 373,000 Canadians in 150 mostly rural communities or remote areas of the country

Transforming Canada's resource endowment into a competitive advantage has met many challenges since the Geological Survey of Canada (GSC) first set out to map and evaluate the potential economic benefits of mineral deposits in 1842. Broadly grouped, and not unique to Canada, these challenges concern: identifying new resources; mining and the environment; mining in support to local communities; and ensuring effective regulation.

Canada has responded to these challenges by generating first class geoscientific knowledge that is driven by innovation, engagement and strong networks for collaboration and information-sharing. It has also worked to promote a fiscal framework that encourages exploration and a policy framework that supports decision-making through clear, predictable rules for development.

2 Responding to challenges: successes and current approaches

As part of Natural Resources Canada, the strength of GSC programming has been to focus on addressing challenges throughout the entire mineral development cycle, starting with land-use planning and pre-exploration, and continuing beyond the closure of a mine, with a consistent commitment to community engagement. Although Canada has carried out government-funded geoscience programs directed at supporting the mineral industry for over thirty years, the current programs serve to illustrate Canada's approach.

2.1 Geoscientific knowledge and expertise

As most mineral developments projects do not advance past the 'discovery' phase, the most pressing priority of Canada's public geoscience approach has been to produce knowledge, information and data to reduce the number of uncertainties associated with exploration. In fact, GSC science results have long been credited with helping industry balance investment risks during the pre-exploration and exploration phases. In large part due to its leadership in generating knowledge around geological settings of mineral deposits and vectoring towards prospective areas, GSC programming has long provided the platform from which industry initiates its search using tectonic settings, new ore deposit models and innovative tools.

The "Targeted Geoscience Initiative" (TGI)[1] is one of

[1] http://www.nrcan.gc.ca/earth-sciences/resources/federal-programs/targeted-geoscience-initiative/10907

the main mineral-based programs of the GSC. First funded in 2000 with a focus on mapping to promote the discoveries needed to sustain base metal mining communities, each renewal of the TGI has been used as an opportunity to strategically refocus the program on the most pressing needs of the mineral exploration industry. The current phase of TGI (2015-2020) focuses on understanding the processes by which metals are collected, transported and accumulated to form a mineral deposit. This new knowledge is allowing the industry to expand their targeted regions for exploration to discover new buried mineral deposits over broader areas. The exploration industry across Canada has integrated TGI geoscience results that were developed during all phases of the program to enhance exploration approaches. For example, in Ontario's Ring of Fire region, industry adopted a TGI enhanced geophysical technique – high resolution gravity surveying – in their base metal exploration program at the Butler prospect (zinc-copper rich volcanogenic massive sulphide occurrences).

TGI has always focused on sustaining discoveries in existing mining camps. With a government increasingly intent on enhancing the economic viability of remote regions – particularly Canada's vast north – in 2008, the GSC launched the Geo-mapping for Energy and Minerals (GEM)[2] program. GEM upgrades the geoscience knowledge base across Canada's North to modern standards to help unlock economic potential and promote responsible land development. This geoscience information supports private sector exploration decisions for many commodities across Nunavut, the Yukon and the Northwest Territories in areas of high potential for precious, base and rare metals as well as leading to the development of new models for hydrocarbon systems. Key activities of the GEM program involve assessing and analysing legacy samples and data, on-the-ground field observations, targeted airborne geophysical surveys and remote sensing and laboratory investigations.

During the first phase of the program (2008–2013), 21 field projects in the three northern territories and the northern parts of six provinces were undertaken, 35 regional geophysical surveys were completed providing new geoscience information for more than 40 percent of northern Canada, over 840 open file releases of new geoscience maps and data were published, and more than 800 technical information sessions were delivered at venues frequented by industry, government and NGOs. Combined, these activities resulted in new exploration investments by over 100 companies, generating $40 million CAD in direct employment opportunities and indirect investments of over $300 million CAD, with still more to come. The second phase of the program (2013-2020) launched initial research activities through 12 field activities during the summer 2014, followed by 15 in 2015, and 13 in 2016.

[2] https://www.nrcan.gc.ca/earth-sciences/resources/federal-programs/geomapping-energy-minerals/18215

GEM has identified areas of high potential for gold, nickel, platinum-group elements, rare earths, base metals and diamonds. In the Yukon, for example, Tarsis Resources' discovery of a gold-copper-silver deposit at White River and Solomon Resources' discovery of the Rosie epithermal gold deposit were announced with direct attribution to GEM results. GEM has also developed new models for hydrocarbon systems, suggesting that large oil and gas potential may exist in new areas not currently explored by industry.

2.2 Driving innovation through engagement and networks

Both TGI and GEM operate under the collaboration principles defined in the Intergovernmental Geoscience Accord (IGA). The IGA represents a commitment by provincial, territorial and federal geological surveys to collaborate and cooperate on the delivery of geoscience. The IGA also lays out the respective roles and responsibilities of the surveys: the GSC focuses on thematic and national programs, including the offshore, while provincial-territorial geological surveys focus on systematic description of the geology and data collection within their jurisdiction.

Strategic collaborations between both programs and academia also represent opportunities for networks to complement GSC expertise and enhance the quality and diversity of knowledge products. For example, GEM's geoscience grants to Canadian universities are proving successful in addressing regional scale thematic geoscience research questions for mineral and hydrocarbon-related development of the Canadian Arctic. The program also benefits from an Advisory Group of Northerners, comprised of representatives from territorial governments, industry, and Indigenous socio-economic development organizations, which provides advice and strategic guidance on the management and delivery of the program.

2.3 Improving environmental performance to promote economic competitiveness

Launched in 2007, with support from the Canadian Institute of Mining, Metallurgy and Petroleum (CIM) and Natural Resources Canada, the industry funded Canadian Mining Innovation Council (CMIC) continues to improve environmental performance while promoting economic competitiveness. With memberships drawn from industry, academia and government, CMIC coordinates and develops research and innovation projects and programs in response to "life of mine" challenges defined by its industry members.

Natural Resources Canada's own Green Mining Innovation (GMI) program addresses challenges across the mining lifecycle, from extraction to closure. Launched in 2009, the program invests in research and development to enhance productivity in the minerals and metals sector. It also supports the commercialization of green mining technologies, and fosters collaboration with industry,

academia, government policy-makers and regulators in Canada and abroad to address environmental and economic challenges. GMI expertise has also benefited mining communities by reducing environmental impacts through innovation in water management, waste minimization and management, improved energy efficiency in mine operations, as well as mine site remediation and ecosystem risk management.

In parallel, and for the benefit of existing and future mining operations, the GSC's Environmental Geoscience program (EGP) is conducted in close collaboration with academia, industry and other levels of government. As with GEM and TGI, such interdisciplinary and multi-stakeholder partnerships have proven to lead to a more comprehensive understanding of complex environmental systems, ensuring that project results are shared directly with risk assessors, environmental managers, and government regulators. Studies carried out through EGP are helping to improve the quality of Canada's environmental regulations and performance, and are providing publically accessible geoscience information in support of decision-making. Research activities focus on issues of strategic importance to Canadians including geoscience for renewable energies, and the characterization of environmental impacts of metals mining. As an example of the latter, GSC experts work to differentiate natural and man-made sources of metal contaminants, their mobility in the environment, and their potential risk to humans, animals and plants. The results of this research are then shared with experts in risk assessment and human health to help develop better environmental quality guidelines and reduce exposure to contaminated sites. EGP scientists use GSC maps that often date back to the late 1800s, now all digitally accessible online. The maps show the locations of old mine workings, mill sites, and mine wastes that are now heavily overgrown in many former mining districts.

2.4 Fiscal and policy decisions that encourage exploration

Canada's exploration and mining sector continues to benefit from government policy choices, in recognition of the significant role it plays in providing employment, especially in rural communities. Measures have included: funding for public geoscience programming; Free Trade and Investment agreements; Flow-through Share mechanisms to help finance exploration and development activities; and tax credits, such as the 15 percent Mineral Exploration Tax Credit with its expanded definition of exploration expenses that now includes costs associated with environmental studies and community consultations.

In 2016, Canada's federal, provincial and territorial natural resources ministers agreed on the importance of strengthening public confidence in the natural resource sectors. This concurred on enhancing community engagement, science and evidence-based decision-making, regulatory frameworks and environmental performance – policy choices aimed at improving environmental performance while protecting economic competitiveness.

While reviews for major projects, such as mines, continue within the current legislative framework, development decisions are based on science, traditional knowledge of Indigenous peoples and other relevant evidence.

3 The future for the GSC

Although Canadian governments support successful mineral discovery in many ways, delivery of public geoscience to stakeholders remains at the core. GSC programming has come a long way since the turn of the century, let alone since its very beginning in 1842. Current priorities focus on completing geological framework mapping of northern Canada in areas with high resource potential, developing new genetic and exploration models of major ore deposit types and mineral districts, and improving predictive capacity for future energy and commodity supplies. Looking beyond 2017, future priorities include conducting targeted resource assessments of key offshore basins in northern Canada, and completing and defending Canada's submission to the Commission on the Limit of the Continental Shelf under the United Nations Convention on the Law of the Sea. As less than 10 percent of the surface of Canada's offshore seafloor has been mapped, and even less is known about the related subsurface, geoscience efforts will focus on filling knowledge gaps through collaborative opportunities. The GSC's geospatial datasets will be integrated into Canada's new Federal Geospatial Platform with derivative knowledge products disseminated promptly.

4 Industry feedback

GEM stakeholders have confirmed, through program evaluation and audit processes, that the program is effectively addressing the need for public geoscience in the North. Socio-economic and social contributions (training and employment) to growth, as evidenced by the uptake of results by the private sector and Northern communities, are clear. Similarly, TGI reviews confirm that the program's collaborative approaches are relevant, in terms of helping ensure industry needs are being addressed. For example, 90 percent of industry respondents to a particular survey exercise indicated that TGI was addressing their organization's needs.

More broadly, the Prospectors and Developers Association of Canada describes the impact of the Canada's approach stating, "public geoscience is the lifeblood of mineral exploration," and "over the long run, the GEM program is expected to stimulate over $500 million [CAD] in exploration expenditures, with potential future mineral discoveries at $12 billion [CAD]."

While Canada's exploration and mining industry stakeholders continue to endorse existing fiscal and policy frameworks currently in place, there are additional

measures being suggested by industry. Those include: further improvements to the regulatory process as it pertains to the mining sector, which accounts for 70 percent of total applications under the Canadian Environmental Assessment Act; additional coordination between federal and provincial environmental assessments; and, more clarity regarding Species at Risk Act as it relates to mining operations.

5 Conclusion

The GSC's leadership is as relevant to Canada's exploration and mining industry today as it was 175 years ago when the first geological surveys were conducted under Sir William Logan's guidance. Looking forward, science organizations will address new sets of challenges including increasing public expectations for quick access to evidence that supports government decisions, and a demand for highly specialized and multidisciplinary expertise. These pressures will provide opportunity to further broaden geoscience programming by examining how science initiatives support the development and evolution of public policy and regulatory decision making, particularly on sustainable development. They also provide opportunity to work to increase scientific literacy, for example, breathing new life into science communications exercises to reach more stakeholders and new target audiences.

We know that public policies are influenced by various elements including environmental risks and changes, economic conditions, public opinion and technological advances, but also the pace of accelerated scientific discovery and the capacity to practice related science diplomacy. With changes now initiated, the GSC is on the right track.

Long-term investment in geoscience has made Finland a top-ranking exploration target

Pekka A. Nurmi, Pasi Eilu, Vesa Nykänen and Jouni Vuollo
Geological Survey of Finland

Abstract: Finland is a traditional mining country and currently one of the most active regions for exploration and mining investments in Europe. Globally, Finland has been ranked in the top 5 in mining investment attractiveness since 2010. The key factors behind the success are the diversified mineral potential, the world's best geodata, an excellent infrastructure and an operating environment supported by the government's pro-mining policy. Readily available, high quality geodata combined with the excellent infrastructure make Finland a cost-effective target for mineral exploration companies.

1 Introduction

Finland has a strong minerals cluster including diverse mining companies, globally known mining technology and service companies, and a strong mineral-based downstream industry. Mining is a traditional business in Finland, which was legally limited to domestic companies until 1994, when Finland changed its legislation preceding membership of the European Union. Since then, international companies have made major investments in mineral exploration and mine development in Finland. Today, the business, especially metal exploration and mining, is dominated by foreign companies.

Finland has been one of the most active countries in Europe in mineral exploration during the past twenty years. The Fraser Institute Annual Survey of Mining Companies has ranked Finland globally in the top 5 in mining investment attractiveness since 2010 (Jackson and Green 2016). Dozens of companies have been active in mineral exploration, with an aggregated annual spending of MEUR 35–80. Exploration has focused on diversified commodities, including Ni, Cu, Zn, and Au, PGMs, diamonds and various hi-tech minerals. Important new discoveries have been made, such as the largest gold mine in Europe (Kittilä), one of the largest nickel mines in Europe (Kevitsa), and the possibly world-class Sakatti Cu-Ni-PGM deposit (Maier etal. 2015).

In this paper, we describe the facts behind the past success, where we are at present and where we are going in the near future, and how this development has benefited from the extensive and persistent contribution through geological mapping and mineral deposit studies by the Geological Survey of Finland (GTK), as well as the supportive government policy.

2 Key issues behind Finland's success

2.1 Mineral potential

The Fennoscandian Shield, of which Finland forms the central part, has historically been one of the most active mining areas of Europe (Weihed et al. 2005; Eilu et al. 2012a, 2016; Maier et al. 2015). Currently, the shield is the most important metal mining region of Europe (Nurmi and Molnár 2014; Reichl et al. 2016). Modern industrial mining in Finland started during the 1920s, and 10 metal and 25 industrial mineral mines are currently in operation (Fig. 1). These include important critical minerals, and the only phosphate, PGM, Co and Cr producing mines within the European Union. Other major products of the mines include Au, Cu, Ni, and Zn, carbonates, talc and wollastonite (Finnish Mining Registry data).

Finland can nevertheless be regarded as largely under-explored. Only four percent of the bedrock is exposed, and intensive drilling has only been carried out in rather few areas. The known deposits and recent positive exploration results associated with typical Precambrian shield geology indicate a good potential for major future discoveries (Eilu et al. 2012b, 2016; Maier et al. 2015).

Current advanced exploration and mine development projects are targeting Ag, Au, Co, Cu, Fe, Li, Ni, PGM, Ti, V, Zn, phosphate and talc (Fig. 1). In addition to the commodities listed above, grassroots exploration is also focused on diamonds and graphite. The ongoing interest in and the indicated mineral potential of Finland is also indicated by the dozen new exploration companies that have come to the country since mid-2016.

2.2 Strong Geological Survey (GTK)

The Geological Survey of Finland (GTK), founded in 1885, is one of the leading European geological survey organisations, with a focus on promoting the sustainable use of mineral resources. GTK presently employs about 450 people and has an annual expenditure of MEUR 45.

GTK has conducted nationwide geophysical, geochemical and geological mapping for over 100 years. For example, Finland has a consistent, country-wide airborne geophysical database including magnetic, electromagnetic and gamma-ray spectrometric measurements systematically performed at a line spacing of 200 m and with a nominal terrain clearance of 30 m (Airo et al. 2014).

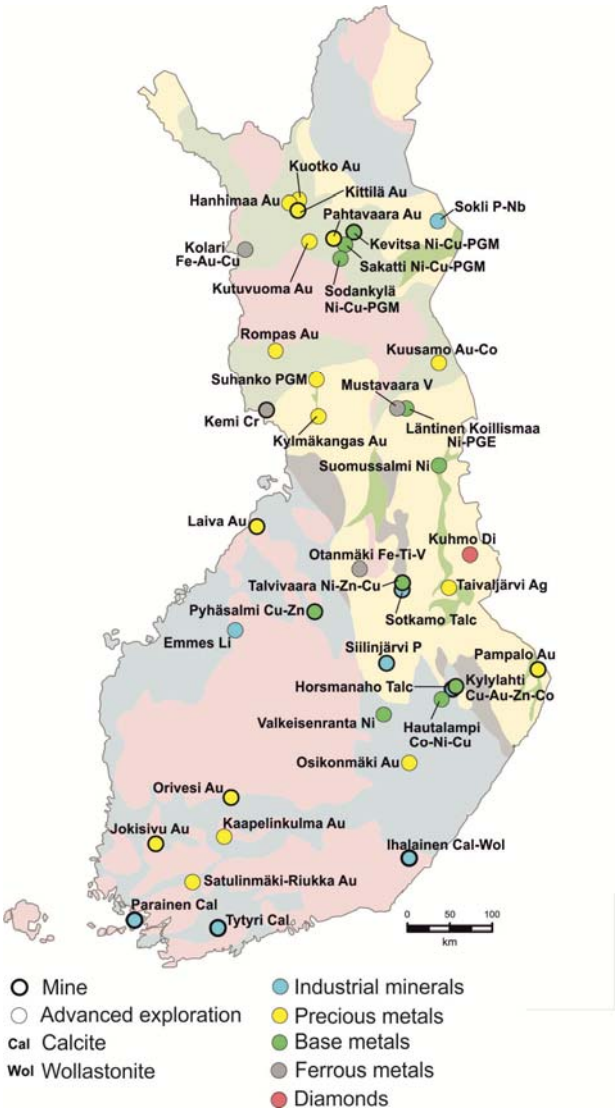


Figure 1. Major mines and exploration projects in Finland.

GTK has over 35 years of experience in digital data management, data architecture, GIS, data analysis, visualization and information delivery. During the last 15 years, GTK has converted all the traditional field data acquisition into a digital format, and since the mid-1990s has gradually placed all its publications and archive reports in the public domain, accessible through the Internet (see: http://hakku.gtk.fi/?locale=en).

All GTK data collected by mining and exploration companies are digitally available online through web-based dissemination services (see GTK map service at: http://gtkdata.gtk.fi/mdae/index.html). The data availability and quality have been assessed for several years in a row as the best in the world by the Fraser Institute annual surveys (Jackson and Green 2016). GTK has also actively promoted the exploration potential and the information available over the past 20 years in global forums.

Over the past decades, GTK has conducted active precompetitive mineral potential mapping. Over 20 mines in Finland have been developed from initial discoveries by GTK. These include the Kevitsa Ni-Cu, Kemi Cr, Talvivaara Ni-Zn, Kittilä Au and Pampalo Au mines (Eilu et al. 2012a; Haapala and Papunen 2015).

Geoscience data are to exploration what road systems are to transport: a precompetitive asset that jurisdictions must provide if they hope to foster a viable and sustainable mining industry (Heffernan 2016). Finland's success story relies on geoscience data that are of high quality, comprehensive and easily accessible, as well as comprehensive research on the Precambrian geology and the associated mineral systems (Lehtinen et al. 2005; Maier et al. 2015).

Mining and exploration companies have been using the geodata and mineral systems understanding provided by GTK in their successful exploration. For example, the discovery of the possibly world-class Sakatti Cu-Ni_PGM deposit was based not only on the persistent exploration strategy of the company, but also on the high-quality airborne geophysical data available from GTK (Brown 2016).

2.3 Stable political environment and excellent infrastructure

Predictable, transparent and long-term strategic policies define Finland. The Fund for Peace has ranked Finland as the most stable country in the world (Messner et al. 2016). This score is based on key political, social and economic indicators and on more than 100 sub-indicators, including public services, income distribution, human rights and the rule of law. Furthermore, Finland has been regularly ranked among the least corrupt nations in the world (Transparency International 2016).

Technology uptake and utilisation is high, with a diverse service sector. Finland welcomes foreign investment as a boost to its economic dynamism, with a corporate tax rate of 20% (Invest in Finland 2017). The World Economic Forum regards Finland as the most competitive country in Europe (World Economic Forum 2014).

An important part of the economy is the skilled workforce. High-quality education can be seen as behind Finland's reputation as a world-class knowledge-based society. Altogether, 14 universities and 24 universities of applied science provide higher education. Education in Finland is free for all, including postgraduate students.

An extensive nationwide road, rail, port and data network covers the whole of Finland. Almost nowhere in the country will an exploration project be more than 5 km from all-year roads and the national power grid. Finland offers competitive energy prices with a robust and diverse energy infrastructure.

Readily available, high quality geodata combined with the excellent infrastructure provide a cost-effective operational environment for mineral exploration.

3 Pro-mining policy

3.1 Finland's mineral strategy

Finland's governments have systematically support the minerals sector in the early 2000s. The mineral potential was well established and it was understood that mining would create welfare for the less populated regions, particularly in eastern and northern Finland, where possibilities for business development in other sectors are limited.

Finland was one of the first European countries to establish a mineral strategy in 2010 (Anonymous 2010, Pokki 2016). The long-term objective of the strategy is to make Finland a global fore-runner in the sustainable mineral industry (Fig. 2). The main pillars of the mineral strategy are: 1) promoting domestic growth and prosperity; 2) solutions for global mineral chain challenges; and 3) mitigating the environmental impacts of mining. These strategic objectives outline the steps that will make Finland a global leader in the sustainable utilisation of mineral resources, and the minerals sector will be one of the foundations of the Finnish national economy.

Finland's diverse mineral resources, new discoveries and excellent exploration potential will form the basis for increases in mineral production in the coming decades. Expertise in the mining technology and service sectors is also a key to promoting the efficient and responsible exploitation of mineral resources globally and creating new international business. The strategy proposes several measures to develop the minerals sector. These include exploration investments to secure raw material supplies, reducing the environmental impacts of mining and strengthening R&D and expertise in the sector.



Figure 2. Finland's mineral strategy (Anon. 2010).

3.2 Green mining

GTK was the driving force in developing Finland's Green Mining (GM) concept as a major tool to implement the mineral strategy (Nurmi and Wiklund 2012, Nurmi and Rasilainen 2015). GM aims to help the mining industry to earn the social licence to operate. It is based on five pillars (Fig. 3). GM promotes material, water and energy efficiency to reduce the environmental footprint of mineral-based product life cycles. It also allows the recovery of all useful minerals and minimises mining waste.

GM aims to ensure the availability of mineral resources for future generations, which requires long-term investment in exploration supported by geoscientific mapping, mineral systems research and the development of exploration techniques. An important goal of GM is to minimise adverse environmental and social impacts in all the stages of the operations, and to maximise local benefits. GM helps to organise the operations in such a way that they are safe and meaningful to employees, and harmless for local residents and the environment. After mine closure, GM helps to restore the mining areas to make them safe and preferably to allow other types of land use. The broad-based participation of local residents and other stakeholders is crucial throughout the mining life cycle, from early exploration to mine closure.



Figure 3. Finland's Green Mining concept.

The Finnish Funding Agency for Innovations (Tekes) operated a major GM programme from 2011–2016 with the aim of making Finland's minerals cluster the world leader in intelligent and minimum impact mining. The programme included over 100 projects with a total budget of MEUR 116, and 185 partners from industry to academia. The results will help the mining industry to improve its performance in all areas of GM, and to make it economically, environmentally and socially more viable and acceptable in the future.

3.3 Mining Finland Programme

The government launched the Mining Finland Programme in 2015 as one of the so-called "growth programmes", which particularly aim to support the development of SMEs in different business areas. The Mining Finland Programme has two major aims: 1) It supports the business development of about 40 mining technology and service companies aiming to expand their exports to the global mining industry; 2) The programme also promotes global exploration investments and assists junior mining companies active in Finland in attracting capital. The programme is led by GTK and has an annual budget of about MEUR 1.

4 Next steps

Finland aims to continue long-term support for the development of the mining industry and the whole minerals cluster as an important part of the "Cleantech" strategy. GTK aims to strengthen its role in RDI in the minerals sector as the national geoinformation centre and in supporting the mineral policy in Finland and in Europe. One of the key issues is to promote mineral exploration and mining, and the sustainable use of mineral resources. GTK is also actively offering its expertize to clients.

The mineral strategy is well supported by GTK's strategic focus areas. These are:

1) Digital solutions: The potential and systemic advantages of digital technology are taken into account in all our processes. This allows innovative operating models, the steady accumulation of data capital and solutions that adapt seamlessly to specific client needs.

2) Cleantech: GTK is well positioned to advance processes and services that reduce waste, increase recyclability and protect our natural endowments.

3) Built environments: We generate the geological information critical to urban development, land-use planning, construction, and infrastructure and associated environmental issues.

4) Mineral economy: We play a key role in advancing mineral-based economies to secure the greater diversity and sophistication of Finnish products and services.

References

Airo M-L Hyvönen E, Lerssi J, Leväniemi H, Ruotsalainen A (2014) Tips and tools for the application of GTK's airborne geophysical data. Geol Surv Finland Rept Invest 215

Anonymous (2010) Finland's Minerals Strategy. The Ministry of Employment and the Economy. http://projects.gtk.fi/export/sites/projects/mineraalistrategia/documents/FinlandsMineralsStrategy_2.pdf. Accessed 21 February 2017

Brown G (2016) Anglo American exploration: key ingredients to a decade (1999−2010) of success. Soc Econ Geol Spec Publ 18:321–329

Eilu P, Boyd R, Hallberg A, Korsakova M, Krasotkin S, Nurmi PA, Ripa M, Stromov V, Tontti M (2012a) Mining history of Fennoscandia. Geol Surv Finland, Spec Paper 53:19–32

Eilu P, Ahtola T, Äikäs O, Halkoaho T, Heikura P, Hulkki H, Iljina M, Juopperi H, Karinen T, Kärkkäinen N, Konnunaho J, Kontinen A, Kontoniemi O, Korkiakoski E, Korsakova M, Kuivasaari T, Kyläkoski M, Makkonen H, Niiranen T, Nikander J, Nykänen V, Perdahl JA, Pohjolainen E, Räsänen J, Sorjonen-Ward P, Tiainen M, Tontti M, Torppa A, Västi K (2012b) Metallogenic areas in Finland. Geol Surv Finland Spec Paper 53:207–342

Eilu P, Hallberg A, Bergman T, Bjerkgård T, Feoktistov V, Korsakova M, Krasotkin S, Lampio E, Lauri, LS, Litvinenko V, Philippov N, Sandstad JS, Shchiptsov V (2016) Fennoscandian Ore Deposit Database. Annual update. http://en.gtk.fi/informationservices/databases/fodd/index.html. Accessed 23 February 2017

Messner JJ, Haken N, Taft P, Blyth H, Lawrence K, Bellm C, Hashi S, Patierno N, Rosenberg L (2016) Fragile States Index 2016. http://library.fundforpeace.org/library/fragilestatesindex-2016.pdf. Accessed 23 February 2017

Haapala I, Papunen H (2015) A history of exploration for and discovery of Finland's ore deposits. In: Maier WD, Lahtinen R, O'Brien H (eds.) Mineral Deposits of Finland. Elsevier, Oxford, pp. 1–38

Heffernan V (2016) Give them data and they will come. Earth Explorer, Expertise, 4 August 2016. http://www.earthexplorer.com/2016/Give_them_data_and_they_will_come.asp. Accessed 15 February 2017

Invest in Finland (2017) Safe playground. http://www.investinfinland.fi/safe-playground. Accessed 22 February 2017

Jackson T, Green KP (2016) Fraser Institute Annual Survey of Mining Companies 2015. Fraser Institute, Vancouver. https://www.fraserinstitute.org/sites/default/files/survey-of-mining-companies-2015.pdf. Accessed 20 January 2017

Lehtinen M, Nurmi PA, Rämö TO, eds. (2005) Precambrian Geology of Finland. Elsevier, Amsterdam

Maier WD, Lahtinen R, O'Brien H, eds. (2015) Mineral Deposits of Finland. Elsevier, Oxford

Nurmi PA, Wiklund M-L (2012) Finland is developing green mining. Géosciences 2012: 15, 36-41

Nurmi PA, Molnár F (2014) The future of metal minerals mining in the EU. European Geologist 37: 12-19

Nurmi PA, Rasilainen K (2015) Mineral resources of Finland. In: Maier WD, Lahtinen R, O'Brien H, eds. Mineral Deposits of Finland. Elsevier, Oxford, pp 753-777

Pokki J (2016) Finland: Mineral Policy. In: Tiess G, Majumder T, Cameron P (eds.) Encyclopedia of Mineral and Energy Policy. Springer-Verlag, Berlin, Heidelberg. http://link.springer.com/referenceworkentry/10.1007/978-3-642-40871-7_45-1. Accessed 21 February 2017

Reichl C, Schatz M, Zsak G (2016) World Mining Data. Vol 31. Austrian Federal Ministry of Science, Research and Economy, Vienna

Transparency International (2016) Corruption Perceptions Index 2016: Full Source Description. http://www.transparency.org/news/feature/corruption_perceptions_index_2016. Accessed 23 February 2017

Weihed P, Arndt N, Billström C, Duchesne JC, Eilu P, Martinsson O, Papunen H, Lahtinen R (2005) Precambrian geodynamics and ore formation: the Fennoscandian Shield. Ore Geol Rev 27:273–322

World Economic Forum (2014) The Europe 2020. Competitiveness Report, Building a More Competitive Europe. The 2014 Edition. http://www3.weforum.org/docs/WEF_Europe2020_CompetitivenessReport_2014.pdf. Accessed 21 February 2017

The Geological Survey of Argentina (SEGEMAR) and its support to the Argentinian mineral industry

Julio Ríos Gómez
Servicio Geológico Minero Argentino

Eduardo Zappettini
Servicio Geológico Minero Argentino

Abstract. The Geological Survey of Argentina was created in 1904 as the Division of Mining, Geology and Hydrology with the responsibility of conducting geological, mineralogical and hydrological exploration. After constitutional and organizational changes and evolution, the Survey became, in 1993, what is today's SEGEMAR. Since its inception, the Geological Survey of Argentina played a fundamental role in providing the geological knowledge and data that formed the basis of advanced exploration. The Survey can also be credited with having played a critical role in discovering a number of world-class deposits. The history of the Geological Survey of Argentina, and its predecessor organizations, clearly illustrates the instrumental role of public geosciences in promoting, supporting and optimizing exploration at various stages. SEGEMAR's current objectives are to continue to provide knowledge and data about Argentina's geology, and to integrate of the wealth of information gathered from the study of mature and emerging mining districts and regions with known mineral endowment for its use by both the industry and government.

> A person who ignores, or who only partially knows the nature of the territory he lives in, is a tenant and not a landowner.
> Martin Doello-Jurado (1939)

1 Background

The Division of Mining, Geology and Hydrology was created by Decree, October 25th, 1904, with the purpose of "performing geological, mineralogical and hydrogeological exploration with an emphasis on studies of fossil fuel and hot springs". Since then, Servicio Geologico Minero Argentino (SEGEMAR) saw its roles and responsibilities go through numerous changes, which also affected its structure and constitution. Despite these changes, the fundamental mission and functions for the most part remained the same, and for this reason, the 1904 Decree is still considered as the founding act of the Geological Survey of Argentina. Indeed, since then, the institutional vision has been to provide the government and the community with expertise about Argentina's geology and resources.

The creation of the Division of Mining, Geology and Hydrology was the result of the merging of the Division of Mining and Geology, which was then directed by Eng. Henry Hoskold, and the Commission for the Study of Groundwater and Coal deposits, directed by Eng. Enrique Hermitte. The Division of Mining and Geology had been established in 1885 as the Mines Section, within the Department of Public Works of the Ministry of Interior with the purpose of conducting geological, mining and hydrogeological studies. At the end of August of the same year, laboratories were built and studies began for the provision of water in the south and southeast of La Rioja, and geological studies in the Velasco, Famatina and Los Llanos ranges, as well as others related to the geology and mineral resources of the Cordoba ranges. Eng. Hoskold, who had acquired a strong reputation throughout the world for having developed a formula to calculate the net current value of a mine in the 1870s, was appointed Director in 1886. During his time, the Division was primarily involved in preparing reports on the description of the country's various mines and their legal status, which were presented at international venues. Thus, Hoskold attended the 1889 Universal Exhibition in Paris and presented the *General and Special Report on Mines, Metallurgy, Legislation and Resources of the Argentine Republic* in Spanish, French and English. This memoir was sent to France, England, Belgium, and Germany among other countries. He has also participated in the 1893 International Exhibition in Chicago and in the 1894 Exhibition in Chile.

The Commission of Studies of Groundwater and Coal deposit was established in 1902 as a subsection of the Mining Industries Section within the Industries Division. The direction of the Commission was entrusted to Eng. Enrique Hermitte who was asked to promote the use of national fuels, thus launching a continuous effort in the exploration, evaluation and promotion of the country's energy resources.

Both the Division and the Commission participated in the promotion of the resources of Argentina at the Universal Fair of Saint Louis in 1904, presenting reports and samples.

2 The early days of the Geological Survey of Argentina

In 1904, with the restructuring of the Ministry of Agriculture and the passing of Hoskold, the Mines, Geology and Hydrogeology Division was created under Hermitte, and systematic drilling, geological mapping and exploration of mineral resources, groundwater, coal and hydrocarbons were initiated.

The progressive acquisition of drilling equipment led to a substantial increase in the drilling program for groundwater research and, derived from this program, the search for fossil fuels. This resulted in the discovery of oil in Comodoro Rivadavia (San Jorge Gulf Basin) in 1907 and in Plaza Huincul (Neuquén Basin) in 1918, thus laying the foundations for the Argentine oil industry. The discovery of oil in Comodoro Rivadavia also marked a milestone in the history of the Geological Survey of Argentina as it helped showcase the value of governmental geological research and the need to intensify regional geological studies before the National Government.

Over the following 70 years, more than 310,000 meters of drilling were completed, ensuring the supply of water to a large number of towns, railway stations and, in parallel, generating an invaluable body of knowledge of the subsoil. The geological studies were organized in a systematic way, with an initial mapping program at a 1: 1,000,000 scale and another at 1: 200,000 scale. The first geological map focusing on mineral resources (on the Córdoba ranges) at a scale 1: 1,000,000 was published in 1905 along with an explanatory report.

At that time, mining studies of deposits and districts continued to enhance knowledge and to promote exploration and exploitation of the country's mineral resources. The methodological compilations of mining knowledge and related metallogenic knowledge began at this stage, which led to the production and publication of syntheses and maps of metalliferous resources, of industrial minerals and dimensional stones, at a scale of 1:5,000,000. In 1907, the first seismological station was set up in Mendoza, and the Division became part of the International Association of Strasbourg.

Hermitte soon made that the organism had to expand and broaden its activities. Consequently, Bodenbender, a German geologist working for the Geological Survey highlighted the necessity to produce an agronomic geological map to investigate the soil's lithological constituents, their origin and the factors that play an important role in plant growth (proportion of constituents, harmful substances, capacity of filtration and absorption, etc.). A few years later, in 1918, the first 1:200,000 geological and economic map and memoire (Bahía Blanca) including agronomic data was published.

The 1930s mark the beginning of geotechnical work by the Survey, more specifically with the characterization of the international Uruguayana-Paso de los Libres bridge area. In addition to its own programs, the Survey carried out studies for other official departments and provided technical advice on applied geology (e.g., dams, roads, railways, trans-Andean tunnel, canals, and study of the 1944 San Juan earthquake).

From 1938 onwards, the activity of the Survey involved the exploration of nuclear minerals, with the first finding of uranium mineralization in Argentina in Calamuchita, Córdoba, and later in La Rioja, San Luis and, the most economically important one, Don Otto mine, in Salta.

In 1941,Bulletin No. 50 "*The mineral deposits and dimensional stones of the Argentine Republic. Its geology and genetic relationships*" was published by Eng. Victorio Angelelli, a landmark in the knowledge of the mineral deposits of Argentina.

From the 1950s onwards, the Survey was responsible for producing the Mining Statistics of the Argentine Republic and there was an important mining promotion component, which resulted in the exploration of deposits and support to the miners, the commercialization, industrialization, export and import of minerals. In 1955, the first reserve estimations of the Sierra Grande iron deposit and the economic study of the Farallón Negro gold deposit were made.

In 1960, studies were carried out including drilling and permeability tests in the Apipé waterfalls, current site of the Yacyretá dam.

3 Prospecting and exploring: the active role of the Survey

Between 1962 and 1963, at the request of the Yacimientos Mineros Aguas del Dionisio (YMAD), the Geological Survey entrusted A. Mezzetti with the study of YMAD's mining property, leading to the identification and definition of Bajo de la Alumbrera as a giant porphyry-type copper deposit and the first estimate of its economic potential.

After its administrative decentralization, in force between 1963 and 1969, the agency, namely National Institute of Geology and Mining (INGM), undertook regional plans for prospecting and exploration in order to promote mining based on an adequate assessment of the mineral and mining potential of the national territory.

This activity gave rise in the 1970s to the first discoveries of disseminated mineralization, such as La Mejicana and Los Bayos, in the province of La Rioja, and Cerro Rico (Agua Rica) and Cerro Atajo, in Catamarca. Important areas of hydrothermal alteration were identified in the Andean Cordillera of La Rioja and the extreme north of San Juan, which include Cerro El Potro, Filo de la Vicuñita, Quebrada de la Frontera and Río Blanco. All these occurrences have been later related to a major gold belt known in Chile as Faja de Maricunga, which soon after saw extensive exploration by private companies in the 1990s.

Between 1980 and 1989 the Valle del Cura region was explored and favorable geological conditions were identified, including hydrothermal alteration, gold and silver anomalies, as well as evidence of significant mineralization. Six areas were declared protected areas (reserves: Del Carmen, Jagüelito, Veladero, Despoblados, La Ortiga and Los Amarillos). Later, the province of San Juan tendered them for development through private companies, constituting one of today's main gold districts of South America.

In the province of Catamarca, the work included regional exploration with selection of areas of interest and the intensive exploration and evaluation of the Bajo de la Alumbrera deposit. Areas such as Diablillos (Au),

Antofalla Este (polymetallic), La Borita (Cu), Filo Colorado (Cu-Mo), Cerro Toronado (Cu-Au), Fiambalá-Zapata (Cu-Ni), and Valle Ancho (Au) were identified as being highly prospective and explored.

Similarly, in the Patagonian region, areas with hydrothermal alteration and mineralization were recognized, such as Cerro Vanguardia, La Josefina, Bajo Pobre, El Dorado-Monserrat and El Macanudo in Santa Cruz, and Cordón Caquel-Cerro Gonzalo-Cerros Colorados, Cordón de Esquel and Huemules in Chubut. Massive sulfide mineralization was found in Tierra del Fuego.

4 The present day Geological Survey of Argentina (SEGEMAR)

During the 1990s the National Government took a series of measures to further promote mining activity in Argentina, favoring risk investments through a new regulatory body, introducing new technologies, and training qualified personnel. Various laws were enacted (e.g., the Mining Investment, Mining Reorganization, and Mining Environmental Protection laws) and the production of geological and thematic maps was established by law. The National Direction of the Geological Survey was thus created in 1993, merging previous National Government technical areas with responsibilities in the fields of geology and mining. And in 1996, the National Direction of the Geological Survey and the Institute of Mining Technology were combined, forming the Servicio Geológico Minero Argentino (SEGEMAR) as a national decentralized agency.

With the participation of international companies and consultants, the professional and technical staff of the Geological Survey were first trained in using remote sensing techniques, which led to the identification of targets in the high mountain ranges of San Juan and La Rioja (e.g., Lama, Valle Ancho and Cordón de la Brea), directly contributing to the mining development.

Through the Argentina - Mining Sector Development Technical Assistance Project (PASMA), which was financed by the World Bank, new áreas of expertise were developed within the Survey. Systematic airborne geophysics, regional geochemistry and metallogenic programs, as well as institutional GIS were implemented with support from various foreing geological surveys (i.e. Canada, the United States and Spain) and a consulting company (WGM Ltd.). Also, provincial mining cadasters were updated, becoming an essential tool to promote investment. Overall, by strengthening the geological infrastructure and mining rights tenure security, the PASMA project led to the creation of a favorable environment for overall sustained growth in mine development-related activities in Argentina.

Other projects directly contributed to the modernization of the Survey, including the Multinational Andean Project, partially funded by C.I.D.A. (led by the Geological Survey of Canada) and the ASTER Project developed with JICA's assistance.

The foundations were laid for the development of the Argentinian mining sector, which led to the initial major mining investments during the 1990s. There are widely recognized milestones in this development, including : 1) Bajo de la Alumbrera, a porphyry Cu-Au deposit (identified in previous decades by the Geological Survey, then evaluated by Musto and currently being mined by Glencore); 2) Cerro Vanguardia, a Au-Ag epithermal deposit (also identified by the Survey, then developed by MINCORP and currently mined by AngloGold-Ashanti); and 3) Salar del Hombre Muerto, a Li deposit (initially identified and evaluated by another State agency, DGFM, and later developed and exploited by FMC).

5 Conclusion

The history of the Geological Survey of Argentina, and its predecessor organizations, clearly illustrates the critical role of public geosciences in promoting, supporting and optimizing exploration at various stages, especially through the generation of geological knowledge and data, helping highlight areas of favorable mineral potential. At present, and looking to the immediate future, SEGEMAR will continue to fill that essential role in generating knowledge and data to be used by mining companies looking for new properties or potential areas to explore and develop. Among SEGEMAR's objectives is the integration of the wealth of information gathered from the study of mature and emerging mining districts and regions with known mineral endowment. This knowledge and data integration will serve to generate a database that will help define improved metallogenetic contexts and generate working hypotheses for the identification of new targets of interest. This highlights the necessity to continuously work at optimizing the interaction between the public and private sectors.

Promoting and assisting mineral exploration: Québec's approach

Patrice Roy, Hugo Dubé-Loubert, Jean Goutier, Mehdi Guemache, Jean-Yves Labbé, Charles Roy, and Robert Giguère
Ministère de l'Énergie et des Ressources naturelles du Québec (MERN)

Abstract. Public geoscience plays an important role in mitigating the risk of mineral exploration. For this purpose, Quebec's approach is based on a blend of innovation, thematic studies and heritage management. Among these, we emphasize four initiatives:

1) the importance of the SIGÉOM database to preserve geoscience heritage and disseminate information;
2) the long-term funding of public geoscience to support the acquisition of new knowledge;
3) Studies on unconventional mineral commodities to support mineral exploration diversification;
4) Promotion of mineral exploration targets to highlight mineral potential following our geological surveys.

In recent years, our geological surveys aimed to complete a basic coverage of the province. We dedicated efforts to rebuild our expertise in Quaternary geology. Also, we developed new products to disseminate the knowledge acquired. These actions have been aligned to Governmental priorities and policies that support the mineral industry.

Our future goals are to adapt our approach to acquire and integrate geoscientific data and facilitate WEB access. We will continue to develop our expertise in Quaternary geology. Finally, we are developing new electronic and searchable reports and maps, new methods of dissemination to the public.

1 The role of public geoscience

In Canada, it is widely acknowledged, by both Industry and Government that public geoscience plays an important role to mitigate the risk of mineral exploration by identifying favourable mineral potential, thus increasing exploration efficiency and effectiveness (Duke 2014; Moore 2014). Aside from guiding private sector investment decisions, public geoscience also guides land and resources management decisions and contributes to the training of highly qualified persons.

2 Important milestones of our success

2.1 Development of the Système d'Information Géominière (SIGÉOM)

The development of our SIGÉOM database began in the 70's with the implementation of a unified lithological legend and field log. When technology was sufficiently advanced, by the end of the 80's, we were able to rapidly build a robust database. This integrated database, that include geological, geochemical, and drillholes data, has been a reference for many years for geological surveys around the world and we think it gave us a strategic advantage. Among the exploration successes, it was mentioned that the SIGÉOM played an instrumental role in targeting the Malartic area that would become the world class Canadian Malartic Mine in 2008 (Wares and Prud'homme 2013).

2.2 Long-term funding for geoscience

Although it is generally acknowledged that it plays an important role in the development of mining industry, funding public geoscience remains a big challenge. And as the mining market is cyclical, funding may wrongly be influenced by these cycles, thus reducing survey efficiency and durability. In Québec, the Government created the mining heritage fund in 2008. Through an act, the Government of Québec established the fund to finance activity that fosters the development of Québec's mineral potential (Québec National Assembly 2008). Most of the fund is dedicated to geoscientific surveys. It is made up of a sum taken out of the duties collected under the Mining Duties Act, so that active mines are actually financing research to reduce the risk to find new ones.

2.3 Original studies to promote mineral diversification

Promoting mineral exploration is aided by anticipating the types of commodities that will see future demand. In Québec, we have had some successes promoting commodities other than base or precious metals. These include graphite, apatite, diamond and architectural stones. Without taking credit for specific mine discoveries, we think that much of our original studies on unconventional commodities have contributed to the diversification of mineral exploration and mining in Québec.

2.4 Exploration targets to highlight mineral potential

Every year since 2007, we have published interpretations of economically interesting targets, identified during our geoscientific surveys. During field work, our geologists identify zones in which the geological context is favourable for mineral exploration. These publications

have two purposes:
1) They highlight the mineral potential of a survey area
2) Following publication, the procedure is to compile mining title activity, which helps us assess the interest of mineral exploration companies in these geoscientific surveys.

3 Current programs and development

3.1 Recent Geoscience Survey Program

The objective of our recent surveys is to complete basic coverage of the province. We completed the coverage in lake-bottom sediment sampling in 2012, with a grid varying from 4 to 12 km. We hope to complete the geological map of Québec at the 1:250 000 scale and aeromagnetic coverage with a 300 meter spacing by 2025. Also, we are conducting more detailed mapping surveys around emerging mining camps in the James Bay region, in easily accessible terrains like the Grenville Province or in more mature areas like the Abitibi belt.

3.2 Surficial Geology Program

With a recent program on groundwater that was launched in 2008, we got an opportunity to rebuild a Quaternary geology expertise in our geological team. We began new surveys for mineral exploration purposes in 2012 as we think that surficial geology as been underused in Québec as a tool for mineral exploration. Till and glaciofluvial sampling proved to be an essential and complementary tool to address problems associated with poor bedrock exposure particularly in region with thick and extensive glacial drift cover. The first heavy mineral results were released in 2014 and generated some positive response from industry, supporting our decision of rebuilding our expertise in this field. The heavy mineral data is supported by detailed surficial mapping as well as by an inventory of glacial landforms and other geomorphic features. Emphasis is also placed on paleo iceflow reconstruction and on the characterization of the glacial dynamics in order to quantify relative transport distance from the bedrock source. The results finally allowed to identify zones with high mineral potential for several metallogenic contexts.

3.3 Online services

In recent years, a new generation of web services were developed to make the database more accessible for consulting and easier to visualize. These take the form of an interactive map and Web Map Services (WMS) with more than 50 layers (Gouvernement du Québec 2017a; 2017b). It is certainly one of the most complete web service available at the moment. Moreover, we recently created a stratigraphic online lexicon that will eventually become the backbone of the geological map (Gouvernement du Québec 2017c).

3.4 Recent input from industry

In Quebec, recent polls still indicate that regional geoscientific surveys are the best way to support mineral exploration, which includes, in decreasing order, geological surveys, geophysical surveys and surficial geology. Without surprise, companies tend to favour surveys taking place in the areas where they have ongoing projects and where there are existing infrastructures. Regarding applied research, regional metallogeny is their favoured theme.

4 Upcoming developments

For future developments, our vision is to innovate in our approach to acquire, integrate and disseminate relevant geoscientific data and to facilitate access to this data by our clients on the WEB. In this regard, we present three development described below that we want to develop in the upcoming years.

4.1 More Surficial Geology

With our recently added expertise in Quaternary geology, we can now look forward to further developments. We are currently working on a database to integrate heavy mineral analyses to our SIGÉOM database. Moreover, a post-doctoral research project was recently initiated, in collaboration woth the Chair in Magmatic Ore Deposits (UQAC), to establish new mining exploration vectors in region with thick glacial sediment cover. The aim of this project is to characterize the geochemistry of the trace elements of sulphides (pyrites, chalcopyrites) present in anomalous till samples in order to specify the metallogenic context and potentially to circumscribe the source. Furthermore, we are working with universities, namely through the industrial research Chair in Mineral Exploration. The ongoing research aims to develop new protocols to automate heavy mineral separation and identification, as well as to provide new discriminant diagram for indicator mineral classification.

4.2 Knowledge acquisition for big data management

The advent of massive and complex databases (big data) and artificial intelligence into mineral exploration necessitate acquisition of various new types of data such as physical properties of rocks or on site analyses of samples. With other technologies simplifying fieldwork, we think that the time is right to introduce new types of data in our surveys, aside from chemical analysis. These new data may also help in speciality fields such as geophysics or for rapid identification of critical geological features to highlight the mineral potential of a given area.

4.3 Development of new online products

Our main WEB 2.0 project is to develop an electronic geological report. This kind of report as many advantages:

1) It will be fully searchable with common internet browsers, giving a direct access to the content of the geological report to the client, without need to browse table of contents or read through tedious text;
2) It will allow a direct access into our databases, our stratigraphic lexicon and the interactive map, thus acting as a link to various sources of information.
3) The interactive nature of the report should make it more convenient and agreeable to read and browse through.

In parallel, we are working to integrate maps from assessment reports completed by industry. If the project is brought to fruition, all the maps would be available through our interactive map.

Acknowledgements

We are grateful to Patrick Mercier-Langevin, David Huston and Karen Kelley for giving us the opportunity to present this contribution. We thank all the team at Géologie Québec, dedicated to improving public geoscience to support mineral exploration.

References

Duke, JM (2014), Public Geoscience for Private Exploration, Atelier Geological Survey of Canada - Prospectors and Developers Association of Canada.

Gouvernement du Québec (2017a) Carte interactive, Ministère de l'Énergie et des Ressources naturelles http://sigeom.mines.gouv.qc.ca/signet/classes/I1108_afchCarteIntr. Accessed 27 February 2017

Gouvernement du Québec (2017b) Services Web Cartographiques. Ministère de l'Énergie et des Ressources naturelles http://sigeom.mines.gouv.qc.ca/signet/classes/I0000_serviceWeb. Accessed 27 February 2017

Gouvernement du Québec (2017c) Lexique stratigraphique du Québec. Ministère de l'Énergie et des Ressources naturelles http://gq.mines.gouv.qc.ca/lexique-stratigraphique/. Accessed 27 February 2017

Maurice C, Lamothe D, Roy C. (2009) Measuring the Economic Impacts of Geoscience Work by Géologie Québec. PRO 2009-06, Ministère de l'Énergie et des Ressources naturelles, Québec.

Moore R (2014) Industry View on Public Geoscience, Exploration Industry Workshop on Public Geoscience, Prospectors and Developers Association of Canada.

Wares R, Prud'homme, S (2013) The Canadian Malartic mine in the southern part of the Abitibi Belt, Québec, Canada: discovery and development of an Archean bulk tonnage gold deposit https://www.mern.gouv.qc.ca/english/mines/quebec-mines/2013-06/malartic.asp. Accessed 27 February 2017

Québec National Assembly (2008) Bill 87, An Act to establish a mining heritage fund, http://www2.publicationsduquebec.gouv.qc.ca/dynamicSearch/telecharge.php?type=5&file=2008C26A.PDF. Accessed 27 February 2017

Precompetitive geoscience for mineral exploration — the Western Australian Government's Exploration Incentive Scheme

Ian M Tyler and Margaret J Ellis
Geological Survey of Western Australia

Abstract. The Western Australian Government's AU$130.6 million Exploration Incentive Scheme (EIS) began in 2009 funded from the Royalties for Regions program. The objective was to promote exploration in Western Australia to increase the discovery rate of economic deposits, emphasising greenfields areas underexplored for mineral deposits and frontier petroleum basins. The flagship Co-funded Government–Industry Drilling Program has contributed to a number of successful exploration programs, including the discovery of the Nova Bollinger nickel mine. The EIS also funds the state-wide acquisition of pre-competitive geology, geophysics, and geochemical and isotopic data. There has been a strong private sector exploration response to EIS and Western Australia improved its Fraser Institute Investment Attractiveness ranking from 17th in 2009 to 1st in 2013. A 3 year, AU$30 million extension (EIS-3) will allow the scheme to continue until 2020. The planned integrated pre-competitive geoscience programs are aligned with the Australian exploration industry-led UNCOVER initiative's AMIRA Roadmap for exploration under cover.

1 The Western Australian Government's Exploration Incentive Scheme

The Western Australian Government's Exploration Incentive Scheme (EIS) was launched in April 2009. Funding of AU$80 million (Fig. 1) was provided from the Royalties for Regions program for a 4.25 year initiative that ran until end-June 2013 (Phase 1). An additional AU$20.6 million was allocated to the scheme from Royalties for Regions funds for 2013–14 (Phase 1A). Funding for EIS (Phase 2) was then extended for 3 years until the end of 2016–17 with AU$30 million from the Consolidated Revenue Fund (CRF). The EIS is managed by the Geological Survey of Western Australia (GSWA), a division of the Western Australian Department of Mines and Petroleum (DMP).

In May 2016, the budget forward estimates provided for a further extension to the scheme with an allocation of Royalties for Regions funding of AU$30 million over three years to end-June 2020.

The objective of EIS is to promote exploration in Western Australia with a particular emphasis on greenfields areas that are underexplored for mineral deposits and on frontier petroleum basins.

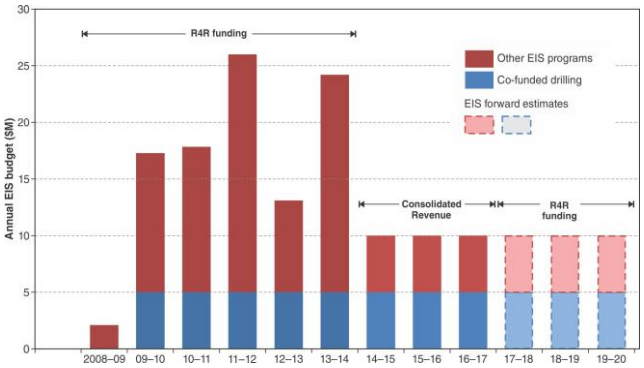


Figure 1. Exploration Incentive Scheme budget 2008–2020

The aim is to maintain investment and exploration activity at levels required for the long-term sustainability of the State's resources sector. This requires an increase in the discovery rate of economic deposits, particularly for gold and base metals (copper, lead, zinc), and steel-industry and specialty metals (includes nickel, vanadium, lithium, rare earth elements), uranium and onshore petroleum.

2 Past successes

2.1 New discoveries

The first new discovery attributable to the Exploration Incentive Scheme was the Nova nickel deposit. GSWA geochemistry and EIS-funded geophysics was used to target the first (EIS-supported) diamond drill hole in the prospect in 2011, with follow-up drilling discovering significant nickel and copper mineralisation in 2012. The first concentrate was shipped from the Nova Bollinger mine in late 2016 with the first export shipment scheduled for June 2017 and full production in mid-2017.

Other successful exploration projects within Western Australia that have benefited from EIS funds include Gold Road Resources Gruyere gold, Rox Resources Mount Fisher East nickel, Sheffield Resources/Centrex Metals Oxley potash, Alloy Resources/Doray Horse Well gold, Encounter Resources Millennium zinc and Panoramic Resources Savannah North nickel–copper–cobalt.

2.2 Beneath the Nullarbor Plain: Understanding the Eucla basement

The Albany–Fraser Orogen and Eucla–Gawler deep crustal seismic reflection and magnetotelluric surveys imaged the Proterozoic rocks forming the basement of the Eucla Basin (Spaggiari and Tyler, 2014; Dutch et al., 2016; Spaggiari et al., 2016, 2017). These rocks are completely covered by the recently uplifted seafloor limestone forming the Nullarbor Plain, and represent perhaps the most challenging greenfields exploration environment in Western Australia.

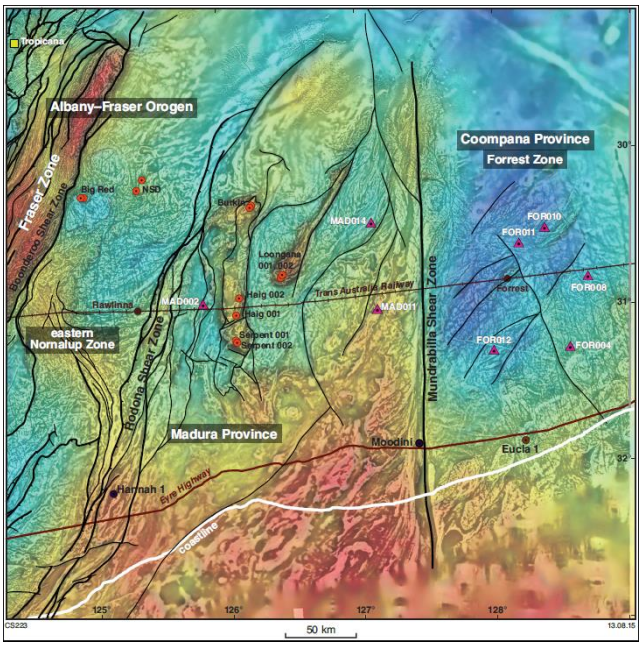


Figure 2. Simplified structures and drill site locations in the Eucla basement plotted on a drape image of gravity (colour) and reduced to pole, first vertical derivative aeromagnetic data (greyscale). The stratigraphic drill sites are shown with pink triangles, EIS co-funded drill sites with orange dots, donated core sites with purple dots, and the Eucla 1 petroleum well with a brown dot (Spaggiari and Smithies, 2015).

- In 2015 GSWA released the results from eight stratigraphic drill cores (Fig. 2) funded by EIS (Spaggiari and Smithies, 2015). The cores provide a wealth of new data, and new ideas about the coming together of the proto-Australian continent between 1.6 Ga and 1.2 Ga, which are significant for developing successful exploration targets in the region.
- The results suggest the presence of ancient oceanic crust, and a 1.4 Ga oceanic island arc caught between the Albany–Fraser Orogen and the Gawler Craton in South Australia.
- There is the potential for volcanic massive sulfide (VMS) or exhalative-style mineralization (SEDEX), as well as magmatic nickel and platinum group elements (PGE), and giant iron oxide–copper–gold (IOCG) deposits.
- Ongoing EIS-funded programs are interpreting the available geophysical images in light of the drilling, together with structural and petrographic analysis, geochronology, and geochemical and isotope studies.

2.3 Fraser Institute rankings

The ranking of Western Australia's Investment Attractiveness in the Fraser Institute's Annual Survey of Mining Companies has improved dramatically since the commencement of EIS from being the least attractive Australian destination for explorers in 2006–07 to being ranked third in the world in the Investment Attractiveness category in 2016 (first in 2013 and 2015), first in the World for Best Practise Mineral Potential in 2015 and 2016, first in the world for geoscience databases in 2016, and ninth in the world in Policy Perception in the 2016 Survey (Fig. 3).

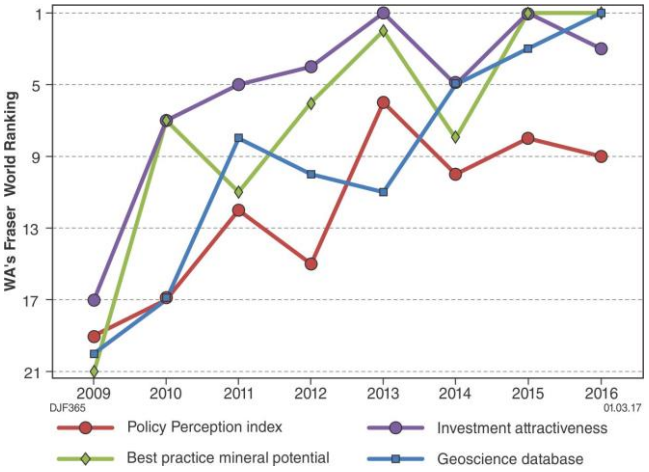


Figure 3. Western Australia's rise in ranking in the Fraser Institute Annual Survey of Mining Companies during EIS

2.4 Economic impact analysis

In late 2014 DMP commissioned an independent economic impact analysis of the EIS to determine multipliers from the perspective of the private sector, employment and the State resulting from the Government's investment into the scheme (ACIL Allen Consulting, 2015).

To determine the net benefit of the EIS to Western Australia, the report considered the source of the additional exploration funds, sector-specific multipliers, and the expected value of future mine developments following additional exploration.

In aggregate, the modelling found that for every $1 million invested in the EIS, the long run expected net benefit to the State, in terms of higher Gross State Product, was $23.7 million (Fig. 4). This comprises:

- $10.3M due to additional exploration activity
- $6.2M in additional taxation and royalty revenue
- $3.9M due to additional construction activity
- $3.3M in new net wealth generated by the development of new mines

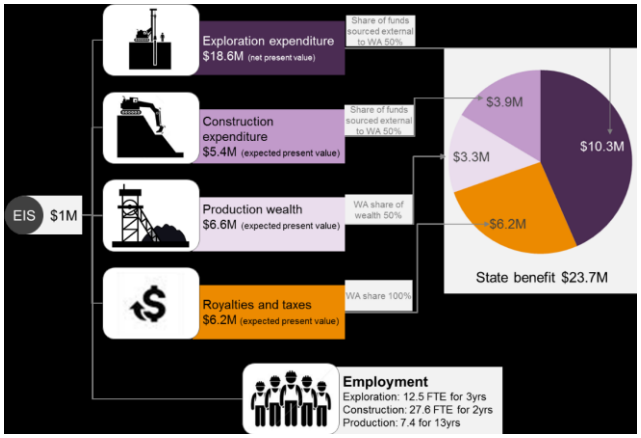


Figure 4. Exploration Incentive Scheme benefit summary (ACIL Allen Consulting, 2015).

The above results, derived from empirical modelling, are large, and the key driver of the result is the strong private sector exploration response to EIS.

3 Recent and current programs

EIS supports five high-level programs, including:

- exploration facilitation
- innovative drilling promotion
- geophysical and geochemical surveys
- 3D prospectivity mapping
- strategic research with Industry

The flagship EIS program is the Co-funded Government–Industry Drilling Program, which is designed to stimulate geoscience exploration of underexplored regions in Western Australia and contribute to their economic development. The program funds high-quality, technically and economically sound projects that promote new exploration concepts and new exploration technologies (Fig. 5).

The Co-funded Drilling Program only funds drilling designed to discover new minerals, or new petroleum or geothermal reservoirs, or for research purposes. Drilling to enlarge an existing mineral or petroleum resource, including for proving the economic viability of a resource, is excluded from the program.

The EIS also funds the acquisition by GSWA of pre-competitive geology, geophysics, and geochemical and isotopic data. The EIS geophysics acquisition program completed coverage of the State by airborne magnetic surveys at a line-spacing of 400 m or less in 2012. The program is now extending the coverage by gravity surveys with stations, or flight lines spaced at 2.5 km. A program of airborne electromagnetic surveys (AEM) is also underway. Availability of medium-spaced, good-quality geophysical data greatly reduces risk and aids exploration targeting in underexplored areas of the State.

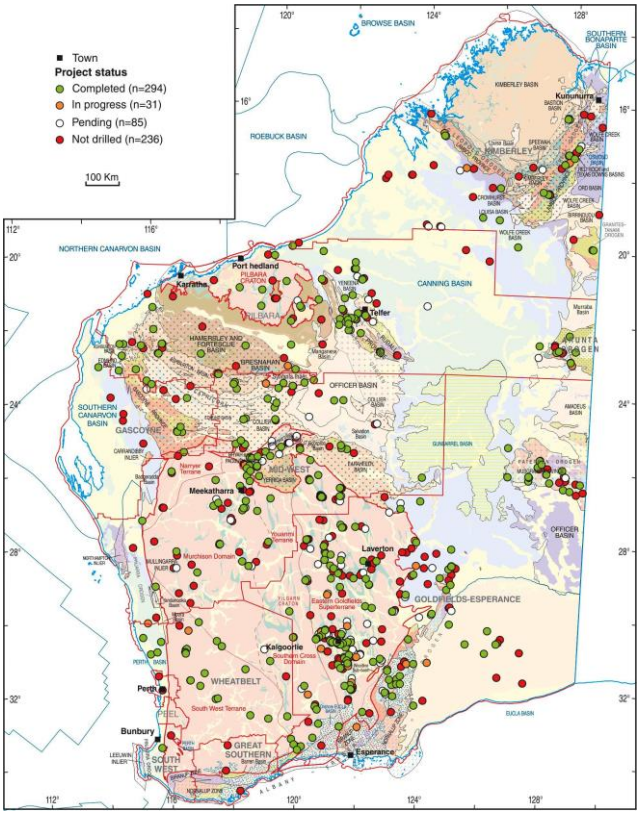


Figure 5. Co-funded Government–Industry Drilling Program projects; all rounds.

GSWA has developed a partnership with the Centre for Exploration Targeting (CET), a joint venture between UWA and Curtin University, and a world leader in mineral system studies, to undertake innovative prospectivity studies, which have been published as a series of GSWA reports (e.g. Occhipinti et al., 2016)

The Capricorn Orogen Distal Footprints of Giant Ore Systems Project is an example of the 'Team WA' approach to collaborative geoscience research in Western Australia involving GSWA, CSIRO, Curtin University and UWA. This project has attracted $16 million of funding from industry, SIEF (the Science and Industry Endowment Fund), the Minerals Research Institute of Western Australia (MRIWA), EIS and the universities, and involves developing innovative exploration targeting techniques.

4 The future

Although the EIS has delivered much in the first two phases of the program from 2008 to 2017, there is a continuing need to maintain Western Australia's ranking as the most attractive minerals investment destination.

The continuation of EIS-3 funding will allow GSWA to implement programs that will deliver integrated pre-competitive geoscience data:

- Innovative Drilling Promotion
  - Government–Industry co-funded exploration drilling

    - Targeted international exploration promotion
- Encouraging exploration through cover
    - Regolith geochemical and resistate mineral surveys
    - Regolith and 3D paleosurface mapping
    - Big data: Exploration data analysis
- Geophysical surveys
    - Airborne and ground geophysical surveys
    - Deep crustal seismic and magnetotelluric surveys
- 3D Prospectivity Mapping
    - WA geology online
    - 3D lithosphere visualization
    - Mineral systems
    - Mapping geodynamic setting
    - Enhanced geochronology and isotopic fingerprinting
    - Petroleum systems
- Promoting strategic research with industry
    - MRIWA support

EIS-3 will also implement a National Drilling Initiative (NDI) in Western Australia.

5 Industry intelligence feedback or input

The design of EIS-3, and ongoing GSWA programs for the next decade, is aligned with the UNCOVER AMIRA Roadmap for exploration under cover.

There is a recognition that near- or at-surface mineral deposits are becoming increasingly more difficult to find in Australia with exploration success declining relative to effort and expenditure. In order to counter the perception among international investors that Western Australia might represent a mature exploration search space, GSWA has been involved with industry, Geoscience Australia and the other State and Territory geological surveys, CSIRO and Australian university research leaders in the UNCOVER roadmap process, facilitated by AMIRA International. The Stage 1 Industry Roadmap identified six themes and 45 focus areas, with 16 focus areas having highest and high priority (AMIRA International, 2015).

The Stage 2 Roadmap is due for release in May 2017 and will deliver detailed, costed programs for the priority activities identified in the Stage 1 Roadmap.

The emphasis will be on innovative pre-competitive geoscience programs characterising and seeing through the cover of soil, sand and sedimentary basins that obscures 80% of Western Australia's economic bedrock.

EIS funding has meant that Western Australia effectively began UNCOVER in 2009.

References

ACIL Allen Consulting (2015) Exploration Incentive Scheme Economic Impact Study. Geological Survey of Western Australia, 78 p.

AMIRA International (2015) P1162. Unlocking Australia's hidden potential. An Industry Roadmap – Stage 1 Final Report. AMIRA International, Melbourne, 97 p.

Dutch RA, Spaggiari CV, Doublier MP, Pawley MJ, Wise T, Kennett BLN, Gessner K, Thiel S, Clark DJ, Holzschuh J (2016) What lies beneath the Nullarbor Plain? Insights into the geology of the Coompana Province from deep crustal seismic reflection profile 13GA-EG1. Geological Society of Australia, Abstracts 118:121.

Occhipinti SA, Metelka V, Lindsay MD, Hollis JA, Aitken AR, Sheppard S, Orth K, Tyler IM, Beardsmore T, Hutchinson M, Miller JM (2016) Prospectivity analysis of the Halls Creek Orogen, northern Western Australia — using a Mineral Systems Approach. Geological Survey of Western Australia, Report 159, 51 p.

Spaggiari CV, Tyler, IM (2014) Albany–Fraser Orogen seismic and magnetotelluric (MT) workshop 2014: extended abstracts. Geological Survey of Western Australia, Rec 2014/6, 182 p.

Spaggiari CV, Smithies RH (2015) Eucla basement stratigraphic drilling results release workshop: extended abstracts. Geological Survey of Western Australia, Record 2015/10, 70 p.

Spaggiari CV, Dutch RA, Doublier MP, Gessner K, Thiel S, Pawley MJ, Kennett BLN, Smithies RH, Wise T, Clark DJ, Holzschuh J (2016) Insights on crustal architecture and evolution of the Madura Province, Western Australia, from deep crustal seismic reflection data. Geological Society of Australia, Abstracts 118:419.

Spaggiari CV, Dutch RA, Doublier MP, Pawley MJ, Thiel S, Wise TW, Kennett BLN, Gessner K, Smithies RH, Holzschuh J, Clark DJ (2017) Geological interpretation of the Madura and Coompana Provinces along the Eucla–Gawler seismic and magnetotelluric line 13GA-EG1. Geological Survey of Western Australia, non-series map.

Living on the edge of the Cambrian Australian proto-continent: potential for subduction-related mineral systems in the Stavely Arc, western Victoria, Australia

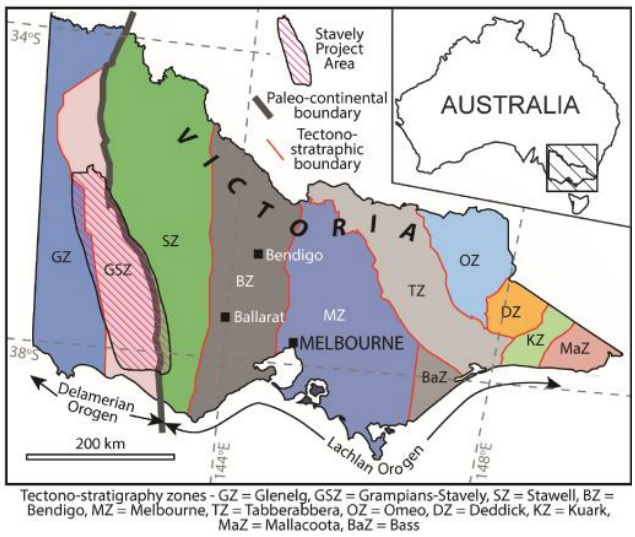
Rob Duncan, Ross Cayley, David Taylor, Phil Skladzien, Cameron Cairns, Mark McLean, Suzanne Haydon, Melanie Middleton, Megan Weatherman
The Geological Survey of Victoria

Anthony Schofield, Chris Lewis, Sarlae McAlpine, David Huston, Evgeniy Bastrakov, James Goodwin, Matilda Thomas, Narelle Neumann, Tim Barton
Geoscience Australia

Abstract. The Stavely Project is a federal and state government collaboration that aims to increase greenfields mineral exploration in western Victoria across an area that preserves a number of structurally dismembered prospective Cambrian volcanic belts (collectively termed the Stavely Arc), the majority of which are under younger cover rocks. These belts developed along with eastern margin of the proto-Australian continent (Delamerian Craton) during west-directed subduction. The region contains numerous features in common with well-endowed volcanic arc terranes worldwide. The project aim was achieved by collecting new geoscientific datasets to better characterise the subsurface Cambrian geology in order to de-risk exploration efforts in the region. Restoration of the volcanic belts to Cambrian-time results in three strike-persistent (~1160 km composite length), sub-parallel belts that are prospective for a series of arc-related mineral systems (porphyry, epithermal and volcanic-hosted massive sulfide deposits). These systems may also occur outside the volcanic belts themselves – this greatly increases the exploration search space in Cambrian rocks. In addition, the region is a potential host of Ordovician- to Silurian-aged orogenic gold systems and Devonian intrusion-related gold and base metal systems. The younger cover rocks host world-class heavy mineral sand resources.

1 Introduction

The Stavely Project (SP) is collaborative project between the Geological Survey of Victoria (GSV) and Geoscience Australia to better understand the geology of western Victoria and to assess mineral systems potential across a ~20,000 km^2 area (Fig. 1). The SP is aligned with the Australian National Mineral Exploration Strategy and the UNCOVER Initiative (led by the Australian Academy of Science) that were developed to address falling mineral deposit discovery rates. The goal is to develop innovative exploration strategies that would make exploration under cover rocks more efficient. Over 95% of the SP area is covered by younger rocks and is under explored (Fig. 2a). Since 2014, land that is available for exploration in the SP area has been progressively incorporated into a land package that is exempt from mineral exploration licences (under Section 7 of the Mineral Resource (Sustainable Development) Act 1990). This land will be made available for exploration in 2017. Currently >63% (~12,600 km^2) of the SP area is held under Section 7.



Tectono-stratigraphy zones - GZ = Glenelg, GSZ = Grampians-Stavely, SZ = Stawell, BZ = Bendigo, MZ = Melbourne, TZ = Tabberabbera, OZ = Omeo, DZ = Deddick, KZ = Kuark, MaZ = Mallacoota, BaZ = Bass

Figure 1. Location of Stavely Project Area in the Grampians-Stavely Zone of Western Victoria – along with the Glenelg Zone it forms the Delamerian Orogen in Victoria and is distinct from the Lachlan Orogen to the east.

The aim of the SP is to improve exploration targeting in the Stavely Arc by better constraining its distribution, internal geological variability and providing an improved geological context for known styles of mineralization. In turn, this would (partially) de-risk future exploration efforts in the region by making it more time and cost efficient.

The outcomes of the SP have been achieved primarily through the acquisition, interpretation, and delivery of >AUD$3.8 million of pre-competitive geoscientific data. The results have been issued as a series of data releases (available from http://www.ga.gov.au/scientific-topics/minerals/unlocking-resource-potential/stavely-project). The detailed project findings are described in a *Regional Geology and Mineral Systems Synthesis* (Schofield et al. 2017). Here we provide an overview of the work completed and its major outcomes that have implications for future exploration in the Cambrian rocks.

The calc-alkaline affinity and arc-related tectonic setting has long been recognised (e.g., Crawford and Keays 1978). However, later interpretations vary widely in terms of the timing of magmatism with relation to subduction,

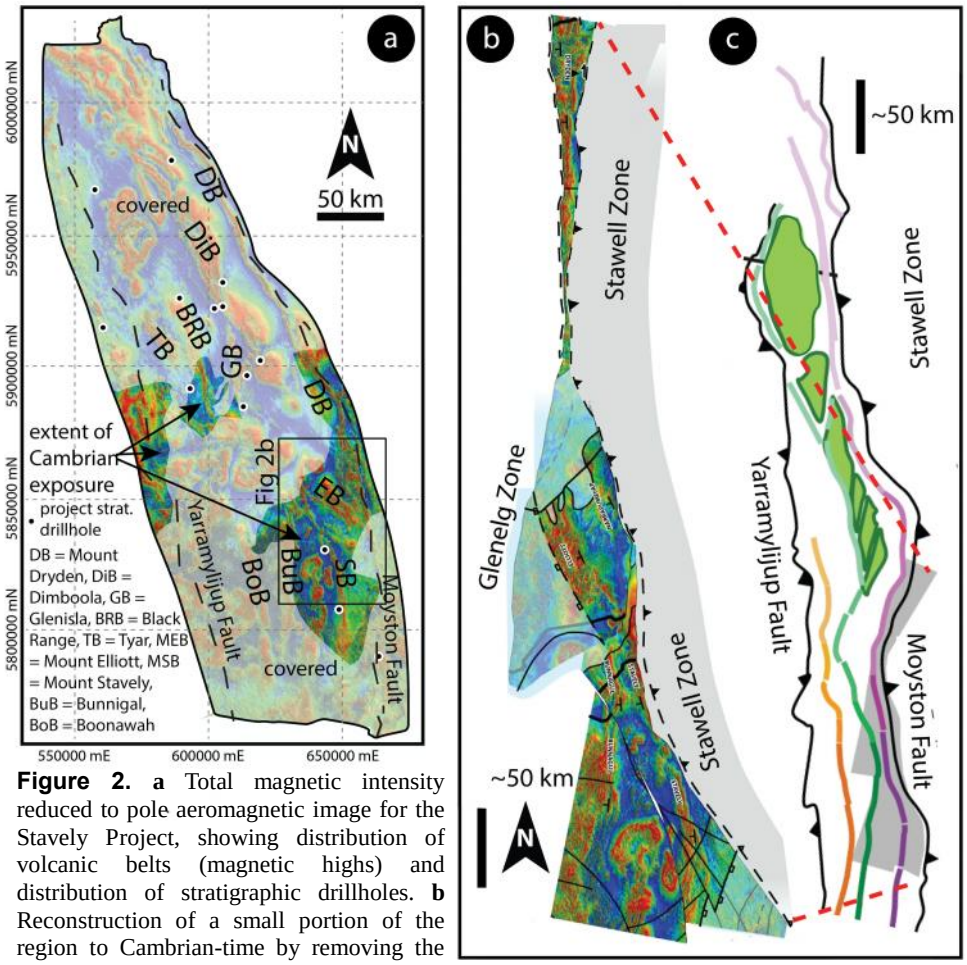


Figure 2. **a** Total magnetic intensity reduced to pole aeromagnetic image for the Stavely Project, showing distribution of volcanic belts (magnetic highs) and distribution of stratigraphic drillholes. **b** Reconstruction of a small portion of the region to Cambrian-time by removing the effect (rotation and translation) of Devonian structures. **c** Reconstruction of entire Stavely Arc to Cambrian-time.

subduction polarity, the involvement of continental crust, and correlation with other volcanic rocks of similar ages (most notably the Mount Read Volcanics that host world-class volcanogenic-massive sulfide deposits in western Tasmania). Uncertainty regarding the geodynamic framework for the Stavely Arc has restricted our understanding of regional metallogenic potential.

2 Geological framework

The SP is located in the Grampians-Stavely Zone that marks the Delamerian Orogen's eastern margin in Western Victoria (Fig. 1). The Cambrian tholeiitic and calc-alkaline volcanic rocks form a series of 3 to 8 km wide north-northwest-trending, fault-bound volcanic belts, collectively termed the Stavely Arc, located between the crustal-scale Moyston and Yarramyljup faults (Fig. 2 and 3). Regional-scale seismic reflection data demonstrate that the faulted belts remain largely intact at depth as an interpreted triangular-shaped volcanic edifice (Cayley et al. 2011). The belts are separated by Cambrian deep marine rocks of the Kanmantoo and Nargoon groups. Rocks have been metamorphosed to prehnite-pumpellyite grade, and this contrasts with amphibolite grade rocks in the adjacent Glenelg and Stawell zones.

The Stavely Arc was folded, faulted, and (locally) tilted at ~500 Ma during the (D1) Delamerian Orogeny (Crawford et al. 2003). A series of large, post-tectonic intrusions of the Bushy Creek Igneous Complex mark the end of the DO. By this time the collision of a micro-continental fragment (Vandieland) had caused the subduction zone to 'jump' eastwards (Cayley 2011).

The Cambrian rocks are overlain in central portions of the SP area by Late Ordovician- to Silurian-aged, fluvial, deltaic, and shallow marine siliciclastic rocks of the Grampians Group. Deformation during the Siluro-Devonian Bindian Orogeny (D2 to D4) generated complex thrust, fold, extensional and strike-slip structures in the Grampians Group and reactivated and reoriented structures in the underlying Cambrian basement. The D4 transtentional deformation is marked by intrusion of a series of syn- to post-tectonic intrusions (and eruption of volcanics) at ~400 Ma. These intrusions were generated by partial remelting of the same sources involved in magmatic activity in the Cambrian intrusions (Hergt et al. 2007). Preservation of D4 structures in the Grampians Group are crucial to unravelling the tectonic evolution that ultimately dismembered the Cambrian volcanics belts and mineral systems that they may host. Since the Devonian the region has been tectonically stable, with Devonian intrusions remaining near-surface since emplacement (Foster and Gleadow 1992), meaning that arc-related mineral system preservation potential is high.

Paleocene to Recent fluvial to shallow marine sediments were been deposited in the intracratonic Murray Basin across the northern section of the project. These sediments thicken northwards and host the world-class heavy mineral sands deposits. Time-equivalent deeper marine sediments accumulated in the Otway Basin in the very southern portion of the region. Miocene to Recent intraplate basaltic flows, typically tens of metres thick erupted in the southern portion of the project area.

3 Historical mineral exploration and known mineralization styles

Mineral exploration in Cambrian rocks in the Stavely Region began in 1969 and continued, albeit sporadically,

Table 1. Summary of major known Cambrian mineral prospects in the Stavely Project Area (Summarized from GSV and Geoscience Australia (2017) and references therein).

Prospect (Belt)	Host rocks	Hydrothermal alteration	Mineralization	Significant intersections
PORPHYRY-STYLE Cu(-Mo-Au)				
Thursday's Gossan[1] (Stavely)	andesitic to rhyolitic volcanics, volcaniclastics, porphyry dykes, sandstone, dacitic to tonalitic, sub-volcanics I-type intrusions	propyllitic (chl-epi-cal), phyllic (qtz-ser-pyr), argillic (ser-ill), advanced argillic (dic-kao-qtz), potassic (bt-kfs-mag)[2]	supergene cc blanket (4 km long x 2 km wide x 20 m thick) best developed over argillic assemblage, hypogene mineralisation associated with qtz-pyr-ccp B vein stockworks (and D veins) associated with advanced argillic and potassic assemblages	supergene zone - 36 m at 1.08% Cu, 73 ppm Mo from 33 m at 0.4% COG[3], including 12 metres at 2.02% Cu, 80 ppm Mo at 1% COG[3] (drillhole STAVRA417), hypogene zone - 229 m at 0.22% Cu at 0.1% COG[3] (drillhole VICT1D4)
Lexington (inter-belt)	granodiorite (considered part of Bushy Creek)	phyllic (qtz-ser-pyr-chl)	supergene cc blanket, hypogene mineralisation qtz-ccp(-mol) and ccp-only stockworks	single diamond drillhole ends in 2 m at 0.4% Cu[4] (drillhole VICT3D1)
VOLCANIC-HOSTED MASSIVE SULFIDE-STYLE Zn-Cu(-Pb-Ag-Au)				
Wickcliffe (Stavely)	hyaloclastitic breccia	qtz-ser-chl(-dol)	massive pyr-ccp-sph-gal as stringers and matrix infill	3.15m at 2.3 g/t Au, 4.9% Zn, 0.2% Cu, 6.9 g/t Ag[4] from 73.4 m depth (drillhole Wickcliffe No1/Pend1W)
Eclipse (Black Range)	dacitic to rhyolitic volcanic and volcaniclastic rocks	qtz-ser-pyr that transitions laterally to chl-ser	supergene cc (plus Au) blanket (0.4 km long x 0.2 m wide), underlying massive sulfide laminated veins and later cal-sulfide veins	107 m at 0.2% Cu, 0.2 g/t Au from 31 m depth, including 37 m at 0.5% Zn from 77 m depth[4] (drillhole RCBR0012)
EPITHERMAL Au-Ag				
Fairview North and South (inter-belt)	sandstone, porphyry dikes	qtz-kao-pyr, qtz-ser-pyr, adu, ab	part of a 4.8 km long Au in soil anomaly, sph-gal-ccp-Au assemblage both as disseminations and veinlets	10 m at 4.2 g/t Au from 6 m depth[4] (drillhole FAC187), 30 m at 1.4 g/At Au from 28 m depth[4] (drillhole unknown)

for supergene chalcocite blanket only Stavely Minerals, 2014; [2]at Junction Prospect ~500 m southeast of Thursday's Gossan; [3]COG = cut off grade; [4]no cut-off grade

Mineral abbreviations: chl = chlorite, epi = epidote, cal = calcite, qtz = quartz, ser = sericite, pyr = pyrite, ill = illite, dic = dickite, kao = kaolinite, cc = chalcocite, ccp = chalcopyrite, sph = sphalerite, gal = galena, dol= dolomite, cal = calcite, ab = albite, adu = adularia

until the 1990s. This period of mineral exploration was restricted to of outcrop and involved stream sediment and soil sampling for a very limited analytical suite that was followed by shallow rotary air blast/air core drilling (average drill hole depth is ~30 m). This work was essentially undertaken blindly because state-wide aeromagnetic data that demonstrated the potential extent of the Cambrian volcanic belts, beyond the areas of exposure, was not collected by the GSV until the mid-1990s (Fig. 2a). Uncertainty over the geological setting, few indicators of historical mining, and the presence of cover rocks meant that there was there was little appetite to continue exploration. New mapping of the exposed Cambrian volcanic belts led to a reinterpretation of the geological setting of the rocks.

The majority of known Cambrian-aged mineral prospects are located in two exposed windows of Cambrian volcanic rocks (Fig. 2a). Table 1 summarises the most well studied Cambrian mineral prospects in the region. It should be noted that there is additional potential for Silurian-aged orogenic gold mineralisation and Devonian-aged intrusive gold and base metal mineralisation – although these are not covered here.

4 Work program

The SP was designed to address four key objectives;

- To characterise sub-surface geology,
- To identify favourable geological environments where mineral systems may have been active,
- To describe the nature of cover units and estimate its thickness across the project area,
- To deliver pre-competitive data to reduce exploration risk in the project area.

The work program focussed around a stratigraphic drilling campaign (14 drill holes, the majority were sonic in cover units (to preserve geological information) and diamond tailed for a total length of 2708.5 m) and was completed to test geological interpretations and to recover material for subsequent analysis. Specific work undertaken included;

- Collection of refraction, reflection and passive seismic geophysical data at drill sites to test the accuracy of these techniques in estimating depth to basement,
- Hyperspectral (HyLogger^{TM}) logging of drill core using the visible and near-infrared, shortwave infrared, thermal infrared wavelength data to understand downhole variations to mineralogy and distribution of hydrothermal alteration minerals,
- Downhole petrophysical properties (density, magnetic susceptibility, P-wave velocity, resistivity, natural gamma),
- 166 high quality whole rock X-Ray fluorescence and inductively-coupled mass spectrometry analyses for lithogeochemical characterization, plus Nd isotopic analyses to assess juvenile/evolved magmatic input,
- 25 sensitive high resolution ion microprobe (SHRIMP) ages for plutonic, (sub-)volcanic, and sedimentary rock units, along with Re-Os model ages on three molybdenite aliquots,
- Orientation surveys of surficial geochemical techniques to detect mineralization under cover (soil gas hydrocarbon, Mobile Metal Ion^{TM}, ionic leach^{TM}),
- Sulfur and lead isotope analyses in sulfides to fingerprint mineralising processes metal sources,
- Laser ablation trace element geochemistry of pyrite, epidote, and chlorite to help fingerprint the origin of mineralization and determine potential distance to mineralization proxies,
- Construction of a 3D geological model for the project area and a reconstruction of original volcanic belt configuration in the Cambrian,

- Compilation of historical exploration datasets for surface geochemistry (~5200 stream sediments, ~25,500 soil and ~2.150 rock chip samples) and drilling (~5,800 drill holes, mostly rotary air blast and air core, for 216,000 metres for metal exploration and ~9,540 drill holes for ~250,000 metres for heavy mineral sands),
- Synthesis of previous mineral occurrence data to help characterise known zones of mineralization.

5 Outcomes – implications for prospectivity

The new data collected during the project has revived support for a continental margin magmatic arc in western Victoria. This is consistent with large-scale seismic and magneto-telluric data that demonstrate the presence of thinned (Proterozoic?) continental crust on which the volcanic arc was built (Cayley et al. 2011; Robertson et al. 2015). Reconstruction of the Stavely Arc, largely based on D2 structures preserved in Silurian rocks, demonstrate that there is a total strike length of ~1160 km prospective volcanic belt stratigraphy (Fig. 2c). Although internally complex the northern portion of the Stavely Arc has undergone little structural re-arrangement and remains relatively intact. The most structurally complex zone occurs around the best exposed portion of the Stavely Arc (compared box on Fig. 2a and reconstruction in Fig. 2b). This highlights that the zone of exposed Cambrian bedrock is not necessarily the best place to elucidate structural controls on potential mineral systems.

It has been recognized that the mineralised porphyries are geochemically similar to post-D1 granites that intruded both the volcanic belts and intervening sedimentary sequences. This means that Cambrian arc-related mineral systems may both be found within and between the volcanic belts (e.g., Lexington and Fairview prospects are both located outside volcanic belts; Table 1) – this finding significantly expands the exploration search space in the region.

Direct evidence of magmatic activity in the Stavely Arc is constrained by U/Pb SHRIMP ~511 Ma age for an unnamed granodiorite in the Stavely Belt and a ~510 Ma age for a quartz dolerite in the Boonawah Belt. However, subduction (and associated igneous activity) may be as old as between ~521 and 524 Ma (the age of volcanics with MORB-like geochemical affinities in the Glenelg Zone that may either represent pre-Delamerian Orogeny passive margin rifting or proto back-arc basin rifting; e.g., VandenBerg et al., 2000 and references therein). There remains the possibility that Stavely Arc magmatism began ~540 Ma (the youngest maximum depositional detrital zircon ages for parts of the Glenthompson that were deposited under passive margin conditions; Fanning and Morand 2002). The majority of new U/Pb zircon ages for Cambrian magmatism are indistinguishable for Re/Os molybdenite model ages from quartz-chalcopyrite-pyrite B-veins at the Thursday's Gossan Prospect.

In simple terms, whole rock geochemistry demonstrates that calc-alkaline igneous rocks with subduction signatures (low LILE and LREE enrichment over HFSE, negative Ti and Nb anomalies) occur throughout the Cambrian volcanic belts in the Stavely Arc. Enrichment of Th, Zr, LREE, and P, and weakly primitive to evolved Nd isotopes in these rocks demonstrate that they were emplaced into or erupted onto an arc setting on thinned continental crust (e.g., Japan, Alaska and parts of the Andean Arc outside the Central Volcanic Zone). In the Boonawah Belt geochemical characteristics, along with weakly developed subduction signatures (relatively low Nb, Zr, TiO_2), suggest they developed in a back-arc basin during active subduction. Whilst the data are not exhaustive they do allow us to predict where porphyry/epithermal and VHMS mineral systems may be preserved.

Uplift and exposure of portions of the Stavely Arc likely occurred during the Siluro-Devonian. These events may have controlled the development of supergene copper mineralization (Table 1). Preservation potential for Cambrian mineral systems is high because the arc appears to have undergone rapid uplift and then was covered by Grampians Group sediments in the Silurian. Since the Devonian there has been little tectonic activity in the region allowing deep weathering zones to develop.

References

Cayley RA, Korsch RJ, Moore DH, Costelloe RD, Nakamura A, Willman CE, Rawling TJ, Morand VJ, Skladzien PB, O'Shea PJ. (2011) Crustal architecture of central Victoria: results from the 2006 deep crustal reflection seismic survey. Aust J Earth Sci 58: 113-156

Crawford AJ, Keays RR (1978) Cambrian greenstone belts in Victoria: marginal sea-crust slices in the Lachlan Fold Belt. Earth Planet Sci Lett 41:197-208

Crawford AJ, Cayley RA, Taylor DH, Morand V, Gray C, Kemp A, Wohlt K, VandenBerg A, Moore D, Maher S, Direen NS, Donaghy A, Anderson J, Black L (2003) Neoproterozoic and Cambrian: continental rifting, continental-arc collision and post-collisional magmatism. Geol Soc Aust Spec Pub 23: 73-93

Fanning CM, Morand VJ (2002) Results of some SHRIMP U-Pb zircon dating of rocks in Victoria. Geological Survey of Victoria Technical Record 2002/1

Foster DA, Gleadow AJW (1992) Reactivated tectonic boundaries and implications for the reconstruction of southeastern Australia and northern Victoria Land, Antartica. Geology 20: 267-270

GSV and Geoscience Australia (2017) An Explorer's Guide for Stavely. Geological Survey of Victoria Technical Record

Hergt JM, Woodhead JD, Schofield A (2007) A-type magmatism in the Western Lachlan Fold Belt? A study of granites and rhyolites from the Grampians region, Western Victoria. Lithos 97:122-139

Robertson K, Taylor D, Thiel S, Heinson G (2015) Magnetotelluric evidence for serpentinization in a Cambrian subduction zone beneath the Delamerian Orogen, southeast Australia. Gond Res

Schofield A, Cayley R, Taylor D, Lewis C, Cairns C, Huston D, Duncan R, Bastrakov E, McAlpine S, Bailey A (2017) Regional geology and mineral systems of the Stavely Arc. Geoscience Australia Record

VandenBerg AHM, Willman CE, Maher S, Simons BA, Cayley RA, Taylor DH, Morand VJ, Moore DH, Radojkovic (2000) The Tasman Fold Belt System in Victoria: geologcy and mineralisation of Proterozoic to Carboniferous rocks. Geological Survey of Victoria Special Publication

Finnish historical and current Ni-Cu-PGE deposits highlight country-wide exploration potential

Jukka Konnunaho
Geological Survey of Finland

Hannu V. Makkonen,
Geological Survey of Finland

Tapio Halkoaho
Geological Survey of Finland

Kalevi Rasilainen
Geological Survey of Finland

Pasi Eilu
Geological Survey of Finland

Abstract. For around one hundred years, Ni-Cu-PGE and Cr-V-Ti-Fe deposits have been economically viable in Finland. Several deposit types, including 1.88 Ga Svecofennian Ni-(Cu), 2.45 Ga layered intrusion related Ni-Cu-PGE and Cr-V-Ti-Fe, and komatiite-hosted Ni-Cu-PGE, highlight the country-wide exploration potential. In addition, active Ni-Cu-PGE exploration, research and mining, as well as Ni-Cu production and stainless steel industry, form a comprehensive value chain in Finland. The Fennoscandian Shield offers similar geology and metallogeny with the Precambrian shields in Canada and Australia. From the exploration point of view, many nickel-potential formations are still poorly understood, as the exploration focus has historically been on the outcropping part of the bedrock. Only a limited amount of modern exploration techniques has been used compared to the famous mining camps in Canada and Australia. The recently discovered Sakatti Cu-Ni-PGE deposit has also highlighted the good exploration potential of Finland. All along its history, the GTK (Geological Survey of Finland) has actively evaluated Ni-Cu-PGE potential related to magmatic deposits across the country. At the moment, the main focus of the Geological Survey of Finland (GTK) is to support the exploration and mining sector in Finland by offering variable services and country wide modern geodata to exploration industry.

1 Introduction

In 2017, Finland celebrates its 100 years of independence, but the mining industry has played an even longer important role in its history even longer. Presently, the most significant magmatic Ni-Cu-Co-PGE (Fig. 1) and Cr-Ti-Fe-V resources of the European Union are located in Finland, within the Fennoscandian shield.

Historical deposits like the Pechenga Ni-Cu and Outokumpu Cu deposits were previously the most important sources of nickel, copper and cobalt in Finland. Several Paleoproterozoic orogenic intrusion-hosted Ni-(Cu) deposits, such as Makola, Hitura, Kotalahti and Vammala, in the central and southern parts of Finland, were important metal sources for the Finnish smelters. The intrusion-related Kevitsa Ni-Cu-PGE, black shale-hosted Talvivaara Ni-Zn-Cu-Co, and layered intrusion-related Kemi Cr deposits include significant metal resources.

Finland's EEA (European Economic Area) agreement in 1994 and entry into the European Union in 1995 opened exploration and mining opportunities for international companies. They have launched several exploration and mining projects in Finland, such as the Kevitsa mine and the Suhanko Ni-Cu-PGE project. However, only a limited amount of exploration has been carried out in Finland compared to Canada and Australia. The recently discovered Sakatti Cu-Ni-PGE deposit has highlighted the good exploration potential of Finland. In addition, the geodata of good quality, available at Geological Survey of Finland, plays important role in exploration success. Active Ni-Cu-PGE exploration, research and mining, as well as Ni-Cu production and the stainless steel industry, form a comprehensive value chain in Finland.

2 Finnish Ni-Cu-PGE deposit types

The main Ni-Cu-PGE deposit types in Finland are related to Archean and Paleoproterozoic mafic-ultramafic rocks, Paleoproterozoic metamorphosed black shales of the Talvivaara type, and the ultramafic and metasomatic calc-silicate rocks of the ophiolitic Outokumpu association. Several komatiite-hosted Ni-Cu-PGE deposits have been discovered in the Archean and Paleoproterozoic greenstone belts in northern and eastern Finland, but only one has been mined, in the 1980s. Many 2.45 Ga mafic-ultramafic layered intrusions in Finland host contact-type PGE-Ni-Cu deposits and significant reef-type PGE deposits; their Ni resources typically are of low grade but large tonnage. Mafic-ultramafic magmatism at ca. 2.06 Ga produced significant Ni-Cu-PGE resources in the Central Lapland greenstone belt, including the Kevitsa and Sakatti deposits. The Svecofennian domain in central and southern Finland contains hundreds of small, ca. 1.88 Ga, mafic-ultramafic orogenic intrusions; many of these host nickel mineralisation (Fig. 1).

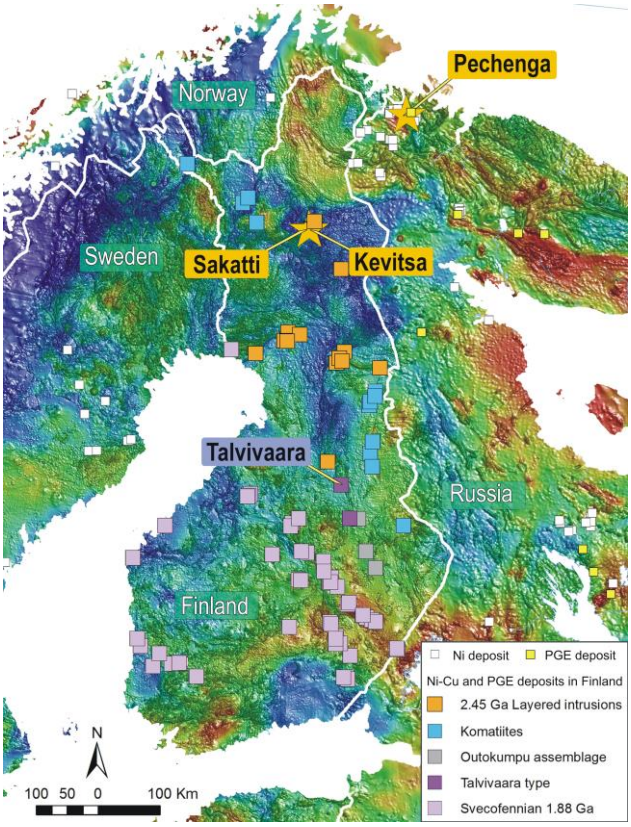


Figure 1. Distribution of Ni-Cu-PGE deposits in Finland, and Ni and PGE deposits in other parts of the Fennoscandian Shield. Yellow stars show location of the Sakatti, Kevitsa and Pechenga deposits. Base map: combined gravimetric + magnetic (red = high gravity, blue = low gravity). Source: Fennoscandian Ore Deposit Database (FODD 2016).

3 Ni-Cu-PGE exploration potential

Significant exploration potential exists in the Fennoscandian Shield, which shares a similar geology and metallogeny with the ancient shields in Canada, Australia, Brazil and South Africa.

The Archean provinces in eastern and northern Finland include komatiites (ca. 2.8–2.9 Ga) and other types of mafic-ultramafic rocks potential for nickel deposits. In the northern Fennoscandian Shield, rifting with mafic-ultramafic magmatism took place in multiple stages during 2.45–2.0 Ga (e.g., Lahtinen et al. 2008). The rifted Archean–Proterozoic boundary is extensively present in the eastern and northern parts of Finland, with the voluminous 2.44 Ga layered intrusions hosting mainly PGE-dominant sulphide deposits. Rift-related greenstone belts of central Lapland host extensive mafic-ultramafic formations with potential for nickel. In particular, the ca. 2.06 Ga rocks (includes the Kevitsa intrusion) have high ore potential.

From the exploration point of view, formations with potential for nickel deposits are still poorly understood, as the exploration focus has historically been on the outcropping part of the bedrock. Exploration potential has also been highlighted by the GTK in permissive tracts (*i.e.*, Ni-Cu-PGE potential areas and belts) and in the assessments of undiscovered Ni-(Cu-PGE) resources in Finland (Fig. 2; Rasilainen et al. 2010a, 2010b, 2012).

4 Ni-Cu-PGE research

Magmatic sulphide ore research in Finland has developed along with the exploration and mining industry. Exploration and research for the Svecofennian (1.88 Ga) nickel deposits began during the 1930s. These deposits were the main focus of nickel deposit research, exploration and mining for several decades (Papunen and Vorma 1985; Makkonen 2015).

In 1960, the Outokumpu Company commenced the Nickel Programme in order to collect a database on Finnish mafic-ultramafic rocks, to be used to enhance nickel exploration. The resulting database includes petrological, mineralogical and geochemical data of more than 50,000 hard rock samples. One of the most important tools developed within the programme was the use of nickel content in mafic silicates to discriminate between barren and nickel-potential formations (Häkli 1971). A follow-up project produced lithogeochemical tools for nickel exploration (Lamberg 2005).

Extensive magmatic sulphide ore research has also been carried out in numerous projects by the Turku and Oulu universities since the late 1960s and by the GTK (Makkonen 2015 and references therein).

Comprehensive compilations of Finnish nickel deposits include the work by Papunen and Gorbunov (1985), where the nickel-copper deposits of the Fennoscandian Shield and Scandinavian Caledonides were described, the work by Puustinen et al. (1995), the public FINNICKEL data base (Makkonen et al. 2009), the nickel chapters in Eilu et al. (2012), the assessment of undiscovered Ni-Cu-PGE resources in Finland (Rasilainen et al. 2010a, 2010b, 2012, 2014) and chapters in Mineral deposits of Finland (Maier et al. 2015).

5 GTK's role in Ni-Cu-PGE exploration

Throughout its history, the GTK has evaluated ore potential related to magmatic deposits across the country. GTK's digital databases are well organized, and regarded the best in the World (e.g., Jackson and Green 2016). Country-wide airborne low-altitude geophysical data, till-geochemical data, and the extensive datasets from mafic and ultramafic rocks and related deposits are available online (Mineral Deposits and Exploration, 2017). Exploration reports of GTK and Finnish exploration companies such as Outokumpu Oy are also available through the GTK online services (online spatial data product database - HAKKU). Also available for the private sector

are the National Drill Core Archive, GTK's Mineral Processing Laboratory with the pilot plant (i.e., MINTEC), research facilities, and the services by several experts specialised in Ni-Cu-PGE deposits.

GTK's main focus is to support the exploration and mining sector in Finland. As a part of this activity, GTK's current nationwide Ni-Cu evaluation project is focused on poorly explored areas and produces new geodata from prospective areas.

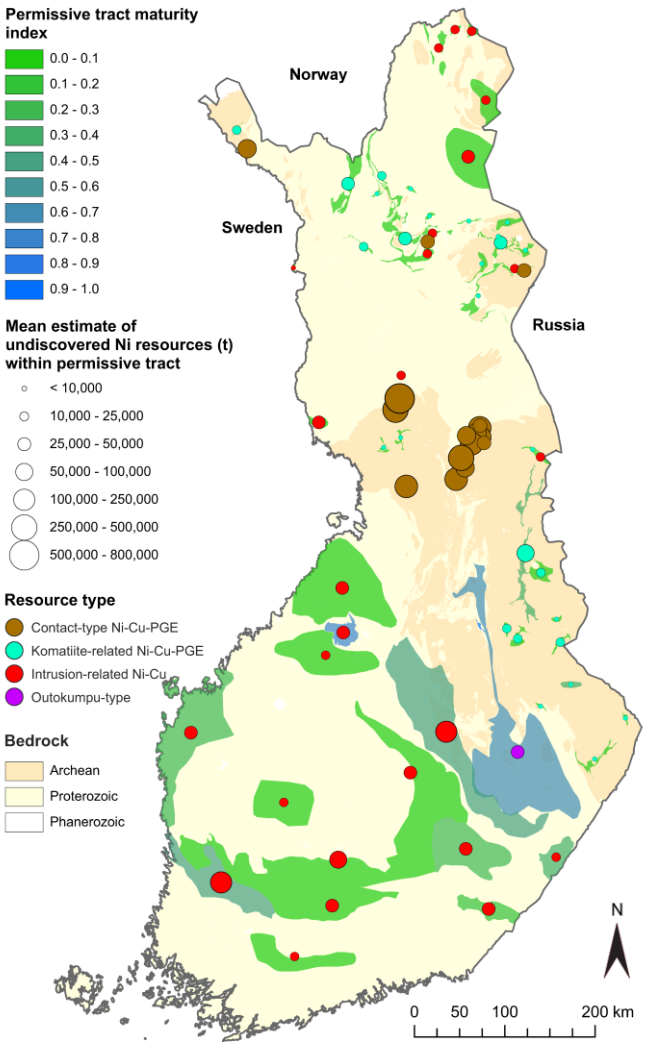


Figure 2. The mean estimate of undiscovered Ni-(Cu-PGE) resources plotted on each permissive tract. The permissive tracts and estimated resources are based on Rasilainen et al. (2010a, 2010b, 2012, 2014). The bedrock map is based on GTK geological map database (Bedrock of Finland – DigiKP).

6 Summary

The following points highlight the good exploration and mining potential of orthomagmatic sulfide and/or oxide deposits in Finland, and these also create favorable ground on exploration industry:

- Favorable Archean and Paleoproterozoic geology similar to famous mining camps in Canada and Australia.
- Several known Ni-Cu-PGE and Cr-V-Ti-Fe deposits and occurrences: 1) Archean and Paleoproterozoic komatiite-hosted Ni-Cu-PGE, 2) 2.45 Ga layered intrusion-hosted Ni-Cu-PGE and V-Ti-Cr-Fe, 3) Paleoroterozoic mafic-ultramafic intrusion-related Ni-Cu-PGE, 4) Talvivaara-type (black shale-hosted) Ni-Zn-Cu-Co, and 5) Outokumpu-type (post-magmatically modified ophiolite) Cu-enriched polymetallic deposits.
- An entire value chain from research to exploration via mining to refinery.
- GTK's services, geological databases and expertise on Ni-Cu-Co-PGE and Cr-V-Ti-Fe deposits.
- Favorable mining law and infrastructure.

References

Bedrock of Finland – DigiKP. Digital map database [Electronic resource]. Espoo. Geological Survey of Finland. Ver 1.0.http://www.geo.fi//en/bedrock.html. Accessed 31 Jan 2017

FODD (2016) Fennoscandian Ore Deposit Database. Annual update. Available at: http://en.gtk.fi/informationservices/databases/fodd/index.html. Last accessed 18 August 2016.

Eilu P, Ahtola T, Äikäs O, Halkoaho T, Heikura P, Hulkki H, Iljina M, Juopperi H, Karinen T, Kärkkäinen N, Konnunaho J, Kontinen A, Kontoniemi O, Korkiakoski E, Korsakova M, Kuivasaari T, Kyläkoski M, Makkonen H, Niiranen T, Nikander J, Nykänen V, Perdahl JA, Pohjolainen E, Räsänen J, Sorjonen-Ward P, Tiainen M, Tontti M, Torppa A, Västi K (2012) Metallogenic areas in Finland, in: Eilu P. (Ed.) Mineral deposits and metallogeny of Fennoscandia. Geol Surv Finland, Spec Paper 53:207-342

Hakku. Online spatial data product database. Available at: http://hakku.gtk.fi/en/reports.

Häkli TA (1971) Silicate nickel and its application to the exploration of nickel ores. Bull Geol Soc Finland 43:247–263

Jackson T, Green KP (2016) Fraser Institute Annual Survey of Mining Companies 2015. Fraser Institute, Vancouver. https://www.fraserinstitute.org/sites/default/files/survey-of-mining-companies-2015.pdf. Accessed 20 January 2017

Lahtinen R, Garde AA, Melezhik VA (2008) Paleoproterozoic evolution of Fennoscandia and Greenland. Episodes 31:20–28

Lamberg P (2005) From genetic concepts to practice – lithogeochemical identification of Ni-Cu mineralised intrusions and localisation of the ore. Geol Surv Finland Bull 402

Maier WD, Lahtinen R, O'Brien H, eds. (2015) Mineral Deposits of Finland. Elsevier, Oxford

Makkonen HV (2015) Nickel deposits of the 1.88 Ga Kotalahti and Vammala belt. In: Maier WR, O'Brien H, Lahtinen R (Eds.) Mineral Deposits of Finland. Elsevier, pp 253-290

Makkonen H, Halkoaho T, Tiainen M, Iljina M, Ahtonen N (2009) FINNICKEL – a public database on nickel deposits in Finland. Version 1. 1, Revised 17.02.2010. Geol Surv Finland. CD-ROM

Mineral Deposits and Exploration (2017) Online Mapservice. http://gtkdata.gtk.fi/mdae/index.html. Accessed 20 January 2017

Papunen H, Gorbunov GI (1985) Nickel-copper deposits of the Baltic Shield and Scandinavian Caledonides. Geol Surv Finland Bull 333

Papunen H, Vorma A (1985) Nickel deposits in Finland, a review, in: H. Papunen and G.I. Gorbunov, eds., Nickel-copper deposits of the Baltic Shield and Scandinavian Caledonides. Geol Surv Finland Bull 333:123–143

Puustinen K, Saltikoff B, Tontti M (1995) Distribution and metallogenic types of nickel deposits in Finland. Geol Surv Finland Rep Invest 132

Rasilainen K, Eilu P, Halkoaho T, Iljina M, Karinen T (2010a) Quantitative mineral resource assessment of undiscovered PGE resources in Finland. Ore Geol Rev 38:270–287

Rasilainen K, Eilu P, Halkoaho T, Iljina M, Karinen T (2010b) Quantitative mineral resource assessment of nickel, copper, platinum, palladium and gold in undiscovered PGE deposits in mafic-ultramafic layered intrusions in Finland. Geol Surv Finland Rep Invest 180

Rasilainen K, Eilu P, Äikäs O, Halkoaho T, Heino T, Iljina M, Juopperi H, Kontinen A, Kärkkäinen N, Makkonen H, Manninen T, Pietikäinen K, Räsänen J, Tiainen M, Tontti M, Törmänen T (2012) Quantitative mineral resource assessment of nickel, copper and cobalt in undiscovered Ni-Cu deposits in Finland. Geol Surv Finland Rep Invest 194

Rasilainen K, Eilu P, Halkoaho T, Karvinen A, Kontinen A, Kousa J, Lauri L, Luukas J, Niiranen T, Nikander J, Sipilä P, Sorjonen-Ward P, Tiainen M, Törmänen T, Västi K (2014) Quantitative assessment of undiscovered resources in volcanogenic massive sulphide deposits, porphyry copper deposits and Outokumpu-type deposits in Finland. Geol Surv Finland Rep Invest 208

S11 – Resources development and perception/acceptability: The role of geosciences

Convenors:
Michel Malo
Michel Jébrak
Yann Gunzburger

Sponsored by:

ios services GÉOSCIENTIFIQUES inc.

Keynote presentation

Social geology applied to mineral deposits

Michel Jébrak
Université du Québec à Montréal, Québec, Canada

Abstract. An ore deposit is a mineral concentration, economically mineable and socially acceptable. Social geology is a needed new discipline that studies the influence of geologic objects on communities and society. Applied to mineral deposits, it should enhance the role of geological features to the analysis and prevision of social change, at a local and global scale.

1 Context

Recent developments in mining exploration and production have shown that the social acceptability of mining activities is a difficult task. During early exploration, the costs of an interrupted project (Davis and Franks 2014) can reach $10,000 per day. For advanced exploration, it can be up to $50,000 per day. And during production, world-class mining project may suffer costs of US$3 million per day of delayed production (Davis and Franks 2014). Social licence to operate has appeared as one of the five major mining business risks (EY 2016).

The salience of this issue could receive many explanations, including the increasing demand for mineral resources, the scaling change in the mineral production, and increasing disjunction between production and consumption. Demand for mineral products (including metal, coal, and cement) has doubled in weight in 20 years, implying the mining of larger low grade deposits that present higher environmental impacts. The development of an ecological consciousness has progressively infused the industry, the governments and the civil society.

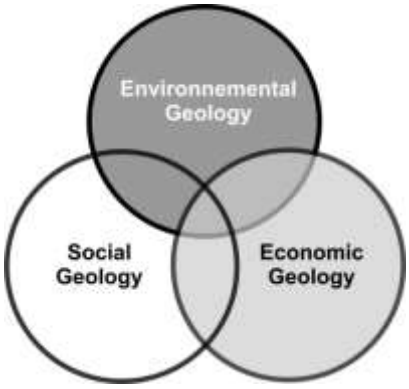


Figure 1. The triple bottom line of sustainable development as reflected by geological sciences

Following the Brundtland report, the triple bottom line has been widely used has an accounting framework that considers social, environmental and financial performance and reporting (Elkington 2004). While this approach may be considered a reductive method, the mining industry has supported the Global Reporting Initiative that follows this triple bottom line concept.

Applied geology was mostly developed to answer key questions of urban and industrial developments. Economic geology was developed in the US at the beginning of the 20th century whereas environmental geology rose in the 1970s. In spite of the existence of numerous activities that are at the boundary between Earth science and social sciences, the concept of social geology has been overlooked and this field of applied geology was never considered with any intensity and depth (Unesco 1998).

The consequences were that the many studies that approach the relationships between society and geology-connected human activities have neglected the very geological object. For instance, numerous studies have approached the social licence to operate or the implication of state governance in the mining industry (Campbell 2009; Prno and Slocombe 2014; Moffat and Zhang 2014). Almost none of them consider the difference between a diamond mine or an iron exploitation. Few of them recognize that each geological object carry its own specificities in term of grade, size, minerals, geometry. Each of these geological parameters has major incidences on the social development of a mining project.

Social geology appears therefore as the missing link between Earth sciences and society.

2 Social geology

The history of social geology is rather short. In 1998, the concept of sociogeoscience was developed in an urban geology report of the UNESCO. The birth of sociogeoscience, a hybrid between sociology and geoscience, is considered as inevitable in the process of the development of human society. It should provide a solid scientific basis in order to realize sustainable development. Sociogeoscience would pay close attention to resources, population and environment.

Mata-Perello et al. (2012) use the term of social geology also in an urban geology context. They focus to the access to drinkable water, human and economic losses related to geological risks, and conflicts related to the control of geological resources. They define social geology as *the discipline of geology that studies the interaction among the geological environment and the social development*, Social geology should provide tools and methodology for a better management of the territory using geological and social criteria.

These early works both emphasize the need for a new discipline constituting a bridge between geology and sociology, between physical sciences and human and social sciences, both rooted in an historical context. Social geology would appear as a cross-disciplinary activity that

could either simply place the two disciplines side-by-side or could be more integrative if we consider it as a new domain (Hansen 2007).

A scientific field should be defined on several dimensions (Kuhn 1962; Krishnan 2009): epistemological (object of research, methods, principles, theories), professional and institutional (community of practice), and didactic and pedagogical (identity, terminologies, discourse).

Focussing on mineral deposits, I would like to demonstrate hereafter that social geology already presents some of these dimensions. The remaining ones may be considered as major questions to be discussed in the future.

3 Social geology applied to mineral deposits

Mineral deposits have multiple incidences on society. As a pioneering industry, mining is often responsible for the establishment of new towns and communities. Mining affects the people and the environment, creates a common culture and fires the imaginations that may become myths.

The geological features of mineral deposits do have a strong impact on society. For instance, the type of mineral deposit defines the size, the grade, and the mineralogy of the mine. The size impacts the environment and the duration of exploitation; the grade controls processing methods and a large part of the potential financial benefit of a mining exploitation; and the mineralogy strongly influences the environmental impact of the exploitation, the processing and even the choice of remediation methods.

Epistemological dimensions: objects and concepts

The rationale for new disciplines is that they deal exclusively with a particular object or topic that is not covered by any other disciplines (Krishnan 2009). The object of social geology is a specific geological feature that presents specific social characters. Such an object could be characterized by its size, its nature, its value and its questions.

Table 1: Scales of social geological objects

Geo / Socio	Local	Global
Small to medium	Corporate social responsibility	Sustainable Development Goals
Large		Land development

The size of the geological object could be small to large, and its impacts on society could affect either large or small communities.

Large geologic objects such as sedimentary basins or mountain ranges have large social implications as they contribute to the birth and development of provinces, kingdoms and states (Table 1). This is implying political approaches. More than a century ago, a great French geographer, André Siegfried (1913) underlined that some areas where both characterized by their geology (granite/limestone) and the long-term political orientation (conservative/liberal). Large geologic objects currently control land development. However, at this scale, numerous other factors, including population and climate, contribute strongly to the social situation and the concept of social geology appears less pertinent.

Small geologic object have dimensions limited to a few km^2 to some hundreds of km^2 (Table 1). This fits with the scale of industrial or urban development projects such as a mine, a winter ski station, a new urbanization project, etc. In 1998, mining industry leaders in London formed the Global Mining Initiative; comprehensive research and numerous consultations led to the Mining, Minerals and Sustainable Development (MMSD) initiative and gave rise to the creation of the International Council on Mining and Metals (ICMM) in 2001. This organization developed 10 principles for guiding change in the industry. Position statements were developed to accompany and strengthen the principles, and were largely implemented in the major companies. The changing situation of the mining industry during the first decade of the 21st century, from boom to burst, revealed new challenges such as the rising pre-eminence of BRICS investors and operators, a better definition and clearer expression in communities' expectations (Buxton 2012) and an emerging decarbonized society.

The social impacts of mining include very diverse concerns such as employment, health and safety, training and education, diversity and equal opportunity, labor practices, human rights, and even culture. The notion is usually very much orientated toward local community and more especially toward indigenous and tribal peoples (United Nations 2007). Social geology would therefore contribute to the consideration of the value of the deposit for local people.

Small to medium geological objects (pluton, local structures, aquifers…) do have an impact on larger societal challenges. For instance, the connection of a mine to the world economy varies with its value and its accessibility to local and world markets (oil, copper…). This is evolving in space and time: the salt market was a major source of income in the Middle Ages, both for Saharan trade and medieval cities. This is not the case anymore.

Interactions between a local geological object such as an ore deposit and broad societal challenges have been explored in several international studies. The Intergovernmental forum on mining exploitation, minerals, metals and sustainable development proposed a global model for optimising the mining contributions to the sustainable development of developing countries (UNCTAD 2010). More recently, the mining industry contributions to the Sustainable Development Goals, adopted in 2015 by the United Nations, have also been specifically declined in a White paper for the World Economic Forum (Lewis 2016).

Social value and social risk should be considered both in their descriptive and perceived, impressionist aspect. The latter implies to know by whom and where the evaluation is done. The perception may considerably vary among cultures, and the results could be interpreted on different grounds. Mining is almost always disturbing the environment and the social structure. After two decades of academic and applied studies, we currently have a better understanding of the social impact of mining

activities, both to local communities and governments. However, the diversity of the ore deposits and the numerous mining methods need now to be taken into account for a predictive approach of the relation between mining and society (Bergeron et al. 2015).

The mining industry is one of the more globalized domains. For several products including metals and energy minerals, it impacts not only the production zones, but the worldwide community of users. Solving the local social challenges may create new difficulties in remote parts of the world, without obvious connection: banning of lead in welds by the European Commission in 2006 led to an increase in tin production as a substitute. This led to the development of cassiterite mines everywhere in the world and especially in the Kivu Province (Eastern Democratic Republic of Congo), with the misery and conflicts engendered (Jébrak 2015).

Therefore, social geology analysis cannot be restricted to local communities in a globalized market/world. For mineral deposits, we need to develop a metric of value that encompasses several scales, like in geopolitical analysis (Subra 2007).

Professional dimensions

Social geology applied to mineral deposit has already been the topics of numerous works, including books and international journals such as *Resources Policy* and *Social and Natural Resources*. A compilation of the papers in these two journals in 2013-2015 shows that the contents of the field mobilizes psychology, sociology, law, communication and public policy, the latter being the most frequent. Major themes have been the sustainability and the resilience of eco- and socio-ecosystems, the management of organisations (Thomson and Boutillier 2011; Stern and Coleman 2015), externalities, the different approaches to democracy, and the social representation of mining.

Social geology also shares strong ties with social impact assessment (Vanclay 2003). This applied anthropological science was developed in the 1990s in response to technocratic assessment undertaken to gain project approval or financing. Social impact assessment should benefit from social geology to form an integrated knowledge.

Social geology should be practiced by geologists especially trained for this purpose. This will be especially useful for the risks definition of a mining project in a formal report (NI-43-101 or JORC) to stock-exchange. The section devoted to this risk in these documents remains weak and poorly defined whereas social risk is presently recognized as a major challenge, both on land and on sea (Baker and Schmidt 2015).

Pedagogical dimensions

Geology and economic sciences have been the two main pillars for the formation of mining explorationists and mine developers. It is not the case anymore! Other new disciplines are already required in order to look toward and to develop more ore deposits. The environmental impacts of mining have been already included in project development. It was relatively straightforward as the dispersion mechanisms of metals and minerals were already integrated in the geochemical cycle.

The need for the integration of human and social sciences is more challenging. This inclusive evolution will have significant consequences for the formation of future ore deposit geologists. For instance, present research projects in Europe and Canada include disciplines such as geography, law, sociology, anthropology, communication, history... All these disciplines require an understanding of the disjunction between so-called objective, cognitive representations of geological objects and economic situations, and affective representations and reactions in the communities and society.

4 Conclusions

The rise of social geology should push the definition of what is a mineral deposit toward new dimensions. It fundamentally associates a geochemical concept, the concentration of a mineral or an element, and an economic concept, the capacity to exploit the ore with benefits. It is now necessary to add social acceptance to the definition of an ore deposit.

We will therefore have to imagine new classification of ore deposits (Mata-Perello et al. 2012) and new mapping techniques that represents socio-geological objects (Kivinen et al. 2015). Hybridizing geology and social sciences will consist of borrowing and lending concepts, methods, theories, and praxes (Dogan 1996).

Social geology will belong to the emerging sustainability science, a more integrative discipline (Wu 2006). Unlocking disciplines is not without risk. One of the difficulty is that "the distance between disciplines can in some cases appear small, in terms of subject matter, but be large in terms of methodology or perspective" (McNeill 1999). Social geology, as a part of social science should also develop critical visions by investigating if any geological object, by its own geological features, can define or modify power relations in society. It could formulate normative perspectives from which a critique of such relations can be made for social change. This will be a tough exercise for geologists that are presently trained to clearly distinguished facts from representation, and science from ideology.

Acknowledgements

I am grateful to KM Bergeron, P Christmann, Y Gunzburger, PY Le Meur, R Marquis and LJ Robb for sharing their ideas with me during preliminary discussions.

References

Baker D, Schmidt R (2015) Environmental and social benchmarking analysis of the Nautilus Minerals Inc. Solwara 1 Project. Nautilus Document Reference SL01-NMN-XE-RPT-0180-001, 174 p.

Bergeron KM, Jébrak M, Yates S, Séguin C, Lehmann V, Le Meur PY, Angers P, Durand S, Gendron C (2015) Mesurer l'acceptabilité sociale d'un projet minier : essai de modélisation du risque social en contexte québécois. Vertigo 15: 3

Buxton A (2012) MMSD+10: Reflecting on a decade. IIED Discussion Paper. International Institute for Environment and Development, London, 34 p.

Campbell B (2009) Mining in Africa: Regulation and Development. Copub. London: Pluto Press, Ottawa : CRDI, Uppsala : The Nordic Africa Institute, 276 p.
Davis R, Franks D (2014) Costs of Company-Community conflict in the extractive sector. Cambridge, MA: Harvard Kennedy School; Corporate Social Responsibility Initiative; Report N°. 66, 56 p.
Dogan M (1996) The Hybridization of Social Science Knowledge In: Palmer CL (ed) Navigating Among the Disciplines: The Library and Interdisciplinary Inquiry, Library Trends 45: 296-314
Elkington J (1997) Cannibals with Forks: the Triple Bottom Line of 21st Century Business. Capstone Pub. Co., Oxford
Ernst & Young (2016) http://www.ey.com/gl/en/industries/mining---metals/business-risks-in-mining-and-metals
Hansen JA (2007) Social epistemology : A journal of knowledge, culture and policy 21: 425-438
Jébrak M (2015) Quels métaux pour demain ? Les enjeux des ressources minérales. Dunod, Paris, 252 p.
Kivinen M, Eilu P, Kangas K, Tuulentie S, Helenius H, Similä J, Meeting BS (2015) Developing tools for the integration of mining with other land uses. In : *Proc*. the13th biennial SGA meeting, Nancy, France, 1535-1538
Krishnan A (2009) What are academic disciplines? Some observations on the disciplinarity vs. interdisciplinarity debate. ERSC National center for research methods, NCRM working paper series 03/09, 59 p.
Kuhn T (1962) The Structure of Scientific Revolutions, Chicago: University of Chicago Press.
Lewis B (2016) Mapping mining to the sustainable development goals: an atlas. White paper to the World Economic Forum,77 p.
Mata-Perello JM, Mata-Lleonart R, Vintro-Sanchez C, Restrepo-Martinez C (2012) Social geology: a new perspective on geology. Dyna. 1-10
Moffat K, Zhang A (2014) The paths to social licence to operate: An integrative model explaining community acceptance of mining. Resources Policy 39: 61-70
Prno J, Slocombe DS (2014) A systems-based conceptual framework for assessing the determinants of a social licence to operate in the mining industry. Environmental Management 53: 672-689
Siegfried A (1913) Tableau politique de la France de l'Ouest, Paris, A Colin, XXVIII, 536 p.
Stern MJ, Coleman KJ (2015) The multi-dimensionality of trust: applications in collaborative natural resource management. Society and Natural Resources 28: 117-132
Subra P (2007) Géopolitique de l'aménagement du territoire, A. Colin, coll. Perspectives Géopolitiques, Paris, 327 p.
Thomson I, Boutilier RG (2011) The social licence to operate. In: Darling, P. (ed), SME Mining Engineering Handbook. Littleton, Co, pp. 1984
UNCTAD/WEB/SUC/2010/3 site web:
https://www.bmz.de/rue/fr/international/igf/index.html
UNESCO (1997-98) Geology for sustainable development. Bulletin 11. Urban Geology, 162 p. Pub. MRAC, Dpt. de Géologie et de Minéralogie, Tervuren (Belgique). Compilation scientifique par P. Lahogue et coordonné par L. Tack
United Nations Declaration on the Rights of Indigenous Peoples (2007)
Vanclay F (2003) Principles for Social Impact Assessment. Impact Assessment and Project Appraisal 21: 5–11
Wu J (2006) Landscape ecology, cross-disciplinarity and sustainability science. Landscape Ecology 21: 1-4

Comparing social risk for mining projects located in different jurisdictions

Kristina Maud Bergeron and Michel Jébrak
Université du Québec à Montréal, Québec, Canada

Christophe Krolik
Université Laval, Québec, Canada

Abstract. Social risk in mining projects has become an issue of great importance in the industry. Like any other risk, it has to be managed. Since it emerges during the exploration stage, an early understanding of the main risk factors is important. Building on the work already done for a Social Risk Index, which identifies characteristics and communicational aspects of mining projects that increase or decrease social risk, the research team has analysed regulatory frameworks in jurisdictions of the Global North to list aspects related to social risk. With these new variables, a comparison of social risk between projects in different jurisdictions becomes possible.

1 Social risk in mining projects

The concept of risk is one that is very well understood in the business world. Just like any other companies, mining companies need to manage financial risk, political risk, operational risk, reputational risk, and other risks. This is also true for social risk, which can be defined as the potential negative consequences on the mining project resulting from difficulties in the relationship between the promoters of a mining project and neighbouring communities or society in general. This definition is tailored to mining companies involved in the exploration stage, during which there are usually few direct impacts on the community, but when communication with residents and local authorities are necessary. At later stages in the mining cycle, when more people and services are needed on site, social risk can also be connected to potential negative consequences for the population affected by the mine, such as social destructuration coming from an influx of workers, increased inequalities, or a change of culture and priorities. At that point, it becomes unclear if the risk is incurred by the local population or by the mining project (see Kemp et al. 2016; in their vocabulary, the work presented here is on social acceptability risk). Of course, a company should also evaluate the potential negative consequences for the population and mitigate them when it becomes clearer that the project could become a mine, but this is not what the Social Risk Index focusses on.

If the expression "social risk" was not widely used previously in the mining world, it is now integrated in the current vocabulary, as shown by a Canadian government document aimed at Canadian mining companies operating abroad (Government of Canada 2015).

Despite the fact that social risk remains poorly described in regulatory documents for disclosure such as the NI 43-101, it has become a major concern of the mining industry. Preventing legal action, problems of access to a site, delays and local recruitment issues require some carefulness and investment. Since we now have an idea of the costs incurred during a project interruption at the exploration stage (up to 10 000 USD per day during initial exploration, and up to 50 000 USD per day during advanced exploration) (Franks et al. 2014), avoiding conflict with neighbouring communities makes sense at a business level and should be a priority.

Understanding risk means evaluating two aspects: the probability of this risk occurring, and the magnitude of its impact if it were to happen. Apprehending the factors constituting the risk leads to a better appreciation of these two aspects and situate a given project on these two scales. To better understand social risk, this is the work that our research team has tackled for the creation of a Social Risk Index for mining projects at the exploration stage.

Managing risk means mitigating some of these factors, i.e. finding the appropriate ways to make them less likely to happen or to diminish their impact. Not all risk factors can be mitigated, and it is important to realize which ones are modifiable and which ones are unchangeable.

The work presented here is about the identification and evaluation of social risk factors, including factors related to the regulatory framework. With the addition of factors coming from the latter, comparison of social risk between mining projects located in different countries or provinces becomes possible. The approach presented has been developed for companies, for investors, for governments, and for communities. It is currently restricted to mining projects located in the Global North.

2 Identifying social risk factors

Social risk analysis can take the form of an extensive case study on the human environment of a mining project (for example, ICMM 2015). This is also the kind of comprehensive exercise required by Social impact assessment. But it is often not possible to realize these complex analyses until later on in the mining cycle. Yet, we know that stakeholders have to be engaged with early on to facilitate processes conducive to the social licence to

operate. So it is important to quickly have an idea of the social risk associated with a project during its first stages, well before the feasibility stage, to know what to pay special attention to and what are the conditions favouring or hindering social acceptability of the mining project.

2.1 Characteristics as social risk factors

As the research team's work on a Social Risk Index shows, there are some social risk factors that are inherent to the initial situation itself, in the sense that they are characteristics of the company, the community, and the project in its natural environment. These factors are relatively objective and can be observed and rated on an established scale by all stakeholders and even by people not directly involved in the project. Characteristics are given, which means that there will be few opportunities to mitigate these risk factors. In a way, they help to see how high the probability of social risk is.

Some projected mines have more environmental and social impacts than others. This in turn has an effect on the social risk of the project in its early stage. For example, a projected underground mine will likely be better accepted than an open pit mine. A projected mine that is located relatively far from any human settlement will likely be better received than one that is very close to a town. If there are fragile sites nearby, environmentally or culturally, resistance to the project will probably be higher.

Communities have a history, an economy and a sociology that may take a long time to fully understand. But there are characteristics that will hint at a higher level of social risk for a mining project. Examples are a low rate of the local economy connected to the mining industry; a high number of cottagers; recent development projects that have left a sour mark on the community.

Something that is not often taken into account in the literature is the perspective that the company promoting the project may itself carry social risk factors. In this perspective, a promising project near a welcoming community can be developed by a company without the right set of skills or sensitivities to prevent conflict and misunderstandings. To identify social risk factors associated with the company, here are examples of questions that can be asked: Is there a local office for the project? Is there a person identified as in charge of community relations that the community can refer to? What is the composition of the board of directors like in this company? If the company has been active on other projects, were there difficulties with communities or environmental infractions recorded?

2.2 Communicational aspects as social risk factors

Some other factors affecting social risk are more subjective, and their interpretation can vary from one person to the other. Relational and communicational aspects of the interactions between actors are possible to evaluate from the outside, but the task is easier (and more meaningful) for actors directly involved in the project. The Social Risk Index includes a questionnaire on these risk factors, which may help to appreciate how serious or disruptive the consequences of the social risk are.

Examples of questions are: Which communication modes have been used by the promoter and by local stakeholders (press release, information leaflet, website, public information session, advertisement, etc.)? Is there enough openness in the position of the promoter and in the position of local stakeholders? In the expressed points of view, are the elements on which there is no consensus about fundamental aspects or more secondary aspects of the project?

The work on the Index is ongoing, but first results are promising. We compared the results obtained with the "characteristics" part of the Index (leaving aside the questionnaire on communication) with results from a press analysis and results from experts' opinions on the same 23 projects (Bergeron et al. 2015). There was a good degree of correspondence between the three classifications of projects.

3 Comparing jurisdictions

For the first phase of this project on social risk, the research was on different mining projects within the same jurisdiction, the province of Québec in Canada. This means that the rules applying were fairly identical for all projects, which explains why the State (and its rules) could be left aside as an actor in mining projects: its influence being fairly equal, it could not create perceptible differences in social risk between projects. With the extension of the project to social risk for mining projects located in other Canadian provinces and other countries, the manner in which laws and regulations applying to mining projects affects social risk has to be taken into account.

3.1 Social risk factors related to the law

A case and literature review led to the identification of a number of variables related to the regulatory framework with an influence on social risk. The focus was kept on the Global North, where the rule of law is taken for granted, even if there can be problems in its application (or lack of) and interferences in its formulation (e.g. the presence of lobbying may distort the definition of the common good). Even if there are commonalities, there are also differences in between the four Canadian provinces that were examined. A first look at Nordic countries also confirms that there is some variability in the laws and regulations governing the development of mineral projects.

The variables related to the regulatory framework are identified in Table 1. As for the other variables in the Index, only the ones with the most impact on social risk have been selected. Tests may lead to a reduction of their number. The following section explains why the whole

mining cycle is considered through these variables.

Indicators	*Components*	*Variables*
Impact assessment study	Characteristics of the impact assessment study	Obligatory nature and scope of the procedure
		Nature of the information that has to be included
		Stage of realisation in the overall project
		Public information during the preparation phase
	Treatment of the impact assessment study	Availability for consultation by the public
		Possibility to request additional precisions
	Consideration of Indigenous peoples' rights	Impacts on Indigenous peoples' communities
Governance	Stakeholders' participation	Stage and modalities of stakeholders' participation
		Decision makers' leeway in relation with stakeholders' opinions
	Project authorization	Nature and scope of planning instruments
	Consideration of Indigenous peoples' rights	Nature and scope of the duty to consult Indigenous peoples
Socio-political aspects	Taxation	Calculation and affectation of royalties
		Transparency of financial transactions
	Benefits plan	Modalities for elaboration and content of the benefits plan
		Specific rules for benefits plan in Indigenous peoples' territory
Project manage-ment	Financial collateral	Amount and payment modalities of the financial collateral
	Land reclamation	Nature and scope of the obligation to reclaim the site
	Project monitoring	Mechanisms for project monitoring

Table 1. Law-related variables with an effect on social risk in mining projects

3.2 Understanding the impact of law on people's perceptions of mining projects

Laws applying to the full mining cycle have been taken into consideration because citizens' perceptions about the quality and the application of the regulatory framework for the mining industry in general affect how they see mining projects even in their early stages. For instance, if people know that rules around remediation are strict and enforced, it incites them to consider mining projects with less apprehension, and thus less social risk is attributed to the projects.

Citizens' expectations toward mining companies are partly structured by the role of the State in society. For example, the availability and validity of information such as contamination measurements, the unemployment rate in a region, or the taxation level for an industry, information which is controlled by public administrations, influence value judgements on the opportunity to allow the development of a mining project. A relative confidence in the institutions and in the people in charge of them is thus connected to social risk; this is also why the work has been focussed on jurisdictions in the Global North.

4 Conclusion

To compare the social risk associated with mining projects located in different jurisdictions, we have to take into account how the jurisdiction's regulatory framework and its application influence citizens' perceptions of mining projects in general. In conjunction with other social risk factors related to the characteristics of the project, the community and the company, as well as social risk factors associated with communicational aspects of the situation, it is possible to assess broadly the level of social risk for a given mining project.

This analysis should be considered as a way to identify opportunities as well as risk. Managing social risk implies getting to know local stakeholders and taking into account local preferences, which is a good way to practice sustainable development. Local support is also an asset for any kind of project. The investments required for its negotiation should not be seen as unessential.

Acknowledgements

The Education and Good Governance Fund of the Québec's Autorité des marchés financiers (Securities Commission) provided funding for this research project. The information, data, and opinions expressed in this paper only engage the liability of the authors. The content of this document does not necessarily reflect the Autorité's opinion and the eventual errors are the sole responsibility of its authors. Additional funding was obtained from Québec's Fonds de recherche Nature et technologies.

Stéphanie Yates, Charles Séguin, Suzanne Durand, Valérie Lehmann, Corinne Gendron, Pierre-Yves Le Meur, were involved in the creation of the first version of the Index and their contribution is ongoing. Philippe Angers also contributed to the first version. Raphaëlle Bach, Philippe Ross, Béatrice D'Anjou, Lucile Tranchecoste, Géraud de Lassus St-Geniès, Gaëtan Marty, Daisy Tiburcio Carneiro, Geneviève Bordeleau and Rebecca Jean-Dufour were all involved as students in different aspects of the work on the new version of the Index and are to be congratulated for their work.

References

Bergeron KM, Jébrak M, Yates S, Séguin C, Lehmann V, Le Meur P-Y, Angers P, Durand S, Gendron C (2015) Mesurer l'acceptabilité sociale d'un projet minier : essai de modélisation du risque social en contexte québécois. VertigO- *la revue électronique en sciences de l'environnement*. doi: 10.4000/vertigo.16737

Franks D, Davies R, Bebbington A, Ali S, Kemp D, Scurrah M (2014) Conflict translates environmental and social risks into business costs. PNAS 111: 7576-7581. doi: 10.1073/pnas.1405135111

Government of Canada (2015) Corporate social responsibility checklist for Canadian mining companies working abroad. Natural Resources Canada, Sustainable Mineral Development webpage.http://www.nrcan.gc.ca/sites/www.nrcan.gc.ca/files/mineralsmetals/pdf/Corporate%20Social%20Responsibility%20Checklist_e.pdf. Accessed 23 February 2017

ICMM (2015) Understanding company-community relations toolkit. http://www.icmm.com/website/publications/pdfs/9670.pdf. Accessed 28 February 2017

Kemp D, Worden S, Owen JR (2016) Differentiated social risk: Rebound dynamics and sustainability performance in mining. Res Pol 50: 19-26

Social acceptability of mining project in Québec: Evidence from stated preference method

Adrien Corneille
Université de Sherbooke, Québec, Canada

Jie He
Université de Sherbrooke, Québec, Canada

Abstract. Nowadays, mining industry raises great challenges of social acceptability (SA). Over the years, the information costs have decreased through the media expansion, when the minimum expectations of the populations have increased. The diversity of the situations met in the mining context makes more difficult the analysis of SA and its field implementation. SA is different among populations, regions, minerals and proponents. Hence, there is still a need to better understand the SA and the underlying factors. In this paper, we propose to assess the SA of mining projects in Québec based on a stated preference method, i.e. choice experiment. We calculate the importance of SA factors and perform some simulations of SA to characterize the observed differences. Our findings suggest that the perceptions of heterogeneous risks play a key role in the observed difference of SA.

1 Introduction

Mining industry progressively moved to best practices of extraction facing new challenges raised by smelter smoke (Cebada 2015). Corporate Social Responsibility (CSR) is an important challenge for mining companies to succeed in balancing the diverse demand of the communities and their needs for environmental protections (Jenkins 2004). As the minimum expectations from the populations increased and the information costs decreased (e.g. mass media, NGOs), more and more social conflicts related to resources extraction occurred. Technology innovations contributed to improve working conditions for employees, limit and better control the mining impacts. Nonetheless, some of these innovations changed the way the mineral being extracted. For instance, the shift from vertical drilling to horizontal drilling led the local population to be differently affected by mining impacts as a result of different concerns (Farrer et al. 2017). Accordingly, public perceptions of new technologies also changed.

In the old days, minerals were just private goods exchanged on the market. The proposal of mining projects was exclusively based on scientific and engineering expertise limiting the populations' interventions in the planning process. Nowadays, minerals are not only private goods but collective goods as well. When a new mine is opening somewhere, local and general populations expected a utility, commonly called the social acceptability (SA), derived from the mining project. Collective goods (e.g. mining project) stand for all the non-exclusive costs and benefits concerning the economic, social and environmental prospects. Even though a new mine opens in a mining town, the mining project is subject to the local acceptance of the population.

At first sight, new mining project is perceived as a windfall through the job creation, investments in transport, social and public infrastructures, decreases in tax, etc. Besides, new mine comes with mining impacts changing the environments space and social interactions radically. It is hard to generalize the diversity of situations within the mining specific context. Reactions from the population seem to be very different according to the various minerals, the localization, the proponent, etc.

There is still a gap to identify the reasons behind success stories and failures when comparing the SA from different mining projects. The present article raises an important question: why do we observe such differences of SA? We propose to fill this gap by estimating the social acceptability of mining projects and analyzing the underlying factors of SA. Our approach focuses the hypothetical scenarios on the notion of SA. The timing of mining project is before the phase of construction when the proponent proposes the project to the population.

2 Methods

The utility can be derived from the questions about the willingness to pay (WTP) or willingness to accept (WTA) related to the implementation of a new project or policy. Several methods from the economics field contribute to estimating the utility: (i) revealed preference and (ii) stated preference. Among revealed preference methods, the hedonic method is used to induce the wellbeing of people through the variation of property value. For example, the construction of a new shale gas well will affect the wellbeing of nearby habitants through variations of the property value (Muehlenbachs et al. 2015). On the Stated Preference side, contingent evaluation is as a "fictive" referendum on the implementation of a new public good; choice experiment (CE) is used to induce the wellbeing through the repetitive decision choices between different goods or policies.

CE approach goes beyond the contingent evaluation in the sense that it allows to take into account the multi-dimensions of a public good instead of the good as a whole. The multi-dimensions of a good are captured by different attributes related to the good included in CE

scenario. CE is particularly relevant for complex goods such as ecosystem, water quality, etc. Minerals are no exception for complex goods as mining projects cover close linkages between economics, social issues and the environment. In a way, minerals are more complicated than the majority of public goods since its extraction influences directly or indirectly several complex goods (e.g. water quality, ecosystem).

Some authors already used CE method within the mining context. Garrod and Willis (2000) assessed the utility from externality of a new quarry project. Ivanova and Rolfe (2010) asked local population for their expectations from a town development program in order to compensate the costs from a new coalmine. Gillespie and Kragt (2010) studied the local wellbeing faced to a new underground coalmine. Rolfe and Windle (2015) analyzed the impact of mining expansion for current mines extracting coal and coal seam gas. Spyce et al. (2012) from aboriginal and non-aboriginal land use faced to cumulative effects of regional development (including mining).

In this article, we use the CE method to assess the social acceptability (SA) of both general and local populations regarding mining projects in Québec (Canada). Both local and general populations could be subject to welfare loss. Local population would suffer from welfare loss once being exposed to mining impacts such as noise, vibrations, and dust. Even if the general population is far away the new mine, they could still perceive a welfare loss. Some of the general populations could have a second home near a mine, have recreational activities next to the mine or even want to preserve the territory from mining activities.

If the respondent were facing a welfare loss, it would be more appropriate to use WTA without particular difficult obstacles (Whittington et al. 2017). When raising WTP questions, the respondent could not believe that they should pay in order to avoid the loss. In the mining context, a new mine will affect the environment space in the long run (despite of all the potential benefits) and seem likely to be perceived as a welfare loss. It would be inappropriate to ask respondents their WTP to avoid the implementation of the new mine.

The sample will include around 1 500 subjects divided into 3 sub-samples for each mineral, i.e. gold, uranium and rare earths. Criteria for mineral choices take into account the mining past (new/usual minerals), the geographical issues' scales and the social use of the minerals. The mode of study includes web survey for the general population in diversified regions and field survey for local population located in resources regions (e.g. Abitibi-Témiscamingue, Côte-Nord, Nord du Québec).

To model the hypothetical scenario, we must select the most important attributes of SA from the mining project. The definition of the attributes is based on an extensive qualitative study and literature review. The qualitative study was realized from June to November 2016 collecting information from around 60 participants belonging to mining shareholders. The participants were asked for the SA factors that seem the most important regarding the population point of view. We declined around 30 SA factors and ranked them each time one factor was mentioned. The SA factors' ranking and the expert judgement help us to select the most relevant factors and include them in the CE scenario. The reference situation for our scenario is the implementation of a new mine near the respondent's house.

3 Findings

At this state of our study, the attributes of our hypothetical scenario are as followed: (i) type of mine (open-pit or/and underground exploitation), (ii) water quality monitoring (a proxy of transparency), (iii) proponent's attitudes during the presentation of the project, (iv) partnership structure and (v) decrease in municipal/regional taxes. Each of these attributes includes several different levels taken from the results of the qualitative study and the expert opinions. Our hypothetical scenario is flexible enough to consider a large part of the situation's diversity met in the mining sector.
Our paper contributes to compare the different perceptions between local and general population regards to new mining project. Most of natural resources' extraction models assume that the risks are evenly distributed. Instead, Farrer et al. (2017) suppose that the risks are heterogeneous depending on the property value and the extracted quantity. Following Farrer et al. findings, we show that risks related to mining projects are heterogeneous according to the technology, the knowledge about mining world and the experience.

We will assess the SA from different mining projects and illustrate the importance of the underlying factors (i.e. attributes). We could calculate the weights of SA factors according to their importance and perform some simulations of SA faced to different combinations of attributes from the mining project. To our knowledge, the current literature does not capture the difference of people wellbeing between the various minerals. Indeed, the CE scenarios do not include the influence of technology on the perception of population through underground or/and open-pit exploitations.

4 Conclusions

Our paper has significant implications for new design policy. Mineral heterogeneity ought to be taking into account as people over-estimate or under-estimate costs and benefits from mining projects. Hence, policy should be designed in a way that reflects the heterogeneous SA. Indeed, we highlight the importance of heterogeneous risks, which provides a partial explanation for the observed differences of perceptions between populations and regions. Innovation plays a key role in the perception of heterogeneous risks by the population. For now the diversity of the mining context makes the understanding of SA more difficult. More research is needed to better understand the mechanism behind the perception of heterogeneous risks.

References

Cebada JDP (2016). Mining corporations and air pollution science before the Age of Ecology. Ecological Economics 123:77-83.

Farrer B, Holahan R, Shvetsova O (2017). Accounting for heterogeneous private risks in the provision of collective goods: Controversial compulsory contracting institutions in horizontal hydrofracturing. Journal of Economic Behavior & Organization 133: 138-150.

Garrod GD, Willis KG (2000). Economic approaches to valuing the environmental costs and benefits of mineral and aggregate extraction. Minerals and Energy 5(4):12-20.

Gillespie R, Kragt ME (2010). Valuing the non-market impacts of underground coal mining (No. 98239)

Ivanova G, Rolfe J (2011). Assessing development options in mining communities using stated preference techniques. Resources Policy 36(3):255-264.

Jenkins H (2004). Corporate social responsibility and the mining industry: conflicts and constructs. Corporate Social Responsibility and Environmental Management 11(1):23-34.

Muehlenbachs L, Spiller E, Timmins C (2015). The housing market impacts of shale gas development. American Economic Review 105(12):3633-3659.

Rolfe J, Windle J (2015). Testing attribute selection and variation in a choice experiment to assess the tradeoffs associated with increased mining development. Land Use Policy 42:673-682.

Spyce A, Weber M, Adamowicz W (2012). Cumulative effects planning: finding the balance using choice experiments. Ecology and Society 17(1).

Whittington D, Adamowicz W, Lloyd-Smith P (2017). Asking Willingness-to-Accept Questions in Stated Preference Surveys: A Review and Research Agenda. Annual Review of Resource Economics 9(1).

Perception regarding mineral resources development and social acceptability in the province of Québec, Canada

Frédéric Malo
Université Laval, Québec, Canada

Karine Bédard
Institut national de la recherche scientifique – Centre Eau Terre Environnement, Québec, Canada

Michel Malo
Institut national de la recherche scientifique – Centre Eau Terre Environnement, Québec, Canada

Christine Rivard
Natural Resources Canada, Geological Survey of Canada, Québec

Roxane Lavoie
Université Laval, Québec, Canada

Abstract. Social acceptability is the key to success for any new industrial development, such as the opening of a new mine. A survey was conducted in the province of Québec in Canada to investigate opinion, perception and social acceptability towards the mining industry. The survey highlighted that Quebecers recognize the importance of the mining industry for the economic development of the province, but they have a low level of trust in the mining industry. Nonetheless, they also recognize their low level of knowledge of this industry. The most important benefit perceived is the job creation, whereas their major concerns are related to environmental issues. The level of trust towards mining companies is in fact the lowest among the different actors of the mining development, whereas the scientific community and the non-profit organisations obtain the highest levels, way above municipal, provincial and federal governments, as well as media. The acceptability of the mining development is mitigated, only 7% of Quebecers are opposed but only 10% encourage its development. Quebecers are less favourable to open pit mines than to underground mine, and become even less favourable to their exploitation if located in their own region. Hydroelectricity is the most socially accepted natural resource exploited in Québec, followed by mineral resources, forests, and oil and gas.

1 Introduction

Social acceptability is becoming an essential requirement for any industrial development in the world. Mining development and the opening a new mining sites cannot avoid this requirement even if the future mine is located in a remote area. The population within the mine area, as well as outside any-mining regions, wants to be consulted prior to any development of an industrial project. In the last twenty years, environmental and health concerns have been raised and the decision to open a mine has no longer been solely based on economic considerations. The mining company must now obtain a "social licence to operate" (Bouchard 2015; Moffat et al. 2014), which strongly depends on the social acceptability of the project. In order to obtain this licence, the main concerns of the population towards mining activities must be known. Interestingly, these concerns in turn depend on the people's perception and knowledge of the mining industry.

In order to find solutions to obtain this social licence to operate in the province of Québec, a survey was conducted to acquire information on the perception and level of knowledge of Quebecers on the mining development in the province. The main objectives of the survey were to understand: (1) the perceived importance of the mining industry in the province, (2) the level of knowledge of the population about the mining industry, (3) people's opinion on the benefits of the mining industry, (4) their apprehensions and concerns about the mining industry, (5) their opinion regarding reputation of different actors in the mining industry, (6) their level of acceptability of mining development, and (7) their level of acceptability about other natural resources.

2 Methodology

A bilingual (French/English) Internet-based survey was created by the INRS (Institut national de la recherche scientifique) team in coordination with survey experts from Leger, a major Canadian polling firm. The survey was inspired by other surveys on mining development in other Canadian provinces or in other countries (Malo et al. 2016; Malo et al. 2015; Moffat et al. 2014). Some questions were open-ended, but most of them were multiple-choice questions with an "I don't know / I prefer not to answer" option available.

Leger conducted the survey on-line, using its web survey panel, a representative sample of Québec's population (French and English-speaking adults as well as male and female representatives). The survey was answered by 1,309 respondents, from September 2 to 14, 2016. By comparison, a probability sample of the same size would yield a margin of error of ±2.7%, 19 times out of 20. The average interview length was 12 minutes.

The representative sample of the Québec population

was obtained by weighting the raw data of the study in order to reflect the actual distribution of population by region, age, sex, mother tongue, education, etc. In addition to conducting the survey, Leger also analyzed results of the survey using different statistical tests.

An oversampling of approximately 100 respondents was made in three mining regions (Abitibi-Témiscamingue, Côte-Nord and Gaspésie-Iles-de-la-Madeleine), to compare the opinion and level of acceptability of people living in mining areas with those living in non-mining regions of the province. The survey results are presented in sections 3 to 9 below.

3 Importance of the mining industry

Most of the Quebecers (69%) recognized the importance of the mining industry in the province of Québec, but it was not ranked as the most important industrial sector, being only seventh out of the eight suggested industrial sectors (after agriculture-forestry-fishery, commerce, technology and communications, finance and insurance, construction, and public services). While not in the top list of industrial sectors, 78% of the respondents believed that Québec should encourage mining development in order to import less mineral resources. In addition, more than 60% of the respondents believed that the mining sector is important for the present-day economy of the province and for the prosperity of the province and its future economic development. The perceived importance of the mining industry was higher (86%) in the three mining regions.

4 Knowledge about the mining industry

When the respondents were asked to indicate their level of knowledge on a scale of 0 to 10 (where 0 meant "not at all" and 10 "very well"), they estimated it to be 3.6, which is quite low. 75% admitted they had a poor knowledge (score between 0 and 5), whereas 17% said they knew the industry well (score of 6 and 7), and only 8% said they know the industry very well (score between 8 and 10). The respondents that highly ranked their knowledge mainly come from the Abitibi-Témiscamingue mining region (33% rated themselves between 8 and 10). The different sources of information for Quebecers about the mining industry appeared to be, in order, television, newspapers, magazines and books, and internet.

5 Benefits of the mining industry

When asked to write the first words that came to mind when thinking about socio-economic benefits of mineral resources, 52% of the respondents answered "I do not know" or "Nothing". From those who provided an answer, 17% mentioned something related to jobs. For the second question, where the respondents had to choose among a list of seven benefits, they ranked "job creation" as being the most important benefit by far (68%), followed by stimulation of the economy (45%) and local economic development (45%) (Fig. 1). Other benefits such as mining royalties (25%), construction of infrastructures in remote regions (23%), job creation for first nation communities (20%) and training of qualified workforce are also worth mentioning.

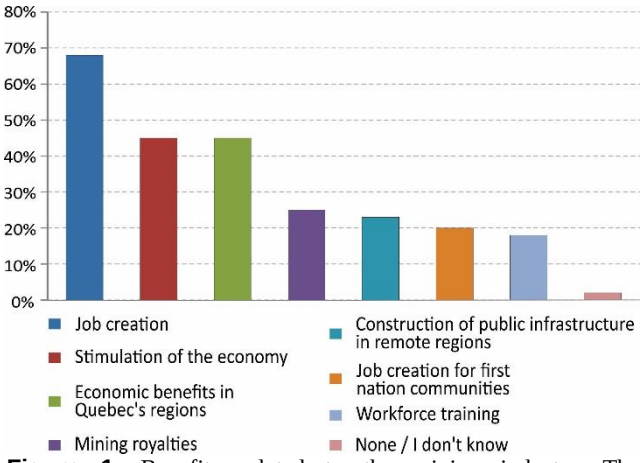


Figure 1. Benefits related to the mining industry. The respondents had to rank benefits according to a list of seven benefits/advantages. Each column of this graph thus shows the percentage of respondents that have chosen this benefit. 2% of the respondents answered "I do not know".

6 Apprehensions and concerns

For the first question on negative impacts of mineral resources exploitation, nearly half of the respondents (48%) said they have no concern. From those who provided an answer, 33% mentioned environmental issues. For the second question, when the respondents were asked to choose three items among a list of twelve concerns (Fig. 2), contamination of surface water and groundwaters appeared as the most important concern (selected by 58% of the respondents). Several other environmental issues were also selected by a significant number of respondents (Fig. 2): soil contamination (32%), loss of biodiversity, faunal and floral habitats (28%), management of mining waste (28%), atmospheric pollution and greenhouse gas emission (26%), destruction of the landscape (23%), abandoned site rehabilitation (19%), air pollution due to dust emission (17%) and noise pollution (5%). The impact on public health and security (18%) and worker security (12%) also received a non-negligible percentage.

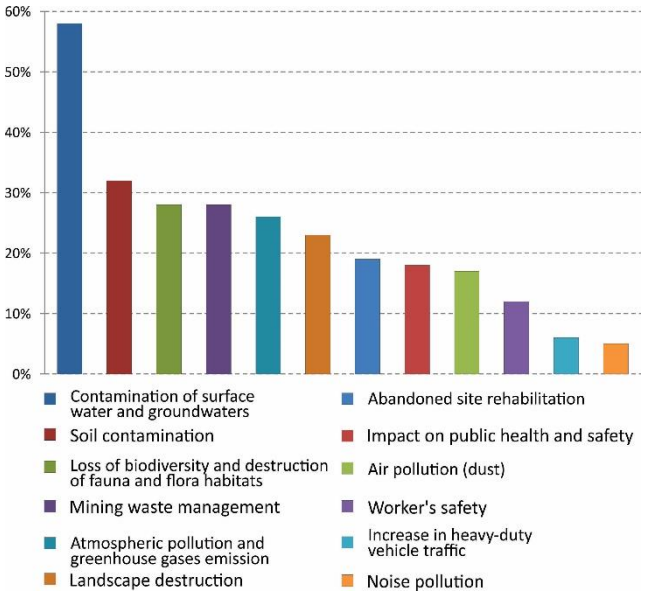


Figure 2. Population concerns related to the exploitation of mineral resources. Respondents had to select three choices among a list of 12. Each column of this graph thus shows the percentage of respondents that have chosen this concern.

7 Reputation

Five statements were used to measure the mining industry reputation (Figure 3). When the respondents had to indicate their degree of agreement with those statements, three statements received a positive score (more or less agree + totally agree). More than half of the respondents agreed that the mining industry has improved their practices over the past years for health and security of workers (63%) and for the protection of the environment (51%). 60% thought that the mining industry is a high-technology industry. However, only 32% of the respondents believed that mining companies are ready to modify their practices according to concerns of impacted communities and only 25% agreed that mining companies consult and respect these communities.

The level of trust towards different actors related to the mining development has been tentatively estimated using a list of organisation/government and a scale of 0 to 10, where 0 meant "no trust at all" and 10 "total trust". The scientific community and universities obtained the highest level of trust (6.9 on 10), whereas mining companies received the lowest score with 4.1. It is worth noting that the levels of trust for municipal (4.8), federal (4.4) and provincial (4.1) governments are close to that of the industry. Non-profit organizations ranked second (6.2 on 10), whereas media arrived third with 4.9, close to the scores attributed to the different levels of government.

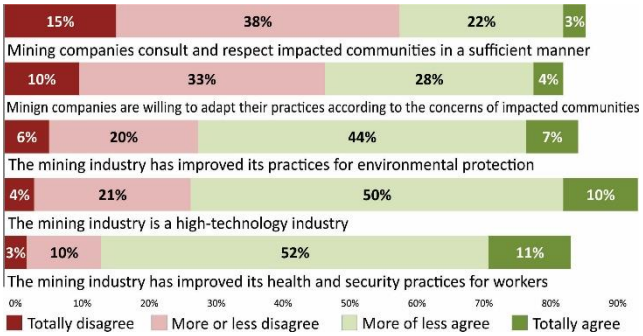


Figure 3. Statements used for judging the reputation of the mining industry along with their responses.

8 Acceptability of mining development

The majority of Quebecers (83%) were not necessarily for or against mining development, in the sense that on both extreme cases (Fig. 4), only 10% encourage it and 7% are opposed. 35% accept the development, 32% tolerate it and 16% approve it (Fig. 4). The highest score for the mining development support was encountered in mining regions (24% compared to 10% for the entire sample), along with the lowest opposition (1%).

	Total (N= 1039)
I **accept** mining development	35%
I **tolerate** mining development	32%
I **approve** mining development	16%
I **encourage** mining development	10%
I am **opposed** to mining development	7%

Figure 4. Acceptability of the mining development.

Beyond these general statements, the level of acceptability depends on the type of exploited resources. For instance, the exploitation of iron, precious metals (gold and silver), base metals (copper, zinc), salt and diamonds are well accepted, whereas the production of uranium and asbestos is not.

The type of mines and its location also plays a role in the acceptability of the mine exploitation (Fig. 5). The respondents were mostly favourable to the development of an underground mine in the province (66%). However, if this underground was said to be located in their own region, they became less favourable (52%). The same phenomena was observed for open pit mine, where the respondents were less favourable to an open pit mine in their region (35%) as compared to an open pit mine elsewhere in the province (47%).

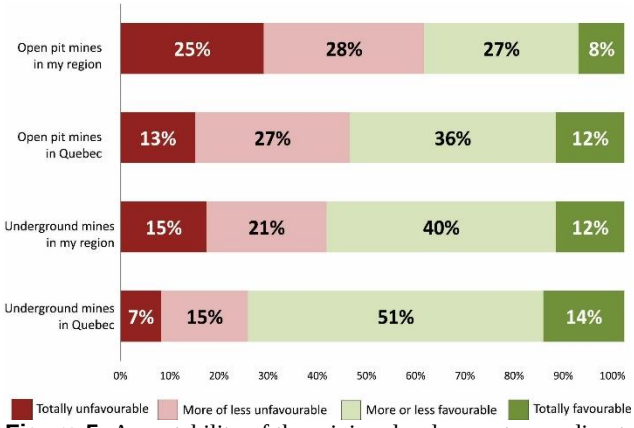


Figure 5. Acceptability of the mining development according to the type of exploitation.

9 Comparison with other natural resources

The support of Quebecers for the exploitation of three other natural resources in the province was compared to that of mineral resources. Hydroelectricity obtained the highest support (88%), then mining development (67%) and forestry (64%) came second and third, respectively. Oil and gas production was ranked the lowest (38%), even if there is no current extraction in the province.

10 Discussion and conclusion

It appears that Quebecers recognize the importance of the mining industry for the economic development of the province, but do not consider it the most important industrial sectors. The most important benefit perceived by Quebecers is the job creation and socio-economic regional development. Quebecers are concerned by surface water and groundwater contamination, as well as other environmental issues. Quebecers recognize their poor knowledge regarding this industry, but the latter clearly suffers from a poor reputation acquired over the past decades. Even if some improvements have obviously been noted over the past years (statements 3 and 5; Fig. 3), the mining industry reputation remains affected by the apparent lack of consultation and respect towards the communities where they currently operate or want to develop a new mine.

Among the different actors of the mining development, the scientific community and the non-profit organisations obtained the highest level of trust, while mining companies, the different levels of governments and media were all ranked quite low.

Most of the respondents accepted, approved or tolerated mining development. Few respondents appeared to have extreme opinion on the subject (either opposed or strongly supportive of the mining development). Support for the mining industry was the highest in the mining regions and the opposition was also the lowest. The type of mine and its location, as well as the type of minerals exploited do make a difference in its acceptability. If a mine was said to be located in their own region, no matter the type of mine, respondents became somewhat less favourable. This result is interpreted to be the expression of the NIMBY syndrome (Not In My Back Yard). In general, Quebecers are also less favourable to open pit mines than underground mines.

The exploitation of water resources for hydroelectricity appears to be by far the best accepted type of exploitation of natural resources in Québec, followed by the exploitation of mineral resources and forests, both of which received a similar level of support. Oil and gas production obtained the lowest level of support.

Acknowledgement

The authors would like to acknowledge the Fonds de recherche Nature et technologies du Québec (FRQNT) and the Ministère de l'Énergie et des Ressources naturelles du Québec (MERN) for their financial support. We also want to thank our industrial partners André Gaumond, Robert Wares and Èva Roy-Vigneault from Osisko Gold Royalties, and Ghislain Poirier from Stornoway. Cynthia Darisse from Leger is thanked for her advice on the survey questionnaire, and Kieren Moffat and Justine Lacey from CSIRO for numerous discussions.

References

Bouchard M (2015) Social licence to operate and the environmental and social challenges of the mining industry. Proceeding 13th SGA Biennal Meeting, Nancy, France, p. 15.

Malo F, Raymond J, Malo M (2016) L'acceptabilité sociale des projets d'énergie géothermique au Québec. Rappot de recherche R1662, INRS Centre Eau Terre Environnement, 58 p. URL :http://espace.inrs.ca/id/eprint/4030.

Malo M, Moutenet JP, Bédard K, Raymond J (2015) Public awereness and opinion on deep geothermal energy in the context of shale gas exploration in the province of Québec, Canada. Proceedings World Geothermal Congress 2015, Melbourne, Australia, 8 p.

Moffat K, Zhang A, Boughen N (2014) Australian attitudes towards Mining: Citizen survey – 2014 Results. CSIRO, Australia, 16 p.

Nickel mining potential for evaluating land-use pressure in the Sodankylä region, Finnish Lapland

Mira Markovaara-Koivisto, Mari Kivinen, Pasi Eilu
Geological Survey of Finland, Espoo, Finland

Abstract. Land-use planning in areas where mining is an important industry is increasingly based on foreseeing the needs of future mining projects together with needs of other land-use forms. The task was tackled in this research by assessing characteristics and spatial distribution of mineral deposits, geological prospectivity and the exploration and mining activities in the Sodankylä region. The different combinations were classified and probable time scales for possible mining activities were given. The produced categorised maps can be used to evaluate the future overlap of different land-use forms in different timescales and to mitigate possible disputes.

1 Introduction

Finland is ranked as one of the top countries in the world for mining and exploration (Jackson and Green 2015). Finnish Lapland can be regarded as having a good potential for gold, copper, and nickel deposits, while the region can be largely regarded as under-explored (Maier et al. 2015). The easiness to enter into exploration and mining in Finland has caused several foreign mining companies start operations in the country since 1995. The local population has awakened to the environmental risks that come along, and the local municipalities to the competition in land-use.

Future coexistence of different land-use needs planning tools and information about the anticipations of different industries. Our research reflects the future changes in the land-use needs and anticipations of nickel mining industry in the Sodankylä region in Finnish Lapland.

2 Materials and methods

This research is based on extensive mining-related datasets gathered in the Geological Survey of Finland (GTK). These include the Mineral Deposit and Exploration Database (MdaE, http://gtkdata.gtk.fi/MDaE/), which contains spatial information of deposits, exploration and mining in Finland; the Fennoscandian Ore Deposit Database (Eilu et al. 2016), which contains numeric information of metallic mines, deposits and significant occurrences in Fennoscandia; and nickel prospectivity assessment for the Sodankylä region (Nykänen et al. 2015). In addition to these data, we applied Mining Register Map Service maintained by TUKES (the Finnish mining permitting authority), which includes knowledge over all mining and exploration tenements in Finland (TUKES 2015, 2017). This information was analysed together in a spatial context to derive new layers of information which we call 'Mining potential' in this article. The research adds to evaluation of land use forms restricting prospecting described in Kivinen et al. (*submitted*).

The idea of the Mining potential is to give an estimation of the minimum time in years needed in a certain location to mining to be established (Table 1). The timeframes are based on mine life cycle presented by Kauppila et al. (2011). Decision over in which class certain mineral deposit or area is placed depends on how advanced they are in a mine life cycle (Fig. 1) and whether there is active exploration or mine development ongoing. A narrative probability (Table 1) is also given for the Mining potential classes. The idea of this probability is to reflect the reality that only a fraction of identified mineral deposits are eventually mined.

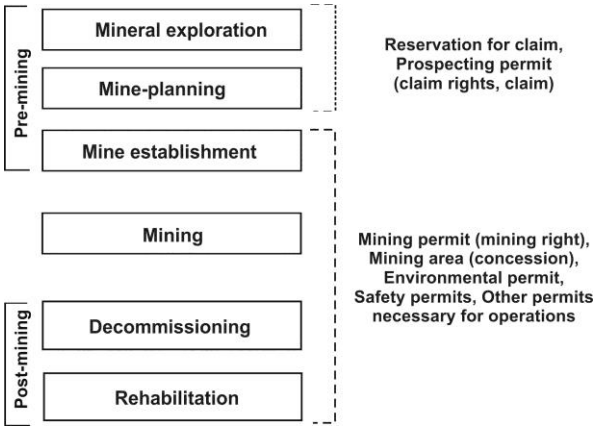


Figure 1. Simplified life cycle for a mining project. Modified after Kauppila et al. (2011).

3 Nickel exploration and mine potential in the Sodankylä region

Sodankylä is a municipality situated in the high north of Finland with a population of about 8900. In recent years, Sodankylä has been a location for active mineral exploration and mining (Brownscombe et al. 2015; Santaguida et al. 2015; Brown 2016). In addition to mineral exploration and mining-related activities, there is nature conservation areas and reindeer herding with extensive land-use needs. The climate in this region corresponds to taiga with cold winters and warm summers but, due to closeness of the warm North Atlantic, no permafrost is present. Bedrock is dominantly composed of Paleoproterozoic supracrustal rocks with ages from 2.50 to 1.96 Ga known as the Central Lapland Greenstone Belt (Hanski and Huhma 2005).

Table 1. Mining potential classes developed for this research.

Mining potential (deposits)			
Class	**Time frame**	**Probability**	**Description**
5	0	In place	Operating or suspended mine. Suspension over 5 years ago -> to be placed in class 4, if over 10 years ago -> to be places in class 1
4	1-10 years	Probable	Mining concession in place; technical and feasibility studies finalised or in review; environmental permit granted or in review
3	5-15 years	Possible	Mining concession in place or applied for, or pre-feasibility study published; resource estimate available; active development (technical studies, environmental impact assessment, feasibility studies) during last 5 years
2	10-25 years	Passable	No resource estimate, active development during last 5 years. If no current holder, deposit/project to be placed in class 1
1	>25 years	Faint	Resource estimate available OR no resource estimate AND no activities during last 5 years. Deposits/projects without current holder to be placed in this class
Mining potential (areas)			
Class	**Time frame**	**Probability**	**Parameters**
2A	10-25 years	Passable	Mineral exploration permit granted AND very high, high or moderate prospectivity
2B	10-25 years	Passable	Mineral exploration permit granted AND low or no prospectivity
1	>25 years	Faint	Areas with prospectivity but no mineral exploration permit

3.1 Nickel mining potential for Sodankylä

Sodankylä region currently hosts one active mine, Kevitsa, which is a Ni-Cu-PGE deposit of magmatic origin within a composite ultramafic intrusion (Santaguida et al. 2015). In addition, there is the Sakatti Ni-Cu-PGE deposit with advanced exploration (Brownscombe et al. 2015) and the Pahtavaara gold mine in care and maintenance. Pahtavaara was excluded from this study as it represents gold, not nickel mining.

The region hosts a marked amount of areas with high to very high nickel prospectivity (Fig. 2) and extensive part of the region is under mineral exploration tenements mostly including the high to very high prospectivity areas.

Nickel mining potential in Sodankylä area was classified according to Table 1. Kevitsa mine falls in the class 5 (in place) as being an operating mine. All of the exploration concession areas fall into class 2 (probability: passable; Figs. 2 and 3), where the estimated time span to develop a mine falls between 10 and 25 years. Sakatti, the only known, unexploited nickel deposit in the studied area also falls in passable probability class, with an expected time span to proceed to mining stage being from 10 to 25 years. For this deposit, the exploration activities are ongoing but no resource estimate has yet been published. The deposit lies under a protected wetland (Fig. 3), and the exploration work is done with a permit from the Supreme Administrative Court of Finland (KHO 2016). This is an example how the other forms of land use can delay or restrict exploration and mining activities. However, according to the current legislation, the only land-use form, with no exception, forbidding mineral exploration by itself is graveyards. In other areas under restricting forms of land use, for example areas designed for nature conservation, mineral exploration can be performed with permission.

Figure 3 shows that there are reasonably large areas under restricted land-use forms in the Sodankylä region, the most important being nature conservation and housing. Restricted areas in places also overlap with high-prospectivity areas and indicate potential land-use conflict locations in the future.

Figure 4 shows the areas which currently fall into the mining potential class 1 (faint probability for mining). This class represents areas without exploration concessions in 2015 but with identified nickel prospectivity. The probability for mining activities to be initiated in these areas prior 25 years is estimated to be faint due to the reason that no attempts to identify new mineral deposits are ongoing. However, it would be reasonable to assume that in the future the exploration activities will move towards the high and very high prospectivity locations within these areas.

Figures 2, 3 and 4 show the situation in Sodankylä in 2015. Yet, new mining concessions are constantly applied and some of the old dropped. As mining potential presented in this paper is based on mineral exploration activity, the maps should be updated frequently to maintain their validity. For example, Figure 5 shows that between 2015 and 2016 exploration concessions have been given out in vast areas south from the Pahtavaara mine even if they were in areas of very high or high nickel prospectivity. On the other hand, exploration permits within Natura 2000 conservation areas were kept regardless the restriction to exploration and mining.

4 Conclusions

To conclude, anticipating the future development of land needs of the mineral exploration and mining industry, concurrent land-use forms in the same region has to be taken into account. In addition, time scales needed prior to possible mining, together with narrative probability of mining activities, helps in adding medium to long term perspectives in land-use planning.

The overlap of mineral exploration and high prospectivity with other forms of land use may cause discrepancy and conflict which can be mitigated by foreseeing the spatial development of the mining industry

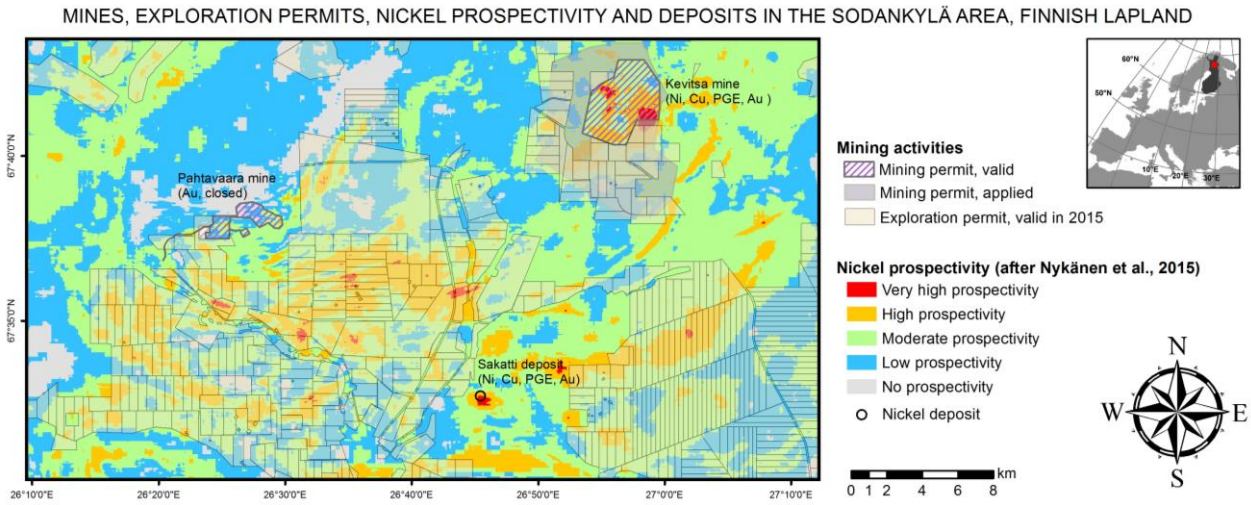


Figure 2. Mining permits and exploration concessions in Sodankylä area in 2015. Prospectivity is defined for magmatic nickel deposits (Nykänen et al. 2015).

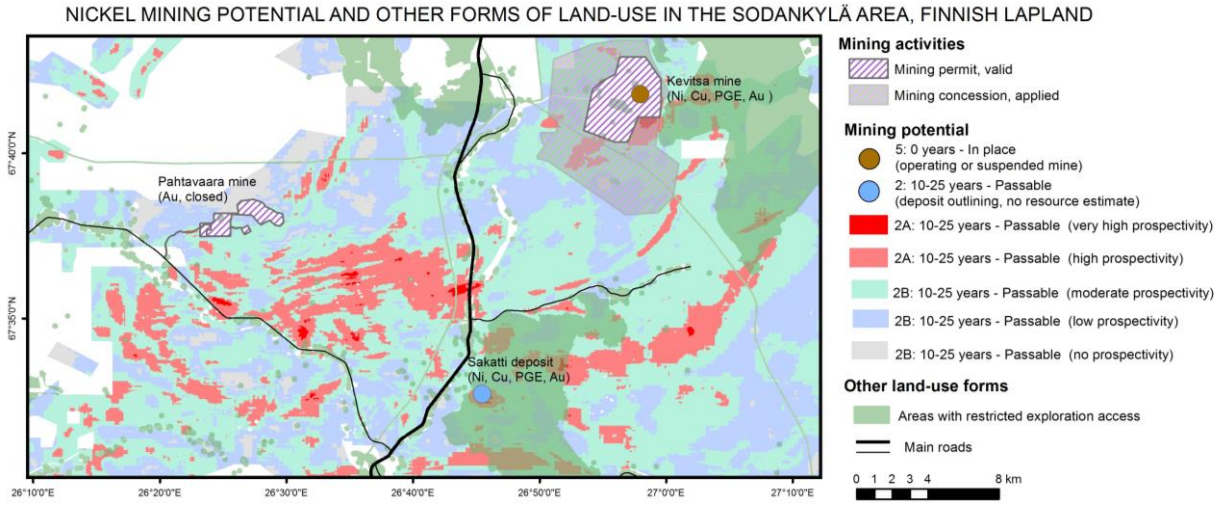


Figure 3. Current nickel mining potential shown together with other forms of land use. Prospectivity is defined for magmatic nickel deposits (Nykänen et al. 2015).

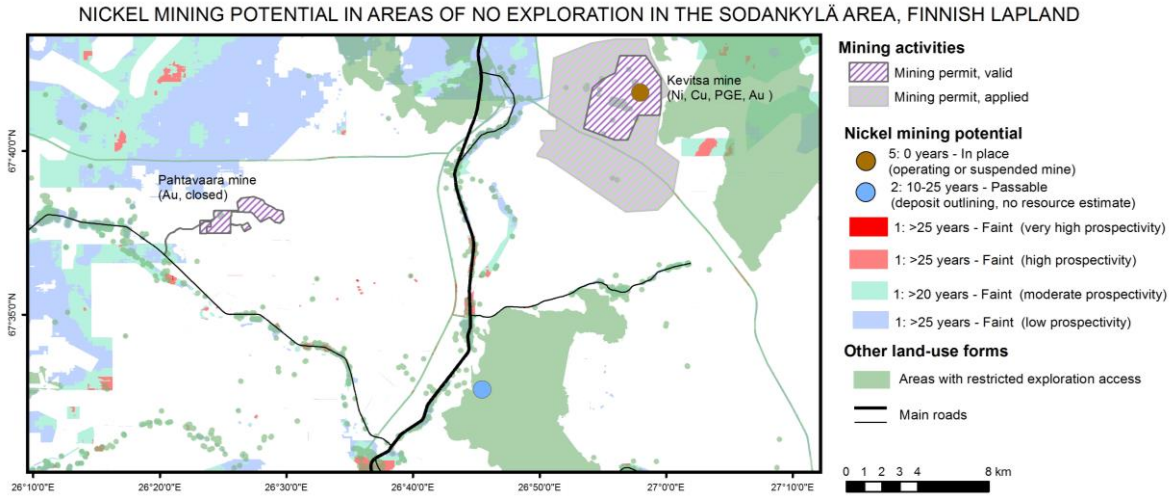


Figure 4. Current nickel mining potential is faint in areas where nickel is not explored. Prospectivity is defined for magmatic nickel deposits (Nykänen et al. 2015).

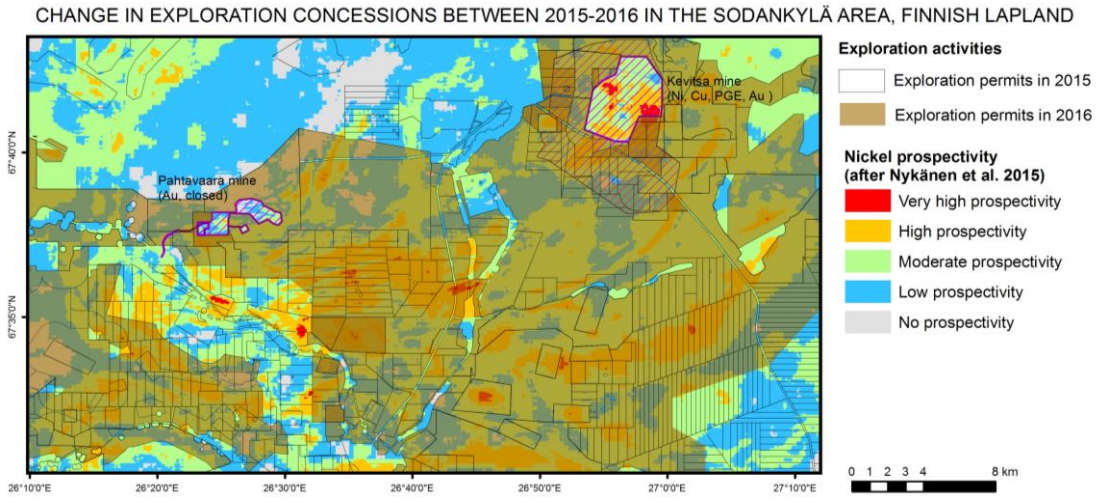


Figure 5. Change in the exploration permissions between years 2015 and 2016 in Sodankylä area. Prospectivity is defined for magmatic nickel deposits (Nykänen et al. 2015).

in a region. In this context, the municipal authorities may play an important role, as the municipality is responsible for regional planning and through that can mitigate clashing of the land use interests.

Acknowledgements

This study is a part of GovAda project in the ARKTIKO Program funded by the Academy of Finland (grant no. 283166).

References

Brown G (2016) Anglo American exploration: key ingredients to a decade (1999−2010) of success. Soc Econ Geol Spec Publ 18:321–329

Brownscombe W, Ihlenfeld C, Coppard J, Hartshorne C, Klatt S, Siikaluoma JK, Herrington RJ (2015) The Sakatti Cu-Ni-PGE Sulfide Deposit in Northern Finland. In: Maier WD, Lahtinen R, O'Brien H. Mineral Deposits of Finland. Elsevier, Amsterdam, 211–252

Eilu P, Hallberg A, Bergman T, Bjerkgård T, Feoktistov V, Korsakova M, Krasotkin S, Lampio E, Lauri, LS, Litvinenko V, Philippov N, Sandstad JS, Shchiptsov V (2016) Fennoscandian Ore Deposit Database. Annual update. http://en.gtk.fi/informationservices/databases/fodd/index.html. Accessed 25 February 2017

Hanski E, Huhma H (2005) Central Lapland Greenstone Belt. In: Lehtinen M, Nurmi PA, Rämö OT. The Precambrian Geology of Finland Key to the Evolution of the Fennoscandian Shield, Elsevier, Amsterdam. 139–193

Jackson T, Green KP (2016) Fraser Institute Annual Survey of Mining Companies 2015. Fraser Institute, Vancouver. https://www.fraserinstitute.org/sites/default/files/survey-of-mining-companies-2015.pdf. Accessed 20 January 2017

Kauppila P, Räisänen ML, Myllyoja S (2011) Best Environmental Practices in Metal Ore Mining. Finnish Environment 29.

Kivinen M, Pokki J, Markovaara-Koivisto M, Aumo R (*submitted*) Discovered and undiscovered mineral resources: Evolving accounts and future prospects of minerals in Finland. Submitted to Mineral Economics

KHO (2016) Decision number 3526/2016. http://kho.fi Accessed 20 February 2017

Maier WD, Lahtinen R, O'Brien H (2015) Mineral Deposits of Finland. Elsevier, Oxford

Nykänen V, Lahti I, Niiranen T, Korhonen K (2015) Receiver Operating Characteristics (ROC) as validation tool for prospectivity models – a magmatic Ni-Cu case study from the Central Lapland greenstone belt, Northern Finland. Ore Geol Rev 71:853–860

Santaguida F, Luolavirta K, Lappalainen M, Ylinen J, Voipio T, Jones S (2015) The Kevitsa Ni-Cu-PGE Deposit in the Central Lapland Greenstone Belt in Finland. In: Maier WD, Lahtinen R and O'Brien H. Mineral Deposits of Finland. Elsevier, Amsterdam, 195–210

TUKES (2015) Mining Register Map Service. http://www.tukes.fi. Accessed 11 March 2015

TUKES (2017) Mining Register Map Service. http://www.tukes.fi. Accessed 20 February 2017

Long–term pollution and impacts on local communities from defunct gold tailings deposits: a case study of Davidsonville, South Africa

Phumzile C. Nwaila
University of Cape Town, South Africa

Glen T. Nwaila
University of Würzburg, Germany

Jennifer L. Broadhurst
University of Cape Town, South Africa

Abstract. Defunct Witwatersrand gold tailings deposits pose significant environmental risks. Environmental impacts associated with gold tailings include formation of acidic water, air and land pollution, and long–term human health impacts. These gold tailings often contain elevated concentrations of deleterious elements and other soluble compounds, such as sulfate. Negative perceptions and concerns in terms of the environmental impacts continue to fuel mine–community conflicts, and currently there is insufficient evidence to support these concerns.

This study demonstrates the application of quantitative environmental analysis combined with a qualitative assessment of stakeholder perceptions of the environmental pollution and associated community, in the case of the Davidsonville area on the West Rand in Gauteng, South Africa. The results indicate that surface waters in the area of the nearby Princess tailings deposit are acidic and contain elevated levels of salts and metals, particularly Fe and Pb. Furthermore, top soils were found to be highly acidic at distances of up to 10 km from the dump. These results support negative perceptions and concerns of the Davidsonville community and external experts. These concerns highlight the need for more comprehensive and systematic monitoring, cause–effect analysis and information dissemination programmes.

1 Introduction

Gold mining has benefited South Africa in various socio–economic aspects for over a century and led to the development of metropolitan districts, such as the greater Johannesburg. Among South Africa's gold provinces, the Witwatersrand Basin is by far the largest single gold–producing province in the world. This province has produced over 53 000 t over a century of mining (Frimmel et al. 2005). The Witwatersrand goldfields are located on the edges of basin. These goldfields and mining waste disposal sites are surrounded by residential areas (both formal and informal). Consequently, many communities (e.g., Davidsonville, Soweto and Riverlea in Johannesburg) that are situated within historic and presently active goldfields run the risk of being exposed to a variety of deleterious elements emanating from the gold tailings dumps (IHRC 2016). The environmental impacts associated with gold mining and mining waste disposal include water, air and soil pollution, which may have negative implications for the health people in the surrounding communities and local flora and fauna (McCarthy 2010; Durand 2012). Certain residential areas such as Carletonville, Westonaria, Khutsong, Kagiso and Randfontein in Gauteng Province fall within areas of a high risk of radioactivity contamination from historic gold tailings (DMR 2008). Tang and Watkins (2011) estimated that 1.6 million people in South Africa live in informal settlements close to mine tailings. As highlighted in the recent report by the Harvard Law School International Human Rights Clinic (IHRC 2016), current efforts by the South African government to mitigate these legacies and associated impacts are inadequate and are failing to meet acceptable standards in term of human rights obligations. Furthermore, although there is currently a renewed interest in the reclamation of the Witwatersrand gold tailings, including those in the Davidsonville area (CRG 2016), this could in fact exacerbate the environmental impacts and gravely affect the community over the short to medium term. The on–going disputes and conflicts between government, local mining and affected communities, as well as the continued failure to implement a coordinated and effective programme to address legacy issues, is underpinned by the lack of adequate supporting data and information and inadequate stakeholder consultation and engagement, both in terms of the risks and the potential mitigation measures (IHRC 2016).

The present study was undertaken to assess the long–term environmental pollution arising from defunct gold tailings deposit and the associated effects on community quality of life, using Davidsonville as a case study (study area coordinates: 26°09'24.8"S 27°51'21.4"E). As indicated in Figure 1, the community of Davidsonville lies in close proximity to the Princess gold tailings dumps, a defunct tailings dam generated during the processing of the Witwatersrand Basin gold ore deposits. This dump covers an area of approximately 25 Ha. In the year 2006, the Department of Mineral Resources (DMR) classified 70 % of the tailings as state property, due to the lack of historic mining documents (DMR 2008). There is currently no

active deposition/dumping of new tailings on the Princess gold tailings dump. The Princess tailings dump is surrounded by the residential settlement of Davidsonville to the north and north–west, a small–scale brick and scrap metal industries to the east and south, and 9 other dormant gold tailings deposits to the south. None of the dormant tailings dumps have been rehabilitated and are often reclaimed by illegal miners (Ngigi 2009).

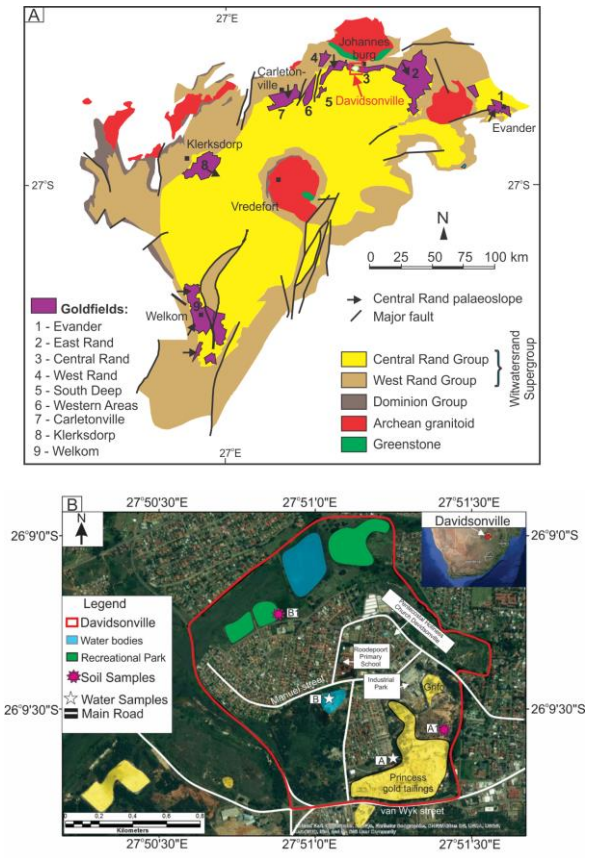


Figure 1. Locality map of the Davidsonville area showing (A) Witwatersrand Basin (modified after Frimmel et al. 2005), and (B) sampling points and key features.

The surface geology of the site is dominated by siliciclastic rocks (e.g., quartzite and conglomerates) of the Central Rand Group, a sub–division of the Witwatersrand Supergroup. These rocks sub–crop the Transvaal Supergroup chemical sedimentary rocks (e.g., dolomites). Fresh hard–rock dolomite is encountered at depths ranging from 0 to 50 m below ground (SACS 2006). A previous study by Dlamini (2014) on the mineralogical composition of the gold tailings from the study area, indicated the presence of sulfides, oxides and a variety of silicates. The site is highly susceptible to erosion which in turn results in a high sediment load that ends up in water streams, increasing the water siltation, water turbidity and decreasing the water quality around the site (Ngigi 2009).

Whilst a number of studies have been done to characterise mine tailings at source, extrapolation of these results to the surrounding environment is fraught with uncertainty and discrepancy, due to the non–linear mechanistic reaction chains, the vast number of influencing factors and the extended spatial and temporal boundaries involved (Hansen et al. 2008). Furthermore, programmes for measuring and monitoring environmental pollution appear to be limited, and the results largely confidential.

This study combines preliminary quantitative analysis of environmental samples in the Davidsonville area with a qualitative assessment of the perceptions of members from community–support organisations in terms of the impacts of the defunct tailings on the local environment and community quality of life.

2 Materials and methods

2.1 Analysis of surface water samples

Two water samples were used in this study. Sample A was sourced from the bottom channels of Princess gold tailings dump. Sample B was sourced from the Davidsonville wetland. The following water variables were measured in order to obtain detailed characteristics of the sampled water: pH, electrical conductivity (EC), total dissolved solids (TDS) and concentration of sulfate and selected metals. Concentrations of the metals Cr, Mn, Co, Ni, Cu, Zn, Mo, Ag, Cd, Bi, and Pb were analysed by inductively coupled plasma mass spectrometry (ICP–MS) (Agilent Technologies 7500 Series), whilst Fe and sulfate were analysed using a Merck Spectroquant Pharo 300 spectrophotometer and Merck reagent kits at Bureau Veritas laboratories (Johannesburg). The standard gravimetric method was used to determine TDS. Measurements such as pH and electrical conductivity were measured during field sampling using a Hanna HI9813–6 pH/EC/TDS/Temperature Meter with CAL Check™ mobile probe. Comparisons were made with South African water quality standards, in order to provide an indication of the relative impacts posed by individual elements.

2.2 Analysis of soil samples

Two soil samples were assessed in conjunction with the water samples. Sample A1 was sourced 5 km from Princess gold tailings dump. The second soil sample, B1 was sourced 10 km away from Princess gold tailings dump close to the Davidsonville wetland. The only measurement performed on these two samples was pH in a depth profile per sample, in order to assess the extent of soil acidification. The pH was measured in the field using a mobile probe. Soils in the study area are predominantly sandy loams and red and yellowish clays.

2.3 Assessment of stakeholder perceptions

Semi–structured interviews were conducted with members of a non–profit organisation concerned with protecting the rights of mining communities, as well as expert

consultants in the area of gold mining and its environmental and social impacts. During the course of the interviews, interviewees were asked to rate specific risks and impacts associated with the gold tailings deposits in the Davidsonville area, as low, moderate or high.

3 Results and discussion

3.1 Water and soil quality assessment

The results of the analysis of water quality and a comparison with current drinking water standards are presented in Table 1. The South African water quality guidelines published by the South African National Standard (SANS 241 2015) serve as the primary source of information for determining the water quality requirements of different water uses, and for the protection and maintenance of the health of aquatic ecosystems. A comparison of field results with SANS 241 drinking water standards can thus be considered as indicative of the relative impacts of the tailings on surface water quality.

Table 1. Davidsonville water quality tests results. All elements are reported in mg/L and EC in mS/m.

Determinant	SANS Limit	Concentration		Enrichment/Depletion[1]		Effect
		Sample A	Sample B	Sample A	Sample B	
pH at 25 °C	≥ 5 ≤ 9.7	2.9	3.1	0.41	0.44	Physical/ Aquatic
Acidity as H+	–	44.9	28.2	–	–	
EC at 25°C	170	368	191	2.16	1.12	Aesthetic
SO_4^{2-}	500	3089	1140	6.18	2.28	Aesthetic/ physical
TDS	1200	4712	1688	3.93	1.41	Aesthetic/ physical
Fe	0.3	627	97	2090.00	323.33	Aesthetic/ physical
Ni	0.07	2.8	1.6	40.00	22.86	Chronic Health
Pb	0.01	9.4	3.2	940.00	320.00	Chronic Health
U	0.015	0.004	0.004	0.27	0.27	Chronic Health
Zn	5	6.3	2.4	1.26	0.48	Chronic Health

The results in Table 1 indicate that both water samples are acidic, with pH values below the acceptable drinking water guidelines, and contain elevated levels of dissolved salts (specifically dissolved sulfate), and the heavy metals, including Fe, Ni, Pb and Zn, which can have adverse aesthetic, physical and toxic effects. Sample A shows higher acidity and toxic metal content when compared to that observed for sample B. This can be attributed to the closer proximity of sample A to the tailings dump. Field observations revealed that the Davidsonville area has undergone change to the extent that its hydrological system can no longer be regarded as a natural system, but rather as a man–made system. This is because the natural features such as streams and wetlands have been impacted upon by the tailings and temporal emplacements of water retention sumps and dams.

The results in Table 2 indicate that the top–soils are acidic, even at distances of up to 10 km downstream from the tailings. These pH profiles within soil samples provided an indication of the extent to which soils in this area may have been affected by mining activities and contaminated run–off from mine tailings in particular. In acidic soils heavy metals cations are most mobile resulting in metal contaminates being available for uptake by plants or to move into water courses and ultimately exposure to humans (SCU 2013; Singh and Agrawal 2008).

Table 2. Davidsonville soil pH test results.

Sample	Location	Depth	Soil colour	pH
A1	5 km from tailings	0.50 m	Yellow	3.5
B1	10 km from tailings	0.35 m	Red	2.8

3.2 Assessment of stakeholder perceptions

The average rating scores and comments in terms of the perceived risks and impacts posed by the gold tailings deposits in the Davidsonville area are summarised in Table 3.

Table 3. Stakeholders environmental risk assessment of pollution and long–term environmental impacts of gold tailings deposits in Davidsonville. Environmental impact significance: 1 = low, 2 = moderate, 3 = high risk.

Risk/Impact	Rating	Comments
Loss of land	3	Impacts future land use as the tailings take up space.
Tailings dam failure	2	Low during mining due to active maintenance and high post mining.
Land pollution and erosion	3	High impact with the added probability of elevated uranium contents particularly in the West Rand region.
Air pollution	3	Tailings are prone to dust and therefore contaminate the air.
Dust	3	Communities residing near tailings are prone to inhale and ingest dust from the tailings.
Underground water quality	1	Impacted by acid mine drainage.
Surface water quality	3	Impacted by acid mine drainage.
Human health	2	Impacted due to air pollution and dust.
Livestock production and health	2	Impacted due to water and land pollution.
Soil fertility	3	Tailings erode to agricultural land and the heavy metals being released by acid mine drainage impact the soil
Crop production and health	3	Impacted by water pollution and land pollution
Aquatic life and health	2	Impacted due to water pollution

The results in Table 3 indicate that stakeholders consider the tailings deposits to have significant impact in terms of loss of land, land pollution, air pollution and dust. The impacts on human and animal health were only

considered to be moderate. Pollution of land and surface water and the subsequent impacts on soil fertility and crop production are attributed mainly to the generation of acid mine drainage and associated release of heavy metals. Thus the potency of environmental impacts by the tailings are long–term.

4 Conclusion

Analysis of the water quality and soil pH indicate that the defunct Princess tailings deposit continues to have a negative impact on the surrounding environment over the long–term. In this regard, the main contaminants of concern are Fe, Pb and, to a lesser extent, Ni and Zn. This data supports the concerns and perceptions of local stakeholders in the Davidsonville area, indicating that environmental contamination arising from the defunct tailings dam is likely to pollute the soil and water as a result of acid mine drainage containing elevated concentrations of heavy metals. The extent of soil pollution affects the potential for crop production whereas heavy metal run–off on the Davidsonville land surface, especially during rainy seasons, could pose health risks to the community. Dust from the dump also creates a pathway for inhalation of, and skin contact with, the contaminants.

Further environmental monitoring and epidemiological studies, coupled with detailed characterization of the tailings deposit could provide a more quantitative understanding of the long–term causal effects of tailings deposits, and assist in informing mitigation approaches. Such interventions will, however, more than likely need to be accompanied by a systematic programme of information dissemination and engagement in order to overcome negative stakeholder perceptions and effectively address their concerns.

Acknowledgments

This work is based on research supported by the South African Water Research Commission (WRC). We would also like to express our thanks to the Bench Marks Foundation for assisting with sample collection and various aspects of the research. Any opinion, finding, conclusion or recommendation expressed in this material is that of the authors and the WRC does not accept any liability in this regard.

References

CRG (Central Rand Gold) (2016) Application of the environmental authorisation for a mining permit application listed in terms of the national environmental management act: EIA regulation (983) 2014 to mine gold ore on portion 167 of the farm Roodepoort 237 IQ, situated in the magisterial District of Johannesburg ref. no.: GP 30/5/1/3/2(10230) MP and GP30/5/1/3/3/2/1(10230) EM

Dlamini TC (2014) Radionuclides and toxic elements transfer the Prince Dump to the surrounding vegetation in Roodepoort South Africa: Potential radiological and toxicological impact on humans. MSc Thesis, University of North West, pp 1–177

DMR (Department of Mineral Resources) (2008) 2008/09 Annual Report. http://www.dmr.gov.za/publications/annual–report.html. Accessed on 19 March 2010

Durand JF (2012) The impact of gold mining on the Witwatersrand on the rivers and karst system of Gauteng and North West Province, South Africa. J Afr Earth Sci, 68, 24–43

Frimmel HE, Groves DI, Kirk J, Ruiz J, Chesley J, Minter WEL (2005) The formation and preservation of the Witwatersrand Goldfields, the largest gold province in the World. In: Hedenquist JW, Thomson JFH, Goldfarb R, Richards J (eds) Economic Geology 100th Anniversary Volume. Society of Economic Geologists, Littleton, Colorado, USA, pp 769–797

Hansen Y, Broadhurst JL, Petrie JG (2008) Modelling leachate generation and mobility from copper sulphide tailings – An integrated approach to impact assessment. Minerals Engineering, 21 288-301

IHRC (Harvard Law School International Human Rights Clinic) (2016) Clinic highlights human rights costs of South African gold mining. Havard Law Today. https://today.law.harvard.edu/clinic–highlights–human–rights–costs–south–african–gold–mining. Accessed on 26 February 2017

McCarthy TS (2010) The decant of acid mine water in the Gauteng city–region – analysis, prognosis and solutions. Provocations Series, Gauteng City–Region Observatory. Universities of the Witwatersrand and Johannesburg, Johannesburg

Ngigi SM (2009) Establishing Effective, Appropriate and Applicable Technologies in treating contaminated surface water as part of a rehabilitation strategy for the Princess dump in Roodepoort, West of Johannesburg. MSc thesis. University of the Witwatersrand

SACS (South African Committee for Stratigraphy) (2006) A revised stratigraphic framework for the Witwatersrand Supergroup. Council of Geoscience, Lithostratigraphic Series 42:1–7

SANS 241–1 (2015) South African National Standard. Edition 2, Water Services Act, 1997 (Act No. 108 of 1997): Regulations relating to the compulsory national standards and measures to conserve water, as published by Government Notice No. 509 (Government Gazette No. 22355) of 8 June 2001, the Foodstuffs, Cosmetics and Disinfectants Act, 1972 (Act No. 54 of 1972), the National Health Act, 2003 (Act No. 61 of 2003), the Constitution of RSA, 1996 (Act No. 108 of 1996), and the Local Government: Municipal Systems Act, 2000 (Act No. 32 of 2000)

SCU (Science Communication Unit) (2013) Science for Environment Policy In–depth Report: Soil Contamination: Impacts on Human Health. Report produced for the European Commission DG Environment, September 2013. Available at: http://ec.europa.eu/science–environment–policy

Singh A, Agrawal M (2008) Acid rain and its ecological consequences. J Environ Biol, 29(1):15–24

Tang D, Watkins A (2011) Ecologies of Gold [online], The Design Observer Group, available from: http://places.designobserver.com/feature/ecologies–of–gold–the–past–and. Accessed on 02 July 2014

Trace metal transfer in the environment: a key issue for the acceptability of mining projects

Rossi, Magali, Camizuli, Estelle, Gasquet, Dominique
EDYTEM, Université Savoie Mont-Blanc-CNRS,Chambéry, Cedex, France

Abstract. Despite low tonnages, hundreds of small Fe, Cu, Pb-Zn and other metal deposits have been mined in the French Alps from Bronze Age to the 20th century. The mining industry was quite important (several million tons of iron, 200 000 t Pb, 100 000 t Zn and 500 t Ag) and contributed to human settlement and economic development. Abandoned during the 19th and the 20th centuries, the mines and their waste dumps are subjected to alteration-lixiviation. These ancient mining districts are thus a perfect area to study long-term trace metal dispersal in the environment. Such knowledge is required to estimate possible environmental contamination of future mining activity and therefore to elaborate strategies to limit or prevent them, which is a prerequisite for new mining project. Geosciences plays a key role to estimate long-term trace metal dispersal by characterizing the geochemical background, the processes of trace metal dispersion from abiotic to biotic compartments, the ore mineralogical assemblage, and thus trace metal speciation and bio- availability. In the French Alps, trace metal dispersion was estimated at regional-scale using statistical analysis of streambed sediment. Work is in progress to assess the transfer processes at the district-scale, using soil analyses.

1 Introduction

Over the last decades, environmental issues have become more and more important for society. Contestation and rejection of mining projects is mostly related to the environmental impacts of mining activity (e.g., Rosia Montana in Romania). Therefore, for a new mining project to be accepted strong environmental guaranties are required: the potential environmental and health impacts have to be estimated and strategies to prevent and limit these impacts have to be established long in advance (sustainable mining, zero wastes policy). Observation of trace metal dispersal in ancient mining territories is a good tool to understand and predict long-term environmental impacts of future mining activity and thus on how to prevent or limit them. It provides data and arguments to contribute to the social debate and perception of a mining project, by learning from the past to protect the future. Such knowledge requires a multidisciplinary approach to understand (i) the dispersion and incorporation processes of trace metals in the environment from mineral-bearing phases to soils and sediments, (ii) the bioavailability from abiotic compartment to biota, and (iii) the environmental parameters controlling trace metals transfer (climate, topography, hydrogeology, trace metals speciation, etc.).

The present study focuses on the Northern French Alps, which experienced many phases of mining from the Bronze Age to the 20th century. A site inventory has shown that the ore deposits (Fe, Cu, Pb, Zn…) are numerous, of small size but widely spread over all the territory. Long-term dispersal of trace metals in the environment is studied by comparing geochemical anomalies with the location of ancient mines. Geochemical anomalies are computed from the available streambed sediment database of the French Geological Survey (BRGM). These sediments represent composite erosion products of rocks outcropping in the catchment area. Their statistical analysis may help to discriminate background to positive geochemical anomalies characterizing areas with high ore deposit potential (Reimann et al. 2008).

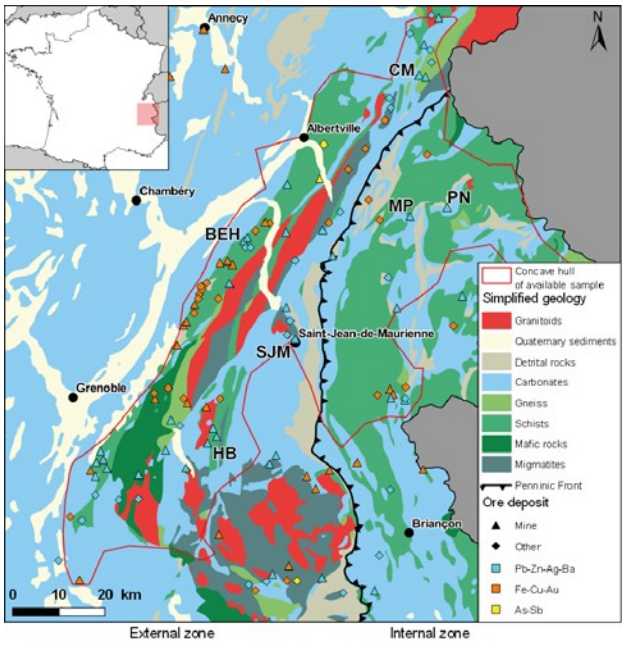


Figure 1. Simplified geological map of the Northern French Alps (One Geology data) showing the location of the ancient mines (triangles) and other ore deposits (diamonds; data from the BRGM sigmines database). BEH: Bourget en Huile, CM : Contamines-Montjoie, HB: Huez-Brandes, MP: Macôt-La Plagne, PN: Peisey-Nancroix, SJM: Saint Jean de Maurienne.

2 Ore deposits and ancient mining activities in the northern French Alps

2.1 Geological setting and ore deposits

The complex Variscan and Alpine orogeneses were associated with fluid flows that were locally responsible for metal concentrations. However, the distribution and size of ore deposits is very heterogeneous depending of the geological setting. If the Eastern Alps host some world class Fe-Cu-Sn deposits still operated as open pits, the

French Alps are characterized by numerous and disseminated small size ore deposits. In the study area, the Northern French Alps, about 150 ore deposits have been reported by the BRGM (Fig. 1).

Iron ore and base-metal deposits (Cu, Pb-Zn-Ag) are the most common in the French Alps. With the exception of some siderolitic iron ores, most deposits occur as vein-type or stratiform mineralisation. They are mainly hosted in the external crystalline massifs or in sediments, at the Permian-Triassic transition, and in Carboniferous rocks of the external Alps (Fig. 1; Meloux 1975; Rossi and Gasquet 2014). Therefore, most ore deposits result from hydrothermal activity associated with the Variscan and Alpine orogenic cycles.

2.2 Past mining activities

The abundance of ore deposits of various metal contents and the development of mining activity strongly contributed to human settlement of the Alps for more than 2 000 years (e.g., Schibler et al. 2011; Py et al. 2014). The mining activity reached its maximum during Middle Age and the 19th century, as evidenced by lead records in lake sediments (e.g., Arnaud et al. 2005; Giguet-Covex et al. 2011; Py et al. 2014). Mining activities contributed to the economic development of alpine territories. Several hundred up to a couple thousand people were employed for the ore extraction and processing. If many local peasants worked in the mines during winter times, the largest mines (Peisey-Nancroix, St-Georges d'Hurtières, …) benefited from immigration of specialists workers and engineers mainly from Italy, Austria, England and Germany. The activity started to decline at the end of the 19th century due to (i) resource depletion in some districts, (ii) the difficulties and costs of operating in high-altitude (most mines are located above 1 500 m. asl.), and (iii) the discovery of world-class deposits with higher metal content and where metal treatment was possible. In France, the last Fe-mine closed in the 1930s and the last Pb-Zn mine closed in the 1970s.

If most mines were artisanal and small-scale underground mines, a few districts were much more important: (i) the Macôt-La Plagne mine was the third provider of French Pb-Ag in the 20th century (total estimate 126 kt Pb and 558 t Ag; Meloux 1975), (ii) the Huez/Brandes district was the most important medieval Pb-Ag exploitation zone in the French Alps, and (iii) the St-Georges d'Hurtières district provided 1.5Mt siderite and more than 10 000 t chalcopyrite between Middle Age and the XXth century. Meloux (1975) estimated that several millions tons of iron, 200 000 t of Pb, 100 000 t of Zn and 500 t of Ag have been mined in the Alps.

3 Streambed sediment analyses

3.1 The BRGM geochemical database

During the 1980s, the BRGM performed a large prospection campaign in the French Alps, from streambed sediment, that led to the collection of 6 892 samples in the study area (Lambert 2005). The entire geochemical dataset is available online at http://sigminesfrance.brgm.fr "Géochimie Inventaire BRGM" database. Concentrations of As, Cd, Cr, Cu, Ni, Pb and Zn show a very positive skewness and locally reach very high values (Table 1). Several statistical methods were used to identify geochemical anomalies that can either reflect a natural contamination (e.g., geology, ore deposits occurrence) or an anthropic contamination (such as mining activity).

Table 1. Descriptive statistics for As, Cd, Cr, Cu, Ni, Pb and Zn concentration for the Northern French Alps (BRGM dataset).

(mg.kg^{-1})	As	Cd	Cr	Cu	Ni	Pb	Zn
LOD	20	2	10	10	10	10	10
%cen	14	93	1	6	3	1	1
Median	42	nc	60	32	40	43	112
Mean	59	nc	71	39	49	66	138
Maximum	1076	45	1700	1530	1571	8900	8190
Skewness	5.66	nc	8.98	14.33	11.92	23.93	23.99

%cen: percentage of samples below the limit of detection (LOD). nc: not calculated.

3.2 Elemental approach

The exploratory data analysis (EDA) is a method statistically robust to the presence of outliers and analytical errors (Monna et al. 2014; Reimann et al. 2008). A transformation procedure was applied to the geochemical data, before computing threshold by EDA, to compare samples from various lithological units. Data were divided in seven groups; the group called "far outliers" allows identification of positive trace metal anomalies (Fig. 2 for lead anomalies).

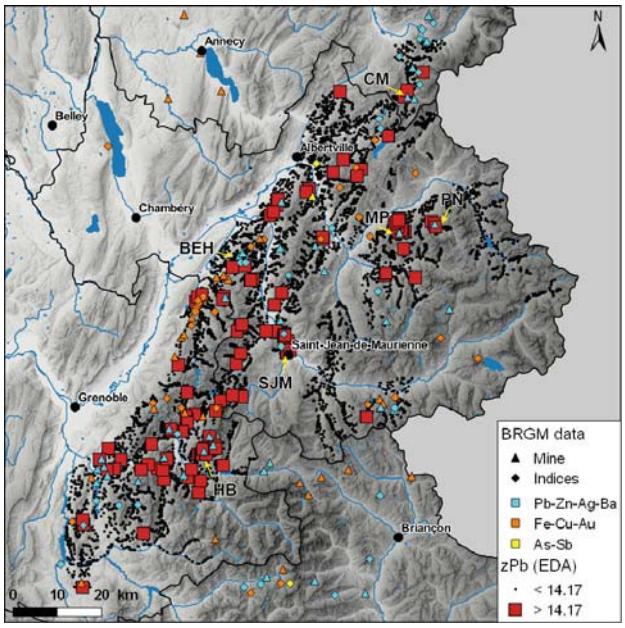


Figure 2. Map of lead anomalies in streambed sediments (zPb > 14.17) and location of the base metal mines reported by the BRGM. See Fig. 1 for abbreviations.

Fig. 2 shows that lead anomalies are very localized, which exclude the effect of geology. Most anomalies are located downstream ore deposits and ancient base metal mines. Downstream the largest mines and mining districts, Pb anomalies are systematics (e.g., Macôt-La Plagne, Peisey-Nancroix, Saint-Jean de Maurienne, Bourget en Huile, Huez/Brandes and Contamines-Montjoie). In places were the anomalies are apparently disconnected with any known ore deposits, field prospection is required in order to determine the origin of the anomalies.

3.3 Multi-elemental approach

The multi-elemental approach is based on the calculation of a sediment quality index (SQI) computed from trace metal concentrations. It describes the overall quality of the streambed sediments when compared to guideline values. The present study uses the "Probable Effect Concentrations" (PEC; MacDonalds et al. 2000) to identify the contaminant concentration above which harmful effects on sediment-dwelling organisms are expected to occur frequently.

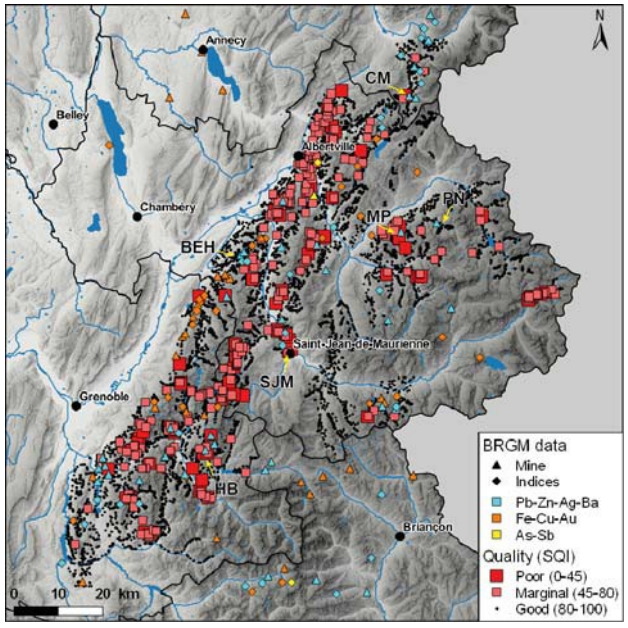


Figure 3. Map of the Sediment Quality Index (SQI) and location of the base metal mines reported by the BRGM. See Fig. 1 for abbreviations.

In the Northern French Alps, “poor” and “marginal” quality represent 1.38% and 3.93% of the analyzed streambed samples, respectively (Fig. 3). The SQI approach allows identification of new areas that were not evidenced from elemental approach. In some cases, these areas are clearly related to the geological background: e.g., in the vicinity of Albertville, the large cluster of “marginal” and “poor” SQI is related to the occurrence of As-rich schists. Similarly, SE of Grenoble, the observed cluster is rather well related to mafic rocks. More localized data are either related to the occurrence of mines or of ore deposits.

In some places no occurrence of mine nor ore deposits have been reported, but the presence of a downstream SQI gradient suggests the occurrence of an unknown ancient mine. However, some areas that showed a lead anomaly have a rather good SQI indicating the limited dispersal of trace metals related to the size of the exploitation (e.g., Peisey-Nancroix).

4 Soil analyses

Geochemical mapping of trace metals in topsoils is required in order to estimate their dispersal in a mining district. Preliminary portable-XRF data indicate that trace metals are still quite abundant several decades to more than 150 years after mine closure. In Peisey-Nancroix (mine closed in the 1860s) the Pb content of topsoils exceeds 200 ppm, and a geochemical gradient is observed around the ore treatment area (up to 10% Pb in waste dumps; Fig. 4). However, SQI results suggest that the dispersal is limited.

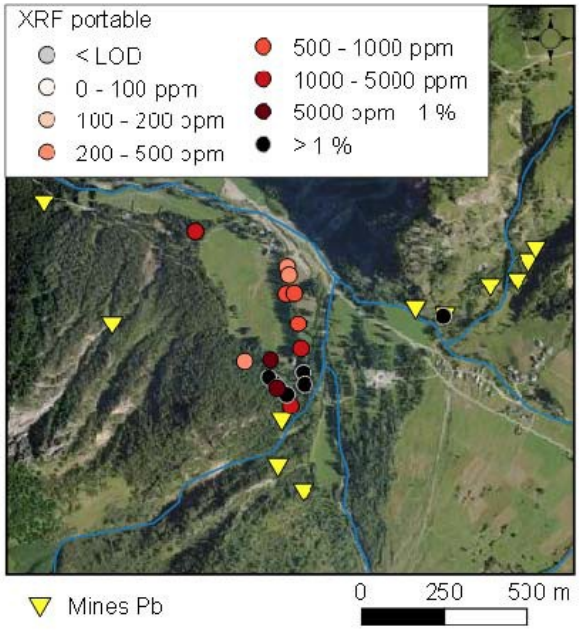


Figure 4. Map of the Peisey-Nancroix Pb-Ag mine, showing the position of the gallery entrances (triangles) and the Pb content of surface soils determined using a portable XRF.

In Macôt-La Plagne, 45 years after the mine closure and the development of a skiing resort right on top of the mining settlement, topsoils still contain more than 1 000 ppm of Pb. In the vicinity of the ancient ore treatment plant, vegetable gardens contain between 2 000 and 4 500 ppm of Pb, despite the supply of uncontaminated earth. Such values are higher than the intervention threshold in the Netherlands (Lynden et al. 2004). However, high trace metal content in soils does not necessarily imply a pollution or danger for human health (e.g., Peijnenburg et al. 2002). Indeed, the speciation and bioavailability have to be established in order to determine

whether trace metals hosted in topsoils can be incorporated into biota. This work is in progress for the study area.

5 Transfer to biota

Transfer from abiotic compartments to biota depends on the biological characteristics of targeted organisms as well as on the bioavailability of the metal, which is influenced by the physico-chemical properties of both the pollutant and the medium (Gestel 2008). On sites that have been contaminated, but are no longer subjected to polluting activities, bioavailability may have drastically decreased due to various physico-chemical processes that immobilize metals in abiotic compartments (Lock and Janssen 2003). Bioavailability is thus a key issue; characterization of trace metal speciation will provide evidence on metal mobility and transfer to biota and up to the trophic chain. In the Northern French Alps, in-situ study of trace metal effects on the functioning of the environment, and on metal speciation is planned. The origin of lead poisoning in big game and bearded vulture communities (*Gypaetus barbatus*) is also investigated. It could be related to ingestion of lead-bearing shot bullets or to mine waste exposure (Sileo et al. 2001; Pain et al. 2009).

The ore mineralogical association is a parameter influencing metal speciation: the occurrence of pyrite can lead to sulfide leaching (e.g. Giéré et al. 2003) and precipitation of soluble secondary phases. Therefore, characterization of ore deposits is of primary importance.

6 Discussion/conclusion

Estimation of long-term environmental impact of mining activity requires very good knowledge of (i) trace metal transfer processes between the various abiotic compartments of the environment, and from abiotic compartments to biota, (ii) the role of the ore mineralogical association, (iii) the climatic and topographic control of trace metal mobility and alteration, as well as (iv) the microbial effect of ore leaching. The multiplication of observation studies in various ancient mining territories, in terms of climatic and topographic conditions, nature of the ore mineralogical assemblage, ore treatment processes, etc. will constrain the conditions of trace metal transfer in the environment.

Realistic scenarios of the future impact of new mining project can be anticipated, and strategies (i) to limit or prevent these impacts, and (ii) for waste dump management can then be proposed. Acceptability and perception of new mining project will depend on the liability of these scenarios and on the strategies to prevent and limit the environmental impacts.

Acknowledgements

This study is supported by the University of Savoie Mont-Blanc (TraMines project) and by the French national program EC2CO-Biohefect of the CNRS (TRACES project).

References

Arnaud F, Serralongue J, Winiarski T, Desmet M, Paterne M (2005) Pollution au plomb dans la Savoie antique (II-IIe s. apr. J.-C.) en relation avec une installation métallurgique de la cité de Vienne. C.R.A.S. Geoscience 338: 244-252

Gestel van CAM (2008) Physico-chemical and biological parameters determine metal bioavailability in soils. Sciences of the Total Environment 406: 385-395

Giéré R, Sidenko NV, Lazareva EV (2003) The role of secondary minerals in controlling the migration of arsenic and metals from high-sulfide wastes (Berikul gold mine, Siberia). Applied Geochemistry 18: 1347-1359

Giguet-Covex C, Arnaud F, Poulenard J, Disnar JR, Celhon C, Francus P, David F, Enters D, Rey PJ, Delannoy JJ (2011) Changes in erosion patterns during the Holocene in a currently treeless subalpine catchment inferred from lake sediment geochemistry (Lake Anterne, 2063 m a.s.l., NW French Alps): The role of climate and human activities. Holocene 21: 651-665

Lambert A (2005) Les données géochimiques et alluvionnaires de l'Inventaire minier du territoire national. Constitution d'une base de données exhaustive. BRGM final report RP-53546-FR, Orléans

Lock K, Janssen CR (2003) Influence of aging on copper bioavailability in soils. Environmental Toxicology Chemistry 22: 1162-6

Lynden van GWJ, Mantel S, Oostrum van A (2004) Guiding principles for the quantitative assessment of soil degradation – with a focus on salinization, nutrient decline and soil pollution. Rome: Food and Agriculture Organization of the United Nations, 73p

MacDonalds DD, Ingersoll CG, Berger TA (2000) Development and Evaluation of Consensus-Based Sediment Quality Guidelines for Freshwater Ecosystems. Archives of Environmental Contamination and Toxicology 39(1): 20-31

Meloux J (1975) Alpes – Nord : Bilan synthétique de dix années de prospection. BRGM report n°75 RME 023 FE, 104p

Monna F, Camizuli E, Nedjai R, Cattin F, Petit C, Guillaumet J.P, Jouffroy-Bapicot I, Bohard B, Chateau C, Alibert P (2014) Tracking archaeological and historical mines using mineral prospectivity mapping, Journ. of Archaeological Science, 49: 57-69

Pain DJ, Fisher IJ, Thomas VG (2009) A global update of lead poisoning in terrestrial birds from ammunition sources. In Watson RT, Fuller M, Pokras M, Hunt WG (eds) Ingestion of Lead from Spent Ammunition: Implications for Wildlife and Humans. The Peregrine Fund, Boise, Idaho, USA, 99-118

Peijnenburg W, Sneller E, Sijm D, Lijzen J, Traas T, Verbruggen E (2002) Implementation of bioavailability in standard setting and risk assessment? Journal of Soils and Sediments 2: 169-173

Py V, Véron A, Edouard JL, de Beaulieu JL, Ancel B, Segard M, Durand A, Leveau P (2014) Interdisciplinary characterisation and environmental imprints of mining and forestry in the upper Durance valley (France) during the Holocene. Quarternary International 353: 74-97

Reimann C, Filzmoser P, Garrett R, Dutter R (2008) Statistical data analysis explained: applied environmental statistics with R. John Wiley & Sons, Chichester, Great Britain

Rossi M, Gasquet D (2014) Panorama géologique des exploitations minières dans les Alpes françaises. Collection EDYTEM 17: 23-40

Schibler J, Breitenlechner E, Deschler-Erb S, Goldenberg G, Hanke K, Hiebel G, Hüster Plogmann H, Nicolussi K, Marti-Grädel E, Pichler S, Schmidl A, Schwarz S, Stopp B, Oeggl K (2011) Miners and mining of the Late Bronze Age: a multidisciplinary study from Austria. Antiquity, 85: 1259-1278

Sileo L, Creekmore LH, Audet DJ, Snyder MR, Meteyer CU, Franson JC, Locke LN, Smith MR, Finley DL (2001) Lead poisoning of waterfowl by contaminated sediment in the Coeur d'Alene River. Archives of Environmental Contamination and Toxicology, 41:364–368

S12 – Gem research: Beautiful windows into Earth's interior

Convenors:
Daniel Marshall
Lee Groat
Gaston Giuliani

Origin of scapolite-hosted sapphire near Kimmirut, Baffin Island, Nunavut, Canada

Philippe M. Belley, Tashia J. Dzikowski, Andrew Fagan, Jan Cempirek, Lee A. Groat, James K. Mortensen
University of British Columbia, Vancouver, Canada

Mostafa Fayek
University of Manitoba, Winnipeg, Canada

Gaston Giuliani
Université de Lorraine, France

Anthony E. Fallick
Scottish Universities Environmental Research Centre, U.K.

Abstract. Gem-quality corundum (sapphire) occurs in scapolite-rich calc-silicate rock hosted in marble of the Lake Harbour Group near Kimmirut, southern Baffin Island. A deposit of blue and colourless gem corundum (Beluga occurrence) is compared to a similar calc-silicate pod generally lacking corundum but containing nepheline (Bowhead occurrence) and located 170 m to the SSW. Corundum formation was made possible by three equally important sequential metamorphic reactions: (1) formation of nepheline, diopside, and K-feldspar (inferred) at granulite facies peak metamorphic conditions; (2) partial retrograde replacement of the peak assemblage by phlogopite, oligoclase, calcite, and scapolite (Me_{50}-Me_{67}) as a result of CO_2-, H_2O-, Cl-, F-bearing fluid influx; and (3) retrograde breakdown of scapolite + nepheline (with CO_2- and H_2O-bearing fluid) to form albite, muscovite, corundum, and calcite. Late, low-temperature zeolite mineralization is common in corundum-bearing zones. Oxy-dravite $\delta^{11}B$ is +3.9 ± 0.7‰. The oxygen isotope composition of corundum ($\delta^{18}O_{VSMOW}$) is 16.4 ± 0.1‰.

1 Introduction

Gem-quality blue corundum (sapphire) accounts for a significant portion of the gemstone market and prices continue to rise in response to demand (Shor & Weldon 2009, Genis 2016). For this reason, there is considerable interest in understanding the genesis of gem-quality corundum so as to constrain the environments in which it forms and produce exploration methodologies that will aid in the development of a Canadian colored gemstone industry that will be competitive on the world market.

Gem corundum deposits have been found in syenite, monzonite, kimberlite, lamprophyre, basalt (xenocrysts), gneiss, amphibolite, marble, skarn, and various contact metasomatic rocks (Simonet et al. 2008, Giuliani et al. 2014). Gem-quality blue and colorless corundum was discovered in 2002 near Kimmirut, southern Baffin Island, Nunavut, Canada, and subsequent exploration led to the discovery of blue, colorless, yellow, and pink gem corundum showings. These occurrences are the first reported examples of gem corundum hosted in scapolite-rich calc-silicate pods in marble. The present study examines two calc-silicate pods, the Beluga deposit, which is blue-corundum-bearing, and the Bowhead occurrence, a nearby calc-silicate pod in which corundum is rare, with the objective of determining the cause and timing of mineralization, and the nature of the protolith.

2 Regional geology

The Beluga and Bowhead calc-silicate pods are hosted by a sequence of marble and calc-silicate rock structurally overlying garnet psammite, semipelite, pelite, and rare orthoquartzite. The marble, calc-silicate rock, and metaclastic rocks form the Lake Harbour Group (LHG) supracrustal suite (Scott 1997, Scott et al. 2002). Prograde granulite facies metamorphism (M_{1A}; 810 °C, 8.0 kbar) occurred ca. 1849 – 1835 Ma and retrograde upper amphibolite metamorphism (M_2; 720°C, 6.2 kbar) occurred ca. 1820 – 1813 Ma (St-Onge et al. 2007).

3 Previous studies

LeCheminant et al. (2005) suggested that calc-silicate rocks at Beluga and Bowhead occurrences formed from a desilicated syenitic magma emplaced in marble late in the D2 deformation event, where corundum formed from the retrograde metamorphism of a nepheline-bearing assemlbage. In a study of nepheline-bearing LHG metacarbonates on Aliguq Island, Butler (2007) determined that nepheline-K-feldspar, a possible precursor for corundum-bearing rocks outside his study area, formed late based on textural relations with forsterite, diopside, and phlogopite. Butler (2007) proposed that this assemblage formed at peak metamorphic conditions (*ca*. 800 °C and 8 kbar) and $X_{CO2} \leq 0.15$. Dzikowski (2013) suggested that the protolith for the Beluga and Bowhead calc-silicate pods was evaporite-black shale.

In this study, we re-evaluate the data presented by Dzikowski (2013) with additional isotopic and petrographic data, and apply the results to refine interpretations on the origin and petrogenesis of gem corundum in Kimmirut-type deposits.

4 Methods

The chemical composition of minerals was determined using electron probe microanalysis (EPMA). Boron isotopes in tourmaline were measured with secondary ion mass spectrometry (SIMS) using a procedure similar to Chaussidon & Albarede (1992). Oxygen isotopes in corundum were measured using the laser fluorination method of Giuliani et al. (2005).

5 Results

5.1 Outcrop description

The Beluga (N 62.828734°, W 69.894072°) and Bowhead (170 m to the SSW) showings are marble-hosted calc-silicate pods with surface exposures of 4.2 × 3.7 m and 2 × 1.5 m, respectively. Contacts with the host marble are sharp, with the exception of parts of the Beluga pod, where euhedral crystals of diopside and scapolite occur in very coarse calcite between the calc-silicate rock and marble.

5.2 Petrography and mineral compositions

Beluga occurrence. The calc-silicate rock at Beluga is coarse to very coarse-grained (5 mm to > 5 cm) and commonly consists of randomly oriented centimeter-scale crystals. The calc-silicate rock can be divided into three distinct mineral assemblages: (1) dark areas composed of phlogopite, oligoclase, diopside, and subordinate calcite; (2) light-colored, scapolite-rich zones, where scapolite is frequently altered to a mixture of fine-grained silicate minerals, generally separating the first assemblage from the corundum-bearing assemblage; and (3) pods or zones of light-colored corundum-albite-muscovite-calcite assemblage containing small amounts of graphite and pyrrhotite.

Fe-, F-, and Ti-bearing phlogopite and oligoclase (Ab_{80}) occur as oriented intergrowths forming coronae around diopside (0.31 Al *pfu*, 0.12 Na *pfu*). The replacement of diopside by phlogopite-oligoclase is substantial (*ca.* 30-80%) with considerable local variation. Minor calcite is present in the coronae and is infrequently visible in hand sample. Titanite, zircon, and apatite are uncommon.

Anhedral, very coarse grained scapolite (Me_{50}-Me_{62}; 0.014 SO_4 *pfu*). Much of the scapolite is pervasively replaced by milky white, fine-grained mixtures of the following mineral phases, identified *via* X-ray powder diffraction: albite with variable quantities of prehnite, analcime, and thomsonite, and small amounts of calcite and muscovite. Uncommon, microscopic fractures cutting scapolite contain albite, calcite, and probable Mg-chlorite; other such fractures contain analcime. Unaltered scapolite fluoresces bright yellow when exposed to long- and short-wave ultraviolet radiation. Pristine scapolite, easily seen when exposed to UV, is generally restricted to the periphery of phlogopite-oligoclase mineralization and as isolated 'pods' within the leucocratic zones, where intensely altered scapolite is always contiguous to corundum-bearing zones. Phlogopite crystals associated with scapolite, occurring on the periphery of phlogopite-oligoclase intergrowths, have well-developed basal faces and no embayed grain boundaries with scapolite, which suggests that these minerals form a stable assemblage.

Small pods and zones, ranging in size from 0.5 × 1 cm to more than 4 × 10 cm, are composed of end-member albite (Ab_{98}), muscovite, idiomorphic blue corundum, subordinate graphite and pale-yellow calcite, and uncommon pyrrhotite. Oxy-dravite ($\delta^{11}B = 3.9 \pm 0.7‰$) occurs very uncommonly at Beluga, as crystals up to 32 mm in length. The corundum-bearing zones locally constitute up to 70% of the rock volume. Parts of the calc-silicate rock with high abundance of phlogopite-oligoclase-diopside (~90% of rock volume) tend to have little or no corundum mineralization. The corundum-bearing zone contains open cavities where the rock surface, including euhedral corundum, is entirely covered by thomsonite, analcime and calcite. LeCheminant et al. (2005) noted thomsonite seemingly penetrating a corundum crystal. The surface of those corundum crystals enclosed in albite-muscovite-calcite and those enclosed in thomsonite are identical in morphology and show no corrosion or alteration.

The corundum crystals ($\delta^{18}O_{VSMOW} = 16.4 \pm 0.1‰$) are euhedral and tapered along the c axis. Most crystals have dimensions in the range of 8 - 14 mm long and 1 – 4 mm wide, but larger crystals are not infrequent (2-4 cm long). The largest crystal recovered intact at Beluga measured 7.7 × 2.1 cm (LeCheminant et al. 2005). The corundum is royal blue, dark blue, or dark greyish blue in hand sample. When observed in cut cross-sections or gemstones, the corundum varies from colorless and light blue to bright blue, dark blue, or dark blue with a grey tinge in oscillatory and sector zoning patterns. The corundum has good transparency and is sparsely included by calcite and apatite. Gem quality is principally controlled by the degree of fracturing. The corundum at Beluga contains an average of 0.08 wt.% TiO2 (range 0.00 – 0.30 wt.%) and 0.07 wt.% FeO (range 0.02 – 0.13 wt.%).

Rare rutile, sanbornite, thorianite, monazite, and uraninite are noted from the Beluga calc-silicate pod (Dzikowski 2013, LeCheminant et al. 2005).

Bowhead occurrence. Mineralization in the Bowhead calc-silicate pod is relatively similar to that at Beluga with the notable exception that it is largely devoid of corundum mineralization whereas nepheline is common. LeCheminant et al. (2005) noted trace corundum in the surface exposure. The rock at Bowhead is composed of coarse to very coarse-grained phlogopite-oligoclase intergrowths (partly replacing diopside), diopside, scapolite, calcite, and nepheline. The diopside and phlogopite at Bowhead are slightly poorer in Ti and Fe relative to Beluga. The oligoclase is slightly more calcic than that at Beluga (Ab_{76}), and scapolite shows the same trend (average Me_{60}, range Me_{50}-Me_{67}). Both nepheline and scapolite have irregular curved boundaries with

calcite. Some scapolite grains appear to embay nepheline, but the contact relationship is unclear. One nepheline grain observed in thin section is entirely surrounded by scapolite. Multiple nepheline grains are in contact with phlogopite-oligoclase intergrowths bordering diopside. The extent of diopside replacement by phlogopite-oligoclase in the nepheline-bearing Bowhead samples (~15-30%) is inferior to the average level of replacement at Beluga and calcite is a major component of the nepheline-bearing rock, whereas it is less abundant at Beluga. A single, 50 µm-wide nodule of muscovite and end-member albite (Ab_{98}) was found in scapolite.

6 Discussion

6.1 Paragenetic sequence

Butler (2007) suggested the following possible nepheline-forming reactions for rocks on Aliguq island:

dolomite + albite → diopside + nepheline + 2 CO_2 (1)

phlogopite + 3 calcite + 3 albite → 3 diopside + 3 nepheline + K-feldspar + 3 CO_2 + H_2O (2)

Based on the inclusion of nepheline by diopside, phlogopite, and forsterite, Butler (2007) ruled out reaction (1), since it occurs at lower metamorphic grade than a forsterite-bearing assemblage. The implied late formation of nepheline and its intergrowth with K-feldspar led Butler (2007) to infer that nepheline formed from reaction (2). A thermodynamic model of the reaction presented by Butler (2007) suggests that at 8 kbar pressure, reaction 2 only occurs at $X_{CO2} < 0.15$. This seems unlikely because the reaction produces CO_2 at a ratio of 3:1 relative to H2O, and therefore the reaction would be self-limiting under these P-T conditions unless X_{CO2} was buffered by a large supply of H_2O-dominant metamorphic fluid. In the Beluga and Bowhead calc-silicate pods, the breakdown of diopside to a mixture of phlogopite, oligoclase, and calcite clearly implies the retrograde reversal of the peak metamorphic assemblage in reaction 2 and is most consistent with the bulk rock composition. Potassium feldspar was not observed in samples from Beluga or Bowhead, but it has been noted in other corundum-bearing calc-silicate pods in the area (Hansen 2008). Thermodynamic modeling of reaction 1 in TWQ v1 (Berman 1988, 1991) places the phase boundary at ~950 °C for 8.0 kbar pressure, far higher in temperature than the determined value for peak metamorphic grades, approximately 810°C (St-Onge et al. 2007). We suggest that error in the thermodynamic properties of minerals used by TWQ may overestimate the P-T conditions in which the nepheline-bearing assemblage is stable, especially since the properties of nepheline used in the thermodynamic data base are preliminary/unpublished data and were not available for comparison with published experimental thermodynamic data. For example, a solution calorimetric study suggests that the thermodynamic properties of nepheline should be considered in a ternary nepheline-kalsilite-$\square^{Si}$ (Si-site vacancy) system, where vacancies at the Si site have an effect on thermodynamic behavior that far outweighs the importance of pressure (Hovis & Roux 1993).

The extent to which the retrograde mineral assemblage replaces the peak assemblage (*i.e.* reversed reaction [2]) is dependent on the availability of CO_2 and H_2O in fluids introduced during this episode of retrograde metamorphism.

Scapolite appears stable with phlogopite since the phlogopite crystals possess well-developed basal faces, and neither mineral embays the other: thus we infer that the scapolite is part of the phlogopite-oligoclase-calcite assemblage, although since it is not present within the phlogopite coronae, it may have formed slightly later from destabilization of nepheline not consumed in the phlogopite-forming reaction. The higher X_{Ca} of scapolite (Me_{50-67}) relative to oligoclase (An_{19-24}) is consistent with compositional data for coexisting scapolite-plagioclase pairs in metamorphic rocks, but F and Cl contents of phlogopite ($X_{Mg} \approx 0.93$, F ≈ 1.39 – 1.96 wt.%, Cl = 0.02 wt.%) are significantly different from values in biotite associated with scapolite in these metasediments ($X_{Mg} \approx$ 0.6, F ≈ 0.6 wt.%, Cl ≈ 0.2 wt.%; Mora & Valley 1989). The relationship between calcite, scapolite, and nepheline near Kimmirut is not abundantly clear since nepheline is in contact with calcite at the Bowhead occurrence. The availability of NaCl in fluid stabilizes scapolite relative to plagioclase in the presence of calcite (Ellis 1978), but the effect of fluid Cl content on the relative stability of nepheline-scapolite-calcite is unknown. In corundum-bearing calc-silicate rock at Pitcairn, New York, rims of NaCl-bearing scapolite separating nepheline from calcite or apatite imply the formation of scapolite from the reaction of nepheline with calcite or apatite and CO_2- and Cl-bearing fluid (P.M. Belley, unpublished data). We suggest that scapolite formation at Beluga and Bowhead may have been limited by Cl availability, whereas fluid Na content may not be a controlling factor since the nepheline is Na-rich. Therefore, the extent of scapolite formation at the expense of nepheline and calcite may be controlled by the availability of Cl introduced to the system concomitant with CO_2- and H_2O-influx during retrograde metamorphism.

Pods and zones of albite, muscovite, calcite, and corundum are always surrounded by pervasively albitized (Ab_{98}) scapolite. A similar phenomenon is observed on a centimetre scale around small corundum-bearing zones in scapolite at Pitcairn, New York, but muscovite is not present at this locality (P.M. Belley, unpublished data). This consistent spatial relationship, together with the presence of calcite in the fine-grained alteration, suggests that the carbonate-bearing scapolite is a reactant in corundum-forming reaction (3), below. Reaction (3) excludes graphite and pyrrhotite, two minerals occurring in the corundum-bearing assemblage at Beluga which probably formed as a result of carbonate and sulphate

(released from scapolite breakdown) reduction, respectively.

Scapolite (Me_{57}) + 0.84 nepheline + 0.60 H_2O + 2.02 CO_2 → 0.76 corundum + 2.35 calcite + 2.14 albite + 0.60 muscovite + 0.66 Cl (3)

Reaction (4), an approximation of reaction (3), was modeled in TWQ:

meionite + 3 nepheline + 3 CO_2 → 3 corundum + 4 calcite + 3 albite (4)

The phase boundary for reaction (4) is in the 650-700 °C range for 2.5-4 kbar pressure. The phase boundary temperature for the breakdown reaction of scapolite and nepheline with CO_2 is probably overestimated by the TWQ thermodyamic model, since Kimmirut scapolite is richer in Na (Me_{50-67}) and end-member meionite becomes stable at higher temperature relative to Na-bearing scapolite (Goldsmith & Newton 1977). Moreover, the TWQ modeled reaction does not take into account the formation of muscovite, an important constituent of the albite-calcite-corundum assemblage at Beluga, however this may not be an important control on mineralization, since muscovite is absent in a similar retrograde corundum-calcite-albite assemblage at Pitcairn, NY.

Conclusions

Sapphire genesis in Kimmirut-type deposits is made possible by granulite facies peak metamorphism and two subsequent amphibolite retrograde metamorphic events. In the Lake Harbour Group, the most prospective areas for gem corundum exploration are expected to be contiguous to the thrust fault separating the LHG and Narsajuaq terranes, where the retrograde, amphibolite facies overprint of the granulite peak assemblages is most pervasive.

Acknowledgements

We are very grateful to the staff and management of True North Gems Inc. for granting access to the area, providing data, maps, and for discussions about the geology. Additional assistance was provided by B. Wilson, A. Brand, A. Cade, R. Sharpe, G. Robinson, and D.J. Lake. Access to Inuit Owned Land was granted by the Qikiqtani Inuit Association and the community of Kimmirut. Financial support was provided by the Northern Scientific Training Program in the form of a grant to PMB, and by the Natural Sciences and Engineering Research Council of Canada in the form of a Discovery Grant to LAG.

References

Berman RG (1991) Thermobarometry using multiequilibrium calculations: a new technique with petrologic applications. Canadian Mineralogist 29:833-855.

Berman RG (1988) Internally-consistent thermodynamic data for minerals in the system Na_2O-K_2O-CaO-MgO-FeO-Fe_2O_3-Al_2O_3-SiO_2-TiO_2-H_2O-CO_2. Journal of Petrology 29:445-522.

Butler JP (2007) Petrogenesis of nepheline- and scapolite-bearing metacarbonates from southwestern Baffin Island, Nunavut, Canada. B.Sc. thesis, Dalhousie University, Halifax, Nova Scotia, Canada.

Chaussidon M, Albarède F (1992) Secular boron isotope variations in the continental crust: An ion microprobe study. Earth and Planetary Science Letters 108:229–241.

Dzikowski TJ (2013) A comparative study of the origin of carbonate-hosted gem corundum deposits in Canada. Doctoral thesis, University of British Columbia, Vancouver, B.C., Canada. 259 p.

Ellis DE (1978) Stability and phase equilibria of chloride and carbonate bearing scapolites at 750 °C and 4000 bar. Geochimica et Cosmochimica Acta 42:1271-1281.

Genis R (2016) Retail gemstone price trends (1975-2015). The Gemstone Forecaster 34. http://www.preciousgemstones.com/gfspring16.html ; Retrieved 20 December, 2016.

Giuliani G, Fallick AE, Garnier V, France-Lanord C, Ohnenstetter D, Schwarz D (2005) Oxygen isotope composition as a tracer for the origins of rubies and sapphires. Geology 33:249-252.

Giuliani G, Ohnenstetter D, Fallick AE, Groat LA, Fagan AJ (2014) The geology and genesis of gem corundum deposits. *In* Geology of Gem Deposits (L.A. Groat, ed.). Mineralogical Association of Canada short course volume 44 (29-112).

Goldsmith JR, Newton RC (1977) Scapolite-plagioclase stability relations at high pressures and temperatures in the system $NaAlSi_2O_8$-$CaAl_2Si_2O_8$-$CaCO_3$-$CaSO_4$. American Mineralogist 62:1063-1081.

Hansen M (2008) A comparison of sapphire bearing and non-sapphire bearing lenses from the Lake Harbour Group, south-eastern Baffin Island. B.Sc. thesis, Carleton University, Ottawa, Ontario, Canada. 61 p.

Hovis GL, Roux J (1993) Thermodynamic mixing properties of nepheline-kalsilite crystalline solutions. American Journal of Science 293:1108-1127.

LeCheminant AN, Groat LA, Mortensen JK, Gertzbein P, Rohtert W (2005) Sapphires from Kimmirut, Baffin Island, Nunavut, Canada. Geochimica et Cosmochimica Acta 69, 10, supplement 280, Abstracts of the 15th annual V.M. Goldschmidt conference.

Mora CI, Valley JW (1989) Halogen-rich scapolite and biotite: Implications for metamorphic fluid-rock interaction. American Mineralogist 74:721-737.

Scott DJ (1997) Geology, U-Pb, and Pb-Pb geochronology of the Lake Harbour area, southern Baffin Island: implications for the Paleoproterozoic tectonic evolution of northeastern Laurentia. Canadian Journal of Earth Sciences 34:140-155.

Scott DJ, Stern RA, St-Onge MR, McMullen SM (2002) U-Pb geochronology of detrital zircons in metasedimentary rocks from southern Baffin Island: implications for the Paleoproterozoic tectonic evolution of Northeastern Laurentia. Canadian Journal of Earth Sciences 39:611-623.

Shor R, Weldon R (2009) Ruby and sapphire production and distribution: a quarter century of change. Gems & Gemology 45:236-259.

Simonet C, Fritsch E, Lasnier B (2008) A classification of gem corundum deposits aimed towards gem exploration. Ore Geology Reviews 34:127-133.

St-Onge MR, Wodicka N, Ijewliw O (2007) Polymetamorphic evolution of the Trans-Hudson Orogen, Baffin Island, Canada: Integration of petrological, structural and geochronological data. Journal of Petrology 48:271-302.

Sapphire corundum anomalies with different gold anomalies in heavy mineral fractions of stream sediments on epithermal-like CLY gold + bismuth telluride prospect, British Columbia, Canada

William R. Howard
Structurally Fine Concepts, Canada

Abstract. Very high counts of locally-sourced corundum grains occur in Heavy Mineral [HM] concentrates prepared from bulk stream sediments on CLY prospect gold quartz vein systems and skarn, south of Nelson in B.C. Most corundum grains [gns] are well-included and 'gritty'; a few are transparent varicolored blue, pink-grey and water-clear sapphire chips from larger gns, Figure 1. HM fractions anomalous in corundum gn counts differ in their gold anomalies. Only LW Ridge stream network has both anomalous recovered Visible Gold [VG] gn counts, Figure 4, and anomalous ppb Au by INAA in the non-magnetic <0.25 mm fine fractions, Figure 5. Other stream networks have only anomalous recovered VG gn counts. N-trending LW Ridge with its steep slopes follows an intrusive contact (map, Figure 3). Evidently glacially pulverized sulphidic skarn contributes fine gold to its W-flowing tributaries.

On CLY Prospect corundum outlines a 2.7 km trend of gold-associated aluminous alteration, with garnets and hercynite. Abundant corundum in HM concentrates can be used as an Indicator Mineral in other covered regions to signal potential for gold deposits with aluminous alteration, including epithermal-style bismuth-telluride enriched vein systems or scheelite (tungsten) + gold skarns. Corundum is not just solely developed by contact metamorphism.

1 Corundum types include sapphire on CLY gold prospect

Abundant grey, well-included 'gritty' corundum grains [gns] and a few clear, varicoloured sapphire chips, Figure 1, occur in several HM concentrates on CLY gold prospect, in southernmost British Columbia Canada, south of Nelson city, Figure 2.

Corundum is aluminum oxide Al_2O_3, the end-member mineral of aluminous hydrothermal alteration in some epithermal gold systems and Cu-Au-Mo-(W) porphyry deposits. CLY showings have sulphides, native gold (or electrum) gns with native bismuth, bismuthinite, joséite-A, joséite-B, hedleyite and various rare bismuth tellurides.

1.1 Unusual abundance of corundum in one sample

Regarding an LW ridge sample, R. Huneault, Overburden Drilling Management Ltd. [ODM] President, commented Jan. 2015: "We do not have a reference where abundant sapphire corundum grains as found in CLY sample HM-18 are present … the 8,000 grains is the highest concentration ... ODM has ever encountered. It is common to find low numbers ... occasionally up to 200 grains but not 8,000 grains". Two duplicate sample pairs have more than 1,700 gns - Figures 4 & 5. Since inception ODM has processed about 25,000 samples for HMs (R. Huneault, p.c.).

As they are often blue-grey ODM names all the corundum gns 'blue sapphire' corundum.

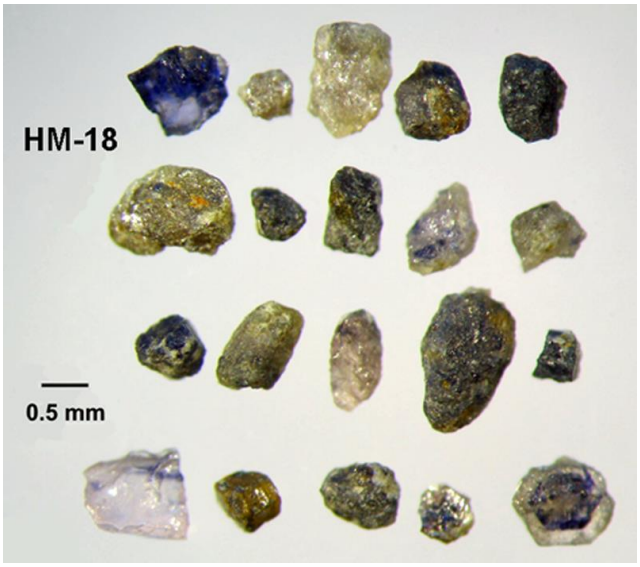


Figure 1. First 20 of 50 representative coarse corundum gns picked from HM-18, LW Ridge. Corundum is 12% of the coarse nonmagnetic fraction or 2,000 gns. Clear corundum overgrows dark blue in the chip at top left. Chip at bottom left has a dark blue fringe. Pink-grey grain at bottom centre may also be a broken chip. Photo by M. Michaud of ODM.

The quality of some clear, blue & pink-grey sapphire chips as precious gems has not been investigated. The source of the exceptionally anomalous corundum in HM-18 Bmin trib watershed (map, Figure 3) is likely banded calc-silicate bedrock exposed in the creek bed.

2 Regional to district scale structural – geologic setting

CLY prospect is located over the continental accretionary suture zone at the Quesnellia - Slide Mountain - Kootenay Terrane boundary, Figure 2.

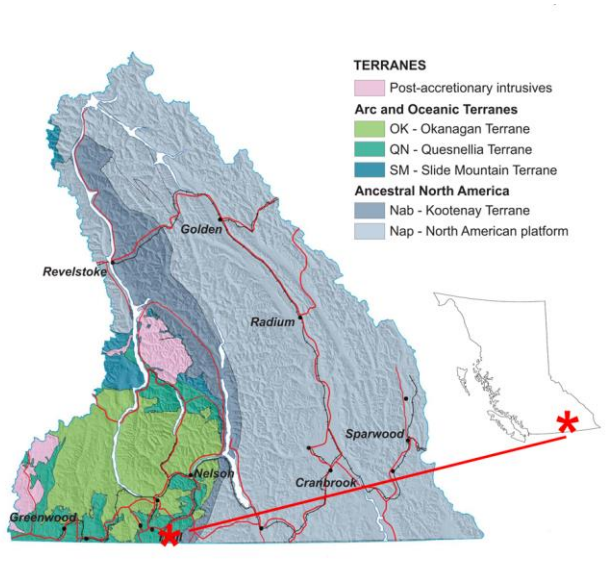


Figure 2. Location of CLY Prospect in south British Columbia over the terrane accretionary boundary, with highways. From Nelson Colpron and Earle (2013).

The layered rock units are metasediments, metavolcanics and ultramafics of the Slide Mountain Terrane Harcourt Ck Assemblage (Tapsoba Part III in Howard Ajibode Tapsoba 2016) and varied carbonaceous, argillaceous limestone and marl beds of the Kootenay Terrane Index Formation. The geologic setting in a fold and thrust belt is complex, with oft-reactivated thrust faults and shear zones (Tapsoba and Howard 2017).

Contact metamorphism by Cretaceous 'S-type' granitoid bodies, including the Wallack Ck stock and the Bunker Hill sill, formed the abundant 'gritty' corundum gns. Siliceous epithermal gold mineralization is associated with Tertiary Eocene age alkalic Coryell suite mafic syenites & lamprophyres. Varicoloured clear sapphire may be neo-formed from 'gritty' opaque corundum. Shallow glacial drift is extensive.

3 Mineralization in the Rossland-Trail-Salmo-Nelson region

The region about CLY prospect is highly mineralized with significant production & reserves in several gold camps, Million oz: Rossland 25 km W, 2.94; Sheep Ck 20 km NE, 0.91; Ymir ~30 km NNE, 0.56; and the Kena KGM zones near Nelson city, 1.89 M. oz NI total reserves. All except the Sheep Ck vein field are along the accretionary boundary, the Waneta – Tillicum Fault system.

3.1 Historic Bunker Hill mine on central CLY

Total recorded production of the Bunker Hill mine 1933 – 1942 from 4 adits and surface trenches totals 375 tons, at average grade 0.30 oz/ton gold and 0.87 oz/ton silver (10.3 g/t Au & 29.8 g/t Ag).

The Bi–Te–S mineralogy, mineral stages, structural setting and age of the associated intrusion is similar to the Liese zone Pogo deposit, AK with 6.5 M. oz *plus*. Mineralization is bismuth and tellurium enriched with several very rare bismuth (sulpho)tellurides, e.g. first occurrences of ikunolite Bi_4S_3 and ingodite Bi(Te,S) in Canada (Cook, Part II in Howard Cook and Ciobanu 2009). At the Bunker Hill mine crossing veins form ore shoots, a Tension Vein Array (Tapsoba and Howard 2017).

4 Bulk stream sediment survey, with two pairs of duplicate samples

For field sampling the standard GSC procedure was used (B. McClenaghan p.c., 2014). In flowing creeks, or nearly dry gullies, use of 4 and 12 mesh screens removed oversize clasts. An average ~8.4 kg of stream sediment (silt) was collected in new 5.7 litre plastic boxes. All equipment was thoroughly washed between samples.

Two pairs of duplicate silts were collected, using the same sampling protocol, close to the anomalous HM-18 site, from Bmin trib below LW Ridge.

5 ODM lab methods

Overburden Drilling Management Ltd. of Ottawa is a leading laboratory in gold grain and Heavy Mineral recovery. They followed typical lab procedures, detail is at http://www.odm.ca/. From CLY prospect ODM tabled 54 bulk stream silts, recovering Visible Gold [VG], scheelite and metallic mineral gns, and prepared 34 Heavy Mineral [HM] fractions, Figures 3 to 5. Over the three year survey D. Holmes did all microscopic identification, counting and picking of the VG and HM gns.

ODM prepared 47 nonmagnetic <0.25 mm fractions sent to Activation Labs Ltd., Ancaster ON, for INAA.

5.1 Re-counts of some suspect counts

The advantage of sampling streams over tills is that fluvial dispersion can be used to check count estimates in silts from the same creek or stream network. Generally upstream concentrations must decrease downstream.

11 of 34 HM samples were re-counted for corundum. Each has 3 gn sizes, thus 33 re-counts. For 12 the counts increased, for 6 they decreased. Often mica coats corundum (and grossular garnet) gns confounding the count estimates. The counts are semi-quantitative data fully sufficient for the survey goal, exploration targeting.

6 Results: recovered visible gold grain counts

ODM recovers a known proportion of the VG gns depending on their size. Anomalous thresholds of gn counts are set at gaps on log normal probability plots. The limits have varied little in 3 survey years (Howard Ajibode and Tapsoba 2016). Anomalies are designated **Class I**, II or *III* in order of decreasing decimal gn counts. As a check, counts of duplicate HMs are often the same anomaly class.

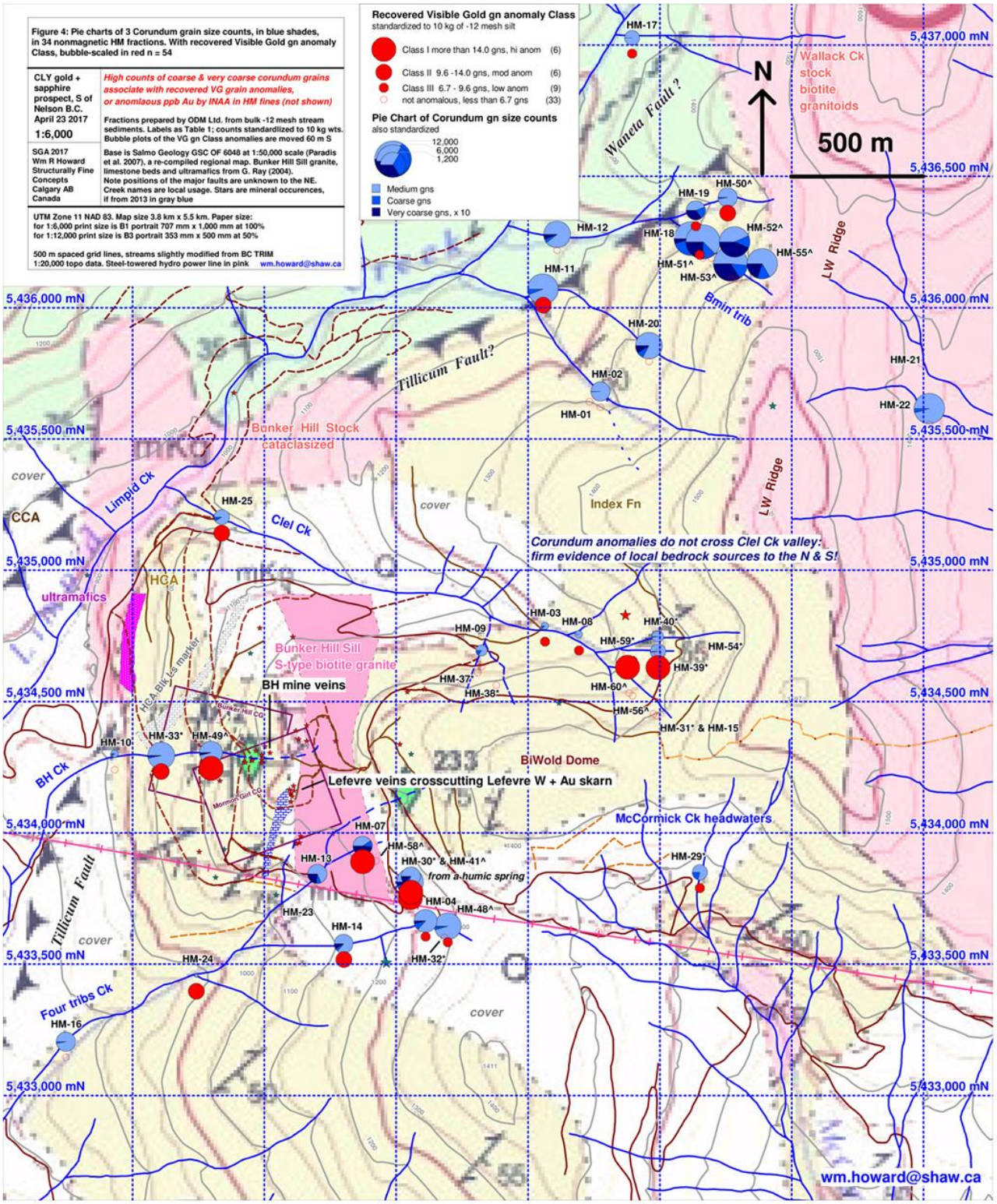


Figure 3: Pie charts of three corundum gn sizes in 34 nonmagnetic HM fractions. Pie sectors in dark & very dark blue represent numbers of coarse and very coarse corundum gns. Recovered Visible Gold gn anomaly classes are bubble-scaled in red, offset to the south for legibility. Fractions with high counts of coarse and very coarse corundum gns always have VG gn anomalies. The reverse co-association is not necessarily true: two **Class I** VG anomalies in upper Clel Ck have very few glacially-dispersed corundum gns. Revealingly, the high corundum counts *do not cross Clel Ck.* This is firm evidence the corundum is locally sourced: *if coarser-sized gns have high counts the corundum sources are restricted to the sampled watershed*. Bowl-like stream headwaters are weathered alpine cirques; W-E trending BiWold Dome is a roche moutonneé (sheep back). Not shown are Au by INAA anomalies in 47 nonmagnetic HM fine fractions.

7 Results: corundum grain counts

For medium size corundum the anomalous thresholds are set at: potentially anomalous 1,100 gns (rather high) and distinctly anomalous 2,200 gns, lines on Figures 4 & 5.

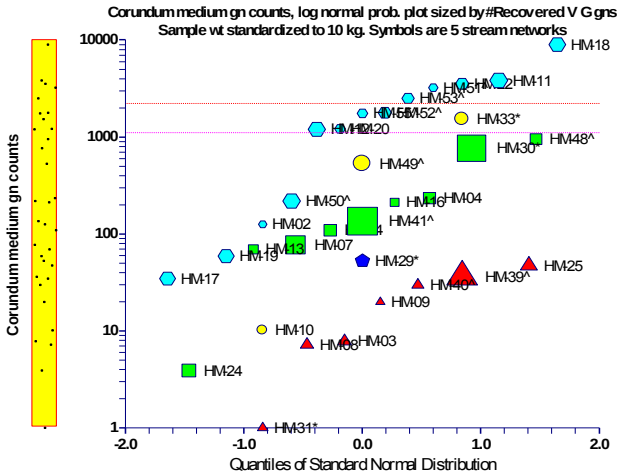


Figure 4: Log normal probability plot of medium corundum gn counts in 34 nonmagnetic fractions, sized by recovered VG gn counts. Purple line is provisionally anomalous threshold, set rather high at 1,100 gns; red line is distinctly anomalous, 2,200 gns. Symbols represent the stream networks: light blue hexagons LW ridge; yellow dots BH Ck; green squares Four tribs Ck; single dark blue pentagon is McCormick Ck; red triangles Clel Ck. Counts standardized to 10 kg of -12 mesh stream sediment.

A duplicate pair of humic spring samples from Four tribs Ck network (green) have the highest recovered VG gn counts, standardized 36.0 and 33.7 gns, both **Class I**.

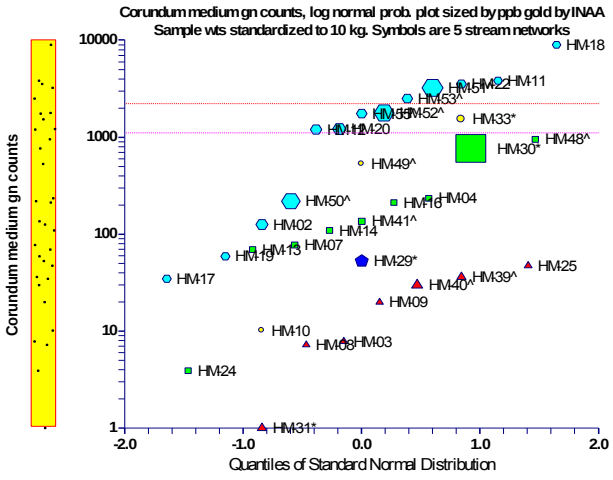


Figure 5: As Figure 4 but sized by ppb Au by INAA in the <0.25 mm fractions. Symbols represent different stream networks like Figure 4. The outlier in green is one analyses of a duplicate from the humic spring in Four tribs Ck network; its other analysis is background. Counts standardized to 10 kg.

Consistently LW ridge HM fines (light blue) have the highest ppb Au by INAA values. **Two BH Ck silts HM-49^ & -33* (yellow) have little ppb Au by INAA.**

8 Conclusion - corundum anomalies have different gold anomalies

Stream networks anomalous in medium corundum gns in HM fractions also have anomalous gold, as recovered Visible Gold (electrum) 'VG' gns, ***or*** ppb Au by INAA in nonmagnetic <0.25 mm HM fine fractions, ***or both***. **Only LW Ridge stream sediments (light blue hexagons) have both.** Bunker Hill [BH] Ck, Four tribs Ck, and Clel Ck networks only have anomalous VG gn counts.

This difference is plausibly due to **more fine particulate gold in sediments from LW Ridge**, from pieces of glacially pulverized sulphidic skarn. LW Ridge has steep W or E facing slopes that follow the intrusive contact of the granitic Wallack Ck stock (map, Figure 3). Figure 4 shows the gold content in the other stream networks is most all as native VG (electrum) gns. Sources in their watersheds are about 500 m or more from intrusive contacts, on moderately sloping land. Examples are the BH mine and Lefevre Au(Ag)-Bi-Te-As-Sb-Pb-W-Fe veins in Four tribs Ck watershed. Long-term weathering in the Tertiary modified most gold grain shapes, enlarging some.

High corundum counts *do not cross Clel Ck* (map, Figure 3). This conclusively shows its sources are local, in the sampled watersheds. Abundant corundum in HM concentrates is one indication of a 2.7 km trend of gold-associated aluminous alteration on CLY prospect. Corundum can be used as an Indicator Mineral in other covered regions to target gold deposits with associated aluminous alteration, possibly with garnet and hercynite. Eocene Coryell mafic alkalic rocks may form gem-quality sapphire from 'gritty', well-included, opaque corundum and epithermal bismuth telluride–associated gold deposits.

References

Howard WR, Cook NJ, Ciobanu CL (2009) Third Mineralogical Report detailing the finding of two 'new' gold-associated bismuth sulphotelluride minerals and identifying other opaque minerals … in claim #516584... southernmost British Columbia Part II by NJ Cook. BC MEMPR AR #30475 Accessed Feb. 18 2017 https://aris.empr.gov.bc.ca/ArisReports/30475.PDF

Howard WR, Ajibode O, Tapsoba B (2016) Surveys of recovered Visible Gold, scheelite & metallic mineral grains and Heavy Mineral grains in bulk stream silts 2013 - 2015 (Part I) ... Field Observations of Geologic Structures … by B Tapsoba (Part III), on CLY Gold + Tungsten polymetallic Prospect. BC MEMPR AR #36076 https://aris.empr.gov.bc.ca/ArisReports/36076.PDF. Accessed Feb. 24 2017

Nelson JL, Colpron M, Earle S (2013) The Cordillera of British Columbia, Yukon and Alaska: Tectonics and Metallogeny. In Tectonics, Metallogeny, and Discovery: The North American Cordillera and Similar Accretionary Settings. Economic Geology Special Publication 17, pp. 53-109

Tapsoba B, Howard WR (2017) Modeling the geometry of shear zone hosted gold-quartz veins at the historic Bunker Hill mine ... south B.C. a covert Tension Vein Array. Accessed Apr. 23 2017 https://cordillerantectonics.files.wordpress.com/2017/02/ctw2017_program_20170220_final_webversion.pdf

Genesis of emerald at Lened, NWT

Donald J. Lake and Lee A. Groat
University of British Columbia, Vancouver, Canada

Hendrik Falck
Northwest Territories Geological Survey, Canada

Jan Cempírek
Masaryk University, Czech Republic

Daniel Kontak
Laurentian University, Ontario, Canada

Daniel Marshall
Simon Fraser University, British Columbia, Canada

Thomas Mulja
Consulting Geologist, Canada

Abstract. The sources of emerald-forming fluids and chromophores at the Lened occurrence were assessed using field relationships, Ar-Ar dating, whole rock geochemistry, stable isotopes (O, C, S), and mineral chemistry; the results clearly show that the ~100 Ma (Ar-Ar muscovite) Lened emerald occurrence is a Type I (igneous) emerald deposit and relates to the proximal ~100 Ma (Ar-Ar biotite) Lened Pluton. Stable isotope analyses suggest the veins formed from a primarily granite-derived fluid with lesser components of meteoric and shale-equilibrated fluids. Beryllium and other incompatible elements (including W, Sn, and F) concentrated in evolved magmatic fluid that exsolved during the last stages of crystallization of the Lened pluton. Local overpressuring of vein-forming fluids under a brittle carapace of early pyroxene-garnet skarn led to fracture and emplacement of quartz-calcite-beryl-scheelite-tourmaline-pyrite veins. Less than 5% of the beryl can be considered pale bluish green emerald. Vanadium concentration in the emerald averages 1563 ppm; Cr averages 75 ppm, and Sc attains concentrations of 782 ppm. The key emerald chromophore vanadium was mobilized by metasomatic breakdown of V-rich black shales (averaging 2000 ppm V) that underlie the emerald occurrence.

1 Geologic context

1.1 Regional geology

The Lened tungsten deposit is located north of the Yukon/Northwest Territories border in the Logan Mountains (62°22' N, 128°38' W; NTS 105/I7). The study area is underlain by largely unmetamorphosed basinal strata consisting of sandstone, shale, chert, and limestone deposited off-shelf in the deeper Selwyn Basin, southwest of the Mackenzie platform; Lened straddles the Cambro-Ordovician shelf edge. The strata formed a wedge of clastic sedimentary units at the western margin of the North American continent from the mid-Proterozoic to mid-Jurassic (Gordey and Anderson 1993).

Argillaceous limestone of the Cambrian-Ordivician Rabittkettle formation (ЄOR) hosts both W skarn and emeraldiferous quartz-carbonate veins. Gritty quartz-rich clastics and siltstone of the Precambrian Vampire formation (PЄV) are stratigraphically below the emerald hosting formation; above are younger carbonaceous black shales that correlate with the Ordo-Silurian Duo Lake Formation (OSD) of the Road River Group or the Portrait Lake formation of the Devono-Mississipian Earn Group (DMP), as seen in Figure 1 (Adie and Allen 1960, Glover and Burson 1986). The Lened quartz-monzonite/granite stock was emplaced ~100 Ma (Ar-Ar, biotite; this study).

1.2 Outcrop geology

Limestone and shale at Lened show evidence of isoclinal folding and development of an axial-plane cleavage fabric. These, along with thrust fault structures, are likely the result of pre- to syn-intrusion compressional tectonics during the Jurassic to Cretaceous (Gordey and Anderson 1993). Undeformed granitic apophyses, dikes, and sills shallowly underlie Lened Ridge (Sergerie 1979) and provide a ready explanation for the presence of skarn forming fluids.

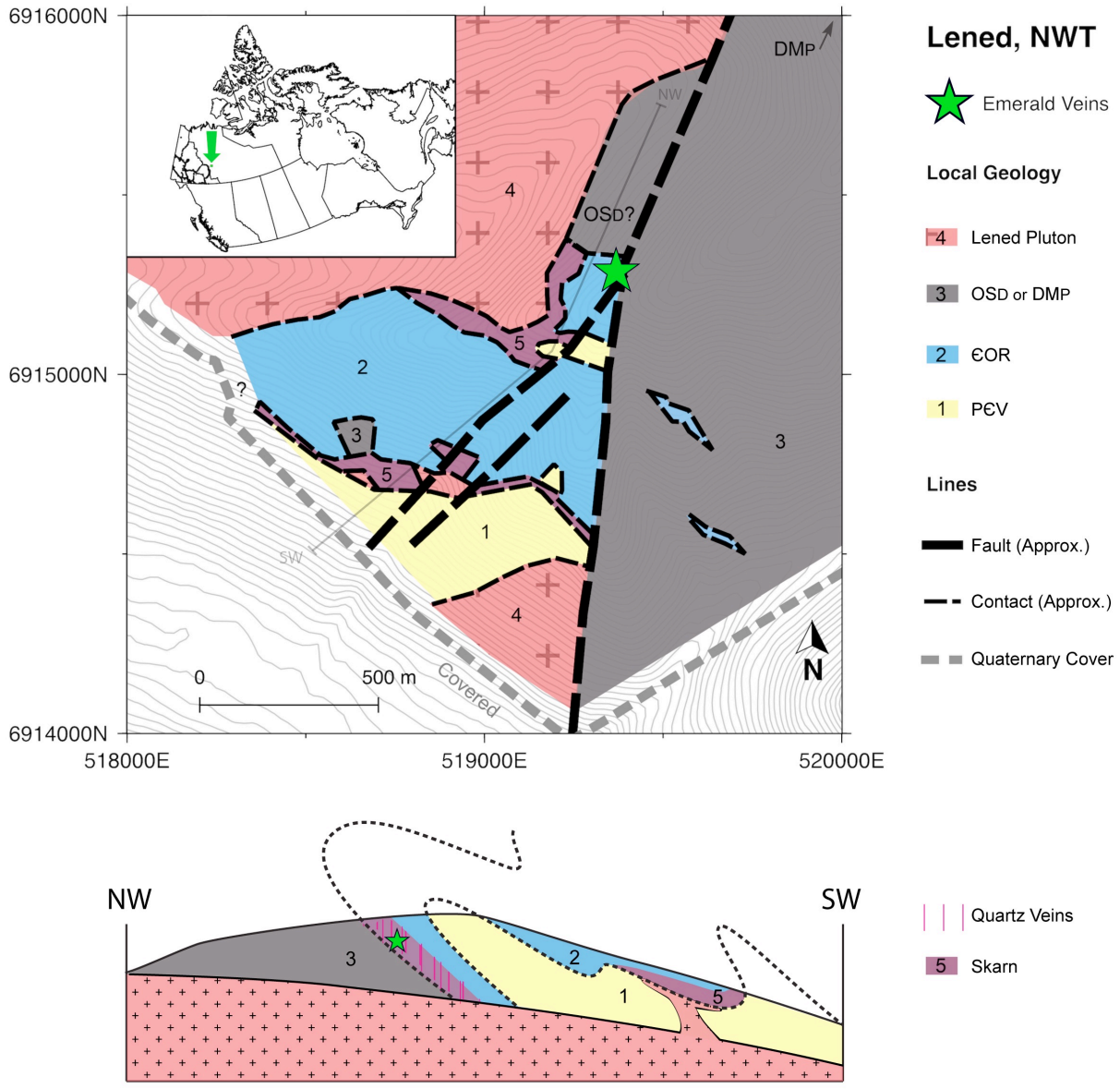


Figure 1. Geology of Lened emerald occurrence and schematic cross-section modified after Adie and Allen (1960), Sergerie (1979), and Gordey and Anderson (1993). See text for unit descriptions. Grid coordinates are UTM (zone 9, WGS 84).

2 Emerald-bearing quartz veins

An array of 26 sub-vertical emerald bearing quartz-carbonate veins at Lened strike southwest, and are hosted by a 20-30 m thick lens of pyroxene-garnet-(±vesuvianite) skarn (Fig. 2). The accepted explanation for black shale to be underlying the emerald vein bearing skarn is that the skarn represents a recumbent fold in the Rabbitkettle limestone, as shown schematically in the cross-section in Figure 1. Emerald veining is shown by field relationships to be syn- to post-plutonism; unaltered veins sharply cut skarnified limestone (and in some cases sericitize selvages).

Emeralds have been found in at least half of the veins. The skarn transitions upwards into less metasomatically altered, finely crystalline, argillaceous limestone. The skarn protolith at the emerald showing is considered to be part of the Rabbitkettle formation (Marshall et al. 2004). The veins only occur in the skarn band, and taper out rapidly at the boundary of the skarn. The veins are composed of quartz (85-90%), calcite (5%), muscovite (5%), beryl (locally up to 3%), scheelite (<1%), tourmaline (<1% dravite), and trace amounts of pyrite.

Beryl occurs as discrete elongate prismatic crystals 0.1-5 mm wide and up to 5 cm in length. Lened beryl is typically a very light yellow to blue-green. Some crystals are nearly colourless; fewer than 5% display a lively blue-green colour. Most crystals are opaque to translucent, though gem-quality beryl of good clarity is known to occur. Faceted gems of good saturation, but very light tone and finished weights to 0.17 ct have been collected from Lened (Fig. 3). Based on electron microprobe analysis (EMPA, n = 88), the emerald is vanadium-rich, averaging 1563 ppm, while Cr averages 75 ppm. Scandium is unusually concentrated in beryl, up

to 782 ppm.

Magnesium-rich dravite is a minor accessory phase and is often found as needle-like euhedral inclusions in quartz and calcite in close proximity to beryl. Slightly smoke-coloured transparent quartz near the vein margin seems to preferentially host tourmaline, and this may represent a secondary quartz phase. Another mode of dravite occurrence is in 1-2 cm patches of parallel-growth aggregates (individual crystals 0.05-1 mm in length) that grow inward from the edge of the vein. The dravite inclusions are typically in the form of radiating sprays or individual broken segments of prismatic dravite.

Scheelite is seen as sporadically occurring 0.5-1 mm solitary white-creamy pink grains and coarse creamy pink subhedral scheelite to 1 cm is intergrown with quartz and occurs mostly near the vein margins.

3 Geochemistry

The Lened emerald vein major element chemistry reflects its dominant composition of quartz and calcite. SiO_2 (80 wt.%) is the major constituent, and the other major contents are CaO (9.95 wt.%), CO_2 (7.5 wt.%), C (2 wt.%), and Al_2O_3 (0.82 wt.%), which can be attributed largely to calcite and muscovite. Beryllium (746 ppm), Sn (108 ppm), and Cs (32.7 ppm) are enriched in the veins. Vanadium (47 ppm) and Cr (180 ppm) are somewhat enriched in the veins and bulk V/Cr is 0.26.

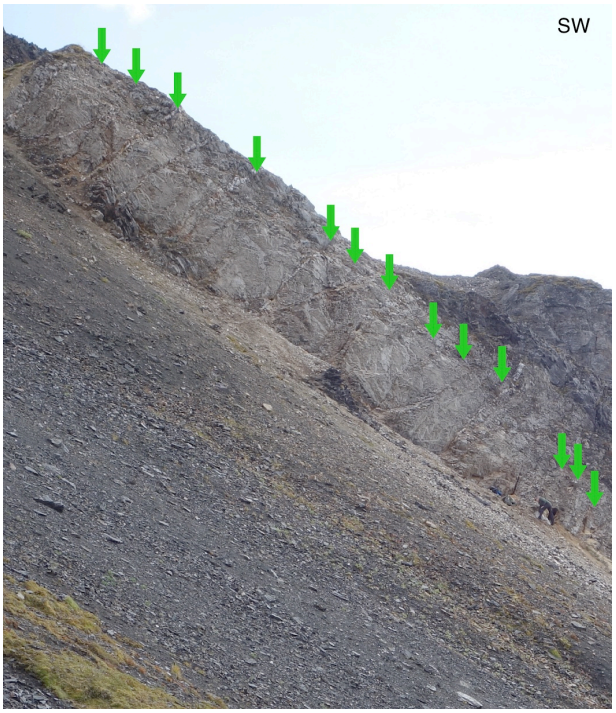


Figure 2. Southwest-facing view of quartz-calcite veins cutting light coloured skarn. Black shale below the skarn can be seen center of frame. Emerald-bearing veins are indicated by green arrows. Bradley S. Wilson provides scale, lower right.

Vanadium is extremely elevated in the black shale unit below the skarn, averaging 2200 ppm over five samples. Skarn at the contact with the black shale shows the highest V enrichment with 4670 ppm (sample HF-14). Chromium is approximately ten times less enriched than V in the shale (V/Cr = 10) and skarn contact, with an average of 208 ppm Cr in the five shale samples. Granitic samples are not enriched in V (average 24 ppm) and show slight enrichment in Cr (average 125 ppm). Chromium values are about five times more enriched than V in the granite. Some shale and clastic sedimentary samples are extremely elevated in Ba (~800-4000 ppm) as is common in black shales throughout the Selwyn Basin (Gordey and Anderson 1993).

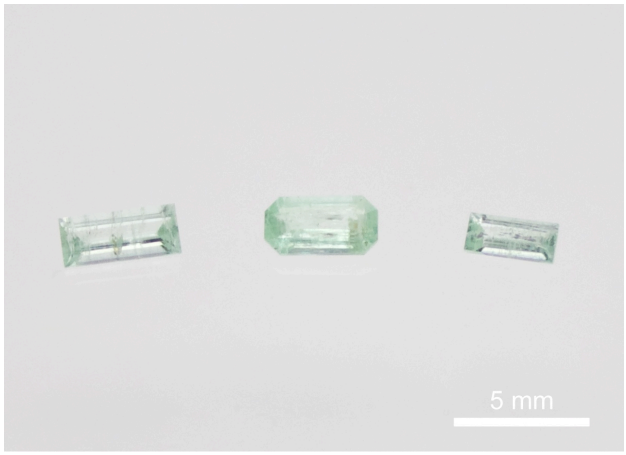


Figure 3. Three pale bluish-green faceted emeralds from Lened. From left to right: 0.14 ct, 0.16 ct, and 0.07 ct.

4 Sources of vein fluids and emeralds

The $\delta^{18}O_{H2O}$ value was calculated for vein and granite-derived fluids using fractionation factors of Matsuhisa et al. (1979). Vein fluids are estimated to be ~10‰ (vein quartz avg. 15.5‰, 350°C) which suggests mixing of the granite-derived fluids (~12‰; magmatic quartz avg. 13.3‰, 600-700°C) with an ^{18}O-depleted fluid such as meteoric water. The dominant emerald chromophore V was mobilized by metasomatic breakdown of V-rich black shales that underlie the emerald occurrence; this is supported by $\delta^{13}C$ data for vein calcite that indicates mixing of the black shale and local limestone reservoirs. Additionally, the similarity of $\delta^{34}S$ values for shale- (avg. 12.2‰) and vein-hosted pyrite (avg. 15.3‰) suggest S was derived from the shale reservoir.

Determining probable sources of Be, B, and V were also important aspects of this study and are key to determining the origin of beryl in this deposit. While low B concentrations are reported at Mactung and Cantung skarns, there is clearly B in the system. Localized volumetrically insignificant tourmaline occurs in aplite dykes (Cantung) and quartz veins (Mactung) (Zaw 1976, Dick and Hodgson 1982, Rasmussen et al. 2011). Similarly, at Lened only a vanishingly small amount of Be and B would have been required to form the small amount of beryl and tourmaline in the veins. Boron might have a

magmatic origin, but it is a highly mobile element and was probably largely sourced from local host rocks by the same breakdown of shales that caused V-enrichment of the vein fluid. Beryllium, on the other hand, is an incompatible element that was likely sourced from the last stages of pluton crystallization. The emerald veins were formed when highly evolved magmatic fluids rich in the incompatible or mobile elements W, Sn, Be, and F (± B) were overpressured and released into fractures within locally embrittled host rocks.

Emplacement of the Lened pluton led to contact metamorphism and metasomatism of overlying black shale and/or associated argillaceous limestone. There is clear evidence of alteration of these units in the vicinity of the emerald veins and skarn. The black shale has in some areas been significantly altered to a grey colour with small amphibole or chlorite porphyroblasts developed throughout. In the unaltered shale, V is most likely bound within illite (or other clay minerals) and organic matter (e.g., Peacor et al. 2000). Breakdown of illite and organic matter in a metasomatic "reaction zone" below the outcrop probably contributed V to both the skarn and emerald veins.

5 Conclusions

The Lened emerald crystals are of Type I igneous origin (see Schwarz and Giuliani 2001 for description of this classification scheme). Emeralds formed in late-stage magmatic-hydrothermal quartz veins resulting from emplacement of the Lened Pluton and development of the Lened W-skarn. The source of Be is likely magmatic and O isotope results imply the vein-forming fluid was largely sourced from evolved granitic fluid. This is supported by magmatic mineral associations (e.g., scheelite), and characteristically magmatic vein chemistry consisting of high W-Be-Sn as in other similar W skarns. Stable isotopes suggest that magmatic-hydrothermal fluids mixed with a small proportion of meteoric and shale-equilibrated fluids (source of V). Metasomatism of black shale and subsequent release of V was therefore an integral part of the process which led to formation of Lened emerald.

Acknowledgements

We thank those who contributed to our study of the Lened emerald occurrence during the past 20 years; these include Dan Marshall, Daniel Kontak, Thomas Mulja and others. This study was supported by the Natural Sciences and Engineering Research Council of Canada in the form of a Discovery Grant to LAG, and by Northern Scientific Training Program grants to DJL.

References

Adie L, Allen TM (1960) Geological report on the Lened tungsten prospect and group of claims, Canex Aerial Exploration Limited, Flat River Area, Mackenzie. Northwest Territories Geoscience Office assessment report 017570

Dick LA, Hodgson CJ (1982) The MacTung W-Cu(Zn) contact metasomatic and related deposits of the northeastern Canadian Cordillera. Econ Geol 77:845–867

Glover JK, Burson MJ (1986) Geology of the Lened tungsten skarn deposit, Logan Mountains, Northwest Territories. In: Morin JA (ed) Mineral Deposits of the Northern Cordillera. Can Inst Mining Met Spec Vol 37:255–265

Gordey SP, Anderson RG (1993) Evolution of the northern Cordilleran miogeocline, Nahanni map area (105I), Yukon and Northwest Territories. Geol Surv Can 428, 214 pp

Marshall DD, Groat LA, Falck H, et al (2004) The Lened emerald prospect, Northwest Territories, Canada: insights from fluid inclusions and stable isotopes, with implications for northern Cordilleran emerald. Can Min 42:1523–1539

Matsuhisa, Y, Goldsmith, JR & Clayton, RN (1979) Oxygen isotopic fractionation in the system quartz-albite-anorthite-water. Geochim Cosmochim Acta 43:1131–1140

Peacor DR, Coveney RM, Zhao G (2000) Authigenic illite and organic matter: the principal hosts of vanadium in the mecca quarry shale at Velpen, Indiana. Clays Clay Min 48:311

Rasmussen KL, Mortensen JK, Falck H (2005) Geochronological and lithogeochemical studies of intrusive rocks in the Nahanni region, southwestern Northwest Territories and southeastern Yukon. In: Yukon Exploration and Geology 2005. Yukon Geol Surv, pp 287–298

Rasmussen KL, Lentz DR, Falck H, Pattison DRM (2011) Felsic magmatic phases and the role of late-stage aplitic dykes in the formation of the world-class Cantung tungsten skarn deposit, Northwest Territories, Canada. Ore Geol Rev 41:75–111

Schwarz D, Giuliani G (2001) Emerald deposits—a review: Aus Gem 21:17-23

Sergerie G (1979) Drill results from the Pan claims. Northwest Territories Geoscience Office assessment report 081031

Zaw K (1976) The Cantung E-zone orebody, Tungsten, Northwest Territories: A Major Scheelite Skarn Deposit. PhD thesis, Queen's University, Kingston, Ontario, 327 pp

The impurities, defects, inclusions and gemological characteristics of diamonds from the M.V. Lomonosov deposit

Tatiana V. Posukhova, G.Yu Kriulina, Victor K. Garanin, Adelya Shaimardanova
Moscow State University, Russia

Abstract. Diamonds from Arkhangelsk and Karpinskaya-1 pipes were studied by optical, Raman and IR-spectroscopy, X-ray tomography methods. Identified the presence, concentration and distribution of structural and non-structural impurities in different crystallographic forms of diamond and their relationship to the color and transparency. Curve-faced dodecahedra and crystals with different shades, with a high degree of transparency dominated. They have a high concentration of hydrogen and nitrogen defects. Diamonds from the studied pipes differ in the form of crystals, in content of crystalline aggregates, in content of colored crystals and content of high-hydrogen crystals. The conditions of formation of diamonds in the studied pipes of the M.V. Lomonosov deposit differ from the conditions of formation of diamonds in kimberlites of Yakutia. Studied diamonds crystallized at lower temperatures.

1 Introduction

Diamondiferous kimberlites were discovered in the northern part of European Russia in the region of the Arkhangelsk Province in 1979. Petrochemical properties and mineral composition of these rocks were described in our previous works (Possoukhova et al., 1999, 2001; Kudryavtseva et al., 2005) and now we point our attention at gemological properties of the diamond. This field is unique in the distribution of the diamonds of various crystallographic forms such as curve-faced dodecahedra or tetra-hexahedra which are rare in other fields. These specific forms have a certain defect-impurity composition, non-standard distribution of defects, structural and non-structural impurities and micro-inclusions, which defines their special gemological quality.

2 Objects and methods of investigation

The objects of research are the diamonds from two pipes of the M.V. Lomonosov deposit (Fig. 1): Arkhangelskaya pipe and Karpinskaya-1 pipe.

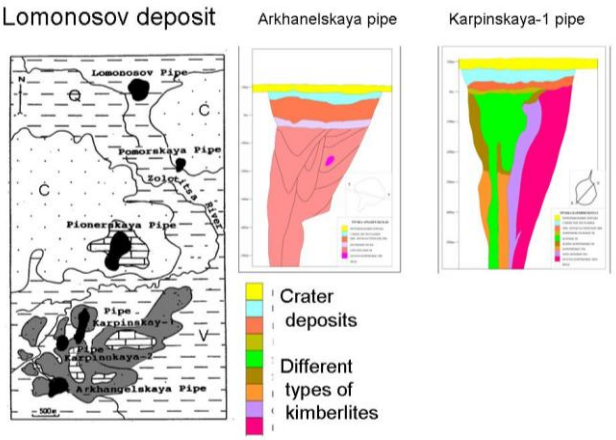


Figure 1. Plan of the M.V. Lomonosov deposit and cross-sections of the pipes

It has been reviewed and described about 500 crystals and around 100 crystals were selected for study in the laboratory of spectral methods. Recording of IR-spectra were done on the VERTEX-70 Fourier spectrometer (Bruker). Recording of Raman spectra of the inclusions in diamonds were held at spectrometer EnSpectr R 532 with the prefix Olympys microscope. Investigation of samples by X-ray computed tomography was carried out on the device SkyScan-1172.

3 Gemological and spectroscopic properties of the diamonds

Investigations have shown that the objects of study differ significantly according to gemological characteristics of diamonds. Comparison of diamonds by color groups were conducted (Fig. 2).

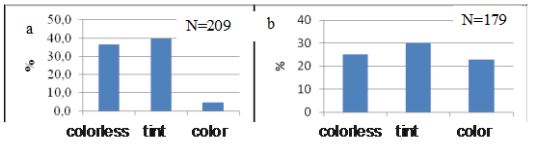


Figure 2. The distribution of diamond crystals acording to a color groups in pipes Arkhangelskaya (a) and Karpinskaya-1 (b)

Diamonds with different shades (brown, yellow, green,

pink, gray) dominated in both cases but the pipes are substantially different in content of colored diamonds: in the Karpinskaya-1 pipe the content of such diamonds more larger (20%). Diamonds with a different color have a different type of spectral characteristics (Fig. 3).

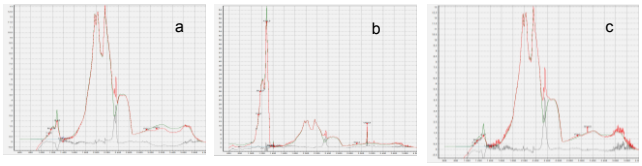


Figure 3. IR spectra of transparent diamond with gray (a), rose (b) and brown (c) colors from pipe Karpinskaya-1 (a) and from pipe Arkhangelskaya (b, c)

Correlations between the color of the crystals and the content of hydrogen defects are not found. The diamonds with low and high concentration of CH-defect are presence in each color group.

We investigated the degree of transparency (Fig.4).

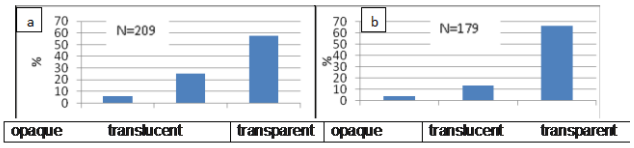


Figure 4. The distribution of diamonds according to degree of transparency in pipes Arkhangelskaya (a) and Karpinskaya-1 (b)

Diamonds with a high degree of transparency dominated (50%) in both pipes. The proportion of non-transparent crystals is low (less than 5%). Spectra of translucent and transparent diamonds vary significantly, either in relation to lattice absorption or in intensity of nitrogen and hydrogen defects (Fig. 5).

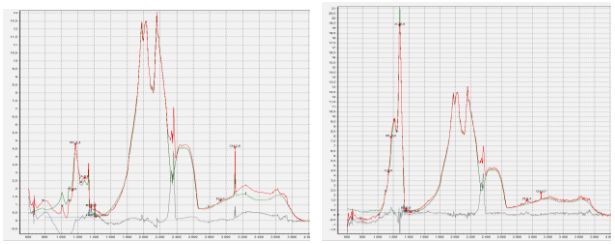


Figure 5. IR-spectra of the transparent crystal from Arkhangelskaya pipe (a) and of the translucent diamond from Karpinskaya-1 pipe (b)

Diamonds with high and low content of hydrogen defects are present in each of the transparency group.

Another important gemological characteristics of diamond is the shape of the crystals. Pipes vary in content of various diamond types of habit (Fig. 6). Crystals in the form of curve-faced dodecahedra prevail in both pipes. Pipes vary in content of octahedra: in the pipe Arkhangelskaya - more than 20% and in the pipe Karpinskaya-1 - less than 5%. Crystals with high and low concentrations of hydrogen defects were established in each groups of habit.

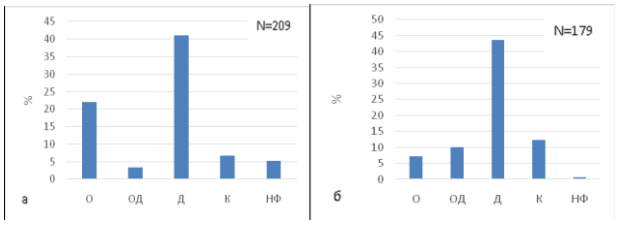


Figure 6. The distribution of diamonds according to habit for pipe Arkhangelskaya (a) and Karpinskaya-1 (b): О- octahedron, ОД- the combination of octahedron-dodecahedra, Д- curve-faced dodecahedra, К- cube, Т - tetra-hexahedra, НФ - indefinite form

Diamonds vary according to mechanism of growth. Crystals of the 3-d and 5-th varieties according to Ju.L. Orlov's classification (1984) identified in Karpinskaya -1 pipe and in the pipe Arkhangelskaya - no. Concentration of nitrogen and hydrogen defects have been calculated, and plotted the content of the diamonds for various types of habit (Fig.7).

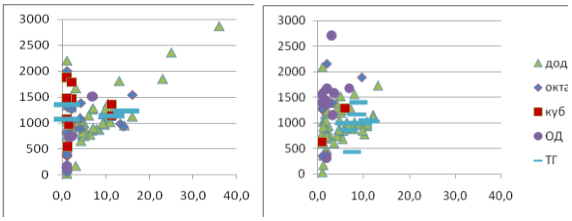


Figure 7. The dependence of the total concentration of nitrogen defects (axis Y) and hydrogen defects (axis X) for the diamond crystals of different types of habit in the Arkhangelskaya pipe (a) and Karpinskaya-1 pipe (b)

The maximum concentration of points for both pipes corresponds with dodecahedra in which the content of nitrogen varies from 500 to 1500, and the content of CH-defects from 0 to 10. Pipes vary in content of diamonds of different habit with high concentrations of nitrogen and low hydrogen. In the pipe Arkhangelskaya it is a cube, and in the pipe Karpinskaya-1 it is O-D crystals. Crystals with high concentrations of hydrogen and nitrogen are present in the pipe Arkhangelskaya and in the Karpinskaya-1 pipe they are absent. We were also studied the content of aggregated and unaggregated nitrogen defects in A and B forms and their correlation with a hydrogen defects (Fig. 8, 9).

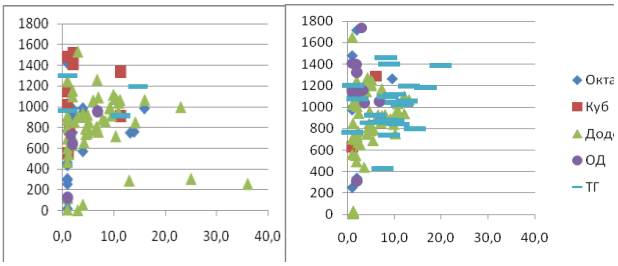


Figure 8. The dependence of the concentration of nitrogen defects in the A form and hydrogen defects in the diamonds of different types of habit in Arkhangelskaya pipe (a) and Karpinskaya-1 pipe (b)

The maximum concentration of points for both pipes corresponds with high content of non-aggregated nitrogen from 600 to 1000 and CH from 0 to 10. On the getting graphs also show that the area of the maximum concentration of points for the two pipe correspond the low concentration of aggregated nitrogen from 0 to 500 and CH from 0 to 10 (Fig. 9).

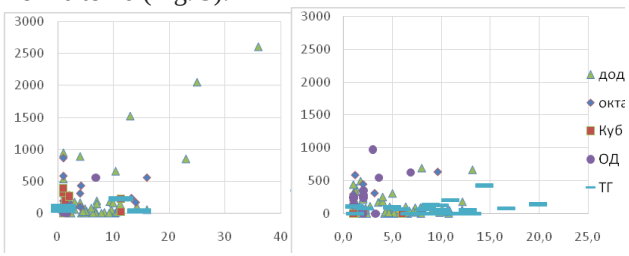


Figure 9. The dependence of the concentration of nitrogen defects in the B form and hydrogen defects in the diamonds of different types of habit in Arkhangelskaya pipe (a) and Karpinskaya-1 pipe (b)

Pipes differ according to the type of the habit of crystals belonging to the area of maximum concentration of the analytical points: in Arkhangelskaya pipe - this is dodecahedra and in the pipe Karpinskaya-1 - this is a tetra-hexahedra. Crystals with high concentration of hydrogen, high concentration of aggregated nitrogen and low concentration of non-aggregated nitrogen established in the pipe Arkhangelskaya, and in the pipe Karpinskaya-1 such crystals are absent.

4 Origin of the diamonds

The differences of gemological and spectroscopic properties of the diamond from studied pipes related to their genetic features. Conditions of diamond formation can be reconstructed based on the study of mineral and fluid inclusions. The peaks of carbonate groups, lines of hydroxyls and water have been identified at the IR spectra of the studied diamonds together with the lattice absorption line, nitrogen line form A-defects (1281sm^{-1}), B1-defect (1175sm^{-1}) and hydrogen CH-defect (3110 cm^{-1}) (Table).

Table Impurity centers and nanoinclusions in diamond crystals detected by local FTIR spectroscopy

Impurity		Lines, см$^{-1}$
Defects associated with nitrogen	C	1345, 1135,1100, 1332
	A	1282
	B (B1)	1175
	P (B2)	1365 , 1350-1370
	N3	1300-1400
Defects associated with hydrogen	CH	**3107,**3237, 2785, 1432, 1404
	OH	3420
	H_2O	1630-1690, 3200-3700 , 1477
	HOH, H_2O	1605
	CH_4	3052
Carbonates	CO_2	**2355**, ~2380, ~660
	CO_3	860-880
Alumino-silicates	SiO_2 и Al_2O_3	900-1200
Oxygen	O^{2-}	1555 - 1500, 1453

We have identified the conditions of formation (T of annealing) according to the degree of nitrogen aggregation (Fig. 10). Diamonds of both tubes are characterized by low temperature annealing or formation (less than 1050 ° C).

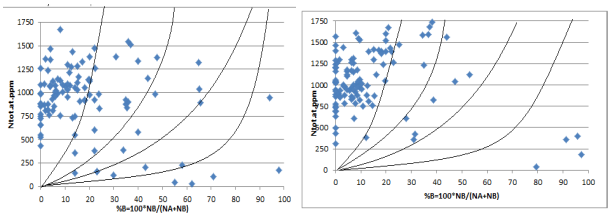


Figure 10. Taylor diagram for diamond crystals from the Arkhangelskaya pipe (a) and pipe Karpinskaya-1 (b)

5 Conclusion

It was established that diamonds in studied pipes have similar gemological characteristics: diamonds with different shades and with a high degree of transparency dominated in both pipes; crystals in the form of curve-faced dodecahedra of the 1-st varieties according to Yu.L. Orlov's classification (1984) predominate and inclusions of graphite, garnet and fluid detected in the diamonds of the both pipes. It was revealed that the diamonds in studied pipes have significant features of the difference: the pipes are different in content of colored diamonds; pipes vary in content of diamonds with different forms of crystals. The differences of gemological and spectroscopic properties of the diamond related to their genetic features.

Acknowledgements

We are grateful to our colleagues for the help in research: Vasilyev E.A from St. Petersburg mining university and D.V. Korost from the Department of Geology of the Lomonosov Moscow State University.

References

Possoukhova TV, Kudryavtseva GP & Garanin VK (1999) Diamonds and accompanying minerals from the Arkhangelsk kimberlite, Russia. In: In"Mineral Deposits: Processes to Processing", Balkema, Rotterdam, v. 1. pp. 667-670

Possoukhova TV, Kudryavtseva GP, Garanin VK, Tikhova M, Verichev EM (2001) Two types of the diamondiferous kimberlites from the Arkhangelsk Province (Russia). In: Mineral Deposits at the Beginning of the 21th Century, Balkema, Rotterdam

Kudryavtseva GP, Posukhova TV, Verzhak VV, et al. (2005) Atlas - Morphogenesis of diamond and satellitic minerals in kimberlites and related rocks of Arkhangelsk kimberlitic province. Arctic Circle, 624 p., in Russian

Orlov Yu. L. (1984) Mineralogy of diamonds.- Moscow: Nauka (in Russian)

GS01 – General session

Convenors:
Pierre-Simon Ross
Patrick Mercier-Langevin

Geochemical survey for rare earth elements in the Hongcheon area, Korea

Joo Sung Ahn, Seung-Jun Youm and Yong-Chan Cho
Korea Institute of Geoscience and Mineral Resources

Abstract. To explore for new ore bodies, a geochemical survey was conducted at one existing carbonatite REE deposit in the Hongcheon area of Korea. Proper sampling strategies and baseline data for the interpretation of the results were determined through a pilot study conducted in the area. Enrichment in the concentration of LREE over that of HREE, which is typical in carbonatite-type deposits, was observed in stream sediments and heavy mineral samples collected during the geochemical survey. Maximum concentrations of LREE were 2,299 ppm and 27,798 ppm for stream sediments and heavy minerals, respectively. Lanthanum and Ce are the dominant components of all REEs, comprising approximately 68 % of mean concentrations. Considering the distribution pattern of La+Ce contents and the associations with the existing outcropping ore bodies, the zone of prospective REE mineralization was determined to be in the south-western part of the area. A detailed follow-up soil survey of the zone found even higher concentrations of La and Ce (2,450 and 3,100 ppm, respectively), and suggested the possible extension of the existing ore bodies.

1 Introduction

The rare earth elements (REEs) are essential for a diverse and expanding array of high-technology applications. REE-containing magnets, metal alloys for batteries and lightweight structures, and phosphors are essential for many current and emerging alternative energy technologies, such as electric vehicles, energy-efficient lighting, and wind power. REEs are also critical for other advanced materials, as well as a number of key defense systems (Long et al. 2010).

Although REEs are relatively abundant in the Earth's crust, they are rarely concentrated into mineable ore deposits. With the exception of surveys of rock outcrops, such as carbonatites, geochemical exploration based on the analysis of stream sediments and/or soils has not been frequently applied to REE mineral prospecting of concealed ore bodies. This paper describes a systematic geochemical survey for REE in the Hongcheon area of Korea. The purpose of this study is to establish the importance and suitability of stream sediment and soil surveys as tools used for the discovery of concealed REE ore bodies.

2 Study area

Due to the supply risk of REEs worldwide, the necessity of developing domestic sources of REE in Korea has been recognized. However, notably few occurrences of mineralization are reported, and the Hongcheon Fe-REE bearing intrusive carbonate rock is the only carbonatite-type ore deposit known in Korea. The total ore reserve of 25,974 Mt was estimated by drilling a total of 1,900 m (13 holes) into the ore bodies (KIGAM 2001). The average ore grade was 2.13 % of total rare earth oxides (TREO). The main rock types in the area are metamorphic rocks of Precambrian age, and granites, felsites and dikes of Mesozoic age (Fig. 1). The metamorphic rocks are mostly biotite gneiss and biotite-hornblende gneiss, which display banded structure. Igneous rocks of Mesozoic age are two-mica granite, porphyritic granite, pink feldspar porphyritic granite and felsite. The banded gneisses contain the northern, middle and southern ore bodies (Fig. 1), which are narrow and long shaped, north-south trending carbonate sill intrusions with widths of 20-50 m and a length of 2,500 m. The mineralization age of the carbonate sills, measured by monazite isochron dating, is 888±42 Ma (KIGAM 2001).

Considering the discontinuous distributions of the 3 ore bodies and the folding structures of the hosting gneiss, there may be extensions to known orebodies or new orebodies, yet to be discovered (Lee and Ryoo 2012). Thus, the REE mineralization in the Hongcheon area was chosen as the most promising site for securing a sufficient supply of the resources. However, with the exception of the ore bodies, the rock outcrops are not well-exposed in the nearby area. Geochemical surveys of stream sediments and soils were used to prospect for the possible concealed ore bodies.

3 Materials and methods

For the geochemical survey on a local scale in the study area (approximately 180 km^2), two stages of sampling were conducted. First, 149 stream sediment and 43 heavy mineral samples were collected to cover the entire study area, which contains 43 catchments. During the second stage, the sampling was targeted at the areas where either the sediments or the heavy minerals displayed elevated REE concentrations. Additional samples of 52 stream sediments and 38 heavy minerals were collected during the second stage. Locations of all samples are shown in Fig. 1. The most prospective zone was designated through the geochemical survey, and higher-density soil sampling was conducted during the final follow-up survey to locate the position of the related anomalies with greater accuracy.

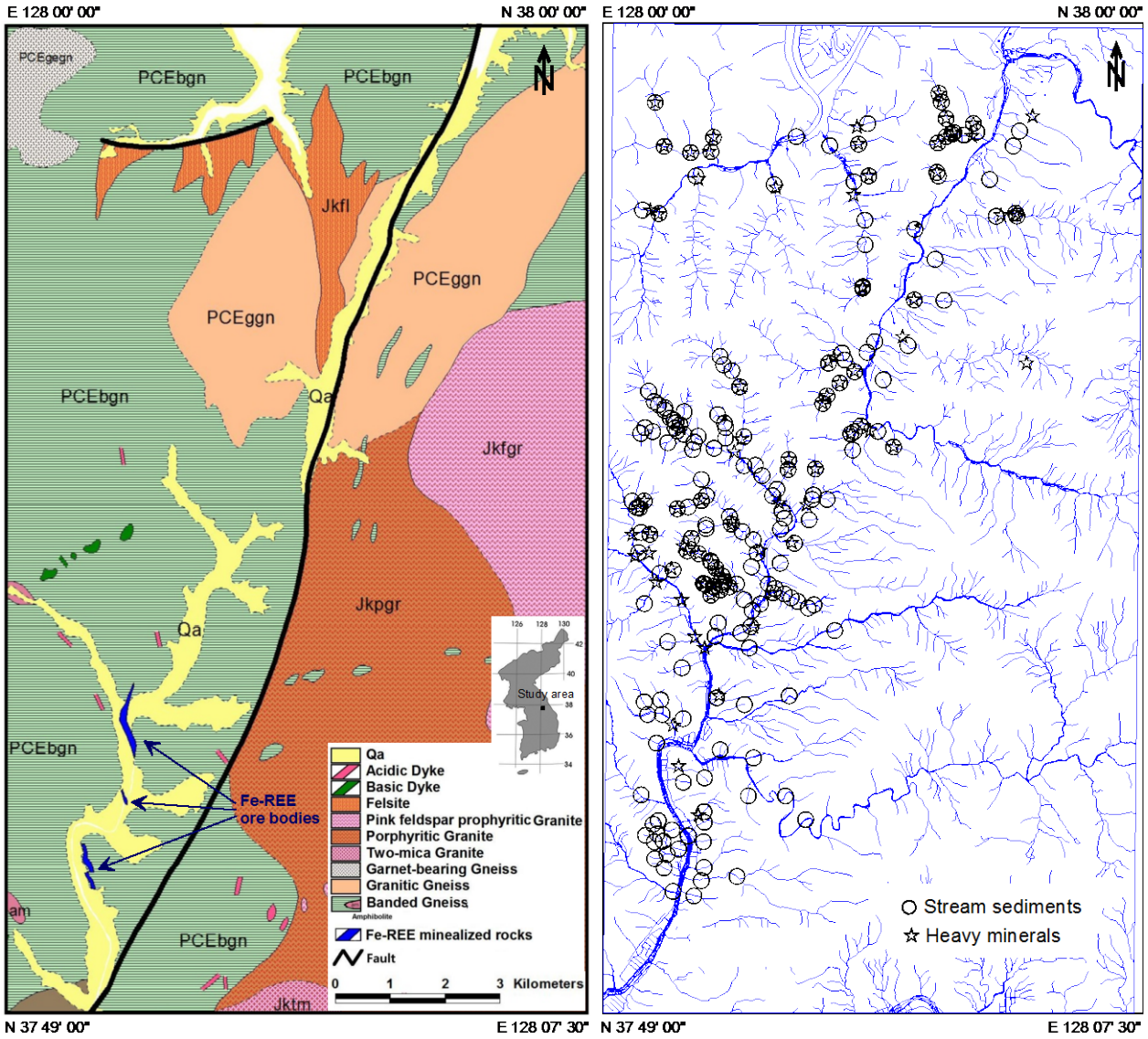


Figure 1. Geologic map and sampling locations of the study area

During the geochemical survey, stream sediment and heavy mineral samples were collected with a density of 0.5-1 sample/km^2. Stream sediment samples were collected at first or second order streams and a minimum of 100 g of samples was obtained by wet sieving through an 80-mesh sieve (< 180 μm). Heavy mineral samples were collected primarily from third order streams by panning; after dried, they were ground to a fine powder. All soil samples were air-dried, sieved through an 80-mesh sieve and ground. A 0.1 g portion of each sample was digested using HF, HNO_3, and $HClO_4$ solutions at 130°C for 24h. The digested product was evaporated to dryness under 220°C and the residue was dissolved in dilute HNO_3 solution. The concentrations of the 15 REEs (Y and the 14 elements of the Lanthanide series excluding Pm) and their related elements (Th, U, Sr, Ba, V, Mo, W, Zr, Nb and Ta) were determined using inductively coupled plasma mass spectrometry (ICP-MS) or atomic emission spectrometry (ICP-AES).

4 Results and discussion

4.1 Geochemical survey of stream sediments and heavy minerals

REE and other related elemental concentrations in the stream sediment samples are summarized in Table 1. The TREE concentrations of 201 stream sediment samples vary from 171 to 2,463 ppm with an average of 464 ppm. The average TREE concentration of the area is approximately 2.8 times greater than that of the upper crust of the Earth (168 ppm) (Wedepohl 1995). LREE (La to Eu) concentrations have a mean value of 421 ppm, approximately 3.1 times higher than the upper crust value (136 ppm) (Wedepohl 1995), while HREE (Gd to Lu and Y) concentrations are approximately 10 times lower than those of LREE and not much greater than those of the upper crust. The concentrations of TREE in the heavy mineral samples ranged from 414 to 28,999 ppm with a mean value of 3,997 ppm, indicating approximately 9 times more enrichment than in the

Table 1. Statistical summary of the data for stream sediments in the study area during the geochemical survey (units in ppm)

Element	N[a]	Min	Max	Mean	Median	SD
La	201	36.0	661	113	86.0	85.0
Ce	201	75.0	1,110	202	157	138
Pr	201	8.5	139	23.8	18.8	16.3
Nd	201	21.0	412	69.0	56.0	43.7
Sm	201	4.8	89.5	12.5	10.6	7.8
Eu	196	0.7	4.9	2.0	1.9	0.7
Gd	201	4.0	72.1	11.2	9.8	6.4
Tb	200	0.5	6.5	1.3	1.1	0.6
Dy	201	1.7	18.9	5.0	4.8	2.0
Ho	184	0.4	2.9	0.9	0.9	0.3
Er	197	0.7	6.8	2.1	2.1	0.8
Tm	35	0.2	1.2	0.4	0.4	0.2
Yb	201	0.4	5.4	1.7	1.7	0.7
Lu	35	0.2	0.6	0.3	0.3	0.1
Y	201	6.2	70.2	20.7	20.0	8.6
TREE	201	171	2,463	464	375	296
LREE	201	149	2,299	421	333	333
HREE	201	13	164	43	41	41
La+Ce	201	112	1,655	314	242	221
Th	200	11.6	254	38.8	31.8	28.9
U	201	0.8	44.9	5.1	4.4	4.6
Sr	184	47.0	709	229	188	144
Ba	201	242	1,441	824	773	241
V	200	25.4	183	83.4	81.0	28.6
Mo	8	10.1	25.0	14.1	11.2	5.9
W	34	10.1	285	21.1	12.1	46.8
Zr	201	27.0	399	69.3	63.0	39.0
Nb	160	7.0	162	44.0	37.0	29.7
Ta	4	21.0	143	71.0	60.0	60.5

[a] Number of samples whose contents are above detection limits

sediment samples. Characteristics of the greater enrichment of LREE than HREE, and the dominance of La and Ce, are also present in heavy minerals

Distributions of La+Ce concentrations in the stream sediments and heavy minerals are plotted in Fig. 2 and are used to search for areas suitable for prospecting for REE mineralization. The concentrations in the stream sediments varied from 112 to 1,655 ppm with a mean of 314 ppm. The maximum value was found at a location in the north-western part of the study area. Six-fold higher values (588 ppm) than that of the upper crust (98 ppm) were found in at least 5 zones, including south-western, mid-western and upper-northern parts of the area.

Within the areas of anomalous La+Ce contents, taking into consideration possible extensions from the existing outcropping ore bodies and close locations of stream sediments of high concentrations, the most prospective zone of LREE enrichment was designated to be in the south-western part of the study area (Fig. 2).

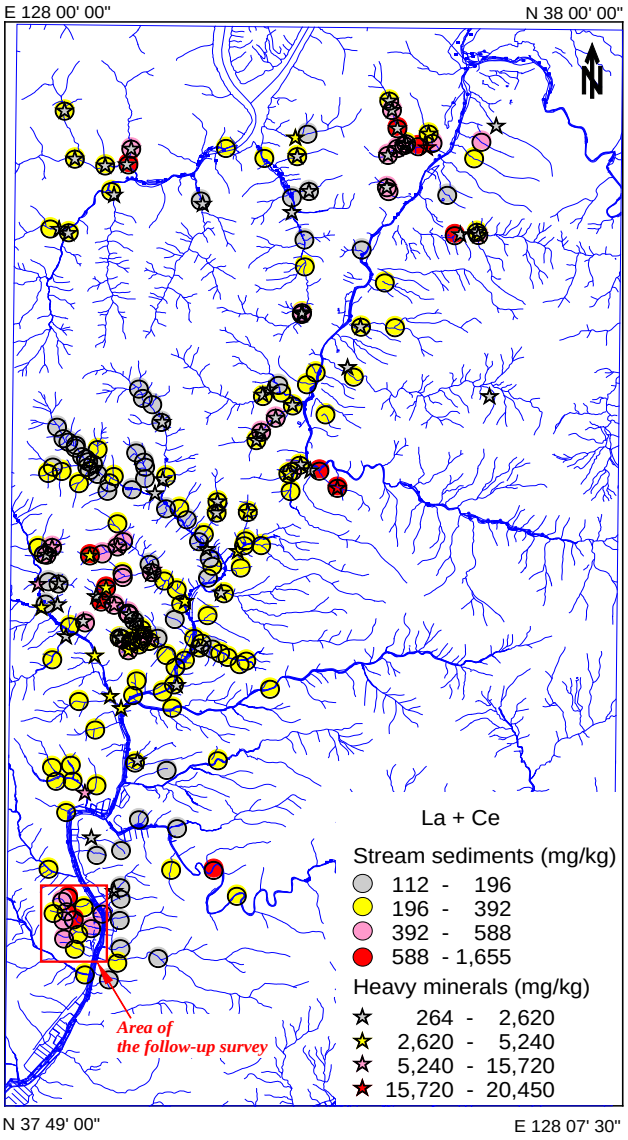


Figure 2. Distribution of La+Ce contents in stream sediments and heavy minerals (Indicated is the area of the follow-up survey)

4.2 Follow-up survey

At the ridges and stream basins of the target prospecting zone (0.6 x 1.3 km^2), 193 soil samples were collected at a spacing of 25 - 50 m. The mean concentrations of La and Ce were 151 ppm (1,100 ppm at maximum) and 237 ppm (1,470 ppm at maximum), respectively. At the site with the highest concentrations of La and Ce, additional 30 grid soil samples were taken at a spacing of 4 m; higher La (2,450 ppm) and Ce (3,100 ppm) concentration values were found at this location.

Approximately 40 rock chips were collected at this location by hand digging to approximately 2 m depth. Among the chips, TREE contents of 2 samples were found to be 4.4 and 2.0 %, which are comparable to values of total rare earth oxide (TREO) grades of the existing ore bodies (0.1 - 4.6%). Monazite minerals containing high

contents of La and Ce were identified from the XRD and SEM-EDS analyses for the rock chip samples (Fig. 3). There is a good possibility that the concealed REE ore body resides beneath this location, and further geophysical and drilling explorations are needed. This area is located at approximately 1 km south of the existing known ore bodies and, in a structural geological sense, could be an extension of the ore bodies. Likewise, it is feasible to conduct a systematic geochemical survey to locate concealed ore bodies in the areas where the mineralization is mostly covered with soil, and rock outcrops are scarce.

Acknowledgements

This research was supported by the Basic Research Project (17-3413) of the Korea Institute of Geoscience and Mineral Resources (KIGAM) funded by the Ministry of Science, ICT and Future Planning of Korea.

References

KIGAM (2001) Mineralization and feasibility study of Fe-REE deposits in Hongcheon area, S. Korea. 2000-R-TI02-P-01, Korea Institute of Geoscience and Mineral Resources (In Korean with English Abstract)

Lee HY, Ryoo CR (2012) Developmental aspects of Hongcheon Fe-REE ore body. Jour Petrol Soc Korea 21:397-403 (In Korean with English Abstract)

Long KR, Van Gosen BS, Foley NK, Cordier D (2010) The principal rare earth elements deposits of the United States—A summary of domestic deposits and a global perspective. Scientific Investigations Report 2010-5220, U.S. Geological Survey

Wedepohl KH (1995) The composition of the continental crust. Geochem Cosmochim Acta 59:1217-1232

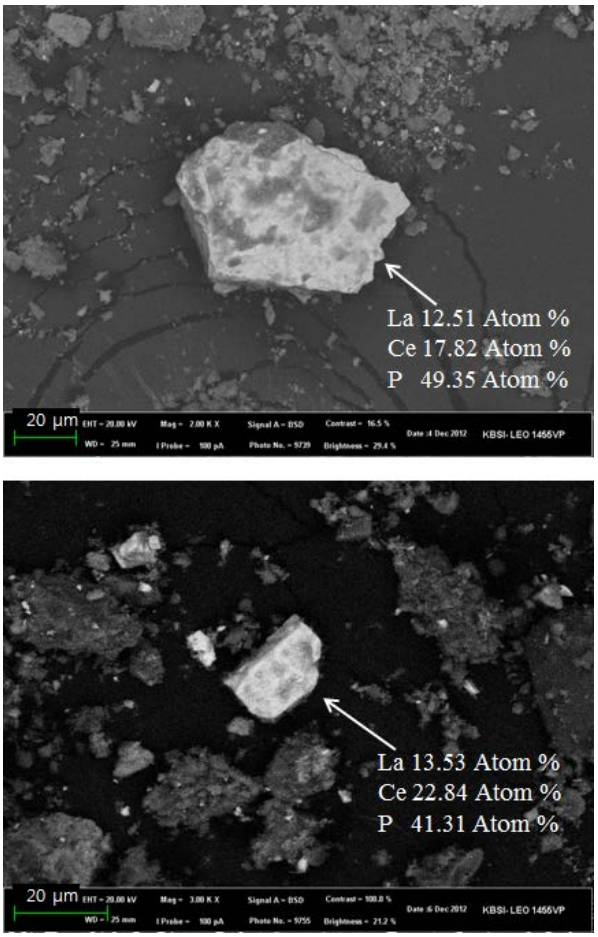


Figure 3. Back-scattered electron images of monazite in rock chip samples from the target zone

The Northern Manitoba Mining Academy: providing resource-related trades training and support for research

Paul Alexandre
Northern Manitoba Mining Academy

Abstract. The Northern Manitoba Mining Academy (NMMA, miningacademy.ca) is a new educational institution located in Flin Flon, Manitoba. It is associated with the University College of the North and is specifically intended to serve the needs of the Northern Manitoban communities with regards to job creation by providing training in a variety of mining, construction, and exploration related areas.

NMMA's mission is to provide innovative and responsible solutions for the creation of a knowledgeable, skilled, and sustainable workforce within a vibrant, mineral-rich resource industry. It facilitates strategic training initiatives and research activities in order to strengthen the social, economic, and environmental benefits of a robust mining and resources sector.

1 Who we are

The Northern Manitoba Mining Academy (NMMA, miningacademy.ca) is a new educational institution located in Flin Flon, Manitoba. It is associated with the University College of the North and is specifically intended to serve the needs of the Northern Manitoban communities with regards to job creation by providing training in a variety of mining, construction, and exploration related areas.

NMMA's mission is to provide innovative and responsible solutions for the creation of a knowledgeable, skilled, and sustainable workforce within a vibrant, mineral-rich resource industry. It facilitates strategic training initiatives and research activities in order to strengthen the social, economic, and environmental benefits of a robust mining and resources sector.

2 Our values

The Northern Manitoba Mining Academy is founded on the bedrock values of:

- Excellence in education and research;
- Dedication to finding solutions to real world problems;
- Respect, celebration and diversity of our students, communities and services;
- Reducing the environmental footprint of all that we do and all that we leave for the future;
- Prudent use of financial, capital and human resources;
- Maximizing social, economic and ecological benefits in a manner benefiting all;
- Providing innovative and responsive solutions; and
- Creating a knowledgeable, skilled and sustainable workforce within a vibrant resource industry.

The Northern Manitoba Mining Academy operates as a wide-ranging partnership between academia (University of Manitoba, University of Winnipeg, Brandon University, University College of the North), industry (Vale, HudBay), Indigenous Peoples in Manitoba groups (Manitoba Métis Federation , Manitoba Keewatinowi Okimakanak), and government (City of Flin Flon, Government of Manitoba, Northern Manitoba Sector Council).

3 Our location

A central premise for the location of the Northern Manitoba Mining Academy in Flin Flon is proximity to the potential students, many of whom come from northern communities and for whom travel and accommodation in the south, for instance Winnipeg, is prohibitively expensive. Proximity to the students' community, but also video conferencing capabilities, accessible through the UCN, are major factors in providing education to those who mostly need it in the best possible conditions. From this point of view, accommodating students at a minimal or no charge is the next challenge that would allow the NMMA to grow and better serve its students. The Academy is in the process of securing funding for a modern, comfortable, and friendly accommodation right on its premises; planned opening of the residence is early 2017. The Academy is actively reaching to people in the North as they are the people most aware of their wants and needs and of what it takes to live and work in the north.

4 The education we provide

In terms of education, NMMA offers its own programs, mostly short courses in health and safety, courses organized by the University College of the North (wilderness safety, prospecting, and exploration), and courses organized in association with the Manitoba Heavy Construction Association (a variety of construction-related trades). However, the programming is not limited to those courses already on the syllabus: the Academy operates on open-doors policy and welcomes people with their unique and diverse needs; it prides itself in its ability to tailor or create specific on-demand courses and deliver them locally in the North.

The NMMA is also becoming increasingly involved in Manitoba health-related training, such as training trauma counsellors and response teams that can be located in northern communities and be prepared for timely and effective intervention. This is an area of increasing

importance and growth for the Academy.

NMMA is hosted in its own building, adjacent to the HudBay Minerals mining complex in Flin Flon, Manitoba, and next door to the University College of the North, Flin Flon Regional Centre. It boasts several classrooms, chemical and computer labs, sample preparation facilities, underground mining heavy equipment simulator, and an assortment of geological microscopes. A full list of facilities and equipment is available on the NMMA's website.

5 Support to field-based research

The Northern Manitoba Mining Academy also provides access to its world-class facilities for field-based undergraduate courses, as well as graduate students and researchers doing field work. Full sample preparation facilities are offered to students and scientists in all natural and environmental sciences. The Academy has a mandate to facilitate and provide support to basic and applied research by establishing a natural resource-related research platform that is primarily inspired and directed from and for the north. Within the framework of this platform, assistance to external resource-related researchers will be accomplished through: a) increasing the general level of knowledge regarding the FFRC and the NMMA and their services; b) identifying the research needs and priorities of northern stakeholders; c) identifying the internal and external resources available to meet northern stakeholder research needs; d) developing long-term partnerships and linkages between research-focused institutions and researchers, relevant industries, and local, provincial and federal research institutions and governments; and e) providing logistic support, such as research facilities, affordable accommodation, and relevant information and connections.

6 Conclusions

The overall goal of the research-supporting platform will be to secure long-term sustainability, economic development, and job-creation and wealth generation in northern Manitoba through natural resource and related research.

In conclusion, the Northern Manitoba Mining Academy is a unique educational partnership with the specific purpose to serve the needs of Northern Manitoba communities in providing practical trades training in very close proximity to where potential students are. The NMMA is actively reaching to the northern communities and residents and proactively helping them become stronger; it is also paying heed to the wants and needs of Northern Manitoba residents. The Academy is growing fast and is ambitious in its aim to serve Northern Manitoba in its job creation endeavours.

Tetrahedrite-freibergite from Ag-Pb-Zn the Prognoz deposit (Russia, Sakha-Yakutia): Implication for ore genesis

Elena Anikina and Nikolay S. Bortnikov
Russian Academy of Sciences

Abstract. Tetrahedrite-Freibergite group, their mineral associations, intergrowths and chemical composition from Silver-Lead-Zinc epithermal Prognoz deposit have been studied. Possibility of using of fahlores as indicators of ore-forming environments of the deposit was shown.

1 Introduction

Fahlores ($M^{+}_{10}\ M^{2+}_{2}\ X^{3+}_{4}\ Y^{2-}_{13}$, where M^{+} = Cu, Ag, M^{2+} = Cu, Hg, Fe, Zn, Pb, Mn, Co, Ni, Cd, X = As, Sb, Bi, Te, Y = S Se) are widespread in of hydrothermal deposits of precious and base metals, occurring in a wide range of settings worldwide. They are among the most common sulphosalts, and are present in larger or smaller amounts in many sulphide deposits throughout the world (Klünder et al. 2003 a, b). Fahlores are the principal source of Ag to the mining industry (Sack et al. 2003). Their characteristic feature is the variety of isomorphous substitutions. Fahlores "sensitively" react to changes in physic-chemical parameters of the environment of mineral-forming. The ability of fahlores for formation of solid solution gives considerable potential for determining of ore deposition environments. It has for a long time attracted the attention of many researchers. The main objective of these researches is the estimation of possibility of using fahlores as petrogenetic indicator of ore-forming processes at the Ag-Pb-Zn deposit..

2 Geological setting

The Ag-Pb-Zn Prognoz deposit is an epithermal deposit in a terrigenous sequence. It is located in the western Verkhoyansk fold–thrust belt (Fig.1, inset), which extends along the north-eastern margin of the Siberian continent. It is confined to a core of an anticline fold broken into blocks by faults of the north-eastern strike. The deposit area is composed of Triassic sandstones with siltstone interlayers (Fig. 1) (Gamyanin et al. 1998) intruded by basic and felsic dikes. Two types of dikes have been identified: pre-ore diorite porphyries and intra-ore subvolcanic quartz porphyries. Ore zones are located in a block bounded by north-striking and northeast-trending strike-slip faults.

Twelve ore bodies are known at the deposit. These are the mineralized fracture zones composed of breccia, veins and disseminated ores of various fabrics. Two stages were revealed, significantly different in mineral composition and in textures. Coarse-blocked, coarse-grained and massive textures are typical for the first stage. These mineralizations are characterized by a low silver content. Main silver minerals of this stage are galena and low-Ag tetrahedrite. The second stage is featured by breccias, banded, crustified, cockade, druse-like textures. The most economically significant silver mineralization of the second stage is superimposed on quartz dikes. It consists of siderite-galena-sphalerite, quartz-sulfide-sulfosalt, quartz-pyrite-sphalerite-ankerite-dolomite, and quartz-calcite assemblages. Several mineral paragenetic association are distinguished in these assemblages. Minerals carrying silver are galena, freibergite, and argentian sulfosalts.

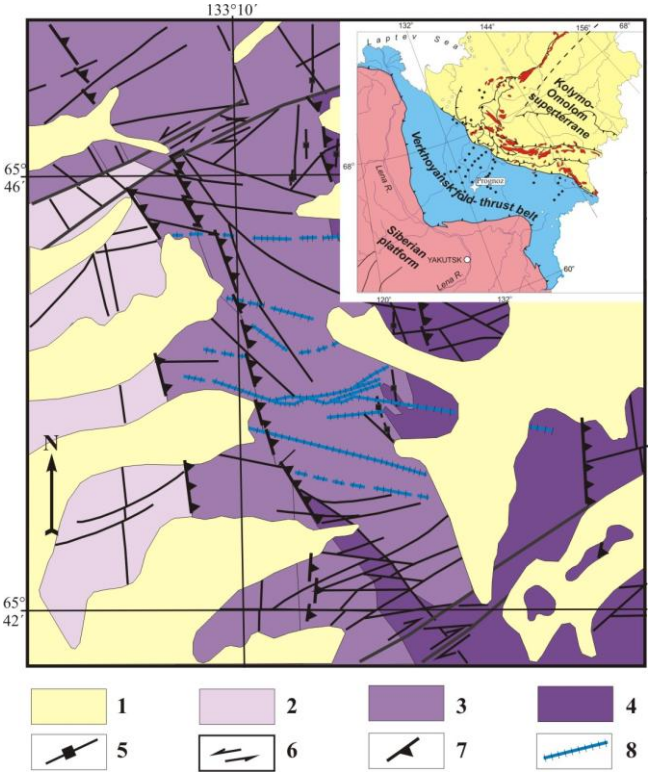


Figure 1. Geological scheme of the Ag-Pb-Zn Prognoz deposit. 1 - Alluvium and deluvium sediments, 2 - Triassic sediments of Norian and Carnian stages, 3 - Triassic sediments of Ladian stage, 4 - Triassic sediments of Anisian stage, 5 - Quartz dykes, 6 -Strike-slip faults , 7 - Upthrust, 8 - Ore bodies. Inset – main tectonic units of the Sakha-Yakutia.

Fahlores observed in several assemblages from both stages: chalcopyrite-bismuthinite-tetrahedrite-galena, sphalerite-galena-tetrahedrite (1-st stage); galena-burnonite-tetrahedrite (freibergite)-Ag-sulphoantimonite,

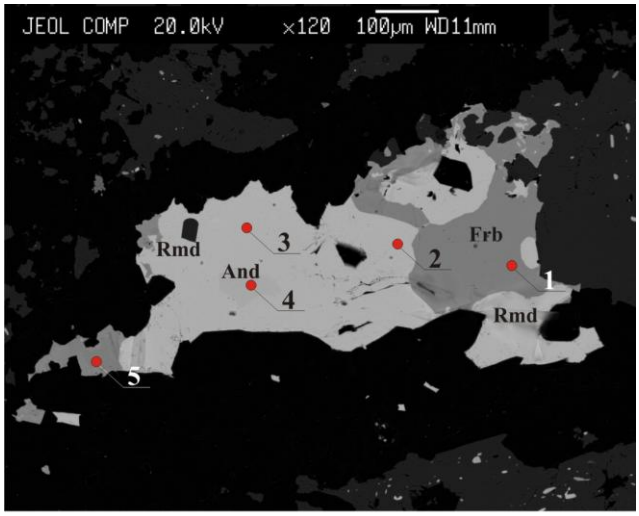
miargirite-pyrargirite-tethahedrite (freibergite)-galena (2-st stage).

3 Mineral associations and intergrowths of fahlores

Two generations of fahlores were identified.

Tetrahedrite-I (1-st stage) is associated with chalcopyrite, sphalerite, and mainly with galena. It occurs as an impregnation and small aggregates with stannite and bournonite in galena.

Tetrahedrite-II (2-nd stage), which belongs to the tetrahedrite– freibergite isomorphous series, is observed as aggregates associated with galena, sphalerite, and various silver-bearing sulfosalts. These aggregates form large (up to 20 cm) patches in siderite and quartz. Tetrahedrite-II forms intergrowths with other minerals of this mineralization (Fig.2), inclusions in other minerals or contains inclusions of sphalerite, galena, chalcopyrite, stannite (Cu_2FeSnS_4), owyheeite ($Ag_2Pb_5Sb_6S_{15}$), andorite ($Ag_4Pb_4Sb_{12}S_{24}$), ramdohrite ($Ag_4Pb_6Sb_{10}S_{23}$), pyrargyrite (Ag_3SbS_3), miargirite ($AgSbS_2$) (Fig. 3 a) and stephanite (Ag_5SbS_4). Fahlores with a heterogeneous chemical composition were observed (Fig. 3 b). The heterogeneity is caused by changes in the concentrations of iron and silver.



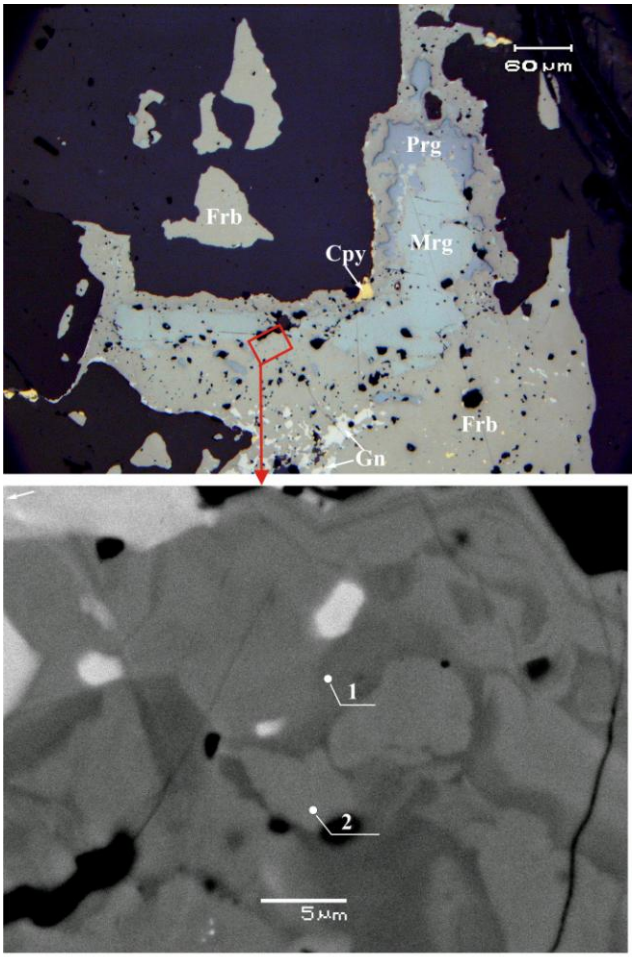
№	mineral	Ag	Cu	Zn	Fe	Pb	Sb	Bi	S	Sum
1	Freibergite	24,0	21,2	0,7	5,6	-	26,2	-	21,5	99,2
2	Ramdohrite	9,2	0,4	-	0,1	33,1	36,4	1,7	18,9	99,8
3	Ramdohrite	9.3	-	-	-	33,2	36,6	3,2	19,3	100,5
4	Andorite	11,5	-	-	-	21,9	43,3	4,5	20,7	101,9
5	Freibergite	23,6	21,8	1,44	4,9	-	26,1	-	21,5	99,3

Figure 2. The intergrowth of ramdohrite (Rmd), andorite (And) and freibergite (Frb) in a quartz cavity. SEM image. № analyses in the table correspond to those in figure.

4 Chemical compositions

Microprobe analyses of fahlores and associated sulfosalts were performed with JXA-8200 electron microprobe (JEOL Ltd., Japan) with five wavelength-dispersive spectrometers at the IGEM RAS. The operating conditions were as follows: a voltage of 20 kV, a beam current of 20 nA and a beam diameter of 1 μm. More than 200 grains of falohres have been studied. Analysis of fahlores is embarrassed due to their heterogeneous textures (zoning, mottling), often intimate intergrowths with other minerals and small sizes of grains. The width of zones in the zonal grains sometimes does not exceed 1 μm that leads to capture of several bands by probe beam.

Fahlores are the most widespread among silver-bearing minerals from the Prognoz deposit. A chemical composition fahlores corresponds to Ag-tetrahedrite and freibergite. According to an IMA report, fahlore containing more than 23 wt % silver are defined as freibergite (Moelo et al. 2008).



№	mineral	Ag	Cu	Zn	Sb	S	Sum
1	freibergite	25,3	18,9	5,1	28,0	22,0	99,3
2	freibergite	33,5	13,7	5,7	27,4	21,1	101,4

Figure 3. a Freibergite (Frb) with inclusions of pyrargyrite(Prg)-miargirite (Mrg) aggregate with slots of galena (Gn) and chalcopyrite (Cpy) in a quartz cavity, optic microscope image. **b** fragment a, two-phase freibergite, SEM image. № analyses in the table correspond to those in figure.

The studied fahlores exhibit a wide range in contents of main components (wt.%): 11.5-37.4 Cu, 0.73-35.6 Ag, 0-7.4 Zn, 0.15-6.2 Fe, 23.4-29.4 Sb, 21.0-24.8 S; they also

contain (wt.%) up to 1.5 Hg, up to 1.7 As, up to 5.46 Bi, up to 2.66 Sn.

The Bi and Sn incorporation in fahlore is exotic. The Bi solubility (Klünder et al. 2003 a) in tetrahedrite –tennanite can reach 0.8 apfu at 350°C. The highest Sn solubility ≈1.6 apfu was observed (Klünder et al. 2003 b). These authors noted that majority of the analyzed tetrahedrite/tennantite grains have a tin content of less than 0.4 apfu. The high Sn content may be due to inclusions of Sn-rich phases (possibly stannite) (George et al. 2017).

The composition of the studied fahlores shows the formulae of $(Ag_{0.11\text{-}6.48},Cu^{+}_{3.52\text{-}9.89})_{\Sigma\ 9.67\text{-}10}(Cu^{2+}_{0.00\text{-}0.52}Fe_{0.00\text{-}1.88},Zn_{0.00\text{-}2.00})_{\Sigma 1.78\text{-}2.33}(Sb_{3.49\text{-}4.17},As_{0.00\text{-}0.4},Bi_{0.00\text{-}0.5})_{\Sigma 3.58\text{-}4.18}S_{12.65\text{-}13.32}$. Antimony dominates over arsenic in all analyses, thus, all fahlores are indentified as the tetrahedrite end-member. This tetrahedrite exibits significant variations in Ag/(Cu + Ag) and Fe/(Zn + Fe) ratios. There is no relationship between these values (Fig.4).

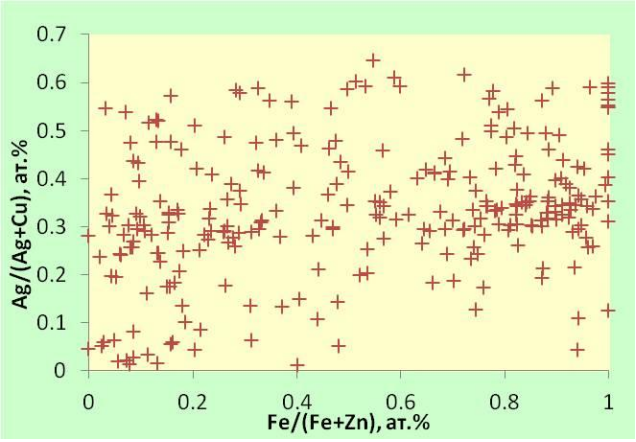


Figure 4. Fe/(Fe + Zn) and Ag/(Ag + Cu) of fahlores from the Prognoz deposits

The Ag content in early and late tetrahedrite generation is dramatically different. The early one contains up to 5 wt % Ag and is a low-iron variety. Tetrahedrite-II displays wide variations in the Ag content that ranges between 0.7 and 35.5 wt %, mostly from 18 to 23 wt %. Oscillations of zinc and iron contents are considerable as well. The (Ag/Ag+Cu) and (Fe/Fe+Zn) ratios vary from 0.01 to 0.67 and from 0 to 1, respectively (Fig. 4). The (Ag+Cu) varies from 9.6 to 10.6 apfu.

The wide compositional variations of this mineral were found in the same sample. Intimate intergrowths of tetrahedrite grains that differ in Cu, Ag, Fe, and Zn contents were observed. The range of Ag content in a same grain may lies within 10 to 20 wt %.

5 Vertical zoning

The distribution of fahlores and other silver sulfosalts in the longitudinal section of the main ore body of the Prognoz deposit has been studied (Gamyanin et al. 2003). A mineral and compositional zonality has been revealed. Fahlores constitute approximately 90% of the total amount of all sulfosalts. The samples of mineral aggregates of the late stage were used, because products of the first stage often were overprinted by later hydrothermal processes. An increase in the amount of silver minerals toward the upper horizons has been revealed. They maximal content was recorded at a depth of 478 m (Fig. 5). This is due to the presence of a so-called structural trap. In this place there is a connection of several ore bodies, and therefore there is an increase of thickness of the ore-hosting structure. On the upper horizons of the deposit, repeating the distribution of sulfosalts, silver-rich areas are grouped.

The blind compositional zoning was revealed due to the variation of Ag/(Ag+Cu) ratio in ores. This value increases with decreasing depth, reaching a maximum in surface workings.

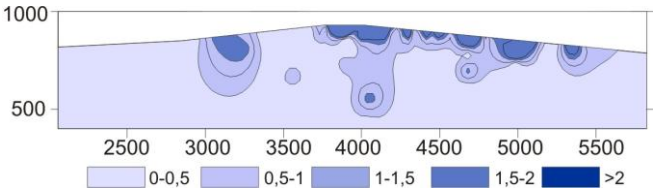


Figure 5. Distribution of sulfosalts in the longitudinal section of the main ore body of the Prognoz deposit.

6 Discussion

The study of fahlores and associated minerals allows us to understand their depositional conditions and the causes of the zonal distribution of fahlores of the various compositions. Hackbarth and Petersen (1984) had been proposed a model of fractional crystallization of fahlores to explain a change in the Ag/(Ag + Cu) ratio. They concluded that tetrahedrite closest to the fluid source is richer in Cu and As as these components are incorporated preferably into this mineral relative to Ag and Sb. Thus, during the mineral crystallization the Cu and As content in a fluid decreases and this results in an increase of Ag and Sb concentration, which caused a gradual enrichment of fahlore in these elements.

Mookherjee and Mishra (1984) suggested that a change in the Ag/(Ag+Cu) ratio in fahlores can depend on changes in NaCl concentration in the fluid. This assumption is based on an assumption that Ag and Cu were migrated as chloride complexes. The exchange reaction between tetrahedrite and chloride complexes of Ag and Cu is as follows:

$$Cu_{10}Fe_2Sb_4S_{13}+x\ AgCl^{2-}= Ag_xCu_{10-x}Fe_2Sb_4S_{13}+x\ CuCl^{0}+x\ Cl^{-} \qquad (0\le x\le 10) \quad (1)$$

This equation shows the equilibrium shift to the right and contributes to an increase in the (Ag/Ag+Cu) ratio in tetrahedrite. The solubility of silver increases with the increasing of temperature, activity of chlorine, f_{O2} and with decreasing of pH and $a_{\Sigma(H2S+HS^-)}$.

A model of retrograde Ag-enrichment in fahlores was proposed (Sack et al. 2002, 2005). Formation of fahlores enriched in Ag is assumed to be result from the Ag-Cu exchange reaction:

A model of retrograde Ag-enrichment in fahlores was proposed (Sack et al. 2002, 2005). Formation of fahlores enriched in Ag is assumed by the Ag-Cu exchange reaction:

$$\underset{\text{Cu-fahlore}}{1/10\ Cu_{10}(Zn,Fe)_2Sb_4S_{13}} + \underset{\text{in galena}}{AgSbS_2} + \underset{\text{galena}}{PbS} =$$

$$\underset{\text{bournonite}}{CuPbSbS_3} + 1/10\ \underset{\text{Ag-fahlore}}{Ag_{10}(Zn,Fe)_2Sb_4S_{13}}, \qquad (2)$$

which occurred during the fluid cooling Hovewer, this mechanism cannot be responsible for the formation of mineral associations at the Prognoz deposit because a distinct population of high-Ag fahlores and coronas of bournonite around fahlores were not observed.

Fluid inclusion studies indicated that mineral deposition at the Prognoz deposit occurred at the decrease of temperature from 225 to 100°C and fluid salinity from 29.0 to 8.0 wt % NaCl-equiv. (Gamyanin et al. 1998). It is possible that the change of these physic-chemical parameters and the metal complex stability has resulted in the compositional variations of fahlores and the blind zonation of the ore body.

Acknowledgements

The study was supported by the Russian Academy of Sciences, Program of Fundamental Research (Program № 72-2) and BES (Program №III.8.3).

References

Gamyanin GN, Anikina EYu, Bortnikov NS et al. (1998) The Prognoz Silver–Polymetallic Deposit, Sakha: Mineralogy, Geochemistry, and Origin. Geol Ore Depos 40(5):391–407.

Gamyanin GN, Anikina EYu, Bortnikov NS, Alpatov VV (2003) The Prognoz Silver–Polymetallic Deposit, Sakha (Yakutia): Chemistry and Zoning of Ore Veins. Geol Ore Depos 45(6):466-480.

George LL, Cook NJ, Ciobanu CL (2017) Minor and Trace Elements in Natural Tetrahedrite-Tennantite: Effects on Element Partitioning among Base Metal Sulphides. Minerals 7(2):17. Doi: 10.3390/min7020017

Hackbarth CJ, Petersen U (1984) A fractional crystallization model for the deposition of argentian tetrahedrite. Econ Geol 79:P.448–460.

Klünder MH, Karup-Møller S, Makovicky E (2003a). Exploratory studies on substitutions in the tetrahedrite-tennantite solid solution series Part III. The solubility of bismuth in tetrahedrite-tennantite containing iron and zinc. N Jahrb Miner-Monatsh 4:153-175.

Klünder HM, Makovicky E, Karup-Møller S. (2003b). Exploratory studies on substitutions in tetrahedrite–tennantite solid solution. Part IV. Substitution of germanium and tin. N Jahrb Miner-Abh: Journ Miner Geochem 179(1):43-71.

Moëlo Y, Makovicky E, Mozgova NN et al. (2008) Sulfosalt systematics: a review. Report of the sulfosalt sub-committee of the IMA Commission on Ore Mineralogy. Eur J Mineral 20:7–46.

Mookherjee A, Mishra B (1984) "Derived" and observed sulphosalt-sulphide phase assembleges compared – A case study from Rajpura-Dariba, India. Min Dep 19(2):112–117.

Sack RO, Fredericks R, Hardy LS, Ebel DS (2005) Origin of high-Ag fahlores from the Galena Mine, Wallace, Idaho, U.S.A. Amer Miner 90:1000–1007.

Sack RO, Kuehner SM, Hardy LS (2002) Retrograde Ag-enrichment in fahlores from the Coeur d'Alene mining district, Idaho, USA. Miner Magaz 66(1):215–229.

Sack RO, Lynch JV, Foit GF Jr (2003) Fahlore as a petrogenetic indicator: Keno Hill Ag-Pb-Zn District, Yukon, Canada. Mineral Magaz 67(5):1023–1038.

The spatial variation of mineralogy in the vanadiferous magnetite deposit of the Lac Doré Complex (Chibougamau, Québec) and its implications on the chemical purity of magnetite concentrates

Jean-Philippe Arguin
Université du Québec à Chicoutimi

Philippe Pagé
Université du Québec à Chicoutimi

Réjean Girard
IOS Services Géoscientifiques Inc.

Sarah-Jane Barnes
Université du Québec à Chicoutimi

Abstract. The incorporation of contaminating elements in vanadiferous magnetite concentrates produced from layered intrusions can lead to expensive complications during vanadium extraction and purification processes. These contaminants may be contained in magnetites, as well as in gangue minerals attached to magnetites after the ore was comminuted. To better understand the flow of contaminating elements incorporated into magnetite concentrates, this project investigates the implications of textural and chemical features of mineralogy on the metallurgical behavior of vanadium ores produced from the Lac Doré Complex in Chibougamau (Québec). *In situ* quantitative mineralogical analysis will be combined with laboratory-scale comminution and magnetic separation tests to develop a framework for a geometallurgical model aiming to improve the process leading to the production of high-purity magnetite concentrates. Results from our preliminary petrographic study reveal that magnetite is preferentially associated with ilmenite, ferrochlorite and ferropargasite in response to magmatic and metamorphic processes. As the mineral abundance, attachments and composition vary greatly in the cumulate pile due to changes in rock type and metamorphic conditions, the chemical constancy of magnetite concentrates will inevitably be affected.

1 Introduction

Vanadium extraction from titanomagnetites by roasting or smelting is very sensitive to the presence of contaminating elements (e.g., Si, Ca and transition metals such as Cr and Mn), which either consume reactants, form refractory phases, or concentrate in the end-product. Consequently, a good knowledge of the distribution of these chemical contaminants in rocks and a good understanding of ore behavior during comminution and mineral separation processes are critical to optimise the extraction of vanadium. Geometallurgy, an emerging approach within the mining industry, aims to integrate geological and metallurgical data to develop predictive models for the improvement of ore processing (e.g., Lamberg 2011). Knowingly, a geometallurgical modeling proves to be an efficient tool to optimize the extraction processes of vanadium produced from heterogeneous titanomagnetite deposits.

VanadiumCorp Resources Inc. plans to extract the vanadium contained in the structure of magnetites from its Lac Doré property (South limb of the Lac Doré Complex, Québec, Canada) to produce a high-purity vanadium electrolyte (99.99%) for the industry of vanadium flow redox batteries. However, due to the presence of contaminating elements in gangue minerals (e.g., ilmenite and silicates such as ferrochlorite and ferropargasite), as well as in magnetites themselves (by diadochic substitution), the extraction process of vanadium may require expensive purification steps. Therefore, obtaining magnetite concentrates with the lowest possible amount of contaminating elements must be optimized for the metallurgical process.

The objective is to assess the implications of textural and chemical variations on the purity of magnetite concentrates produced from a 122-metre-long transect line chosen to represent the stratigraphy of the East deposit (Lac Doré property). A detailed mapping of this transect was carried out in the summer of 2016 (Fig. 1). Two main problems will be investigated to develop a framework for a geometallurgical model: (1) the implication of textural variations on magnetite liberation during comminution processes; and (2) the implication of mineral composition and its variations on the incorporation rate of contaminating elements in vanadiferous magnetite concentrates. Given that the project is in its early stages, this short paper only includes preliminary results that encompass some textural features for magnetitites and magnetite-bearing anorthositic rocks sampled along the studied transect.

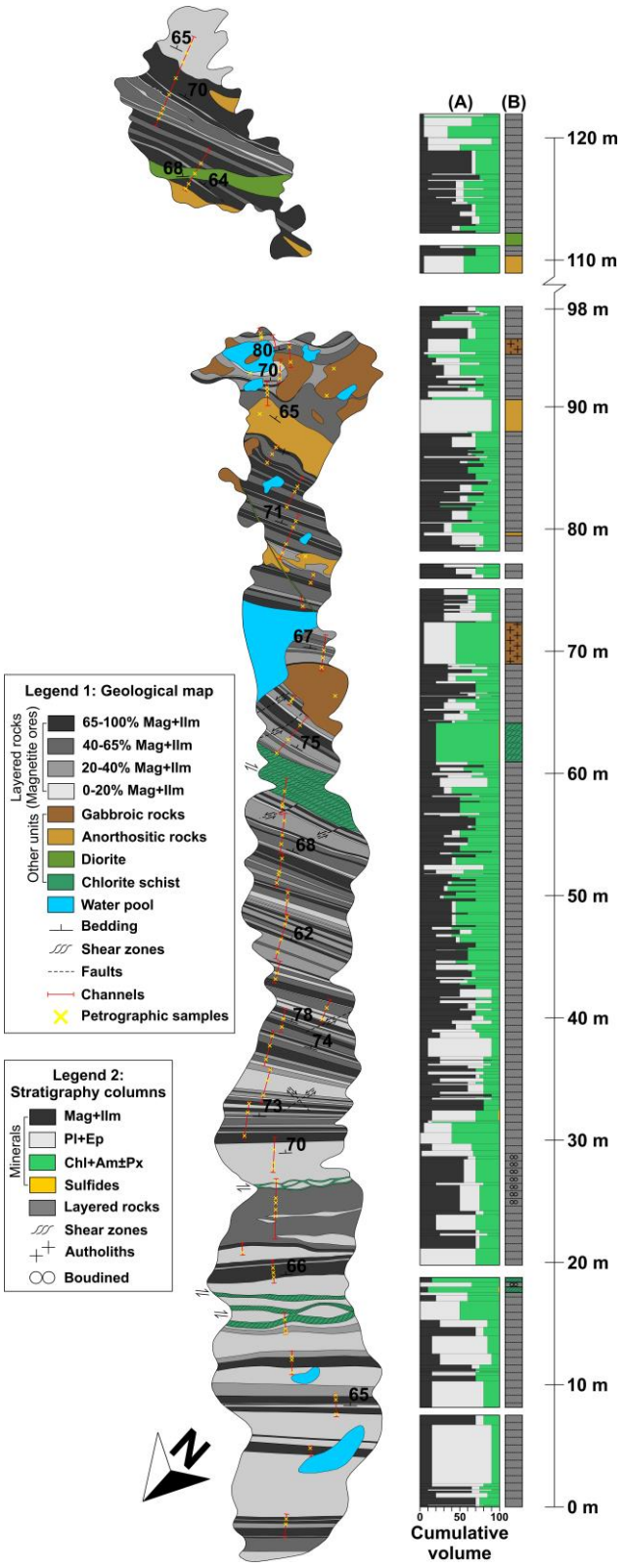


Figure 1. Detailed geological map of the trench 19+50E from the Lac Doré property (VanadiumCorp Resources Inc.). The stratigraphic columns show the estimated modal proportion of minerals (a) and the different types of lithology including layered rocks and non-stratigraphic units (b). Am, amphibole; Chl, chlorite; Ep, epidote; Ilm, ilmenite; Mag, magnetite; Pl, plagioclase; Px, pyroxene.

2 Geological background

The Lac Doré Complex (LDC) is an Archean layered intrusion (2728.3+1.2 / -1.1 Ma; Mortensen 1993) located in the eastern end of the Abitibi greenstone belt in Québec, Canada. Based on the work of Allard (1976) and Daigneault and Allard (1990), the LDC includes from base to top the following stratigraphic levels: (1) the Lower Series; (2) the Layered Series; and (3) the Upper Series. The Layered Series is well known for their vanadium-bearing titanomagnetite deposits, which are mainly represented by a mineralized horizon that extends along the North and South limbs of the LDC (e.g., Allard 1976; Daigneault and Allard 1990; Girard and D'Amours, 2015). The most documented magnetite deposit is in the South limb and consists of an almost continuous mineralized horizon that is typically 60 to 100 metres thick, increasing to more than 200 metres in its most eastern part. According to Girard and D'Amours (2015), the titanomagnetite-rich horizon is steeply dipping to the southeast and extends for 17 km following a NE-SW trend from the Grenville Front toward the southwest. These authors claim that the typical V content of titanomagnetite decreases from 1.47 to 0.86 wt % V_2O_3 towards the top of the Layered Series within the Lac Doré property, while the Ti content increases.

3 Exsolution features

One of the most important problems related to the effects of mineralogy on the purity of vanadiferous magnetite concentrates concerns the presence of fine exsolutions, which are too small to separate from their host magnetite during communition processes. The systematic incorporation of these exsolutions into the concentrates may result in a significant contamination and a dilution of the V content.

In the Layered Series of the LDC, exsolutions are ubiquitous. The most common features are related to the magnetite-ulvöspinel miscibility gap of which the upper consolute temperature, as determined from various experiments, ranges from about 450 to 600°C (e.g., Price 1981; Lilova et al. 2012). In the studied section, two types of exsolution occurred from the mixing of these two components: (1) ilmenite exsolutions resulting from the oxidation of the ulvöspinel component at temperatures above the solvus of the magnetite-ulvöspinel solid solution; and (2) ilmenite exsolutions resulting from the oxidation of exsolved ulvöspinels. According to Buddington and Lindsley (1964), both types can be referred to as oxy-exsolution.

Oxy-exsolutions in the East deposit exhibit a wide range of textures mainly resulting from the spatial variation of the diffusion rate during cooling. Based on textural evidence, increasing degrees of diffusion result in a systematic textural continuum for both types. Type 1 exsolutions progress from (1) broad trellis- or sandwich-textured lamellae along {111} planes of magnetite (Fig. 2a); through (2) internal granules; to (3) external granules.

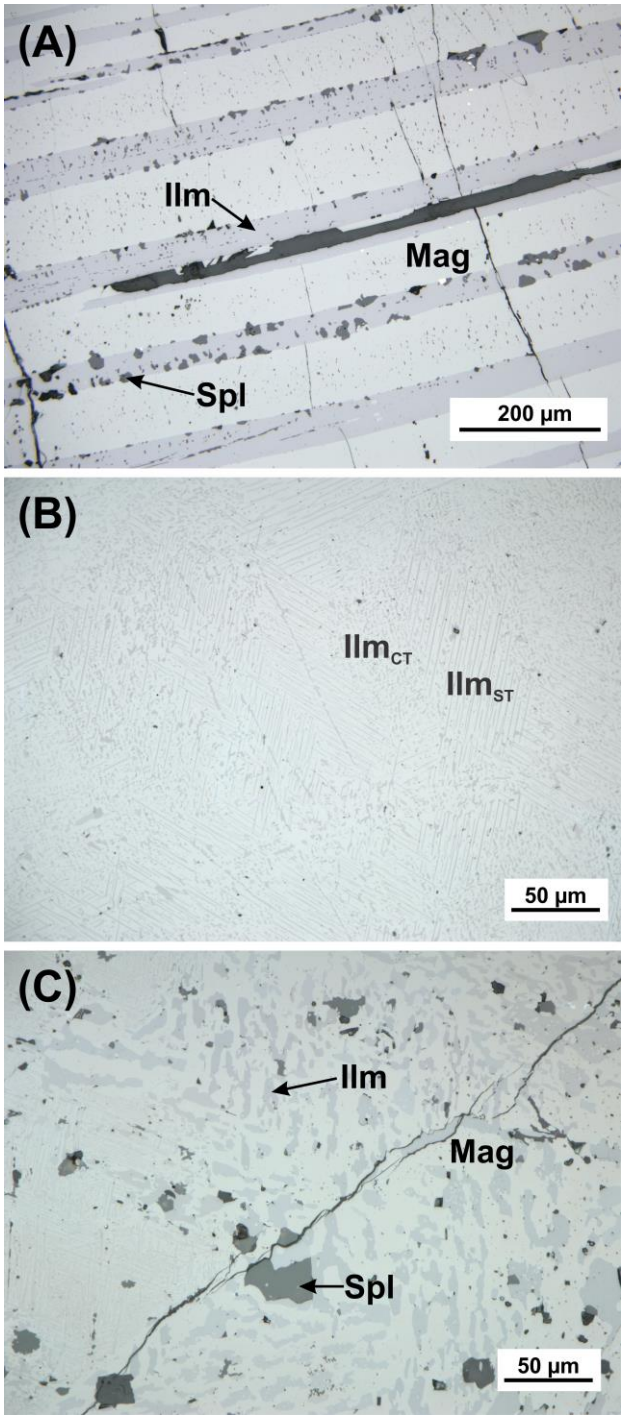


Figure 2. Microphotographs showing some exsolution features in titanomagnetites from the Layered Series of the LDC: (a) broad sandwich-textured lamellae containing small granules of aluminous spinel; (b) contiguous patches of cloth-textured (CT) and sandwich-textured (ST) proto-ilmenite; and (c) pseudo-oriented irregular patches of proto-ilmenite containing very small blebs of magnetite (composite intergrowths). Ilm, ilmenite; Mag, magnetite; Spl, spinel.

On the other hand, type 2 exsolutions [also termed proto-ilmenite by Willemse (1969) and Von Gruenewaldt et al. (1985)] progress from very thin cloth-textured lamellae or prisms (pseudomorphised ulvöspinel exsolutions; Fig. 2b); through (2) contiguous patches of very thin lamellae forming a second generation of trellis- or sandwich-type texture (Fig. 2b); (3) composite intergrowths (ilmenite ± magnetite) forming irregular, vermicular or lenticular patches (Fig. 2c); to (4) small external granules. Proto-ilmenite appears to be almost entirely confined in a 30-metre-thick continuous sequence (from 68 to 98 m in Fig. 1). In cases where the proto-ilmenite is dominant, type 1 exsolutions are absent or much less abundant than in the rest of the studied transect.

Aluminous spinels such as those from the hercynite-gahnite solid solution series are also present as exsolution intergrowths in titanomagnetites from the Layered Series. Although their abundance is low compared to ilmenite and varies greatly from one sample to another, they are ubiquitous throughout the transect and occur as very thin discs along {100} planes of magnetite or as very small granules regularly included into broad ilmenite lamellae (Fig. 2a).

4 Silicates and primary ilmenite

Silicates and primary ilmenite (i.e., produced by primary crystallization) in magnetitites and magnetite-bearing anorthositic rocks from the Layered Series are also considered as a part of the problem related to the incorporation of contaminating elements in magnetite concentrates. The association of magnetite with a specific mineral may be preferential or not depending on the nature of the mineralogical textures.

The main silicates in the studied transect are those resulting from the metamorphism of rocks at greenschist facies conditions. This includes ferrochlorite, ferropargasite, epidote and albite. The last two are less problematic because they rarely share a common perimeter with magnetite. On the other hand, most of the preferential associations between magnetite and both, ferrochlorite and ferropargasite, can be attributed to the metamorphism of plagioclase, which is responsible for the following features: (1) the presence of kelyphitic rims of ferropargasite resulting from a reaction between magnetite (or ilmenite) and plagioclase with water interaction (in this case the core of plagioclase grains is replaced by a mixture of epidote and albite); (2) the preferential replacement of plagioclase by ferropargasite (±epidote) due to sustained water interaction; and (3) the preferential replacement of plagioclase by ferrochlorite (±epidote) due to more sustained water interaction. This latter case is peculiar to the magnetitites and could be related to the abundance of fractures in magnetites. Magnetite-ferrochlorite association can also be attributed to the replacement of magnetite along fractures and grain margins.

Primary granular ilmenite is ubiquitously associated with magnetite in the Layered Series. This association results from the primary crystallization of both minerals together (or one after the other) as cumulus or intercumulus phases. As suggested by our petrological

observations, the magnetite/ilmenite ratio of magnetitites tends to decrease towards the top of the sequence with values ranging from 14.00 to 1.80.

5 Quantitative analysis: a foretaste

Geological data derived from a quantitative mineralogical analysis is the key information to understand ore behavior during mineral processing (comminution, mineral separation and resource extraction). In the course of our study on the East vanadium deposit, we will collect quantitative data sets from *in situ* (on thin sections) analyses of textures and mineral chemistry. The bulk of data will be acquired using the following methods:

(1) *In situ* textural data including, modal mineralogy, exsolution proportion, mineral associations, grain size and contact roughness, will be acquired from colorized backscattered electron (BSE) and energy-dispersive X-ray spectrometry (EDS) images. BSE and EDS images will be obtained using a Zeiss EVO MA scanning electron microscope, and then processed and analysed with the proprietary software ARTSection. Figure 3 shows an example of a colorized BSE image.

(2) *In situ* determination of mineral chemistry will be done by EDS and laser ablation inductively coupled plasma mass spectrometry (LA-ICP-MS). Both methods will be used to measure the major, minor and trace element content in minerals such as magnetite, ilmenite, ferropargasite and ferrochlorite.

Combined with laboratory-scale comminution and magnetic separation tests, the *in situ* data will be used to determine the implications of mineralogy on mineral processing in order to develop a framework for a geometallurgical model allowing the improvement of processes leading to the production of magnetite concentrates as pure as possible.

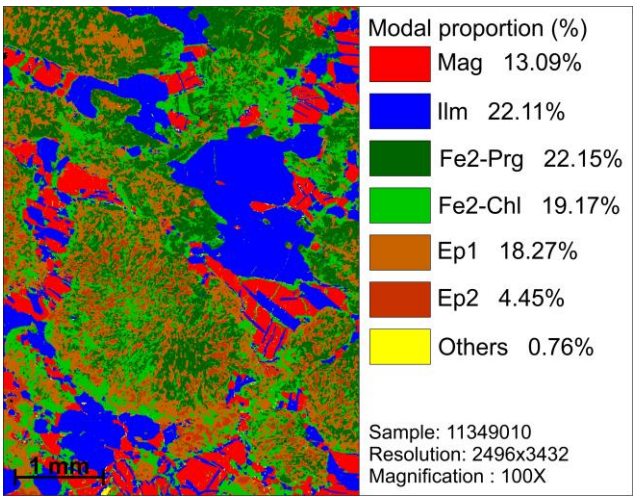


Figure 3. Example of a colorized BSE image showing the modal proportion of minerals. Shades of grey from a mosaic of BSE images have been processed with ARTSection to extract mineralogical parameters. Ep, epidote; Fe2-Chl, ferrochlorite; Fe2-Prg, ferropargasite; Ilm, ilmenite; Mag, magnetite.

6 Concluding remarks

Mineralogical variations in the vanadiferous magnetite deposit of the LDC are expected to affect the purity of magnetite concentrates, and therefore, the efficiency of vanadium extraction processes. One of the main issues related to the effects of mineralogy on mineral processing concerns the eventual control of associated gangue minerals on magnetite liberation, and by extension, on the contamination of magnetite concentrates. As observed during our preliminary petrological study, magnetite in the Layered Series can be associated with (1) ilmenite produced by (i) oxy-exsolution processes or (ii) primary crystallization, (2) ferropargasite and ferrochlorite derived from the metamorphism of plagioclase, and (3) ferrochlorite formed by the replacement of magnetite itself along fractures and grains margins. Each of these associations will be considered as critical features during future work, which will include quantitative mineralogical analyses and laboratory-scale comminution and magnetic separation tests.

Acknowledgements

This work encompasses early stages of the PhD research project of J.-P. A. Valérie Lecomte and Alexandre Néron from IOS Services Géoscientifiques Inc. are thanked for their assistance and advice for BSE image processing and analysis. Annual bursary awarded to the first author to cover living expenses and fees were supported by the Mitacs-Accélération program: grant # IT07474.

References

Allard, GO (1976). Doré Lake Complex and its importance to Chibougamau geology and metallogeny. Ministère des Richesses Naturelles, Québec, DP-368.

Buddington, AH, Lindsley, DH (1964) Iron-titanium oxide minerals and synthetic equivalents. J Petrol 5: 319-357.

Daigneault, R, Allard, GO (1990) Le Complexe du Lac Doré et son environnement géologique (Région de Chibougamau – sous-province de l'Abitibi). Ministère de l'Énergie et des Ressources, Québec, MM 89-03.

Girard, R, D'Amours, C (2015). The Lac Doré Vanadium Project: first resource estimate. Chibougamau, Québec, Canada, NI 43-101 Technical Report presented to VanadiumCorp Resource Inc.

Lamberg, P (2011) Particle – the bridge between geology and metallurgy. Conference in mineral engineering, Lulea, Sweden, Proceedings: 1-16.

Lilova, KI, Pearce, CI, Gorski, C, Rosso, KM, Navrotsky, A (2012) Thermodynamics of the magnetite-ulvöspinel (Fe_3O_4-Ti_2TiO_4) solid solution. Amer Miner 97: 1330-1338.

Mortensen, JK (1993) U-Pb geochronology of the eastern Abitibi Subprovince. Part 1: Chibougamau-Matagami-Joutel region. Can J Earth Sci 30: 11-28.

Price, GD (1981) Subsolidus phase relations in the titanomagnetite solid solution series. Amer Miner 66: 751-758.

Von Gruenewaldt, G, Klemm, DD, Henckel, J, Dehm, RM (1985) Exsolution features in titanomagnetites from massive magnetite layers and their host rocks of the Upper Zone, eastern Bushveld Complex. Econ Geol 80: 1049-1061.

Willemse, J (1969) The vanadiferous magnetic iron ore of the Bushveld Igneous Complex. Econ Geol Monograph 4: 137-208.

Estimate of alteration zones and type of deposit by multispectral satellite image interpretation and correlation with geology and geochemistry in the SW Loja-Ecuador Province

Caiza Cañar Evelyn Karina
Central University of Ecuador

Abstract. This study aims to contribute to the investigation and search for new areas with geological-mining potential in Ecuador determining types of ore deposits by estimating hydrothermal alteration zones using ASTER satellite image interpretation with their respective validation by creating a record of spectral signatures. Additionally, a geological correlation is necessary where volcanic rocks of Piñon Formation of lower cretaceous age host polymetallic mineralization as result of a granitic to granodioritic igneous body intrusion of upper cretaceous age. Zones of geochemical anomalies determined by a geostatistical analysis of stream sediment that were collected by the National Institute of Geological Metallurgical and Mining Research (INIGEMM) are displayed within the study area. The most important anomaly of first order matches with a hydrothermal alteration zone on the Rio Playas valley where anomalous samples of Cu, Pb, Zn and Mo matches with a possible disseminated mineralization copper-molybdenum and veined; these zones with anomalies are associated with the margin of intrusive igneous body which have a NE-SW trend related to the main fault system in the study area.

1 Introduction

The estimate of zones of hydrothermal alteration using digital interpretation of satellite images ASTER with their respective validation by creating a record of spectral signatures, will be correlated with geological information which discloses the type of rocks that host polymetallic mineralization, with geochemical information through determination of anomalic zones of Cu, Pb, Zn and Mo which are closely related to zones with disseminated and veined mineralization type; and finally with a main fault system in NE-SW direction which is related to the trend of the anomalic zones. This correlation allows certain way to estimate a possible type of ore deposit to be responsible for polymetallic mineralization in the study area.

2 Geological and structural framework

2.1 Geological framework

In the study area mostly outcropping volcanic rocks of lower cretaceous of Piñon Formation (Feininger 1980), which are angular discordance with sedimentary rocks like black and silt shales of Alamor Group (Duque 2010) that (Kennerley 1973) divides it into two formations: Ciano Formation and Zapotillo Formation of upper cretaceous age (Kennerley 1973); this group is underlying by conglomerates and semiconsolidated clays of Rio Playas Formation of tertiary age (Villemur 1967). Covering the above units have the quaternary deposits (Fig. 1).

The volcanic rocks of Piñón Formation are of great importance because in them the polymetallic mineralization and hydrothermal alteration zones as a cause of the intrusion of the Tangula Batholith of granitic to granodioritic composition of upper cretaceous age (Snelling et al. 1970), these volcanic rocks host large metal deposits in the country mainly epithermal high and low sulphidation and porphyry copper deposits.

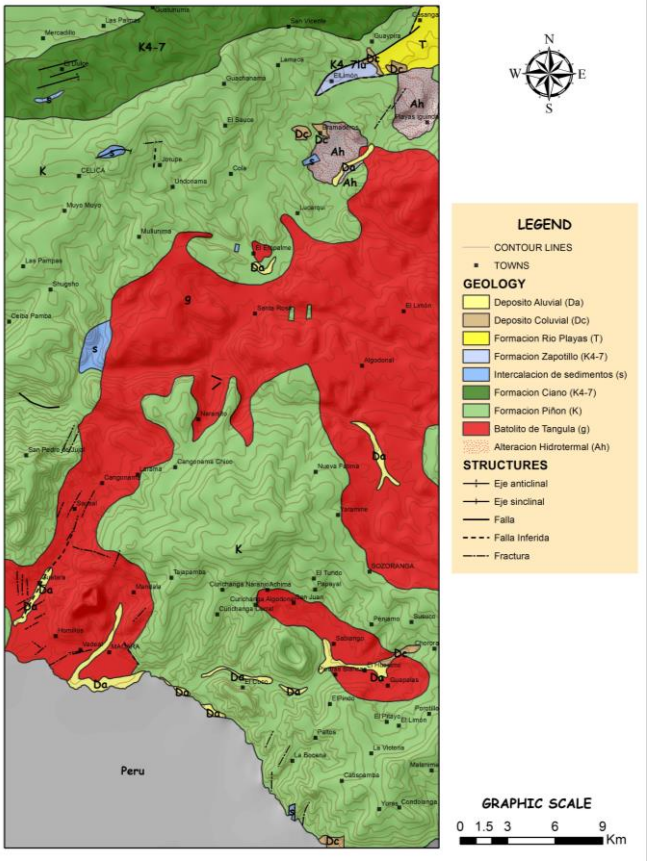


Figure 1. Geological map of the study area.

2.2 Stratigraphy

The stratigraphy of the area is made up of units ranging from the Cretaceous to Quaternary age. In the Early Cretaceous volcanic rocks has mainly interbedded sediments represented by Piñón Formation; while in the

Upper Cretaceous you have an interbedded of sedimentary rocks like black shales and silts with volcanic rocks corresponding to Alamor Group. In the Tertiary the presence of Rio Playas Formation consisting of conglomerates and clays semiconsolidated, while the Quaternary is made up of alluvial and colluvial deposits.

Covering most of the study area is an intrusive of granitic to granodioritic composition of upper cretaceous age (Snelling et al. 1970) responsible for the mineralization and hydrothermal alteration in the volcanic rocks of Piñon Formation.

EARLY CRETACEOUS

Piñon Formation. - This unit outcrops in the central part of the study area and consists of volcanic rocks as andesites with texture porphyritic whose phenocrysts constitute 50% of the rock; mafic phenocrystals consist hypersthene, diopside and augite, many of feldspathic phenocrystals are altered to kaolin and sericite. This formation intruded by the Batholith Tangula of upper cretaceous age (Snelling, et al, 1970) and has zones of hydrothermal alteration and mineralization.

UPPER CRETACEOUS

Alamor Group. - Two formations of Alamor Group are present in the study area, the Ciano Formation and Zapotillo Formation. The Ciano Formation outcrops in the zone NW and consists of laminated shales, siltstones, and volcanic rocks like tuffs with andesitic composition. The Zapotillo Formation is located between two blocks failed in the zone NE and consists of black shales.

TERTIARY

Rio Playas Formation.- This unit outcrops NE of the study area and consists of clays and conglomerates semiconsolidated containing shingle the pebbles black limestone derived of Alamor Group of upper cretaceous age (Kennerley 1973).

QUATERNARY DEPOSITS

The alluvial deposits are confined to the valleys of Catamayo, Playas, Santa Ana and Subiango Rivers and in particular, to areas where the intrusive presents a granitic composition because the grained rock is easily broken by weathering processes. Several sections with colluvial material found on the Rio Playas valley.

INTRUSIVE

The Tangula Batholith dominates the study area and its composition varies from granite to granodiorite. The composition granitic appears in the north of the batholith while the granodiorite composition appears in the south of the batholith characterized mainly by high biotite. The batholith crosses the Piñon Formation suggesting to intrusion of late cretaceous age (Snelling et al. 1970). Hydrothermal alteration in the Rio Playas valley and mineralization in rocks of the Piñon Formation would be associated with the intrusion of the batholith.

2.3 Structural geology

The main structural feature in the study area is clearly a system fault with NE-SW trend, which causes an average degree of fracturing in the Tangula Batholith. In the northern part of the study area the presence of two normal faults which uplifted blocks belong to the volcanic rocks of the Piñon Formation is observed, the raised block the SE area has an average degree of fracturing whose fractures are filled with mineralization and affected by hydrothermal alteration zones (Fig. 2).

Additionally worth mentioning that in the NW zone of the study area the Ciano Formation folded with E-W axis direction, this folding extends into the Piñon Formation where there are intercalated sediments (Villemur 1967).

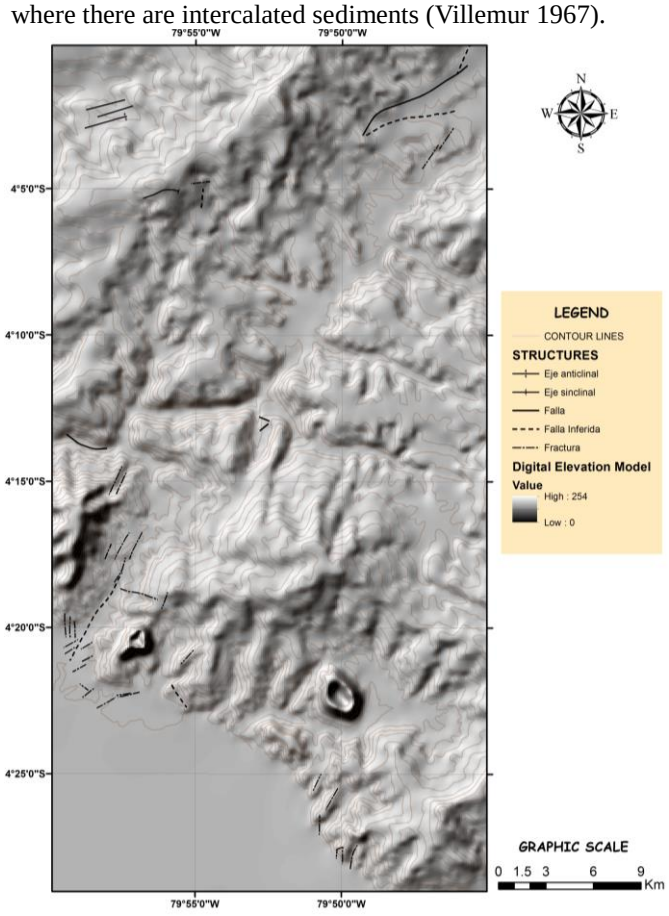


Figure 2. Structural map – Digital Elevation Model

3 Geochemical interpretation and zones of hydrothermal alteration

3.1 Interpretation geochemistry

Geochemical analysis conducted in the study area builds on the realization of a geostatistical analysis of stream sediment geochemical data collected by the National Institute of Geological Metallurgical and Mining Research (INIGEMM); these data were raised to 1: 50,000 scale, taking one sample per 25 km and comprises a total of 1000 data stream sediments.

The geochemical data processing yields as a result the location of four anomalous areas within the study area: The most important first-order anomaly coincides with a zone of hydrothermal alteration in the valley of the Rio Playas where anomalous samples of Cu (830-350 ppm with background 25 ppm), Pb (52-250 ppm with background 20 ppm), Zn (230-600 ppm with background

60 ppm) and Mo (6-18 ppm with background 1ppm) coincide with a possible disseminated mineralization copper-molybdenum (Fig. 3).

The following three anomalous areas are of second order like: Near the village La Zanja anomalous samples of Cu (75-140 ppm with background 50 ppm) and Zn (300 ppm to 80 ppm background) are associated with veined mineralization type. SW of the town La Florencia anomalous samples of Cu (60-270 ppm with background 25 ppm) match with chalcopyrite streaks in granodiorite. Finally in the SW of the study area near the town Miraflores they were recorded anomalous samples of Cu (240-270 ppm to 80 ppm background) and (85-240 ppm with background 30ppm) (Fig. 3).

Areas with anomalies obtained in the study area are associated with the margin of the Tangula Batholith which are trending NE-SW related to the main fault system and the volcanic rocks of Piñon Formation which host the mineralization polymetallic and hydrothermal alteration zones.

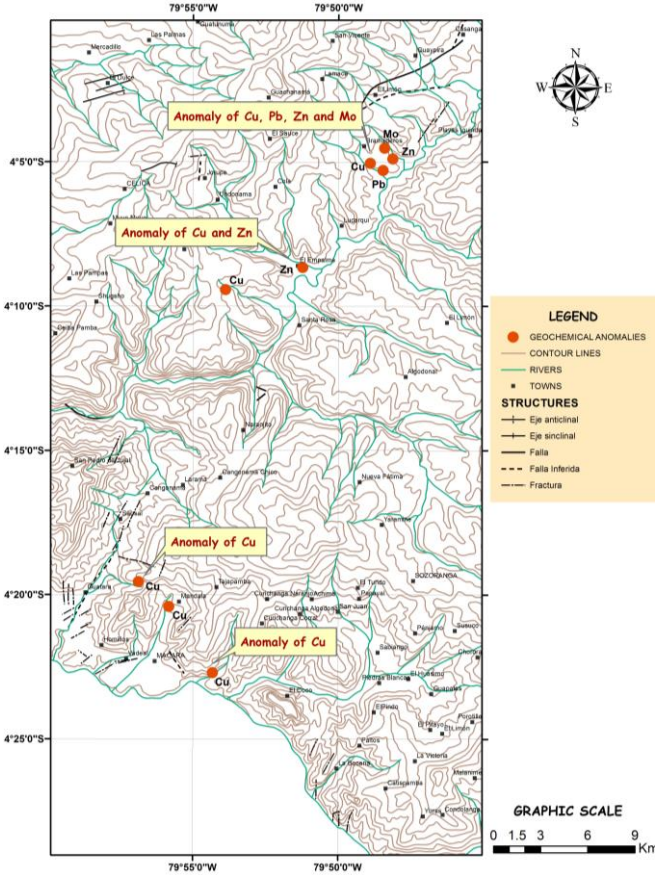


Figure 3. Geochemical Anomalies Map

3.2 Spectral interpretation of hydrothermal alterations

Satellite images of remote sensors are very useful to highlight and identify certain characteristics of the earth's surface, so satellite images ASTER with 14 bands are used and by performing a combination of bands subsystems VNIR and SWIR can be recognized different features within the study area like lithology, structures, hydrothermal alteration zones, geomorphology, vegetation, etc. The combination of bands together with the determination of ratios bands can identify a zone of argillic alteration extensive in the NE zone of the study area and a less extensive propylitic alteration with main minerals are: alunite, kaolinite, dickite, montmorillonite, sericite, chlorite, epidote and illite, their specters can be differentiated by the spectral resolution that has ASTER.

The spectres obtained by processing satellite images must be validated through a comparison with the spectres obtained from the rocks taken in field. Finally a correlation between maps obtained: geological, structural, geochemical and hydrothermal alteration zones allows certain way to estimate a possible type of deposit which is responsible for polymetallic mineralization in the study area.

Acknowledgements

I acknowledge the Faculty of Engineering in Geology, Mines, Oil and Environmental of the Central University of Ecuador for the years of learning and as the final stage of my studies is the development of this research in conjunction with National Institute of Geological Metallurgical and Mining Research (INIGEMM).

References

Duke P (2010) Short Stratigraphic Lexicon of Ecuador. Alamor Group 11-12

Feininger T (1980) Historical Geology Cretaceous and Paleogene of the Ecuadorian Coast. Geology Unit 7-8

Kennerley J. B (1973) Geology of Loja Province Southern Ecuador. Geology and Mineral Resources, Photogeological Unit 23-24

Snelling N, Ingram I, Chan K (1970) K-Ar age Determinations on Samples from Ecuador. Isotope Geology Unit Report 70-71

Villemur J. R (1967) Study of geological-mineralogical recognition of the Province of Loja. Geology Unit 12-14

Heavy minerals related to nepheline syenites in the Guaviare Department, southeastern Colombia

Héctor Ricardo Campos Rodríguez
Universidad Nacional de Colombia

José Alejandro Franco Victoria
Universidad Nacional de Colombia

Duván Fernando García Romero
Universidad Nacional de Colombia

Thomas Cramer
Universidad Nacional de Colombia

Amed Bonilla Pérez
Universidad Nacional de Colombia. Universidad Santo Tomás

Zeze Amaya Perea
Universidad Nacional de Colombia

Abstract. In the NW part of the Amazonian Craton in southeastern Colombia the nepheline syenite of San José del Guaviare (NSSJG) outcrops, composed mainly of K-feldspar, nepheline, plagioclase and minor amounts of biotite, sodium amphibole and calcite. This unit contains heavy minerals such as ilmenite and magnetite. Also large zircons of more than 1cm of diameter have been found in both active sediment and colluvial deposits near to the outcrops of the NSSJG. It is believed, that these large zircons comes from dykes intruding the unit, but no zircons have been found *in situ* yet. Petrographic and geochemical analysis (petrography, XRF, SEM) of both igneous rock samples and minerals present in the dykes indicate metaluminous and peralkaline intrusive silica undersaturated rocks with A-Type granite characteristics, intruded in a within-plate setting. The main heavy minerals are magnetite, ilmenite (which have been found *in situ*) and zircons, which have been only found in colluvial deposits and active sediment. The study of these heavy minerals and the characterization of NSSJG may be used as the first steps to explore elements like Hafnium and other rare elements (RE) in this area.

1 Geological setting

The Amazonian Craton is one of the largest and least known Archean-Proterozoic areas of South America, and one of the main tectonic units in the continent. The craton is divided into two Precambrian shields: the Guatapore shield and the Guyana shield, which are separated by the Paleozoic sedimentary basin of the Amazon. Many models have been proposed to describe the craton, among them by Santos et al. (2000), who divides it in seven geochronological provinces and one shear belt: 1) Carajás-Imataca (3.2-2.53 Ga). 2) Transamazónica (2.25-2.0 Ga). 3) Tapajós-Parima (2.10-1.87 Ga). 4) Amazonia Central (1.88-1.70 Ga). 5) Rio Negro (1.86-1.52 Ga). 6) Rodonia Juruena (1.76-1.47 Ga). 7) Sunsas (1.33-0.99), (which includes the K'Mudku shear belt with ages of 1.33-1.10Ga)

The nepheline syenite of San José del Guaviare outcrops in the area of San José del Guaviare (Guaviare Department) as part of the Rio Negro Province (Santos et al. 2000).

The very few studies about the nepheline syenite of San José del Guaviare made by Ingeominas (current Colombian Geological Survey, SGC) and university researchers describe it as an igneous body composed of microcline, nepheline, albite, cancrinite (aureols), with smaller amounts of biotite, magnetite, zircon, sphene, monazite, apatite and pyrochlore? (Galvis et al. 1979; Celada et al. 2006; Arango et al. 2012; García and Cramer 2015).

Pinson et al. (1962) obtained a K / Ar age in biotite of 445-495Ma, whereas Arango et al. (2011), with U/Pb in 29 zircons obtained an age of 577.8 ± 6.3 Ma, interpreted as rock crystallization age; Ar/Ar ages of 494 ± 5 Ma were interpreted as closing age of the cooling process. The rocks are of peralkaline character and geochemically fall in the field of intraplate granites.

Celada et al. (2006) report these rocks as possible sources for rare earths elements in the surroundings of San José del Guaviare in a potential area of 200 km^2.

Arango et al. (2011) performed geochemical analyzes, which indicate that nepheline syenite rocks are enriched in RE like Rb, Zr, Ba, Th, U, Nb and K; and impoverished in RE like Dy, Ho, Er, Tm, Yb, and Lu.

2 Petrography

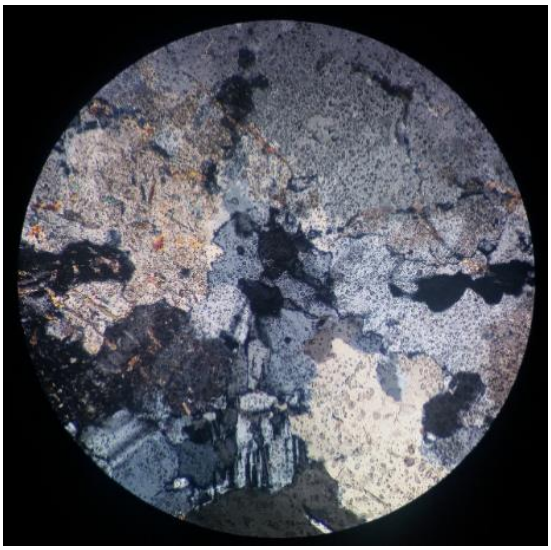


Figure 1. Nepheline syenite. Photomicrograph in cross-polarized light, 4X.

Petrographic analysis show two different types of lithologies: non-silica-saturated igneous rocks, mainly foid monzosyenite, and metamorphic rocks such as syenite gneisses, foid monzosyenite gneisses and gneisses of quartz and feldspar.



Figure 2. Minerals found in active sediments and colluvial deposits near the NSSJG outcrops.

The NSSJG was intruded by acid dykes with more than 1cm thick minerals, which are mainly magnetite and ilmenite. Other heavy minerals (see Fig. 2) have been found in sediments near to the outcrops of the NSSJG.

3 Geochemical analysis

All rock samples analyzed by means of XRF fall in the shoshonitic series field (Peccerillo and Taylor 1976), as commonly feldspathoids do (Fig. 3).

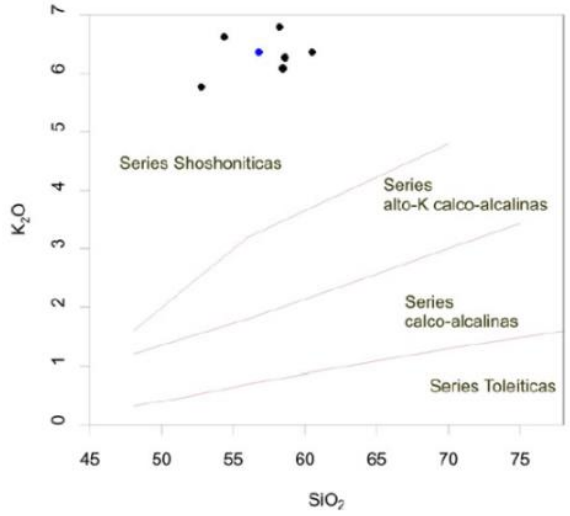


Figure 3. SiO_2 vs K_2O Diagram (Peccerillo and Taylor 1976). García and Cramer (2015).

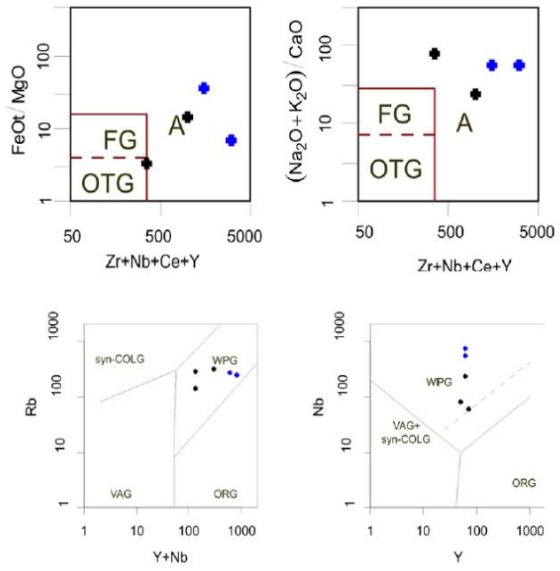


Figure 4. Tectonic discrimination diagrams (Whalen et al. 1987). **FG:** Fractionated granites. **OTG**: Non-fractionated granites M-S type. **A:** Granitoids A-type (Pearce et al. 1984). **Syn-COLG:** Syncollisional granites. **WPG:** Within-plate granites. **VAG**: Volcanic arc granites. **ORG:** Ocean ridge granites. García and Cramer (2015).

In the Tectonic discrimination diagrams after Whalen et al. (1987) the rocks fall in the Anorogenic-type (A-Type) granites field; the Y+Nb/Rb and Y/Nb diagrams (Pearce et al. 1984) situate them in an intra- plate setting (Fig. 4).

Table 1. XRF analysis of zircons.

Element	XRF-4301 M-Zircon Jordán-wt%
ZrO_2	61. 809
SiO_2	31. 937
HfO_2	1. 550
Fe_2O_3	1. 336
Al_2O_3	1. 267
TiO_2	0. 634
CaO	0. 335
Y_2O_3	0. 314
P_2O_5	0. 109
ThO_2	0. 106
MnO	0. 095
W	0. 090
MgO	0. 088
Nd	0. 076
Yb	0. 071
S	0. 063
Ti	0. 049
K_2O_8	0. 047
Co	0. 023

XRF analyses of the heavy minerals in the sediments confirm that they are mainly zircons (see Table 1) with 1.55%wt HfO_2, which correspond to normal Hf-values in nepheline syenites between 0.55-1.78%wt (Pavlenko et al. 1957).

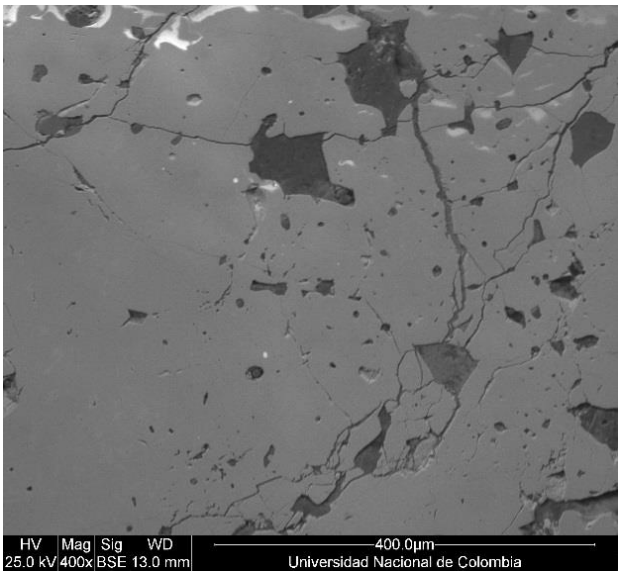


Figure 5. SEM. Zircon, with inclusions, found in active sediment near the NSSJG outcrops.

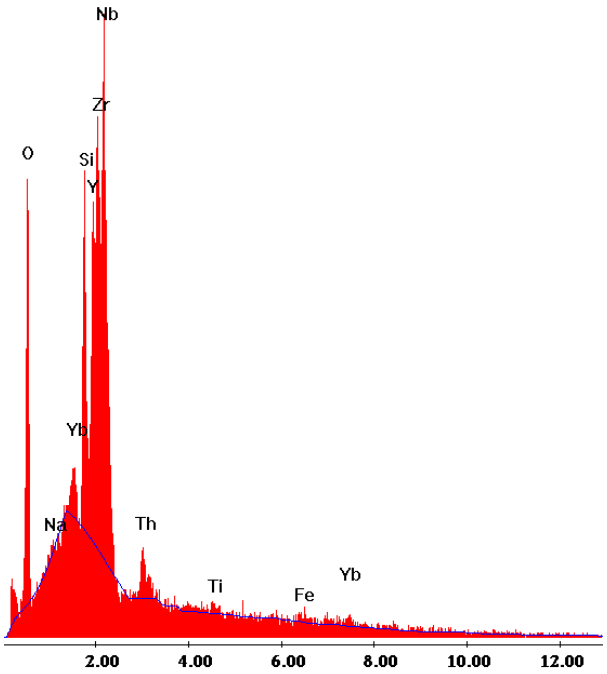


Figure 6. SEM-EDX of a pyrochlore (?) inclusion.

Scanning Electrone Microscopy (SEM) (Figs. 5 and 7) and SEM-EDX revealed the heterogeneous character of some of the zircons (Figs. 6 and 8) with inclusions of monazite and Nb-rich pyrochlore (?) (Fig. 6).

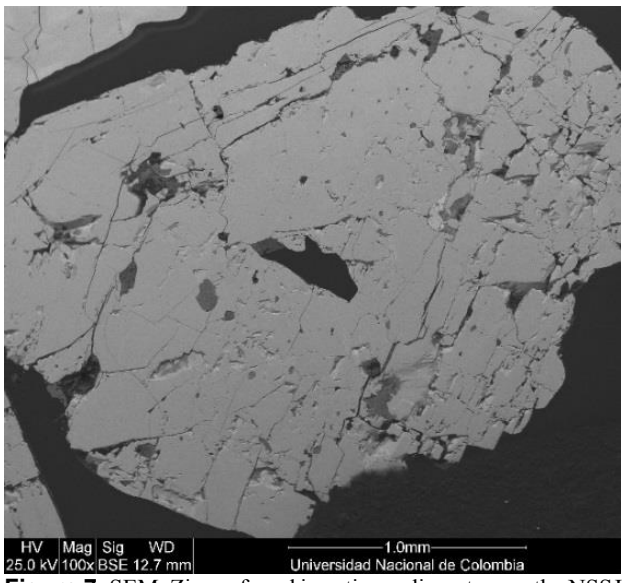


Figure 7. SEM. Zircon found in active sediments near the NSSJG outcrops.

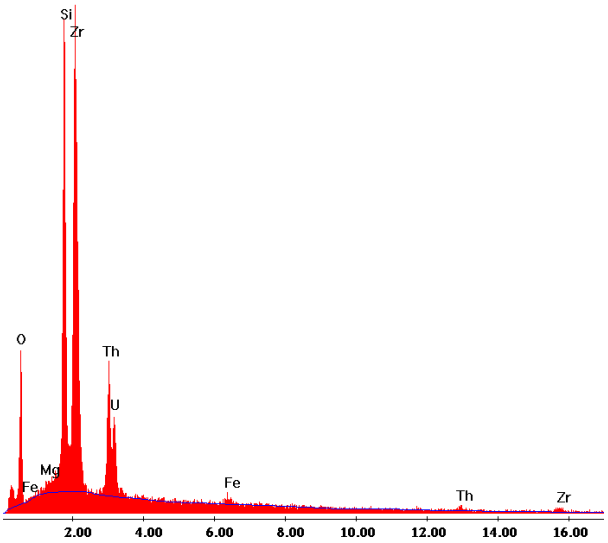


Figure 8. SEM-EDX of zircons.

4 Conclusions

The metamorphic rocks can be separated in two groups, rocks with less than 5% of quartz, like syenite gneisses; and rocks with more than 5% of quartz, like quartz-feldspar gneisses.

The main plutonic rock in both the unit and dykes is foid monzosyenite (Streckeisen 1976).

Geochemically, the analyzed syenite rock samples fall in the A-Type granite field related to within –plate magmatism.

Heavy minerals present in the NSSJG are mainly ilmenite and magnetite (with more than 1cm of thickness).

Zircons present in both active sediment and colluvial deposits near to the outcrops of the NSSJG come from this unit. No other possible source of these zircons was found.

Zircons have different types of inclusions, mostly of monazite or pyrochlore crystals.

Acknowledgements

We express our gratitude to the communities of San José del Guaviare and El Retorno for allowing our studies in their areas.

References

Arango MI, Zapata G, Martens U (2012) Caracterización petrográfica, geoquímica y edad de la Sienita Nefelínica de San José del Guaviare. Boletín Geol 34:15–26.

Celada CM, Garzón M, Khurama S, et al (2006) Potencial de recursos minerales en el oriente Colombiano : Compilación y análisis de La información geológica disponible. Instituto Colombiano de Geología y Minería (INGEOMINAS), Bogotá D.C.

Galvis J, Huguett A, Ruge P (1979) Geología de la Amazonía Colombiana. Boletín Geológico 22:3–86.

García D, Cramer T (2015) Petrografía y geoquímica de las rocas aflorantes al sur de San José del Guaviare. Dissertation, Universidad Nacional de Colombia

Pavlenko AS, Vainshtein EE, Shevaleevskii ID (1957) On the Hafnium-Zirconium Ratio in Zircons of Igneous and Metasomatic Rocks. Geokhimiya 5:411–430.

Pearce JA, Harris NW, Tindle AG (1984) Trace Element Discrimination Diagrams for the Tectonic Interpretation of Granitic Rocks. J Petrol 25:956–983.

Peccerillo A, Taylor SR (1976) Geochemistry of Eocene Calc-alkaline Volcanic Rocks from Kastamonir area, Nortgern Turkey. Contrib to Mineral Petrol 58:63–81.

Santos JOS, Hartmann LA, Gaudette HE, et al (2000) A New Undestanding of the Provinces of the Amazon Craton Based on Integration of Field Mapping and U-Pb and Sm-Nd Geochronology. Gondwana Res 3:453–488.

Streicksen A (1976) To Each Plutonic Rocks its Proper Name. Earth Sci Rev 12:1–33.

Whalen JB, Currie KL, Chappell BW (1987) A-type Granites: Geochemical Characteristics, Discrimination and Petrogenesis. Contrib to Mineral Petrol 407–419.

Measurements of gold in ores by laser-induced breakdown spectroscopy (LIBS)

Maryline Castello
Université Laval, Québec, Canada

Marc Constantin
Université Laval, Québec, Canada

Marcel Laflamme
Université Laval, Québec, Canada

Kheireddine Rifai
Conseil national de recherches, Canada

Blandine Nguegang Kamwa
Université Laval, Québec, Canada

Abstract. Numerous rock samples are taken from gold mines on a daily basis and sent to laboratories for gold determination by fire assay. A 48-hour delay in the delivery of results may force mining operators into either making operational decisions prior to knowing the results, or delaying work progress. In both cases, the decisions made can lead to significant losses for the mine. Real-time measurement of gold content in ores may provide a solution to this problem. Such an approach could be achieved by the emerging technology known as Laser-Induced Breakdown Spectroscopy (LIBS), which provides in-situ real-time quantitative gold analysis. In order to achieve this goal, the purpose of the project was to calibrate and validate the current technique. The following steps were taken: petrographic and mineralogical study for the determination of macrofacies and the gold grain distribution; x-ray fluorescence (XRF) quantitative analysis for the classification of samples; gold measurements in rock cores and grab samples by LIBS and validation with chemical fire assay.

1 Introduction

Current challenges faced by the mining industry include but are not limited to an increasing complexity of exploration, as high-grade deposits, located at shallow depths, and containing simple mineralization with a zero or low impurity level, become scarce. This leads to an increase in production and exploration costs. To deal with this problem, the project "Portable Gold Analyzer for Mining Samples Using Laser Induction Spectroscopy (LIBS)" was implemented on account of several advantages:

- Fast real-time analysis, almost one second per spectrum
- Multi-element analysis;
- Remote scanning (suitable for hostile environments);
- Possible analysis regardless of the sample state: solid, powder, liquid, sludge and gas;
- Little or no preparation of the sample needed;
- Almost non-destructive: the ablated mass is on the order of 100's of nanograms.

In order to develop and improve this technique, this project combines several areas of expertise: geochemistry, physics and statistics. This document will focus on the geochemical aspects.

2 What is LIBS and why is it useful?

Laser-Induced Breakdown Spectroscopy is an approach based on a laser paired with a spectrometer. Through the use of a mirror set, the laser meets the sample and creates a plasma (electron excitation) at the surface of the sample. Subsequently, this plasma is identified by a spectrometer by comparison with all the elements of the periodic table (Rifai et al. 2013; 2017 (in prep.)). The wavelength of 267.59 nm corresponds to the gold line used to calculate the gold content of the samples. It will therefore be necessary to calibrate it in the concentration ranges desired by the mines by improving the sensitivity and the resolution of this line:

Several techniques, such as X-ray fluorescence, are available for the in-situ real-time identification of metal contents in the solid state. XRF has been applied successfully to several base metals such as copper, zinc and nickel. However, portable XRF analyzers have a detection limit for gold of 50 ppm, which is inadequate for gold deposits as detection limits 50 to 100 times lower are required (Brand and Brand 2014). A first attempt to improve the LIBS technique brought the gold detection limit to about 0.8 ppm on all types of samples (powders, rocks, etc.) and this, regardless of their matrix (siliceous, ferrous, etc.: Rifai et al. in prep.). This result is consistent with the desired application requiring a detection limit of about 1 ppm for gold deposits.

Although the LIBS technique is a promising method, there is still improvement to be made regarding the calibration and validation of this technique in order to obtain reliable analyses of mining samples in the field. Indeed, it is important to control the parameters which

may affect the accuracy of the gold concentration measurement. One such factor is the "matrix effect", which make it necessary to characterize the rock homogeneity.

The qualitative and quantitative analyses by XRF and petrographic studies will allow for improvement and better understanding of the LIBS signal, and will lead to the establishment of a database characterizing the deposits and fitting of proper calibration curves. Finally, the method will be validated by laboratories external to the project which will determine gold contents by neutron activation analysis, atomic absorption and gravimetric analysis.

3 Geology of deposits

A total of four mining companies are involved in this project. Data from six mines of the Abitibi region were made available:

- Agnico Eagle: Lapa, Laronde and Goldex mines.
- Yamana Gold and Agnico Eagle: Canadian Malartic mine
- Hecla Québec: Casa Berardi mine.
- Iamgold: Westwood mine.

All mines are located in the Superior Province of the Canadian Shield, more precisely in the Abitibi subprovince. Five out of six mines are either in the vicinity or directly located on the Cadillac-Larder Lake fault (CLLF) (Figure 1).

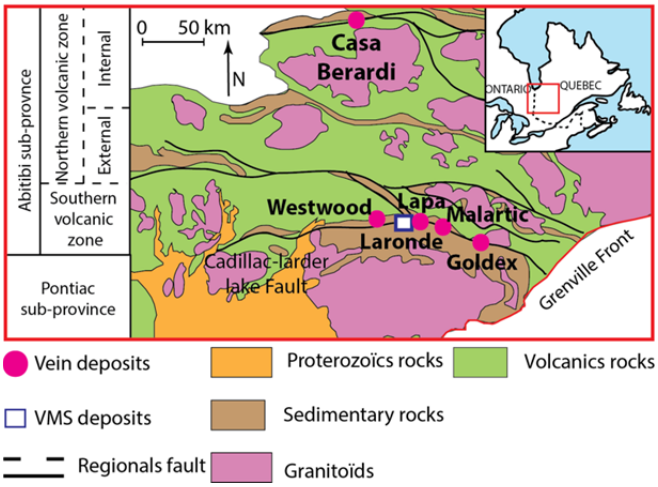


Figure 1. Location of the area under study and participating mines (modified from Chown et al. 1992).

Sample collection took place during internships at the partnered mines:

- The Canadian Malartic open-pit mine, located next to the CLLF, is an orogenic gold deposit. Gold is hosted and disseminated in vein stockwork in turbiditic metasedimentary rocks and porphyritic intrusions (De Souza et al. 2015). It is a low-grade high-tonnage deposit (343.7 Mt @ 0.97 g/t Au: Belzile and Gignac 2011)
- The Goldex mine is an underground mine located north of the CLLF. The ore is hosted in a quartz-tourmaline-carbonate vein stockwork in a granodiorite. It is a low grade deposit (7.6 Mt @ 1.5 g/t Au) (Hudyma et al. 2010).
- The Laronde mine is an underground mine located in the Blake River Group. The mine corresponds to a polymetallic volcanogenic massive sulphide deposit (Mercier-Langevin et al. 2011). The sulphide mineralization is massive to disseminated, making up a high grade and tonnage deposit (58.8 Mt @ 4.31 g/t Au). .
- The Westwood mine is an underground mine also located in the Blake River Group and composed by metavolcanic rocks. The mineralization is present in two forms: veins (pyrite-rich quartz veins, sphalerite and chalcopyrite) and semi-massive to massive sulphides. It is a high-grade deposit of 14.2 Mt @ 7.6 g/t Au (Yergeau et al. 2015).
- The Lapa mine is an underground mine located in the CLLF zone. In this property, the contacts between the Cadillac and Pontiac metasedimentary rocks and the metavolcanic rocks of the Piché group are visible. Mineralization occurs as quartz veins associated with biotite alteration zones. It is a high-grade low-tonnage deposit of 1.77 Mt @ 5.84 g/t Au (Simard et al. 2013).
- The Casa Berardi mine is the northernmost mine of this study located 95 km north of the town of La Sarre. The ore is hosted in quartz vein in sedimentary and metavolcanic rocks. It is a high-grade deposit of 8.45 Mt @ 5.3 g/t Au (Pilote et al. 1990; Fayol et al. 2016).

4 Methodology

As stated above, the main objective of this project is to calibrate the LIBS method for gold determination. Thus, it is necessary to properly characterize the samples in order to establish a database representative of the different gold deposits while classifying the different types of ore and associating each deposit with the proper calibration curve. Sample characterization is done by combining petrographic analysis (macroscopic descriptions of the samples) with a bibliographic study in order to establish macrofacies. Several criteria are taken into account such as grain size, mineralogy, gold distribution, rocks, deposit and mineralization types.

Geochemical analyses by X-ray fluorescence were performed as a complement to this study. A Bruker Tracer III SD portable XRF was used to determine major element contents (MgO, Al_2O_3, SiO_2, S, CaO, Fe_2O_3 and ZnO) in ore samples. Powdered certified reference samples were used. In total, 54 reference materials were used: 35 for the calibration itself and 19 for its validation. Figure 2 shows the calibration curve used for silica. Calibration was performed for all major elements.

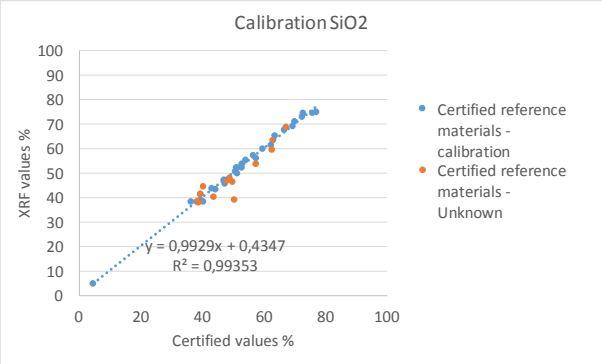


Figure 2. Calibration curve used to quantify the SiO_2 content of unknown mining samples

Subsequently, 171 unknown samples from the 6 mines were characterized by XRF.

The main objective of this project was to validate the LIBS technique for gold measurements. Comparisons on the same samples with other spectral methods such as neutron activation analysis (NAA), atomic absorption and gravimetric analysis were used for cross validation of gold measurements by LIBS.

In a first study, the chemometrics method known as Principal Component Analysis (PCA) was performed on available measurements, thus showing a division of data into two types of matrix: silica-rich and iron-rich. Two calibration curves were developed by doping powdered reference material with known amounts of gold in solution; one curve for each of the sample matrix was thus obtained (Fig. 5; Rifai et al. in prep.). The gold contents of doped materials were measured by NAA at the Slowpoke laboratory in Montreal.

Gold measurements obtained with LIBS on ore samples (unknown) were compared to results from other methods and laboratories: one from a partnered mine and the other being ALS laboratory. This allowed for the double verification of gold content in ore samples. In addition to this, the assessment of results shed light on the distribution of gold by mine and type of deposit, and also on the reproducibility of results, due to the same materials being analyzed in different forms: ¼ core, rejects, drill cutting, pulp and powder.

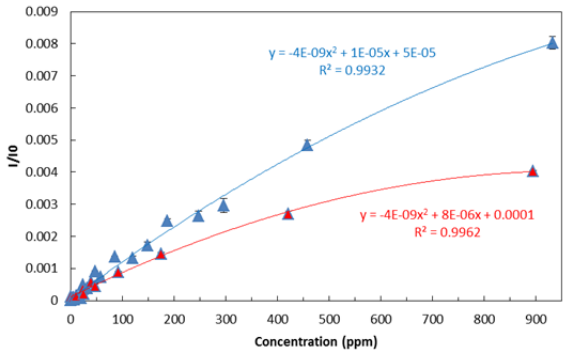


Figure 3. Calibration curves using the gold 267.59 nm line for samples from a silica-rich matrix (blue) and from an iron-rich matrix (red) (Rifai et al. in prep.).

Results were also used to implement a sampling strategy for all such sample forms present in an operating mine.

5 Results

XRF analysis makes it possible to group mines by matrix and to perform the geochemical characterization of samples regardless of their form: pulp, powder, tailing, drill cutting and rock. The results obtained by XRF were used to determine the geochemical signature of each deposit based on the lithological nature of materials analyzed (Figure 4).

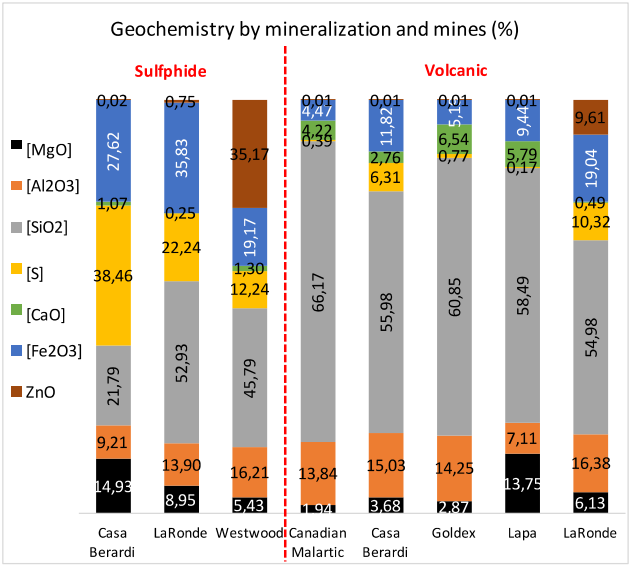


Figure 4. Geochemistry by mineralization and by mine

Proper calibration curves can then be associated to the unknown mining samples analyzed by LIBS. For instance, at the Canadian Malartic and Lapa mines, the calibration curve for Si-rich samples will be commonly used, whereas at the Westwood and LaRonde mines, the calibration curve for Fe-rich matrices will mostly be used. The Casa Berardi mine will require the use of both calibration curves. In the latter case, it is possible to specify a limit value for the concentration of silica or iron to help determine which curve to use.

In Table 1 below, prediction of gold concentration in unknown Si-rich samples and using the blue calibration curve from Figure 3 yielded values similar to those obtained in the laboratory, with a correlation coefficient equal to 0.9973 and an average square deviation error of 3.5 ppm (Rifai et al. in prep.).

Table 1. Results comparing predicted gold concentration vs LIBS analysis laboratory (Rifai et al. in prep.).

Predicted Gold concentration (ppm)	Lab Assay gold concentration (ppm)
25	25,4
198	195,8
119	122,9

Finally, a sampling strategy was developed by grouping all results by performed analysis (
Table **2**).

At the current stage of the project, mining samples have been analyzed on all three types of material. The most promising results to date were obtained from pulps, tailings and ¼ cores. The fact that some results are better reproduce than others is explained by the degree of homogeneity of gold within the samples.

6 Conclusion

The portable gold analyzer project relates to several fields of study. Each specific domain allows for a better understanding of the system as a whole.

Physics is the essence of the project as it underlies the LIBS technique. It is a promising method for the in-situ real-time measurement of gold grade. Indeed, the measurements of the gold, obtained with LIBS, are reproducible. And variations in concentrations are caused by the heterogeneous distribution of gold in natural samples.

Geochemistry and geology are involved in defining the parameters that may affect the measurements and in better understanding the results. They contribute to the knowledge of the matrix and therefore to the choice of calibration curve during the LIBS analysis.

Statistics helps establish confidence in measurements and to make them independent from certain parameters such as the “nugget effect”.

Table 2. Summary table of the results obtained from the various analyzes present in the framework of this project.

Name	[Au] ppm					Number of total shots			XRF (%)							Macrofacies
	External Laboratory		LIBS													
	Lab 1	Lab 1 bis	Core	Rejects	Pulpes	Core	Rejects	Pulpes	MgO	Al2O3	SiO2	S	CaO	Fe2O3	ZnO	
LAR-33	53,61	50,07	21,3	49,54	69,5	20952	500	500	3,00	13,96	73,01	5,04	0,33	11,97	0,01	Black River Group:
LAR-29	1,63	1,85	7,2	7,04	1,61	9600	500	500	5,22	14,08	65,92	5,67	0,72	15,91	0,02	Volcanic rocks with
LAR-30	2,99	4,04	10,1	13,46	1,64	20055	500	500	4,07	14,28	63,67	5,01	0,32	15,37	0,01	homogeneous gold

Acknowledgements

The authors would like to thank Agnico Eagle and their staff of the geology department of the LaRonde, Goldex and Canadian Malartic mines for their participation in the realization of this project. They also address a particular word of thanks to all professors, technicians and colleagues for their support in the preparation of this paper.

References

Belzile E, Gignac L-P (2011) Update resources and reserves estimates for the Canadian Malartic Project, Malartic, Québec, NI 43-101, Technical report prepared by Belzile Solutions Inc and G Mining Services on behalf of Osisko Mining Corporation.

Brand NW, Brand CJ (2014) Performance comparison of portable XRF instruments. Geochemistry: Exploration, Environment, Analysis 14:125–138. doi: 10.1144/geochem2012-172

Chown EH, Daigneault R, Mueller W, Mortensen JK (1992) Tectonic evolution of the Northern Volcanic Zone, Abitibi belt, Quebec. Canadian Journal of Earth Sciences 29:2211–2225. doi: 10.1139/e92-175

De Souza S, Dubé B, McNicoll VJ, Dupuis C, Mercier- Langevin P, Creaser RA, and Kjarsgaard IM (2015) Geology, hydrothermal alteration, and genesis of the world- class Canadian Malartic stockwork-disseminated Archean gold deposit, Abitibi, Quebec, In: Targeted Geoscience Initiative 4: Contributions to the Understanding of Precambrian Lode Gold Deposits and Implications for Exploration, (ed.) B. Dubé and P. Mercier-Langevin; Geological Survey of Canada, Open File 7852, 113-123

Fayol N, Jébrak M, Harris LB (2016) The magnetic signature of Neoarchean alkaline intrusions and their related gold deposits: Significance and exploration implications. Precambrian Research 283:13–23. doi: 10.1016/j.precamres.2016.07.009

Hudyma MR, Frenette P, Leslie I (2010) Monitoring Open Stope Caving at Goldex Mine*. Caving 2012-Second International Symposium on Block and Sublevel Caving 1–13.

Mercier-Langevin P, Hannington MD, Dubé B, Bécu V (2011) The gold content of volcanogenic massive sulfide deposits. Mineralium Deposita 46:509–539. doi: 10.1007/s00126-010-0300-0

Pilote P, Guha J, Daigneault R, Robert F, Golightly JP, (1990) Contexte structural et minéralisations aurifères des gîtes Casa-Berardi, Abitibi, Québec. Canadian Journal of Earth Sciences 27:1672–1685. doi: 10.1139/e90-175

Rifai K, Vidal F, Chaker M, Sabsabi M (2013) Resonant laser-induced breakdown spectroscopy (RLIBS) analysis of traces through selective excitation of aluminum in aluminum alloys. Journal of Analytical Atomic Spectrometry 28:388–395. doi: 10.1039/c3ja30308j

Simard M, Gaboury D, Daigneault R, Mercier-Langevin P (2013) Multistage gold mineralization at the Lapa mine, Abitibi Subprovince: insights into auriferous hydrothermal and metasomatic processes in the CadillacñLarder Lake Fault Zone. Mineralium Deposita 48:883–905. doi: 10.1007/s00126-013-0466-3

Yergeau D, Mercier-Langevin P, Dubé B, Malo M, McNicoll V, Jackson SE, Savoie A, La Rochelle F (2015) The Archean Westwood Au deposit, southern Abitibi: Telescoped Au-rich VMS and intrusion-related Au systems. InTargeted Geoscience Initiative 4: Contributions to the Understanding of Precambrian Lode Gold Deposits and Implications for Exploration. Edited by B. Dubé and P. Mercier-Langevin. Geological Survey of Canada, Open File 7852: 177-191

Replacement processes of the early-stage sulphides in the Kupferschiefer series of SW Poland

Andrzej Chmielewski and Sławomir Oszczepalski
Polish Geological Institute, National Research Institute

Abstract. The early-stage iron sulphides in the lowermost Zechstein rocks are represented by pyrite occurring in various forms and textures. As the earliest sulphide, pyrite is preferentially replaced by later-stage minerals including: marcasite, sphalerite, galena and copper-poor sulphides (chalcopyrite, bornite) followed successively by copper-rich sulphides (covellite, digenite and chalcocite) or locally by As-Sb sulphosalts, Co-Ni-Fe arsenides and other minerals. Replacements of pyrite by Cu, Pb, Zn sulphides and other minerals indicate that metal-bearing phases were formed at the expense of the earliest iron sulphides thus destructing the original components. Transformation of early iron sulphides are observable at different levels of copper-bearing series. Replacements of iron sulphides by later-phase Cu, Pb and Zn minerals are present only in profiles affected by fluid/rock interaction during the evolution of the mineralizing system. Consequently, recognition of pyrite composites is vital to the interpretation of their origin and post-depositional history.

1 Introduction

This paper concerns the nature of transformation processes of the early-stage mineralization in the Kupferschiefer-related copper-bearing series observed in core materials from wells located within the Fore-Sudetic Monocline (Fig. 1), demonstrating different types of mineral distribution patterns.

The initial and overprinting mineralization are confined to the Kupferschiefer series representing the contact zone between the Rotliegend continental red beds (P1) and the Zechstein marine sediments comprising: the Weissliegend sandstones (Ws), the Kupferschiefer shales (T1), the Zechstein Limestone carbonate rocks (Ca1) and locally the base of Lower Anhydrite (A1) (Fig. 2). The distribution of the Kupferschiefer-type mineralization is closely associated with a range of different geochemical zones, including the Rote Fäule hematitic footwall alteration (Rydzewski 1978; Oszczepalski 1989, 1999, Speczik 1995, Chmielewski et al. 2015).

New research findings on the relations between mineral textures and ore structures with respect to geochemical zones are based on a compilation of reflected-light microscopy, CAMECA SX 100 electron microprobe studies and scanning electron microscope observations and measurements. A particular attention was paid to the upper part of copper-bearing series, where the early-stage iron sulphides display the very clear state of preservation and the most interesting mineral textures.

Most of the ore minerals present in the Lower Zechstein sediments are characterized by fine-grained forms irregularly distributed in rocks or less likely veinlets, tiny crystals, large agglomerates and aggregates or nodules (Rydzewski 1969a; Wodzicki and Piestrzyński 1994). Recognition of mineral textures and their interpretation provide information valuable to the understanding of the evolution the mineral system.

2 The early-stage mineralization in the Kupferschiefer series

Pyrite is the most common and the earliest iron sulphide deposited during early anoxic diagenesis, typically forming grains, spherules, framboids, euhedral and anhedral crystals as well as large irregular aggregates, agglomerates or nodules, commonly occurring in reduced facies of the lowermost Zechstein rocks (Rydzewski 1969a, b; Oszczepalski 1989, 1999; Oszczepalski and Rydzewski 1997; Jowett et al. 1991; Sawłowicz 1992, 1993). Detailed examination of Bułaków and Pogorzela profiles with rocks not subjected to base metals mineralization revealed that the distribution of pyrite exhibits some regularities involving highly elevated amounts of pyrite generally encountered in rocks enriched in organic matter, as described below.

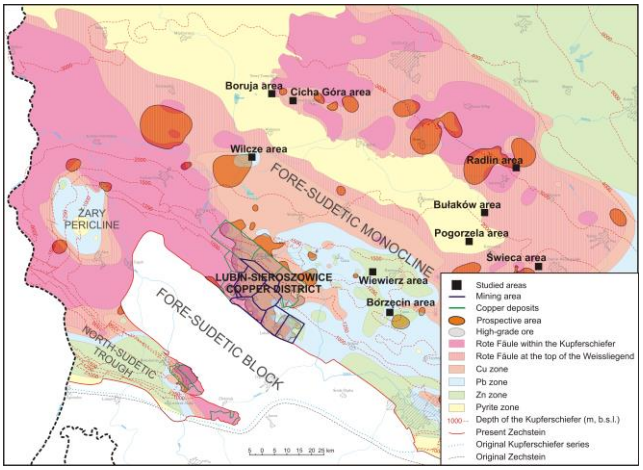


Figure 1. Map showing location of the studied areas in relation to copper prospects, Rote Fäule areas and metal zoning patterns in the Zechstein copper-bearing series of SW Poland.

Individual spherules (up to 5μm in diameter) are spherical bodies of pyrite whereas pyritic grains occur as irregular forms (up to 100μm in diameter) and they are both usually scattered through the rocks of the studied profiles (Fig. 3A) but locally they can be also partially or entirely grouped into large lenses and occasionally packed

loosely either densely into agglomerates.

Pyrite framboids, composed of pyrite idiomorphs (microlites), occur usually in framboidal forms but slightly elongated shapes are also common. The diameters of most of framboids detected in examined rocks varies between 10µm and 50µm. Nevertheless, pyrite framboids are well preserved with only few incorporated products occurring on surfaces like clay or carbonate minerals. Pyrite framboids are frequently observed in close spatial and mutual relationships with other minerals reaching up to few millimeters in diameter (Fig. 3B, C). Single, isolated octahedral or cubic microlites are common in pyrite framboids and any deviation from this shapes are typical of densely packed assemblages (Fig. 3B, D) where crystals seem to grown together as a result of later aggradational formation (Fig. 4A). Characteristically, small framboids are composed of tiny microlites and large framboids have relatively larger microlites. Large aggregated masses with indistinctive individual framboids are also present (Fig. 4C). Typically, most of the framboids exhibit smooth surfaces but sporadically they may display slightly rough surfaces which is the result of diagenetic fluids resorption during later evolution of sediments. Most framboids grouped in aggregates seem to have grown simultaneously, until the free space was filled as evidenced by no overgrowth or disruption of framboidal structures.

The space between pyrite microlites of framboids is rarely open and generally taken up by cementing material, such as clay or carbonate minerals. The cement of framboids contains strongly elevated values of Si, Al, K and Ca which are typical elements for the host rocks. Individual framboids never display bimodal microcrystal size distribution indicating that they crystallized in one phase but size of microlites in various framboids are not usually the same.

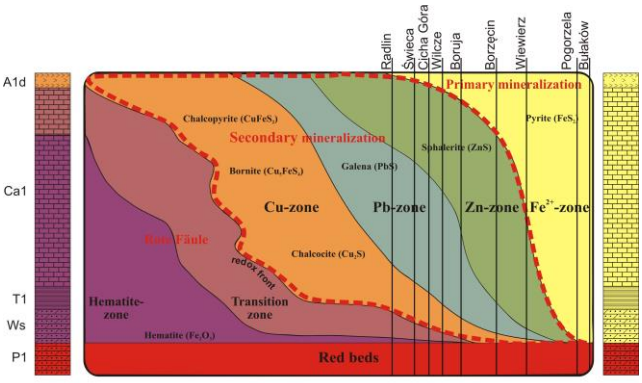


Figure 2. Schematic section of the Kupferschiefer series showing the spatial relationship between the early-stage pyrite mineralization and later ore mineralization in relation to the oxidized Rote Fäule front position and the metal zoning.

Euhedral and anhedral pyritic crystals (with the size up to several mm) are rare and usually they are disseminated unevenly in the examined rocks, only sporadically arranged in large irregular aggregates or masses (up to 2cm in diameter). Pyrite nodules are small irregularly rounded balls, lumps or tubes consisting of crystals radiating from a central point towards the edge of these forms (with size up to 1cm in diameter). Rarely they have preserved remnants of original bedding.

Marcasite is also common in the studied rocks, and it is usually associated with pyrite mineralization. Pyrite and marcasite are often intergrown forming irregular aggregates, but pyrite appears to pre-date marcasite. Marcasite forms either aggregates of equant euhedral crystals (up to 300µm) or aggregates of tabular crystals (up to 1cm) irregularly scattered throughout the rocks. Sporadically framboidal pyrite can be either invaded or overgrown with marcasite or even surrounded by marcasite groundmasses.

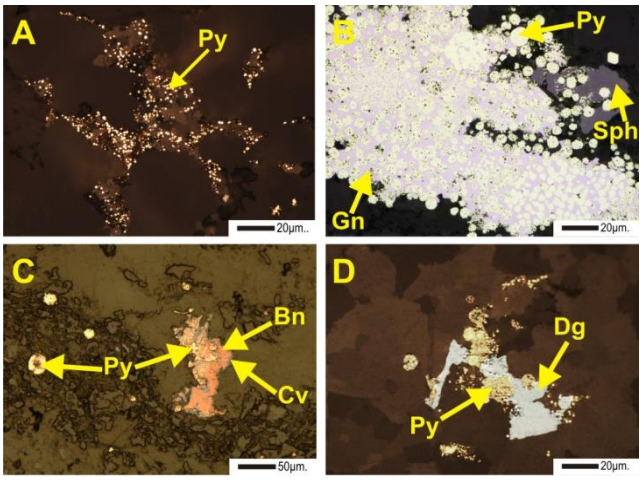


Figure 3. Selected micrographs of sulphide mineralization. **a** Tiny spherules of pyrite (Py) irregularly dispersed between carbonate spar. **b** Pyrite framboids (Py) with different density of packing cemented by galena (Gn) and sphalerite (Sph). **c** Irregular composites of bornite (Bn) and covellite (Cv) with remnant pyrite (Py). **d** Digenite (Dg) partly replacing the pre-existing pyrite framboids (Py).

Although, the early diagenetic iron sulphides are ubiquitous in the Zechstein copper-bearing series, there is a little attention paid for their evolution during further diagenesis (Sawłowicz 1990, 1992, Large et al. 1995).The recognition and description of successive transformation phases of early-stage mineralization in relation to the ore deposits formation is crucial for establishing the evolution of the early-stage mineralization and understanding the role of syn-diagenetic, diagenetic and epigenetic processes.

3 Secondary textures resulting from replacements of the early-stage iron sulphides

Replacements of pyrite by other sulphides are common in the other profiles studied, such as: Borzęcin, Boruja, Cicha Góra, Radlin, Świeca, Wiewierz and Wilcze (Fig. 1) that are characteristic for rich base metals mineralization. Primary pyrite mineralization in these rocks was successively replaced by the secondary mineralization

phase represented by: marcasite, sphalerite, galena and copper-poor sulphides (chalcopyrite, bornite) followed successively by copper-rich sulphides (covellite, digenite and chalcocite) as evidenced by micrographs (Figs. 3B-D; 4A-D; 5A-D). This is consistent with the distinct metal zonation and mineral distribution pattern (Wodzicki and Piestrzyński 1994; Oszczepalski and Rydzewski 1997; Pieczonka 2011). Generally, pyrite prevail in zones barren in Cu, Pb and Zn sulphides, occupying mostly the upper parts of copper-bearing series lying directly above the late-stage base metals enrichments but minor pyrite is also sporadically encountered within Cu, Pb or Zn mineralized zone (Fig. 2; Fig. 5A, B)

In the initial phase of pyrite replacement by the late-stage sulphides any changes in textural development are readily identified where primary phase remains and the original crystals boundaries are still recognizable (Fig. 3B). Consequently, in more advanced stages, the original phase may be reduced to 'islands' floating in a matrix of the replacing mineral (Fig. 3C, D). Numerous remnants of pyrite are found in the center of aggregates, agglomerates or irregular framboids consisting of zinc, lead or copper sulphides (Fig. 4A) although unaffected pyrite is also common (Fig. 4B). Pyrite framboids and aggregates often consist of more than one mineral and individual microlites in framboids are commonly cemented with different Cu, Pb and Zn minerals.

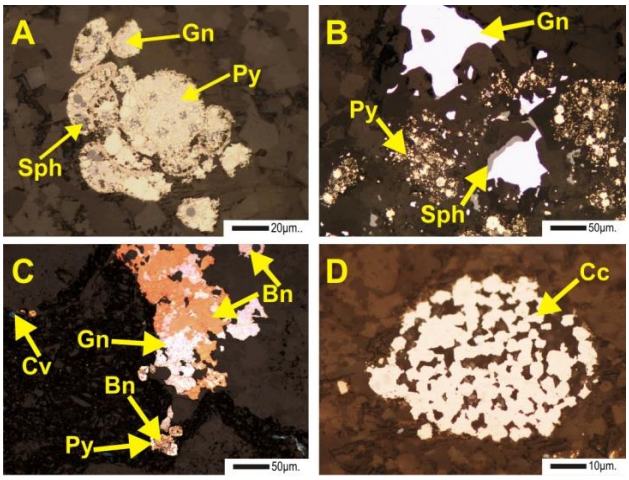


Figure 4. Selected micrographs of the late-stage sulphide mineralization. **a** Foram chambers filled with pyrite (Py) partly replaced by galena (Gn) and sphalerite (Sph). **b** Mineral association consisting of galena (Gn), sphalerite (Sph) and pyrite framboids (Py). **c** Bornite (Bn) intergrown with galena (Gn) accompanied by covellite (Cv) and relics of pyrite (Py) in replacing bornite (Bn). **d** Complete replacement of framboidal pyrite by chalcocite (Cc).

Very typical textures are pseudomorphs of copper, lead and zinc sulphides after framboidal pyrite with enhanced single microlites conversion (Fig. 4D). Very common are irregular intergrowths of chalcocite and digenite, chalcocite and bornite, bornite and galena (Fig. 4C), galena and sphalerite with chalcopyrite (Fig. 5A) or bornite and chalcopyrite (Fig. 5B). Digenite (Fig. 3D) and chalcocite with remnants of pyrite microlites are also common. Very fine coatings of sphalerite (Fig. 5C) or galena around framboidal pyrite are common as well.

Pyrite spherules, grains, framboids, euhedral and anhedral crystals, agglomerates and aggregates partly replaced by other sulphides differ slightly between each other depending on mineral zone patterns. In copper-mineralized zone, strongly elevated concentrations of Cu are measured within pyrite relicts, whereas in galena or sphalerite-mineralized zones higher concentrations of Pb and Zn in remnant pyrite are respectively found. Furthermore, outer margins of framboids are composed of Cu, Pb or Zn-rich pyrite, though inner zones are represented by pyrite with minor Cu, Pb and Zn admixtures in particular mineral zone pattern respectively (Fig. 5D). The presence of pyrite with a variable chemical composition from high-copper, lead or zinc admixtures in pyrite to poorly-enriched in these metals pyrite or even pure-pyrite forms are ordinarily registered. These changes correspond with gradual depletion of metals from bottom to the top of copper-bearing series.

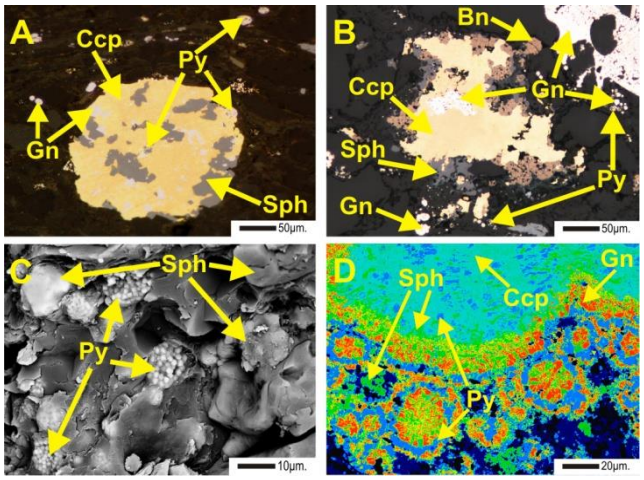


Figure 5. Selected micrographs (A and B) and BSE images (C and D) of the pyrite post-dated mineralization. **a** Composite grain of chalcopyrite (Ccp), sphalerite (Sph) and galena (Gn) with remnants of pyrite microlites and tiny framboids (Py). **b** Mineral aggregate of bornite (Bn), chalcopyrite (Ccp), galena (Gn) and sphalerite (Sph) accompanied by pyrite (Py). **c** Pyrite framboids (Py) partially replaced by sphalerite (Sph). **d** Mineral assemblage consisting of chalcopyrite (Ccp), sphalerite (Sph), galena (Gn) and remnant pyrite (Py).

Other scarcely encountered minerals partly replacing pyrite and copper, zinc and lead sulphides are: As-Sb sulphides (tenanntite-tetrahedrite, enargite) and Co-Ni-Fe arsenides (gersdorfite, cobaltite, nickeline, löllengite and arsenopyrite). Several other mineral components including: alabandite, carrollite, idaite, mckinstryite, native bismuth, native silver, nowackite, silver amalgams and sylvanite are later then Cu, Pb, and Zn mineralization as is confirmed by secondary textures.

Replacement processes essentially influenced the

textural development of the later-phase mineralization affecting the final shape of ore bodies. The advancement of these processes corresponds with the content of pyrite mineralization in examined rocks indicating that Cu, Pb and Zn sulphides postdated the pre-ore pyrite mineralization. The preservation of the early pyrite relict mineralization as well as the occurrence and the location of the later Cu-Pb-Zn mineralization are closely dependent on the distance from the Rote Fäule zone and its vertical position in the profile of copper-bearing series (Fig. 2).

The emplacement of the late-stage sulphide mineralization in areas distal from the Rote Fäule is located in Weissliegend sandstones and its position rises gradually towards the center of the Rote Fäule areas through the Kupferschiefer shales and the Zechstein Limestone carbonates reaching as high as the base of Lower Anhydrite in profiles with the highest location of hematitic footwall alteration (Fig. 2).

The late-stage sulphide mineralization is a result of replacement processes of the early-stage sulphides during diagenesis of the Zechstein sediments producing high variability of mineral associations and complexity of mineral textures observed in investigated profiles (Figs. 3; 4 and 5).

4 Conclusions and implications

Similar sizes of the early-stage iron sulphides and their occurrence as ordinary spherules, grains and framboids through euhedral and anhedral crystals to aggregates and agglomerates or nodules suggest formation in relatively stable reducing conditions.

The complex secondary textures of pyrite are regularly observed in many different forms. Compared to other sulphides, pyrite is significantly earlier, which is evidenced by both pyrite replacements by Cu, Pb and Zn minerals and the presence of pyritic crystals, spherules and framboids within the late-stage Cu, Pb and Zn sulphide enrichments. Marcasite post-dates formation of framboidal pyrite. Textures and mineral distribution patterns of the late stage sulphides provide insights into evolution in the formation of the replacements of early-phase sulphides, which was presumably caused by the introduction of mineralizing solutions into the lowermost Zechstein rocks during diagenesis of the host rocks.

Transformation of pre-ore iron sulphides into overprinting Cu, Pb and Zn minerals and other phases contributed to extensive destruction of the primary components. As a result of mineralizing fluid flow, base metal sulphide enrichments were formed in the most intensive process of pyrite replacement at locations proximal to the Rote Fäule area. The early-stage mineralization occupies the highest position in copper-bearing profiles and this is typical for places where the process of pyrite replacement has not been implemented. Replacement processes of pre-ore sulphides by later-phase minerals are the most intense in profiles highly mineralized with copper sulphides where the highest vertical extent of mineralizing fluids is highlighted and processes of replacement are the strongest. There is no late-stage base metals enrichments in places where rocks were not affected by fluid/rock interaction and these rocks typically containing unaltered pyrite mineralization Therefore, the current location of the late-stage Cu, Pb and Zn enrichments indicates the final extent of upwelling and spreading of mineralizing solutions.

Acknowledgements

The main support to ACh and SO was provided by PGI-NRI Grant no. 61-6505-1501-00-0 and 61-2601-1601-00-0. Extended thanks are also expressed to PGNiG for granting access to the cores.

References

Chmielewski A, Oszczepalski S, Speczik S (2015) Relict mineralization in the transition zone, Kupferschiefer series of SW Poland. In: Andre-Mayer AS, et al. (eds) Mineral resources in a sustainable world, Proceedings Volume 5, Universite de Lorraine, pp 1897-1900

Jowett EC, Roth T, Rydzewski A, Oszczepalski S (1991) "Background" δ^{34} values of Kupferschiefer sulphides in Poland: pyrite-marcasite nodules. Mineral Deposita 26:89-98

Large DJ, MacQuaker J, Vaughan DJ, Sawłowicz Z, Gize AP (1995) Evidence for low-temperature alteration of sulfides in the Kupferschiefer copper deposits of southwestern Poland. Econ Geol 90:2143-2155

Oszczepalski S (1989) Kupferschiefer in southwestern Poland - sedimentary environments, metal zoning, and ore controls. In: Boyle RW, Brown AC, Jowett EC, Kirkham RV (eds), Sediment-hosted stratiform copper deposits. Geol Assoc Can Spec Paper 36:571-600

Oszczepalski S (1999) Origin of the Kupferschiefer polymetallic mineralization in Poland. Mineral Deposita 34:599-613

Oszczepalski S, Rydzewski A (1997) Metallogenic Atlas of the Zechstein Copper-bearing Series in Poland. Polish Geological Institute, Warsaw

Pieczonka J, (2011) Factors controlling distribution of ore minerals within copper deposit, Fore-Sudetic Monocline, SW Poland. Wydawnictwa AGH, Kraków pp. 1-195.

Rydzewski A (1969a) Petrography of the copper-bearing Zechstein shales in the Fore-Sudetic monocline (Lower Silesia). Biul Inst Geol 217:113-167

Rydzewski A (1969b) The problem of occurrence and genesis of pyrite in the Zechstein rocks of the Fore-Sudetic Monocline Geol Quart 13:811-825

Rydzewski A (1978) Oxidated facies of the copper-bearing Zechstein shale in the Fore-Sudetic monocline. Przegl Geol 26:102-108

Sawłowicz Z (1990) Primary copper sulphides from the Kupferschiefer, Poland. Mineral Deposita 25, 262-271

Sawłowicz Z (1992) Primary Sulphides in the Cu-Fe-S Zones of the Kupferschiefer Bed, Fore-Sudetic Monocline, Poland. Trans Instn Min Metall 101: B1-B8

Sawłowicz Z (1993) Pyrite framboids and their development: a new conceptual mechanism. Geol Rundsch 82:148-156.

Speczik S (1995) The Kupferschiefer mineralization of Central Europe: New aspects and major areas of future research. Ore Geol Rev 9:411-426

Wodzicki A, Piestrzyński A (1994) An ore genetic model for the Lubin-Sieroszowice mining district, Poland. Mineral Deposita 29:30-43.

Mineral exploration guidelines for the Ba-Sr ore deposits of the Neuquén Basin, West Argentina

Raúl E. de Barrio
INREMI-Facultad de Ciencias Naturales y Museo, Argentina.

Abstract. Numerous Ba-Sr deposits are found along the 70°W longitude in the Neuquén Basin, west Argentina. They show a close relationship with the Jurassic-Cretaceous sequence revealing a strong stratabound character. They are mainly composed by barite and celestite with, in some cases, very minor amounts of Pb-Zn sulfides. The deposits appear in three ways: stratiform ("mantos"), veins and irregular bodies. Most of the mineralizations are due to the epigenetic replacement of favorable lithologies as boundstones and gypsum-rich beds. Based on the recognized general geological features, most of these mineralizations can be permissively classified as Mississippi Valley-type (MVT) deposits. Geologic and metallogenic investigations allowed to establish some mineral exploration guidelines for the Ba-Sr deposits of the Neuquén Basin.

1 introduction

The Neuquén Basin is located on the western side of Argentina, between 32° and 40°S latitude (Fig. 1). It represents a large morphostructural unit characterized by a stratigraphic sequence, more than 6,000 m thick, deposited between the Late Triassic and the Lower Tertiary (Legarreta and Gulisano 1989, Howell et al. 2005). It hosts numerous stratabound carbonate-hosted hydrothermal deposits mainly of celestite and barite as ore minerals. They are mainly distributed along the 70°W longitude between Chos Malal and Zapala localities (Brodtkorb et al. 1982, 1989) and appear in three ways: stratiform ("mantos"), veins and irregular bodies in cavities by karstic dissolution (de Barrio et al. 2014). Their origin is mostly related to epigenetic processes of replacement of Mesozoic carbonate or evaporitic rocks. Only Arroyo Nuevo Ba mineralization is syngenetic, formed by sedimentary-exhalative deposition onto the seafloor. Barite and celestite ore minerals also are accompanied, in some cases, by very minor proportions of galena, sphalerite, chalcopyrite, dolomite, calcite, and quartz. In the last years, several metallogenic studies allowed to establish some mineral exploration guidelines for the Ba-Sr ore deposits of the Neuquén Basin.

2 Geological setting

The sedimentary sequence of the Neuquén Basin is constituted by clastic, carbonate, evaporitic, pyroclastic and magmatic rocks (Legarreta and Gulisano 1989). It was developed from the Upper Triassic to the Lower Tertiary, near the western edge of the South American Plate, between a volcanic arc to the west and the eastern flank of the foreland (Howell et al. 2005). The tectonostratigraphic history of the Neuquén Basin involves the development of several alternating marine and continental cycles mainly during the Jurassic-Cretaceous. Moreover, the andesitic magmatism represented by the Naunauco Group (Colipilli and Cayanta Formations, Llambías and Aragón 2011) is an important tectonomagmatic event developed in the Late Cretaceous-Eocene. This magmatism is represented by outcrops of intrusive bodies (sills, dikes and stocks) and extrusive lava series.

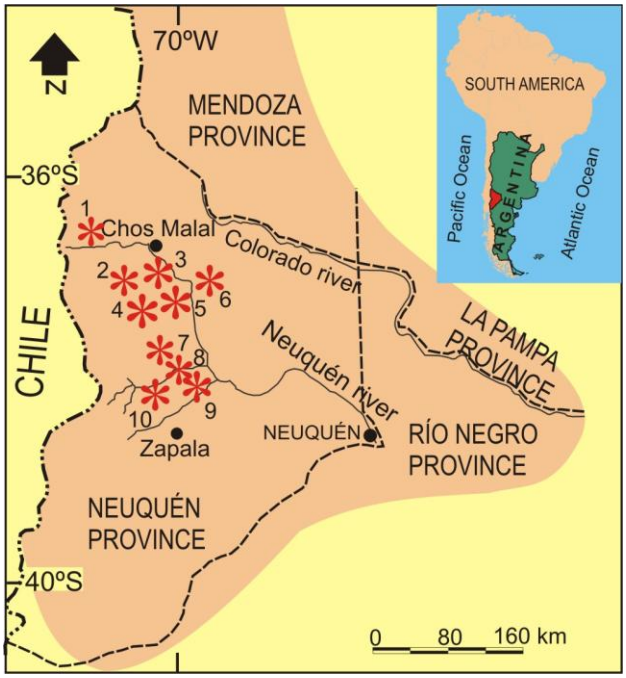


Figure 1. Location map of the Neuquén Basin and distribution of the main Ba-Sr ore deposits. 1. Arroyo Nuevo mine, 2. Colipilli district, 3. Naunauco-Taquimilán district, 4. Loncopué district, 5. Continental Group, 6. Barda Klein mine, 7. Bajada del Agrio district, 8. Llao Llao mine, 9. Achalay mine, 10. San Charbel mine.

3 Mineral exploration guidelines

The mineralizations present conspicuous geological features which may help to mineral exploration programs. Table 1 shows a summary of the main characteristics of representative Ba-Sr ore deposits in the Neuquén province. The mineralizations are catalogued in three groups: a) sedimentary exhalative deposits (SEDEX-Ba), b) epigenetic hydrothermal deposits spatially linked with

igneous rock outcrops, and c) epigenetic hydrothermal deposits no spatially linked with igneous rock outcrops. Most of the celestite deposits are distributed in areas without magmatic activity while the barite deposits are grouped in sectors with igneous rock outcrops. However, both groups show stable isotope data compatible with a non magmatic origin.

The Ba-Sr deposits show a marked stratabound character. They are closely spatially related to the Jurassic-Cretaceous sequence where the carbonate-evaporite and siliciclastic stratigraphical units played a significant role for the genetic processes. These deposits mainly occur in different sedimentary formations: Tábanos Fm. (Middle Jurassic, Fig. 2), Auquilco Fm. (Upper Jurassic) and Huitrín Fm. (Lower Cretaceous), all of them constituted by platform carbonate-evaporitic sequences. Laminated microbial limestones (boundstones) are conspicuous layers in numerous deposits. They constituted favourable beds for the circulation of mineralizing fluids and subsequent selected replacement and infilling processes.



Figure 2. Celestite layer showing carbonate relict at San Charbel mine (Tábanos Formation, Middle Jurassic).

The celestite and barite beds have a length of hundreds of meters and tabular- to lensoid-shapes. Their color varies from light blue to light brown and yellowish white. They are of a few centimetres up to 1.8-2 m thickness lying conformable with the general bedding. Zebra or rhythmite textures (Fig. 3) are very common in the stratiform deposits. They are composed by a laminae alternation of a few millimeters to some centimeters thickness. The texture shows dark and light bands of carbonate and celestite or barite, respectively.

The areal distribution of the deposits is controlled by several regional lineaments and folded structures of N-S general strike. At the present, their attitude depends on local fold structures. Thus, in some places the celestite-barite beds are horizontal while in others, they are near vertical. This variation complicates the mining works.

4 Conclusions

The Ba-Sr deposits of the Neuquén Basin represent a large group of widely distributed mineralizations mostly linked to Middle Jurassic-Lower Cretaceous carbonate-evaporitic sequences showing strong regional stratabound behaviour. The mineralizations form several clusters of deposits showing similar metallogenic features.

The mineralogical, petrographic and textural data support an epigenetic style for the bedded Ba-Sr deposits and point out a replacement of carbonate and gypsum layers by hydrothermal fluids likely formed from basinal brines that were mobilized possibly during the Lower Tertiary. Later, remobilization processes generated infilling of fractures and holes resulting in veins and breccia deposits. Finally, lining of paleokarstic cavities in carbonate rocks occurred (Fig. 4).



Figure 3. Zebra texture at Ba-Sr Santa Elena mine (Lower Cretaceous, Continental Group) in underground works.

The general geological characteristics of the Ba-Sr deposits of the Neuquén Basin are similar to those of the Ba-Sr mineralizations of the Coahuila State, NE México which were considered as MVT deposits (Tritlla et al. 2006, González Sánchez et al. 2009). The indicated features represent useful tools of mineral exploration for the Ba-Sr deposits in a very large region with up to the present scarce exploration programs.



Figure 4. Karstic cavities with remobilized barite at La Luisiata mine (Huitrín Formation, Lower Cretaceous).

TIPOLOGY	AREA/ DISTRICT	ORE DEPOSIT/ MINE	SHAPE OF ORE BODY	MINERAL ASSOCIATION	ORE TEXTURE	HOST ROCK/ FORMATION	ALTERATION STYLE	MAIN GENETIC PROCESSES
SEDIMENTARY EXHALATIVE DEPOSIT (SEDEX Ba)	Cura Mallín	Arroyo Nuevo	stratiform ("manto")	Brt >>> Py ± Gn ± Sp ± Ccp ± Qz	coarse grains	black shales/Los Molles Fm	oxid, sil	sea-floor deposition
			vein	Brt >>> Gn	tabular grains	sandstones/Los Molles Fm	oxid	remobilization/infilling
EPIGENETIC HYDROTHERMAL DEPOSITS SPATIALLY LINKED WITH IGNEOUS ROCK OUTCROPS	Loncopué	La Rosita	stratiform ("manto")	Brt	fine tabular grains	limestones/Tábanos Fm	sil	replacement
			vein	Brt	tabular grains	sandstones/Lotena Fm	minor sil	infilling
		La Florcita	vein	Brt >>> Sp	tabular grains	sandstones/Lotena Fm	minor sil	infilling
	Mallín Quemado Hill/ Cuchillo Cura range	Achalay	stratiform ("manto")	Brt >>> Gn ± Py	comb, tabular grains	limestones/Auquilco Fm	oxid, chlor	infilling/replacement
			breccia	Brt >> Gn ± Ccp	coarse grains	limestones, sandstones, gypsum, and barite blocks	sil, chlor, oxid	hydraulic fracturation/infilling
			vein	Brt >> Gn ± Sp ± Ccp ± Py ± Qz ± Adl	coarse grains	sandstones/Tordillo Fm	ser, sil, arg	infilling
			dissemination	Clt	fine grains	sandstones/Tordillo Fm	arg	infilling
		Río Agrio	vein	Brt >> Ccp ± Gn ± Cal ± Qz ± Adl	coarse grains	sandstones/Tordillo Fm	ser, sil	infilling
		La Porfía	vein	Brt	coarse grains	sandstones/Tordillo Fm	ser, sil	infilling
		Llao Llao	stratiform ("manto")	Clt	massive, fine tabular grains, rhythmites	limestones/Auquilco Fm	pyr, sil, oxid	replacement
			stratiform ("manto")	Brt >> Py	massive		pyr	replacement/infilling
	Colipilli	San Eduardo	vein/stratiform ("manto")	Brt >> Gn ± Ccp	rhythmites, breccia	limestones/Troncoso superior Member, Huitrín Fm	oxid	replacement/infilling
		La Bienvenida	stratiform ("manto")	Brt > Gn	rhythmites	sandstones/ Troncoso inferior Member	oxid	replacement/infilling
		Julio César and others	vein	Brt >> Gn ± Hem	tabular grains, breccia	limestones/Chorreado Member, Agrio Fm	oxid, prop	infilling
	Naunauco	Don Candelario, Clementina	stratiform ("manto")	Clt >>> Py	equant grains	limestones, gypsum/ Troncoso superior Member, Huitrín Fm	weak dol	replacement
	Tralalhue stream	Diablo Hill	vein	Brt >> Gn ± Sp ± Au ±Hem	Tabular grains	Diorite-andesites Naunauco Group/ black shales of Vaca Muerta Fm/ sandstones of Mulichinco Fm	prop	infilling
EPIGENETIC HYDROTHERMAL DEPOSITS NO SPATIALLY LINKED WITH IGNEOUS ROCK OUTCROPS	Cuchillo Cura	San Charbel	stratiform ("manto")	Clt	tabular-prismatic grains, rhymithes	limestones/Tábanos Fm	weak dol	replacement
	Bajada del Agrio	3, 4 and 5 de noviembre, Santa Bárbara, Santa Ana	stratiform ("manto")	Clt > Bar	rhythmites	limestones, gypsum/ Troncoso superior Member and La Tosca Member, Huitrín Fm	weak dol	replacement/infilling
	Salado Range	Dios Alado	stratiform ("manto")	Clt > Brt	rhythmites		weak dol	replacement
		Continental Group (Cecilia mine and others)	stratiform ("manto")	Clt > Brt	rhythmites		calc	replacement
			stalactitic	Brt	crustiform-banded		weak dol	infilling of cavity
			cavity infilling	Brt	druse/geoda		calc	remobilization/ infilling
		Santa Elena	stratiform ("manto")	Clt > Brt	rhythmites		weak dol	replacement/infilling
	Picún Leufú Stream	Puesto Gregor	stratiform ("manto")	Sp > Gn ± Dol ± Cal	disseminated	sandstones/ Las Lajas Fm	dol	replacement

Table 1: Summary of the main characteristics of representative Ba-Sr ore deposits in the Neuquén province, Argentina. References: chlor: chloritization; oxid: oxidation; sil: silicification; ser: sericitization; arg: argilization; pyr: pyritization; prop: propilitization; dol: dolomitization; calc: calcitization. Mineral abbreviations after Whitney and Evans (2010).

Acknowledgements

Thanks to National University of La Plata (UNLP) and the National Research Council of Argentina (CONICET) which supported this investigation.

References

Brodtkorb MK de, Ramos VA, Barbieri M, Ametrano S (1982) The evaporitic celestine-barite deposits of Neuquén, Argentina. Miner Depos 17:423-436

Brodtkorb MK de, Schalamuk IB, Ametrano S (1989) Celestine and barite stratabound orefields in Argentina. In: Brodtkorb MK de (ed) Non-Metalliferous stratabound orefields, Van Nostrand, New York, pp 41-68

de Barrio RE, Etcheverry RO, Del Blanco MA, Domínguez EA, Recio Hernández C, Escobar RI, Salvioli MA (2014) Nuevos datos y esquemas genéticos de los depósitos barítico-celestínicos vinculados a la secuencia jurásico-cretácica de la Cuenca Neuquina en la provincia del Neuquén. Rev Asoc Geol Arg 71(2): 184-200

González-Sánchez F, Camprubí A, González-Partida E, Puente-Solís R, Canet C, Centeno-García E, Atudorei V (2009) Regional stratigraphy and distribution of epigenetic stratabound celestine, fluorite, barite and Pb–Zn deposits in the MVT province of northeastern Mexico. Miner Depos 44:343–361

Howell JA, Schwarz E, Spalletti LA, Veiga G (2005) The Neuquén Basin: an overview. In: Veiga GD, Spalletti LA, Howell JA, Schwarz E (eds) The Neuquén Basin, Argentina: A case study in sequence stratigraphy and basin dynamics. Geol Soc London, Spec Publ 252:1-14

Legarreta L, Gulisano C (1989) Análisis estratigráfico secuencial de la Cuenca Neuquina (Triásico superior-Terciario inferior). In: Chebli G, Spalletti L (eds) Cuencas Sedimentarias Argentinas, Ser Correl Geol 6, Inst Sup Correl Geol, National University of Tucumán, Argentina, pp 221-243

Llambías EJ, Aragón E (2011) Volcanismo Paleógeno. In: Leanza H, Arregui C, Carbone O, Danieli JC, Vallés J (eds) Relatorio Geología y Recursos Naturales de la provincia del Neuquén, 23:265-274

Tritlla J, Levresse G, Corona-Esquivel R, Banks D, Lamadrid H, Bourdet J (2006) Depósitos de Pb-Zn-Cu-Ba-F-Sr epigenéticos estratoligados en series sedimentarias en relación con salmueras de cuenca: depósitos de tipo "Mississippi Valley" (MVT) y similares en México. Bol Soc Geol Mex 58:103-139

Whitney DL, Evans BW (2010) Abbreviations for names of rock-forming minerals. Am Mineral 95:185-187

The potential of phosphate and associated critical raw materials in Europe

Sophie Decrée
Geological Survey of Belgium, Royal Belgian Institute of Natural Sciences

Peter M. Ihlen, Henrik Schiellerup
Geological Survey of Norway

Anders Hallberg
Geological Survey of Sweden

Alecos Demetriades
Instituto Geologico y Minero de Espana (IGME)

Margus Raha
Estonian Ministry of Economic Affairs and Communication

Alvar Soesoo
Tallinn University of Technology, Estonia

Abstract. Phosphate rocks (sedimentary and igneous in origin) and their potential by-products (Rare Earth Elements and F) are listed as Critical Raw Materials (CRMs) by the European Commission, emphasizing the existing pressure to ensure the supply of these materials to the European Union. However, sedimentary phosphorite deposits are widespread throughout Europe, and several igneous-related phosphate deposits (associated with alkaline/carbonatite magmatism, anorthosites and monzonitic complexes) are located within the Fennoscandian Shield. This abstract aims to provide a short review of the most important phosphate deposits in Europe, with up-to-date data (abstracted from bibliography) relating the reserves/resources and grades of the deposits.

1 Interest for P and CRMs in Europe

The European Union (EU) does not produce enough of the raw materials needed for its industries, especially those oriented towards new technologies (EC 2015). In order to ensure the supply of these materials, and guarantee the European industrial competitiveness, the EU identified 14 critical raw materials (CRMs) in 2011 (EC 2011). This list was extended in 2014 and now comprises 20 CRMs, including phosphate rock (EC 2014). The EU imports about 4,000,000 tonnes of natural phosphate-rich material per year (EC 2015), mostly to produce fertilizers.

Phosphorus can be exploited from sedimentary phosphorite deposits (onshore and offshore), island (guano) deposits or igneous phosphate deposits. The phosphorite deposits are by far the main source of P, which occurs as francolite (carbonate fluorapatite) (EC 2015).

Besides P, the rare earth elements (REEs) can be recovered from phosphate deposits. These elements are also listed as CRMs by the EU. About 8,000 tonnes of REE compounds, metals and alloys are imported every year in the EU (EC 2015). The potential of phosphate deposits as a source of REE has recently been put into the forefront (Christmann 2014; Ihlen et al. 2014; Emsbo et al. 2015; Goodenough et al. 2016). Emsbo et al. (2015) have shown that the REE content of sedimentary phosphate deposits occurring in the USA is as important as any known resource. The concentration of REEs in these deposits is highly variable; it reaches 0.15% in the sedimentary phosphorite deposits (Notholt 1980; Chrismann 2014), while contents over 0.35% are observed in magmatic apatite (Ihlen et al. 2014). The sedimentary deposits usually show higher grades than the igneous phosphate ones. Nevertheless, the latter usually has lower contents of unwanted contaminants for exploitation, such as Th and U (Ihlen et al. 2014; Ahokas 2015). Compared to the conventional deposits (where the REEs are exploited as monazite or fluorocarbonates), their extraction from apatite is possible during the production of phosphoric acid, or from waste phosphoric acid and phosphogypsum (e.g., Pereira and Bilal 2012; Christmann 2014; Emsbo et al. 2015). Moreover, this recovery is less harmful to the environment than REE exploitation from conventional deposits (Emsbo et al. 2015).

In addition to P and REEs, fluorspar (the commercial name of fluorite) is another CRM that can be recovered from phosphate deposits. The EU imports F (that is mainly used to produce hydrofluoric acid) at a level reaching 8-15 times the exported products (EC 2015). Up to 3-4% F is present in phosphate deposits. It can be recovered as fluosilicic acid during the course of the phosphate chemical processing, and processes to transform this fluorine compound into calcium fluoride exist (McKelvey 1967; Ayres et al. 2001). Phosphate rocks therefore represent a secondary and perspective source of fluorine (McKelvey 1967; Gorecki 1994).

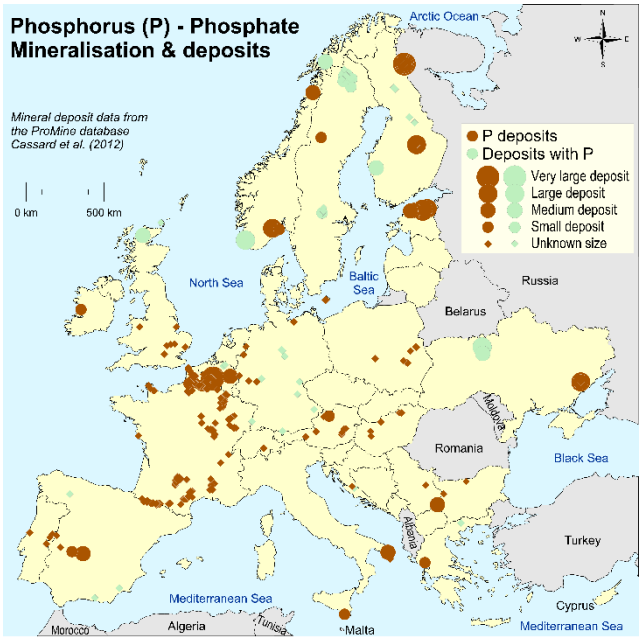


Figure 1. Phosphorus and phosphate mineralization and deposits (figure modified from Demetriades and Reinmann 2014, and ProMine database from Cassard et al. 2012). Deposit size: Small (>X) 2,000,000; Medium (>X): 20,000,000; Large (>X): 200,000,000; Very large (>X): 2,000,000,000 tonnes

2 Phosphate deposits in Europe

2.1 Sedimentary phosphorite

Sedimentary phosphate deposits/occurrences are widespread in Europe and are distributed in rocks from the Proterozoic to the Cenozoic (Fig. 1). Deposits with available data about resources/reserves and grade are reported below.

The Proterozoic and Lower Paleozoic phosphorites constitute most of the phosphorite deposits in Europe. They indicate the existence of a phosphogenic province within the Avalon and the Baltic Platforms. These deposits/occurrences are commonly hosted within glauconitic sediments or black shale (Notholt and Brasier 1986). Proterozoic phosphorite deposits only occur in the Fennoscandian Shield (Notholt et al. 1989). Among these, the Lampinsaari deposit (Finland) is made of a lenticular bed of apatite-bearing dolomite, skarn and apatite-rich gneiss (Notholt and Brasier 1986). It accounts for 39 million tonnes at a grade of 2.6% P_2O_5 (Notholt et al. 1989), with more than 230 ppm REE in the apatite concentrates (Rehtijärvi 1983). Cambro-ordovician phosphorite deposits are widely distributed in Europe. The early Cambrian Fontanarejo deposit (phospharenite and phospharenorudite; Gabaldon et al. 1987) has resources of about 2,000,000 tonnes (Notholt et al. 1989), with about 190 ppm REEs (Alvaro et al. 2015). Ordovician phosphorite deposits (metamorphosed phosphatic sandstone) of economic interest occur in Serbia (Notholt et al. 1989). They present 95 million tonnes of mineral resources at ~10% P_2O_5 (Torbica and Lapčević 2012). In northern Estonia, Cambrian – Ordovician sandstone with variable amounts of phosphatic linguloid brachiopod shells account for deposits of 750-800 million tonnes of P_2O_5 (Raudsep 1997), with average total REE contents of 1350 ppm. Middle to Upper Palaeozoic phosphorite deposits are also encountered in Europe. One notable deposit is present in Ireland (County Clare), where the resources of Upper Carboniferous sedimentary phosphate rocks (occurring in a condensed sequence) have been estimated at 1.25 million tonnes, with a grade of 20-25% P_2O_5 (Notholt et al. 1979).

A significant phosphogenic episode is known during Cretaceous time on the NE margins of the Anglo-Paris Basin (Jarvis 1992). In the Mons and Paris Basins (Belgium and France, respectively), the deposits consist of phosphatic chalk, enriched pockets of residual phosphates, and phosphatic channels infills (Monchiardini 1989; Robaszynski 1989). An estimation of the total resources lead to 600-900 million tonnes at 8-10.5% P_2O_5 in the Mons Basin (Robaszynski 1989), and 12-15 million tonnes at 7-14% P_2O_5 in the Paris Basin (Monchiardini 1989). In the UK, the Taplow Cretaceous phosphate chalk has an economic potential, with reserves estimated at 500,000 tonnes in its southwestern side. In addition, in Cambridge Greensand (UK), reserves of 246,000 tonnes can be found in Cenomanian condensed glauconitic marl comprising phosphate nodules (Notholt et al. 1979). In Lower Saxony (Germany), the Lengede-Broitstedt deposit (made of phosphate nodules beds) is considered as an economic source of phosphorus, with a grade of about 4% P_2O_5 (Notholt et al. 1979). In Bavaria (Oberpfälz district, Germany), phosphatic beds associated with iron ore accounts for at least 30,000 tonnes at 20% P_2O_5 (Notholt et al. 1979). In western Hellas (Greece) there are two extensive phosphatized limestone horizons of Cretaceous age, with the Drimonas deposit having about 7 Mt at ~25% P_2O_5, and with a U and REEs potential (Koukouzas et al. 1978; Tzifas et al. 2014).

Major phosphogenic episodes have been identified during the Cenozoic (Arthur and Jenkyns 1981). Miocene phosphate-rich sediments in the area of Salento (Italy) account for at least 60 million tonnes of phosphatic limestone with 7-8 % P_2O_5, and Upper Pliocene (?) nodular phosphates in the same zone could account for additional 10 million tonnes at a grade in the range 10.5-20.5 % P_2O (Notholt et al. 1979). In Sicily, Oligo-Miocene phosphatic nodule-rich formations are present (Cultrone et al. 2008), with resources of 7 million tonnes at about 15% P_2O_5 at Donnalucata (Notholt et al. 1979). In Germany, the Lahn phosphorite deposits associated with Lower Tertiary Fe and Mn oxide ores, which are spatially associated with weathered basic pyroclastic rocks, account for 750,000 tonnes of mineral resources at above 20% P_2O_5 (Notholt et al. 1979).

2.1 Igneous phosphate deposits

Most of the igneous apatite deposits in Europe are associated with alkaline complexes, carbonatite, massif-type anothosite and monzonitic complexes (the latter two

complexes carrying apatite-iron- titanium oxide, AITO, ores; Notholt et al. 1979; Ihlen et al. 2014; Goodenough et al. 2016). Apart from few exceptions, all these deposits occur within the Fennoscandian Shield. Only a few examples of these deposits are given below.

In Finland, the Precambrian deposit of Siilinjärvi, which is related to an Archean carbonatite complex, is interesting regarding P and REEs. It comprises 1617 million tonnes of phosphate rocks (Ahokas 2015; Yara 2016). The total concentration in REEs is about 3000-4000 ppm in the apatite concentrates (Hornig-Kjarsgaard 1998). At Sokli, the reserves in phosphate associated with the Devono-carboniferous alkaline complex reaches 190 million tonnes (Ahokas 2015). There, the apatite concentrate shows contents of 4108 and 5569 ppm of REEs (Hornig-Kjarsgaard 1998). Phosphate deposits are also found in association with the Paleoproterozoic gabbro of Southern Ostrobothnia (Ahokas 2015; Kärkkäinen and Appelqvist 1999).

In Sweden, apatite iron ores are found in the Northern Norrbotten district, northern Sweden, and in the Bergslagen district, south central Sweden. In the Northern Norrbotten district, the deposits at Kirunavaara and Malmberget have produced more than 1500 Mt with c. 60% Fe and 1.37% P_2O_5 during the last 110 years (Hallberg et al 2016). Smaller deposits in the district account for c. 100 Mt at similar grades. Apatite iron ore resources for the district are estimated to 2000 Mt. In the Bergslagen district the Grängesberg mine produced 133 Mt with 44.5% Fe and 3.18 % P_2O_5 during its lifetime. Estimated resources are 148 Mt. The apatite in the ores always carries REEs, though very little have been recovered and resource estimates for the REEs have not been published.

At Fen (Norway), some apatite-rich facies have been recognized among the rocks constituting the carbonatite complex (up to 29% apatite in apatite-rich cumulates; Ihlen et al. 2014). Apatite concentrates from Fen show total REE contents varying between 3752 and 5220 ppm (Hornig-Kjarsgaard 1998). The Tappeluft pegmatitic gabbro (Precambrian to Cambrian alkaline complexes of the Seiland Igneous Province) contains P_2O_5 contents ranging from 1.88 to 4.29%. In the Lillebukt Complex, carbonatitic facies and clinopyroxenite dykes are both characterized by an average content of 3% P_2O_5; apatite comprising a few thousand ppm of REEs. The pyroxenite of the Misvaerdal Complex hosts apatite, with grade ~2.38% P_2O_5 for the whole massif. Apatite shows total REEs enrichment ranging from 1234 to 11,180 ppm (Ihlen et al. 2014). A volume of 30 Mt with more than 4 % P_2O_5 has been identified. Other phosphate deposits in Norway are associated with the Precambrian anorthositic complexes. In the Rogaland Anorthosite Province, large apatite rich zones (up to 10 kilometers along strike, and up to 170 m in thickness), show about 7.8-10.2% of apatite, depending on the zones position in the intrusion (Ihlen et al. 2014). The Bjerkreim-Sokndal intrusion has resources of above 300 Mt, with 8.0-10.2% apatite containing also ilmenite and vanadium-rich magnetite (Ihlen et al. 2014). Another type of phosphate deposit, associated with monzonitic complexes, such as in the Paleoproterozoic Lofoten-Vesteralen Mangerite Complex, nelsonite veins and dykes are reported with P_2O_5 varying between 2.75 and 4.23%. The apatite concentrate shows high REE content reaching about 5000 ppm (Ihlen et al. 2014). Another deposit, associated with a monzonitic complex is the Kodal deposit, has reserves of 70 Mt at 4.9 % P_2O_5. Finally, apatite is present in Kiruna-type apatite-iron ore (AIO) and in metasomatic deposits. In the Precambrian Mesoproterozoic Søftestad deposit, the ore is dominated by magnetite, and may contain up to 8% P_2O_5. Reserves left are ~0.5 Mt at 55% Fe and 3.9% P_2O_5 (Ihlen et al. 2014, and references therein). About 250,000 tonnes of apatite have been produced in the Bamble-Lillesand Block, where phosphate veins and lenses are associated with regional metasomatism. About 5000-6000 ppm REEs are normally hosted within apatite (Ihlen et al. 2014). At Rossavika, an enigmatic deposit is made up by pseudo-carbonatitic lenses grading from 7.63 to 21.34% P_2O_5, with a low total REE content of 3806 ppm (Ihlen et al. 2014).

3 Perpectives

This short reviews aims to show that the potential in terms of phosphate deposits in Europe is significant and could – at least partly – secure the access to phosphate rocks (and other by-products considered as CRMs) in Europe. However, it appears from this review that more efforts are needed to study sedimentary phosphate deposits. Excepting for a few of them, no careful chemical characterization and up-to-date estimation of the reserves/resources have been done since a few decades.

In addition, it is worth mentioning that part of the phosphorate deposits (especially the Proterozoic- Lower Palaeozoic ones) are hosted within black shale. The latter could be particularly interesting regarding the (precious) metals/metalloids they can potentially contain (McKelvey 1967), more particularly Be, Sb, Co, Cr and platinum group metals that are also listed as CRMs by the EU (EC report 2014).

Acknowledgements

D. Papanikos and Y. Marantos (Institute of Geology and Mineral Exploration) are thanked for the information on the hellenic P deposits.

References

Ahokas K (2015) Finland's phosphorus resources are more important than ever. Geofoorumi 2: 10-12

Álvaro JJ, Shields-Zhou GA, Ahlberg P, Jensen S, Palacios T (2015). Ediacaran–Cambrian phosphorites from the western margins of Gondwana and Baltica. Sedimentology 63: 350–377

Arthur MA, Jenkyns HC (1981) Phosphorites and paleoceanography. Ocean Acta, Special issue: 83-96

Ayres RU, Holmberg J, Andersson B (2001) Materials and the global environment: Waste mining in the 21st century. MRS Bull 26: 477-480

Cassard D, Bertrand G, Maldan F, Gaàl G et al (2012) ProMine pan-European Mineral Deposit database: a new dataset for assessing

primary mineral resources in Europe. Workshop on: Mineral Resources Potential Maps: a Tool for Discovering Future Deposits. 12th-14th March 2012, Nancy, France, Proceedings: 9-13

Christmann P (2014) A forward look into rare earth supply and demand: a role for sedimentary phosphate deposits? Proced Eng 83: 19-26

Cultrone G, Anfuso G, Sebastián E (2010) Mineralogy of Miocene phosphatic nodules in SE Sicily (Italy). Geol Q 52: 61-70

Demetriades A, Reimann C (2014) Mineral deposits in Europe - Chapter 3. In: Reimann C, Birke M, Demetriades A et al (eds) Chemistry of Europe's agricultural soils – Part B: General background information and further analysis of the GEMAS data set, Geol Jahrbuch (Reihe B103), Schweizerbarth, Hannover, pp 71-78

Emsbo P, McLaughlin PI, Breit GN et al (2015) Rare earth elements in sedimentary phosphate deposits: Solution to the global REE crisis? Gondwana Res 27:776-785

European Commission (EC) (2011) Tackling the challenges in commodity markets and on raw materials. http://eur-lex.europa.eu/legal-content/EN/TXT/PDF/?uri=CELEX:52011DC0025&from=EN. Accessed on 9 December 2016

European Commission (EC) (2014) On the review of the list of critical raw materials for the EU and the implementation of the Raw Materials Initiative. http://eur-lex.europa.eu/legal-content/EN/TXT/PDF/?uri=CELEX:52014DC0297&from=EN. Accessed 9 December 2016

European Commission (EC) (2015) Report on Critical Raw Materials for the EU. Critical Raw Materials Profiles. http://ec.europa.eu/DocsRoom/documents/11911/attachments/1/translations. Accessed 9 December 2016

Gabaldon LV, Hernandez Urroz J, Lorenzo Alvarez S et al (1987) Sedimentary facies and stratigraphy of Precambrian-Cambrian phosphorites on the Valdelacasa anticline, Central Iberian Zone, Spain. In: Cook PJ, Shergold JH (eds) Phosphate Deposits of the World: volume 2. Proterozoic and Cambrian Phosphorites, Cambridge University Press, Cambridge, pp 422–428

Goodenough KM, Schilling J, Jonsson E et al (2016) Europe's rare earth element resource potential: An overview of REE metallogenetic provinces and their geodynamic setting. Ore Geol Rev 72: 838-856

Gorecki HJ (1994) Utilization of fluorine from phosphate fertilizer plants. In: Hodge CA, Popovici NN (eds) Pollution control in fertilizer production, CRC press, pp 299-336

Hallberg A, Bergman T, Gonzalez J et al (2016) Chapter 7 – Sweden. In: Boyd R, Bjerkgård T, Nordah B et al (eds) Mineral Resources in the Arctic. Geological Survey of Norway Special Publication, http://www.ngu.no/upload/Aktuelt/CircumArtic/7_Sweden.pdf

Hornig-Kjarsgaard I (1998) Rare earth elements in sövitic carbonatites and their mineral phases. J Petrol 39, 2105-2121

Ihlen PM, Schiellerup H, Gautneb H, Skår Ø (2014). Characterization of apatite resources in Norway and their REE potential—a review. Ore Geol Rev 58: 126-147

Kärkkäinen N, Appelqvist H (1999) Genesis of a low-grade apatite-ilmenite-magnetite deposit in the Kauhajärvi gabbro, western Finland. Miner Dep 34: 754-769

Koukouzas K, Grigoris P, Papastavrou S et al (1978) Preliminary report on U-bearing phosphorite occurrences and radioactive anomalies in Epirus-Ioannina district. Open File Report, Institute of Geology and Mineral Exploration, Athens

Martinsson O, Billström K, Broman C et al (2016) Metallogeny of the Northern Norrbotten Ore Province, northern Fennoscandian Shield with emphasis on IOCG and apatite-iron ore deposits. Ore Geol Rev 78: 447-492

McKelvey VE (1967) Phosphate deposits (No. 1252-D), USA Govt Print Off

Monciardini C (1989) The Senonian (Cretaceous) phosphatic chalks of the Paris Basin, France. In: Notholt AJG, Sheldon RP, Davidson D (eds) Phosphate deposits of the world: volume 2, phosphate rock resources, Cambridge University Press, Cambridge, pp 407-410

Notholt AJG, Highley DE, Slansky M (1979) Raw Materials Research and Development IV. Dossier on Phosphate, Commission of the European Communities, Brussels

Notholt AJG, Brasier MD (1986) Proterozoic and Cambrian phosphorites-regional review: Europe. In: Cook PJ, Shergold JH (eds) Phosphate deposits of the world: volume 1, Proterozoic and Cambrian phosphorites, Cambridge University Press, Cambridge

Notholt AJG, Sheldon RP, Davidson D (1989) Europe-Introduction. In: Notholt AJG, Sheldon RP, Davidson D (eds) Phosphate deposits of the world: volume 2, phosphate rock resources, Cambridge University Press, Cambridge

Pereira F, Bilal E (2012) Phosphoric acid extraction and rare earth recovery from apatites of the Brazilian phosphatic ores. Rom J Miner Dep 85: 49-52

Raudsep R (1997) Phosphorite. In: Raukas A and Teedumäe A (eds) Geology and mineral resources of Estonia, Estonian Academy Publishers, 436 p

Rehtijarvi P (1983) REE patterns for apatites from Proterozoic phosphatic metasediments, Finland. Bull Geol Soc Finl 55, 77-82

Robaszynski F (1989) The phosphatic chalk of the Mons Basin, Belgium. In: Notholt AJG, Sheldon RP, Davidson D (eds) Phosphate deposits of the world: volume 2, phosphate rock resources, Cambridge University Press, Cambridge, pp 370-375

Torbica S, Lapčević V (2012) Concept of underground mining of phosphate deposits in Lisina near Bosilegrad. Podzemni radovi: 23-29

Trappe J (2006) Phanerozoic phosphorite depositional systems: a dynamic model for a sedimentary resource system (Vol. 76), Springer

Tzifas IT, Godelitsas A, Magganas A et al (2014) Uranium-bearing phosphatized limestones of NW Greece. J Geochem Explor 143: 62-73

Yara (2016) Siilinjärvi Phosphate Mine – fourth decade ongoing. http://fem.lappi.fi/c/document_library/get_file?folderId=1405164&name=DLFE-20769.pdf. Accessed 9 December 2016

Mineralizing events in the Vosges massif: insights from the Mn-W Haut-Poirot deposit (NE France)

Augustin Dekoninck, Gaëtan Rochez, Johan Yans
Université de Namur, Namur, Belgique

Pierre Fluck
Université de Haute-Alsace, Mulhouse, Cedex, France

Abstract. Vosges (NE France) and Schwarzwald (SW Germany) massifs are well known for their numerous structure-related base-metal deposits. Mineralization events are linked to activation and reactivation of crustal faults as well as hydrothermal episodes in relation with the Variscan orogenic cycle, Jurassic hydrothermalism and Cenozoic rifting. Some manganese veins have been studied in Schwarzwald (i.e. Eisenbach deposit) and provide K/Ar cryptomelane ages correlated to the aforementioned hydrothermal events but also to intense weathering during the Miocene. In the Vosges, the manganiferous Haut-Poirot deposit is hosted in biotite granite and took place at the end of the Variscan orogeny, based on geochemistry and the relatively high temperature assemblage of the primary ore. Despite the lack of datable manganese oxides, this deposit shows a multistage character that could be related to important mineralizing events as reported in the Eisenbach deposit located in Schwarzwald.

1 Introduction

In Western Europe, the Variscan belt outcrops in several massifs that represent some portions of the collision between three continents: Larussia, Baltica and Gondwana (e.g. Friedl et al. 2011). Within this belt, the massifs of Vosges and Schwarzwald (or *Black Forest*) take a linking position between the Massif Central and Bohemian massif (Fig. 1a, e.g. Echtler and Alther 1993). The Baden-Baden (Schwarzwald) and Lalaye-Lubine (Vosges) shear zones define the Saxothuringian (North) and Moldanubian (South) parts of the orogenic belt (Fig. 1a, b, Wickert et al. 1990). Numerous mineral deposits are related to this major geodynamic event, well-documented in Central and Western Europe (e.g. Chantraine et al. 1994; Dallmeyer et al. 1995).

The meso-cenozoic evolution of Vosges and Schwarzwald massifs and their respective break-up on the flanks of the Rhine Valley is attributed to intensive Cenozoic rifting, in relation with the Alpine orogeny (Fig. 1b, Prodehl et al. 2006). The evolution of the Cenozoic Upper Rhine Graben was controlled by a repeatedly changing stress field and reactivation of a complex set of crustal discontinuities originated from the Variscan orogeny (e.g. Hinsken et al. 2007), leading to deposition of mineral vein-type deposits (Fluck and Stein 1992).

The occurrence of numerous veins of base-metal (Ag-Co-Cu-Fe-Mn-Mo-Au-Pb-Zn-Ba-F) in Vosges and Schwarzwald has led to a long duration mining activity during the past centuries. The Haut-Poirot deposit has been mined intermittently from 1890 and the end of the Second World War for its manganese and tungsten content (Fig. 1b, Lougnon 1981). Here, we refine the mineralogy and petrography of this deposit to correlate observations with the general chronologic framework and mineralizing events occurring in Vosges and Schwarzwald.

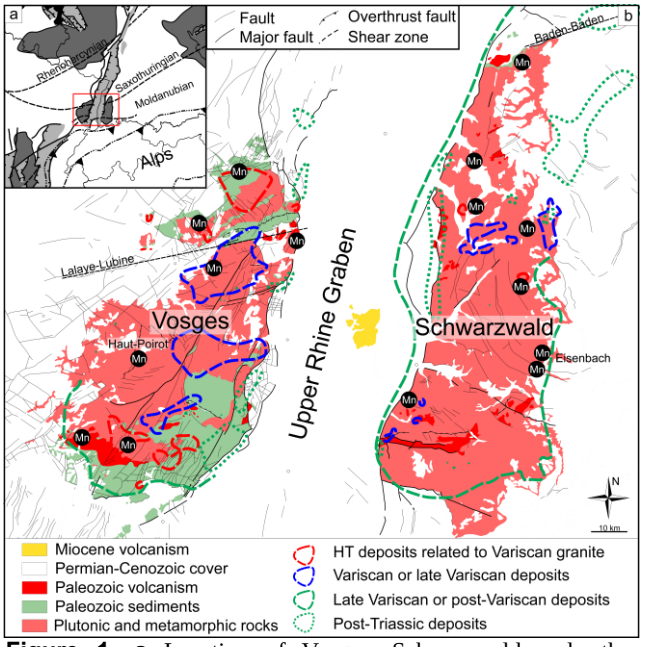


Figure 1. a Location of Vosges, Schwarzwald and other Variscan massifs of Western Europe (modified after Dèzes et al. 2004). **b** Metallogeny map of Vosges and Schwarzwald, and location of manganese deposits (modified after Fluck and Weil 1976).

2 Metallogeny of Vosges and Schwarzwald

The common evolution of Vosges and Schwarzwald has has led to consider their metallogenic features together (Fluck and Weil 1976; Fluck 1977).

2.1 Classification of mineral deposits

Sedimentary deposits are missing in Paleozoic series and occur only in the Mesozoic cover: Triassic uranium and coal deposits (Southern Vosges), Jurassic evaporites (Vosges and Schwarzwald) and Fe-oolithe (Schwarzwald), and K-rich basins (Rhine Valley).
Structure and/or magmatic-related are the most common deposits, but their complexity is somewhat difficult to provide clear classification between the two regions. Based on structural interactions, Fluck and Weil (1976) proposed

these deposits to be associated directly to plutonic rocks or post-Triassic faults that clearly cross-cut the Triassic cover or follow the flanks of the Upper Rhine Graben (Ba, Ba-Fe, F and Q veins). However most of the tectonic-related veins are randomly distributed. Actually their source could be related to three periods: Variscan, post-Variscan or post-Triassic (Fig. 1b).

2.2 Mineralizing events

The timing of the numerous ore veins has long been unclear, mainly because of the lack of datable materials. However, several hydrothermal events are mentioned to explain the formation of structure-related deposits:

1) The Carboniferous is associated to a magmatic-metallogenic period (±330-280 Ma) corresponding to a high temperature hydrothermal activity. This phase is recognized in other Variscan massifs and is connected to intensive, short-duration endogenic processes. It is responsible for late granitoid rocks and related Sn-W associations (Thomas and Tischendorf 1987). Sn, W, Mo, Cu, Fe, Mn, Au occurring in late two-mica granite are directly related to magmatic bodies (Fluck and Weil 1976).
2) The Permian corresponds to the initiation peak of long duration hydrothermal activity (280-260 Ma) at lower temperatures responsible for Ba-F and associated base-metal mineralization (e.g. Segev et al. 1991).
3) Early Jurassic is probably the most prominent mineralizing event recorded along basement faults in Vosges and Schwarzwald massifs (Clauer et al. 1996). Four successive pulses characterize this activity around 200 Ma, 180 Ma, 170 Ma and 150 Ma. Hydrothermal activity is synchronous with episodes of enhanced subsidence. As large parts of Europe were affected by an extensional stress regime, it is suggested that hydrothermal activity and subsidence resulted from extension, and pre-existing faults became reactivated (e.g. Wetzel et al. 2003). The granitoid rocks register temperature of mineralizing fluids up to 230°C (e.g. Clauer et al. 1996).
4) The Cretaceous corresponds to a weaker but higher temperature hydrothermal episode (±100 Ma) relative to the former stage (Segev et al. 1991, Wetzel et al. 2003) linked to a large domal uplift (Illies 1977, Geyer et al. 2011).
5) The Cenozoic renews a higher temperature magmatic-metallogenic activity related to riftogenic activity (Segev et al. 1991, Fluck and Stein 1992).
6) Recent low temperature hydrothermalism is still present with temperatures of about 140-160°C (e.g. Clauer et al. 1996) that leads to geothermal activity in the Upper Rhine Graben (Bailleux et al. 2013).

2.3 Weathering

Emersion periods from the Cretaceous to Paleocene periods suggest weathering processes to be registered in Vosges and Schwarzwald area. However, the first clear signs of weathering are related to the recent uplift of Vosges and Schwarzwald simultaneously with the Upper Rhine Graben rifting by the early Eocene in the Vosges (Fluck and Weil 1976) and at least Miocene in Schwarzwald (Hautmann and Lippolt 2000), leading to the formation of Fe or Mn gossans (Fluck and Weil 1976).

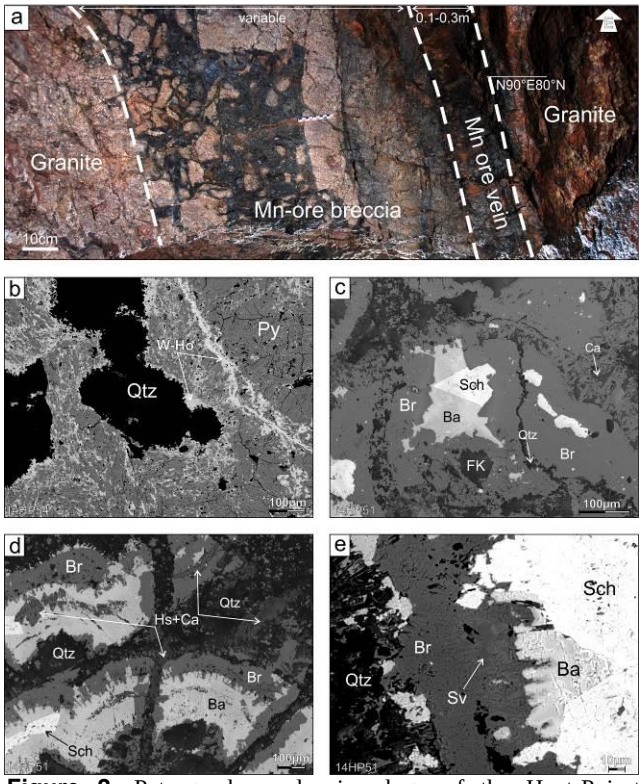


Figure 2. Petrography and mineralogy of the Haut-Poirot deposit. **a** Underground picture of the main ore vein and the associated manganiferous breccia. **b** Replacement texture of pyrolusite by W-rich hollandite. **c** Replacement texture of K-feldspars by braunite. Successive crystallisation of scheelite and barite onto braunite crystals. **d** Secondary brecciation of the main ore. **e** replacement texture of braunite by svabite. FK=K-feldspar; Qtz=quartz; Ho=hollandite; Py=pyrolusite; Br=braunite; Sch=scheelite; Ba=barite; Ca=manganoan calcite; Hs=hausmannite; Sv=svabite.

3 Mn-W Haut-Poirot deposit

Numerous manganese veins occur in Vosges and Schwarzwald in association with some structures and faults (Fig. 1b). Manganese minerals might be decoupled from iron minerals and the veins are hosted both in the Variscan bedrock and the post-Variscan cover (Fluck and Weil 1976). Some of them have been considered in Schwarzwald to provide useful K/Ar and $^{40}Ar/^{39}Ar$ ages obtained on cryptomelane crystals (Segev et al. 1991; Hautmann and Lippolt 2000) in order to determine the

timing and processes responsible for their formation.

3.1 Manganiferous veins

The veins are located in the Haut-Poirot and Lyris woods in the Central Vosges Mountain, 7 km westward of Gérardmer (Fig. 1b, France). The mineralized veins are mainly hosted in biotite and in two-mica granite, part of the Central Vosges Granites (CVG), formed between 330 to 320 Ma during the Variscan cycle (Tabaud *et al.* 2014). The orebodies form two subparallel veins oriented N90° to N120° in a well-fractured zone. The vein 1 is ~600 m long with a thickness ranges from 1 to 0.4 m and a dip angle of 80°N. The second vein is subdivided in two segments with a thickness of about 0.4 m (Bonhomme 1958, Lougnon 1981).

3.2 Mineralogy and petrography

The main ore forms a tectonic breccia (Fig. 2a) filled by pyrolusite, braunite in a barite and quartz gangue (Fig. 2b, c). Scheelite and hollandite *s.s.* are associated to the ore (Fig. 2b, c), as well as U-minerals (francevillite, chalcolite and autunite, Jurain 1956, Weil *et al.* 1959, Lougnon 1981), bornite and chalcocite (Lougnon 1981) that have been described in the ore and host rock granite. The ore is brecciated itself enabling the formation of hausmannite cemented in manganoan calcite and quartz (Fig. 2d). Svabite ($Ca_5[AsO_4]_3F$) replaces locally braunite (Fig. 2e). Iron oxides are nearly absent in the main ore vein.

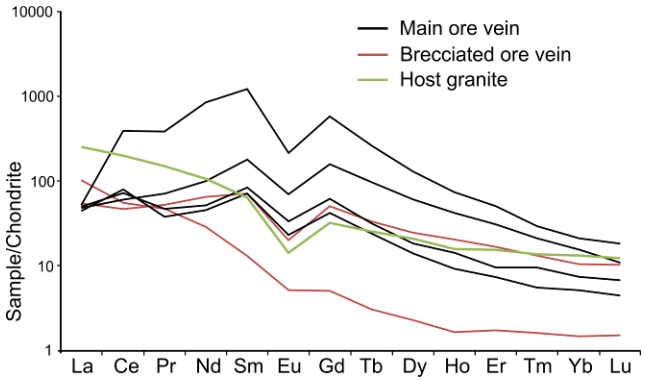


Figure 3. REE pattern of the host rock and manganese ores of the Haut-Poirot deposit normalized to chondrite.

3.3 Geochemistry

The peraluminous host granite shows typical concentration in manganese compared to mean value of granitoid rocks (Li 2000), as well as REE patterns characterized by Eu negative anomaly and enrichment in LREE compared to HREE (Fig. 3).

Mn ores of the Haut-Poirot deposit are characterized by high grade manganese (69.57-72.02 wt. % MnO), silica (3.87-12.39 wt. % SiO_2), tungsten (0.48-0.89 wt. % W) and copper (0.05-0.25 wt. %) and very low phosphor (0.03-0.08 wt. % P_2O_5) and iron (0.08-0.14 wt. % Fe_2O_3). Arsenic, antimony and REE are substantially enriched to thousands of ppm in some samples. The geochemical signature of the ore is typical for hydrothermal deposits (Nicholson 1992) and REE patterns follow the granite trend for HREE and MREE, while LREE are depleted compared to the host granite (Fig. 3).

3.4 Timing and origin of the ore

The most striking feature of the manganiferous vein in the Haut-Poirot deposit is the occurrence of, at least, two distinct mineral assemblages (Fig. 4): 1) the main ore stage is marked by the formation of relatively high temperature paragenesis (braunite and scheelite, Fig. 2c) followed by a O_2-rich mineral assemblage with pyrolusite and then barite (Fig. 2b), after the brecciation of the granite; 2) the brecciation of the ore itself, characterizes a second minor mineralizing event marked by carbonates, hausmannite and probably arsenate (svabite, Fig. 2d, e) corresponding to reduced conditions of the mineralizing fluid. A pre-ore stage is identified by Weil et al. (1959) and corresponds to the formation of quartz-hematite breccia. Weathering processes are poorly recorded such as typical Mn-rich gossan that could be found in other hydrothermal deposits worldwide. However, we could expect some of the observed textures and minerals to be attributed to such processes. For example, it is complex to assign hollandite s.s. to hydrothermal alteration, or weathering processes (Fig. 2b). Coronadite and Pb-rich hollandite occur in the Haut-Poirot deposit as replacement material for biotite in the wall-granite. Biotite is sensitive to oxidation at surface conditions, and can then be easily weathered into oxide minerals, such as Mn-oxides. Lead enrichment in hollandite might be assigned to weathering processes, while pure and tungsten-rich hollandite could be formed by hypogene and/or supergene processes (Fig. 2b). Some of the pyrolusite could form during supergene processes by replacing coronadite crystals.

Despite the occurrence of hollandite group minerals, their sizes are too small in the Haut-Poirot deposits to be dated by K/Ar or $^{40}Ar/^{39}Ar$ methods. However, considering the close genetic relationship between Vosges and Schwarzwald massifs and especially the similarities with the Eisenbach deposit in Schwarzwald (Segev et al. 1991), we could expect manganiferous veins to be affected by the relatively same processes. Although the geochemistry together with the high temperature mineral assemblage observed in the main ore of the Haut-Poirot veins could only be related to Variscan magmatic bodies, the multistage/polyphased character (Fig. 4) allows the ore to be (re)activated several times, probably during faulting and hydrothermal periods registered in the whole area. As an example, Segev et al. (1991) show that the main manganese mineralizing event in the Eisenbach deposit are associated to post-Variscan mineralization periods at relatively low temperature. Intensive tectonic movements related to riftogenic regime of the Upper Rhine Graben lead to Cretaceous ages, corresponding to the initiation of rift activity. Hautmann and Lippolt (2000) show intense weathering of manganese deposits during the Miocene, in

relation with the uplift of Schwarzwald and Vosges. Weathering periods could also be extended to Cretaceous considering that most of the ancient massifs in Western Europe are exposed during that time (e.g. Quesnel 2003), explaining the Early Cretaceous ages obtained by Segev et al. (1991) as well as the lack of Cretaceous sediments.

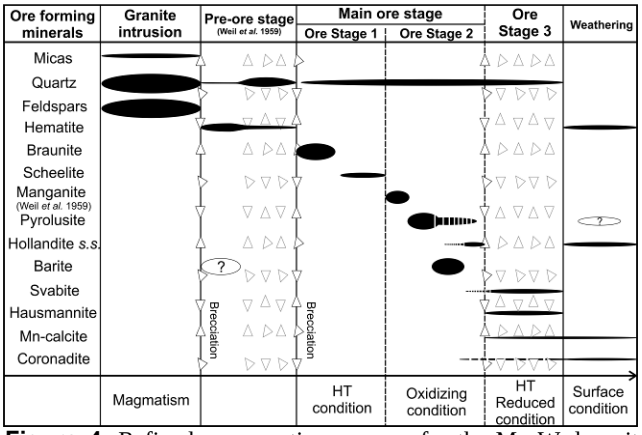


Figure 4. Refined paragenetic sequence for the Mn-W deposit of the Haut-Poirot. Triangles=main brecciation events; HT=High Temperature.

4 Conclusion

In conclusion, the petrology and mineral assemblages observed in the manganiferous Haut-Poirot deposit corroborate the multistage/polyphased character of manganese veins in the Vosges, which could be correlated to the mineralizing events reported in several deposits in Schwarzwald.

Acknowledgements

Thanks are due to Ms. Szöke for early works on the Haut-Poirot samples. Useful discussions with Mr Mortier, especially about the Bagenelles, improved the overview of Vosges. We also thank Mr Charlier for field facilities.

References

Baillieux P, Schill E, Edel JB, Mauri G (2013) Localization of temperature anomalies in the Upper Rhine Graben: insights from geophysics and neotectonic activity. Int. Geo. Rev. 55:1744-1762

Bonhomme M (1958) Contribution à l'étude d'une mine de manganèse dans la région de Gérardmer. Master thesis

Chantraine J, Rolet J, Santallier DS, Piqué A, Keppie JD (1994) Pre-Mesozoic Geology in France and Related Areas. Springer Berlin Heidelberg

Clauer N, Zwingmann H, Chaudhuri S (1996) Isotopic (K-Ar and oxygen) constraints on the extent and importance of the Liassic hydrothermal activity in Western Europe. Clay Miner 31:301–318

Dallmeyer RD, Franke W, Weber K (1995) Pre-Permian Geology of Central and Eastern Europe. Springer Berlin Heidelberg

Dèzes P, Schmid SM, Ziegler PA (2004) Evolution of the European Cenozoic Rift System: interaction of the Alpine and Pyrenean orogens with their foreland lithosphere. Tectonophysics 389:1–33

Echtler HP, Altherr R (1993). Variscan crustal evolution in the Vosges Mountains and in the Schwarzwald : guide to the excursion of the Swiss Geological Society and the Swiss Society of Mineralogy and Petrology (3-5 October, 1992). Schweiz Miner Petro 73:113–118

Fluck P (1977) Metallogeny of Vosges. *Freiberger Forschungshefte*, C 345, Topical Report of IAGOD *(International Association for the Genesis of Ore Deposits)*, Salamanca, 8:83-93

Fluck P, Stein S (1992). Espèces minérales des principaux districts miniers du massif vosgien. Pierres et Terre 35:107–115

Fluck P, Weil R (1976). Géologie des gîtes minéraux des Vosges et des régions limitrophes. Corrélation métallogénique Vosges - Forêt-Noire. Mémoires du B.R.G.M

Friedl G, Cooke RA, Finger F, McNaughton NJ, Fletcher IR (2011) Timing of Variscan HP-HT metamorphism in the Moldanubian Zone of the Bohemian Massif: U-Pb SHRIMP dating on multiply zoned zircons from a granulite from the Dunkelsteiner Wald Massif, Lower Austria. Miner Petrol 102:63–75

Geyer OF, Gwinner MP, Geyer M, Nitsch E, Simon T, Ellwanger D (2011) Geologie von Baden-Württemberg. Schweizerbart, Stuttgart

Hautmann S, Lippolt H (2000) $^{40}Ar/^{39}Ar$ dating of central European K–Mn oxides — a chronological framework of supergene alteration processes during the Neogene. Chem Geol 170:37–80.

Hinsken S, Ustaszewski K, Wetzel A (2007) Graben width controlling syn-rift sedimentation: the Palaeogene southern Upper Rhine Graben as an example. Inter J Earth Sci 96:979–1002

Illies JH (1977) Ancient and recent rifting in the Rhinegraben. Geol Mijnbouw 56:329–350

Jurain G (1956) Présence d'uranium dans quelques gîtes de manganèse dans les Vosges méridionales et centrales. CR Acad Sci 243:1044–1045

Li YH (2000) A compendium of geochemistry: from solar nebula to the human brain. Princeton University Press, Princeton.

Lougnon J (1981). Ressources minières françaises : les gisements de manganèse. BRGM

Nicholson K (1992) Genetic types of manganese oxide deposits in Scotland; indicators of paleo-ocean-spreading rate and a Devonian geochemical mobility boundary. Econ Geol 87:1301–1309

Prodehl C, Mueller S, Haak V (2006). The European Cenozoic rift system. In: Developments in Geotectonics. Elsevier, pp 133–212

Quesnel F (2003) Paleoweathering and paleosurfaces from northern and eastern France to Belgium and Luxembourg: geometry, dating and geodynamic implications. Geol France 1:95–104

Segev A, Lang B, Halicz L (1991) K-Ar dating of manganese minerals from the Eisenbach region, Black Forest, southwest Germany. Schweiz Miner Petro 71:101–114

Tabaud AS, Whitechurch H, Rossi P, Schulmann K, Guerrot C, Cocherie A (2014) Devonian-Permian magmatic pulses in the northern Vosges Mountains (NE France): result of continuous subduction of the Rhenohercynian Ocean and Avalonian passive margin. Geol Soc London 405:197–223

Thomas R, Tischendorf G (1987) Evolution of Variscan magmatic-metallogenetic processes in the Erzgebirge according thermometric investigations. Z Geol Wissenschaft 15:25–42.

Weil R, Stat A, Meister L, Bonhomme M (1959) Les espèces minérales du gisement de manganèse du Haut-Poirot, près de Gérardmer (Vosges). Bulletin du Service de la Carte Géologique d'Alsace et de Lorraine 2:49–59

Wetzel A, Allenbach R, Allia V (2003) Reactivated basement structures affecting the sedimentary facies in a tectonically "quiescent" epicontinental basin: an example from NW Switzerland. Sediment Geol 157:153–172

Wickert F, Altherr R, Deutsch M (1990) Polyphase Variscan tectonics and metamorphism along a segment of the Saxothuringian-Moldanubian boundary: The Baden-Baden Zone, northern Schwarzwald. Geologische Rundschau 79:627–647

Geochronology and mineralogical evolution of the Koudiat-El-Hamra silver ore veins deposit (Central Jebilet, Morocco)

Amal El Arbaoui, Amina Wafik, Abderrahim Essaifi and Abdelmajid Jarni
Cadi Ayyad University, Morocco

Lou Maacha
Managem Mining Company

Abstract. In the Hercynian Central Jebilet Massif, the Ag-rich Koudiat-el-Hamra Pb-Zn-Cu-Co-As-Sb-Sn vein ore deposit is hosted in the visean volcanosedimentary sarhlef series. The principal ore vein is generally sub-parallel to the regional schistosity. This vein was fragmented and extruded during the syn-schist deformation indicating probably that the mineralization pre-main deformation. Textural relationships indicate that stock metal deposit forming the Koudiat El Hamra mineralization was carried out in a single stage marked by assemblages of quartz-chlorite-carbonate. Silver minerals are freibergite, miargyrite, pyrargyrite, polybasite, argentopyrite, and native silver. The sulfides minerals are pyrite, pyrrhotite, arsenopyrite, galena, sphalerite and chalcopyrite with Ag-Pb-Sb sulfosalts that are inclusions in galena. The geochronology and mineralogical evolution of the Koudiat-el-Hamra ore deposit may be linked to the Bamega Tabouchennt granite. The paragenetic minerals could be explained by the mineralogical and geochemical differentiation followed by more advanced remobilization attested by the mineralized veins recovery in new folded stage, a temperature lowering and supergene weathering conditions.

1 Introduction

The Koudiat-el-Hamra Ag-rich Pb-Zn-Cu-Co-As-Sb-Sn vein deposit, situated 26 km north western Marrakech (Fig. 1), is hosted in the visean volcano sedimentary sarhlef series (Huvelin 1977) that is affected by both regional and contact metamorphism.

The silver has been mined in Roc Blanc deposit (Huvelin et al. 1978; El Arbaoui et al. 2015). In Koudiat-el-Hamra, the ore deposit consists of four mineralized veins having direction ranging from 120°E to 170°E. The veins are hosted in the Sarhlef formation.

Detailed microscopic description shows that Koudiat-El-Hamra ore is composed primarily of pyrite, arsenopyrite, sphalerite, pyrrhotite, chalcopyrite, galena, silver minerals, Pb-Ag-Sb sulfosalts and native silver. The gangue mineral includes quartz, chlorite dolomite, siderite and barite. These minerals form a single paragenesis and they precipitate in a single mineralizing fluid.

This paper describes the geological and mineralogical characteristics of the Koudiat-el-Hamra Pb-Zn-Ag deposit. Various aspects of the mineralization have been discussed previously by (Huvelin 1977, Huvelin et al. 1978, Huvelin et al. 1980). This preliminary information is integrated with additional data on the geological setting, ore mineralogy and geochemistry, with a view to understanding the genesis of the Pb-Zn-Cu-Co-As-Sb-Sn and the Koudiat-el-Hamra hydrothermal system.

2 Geological setting

The Jebilet massif, 7 km north of Marrakech in north central Morocco, forms a component of the Western Meseta, part of the North African Variscan Belt (Fig. 1A). The massif, 170 km long and 40 km wide, is dominated by a succession of sedimentary rocks, deposited in the shallow marine environment of a Devonian-Carboniferous, continental margin, transtensional rift basin (Huvelin 1977; Aarab and Beauchamp 1987; Moreno et al. 2008). The Jebilet massif consists of three tectono-stratigraphic units subdivided as Eastern, Central and Western Jebilet (Huvelin 1977; Bordonaro et al. 1979). Their original sedimentary relationships are masked by complex tectonized contacts. The Western Meseta Shear Zone separates the western and central units (Pique et al. 1980) and the Marrakesh Shear Zone separates the Central and Eastern units (Lagarde and Choukroune 1982).

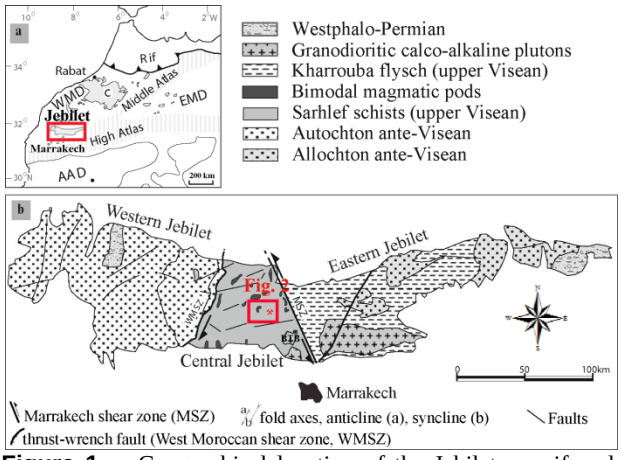


Figure 1. a Geographical location of the Jebilet massif and study area. **b** Geological map of Central Jebilet Massif (Huvelin 1977).

The Western unit consists of weakly deformed and metamorphosed Cambrian and Ordovician rocks, whereas the Central unit is a block of low-grade metamorphosed, schistose, marine visean shale (Sarhlef schist). The Eastern unit is composed of Visean rocks including allochtoneous terranes of Ordovician to Devonian age. The Central unit of the Jebilet Massif, which hosts the Koudiat-El-Hamra deposit, includes several pyrrhotite-rich massive sulfide deposits. Syn-

tectonic magmatism comprising an ultramafic to granitoid bimodal association (>65% mafic-ultramafic, the remainder is felsic) is widespread, associated with peraluminous granodiorites emplaced at ca. 330 Ma, intruded by younger (300 Ma) leucogranites (Fig. 1B). The bimodal plutonism occurs principally in three lineaments parallel to shear zones (Essaifi et al. 2014).

The Koudiat-el-Hamra deposit is hosted within the Sarhlef series. These series consists of pellite and sandstone intercalations, bioclastic limestones, finely banded calcareous and massive sulphide deposits (Kettara pyrrhotite, Koudiat Aicha and Draa Sfar deposits). The study area contains many intrusive bodies of gabbros and dolerite, it was intersected by long veins of microdiorite, and finally by numerous quartz-carbonate veins with sulphide paragenesis (veins of Jbel Sarhlef ‘‘Pb-Zn’’) (Fig. 2).

3 Morphology of mineralized veins

The quartz-chlorite veins had generally small size. Their thickness and their extension vary from few mm to a many decameters and are frequently grouped into anastomosing networks. These veins are generally sub-parallel to the regional schistosity intersecting clearly the corresponding folds. This is particularly the casealong the main Koudiat-el-Hamra and Jbel Sarhlef veins trips that are both sub-meridian having East dip.

Silver-mineralized veins (Fig. 2) are less abundantin the area. These veins were fragmented and extruded during the syn-schist deformation. The main Koudiat-el-Hamra vein is by far the most mineralized. This vein is staked approximately along 300m by the ancient works. It has an average of 45° E dips, substantially the same as that of the schistosity, but with a slightly inclined direction. The opening exceeds rarely 50 cm, and is found often between 10 and 30 cm, with rapid variations. The mineralization is very complex and is mainly composed of sulphide hosted in an irregular gangue composed of chlorite, quartz, and carbonates (siderite, dolomite and calcite). However, because of its richness in silver, it has been the subject of quite developed mining work (Huvelin 1977), particularly from 1930 to 1948. Between the 25 and 45m depth levels, the ore is banded having irregular thickness, varying from 1 to 25 cm (10 cm average), generally located outside a filling of pyrite and quartz. It can be located also at the wall, at the roof rat both sides (Clariond 1932). Across the entire deposit, the reduced sulphide thickness was estimated at 5 cm around the 45 m level.

In contrast to the main Koudiat-el-Hamra vein deposit and to that of Jbel Ergab-el-Beida, other veins (Fig. 2, map of the area) are clearly oblique to the schistosity. These are Madeleine vein having a 75° NE dips; the vein A with 15° to 45 ° ENE dips and the vein B, at 200 m SE of vein A at 35° to 45° E dips (Fig. 2).The works, which concerns the Madeleine vein, seem to have followed a recent break with quartz, barite and galena filling (Fig. 2), of the same type as that of the Jbel Sarhlef lead mine, but also highlighted Ag-rich ores in a quartz gangue accompanied by chlorite.

4 Paragenetic sequences

The Koudiat-el-Hamra mineralization corresponds quite accurately to a classical paragenetic type: the zinc-lead

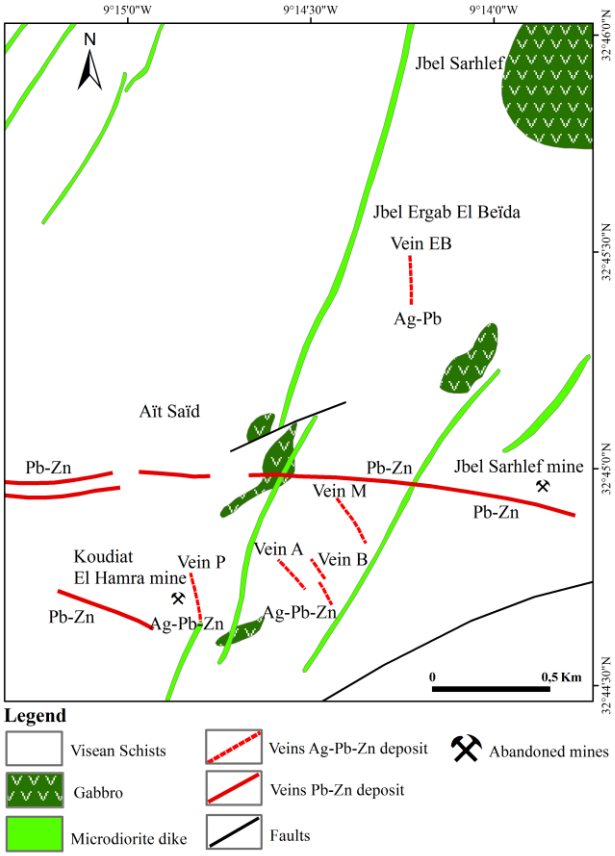


Figure 2. Geological map of the Koudiat-El-Hamra area (this study).

paragenesis with copper and silver that have magmatic originas defined by (Oelsner 1965). According to this author paragenesis features in its variant of high temperature are: (1) massif ore vein without banded texture; (2) significant grade of iron sulphide in the mineralization; (3) initial deposition of Fe-rich minerals that are arsenopyrite, pyrrhotite and pyrite accompanied by Cassiterite, then sphalerite-chalcopyrite group minerals including stannite, and finally galena-tetrahedrite Ag-rich group minerals; (4) exsolution phenomenon reflecting the high crystallization temperature of the sulphides: pyrrhotite and chalcopyrite exsolutions in sphalerite and pyrite exsolution in chalcopyrite. This lets say that for the most part of the stock metal deposit constituting the Koudiat-el-Hamra mineralization was carried out in a single stage. Subsequent processes as recovery vein in new folding phases and lowering temperature have led to limited ore transformations particularly in its mineralogical expression mode.

5 Koudiat-el-Hamra mineralization features

Among mineralizations known in the central Jebilet, a detailed metallographic study shows two sulphide mineralizations that are comparable to that of Koudiat-el-Hamra. The Roc Blanc mineralization and this of

North Draa Sfar mine (Table 1).

Table 1. Comparison of the primary sulphide parageneses of the Koudiat-el-Hamra, North Draa Sfar mine and Roc Blanc deposits.

Mineralogical and chemical characteristics	Fe/S ratios	Sn & Ge	Co	Chalcopyrite	Copper gray	Other frequent sulfosalts	Trace elements expressed mineralogically
North Draa Sfar mine	dominated pyrrhotite	SnO2	cobaltite	dominated	-		Bi, Se, Au, Ag
Koudiat El Hamra deposit	pyrite, pyrrhotite	SnO2 – Cu2FeSn S4	ullmannite	minor	argentiferous tetrahedrite	Pb-Sb sulfosalts	Ni
Roc Blanc deposit	pyrite = pyrrhotite	Sn –Ag8GeS6	ullmannite	minor	argentiferous tetrahedrite	Pb-Ag-Sb & Sb-Ag sulfosalts	Ni

We note that for many characters, the Koudiat-el-Hamra mineralization is intermediate between the Roc Blanc and the North Draa Sfar mine mineralization. The character that seems decisive corresponds to the pyrrhotite-pyrite ratio for the first generation associated with arsenopyrite reflecting different degrees of sulphidation ores. The North Draa Sfar mine dominant-pyrrhotite appears to be significant in sulfur, relatively to metals, in contrast to the Roc Blanc deposit where pyrrhotite veins filling cm-scale (0.1-20 cm) crosscut metapelite (El Arbaoui et al, 2015).

According to this character, at the North Draa Sfar mine, the tin is in the oxidized form [SnO_2], while in Koudiat-el-Hamra, we note the oxidized tin (Cassiterite) and sulfide tin (Stannite) association. At the Roc Blanc deposit, tin was detected only in its sulphide form (traces in sphalerite), and that the germanium is expressed in sulphide form (Argyrodite) [Ag8GeS6]. This gradation is in agreement with an increasing sulphidation potential of the ore-generating environment. In addition, we note also: (1) The individualization of cobalt (cobaltite) at north Draa Sfar mine, while it is expressed only in the Co-rich arsenopyrite and ullmannite form in Koudiat-el-Hamra deposit, variety which is occurs in Co-rich ullmannite at the Roc Blanc deposits; (2) The content of Bi, Se, Au and Ag at more expression in the North Draa Sfar mine in contrast to the other two deposits; (3) The increasing abundance of silver and antimony-bearing minerals in the Roc Blanc and Koudiat-el-Hamra deposits, and a decreasing abundance of copper bearing minerals, in the North Draa Sfar and the Roc Blanc deposits.

The comparative paragenetic study of these three mineralizations allows obtaining a coherent ensemble of mineralogical and geochemical gradients. At the Fe/S ratio variation, explained by pyrrhotite-pyrite ratio of the first generation, correspond variations in the minor or trace elements content, in particular Ag and Cu. There may be a useful guide to determine which ones are the most likely to have interesting silver or copper content.

6 Conclusion and discussion

The Koudiat-el-Hamra Ag-rich veins deposits constitute a special case, because their establishment in the hercynian Central Jebilet orogeny and gitology remains to be discussed.

A tectonic point of view, these veins are extruded and fragmented. In addition, they are affected by late folding and a Kink bound schistosity (S2) that is clearly post contact-metamorphism. This is justified by the presence of crystallization tail and pressure shadow areas of andalusite following the main schistosity (S1).

Gitologic point of view, Koudiat-el-Hamra Ag-rich veins deposits present certain analogy with those of North Draa Sfar mine (Huvelin et al. 1978), and Roc Blanc veins deposits that are linked to Bramram-Tabouchant-Bamega granite (BTB) (Huvelin et al. 1980; El Arbaoui et al. 2015).

According to these observations, one as sumption could be convincingly. This hypothesis stipulates that the stock metal constituting the Koudiat-el-Hamra mineralization was carried out in a single stage. The paragenetic succession evolution could be explained by mineralogical and geochemical differentiation followed by more advanced remobilization attested by the mineralized veins recovery in new folded stage, a temperature lowering and supergene weathering conditions.

Reference

Clariond L, (1932) Note concernant les travaux exécutés par le BRPM sur les filons argentifères de Koudiat el Hamra, Rapport BRPM, Rabat, inédit.

El Arbaoui A, Wafik A, Ndiaye I, Maacha L, Zouhair M, Ouadjou A, Radnaoui, A, (2015) Mineralogical Evolution of the Polymetallic Vein Mineralization at the Roc Blanc Silver Deposit (Jebilet Massif, Variscan Belt, Morocco). Mineral Resources in a Sustainable World. 13th Biennial SGA-SEG Meeting, Nancy-France, August 2015. Proceedings, Volume 2, pp. 449-452.

Essaifi A, Samson S, Goodenough K, (2014) Geochemical and Sr–Nd isotopic constraints on the petrogenesis and geodynamic significance of the Jebilet magmatism (Variscan Belt, Morocco). Geological Magazine 151, 666–691.

Huvelin P, (1977) Etude géologique et gîtologique du massif hercynien des Jebilets (Maroc occidental). Note et Mémoires du Service Géologique du Maroc, 232 bis, 307pp.

Huvelin P, MOELO Y, PERMINGEAT F. & PICOT P, (1978) Sur la mineralisation du champ filonien polymetallifere du Roc Blanc (Jebilet centrales, Maroc). Notes Serv. Geol. Maroc, t. 40, n° 275, 239-248.

Huvelin P, Ortelli L, Permingeat, F, Picot, P, (1980) Présence de filons stannifères dans le granite hercynien du Baramram-Tabouchennt (Jebilet centrales, Maroc). Notes Serv. Geol. Maroc, t. 41, n° 285, 231-236.

Lagarde JL, Choukroune P, (1982) Cisaillement ductile et granitoïdes syntectoniques: l'exemple du massif hercynien des Jebilet (Maroc). Bull SocGéol Fr 24:299–307.

Moreno C, Sáez R, González F, Almodóvar G, Toscano M, Playford G, Alansari A, Rziki S, Bajddi A (2008) Age and depositional environment of the Draa Sfar massive sulphide deposit, Morocco. Miner Deposita 43:891-911.

Oelsner (1965) Atlas des principales paragenèses minérales vues au microscope (traduit par R. Mignon). Gauthier-Villars Paris. Edition Leipzig.

Piqué A, Jeannette D, Michard A, (1980) The Western Meseta shear zone, a major and permanent feature of the Hercynian belt of Morocco. J StructGeol 2:55–61.

Geology and genesis of El-Dob tungsten ore deposit (North Eastern Desert, Egypt): Insights from fieldwork, petrography and remote sensing

Hamdy El Desouky
Egyptian Academy of Scientific Research & Technology, Menoufia University, Egypt

Maher Dawoud and Mohamed Salah
Menoufia University , Egypt

Abstract. El-Dob ore deposit is one of twelve tin-tungsten mineral occurrences located in the Egyptian basement complex. Detailed fieldwork, petrography and remote sensing investigations were performed to map the area and to shed light on the genesis of the tungsten mineralization. The area is covered by syn-orogenic granodiorite, intruded by gabbro and late- to post-orogenic monzogranite and alkali-feldspar granite. The mineralization occurs as wolframite-bearing quartz veins, associated with greisen alteration zones, cutting through the granodiorite and monzogranite. The wolframite occurs as large, prismatic cm-size crystals, which are often concentrated and radially oriented in large nodules with up to 20 cm radius. Various image enhancement techniques, such as band combinations, band ratios, principle component analysis and minimum noise fraction, have been applied on ASTER and ETM+ datasets to perform detailed lithological and hydrothermal alteration mapping on the area. The mineralization is hosted by two alteration zones, which are spatially associated with the alkali-feldspar granite. Likely, during the post-orogenic extensions and magmatism, a magmatic-hydrothermal fluid was released, along with the incompatible tungsten, from the differentiating granitic melt phase. Intense interaction between this fluid and the surrounding granodiorite and monzogranite developed the greisen hydrothermal alteration zones and facilitated fluid cooling and the W mineralization.

1 Introduction

Twelve tungsten, tin-tungsten and tin mineral occurrences were discovered in the basement complex of the Egyptian Eastern Desert (ED). The deposits are often associated with granitic intrusions and were mined for the production of wolframite, scheelite and cassiterite, during the Second World War (Takla et al. 1976). During the war, there was a high demand for these minerals in weapon production. Thus, the mining activity ceased shortly after the war. Recently, there is an increased interest in the assessment, development and reopening of the ancient mines. The historic El-Dob tungsten mine is located in the North Eastern Desert (NED) at around 415 km south east Cairo and around 50 km to the west of the Safaga city.

Recent development of multi-spectral remote sensing systems, such as the Advanced Spaceborne Thermal Emission and Reflection Radiometer (ASTER) and Landsat Enhanced Thematic Mapper plus (ETM+) sensors, offer geologists a potentially cost-effective alternative to expensive and time-consuming regional mineral exploration and geological mapping (e.g. Rowan et al. 2003). Thus, ASTER and ETM+ data have been used increasingly in the last decade for geological and hydrothermal alteration mapping (e.g. Rajendran et al. 2013). Despite these numerous studies, the remote sensing technique for geological and hydrothermal alteration mapping is rarely applied to areas with tungsten mineralization.

The aim of this study is to investigate the geology and petrography of El-Dob tungsten ore deposit, to perform a detailed lithological and hydrothermal alteration mapping of the area and to shed light on the genesis of the tungsten mineralization. Detailed image processing techniques were performed in ASTER and ETM+ satellite imagery to identify the different rock units and hydrothermally altered zones. Furthermore, detailed fieldwork and petrographic examinations were performed to investigate the field relationships, the mineralogical compositions and textures. This integrated approach will have implications on the mineralogical potential of the study area and will enhance the exploration of similar ore deposits in the region.

2 Regional geological setting

The Precambrian basement rocks of the ED of Egypt form an elongate mountainous belt along the western flank of the Red Sea. It constitutes the extreme north western part of the Arabian–Nubian Shield (ANS), which extends from Egypt in the west to Saudi Arabia and Oman in the east and from Jordan in the north to Eritrea and Ethiopia in the south. The ANS consists primarily of Neoproterozoic juvenile crust and represents an area of suturing between East and West Gondwana before the Palaeozoic (Stern 1994). It formed through the accretion of numerous, mainly inter-oceanic, island arcs along ophiolite-lined suture zones and gneissic fault zones between 900 Ma and 550 Ma when the Mozambique ocean closed (Stern 1994). The Neoproterozoic basement rocks of the ED include gneisses, ophiolitic mélange represented by serpentinites, metagabbro, and metabasalt that were subsequently intruded by volcanics and abundant granitoids, and overlain by molasse-type sediments (Hassan and Hashad

1990; Stern et al. 2004). Based on composition, field relationships and timing relative to the development of the ANS, the granitoid intrusions are widely classified to older granitoids, with a syn-orogenic origin and younger granitoids, with a late- to post-orogenic origin (Hassan and Hashad 1990).

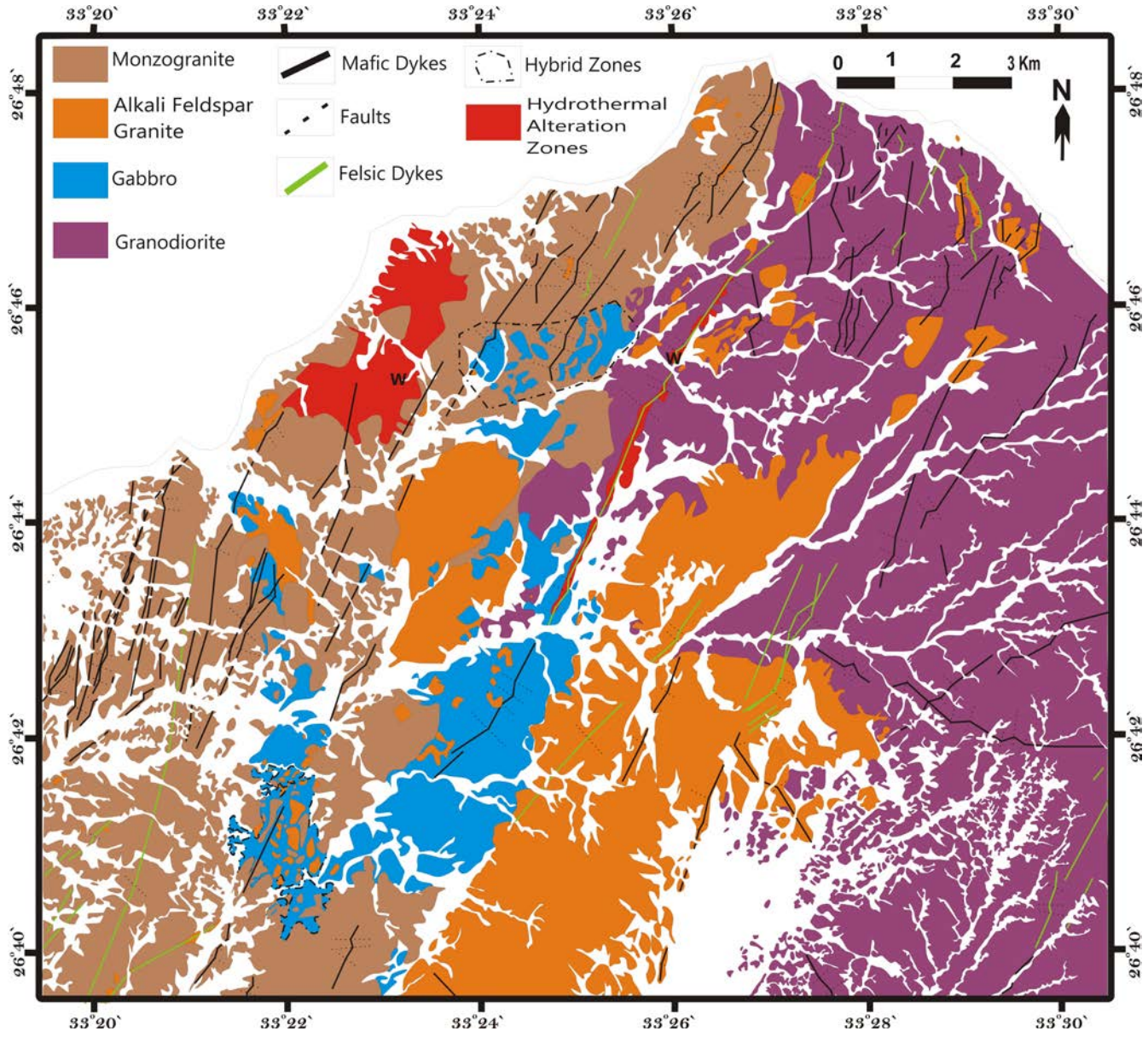


Figure 1. Detailed lithological and hydrothermal alteration map of El-Dob area prepared from detailed remote sensing analysis and fieldwork verification. W = location of the wolframite beating quartz veins, hosted in alteration zones in granodiorite and monzogranite

3 Methodology

Detailed field observations and sampling were performed during a field campaign in April 2016. During this campaign, the different field relationships were described and photographed and fresh samples were collected from the different rock units, the hydrothermally altered zones, and the mineralized and barren quartz and carbonate veins. Representative thin sections were carefully prepared and detailed petrographic examination was carried out using a polarized optical microscope equipped with a high-quality digital camera.

For remote sensing analysis, cloud-free ETM+ and ASTER images, acquired respectively on September 2000 and November 2003 were used. The ETM+ image is composed of 4 bands in the visible-near infra-red (VNIR) and 2 bands in the short-wave infra-red (SWIR) with 30m spatial resolution, a thermal band (TIR) with 60m resolution and a panchromatic band with a 15m resolution. The panchromatic band was fused with the 6 VNIR-SWIR bands to enhance their spatial resolution to 15m. The ASTER image is composed of 14 spectral bands with different spatial resolutions (3 VNIR at 15m, 6 SWIR at 30m and 5 TIR at 90m). Spectral resampling has been

used to downscale the spatial resolution of the 6 SWIR bands of the ASTER data to 15 m.

The image data was processed using ENVI to identify the different rock units and alteration zones. The processed images were imported as layers into a GIS software and on-screen digitizing of various geological classes was performed to carefully prepare the geological map. Finally, the map was further adapted based on field verifications.

4 Geology and petrography

Field observations and petrographic examinations indicate that El-Dob area is covered by the following four rock units (respectively from older to younger): granodiorite, gabbro, monzogranite and alkali-feldspar granite (Fig. 1). These rock units are crosscut by mafic and felsic dyke swarms with a predominant NE to NNE orientation, especially in the northern and western parts of the study area (Fig. 1).

The granodiorite is the oldest and most dominant rock unit in the area, it occurs as large low-relief plutons with discordant contacts in the eastern and central parts (Fig. 1). It is characterized by grey colour and clear schistosity and often has a sharp contact with the other rock units. Microscopically, it is characterized by equigranular medium- to coarse-grained hypidiomorphic texture and is mainly composed of plagioclase, quartz, k-feldspar and abundant biotite. This rock unit belongs to the older granitoid intrusions, which have a syn-orogenic origin (Hassan and Hashad 1990).

The gabbro is exposed as a U-shape pluton in the central part of the area (Fig. 1). Although the contacts of the gabbro are often sharp, a transitional to defuse boundaries were observed in the northern and southwestern parts of the pluton, which are marked by hybrid zones with the granitic rocks. At these zones, the gabbro is intercalated with the monzogranite and alkali-feldspar granite. The gabbro is unlayered and characterized by dark greenish colour and medium to coarse-grained hypidiomorphic texture. It is mainly composed of plagioclase, hornblende and minor pyroxene.

The monzogranite is widely cropping out in the northern and western parts of the area (Fig. 1). It is characterized by pinkish grey to light reddish colour. In the western part, it is crosscut by NE-SW oriented mafic to felsic dyke swarms with narrow spacing. Abundant rock fragments from these dykes are scattered over the monzogranite outcrops (Fig. 2). Microscopically it consists of plagioclase, k-feldspar, quartz and biotite with equigranular coarse-grained hypidiomorphic texture and characterized by abundant perthite.

The alkali-feldspar granite occurs as a NE-SW elongated belt, which is characterized by a high relief relative to the other rock units. This trend is parallel to the main structure features in the area and to the elongation of the dyke swarms (Fig. 1). The alkali-feldspar granite is the youngest granitic rock unite in the area and is characterized by reddish to pinkish colour and composed mainly of K-feldspar, quartz and plagioclase. This granitic unite along with the monzogranite belong to younger granitoid intrusions, which have a late- to post-orogenic origin (Hassan and Hashad 1990).



Figure 2. Field photograph showing abundant fragments from a large mafic dyke (see top arrows) scattered over the monzogranite outcrops (see bottom arrow)

5 Tungsten mineralization

The mineralization occurs as wolframite-bearing quartz veins cutting through the granodiorite and monzogranite. The veins have a predominant NE to NNE strike and characterized by steep dip angles (between 50^{o} and 70^{o}) respectively toward the SE and ESE directions. The veins are discontinues and display variable thickness ranging between 5 cm and 70 cm and are often associated with greisen alteration zones, up to 1 m thick. In these zones, the host granite is partially to completely replaced by sericite, mica and locally kaolinite. The veins and the greisen zones are spatially associated with thin mafic dykes with a basaltic composition.

The mineralization is visually observed and is characterized by a heterogeneous distribution in the veins. The wolframite occurs as euhedral to subhedral large, prismatic cm-size crystals, which are often concentrated and radially oriented in large nodules with up to 20 cm radius (Fig. 3). In addition to wolframite, sulphides (pyrite and chalcopyrite) and iron oxides are locally observed in the nodules. The mineralized quartz veins are stained with reddish brown to black colours along cracks (Fig. 3) and the fresh quartz is massive with milky to light grey colour, whereas the unmineralized veins are typically white. Most of the mineralized quartz veins are historically exploited at and near the surface.

6 Lithological and hydrothermal alteration mapping

The special geological setting of the area resulted in three challenges during the lithological mapping: (1) the area is

mostly covered by granitic rocks with variable compositions (Fig. 1), which apparently lock similar in the satellite imagery; (2) the hybrid zones between the gabbro and the granitic rock units complicated mapping their boundaries; and (3) the abundant mafic dyke fragments, which cover the monzogranite outcrops at the southwestern part of the area (Fig. 2), provided misleading signatures. The integration between remote sensing investigations and fieldwork verifications allowed overcoming these challenges.

For detailed lithological and hydrothermal alteration mapping, several image enhancement techniques were applied on the ASTER and ETM+ datasets including, band combinations, band ratios and the Minimum Noise Fraction (MNF) and the Principal Component Analysis (PCA) transformations. The band combinations of ETM+ 541 in RGB and ASTER 741 in RGB along with the ETM+ band ratios 7/5, 5/4, 3/1 in RGB were used to identify the main rock units and the mafic and felsic dykes. Further lithological decimation was done by applying a covariance PCA transformation on the 9 VNIR and SWIR bands of ASTER and assigning the principal components 1, 2 and 9 to the RGB colour channels.

The hydrothermal alteration zones in the area were identified using the altered minerals OH-bearing Index (OHI) and the Kaolinite Index (KLI). The OHI index was calculated by applying the following formula to the ASTER SWIR bands (B7-B6)*(B4-B6) and was displayed in grey scale. Similarly, the KLI index ((B4-B5)*(B8-B6)) was calculated from the ASTER SWIR data and displayed in grey scale. Further confirmation and colour representation of the hydrothermally altered zones was performed by displaying the ASTER PCA components 2, 5 and 4 in the RGB colour channels and by applying the MNF transformation on the ASTER SWIR bands and displaying the MNF components 3, 2 and 1 in RGB.

7 Discussion

The wolframite-bearing quartz veins are hosted in two elongated alteration zones that are spatially associated with the alkali-feldspar granite, the youngest granitic intrusion in the area (Fig. 1). The predominant strike of the W-bearing quartz veins is parallel to the elongation of the host alteration zones and the alkali-feldspar granite belt. Based on this information, the absence of visible W-bearing quartz veins in the alkali-feldspar granite and the typical association of W deposits in Egypt and worldwide with granite intrusions, a genetic relationship between the emplacement of the post-orogenic alkali-feldspar granite and the W mineralization is suggested. Likely, during the post-orogenic extensions and magmatism, a magmatic-hydrothermal fluid was released out, along with the incompatible tungsten, from the differentiating granitic melt phase (cf. Hulsbosch et al. 2016). Intense interaction between the released hot fluid and the surrounding granodiorite and monzogranite belts developed the greisen hydrothermal alteration zones. Likely, this interaction facilitated the fluid cooling and the W-mineralization in the quartz veins to develop. The nature of this hydrothermal mineralizing fluid is the aim of an ongoing fluid inclusion study.

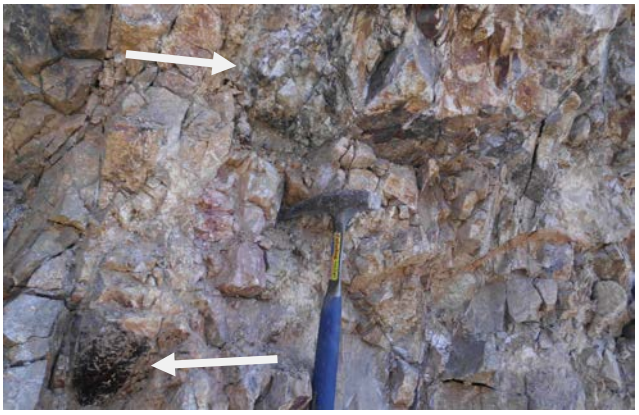


Figure 3. Field photograph showing a large quartz vein with wolframite crystals concentrated in large nodules with up to 20 cm radius (see arrows)

Acknowledgements

The financial support of the Egyptian Academy of Scientific Research & Technology and the Menoufia University to H. El Desouky is highly acknowledged. This contribution is a part of the research thesis of M. Salah.

References

Hassan MA, Hashad AH (1990) Precambrian of Egypt. In: Said R (ed) The geology of Egypt. A. A. Balkema, Rotterdam/Brookfield, pp 201-245

Hulsbosch, N, Boiron, M-C, Dewaele, S, Muchez, Ph (2016) Fluid fractionation of tungsten during granite–pegmatite differentiation and the metal source of peribatholitic W quartz veins: Evidence from the Karagwe-Ankole Belt (Rwanda). Geochim Cosmochim Acta 175: 299-318

Rajendran, S, Nasir, S, Kusky, TM, Ghulam, A, Gabr, S, El-Ghali, M A (2013) Detection of hydrothermal mineralized zones associated with listwaenites in Central Oman using ASTER data. Ore Geol Rev 53: 470-488

Rowan, L, Hook, SJ, Abrams, MJ, Mars, JC (2003) Mapping hydrothermally altered rocks at Cuprite, Nevada, using the Advanced Spaceborne thermal emission and reflection radiometer (ASTER), a new satellite-imaging system. Econ Geol 98: 1019-1027

Stern, RJ, Johnson, P, Kröner, A, Yibas, B (2004) Neoproterozoic ophiolites of the Arabian–Nubian shield. In: Kusky, TM (Ed.), Precambrian Ophiolites and Related Rocks. Elsevier, Amsterdam, pp. 95-128

Stern RJ (1994) Neoproterozoic (900-550 Ma) arc assembly and continental collision in the East African orogen: implications for the consolidation of Gondwanaland. Annu Rev Earth Planet Sci 22: 319-351

Takla, MA, Basta, EZ, El-Sharkawy, MA, Fawzie, E (1976) The mineralogy of some wolframite veins from Egypt: Bull Fac Sci, Cairo Univ., Cairo, Egypt: 49, 415-43

The Filon 7/5 (Bou Azzer district, Morocco): an example of Co-Ni ores formation under disequilibrium conditions

Isabel Fanlo, Enrique Arranz and Ignacio Subías
Universidad de Zaragoza, Spain

Fernando Gervilla
University of Granada, Spain

Abstract. Filon 7/5 is one of the most relevant orebodies in the Bou Azzer mining district. It is composed of a complex sequence of Co-Ni-Fe diarsenides, triarsenides and sulphoarsenides with extensive development of solid solutions between the end-members in each group. The textural relationships and the composition of the phases indicate a general evolution at high temperatures (about 650ºC), from Ni-ores to Co-ores through changing fugacities of As and S in the mineralizing fluid. This evolution leads to a very common development of replacement textures. The wide compositional variation of each of the analysed minerals is proposed to be the result of progressive reequilibration with fluids of changing composition, replacing early-formed phases by later ones. This process is supported, for example, by the remnants of high temperature phases (krutovite) inside As-gersdorffite or by the compositional inheritance of krutovite/rammelsbergite showed by the cobaltite-gersdorffite crystals that replace them.

1 Introduction

The Bou Azzer mining district includes nearly a hundred Co-Ni-Fe-arsenide orebodies scattered along the Bou Azzer-El Graara inlier, in the central part of the Moroccan Anti-Atlas. Leblanc and co- workers (e.g. Leblanc 1975, Leblanc and Billaud 1982; Leblanc and Fisher 1990) described the general features of the deposits, their mineralogy and composition and interpreted the origin of metals. More specific studies (En-Naciri 1995; En-Naciri et al. 1997; El Ghorfi et al. 2008; Oberthür et al. 2009) have focused on the nature of mineralizing fluids, the age of the mineralization and on some of the associated chromitite orebodies. Detailed research on some of the mineralized areas or mineral groups, including the mineral chemistry, the paragenesis and phase relationships are still scarce (Ahmed et al. 2009, Gervilla et al. 2012; Fanlo et al. 2015).

This contribution is focused on the mineral composition, paragenesis and phase relationships in the so called "Filon 7/5" (Bou Azzer mine), one of the most representative Co-Ni-Fe orebodies in the district.

2 Geological setting

The Bou-Azzer-El Graara inlier is one of several exposures of Precambrian rocks inside the Anti-Atlas Palaeozoic fold belt (Fig. 1). These exposures (inliers or "boutonnières") include Paleoproterozoic sequences, deformed during the Eburnean orogeny (2.1 to 2 Ga) which are covered by Neoproterozoic rocks. All these Precambrian rocks were deformed during the Pan-African orogeny (760-550 Ma), as they were located in the northern margin of the West African Craton (Walsh et al, 2012). Neoproterozoic oceanic crust was obducted in some parts of this margin in the form of ophiolitic units.

The Bou-Azzer ophiolitic complex includes slices of mafic and ultramafic rocks (serpentinized peridotites, mafic cumulates) and volcanic rocks, intruded syntectonically by quartz-diorite bodies (Dolansky 2007). Filon 7/5 includes a group of orebodies emplaced either along the subvertical serpentinite-quartz diorite contacts (Filon 7) or emplaced as lenses within the quartz diorite (Filon 5). Ore minerals occur as massive bodies, as a cement in brecciated units or disseminated within the host rock, with a strong structural control.

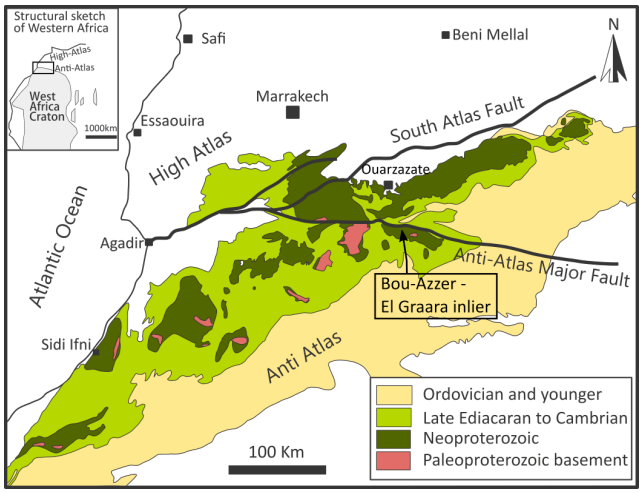


Figure 1. Simplified geological map of the Anti-Atlas fold belt (modified from Gasquet et al. 2005) with location of the Bou-Azzer inlier.

3 Mineralogy and textures

The Filon 7/5 mineralized bodies include a complex sequence of Co-Ni-Fe arsenides, sulphoarsenides and sulphides, along with molybdenite and minor Cu, Fe and Pb sulphides and brannerite. The paragenetic sequence has been reconstructed integrating observations in samples

obtained at different levels of the orebodies, under the optical microscope and SEM, complemented with compositional data and structure identification by electron probe micro-analysis (EPMA) and electron backscatter diffraction (EBSD).

The first mineral in the paragenetic sequence is nickeline (Nc); in samples without Nc, the first phase is a nickel-rich skutterudite (Sk I; up to 17% Ni) which presents a typical alteration following mineral growth zones (Fig. 2A). Where both phases are present, Sk I replaces Nc along cracks. Both phases are preserved as irregular patches mantled by diarsenide solid solutions: rammelsbergite-safflorite ($RS_{ss}I$), safflorite-löllingite ($SL_{ss}I$) or even ternary solutions (RSL_{ss}) forming irregular masses, cuspate aggregates or, in some cases, alternating layers of both solid solutions. These are followed by sulphoarsenides, either cobaltite (Cob), gersdorffite (Ger) or, as a general case, members of the solid solution cobaltite-gersdorffite (CG_{ss}). These minerals occur commonly as isolated euhedral crystals or masses composed of individual euhedral and sometimes skeletal grains. They can include earlier minerals (e.g. Nc) or cover the surface of previous phases (RS and SL solid solutions), frequently showing replacement textures (Fig. 2B). Some of the nuclei of Ger of CG_{ss} crystals are very rich in As and have the structure of krutovite, as determined by EBSD. This As-rich phase, according to textural relationships, clearly predates Ger or CG_{ss} crystals (Fig. 2C).

The second generation of skutterudite (SkII) is the most abundant phase in most of the samples, forming euhedral crystals which can show oscillatory zoning or skeletal forms. It overgrows all the previously described phases, which can occur as isolated remnants inside SkII. This mineral is followed in some samples by a second generation of diarsenide solutions ($RS_{ss}II$, $SL_{ss}II$) or even safflorite or löllingite in well-developed sub-millimetre crystals. These minerals commonly form arborescent aggregates with replacement textures developed around previous phases. Euhedral to subhedral alloclasite is next in the sequence, either as individual crystals dispersed in the matrix, filling voids or cracks or replacing previous phases (Fig. 2A). Skutterudite (SkIII; Figs. 2A, 2B) is the last Co ore in the sequence, filling the internal parts of small veins (anhedral) or as individual euhedral crystals dispersed in the matrix. The last minerals in the sequence are occasional arsenopyrite, molybdenite –which is very common in some samples, as masses or aggregates of laminar crystals, sometimes replacing previous phases–, pyrite, chalcopyrite, brannerite, galena and realgar-orpiment. These minor phases are dispersed in the samples and fill voids, cracks or spaces in the rock and in the main ore minerals, but no textural relationships have been observed amongst them allowing for a precise timing of their formation.

4 Mineral chemistry

The compositions in nickeline are very homogeneous and stoichiometric. Skutterudite (Fig. 2D) is much more variable; the first generation of this mineral (Sk I) shows a wide compositional variability related to substitution of Co for Ni and Fe, and As for S [$(Co_{0.18\text{-}0.86}\ Ni_{0.06\text{-}0.80}\ Fe_{0.03\text{-}0.39})\ As_{2.69\text{-}2.96}\ S_{0\text{-}0.30}$]. Later skutterudite (Sk II) is more homogeneous [$(Co_{0.83\text{-}1}\ Ni_{0\text{-}0.08}\ Fe_{0.03\text{-}0.17})\ As_{2.68\text{-}2.91}\ S_{0.8\text{-}0.22}$]

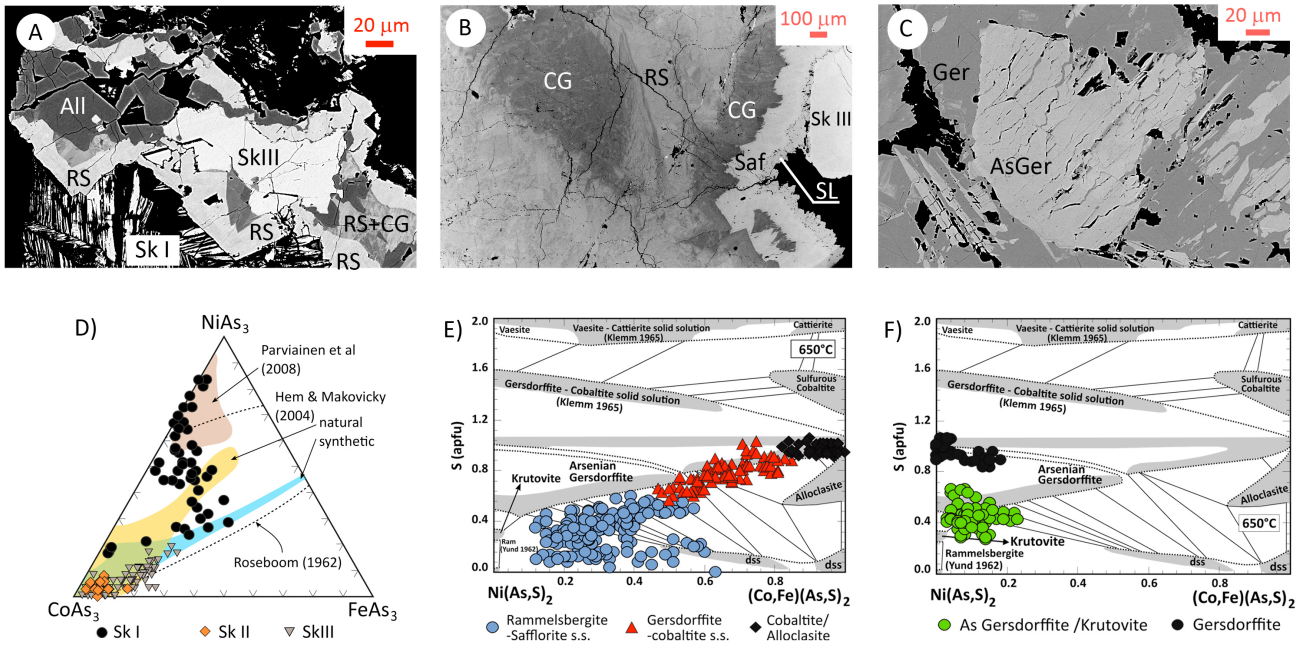


Figure 2. **a**, **b**, **c** SEM images of textural relationships amongst the described phases. **d** Composition of the three skutterudite generations, with indication of the fields and limits defined by previous authors. **e** and **f** Composition of diarsenides and sulphoarsenides in the studied samples. Stability fields according to Hem (2006) at 650ºC, Klemm (1965) and Yund (1962).

and Sk III is richer in Ni and Fe [$(Co_{0.61-1}\ Ni_{0-0.20}\ Fe_{0.03-0.28})\ As_{2.69-2.97}\ S_{0.03-0.28}$] than SkII.

The diarsenides develop complex solid solutions, either on the Ni-Co join (RS_{ss}), on the Co-Fe join (SL_{ss}) or ternary Co-Ni-Fe solid solutions (RSL_{ss}). RS_{ss} (Fig 2E: $(Co_{0.14-0.59}\ Ni_{0.45-0.89}\ Fe_{0-0.07})\ As_{1.36-1.97}\ S_{0-0.63}$) and SL_{ss} [$(Co_{0.25-0.85}\ Ni_{0-0.04}\ Fe_{0.18-0.78})\ As_{1.68-1.97}\ S_{0-0.3}$] are quite variable in their respective cation proportions and sometimes include a relevant proportion of S. Löllingite [$(Co_{0.06-0.1}\ Ni_{0-0.26}\ Fe_{0.70-0.95})\ As_{1.77-1.94}\ S_{0.02-0.18}$] and Safflorite [$(Co_{0.79-0.96}\ Ni_{0-0.17}\ Fe_{0.06-0.20})\ As_{1.42-1.94}\ S_{0.02-0.55}$] are, as described, less common and normally associated to a second formation stage.

The Ni-Co sulphoarsenides are commonly replacing previous phases, forming cobaltite-gersdorffite solid solutions (Fig. 2E: [$(Co_{0.18-0.85}\ Ni_{0.15-0.77}\ Fe_{0.02-0.07})\ As_{0.98-1.41}\ S_{0.57-1.03}$]). In some samples, gersdorffite [$(Co_{0-0.19}\ Ni_{0.82-1}\ Fe_{0-0.03})\ As_{0.93-1.18}\ S_{0.84-1.09}$] and As-gersdorffite [$(Co_{0.05-0.23}\ Ni_{0.77-0.97}\ Fe_{0-0.04})\ As_{1.30-1.71}\ S_{0.27-0.67}$] (Fig. 2F) are the most abundant phases. Some of the As-gersdorffite crystals are clearly identified in SEM images in the nucleus of gersdorffite masses (Fig. 2C) and according to their structure parameters, identified by EBSD, represent remnants of krutovite crystals. Their composition fits with the limits described by Hem & Makovicky (2004).

Cobaltite and alloclasite are the last sulphoarsenides in the paragenetic sequence (Fig. 2E). Cobaltite [$(Co_{0.68-0.99}\ Ni_{0-0.21}\ Fe_{0.02-0.25})\ As_{0.91-1.19}\ S_{0.80-1.10}$] grows in continuity with CG_{ss} forming thin rims. Alloclasite [$(Co_{0.66-0.95}\ Ni_{0.05-0.21}\ Fe_{0.03-0.16})\ As_{0.93-1.03}\ S_{0.93-1.03}$] shows a good stoichiometry in its As:S ratio, as it fills fractures and cracks without replacement of previous phases (Fig. 2A).

5 Discussion

The described phases represent a succession of high temperature assemblages as previously described in other Anti-Atlas Co-Ni-Fe orebodies (eg Aghbar, Gervilla et al. 2012). Textural relationships between the studied phases, the formation of several generations for a single phase and the observed replacement textures indicate that the mineralizing fluids were episodically changing, leading to a general evolution from Ni-ores to Co-ores in the latest stages, accompanied by significant variations in As and S fugacities. Therefore, disequilibrium conditions were probably dominant during the whole process.

In Filon 7/5, the obtained compositions are outside the solid-solution stability fields defined by Hem (2006) for 650º C (Fig. 2E, 2F). As seen in these figures, there seems to be a compositional continuum between cobaltite, members of gersdorffite-cobaltite solid solution and members of rammelsbergite-safflorite solid solution. After experimental data from Hem & Makovicky (2004), a complete solid solution between diarsenides and sulphoarsenides only exists for pure Ni end-members (krutovite-gersdorffite) and natural data from Spiridonov & Chvileva (1995), Fanlo et al. (2004) and this study, support these findings. However, in equilibrium conditions experimental data deny a solid solution between Co- Ni-diarsenides and sulphoarsenides.

The main evidence of disequilibrium is the general development of replacement textures that lead to mineral phases with anomalous compositions. The first example of this is SkI, with Ni-rich compositions as the result of partial or complete replacement of previous nickeline. Another significant example is the relationship between gersdorffite and As-gersdorffite (Fig. 2F). This latter phase has the structure of krutovite (pyrite-type structure, *Pa3*) and is the high-temperature polymorph of rammelsbergite. According to Hem & Makovicky (2004), gersdorffite and krutovite can coexist in equilibrium at 650ºC and thus the analysed As-rich gersdorffite could represent the remnants of original krutovite, but partially or completely replaced by As-rich gersdorffite as later S-richer fluids interacted with previous minerals.

Regarding the compositional trend shown in Fig. 2E, textural relationships evidence that the primitive phase involved was of krutovite/rammelsbergite composition, which was destabilized as the chemistry of the percolating fluids was evolving to S- and Co- richer compositions. Therefore, there was a continuous re-equilibration between the fluid, the original phases and the newly precipitating ones leading to a compositional and irregular zoning (Fig. 2B) and to the dominance of complex solid solutions with wide variations in Ni:Co and S:As ratios. Further changes in the composition of the fluid, becoming rich in Fe, lead to a modification of the composition of diarsenides by the solid–fluid reaction described, towards the safflorite-löllingite binary. If so, cobaltite-gersdorffite crystals with high As-contents began to precipitate at the same time as rammelsbergite–safflorite crystals were dissolved.

These replacement processes imply not only compositional changes but also modifications of the structure. Further investigations on the structure of these mineral assemblages are being carried out and the preliminary results seem to confirm the proposed reaction scheme.

Acknowledgements

We greatly acknowledge the kindness of Marc Leblanc providing us with his complete collection of samples from his Ph. D. Thesis. This paper is a contribution to the MINECO-FEDER project CGL2014-55949- R; additional support from the Regional Government of Aragón to the E-45 Consolidated Research Group (Recursos Minerales)-IUCA is also acknowledged.

References

Ahmed AH, Arai S, Ikenne M (2009) Mineralogy and Paragenesis of the Co-Ni arsenide ores of Bou Azzer, Anti-Atlas, Morocco. Econ Geol 104:249-266

Dolansky LM (2007) Controls on the genesis of hydrothermal cobalt mineralization: insights from the mineralogy and geochemistry of the Bou Azzer deposits, Morocco. Unpublished Ph. D. Thesis, Montreal, Canada, McGill University, 182 pp

El Ghorfi M, Melcher F, Oberthür T, El Boukhari AE, Maacha L, Maddi A, Mhaili M (2008) Platinum group minerals in podiform chromitites of the Bou Azzer ophiolite, Anti Atlas, Central Morocco. Mineral Petrol 92 :59-80

En-Naciri A (1995) Contribution a l´étude du district a Co, As (Ni, Au, Ag) de Bou Azzer, Anti atlas (Maroc), données mineralogiques et geochimiques; étude des inclusions fluides: Unpublished PhD thesis, Orleans, France, Université Orleans, 238 pp

En-Naciri A, Barbason L, Touray JC (1997) Brine inclusions from the Co-As(Au) Bou Azzer district, Anti-Atlas Mountains, Morocco. Econ Geol 92:360-367

Fanlo I, Subías I, Gervilla F, Paniagua A, García B (2004) The composition of Co–Ni–Fe sulfarsenides, diarsenides and triarsenides from the San Juan de Plan deposit, central Pyrenees, Spain. Can Mineral 42:1221-1240

Fanlo I, Gervilla F, Colás V, Subías I (2015) Zn-, Mn- and Co-rich chromian spinels fron the Bou-Azzer mining district (Morocco): constraints on their relationship with the mineralizing process. Ore Geol Rev 71:82-98

Gasquet D, Levresse G, Cheilletz A, Azizi-Samir MR, Mouttaqi A (2005) Contribution to geodynamic reconstruction of the Anti-Atlas (Morocco) during Pan-African times with the emphasis on inversion tectonics and metallogenic activity at the Precambrian-Cambrian transition. Precamb Res 140:157-182.

Gervilla F, Fanlo I, Colás V, Subías I (2012) Mineral compositions and phase relations of Ni-Co-Fe arsenide ores from the Aghbar mine, Bou Azzer, Morocco. Can Min 50:447-470

Hem SR (2006) Solid solutions in the Fe-Co-Ni-As-S system. Chem Geol 225:231-303

Hem SR, Makovicky E (2004) The system Fe-Co-Ni-As-S. II. Phase relations in the (Fe,Co,Ni)$As_{1.5}S_{0.5}$ section at 650ºC and 500ºC. Can Min 42:63-86

Klemm DD (1965) Synthesen und Analysen in den Dreiecksdiagrammen FeAsS-CoAsS-NiAsS und FeS_2-CoS_2-NiS_2. N Jb Miner Abh 103:205-255

Leblanc M (1975) Ophiolites précambriennes et gîtes arseniés de cobalt (Bou Azzer-Maroc): Unpublished PhD thesis, Paris, France, Université de Paris, 367 pp

Leblanc M, Billaud P (1982) Cobalt arsenide orebodies related to an upper Proterozoic ophiolite, Bou Azzer (Morocco). Econ Geol 77:162–175

Leblanc M, Fischer W (1990) Gold and platinum group elements in cobalt arsenide ores: Hydrothermal concentration from a serpentinite source-rock. Mineral Petrol 42:197–209

Oberthür T, Melcher F, Henjes-Kunt F, Gerdes A, Stein H, Zimmerman A, El Ghorfi M (2009) Hercynian age of the cobalt-nickel-arsenide-(gold) ores, Bou Azzer, Anti Atlas, Morocco: Re-Os, Sm-Nd, and U-Pb age determinations. Econ Geol 104: 1065-1079

Parviainen A, Gervilla F, Melgarejo JC, Johanson B (2008) low-temperature, platinum-group elements-bearing Ni arsenide assemblage from the Atrevida mine (Catalonian Coastal Ranges, NE Spain). N Jb Miner Abh 185/1:33-49

Roseboom EH (1962) Skutterudites (Co,Ni,Fe)As_{3-x}: composition and cell dimensions. Am Mineral 47: 310-327

Spiridonov EM, Chvileva TN (1995) On the boundary between gersdorffite NiAsS and krutovite NiAs2. Dokl Acad Sci USSR Earth-Sci Sect 341:119-123

Walsh GJ, Benziane F, Aleinikoff JN, Harrison RW, Yazidi A, Burton WC, Quick JE, Saadane A (2012) Neoproterozoic tectonic evolution of the Jebel Saghro and Bou Azzer-El Graara inliers, eastern and central Anti-Atlas, Morocco. Precambrian Res 216-219:23-62

Yund RA (1962) The system Ni-As-S: phase relations and mineralogical significance. Am J Sci 260: 761-782

Volcanic stratigraphy and mineralisation of the Archean Colomb-Chaboullié greenstone belt, James Bay, Québec, Canada

Sarah Galloway and Pierre-Simon Ross
Institut national de la recherche scientifique-Centre Eau Terre et Environnement, Canada

Daniel Bandyayera and Yannick Daoudene
Ministère de l'Énergie et des Ressources naturelles, Canada

Abstract. The small Archean Colomb-Chaboullié greenstone belt, located at the contact between the Nemiscau and Opatica Subprovinces, contains a series of base and precious metal-bearing sulphide prospects that indicate exploration potential in the area. The Colomb-Chaboullié greenstone belt is composed of volcanic, mafic/ultramafic intrusives, and metasedimentary units. Within this belt, sulphide mineralisation occurs as massive and semi-massive bodies dominantly located in the volcanic units, and as disseminated sulphide zones infilling the inter-pillow basalt material of the pillowed facies. Disseminated sulphide veins also occur in massive basalt flows, infilling fractures. This study will help future exploration of greenstone belts in the northern region of the Superior Province that are underexplored in comparison to the Abitibi greenstone belt.

1 Introduction

The Colomb-Chaboullié greenstone belt is a NE-SW to E-W trending volcano-metasedimentary belt, located in the contact zone between the Nemiscau and Opatica Subprovinces of the Archean Superior Province, in the James Bay area, Québec, Canada (Fig. 1).

1:50,000 scale mapping was completed here by the *Ministère de l'Énergie et des Ressources naturelles*, Québec (MERN) in 2015.

This project aims to determine the origin of the precious-metal sulphide prospects, as it was unclear whether they are volcanogenic or tectonic in origin. This project also aims to gain more knowledge about the geological and tectonic setting of the Colomb-Chaboullié belt using geochemical and petrographic analysis, as it is unclear to which of the Opatica or Nemiscau subprovinces this belt belongs.

2 Regional Geological Context

The Opatica Subprovince, which lies to the south of the Colomb-Chaboullié, is made up of five plutonic units (Bandyayera and Daoudene in prep.). The northernmost unit, the Lac Rodayer pluton is adjacent to the Colomb-Chaboullié belt. This is a large intrusive complex that consists of four different subunits; 1) a quartz-diorite and diorite complex (Arod1), 2) hematised and foliated tonalite with injections of granitic pegmatite (Arod2), 3) foliated tonalite and quartz-diorite (Arod3), and 4) magnetic, hematised, foliated tonalite with biotite-magnetite granite injections (Arod4) (Fig. 2). U-Pb ziron ages around 2825 Ma for the Lac Rodayer pluton were determined by Davis, et al. (1995). Overall, the Opatica has a younging direction towards the south, away from the Colomb-Chaboullié belt (Davis et al. 1992).

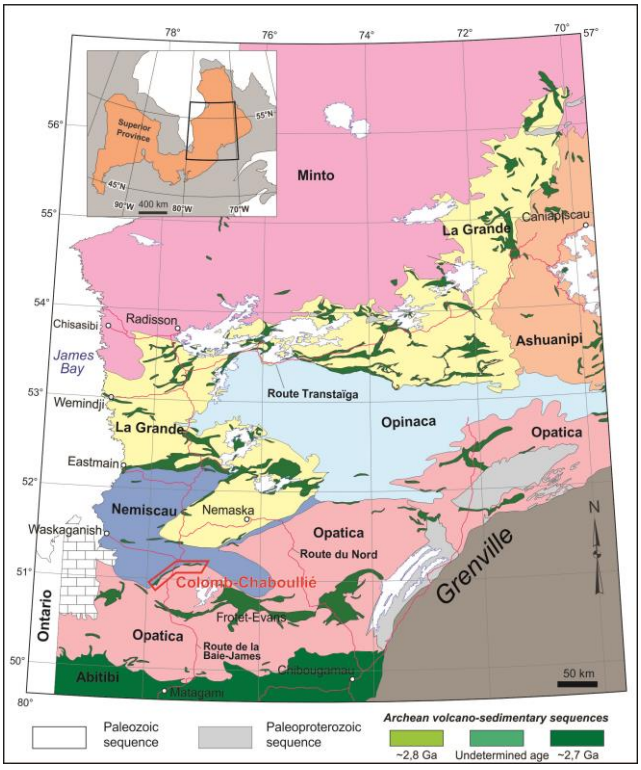


Figure 1. Location of the Colomb-Chaboullié greenstone belt (Bandyayera and Daoudene in prep.).

The Nemiscau subprovince, located to the north of the Colomb-Chaboullié, comprises metasedimentary assemblages (Bandyayera and Daoudene in prep.). According to Hocq (1994), the Nemiscau can be subdivided into two different zones; a plutonic terrain that is composed of monzonite to granodiorite lithologies, and a metasedimentary terrain. A further division has been proposed by Bandyayera and Daoudene (in prep.); the Rupert Group, which is based on the fieldwork carried out by the MERN in 2015. This group is made up of: a biotite

+ hornblende paragneiss (Aru1), migmatised biotite + hornblende paragneiss (Aru2), metatexite that has undergone up to 50% melt (Aru3), diatexite with melt fractions of 50-90% (Aru4), and a pegmatitic material that is granitic in nature, containing biotite ± garnet ± muscovite (Aru5) (Fig. 2).

3 Methodology

The study area, located in the central part of the Colomb-Chaboullié belt, was mapped on a scale of 1:20,000 in August 2016. The Route de la Baie-James bisects the belt in an N-S direction which allowed an N-S transect to be extensively sampled for geochemical analysis (Fig. 2). Samples were taken outside of this transect, in order to define the units not represented in this traverse.

The hand samples collected cover all the volcanic lithologies in the greenstone belt as well as high-grade metasedimentary and massive sulphide units for geochemical and petrographic analysis.

Outcrop-scale mapping was carried out on an outcrop in the western sector of the study area, where the Lac Marcaut gold showing has previously been reported (Riopel 1994), to help establish the origin and relationship of the massive sulphides with the surrounding host rock.

4 Volcanic assemblages

The dominant lithology within this greenstone belt consists of amphibolised, massive to pillowed basaltic flows (Acch1). This makes up about 80% of the Colomb-Chaboullié belt (Bandyayera and Daoudene in prep.). These basalts are very fine-grained, and in thin section contain ca. 50% amphibole crystals, with up to 40% plagioclase. A schistosity is defined by the common orientation of the amphibole and plagioclase crystals, displaying a nematoblastic texture. The pillowed facies dominates this unit, where pillows are highly deformed, flattened and elongated (Fig. 3a). The occurrence of a dark coloured hyaloclastite material is common in the pillow borders, however this is typically chloritised. Disseminated sulphides and garnet crystals (<5 mm) are also present in this inter-pillow material. The occurrence of sulphides within the inter-pillow material suggests that mineralisation occurred early on, before diagenesis.

The porphyritic andesites (Acch2) form long, thin bands within Acch1. Two types of andesites were identified, the first being a porphyric massive unit with 1-2 mm, tabular phenocrysts of plagioclase that make up ca. 20% of the rock (Acch2). The second andesite (Acch2a), located in the northeastern section of the belt, is pillowed. These pillows are also deformed and elongated in an E-W direction. These andesites are composed of a fine grained groundmass and contain phenocrysts of idiomorphic plagioclase crystals measuring 3-5 mm in length and 2-8mm hornblende crystals. Microphenocrysts and glomerophenocrysts make up 10-20% of the rock. These glomerophenocrysts also contain lesser amounts of biotite. These are embedded in a fine-grained groundmass composed of quartz, plagioclase and minimal amounts of biotite.

The final volcanic facies in this belt is composed of felsic to intermediate volcaniclastic rocks (Acch3). These occur as thin, elongate bodies within the amphibolitised basalts. These rocks are aphyric and banded, where the bands are defined by a colour change from white to green. In one of these Acch3 outcrops, elongate lapilli are present. In thin section, the mineralogy consists of quartz, biotite, chlorite and augite.

5 Metamorphic and sedimentary assemblages

Two small paragneiss units (Acch7) are present in the Colomb-Chaboullié belt, one in the north western part of the study region and the other at the very western end of the greenstone belt. This highly deformed paragneiss, rich in biotite (30-60%), is fine-grained and foliated. The mineralogy in thin section consists of quartz, plagioclase, biotite, chlorite, iron oxides and zircon. There are isolated garnets within this metasediment ca. 2mm in size, which suggests high metamorphic grades. Veins and injections that are tonalitic in nature are also present in this unit.

Definite sedimentary units include polymict conglomerates (Acch8) and, beyond the study area, a quartzite/iron formation. The polymict conglomerate comprises elongate clasts of diorite, gabbro, basalt, tonalite, porphyric andesite and intermediate lithologies which originate from the surrounding units. The presence of these clasts suggests that this conglomerate is younger than the surrounding lithologies. The banded quartzite/iron formation marks a pause in the volcanism in the region. The unit contains high levels of magnetite which are interbedded with silica-rich layers. Some pyrrhotite-rich sulphide patches also occur within this unit.

6 Massive sulphides

The massive to semi-massive sulphide occurrences are situated close to lithological contacts, following the regional tectono-stratigraphic orientation of the region (Fig. 2). Two of these previously recorded showings are located with the amphibolised basalt, close to the Acch7 unit. The remaining two gold occurrences are present in felsic to intermediate volcaniclastic lenses that are surrounded by the basalt.

These sulphides contain rounded, silica-rich clasts hosting minor amounts of pyrite, which are embedded within a pyrrhotite matrix (Fig. 3b). The Lac Marcaut gold showing (Fig. 2, outcrop 3521 and Fig. 3b) is the best known volcanogenic derived mineralisation in the Colomb-Chaboullié belt. Bandyayera and Daoudene (in prep.) have reported a polymetallic composition of pyrrhotite (40-90%) and pyrite (40-50%), with minor amounts of chalcopyrite, galena, and arsenopyrite at this locality.

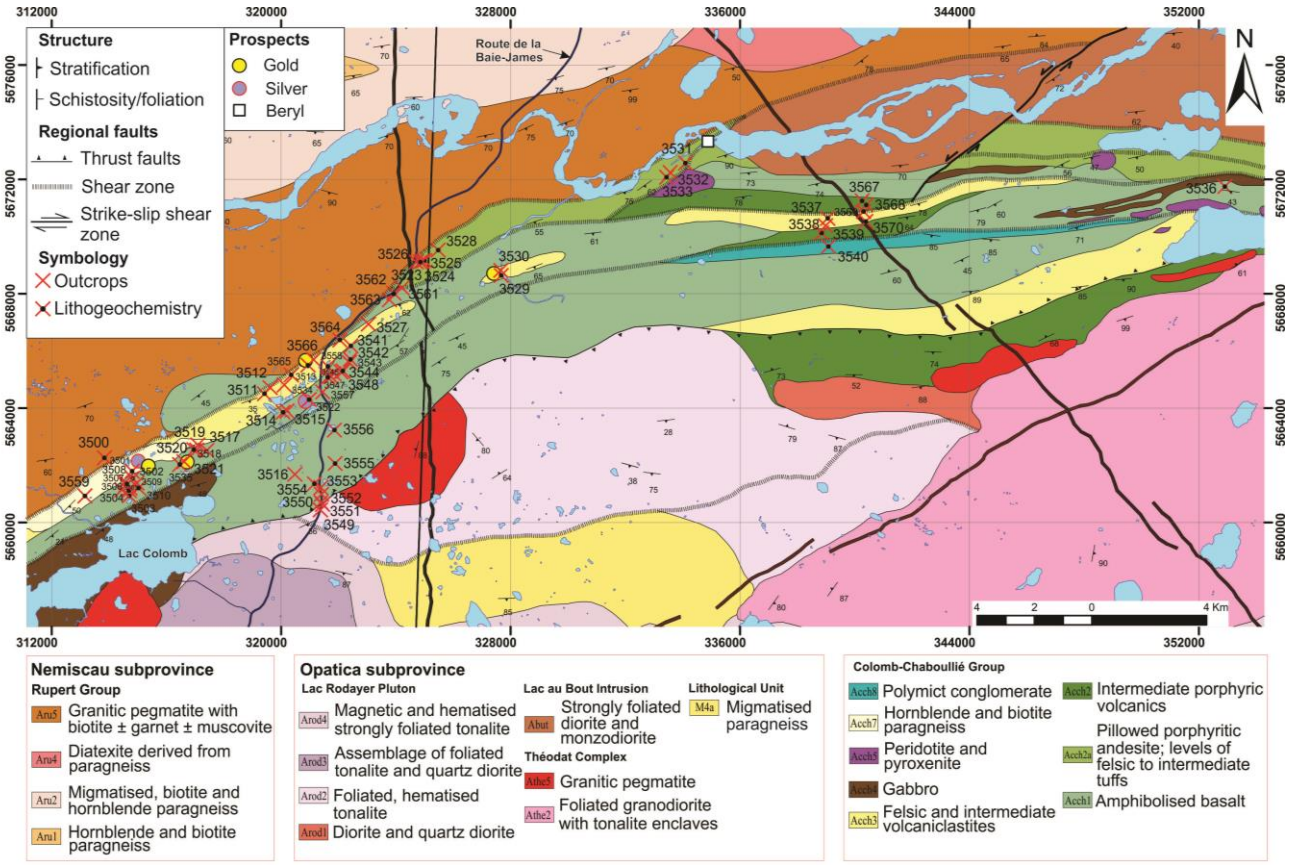


Figure 2. Geological map of the Colomb-Chaboullié greenstone belt showing the location of the outcrops mapped in 2016 by the first author, the location of the lithogeochemical samples, and the locations of previously recorded mineralisation in the study area.

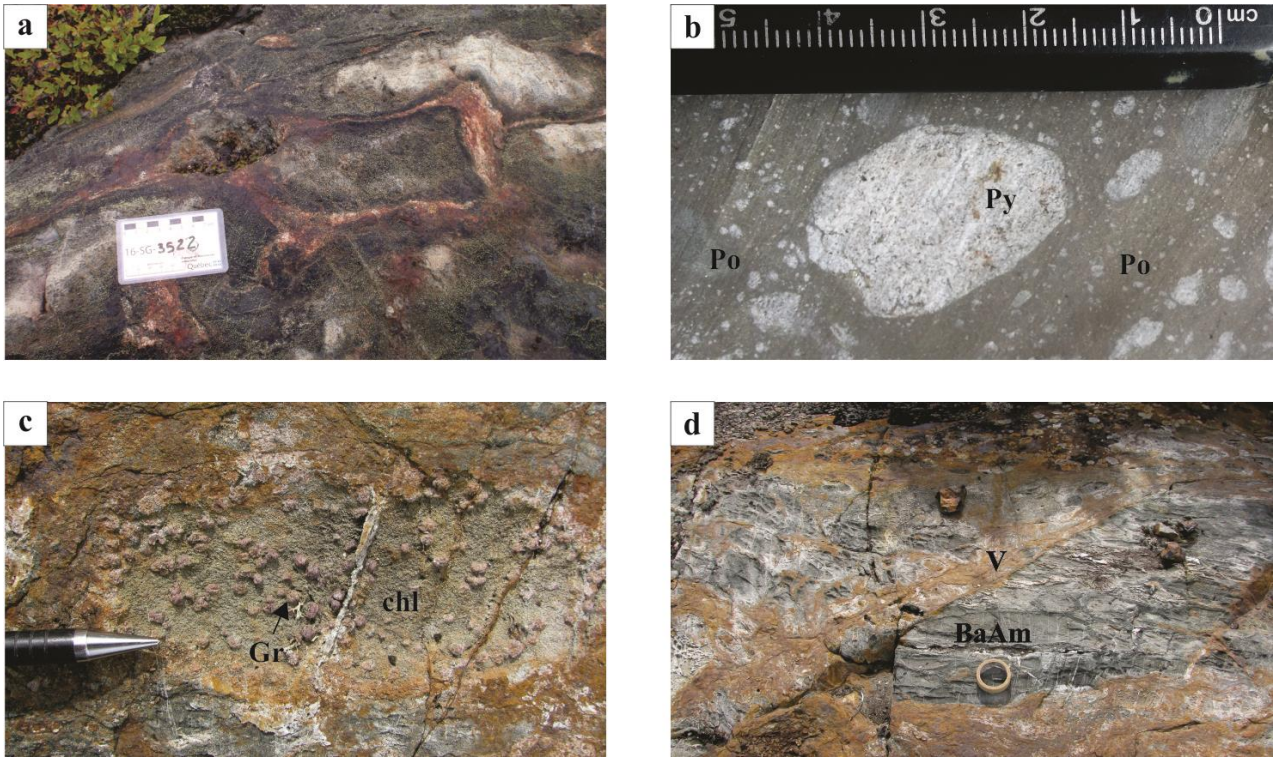


Figure 3. a Deformed pillowed basalt with rusted inter-pillow material which suggests the early circulation of hydrothermal fluids. **b** Sample from the Lac Marcaut outcrop, containing gold values. Rounded siliceous fragments containing pyrite (Py) are embedded in a matrix of pyrrhotite (Po). **c** Basalt showing synvolcanic alteration of recrystallized chlorite (chl) and garnet (Gr) in the pillow margins. **d** Veins of sulphides (V) in the amphibolised basalt (BaAm) showing a stockwork pattern.

Disseminated sulphides are present in both the pillowed and massive basalt flows. In the pillowed basalts, these sulphides occur in the interpillow material, often surrounded by chlorite and garnet which suggests synvolcanic pillow margin replacement (Fig. 3c). In the massive flows, the sulphides form a network of infilling fractures (Fig. 3d). Within this stockwork, only iron sulphides were identified in the field, however gold and silver values are recorded in historical work and from the 2015 MERN samples.

7 Geochemistry of the Colomb-Chaboullié volcanic rocks

Lithogeochemical analysis was carried out by the MERN, after the field mapping campaign of 2015 (Bandyayera and Daoudene in prep.). In figure 4a, it can be seen that the volcanic rocks of the Colomb-Chaboullié belt span the SiO_2 range from sub-alkaline basalts to rhyolites. In the magmatic affinity plot from Ross and Bédard (2009), there are two distinct geochemical groups; tholeiitic to transitional basalts, and a more evolved calc-alkaline suite containing andesites and intermediate to felsic volcaniclastic rocks and tuffs (Fig. 4b).

8 Future work

Geochemistry will be used to compare the Colomb-Chaboullié greenstone belt with greenstone belts in the Opatica Subprovince such as the Frotet-Evans Greenstone Belt, and smaller belts in the Nemiscau Subprovince, in order to help with future exploration campaigns north of the Abitibi Subprovince.

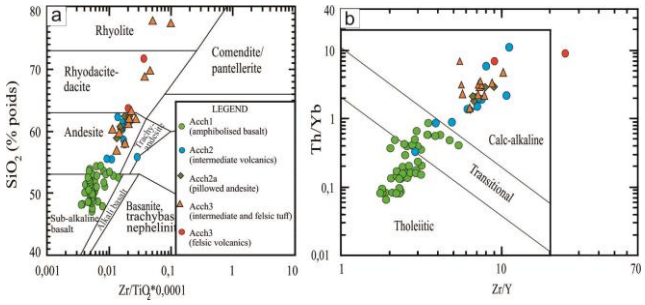


Figure 4. Geochemical results from the 2015 mapping campaign (Bandyayera and Daoudene in prep.). **a** Winchester and Floyd (1977) classification diagram. **b** Magmatic affinity diagram from Ross and Bédard (2009).

Acknowledgements

This research is funded by the *Ministère de l'Énergie et des Ressources naturelles*, Québec.

References

Bandyayera D, Daoudene Y (in preperation) Géologie de la région du lac Nemiscau, secteur du lac Royayer (SNRC 32K13, 32K14, 32N03 et 32N04-SE). MERN report.

Benn K, Moyen JF (2002) The Late Archean Abitibi-Opatica terrane, Superior Province; A modified oceanic plateau. Special Paper 440. The Geological Society of America:173-197

Davis WJ, Sawyer E, Machado N, Gariépy C, Benn K (1992) U-Pb geochronologyof Plutonism and Metamorphism in the Opatica Belt: Initial Results. Lithoprobe report 33, pp 147-149

Davis WJ, Machado N, Gariépy C, Sawyer EW, Benn K (1995) U-Pb geochronology of the Opatica tonalite-gneiss belt and its relationship to the Abitibi greenstone belt, Superior Province, Quebec. Can Jour Earth Sci 32:113-127

Hocq M (1994) La Province du Supérier. In: Dubé C (ed) Géologie du Québec, vol. les publications du Québec, pp 7-20

Mercier-Langevin P, Gibson HL, Hannington MD, Goutier J, Monecke T, Dubé B, Houlé MG (2014) A Special Issue on Archean Magmatism, Volcanism, and Ore Deposits: Part 2. Volcanogenic Massive Sulfide Deposits. Econ Geol 109:1-9

Riopel J (1994) Rapport technique des travaux, campagne 1994, propriété lac Marcaut. Rapport statutaire déposé au Ministère des Ressources naturelles, Québec. GM 53629, pp 1-328

Ross P-S, Bédard JH (2009) Magmatic affinity of modern and ancient subalkaline volcanic rocks determined from trace-element discriminant diagrams. Can Jour of Earth Sci 46:823-839

Winchester JA, Floyd PA (1977) Geochemical Discrimination of Different Magma Series and their Differentiation Products using Immobile Elements. Chem Geo 20:325-343

First record of garnierite in serpentinites from the Eastern Desert of Egypt: a witness to Ni-laterization in the Arabian Nubian Shield

Mohamed Mahmoud Hamdy, Mohamed A. Abdel Wahed
Tanta University, Egypt

Hamed Gamal El Dien
Tanta University,Egypt, University of New Brunswick, Canada, and Kanazawa University, Japan

Tomoaki Morishita
Kanazawa University, Japan

Abstract. This paper records, for the first time, the garnierite in Wadi Dubur Neoproterozoic serpentinites from the Central Eastern Desert of Egypt. Garnierites (népouite) occur in two types of infillings in the altered and faulted serpentinite. The *Type I garnierite* is Fe-richer [$Mg_{0.26-0.71}$ $Ni_{1.22-1.79}$ $Fe_{1.28-3.05}$ $Al_{0.0-0.02}$ $Si_{1.11-1.73}$ $O_5(OH)_4$] showing preferential zoning, while the *Type II garnierite* is homogenous with higher Si and Mg [$Mg_{0.54-0.94}$ $Ni_{1.38-2.04}$ $Fe_{0.38-1.29}$ $Al_{0.0-0.01}$ $Si_{1.66-2.10}$ $O_5(OH)_4$]. The serpentinization of the peridotite protolith and the associated alteration of chromite and Ni-sulfides were important for the early liberation of Ni. It is proposed that the unweathered serpentinites represent the bedrock, while the altered garnierite-bearing ones represent the saprock. The early weathering of serpentinites contemporaneous with the post-obduction tectonic activation caused *in situ* precipitation of *Type I garnierite* in veins. With the faulting repetition and progressive alteration Ni, Si, and Mg were transferred to the percolating meteoric solutions downward precipitating the *Type II garnierite* in gouges. Although the Dubur garnierite represents a narrow Ni-laterization, nickel ore in the Arabian–Nubian Shield of the Eastern Desert of Egypt.

1 Introduction

Despite that supergene enrichment mineralization in Arabian-Nubian Shield (ANS) ultramafics of the Eastern Desert of Egypt are evident (Shalaby and Moharem 2001; Harraz and Hamdy 2010; Hamdy and Aly 2011;) none of these rocks has been exploited for its potentiality to generate Ni laterite. Herein, the first author recorded, for the first time, the occurrence of garnierite in the serpentinite from Wadi Dubur from the ANS of the Eastern Desert of Egypt. The present study presents a preliminary evaluation of the data about field geology, mineralogy, and geochemistry of garnierite and its hosting serpentinites, providing an examination about the possibility of the Ni-laterization in the Arabian–Nubian Shield of the Eastern Desert of Egypt, which is usefulfor future exploration of Ni resources in this region.

2 Geological and structural settings

The Wadi (W.) Dubur area is located within the catchment of W. Dubur basin as a part of the Central Eastern Desert, north of Idfu-Marsa Alam highway (Fig. 1). W. Dubur serpentinites representing the base of a remnant ophiolite sequence occur as both NE–SW directed tectonized and mélange bodies in the arc metavolcanic rocks. Metasediments are schist having foliation warped around serpentinite sheets and close to contacts with the intrusive rocks. Two major slightly symmetric folds exist in metasediments. The major synform is cored by a weathered brown and reddish brown serpentinite, which encloses a fresh blocky joined serpentinite (Fig. 1). At the border with the mélange metasediments (up to 1 km wide), W. Dubur serpentinites were displaced sinistrally by a NNW-SSE striking strike-slip fault and dextrally by NE-trending shear zones. The faulted and sheared serpentinites display a different degree of the alteration and weathering. The more alteration and weathering is observed along joints and fractures. The weathered and sheared serpentinites (D-G) zone (1 to 7 m) overlies the unweathered one (D-S) with an irregular and gradualcontact and is commonly loose, porous friable and well developed along the gentle slopes, but to a less extent in the highland (Fig.1). The D-G serpentinites contain garnierite as mm-cm infilling veins and coatings on joints and fractures.

3 Samples of study and results

3.1 Serpentinites

The unweathered garnierite-free serpentinite (D-S), and the garnierite-bearing serpentinite (D-G) are completely serpentinized. Chromian spinel occurs as strongly altered unzoned small to big (0.5-2 mm) cracked grains. A variety of the Fe-Ni-Co sulfides (20-60 μm) including pentlandite to cobaltiferous pentlandite with magnetite overgrowth occur only in D-S serpentinites. The late shearing and faulting obliterate the primary textures producing mylonitic, cataclastic, and brecciated textures. Magnetite is obviously highly concentrated in D-G serpentinites. Garnierite is recognized in two types of infillings. *Type I garnierite* (Fig. 2) is the most common occurring in veins and veinlets, intergrown with Fe oxyhydroxides show banding. *Type II garnierite* (Fig. 2) is less common occurring as disseminated homogeneous fine (50-100 μm) sub- to euhedral highly

fractured fragments filling the fault gouges and fractures.

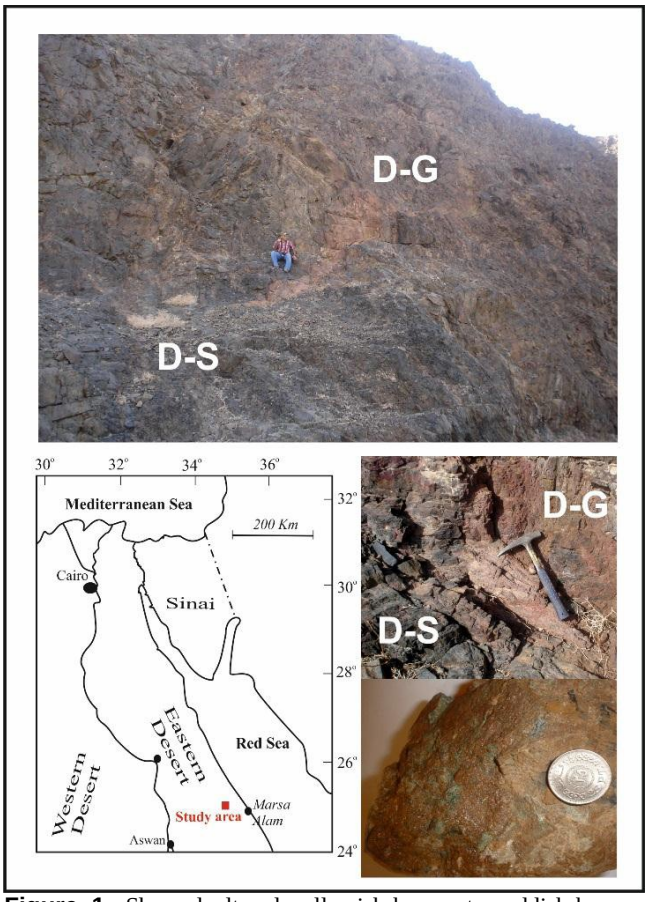


Figure 1. Sheared altered yellowish-brown to reddish-brown serpentinites (D-G) overlie and sometimes enclose the unweathered serpentinites (D-S). Hand sample is jade-green colored garnierite filling veins, gouges and coatings on joints and fractures of the altered serpentinites (D-G).

Electron probe microanalyses show that serpentine minerals differ, but slightly, in their compositions among the D-G and the D-S serpentinite. However, serpentine from the garnierite-bearing samples have more Ni + Fe, moving continuously between the serpentine and the népouite end members are like phases examined in other worldwide Ni- lateritic deposits. Spinel in D-G rocks are intensely altered having the chromian magnetite composition and corresponds to the metamorphogenic magnetite. A variety of the Fe-Ni-Co sulfides occur only in D-S serpentinites including pentlandite to cobaltiferous pentlandite and heazlewoodite, with magnetite overgrowth. Raman peaks include 378 cm^{-1} (for lizardite) and 395 cm^{-1} (for antigorite) bands to the vibrations of the SiO_4 tetrahedra, intense band at 675 cm^{-1} (antigorite) and 683 cm^{-1} (lizardite) produced by symmetric stretching modes of Si–Ob–Si linkages.

The whole-rock elemental data obtained show that the studied W. Dubur serpentinite rocks (ave. = 0.28 wt%) don't have the highest nickel content among other serpentinites from the Eastern Desert of Egypt. However, the distribution pattern of elements in W. Dubur serpentinites is identical to those of bedrocks of the nickel laterites elsewhere in the world (e.g., Thorne et al. 2012; Fu et al. 2014; Al-Khirbash 2015). Coupled with their enrichment in Ni the garnierite- bearing serpentinites are enriched in Si, Mg, Cr, Co, V, and Pb, but depleted in Fe, Al, Mn, Ca, Cu, Sr, and Ba.

3.2 Garnierite

Most of the studied garnierites are Al-poor but Fe-rich. The *Type I garnierite* (Fig. 2) is usually Fe-richer and Si-poorer [$Mg_{0.26-0.71}$ $Ni_{1.22-1.79}$ $Fe_{1.28-3.05}$ Al $_{0.0-0.02}$ $Si_{1.11-1.73}$ $O_5(OH)_4$], while the *Type II garnierite* (Fig. 2) has the composition of $Mg_{0.54-0.94}$ $Ni_{1.38-2.04}$ $Fe_{0.38-1.29}$ Al $_{0.0-0.01}$ $Si_{1.66-2.10}$ $O_5(OH)_4$.

Most of the analyzed garnierites plot within the field limited by serpentine–népouite series (Fig. 3), but closer to the népouite endmember. Some spot *Type II garnierite* analyses located in between the népouite-serpentine and the karpinskite-Ni karpinskite lines, but closer to the Ni karpinskite endmember (Fig. 3). Iron oxide phases are most common with the *Type I garnierite*, having lower Mg and Si and higher Fe compared to the saprolite in literature. Analyses of the Fe-richer phases plot continuously in a wide range of compositions between the serpentine endmember, *the Type II garnierite* and the Ni corner of the triangle. Raman spectra bands at 212-214, 270-275, and 290-293 cm^{-1} were obtained characteristic for hematite. Ni-substitution does result in a more poorly crystalline limonite structure.

Of the elemental maps acquired notable observations were only made for Si, Mg, Ni, Fe, and Co. The *Type I garnierite* is enriched in Fe, but Si-poor, showing a preferential zoning in the colloform texture and wrapping by Ni-poor serpentine. Contrastingly, the elemental maps of the *Type II garnierite* show that the Ni enrichment is mirrored by Si enrichment and Fe deficiency, with a slight enrichment in Co. Grains of this garnierite type are chemically homogeneous.

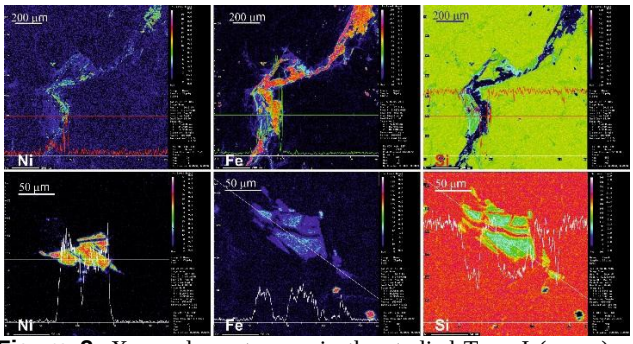


Figure 2. X-ray element maps in the studied Type I (upper) and Type II (lower) garnierites

Discussion and conclusions

The concentrated Ni and the formed garnierite are the weathering products of exposure of the W. Dubur ultramafic rocks and were most probably not the result of recrystallization of the lizardite into antigorite during the

progressive metamorphism of the serpentinites. Fluid activity during serpentinization due to the prevalence of oxidation conditions is largely responsible for the modification of the chromite by loss of Cr, Al, and Mg and incorporation of Fe^{3+}, Ti, Ni, and Mn, and remobilization of S, Fe, Ni, and Co included in the primary magmatic assemblage, thus introducing Ni into the weathering solutions. This ion exchange reaction is greatly favourable under the alkaline condition (Burns 1993).

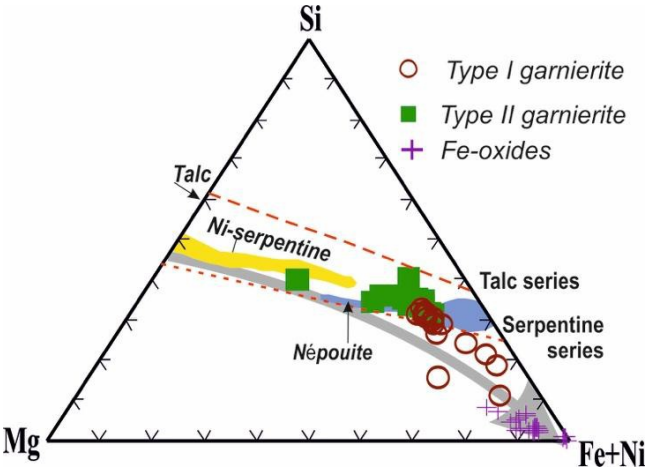


Figure 3. Triangular diagrams of Si-M g-(Ni+Fe) of the mineral phases in the studied serpentinites.

It is proposed that while the garnierite-bearing serpentinite represents a saprock (i.e., a transition zone between bedrock and an overlying saprolite) (Fritsch et al. 2016) within a weathering profile of a probable Ni-laterite, the garnierite-free serpentinites may represent the bedrock of this Ni mineralization (Fig. 4).Also, presence of the népouite garnierite in W. Dubur serpentinites (D-G), which locate in the bottom of the proposed weathering profile, is like other hydrous Mg silicate-type deposits worldwide. However, presence of the ferruginous weathering horizon locally overlying the unweathered serpentinite (bedrock) in W. Dubur area most probably refer to that the most favorable weathering products at the beginning of the lateritization under oxidizing conditions were the ferruginous minerals.

Nickel in the serpentinite-hosted népouite garnierites most probably transported from an overlying saprolite or Fe-Ni laterite horizon. With the continuous weathering of the saprock (D-G serpentinite) Ni released from the crystal lattice of the primary minerals, leading to a residual accumulation of Fe and Ni, along with other less mobile elements, forming a saprolite zone overlain by a nickel-rich ferruginous weathering one (Freyssinet et al. 2005).

Mineral chemical analyses suggest the existence of complete solid solution between the two types of the studied népouite garnierites and their hosting serpentines. This indicates that Ni was most probably incorporated first in the Ni-bearing serpentines (Pelletier, 1996), till the serpentine became saturated, as the excess of Ni gave the garnierites. The *Type I garnierite* most probably formed by an early alteration of the serpentine species and with a fracturing control. This caused *in situ* precipitation of Ni and Fe, since ferrous Fe in serpentine and sulfide minerals was largely oxidized to insoluble Fe^{3+} (Fig. 4). On the other hand, Si and Mg were transferred to the weathering solutions away from the serpentinite saprock. With progressive post-obduction deformation and weathering of the Dubur serpentinites the early formed hydrous Mg-Ni silicates would be a source feeding the upper weathering saprolite and ferruginous horizons with nickel. Meanwhile Fe is insoluble in the chemical weathering solutions, nickel combined with Si and Mg were transferred by the percolating acidic solutions (Brand et al. 1998; Freyssinet et al. 2005) moving downward through the weathering profile. This caused precipitation of neoformed népouite-garnierite in gouges and voids (*Type II garnierite*). In addition, some *Type II garnierite* analyses show a composition between the népouite-serpentine and the karpinskite-Ni karpinskite; being an indication for the increase of Si activity in the weathering solutions.

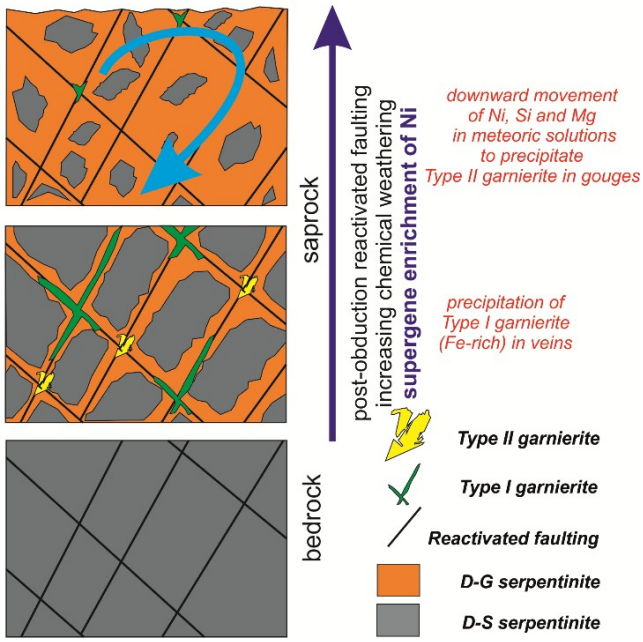


Figure 4. Schematic model for the supergene enrichment of Ni and formation of garnierite in W. Dubur serpentinites.

It is proposed that fractures, faults, and shear zones strongly controlled the Ni mineralization in the Dubur altered serpentinites. The coexistence of the two garnierite types within the same fault zone in the studied mineralized serpentinites suggests reactivation of faulting, while progressive alteration was maintained. Deformation of W.

Dubur serpentinite rocks caused cracking and/or damaging the crystal structure of minerals, which enclosing tightly bound Ni and Fe, and consequently, increased the effect of the weathering solutions. Both normal and strike-slip faults are rooted in serpentinites and are likely due to the reactivation of older faults. Faults usually generate very

steep slopes that allow the base of the weathering profile to be exposed. Evidence for long-lasting syntectonic weathering is provided by faults that are now located in Ni- rich serpentinites.

Weathering of the serpentinized peridotite at W. Dubur began upon exposure to a tropical climate during the Neoproterozoic where the nickel mineralization was formed. Low tectonic activity, moderate to low relief, and a high-water table responding to continued uplift increased the effect of weathering, accumulation, and preservation of its Ni mineralization products. Dubur Ni-mineralization occurs within the fault zone of the altered serpentinites, where this fault zone affected the associated metasedimentary rocks. Therefore, the Ni-laterization within Dubur serpentinites most probably took place in the presence of the Neoproterozoic metasediments. The proposed model of the Ni-concentration and garnierite formation in Dubur serpentinites strongly imply Ni-laterization within the weathering hydrous silicate and ferruginous horizons in the ANS of the Eastern Desert of Egypt. We recommend carrying out more detailed and large- scale petrological, structural, drainage analysis, paleoclimate, mineralogical and geochemical studies for the Dubur area and other similar regions in the Arabian Nubian Shield for prospection and exploration of nickel and other new residual enrichment mineralization.

Acknowledgment

The authors thank T. Mizukami from the Department of Earth Sciences of Kanazawa University for his kind assistance during carry out of some analyses. Prof. D. Lentz is appreciated for helping in language editing. Field work was supported by the Tanta University, Egypt that is gratefully acknowledged.

References

Al-Khirbash S (2015) Genesis and mineralogica l classification of Ni-laterites, Oman Mountains. Ore Geol Rev 65:199–212.

Brand NW, Butt CRM, Elias M (1998) Nickel laterites: classification and features. AGSO Journal of Australian Geology & Geophysics 17(4):81-88

Burns RG (1993) Mineralogical Applications of Crystal Field Theory. Cambridge University Press, p. 551.

Freyssinet P, Butt CRM, Morris RC, Piantone P (2005) Ore- forming processes related to lateritic weathering. Econ Geol 100th Anniversary:681–722.

Fritsch E, Juillot F, Dublet G, Fonteneau L, Fandeur D, Martin E, Caner L, Auzende A-L, Grauby O, Beaufort D (2016) An alternative model for the formation of hydrous Mg/Ni layer silicates (‘deweylite’/‘garnierite’) in faulted peridotites of New Caledonia: I. Texture and mineralogy of a paragenetic succession of silicate infillings. Eur J Mineral 28: 295– 311

Fu W, Yang J, Yang M, Pang B, Liu X, Niu H, Huang X., 2014. Mineralogical and geochemical characteristics of a serpentinite-derived laterite profile from East Sulawesi, Indonesia: Implications for the lateritizatio n process and Ni supergene enrichment in the tropical rainforest. J Asian Earth Sci 93:74–88.

Hamdy MM, Aly GA (2011) Preliminary results of a first record of gold and uranium in marble from Central Eastern Desert, Egypt: a witness for (syn and post?)– metamorphic mineralization in metasediments. Arab J Geosc 4:25-43.

Harraz HZ, Hamdy MM (2010) Interstratified vermiculite-mica in the gneiss-metapellite- serpentinite rocks at Hafafit area, Southern Eastern Desert, Egypt: from metasomatism to weathering. J Afr Earth Sci 58:305–320

Pelletier B (1996) Serpentines in nickel silicate ore from New Caledonia. Australasian Institute of Mining and Metallurgy Publication Series - Nickel conference, Kalgoorlie (Western Australia) 6/96, p. 197–205.

Shalaby MH, Moharem AF (2001) Geochemistry and radioelement distribution in the fresh and altered Hammamat sedimentary rocks along Wadi Belih, southern Gabal Um Tawat, north Eastern Desert, Egypt. Egypt Sediment 9:123–134.

Thorne R., Roberts S., Herrington R. 2012. The formation and evolution of the Bitincke nickel laterite deposit, Albania. Miner Deposita 47:933–947.

What's inside the Temagami geophysical anomaly, Sudbury district, Ontario?

Alexander Kawohl and Hartwig E. Frimmel
University of Würzburg, Germany

Andy Bite and Wesley Whymark
Inventus Mining Corp.

Abstract. The Temagami anomaly is similar in size and extent to the geophysical anomaly that marks the Sudbury Igneous Complex (SIC) in its immediate vicinity but its geological cause and potential link to the Sudbury impact structure have remained elusive. A first analysis of the lithology and alteration of a diamond drill core intersecting the area of maximum magnetic anomaly revealed that the anomaly cannot be explained by a layered mafic complex related to the SIC. Instead, the units intersected below Huroninan sedimentary cover rocks can be correlated with those of the 2.7 Ga Temagami greenstone belt. Extensive alteration noted throughout the core may be, at least in parts, responsible for the extreme geophysical signal. The cause of this hydrothermal alteration is suggested to be either related to 1.74-1.93 Ga carbonatitic to lamprophyric magmatism or to hydrothermal fluid circulation immediately following the 1.85 Ga Sudbury impact. Alternatively, the magnetic anomaly may be related to deep-seated magnetite-rich mafic rocks.

1 Introduction

The Temagami Anomaly (TA) is one of the largest positive but hitherto unexplained magnetic features on the Canadian Shield. Located in the Palaeoproterozoic Huronian basin fill, some 50 km northeast of Sudbury, Ontario, the anomaly extends over an area of approx. 1200 km^2 (Fig. 1), and a maximum magnetic intensity exceeding 10,000 nT has been measured. Moreover, a significant local gravity high coincides with the eastern extension of the TA.

Due to the close resemblance in terms of size and shape, a genetic link between the TA and the neighbouring Sudbury Igneous Complex (SIC) has long been speculated (cf. Fig. 1). Some authors (e.g. Naldrett 2004) assume an (ultra-)mafic intrusion of the ~2.48 Ga East Bull Lake Suite instead.

Since its discovery in the 1960s only few studies have been carried out on the TA and its geological cause remains enigmatic. Geophysical modelling by Card et al. (1984), for example, demonstrated that banded iron formation is likely to contribute partly to the 10,000 nT anomaly, and a deep seated (~5 km) intrabasement body containing 6 vol% magnetite is required. Coles et al. (1981) and recent modelling (Alan King, pers. comm.) arrived at similar conclusions. In their evaluation of a seismic transect across the TA, Milkereit and Wu (1996) interpreted the broad zone of low reflectivity beneath the thick Huronian strata as a large mid-crustal body, extending to a depth of 10-15 km, in agreement with previous studies. Furthermore, they speculated on the possibility of a larger IOCG-system, similar to Olympic Dam, as a potential cause for the TA. With a profound lack of surface outcrop, no conclusive explanation for the TA could be established. In 2014 Canadian Continental drilled into the anomaly to a depth of 2200 m. Here we report on the intersected lithology and its implications on the possible cause of the TA.

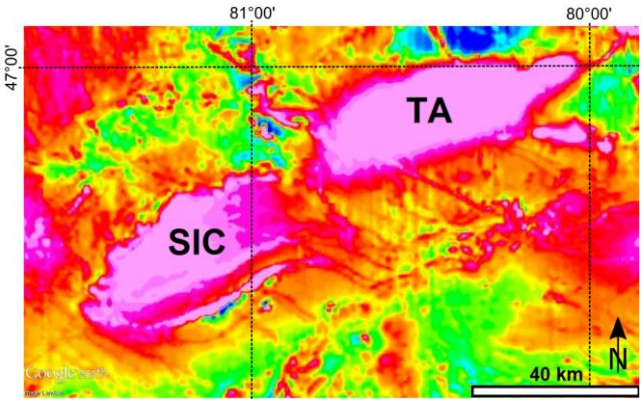


Figure 1. Aeromagnetic map of the Sudbury Igneous Complex (SIC) and the Temagami Anomaly (TA). Source: Ontario Geological Survey.

2 Geological Setting

Archaean units within the study area (also known as the Cobalt Embayment) are granite-greenstone terranes, the nearest to the anomaly of which is the Temagami Greenstone Belt (Fig. 2). This supracrustal assemblage of predominantly felsic and minor mafic metavolcanic, pyroclastic, and clastic sedimentary rocks, as well as banded iron formation and syn-volcanic intrusive bodies (TTGs with subordinate lamprophyre and ultramafic plutons) has been dated at ~2.7 Ga (Bowins and Heaman 1991) and is exposed as a southwest-plunging syncline east of Lake Temagami.

Subsidence of the Huronian basin began at the Archaean-Proterozoic boundary and deposition of the basin infill lasted until 2.2 Ga. The Huronian Supergroup comprises rift-related bimodal volcanic rocks at is base

and three sedimentary cycles that are likely to reflect glaciations. A maximum thickness of 12 km is reached southeast of Sudbury (Young et al. 2001) and a thickness of ~1.5-3.4 km is assumed within the area of the TA (Dressler 1982, 1986; Milkereit and Wu 1996). Rocks of the Huronian Supergroup were subjected to very low-grade sub-greenschist-facies metamorphism and deformation related to the Penokean and Grenville orogenies. There is evidence of a metasomatic event to have occurred around 1.74-1.93 Ga, which is ascribed to contemporaneous alkaline magmatism in the area (Schandl et al. 1994; Fedo et al. 1997; McLennan et al. 2000).

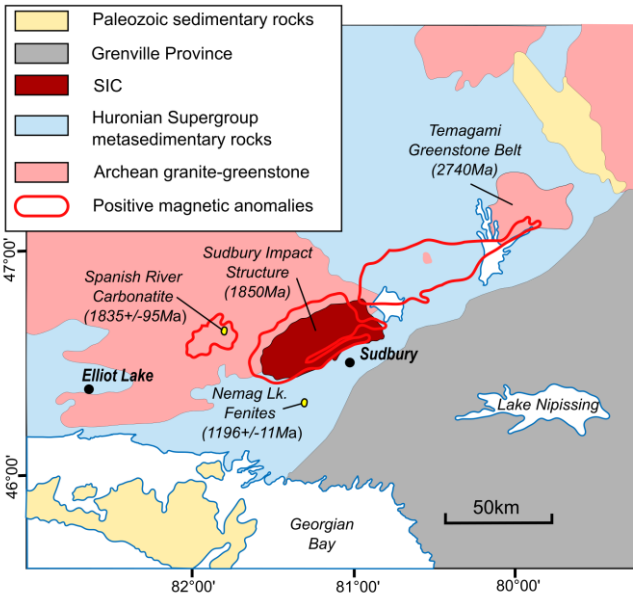


Figure 2. Regional geological setting of the Temagami Anomaly (after Lightfoot 2016).

Both the Archaean basement and the Huronian Supergroup rock were repeatedly affected by igneous activity, that is, the emplacement of (i) very widespread mafic sills and dykes of the 2.2 Ga Nipissing Diabase, (ii) intrusion of ultrabasic magma forming the 2.48 Ga East Bull Lake Suite and associated feeders known as the Matachewan dyke swarm, (iii) granitoid plutons of roughly the same age, (iv) alkaline complexes such as the 1.84 Ga Spanish River Carbonatite and the 1.2 Ga Nemag Lake Fenite (Lightfoot 2016).

Formation of the Sudbury Structure is attributed to a 1.85 Ga large asteroid impact. Vast volumes of granodioritic impact melt filled the centre of the resulting multi-ring basin and subsequently differentiated into a ~3 km thick sequence of, from bottom to top, xenolith-bearing "contact sublayer" of noritic composition discontinuously overlying the brecciated footwall country rocks, mafic quartz-norite, felsic norite, apatite- and oxide-rich quartz monzogabbro, and granophyre (Therriault et al. 2002; Naldrett 2004; Lightfoot 2016). The term "offset sublayer" is applied to <100 m wide dyke-like intrusions of quartz-dioritic composition, extending as much as 30 km from the SIC into the footwall rocks (Grant and Bite 1984). The SIC experienced tilting and NW-SE shortening during the Penokean Orogeny and is nowadays exposed as funnel-shaped, elliptical 60 x 30 km large structure, overlain by fall-back breccias and Palaeozoic sedimentary rocks of the Whitewater Group. The SIC is not only the prime natural laboratory to study impact processes but it also hosts world-class Ni-Cu-PGE deposits directly related to the impact. Massive to disseminated sulfide mineralization affected the contact sublayer, the brecciated country rocks and the inclusion-bearing facies of quartz-diorite offsets (see Lightfoot 2016 for a review).

3 Preliminary Results

The studied diamond drill hole, targeting the peak of the magnetic anomaly west of Emerald Lake, Afton Township, was the first to penetrate the Nipissing Diabase and Huronian overburden, and encountered Archaean basement at a depth of 600 m. The Archaean succession is dominated by felsic porphyric volcanic rocks, with intercalated intermediate/felsic pyroclastic and volcaniclastic rocks, banded iron formation (BIF) and siliciclastic metasedimentary rocks. BIF of the oxide facies occurs at several stratigraphic positions, with thickness varying from tens of centimetres to over 100 m. The BIF units dip in places steeply. In addition, a ~200 m thick graphitic argillite, containing abundant nodular pyrite, is present. Overall the Archaean section of the core is remarkably similar, both in lithology and stratigraphy, to the Temagami Greenstone Belt (cf. Fyon et al. 1988; Jackson and Fyon 1991; Ayer et al. 2006).

Of specific interest are the lowermost 200 m of the core as they contain the only mafic lithology within the sub-Huronian portion of the core and which might provide clues as to the magnetic anomaly. Two mafic intrusive units, 52 m and 25 m thick, were found in sharp contact with the felsic volcanic rocks. These mafic units are characterized by an anomalous strong magnetic susceptibility, which we can now attribute to a high modal amount of magnetite (5-10 vol%), evenly dispersed throughout the rock. The mafic rocks are fine-grained, free of inclusions, show a diabase texture and are composed of plagioclase, epidote, biotite, magnetite and ±actinolite. Primary ferromagnesian minerals were either completely destroyed or the matrix was originally composed of glass. No sulfide mineralization was found.

Geochemical analyses reveal a low-Ti tholeiitic to subalkalic composition (on average 55 wt% SiO_2, 1.1 wt% TiO_2, 12 wt% Fe_2O_3t, 3.7 wt% MgO), which is – in consideration of the alteration – within the compositional range of the Nipissing Diabase (Conrod 1989; Lightfoot and Naldrett 1996 and references therein). However, the mafic units differ significantly regarding their mineralogy and texture from the Nipissing Diabase in the same core. No evidence of a correlation with the SIC and its offset dykes could be found.

The entire 2200 m of the drill core were affected by intense alteration to an extent not previously reported for

the Temagami Greenstone Belt. Styles of alteration include the following:

- Propyltic alteration of the Nipissing Diabase and mafic intrusives,
- chlorite veins,
- extreme sericitization, especially of aphyric volcanic rocks and tuff,
- pervasive alkali-metasomatism, indicated by stilpnomelane veins of several centimetres thickness, cutting across BIF, as well as ominipresent biotitization, and
- carbonate alteration in spatial association with potassic alteration.

Primary minerals of the Nipissing Diabase were converted to amphibole, clinozoisite, leucoxene and chlorite, whilst the felsic volcanic rocks were altered to sericite, biotite, carbonate and albite. Some of the originally felsic volcanic rocks are almost solely composed of sericite and their igneous texture is no longer apparent. BIF beds are cut by veins of, and have been altered to, stilpnomelane, carbonate, chlorite and pyrite. Stilpnomelane was, in places, replaced by chlorite. The most prominent alteration feature, however, is a pervasive biotitization of almost all rocks beneath the Huronian cover. Some lithotypes of likely pyroclastic origin contain as much as 80 vol% biotite. The potassic alteration is typically accompanied by moderate to strong carbonatization and/or chloritization.

4 Discussion and conclusions

The petrographic analysis of the drill core revealed that no connection exists between the intersected mafic units and the SIC. The hypothesis of a SIC-related layered mafic complex being responsible for the TA has to be discarded. Instead, the rocks that were intersected below the Huronian cover can be correlated with those of the 2.7 Ga Temagami Greenstone Belt cropping out east of Emerald Lake.

The remarkable extent of alteration observed in the core raises the questions of the ultimate cause of this alteration and whether it could provide an explanation for the magnetic anomaly. A genetic link between the alteration in the studied core and carbonatitic as well as lamprophyric magmatism in the region is possible. Alternatively, it might be related to a basin-wide hydrothermal event immediately after the Sudbury impact. A first, preliminary, highly imprecise U-Pb monazite age of 1775 ± 76 Ma (D.W. Davies, unpubl. data) is interpreted as approximating the age of hydrothermal alteration in the core. This age, bearing in mind its large uncertainty, does not permit to distinguish between the two above genetic possibilities as both 1.7-1.8 Ga alkali magmatism and hydrothermal alteration following the 1.85 Ga impact took place within a relatively short, so far poorly resolved time span.

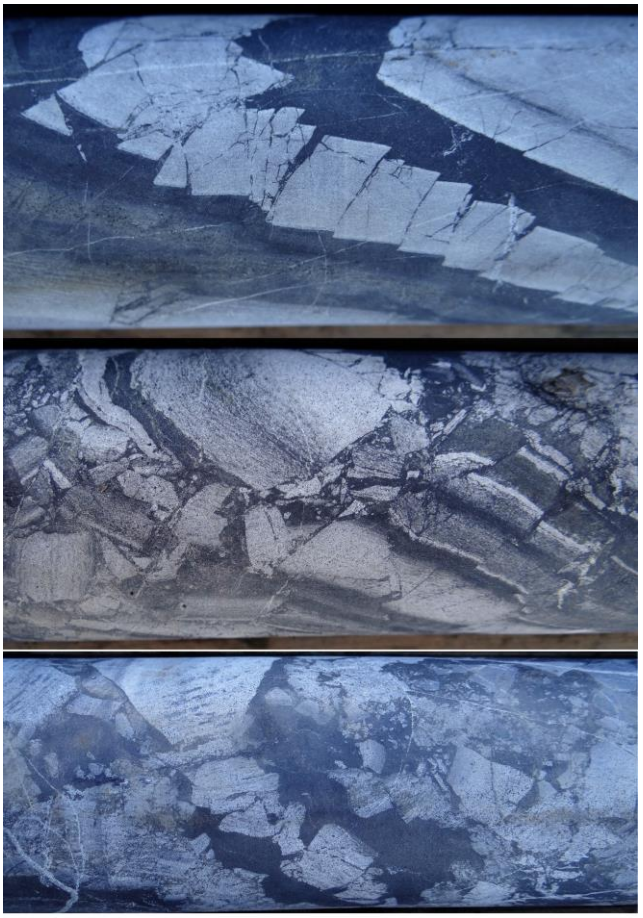


Figure 3. Drill core (4.5 cm diameter) at c. 2040 m showing brecciated banded iron formation. Chert fragments are embedded in a matrix of secondary magnetite.

While the amount of sedimentary BIF in the study area cannot account alone for the observed magnetic anomaly, regional mobilization of magnetite into secondary, hydrothermal magnetite (Fig. 3) could provide a potential explanation. Its spatial association with extensive potassic alteration bears some similarity with alteration patterns typically found around IOCG deposits in connection with regional alkaline magmatism – a link that will be tested in the next phase of this project.

Alternatively the TA might be related to a large volume of magnetite-rich mafic rocks at depth. The age and stratigraphic position and correlation of these mafic rocks remains unresolved at this stage and will be tested by forthcoming detailed geochemical analyses.

All in all, our first results on the nature of the TA have already helped in excluding some initial work hypotheses, that is the presence of a mafic layered complex linked to the SIC, but at the same time leave a number of other metallogenetic possibilities open. This has far-reaching implications for future exploration efforts in the region.

Acknowledgements

We thank Canadian Continental and Inventus Mining for financial and logistic support, respectively. The former company, specifically T. Obradovich, is thanked for the permission to present these findings.

References

Ayer JA, Chartrand JE, Grabowski GPD, Josey S, Rainsford D, Trowell NF (2006) Geological compilation of the Cobalt–Temagami area, Abitibi greenstone belt. Ontario Geological Survey, Preliminary Map P.3581, scale 1:100 000

Bowins RJ & Heaman LM (1991) Age and timing of igneous activity in the Temagami greenstone belt, Ontario: a preliminary report. Can J Earth Sci 28:1873-1876

Card KD, Gupta VK, McGrath PH, Grant FS (1984) The Subdury Structure: its regional geological and geophysical setting. In: Pye EG, Naldrett AJ, Giblin PE (eds) The Geology and Ore Deposits of the Sudbury Structure, Ontario Geological Survey, Spec Vol 1: 25-43

Coles RL, Haines GV, Hannaford W (1981) Broadscale magnetic anomalies over central and eastern Canada: a discussion. Can J Earth Sci 18:657-661

Conrod DM (1989) The Petrology and Geochemistry of the Duncan Lake, Beaton Bay, Milner Lake, and Miller Lake Nipissing Intrusions within the Gowganda Area, District of Timiskaming. Ontario Geological Survey, Open File Report 5701, 210 pp.

Dressler BO (1982) Geology of the Wanapitei Lake Area, District of Sudbury. Ontario Geological Survey, Report 213, 121 pp.

Dressler BO (1986) Geology of the Chiniguchi Lake Area, District of Sudbury, Ontario Geological Survey, Report 242, 19 pp.

Fedo CM, Young GM, Nesbitt, HW, Hanchar JM (1997) Potassic and sodic metasomatism in the Southern Province of the Canadian Shield: evidence from the Paleoproterozoic Serpent Formation, Huronian Supergroup, Canada. Precambrian Res 84:17-36

Grant RW, Bite A (1984) Sudbury quartz diorite offset dikes. In: Pye EG, Naldrett AJ, Giblin PE (eds) The Geology and Ore Deposits of the Sudbury Structure, Ontario Geological Survey, Spec Vol 1:275-300

Jackson SL, Fyon JA (1991) The western Abitibi Subprovince in Ontario. In: Thurston PC, Williams HR, Stutcliffe RH, Stott GM (eds) Geology of Ontario. Ontario Geological Survey, Spec Vol 4, Part 1:404-482

Lightfoot P, Naldrett AJ (1996) Petrology and geochemistry of the Nipissing Gabbro: exploration strategies for nickel, copper, and platinum group elements in a large igneous province. Ontario Geological Survey, Study 58, 81 pp.

Lightfoot P (2016) Nickel sulfide ores and impact melts: Origin of the Sudbury Igneous Complex. Elsevier.

McLennan SM, Simonetti A, Goldstein SL (2000) Nd and Pb isotopic evidence for provenance and post-depositional alteration of the Paleoproterozoic Huronian Supergroup, Canada. Precambrian Res 102:263-278

Milkereit B, Wu J (1996) Seismic image of an early Proterozoic rift basin. Tectonophysics 264:89-100

Naldrett AJ (2004) Magmatic sulfide deposits: Geology, geochemistry and exploration. Springer, Berlin and Heidelberg.

Schandl ES, Gorton MP, Davis DW (1994) Albitization at 1700±2 Ma in the Sudbury-Wanapitei Lake area, Ontario: implications for deep-seated alkalic magmatism in the Southern province. Can J Earth Sci 31:597-607

Therrriault AM, Fowler AD, Grieve RAF (2002) The Sudbury Igneous Complex: a differentiated impact melt sheet. Econ Geol 97:1521-1540

Young GM, Long DGF, Fedo CM, Nesbitt HW (2001) Paleoproterozoic Huronian basin: product of a Wilson cycle punctuated by glaciations and a meteorite impact. Sediment Geol 141-142:233-254

The association between granitoids and skarn mineralisation in the Taebaeksan mineralized province, South Korea

Gyoo-bo Kim, Seon-Gyu Choi, Eun Joo Choi, Chang Seong Kim and Jeong Geuk Kang
University of Korea

Jieun Seo
National University of Kyungpook, South Korea

Sang-Tae Kim
University of McMaster, Canada

Abstract. Diverse skarn deposits occur in the southern part of the Taebaeksan Basin, South Korea. This province is an important ore district and contains polymetallic skarn mineralization such as the Geodo Fe–Cu(–Au), Shinyemi Fe–Zn–Mo(–Pb), Sangdong W–Bi(–Au), and Gagok Zn–Pb(–Ag) deposits. Ore bodies are hosted mainly in Cambrian to Ordovician carbonate beds in the lower part of the Choseon Supergroup. Skarn mineralization consists of stratiform, pipe, and massive bodies in the carbonate rocks adjacent to the granitoid intrusions. The Cretaceous granitoids provided the magmatic fluids for the skarn deposits. Geochemical analysis generally shows that the granitoids are subalkaline, high-K calc-alkaline, and metaluminous in composition and were emplaced at relatively shallow depths (<300 m). In contrast, the Sangdong granite was emplaced below 1 km the surface and shows a composition intermediate between that of metaluminous and peraluminous. Each granitoid has a different oxidation state and distinct geochemical features. In addition, the mineralization ages of the skarn deposits are similar to the ages of the associated granitoids: Geodo (98.4 Ma), Sangdong (83.6 Ma), Shinyemi (76.2 Ma), and Gagok (78.8 Ma). The Geodo Fe skarn deposits are associated with low ratios of clinopyroxene to garnet and show a relatively oxidized mineral assemblage, whereas the Sangdong W–Mo skarn deposit is characterized by high ratios of clinopyroxene to garnet and a relatively reduced mineral assemblage.

1 Introduction

The Taebaeksan mineralized province, located in eastern South Korea, is an important skarn district that is known globally and is rich in zinc–lead–tungsten–iron–copper–molybdenum–silver–gold mineral resources. Here we present geological, geochemical, and mineralogical data

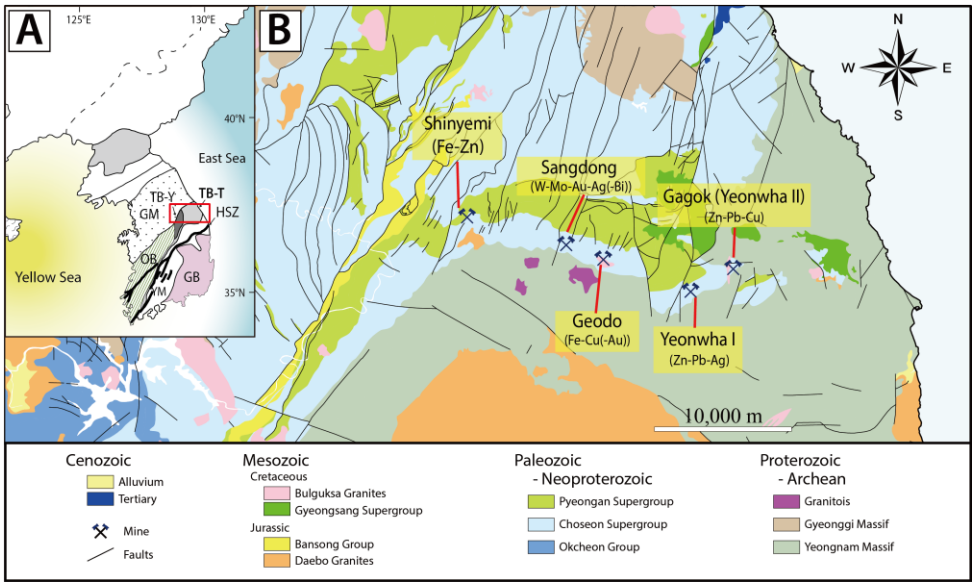


Figure 1. Geological map of the Taebaeksan mineralized province, South Korea. **a** Study area and tectonic framework in South Korea. **b** Geology of the Taebaeksan Basin showing the location of deposits discussed in the text. GM: Gyeonggi Massif; TB-Y: Taebaeksan Basin (Yeongwol type); TB-T: Taebaeksan Basin (Tuwibong type); OB: Okcheon metamorphic Belt; HSZ: Honam Shear Zone; YM: Yeongnam Massif; GM: Gyeongsang Basin.

from both the skarn deposits and their associated intrusions, and discuss the geochemical relationships between granitoids and skarn mineralization in the Taebaeksan mineralized province. These deposits principally coexist in time and space with magmatic hydrothermal deposits such as skarn, hydrothermal replacements, and mesothermal vein deposits. The region contains several important ore deposits, including the Geodo Fe–Cu–Au, Shinyemi Fe–Zn–Pb–Mo, Sangdong W–Mo–Bi, and Gagok-Yeonhwa 1 Zn–Pb deposits. These are hosted most commonly in lower formations (Upper Cambrian Punchonn Limestone, Table 1) and in the underlying interbedded limestone in Cambrian Myobong slate and upper formations of the Great Limestone Group (Ordovician Maggol limestone, Table 1). These deposits contain a diverse group of metal elements, because each type of skarn deposit formed from a distinct plutonic episode. Previous researchers have tried to relate skarn mineralization to granitoids of individual skarn deposits in this province (Kim 1986; Moon 1993; Choi et al. 2010; Koo 2012; Choi et al. 2014). Based on mineralogical and geochemical methods, this study focuses on the geochemical characteristics of granitoids, skarn mineralization, and compares four typical skarn deposits. The results can be used to explore new targets that may have similar potential for mineralization. A systematic geochemical study of a variety of ore deposits and an assessment of the relations between skarns and associated plutons may provide new insights that aid exploration for hidden ore deposits.

2 General Geology

The geological units in the southern part of Taebaeksan province consist of Precambrian gneisses, Paleozoic sedimentary rocks, and Jurassic and Cretaceous subvolcanic granitoids (Fig. 1). The Paleo-Mesozoic sediments are part of the Choseon and Pyeongan supergroups. The Choseon Supergroup consists of marine

Table 1. Diverse skarn deposits controlled by favorable stratigraphic sequence of the Choseon Supergroup.

Group		Formation	Rocks	Orebody
Choseon Supergroup	Ordovician	Duwibong	limestone, calcareous shale	
		Jigunsan	shale, limestone	
		Maggol	calcareous mudstone, dolostone, limestone	Sinyemi: Fe-Zn-Mo
		Dumugol	limestone, dolostone	
		Dongjeom	sandstone, calcareous shale	
	Cambrian	Hwajeol	calcareous shale/mudstone	Yeonhwa I: Zn-Pb-Ag Geodo: Cu-Au
		Sesong	shale/limestone	
		Daegi	massive limestone, oolitic limestone	Yeonhwa I: Pb-Zn-Ag Gagok: Zn-Pb Sangdong: W-Bi
		Myobong	sandstone, limestone, slate/shale	Yeonhwa I: Zn-Pb-Ag Gagok : Zn, Geodo: Fe-Cu Sangdong: W-Bi
		Jangsan/ Myeonsan	sandstone, conglomerate	Sangdong: Mo

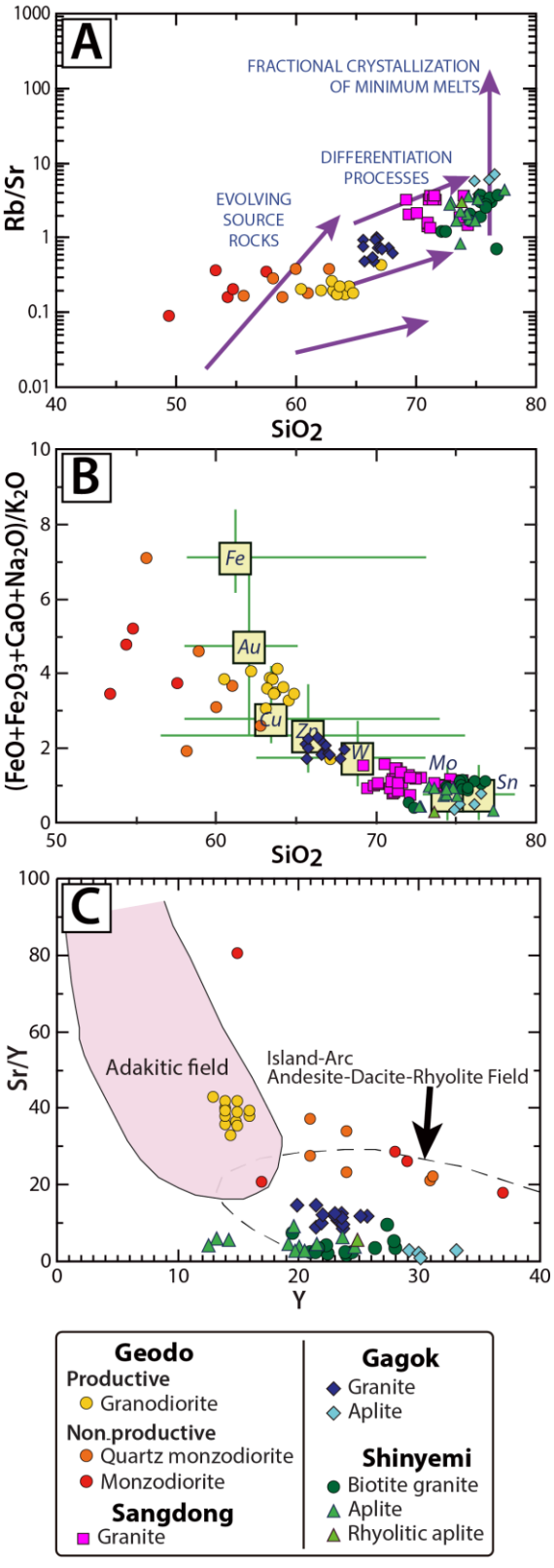


Figure 2. **a** Rb/Sr vs. SiO_2 diagram for differentiation degree (Blevin and Chappell 1996), **b** Discriminant diagram of metal commodities (Meinert 1991), **c** Sr/Y vs. Y diagram for adakitic composition of granitoids.

clastic sedimentary and carbonate rocks, the Jangsan quartzite, the Myobong slate (Cambrian), and the Cambrian to Ordovician Great Limestone Group. The most important skarn deposits occur in the limestone layers in the southern part of the Taebaeksan Basin. The rocks in this region generally strike N70°–80°E and dip 25°–35°NW, while the rocks in the northern part pf the basin have variable orientations.

3 Methodology

In this study, relatively fresh granitoids, collected from each skarn deposits, are analysed. Whole-rock major, trace, and rare earth element (REE) concentrations were determined using inductively coupled plasma–atomic emission spectrometry (Termo JarrelAsh ENVIRO II), inductively coupled plasma–mass spectrometry (Perkin Elmer Optima 3000), and instrumental neutron activation analysis at Activation Laboratories Ltd., Canada. Geochemical compositions of skarn minerals were determined using JEOL JXA-8600 SX electron microprobe at Korea University.

4 Results

There are various skarn ore deposits in the Taebaeksan mineralized province. Most of the ore bodies such as Geodo, Gagok, and Sangdong deposits are hosted in the lower part of the Cambrian limestone, in the Daegi limestone, and in interbedded limestone in the Myobong slate. The ore bodies hosted in the lower part of the Choseon Supergroup are associated with calcic skarn. In contrast, the Shinyemi ore body is hosted within a dolomitic carbonate bed in the upper part of the Choseon Supergroup, in the Maggol Formation. These ore bodies are found within the same formation and have similar geochemical compositions. The Fe ore bodies at the Shinyemi Deposit are closely associated with magnesian skarn.

Granitoids in the Taebaeksan province intruded marine clastic sedimentary rocks and are Cretaceous in age; e.g., granodiorite at Geodo (107 Ma), granite at Sangdong (87.5 Ma), biotite granite at Gagok (78 Ma), and biotite granite at Shinyemi (74.7–77.2 Ma). These granite ages are similar to the reported mineralization age at Geodo (98 Ma), Sangdong (82–83 Ma), Gagok (73–78 Ma), and Shinyemi (75–78 Ma). Field relationships suggest that these Cretaceous subvolcanic intrusions are the source of the metals, heat, and fluids responsible for the diverse metallic mineralization. The intrusions are generally silica-rich and are of the high-K series with a metaluminous to slightly peraluminous affinity. They are I-type granites that were emplaced at very shallow levels (≤300 m). They generally have a porphyritic, medium- to fine-grained texture and occur as stocks, pipes, and occasionally breccia. The granodiorite at Geodo has a high Sr/Y ratio (average of 38.6), similar to adakites (Fig. 2 **c)**. The granite at Sangdong, however, occurs 1 km below the surface and is classified as a subalkaline, high-K calc-alkaline granite with molecular A/CNK ratio of 1.01–1.55. Therefore, it is intermediate in composition between metaluminous and peraluminous. Rb/Sr ratios indicate that granitoids at Shinyemi, Sangdong, and Gagok are more highly differentiated than the Geodo granodiorite (Fig. 2 **a**). All of the granitoids, each related to a specific type of ore body, contain distinct major and by-product metals (Fig. 2 **b**).

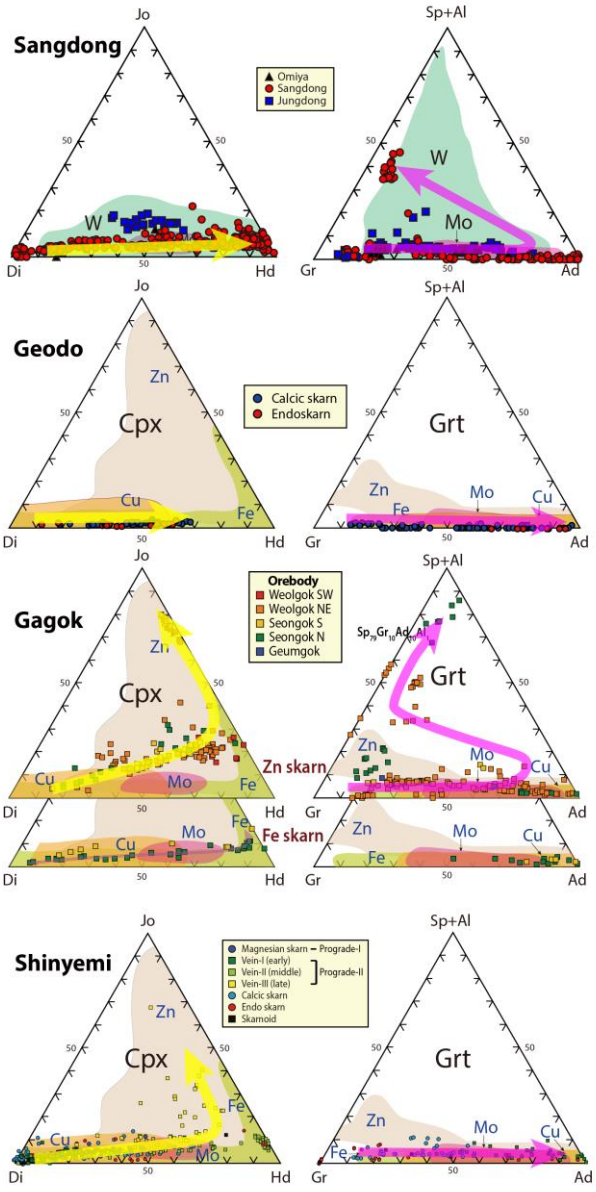


Figure 3. Evolution trend of garnet and clinopyroxene from Taebaeksan skarn deposits. Ad: Andradite; Al: Almandine; Cpx: Clinopyroxene; Di: Diopside; Gr: Grossular; Grt: Garnet; Hd: Hedenbergite; Jo: Johannsenite; Sp: Spessartine (Einaudi et al. 1981; Meinert et al. 2005).

The chemical compositions of garnet and clinopyroxene are also compared in detail for these four skarn deposits in Taebaeksan province (Fig. 3). Ca–Fe^{3+}-garnet and diopsidic clinopyroxene from Geodo occur in Fe- and Cu-type skarn mineralization, indicating an oxidized-type skarn. The composition of garnet and clinopyroxene from the Gagok and Shinyemi deposits is consistent with Fe- and Zn-type skarn mineralization, and these minerals become more Mn-rich with time. Sub-calcic garnet and hedenbergitic clinopyroxene from the Sangdong deposit formed during W-type skarn mineralization. These Mn–Fe^{2+}-garnets indicate an intermediate reduced-type skarn and the mineral assemblages indicate a reduced-type skarn. The tungsten concentration at Sangdong during the retrograde stage of metasomatism (e.g. fluorite and muscovite) may have resulted from relatively high fluorine activity.

5 Discussion and conclusion

Through a review of four skarn deposits in South Korea, at the Geodo (Cu–Fe–Au), Shinyemi (Zn–Fe–Mo), Gagok (Zn–Pb), and Sangdong (W–Mo), we obtained the following conclusions. Most of the granitoids in the Taebaeksan mineralized province have a sub-alkaline and high-K calc-alkaline composition and are metaluminous. The Sangong granite, however, exhibits characteristics that are intermediate between metaluminous and peraluminous. The high A/CNK ratio reflects depleted alkaline contents as a result of phyllic alteration. These granitoids formed in a post-orogenic environment. The Cretaceous age of each granitoid is well correlated with the mineralization age of each ore body. New and existing geochemical data from related granitoids show that these plutons are closely affiliated with metals in various skarn deposits in the Taebaeksan province.

Based on the quantitative correlation between garnet and clinopyroxene, the dominant diopsidic clinopyroxene and andriditic garnet at the Geodo Fe–Cu skarn deposit are useful indicators of oxidized-type skarn. While diopsidic clinopyroxene and andraditic garnet are observed similarly in early stage skarn, garnet was replaced by Fe^{2+}–Mn-garnet such as almandine and spessartine in the late-stage skarn. This transition in mineral composition indicates a reduced-type skarn. At the Gagok mine, diopsidic pyroxene and rhodonite are more common than andraditic garnet in the upper part of the Zn skarn zone. Andriditic garnet is dominant in the lower part of the Fe skarn zone, indicating an oxidized-type skarn. Most skarn deposits, such as at the Geodo, Gagok, and Sangdong (but not Shinyemi), are hosted in interbedded limestone within the Myobong Slate and the Pungchon Limestone, in the lower part of the Choseon Supergroup. The results suggest that the difference in oxidation state of magmatic fluids from each pluton resulted in the diverse types of skarn ore bodies.

Acknowledgements

This research was supported by a grant from the Korea Institute of Energy Technology Evaluation and Planning (KETEP) (No.20152510101970).

References

Blevin PL, Chappell BW (1996) The role of magma sources, oxidation states and fractionation in determining the granite metallogeny of eastern Australia. Trans Royal Soc Edinburgh Earth Sci 83: 305–316.

Choi BG, Choi SG, Seo J, Ryu IG, Kang HS, Koo MH (2010) Mineralogical and geochemical characteristics of the Wolgok-Seongok orebodies in the Gagok skarn deposit: Their genetic implications, Econ Environ Geol 43: 477-490

Choi EJ, Choi SG, Seo J, Kim CS, Park SG (2014) Geology, mineralogy and geochemistry of the Shinyemi iron deposit, Korea: Implications for a genetic model, Acta Geologica Sinica 88:1083-1084

Einaudi MT, Meinert LD, Newverry RJ (1981) Skarn deposits, In: Skinner BJ (ed) Economic Geology 75th Anniversary Volume, Society of Economic Geologists, El Paso, Texas, USA, pp 317-391

Kim GH (1986) Geochemical characteristic of the Sangdong granite, Unpublished MS Thesis, Kyungbuk National University, Korea, p 80

Koo MH (2012) Skarn evolution and zinc-lead-iron mineralization at the Gagok mine, Unpublished MS Thesis, Korea University, Korea p 80

Meinert LD (1991) Skarns and skarn deposits. Geoscience Canada 19: p 145-162.

Meinert LD, Dipple GM, Nicolescu S (2005) World skarn deposits, In: Hedenquist JW, Thomson JFH, Goldfarb R, Richard J (eds) Economic Geology 100th Anniversary Volume, Society of Economic Geologists, Littleton, Colorado, USA, pp 299-336.

Moon GJ (1993) Skarn ore deposits at the southern limb of the Baegunsan syncline in the Taebaeg Basin of south Korea - A review, In: Ohmoto H, Watanabe M, Nakashima S, Ishihara S, Matsueda H, Tsusue A, Hayashi K, Shikazono N (eds) Proceedings of the 29th International Geological Congress, Tokyo, Japan. Res Geol Special Issue, 15: pp 97-110

Impacts of the ore mining and processing on the environment in the Berg Aukas area, Namibia

Bohdan Kříbek, Vladimír Majer, Jan Pašava, Ilja Knésl
Czech Geological Survey

Frederick Kamona, Benjamin Mapani
University of Namibia

Ondra Sracek
Palacký University, Czech Republic

Abstract. As revealed by environmental-geochemical mapping, soils and agricultural products are affected to various degrees by industrial pollution in the area of the former Berg Aukas Pb–Zn–V mine. The most important sources of contamination are airborne particles from slag and tailing deposits. The degree of regional industrial pollution of soils can be best evaluated using the Coefficient of the Industrial Pollution (CIP), which is expressed as a sum of the concentrations of As, Cd, Cu, Pb and Zn in topsoil at the individual sampling points, divided by the median values of the same metals in topsoils of the studied region. Crops grown at the local National Youth Service Cooperative Farm contain high concentrations of potentially toxic elements (PHEs) that are deleterious to health. The analysed cassava and sweet potato leaves as well as sweet potato tubers are characterized by As, Pb and Zn values in excess of WHO limits for food. Based on this study, measures to reduce environmental risks in the Berg Aukas area are suggested.

1 Introduction

A comprehensive environmental-geochemical survey was conducted in the abandoned Berg Aukas mining district. The aims of the survey were: to analyze the contamination of soils and agricultural plants by potentially toxic elements (PHEs); to determine the effect of ore mining and processing on the environment and; to formulate recommendations and concepts that should ensure protection of the environment after mining operations.

2 Location of the Berg Aukas area

Berg Aukas is located 15 km east of Grootfontein on the Berg Aukas 593 farm, in the Otavi Mountain Land, Namibia (Fig. 1). Currently, the National Youth Service Cooperative Farm is located at this former mine site, conducting training programs in agriculture.

3 Ore deposit

The Pb–Zn–V mineralization can be divided into (a) the Northern ore horizon consisting of lenses with oxidized sulfide bodies with primary descloizite $(Pb,Zn)_2(OH)VO_4$, sphalerite ZnS, galena PbS, and subordinate pyrite FeS_2; and (b) the Central ore body found in recrystallized dolomite and arranged in an en-echelon pattern. The principal primary minerals are galena, sphalerite, and minor descloizite. Other reported V minerals are mottramite $PbCu(VO_4)(OH)$, and vanadinite $Pb_5(VO_4)_3Cl$ (Bezing et al., 2008). Vanadium mineralization is assumed to be formed at low-temperature conditions (40–50 °C) by meteoric waters interacting with Proterozoic rocks in a karst environment (Boni et al. 2007). Secondary minerals are represented by secondary descloizite, willemite Zn_2SiO_4, cerussite $PbCO_3$, and smithsonite $ZnCO_3$.

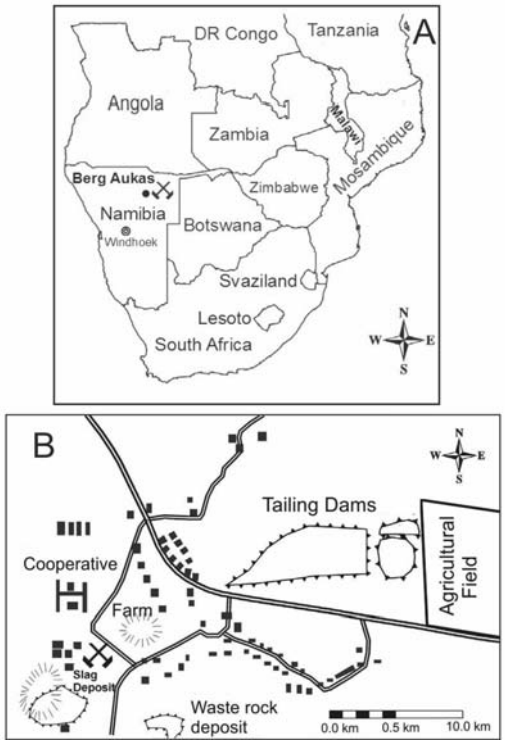


Figure 1. Location of Berg Aukas (A) and position of waste rock deposit, slag, tailing dams and agricultural field where cassava and sweet potato were sampled (B).

4 Mining and mining remnants

The Berg Aukas deposit was discovered in 1913. Mining started in 1920 and was terminated at the groundwater level in 1928. In 1950, the mine was reopened, and vanadinite and sulfide concentrate was produced and roasted on the spot. The ore reserves at the time of mine closure in 1978 were estimated as 1.65 Mt grading 0.6 % V_2O_5, 5% Pb and 17% Zn

(Misiewicz 1988). Remnants of waste rock heaps are located directly in the area of the former mining and metallurgical complex (Fig.1). The slag deposit is also located within the mine area. Slime (tailing) dams are located north-east of the mining area. The total volume of the slimes is estimated at 343,500 m^3 (Mapani et al. 2010).

5 Materials and methods

Six tailing and slag samples as well as thirty soil samples and twenty plant samples (cassava and sweet potato tubers and leaves) were collected around Berg Aukas using the methodology recommended for the regional geochemical mapping by the FOREGS Geochemistry Working Group (Salminen et al. 1998).

Soils, slimes, and slag were analyzed for S_{tot}, C_{org}, C_{carb}, As, Cd, Cu, Fe, Hg, Mo, Pb, V, and Zn. Details of analytical procedures are given in Dempírová and Vitková (2002). Statistical characteristics of analytical data were obtained using S-plus non-parametric statistical program (MathSoft, USA). Geochemical data were expressed in the form of spot or isoline maps using SURFER (Golden Software Inc.) program. Agricultural products (cassava and sweet potato leaves) were properly washed by tap and distilled water and dried. Cassava and sweet potato roots were peeled, washed and dried. The plant samples were combusted in a muffle oven at the temperature of 400 °C. The amount of ash was scaled and the metals were analytically determined in HNO_3 and HCl leachate as described for the soil samples.

6 Results and discussion

6.1 Sources of contamination

The tailings contain high amounts of Zn, V, Cd, As, and Hg (Table 1). Approximately 18 % of the tailings consist of particles of less than 8 μm in diameter (PM8s). These particles pose the most serious health effects, as they enter the lungs. The slag is rich in Zn, Pb, V, Cu and As (Table 1). The amount of PM8s particles in the slag dust is low (1.3 %).

6.2 Distribution of metals and arsenic in soils

To differentiate between a geological source, i.e. primary geochemical regional background of elements in soils, and anthropogenic contamination, the concept of correlation between their concentrations in topsoil and in the subsurface soil horizon (70 to 90 cm depth) was accepted. Using this concept, higher concentrations of elements in the surface layer of soil compared to the deeper soil horizon were considered to represent anthropogenic contamination caused mainly by airborne dust particles. In contrast, higher concentrations of elements in the lower soil horizon compared with topsoils were considered to reflect the natural geochemical contribution from bedrock. For example, very high concentrations of As in surface soil (topsoil) compared with low concentrations of As in subsurface soil (Fig. 2), are interpreted to represent dust contamination.

Table 1. Average chemical composition of tailings and slag at Berg Aukas. S_{tot}, C_{org}, C_{carb} and Fe in wt.%, other elements in ppm.

	Tailings	Slag
S_{tot}	0.03	0.11
C_{org}	0.42	<0.01
C_{carb}	37.16	6.04
Fe	1.68	3.98
V	704	832
Zn	52 100	22 400
Mo	<5	13
Cd	352	<0.8
Cu	184	640
Pb	< 10	11 600
As	109	383
Hg	2.2	0.03

It was established that the degree of industrial contamination may be best expressed using the Coefficient of Industrial Pollution (CIP; Kříbek et al., 2010), which is a sum of the concentrations of selected potentially harmful elements in topsoil at the individual sampling points, divided by the median values of the same elements in topsoil of the whole region:

$$CIP=\left(\frac{As}{m}+\frac{Cd}{m}+\frac{Cu}{m}+\frac{Hg}{m}+\frac{Pb}{m}+\frac{Zn}{m}\right)/6,$$

Where m is a median value of the metal concentration.

At Berg Aukas, CIP values show an elongated halo in the downwind direction. The highest CIP values are located in the vicinity of mine wastes, slag deposits and tailing dams. The concentrations of trace metals in soils in the study area were compared with the Canadian soil quality limits for trace elements (CCME 2007). The Canadian guidelines for soils have different levels for agricultural, commercial and industrial land uses. Concentrations of metals above these limits are expected to be associated with adverse biological effects. It was found that 34 % of topsoil samples in Berg Aukas area exceed the Canadian limits for agricultural use in the case of Cu, 29 % in the case of Pb, 20 % in the case of Zn, and 12 % in the case of As. A small part of samples exceed the limits for Cd (3.4%) and Mo (1.7 %). The proportion of soil samples exceeding the limits for commercial and industrial land use is high only in the car of Cu (25.8%), Pb (13.8%) and Zn (6.9%).

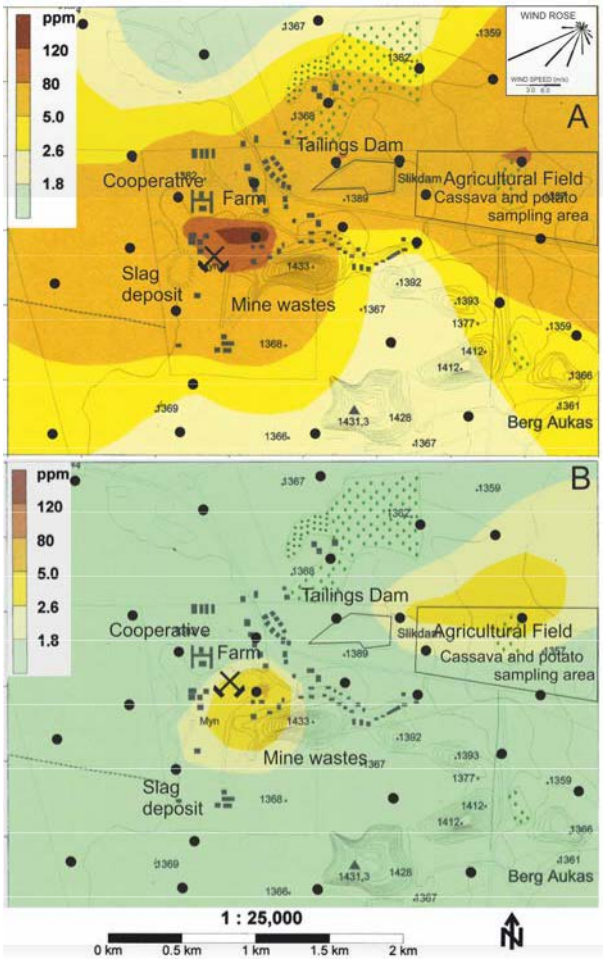


Figure 2. The distribution of As in topsoil (A) and in the subsurface soil horizon (70 to 90 cm depth; B).

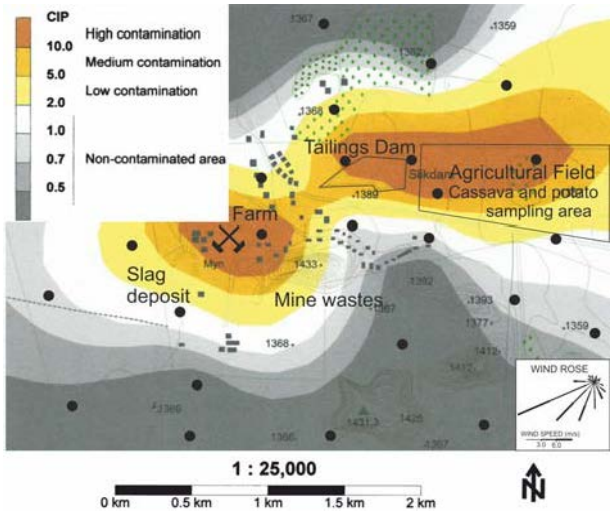


Figure 3. A contour map of the Coefficient of Industruial Pollution (CIP) in surface soils in the Berg Aukas area. Sampling points are marked by black dots. Exceeding the limits for commercial and industrial land use is high only in the case of Cu (25.8 %), Pb (13.8 %) and Zn (6.9 %).

6.2 Distribution PHEs in plants

The median and standard deviation values for cassava and sweet potato sampled in the region of the Berg Aukas mine are summarized in Tables 2 and 3.

Table 2. The median and standard deviation values for the concentrations of selected elements in cassava tubers and leaves. Data in mg.kg^{-1} on dry weight. Number of samples: 8.

Element	Cassava tubers		Cassava leaves	
	Median	2σ	Median	2σ*
As	0.28	0.03	0.73	0.15
Cd	0.1	0.05	0.76	0.22
Cu	3.4	0.9	7.1	0.33
Mo	0.25	0.02	1	0.94
Pb	4	2.3	65	18.7
Zn	49	11.1	359	98

* Standard deviation

Table 3. The median and standard deviation data for the concentrations of selected elements in sweet potato tubers and leaves. Data in mg.kg^{-1} on dry weight. Number of samples: 12.

Element	Sweet potato tubers		Sweet potato leaves	
	Median	2σ	Median	2σ*
As	1.15	0.37	2.17	0.37
Cd	0.1	0.06	1.0	0.18
Cu	4.52	1.83	7.45	1.52
Mo	0.025	1.41	0.025	0.39
Pb	25.5	19.1	166	33.8
Zn	103	63.6	771	121

* Standard deviation

All the studied cassava and sweet potato leaves and sweet potato tubers collected at the agricultural field located east of the tailing dams are characterized by As, Pb and Zn values in excess of WHO limits for food (Codex Alimentarius, WHO/FAO 2012, Fig. 4). Generally higher concentrations of PHEs occur in leaves than in roots. This corresponds with the higher bioaccumulation potential of leaves of both plants compared with tubers, as shown by Kříbek et al. (2014) in the Zambian Copperbelt. However, it is very probable that fine dust particles contribute to the high content of PHEs in leaves. Although leaves were properly washed, dust particles that settle on the sticky surface of leaves are very difficult to remove (Kříbek et al. 2014). The correlation coefficient values for individual PHEs in soil, cassava and sweet potato leaves and tubers were found to be low at individual sampling sites. This is believed to be due to the mixing of strongly contaminated topsoil with the deeper horizons in the soil profile caused by hoeing among the plants.

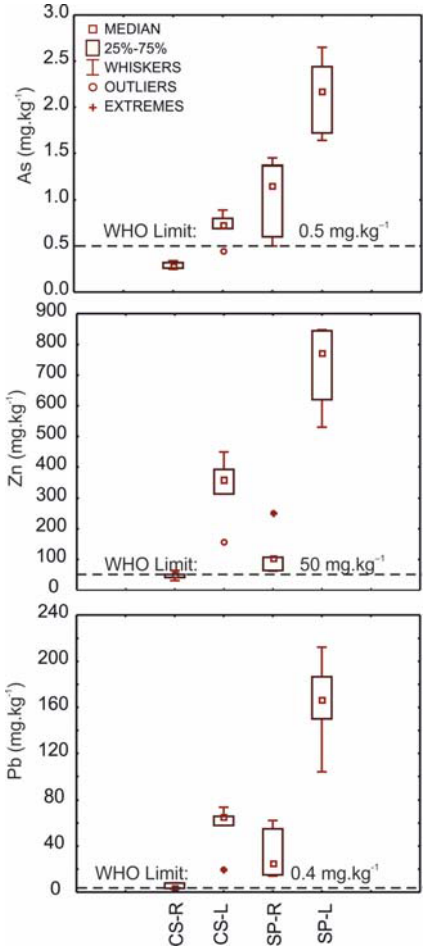


Figure 4. Statistical distribution (box-plots) of As, Zn and Pb concentrations in cassava and sweet potato peeled tubers and washed leaves and WHO/FAO limit values for food. Concentrations are expressed in dry weight. *Explanation:* CS-R: Cassava tuber, CS-L: Cassava leaves, SP-R: Sweet potato tubers, SP-L: Sweet potato leaves.

7 Conclusions and recommendations

The study shows that parts of the soil and vegetation in the Berg Aukas area are severely contaminated by As, Cd, Cu, Pb, Hg and Zn. The contamination dates back to historic ore roasting and wind-blown dust from slag dumps and tailings. People living and working at Berg Aukas face health risks from inhalation and ingestion of the dust as well as from ingestion of contaminated crops grown on contaminated soils. If humans are exposed to these heavy metals for longer periods, they may be subject to various heavy metal-triggered diseases and disorders.

There is an urgent need to react to the results of this study in the following ways:

(1) Awareness about the hazards associated with living conditions in the area must be created. This needs to be communicated to the residents as well as the local politicians.

(2) Heavily contaminated areas have to be delineated as no-go areas.

(3) Contaminated urban areas have to be remediated, e.g., by covering topsoil with organic matter and grasses or by pavement.

(4) It is recommended to cease crop production northeast of Berg Aukas, in the vicinity of the tailing dams.

Acknowledgements

This study was carried out within the framework of the Czech Science Foundation grant 16-13142S, Mining and Processing of Ores in Sub-Saharan Africa.

References

Boni M, Terracciano R, Evans NJ, Laukamp, C, Schneider J, Bechstädt T (2007) Genesis of vanadium ores in the Otavi Mountainland, Namibia. Econ Geol 102:441–469

Bezing L, Bode R, Jahn S (2008) Namibia Minerals and Localities.Edition Schloss Freudenstein, Bode Verlag GmbH, 263 p

CCME (Canadian Council of Ministres of the Environment) (2007) Canadian soil quality guidelines for the protection of environmental and human health. Summary tables, Update 7.0. CCME Ottawa, Canada. http://www.ccme.ca/assets/pdf/rev_soil_summary_tbl_7.0_e.pdf. Visited 14-01-2017

Dempírová L, Vitková H (2002) Methods of certified chemical analyses. MS., Czech Geological Survey, Prague, p. 230 (in Czech with English summary)

Kříbek B, Majer V, Veselovský F, Nyambe I. (2010) Discrimination of lithogenic and anthropogenic sources of metals and sulphur in soilsof the central-northern part of the Zambian Copperbelt Mining District: A topsoil vs. subsurface soil concept. J African Earth Sci 104:69–86

Kříbek B, Majer V, Knésl I, Nyambe I, Mihaljevič M, Ettler V, Sracek O (2014) Concentrations of arsenic, copper, cobalt, lead and zinc in cassava.(*Manihot esculenta* Crantz) growing on uncontaminated and contaminated soils of the Zambian Copperbelt. J African Earth Sci 99,713–723

Mapani B, Ellmies R, Kamona F, Kříbek B, Majer V, Knésl I, Pašava J, Mufenda M, Mbingeneeko F (2010) Potential human health risks associated with historic ore processing at Berg Aukas, Grootfontein area, Namibia. J African Earth Sci 58:634–647

Misiewicz JE (1988) The Geology and Metallogeny of the Otavi Mountain Land,Damara Orogen, SWA/Namibia, with Particular Reference to Berg Aukas Zn–Pb–V deposit: A model of genesis. M.Sc. Thesis, Rhodes University, Grahamstown, South Africa, p. 125.

Salminen R, Tarvainen T, Demetriadis, Duriš M, Fordyce FM, Odor L, Plant JA, Siewers U, Williams L (1998) FOREGS geochemical mapping field manual. Geological Survey of Finland, Guide 47. Geological Survey of Finland, Espoo, p. 89

WHO/FAO (2012) Codex Alimentarius. Official web site. www.codexalimentarius.net/web/index-en.jsp visited 20-01-2015

Greisenisation and permeability changes in granitic intrusions related to Sn-W deposits: case of Panasqueira

Gaëtan Launay, Stanislas Sizaret , Laurent Guillou-Frottier, Eric Gloaguen, Jérémie Melleton, Michel Pichavant and Rémi Champallier
Institut des Sciences de la Terre d'Orléans, BRGM, France

Filipe Pinto and Paulo Ferraz
Beralt Tin & Wolfram S.A.

Abstract. The W-Sn veins of Panasqueira are connected with a massive quartz-muscovite greisen cupola. This greisen results from interactions between granitic rock and acid Sn-W hydrothermal fluid, which causes the destruction of feldspars of the Panasqueira granite. Greisenisation can constitute an important factor of control on fluid flow, and its role on metal transport remains to be established. Mineral reactions of greisenisation involve a decrease of the rock volume and thus an increase porosity (~6%). Consequently permeability increases significantly (10^{-20} to 10^{-17} m²) enhancing fluid flow in the greisen cupola and promoting further hydrothermal alteration and transport of metals. Finally a part of the mineralization is trapped in this porosity, with precipitation of cassiterite and sulfides. Therefore, Sn-W fluids are able to generate their own pathways in initial impermeable granite via greisenisation reactions.

1 Introduction

Permeability is a critical parameter in processes of hydrothermal fluid flow and metals transport in magmatic-hydrothermal systems. Nowadays, fluid flow controlled by deformation and fracture permeability may be the most studied aspect of hydrothermal circulation in granitic intrusions. Greisenisation is a common type of hydrothermal alteration in apical parts of granitic intrusion related to Sn-W mineralization (Scherba 1970, Pirajno 1992). This metasomatic process can constitute another important controlling factor in hydrothermal fluid flow. Indeed, several authors have highlighted the impact of hydrothermal reactions on fluid flow via porosity and permeability changes (Yardley 1986, Ingebritsen and Appold 2012). Gain and loss of elements induced by mineral replacement reactions occurring during greisenisation can modify significantly the volume and the density of the rock (Stemprok et al. 2005, Halter 1996), and consequently affects fluid pathways by porosity and permeability changes. This time-dependant feature of the permeability is called hereafter 'dynamic permeability'.
This in turn can directly affect the continuation of hydrothermal circulation via potential feed-back between greisenisation and fluid circulation. However effects of greisenisation on the dynamic permeability that ultimately leads to fluid circulation and metals transport in granitic intrusion remains an important research topic. In order to investigate effects of greisenisation reactions, petrological study and experimental determinations of porosity and permeability have been combined for different granite alteration levels and various petrographic types from Panasqueira.

2 Geological setting of Panasqueira

The W-Sn-(Cu) Panasqueira deposit is located in the Central Iberian zone of Portugal (Fig. 1). This region is essentially composed of a flyshoïd series of schist and greywacke (Schist-Greywacke complex) folded and metamorphosed to lower greenschist grade during the Variscan orogeny. In the Panasqueira district, these schists are converted to spotted schist during the thermal metamorphism induced by the emplacement of the non-outcropping Panasqueira granite. The Sn-W mineralization occurs as dense network of sub-horizontal quartz-wolframite-cassiterite-sulfides veins concentrated in the vicinity of a hidden greisen cupola (Thadeu 1951, Kelly and Rye 1979) (Fig. 1). This greisen cupola represents the upper apex of the buried Panasqueira granite. Greisenisation of the granite results from interactions between granitic rocks and acid hydrothermal fluids which transport the Sn-W mineralization.

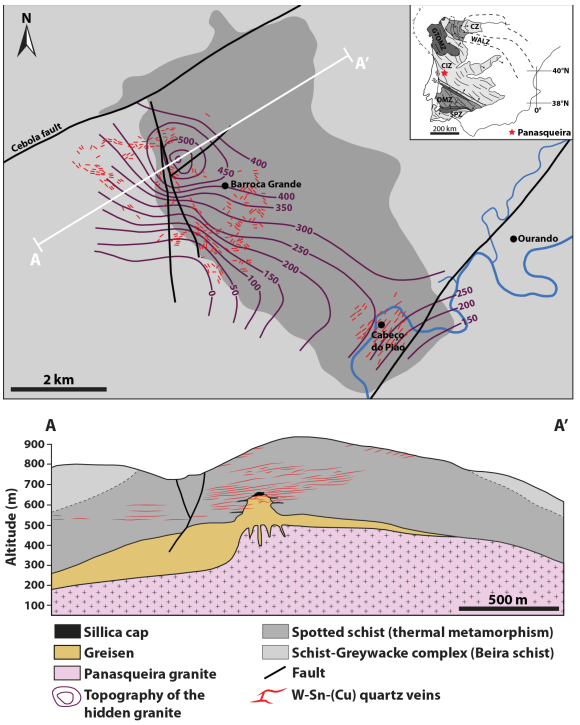


Figure 1. Location and cross-section of the Panasqueira deposit illustrating relationship between W-Sn veins and greisen.

3 Greisenisation and volume change

3.1 Alterations reactions

At Panasqueira, drill holes allow to follow the progressive transformation of the initial porphyric two micas granite in quartz-muscovite greisen from the deeper part to the apical part of the granitic body (Fig. 2). To determine mineralogical reactions involved by greisenisation, samples used in this study were selected in different levels of alteration between unaltered granite and the endmember muscovite-quartz greisen. Petrographic observations show that greisenisation caused destabilization and the total destruction of feldspars (Fig. 2b and 2d) and biotite (Fig. 2c) to produce the quartz muscovite assemblage (Fig. 2a) characteristic of the greisen. On the base of these observations we can define alteration reactions which occurred during greisenisation (Table 1).

3.2 Volumetric effects of greisenisation

The volume changes induced by alteration reactions defined previously can be calculated from molar volume data of each mineral phase and their stoichiometric coefficients. The molar volume change percentage (ΔV) is defined as the percent difference between the respective products of the stoichiometric coefficients and molar volumes of reactants and products:

$$\Delta V\ (\%) = 100.(\Sigma x^{p}_{i}.V_i - \Sigma x^{r}_{i}.V_i)/(\Sigma x^{r}_{i}.V)$$

With x^{p}_{i} and x^{r}_{i} which are respectively stoichiometric coefficients of product and reactant minerals and V_i the molar volumes of associated mineral. Hydrothermal fluid and its dissolved species are absent before and after alteration processes, so only solid phases are taken in consideration. Calculations of molar volume changes were made based on the thermodynamic database of SUPCRT92 (Johnson et al. 1992) for 1 kbar and 450°C. Results of volume changes induced by each alteration reactions are summarized in the following table.

Table 1 Alteration reactions and molar volume changes induced by greisenisation.

Greisenisation reactions	ΔV (%)
3 K-feldspar + 2 H^+ = Muscovite + 6 Quartz + 2 K^+	-15.3
3 Albite + 2 H^+ + K^+ = Muscovite + 6 Quartz + 3 Na^+	-7.7
3 Biotite + 0.65 O_2 + 12.6 H^+ = 2 Muscovite + 3 Quartz + K^+ + 4.8 Fe^{2+} + Mg^{2+} + 7.3 H_2O	-8.8

The replacement of biotite by muscovite and quartz is characterized by a volume decrease of 8.8%. Alteration reactions of K-feldspars and plagioclase are respectively associated with 15.3% and 7.7% of volume decreases. Feldspars are the most abundant minerals in the Panasqueira granite, thus their breakdown is able to generate significantly porosity in greisen. These results are compatibles with the presence of (i) vugs in altered sections of feldspars (Fig. 2b) and (ii) the vuggy texture of the endmember quartz-muscovite greisen (Fig. 2a).

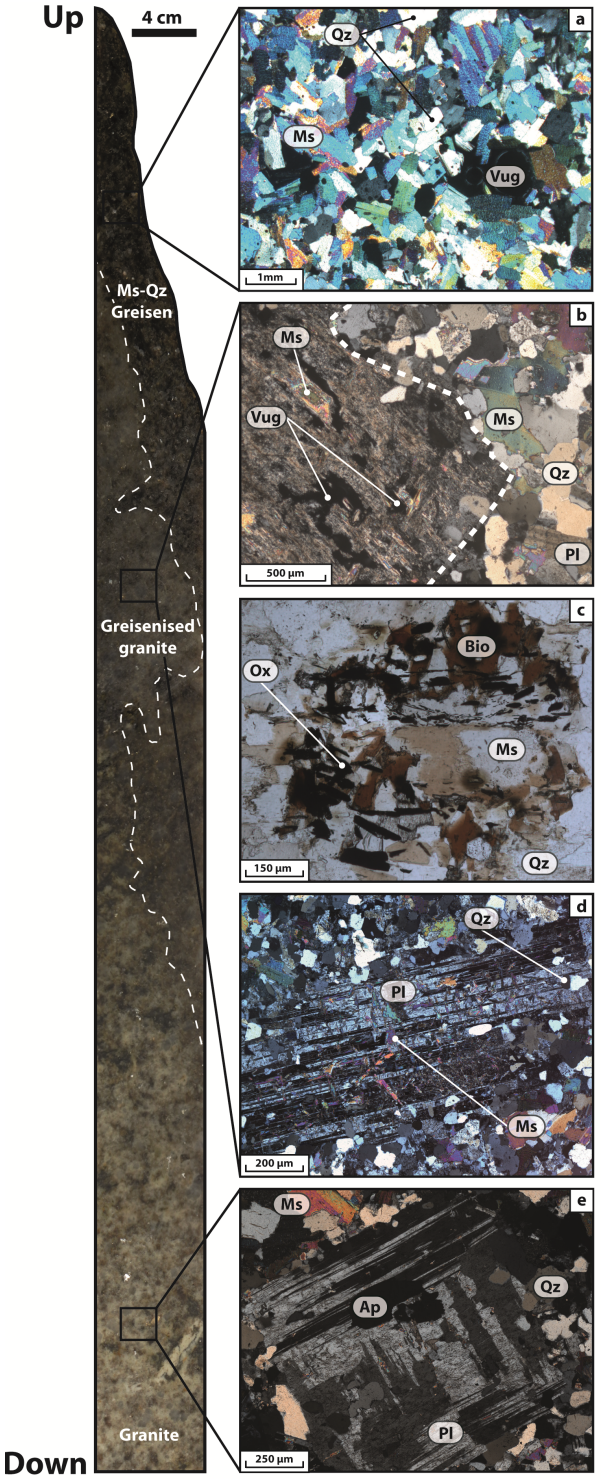


Figure 2. Zoned greisenisation of the Panasqueira granite in drill core section. **a** Section of the quartz-muscovite greisen endmember. **b** Section of K-feldspar replaced by muscovite. **c** Section of biotite bleached and partially transformed in muscovite. **d** Section of plagioclase partially altered and **e** section of fresh plagioclase in the unaltered granite.

4 Porosity and permeability changes with greisenisation

4.1 Experimental methods

Connected porosity and bulk density were measured by gravimetric method which consists of measuring mass changes when samples are saturated by a fluid. Mass of water in saturated samples allows calculating volumetric water contents and consequently the connected porosity of samples. Mass ratio between dry samples and difference between saturated and dry samples allow calculating the bulk density of samples.

Permeability measurements were performed with Paterson apparatus following the method described by Coelho et al. (2015). Experiments were performed at 400°C, 1 kbar of confinement pressure (Pc) and with 500 bar of pore fluid pressure (deionized water). Permeability was measured using steady-state flow method for Darcian flow which defines the flow rate (Q) proportional to the permeability (k) for an imposing pressure difference ($\Delta P \approx 5$ MPa) across the core sample:

$$k = (\mu * L * Q)/(A * \Delta P)$$

Where μ is the water viscosity at 400°C and 500 bar L (in m) and A (in m²) are respectively the length and the cross-sectional area of core samples. Fluid flow (Q in $m^3.s^{-1}$) across samples was calculated from the volume of fluid injected in samples over experiment time.

4.2 Results

Evolution of density and connected porosity are plotted in function of alteration index of the rock (Al_2O_3/Na_2O+K_2O) based on the progressive transformation of feldspars in muscovite during greisenisation (Fig. 3a and 3b). The initial granite is characterized by a bulk density of 2.65 $g.cm^{-3}$ and a low connected porosity of 0.56%. Evolutions of bulk density and connected porosity are positively correlated with index of alteration (Fig. 3a and 3b). Value of bulk density increases from 2.65 to 2.87 $g.cm^{-3}$ and connected porosity strongly increases from 0.56 to 5.86%. As expected, the endmember quartz-muscovite greisen is more porous than unaltered granite. Permeability evolution is reported in function of the connected porosity (Fig. 3c). The unaltered granite is impermeable and presents a permeability value of 10^{-20} m², comparable to the average of permeability in granitic rocks. The porosity increase induced by hydrothermal alteration progression causes an important permeability increase following the theoretical relation between permeability and porosity of rock proposed by Wark and Watson (1998). Consequently, the important increase of connected porosity in greisen clearly implies a significant increase of permeability in the muscovite-quartz greisen (10^{-17} m²).

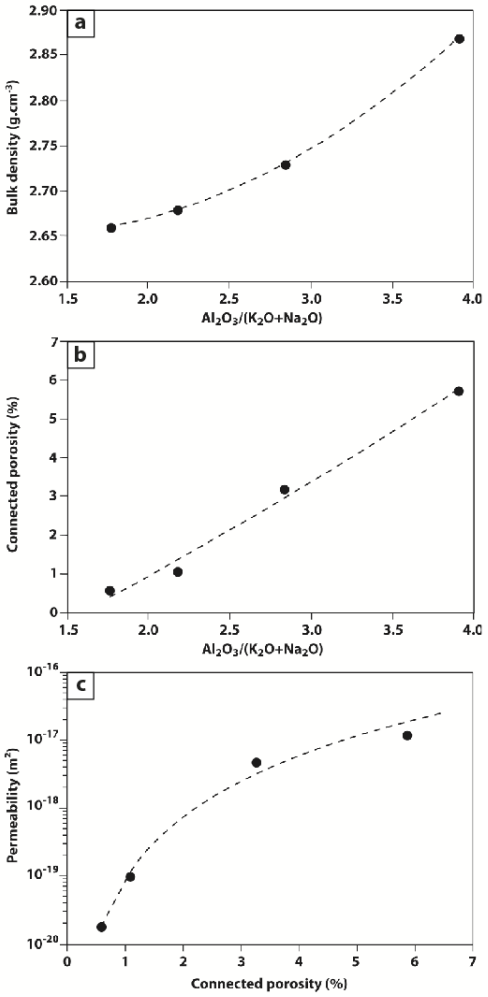


Figure 3. Evolution of **a** bulk density and **b** connected porosity in function of the alteration index $Al_2O_3/(Na_2O+K_2O)$. **c** Evolution of permeability in function of connected porosity.

5 Numerical modelling of greisenisation effect on fluid flow

5.1 Model geometry and parameters

Previous results suggest that permeability of granitic intrusion evolves significantly during greisenisation. This permeability change have been integrated in numerical modelling performed with Comsol Multiphysics™ by coupling Darcy's law and heat equation to determine effect of greisenisation on Sn-W fluid flow. The granite is characterized by an initial temperature of 850°C and an initial permeability of 10^{-20} m². With time, the granite cools progressively and its permeability increase in function of the pressure gradient which constrain preferential sites of hydrothermal alteration. The parameters of the matrix are based on schist properties. A fixed pressure is imposed on top boundary while no flow is allowed on others and there is no heat flow on lateral boundaries.

5.2 Numerical results

Preliminary results show that greisenisation can play a key role on fluid flow in and around granitic intrusion. Dynamic time-varying permeability in the apex and along the roof of the intrusion increases significantly and is self-sustaining during the greisenisation (Fig. 4a). This permeability increase causes the enlargement of the fluid pathways in the upper part of the granitic intrusion and increases significantly fluid velocity above the apex (Fig. 4b), and consequently enhances metal transport (Sn-W) in the apical part of granitic intrusion.

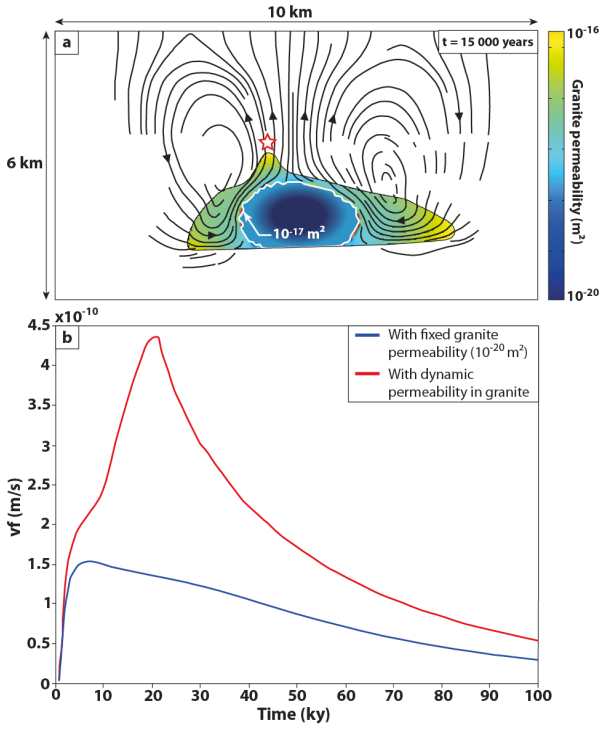


Figure 4. **a** Numerical solution (at 15 000 years) of fluid flow around granitic intrusion with dynamic permeability in the granite **b** fluid velocity above the apex (red star) between with fixed and dynamic permeability in the granite.

6 Discussion and conclusion

In the W-Sn veins-greisen system of Panasqueira, the intense fluid flow in the upper part of the granitic intrusion strongly changes the mineralogy of the granite. The total breakdown of feldspars during greisenisation causes a mineral volume reduction of 6%. This process of mineral volume reduction has direct effects on petrophysical and hydrodynamic features of granitic rock. First, the remaining mass of rock is reduced in a lower mineral volume, consequently the rock density increases progressively with progression of greisenisation. Second, the mineral volume decrease implies connected porosity creation and expansion in greisen, thus increasing the permeability of the intrusive body. As a result, greisenisation induced by W-Sn fluid flow in granite enhances fluid circulation by enlarging the network of fluid pathway. In this case, hydrothermal alteration has a positive feedback on permeability and consequently on metal transport by focussing of fluid in the most permeable zone of granitic intrusion. Presence of cassiterite (Fig. 5a) and sulfides (Fig. 5b) which infill partially the porosity confirms that fluids which transport metals have flowed in the greisen via the neo-formed porosity.

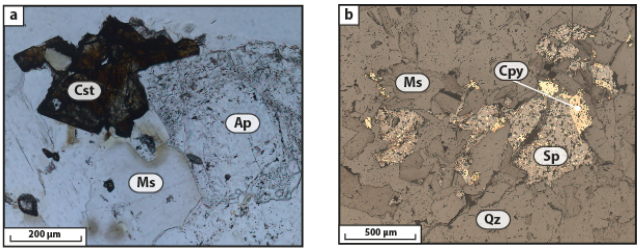


Figure 5. Infilling of vugs generated during greisenisation by **a** cassiterite and apatite **b** sphalerite and chalcopyrite.

In conclusion hydrothermal fluids at the origin of the Panasqueira deposit made their own pathway in the granite via greisenisation reactions which improve significantly fluid circulation and focusing it in the apical part of granitic intrusion. The greisenisation is not just a passive process of hydrothermal circulation but can play a key role during fluid flow in Sn-W ore deposit system.

References

Coelho G, Branquet Y, Sizaret S, Arbaret L, Champallier R, Rozenbaum O (2015) Permeability of sheeted dykes beneath oceanic ridges: Strain experiments coupled with 3D numerical modeling of the Troodos Ophiolite, Cyprus. Tectonophysics 644:138-150

Halter WE (1996) The role of greisenization in cassiterite precipitation at the East Kemptville tin deposit, Nova Scotia. Econ Geol 91(2):368-385

Ingebritsen SE, Appold MS (2012) The physical hydrogeology of ore Deposits. Econ Geol 107:559-584

Johnson JW, Oelkers EH, Helgeson HC (1992) SUPCRT92: A software package for calculating the standard molal thermodynamic properties of minerals, gases, aqueous species, and reactions from 1 to 5000 bar and 0 to 1000°C. Computers and Geosciences 18(7):899-947

Kelly WC, Rye RO (1979) Geologic, fluid inclusion, and stable isotope studies of the tin-tungsten deposits of Panasqueira, Portugal. Econ Geol 74(8):1721-1822.

Pirajno F (1992) Hydrothermal Mineral Deposits: Principles and Fundamental Concepts for the Exploration Geologist. Springer-Verlag, Berlin, Heidelberg, New York, London, Paris, Tokyo, Hong Kong

Scherba GN (1970) Greisens: International Geology Review 12:114-150

Štemprok M, Pivec E, Langrová A (2005) The petrogenesis of a wolframite-bearing greisen in the Vykmanov granite stock, Western Krušné hory pluton (Czech Republic). Bull Geosci 80(3):163-184

Thadeu D (1951) Geologia do Couto Mineiro da Panasqueira. Comunicações dos Serviços Geológicos de Portugal 32:5-64

Wark DA, Watson EB (1998) Grain-scale permeabilities of texturally equilibrated, monomineralic rocks. Earth Planet Sci Lett 164:591-605

Yardley BWD (1986) Fluid migration and veining in the Connemara Schists, in Walther JV, Wood BJ, eds. Fluid-rock reactions during metamorphism: Advances in Physical Geochemistry. Springer-Verlag, New York, 5:109-13.

Petrogenesis and tectonic implications of the Triassic granitoid plutons in west Qinling Mountains, China: insights from LA-ICP-MS zircon U-Pb ages, and Lu-Hf isotope of the Zhongchuan pluton

Jiajun Liu, Shangsong Yang, Degao Zhai, Jianping Wang, Yinhong Wang, Zhenjiang Liu, Fangfang Zhang, Feng Yuan
China University of Geosciences, Beijing, China

Abstract. The Zhongchuan pluton is one of the most important acidic–intermediate plutons in the western Qinling orogenic belt. The authors collected geochemical and geochronologycal data for the Triassic granitoid plutons of the west Qinling Mountains and found that nearly all plutons share the similar features with the Zhongchuan pluton. We present new LA-ICP-MS zircon U-Pb ages, major and trace element geochemistry, and zircon Hf isotope systematics for the granites of the Zhongchuan pluton to elucidate the evolution of granitoid plutons in the western Qinling Mountains during the Triassic. LA-ICP-MS zircon U-Pb dating indicates that the Xujiaba and Guandigou units formed at 220.1±1.2 Ma and 215.9±0.85 Ma, respectively, reflecting the time of the Late Triassic. The zircon Hf isotope dating indicates that the Xujiaba and Guandigou units have an inhomogeneous $\varepsilon_{Hf}(t)$ and two-stage Hf model ages. The isotopic data imply that the granites of each unit share the same origin, which probably derived from the partial melt of metagreywackes and then mixed with the mantle-derived magma. Based on the regional geological history, petrographic characteristics and new geochemical and isotopic data of the Zhongchuan pluton, we suggest that the Triassic magma was derived from the partial melts of metagreywackes and was influenced by the mantle-derived melt during the collision of the Yangtze and Qinling plates.

1 Introduction

The western Qinling orogenic belt is characterized by a number of acidic–intermediate plutons and many types of ore deposits such as gold, lead, zinc, uranium and molybdenum. Most of deposits are situated along granitoid contacts or hosted by the intrusion directly. Though the relationship between metallogeny and magma activities in the western Qinling Mountains still remains controversial, it is accepted that the granitoid bodies can define the maximum age of the gold mineralization (Zeng et al. 2012; Zhu et al. 2013), which means precise and accurate ages of granitoid bodies are not only very essential for the research of tectonic evolution, but also very important for understanding metallogenesis.

The Zhongchuan pluton (Fig. 1) is one of the very important granitic plutons in this area with abundant gold resources such as the Liba, Maquan, Minhua and Jinshan gold deposits. Different formation ages for the pluton have been obtained from diverse techniques, such as from 232 to 199 from K-Ar dating (Song et al. 1997), 232.9 ± 14Ma from Rb-Sr dating (Song et al. 1997), and 264.4 ± 1.3 to 207 ± 1 Ma from U-Pb dating (Zhu et al. 2013; Nie, 2015).

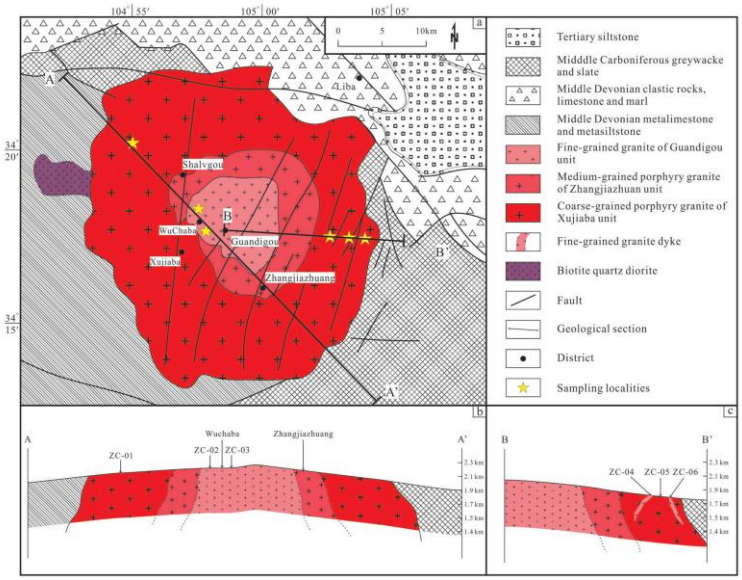


Figure 1. a Distribution plan of the Zhongchua composite granite intrusion (modified after Li et al. 2012; Zhu et al. 2013); **b** Geological section of A-A'; **c** Geological section of B-B'

In terms of the petrogenesis, several researchers have classified the granites of the Zhongchuan pluton to S-type granites, which were formed by crustal melt (Li et al. 2012). Nie (2015) proposed that they were metaluminous or peraluminous high K calc-alkaline series and I-type granites. However, Peng (2012) suggested that the rock group includes S-and I-type granites, with the S-type being the main type. With respect to the relationship with metallogeny, many researchers supported the view that the pluton provides the metallogenic heat but no metallogenic material for the deposits nearby (Song et al. 1997; Zhang and Zhang, 2008).

However, the large range and poor precision of the pluton age limited the understanding of the relationship between pluton and metallogeny. To better constrain the petrogenesis and geodynamic setting of the Zhongchuan pluton, we use the in situ U-Pb and Hf data of zircons to constrain the genesis and geodynamic setting of the Zhongchuan pluton in the west Qinling Mountains.

2 Petrography of the Zhongchuan pluton

The Zhongchuan pluton has an exposed area of 210 km^2 and intruded into clastic rocks, Devonian limestone and Carboniferous greywacke slate (Fig. 1a). It is surrounded by alteration zones such as the andalusite-cordierite zone, biotite zone and sericite-chlorite zone from the inside to outside. The width of each alteration zone is generally 5 km. The shape of the Zhongchuan pluton is close to a concentric circle. It mainly consist of monzogranite with different structures. From the inside out, the pluton can be divided into three granitic units, known as the Guandigou, Zhangjiazhuang and Xujiaba units (Fig. 2a) (Song et al. 1997; Peng 2012), which have no clear boundaries. Moreover, the Xujiaba unit hosts several fine-grained granite dykes (Figs. 1c and 2a) and mafic microgranular enclaves (MMES) (Fig. 2b)

The main lithology of the Zhongchuan pluton is monzogranite. With respect to spatial variation, the granularity of the monzogranite changed from coarse-grained to fine-grained and the number of phenocrysts (2-10 mm euhedral K-feldspar and a few plagioclases) decreased from the Xujiaba to Guandigou units. The monzogranite of the Zhongchuan pluton is pale brown and mainly composed of K-feldspar (30~40%, xenomorphic granular with simple or crosshatched twins), plagioclase (25~30%, euhedral-subhedral granular with oscillatory zoning and polysynthetic twins), quartz (25~30%, xenomorphic granular), and biotite (10~15%, euhedral schistose and xenomorphic granular). Accessory minerals include monazite (euhedral columnar granular with oscillatory zoning), apatite, zircon, allanite and magnetite. The main rock of the granite dykes in the Xujiaba unit is fine-grained monzogranite, with a mineral composition similar to that of the Zhongchuan host granitoids. The mafic microgranular enclaves have mainly irregular and sub-rounded or ellipsoid shapes, showing a fine-grained structure and massive texture. They are composed of biotite (15-20%), amphibole (15-20%), quartz (5-10%), plagioclase (35-45%) and K-feldspar (~5%) (Nie 2015).

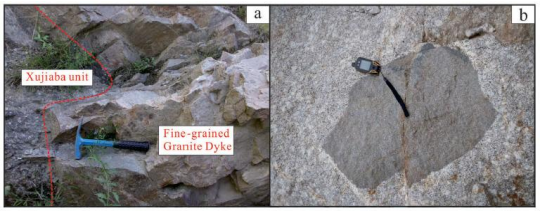


Figure 2. The characteristic photos of the Zhongchuan granites. **a** The granitic dyke in the Xujiaba unit; **b** The mafic microgranular enclaves (MMES) in the Xujiaba unit

3 Zircon U-Pb ages

Two representative granite samples from the Zhongchuan pluton (sample ZC-05 from the Xujiaba unit and ZC-03 from the Guandigou unit) were analyzed by zircon LA-ICP-MS dating. Based on the CL images, the zircons of the two samples are transparent, colorless, euhedral crystals, commonly exhibiting concentric oscillatory zones with length-width ratios from 3:1 to 4:1 (Fig. 3a, b), which indicate that the crystals are typical magmatic zircons.

The sample ZC-05 was collected in the east of the pluton (Xujiaba unit). A total of 35 zircons were chosen for LA-ICP-MS U-Pb analyses. Seven of the zircons own a little older ages, which might be infected by the inherited obtained from the remaining 26 concordant samples vary zircons and represent mixed ages. The $^{206}Pb/^{238}U$ ages from 225 to 213 Ma, yielding a weighted mean $^{206}Pb/^{238}U$ age of

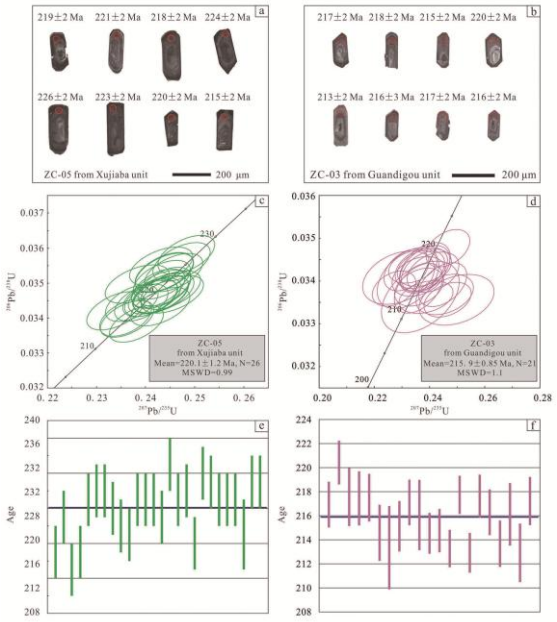


Figure 3. **a** and **b** Cathodoluminescence images of representative zircon grains; **c** and **d** The zircon U-Pb concordia diagrams for Xujiaba and Guandigou units; **e** and **f** $^{206}Pb/^{238}U$ probability density histograms for Xujiaba and Guandigou units

220.1 ± 1.2 Ma (MSWD=0.99; Fig. 3c, e), which is interpreted to represent the formation age of the Xujiaba unit.

The sample ZC-03, collected close to the center of the pluton, is a good representative of the Guandigou unit. Twenty-one of the 27 analyses on 27 zircons grains show that the $^{206}Pb/^{238}U$ ages vary from 207 Ma to 220 Ma, yielding a concordant group with a weighted mean age of 215.9 ± 0.85 Ma (MSWD=1.1) (Fig. 3d, f), which is interpreted as the best estimate of the crystallization age of the granite from the Guandigou unit. Spot 7 (207 Ma) is slightly younger than the other spots due to hydrothermal activities. The other five zircon ages (spot 4, 13, 18, 22 and 23) range from 483 Ma to 1655 Ma, which may reflect the age of inheritable zircons.

4 Discussion

4.1 Geochronology

Zircon, one of the most common accessory minerals, has been chosen as the most ideal object for U-Pb dating because of its stable crystal texture, low common lead concentration and high sealing temperature (Wilde et al. 2001). We chose the most likely magmatic zircons of the sample ZC-05 and ZC-03 for U-Pb dating and obtained the weighted mean $^{206}Pb/^{238}U$ ages of 220.1 ± 1.2 Ma (MSWD=0.99) and 215.9 ± 0.85 Ma (MSWD=1.1) (Fig. 3), respectively, which are interpreted as the best estimate of the crystallization age of the granites of the Xujiaba and Guandigou units and indicate that the granites become younger from the outside to the inside.

4.2 Petrogenesis

In recent years, based on zircon U-Pb age and Hf-O isotopic research, two important views about the origin of the I-type granitoids have been proposed; the melt of the sediment can produce I-type granitoid under the influence of the mantle source magma (Kemp et al. 2007; Zhu et al. 2009) and the decrease of the sediment contribution during crust thinning can also produce the I-type granitoid (Collins and Richards, 2008; Zhu et al. 2009). In Fig. 4a, the younger zircons own lower $\varepsilon_{Hf}(t)$ values, which means that the sediment contribution was increasing during the magma process. The inhomogeneous calculated $\varepsilon_{Hf}(t)$ values (-4.425 to 1.067 for ZC-05 and -4.920 to 2.042 for ZC-03's magmatic zircons)(Fig. 4) illustrate that there was an open system causing the changes of the melt $^{176}Hf/^{177}Hf$ ratio when the magma intruded (Kemp et al. 2007; Zhu et al. 2009). This open system is considered the mantle source material with more radiogenic Hf (Kemp et al. 2007; Zhu et al. 2009). Experimental studies have shown that melts from the basaltic lower crust have low Mg# values of less than 40 regardless of the melting degree (Guan et al. 2012), which implies that the Zhongchuan granites with a Mg# of 28-54 (most are greater than 40) were associated with mantle components. Furthermore, the existence of mafic microgranular enclaves (MMES) (Fig. 2b), which

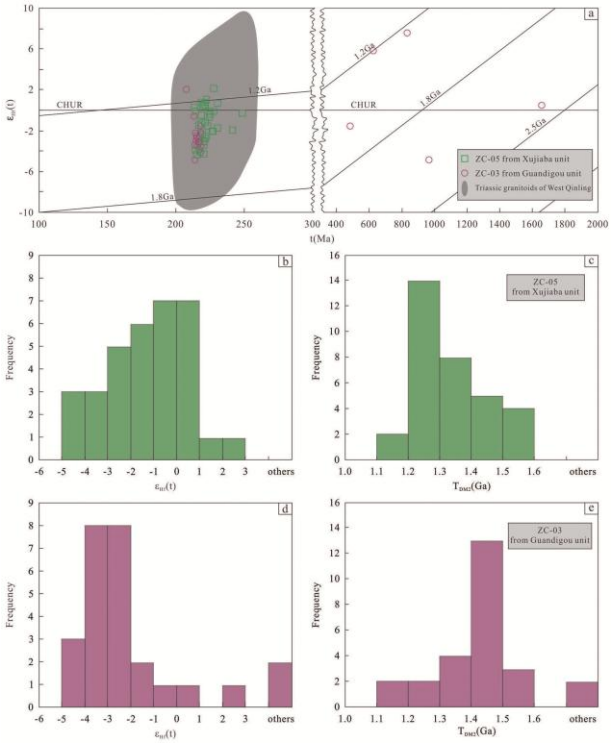


Figure 4. a Correlation diagram of zircon $\varepsilon_{Hf}(t)$ versus U-Pb ages of the Zhongchuan pluton (after Rollinson 1993); **b** and **d** Histograms of zircon $\varepsilon_{Hf}(t)$ values; **c** and **e** Histograms of zircon T_{DM2}. The data for Triassic granitoids of West Qinling are mainly from Jiang et al. (2010), Lei et al. (2011), Yang et al. (2014) and Li et al. (2015).

has been confirmed to be derived from partial melting of the continental lithospheric mantle (Zhu et al. 2013), also provides evidence for the addition of mantle-derived magma.

Because most Triassic granitoid plutons share similar petrographic features, geochemical characteristics and isotopic composition (Fig. 4) to the Zhongchuan pluton, we conclude that the Triassic granitoid magma of the west Qinling Mountains originated from the partial melting of metagreywackes. The magma gradually transformed into I-type granite under the influence of mantle-derived magma as the magmatic activity continued, leading to the I-type characteristics of the granitoids.

The Zhongchuan pluton with concentric circle texture has been divided into three different lithologic units from the inside out, but there are no clear boundaries between each unit. Song et al. (1997) have reported that the transition relations between the older and younger units are shown clearly near Shalvgou (Fig. 1). The granites of the three units have similar geochemical compositions, which means that the Zhongchuan pluton formed from the same parent magma and experienced similar evolution process. According to the isotope data, the forming ages of Xujiaba and Guandigou units are too close for repeated crustal melting. Furthermore, the similar Hf isotopic composition indicates that the two units came from the same source (Fig. 4). Therefore, we suggest that the different units of Zhongchuang pluton formed from the same parent magma

after continuous and repeated intrusion, and the fractional crystallization was more important during the evolution process.

4.3 Geodynamic setting

The formation of the Triassic plutons in the west Qinling Mountains is related to the northward subduction of the Yangtze plate. In the Late Indosinian, the Yangtze plate subducted northward and collided with the Qinling plate, which resulted in the closing of the Paleo-Tethys Ocean (Fig. 5). Under this structural setting, the continental crust thickening caused the old crust melt to produce S-type granitic melt. The mantle-derived magma injected into the S-type melt when the S-type melt intruded into the Devonian and Carboniferous strata, which lead to the gradual transformation to I-type melt. The incompletely mixed mantle-derived magma formed the mafic microgranular enclaves (MMES). Furthermore, the continuity and multiplicity of the Zhonghuan magma intrusion process caused the concentric structure of the Zhongchuan pluton, with three transitional lithologic units and granite dykes in the Xujiaba unit.

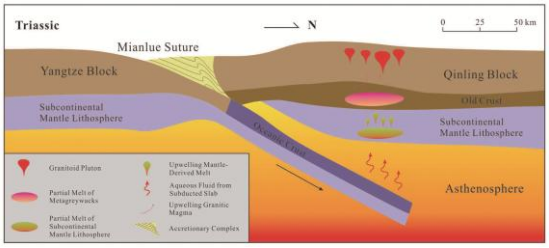


Figure 5. Schematic illustration for the formation of the Late Triassic granitoids in west Qinling

5 Conclusions

(1) The Zhongchuan pluton formed at 220.1±1.2 Ma to 215.9±0.85 Ma, corresponding to Triassic magmatism in the west Qinling Mountains.
(2) The Triassic granitoid magma of the west Qinling Mountains originated from the partial melting of old crust, mainly composed of clay-poor psammitolite, and were changed by mantle-derived magma, resulting in that the host granitoid show both characteristics of I- and S-type granites.
(3) Based on the regional geological history and new geochemical data, we suggest that the Triassic plutons in the west Qinling Mountains are the product of the collision of the Yangtze and Qinling plates.

Acknowledgements

This research was supported financially by the National Natural Science Foundation of China (Grants 41573036 and 41030423) and the Chinese “111” project (Grant B07011).

References

Collins WJ, and Richards SW (2008) Geodynamic significance of S-type granites in circum-Pacific orogens. Geol 36: 559–562
Guan Q, Zhu DC, Zhao ZD, Dong GC, Zhang LL, Li XW, Liu M, Mo XX, Liu YS, Yuan HL (2012) Crustal thickening prior to 38 Ma in southern Tibet: evidence from lower crust-derived adakitic magmatism in the Gangdese Batholith. Gondwana Res 21: 88–99
Kemp AIS, Hawkesworth CJ, Foster GL, Paterson BA, Woodhead JD, Hergt JM, Gray CM, Whitehouse MJ (2007) Magmatic and crustal differentiation history of granitic rocks from Hf-O isotopes in zircon. Sci 315: 980–983
Jiang YH, Jin GD, Liao SY, Zhou Q, Zhao P (2010) Geochemical and Sr–Nd–Hf isotopic constraints on the origin of Late Triassic granitoids from the Qinling orogen, central China: Implications for a continental arc to continent–continent collision. Lithos 117: 183–197
Lei M, Wu CL, Wu XP, Gao YH, Wu SP, Chen QL, Qin HP (2011) Zircon SHRIMP U-Pb datings of granite and its enclave from Xinyuan pluton, Southern Qinling Mountains, and their geological significance. Geol Rev 57: 889–899 (in Chinese with English abstract)
Li N, Ulrich T, Chen YJ, Thomsen TB, Pease V, Pirajno F (2012) Fluid evolution of the Yuchiling porphyry Mo deposit, East Qinling, China. Ore Geol Rev 48: 442–459
Li XW, Mo XX, Huang XF, Dong GC, Yu XH, Luo MF, Liu YB (2015) U–Pb zircon geochronology, geochemical and Sr–Nd–Hf isotopic compositions of the Early Indosinian Tongren Pluton in West Qinling: Petrogenesis and geodynamic implications. J Asian Earth Sci 97: 38–50
Nie ZR (2015) Age, geochemistry, Magma mixing of Zhongchuan granitoid pluton in the Western Qinling. China University of Geosciences (Beijing), pp 1–90 (in Chinese with English abstract)
Peng X (2012) Magmatic consanguinity and tectonic significance of Zhongchuan rock group in western Qinling. Chang'an University, pp 1–71 (in Chinese with English abstract)
Rollinson HR (1993) Using geochemical data: Evolution, presentation, interpretation. Longman Scientific and Technical, New York, pp 1–352
Song ZB, Feng YM, He SP (1997) Characteristics of tectono–magmatism of Zhongchuan granite and its ore-forming process. J Xi'an Engin Univ 4: 48–52 (in Chinese with English abstract)
Wilde SA, Valley JW, Peck WH, Graham CM (2001) Evidence from detrital zircons for the existence of continental crust and oceans on the Earth 4.4 Gyr ago. Nature 409: 175–178.
Yang PT, Liu SW, Li QG, Wang ZQ, Zhang F, Wang W (2014) Chronology and petrogenesis of the Hejiazhuang granitoid pluton and its constraints on the Early Triassic tectonic evolution of the South Qinling Belt. Sci China (Earth Sci) 57: 232–246
Zeng QT, McCuaig TC, Hart CJR, Jourdan F, Muhling J, Bagas L (2012) Structural and geochronological studies on the Liba goldfield of the West Qinling Orogen, Central China. Mineral Deposita 47: 799–819
Zhang YL, Zhang CZ (2008) Discussion on the genesis of Zhongchuan uranium deposit. Uranium Geol 24(5): 275–281 (in Chinese with English abstract)
Zhu DC, Mo XX, Wang LQ, Zhao ZD, Niu YL, Zhou CY, Yang YH (2009) Petrogenesis of highly fractionated I-type granites in the Chayu area of eastern Gangdese, Tibet, Constraints from zircon U-Pb geochronology and Sr-Nd-Hf isotopes. Sci China (Earth Sci) 39: 833–484 (in Chinese)
Zhu LM, Zhang GW, Yang T, Wang F, Gong HJ (2013) Geochronology, petrogenesis and tectonic implications of the Zhongchuan granitic pluton in the Western Qinling metallogenic belt, China. Geol J 48: 310–334

Trace elements in sphalerite from the Stan Terg Pb-Zn deposit, Kosovo

Sławomir Mederski, Joanna Kołodziejczyk and Jaroslav Pršek
AGH University of Science and Technology, Kraków, Poland

Abstract. Trace elements in sphalerite from the Stan Terg deposit hydrothermal system (Kosovo) were measured by LA-ICPMS. Stan Terg is world class Pb-Zn deposit located in the Trepça Mineral Belt, central Balkan Peninsula, Kosovo. Deposit was classified as Pb-Zn-Ag skarn, or as a carbonate replacement deposit type. The most important minor elements in sphalerite are Fe, Mn and Cd, on average 9.69 wt.%, 0.43 wt.% and 0.15 wt.%, respectively. Copper, Sn and In are another significant minor elements. The highest Sn contents were observed in the northern part of the deposit (336 and 204 ppm). Sphalerite in the central part of the deposit (skarn mineralization) is depleted in the trace and minor elements, but has the highest Hg content (14 ppm). The highest concentrations of In in sphalerite were found in samples from the southern part of the deposit (up to 97 ppm).

1 Introduction

Trace elements content in sphalerite may provide petrogenetic information about metal source and the crystallization temperature (Cook et al. 2009). In the recent years there were many attempts to assign chemistry of sphalerite to ore deposit types (e.g. Cook et al. 2009; Ye et al. 2011; Belissont et al. 2014).

In this project trace element analyses were used to describe diversification in Stan Terg orebodies and its mineralization styles for the entire hydrothermal system, which extend about 2 km horizontally and over 700 meters below surface.

2 Samples and investigation methods

2.1 Investigated material

Sphalerite and galena are the main ore minerals in the Stan Terg deposit. Sphalerite occurs as black colour variation and in coarse-grained form. Representative samples of various ore types (skarn, hydrothermal-replacement, rhodochrosite-style, vein) were collected in the various orebodies at different mining horizons. Orebodies in the Stan Terg hydrothermal system have almost vertical manto-like, shape. Samples collected in 147C, 147B0 stopes in southern part of the deposit are marked in this work as "x7". They are abundant with typical hydrothermal mineralization, as well as banded-rhodochrosite type of mineralization. Samples collected in stopes No. 80, 90, 100, 140, 150 are from so called central orebody, and are marked as "x0" and have skarn or hydrothermal-replacement character. Samples collected in "x1" (stope No. 141 with skarn mineralization), "x8" (stopes No. 148, 148a, 148-43 with hydrothermal-replacement mineralization) and "x9" from stopes No. 149, 149-C2, 149-C3, 149e, 149F with skarn, hydrothermal, vein and rhodochrosite type of mineralization. Sphalerite crystals selected for trace element analyses are free of mineral inclusions visible in reflected light and BSE images.

2.2 Analytical techniques

Preliminary chemical analyses of sphalerite were carried out by electron microprobe (EPMA) at the Critical Elements Laboratory AGH-KGHM in Kraków, Poland. Operating conditions were an accelerating voltage of 20 kV, a beam current 20 nA, peak time of 20 sec, and a background time of 10 sec. Natural mineral standards (FeS_2, ZnS) and syntetic standards (CdS, InAs, Cu, SnS, HgTe, MnS, Ag, GaP, GeS) were used for calibration.

Trace elements analyses were performed by laser ablation inductively coupled plasma mass spectrometry (LA-ICPMS) using 193 nm New Wave UP193FX laser ablation system linked to a Perkin-Elmer Sciex ELAN DRC-e quadrupole ICPMS at the Geological Institute of the Bulgarian Academy of Science in Sofia, Bulgaria. The following isotopes were monitored ^{49}Ti, ^{51}V, ^{53}Cr, ^{55}Mn, ^{57}Fe, ^{59}Co, ^{62}Ni, ^{65}Cu, ^{66}Zn, ^{69}Ga, ^{74}Ge, ^{75}As, $^{82/77}$Se, ^{95}Mo, ^{107}Ag, ^{111}Cd, ^{115}In, ^{118}Sn, ^{121}Sb, ^{125}Te, ^{181}Ta, ^{182}W, ^{197}Au, ^{202}Hg, ^{205}Tl, ^{208}Pb and ^{209}Bi. Ablation was done using 35 μm diameter spot size; laser energy density was > 9 J/cm^{-2} with pulse frequency of 10 Hz. External standards MASS1 sulphide standard (USGS) and NIST SRM 610 were used for calibration. Data reduction was undertaken using Zn (determined by EPMA) as internal standard and by SILLS software (Guillong et al. 2008). Content of zinc was systematically checked in all analyses and they were not any fluctuation in the content in the individual grains. For the LA-ICP-MS calculations were used direct values for the proper grains. Concentration of elements was calculated on LA-ICPMS spectra with no clearly visible micro-inclusions.

3 Geology

Stan Terg Pb-Zn deposit is located in the Trepça Mineral Belt, which is related to the NW-SE trending Vardar Zone, between the Dinaride Alpine Belt and the Serbo-Kosovaro-Macedonian Massif (Hyseni et al. 2010, Strmić Palinkaš et al. 2013).

The main tectonic structure in the deposit is an anticline plunging at about 40° NW, with a volcanic breccia pipe along the hinge of the asymmetric anticline. The anticline core of the structure consists of Upper Triassic carbonates (marbles and metamorphosed limestones) surrounded by sericite schist (Hyseni et al. 2010). The contact between carbonates and sericite schist is marked by the presence of the breccia pipe and parallel stretching orebodies (e.g. Schumacher 1950, Féraud et al. 2007). Most of the orebodies are characterized with columnar manto-shape (Fig. 1). Some orebodies are related to skarn alteration, but most of ore has hydrothermal-replacement character or is filling karst cavities (Féraud and Deschamps 2009).

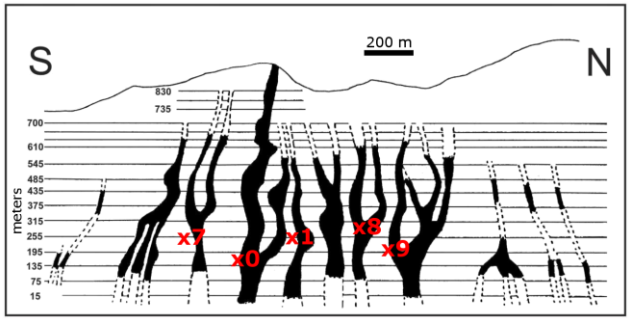


Figure 1. Simplified cross section through columnar-shaped orebodies at Stan Terg hydrothermal system along unfolded contact of carbonates with schists (modified after Féraud and Deschamps 2009).

There are two main ore mineralization styles in Stan Terg deposit: hydrothermal-replacement and skarn (Kołodziejczyk et al. 2016). Hydrothermal-replacement ore is massive and consists of sphalerite, galena, pyrite, arsenopyrite, pyrrhotite, chalcopyrite, boulangerite with minor tetrahedrite and stannite. Skarn-type of mineralization, mostly galena, pyrrhotite, pyrite, with minor sphalerite, chalcopyrite, Bi-minerals is accompanied by gangue minerals as ilvaite, hedenbergite, actinolite, garnet and magnetite. The other mineralization styles, like rhodochrosite-style (mostly sphalerite and boulangerite), vein (galena, pyrite), breccia style (mix of various ore pieces) are less common.

4 Chemical composition of sphalerite

Average trace and minor elements in sphalerite from Stan Terg deposit are reported in Table 1.

Fe, Mn, and Cd occur in high concentrations, and should be discussed as minor elements. Significant trace elements in Stan Terg deposit are Sn, In, Ag, and Hg.

Sphalerite crystals from the Stan Terg are characterized by high Fe content (up to 14.9 wt.%), average wt. 9.7%. In the sphalerite from orebody x8 occur the highest average content of some elements: Fe (10.18 wt.%), Mn (0.68 wt.%) and Cu (0.05 wt.%). In other orebodies Mn and Cu content are lower: 0.04 wt.% (Mn) and 0.02 wt.% (Cu).

The most significant trace elements are In and Sn. Sphalerite from orebody x1 have the lowest indium content (6.58 ppm), in other orebodies there are high In contents (29 in x8 orebody – 97 ppm in x7 orebody). Tin content in sphalerite varies from 66 to 336 ppm. The highest contents are present in x8 and x9 orebody, which are likely due to the presence of tiny stannite inclusions in sphalerite. Most sphalerite samples have low Tl (0.08 – 0.11 ppm), x1 orebody has Tl content below the detection limit (0.08 ppm).

Low content of Co was recorded in x1 and x7 orebody, in other orebodies Co value is in average 5 ppm. Ni content in sphalerite is uniform in all orebodies (1.51 – 2.21 ppm), besides orebody x1, where Ni content is below the detection limit (1.38 ppm).

Table 1. Average element concentrations (in ppm) in sphalerite from Stan Terg deposit by LA-ICPMS. Zn is from EPMA (wt. %).

	Orebody x7	Orebody x0	Orebody x1	Orebody x8	Orebody x9
^{55}Mn	3,981	4,006	4,586	6,787	4,085
^{57}Fe	97,362	97,097	97,075	101,778	95,414
^{59}Co	0.15	5.95	<MDL	5.87	4.14
^{62}Ni	1.54	1.51	<MDL	2.21	1.86
^{65}Cu	227	226	212	506	366
^{66}Zn	54.77	55.36	54.63	54.65	54.98
^{69}Ga	3.91	6.07	6.56	10.53	6.95
^{74}Ge	0.64	0.66	<MDL	0.76	0.74
^{75}As	9.09	7.27	<MDL	1.33	7.70
$^{82/77}$Se	14	13	14	14	14
^{95}Mo	0.61	0.91	<MDL	<MDL	0.57
^{107}Ag	1.06	1.10	0.77	2.39	1.93
^{111}Cd	1,322	1,677	1,757	1,776	1,443
^{115}In	97	70	6.58	29	42
^{118}Sn	66	83	103	336*	204*
^{121}Sb	3.42	1.28	<MDL	42**	6.00
^{125}Te	1.59	2.51	<MDL	1.55	1.70
^{197}Au	0.07	0.07	<MDL	0.06	0.23
^{202}Hg	6.01	8.57	14	7.90	8.42
^{205}Tl	0.09	0.08	<MDL	0.11	0.09
^{208}Pb	1.30	1.16	0.66	69**	2.08
^{209}Bi	0.07	0.15	<MDL	0.10	0.08

MDL - minimum detection limit, some results have elevated values by nano-inclusions of *Sn-minerals, **boulangerite

Sphalerite from orebody x1 has low concentrations of minor and trace elements. The only exception is Hg content (14 ppm), which in other orebodies varies between 6.01 – 8.42 ppm of Hg.

The highest Ga content was recorded in orebody x8 (10.53 ppm), the lowest in x7 (3.91 ppm), in the rest of the orebodies sphalerite contains 6.07 – 6.95 ppm Ga. Content of Ge in all orebodies is similarly low (0.64 - 0.76 ppm) or below detection limit.

Low content of As (below 1.33 ppm) was recorded in x8 and x1 orebody, in other orebodies As content is 7.27 – 9.09 ppm. Antimony has similar concentrations to As, in range of 1.28 to 6.00 ppm. Sphalerite from x8 orebody has elevated concentrations of Sb and Pb, up to 42 ppm and 69 ppm, respectively. This might be related to presence of nano-inclusions of boulangerite, which is abundant minor mineral in ore samples from this part of the deposit.

Silver content in sphalerite is uniform (0.77 - 2.39 ppm) with the highest recorded value in x8 orebody.

5 Discussion

In our data, there is an evidence for coupled substitution Cu + Ag versus Ge + Ga + Sn + In, starting from 100 ppm of Ge + Ga + Sn + In (Fig. 2). Concentrations of Cu and Ag are relatively higher in sphalerite with lower contents of Ge + Ga + Sn + In.

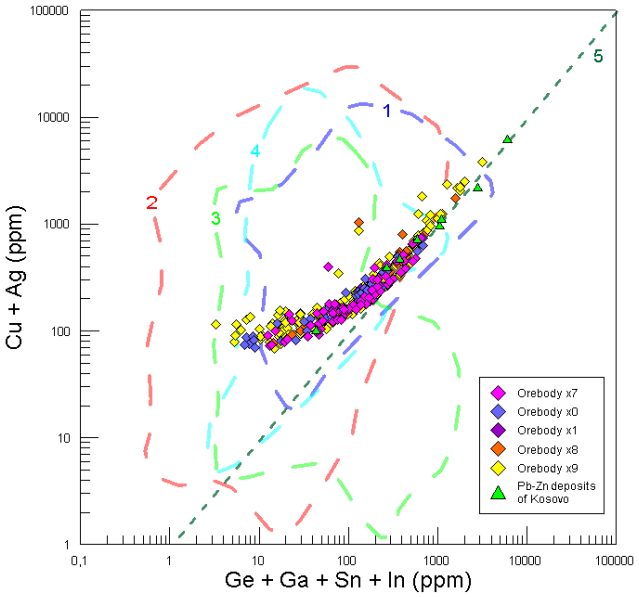


Figure 2. Correlation plots of Cu + Ag vs. Ge + Ga + Sn + In in sphalerite from the Stan Terg deposit, colour lines show fields for genetic types of Pb-Zn deposits after Cook et al. (2009). 1) Epithermal, 2) Skarns, 3) Carbonate replacement, 4) VMS, 5) Theoretical 1:1 correlation.

Tin content in sphalerite from the Stan Terg is high (up to 0.31 wt.%) and it is likely due to the presence of tiny stannite inclusions or veinlets, or it may indicate a solid solution of stannite in sphalerite. Sn concentrations are not as high as in other deposits in Kosovo, where Sn content were reported up to 0.59 wt.% in Artana deposit (Kołodziejczyk et al. 2015). Sphalerite enriched in Sn was not reported for other Pb-Zn deposits elsewhere, and our results are first report of this phenomena (Fig. 3).

In our data we have proof for Zn^{2+} <-> Cu^{+} + Ag^{+} coupled substitution, which is visible on Cu versus In graph (Fig. 4) in sphalerite samples from the southern part of the deposit. These values and substitution mechanism are similar to other sphalerite compositions reported from various genetic types (Cook et al. 2009). Some sphalerite has elevated Cu content (especially in x8 and x9 orebodies), what might be linked to presence of nano-inclusions of chalcopyrite.

Our results fall in similar field as sphalerite from other localities in terms of Cu + Ag versus Ga (Fig. 5). There is no trend visible, and there must be other elements, like Ga, Sn, In that are involved in substitution processes (compare to Fig. 2).

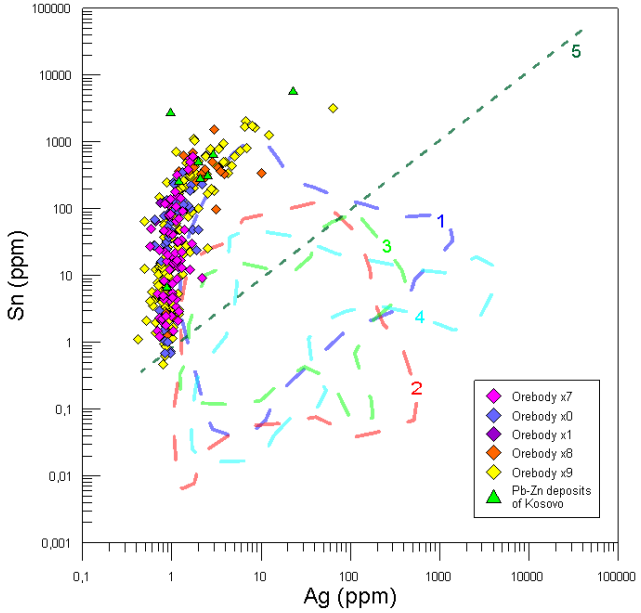


Figure 3. Correlation plots of Sn vs. Ag in sphalerite from the Stan Terg deposit, colour lines show fields for genetic types of Pb-Zn deposits after Cook et al. (2009). 1) Epithermal, 2) Skarns, 3) Carbonate replacement, 4) VMS, 5) Theoretical 1:1 correlation.

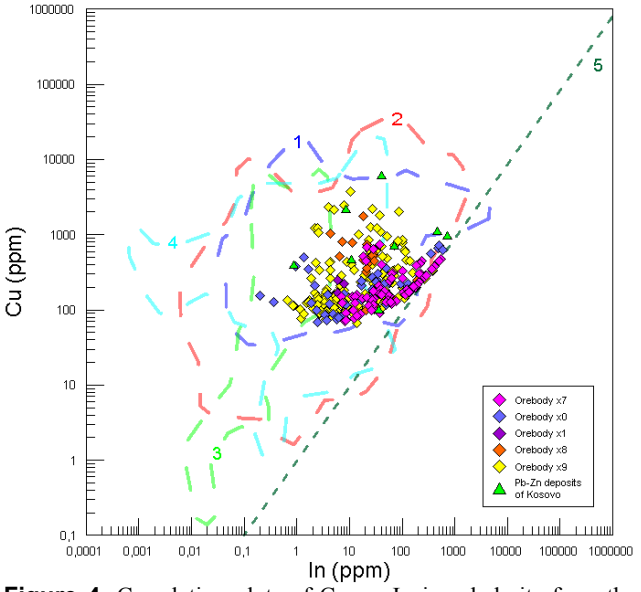


Figure 4. Correlation plots of Cu vs. In in sphalerite from the Stan Terg deposit, colour lines show fields for genetic types of Pb-Zn deposits after Cook et al. (2009). 1) Epithermal, 2) Skarns, 3) Carbonate replacement, 4) VMS, 5) Theoretical 1:1 correlation.

Comparing Stan Terg sphalerite crystals to sphalerite from other Pb-Zn deposits of skarn / carbonate replacement origin, sphalerite from Stan Terg have elevated Sn content. Many similarities exist with the Majdanpek deposit in Serbia, like similar content of Fe (9.04 wt.%), In (56 ppm) and Ge (0.80 ppm). Differences can be observed in Sn, Sb and Ga contents, which are higher in Stan Terg. Majdanpek deposit is characterised by higher Co content, 34 ppm (Cook et al. 2009).

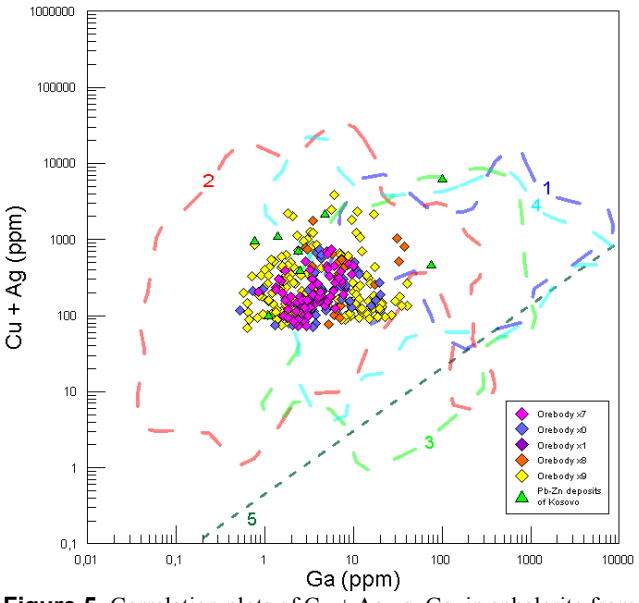


Figure 5. Correlation plots of Cu + Ag vs. Ga in sphalerite from the Stan Terg deposit, colour lines show fields for genetic types of Pb-Zn deposits after Cook et al. (2009). 1) Epithermal, 2) Skarns, 3) Carbonate replacement, 4) VMS, 5) Theoretical 1:1 correlation.

Co content in sphalerite in most samples reaches 5 ppm. In x1 and x7 orebodies Co content is near detection limit. These values are low in comparing to sphalerite from other deposits in Kosovo (e.g. 29 ppm Co in Drazhnje deposit) (Kołodziejczyk et al. 2015), and also other Pb-Zn skarn deposits from elsewhere. For example Cook et al. (2009) reported higher concentrations of Cu (up to 0.23 wt.%), Ag (up to 107 ppm), Cd (up to 7.38 wt.%) and lower As content (0.2 – 2.6 ppm) from Romanian skarn deposits.

In similar skarn deposits from China the common feature of sphalerite is elevated Co and Mn content, but also low In concentrations in distal deposits (Ye et al. 2011). Sphalerite from some localities is enriched in Ge, for example in vein Pb-Zn mineralization from the Noailhac – Saint-Salvy deposit (Bellisont et al. 2014) Ge content reaches up to 0.25 wt.%. Radosavljević et al. (2012) reported up to 6.47 wt.% Hg content and up to 2.60 wt.% Cd content in sphalerite from Rujevac deposit (EPMA data). Sphalerite from Čumavići deposit contain: Sn (up to 0.53 wt.%), In (up to 0.11 wt.%), As (up to 0.54 wt.%), Sb (up to 1.62 wt.%) and Pb (up to 3.08 wt.%) (EPMA data) (Radosavljević et al. 2016).

Sphalerite from Stan Terg hosts typical minor and trace elements, like Fe, Mn, Cd, Sn, In, Ga and traces of Ag, Hg, Sb, As, Ge and their concentrations are typical when comparing to other skarn and carbonate-replacement deposits. Stan Terg sphalerite, however, is relatively depleted in Co and Ag and increased in Sn, what is a characteristic feature for this locality. Study of rare elements in the sphalerite is the another nice example of the variation of sphalerite composition due to different hydrothermal conditions.

Acknowledgements

Research was founded by SEG Student Research Grant to JK in 2014 and 2015 years and AGH grants No. 11.11.140.320 and 15.11.140.636.We are grateful to Trepça Mining Company for allowing sample collection and to Dimitrina Dimitrova from Geological Institute of Bulgarian Academy of Sciences for help in LA-ICPMS data collection.

References

Belissont R, Boiron MC, Luais B, Cathelineau M (2014) LA-ICPMS analyses of minor and trace elements and bulk Ge isotopes in zoned Ge-rich sphalerites from the Noailhac–Saint-Salvy deposit (France): Insights into incorporation mechanisms and ore deposition processes. Geochim. Cosmochim. Acta 126:518-540

Cook NJ, Ciobanu CL, Pring A, Skinner W, Shimizu M, Danyushevsky L, Saini-Eidukat B, Melcher F (2009) Trace and minor elements in sphalerite: A LA-ICPMS study. Geochim. Cosmochim. Acta 73:4761-4791

Guillong M, Meier DL, Allan MM, Heinrich CA, Yardley BWD (2008) Appendix A6: SILLS: A MATLAB based program for the reduction of laser ablation ICPMS data of homogeneous materials and inclusions. In: Sylvester P (ed). Laser Ablation ICP–MS in the Earth Sciences: Current Practices and Outstanding Issues. Vancouver, Mineralogical Association of Canada, Short Course 40:328-333

Féraud J, Deschamps Y (2009) French scientific cooperation 2007-2008 on the Trepça lead-zinc-silver mine and the gold potential of Novo Brdo/Artana tailings (Kosovo). BRGM Report No RP-57204-FR

Hyseni M, Durmishaj B, Fetahaj B, Shala F, Berisha A, Large D (2010) Trepça Ore Belt and Stan Terg mine – Geological overview and interpretation, Kosovo (SE Europe). Geologija 51:87-92

Kołodziejczyk J, Pršek J (2015) Incorporation of trace elements into sphalerite: case study from Pb−Zn mineralizations in Vardar Zone, Kosovo. In: André - Mayer AS (ed). Mineral resources in a sustainable world: 13th SGA biennial meeting: Nancy – France, 24–27 August. Proceedings Volume 2:599-602

Kołodziejczyk J, Pršek J, Voudouris P, Melfos V, Asllani B (2016) Sn-Bearing Minerals and Associated Sphalerite from Lead-Zinc Deposits, Kosovo: An Electron Microprobe and LA-ICP-MS Study. Minerals 6:42

Radosavljević AS, Stojanović NJ, Pačevski MA (2012). Hg-bearing sphalerite from the Rujevac polymetallic ore deposit, Podrinje Metallogenic District, Serbia: compositional variations and zoning. Chem. Erde-Geochem. 72:237–244

Radosavljević AS, Stojanović NJ, Radosavljević-Mihajlović SA, Vuković SN (2016) (Pb–Sb)-bearing sphalerite from the Čumavići polymetallic ore deposit, Podrinje Metallogenic District, East Bosnia and Herzegovina. Ore Geol Rev 72:253–268

Schumacher F. (1950) The ore deposits of Yugoslavia and the development of its mining industry. Econ Geol 49:451–492

Strmić Palinkaš S, Palinkaš L, Renac C, Spangenberg J, Lüders V, Molnar F, Maliqi G (2013) Metallogenic model of the Trepča Pb-Zn-Ag Skarn deposit, Kosovo: Evidence from fluid inclusions, rare earth elements, and stable isotope data. Econ. Geol. 108:135–162

Ye L, Cook NJ, Ciobanu CL, Yuping L, Qian Z, Tiegeng L, Wei G, Yulong Y, Danyushevskiy L (2011) Trace and minor elements in sphalerite from base metal deposits in South China: A LA-ICPMS study. Ore Geol Rev 39:188-217

Rare earth elements in the Marinkas Quellen carbonatite, southwestern Namibia

Ibiyemi Ogungbuyi, Philip Janney and Chris Harris
University of Cape Town, South Africa

Abstract. The Marinkas Quellen (MQ) Carbonatite Complex of southern Namibia forms part of the Kuboos Bremen Line (KBL) of alkaline igneous rocks (Smithies 1992). The carbonatite varieties present include calciocarbonatites, magnesiocarbonatites and ferrocarbonatites. They are characterized by different degrees of enrichment in incompatible elements such as Ba, Nb, Th, Sr and light rare earth elements (LREE). These elements are present at significantly higher concentrations in the ferruginous calciocarbonatites, which have La concentrations of 1,485 to 45,600 times chondrite with $(La/Yb)_N$ values between 116 and 3,312. The ferruginous calciocarbonatites contain the highest values of total rare earth oxides (TREO) ranging from 0.3 to 4 wt.% with an average of 1.8 wt.% and high Th (233-720 ppm) content. In the calciocarbonatites and magnesiocarbonatites TREO values fall between 0.02 and 0.6 wt.% with an average of 0.13 wt.%. BaO and SrO have high concentrations, varying from 0.47 to 4.93 wt% and 0.01 to 2.5 wt%, respectively.

1 Introduction

Carbonatites are alkaline igneous rocks consisting of greater than 50 wt% carbonate minerals, and which contain less than 20 wt.% SiO_2 (e.g. Le Maitre 2002). Carbonatites are unusual rocks that are often extremely enriched in rare earth elements (REE) and other economically valuable rare metals (e.g., Nb, Ta) and therefore, can form important deposits of these resources. The industrial and economic uses for rare earth elements are rapidly increasing, and the demand for these elements has not been met. At the moment, China is the largest producer of REE and controls between 50 and 90% of the world's supply. There is thus an urgent need to discover new REE deposits, due to their importance in the energy and electronics sectors.

Aside from their economic utility, carbonatites represent a very unusual and scientifically interesting expression of mantle-derived magmatic activity. The petrogenesis of carbonatite complexes remains poorly understood in many cases, especially in southern Africa. The 525 Ma Marinkas Quellen (MQ) complex of southern Namibia (Fig. 1), part of the Kuboos-Bremen Line (KBL) of alkaline igneous centers (e.g. Smithies 1992) consists of granites, nepheline syenites and carbonatites and is the only carbonatite locality in the KBL (Smithies 1992). MQ carbonatites include calciocarbonatites, ferruginous calciocarbonatites, magnesiocarbonatites, and ferrocarbonatites. Some petrological and isotopic studies of MQ carbonatites have been done previously (Smithies and Marsh 1998). Detailed REE resources and reserves have not been studied.

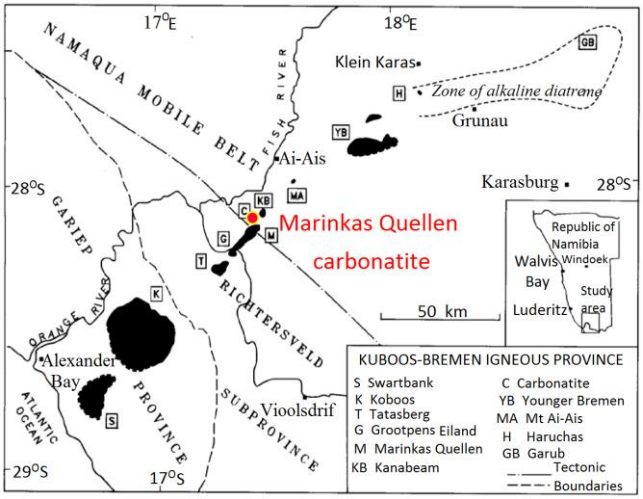


Figure 1. Simplified geological map showing terrane boundaries in SW Africa, and the location of the Kuboos-Bremen Igneous Province, modified after Reid (1991).

2 Trace element geochemistry

The MQ carbonatites are characterized by varying degrees of enrichment in incompatible elements such as Ba, Nb, Th, Sr and LREE. All the carbonatites are characterised by large Zr, Hf, Ti depletions, elevated Sr (0.46-4.9 wt.% SrO), variable Ba (0.001 to 2.5 wt.% BaO) and highly variable LREE enrichment ($(La/Yb)_N$ = 30 to 3312; Fig. 2) and they lack Eu anomalies (Fig. 2).

The ferruginous calciocarbonatites contain the highest values of total rare earth oxide (TREO; Table 1), with data ranging between 0.33 and 4.0 wt.% having an average of 1.8 wt.%. In the calciocarbonatites and magnesiocarbonatites, TREO values fall between 0.11 to 0.14 wt.% and 0.02 to 0.10 wt.%, respectively. The ferruginous calciocarbonatites are also more enriched in Mn, Ba and Th (Figs. 2 and 3) in comparison to the other carbonatite types in the complex. Their enrichment in the LREE (La to Nd) is significantly greater than other carbonatite varieties, with La concentrations ranging from 1485 to 45,600 times chondrite, and (La/Yb)N ratios between 116 and 3312.

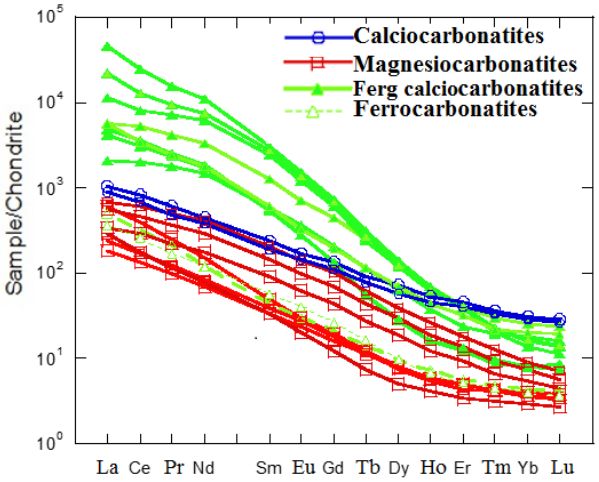


Figure 2. Chondrite normalised REE patterns for carbonatites. REE normalization values from Evensen et al. (1978).

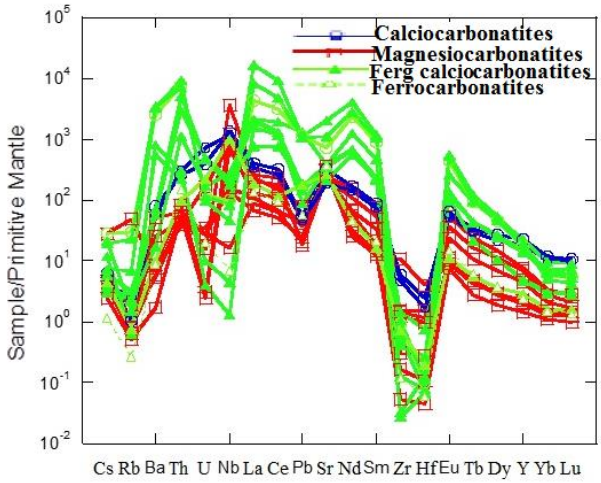


Figure 3. Primitive mantle normalized incompatible element patterns for carbonatites. Normalisation factors from Sun and McDonough (1989).

The carbonatites have steep negative sloping REE patterns (Fig. 2). The higher the fractionation of the REE, the less the actual value of the total REE present, due to higher prices for middle and heavy REE. LREE oxides such as La_2O_3 and Ce_2O_3 are sold at cheaper rate (≈US$4 to 8 per kg), while the prices are much higher for Pr_2O_3 and Nd_2O_3 (≈US$60 to $120 per kg). Middle and heavy rare earths (Eu_2O_3, Tb_2O_3 and Dy_2O_3) attain substantially higher prices (≈US$400 to $800 per kg) on the global market. However, the monetary value of the rare earth element present in the Marinkas Quellen carbonatites will be

Table 1. Concentrations of total rare earth oxides and other elements in Marinkas Quellen carbonatites.

Name	Sample No	Th(ppm)	U(ppm)	TREO(wt%)	BaO(wt%)	SrO(wt%)
Calcio	MKC-29	21.19	7.97	0.14	0.06	0.08
Calcio	MKC-52	24.17	14.89	0.11	0.04	0.05
Fer. Calciocarb	MKC-16	233.22	10.33	0.33	0.04	0.49
Fer. Calciocarb	MKC-17	413.83	9.58	0.83	0.05	0.89
Fer. Calciocarb	MKC-20A	631.43	2.23	1.44	1.86	1.70
Fer. Calciocarb	MKC-20AN	720.57	1.96	2.21	2.45	2.59
Fer. calciocarb	MKC-20B	556.88	2.5104	4.00	2.53	4.93
Magnesiocarb.	MKC-4	3.51	3.43	0.06	0.02	0.66
Magnesiocarb.	MKC-25	3.09	0.72	0.02	0.01	0.07
Magnesiocarb.	MKC-25MS	3.84	0.56	0.03	0.00	0.77
Magnesiocarb.	MKC-34	6.63	0.06	0.08	0.01	0.55
Magnesiocarb.	MKC-34MS	4.40	0.05	0.05	0.00	0.54
Magnesiocarb.	MKC-35	5.07	0.55	0.03	0.04	0.83
Magnesiocarb.	MKC-45	4.65	0.32	0.10	0.00	0.60
Mag-Ferrocarb	MKC-27A	18.14	0.20	0.52	0.42	0.87
Mag-Ferrocarb	MKC-27B	24.71	0.08	0.56	0.60	0.90
Mag-Ferrocarb	MKC-48	87.24	3.37	0.58	0.01	0.80
Ferrocarb.	MKC-7	7.70	4.53	0.05	0.01	0.62
Ferrocarb.	MKC-62	12.38	0.42	0.04	0.01	0.88

determined by the ease with which the REEs are liberated from their host minerals.

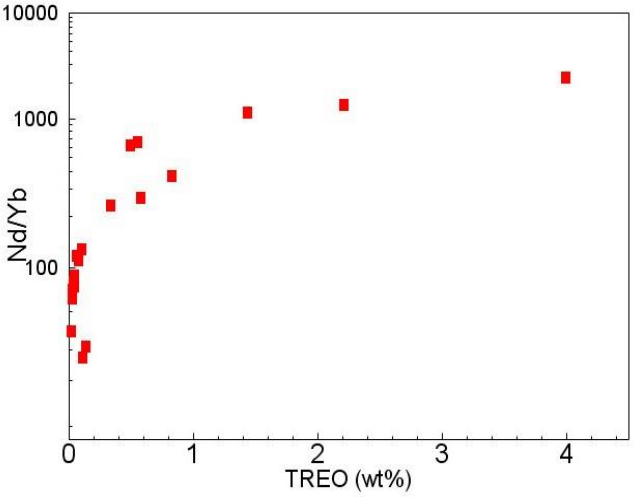


Figure 4. Plot of Nd/Yb ratio against TREO.

Figure 4 shows the ratio of Nd/Yb (a LREE/HREE ratio) plotted against TREO (wt. %) in order to evaluate rare earths in high demand. In Marinkas Quellen, as in most

other carbonatites, increase in TREO content is related to LREE enrichment, and the samples with lower LREE/HREE ratios have lower TREO contents. This pattern is typical of magmatic REE enrichment followed by late-stage mineralisation by carbonatitic fluids.

3 Conclusions

Different carbonatite varieties occur in the Marinkas Quellen complex, including calciocarbonatites, ferruginous calciocarbonatites, magnesiocarbonatites and ferrocarbonatites. REE concentrations in the carbonatites are several orders of magnitude higher in the ferruginous calciocarbonatites than other carbonatite varieties. The REE in the MQ carbonatites are highly fractionated. REE enrichment in the ferruginous calciocarbonatites is extremely high, with concentrations up to 4% TREO. But TREO contents are less than 0.59% in the magnesiocarbonatites and even lower (<0.15%) in the calciocarbonatites and ferrocarbonatites. The pattern displayed on the Nd/Yb against TREO plot is characteristic of magmatic enrichment with subsequent late stage mineralization by carbonatitic fluids. The monetary value of the rare earth element present in the Marinkas Quellen carbonatites will be determined by the ease with which the REEs are liberated from their host minerals.

References

Evensen NM, Hamilton PJ, O'Nions RK (1978) Rare earth abundances in chondrite meteorites. Geochim et Cosmochim Acta 42:1199-1212

Le Maitre R (2002) Igneous rocks: a classification and glossary of terms in igneous rocks. Cambridge University Press, UK

Reid DL (1991) The alkaline rocks of the Kuboos-Bremen igneous province, southern Namibia: the Kanabeam multiple ring complex. Communications, Geol Survey of Namibia 7:3-13

Smithies RH (1992) Geochemical evolution of three alkaline complexes in the Kuboos-Bremen igneous province, southern Namibia. Ph.D. Thesis, Rhodes University, South Africa, 197 p

Smithies RH, Marsh JS (1998) The Marinkas Quellen carbonatite complex, southern Namibia: carbonatite magmatism with an uncontaminated depleted mantle signature in a continental setting. Chem Geol 148:201–212

Sun SS, McDonough WF (1989) The chemical and isotopic systematics of oceanic basalts: implications for mantle composition and processes. In: Saunders AD, Norry MJ (eds) Magmatism in the ocean basins. Geol Soc London Spec Publ 42:313–345

·

New data on the origin of the Fe-Cu-As skarn deposit at Obří důl, West Sudetes, Bohemian Massif

Jan Pašava, František Veselovský, Petr Dobeš, Vojtěch Erban, Ondřej Pour
Czech Geological Survey

Karel Žák, Lukáš Ackerman, Eva Haluzová
Institute of Geology of the Czech Academy of Sciences

Robert Creaser
University of Alberta, Canada

Radko Tásler
Czech Speleological Society

Abstract. The Obří důl Fe-Cu-As sulfide deposit is hosted in metamorphosed lenses of marble, calc-silicate rocks and skarns. The deposit is located up to a few hundred meters away from the contact of the large, late-orogenic Variscan Krkonoše-Jizera Plutonic Complex (KJPC). Mineralogical and fluid inclusion studies of the Gustavská ore lens show that the main sulfide stage, dominated by pyrrhotite, chalcopyrite and arsenopyrite, originated from water-rich hydrothermal fluids with salinities up to 8 wt.% NaCl eq. at temperatures ranging from 324 to 358°C.These fluids replaced mainly the carbonate-rich lithologies. The $\delta^{34}S$ values indicate a magmatic source of sulfur and Re/Os dating of molybdenite are consistent with simultaneous formation of the main sulfide stage ore and the KJPC.

1 Introduction

Skarns are commonly associated with exploitable accumulations of ore minerals of a wide range of metals – Fe, Cu, Zn-Pb, Mo, Sn, W, (or Sn-W), more rarely Au – although skarns without economic ore exist as well. The presence of these economically important components defines up to seven geochemically distinct skarn types, each usually associated with a specific type of plutonic rock (Einaudi et al. 1981, 1983; Meinert et al. 2005 and references therein).

The Obří důl Fe-Cu-As skarn deposit is developed in a metamorphosed series containing lenses of marble, calc-silicate rocks and skarns, at a site located up to a few hundred meters away from the contact of a large late-orogenic Variscan Krkonoše-Jizera Plutonic Complex (KJPC) – Fig. 1.

The deposit consists of two sulfide-rich ore lenses Gustavská and Helenská (1–12 m thick) and one smaller Václavská ore lens. The deposit has a long mining history with a monopoly position in the Bohemian market for arsenic in the period 1828–1868 and copper 1830–1853. Recently, a part of the underground workings of the Gustavská ore lens became a heritage site and is accessible to the general public.

Several different models for the origin of the Obří důl skarn deposit were published including replacement metasomatism of carbonate rocks in pre-Variscan or early-Variscan times followed by Variscan regional metamorphism (e.g., Bubal and Dolejš 2013 and references therein) or a model of metamorphic reworking of sedimentary/volcanosedimentary Fe-rich successions (e.g., Pertold and Kopecký 1979). The Obří důl deposit is in some aspects similar to the Czarnów deposit on the Polish side of the border, for which several genetic concepts are also proposed (Mikulski 2010; Mochnacka et al. 2015 and references therein).

In this paper, we report new Re-Os age data on the formation of the main sulfidic phase of the Obří důl deposit, accompanied by further mineralogical, petrologic, geochemical and isotope studies of the sulfidic and carbonate minerals of this deposit. Preliminary fluid inclusion data are also reported.

2 Results and discussion

2.1 Samples and methods

All studied samples were collected in the Gustavská ore lens (50.7279 N, 15.7312 E, altitude of the current mine entrance – Barbora adit – is 1014 m a.s.l.), i.e. the only part of the deposit easily accessible in the underground galleries and shafts of the historical heritage mine. The sampling focused on sulfide mineralization and on all rocks with presence of carbonate for C, O and Sr isotope study.

The polished sections with sulfide minerals were first studied using a Nikon ECLIPSE E 600 and selected mineral phases were analyzed by CAMECA SX 100 electron probe micro analyzer in the Joint Laboratory of Electron Microscopy and Microanalysis of the Czech

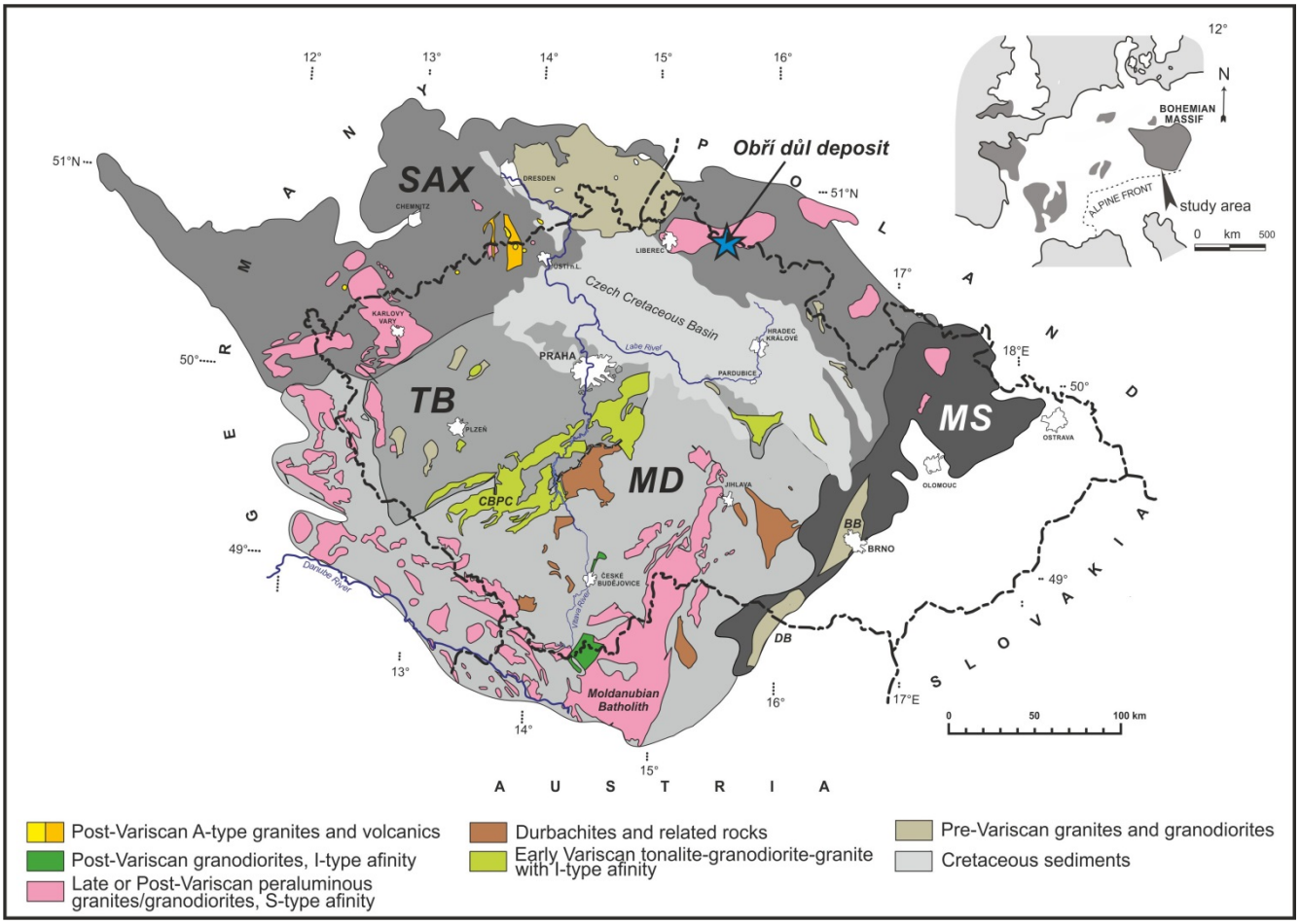


Figure 1. Geological map of the Bohemian Massif with location of the Obří důl skarn deposit. TB – Teplá-Barrandian Unit, SAX – Saxothuringian Unit, MD – Moldanubian Unit, MS – Moravo-Silesian Unit, CBPC – Central Bohemian Plutonic Complex, DB – Dyje Batholith, BB – Brno Batholith (adapted from Ackerman et al. 2016).

Geological Survey and Masaryk University in Brno (R. Škoda, analyst). Fluid inclusions (FI) were studied in double-polished sections 0.3 mm thick by the methods of optical microthermometry using a Chaixmeca heating and freezing stage (Poty et al., 1976) in the laboratories of the Czech Geological Survey in Prague. The Re-Os dating of molybdenite was undertaken in the Crustal Re-Os Geochronology Laboratory of the University of Alberta (UofA lab).

Sulfur isotope composition in pyrrhotite, chalcopyrite and arsenopyrite was determined in the Stable Isotope Laboratory of the Czech Geological Survey in Prague (decomposition under vacuum with CuO and analyses on Finnigan MAT 251 IRMS; Z. Lněničková analyst), where also C and O isotope study of the carbonates was performed (usual decomposition with H_3PO_4 followed by measurement on Thermo Scientific Delta V IRMS). Sr isotopic analyses from selected carbonates were performed at the Czech Geological Survey on Thermo Neptune MC-ICP-MS. More details on the used methods are available in Veselovský et al. (in preparation).

2.2 Mineralogy

The earliest ore mineral is arsenopyrite, followed by pyrrhotite, chalcopyrite, sphalerite, stannite and other ore minerals (e.g., native Bi, bismuthinite, Bi-Pb-Ag-S phases, molybdenite, cassiterite, scheelite, malayaite, stokesite and Te-canfieldite). The arsenopyrite has variable As/S ratio and can contain up to 0.1 wt.% Co. Non-altered pyrrhotite ($Fe_{1-x}S_1$) has lower Fe values than altered pyrrhotite, with "x" ranging from 0.12 to 0.16 documented by electron microprobe study (Fe = 57.5–59.2 wt.% and S = 38.3–39.7 wt.%), in places with Pb values of 0.01–0.2 wt.%. Chalcopyrite contains up to 0.17 wt.% Pb, and Zn and Ag concentrations of 0.04 wt.% and 0.1 wt.%, respectively. Locally, it hosts micro-inclusions of Ag-Bi-S phase (matildite?). Sphalerite is mostly associated with chalcopyrite and less frequently with pyrrhotite, and

locally bears inclusions of stannite. Sphalerite contains 9–11.6 wt.% Fe, 1.2–1.6 wt.% Cd, 0.8–1.6 wt.% Cu, up to 0.6 wt.% Mn, and up to 0.02 wt.% In. Molybdenite from the skarn assemblage showed micro-inclusions of native bismuth and an Ag-S phase. Native bismuth is the most abundant accessory mineral which contains up to 0.2 wt.% Zn and up to 0.6 wt.% Cd.

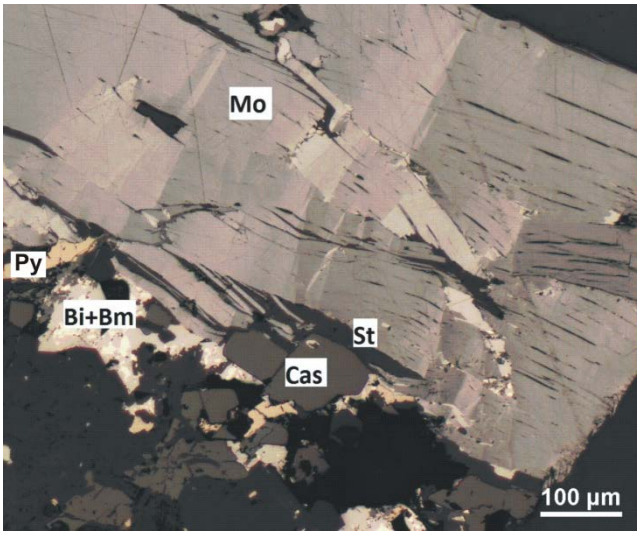


Figure 2. Back scattered electron (BSE)/Scanning electron microscope (SEM) image of molybdenite (Mo) in association with pyrite (Py), cassiterite (Cas), native bismuth (Bi) – light, in the core of grain, bismuthite (Bm) – darker, surrounding native Bi and stokesite (St) – black, filling a space in the vicinity of cassiterite and molybdenite grains.

2.3 Fluid inclusions

Three types of paleofluids were identified in our samples: (1) H_2O-type fluids in diopside with Th = 387–424 °C and salinity up to 8 wt.% NaCl equivalent, (2) H_2O-type fluids with low CO_2 values in quartz veins with sulfide mineralization (minimum temperature of sulfide formation Th = 324–358 °C, salinity 4.0–8.8 wt.% NaCl equivalent and indicated presence of Mg and Fe chlorides), and (3) H_2O-type fluids in carbonate veins and younger quartz veins with Th = 113–168 °C, salinity up to 8 wt.% NaCl equivalent and indicated presence of K-Mg-Fe chlorides. Our data are in agreement with those published by Kwak (1986) and others who reported that skarn type deposits contain fluids characterized by extreme range in both temperatures and salinities. They reflect changes in the evolution of fluid system from magmatic (and/or metamorphic) fluids of early stages to epithermal fluids dominating during later stages. Temperatures and salinities generally decrease away from the solution source, both in time and space. The gradients found at greater distances from the source in distal (far from contact) skarns tend to be less (e.g. 210-350°C) for a particular skarn stage to that in proximal (near contact) skarns (e.g. 400–450°C). High KCl contents are found in skarns adjacent to high K granitoids, whereas high NaCl contents are found in skarns adjacent to calcic granitoids.

2.4 Sulfur isotopes in sulfides

$\delta^{34}S$ values in massive pyrrhotite range from 0.9 to 2.7 ‰. Similar values were found in chalcopyrite ($\delta^{34}S$ = 2.7 to 3.1 ‰), while arsenopyrite showed slightly higher values ($\delta^{34}S$ = 4.1 to 4.8 ‰). The range of sulfur isotope values in the studied sulfides (0.9 to 4.8 ‰) is very close to that reported from different skarn-type deposits (e.g., Zahedi et al. 2014). The data indicate a homogeneous sulfur source and dominantly reducing conditions during the formation of sulfides (i.e., low proportion of sulfate in the fluids during the formation of sulfidic minerals). The sulfur source is difficult to ascertain, since the background data defining the sulfur isotopic composition of the KJPC and of the metamorphic series hosting the ODSD are unknown. Nevertheless, the whole range of sulfur isotope data (0.9 to 4.8 ‰) is in agreement with the range commonly observed in magmatic rocks of the Bohemian Massif (e.g., Bernard and Žák 1992).

2.5 Carbon and oxygen isotopes in carbonates

The carbonates in skarns and Ca-Si rocks mineralized by sulfides represent a heterogeneous group, since the microscopic study indicates calcite as one of the youngest minerals in skarns, while the mineralized Ca-Si rocks still retain a lot of original carbonate. All carbonates in Ca-Si rocks show large $\delta^{18}O$ shifts from the field of both hypothetical protolith limestones, and the field of unmineralized Ca-Si rocks (carbonate $\delta^{18}O$ values ranging from -13.41 to -25.21‰ vs. V-PDB). Carbonates from skarns and mineralized Ca-Si rocks are therefore totally overprinted by channelized metasomatic fluid flow, which is most probably related to the intrusion of the KJPC.

2.6 Strontium isotopes in carbonates

Five samples of carbonates were analyzed for $^{87}Sr/^{86}Sr$ isotope ratios. The obtained data roughly correlate with both C and O isotopes: the least radiogenic sample ($^{87}Sr/^{86}Sr$ = 0.7098) also has the highest $\delta^{13}C$ and $\delta^{18}O$ values, closest to the presumed marine carbonate (Veizer et al. 1999). The most radiogenic Sr value (0.7190) found in later vein-type carbonate most likely reflects a contribution of Sr leached from surrounding mica schists by fluids mobilized by the intrusion of the KJPC.

2.7 Re-Os geochronology

Molybdenite from the Obří důl skarn deposit was dated using the Re–Os method has an age of 312.7 ± 1.4 Ma (Ackerman et al. 2016). The KJPC has been recently dated by the high-precision CA-ID-TIMS U–Pb zircon method, providing identical ages of 312.5 ± 0.3 and 312.2± 0.3 Ma for two different granite facies (Kryza et al. 2014). These Re-Os and U-Pb ages data support the simultaneous

formation of polymetallic skarn and intrusion of the KJPC.

Acknowledgements

This research was supported by the Czech Science Foundation (13-15390S to L.A. and J.P.). We thank Z. Lněničková for sulfur isotope analyses, R. Škoda for EMPA and P. Simon for useful comments.

References

Ackerman L, Haluzová E, Creaser RA, Pašava J, Veselovský F, Breiter K, Erban V, Drábek M (2016) Temporal evolution of mineralization events in the Bohemian Massif inferred from the Re–Os geochronology of molybdenite. Miner Deposita, doi 10.1007/s00126-016-0685-5

Bernard JH, Žák K (1992) Stable isotope study of Variscan vein Pb-Zn-Ag mineralization of the Bohemian Massif. Explor Mining Geol 1: 81–84

Bubal J, Dolejš D (2013) Magnetite chemistry in skarns of the Bohemian Massif: evaluating competing effects of protolith inheritance, crystal chemistry, fluid composition and pressure-temperature conditions. In: Jonsson E. (ed) Mineral deposit research for a high-tech world. The 12th SGA Meeting, August 2013 Uppsala, Sweden, Proceedings Volume 1: 264–267

Einaudi MT, Meinert LD, Newberry RJ (1981) Skarn deposits. Economic Geology 75th Anniversary Volume. Society of Economic Geologists, Littleton, Colorado, USA, pp 317–391

Einaudi MT, Burt MD (1982) Introduction – terminology, classification, and composition of skarn deposits. Econ Geol 77: 745–754

Kryza R, Schaltegger U, Oberc-Dziedzic T, Pin C, Ovtcharova M (2014) Geochronology of a composite granitoid pluton: a high-precision ID-TIMS U–Pb zircon study of the Variscan Karkonosze Granite (SW Poland). Int J Earth Sci 103:683–696.

Kwak TAP (1986) Fluid inclusions in skarns (carbonate replacement deposits). J Metamorph Geol 4: 363–384

Meinert LD, Dipple GM, Nicolescu S (2005) World Skarn Deposits. Economic Geology 100th Anniversary Volume. Society of Economic Geologists, Littleton, Colorado, USA, pp 299-336

Mikulski SZ (2010) The characteristic and genesis of the gold-bearing arsenic polymetallic mineralization in the Czarnów deposit (West Sudetes). Biul Państw Inst Geol 439: 303–320 (in Polish with English summary)

Mochnacka K, Oberc-Dziedzic T, Mayer W, Pieczka A (2015) Ore mineralization related to geologic evolution of the Karkonosze-Izera Massif (the Sudetes, Poland) – Towards a model. Ore Geol Rev 64: 215–238

Pertold Z, Kopecký L (1979) Origin of the Obří důl deposit and problems of skarns in the Giant Mts. In: Proceedings 22. Konference Čs spol pro mineralogii a geologii. Geoindustria, Prague: 235–241 (in Czech)

Poty B, Leroy J, Jachimowicz L (1976) Un nouvel appareil pour la mesure des temperatures sous le microscope: L'installation de microthermometrie Chaixmeca. Bull Soc géol Mineral Cristallogr 99: 182–186

Veselovský F, Ackerman L, Pašava J, Žák K, Haluzová E, Creaser R, Dobeš P, Erban V, Tásler R. (in prep.) Multiphase formation of the Obří důl polymetallic skarn deposit, West Sudetes, Bohemian Massif: Geochemistry and Re-Os dating of the sulfidic mineralization. Miner Deposita

Zahedi A, Boomeri M, Nakashima K, Mackizadeh M, Ban M, Lentz D (2014) Geochemical Characteristics, Origin, and Evolution of Ore-Forming Fluids of the Khut Copper Skarn Deposit, West of

New insights into hydrothermal Zn-Cu mineralization in the West Troms Basement Complex, northern Norway

Hanne-Kristin Paulsen, Sabina Strmic Palinkas, and Steffen G. Bergh
University of Tromsø, Norway

Abstract. The structurally controlled Zn-Cu hydrothermal mineralization on the island of Vanna is located in the West Troms Basement Complex, a western continuation of the Vannareid-Burøysund brittle fault zone along a contact between ductilely sheared Archean basement gneisses. It occurs as veins and hydrothermal breccia infills composed mostly of sphalerite, chalcopyrite, quartz and calcite. The stable isotope composition of calcite overlaps with the $\delta^{13}C$ vs. $\delta^{18}O$ values of primary magmatic carbonates. Fluid inclusion studies show that low salinity (~1 wt. wt. % NaCl equ.) mineralizing fluids were composed of $H_2O+CO_2+NaCl+LiCl$. Sulphide minerals were likely deposited by different mechanisms including boiling and cooling. From microstructures displayed by the vein system, it can be inferred that mineralization occurred in an extensional setting after the last metamorphic event. This could correspond with existing Permian ages of illite growth in this fault, and it is possible that mineralization at Vannareid has occurred in a post-orogenic setting and is younger than the Palaeoproterozoic age previously suggested.

1 Introduction

The exploration company, Store Norske Gull (SNG), evaluated in 2012 an alteration zone in the Vannareid-Burøysund (VB) Permian brittle fault zone on the island of Vanna in northern Norway. Based on observed geochemical anomalies and magnetic and IP geophysical surveys, 880 m of drill core (7 drill holes) was bored and Zn-Cu mineralization was identified over a strike length of 250 m. The mineralization is open along strike, but the grade and extent of mineralization at the VB occurrence as outlined today has no economic potential.

This occurrence represents the only structurally hosted hydrothermal Zn-Cu occurrence in the West Troms Basement Complex (WTBC) and is therefore of great interest. The VB fault hosting mineralization is a part of the regional Vestfjorden-Vanna complex (Indrevaer 2013). By better understanding the mineralizing processes in the VB fault, other faults in the regional complex could be evaluated as exploration targets.

In addition, deposition post-dates peak metamorphism in the area and this occurrence provides a unique opportunity to contribute to the larger tectonostratigraphic puzzle that comprises the WTBC.

1.1 Geological setting

Vanna is an island located in the Neoarchaean to Palaeoproterozoic WTBC. The WTBC lies west of the Caledonian Nappes in northern Norway, is composed of TTG gneisses (2.9-2.6 Ga) intruded by mafic dyke swarms (2.4-2.2 Ga) and plutonic complexes (c. 1.8 Ga), and overlain by variously aged (2.8-1.9 Ga) greenstone belts (Bergh et al. 2007; Bergh et al. 2010). The WTBC is thought to be a western continuation of the Fennoscandian shield but also shows many similarities to the Lewisian in Scotland, and similar aged crustal segments in Greenland (Bergh et al. 2012).

The WTBC has a complex architecture of metamorphic, igneous and supracrustal rocks subdivided into a series of segmented blocks that were brought together during the Svecofennian (c. 1.8-1.6 Ga) and/or younger tectono- thermal events. Despite recent advances in the geological knowledge of the region, the metallogeny is still poorly understood.

1.2 Geology of VB Zn-Cu occurrence

Mineralization is hosted by the ENE-WSW trending, south dipping VB fault. The VB fault separates variably deformed tonalitic gneisses intruded by mafic dikes, diorite and gabbro, in the footwall, from mylonitized tonalite in the non-mineralized hanging wall (Opheim and Andresen, 1989). The hydrothermal mineralization in the brittle VB fault consists of brecciated mafic and tonalitic host rocks and numerous carbonate and quartz filled veins, previously interpreted as a Paleoproterozoic VMS springer zone (Ojala et al. 2013; Monsen 2014). Normal movement along the fault has been dated by Davids et al. (2013) using K-Ar method on illite in the cataclastic fault rocks yielding a late-Carboniferous through early Permian age of illite growth. This is concurrent with post-Caledonian extension and incipient rifting of the Atlantic Ocean.

2 Methods

Mineralogy and textural associations were examined using reflected and transmitted light microscopy and representative samples were selected for fluid inclusion studies. Preliminary fluid inclusion data were obtained from quartz veins. Homogenisation (T_h) and final ice melting temperatures (T_m) were recorded on fluid inclusions in double polished sections (100 to 250 µm) using a LINKAM heating and cooling stage at University

of Tromsø (UiT). All drill core samples were analysed for whole rock geochemistry by SNG using ME-XRF06 and 48-element suite using ME-MS61. The ore grade Zn and Cu was reanalysed using Cu-ICP81, Zn-ICP81 and ZN-OG62. PGM elements were analysed using PGM-ICP24. Stable isotope analyses of carbonates determining $\delta^{18}O$ and $\delta^{13}C$ values were carried out using a Thermo-Fisher MAT253 IRMS with a Gasbench II at UiT.

3 Results

3.1 Mineralization, textures, and host rocks

The mineral assemblage in the veins and breccia infill at the VB occurrence is relatively simple. Sphalerite, chalcopyrite, quartz and calcite are the main constituents of the veins, but they vary in abundance from place to place and between different host rocks. Pyrite, Pb-Bi-Ag sulphide and fluorite are minor constituents, generally restricted to late-stage veins. The grain size of the minerals vary from fine (<0.1 mm) to coarse (<20 mm).

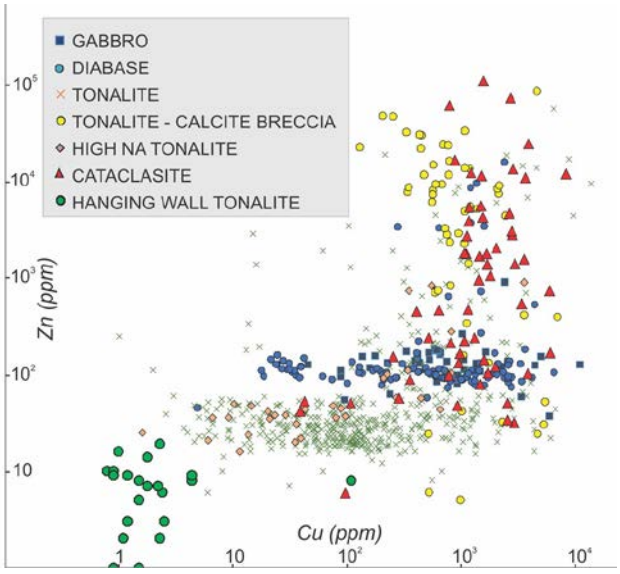


Figure 1. Zn and Cu grade plotted by host rock type. High grade Zn is hosted by cataclasite and hydrothermal calcite breccia in tonalite.

The ore grade is controlled by host rocks (Figure 1) and mineralization type. The hydrothermal calcite breccias in tonalite and quartz-calcite veins in cataclasite carry the highest Zn and Cu grades. These different mineralization styles will be described below.

The term cataclasite is here used to describe a polymict milled matrix supported breccia (80% matrix) that tends to form at the contact between mafic dikes and tonalite. Clasts are composed of tonalite, quartz- or calcite veins, or previously cemented cataclasite matrix. They are commonly rounded and <10 mm. Very fine-grained rock flour matrix is deposited both as syn-sedimentary banded structures and as infill within hydrothermal breccias, indicating multiple movement events (Figure 2A). The mineralization in cataclasite occurs both as disseminated fine-grained sphalerite and chalcopyrite, and as quartz veins and veinlets (<100 mm) crosscutting consolidated rock flour and breccia clasts. The majority of chalcopyrite has deposited on veins salvages, in contact with the host rock (Figure 2A).

Two different mineralization styles are hosted by tonalite. In the upper parts of the deposit, a matrix supported, hydrothermal calcite breccia, with angular clasts of calcite (<10 mm), is cemented by calcite, sphalerite, chalcopyrite, and minor chlorite (Figure 2B). The breccia is cut by later white calcite veins with sphalerite and chalcopyrite along margins. Sphalerite is yellow-brown and can exhibit well- defined zonal colour banding defined by variations in Fe content (Figure 2C).

The second mineralization style hosted by tonalite consists of veins, veinlets and minor breccia infill composed of euhedral quartz and minor calcite. Quartz veins are characterised by euhedral, crustiform crystals, commonly zoned with minor inclusions of sphalerite. Sphalerite with triangular texture has infilled interstitially around the euhedral quartz, and displays simple intergrowth with the later chalcopyrite. Calcite veins and infill are common, and occur late in the sequence (Figure 2E).

Within diorite and gabbro, the mineralization is restricted to narrow quartz chalcopyrite veinlets (1-20 mm wide), with minor sphalerite (Figure 2D). Similar to the quartz veins in the tonalite, quartz occurs in forms of euhedral crystals, and sphalerite, where present, shows triangular textures and intergrowth with subsequent chalcopyrite that commonly overgrows cubic pyrite or has a pyrite core. Minor calcite occurs as the last stage infill in some veinlets.

3.2 Parageneses

Paragenesis studies, mainly involving analysis of the superposition of mineralized veins and breccias, have revealed four mineralizing stages:
1) The first sulphide stage includes sphalerite that occurs as zoned inclusions in euhedral quartz in tonalite. Minor sphalerite also occurs as infill between the euhedral quartz crystals; 2) Later chalcopyrite with quartz shows simple intergrowth with sphalerite. Chalcopyrite also occurs in crosscutting quartz veins in tonalite (Figure 2E), and within diorite (Figure 2D); 3) High-grade sphalerite and chalcopyrite mineralization deposited within hydrothermal calcite breccia. This calcite is likely the same event as the late-stage calcite infill in quartz veins; 4) Narrow (<5 mm) crosscutting veins composed of quartz, calcite, fluorite, a Pb-Bi-Ag sulphide mineral, and minor chalcopyrite.

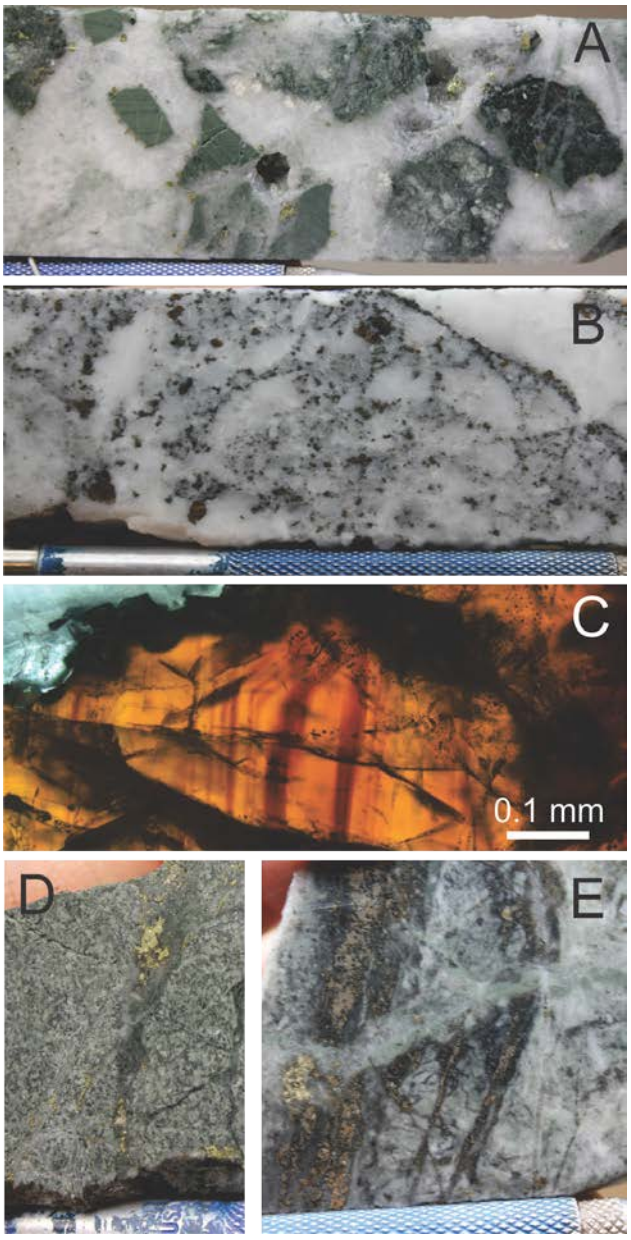


Figure 2. Photos of drill core from VB occurrence; A) quartz matrix supported breccia with rounded clasts of previously brecciated tonalite and angular clasts of cemented cataclasite. Chalcopyrite is deposited on vein salvages; B) hydrothermal calcite breccia with dark sphalerite; C) zoned sphalerite grain from calcite breccia; D) quartz-chalcopyrite veinlet in diorite; E) tonalite with early sphalerite-quartz veins cut by a later chalcopyrite-quartz vein. Pen for scale is 5 mm wide.

3.3 Isocon diagrams

Isocon diagrams (Grant 2005) have been plotted for different mineralization stages in diorite and tonalite host rocks (Figure 3). The isocon plot of diorite shows that Zn-Cu quartz vein mineralization is associated with an increase in Hg, Au, Cd, Bi, As, and Pb, while Sr, Na_2O and CaO are depleted.

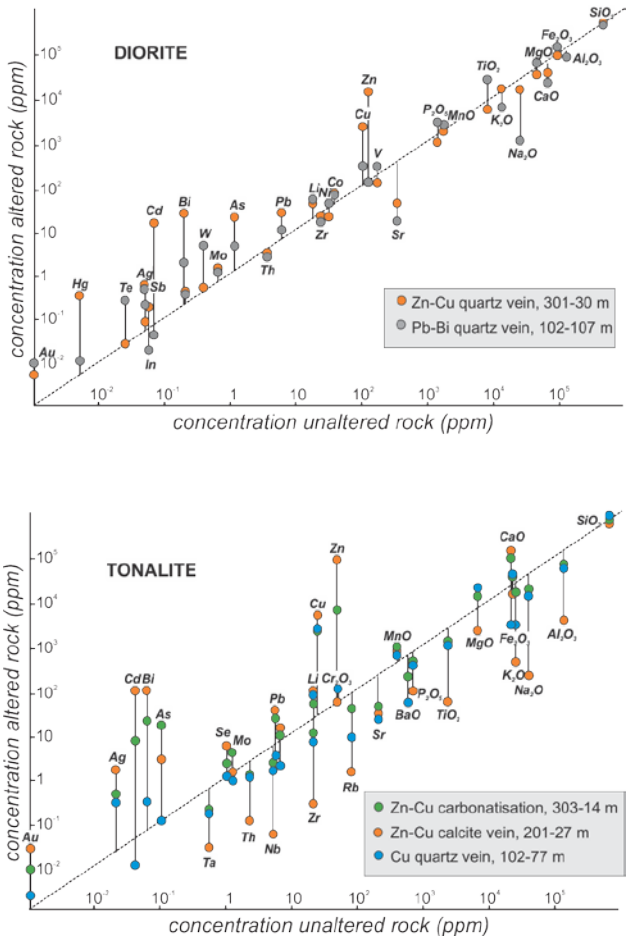


Figure 3. Isocon diagrams depicting increase and depletion of elements with mineralization in relation to unaltered host rock. Top diagram shows mineralization in diorite while bottom diagram shows tonalite host rock.

In the tonalite, Zn-Cu calcite mineralization is associated with enrichment in Au, Ag, Cd, Bi, As, Pb, and MnO while most of the major elements are depleted. This apparent major element depletion is also a result of the relative amount of host rock being smaller when massive calcite is present, as most of the immobile elements plot along the same trend.

3.5 Fluid inclusion studies

Preliminary fluid inclusion data from late Cu-bearing quartz veins indicate that the mineralizing fluids were composed of H_2O+CO_2+NaCl+LiCl (Dubois et al. 2010). The final ice melting temperature corresponds to the salinity of approximately 1 wt % NaCl eq. A fluid with such low salinity does not have the capacity to transport base metals, with an exception of Cu which can be transported in forms of bisulphide complexes. Fluid inclusion assemblages containing both monophase vapour (V) inclusions and liquid-rich two-phase (L+V) inclusions has also been recorded, indicating that boiling has occurred.

3.6 Stable isotopes

The stable isotope composition of six hydrothermal samples from different mineralization styles in the VB occurrence were measured. The $\delta^{13}C_{VPDB}$ values range from -4.4 to -6.1 ‰ and $\delta^{18}O_{SMOW}$ values range from 9.3 to 11.0 ‰. These values overlap with values of primary igneous carbonates defined by Taylor (1967).

4 Discussion

The mineral assembly indicates that the fluids were near neutral, and limited chlorite alterations suggests a temperature of around 200-350^{O}C. The paragenetic sequence show that Zn was deposited prior to Cu. One explanation could be that Zn and Cu have been carried by different ligands, and could therefore have different deposition mechanisms. These mechanisms include fluid mixing or phase separation (boiling). In addition, deposition of chalcopyrite is also controlled by wall rock interactions, as it commonly deposits on the edges of veins where they are in direct contact with mafic minerals, which could be the source of Fe. This is supported by the low salinity (1 wt %) of the mineralising fluid identified by fluid inclusion studies. A fluid with this low salinity would not have the capacity to carry Fe. Cubic pyrite could also have been a nucleation seed for chalcopyrite growth. No fluid inclusions in sphalerite have so far been measured, and it is possible that Zn was carried by a fluid with higher salinity.

From microstructures displayed by the vein system it can be inferred that mineralization occurred in an extensional setting after the last metamorphic event, the Svecofennian orogeny around 1.8 Ga. Permian ages of this fault from Davids (2013) corresponds to other normal, brittle, and post-Caledonian faults in the region. It is likely that mineralization at Vannareid is younger than the Palaeoproterozoic age interpreted by previous workers.

Conclusions

-Mineralization is structurally controlled and cataclasite fault gauge has likely acted as fluid pathways.
-Deposition of sulphides is partly controlled by wall-rock interactions, boiling, and cooling.
-The VB occurrence is the only known post-orogenic hydrothermal Zn-Cu mineralization in the WTBC, and is therefore an exciting regional exploration target.

Acknowledgements

We would like to thank Øystein Rushfeldt with Nussir ASA and Harald Hansen with Store Norske Gull for generously sharing their knowledge and data. We also would like to extend a thank you to Matteus Lindgren at UiT for stable isotope analyses and Kai Neufeld for aid with SEM analyses.

References

Bergh SG, Corfu F, Myhre PI, Kullerud K, Armitage PEB, Zwaan KB, Ravna EJK, Holdsworth RE, and Chattopadhya A (2012) Was the Precambrian basement of Western Troms and Lofoten-Vesterålen in Northern Norway linked to the Lewisian of Scotland? A comparison of crustal components, tectonic evolution and amalgamation history. In: Sharkov E (ed) Tectonics - recent advances, 1st edn. InTech, pp 283-330

Bergh SG, Kullerud K, Armitage PEB, Zwaan KB, Corfu F, Ravna EJK, Myhre PI (2010) Neoarchean to Svecofennian tectono-magmatic evolution of the West Troms Basement Complex, North Norway. Nor J Geol 90:21-48

Bergh SG, Kullerud K, Corfu F, Armitage PEB, Davidsen B, Johansen HW, Pettersen T, and Knudsen S (2007) Low-grade sedimentary rocks on Vanna, North Norway: a new occurrence of a Palaeoproterozoic (2.4-2.2 Ga) cover succession in northern Fennoscandia. Nor J Geol 87:301-318

Davids C, Wemmer K, Zwingmann H, Kohlmann F, Jacobs J, Bergh SG (2013) K-Ar illite and apatite fission track constraints on brittle faulting and the evolution of the northern Norwegian passive margin. Tectonophysics 608:196-211. doi: 10.1016/j.tecto.2013.09.035

Dubois M, Monnin C, Castelain T, Coquinot Y, Gouy S, Gauthier A, Goffè B (2010) Investigations of the H2O-NaCl-LiCl system: a synthethic fluid inclusion study and thermodynamic modeling from -50^{O} to +100^{O}C and up to 12 mol/kg. Econ Geol 105:329-338. doi: 10.2113/gsecongeo.105.2.329

Grant JA (2005) Isocon analysis: a brief review of the method and applications. Phys Chem Earth 30:997-1004. doi: 10.1016/j.pce.2004.11.003

Indrevaer K, Bergh SG, Koehl JB, Hansen JA, Schermer E, Ingebrigtsen A (2013) Post-Caledonian brittle fault zones on the hyperextended SW Barents Sea margin: New insights into onshore and offshore margin. Nor J Geol 93:167-189

Monsen, K (2014) Hydrothermal Cu-Zn mineralization at Vanna, West Troms Basement Complex. Dissertation, University of Tromsø

Ojala JV, Hansen H, Ahola H (2013) Cu-Zn mineralisation at Vannareid, West Troms Basement Complex: a new Palaeoproterozioc VMS occurrence in the northern Fennoscandian Shield. Proceedings of the 12th Biennial SGA Meeting, Uppsala, Sweden.

Opheim JA, Andresen A (1989) Basement-cover relationships on northern Vanna, Troms, Norway. Nor Geol Tidsskr 69:67-81

Taylor HP, Frechen J, Degens T (1967) Oxygen and carbon isotope studies of carbonatites from the Laacher See district, West Germany and the Alnö District, Sweden. Geochim Cosmochim Acta 31:407-430. doi: 10.1016/0016-7037(67)90051-8

Mn deposits in karstic and pseudo-karstic landforms in the Iberian Range (Teruel, NE Spain)

Ignacio Subías, Isabel Fanlo, Ana Ester López Pomar and Gonzalo Ares
Universidad de Zaragoza, Spain

Abstract. Manganese deposits hosted by the Upper Jurassic limestones (Camañas mine) and the Lower Cretaceous sandstones (Crivillén mine) of the Iberian Range occurs in karstic and pseudo-karstic landforms, sometimes related to E-W and ESE-WNW striking faults. Two distinct morphologies have been observed at Camañas mine: veins and pocket or nest-like bodies, of metric to decimetric scale. This mineralization is marked by an assemblage composed by pyrolusite, romanechite, quartz, and calcite and rare Fe-rich chlorite and barite. In the case of the Crivillén deposit, mineralization consists of cavity fillings of metric to decimetric scale. The internal structure of the orebodies is typically laminated. Ore mineral assemblage is made up of pyrolusite, romanechite and strontiomelane. The presence of hydrothermal minerals and also fluid inclusions in quartz crystals, point to hydrothermal process being responsible for both cavities and ore formation. This ore-forming fluid was reduced and acid since manganese is a soluble and mobile element with a bivalent state (Mn^{2+}) in such conditions. The (pseudo)-karst system could provide enhanced fluid percolation and fluid/rock interaction promoted oxidation and increasing pH by cement dissolution that was responsible for oxide and oxyhydroxide deposition. Also, the increasing pH lead to the decoupling of Mn from Fe.

1 Introduction

Mining Mn operations in the Iberian Range can be dated back to the seventeenth century, the Crivillén mine being the first Spanish Mn exploitation. During the latter part of the nineteenth and the first half of the twentieth centuries, Teruel was the leading Spanish manganese producers. The total production is slightly over 50 000 t of which almost 37 000 t have been exploited in the Crivillén deposit.

The goals of this study are to improve the understanding of the geology and mineralogy of the manganese deposits in the Iberian Range, and to propose a genetic model for these deposits.

The achievement of these goals was obtained by means of detailed mapping on outcrops and underground adits, X-Ray Diffraction (XRD), optical microscopy and field-emission scanning electron microscopy (FESEM).

2 The Iberian Range: synthesis

The Iberian Range, located between the Pyrenean and Betic alpine belts, forms two parallel, elongated Mesozoic massifs cored by Paleozoic basement separated by basins filled by Tertiary and Quaternary detrital rocks (Figure 1). The basement is composed of Precambrian to Permian rocks folded in northwest-southeast to north-south directions and overthrust during the Variscan orogeny. During the late Variscan, northwest-trending kilometre-scale strike-slip faults also affected the Iberian Range.

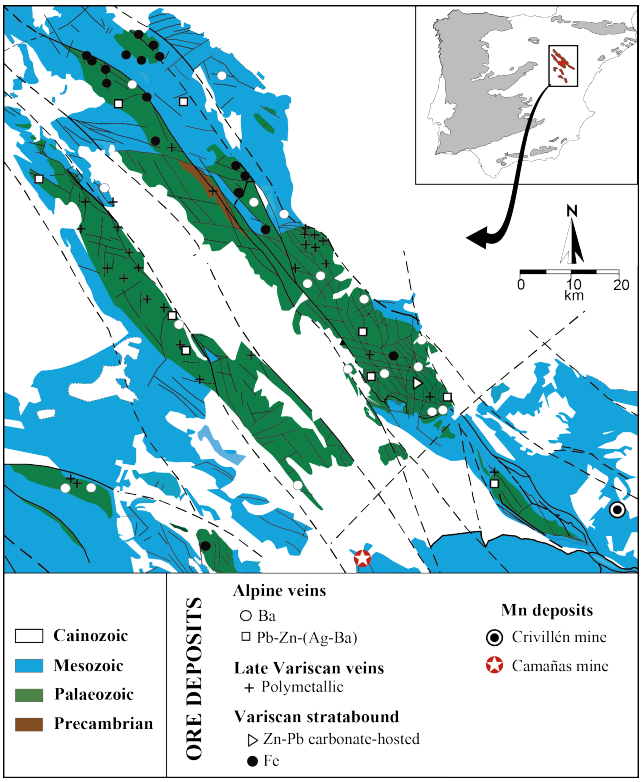


Figure 1. Geological map of the Iberian Ranges, showing the location of the ore deposits discussed in the text.

During the Alpine orogeny (Tertiary), the intracratonic Iberian basin (Iberian Range, Ebro basin, and Catalan Range) was developed. It was initially filled by fluviatile clastic sequences related to the first phases of formation of an aulacogen. Subsequent deposition of marine shallow-water carbonates occurred in an epicontinental sea, and significant siliciclastic deposits accumulated in the adjacent marginal areas. Salas and Casas (1993) interpreted the Iberian Range as a well-developed Mesozoic rift with a northwest-trending crustal root resulting from the collision of the Iberian plate and the Ebro block during the Paleogene.

Apart from manganese deposits, metallogenetic

studies of the Iberian Range report different types of ore deposits related to the Variscan and Alpine orogenic episodes: Alpine-type Ba-Zn-Pb-Cu, low-temperature vein and stratabound deposits as well as several different types of Fe deposits. These include stratiform and vein-type deposits of hematite that occur at a specific stratigraphic level of Early Cambrian age and at a pre-Triassic unconformity. In addition, several massive ironstone horizons occur in Ordovician siltstones, and they have oolitic textures, containing iron oxides, silicates, and carbonates.

2 Geology of manganese deposits

3.1 The Camañas mine

Two distinct morphologies have been observed in the Camañas mine: veins and pocket or nest-like bodies (cavity-fillings) filled by Mn oxides, quartz and calcite (Figures 2A and 2B).

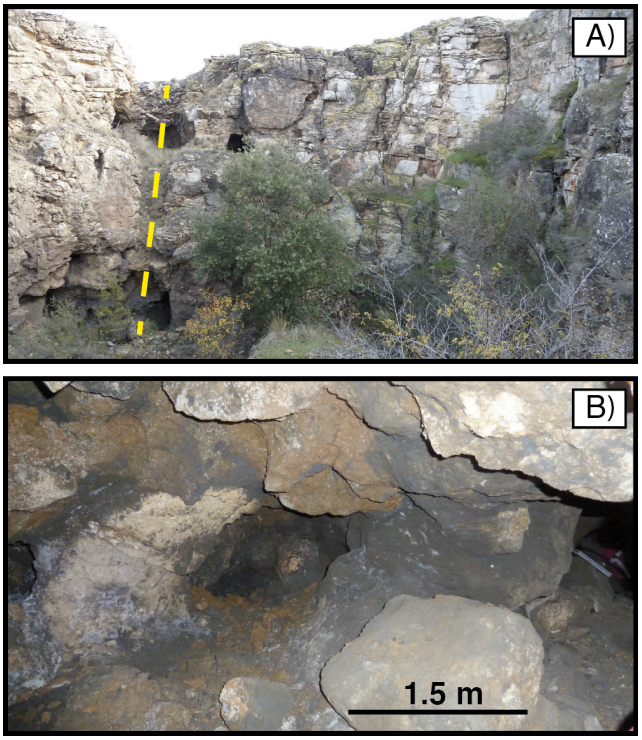


Figure 2. **a** main portals related to a vertical fault (yellow dashed line). **b** dissolution cavity filled by Mn ores (black masses) cementing host limestones fragments).

These ore bodies are hosted by the Higueruelas limestones Formation, Late Jurassic in age (Tithonian) and are related to E-W and ESE-WNW striking faults. The pinching out of these veins (the downward or upward disappearance of the mineralization) do not allow us to decipher if karst cavities are the result of meteoric or of hydrothermal event/s. Ores are often fractured and partly or totally filled by variable clasts composed of in situ brecciated host limestones and Mn minerals. Also, Mn oxides are being recognized as cements in Miocene conglomerates as a consequence of the remobilization of primary ores.

Mn oxides (pyrolusite and romanechite) along with barite, chamosite, quartz and calcite have been identified in the mineralized zones.

Romanechite $(Ba,H_2O)_2(Mn^{+4},Mn^{+3})_5O_{10}$ appears as homogeneous masses or collomorphous aggregates with Ba, O, and Mn energy peaks and Sr or K impurities. Pyrolusite occurs as coarse prismatic crystals filling veins and replacing host limestone. Pyrolusite also surrounds and fills small micro veinlets in romanechite, indicating that pyrolusite postdates the formation of romanechite (Figure 3). Quartz occurs as isolated crystals in the Mn oxides masses or as veinlets. In some samples, barite and chamosite are present as small patches in romanechite/pyrolusite masses, indicating both minerals occur at the end of the sequence. Sparry calcite veinlets occur as small infill of thin veinlets affecting ore bodies.

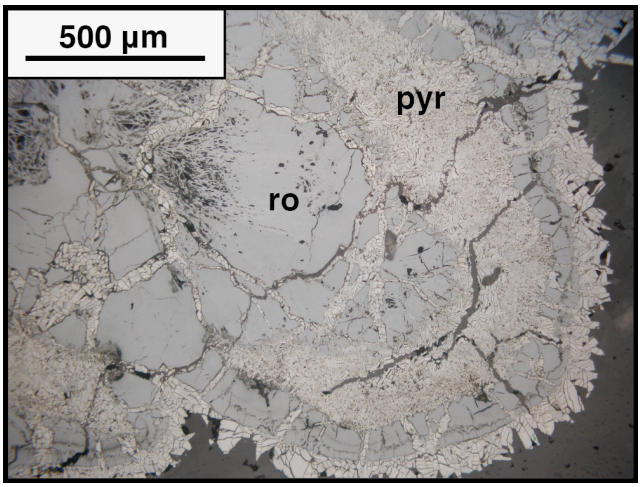


Figure 3. Pyrolusite (pyr) replacing and filling fractures in romanechite (ro).

3.2 The Crivillén mine

The deposit consists of pocket bodies (cavity fillings) of metric to decimetric scale, hosted by the Utrillas Formation sandstones. In other words, the specific characteristic of this deposit is the occurrence of dissolution cavities affecting sandstones (Figure 4A). This karst-like morphology (pseudokarst) was produced by a process other than dissolution of carbonates, mainly the removal of particles of granular and poorly insoluble rocks by channelized ground water flow (piping). The internal structure of the orebodies is typically laminated (Figure 4B).





Figure 4. **a** mining works in the Utrillas Formation sandstones. **b** laminated ores filling a metric cavity in the Utrillas sandstones. Paleogene conglomerates fossilizing ore bodies.

Ore mineral assemblage is made up of pyrolusite, romanechite and a mineral belonging to the Hollandite Supergroup. The chemical composition of this latter mineral has been obtained by means of energy-dispersive X-ray spectroscopy what allow one to identify it as strontiomelane: $(Ba,K,Sr)(Mn^{4+},Mn^{3+})_8O_{16}$.

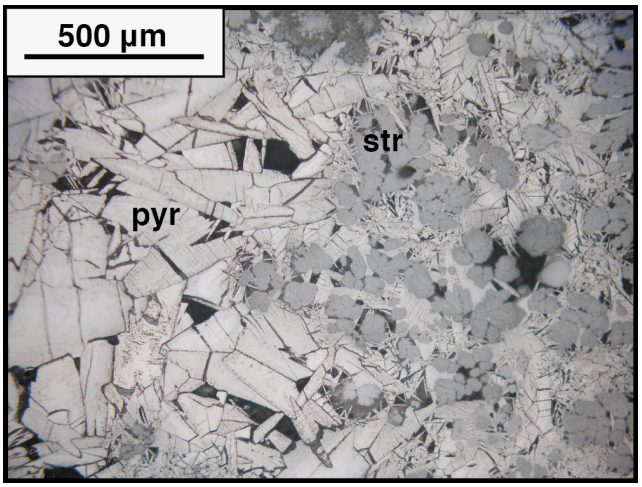


Figure 5. Strontiomelane (str) replacing pyrolusite (pyr) following cleavages and cracks.

Petrographic studies show that the manganese minerals occur as intergranular cement replacing previous diagenetic calcite cement. On the other hand, we have investigated the relative arrangement of Mn minerals to propose a paragenetic sequence. It starts after dissolution processes affecting the host rocks by pyrolusite, which does appear before strontiomelane because strontiomelane crystals grow onto pyrolusite following its cleavages/fractures/cracks (Figure 5). There is no spatial relationship between pyrolusite, strontiomelane and romanechite. For this reason, we have assumed that romanechite represents the early stage of Mn deposition as occurs in the Mn deposit at Camañas.

4 Metallogenetic considerations

The main outcome of this study is the recognition that the manganese orebodies are strata-bound and related to cave deposits formed during karstic and pseudokarstic solution collapse of the country rocks, a Late Jurassic limestone (López Pomar 2014) succession and an Early Cretaceous sandstone formation (Ares 2016).

Dissolution of the host rocks to form a strata-bound cave system could only lead to in situ accumulation of insoluble siliciclastic residue a few centimeters thick at most and with little associated manganese. Therefore, the strata-bound manganese ore filling the ancient cave system must have been introduced from external sources.

The presence of Mn ores along with barite, chamosite and associated elements (Ba, K, Sr) in the mineralizing fluids indicates their possible hydrothermal nature. If so, karstic and pseudokarst cavities could be the result of this hydrothermal event. This ore-forming fluid was reduced and acid since manganese is a soluble and mobile element with a bivalent state (Mn^{2+}) in such conditions. The karst/pseudokarst system could provide enhanced fluid percolation and fluid/rock interaction promoted oxidation and increasing pH by cement dissolution that was responsible for oxide and oxyhydroxide deposition. Also, the increasing pH lead to the decoupling of Mn from Fe.

The source of the metal association (Mn, Ba, K) in the studied manganese mineralization may be the basement rocks and specifically the detrital sequence of the Iberian Range, because even at low temperature metamorphic K-feldspar will break down and act as metal source (Stefansson and Arnorsson 2000). Furthermore, these basement rocks are known to be richly endowed in base metal and barite deposits. Consequently, inheritance and/or remobilization of components from the mentioned ore deposits cannot be ruled out (Subías et al. 2010).

Although the absolute age of (pseudo)-karstification and manganese ore formation is unknown, the observed field relationships: Paleogene (Miocene) conglomerates fossilized orebodies (Figure 4B) or are cemented by manganese ores, allow us to infer that Mn deposition took place prior to deposition of Miocene conglomerates. In other words, Mn deposition most probably took place in a time span between the beginning of the Late Cretaceous and Miocene times.

It is worthy to consider that many authors invoke hydrothermal activity related to the break-up of Pangea during the Mesozoic (185 to 86 Ma; Cathelineau et al. 2012 and references therein), not only in the Variscan belt of Iberia but in Western Europe as well, what it is in line with our time reconstruction.

Acknowledgements

This research has been made possible by Gobierno de Aragón grant E45 belonging to Grupos de Investigación scheme.

References

Ares G (2016) Geología del yacimiento de Mn de Crivillén (Teruel). End-of-Degree Project, Universidad de Zaragoza

Cathelineau M, Boiron MC, Fourcade S, Ruffet G, Clauer N, Belcourt O, Coulibaly Y, Banks DA, Guillocheau F (2012) A major late Jurassic fluid event at the basin/basement unconformity in western France: $^{40}Ar/^{39}Ar$ and K-Ar dating, fluid chemistry and related geodynamic context. Chemical Geology 322-323:99-120. doi: 10.1016/j.chemgeo.2012.06.008

López Pomar AE (2014) Depósitos de Mn en Camañas (Teruel): geología y mineralogía. End-of-Degree Project, Universidad de Zaragoza

Salas R, Casas A (1993) Mesozoic extensional tectonics, stratigraphy and crustal evolution during the Alpine cycle of the eastern Iberian basin. Tectonophysics 228:33-55. doi: 10.1016/0040-1951(93)90213-4

Stefansson A, Arnorsson S (2000) Feldspar saturation state in natural waters. Geochimica et Cosmochimica Acta 64:2567–2584. doi: 10.1016/S0016-7037(00)00392-6

Subías I, Fanlo I, Mateo E, Billström K, Recio C. (2010) Isotopic studies of Pb-Zn-(Ag) and barite alpine vein deposits in the Iberian Range (NE Spain). Chemie der Erde 70 149-158. doi: 10.1016/j.chemer.2009.12.004

Mineral survey and characterization of talc indices of Bodi, north of Boumnyebel, Cameroon

Emmanuel Tangko and Charles Nkoumbou
Université Yaoundé, Cameroun

Abstract. Bodi is located north of Boumnyebel where the Pan-African formations of the Yaoundé Group comprise of quartzite, micaceous quartzite, garnet-micaschist, talcschist, garnet-amphibolite and amphibolite. Talc indices of Bodi are hosted in a garnet and muscovite-bearing micaschist. Structural analysis shows that the micaschists and quartzites have been affected by three phases of deformation D1, D2 and D3. D1 phase is characterized by S1 schistosity, Fo1 foliation, Ln1 lineation, B1 boudinage and F1 folds. D2 phase is a major phase characterized by S2 schistosity, Fo2 foliation, C2 shearing. D3 phase is characterized by brittle deformations. Petrographic studies show a mineral assemblage comprising Qtz+Pl+Fk+Amp+Gt+Spn+ Opaque minerals indicating that metamorphic conditions of Bodi are those of the amphibolite facies. The mineralogy of talcschists of Bodi is mainly composed of talc (>90%) and traces of chlorite, amphibole and phlogopite. The geochemistry of talcschists indicates an ultrabasic composition as shown by the high concentration of Ni (3302-4862ppm) and Cr (1200-2830ppm). The absence of toxic elements such as As, Cd, Pb, U shows that it could be useful in ceramics, cosmetics and pharmaceuticals.

1 Introduction

Geological research in Cameroon started as far back as the colonial period as the reconnaissance geologic map of Cameroon was established in 1956 (Champetier de Ribes et Aubague 1956; Gazel et Guiraud 1956), but these maps do not bear talc indices, except the work of Laplaine (1969) mentioning four indices of Amiant-Talc in Boania and Mayo Boula (North Cameroon), Bayara in the North East of Meiganga (Adamawa) and Ngambé located between Bafia and Edéa. Thus much research work carried out lately shows the presence of Talc indices in Boumnyebel in the Centre region of Cameroon (Yakeu 1999; Nkoumbou et al. 2006). Talc indices in Boumnyebel are spotted in the localities of Pout Kellé Nsimikellé, Bot-Makak, Bibodi Lamal and Memel.

The present work goes further to discover talc indices at Bodi, a small village located north of Boumnyebel, between latitude 4˚ 07' and 4˚ 12' N and longitude 10˚50' and 10˚54' E making a total surface area of about 70 km^2.

2 Geologic setting

The Yaoundé Group belongs to the North Equatorial Pan-African belt (Nzenti et al. 1988). The tectono-metamorphic evolution is monocyclic (Ball et al. 1984) and results in two successive phases of deformation D1 and D2 (Nzenti et al. 1988). The D1 phase is characterized by a development of granulitic assemblages and a calco-alkaline plutonism. This deformation phase dated 620 ±10Ma (Penaye et al. 1993). The D2 phase is characterized by a large migmatisation and a large shear movement parallel to the stretching lineation L_2 with average attitude N030 13 (Feybesse et al. 1987; Mvondo et al. 2003), with a direction of transport southwards (Toteu et al. 1994).

The high-grade metamorphism in the Yaounde region is constrained between 620 and 610 Ma (Oliveira et al. 2006; Toteu et al. 2006). D2 deformation is aged 565 Ma (Lassere and Soba 1979). The data for Sm-Nd shows that the Yaoundé Group is of the upper Proterozoic age (Penaye et al. 1993). It is deposited in an environment (on the border or on continental crust) almost comparable to that of the Lom series (Toteu 1987; Soba et al. 1991). Yaoundé Group is the product of detritus from Neoproterozoic magmatic arcs and the Paleoproterozoic igneous basement of Adamawa-Yade Domain with few Archean xenocrysts (Toteu et al. 2004; 2006). This study deals with the westwards extension of the Yaounde´ Group known for the presence of mafic rocks and talcschists (Nkoumbou et al. 2006a; b) (Fig. 1)

3 Methodology

It consisted of a fieldwork during which rock samples were obtained, petrographic study of various rock samples and chemical analysis using X-ray florescence and diffraction on the three talcshist samples.

4 Results

4.1 Petrography

Microscopic observation reveals the following rock types: garnet-micaschist, quartzite, micaceous quartzite, garnet-amphibolite and amphibolite. The main minerals are quartz, biotite, hornblende, muscovite, garnet, plagioclase, and orthoclase. Some of these minerals occur as inclusions in others; some occurred freely in the rock while others were aligned with a preferred orientation.

The mineral assemblage is Qtz+Pl+Amp(Hbl) +Gnt+Spn showing that the metamorphic conditions (P-T) at Bodi correspond to those of the amphibolite facies with reference to Eskola's classification scheme.

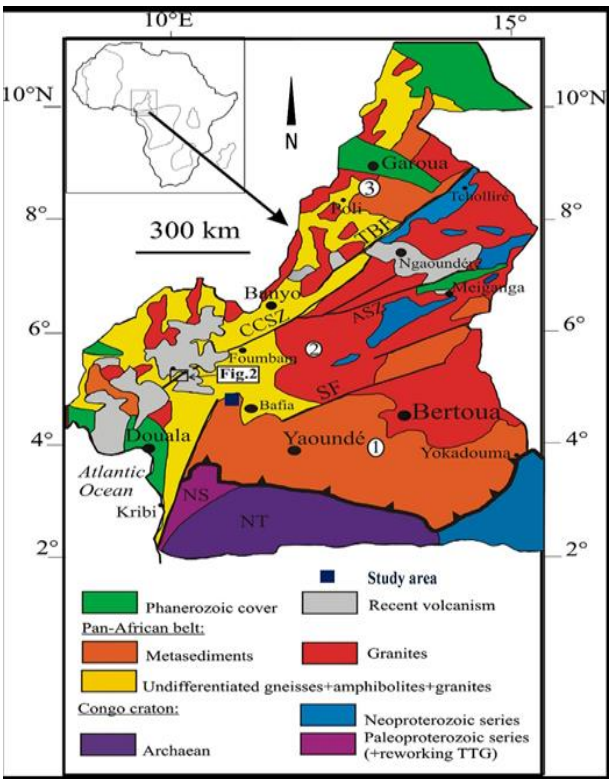


Figure 1. Geology map of Cameroon, showing the major lithotectonic domains; ASZ, Adamawa shear zone; SF, Sanaga fault; TBF, Tcholliré-Banyo fault; CCSZ, Central Cameroon shear zone; NT, Ntem complex; DS, Dja group; NS, Nyong group; 1 = southern; 2 = central domain (Adamawa-Yadé domain of Toteu et al. 2004); 3 = northern domain

4.2 Mineralogy

The X-ray Diffraction studies were carried out in order to determine the mineralogical composition of talcschist: powders of representative samples (TA04, TAO7 and TAO9) of three talcschist bodies (Fig. 4) were examined using a Philips-PW1011 model diffractometer. The diffractograms were recorded using a scanning rate 2Θ/Th with a Ni filtered Fe K-alpha radiation. Loss on ignition test was also carried out at laboratoire de Physico-chimie des Materiaux Mineraux (L.P.M_2) University of Yaounde I to confirm those carried out at MIPROMALO.

Results of the X-ray diffraction show conspicuous peaks of talc and minute traces of chlorite and amphibole (Fig. 2). All the whole rock samples patterns are dominated by the 00l reflections of talc as for pure talc (Ferrage et al. 2003). From the diffractograms of powder samples, talc constitutes the most abundant mineral accounting for about 90% of the total rock volume.

4.3 Geochemistry

Three samples of the crude talc (TA04, TA07 and TA09) were analysed for major and trace elements composition (Fig. 4) by X-ray fluorescence method at Mission de Promotion des Matériaux Locaux (MIPROMOLO), Yaoundé-Cameroon.

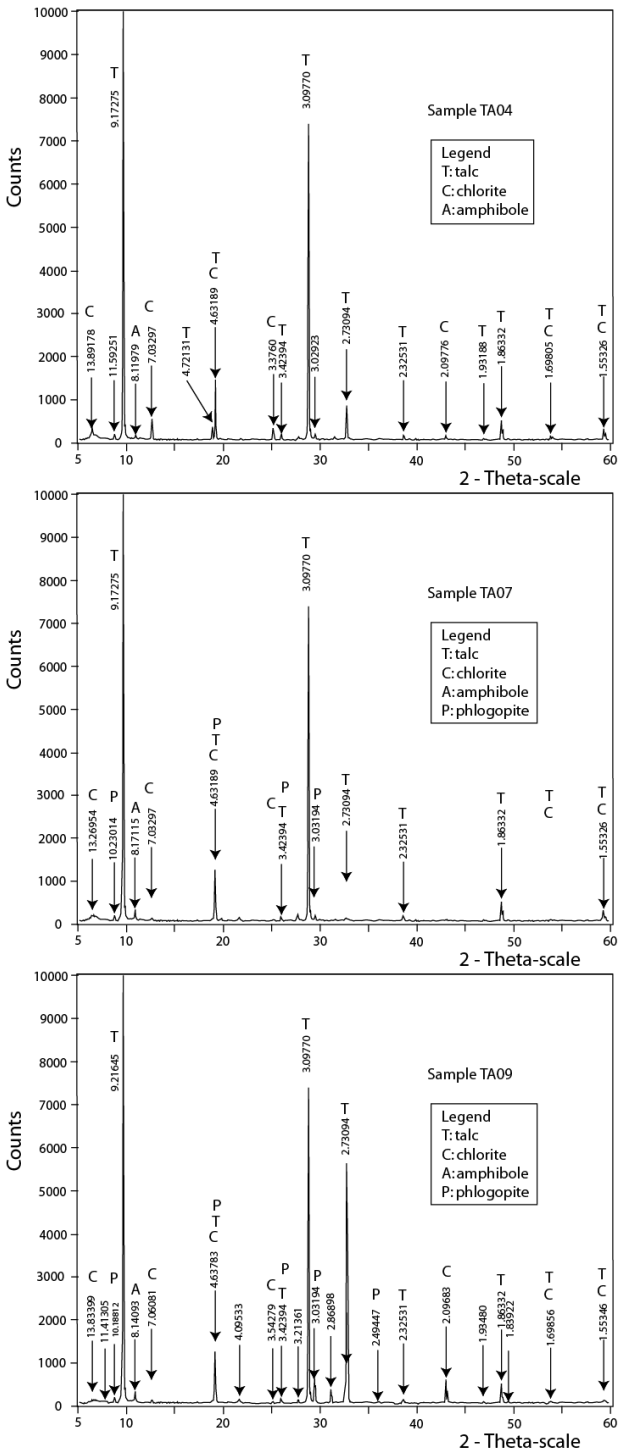


Figure 2. XRD diagrams of talcschist samples from Bodi

4.3.1 Major elements

The results of chemical analyses show that the crude talc samples are made up of SiO_2 (28.06-49.43 wt. %), MgO (20.65-29.38 wt. %), Fe_2O_3 (15.74 and 27.49 wt. %) and CaO (0.128-2.169 wt. %). Na_2O content is below detection limits and K_2O varies from (0-0.0749 %). Their Al_2O_3 concentration is low (0.185-0.668wt. %). The loss on ignition (L.O.I) values range from 0.99 wt. % to 20.74 wt. %. On the tholeiitic-komatiite classification scheme of Naldrett and Cabri (1976), talcschists of Bodi plot in the field of tholeiite (Fig.3).

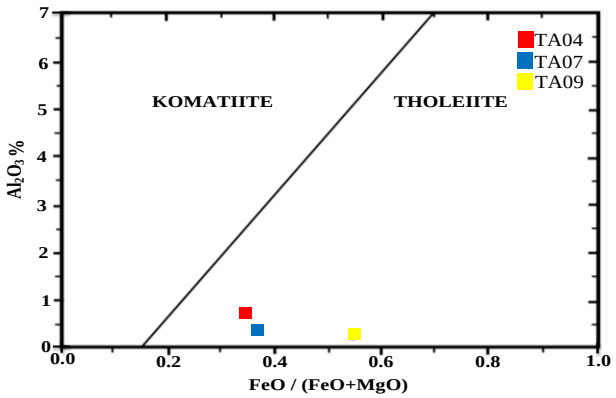


Figure 3. Variation of Al_2O_3 with FeO/(FeO + MgO)% ratio in talcschists of Bodi: limit between tholeiite and komatiite determined by Naldrett and Cabri (1976).

4.3.2 Trace elements

The analyses of trace elements show that the crude talc contains high level of Ni (3302-4862 ppm), Cr (1200-2830 ppm), Cu (0-70 ppm) Zn (60-90 ppm) whereas cobalt is below detection limit.

5 Discussion

Talc accounts for more than 90% of the talcschists of Bodi similar to the talcschist from Boumnyebel (Nkoumbou et al. 2006) making it suitable for use in cosmetics, baby powder, pharmaceuticals, steatite ceramics, pitch control in the paper industry and as a filler in rubber (Zazenski et al. 1995).

The SiO_2 content of these samples varies from 28.06-49.43 wt. %. Values of SiO_2 greater than 45% are generally regarded as upper limit for ultrabasic igneous rocks (Olorunfemi et al. 2010). However, the seemingly high SiO_2 content may suggest possible syntectonic metamorphic silicification of the rock (Olorunfemi et al. 2010). Moreover, on the tholeiitic-komatiitic classification scheme of Naldrett and Cabri (1976) talcschist of Bodi plot in the field of tholeiite. Considering the above, and in comparison with rocks of analogous composition, the overall major element chemical composition of the rock confirms an ultrabasic igneous rock origin. Even though the iron content is high, the composition of these major elements are similar to those of the talcschist of Memel (Nkoumbou et al. 2008). They are also similar to those mined in Trimouns in France, Rabenwald in Australia (Moine et al. 1989), Ponta Grossa, Castro zones in Brazil (Gondim and de Loyala 2002), the lower Skagit Valley, Washington in USA (Benard et al. 1976) and Eastern Desert of Egypt (El-Sharkawy 2000). The SiO_2 and MgO contents, make talcschists of Bodi suitable for cordierite ceramics (Nkoumbou et al. 2008). Na_2O is below detection limit and K_2O is very low (0-0.0749%). This may possibly be due to hydrothermal leaching.

Trace elements analyses show that the crude talc contains high level of Ni (3302-4862 ppm), Cr (1200-2830 ppm) and Zn (60-90 ppm). Ni, Cr, and Co are important elements for the identification of origin of talcs.



Figure 4. A. sample TA04 (talcschist from Bodi), **B.** sample TA07 (talcschist from Malohe), **C.** sample TA09 (talcschist from Bodi

Their abundances are low in Mg-carbonatic talc, but are concentrated in ultramafic talcs (Prochaska 1989). The high Ni, Cr and Fe contents characterize talc formed from ultrabasic rocks making it similar to the talcschist from Bibodi and Memel (Nkoumbou et al. 2008). It also matches with the trace elements geochemistry of talcose rock of Esie area, southwestern Nigeria (Olorunfemi et al. 2010). Trace elements concentration of talc from Bodi ties with the concentration of the major talc deposit in eastern USA (Rohl et al. 1976). The concentrations of trace elements Ni and Cr in the rock samples is also similar to those of peridotites (Divakara Rao et al. 1975). High Ni, Cr and MgO contents point to the existence of a high Ni-phase, presumably olivine in the parent rocks (Hawkesworth and O'Nions 1977). Co and Ni are often thought to have similar geochemical behavior, although the distribution coefficient of Co in olivine/liquid is in general lower than that of Ni (Duke 1976; Leeman 1974). Arndt (1976) has shown that the liquidus phases in a melt with MgO > 20% are olivine and chromite; if MgO is between 2 to 12%, olivine + pyroxene; and with MgO < 12%, pyroxene + plagioclase. By the same argument, the high Cr-phase may be spinel or Cr-rich orthopyroxene. Most of the very small concentrations of toxic elements like As, Cd, Pb, U, except Al could not be detected under the analytical conditions. It may therefore indicate a potential cosmetic and pharmaceutical use (Nkoumbou et al. 2008, Rohl et al. 1976). Also, Cu and Zn may be beneficial, particularly for the use of talc in medical applications such as skin care and mud baths (Olabanji et al. 2005).

Conclusion

The Bodi area is principally composed of meta-sedimentary (garnet-mica schist, micaceous quartzite and quartzite) and meta-igneous (garnet amphibolite, amphibolite and talcschist) rocks which have been affected by three phases of deformation. Three talc indices embedded in a Pan-African garnet and muscovite-bearing micaschist of theYaounde series were discovered at Bodi (Cameroon).

Mineralogical and geochemical analyses of talschists point to an ultrabasic protolith as indicated by high Cr and Ni contents. Also following the classification

scheme of variation of Al_2O_3 with FeO/(FeO + MgO)% ratio (Naldrett and Cabri, 1976), samples plot in the field of tholeiitic rocks. X-ray diffraction analyses show that talc accounts for approximately more than 90%; chemical analyses show high SiO_2 and MgO concentrations coupled with the absence of small concentration of toxic elements such as As, Cd, Pb and U which could not be detected under the analytic condition; it therefore indicates that, the talc of Bodi could be suitable for industrial applications such as ceramics, cosmetic and pharmaceutical, pitch control in the paper industry and as a filler in rubber.

Acknowledgement

The first author extends his gratitude to his family for their moral and financial support. We appreciate the very thorough review of P.-S. Ross and F. Martin.

Reference

Arndt NT (1976) Melting relations of ultramafic lavas (komatiite) at 1 atm and high pressure. Yb. Carnegie Instn. Wash. 75, 555-62

Ball E, Bard JP, Soda D (1984) Tectonique tangentielle dans la catazone pan-africaine du Cameroun. Les gneiss de Yaoundé: Journal of African Earth Science, V. 2, 91-95

Champentier de Ribes G, Aubague M (1956) Carte géologique de reconnaissance à l'échèle 1/500000 ; feuille Yaoundé Est avec notice explicative. Dir. Min. Geol. Cameroun, 35p

Divakara RV, Satyanarayana K, Navovi SM, Haussain SM (1975) Geochemistry of Dharwar ultramafics and the Archean mantle. Lithos, 8, 77-91

Duke JM (1976) Distribution of the period four transition elements among olivine Calcic clinopyroxene and mafic silicate liquid: experimental results. J. Petrology, 17,499-521

El-Sharkawy MF (2000) Talc mineralization of ultramafic affinity in the Eastern Desert of Egypt. Mineralium Deposita (2000) 35: 346-363

Ferrage E, Martin F, Micoud P, Petit S, De Parseval P, Beziat D, Ferre TJ (2003) Cation site distribution in clinochlores: a NIR approach. Clay Minerals, 38, 331-340

Feybesse JL, Johan V, Maurizot P, Abessolo A (1987) Evolution tectono-métamorphique libérienne et éburniénne de la partie NW du craton du Congo zaïrois (SW Cameroun). In: Current Res. In Afr. Earth sci., Matheis G. & Schandelmeier H. (Ed), Balkema-Rotterdam, 9-12

Ganno S, Nzenti JP, Ngnotue T, Kankeu B, Kouankap NGD (2010) Polyphase deformation and evidence for trangressive tectonics in the Kimbi area, Norwestern Pan-African fold belt. Journal of Geology and mining Research Vol. 2 (1) pp 001-015

GazeL J, Guiraud CH (1956) Carte géologique de reconnaissance du Cameroun à 1/500000. Notice explicative de la feuille Abong Mbang Ouest, Dir. Mines Géol. Cameroun.

Gondim AC, De Loyola LC (2002) The composition and structure of minesotaite, a common iron silicate in iron formation. American Mineralogist 29, 363Ponta Grossa and Castro zones in Parana talc district, Brazil, ore properties and mineral industry. Boletim Paranaense de Geociencias 50, 9-14

Hawkesworth CJ, O'nious KR (1977) The petrogenesis of Archean Volcanic rocks from South Africa. J. Petrol., 18, 487-520

Laplaine L (1969) Indice minéraux et ressources minérales du Cameroun. Bull. Dir. Mines la Géologie, Cameroun (5), 1-184

Lassere M, Soba D (1979) Migmatisation d'âge pan-africaine au sein des formations camerounaise appartenant à la zone d'Afrique Central. C. R. Somm. Soc. Géol. Fr., 2, p 64-68

Leeman WP (1974) Experimental determination of partitioning of divalent cations between olivine and basaltic liquid. Ph.D. Thesis, University of Oregon

Moine B, Fortune JP, Moreau P, Viguier F (1989) Comparative mineralogy, geochemistry, and conditions of formation of two metasomatic talc and chlorite deposits: Trimouns, (Pyrenees, France) and Rabenwald (EasternAlps, Austria): economic geology, v. 84, p 1398-1416

Mvondo H, Den Brok SWJ, Mvondo OJ (2003) Evidence of symmetric extension and exhumation of the Yaounde´ nappe (Pan- African fold belt, Cameroon). J. Afr. Earth Sci. 36, 215-231

Naldrett AJ, Cabri LJ (1976) Ultramafic and related mafic rocks: their classificationand gensis with special reference to the concentration of nickel sulphides and platinum-group elements. Econ. Geol., 71, 113–115

Nkoumbou C, Njopwouo D, Villieras F, Njoya A, Yonta NC, Ngo NL, Tchoua F, Yvon J (2006a) Talc indices from Boumnyebel (central Cameroon), physico-chemical characteristics and geochemistry. Journal of African Earth Sciences, 45, 61-73

Nkoumbou C, Villieras F, Njopwouo D, Yonta NC, Barres O, Pelletier M, Razafitianamaharavo A, Jacques Y (2008) Physicochemical properties of talc ore from three deposits of Lamal Pougue area (Yaounde Pan-African Belt, Cameroon), in relation to industrial uses. Clay Minerals, 43, 317-337

Nzenti JP, Barbey P, Macaudiere J, Soba D, (1988) Origin and evolution of the late Precambrian high-grade Yaounde gneisses (Cameroon). Precambrian Research 38, 91-109

Olabanji SO, Ige AO, Mazzoli C, Ceccato D, Ajayie OB, De Poli M, Moschini G (2005) Quantitative elemental analysis of industrial mineral talc, using accelerator-based analytical technique. Nuclear Instruments and Methods in Physics. Research B 240, 327-332

Olorunfemi AO, Olarewaju VO, Okunlol OA, (2010) Petrochemistry and genetic indicators of talcose rock of Esie area, southwestern Nigeria. RMZ–Materials and Geoenvironment, Vol. 57, No. 3, pp 363-386

Penaye J, Toteu SF, Van Schmus WR, Nzenti JP (1993) U-Pb and Sm-Nd preliminary geochronologic data on the Yaounde´ series Cameroon: Signification of the granulitic rocks in the « Centrafrican » belt. C.R. Acad. Sci. Paris Se´ r. II 317, 789-794

Prochaska W (1989) Geochemistry and genesis of Austrian talc deposits. Applied Geochemistry 4, 511-525

Rohl AN, Langer AM, Selikoff IJ (1976) Consumer talcums and powders: mineral and chemical characterization. J Toxicol Environ Health, 2:255-284

Soba D, Michau A, Toteu SF, Morman DI, Penaye J, Ngako V, Nzenti JP, Dautel D (1991) Données géochronologique nouvelles (Rb. 55) Rb-Pb et Sm-Nd) sur la zone mobile panafricaine de L'Est-Cameroun : âge Protérozoïque supérieure de la série de Lom. C.R .Acad. Sci. Paris, 31, série II; 1453-1458

Toteu SF, Michard A, Bertrand JM, Rocci G (1987) U-PB dating of Precambrian rocks from Northern Cameroon, orogenic évolution and geochronology of the Pan-African Belt of Central Africa. Precambrian Research, 37, 71-87

Toteu SF, Van SE, Penaye J, Nobe JB (1994) U-Pb and Sm-Nd evidence for Eburnean and panafrican high-grade metamorphism in cratonic rocks of Southern Cameroon. Precambrian Research, 67, 321-347

Toteu SF, Penaye J, Poudjom YD (2004) Geodynamic evolution of the Pan-African belt in central Africa with special references to Cameroon. Canadian Journal of Earths Sciences, 41: 73-85

Toteu SF, Penaye J, Deloule J, Van SE, Tchameni WR (2006) Diachronous evolution of volcano-sedimentary basins north of the Congo Craton: Insights from U-Pb ion microprobe dating Zircons from Poli, Lom and Yaoundé Group (Cameroon). J. of Afr. Earth Sci., 44, 428-442

Yakeu NM (1999) Etude du massif de Boumnyebel et ses relations avec les roches environnantes. Mem. Maitrise Univ. Yaoundé I. 63p

Zazenski R, Ashton WH, Briggs D (1995) Talc: occurrence, characterization, and consumer applications. Regul Toxicol Pharmacol, 21:218-229

Graphite veins mineralization in the Beni Bousera massif (Internal Rif, Morocco)

Amina Wafik and Zaineb Hajjar
Cadi Ayyad University, Morocco

Fernando Gervilla
Universidad de Granada, Spain

Rachida Bendaouad
Cadi Ayyad University, Morocco

Abstract. This paper describes Raman Spectroscopy and X-ray data of graphite from unusual sulfide and graphite deposits in ultramafic rocks from Beni Bousera massif (Morocco). These deposits occur as veins, stockworks and irregular masses, ranging in size from few cm to a few m in thickness. The primary mineral assemblages consist mainly of Fe–Ni–Cu sulfides (pyrrhotite, pentlandite, and chalcopyrite) and minor sulfoarsenides and arsenides, graphite and chromite. Weathering occurs in some deposits; the mineralized structures are mainly composed of graphite (up to 90%), chromite and iron oxides. These mineralogical assemblages confirm that graphite is crystallizing shortly before or during the formation of sulfides and chromite. Graphite has been probably crystallized at the temperature ranging from 660 to 850 °C, as indicated by X-Ray geothermometer based on c0 parameter. Therefore, Raman cartography of disordered graphite, in Malikath deposit, involves the presence of inclusions of nonodiamond crystal (<1 μm).

1 Introduction

Carbon is present in the mantle under two crystalline forms: diamond and graphite; the first one is restricted to kimberlites in cratonic areas; however, graphite is present in many environmental rocks (e.g. Luque et al. 1992; Deines 2002). Carbon origin in mantle derived rock removes some controversial proposition. For diamond in peridotitic rocks, carbon is thought to be indigenous to the mantle or has been incorporated into the mantle via subduction of crustal rocks (e.g. Pearson and Nixon, 1996). However, graphite can be resulted from diamond pseudomorph or assimilated from carbonaceous country rocks during magmatic ascent or emplacement (Barrenechea et al. 1997; Luque et al. 1998). Raman spectroscopy is a standard nondestructive tool for the characterization of crystalline, nanocrystalline and amorphous carbons; thus the Raman spectra of diamond consists of 1332 cm-1, but this of graphite show two quite sharp modes, the G peak around 1580-1600 cm-1 and the D peak around 1350 cm-1 (Ferrari 2007).

Vein graphite in ultramafic rock is a singular type of graphite mineralization presently known in the ultramafic massif of Beni Bousera (northern Morocco) and Serranía de Ronda (Southern Spain). These graphite occurrences were associated to sulfide mineralization in both massifs (S-G type; Gervilla 1990). In latest century, graphite mineralization was studied to understand its genesis. Crespo et al. (2006) link graphite occurrences associated to sulfide to a carbonaceous assimilation during mantle exhumation. In this paper, we try to determine the temperature of formation of graphite according to X-Ray Geothermometer.

2 Geological setting

The ultramafic massif of Beni Bousera massif (northern Morocco) is located in the Betic-Rifan orogenic belt; which is the westernmost part of the Mediterranean Alpine belt. The Beni Bousera massif is a portion of an old subcontinental lithospheric mantle that suffered partial melting, just before its tectonic emplacement, probably during the Middle Miocene (Afiri et al. 2011; Frets et al. 2014). Peridotites are the most common facies at the massif, and contain pyroxenites layers (Gysi et al. 2011; Chetouani et al. 2016).

The Beni Bousera massif is characterized by the presence of two types of small-scale magmatic deposits: the first one consists mainly of chromite and Ni arsenides (Cr-Ni ores), and the second one includes Fe-Ni-Cu sulphides containing variable proportions of graphite and minor chromite (S-G ores). Graphite mineralization appears as small pockets and veins. According to Gervilla (1990), they belong to Fe-Ni-Cu sulfides-graphite ores defined for ultramafic rocks in Beni Bousera and Serranía de Ronda massifs. In addition to this type of graphite, same pyroxenites layers are found as disseminated clocks.

The S-G mineralization is mainly composed of sulfides (pyrrhotite, pentlandite, and chalcopyrite) with low amounts of arsenides (maucherite, nickeline) and sulfarsenides (cobaltite) ± chromite ± graphite. This primary assemblage is associated with silicate gangues as phlogopite, pyroxene, and plagioclase (Gervilla 1990; Piña et al. 2013). Graphite occurrences in this type of mineralization,are present in a poor sulfides ores (< 10% of sulfides), and are associatedwith chromite and iron oxides which result from supergene alteration of sulfides.

3 Analytical methods

Six samples were collected from S-G ore-type especially from a poor sulfides ores; such as Malikath, and Amasiden deposit. All of these samples were confectioned as thin polished sections for optical microscopy studies (at department of geology, Faculty of Sciences Granada,

Spain). They are analyzed by X-Ray technique with a Cu anode (at chemistry department, Cadi Ayyad University, Marrakech, Morocco). This XRD data were treated in X Pert HighScore software to determine graphite structure, and other X-Ray diffraction parameters such as d0 spacing. Graphite minerals were determined by Raman spectra obtained at Lille 1 University (France). The Raman spectra were recorded with a LabRam HR800 Jobin-Yvon-microspectrometer equipped with 1800 g/mm gratings and using 532.28 nm (green) laser excitation. Acquisition time span varied from 10 to 20 s during five accumulating cycles. The spectra regions scanned were in the range 1000-2000 cm^{-1}. One sample was analyzed and cartographies by Raman spectroscopy in ThermoFisher Scientific lab to determine the distribution of graphite. We have been collected 20590 Raman Spectra with one µm mapping stage on X and Y axis, in thin section, without varying the depth profile. The Raman spectra were recorded with a DxRxi Raman microscope equipped with 1200 lines/mm gratings and using 455 nm laser. Acquisition time is 0.0083 s and 64 exposures number. The spectra regions scanned were in the range 86.9611-3500.3474 cm^{-1}.

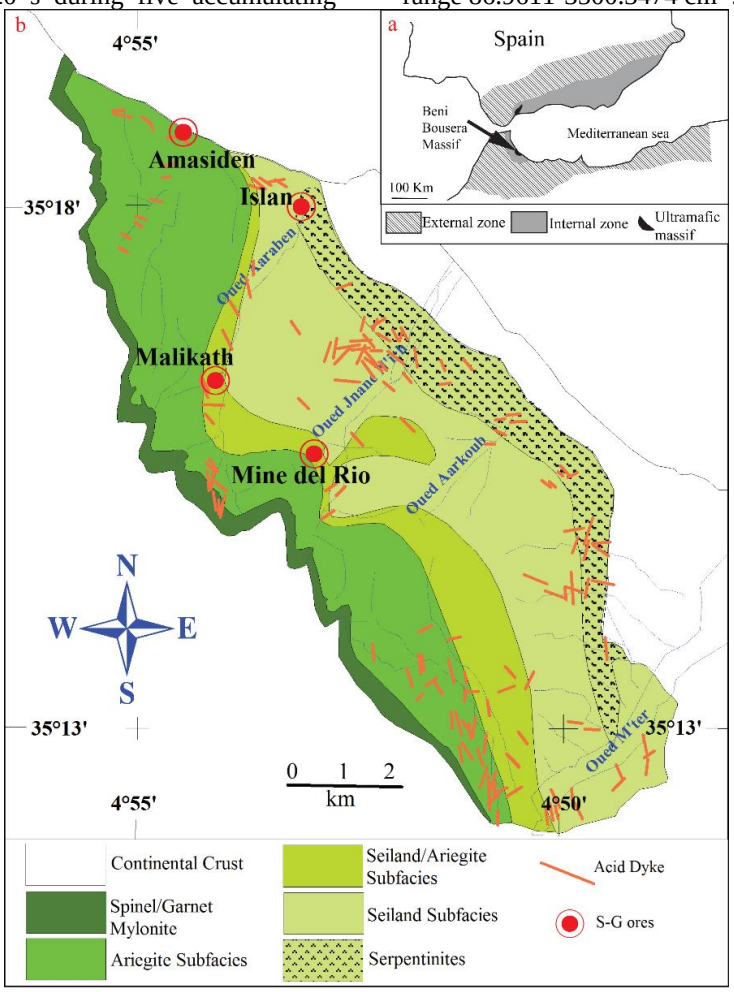


Figure 1. a Sketched map of the Rif Betic mountain belt showing the location of the Beni Bousera massif. **b** Structure of the Beni Bousera peridotite, with the localization of S-G ores (Modified from Frets et al. 2014; it includes the serpentinized area mapped by Reuber et al. 1982).

4 Results

4.1 Graphite vein deposit

Graphite veins are present in some deposits in Beni Bousera massif; the most important deposits are Malikath located in upstream of Ouad Araben, Mina del Rio and Islam in upstream of Ouad Jnane Nich (Fig. 1).

Graphite veins are composed of 80 to 90 % graphite and minor amounts of chromite (5-10 %) accompanied by variable amounts of iron oxides and hydroxides. Except in Mina del Rio deposit where graphite is associated with sulfides minerals. Graphite shows two different morphologies, appearing as randomly oriented flakes and as small nodules (up to 5 mm). The first one is present in the relatively fresh samples, and the second one is associated to iron oxides and hydroxides. The study of paragenetic succession reveals that graphite crystallizes shortly before or during the formation of sulfides and chromite formation.

4.2 Graphite Raman spectra

Raman spectra characterization of graphite shows that it is mainly disordered graphite (Fig. 2A). The main feature in

the Raman spectra of graphite is the so-called G and D peaks which lie at around 1582 and 1350-1354 cm^{-1} respectively. In Malikath samples we describe another type of graphite with G and D peaks at around 1582 and 1347-1349 cm-1 respectively (Fig. 2A). We remark that the G peak does not vary very well, comparatively to the D peak; so disorder in graphite structure can be monitored via the D peak; as it is described in the experimental study of Ferrari, (2007).

The Raman map of graphite from Malikath deposit, has allowed us the presence of disordered graphite, nanodiamond (1µm) and amorphous carbon (Fig. 2B, C, D). The presence of amorphous carbon in the weak structure and gaps can reflect polishing defect. The presence of nanodiamond crystal included in graphite may reflect the pseudomorphose of diamond to graphite.

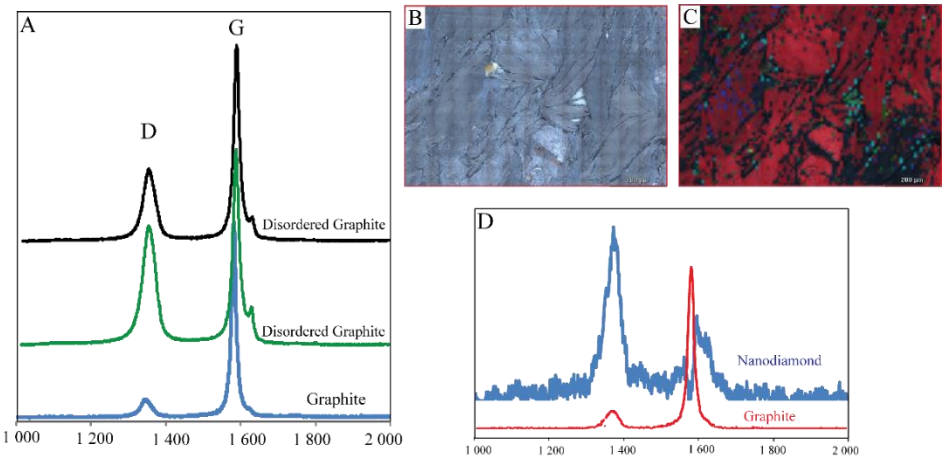


Figure 2: Raman spectroscopy data of graphite in S-G ores. **a** Raman shift of graphite. **b** image of mapped zone by Raman. **c** image resulting from Raman mapping (Red point: graphite; bleu points nanodiamond; green points: amorphous carbon). **d** Raman shift of graphite and nanodiamond obtained by Raman mapping.

4.3 Graphite temperature

Structural and thermal characteristics of graphite from the studied occurrences are given in Table 1. The structural characteristics of graphite by XRD technique show that basal spacing d002 is around 3.36 A°. Only rhombohedral structures are observed in those samples; but in the samples analyzed by Crespo et al. (2006), they describe only hexagonal structure. In any case, the c0 parameter, crystallite size (Lc) and graphitization degree (GD) reveals high crystallinity for graphite. Projection of c_0 parameter in Shengelia et al. (1979)'s geothermometer, demonstrate that minimum temperature of formation of graphite is in the range between 660 and 840°C.

5 Discussion

Graphite in mafic and ultramafic rocks has been traditionally interpreted as resulting from crustal assimilation or the reaction of organic carbon during the emplacement of these rocks (Hollister, 1980), or generated in relation to secondary process such as serpentinization (Pasteris 1981, 1988)

Table 1: XRD and thermal data of graphite from the studied S–G occurrences

	Amasiden	Malikath				Mina del Rio
Occurrences	28	36	38 a	1	39	MR
Parameters						
d 002 (A°)	3,347	3,352	3,347	3,354	3,357	3,347
c0	6,694	6,704	6,694	6,708	6,71	6,694
FWHM	0,34	0.1181	0,30	0,23		0,16
T (°C)	850	750	850	700	650	860

Graphite veins in sulfide-poor mineralizations in the Beni Bousera massif, analogous to those of Serranía de Ronda massif (Southern Spain), are described as the alteration products of magmatic mineralization like that studied in Mina del Rio (Gervilla, 1990; Gervilla et al., 1996, Gervilla et al., 2002). The magmatic crystallization of graphite is supported by the described textural relationships in primary, non-altered ores (e.g. graphite inclusions in chromite), as well as by its crystallization temperature (from 850 to 660 °C; calculated from its co parameter (Table 1; Luque et al., 1992). The origin of carbon in graphite, based on δ14C data, revealsthat graphite was generated in primary S-G ores by carbonaceous contamination during magmatic ascent (Crespo et al., 2006). Raman spectra of graphite indicate the existence of disordered graphite and graphite (s.s). In a sample from Malikath mapped by Raman spectroscopy, we can observe the presence of nanodiamond crystal (1 µm) included in

disordered graphite. This observation completed with SEM image of a nodule-like graphite aggregate from Mina Marbella (Serranía de Ronda) showing a nucleus with cubic morphology surrounded by laminar graphite crystals, was interpreted as relicts of graphitized diamonds by Crespo et al., (2006). These features support an origin of this mineral from graphite pseudomorphosed after diamond in S-G mineralizations both in Beni Bousera and in the Serranía de Ronda massifs. Graphitized diamonds have been described too in pyroxenites of the Beni Bousera massif (Pearson et al., 1989)

Thus, the formation of graphite veins in the Beni Bousera massif are difficult to explain by single serpentinization processes but their genesis fits better with a model based on primary magmatic concentration in the parent sulfide melts of S-G ores followed by late, low temperature hydrothermal alteration, most probably related with serpentinization fluids. Serpentinization does not affect graphite crystallinity; it only influenced some local characteristics of the graphite vein mineralization (Luque et al., 1992).

6 Conclusion

The graphite–sulfide deposits in the ultramafic rocks of the Beni Bousera are an unusual type of magmatic mineralization. They represent volumetrically large carbon accumulations in mantle-derived rocks. Geological and mineralogical characteristics of graphite vein deposits in this type of ore indicate that the temperatures of formation range from 660 to 850 °C. The metallogenic model of formation of graphite associated to Fe-Ni-Cu sulfide in this massif predicts a formation after residual melts that resulted from partial melting (and melt–rock reactions) of peridotites and pyroxenites by asthenospheric-derived melts. This Remarque was supported by its crystallization shortly before or during the formation of sulfides and chromite formation. These residual melts concentrated volatile components (mainly CO2 and H2O), as well as S, As, and chalcophile elements.

Acknowledgements

This study was supported by the FP7-PEOPLE-2013-IRSES MEDYNA project funded under Grant Agreement PIRSES-GA-2013-612572 (WP3 -Deep structures and mantle processes).

References

Afiri A, Gueydan F, Pitra P, Essaifi A, Précigout J (2011) Oligo-Miocène exhumation of the Beni Bousera peridotites through à lithosphère scale extensional shear zone. Géodynamica, 24/1, pp 49-60

Barrenechea J.F, Luque FJ, Rodas M, Pasteris JD (1997) Vein-type graphite mineralization in the Jurassic volcanic rocks of the external zone of the Betic Cordillera (southern Spain). Canadian Mineralogist 35, 1379–1390.

Chetouani K, Bodinier JL, Garrido CJ, Marchesi C, Amri I, Targuisti K (2016) Spatial variability of pyroxenite layers in the Beni Bousera orogenic peridotite (Morocco) and implications for their origin. C. R. Geoscience 348. 619–629

Crespo E, Luque FJ, Rodas M, Wada H, Gervilla F (2006) Graphite–sulfide deposits in Ronda and Beni Bousera peridotites (Spain and Morocco) and the origin of carbon in mantle-derived rocks, Gondwana Research 9, pp. 279 – 290

Deines P (2002) The carbon isotope geochemistry of mantle xenoliths. Earth- Science Reviews 58, 247– 278.

Ferrari AC (2007) Raman spectroscopy of graphene and graphite: Disorder, electron–phonon coupling, doping and nonadiabatic effects. Solid State Communications 143: 47–57

Frets E, Tommasi A, Garrido CJ, Mainprice D, Targuisti K, Amri I (2014) The Beni Bousera Peridotite (Rif Belt, Morocco): an Oblique-slip Low-angle Shear Zone Thinning the Subcontinental Mantle Lithosphere. J Petrol. doi:10.1093/petrology/egt067

Gervilla F, (1990) Mineralizaciones magmaticas ligadas a la evolución de los rocas ultramaficas de la Serranía de Ronda (Malaga, España). Thesis doctoral, Universidad de Granada, 171p

Gervilla F, Leblanc M, Torres-Ruiz J, Fenoll Hach-Ali P, (1996) Immiscibility between arsenide and sulfide melts: a mechanism for the concentration of noble metals. Canadian Mineralogist 34, 485–502.

Gervilla F, Gutierrez-Narbona R, Fenoll P, (2002) The origin of different types of magmatic mineralizations from small-volume melts in the lherzolite massifs of the Serranía de Ronda (Ma´laga, Spain). Boletin de la Sociedad Espanola de Mineralogia 25, 79–96.

Gysi AP, Jagoutz O, Schmidt MW, Targuisti K (2011) Petrogenesis of Pyroxenites and Melt Infiltrations in the Ultramafic Complex of Beni Bousera, Northern Morocco, Journal of Petrology, Vol. 0, N° 0, pp 1-57.

Hollister VF, (1980) Origin of graphite in the Duluth Complex. Economic Geology 75, 764– 766.

Luque FJ, Rodas M, Galan E (1992) Graphite vein mineralization in the ultramafic rocks of southern Spain: mineralogy and genetic relationships. Mineralium Deposita 27, 226– 233.

Luque FJ, Pasteris JD, Wopenka B, Rodas M, Barrenechea JF (1998) Natural fluid-deposited graphite: mineralogical characteristics and mechanisms of formation. American Journal of Science 298, 471–498.

Pasteris JD (1981) Occurrence of graphite in serpentinized olivines in kimberlites. Geology 9:356-359

Pasteris JD (1988) Secondary graphitization in mantle derived rocks. Geology 16:804-807

Pearson DG, Davis GR, Nixon PH, Milledge DP (1989) Graphitized diamonds from a peridotite massif in Morocco and implications for anomalous diamond occurrences. Nature 338:60-62.

Pearson DG, Nixon PH (1996) Diamonds in young orogenic belts: graphitised diamonds from Beni Bousera, N. Morocco, a comparison with kimberlite-derived diamond occurrences and implications for diamond genesis and exploration. Africa Geoscience Reviews 3, 295– 316.

Reuber I, Michard A, Chalouan A, Juteau T, Jermoumi B (1982) Structure and emplacement of the alpine-type peridotites from beni bousera, Rif, Morocco: a polyphase tectonic interpretation, Tecmnophysics. 82, pp. 23 l-25.

Piña R, Gervilla F, Barnes SJ, Ortega L, Lunar R, (2013) Partition coefficients of platinum-group and chalcophile elements between arsenide and sulfide phases as determined in the Beni Bousera Cr-Ni mineralization (North Morocco), Economic Geology, v. 108, pp. 935–951

Shengelia DM, Akhvlediani RA, Ketskhoveli DN (1979) The graphite geothermometer. Dokl. Acad. Nauk SSSR 235:132-134.

Mineralization in the serpentinites from the Kizhnica area, Kosovo

Katarzyna Werner
AGH University of Science and Technology, Poland

Abstract. The Kizhnica area is an example of two big overlapping tectonometamorphic and metallogenic events of regional importance: serpentinization of Jurassic ophiolitic complexes and hydrothermal activity related to Tertiary volcanic rocks. The purpose of the research was to describe ore mineralization present in serpentinite bodies in the surroundings of a former lead-zinc- s ilver mine. The s tudy, carried out using field observation, both reflected and transmitted light microscopy and E DS analysis, led to the observation of two different types of mineralization. The firs t type, chromium mineralization, was not present in a s ignificant amount. On the other hand, the notable presence of copper mineralization, linked to Tertiary igneous activity, suggests that hydrothermal processes are more widespread in the area than it was assumed in previous works and could help to predict the presence of other mineralization types which were not formerly reported. C opper mineralization is mineralogically poor and only chalcopyrite, bornite and pyrite with secondary minerals (azurite and malachite) were identified in the tectonic zones up to a few metres from the contact of serpentinite with micro-diorite bodies. All occurrences of copper mineralization were found in the tectonic zone running approximately in the NE -S W direction.

1 Location

The place of the research, Kizhnica is located in the eastern part of Kosovo, around 15 km southeast from Prisztina, the capital city of Republic of Kosovo. The geographical coordinates of the central part of the village are 42°36'3" North and 21°13' 3"East. Kizhnica is located in the mountainous region named Goljak Mountains. This unit belongs to the Rhodope system, that is one of the oldest in Europe. The field work was carried out around 500 meters from the former Kizhnica lead-zinc mine so it should be assumed that the mineralization that was found in small serpentinite quarries (Fig.1.) close to Kizhnica is connected with the mineralization occurring in the mine.

2 Serpentinites as a host rocks

Serpentinite rocks are the product of hydrothermal metamorphism. Besides opportunities of using them as decorative and crushed stones, they could host economically valuable deposits. The most important serpentinite-related commodities are chromite, talc, soapstone, asbestos and nickel laterite ore deposits (Pearre N, Hey l A, 1960). Finally, serpentinites (or the contact of serpentinites with other rocks) could be host rocks for various type of hydrothermal vein mineralizations. Usually lead-zinc, nickel or polimetalic mineralization occur in such environment (Borojevič-Šoštarič S, et al. 2013)

3 Methodology

In conducting this research, following methods were use: the field trip observations, the sampling, polarizing microscopy and Electron-Dispersive X-Ray Spectroscopy.

4 Results

Host rocks were divided into three groups according the mineralization they bear.

The first category is represented by samples of igneous rocks, micro diorite and peridotite. The occurrence of ore minerals that are present in the sample is too scarce to use the term mineralization.

Samples of serpentinite, carbonatized serpentinite and hydrothermal breccia belong to the second category, that is characterized by content of ore minerals around 1-3% ore minerals. Main ore mineral is chromite occurring in form of euhedral and subhedral grains accompanied by hematite and magnetite.

5 Serbo-Macedonian metallogenic province

Serbo-Macedonian metallogenic province covers the Central Balkan Peninsula. This province was assigned because of several similarities that occur within a large area. Genetic relation of magmatism and the ore deposition was indicated on the base on examining geochemical evolution trends of magmatism and isotopic composition of Pb and S. Mineralization was formed during the Alpine metallogenic epoch. It is associated with the calc-alkaline volcano-intrusive magmatic complexes. The age of those complexes is Tertiary. Volcanic and intrusive activity was the most intensive in the turn of Eocene-Pliocene. Later during Pliocene and Miocene the importance of these processes had declined. Within the province a few ore-forming stages were described. The most significant is the hydrothermal stage (Jankovic, 1974).

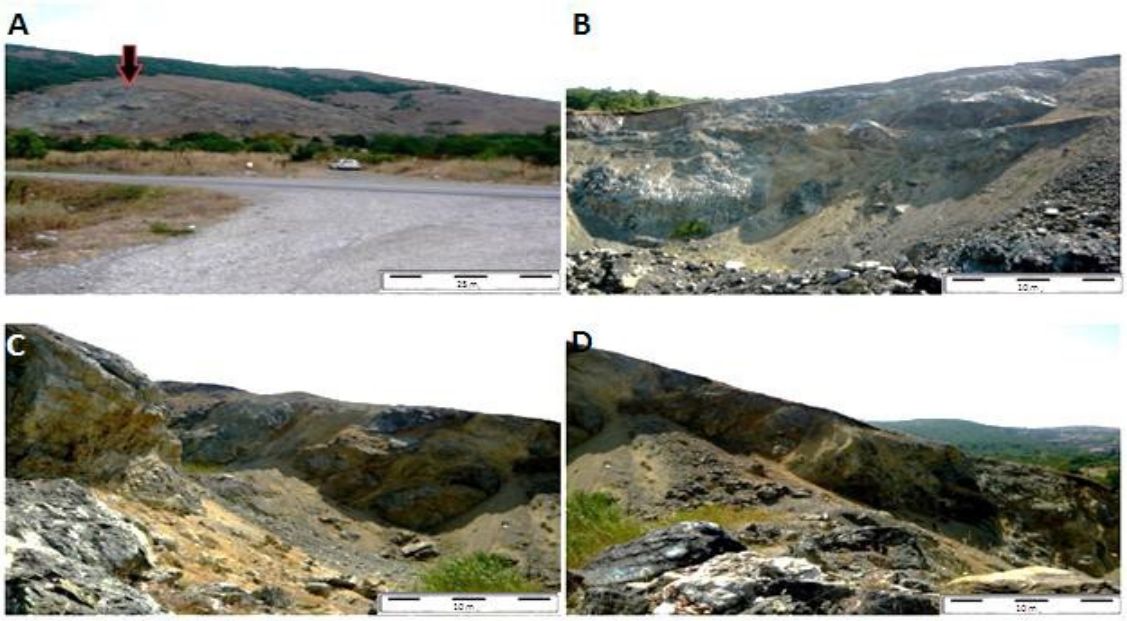


Figure 1. The serpentites quarry in Kizhnica. A (top lelt). The view from the road M-25- 2 on Kizhnica quarry B-D.

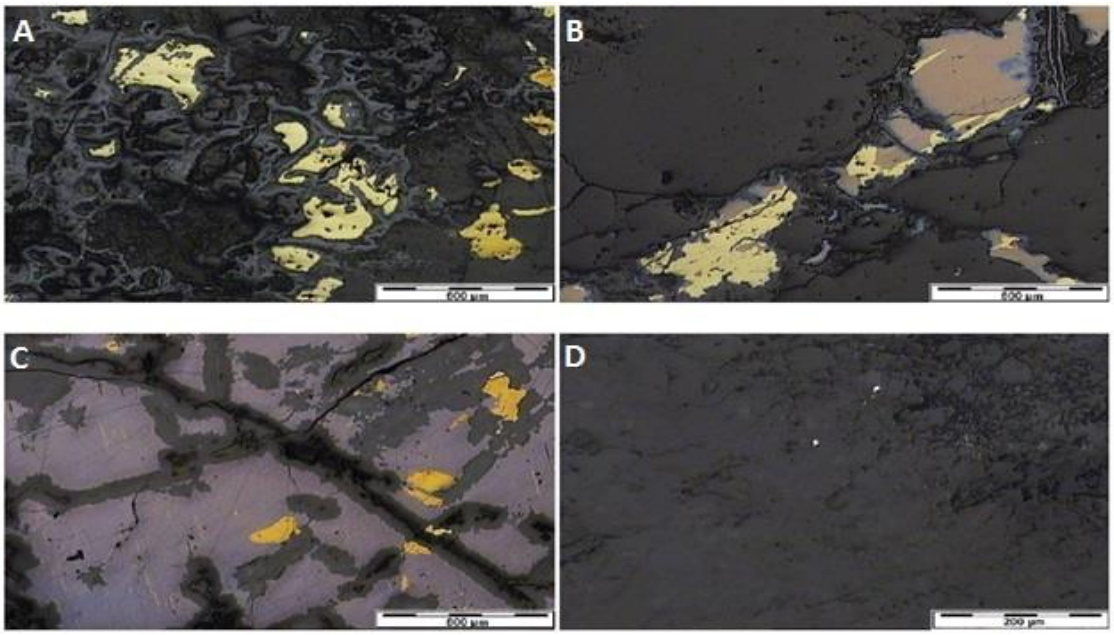


Figure 2. The copper mineralization observed under reflected light. Samples from top left: chalcopyrite with digenite top right: chalcopyrite, bornite and covellite; bottom left: bornite with chalcopyrite; bottom right: Mineral X.

Third category is composed of fragments of hydrothermal veins sampled in various part of the quarry (Fig.2.). The mineralization found here is composed of copper minerals such as chalcopyrite, bornite, covellite and digenite. In this group iron-bearing minerals, pyrite, sphalerite, goethite and lepidocrocite were observed as well. Mineral X found only in the third category was too small to be recognized by using polarizing microscopy. Electron Dispersive X-Ray Spectroscopy results indicate the presence of very pure form of galena.

6 Conclusion

The presence of serpentinite rocks indicates the possibility of the mineral deposit occurrences such as chromite, magnetite, rutile, talc or Ni-minerals. Also position of the area on the contact of serpentinite rocks with younger volcanites of andesitic composition give other possibilities for different hydrothermal mineralization. Only the two first minerals were found in the serpentinite quarries close to Kizhnica quarry in a significant amount. The occurrence of chromite can be described as a "birdseye" (disseminated) form. In some samples, the chromium content is quite big 2-3 %.

Surprisingly, the field work has provided new data about the existence of hydrothermal copper mineralization occurring in veins form in the contact zones between serpentinite bodies and micro-diorite dykes. The crystals of primary minerals like chalcopyrite and bornite occur in veins, that filled cracks. In the field, copper minerals were observed in much bigger amounts than chromite mineralization. Although there is no indication of lead-zinc- silver minerals that are a peculiarity of the Kizhnica open pit mine (Wojciechowski, 2014) hydrothermal changes such as sillification, silification, carbonatization, talcitization are exactly the same as in the former mine (Jankovic et al.,1997).

Acknowledgement

I would like to thank Dr. Krzysztof Dudek and MSc. Joanna Kołodziejczyk for their help in collecting data for the thesis and for their practical tips, which improve the quality of my work.

References

Borojevič-Šoštarič S, Huraj V, Neubauer F, Genser J, (2013) Silver-base metal epithermal vein and listwanite hosted deposit Crnac, Rogozna Mts., Kosovo, part II: A link between magmatic rocks and epithermal mineralization, Ore Geology Reviews, February 2013

Jankovič S,(1974) Metallogenic provinces of Jugoslavia in time and space.[in] Metallogeny and Concepts of the Geotectonic Evolution of Jugoslavia, Belgrade. pp 37-63.

Jankovič S, Serafimovski T, Jelenkovic R, Cifliganec V, (1997). Plate Tectonic Aspects of Alpine Metallogeny in the Carpatho-Balkan Region.[in] Magmatism, methamorphism and metallogeny of the Vardar Zone and Serbo-Macedonian Massif Štip-Dojran. Symposium, Annual Meeting, Faculty of Mining and Geology. pp 29-67.

Pearre N, Hey l A, (1960). Chromite and other mineral deposits in serpentine rocks of the piedmont upland, Maryland, Pennsylvania, and Delaware. Contributions to Economic Geology. Geological Survey Bulletin 1082-K, UNITED STATES GOVERNMENT

Vaskovic N, Matovic V, (2010). Ophiolites of the Vardar zone and Dinarides. Szeged:Acta Mineralogica-Petrographica.

Wojciechowski K, (2014). Pb-Zn okruszcowanie złoża Kizhnica, Kosowo. Krakow. University of Science and Technology, Faculty of Economic Geology.

The $^{234}U/^{238}U$ isotopic ratio as a vector to kimberlite pipes: the example of the Arkhangelsk diamondiferous province, Russia

Evgenii Yakovlev and Sergey Druzhinin
Federal Centre for Integrated Arctic Research (FCIAR)

Abstract. Abstract. Recently, the effectiveness of the use of traditional methods of search kimberlite pipes (magnetic survey) in the Arkhangelsk region has dropped greatly. For this reason there is need to develop new methods of searches of kimberlites. Studies conducted by us revealed new patterns in the distribution of radioactive isotopes within the kimberlite fields, in particular the isotopes of uranium (^{234}U and ^{238}U). The isotopic radio-geochemical studies has shown that that the kimberlite pipes are characterized by local radio isotope anomalies, on surface and along exploration drill core. Especially clearly it is manifested in the formation of non- equilibrium anomalous isotopic composition of uranium in the surrounding rocks of near-contact zone of the pipes. The revealed features of the distribution of uranium isotopes can be used to search kimberlites in other areas with similar geological conditions.

1 Introduction

Currently, the application of traditional methods of prediction and exploration for diamond deposits, such as magnetic surveys, in the Arkhangelsk diamondiferous province has become inneficient (Stognij and Korotkov 2010). Many other geophysical and geochemical methods, proven to solve the problem of search the primary diamond deposits did not show sustained efficiency (Kontarovich and Babayants 2011). The main complicating factors in the search for kimberlites in the territory are due to the peculiarities of the geological structure of the territory and the material composition of kimberlites (Androsov et al. 2004). In this regard, particular efforts are necessary to develop new approaches to solving the problems of searching diamond deposits and put them into practice prospecting.

One of the promising directions in the development of new technologies in the search for kimberlite bodies is the isotopic radiogeochemical method based on the whole complex of the radioisotopic features inherent to alkaline-ultramafic rocks (Yakovlev et al. 2016).

Most clearly it has been manifested in nonequilibrium uranium fixed in the exploration drill core. Previous studies have empirically revealed that at the endocontacts of kimberlite rocks the activity of ^{234}U isotope higher than its parent nuclide – ^{238}U. This isotope ratio $\gamma = {}^{234}U/{}^{238}U$ is higher than 1. The theoretical model of radioactive decay for ancestor and its daughter products foresees the oncoming of the secular equilibrium consisting in nuclide activity equation after a lapse of time (in comparison with duration of geological processes). For under consideration uranium series (isotopes ^{238}U and ^{234}U) this period is about 1 million years. Accordingly, in natural compounds occurred more than 1 million years ago in uranium series the secular equilibrium should be observed. Numerous studies of the isotopic composition of uranium of various rocks and minerals demonstrate significant deviation ratio of $\gamma={}^{234}U/{}^{238}U$ from equilibrium (Chalov 1975). As a rule, recent beds, such as peat, bottom sediments, soils, are significantly enriched by U-234. This is due to the fact that the ^{234}U atoms remote from bed rock accumulate in the re-deposited rocks exposed to natural waters (Rosholt 1983). Uranium-234 enrichment is also characteristic for the recent volcanic deposits (Cherdyntsev 1969). For the ancient rocks the activity ratio of even uranium isotopes for the above reasons, comes close to the equilibrium.

The values of the $^{234}U/^{238}U$ isotopic ratio in the rocks at the contact with kimberlites can reach up to 3.5 units, which were observed on Pioneerskaya pipe of Zolotitskoe ore field (Yakovlev et al. 2016). Furthermore, it was shown that the depending of the $^{234}U/^{238}U$ isotopic ratio on age and type of rock is not observed.

For obtaining new evidences of the detected phenomenon relative to some other kimberlite pipes and also for detection of general features of distribution of naturally occurring radioactive isotopes there is need to carry out detailed study. For this reason we have carried out studies of uranium isotopic composition in kimberlites and surrounding rocks the example of Arkhangelskaya and Karpinskaya-1 pipes of the Arkhangelsk diamondiferous province.

2 Methods

For the analysis of the uranium isotopic composition in the total uranium of rocks specimens were prepared by complete rock dissolving when subjected to strong acid mixture $HClO_4$ and HF in the ratio 4:1. The sample fully unsealed in such way was transformed into the nitric acid solution from which uranium isotopes were extracted with tributyl phosphate with subsequent purification from interfering radionuclides with similar energies of alpha particles.

The activity of uranium isotopes precipitated electrolytically on stainless steel disks was measured using the alpha-spectrometer "Progress" with a

semiconductor detector. Uranium output was controlled by the activity of indicator - synthetic isotope ^{232}U, added in the specimen.

3 Results and discussion

The $\gamma=^{234}U/^{238}U$ isotope ratio in Arkhangelskaya pipe ranges from 0.86 to 1.60 (Fig. 1).

In the rocks, whose age is more than 1 million years a close to the equilibrium value of γ should be observed by reason of radiogenic decay of uranium-234 atoms. However, in many samples the isotopic equilibrium is disturbed, the value of non-equilibrium uranium forms halo of the γ as concentric form with the values more than 1.1. The Halo of non-equilibrium uranium is pertained to near-contact zone of pipe and it is found in the Vendian enclosing rocks and sedimentary-volcanogenic sediments of crater facies in the contact with the Vendian. The average deviation from equilibrium in the Vendian sediments is 1.27, reaching values of up to 1.6. In the Carboniferous formation rocks the average isotope ratio of uranium is equal to 1. Autolithic breccias and tuffaceous sedimentary rocks of the lower section of the crater facies are characterized the equilibrium isotopic composition of uranium. The Quaternary sediments also are noted with the equilibrium value of γ.

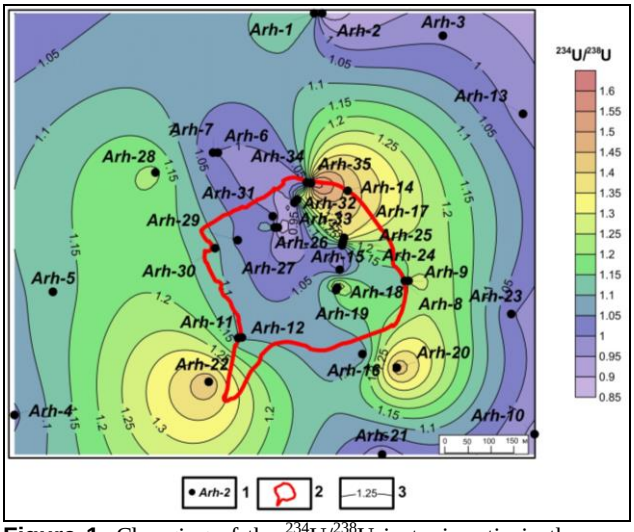


Figure 1. Changing of the $^{234}U/^{238}U$ isotopic ratio in the near-contact zone of Arkhangelskaya pipe. 1 - sampling point; 2 - circuit of Arkhangelskaya pipe; 3 - contour lines of the $^{234}U/^{238}U$.

Uranium concentration studied alpha spectrometry ranges from 0.6 to 4.07 ppm (Fig. 2). Autolithic breccia is characterized by a low concentration of uranium. It is also typical for bottom rocks of the crater facies of the pipe. The average uranium content in the rocks of the Carboniferous formation is about 1.2 ppm.

The uranium content in the Quaternary sediments is 1.4 ppm. The spatial pattern of distribution of uranium on alpha spectrometric data is different from spatial pattern of isotopic ratio however the increased concentration of uranium is also pertained to the Vendian rocks and of the crater rocks in contact with Vendian sandstones and siltstones. The average uranium content in these rocks is about 1.8 ppm. The spatial position of elevated uranium concentrations tends to the pipe contour. High concentration of uranium is localized in two areas on the northern and southern borders of the pipe.

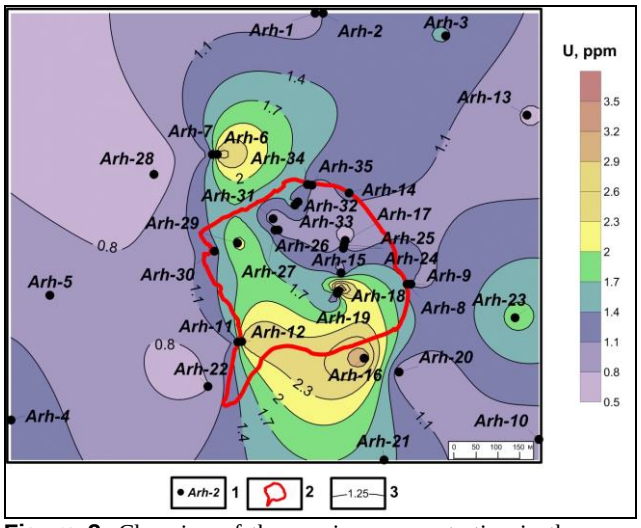


Figure 2. Changing of the uranium concentration in the near-contact zone of Arkhangelskaya pipe. 1 - sampling point; 2 - circuit of Arkhangelskaya pipe; 3 - contour lines of the uranium concentration.

The isotopic composition of uranium in kimberlites of Karpinskaya-1 pipe is changed varies from 0.99 – 1.04, the uranium concentration from 0.64 to 1.07 ppm. Sedimentary-volcanogenic sediments of crater facies is characterized by a wide range of variation of the γ value, which ranges from 1.05 to 1.23, and uranium concentrations ranging from 0.79 to 2.44 ppm. In the Carboniferous sandstones the average isotope ratio varies in the range 0.96 - 1.01, the uranium concentration is in the range 0.68 – 1.30 ppm. In the Quaternary formations represented a mixture of sand and gravel are observed gamma values, varying from 0.93 to 0.96, while changing of the concentration of uranium is in the range 1.33 – 1.91 ppm. Vendian enclosing rocks represented by sandstones are characterized the changing values of the γ in the most widely among from 0.89 to 1.54. Uranium concentration is changed from 0.63 to 1.89 ppm. The obtained evidence suggests that the isotopic composition of uranium in the studied samples is far from equilibrium, as required by the law of radioactive decay of uranium. In general, this is true for the studied Middle Carboniferous rocks, they are characterized by the equilibrium isotopic composition of uranium, it is also characteristically for the section of the overlying Quaternary rocks. Autolithic breccia has a close to equilibrium the isotopic composition of uranium.

An entirely different picture is characterized for the enclosing sediments of near-contact zone of the pipe that represented by Vendian sandstones, as well as tuffaceous sedimentary formations of crater facies referential to endocontacts of the pipe. The value of γ reaches 1.54,

which is characterized as a significant imbalance of isotopic equilibrium, which takes place at the contacts of enclosing rocks with the kimberlite pipe.

Thus, observed patterns of value of the $^{234}U/^{238}U$ isotopic ratio for Karpinskaya-1 pipe's specimens are in good agreement with data obtained for Arkhangelskaya pipe and confirm the unified nature of formation the excess uranium-234.

Probably, the structural and geological features of kimberlite pipes are cause of significant imbalance of the $^{234}U/^{238}U$ isotopic ratio in the near-contact zone of the pipes. This version is confirmed by the results of research, during which faults were recorded in the near-contact zone of Arkhangelskaya pipe (Ignatov 2009). Tectonic disturbances are detected in enclosing and overlying sediments of the pipe and reliably installed in Urzugskaya suite of the Carbon and Padunskaya suite of the Vendian (Vasiliev 2010). Furthermore, the endogenous bleaching of the Vendian rocks was discovered in the near-contact zone of the pipe (Ignatov et al. 2015). The halo of bleaching has a similar configuration with the halo of the $^{234}U/^{238}U$ isotopic ratio. The endogenous bleaching is fixed all around the perimeter of the pipe directly in the tectonic contacts of crater facie and at a distance of 300 m from the pipe (Ignatov et al. 2015).

The features of distribution the halo of the non-equilibrium uranium, more likely, also are caused with development of tectonic faults in the near-contact zone of the pipes. The features of ^{234}U distribution are in good agreement with the data on tectonic and material changes in the rocks of the near-contact zone. In this case the probable cause of isotopic nonequilibrium is the process of dynamics and circulation of groundwater through tectonic fractures in the surrounding rocks of near-contact zone. The change of groundwater circulation in near-contact zone by mixing saline water of the Vendian complex with fresh infiltration water creates the conditions for the deposition of uranium around the pipe. During these processes, the uranium mineral phases are formed and as a result, there is a modern active fractionation ^{234}U and ^{238}U in the near-contact zone.

4 Conclusion

In the Vendian surrounding rocks of the near-contact zone of Arkhangelskaya and Karpinskaya-1 pipes the excess ^{234}U has been detected. Probably, the high values of the $^{234}U/^{238}U$ isotopic ratio is associated with features of geological structure of near-contact zone of the pipes. The pattern of distribution of excess ^{234}U is consistent with the data on tectonic and material changes in the Vendian enclosing rocks. The reason of significant imbalance of uranium isotopic equilibrium is explained as a process of dynamics and circulation of groundwater through tectonic fractures limiting pipes.

Size of the halo of nonequilibrium uranium is up to two pipe diameters and it can be regarded as a local prospecting indicator of kimberlite pipes. The revealed features of the distribution of uranium isotopes can be used to search kimberlites in other areas with similar geological structure.

Acknowledgements

We like to acknowledge staff of the radiological laboratory FCIAR and all the people associated with us who have created an opportunity to engage these studies.

This work was supported by grant 16-35-00153 from the Russian Foundation for Basic Research.

References

Androsov EA, Verzhak VV, Larchenko VA (2004) On the structural control of the placement of kimberlite bodies on the example of the Arkhangelsk kimberlite province. VSEGEI 50: 9-18

Babayants PS, Kertsman VM, Levin FD, Trusov AA (2015) Special features of the state-of-the-art airborne gamma-spectrometry. Prospect of mineral resources 12:10-15

Chalov PI (1975) Isotopic fractionation of natural uranium. Ilim, Frunze

Cherdyntsev VV (1969) Uranium-234. Atomizdat, Moscow

Ignatov PA, Bolonin AV, Vasilyev ID (2012) Skladchatyye i razryvnyye deformatsii vo vmeshchayushchikh i perekryvayushchikh tolshchakh v kar'yere kimberlitovoy trubki Arkhangel'skaya. Rudy i metally 1:42-48

Ignatov PA, Zaripov NR, Kim V (2015) Tipy osvetlennykh krasnotsvetnykh kimberlitovmeshchayushchikh porod venda-kembriya Zimneberezhnogo rayona Arkhangel'skoy oblasti. Geologiya i razvedka. Izvestiya vuzov 2:15-21

Rosholt JN (1983) Isotopic composition of uranium and thorium in crystalline rocks. J. Geophys 88:7315-7330

Stogniy VV, Korotkov YuV (2010) The Search of the Kimberlite Bodies by Transients. Malotirazhnaya tipografiya 2D, Novosibirsk

Vasilyev ID (2010) Geologicheskiye struktury v okolotrubochnom prostranstve trubki Arkhangel'skaya i ikh ispol'zovaniye dlya poiskov korennykh mestorozhdeniy almazov v Zimneberezhnom rayone. Dissirtation, MGRI-RGGRU

Yakovlev EY, Kiselev GP, Druzhinin SV (2016) Non-equilibrium uranium in kimberlites and host rocks Pionerskaya pipe of the M.V. Lomonosov deposit. Vestnik of Northern (Arctic) Federal University 1:19-28

Genesis of the mottramite-bearing Jbel Haouanit Cu–Pb–Zn–V supergene ore deposit (Eastern High Atlas, Morocco)

Johan Yans, Michèle Verhaert, Augustin Dekoninck *University of Namur, Belgium*

Alain Bernard
Université Libre de Bruxelles, Belgium

Cécile Gautheron
Université Paris-Sud, France

Omar Saddiqi
University Hassan II, Morocco

Abstract. The Jbel Haouanit ore deposit, hosted in dolomitized Jurassic limestones, is located in the Oriental High Atlas (Morocco). Pb-Zn mineralizations have been exploited in an ancient underground mine, while Cu-Pb-V occurrences are currently mined in handmade ("artisanal") excavations. The primary sulfides of Jbel Haouanit, galena, sphalerite, pyrite, and chalcopyrite, underwent weathering processes leading to the precipitation of typical supergene minerals, mainly carbonates. Their formation was allowed by the buffering of the fluids acidity associated with the oxidation of sulphides, through the dissolution of the dolomitic host rocks. The paragenetic sequence is rather simple: galena has been successively replaced by anglesite and cerussite, sphalerite has been weathered in smithsonite, which was later replaced by hydrozincite, and pyrite has been pseudomorphosed in hematite and goethite. The weathering of chalcopyrite successively lead to the precipitation of chalcocite, covellite, malachite, and goethite. Late iron oxyhydroxides are mainly found at the top of the deposit. Occurrences of mottramite indicate that V-rich fluids have circulated in the deposits. The presence of secondary sulfides (galena, covellite) and mottramite is related to local fluctuations of the hydrostatic level.

1 Introduction

Morocco hosts a wide range of supergene deposits distributed along the High Atlas and the Anti-Atlas. The renewal of interest in these ore deposits, leading to new exploration and mining projects, has been induced by the rise of metal prices since the 2000s, the introduction of modern prospecting tools, and the increasing demand for metals for new technologies. Moreover, supergene metal deposits are easier and faster accessible and extractable than the primary minerals, and their metals and REE contents are typically higher (e.g. Reich and Vasconcelos 2015).

Here we focus on the Jbel Haouanit deposit, located close to the Moroccan city of Bou Arfa. The deposit is mostly known for its Pb-Zn mine that was exploited during the first half of the 20th century (until 1954), providing 150 000 tons of ore. Handcrafted excavations are currently exploited 2.5km away from the principal mine, for Cu and Cu-Pb-V ores. The purposes of this study are to 1) characterize the supergene mineral assemblages, 2) establish a mineral inventory, 3) identify the parageneses, and 4) propose a genetic model that includes the various mineralizations of the deposit, while giving some particular attention to the uncommon Cu-Pb-V occurrences.

2 Geological setting

The Jbel Haouanit mine is located at the northern edge of the Oriental High Atlas (Fig. 1). This intracontinental mountain belt was built in several steps, the two most dominant being the Mesozoic rifting and the Cenozoic tectonic inversion and uplift. The rifting, lasting from Permian to Middle Jurassic, has been induced by the break-up of Pangaea and the opening of the Tethys and Atlantic Oceans. The Late Cretaceous opening of the Atlantic Ocean modified the drifting direction of the African plate from heading E to NE, and made it converge with the Iberian (Eurasiatic) plate, triggering the basin inversion and generating fracturing, folding and sometimes detachment of the Mesozoic and Cenozoic cover units from the Variscan basement (e.g. Frizon de Lamotte et al. 2000, and references therein). In the studied area, three major episodes of Cenozoic uplift are defined by Leprêtre et al. (2015): late Eocene, early to middle Miocene, and late Pliocene to Quaternary. The paroxysmal compressional phase happened during Pliocene. These crustal processes coupled with a high asthenospheric heat flow are responsible for the current topography of the Atlas Chain (Missenard et al. 2006).

The Pb-Zn, Cu and Cu-Pb-V ores of Jbel Haouanit are hosted in Jurassic dolomitized series most likely Dogger in age, between Aalenian and Bathonian (Chefchaouni et al. 1963; Fig. 1). These limestones are strongly fractured, moderately folded, and lie unconformably on the Paleozoic schist basement. Numerous faults affect the Triassic, Jurassic and Cretaceous strata of the Bou Arfa region, in the E-W, NE-SW, and WNW-ESE directions; a major E-W oriented fault may be observed close to the main mine (Chefchaouni et al. 1963; Fig. 1).

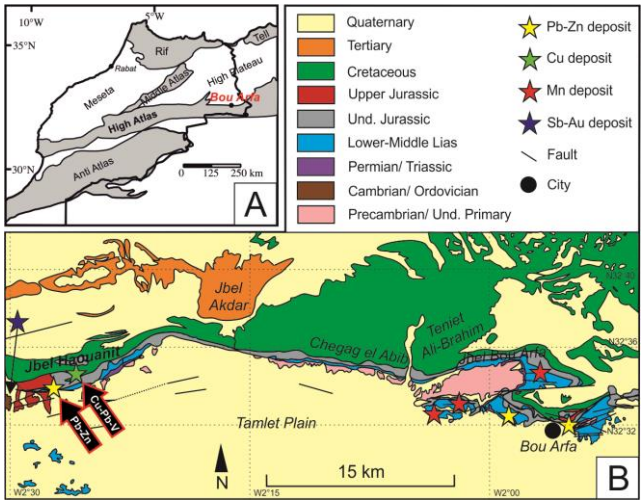


Figure 1. **a** Simplified geologic map of Morocco showing the location of Bou Arfa. **b** Synthetic geologic map of the Bou Arfa region showing the location of the Jbel Haouanit ore deposit in undetermined Jurassic dolostones (modified zoom of the geological map of Chefchaouni et al. 1963).

3 Materials and analytical methods

Field observation has been complemented by a multidisciplinary approach (transmission and reflection optical microscopy, XRD (X-Ray Diffraction), SEM (Scanning Electron Microscopy), geochemistry) for the mineralogical characterization.

4 Results and discussion

4.1 Host rock

The Jurassic host rock consists of a xenotopic recrystallized matrix of microcrystalline dolomite punctuated by rare iron oxyhydroxides, which results from the replacement of the primary limestone by dolomite. The presence of carbonates in the host rock has been of a major importance during the weathering, as it enabled the buffering of the fluids acidity and the precipitation of secondary minerals.

4.2 Cu and Cu-Pb-V mineralization

The copper ores mined in the small ("artisanal") excavations consist of highly brecciated chalcocite successively weathered in covellite and malachite, associated to botryoidal goethite (Fig. 2A, 3). Ore veins are 0.5 to 5 centimeters wide. Chalcopyrite and pyrite are thought to be the primary sulfides: the circulation of acidic, Cu-rich fluids in the deposit triggers the replacement of chalcopyrite in chalcocite, and the remobilization and precipitation of iron in goethite (Fig. 3). Covellite then replaces the highly fractured chalcocite, from the edges to the center, when fluids become less enriched in Cu (Fig. 2A, 3). Malachite finally replaces both chalcocite and covellite, by recombination of dissolved copper and bicarbonate ions (Fig. 2A, 3). Covellite often contains acanthite inclusions that are typically found in supergene oxidation zones, associated with low temperature secondary sulfides (Ramdhor, 1980). Small grains of partly oxidized pyrite, barite, copper-lead sulfosalts and phospho-arsenates are disseminated in the ore. Malachite also contains numerous small crystals of mottramite, a Cu-Pb hydrated vanadate.

Some excavations exhibit veins containing euhedral crystals of mottramite surrounded by (ferriferous) calcite and dolomite (Fig. 2B). Mottramite is typically found in oxidized zones of vanadium-bearing supergene deposits, but may also be abundant within/around Cu-sulfides ores. It is observed in the southern part of Africa (Namibia, Angola, Zambia) (Boni 2007, and references herein). This vanadate forms at low temperatures (40–50°C), in arid (Takahashi 1960), acidic and slightly reduced environments, such as the boundary between the phreatic and vadose zones (Boni et al. 2007).

Jbel Haouanit mottramite shows a positive Ce anomaly, suggesting its neoformation in relation with Eh variations (Leybourne et al. 2000). The slight enrichment in LREE (Light Rare Earth Elements), compared to HREE (Heavy Rare Earth Elements) in mottramite, also indicates that this mineral may have precipitated from slightly more acidic fluids than the other supergene minerals, where LREE are more soluble than HREE (De Putter et al. 1999).

Vanadium was initially restricted in minor quantities in the primary sulfides (e.g. galena) and in the host dolostone of Jbel Haouanit, in the range of 5–10 ppm. V was released with other ions during weathering. It was probably transported as calcium metavanadate ($Ca[VO_3]_2$) far away from its source (Van der Westhuizen et al. 1988) and precipitated by recombination with metal cations in favourable environments. Following Boni et al. (2007), the released Ca may then have reacted with bicarbonate ions to form dolomite and calcite.

All the Jbel Haouanit samples are V-rich, and Calamine rocks are also enriched in this metal compared to galena, suggesting that V-bearing fluids may have percolated in the whole deposit, and that mottramite may result from the same weathering step as the other secondary minerals. Once formed, mottramite does not seem to undergo further weathering. Note that descloizite, the Zn analogue of mottramite, was not found in this deposit.

4.3 Pb-Zn mineralization

In the Pb-Zn ore, mineralized veins are 1 millimeter to 20 centimeters wide, and mostly contain galena surrounded by lead and zinc weathering minerals (here designated as calamine; Fig. 2C). The principal primary sulfide observed in the ore is galena, but pyrite and sphalerite were likely initially present, as their weathering products (relics and pseudomorphs) are found in significant quantities (Fig. 3). The supergene mineral assemblage resulting from the weathering of these sulfides, under slightly acidic and oxidizing conditions, is dominated by carbonates. The predominant position of cerussite suggests a low acidity of

the mineralizing fluids, due to an efficient buffering of the acidity by dissolution of the carbonated host rocks.

Galena has been weathered to anglesite and cerussite: anglesite is found in fractures and cleavages, whereas cerussite also surrounds galena (Fig. 2C, 3). This divergence is related to the stability domains of these minerals: cerussite is stable under slightly acidic to basic conditions (pH >5), whereas anglesite usually forms in acidic environments (pH <5), where sulfate ions activity is high. These last specific conditions are typically found close to weathering-ongoing pyrite that causes locally substantial drops of pH, or in favorable microenvironments as fractures and cleavages. With increase of pH, anglesite is replaced by cerussite (Reichert 2007). At Jbel Haouanit, covellite is often observed at the contact between galena and cerussite/anglesite, and secondary galena is found in cavities, close to cerussite. The occurrence of these secondary sulfides suggests that, locally, slightly reduced conditions prevailed or that the environment was fluctuating between oxidizing and reduced conditions due to local variations of the hydrostatic level (Choulet et al. 2014).

Weathering of sphalerite in smithsonite began along cleavages and fractures, and later affected the whole crystal (Fig. 2D, 3). Smithsonite is only stable at pH lower than 7, and high CO_2 partial pressures, typically observed in percolating fluids that are not in equilibrium with the atmospheric CO_2. At the end of the weathering processes, when CO_2 pressure turned to atmospheric values, smithsonite became unstable and has been replaced by more stable hydrozincite (Reichert 2007). Smithsonite encloses anhedral inclusions of acanthite that are responsible for a remarkable enrichment in Ag (up to 450-550 ppm). The lack of Zn silicates at Jbel Haouanit indicates that the mineralizing fluids did not contain significant amounts of Si, which is quite rare in calamine deposits, but consistent with the low content in detritic elements of the host rock dolostone.

Small crystals of pyrite have been pseudomorphosed in iron oxyhydroxides: hematite and goethite are respectively observed at the center and external rim of the pseudomorphs. Goethite precipitates under acidic conditions, whereas hematite forms under more neutral pH conditions (Fig. 3; Jönsson et al. 2006, and references therein); goethite often replaces hematite. Iron oxyhydroxydes are the most enriched in REE, and are characterized by the highest contents in immobile elements, which is related to their low solubility and their in-situ precipitation. Large veins of hematite, goethite, and late (ferriferous) dolomite and calcite also surround the Pb- Zn ores.

The relative resistivity of galena to weathering, in comparison with the other sulfides, and its subsistence among the supergene mineralizations, is related to the geochemical behaviour of Pb. Because Pb is an immobile element, galena is replaced in situ by its quite insoluble weathering products that precipitate directly around the sulfide, creating an armoring protecting galena from further weathering and oxidation by (partially) hindering contact with the oxidizing agents (Reichert 2007). As Zn ions are particularly mobile under acidic conditions, sphalerite does not have such a protective layer, and is totally weathered.

Calamine samples and galena are rich in Ge (up to 16.5 ppm): in the sulfide, this enrichment is due to the common substitution, involving elements such as Fe, Cu, Ag, to Zn (Cook et al. 2009). When sphalerite is oxidized, Ge is released and may then accumulate in calamine samples (here particularly in smithsonite), by substituting Zn. All samples are also enriched in U, which is a typical supergene pattern.

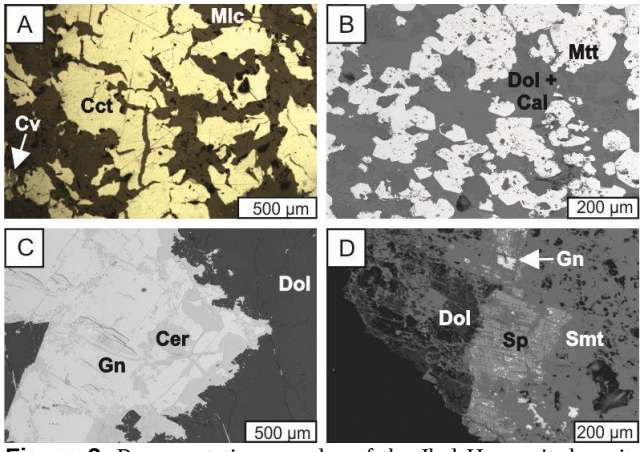


Figure 2. Representative samples of the Jbel Haouanit deposit: reflected light photomicrograph (**a**), and SEM microphotographs in backscattered electrons mode (**b**, **c**, **c**). **a** Lattice of chalcocite (Cct), covellite (Cv) and malachite (Mlc). **b** mottramite (Mtt) surrounded by dolomite and calcite (Cal). **c** weathering of galena (Gn) in cerussite (Cer), surrounded by dolomite (Dol). **d** sphalerite (Sp) weathered in smithsonite (Smt), close to galena and dolomite.

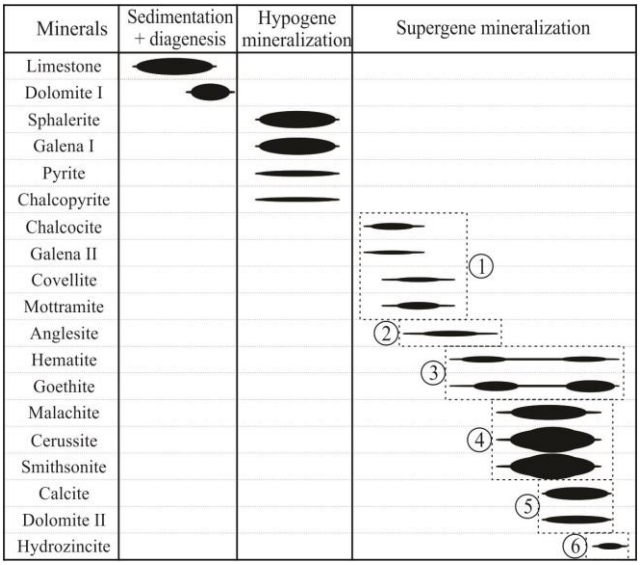


Figure 3. Tentative paragenetic sequence for the Jbel Haouanit deposit.

5 Conclusion: weathering profile in the ore

Clear parageneses are easily identified at Jbel Haouanit. The hypogene galena has been successively replaced by anglesite and cerussite, whereas sphalerite has been weathered in smithsonite and hydrozincite. The occurrence of copper minerals and mottramite indicates that Cu, Pb, V bearing fluids have also circulated through the Jurassic host rocks. As shown in Figure 4, the weathering of the hypogene sulfides led to the formation of several mineralogical zones: the primary sulfides zone (chalcopyrite, pyrite, galena, sphalerite), the secondary sulfides zone (chalcocite, covellite, mottramite), the oxidized ores zone (cerussite, anglesite, smithsonite, hydrozincite, malachite, mottramite, iron oxyhydroxides), and the leached zone (iron oxyhydroxides and late calcite and dolomite, principally). The secondary sulfides zone of the Pb-Zn deposit is quite reduced, in comparison to that of the Cu and Cu-Pb-V occurrences.

No dating has yet been performed on these supergene mineralizations, although it could bring very useful information on the refined chronology of this deposit. Geochronological data are also essential to insert supergene ore genesis in the climate and geodynamic evolution of the metallogenic province (i.e. relations between the supergene mineralizations and the Cenozoic High Atlas uplifts). For this purpose, (U-Th)/He chronology will be carried out on some supergene goethite and hematite.

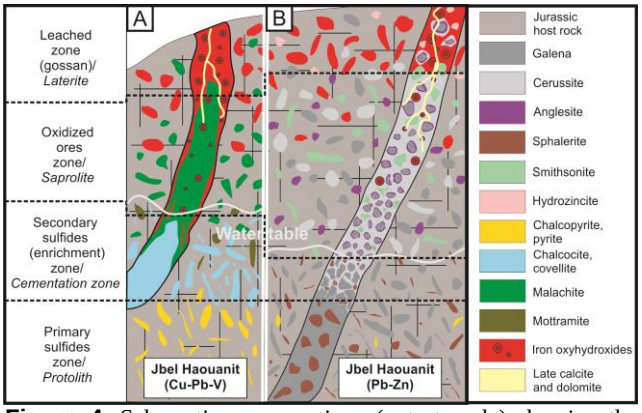


Figure 4. Schematic cross-sections (not at scale) showing the mineralogical zones of the Jbel Haouanit supergene ore deposits and the most common mineral phases. **a** Cu-Pb-V deposit of Jbel Haouanit. **b** Pb-Zn deposit of Jbel Haouanit (adapted after Robb 2005).

Acknowledgements

Michèle Verhaert thanks the Belgian Fund for Scientific Research (FNRS-FRIA), for providing a FRIA PhD grant. The authors are grateful to the administration of Bou Arfa for its role in providing field access. Georges Zaboukis (ULB), Patrick Kubben (ULB), and Gaëtan Rochez (UNamur) are thanked for the confection of thin and polished sections, and technical help for XRD data.

References

Boni M, Terracciano R, Evans NJ, Laukamp C, Schneider J, Bechstädt T (2007) Genesis of vanadium ores in the Otavi Mountainland, Namibia. Econ. Geol. 102:441–469

Chefchaouni YC, Diouri M, Choubert G (1963) Carte géologique du Haut Atlas oriental, feuilles Bou Arfa, Iche, Talzaza et Figuig. Notes et Mém. Serv. Géol. Maroc 158 (French)

Choulet F, Charles N, Barbanson L, Branquet Y, Sizaret S, Ennaciri A, Badra L, Chena Y (2014) Non-sulfide zinc deposits of the Moroccan High Atlas: multi-scale characterization and origin. Ore Geol. Rev. 56:115–140

Cook NJ, Ciobanu CL, Pring A, Skinner W, Shimizu M, Danyushevsky L, Saini-Eidukat B, Melcher F (2009) Trace and minor elements in sphalerite: A LA-ICPMS study. Geochim. Cosmochim. Acta 73:4761–4791

De Putter T, Charlet JM, Quinif Y (1999) REE, Y and U concentration at the fluid-iron oxide interface in late Cenozoic cryptodolines from Southern Belgium. Chem. Geol. 153:139 – 150

Frizon de Lamotte D, Saint Bezar B, Bracène R (2000) The two main steps of the Atlas building and geodynamics of the western Mediterranean. Tectonics 19/4:740–761

Jönsson J, Jönsson J, Lövgren L (2006) Precipitation of secondary Fe(III) minerals from acid mine drainage. Appl. Geochem. 21:437–445

Leprêtre R, Missenard Y, Saint-Bezar B, Barbarand J, Delpech G, Yans J, Dekoninck A, Saddiqi O (2015) The three main steps of the Marrakech High Atlas building in Morocco: structural evidences from the southern foreland, Imini area. J. Afr. Earth Sci. 109:177–194

Leybourne MI, Goodfellow WD, Boyle DR, Hall GM (2000) Rapid development of negative Ce anomalies in surface waters and contrasting Rare Earth Elements patterns in groundwaters associated with Zn-Pb massive sulphide deposits. Appl. Geochem. 15:695–723

Missenard Y, Zeyen H, Frizon de Lamotte D, Leturmy P, Petit C, Sébrier M, Saddiqi O (2006) Crustal versus asthenospheric origin of relief of the Atlas Mountains of Morocco. J Geophys Res: Solid Earth, 3, 1-13

Ramdohr P (1980) The ore minerals and their intergrowths, second edition, vol. 2, Pergamon Press, Oxford, United Kingdom

Reich M, Vasconcelos PM (2015) Geological and economic significance of supergene metal deposits. Elements 11, 305 -310.

Reichert J (2007) A metallogenetic model for carbonate-hosted non-sulphide zinc deposits based on observations of Mehdi Abad and Irankuh, Central and Southwestern Iran. Thesis at the Martin-Luther-Universität Halle-Wittenberg

Robb LJ (2005) Introduction to ore-forming processes. Blackwell Science LtD, USA

Takahashi T (1960) Supergene alteration of zinc and lead deposits in limestone. Econ. Geol. 55:1083–1115

Van der Westhuizen WA, Tordiffe EA, de Bruiyn H, Beukes GJ (1988) The composition of descloizite-mottramite in relation to the trace element distribution of Pb, Zn, Cu and V in the Otavi Mountain Land, South West Africa/Namibia. J. Geochem. Explor. 34:21–29

Zircon U-Pb dating and Sr-Nd-Pb-Hf isotopes of the ore-associated granite porphyry at the Longgen Pb-Zn deposit, Tibet

Yong-Chao Zhang, You-Ye Zheng, and Shun-Bao Gao
China University of Geosciences, Beijing, China

Abstract. Longgen is one typical Pb-Zn skarn deposit form- ed in the Nyainqentanglha metallogenic belt, Western Tibet. Lead-zinc mineralization mainly occurs as vein or lenticular in the external contact belt of skarnization limestone. Granite porphyries yield a weighted average zircon $^{206}Pb/^{238}U$ age of 64.3±0.7Ma, slightly older than the molybdenite Re-Os isochron age of 61.5±0.6 Ma, suggesting that the Longgen was formed in the Palaeocene. Granite porphyries show high contents of SiO_2, K_2O and CaO, low contents of TiO_2 and P_2O_5, and peraluminous high-K calcalkaline of S-type granite, with obvious LREE enrichment and negative Eu anomalies. They have low $(^{87}Sr/^{86}Sr)_i$ ratios of 0.71262 to 0.71482, εNd(t) values of -6.78 to -6.13, and T_{DM2}(Nd) ages of 1.37 to 1.42 Ga. Their $(^{206}Pb/^{204}Pb)_t$, $(^{207}Pb/^{204}Pb)_t$ and $(^{208}Pb/^{204}Pb)_t$ values are 18.581-18.735, 15.653-15.713, and 38.932-39.158, respectively. Zircons εHf(t) values of the granite porphyry range from -4.57 to -2.65, with T_{DM2}(Hf) ages of 1.30-1.43 Ga. These geochemical and isotopic data imply that the Longgen granite porphyry originated mainly from partial melting of ancient continental crust materials of Gangdese micro-continent accompanied by fractional cryst- allization during the main collision between Indian and Asian. In addition, we conclude that the India–Asia continental initial collision started no later than 65 Ma.

1 Introduction

The Gangdese metallogenic belt within the Lhasa terrane is one of the most important metallogenic belts in China, including the Gangdese porphyry Cu-Mo belt (GPCB) in the southern Lhasa subterrane and the Nyainqentanglha Pb-Zn-Fe-Ag polymetallic belt (NTPB) in the central Lhasa subterrane immediately north of Gangdese porphyry copper belt. In recent decades, a large number of large Pb-Zn (Fe-Cu) polymetallic deposits were found in NTPB (Tang et al. 2012; Hou et al. 2015; Wang et al. 2016; Zhao et al. 2016). Based on systematic reviews of the key metallogenic settings and resultant collision-related ore deposits, Hou and Cook (2009) suggested that the mineralization can be divided into three principal metallogenic epochs in the Gangdese metallogenic belt: (1) a main collisional convergent setting (~65 to 41 Ma); (2) a late-collisional transform structural setting (~40 to 26 Ma); (3) and a post-collisional crustal extension setting (~25 to 0Ma).

Longgen is considered as a highly prospective deposit in western of NTPB. However, the petrology, geochemistry, isotope systematics and genesis of the granite porphyry at the deposit are lacking. In addition, the metallogenic geodynamic settings of the belt remain unclear. Moreover, the age of the initial collision of Indian and Asian continents is still controversial.

In this contribution, we report new data for the granite porphyry related to Pb-Zn mineralization in Longgen deposit, including major and trace elements and zircon U-Pb isotopes, zircon Hf isotopes, and Sr-Nd-Pb isotope compositions. And thereby, comprehensively define the age and genesis of the granite porphyry, discuss the tect- onic setting of Longgen skarn Pb-Zn system. Furthermore,we discuss the time of India–Asia continental initial collision.

2 Geology

Longgen Pb-Zn skarn deposit, located in the western of NTPB, has 63,000 t Pb with average grade of 3.21 %, 57,000 t Zn with average grade of 2.43 % and 109.1 t Ag with average grade of 46.74 g/t.

The strata are mainly the Middle Permian Xiala Formation and the Eocene Nianbo Formation (Fig. 1). The Xiala Formation mainly contains fine grained clastic rocks and limestone. The Nianbo Formation exposed in the central eastern part, mainly consists of tuff. The main structure in the deposit is NW-striking fault. The Xiala Formation was intruded by granite porphyry related to skarn and mineralization. Skarn present at the contact between the granite porphyry and the limestone (Fig. 1).

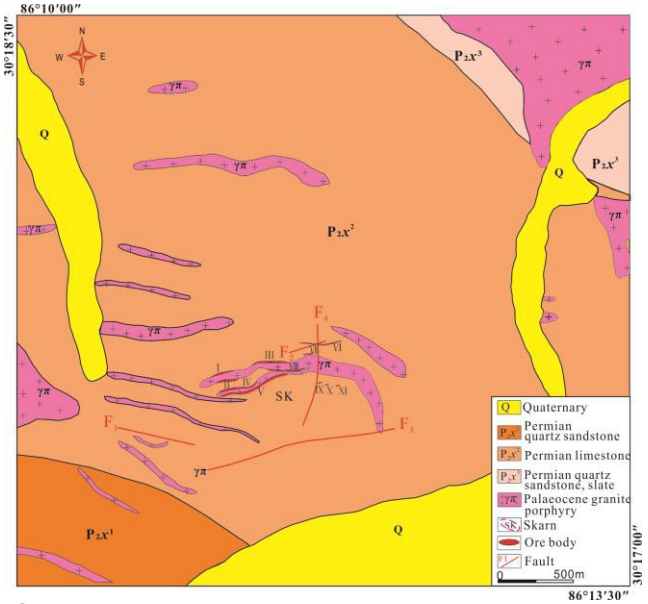


Figure 1. Geological map of the Longgen Pb–Zn skarn deposit

The deposit consists of eleven Pb-Zn polymetallic orebodies. Most of the orebodies are stratiform, lenticular and vein, occurred in the skarn between the Xiala Formation and the granite porphyry. Ore textures are mainly disseminated, banded and massive. Primary ore minerals are sphalerite and galena, with minor chalcopyrite, pyrite, magnetite and pyrrhotite. Gangue minerals are quartz, calcite, diopside, garnet, actinolit, epidote and chlorite.

3 Results and discussion

Zircon grains from granite porphyry at Longgen yield a weighted mean $^{206}Pb/^{238}U$ age of 64.3 ± 0.7 Ma. These zircon U-Pb ages are also geologically consistent with the molybdenite Re-Os ages of 61.5 ± 0.6Ma (Gao et al. 2012). They suggest that the Longgen Pb-Zn skarn mineralization was formed in the period of 65 to 61 Ma, the main collision setting of the collision between Indian and Asian.

The granite porphyries have high contents of SiO_2 (72.02–74.26%), alkalis (Na_2O+K_2O = 5.78–8.31%) and Al_2O_3 (12.43–13.8%), but low contents of TiO_2 (0.2–0.26%) and P_2O_5 (0.05–0.07%). The values of K_2O/Na_2O, A/CNK and $Mg^{\#}$ are 1.55–2.06, 1.01–1.15 and 27–33, respectively. All the studied samples have ΣREE+Y contents of 217 to 233 ppm, showing steep LREE and flat HREE patterns (Fig. 2a) with $(La/Yb)_N$ ratios of 11.3 to 12.7, and obvious Eu depletions with δEu of 0.52 to 0.61. They exhibit strong peaks of Rb, Th, U, K, Ta and Hf, and troughs of Eu, Nb, Sr, Ba, P and Ti in the primitive mantle-normalized diagram (Fig. 2b). The geochemical characteristics suggest that the Longgen granite porphyry belong to the peralumin- ous high-K calcalkaline of S-type granites, indicating that the intrusion is crust-sourced granite, and underwent high degree of differentiation evolution in continental collision geodynamic background.

The granite porphyries have $^{87}Rb/^{86}Sr$ and I_{Sr} values of 1.4433−4.1801 and 0.70927–0.71350. Their εNd(t) and TDM_2(Nd) values are -6.78–-6.13 and 1.37–1.42 Ga. Which are identical to an ancient continental crust source (Fig. 4). The $(^{206}Pb/^{204}Pb)_t$, $(^{207}Pb/^{204}Pb)_t$, and $(^{208}Pb/^{204}Pb)_t$ values of granite porphyries are 18.581–18.735, 15.653–15.713 and 38.932–39.158, respectively, suggesting a upper crust and orogen mixed Pb isotopic signature. Furthermore, the initial ratios of $^{176}Hf/^{177}Hf$ are between 0.282604 and 0.282658, εHf(t) values range from -4.57 to -2.65 (Fig. 3), with corresponding TDM_1 of 0.84–0.93 Ga and TDM_2 of 1.30–1.43 Ga. These isotope compositions are generally indicative of Longgen granite porphyry originated mainly from partial melting of ancient continental crust materials of Gangdese micro-continent (Zhu et al. 2009, 2011).

Dynamic modeling of slab detachment predicts that there are 10 to 20 Ma delay times between the initiation of continental collision and the occurrence of slab break-off (Hunen and Allen 2011). So studies the time of break–off can constrain the initiation of continental collision.

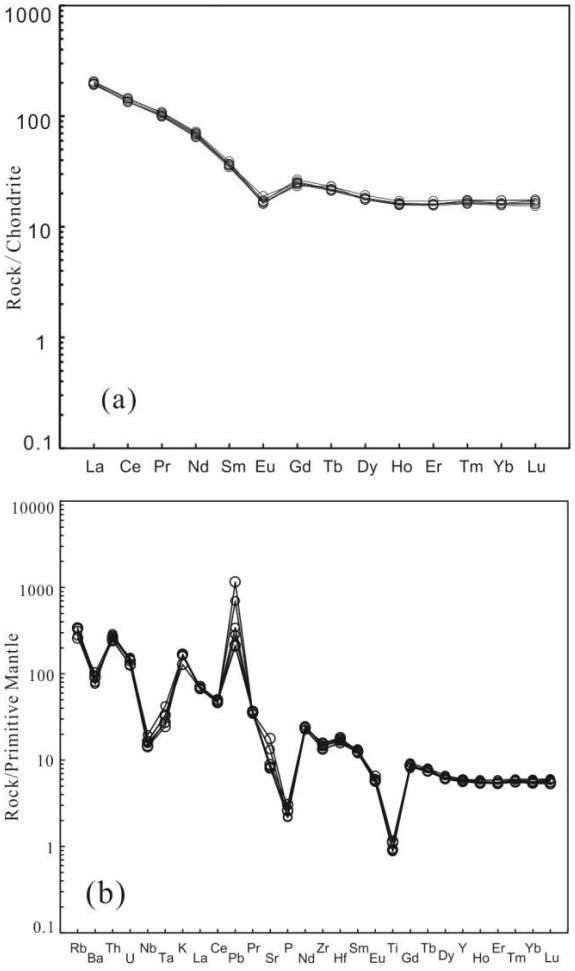


Figure 2. Chondrite-normalized REE patterns (a) and primitive mantle-normalized trace element patterns (b) of the Longgen granite porphyry. Reference data of chondrite and primitive mantle are from (Sun and McDonough 1989)

Linzizong volcanic rocks were formed during the break– off of the subducted Neo–Tethyan slab (Lee et al. 2012), The Pana Group who is the upper Linzizong Formation was formed at 53.9–47.1 Ma (e.g., Lee et al. 2004; Fu et al. 2014). Thus, the break–off of the Neo–Tethyan slab occurred no later than 53.9–47.1 Ma. Abundant magmatic rocks were produced during collision between Indian and Asian. These magmatic rocks formed between 68.8 and 51.5 Ma (e.g., Zhao et al. 2014, 2016; Hou et al. 2015; Zheng et al. 2015) associated with Pb-Zn (Fe-Cu) poly- metallic deposits, such as Narusongduo Pb-Zn, Yaguila Pb-Zn-Ag, Dongzhongsongduo Cu-Pb-Zn, Dongzhongla Pb-Zn-Cu-Ag, Mengya'a Pb-Zn-Ag, Chagele Pb-Zn-Cu, Jialapu Fe, Lietinggang Fe polymetallic, Silongduo Fe pol- ymetallic deposit. Therefore, we conclude that the India– Asia continental initial collision started no later than 65 Ma.

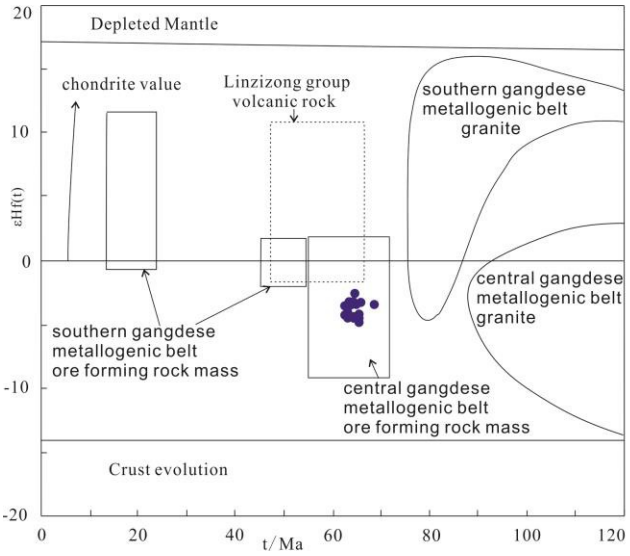


Figure 3. εHf(t) vs. T (Ma) diagram of the Longgen granite porphyry

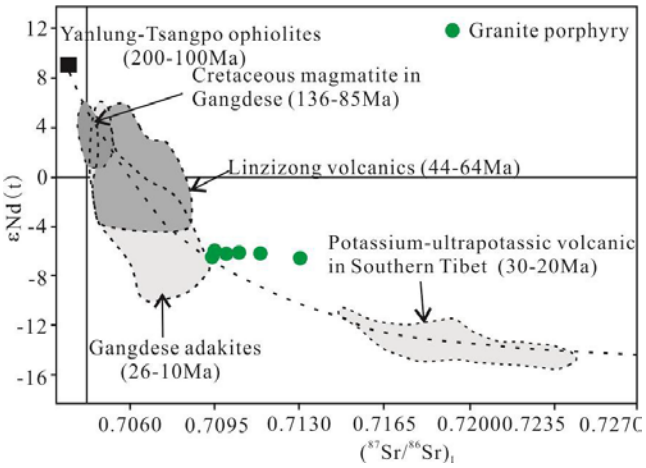


Figure 4. Sr and Nd isotopic compositions of Longgen granite porphyry

4 Conclusions

1. Zircons from the Longgen granite porphyry yield a weighted average $^{206}Pb/^{238}U$ age of 64.3 ± 0.7 Ma, slightly older than the molybdenite Re–Os ages of 61.5 ± 0.6 Ma, constraining that the Longgen skarn Pb-Zn system occurred in the span of 65–61 Ma.
2. The element geochemistry, the Sr-Nd-Pb isotope system- atics and the zircon Hf isotopes signature of the granite porphyry indicate that Longgen Skarn Pb-Zn system has originated mainly from partial melting of ancient continental crust materials of Gangdese micro-continent in the main collision setting of the collision between Indian and Asia.
3. We conclude that the India–Asia continental initial collision started no later than 65 Ma.

Acknowledgements

Research for this paper was supported by the Commonweal Project from China Geological Survey (DD2016027 and 12120101000015014).

References

Fu WC, Kang ZQ,Pan HB (2014) Geochemistry, zircon U-Pb age and implications of the Linzizong Group volcanic rocks in Shiquan River area, western Gangdise belt, Tibet. Geol Bull Chin 33: 850-9(in Chinese with English abstract)

Gao, SB, Zheng, YY, Tian, LM, Zhang Z, Qui WJ,Liu MY (2012) Geochronology of Magmatic Intrusions and Mineralization of Chagele Cu-Pb-Zn Deposit in Tibet and its Implications. Earth Sci, 37(3):507-514(in Chinese with English abstract)

Hou Z, Cook NJ,Zaw K (2009) Metallogenesis of the Tibetan collisional orogen. Ore Geol Rev 36: 2-24

Hou Z, Duan L, Lu Y, Zheng Y, Zhu D, Yang Z, Yang Z, Wang B, Pei Y, Zhao Z,McCuaig TC (2015) Lithospheric Architecture of the Lhasa Terrane and Its Control on Ore Deposits in the Himalayan-Tibetan Orogen. Econ Geol 110: 1541-75

Hunen JV,Allen MB (2011) Continental collision and slab break-off: A comparison of 3-D numerical models with observations. Earth Planet Sci Lett 302: 27-37

Lee HY, Chung SL, Wen DJ, Lo CH, Ji J, Qian Q, Lee TY(2004) New age and geochemieal constraints of the origin of the Linzizong volcanic successions, soutern Tibet. . Eos Trans. AGU, Western Pacific Geophysics Meeting Abstracts Honolulu 164p

Lee HY, Chung SL, Ji J, Qian Q, Gallet S, Lo CH, Lee TY,Zhang Q (2012) Geochemical and Sr–Nd isotopic constraints on the genesis of the Cenozoic Linzizong volcanic successions, southern Tibet. J Asian Earth Sci 53: 96-114

Sun SS, McDonough WF (1989) Chemical and isotopic systematics of oceanic basalts: implications for mantle composition and processes. Geol Soc Lond Spec Pub 42: 313-45

Tang, JX, Duo,J, Liu, HF, Lang XH, Zhang JS 2012. Minerogenetic Series of Ore Deposits in the East Part of the Gangdese Metallogenic Belt. Acta Geos Sinica 33(04):393-410(in Chinese with English abstract)

Wang L, Cheng W, Tang J, Kang H, Zhang Y,Li Z (2016) U–Pb geochronology, geochemistry, and H–O–S–Pb isotopic compositions of the Leqingla and Xin'gaguo skarn Pb–Zn polymetallic deposits, Tibet, China. J Asian Earth Sci 115: 80-96

Zhao J, Li G, Evans NJ, Qin K, Li J,Zhang Xn (2016) Petrogenesis of Paleocene-Eocene porphyry deposit- related granitic rocks in the Yaguila-Sharang ore district, central Lhasa terrane, Tibet. J Asian Earth Sci 129: 38-53

Zhao J, Qin K, Li G, Li J, Xiao B, Chen L, Yang Y, Li C,Liu Y (2014) Collision-related genesis of the Sharang porphyry molybdenum deposit, Tibet: Evidence from zircon U–Pb ages, Re–Os ages and Lu–Hf isotopes. Ore Geol Rev 56: 312-26

Zheng YC, Fu Q, Hou ZQ, Yang ZS, Huang KX, Wu CD, Sun QZ (2015) Metallogeny of the northeastern Gangdese Pb-Zn-Ag-Fe -Mo-W polymetallic belt in the Lhasa terrane, southern Tibet. Ore Geol Rev 70: 510-32

Zhu DC, Mo XX, Niu Y, Zhao ZD, Wang LQ, Liu YS,Wu FY (2009) Geochemical investigation of Early Cretaceous igneous rocks along an east–west traverse throughout the central Lhasa Terrane, Tibet. Chem Geol 268: 298-312

Zhu DC, Zhao ZD, Niu Y, Mo XX, Chung SL, Hou ZQ, Wang LQ,Wu FY (2011) The Lhasa Terrane: Record of a microcontinent and its histories of drift and growth. Earth Planet Sci Lett 301: 241-55

100 YEARS 1917 - 2017



FutureSmart™ mining applies cutting-edge technological advances and broad innovative thinking to find safer, more efficient and more sustainable ways to mine the metals and minerals that the world needs.

www.angloamerican.com

THE FUTURE IS FUTURESMART™ MINING

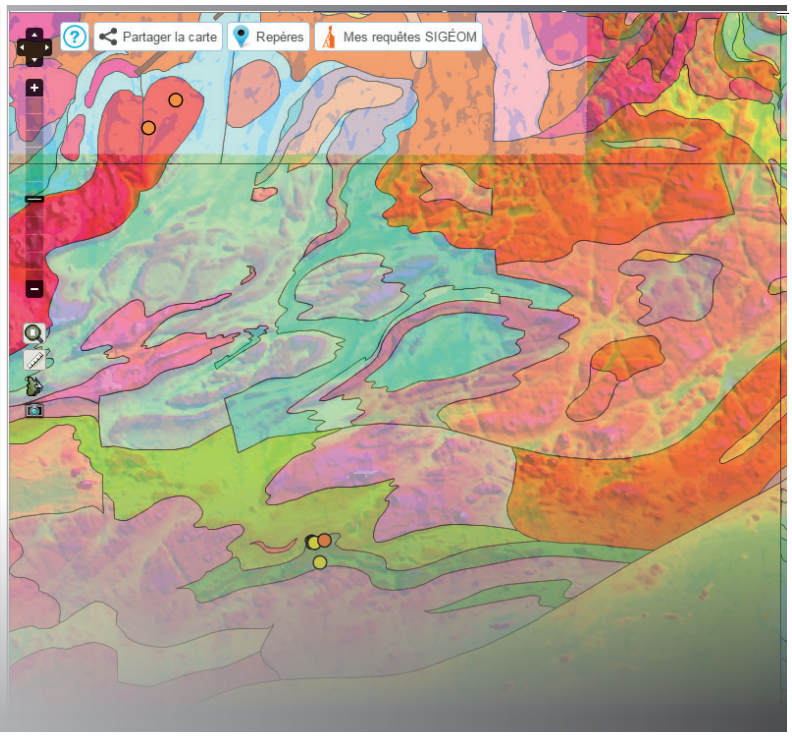
AngloAmerican

Real Mining. Real People. Real Difference.

SIGÉOM

Plus de 150 ans de données géoscientifiques du Québec recueillies dans un système à référence spatiale unique.

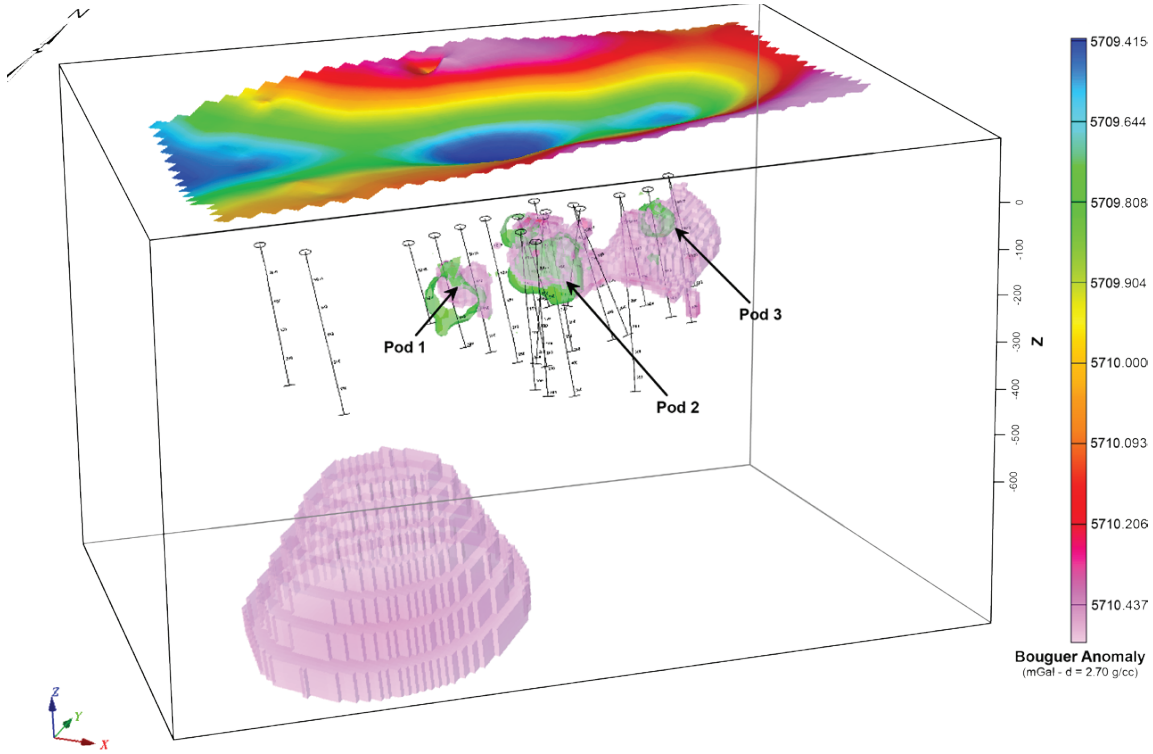
More than 150 years of geoscientific data from Québec, gathered together in a unique spatial reference system.



sigeom.mines.gouv.qc.ca

ENSEMBLE on fait avancer le Québec

Québec



INNOVATION IN GEOSCIENCE

As a world leader in the discovery of uranium deposits, AREVA's team of geophysicists, geologists, and geochemists use innovative new concepts in deposit formation study and exploration methods.

arevaresources.ca

AREVA

QUÉBEC MINES

LE CONGRÈS PAR EXCELLENCE
DE L'INDUSTRIE MINIÈRE QUÉBÉCOISE

THE QUÉBEC MINING INDUSTRY'S
LEADING CONGRESS



QuebecMines.gouv.qc.ca

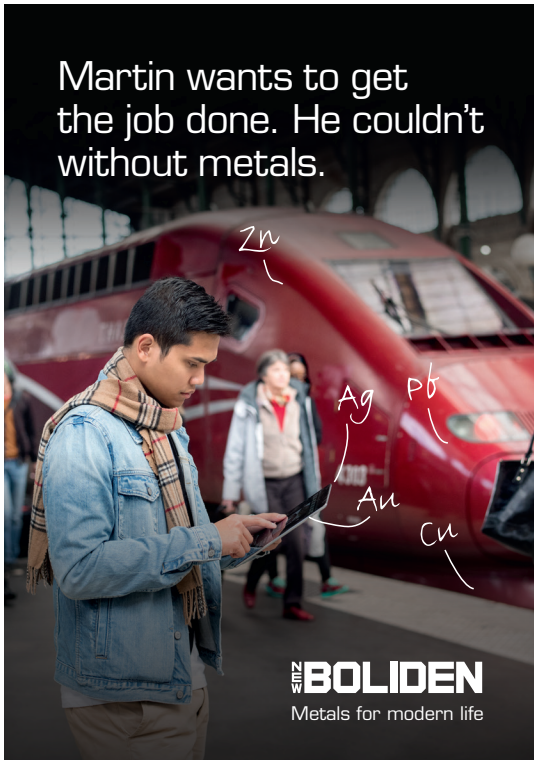
20 au 23 novembre 2017
November 20 to 23, 2017 • Québec

ENSEMBLE on fait avancer le Québec

Québec

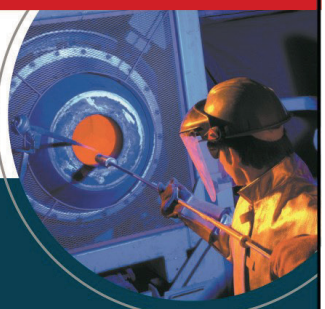
newgold

PROUD SPONSOR OF
SGA 2017



LE PARTENAIRE POUR UNE SOLUTION COMPLÈTE ET INNOVANTE
THE PARTNER FOR A COMPLETE AND INNOVATIVE SOLUTION

COREM



EXPERTISE DE CALIBRE INTERNATIONAL EN TRAITEMENT DE MINERAIS

WORLD-CLASS EXPERTISE IN MINERAL PROCESSING

corem.qc.ca



FRAGMENTATION	COMMINUTION
SÉPARATION PHYSIQUE	PHYSICAL SEPARATION
FLOTTATION	FLOTATION
MÉTALLURGIE EXTRACTIVE	EXTRACTIVE METALLURGY
AGGLOMÉRATION	PELLETIZING
PROCÉDÉS THERMIQUES	THERMAL PROCESSES
CARACTÉRISATION	CHARACTERIZATION
MINÉRALOGIE	MINERALOGY



Québec
• Ministère de l'Énergie et des Ressources naturelles
• Ministère de l'Économie, de la Science et de l'Innovation

Développement économique Canada pour les régions du Québec
Canada Economic Development for Quebec Regions
Canada



TOGETHER, WE ROCK

We do more than mine gold. Goldcorp creates social and economic benefits in the communities where we live and work. Thousands of jobs. Local purchasing. Responsible operations. And support for programs that create healthy, vibrant and engaged communities.

NYSE: GG | TSX: G
goldcorp.com

GOLDCORP

International workshop announcement in **Nancy, France**

Geochemical cycle of Ni, Co and Sc : from mining exploration to ecotoxicity

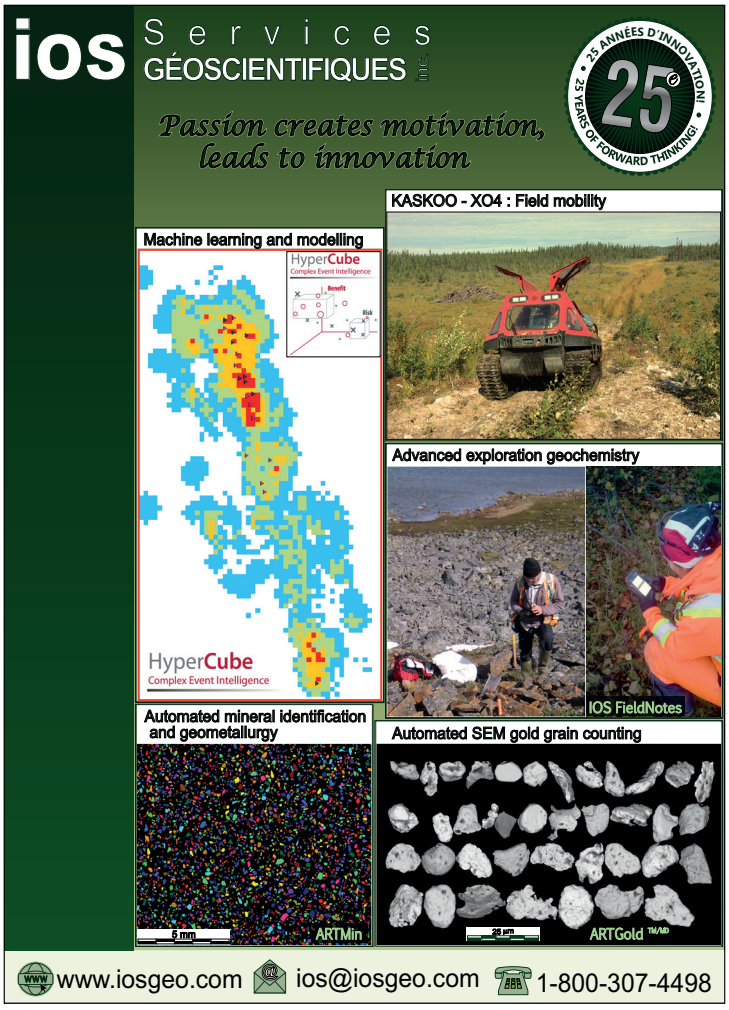
October 17-19, 2017

The Laboratory of Excellence *RESSOURCES21*
and the Lorraine Earth and Environment observatory OTELO,
will host in Nancy, France, the 1st International Workshop on the geochemical cycle of nickel, on October 17 to 19, 2017.

This is a call for transdisciplinary submissions to cover analytical advances in all topics related to low-temperature geochemistry of nickel and allied elements; to address key questions in the domain of Ni laterites from exploration to mining and processing.

• Ni mineralogy (serpentinisation and formation of Ni silicate ores) • The geochemical cycle of elements allied to Ni: Sc, Mn, and Co • Geometallurgy of Ni ores, including flotation and hydrometallurgy • Ni in soils and plants: Ni isotope geochemistry, Ni hyperaccumulators, remediation of soils on ultrabasic rocks, Agromining • Ni ecotoxicity and the hydrosphere

Please send the title of your submission to ressources21-contact@univ-lorraine.fr from now on - Registration and Abstracts deadlines by September 1st, 2017 http://ressources21.univ-lorraine.fr/content/registration



OSISKO
GOLD ROYALTIES



THE LEADING
INTERMEDIATE GOLD ROYALTY COMPANY

www.osiskogr.com **TSX & NYSE:OR**

FUNDING THE SEARCH FOR CANADA'S NEXT GOLD MINES

TWO OF THE PREMIER GOLD ROYALTIES IN THE WORLD

SAFE EXPOSURE TO GOLD & LEVERAGE THROUGH RESOURCE GROWTH

HIGH QUALITY EXPLORATION STAGE ROYALTIES

STRONG MANAGEMENT WITH PROVEN TRACK RECORD



OSISKO MINING



WINDFALL PROJECT

www.osiskomining.com | **TSX:OSK**



FALCO RESOURCES

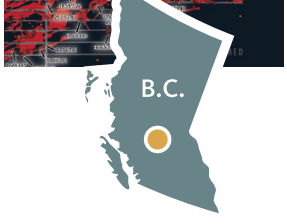


HORNE 5 PROJECT

www.falcores.com | **TSXV:FPC**



BGM BARKERVILLE GOLD MINES



CARIBOO PROJECT

www.barkervillegold.com | **TSXV:BGM**

